Proceedings of the Eighth U.S.-Japan Workshop on Earthquake Resistant Design of Lifeline Facilities and Countermeasures Against Liquefaction

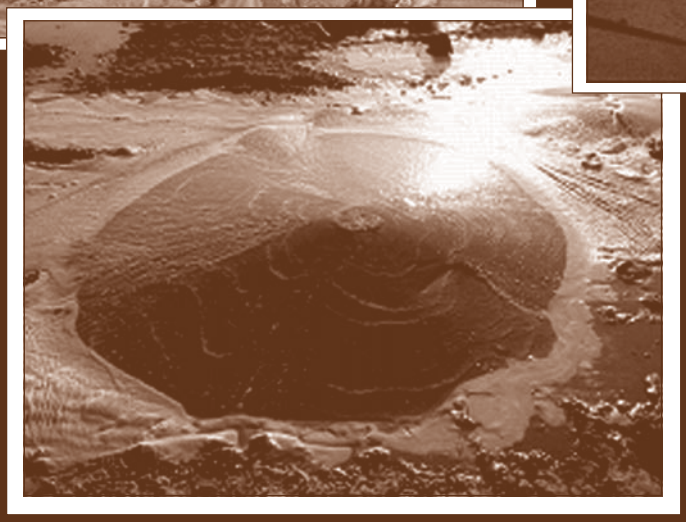

Edited by

Masanori Hamada
Department of Civil Engineering
Waseda University
3-4-1 Okubo Shinjuku-ku
Tokyo 169 Japan

Jean-Pierre Bardet
Department of Civil/
Environmental Engineering
University of Southern California
Los Angeles, California 90089-2531

Thomas D. O'Rourke
School of Civil and
Environmental Engineering
Cornell University
Ithaca, NY 14853-3501

MCEER
MULTIDISCIPLINARY CENTER FOR EARTHQUAKE ENGINEERING RESEARCH
A National Center of Excellence in Advanced Technology Applications

ISSN 1520-295X

Technical Report MCEER-03-0003
June 30, 2003

This workshop was held December 16-18, 2002 at the Edmont Hotel, Tokyo, Japan, and was supported primarily by the Earthquake Engineering Research Centers Program of the National Science Foundation under award number EEC-9701471.

NOTICE

This report was prepared by Waseda University, University of Southern California and Cornell University as a result of research sponsored by the Multidisciplinary Center for Earthquake Engineering Research (MCEER) through a grant from the Earthquake Engineering Research Centers Program of the National Science Foundation under NSF award number EEC-9701471 and other sponsors. Neither MCEER, associates of MCEER, its sponsors, Waseda University, University of Southern California, Cornell University, nor any person acting on their behalf:

a. makes any warranty, express or implied, with respect to the use of any information, apparatus, method, or process disclosed in this report or that such use may not infringe upon privately owned rights; or

b. assumes any liabilities of whatsoever kind with respect to the use of, or the damage resulting from the use of, any information, apparatus, method, or process disclosed in this report.

Any opinions, findings, and conclusions or recommendations expressed in this publication are those of the author(s) and do not necessarily reflect the views of MCEER, the National Science Foundation, or other sponsors.

Cover Photo/Illustration Credits

Example of liquefaction in Adapazari, taken from "Measurement of Ground Deformation Induced by Liquefaction and Faulting in the Earthquake Area of the 1999 Kocaeli Earthquake," by O. Aksu, J. P. Bardet, V. O. Atak, M. Onder and Ö. Aydan, pages 541-546.

Sand boil after the first experiment, taken from "Observed Behavior of Lifelines Subjected to Lateral Spreading: Tokachi Blast Experiment," provided by S. A. Ashford and T. Juirnarongrit, pages 547-558.

Collapse of Daikai station, taken from "Actual Observations and Numerical Simulations of Surface Fault Ruptures and Their Effects on Engineering Structures," by Ö. Aydan, pages 227-238.

MULTIDISCIPLINARY CENTER FOR EARTHQUAKE ENGINEERING RESEARCH

A National Center of Excellence in Advanced Technology Applications

Proceedings of the Eighth U.S.-Japan Workshop on Earthquake Resistant Design of Lifeline Facilities and Countermeasures Against Liquefaction

Held at
Edmont Hotel
Tokyo, Japan
December 16-18, 2002

Edited by
Masanori Hamada[1], Jean-Pierre Bardet[2] and Thomas D. O'Rourke[3]

Publication Date: June 30, 2003

Technical Report MCEER-03-0003

NSF Master Contract Number EEC-9701471

1 Professor, Department of Civil Engineering, Waseda University
2 Professor, Department of Civil and Environmental Engineering, University of Southern California
3 Thomas R. Briggs Professor of Engineering, School of Civil and Environmental Engineering, Cornell University

MULTIDISCIPLINARY CENTER FOR EARTHQUAKE ENGINEERING RESEARCH
University at Buffalo, State University of New York
Red Jacket Quadrangle, Buffalo, NY 14261

Preface

The Eighth US-Japan Workshop was a forum for U.S. and Japanese colleagues to share their ideas about earthquake damage to lifelines and explore advanced technologies for characterizing liquefaction, mitigating risk to hazardous sites, and improving post earthquake response and recovery. The Eight US-Japan Workshop was held at the conclusion of the *U.S.-Japan Cooperative Research Program on Urban Earthquake Disaster Mitigation*. This program was launched by the U.S. National Science Foundation (NSF) and the Japanese Ministry of Education, Science, Sports, and Culture in the aftermath of the 1994 Northridge and 1995 Hyogoken-Nanbu (Kobe) earthquakes. The researchers, who organized this workshop, were supported by the *U.S.-Japan Cooperative Research Program on Urban Earthquake Disaster Mitigation*, and acknowledge the support received from and accomplishments achieved by this collaboration. The Eight US-Japan Workshop provided an opportunity to discuss the construction of the George E. Brown, Jr. Network for Earthquake Engineering Simulation (NEES), and allowed U.S. and Japanese colleagues to exchange information and ideas for future collaboration within the novel framework of NEES. It is our hope that the research results in these proceedings will be applied in engineering decisions and that the workshop will act as a catalyst in promoting the transfer of technology from theory to practice.

J.P. Bardet
Professor, University of Southern California

M. Hamada
Professor, Waseda University

T.D. O'Rourke
Professor, Cornell University

U.S.-Japan Cooperative Research and Workshops

The proceedings of this workshop are part of a longstanding US-Japan cooperative research activity that focuses on earthquake resistant design of lifeline facilities and countermeasures against soil liquefaction. Since its inception, this activity has assisted other research agendas, such as cooperative research among the U.S. Earthquake Engineering Research Centers and the *U.S.-Japan Cooperative Research Program on Urban Earthquake Disaster Mitigation*. In the future, US-Japan cooperative research on lifelines and liquefaction will benefit from collaborative experimentation and analytical modeling at many of the superb testing facilities both in Japan and within the George E. Brown, Jr. Network for Earthquake Engineering Simulation (NEES).

U.S.-Japan Cooperative Research on Earthquake Resistant Design of Lifeline Facilities and Countermeasures Against Soil Liquefaction

U.S.-Japan research on earthquake resistant design of lifeline facilities focuses on the earthquake performance of lifelines, with emphasis on liquefaction-induced large ground deformations. Large ground deformations are the principal cause of subsurface structural damage during earthquakes. Currently, there is a growing recognition in the civil and earthquake engineering communities of the importance of large ground deformations. Our understanding of the mechanisms of large ground deformations and their effects on lifeline facilities, and our ability to predict the magnitude and distribution of ground displacements have improved substantially in recent years to provide a rational framework for design and protective measures. Both Japanese and U.S. researchers have been working on this topic, and it was recognized that considerable benefits will result from their cooperative efforts to collect case history data and recommend the most appropriate analytical methods and design procedures.

The program was initiated formally in November, 1988 with the signing of a Memorandum of Understanding between the Japanese and U.S. sides. The document was signed at a ceremony during a workshop in Tokyo, Japan by K. Kubo, Professor Emeritus of Tokyo University, and M. Shinozuka, the Champion Professor of Civil Engineering at the University of Southern California. Professor Kubo signed on behalf of the Association for the Development of Earthquake Prediction (ADEP), the Japanese sponsoring agency. Professor Shinozuka signed on behalf of Robert L. Ketter, then Director of the National Center for Earthquake Engineering Research (NCEER), the U.S. sponsoring agency.

Since 1988, the US-Japan research has materialized into a series of eight workshops:

1. Tokyo, Japan, November 16-19, 1988.
2. Buffalo, NY, September 26-29, 1989.
3. San Francisco, CA, December 17-19, 1990.
4. Honolulu, HI, May 27-29, 1992.
5. Snowbird, UT, September 29-October 1, 1994.
6. Waseda University, Tokyo, Japan, June 11-13, 1996.
7. Seattle, WA, August 15-17, 1999.
8. Tokyo, Japan, December 16-18, 2002.

The research program has concentrated on case histories of earthquake-induced ground deformations and their effects on lifeline facilities. In addition to the publication of the case history volumes, the products of the cooperative research include U.S.-Japan workshops and associated publications of the proceedings covering case history data, analytical modeling, experimental studies and recommendations for improved practices.

The U.S.-Japan workshop program is a major instrument for collaboration and cooperative exchange. To date, there have been seven workshops. The first was held in Tokyo and Niigata, Japan on November 16-19,

1988. The proceedings of this workshop were published by the Association for the Development of Earthquake Prediction, and are available from the Multidisciplinary Center for Earthquake Engineering and Research (MCEER).

U.S.-Japan Cooperative Research Program on Urban Earthquake Disaster Mitigation

The *U.S.-Japan Cooperative Research Program on Urban Earthquake Disaster Mitigation* was launched by the National Science Foundation (NSF) and the Japanese Ministry of Education, Science, Sports, and Culture in the aftermath of the 1994 Northridge, California, and 1995 Hyogoken-Nanbu, Japan earthquakes. In 1997, support from this program was extended to the U.S.-Japan collaborative research team to investigate soil liquefaction and its effects on foundations and lifeline systems.

On the U.S. side, the research team involved professors and students from Cornell University, Rensselaer Polytechnic Institute (RPI), the University of Southern California (USC), and several U.S. government and industry organizations including, the Multidisciplinary Center for Earthquake Engineering Research, Los Angeles Department of Water and Power (LADWP), Pacific Gas & Electric Company, U.S. Army Corps of Engineers, U.S. Geological Survey, and URS Corporation. On the Japanese side, the research team consists of professors and students from Kyoto University, Tokyo Institute of Technology, University of Tokyo, Waseda University, and Yamaguchi University, as well as several Japanese government and industry organizations. The main research objective was to investigate the effects of liquefaction-induced deformation on foundations and lifelines systems in the 1994 Northridge and 1995 Hyogoken-Nanbu earthquakes, and to propose engineering solutions that mitigate these devastating effects in future earthquakes.

George E. Brown, Jr. Network for Earthquake Engineering Simulation (NEES).

NEES is a major research equipment project of the U.S. National Science Foundation (NSF) that focuses on integrated experimentation, computation, databases, and model-based simulation. NEES includes 15 U.S. engineering equipment sites networked through the high performance Internet. NEES will involve advanced experimental and simulation capabilities and provide end-to-end system connectivity to operate distributed experimental research equipment, including teleobservation and teleoperation, thereby enabling computation and distributed simulation for earthquake engineering experimentation. Through NEES, researchers will have remote access to a curated repository of databases, user-developed simulation software, and models for use in model-based simulation and visualization. NEES is an integrated network that facilitates interdisciplinary global collaboration among scientists and engineers. It enables participation from many in the earthquake engineering community, including educators, students, practitioners, and public sector.

The Eighth U.S.-Japan Workshop on Earthquake Resistant Design of Lifeline Facilities and Countermeasures Against Soil Liquefaction

This eighth U.S.-Japan workshop capitalizes on the success of past U.S.-Japan collaborations in geotechnical and lifeline earthquake engineering. The workshop proceedings summarize the findings of U.S.-Japan collaboration on earthquake resistant design of lifelines and remediation against soil liquefaction. It also defines directions for future U.S.-Japan collaboration in geotechnical earthquake engineering. The workshop was co-organized by Prof. M. Hamada, Waseda University, Japan, Prof. T. D. O'Rourke, Cornell University, and Prof. J. P. Bardet, University of Southern California. The workshop took place at the Edmont Hotel, in Tokyo, Japan on December 16-18, 2002. The U.S. participants came from the following universities, federal agencies, engineering consulting firm and local/municipal agencies:

- Brigham Young University, Provo, UT
- Cornell University, Ithaca, NY
- Rensselaer Polytechnic Institute, Troy, NY,
- University of California at Davis, Davis, CA

- University of California Berkeley, Berkeley, CA
- University of California Los Angeles, Los Angeles, CA
- University of California, San Diego, CA
- University of Southern California, Los Angeles, CA
- University of Texas Austin, Austin, TX
- U.S. Geological Survey, Menlo Park, CA
- ABS Consulting, Inc., Oakland, CA and Seattle, WA
- LA Dept of Water & Power, Los Angeles, CA

On the Japanese side, the participants originate from the following universities, government agencies and industrial firms:

- Chuo University
- Kanazawa University
- Kanto-Gakuen University
- Kyoto University
- Musashi Institute of Technology
- Tokai University
- Tokyo Institute of Technology
- University of Tokyo
- Waseda University
- Yamaguchi University
- Tokyo Metropolitan University
- Kogyokusha College of Technology
- Konoike Construction Co.
- JFE Co
- Railway Technical Research Institute
- Tokyo Soil Research Co., Ltd.
- Ohbayashi Corporation
- Building Research Institute
- Public Work Research Institute
- National Institute of Advanced Industrial Science and Technology
- Osaka Gas Co.,Ltd.
- Tokyo Gas Co.,Ltd.
- Kajima Corporation
- Taisei Corporation
- Shinozuka Research Institute
- Oyo Corporation
- Sumitomo Metal Industries Ltd.
- Tobishima Corporation

The workshop findings are released on the Internet through the webserver of the University of Southern California (*http://gees.usc.edu/Tokyo2002*), and are published as a hardcopy proceedings distributed by MCEER.

Acknowledgements

The workshop co-chairs acknowledge and thank the Japanese Ministry of Education, Science, Sports and Culture and the U.S. National Science Foundation (NSF). In particular the U.S. co-chairs thank Dr. Mira McAuliffe from the international program of NSF for her encouragement and support. The co-chairs also acknowledge the Multidisciplinary Center for Earthquake Engineering Research (MCEER) for its support with partial travel reimbursements of workshop participants as well as the publication of the proceedings.

Contents

Invited Lecture

Lessons Learned from the World Trade Center Disaster about Critical Lifeline Systems

T. D. O'Rourke

Lessons Learned from the World Trade Center Disaster about Critical Lifeline Systems

Thomas D. O'Rourke, Arthur J. Lembo, and Linda K. Nozick

ABSTRACT

The terrorist attack on the World Trade Center (WTC) in New York City (NYC) of September 11, 2001 was unprecedented in terms of damage and repercussions on civil infrastructure for an event not related to declared military operations. There were 2,830 people killed and 10 major buildings destroyed or subjected to partial collapse. Approximately, 2.8 million m^2 of commercial office space were removed from service, of which 1.1 million belonged to the WTC Complex [1].

The WTC site is located within an intricate complex of infrastructure systems. It is important, therefore, to assess the consequences of such severe damage on the interdependent systems connected to the site.

In this paper, the consequences of the WTC Disaster on civil infrastructure systems is explored, and a summary of performance is provided for water supply, electrical power, telecommunications, natural gas, and steam energy. The effects of water distribution system damage on fire fighting are addressed. The characteristics of damage and systems performance resulting from the WTC Disaster are compared with those of other major incidents in NYC. Preliminary conclusions are drawn with respect to causes of damage, factors affecting the spread and constraint of damage, and factors that contribute to both the resiliency of urban infrastructure and the attendant services necessary to respond effectively to extreme events.

Thomas D. O'Rourke, Professor, School of Civil and Environmental Engineering, Cornell University, 273 Hollister Hall, Ithaca, NY 14853
Arthur J. Lembo, Sr. Research Associate, Crop and Soil Science, Cornell University, 1001 Bradfield Hall, Ithaca, NY 14853
Linda K. Nozick, Professor, School of Civil and Environmental Engineering, Cornell University, 323 Hollister Hall, Ithaca, NY 14853

BUILDINGS

The building performance at the WTC Complex has been described in considerable detail [1], and only select features of the building response are described herein. On September 11, two hijacked aircraft were flown into the WTC towers. At 8:46 am the north face of the north tower (WTC1) was struck, and at 9:03 am the south face of the south tower (WTC2) was struck. At 9:59 am and 10:29 am, WTC2 and WTC1, respectively, collapsed.

Figure 1 shows the area of the collapse debris impact as depicted by FEMA [1]. Buildings surrounding the towers are also shown, with special emphasis (dark shading) provided for those that were destroyed as a consequence of being struck and/or ignited by debris from the collapsing towers. The inner circles indicate the approximate radius of inner steel column collapse and other heavy debris. The outer circles indicate the approximate radius of fallen aluminum cladding and other relatively light debris. Of special interest for electric power and telecommunications are WTC7 and the Verizon Building located along Vesey St. immediately north of the WTC Complex.

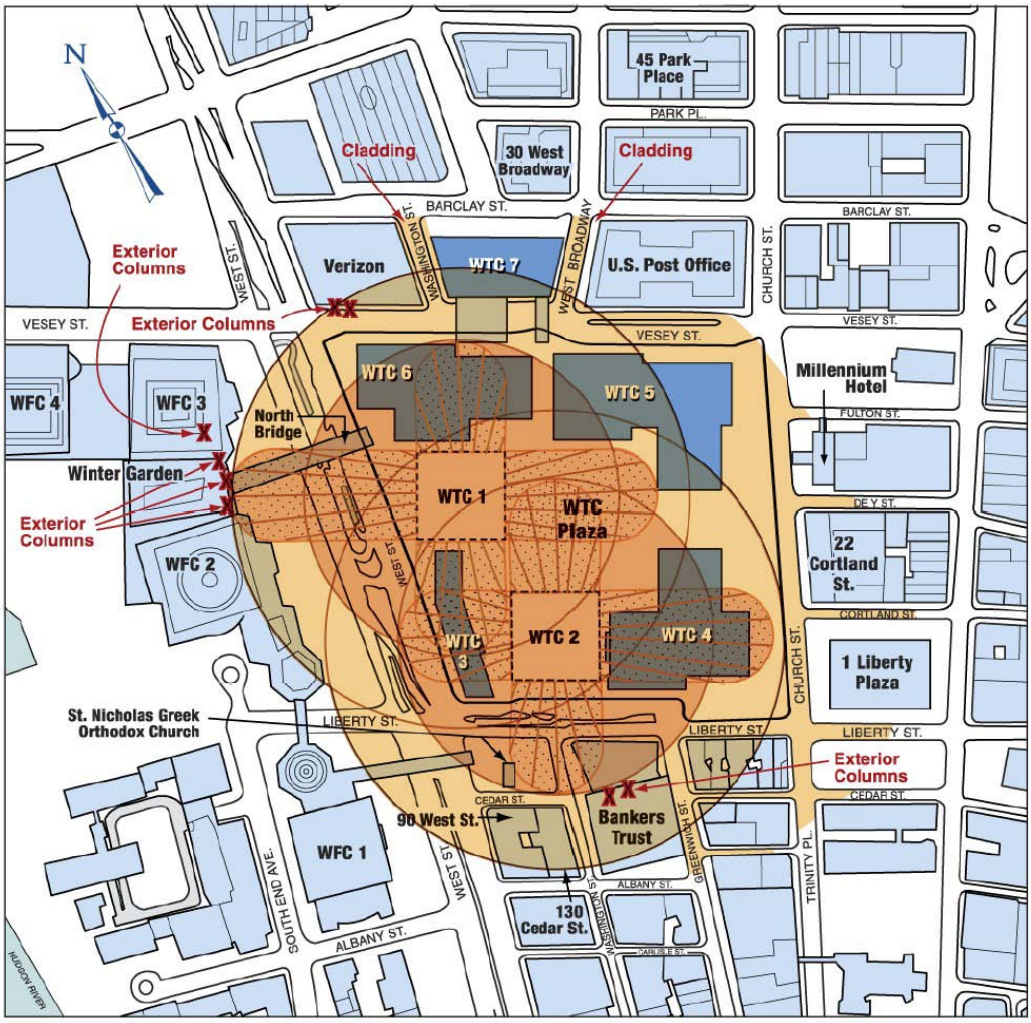

Figure 1. Schematic Depiction of Areas of Collapse Debris Impact (After FEMA, 2002)

Figure 2 presents a map of the buildings surrounding the Complex as published by FEMA [1]. The map shows the damage assessment of surrounding structures based on the inspections of 406 buildings on September 14 and 15 by NYC structural engineers. The building inspection procedures and damage classification were adopted from guidelines developed for rapid assessment of buildings after earthquakes [2].

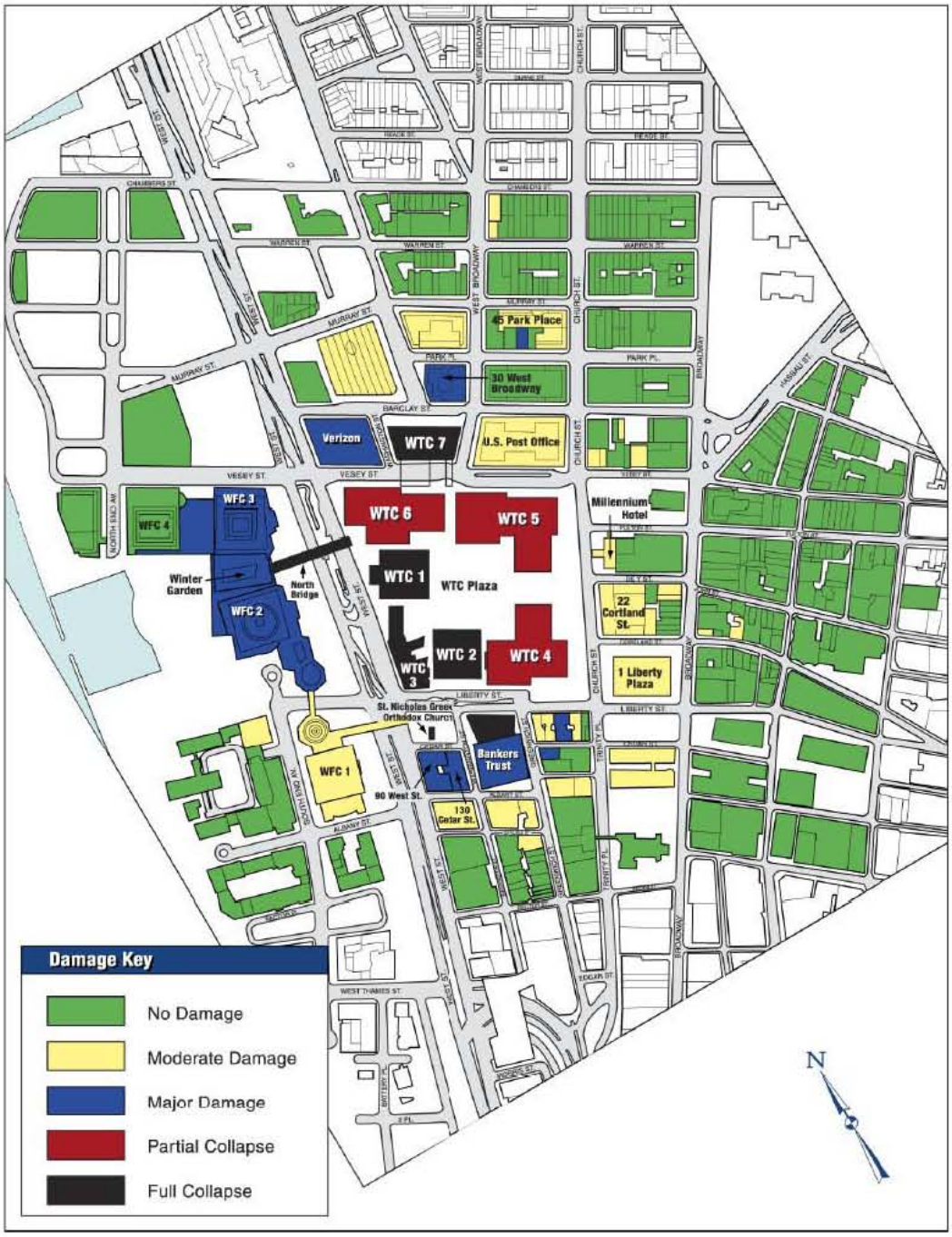

Figure 2. New York City DDC/DoB Cooperative Building Damage Assessment Map of November 7, 2001 (After [1])

As mentioned previously, the damage to buildings was of unparalleled proportions for a disaster perpetrated independently of official military operations. Of significance also was the damage sustained by other civil infrastructure systems, which are described briefly in the following sections of this paper.

WATER SUPPLY

The NYC water supply is maintained and operated by the NYC Department of Environmental Protection (DEP) About 90% of water provided to NYC is conveyed through City Water Tunnels 1 and 2, which were commissioned in 1917 and 1938, respectively. Since commissioning, neither tunnel has been dewatered for inspection so that their state of repair can only be inferred indirectly. City Tunnel 1 is the backbone of supply for Manhattan. The tunnel is about 183-213m below street surface and transmits water to the distribution pipeline system through riser shafts. Some valves in the tunnel and shafts have not been used in many years, and no attempt is made to operate them because of concerns about malfunctioning and corresponding impact on the system. A third tunnel, City Tunnel 3, is currently under construction. This tunnel will supplement supply and allow for dewatering sections of City Tunnels 1 and 2 for maintenance and repair.

Four shafts in lower Manhattan provide water for the distribution system that serves the WTC area and nearby neighborhoods. The shafts are equipped with regulators to decrease pressure to a level compatible with the capacity of the trunk and distribution pipelines. Continuous flow measurements are performed at each shaft. Because the pressure at each shaft is regulated, the resulting flow measurements provide accurate data on rate of flow at constant pressure.

Collapse of the WTC towers and the subsequent collapse of WTC 7 resulted in about 10 locations of ruptured water mains within the disaster area. These locations do not include the loss of a 406-mm-diameter water main that was situated beneath the WTC Complex. Damage to 508-mm- and 305-mm-diameter water mains was caused primarily by direct impact from collapsing structures and falling debris.

On September 11, maximum total water flow recorded at four shafts in lower Manhattan was 7140 liters/sec compared with 5610 liters/sec on September 10. This resulted in an increase of 1530 liters/sec relative to normal usage. Water from the shaft closest to the WTC site accounted for about half the increased flow relative to normal usage. However, the usage was not normal on September 11. A close inspection of the DEP flow measurements shows water demand from the four shafts declining to about 4380 liters/sec before the collapse of the WTC towers. After collapse, water flow jumped to 6790 liters/sec, and then rose gradually to a peak of 7140 liter/sec. The initial jump of 2410 liters/sec represents water lost through broken water mains beneath and surrounding the WTC Complex. The additional 350 liters/sec represents the draw from fire hydrants that were used to fight fires in adjacent buildings.

An independent assessment of water drawn from the distribution system was made by interviewing deputy fire chiefs, who were in command on the eastern and western sides of the WTC complex. The chiefs were able to identify hydrants, hoses, and fire engines used at the site from which it was estimated that approximately 280 liters/sec were being drawn from the water distribution system. Hence, the estimate obtained from fire department commanders and the rate shown by the flow measurements are in reasonably good agreement.

Water pressures at hydrants adjacent to the WTC Complex declined throughout the afternoon. Measurements performed by DEP at 6pm show pressure 2 to 3 blocks from the site at a level approximately one third of that under normal conditions. Fire fighting was impaired by the declining pressures. From about 6pm to 2am, DEP personnel shut gate valves in the pipeline network surrounding the site to isolate damaged pipelines from the rest of the system. Isolating the broken mains restored pressure in the intact system outside the perimeter of closed gate valves.

The area initially isolated was relatively large to provide sufficient coverage and confidence that the then unknown locations of damage would be included within the isolated zone. The area was bounded on the north by Murray St., and on the east by Broadway (see Figure 2). The isolation area extended to the western side of the World Financial Center and as far south as Morris St. The isolation zone was eventually reduced to include only the streets immediately adjacent to the WTC Complex.

FIRE FIGHTING

Fires at and adjacent to the WTC Complex were fought in essentially two theaters of action. On the eastern side, three tower ladders were deployed to attend to fires at WTC 4, 5, and 7. In the afternoon of September 11, the decision was made to abandon WTC 7, which collapsed about 5pm.

On the western side, fires were fought primarily with water from the Hudson River, which is two to three blocks from the WTC Complex. The NYC Fire Department, Marine Division, dispatched four fire boats to the WTC site: Firefighter (1260 liter/sec capacity), John D. McKean (1200 liter/sec capacity), Smoke II (130 liter/sec capacity), and Kevin C. Kane (410 liter/sec capacity). The McKean arrived within 15 minutes, just before the second aircraft struck WTC 2. The Smoke arrived shortly thereafter. Initially, the McKean and Smoke were used to ferry wounded and fleeing people to New Jersey City. Between approximately 10 and 11am, the four fire boats took up positions. The Firefighter docked on the Hudson River at Vesey St. The Smoke and the Kane docked in North Cove, and the McKean docked on the Hudson River at Albany St.

A review of the pumping records, interviews with Marine Division personnel, and inspection of high resolution aerial photographs were used to estimate the amount of water supplied to the WTC Complex and surrounding buildings. All fire boats were pumping at high capacity from the Hudson River. However, not all the water was relayed to fire engines. Excess water, unable to flow through hoses and land-based equipment was discharged into the river without specific measurement. Hence, the fire boat pumping records do not provide a direct measure of water actually used at the WTC site, but an upper bound estimate. An alternate estimate was made by obtaining information about the number of hose lines deployed from each boat, and approximating the flow based on hose diameters and distances from boats to fire engines that were relaying the water.

The estimated total flow during September 11 from Marine Division equipment is between 630 and 1260 liter/sec, with the actual value likely to be closer to 630 liter/sec. Hence, fireboats played an important and highly significant role in suppressing fires on and immediately after September 11. During the critical hours following the collapse of the WTC towers, they provided from two to four times the amount of flow that was pumped from intact water distribution mains near the site.

ELECTRIC POWER

Almost all the electric power for NYC is supplied by the Consolidated Edison Company of New York, Inc. (Con Edison). Con Edison serves the most dense electrical *load pocket* in the world. It supplies over 3.1 million customers in an area of 1564 km^2 served by more than 145 thousand km of underground distribution cable and 255,000 manholes and service boxes. Within NYC electric power is transmitted by high voltage cables (typically 138 kilovolt [kV]), which are encased in butyl-oil-filled steel pipelines. They connect with electric substations where the power is converted to low voltage (27 or 13.8 kV) feeders. Con Edison uses a *distribution network* concept. The networks are grids supplied by the 13.8 kV feeders that cover anywhere from several city blocks to several square kilometers. The networks are mostly underground, beneath the streets and sidewalks. The Con Edison system includes about 55 distribution networks within the city limits, of which 33 are in Manhattan. Each network is independent of its neighboring networks and is fed from multiple distribution feeders. Con Edison has 50% of all the distribution networks in the world, and its engineers are experts who often act as consultants for other distribution networks.

Because each distribution network is virtually independent, local damage will generally not affect the operation of other networks. Moreover, there is redundancy in the number of 27 or 13.8 kV feeders supplying a given network. Even if multiple feeders are lost, there is reserve capacity to sustain power. The basic design of the network system provides for overall high reliability. According to Con Edison representatives, the annualized power outage per customer is 2.6 minutes in Manhattan compared with a US national average of 111 minutes.

Debris falling from the collapse of WTC 1 damaged and ignited WTC 7, which contained two electric substations. Approximately one hour before the collapse of WTC 7, the NYC Fire Department requested that the substation be de-energized. Con Edison had been preparing for this event and power was immediately shutdown to three networks. The World Trade Center complex had lost power earlier in the morning as a direct result of the fires in the twin towers. The substations were totally destroyed when WTC

7 burned and collapsed. This collapse also resulted in damage to five 138 kV cables. The faults generated by the damaged cables triggered switches that disconnected an additional substation at the lower east side of Manhattan. Thus, five local distribution networks lost power as a result of the events. A sixth network, which services the New York Stock Exchange (NYSE) area, lost six 13.8 kV feeders. It continued to function from the remaining ten feeders, which supplied the local distribution network from a substation located north of the WTC Complex. The total power loss throughout all affected portions of the system was approximately 450 megawatts (Mw).

Restoration of power to the lower west side of Manhattan involved running 58 km of 13 kV cables above ground from areas that had power to the areas that did not have power. This process was completed in 8 days. The first network was restored in 3 days by this method.

Restoration to the lower east side of Manhattan required that the 138 kV cables into the WTC Complex be isolated and repaired. Cable repair involved freezing the butyl-oil-filled pipelines with liquid nitrogen, cutting both the pipeline and three cables contained in each pipe, then capping the cables and pipes, filling and pressurizing each pipe with oil, and soaking the cables. The first damaged 138 kV cable was restored by Monday morning, 17 September.

Con Ed crews worked 24 hrs a day to complete the restoration work Con Ed also set up 82 mobile, diesel generators, each with a capacity of 1.2 to 1.8 Mw, throughout lower Manhattan to supply emergency power to parts of Wall St., Battery Park City, the Merchantile Exchange, and World Financial Center. The combination of emergency generators and repairs to the area's power system were required to be ready for opening of the NYSE on Monday, September 17.

TELECOMMUNICATIONS

A major telecommunications central office is located immediately north of the WTC Complex at 140 West St., known as the Verizon Building. The structure was built in 1928 and is 32 stories high. Telecommunications equipment was located on the 1st through 9th floors. A cable vault, transformers, generator, and fuel tanks were housed in the five basement levels of the building.

Verizon claims that the telecommunications capacity of the 140 West St. central office was one of the largest in the world and equivalent to that of Austria, Denmark, and Egypt combined. The building housed 4 digital switches, 500 optical transport systems, 1500 channel banks, 17,000 optical fiber lines, 4.4 million data circuits, and 90,000 message trunks.

The building was damaged from the collapse of WTC 1 and WTC 7. Damage from the collapse of WTC 7 was especially severe on the eastern side from about the 9th floor down where most of the telecommunications equipment was located.

The worst physical damage to telecommunication facilities occurred in the cable vault and on 1st, 4th, 7th, and 9th floors. The emergency 911 system failed instantly, but switched to a back-up node at the Verizon central office at Metrotech, Brooklyn. Due to the 911 design, switching occurred immediately, and the new center never missed a call. There were approximately 38,000 calls on the 911 system on September 11, which is 71% higher than normal volume.

Three class 5ESS switches were located on the 7th floor, and one was located on the 9th floor. Each switch consists of 40 frames and supports 60,000 customer lines. Remarkably, there was very little direct physical damage to the switches. Telecommunication equipment is designed and operated in compliance with the Network Equipment Building System (NEBS) standards (e.g., [3]). These standards have been developed with significant input from experience during natural disasters, including the 1989 Loma Prieta and 1994 Northridge earthquakes. In general, the telecommunication equipment remained intact and continued to function at reliable levels even though severe damage was sustained by the structural and building elements surrounding them. Three of the four switches were scheduled for replacement within two years of the disaster because dust had entered the equipment, clogging the filters and impairing reliable operation. Dust also had a deleterious effect on the turbines and cooling systems within the building.

Steel beams and debris, primarily from the WTC 2 collapse, penetrated the cable vault on West St., severing 70,000 copper pairs and additional fiber optic lines. Water flooded the cable vault. Nearly 41600 m^3 of water had to be pumped from the vault during recovery. There was also water damage on the 7th and 9th floors where fire fighters sprayed water on adjacent buildings.

As a result of the damage, Verizon lost 200,000 voice lines, 100,000 private branch exchange (PBX) lines, 4.4 million data circuits, and 11 cell sites. Over 14,000 business and 20,000 residential customers were affected.

Telecommunications traffic was switched from the Verizon Building to other central offices. Of special importance were the Security Industry Data Network (SIDN) and the Security Industry Automation Corporation (SIAC) circuits that are used to execute and confirm block trades on the stock exchange. These circuits were necessary to resume trading and financial activity. The SIDN and SIAC circuits were rerouted from a central office in mid-town Manhattan to by-pass the Verizon Building. This was accomplished by routing traffic through a facility north of the WTC Complex to another large central office in lower Manhattan, from which they were connected with the NYSE.

AT&T lost two local transport nodes in WTC 2, which burned and collapsed. Two other network switches located in the vicinity of the WTC Complex were not accessible because of damage, evacuations, and response activities. The equipment was powered down as the offices were evacuated to provide for easier restoration of service later. Telecommunication equipment showed resilience similar to that in the Verizon Building. AT&T Internet Protocol transport and other equipment in a sub-basement level of WTC 2 continued to work even after the building collapsed.

As a result of the WTC Disaster, the two largest AT&T local transport nodes in New York City were destroyed. Six other transport nodes in Manhattan were fully functional, and were rapidly configured to reroute traffic. In total, two switches were lost due to building collapse; two others were temporarily out of service because of lost power. Seven other switches in Manhattan remained in operation.

Two switches were restored by the fourth day after the attack, an optical remote module was upgraded to a full switch within six days, and a third local switch was restored within 18 days. Broadband wireless capacity was established whenever possible. Within 24 days of the attack, 24 38-GHz radio systems, including antenna and back-up equipment, were deployed throughout the affected area.

A team of telecommunication companies, brokerages, exchanges, and municipal leaders, in combination with Federal authorities, developed a plan to restore services so that the NYSE could be reopened on September 17. Reliable telecommunications service could have been supplied on Friday, September 14. However, brokerages and financial banking institutions with offices adjacent to the WTC Complex could not have been linked to the NYSE on that date because of disrupted telecommunication services. These organizations were potentially at a significant competitive disadvantage. Additional routing of cables and fiber optic lines to connect with these organizations was performed over the weekend to prepare for the NYSE opening.

On September 11, 2001, the wireless telecommunication industry experienced a 50% increase in call attempts nationally. In contrast, calls increase nationally by about 30% on Mother's Day. Figure 3 shows a bar chart of wireless traffic demand and blocked call percentages for normal conditions in contrast with September 11 conditions for the Northeastern U.S., Washington, DC, NYC area averaged over the entire day, and NYC at approximately 11AM. In the 9-11AM period on September 11, there was an approximate 1300% increase in wireless call attempts experienced by one carrier before the call-count administrative controls were discontinued to support call processing.

At 11AM, roughly 92% of wireless calls were blocked in the NYC area. Restoration of wireless service was rapid, as shown by the plot of equivalent site capacity near the WTC Complex versus time in Figure 4. Equivalent capacity to restore lost wireless sites was provided by restoring sites; deploying portable wireless cells, known as cellulars on wheels (COWs); and increasing the radio frequency range allocated to telecommunication providers.

Emergency operations were underway at Verizon, AT&T, and other telecommunication providers immediately after the WTC attack. AT&T, for example, followed a strict and well-rehearsed telephone system protocol in which command-and-control operations were established with multiple technical bridges from upper management to personnel in the field. All telecommunications facilities in the WTC area were secured, and services were restored using the Telecommunications System Priority (TSP) program [5] to assure that critical services received the highest priority. The TSP program is the administrative and operational framework, overseen by the Federal Communications Commission (FCC), for priority restoration and provisioning of telecommunication services in times of crises and events that threaten the U.S. population and national security. Large AT&T trailers containing telecommunications equipment were mobilized and placed in service at a site in New Jersey within 48 hours of the attack.

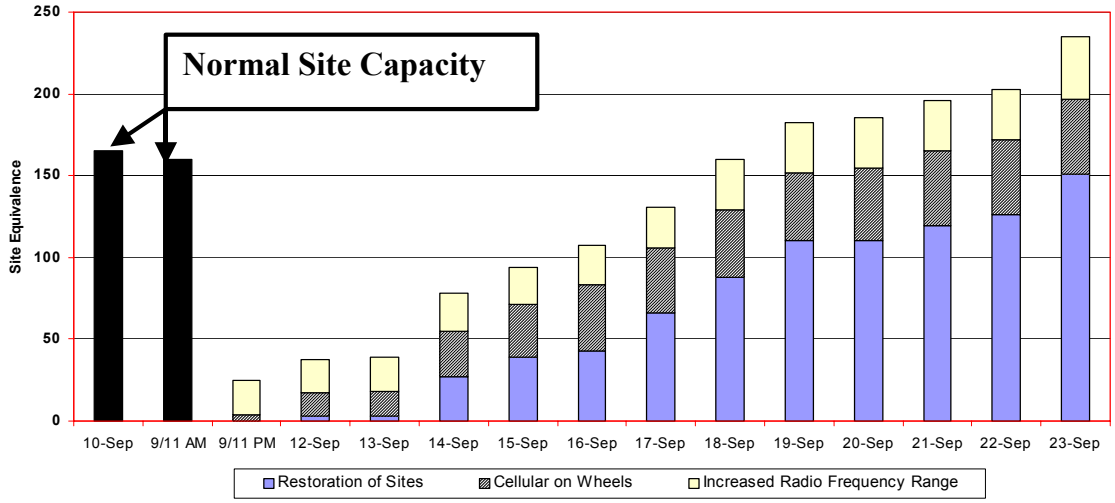

Figure 3. Cellular Traffic and Blocked Call Rate on September 11, 2001 (after [4])

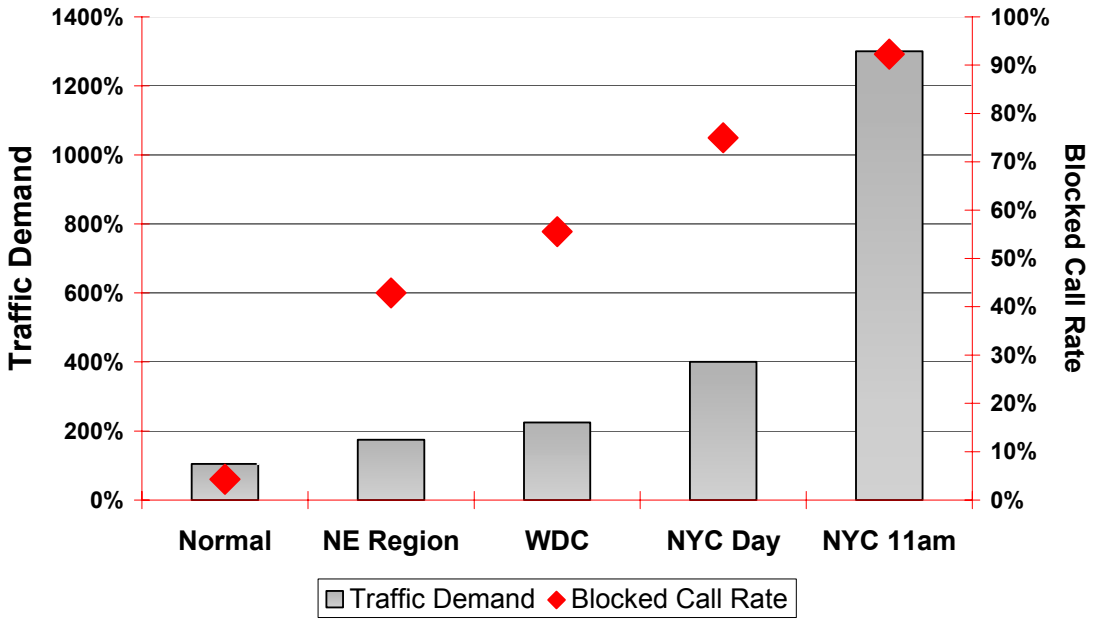

Figure 4. Restoration of Cellular Telecommunications in the Vicinity of WTC (after [4])

Redundant, dispersed facilities and the ability to rapidly by-pass damaged central offices were key aspects of the telecommunications performance. Verizon reports that it was able to process approximately twice the normal daily volume of cell phone calls on September 11.

WIRELESS E MAIL

Discussions with representatives of the NYC Mayor's Office, FEMA Region II, and the Port Authority of New York and New Jersey confirm that cell phone and landline voice communications were impaired by delays and busy signals after September 11. To facilitate emergency communication, the IBM Crisis Response Team assisted both the Red Cross and NYC Mayor's Office after the WTC Disaster. The team

organized a secure information system for the Mayor's office with linkages to wireless e mail. The e mail system employed BlackBerry handheld units operating on the Cingular Mobitex system. IBM distributed about 70 units to the Mayor's Office and approximately 11 units to the New York State Governor's Office.

Cingular lost connectivity to most of its base stations in lower Manhattan because of failed telecommunication interconnections and interruption of electric power. Service, however, was able to continue because the handheld devices simply roamed to other non-affected base stations in New Jersey and Brooklyn that provided overlapping coverage to lower Manhattan.

The e mail system is based on the transmission of information packets, each of which may travel by different routes and be separated in time intervals that exceed those required for voice messages. Because e mail is asynchronous, message routing is more flexible and able to accommodate heavy traffic more easily than voice communication, which requires synchronous transmissions. Therefore, e mail communications experienced less disruption than voice communications.

The wireless e mail system also has queuing capability. If a message is not sent because of congestion, there is an automatic retry algorithm built into the system so that transmissions initially delayed are sent. In a voice network there is no queuing. The e mail system is also able to save messages so that retrieval can occur at significant lengths of time after initial transmission.

The use of handheld e mail devices greatly facilitated communications and contributed to substantial improvements in efficiency. Some advantages of wireless e mail communication that were identified by handset users include reliability and consistency. Communications are not impeded by background noise, which can be troublesome with voice communication in emergency situations. E mail communications are in text format so no notes have to be taken. Note taking can be difficult when using voice communication devices in the field. Moreover, e mail messages are automatically logged and can be archived for future record keeping.

NATURAL GAS DISTRIBUTION

New York City is served by a natural gas distribution system that involves over 10000 km of pipelines. Natural gas distribution in Manhattan is provided by Con Edison through approximately 1000 km of underground piping.

After the WTC towers collapsed, Con Edison crews were dispatched to the disaster area. The gas company personnel could gain access to only a limited number of curb valves to turn off gas flow because debris, vehicles, and equipment were blocking access. To ensure stoppage of gas flow into areas of greatest damage and because of uncertainties regarding the extent of damage, a relatively large section of the distribution network was isolated. Isolation was performed by cutting and capping mains until an area, which was bounded by Chambers St., Broadway, Rector St., and the Hudson River, was disengaged from the remainder of the system. The isolation process required approximately 24 hrs.

Leakage on September 11 was confirmed in the near vicinity (within one block) of the WTC Complex at only 4 locations at which steel and cast iron mains were situated. Most of these locations coincide with areas of fallen debris and projectile penetration of street cover.

The gas distribution network was restored by returning service successively to 9 different sectors. Sectors at the perimeter of the isolated area were restored first, followed by those closer to "ground zero". The last sector, which surrounds the WTC Complex, was not restored for over a year after the disaster because of ongoing construction and the absence of customers who did not re-occupy their businesses. Approximately 90% of gas service was restored within one week of the disaster. There were about 300 Con Edison personnel in total engaged in the isolation and restoration efforts, working 24 hrs. per day.

STEAM ENERGY

New York City is served by a steam energy system consisting of seven steam generating plants and over 160 km of steel transmission and distribution pipelines. The system is operated by Con Edison. The pipelines are typically 254 to 762-mm-diameter, and are operated at internal pressures of 1360 to 2720 kPa and temperatures of 212 to 246^{o}C. The steam is used for heating, cooling, and processing.

There was damage to several steam pipelines, surrounding the WTC Complex caused by structural collapse or direct hit by projectiles and falling debris. A 762-mm-diameter steam line within the WTC

Complex was lost. Steam line ruptures in 406 to 610-mm-diameter lines were confirmed by video inspection at four locations. On several streets adjacent to the WTC Complex, where building damage was especially severe, steam pipelines were cut and capped with no inspection.

Monitoring stations within the distribution network showed a steady drop in steam pressure after the WTC towers collapsed. By 11am on September 11, the decision was made to shut down the steam distribution network south of Grand and 7th Avenue. This decision was made to preserve service in areas unaffected by damage. The area isolated was chosen conservatively to be sufficiently large to cover locations of damage that were unknown at the time. It was also chosen to expedite the isolation process. In the vicinity of Grand and 7th Avenue, the system configuration was such that only five valves were shut to isolate approximately 30% of the system in lower Manhattan.

It took six days to restore most of the steam service to lower Manhattan. There were several temporary boilers installed and run for several weeks to supply buildings disengaged from the network. Several new mains were installed. The steam system in the immediate vicinity of the WTC Complex remained isolated for over a year after the disaster because of construction in damaged buildings and the continued absence of customers who once had occupied the area.

OTHER INCIDENTS

Two incidents, which occurred in NYC before September 11, 2001, are used in this paper to show the potential for escalating damage originating from the failure of a single component. There have been similar incidents in other cities. The incident descriptions are taken directly from O'Rourke [6].

Hellgate Incident

On December 29, 1989, a 750-mm-diameter gas transmission line exploded in the Hellgate area of the Bronx, NY. The explosion killed one person and injured six others, who had been working with a backhoe near the pipeline. The explosion and fire severely damaged a recycling plant, shattered windows, forced the evacuation of several nearby buildings, including a regional bus terminal. If confined to the nearby area, this incident would be regarded as serious by any standard. The accident, however, had much greater repercussions.

Heat and fire from the pipeline caused all electric power to be shut off at the adjacent Hellgate Plant. This cut off electricity to about 135,000 customers, including households and entire buildings, and blacked out an area of 5 km^2 on the Upper East Side of Manhattan and 7.5 km^2 in the Bronx. Traffic lights switched off, forcing substantial traffic jams. The loss of electricity suspended service on eight separate subway lines. Although subway trains operate on direct current from the third rail, the station lights and track signaling are operated by utility-supplied electricity. Evacuation of the bus terminal near the fire left 200 buses stranded. As a result, there was severe disruption of bus service on 12 routes in Manhattan and the Bronx.

The accident occurred on Friday afternoon at about 2:00 p.m., just before the start of weekend rush-hour traffic before New Years Eve. Hundreds of thousands of commuters were left stranded and a similar number of businesses and buildings incapacitated by the blackout, which lasted from three to five hours over major portions of the city.

Garment District Incident

On August 10, 1983, a 300-mm-diameter cast iron water main ruptured near the intersection of 38th Street and 7th Avenue. Water from the burst main flooded an underground electric substation, shorting electric circuits and touching off an immense fire. Loss of the substation blacked out approximately 3 km^2, including the Garment District and neighboring areas of the city. This involved over 10,000 customers, including Macy's and Gimbel's Department Stores. The blackout affected telephone company central office, interrupting telecommunication service to tens of thousands of customers until emergency power was switched on. Phones using electric utility power were lost for a considerably longer time.

The accident occurred during Market Week in the Garment District, when most out-of-town buyers come to NYC to order next year's spring clothing lines. Direct and indirect business losses during this critical time have been estimated in the tens of millions of dollars.

Fire in the substation caused heat so intense that firefighters could not approach the blaze directly, but had to attack it with more than 2000 m^3 of foam. The blaze flared up an air shaft, igniting the roof of a 25-story building. Burning transformers released polychlorinated biphenyls (PCBs), thereby generating hazardous emissions. The fire took 16 hours to extinguish.

Electric power was not fully restored for over five days. Distribution substations are designed to operate in isolation from the remainder of the system to reduce the chance of one station's failure overloading neighboring substations. This isolation strategy means, however, that bypassing a given station cannot be accomplished easily. Power was diverted from other substations by the time-consuming process of splicing underground lines, all during a period when many electric utility workers were on strike.

It is clear from these incidents that there was sudden and extensive escalation of damage from an otherwise local event. This process of escalating damage was referred to by O'Rourke [6] as the cascade effect. Figure 5 shows an event tree for the Garment District incident, which illustrates the cascade effect. The pipeline rupture, at first, caused local disruption through flooding and undermining in its vicinity. When the electric substation was flooded, causing fire, disruption was transferred to a much larger area by electric power outage. Loss of electricity, in turn, affected business, transportation, and telecommunications. The figure shows three principal tiers, or levels, of disruption generated by the pipeline failure. As the damage cascaded from one level to another, losses were sustained in increasingly larger and complex systems.

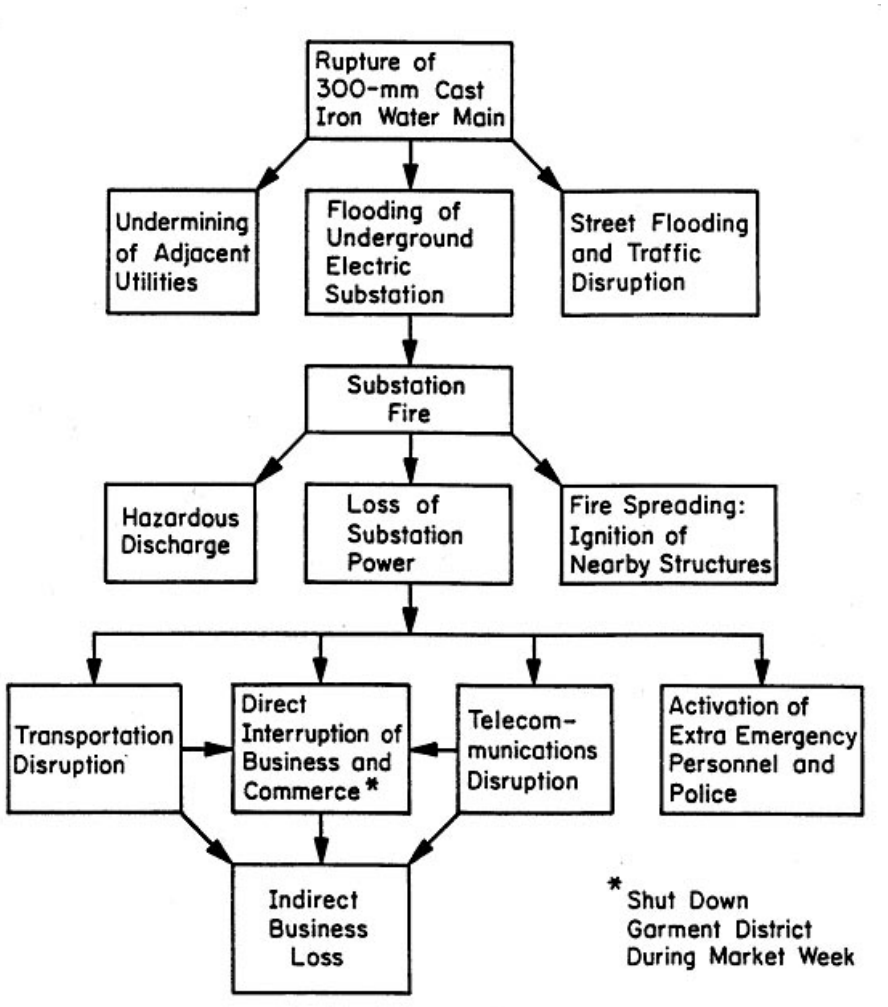

Figure 5. Event Tree for Garment District Incident [6]

LESSONS LEARNED

The WTC Disaster was an immense and complex event. The lessons learned, as presented in this paper, should be viewed as preliminary. Work is in progress to collect additional information that will lead to refinements in the databases and further clarification of the issues raised by the disaster. Lessons learned are summarized under the five subheadings that follow.

Damage to Underground Facilities

September 11 damage to underground water, gas, and steam pipelines and telecommunication conduits was caused by direct impact from falling debris or projectile penetration of the ground. There is no direct evidence of damage caused by ground vibrations and secondary effects, such as water hammer. There are records of gas leakage in streets traversed by heavy construction vehicles, but such instances were not exceptional or unanticipated by gas personnel. Virtually all damage of major consequence was the result of direct impact. Consequently, the areal extent of damage to critical water, telecommunications, gas, and steam conduits was confined principally to the zones of debris impact (see Figure 1). This lesson is significant for establishing planning and emergency response scenarios. It indicates that underground infrastructure damage from building collapse will likely be confined within the near vicinity of the failed structures.

Loss of Infrastructure Systems

Although physical damage to water, gas, and steam pipelines was confined principally to the area of debris impact surrounding the WTC Complex, the temporary loss of these systems extended far beyond this perimeter. After collapse of the WTC towers, there was the need to isolate damaged zones of the water and steam systems to preserve pressure and flow in undamaged sections. There was the need to shut off gas pipelines to suppress leakage and potential ignition. Because the extent of damage was unknown, conservative decisions were made about the size of the isolation zones. The initially isolated portions of the water, gas, and steam systems covered approximately 0.8 km^2, 1.2 km^2, and 3.4 km^2, respectively. One to two weeks were required for restoration of the isolated zones, with the exception of the physically damaged conduits immediately adjacent to the WTC site.

In extreme events, conservative decisions under emergency conditions are likely to result in a substantial zone of temporarily lost service. For planning purposes, significant system disruptions should be anticipated.

Water Supply

Damage to water distribution pipelines surrounding the WTC site was sufficiently severe that pressure losses interfered with fire fighting until isolation of damaged water lines could be achieved. Between two and four times the amount of water taken from distribution pipelines was supplied from fireboats during the critical hours following collapse of the WTC towers.

The WTC experience is similar to experience gained during the 1989 Loma Prieta earthquake. Water supplied by fire boat and relayed with a Portable Water Supply System (PWSS), consisting of hose tenders and above ground hydrants, was responsible for suppressing the fire in the Marina and averting a much more serious conflagration [6]. The deployment of fireboats and the strategic use of bay water plays a critical role in emergency earthquake planning for San Francisco, Oakland, and Berkeley, CA, as well as Vancouver, BC. September 11 experience supports a similar strategy for extreme events of non-earthquake origin. Fire boat deployment and implementation of PWSS concepts should be considered for supplying water under extreme emergency conditions. Water supply from fireboats to land-based locations is especially important where significant damage to the distribution pipeline system has occurred or where the capacity of the system to deliver water is limited.

Substantial amounts of water were supplied to WTC sites at significant distances inland from marine locations. Experience in the San Francisco Bay Area during and after the Loma Prieta earthquake [6] reinforces the WTC experience and demonstrates that water can be conveyed rapidly from marine locations for distances of 1 to 1.5 km, provided that appropriate planning and equipment acquisition have been undertaken. In a post September 11 world, it is important to include marine-based fire protection as part of

strategic planning for disaster response.

The NYC fire boats with greatest pumping capacity were commissioned in 1938 and 1954. When decisions are made for commissioning new fire boats, it will be advantageous to provide for pumping capacity that is comparable to or exceeds the capability of the current fleet.

Telecommunications

As described previously, redundant, dispersed facilities and the ability to rapidly by-pass damaged telecommunication nodes were important factors contributing to the performance of the telecommunications system. Even so, cell phone and landline traffic were impaired, and substantial repairs in the telecommunication service had to be implemented before reliable circuits were restored.

There are many central offices in lower and mid-town Manhattan. The proximity of many telecommunication facilities was a distinct asset during response and recovery. Similar configurations may not be present in other urban centers, thereby prompting consideration of additional facilities and dispersion of facilities where loss of business and commercial activity can have severe regional and national consequences. Special consideration should be given to facilities that affect urban, state, and national programs.

In general, the telecommunication equipment performed very well. The successful performance of telecommunication equipment encourages continued testing and evaluation of critical facilities, guided by observations of performance during extreme events.

The emergency procedures enacted by telecommunication companies worked well. The telecommunication industry operates with a formal, well-rehearsed protocol whereby command-and-control operations are rapidly established, with multiple communication pathways between upper management and field personnel. The U.S. telecommunications industry is served by a National Coordinating Center (NCC) that consists of government and industry representatives, who coordinate telecommunication services for national security and emergency preparedness. NCC uses information sharing and analysis to evaluate the experience of industry participants, including lessons learned during emergency operations. The Network Reliability and Interoperability Council (NRIC) provides recommendations to the telecommunications industry and the FCC for operating telecommunication networks under various conditions, including natural disasters and both cyber (e.g., computer viruses, network intrusion, etc.) and physical attacks. The best practices, compiled by NRIC, have benefited from lessons learned during previous natural disasters, including the Loma Prieta and Northridge earthquakes (e.g., [7]).

Wireless e mail proved to be a valuable asset after September 11. The use of handheld e mail devices greatly facilitated communications and contributed to substantial improvements in emergency response efficiency.

Electric Power Systems

Perhaps the most important observation from the WTC Disaster and other incidents described in this paper is that damage becomes most pervasive when it interferes with the electric power system. Both the Hellgate and Garment District incidents show that power outages were responsible for major escalation of initial damage. The electric power system is, in effect, the gateway for local damage to escalate or cascade into other systems.

The effects of local damage appear to be influenced by the proximity of damage to an electrical substation. When damage affects a NYC substation, its potential for cascading consequences increases dramatically, but nonetheless is capped by the configuration of the electrical network. Because the NYC system is compartmentalized into local distribution networks, substation loss tends to be limited to the one or two local distribution networks that are linked to that substation.

Systems that are configured differently will not react to damage in the same way. In other systems, for example, damage may trigger switching stations that isolate several substations, thereby resulting in power loss over a substantial area. Other systems do not have the redundancy embodied in the NYC system so that loss of one or two transmission lines or primary distribution feeders may compromise a significant part of the overall network.

The damage on September 11 was so extensive that disruption spread through five distribution networks, with a sixth impaired through the loss of six 13.8 kV feeders. Extensive isolation, repairs, and

new feeder installation were required for power restoration to financial centers in lower Manhattan and the resumption of Stock Exchange activities. Rehabilitation on such a scale within the short time frame required for the resumption of financial trading activities was only possible through extensive stockpiling of specialized parts and the availability of many trained, highly motivated and well-equipped staff. System resilience depended on organizational resilience that was embedded in the planning and preparations that had been developed for emergency response.

BRAVE NEW WORLD

The events of September 11, 2001 have changed not only the way we think about urban infrastructure, but the way we treat infrastructure information. In the "brave new world" after September 11, knowledge is power both for those who wish to build and those who want destruction. It is therefore logical and responsible for the managers of infrastructure to be cautious about providing information that involves critical facilities. The notable lack of maps (except those available at the FEMA website) and graphical details in this paper is a testament to this caution. Although detailed information was collected in the preparation of this paper, it is not appropriate for the authors to provide further details until review and clearance of the information can be obtained. Such clearance may take many months or longer.

To benefit from the revolution in information technology, it is necessary to have access to information. It is ironic that the power of information technology may seriously inhibit its beneficial use because we are unable to decide the intentions of those who wish to use it. From an engineering and scientific viewpoint, there has never been a more opportune time for advancing the state-of-the-art and practice for characterizing and modeling complex infrastructure systems. Advanced GIS, remote sensing, condition monitoring, model-based simulation, and systems engineering coupled with the capability of producing precise digital base maps, which can integrate the spatial characteristics of infrastructure, provide unparalleled opportunities. Legitimate concerns about security and attendant restrictions on information are equally important factors that may become barriers, unless we develop suitable procedures for information accessibility and dissemination. It is extremely important to develop a consistent policy regarding the need to know vs. the need to secure information and databases about critical infrastructure systems.

In addition to improved protocols for information accessibility, there is the need to integrate and utilize the talent and resources of those working on extreme events. As described in this paper, the rapid inspection procedures for buildings adjacent to the WTC Complex and the resiliency of telecommunications equipment can be attributed in part to experience gained from earthquakes. Collectively, the professionals and research specialists, who focus on natural disasters, have expertise in risk assessment for the built environment, design procedures under conditions of uncertainty, strengthening of structures for multiple loadings, simulation of complex infrastructure under various damage states, emergency response, and community recovery. Such expertise is an asset when developing procedures for countering terrorism. An effective approach to homeland security requires that the parties responsible for implementing security have the vision and intelligence to engage those involved in natural hazards. Homeland security should integrate and harmonize the technologies for mitigating natural and terrorist disasters to create communities resilient to all hazards.

ACKNOWLEDGEMENTS

The authors acknowledge the support of the National Science Foundation under Award No. CMS-0207266. We thank Drs. Priscilla Nelson and Miriam Heller for their encouragement and assistance. We also express our deep gratitude for the help of talented and dedicated personnel at the Consolidated Edison Company of New York, Inc., New York City Fire Department and Department of Environmental Protection, AT&T, Verizon, Cingular Interactive, and IBM Global Services. We appreciate the support of the Institute for Civil Infrastructure Systems in conducting the research leading to this paper, and acknowledge Professor Rae Zimmerman of New York University for her leadership and continuing assistance.

REFERENCES

[1] FEMA, "World Trade Center Building Performance Study", FEMA 403, May, 2002, Federal Emergency Management Agency, Washington, DC.

[2] ATC, "Procedures for Postearthquake Safety Evaluation of Buildings", ATC-20, 1989, Applied Technology Council, San Francisco, CA.

[3] Verizon Communications, "System Integration and Testing NEBS Compliance Checklist" SIT.NEBS.TE.NPI.2000.004, Revision 1, Oct., 2001, retrieved 30 Sept.02, www.verizonnebs.com/nebs_d.doc

[4] Condello, K., "Wireless Industry: Impact and Recovery Efforts Summary Report", NRIC Meeting, Oct., 2001, retrieved 26Sept.02, www.nric.org/meetings/meeting20011030.html.

[5] National Coordinating Center for Telecommunications, "Telecommunications Service Priority Program", retrieved 21 Oct. 02, www.ncs.gov/ncc/main.html.

[6] O'Rourke, T.D., "Prospectus for Lifelines and Infrastructure Research", The Art and Science of Structural Engineering, N.K. Khachaturian, Ed., Prentice-Hall, Inc., April 1993, pp. 37-58.

[7] Network Reliability Council, "Network Reliability – The Path Forward", Alliance for Telecommunications Industry Solutions, Washington, DC, retrieved 26 Sept. 02, www.nric.org/pubs/index.html.

Response and Design of Pipelines Subject to Permanent Ground Deformations

Requirements for Designing Safe and Cost Effective Pipelines in Seismic Areas

Serghios T. Barbas
ExxonMobil Upstream Research Company

ABSTRACT

Through an active research program, ExxonMobil has identified safe and cost effective design practices for pipelines in seismic areas. As part of this work, we have developed analytical methods and models to assess the impact of seismic hazards on the pipeline and quantify the loads, stresses and strains that develop in the pipeline as a result of the seismic hazards. In addition, we have developed analytical models and have conducted tests to quantify the capacity of the pipe and its welds to accommodate the loads and strains generated by the seismic events.

This paper will describe some of ExxonMobil's work in this area, present results from case studies considered to date which highlight some of the key challenges in designing pipelines to operate safely in seismic areas, and discuss design approaches that can be used to overcome these challenges and produce safe and cost effective pipeline designs. The paper will also discuss some of the limitations found in existing industry Standards for addressing seismic hazards and explain how limit state design approaches can be used to develop rational design criteria for such pipelines.

INTRODUCTION

ExxonMobil Corporation's current and future interests include the need to design, install and operate oil and gas facilities in various areas around the world where seismic activity is high. In such areas, a very important objective is to design these facilities to operate safely in a manner that preserves health, safety and the environment. A second important objective is to ensure that these facilities maintain high operability standards following major seismic events in order to minimize downtime and service interruptions.

Industry Codes and Standards provide general guidelines on how to produce safe designs for pipelines in seismic areas, but rarely provide explicit design criteria or performance standards on how to achieve this important objective. Quite often, operators considering installation of pipelines in seismic areas find it necessary to supplement the guidelines found in existing Codes and Standards with project specific design criteria. These criteria are carefully selected to be consistent with the spirit and intent of the Standards and provide more direct guidance to designers on how to achieve the desired objectives.

This paper provides an overview of various ExxonMobil research and development activities that are either completed or are ongoing, which aim to enhance our ability to produce safe and cost effective pipeline designs in seismic areas. This work covers both onshore and offshore pipelines, and addresses both buried and unburied pipelines.

DESIGN OBJECTIVES

The main objective of seismic pipeline design is to make the pipeline and pipeline facilities resistant to the effects of potential earthquakes that may occur during the operating lifetime of these facilities, and prevent failures that can adversely impact health, safety and the environment. A second, but also very important objective, is to minimize capital loss and disruptions to operations.

Buried and above-ground pipelines can be affected by permanent ground deformation (PGD) and transient ground deformation (TGD). PGD involves irrecoverable movement of the ground that results primarily from earthquake-induced soil liquefaction, surface faulting, and landslides. TGD results from seismic wave propagation associated with strong ground shaking. Small ground cracks and fissures may also result from seismic shaking, but the size of these cracks is generally much smaller than the magnitude of ground displacements caused by large scale soil liquefaction, surface faulting and landslides.

Industry experience from past earthquakes indicates that modern steel pipelines joined by good quality full penetration girth welds are highly resistant to TGD, but may be vulnerable to PGD when substantial localized displacements occur [1]. During detailed design of the pipelines, the effects of TGD and PGD on the pipelines need to be investigated in detail, and design solutions must be found to protect the pipelines from all seismic hazards. Buried pipelines are primarily affected by hazards that cause large ground deformation. Above-ground pipelines are primarily affected by the dynamic effects of ground shaking, but can also be affected by large ground movements.

Supporting pipeline facilities must also be designed to withstand the effects of seismic events. Critical pipeline facilities include main line pumps, control systems, communication systems, data gathering systems, remote valves, and emergency systems. After major earthquakes in the past, pipelines have survived the earthquake intact, but damage to these supporting facilities has often resulted in unnecessary downtime for the entire pipeline system. Since most of these supporting facilities are above ground, the primary seismic threat to them is ground shaking during the earthquake. Pipeline support facilities must obviously also be sited to avoid PGD hazards. On-line or back-up power supplies for critical systems are also essential and must remain operational after large earthquakes.

Buildings that house critical systems and personnel must also be designed to withstand the effects of design level earthquakes. While some degree of damage may be unavoidable after extreme seismic events, the buildings should not fail catastrophically or in such a manner as to interfere with the function of critical systems or threaten personnel safety.

DESIGN PHILOSOPHY

Seismic design criteria for pipelines and pipeline facilities typically follow a two-tier design approach. Specifically, two levels of earthquake hazards are considered for design - the Strength Level Earthquake (SLE) and the Ductility Level Earthquake (DLE). The SLE is a lower intensity earthquake that has a small but finite likelihood of occurring during the lifetime of the pipeline. The return period of the SLE event is typically in the 100-200 year range. The DLE is a rare, intense earthquake which has a very small likelihood of occurring during the lifetime of the pipeline. The DLE typically has a mean return period on the order of 1000-2000 years. Pipelines and pipeline facilities are typically designed to meet the following performance objectives for the SLE and DLE events:

1) SLE – the pipelines and critical pipeline facilities should withstand seismic shaking and permanent ground movements without significant damage and with minimal interruption of normal operations. Some damage can be tolerated in less critical pipeline facilities that are not essential for continued operation following the SLE.

2) DLE – the pipeline and pipeline facilities should survive seismic shaking and ground movements without leaks, ruptures, collapse, loss of life, or significant damage to the environment, but with a distinct possibility of damage that would interrupt operation and require repairs. The amount of permissible damage varies according to the type of structure or component and its function. The functionality of essential control, communications and emergency systems should be maintained without interruption during and after a DLE event.

Seismic design of above-ground pipelines and pipeline facilities must follow well-established analysis and design procedures to predict deformations, stresses and strains in all key components resulting from ground shaking. Seismic design of buried pipelines must follow analytical and modeling procedures which adequately account for the pipe-soil interaction under PGD and TGD movements.

Working stress based design procedures currently incorporated in some Industry Standards are often inadequate for addressing potential pipeline failure modes that may occur after major earthquakes. A more rational approach for preventing such failures is to conduct more thorough

evaluations during design using limit state methods. Limit state design methods are much more useful for finding solutions to prevent pipeline failures after large earthquakes, because they can directly focus on specific failure modes that must be prevented. Industry acceptance of limit state design methods has increased tremendously over the last few years, due to significant advancements in computational power and nonlinear finite element technology that have made the use of such methods more practical and more accessible to designers. As a result, design approaches based on limit state methods are gradually finding their way in new or updated Industry Standards or project specific design criteria.

METHODS FOR QUANTIFYING STRAIN DEMAND ON PIPELINE

Buried and unburied pipelines must be designed to withstand the effects of seismic hazards while meeting the design objectives stated above for the SLE and DLE design events. For proper design, the stresses and strains that develop in the pipeline due to all relevant seismic hazards must be carefully quantified, to ensure that the pipeline can safely accommodate these strains without failures.

ExxonMobil has developed advanced analysis methods for assessing the impact of seismic hazards on pipelines. These methods are based on nonlinear finite element models, which can be used to assess both the static and dynamic response of the pipeline due to a variety of seismic hazards. These models account for the nonlinear material behavior of the pipe and its welds, the large deformations that occur due to significant ground movements which often accompany major seismic events, and the nonlinear interaction between the soil and the pipeline as the pipe is pushed through the soil.

While detailed description of the analytical models used by ExxonMobil to quantify the strain demand on the pipeline due to seismic hazards is beyond the scope of this paper, results from a few representative analyses are provided in the paper to illustrate some of the available methods and tools for addressing seismic hazards.

Assessment of Fault Crossings

Figure 1 shows the longitudinal strain that develops in a buried pipeline at a fault crossing. As can be seen, significant tensile and compressive strains can develop in the pipeline as a result of the ground movement. Initially the strains increase rapidly with ground movement, but eventually reach a plateau as the pipe starts shearing through the soil.

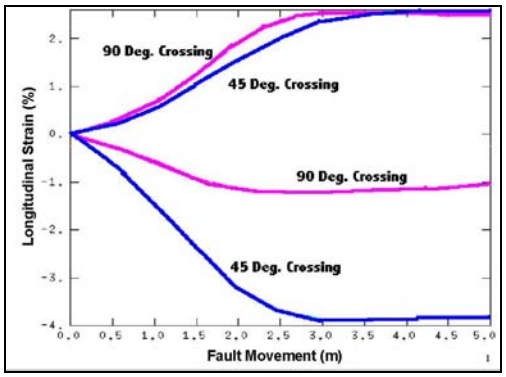

Figure 1. Longitudinal Strain in Pipe vs Ground Movement at Strike Slip Fault Crossing

Pipe-soil interaction models that can be used to capture the soil resistance to pipe movement in the axial, lateral and vertical directions can be found in [2]. Quantifying the amount of ground movements anticipated at specific fault crossings requires careful evaluation of the fault of interest based on detailed geological assessments and seismotectonic models such as those described in [3]. Empirical relationships based on historical accounts from past earthquakes such as those described in [4] are also sometimes used to quantify expected fault movements at specific locations.

As shown in Figure 1, the crossing angle between the pipe and the fault can have a significant effect on the calculated strains, and must be evaluated over a reasonable range of values to account for uncertainties in estimating this angle at specific crossing locations. Although the example shown in Figure 1 is for a strike slip fault where the ground movement occurs in a single plane, quite often ground movements caused by seismic events can have displacement components in all three directions. The finite element models used by ExxonMobil for these types of analyses can simulate movements in all three directions.

For fault crossings, it is often advantageous for designers to orient the pipeline in a way where the ground movements generate tensile loads in the pipeline. Compressive loads reduce the buckling capacity of the pipe and should be avoided. It is also advantageous to build as much flexibility in the pipeline as possible, by either bringing the pipeline above ground or by burying it in shallow trenches with loose backfill material which allows as much pipe movement as possible.

Assessment of Pipe Behavior due to Lateral Spreading Caused by Soil Liquefaction

Figure 2 shows results for a buried pipeline subjected to ground movements due to lateral spreading caused by soil liquefaction. Lateral spreading generally occurs when a layer of soil liquefies right beneath a competent layer of soil near the ground surface which does not liquefy. When this occurs, the top layer loses its support and can move in a down-slope direction due to gravity loads and inertia loads caused by seismic shaking. Quite often, pipelines are buried in this top soil layer and are thus subjected to significant displacements as the top ground layer moves.

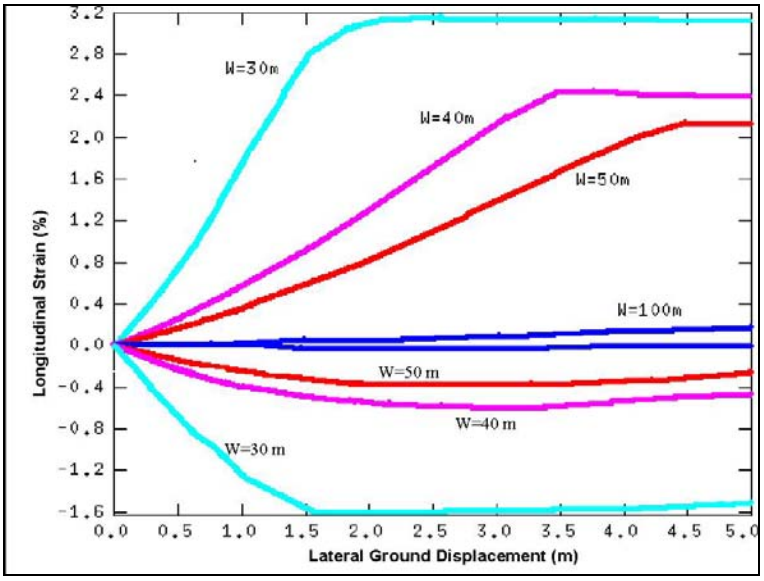

Figure 2. Longitudinal Strain in Pipe vs Ground Movement Due to Lateral Spreading. (W = Lateral Spread Width)

For the example shown in Figure 2, the soil movement is assumed to be perpendicular to the pipeline. However, ground movements due to lateral spreading can theoretically occur in any direction, since local ground slopes can vary significantly along the pipeline route. As a result, for a long pipeline crossing multiple areas that may be prone to soil liquefaction, the analyses must consider possible ground displacements directed at various angles relative to the pipeline.

Pipe strains generated by lateral spreading can be very significant if the ground movements are large. Ground movements of several meters have been observed due to lateral spreading after major past earthquakes, and movements of this magnitude have been known to cause some damage to buried pipelines. As a result, the potential effects of lateral spreading merit serious consideration during the detailed design of buried pipelines in areas where soil liquefaction can occur.

Assessment of Effects of Seismic Wave Propagation

Seismic wave propagation can induce significant ground displacements and strains at distances several hundred kilometers away from the seismic source. As a result, seismic waves can affect significant portions of long pipelines, especially for pipelines buried deep in the ground, where a large percentage of the ground strain is transmitted directly to the pipeline by the surrounding soil. However, pipe strains resulting from seismic wave propagation are generally much smaller than those seen at fault crossings or in areas where lateral spreading occurs, and are therefore rarely a serious threat to the pipeline.

Figures 3 and 4 show typical displacement and strain patterns that can develop in surface ground layers due to seismic wave propagation. In this example, it is assumed that the seismic wave is propagating along the longitudinal axis of the pipeline, thereby generating axial deformation and loads in the pipe. These displacement and strain patterns were calculated using the simplified methods recommended in [5]. They correspond to seismic waves with a wavelength of approximately 220 meters travelling through a soil layer with a natural period of 0.7 seconds. Such waves produce maximum ground strains of approximately 0.4%, as shown in Figure 4.

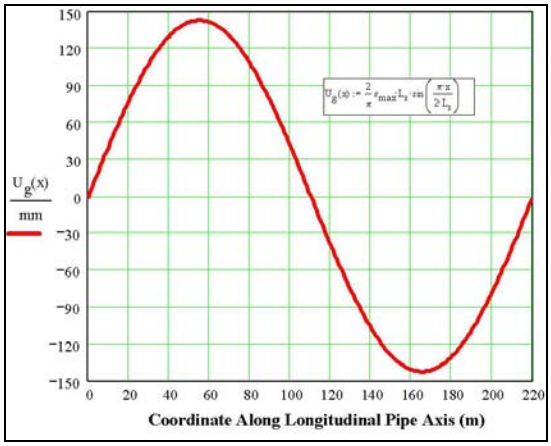

Figure 3. Ground Displacement Caused by Seismic Wave Propagation

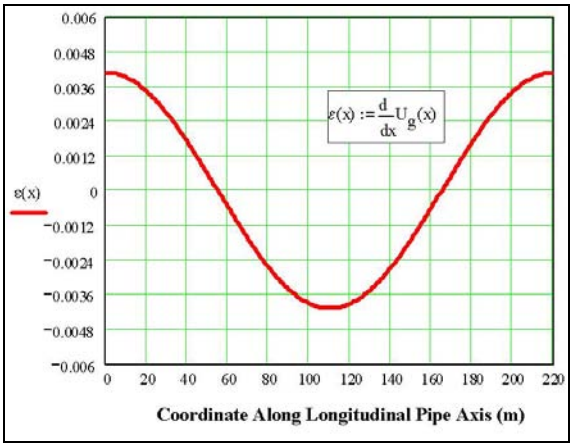

Figure 4. Ground Strain Caused by Seismic Wave Propagation

Figure 5 shows the axial strain resulting in the pipe for the ground strain shown in Figure 4. Results are shown for both "high" and "low" skin friction between the pipe and the surrounding

soil. In the case of high friction (i.e. deep burial in dense backfill), the pipe moves with the soil and the pipe strains are essentially the same as those of the surrounding soil. For low friction (i.e. shallow burial in loose backfill), however, significant slippage usually occurs between the pipe and the surrounding soil. As a result, the strain transmitted to the pipe is much lower than the strain in the surrounding soil.

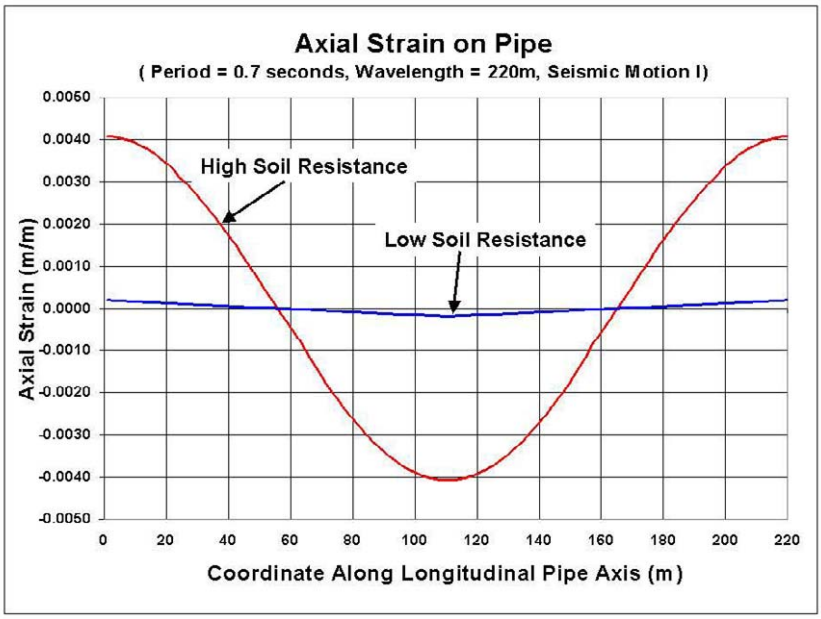

Figure 5. Axial Strain in Pipe Resulting from Seismic Wave Propagation

Assessment of Dynamic Effects for Above Ground Pipelines

For above ground pipelines, dynamic effects due to ground shaking can be significant and should be investigated along with the effects of PGD hazards that may also impact such pipelines. Above ground pipelines include elevated pipelines on discreet supports or pipelines resting on the ground (onshore) or on the seafloor (offshore).

The most challenging aspect of these analyses is to properly model the acceleration time histories transmitted from the ground to the pipe. These histories can vary significantly along the length of a very long pipeline, and this spatial variability must be properly captured by the analysis.

Figure 6 shows the combined stress generated in a pipeline resting on the seafloor due to dynamic effects caused by seismic shaking. In this analysis, identical acceleration time histories are applied along the length of the pipeline, but with some time delay to account for wave passage effects along the length of the pipeline. This time delay results in out of phase displacements at various points along the length of the pipeline, which can produce significant axial loads in the pipeline. Incoherence effects due to varying soil conditions along the pipeline route produce a similar effect and should also be considered. Due to the high flexibility of unrestrained pipelines lying on the seafloor, such pipelines can accommodate these axial loads very efficiently by deflecting slightly in the lateral direction. The resulting stresses in the pipeline may exceed the yield strength of the pipe material, as shown in Figure 6, but the resulting plastic strains are generally very small and can be safely accommodated through proper design.

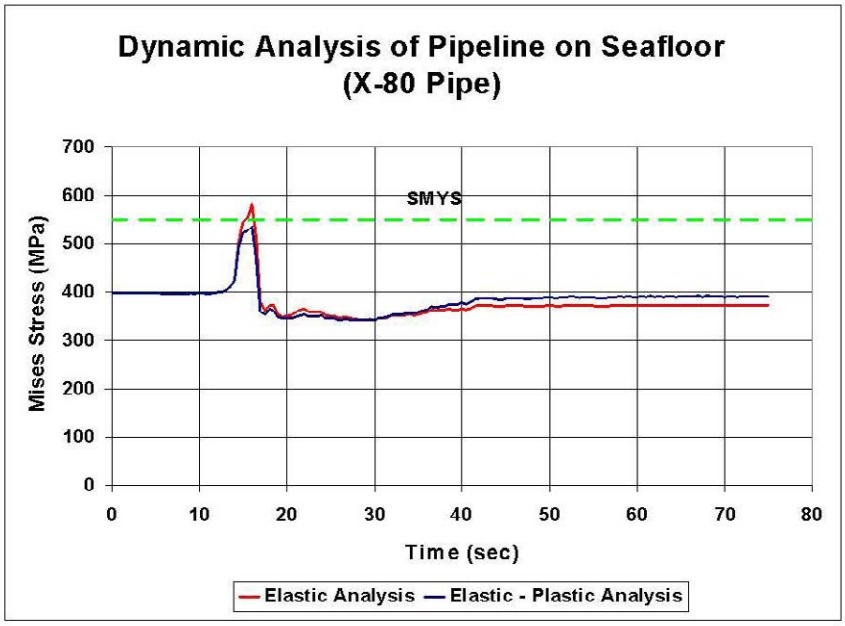

Figure 6. Stresses in Pipeline on Seafloor Subjected to Seismic Shaking

METHODS FOR QUANTIFYING STRAIN CAPACITY OF PIPE

For proper pipeline designs in seismic areas, the need to accurately assess the capacity of the pipe and its welds to accommodate the loads and strains generated by the seismic event is just as high as the need to accurately quantify the seismic loads and strains that develop in the pipeline. Fortunately, recent advances in computational power and nonlinear finite element technology have made such assessments not only technically feasible, but also quite accessible to pipeline designers.

ExxonMobil has developed advanced analytical models and has conducted or is currently conducting various test programs to properly assess the impact of seismic hazards on pipelines. The knowledge gained from these programs has allowed us to identify designs for pipelines in seismic areas that are highly resistant to seismic hazards. This section will discuss some of the analytical methods we use for such assessments, and show results from a few example analyses. The next section will discuss parallel test programs we have undertaken to validate our analytical models and study effects difficult to assess entirely through analytical methods.

Assessment of Buckling Capacity of Pipe

Figure 7 shows results from a 3-D finite element analysis model to assess the buckling capacity of the pipe. This model is constructed from 3-D shell elements that can capture the nonlinear response of the pipe material and the large deformations that occur in the pipe cross-section when the pipe is subjected to seismic loads. These models take into consideration all pipeline operational loads, plus all loads generated by the seismic event such as axial tensile and compressive loads and bending moments. Such models show excellent agreement between analytical and experimental results, not only in predicting the onset of the buckling instability, but also in capturing the deformation that occurs in the pipe well beyond the point of instability.

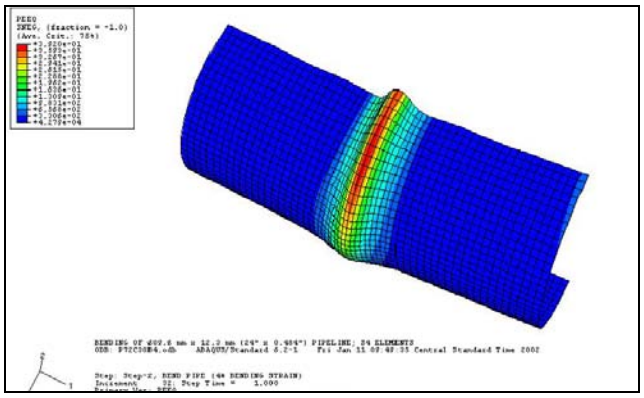

Figure 7. FEA Model to Assess Buckling Capacity of Pipe

Figure 8 shows visual comparisons between FEA model predictions and test results for a case where the pipe is bent well beyond the point of first instability. Analyses such as this are very important for predicting the extent of damage that can occur under extreme seismic loads, and for finding solutions to prevent catastrophic failures under such events. These analyses provide significant insight regarding the impact of various loads on the capacity of the pipe to resist buckling, something that is very difficult and very costly to determine experimentally.

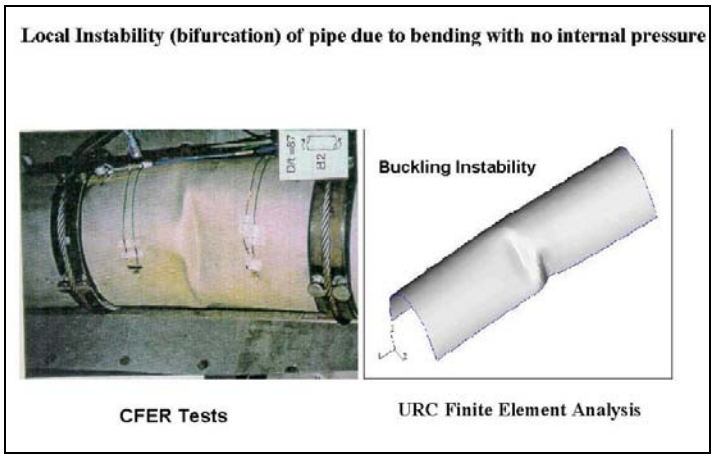

Figure 8. Buckling Failure Mode - Visual Comparison of Test Results and FEA Predictions

Figure 9 shows the moment vs bending strain response of a pipe subjected to bending in the presence of high axial loads and internal pressure. In general, the applied loads affect both the magnitude of the peak moment that can develop in the pipe just prior to the buckling instability, as well as the magnitude of bending strain the pipe can accommodate before the instability occurs. As observed from Figure 9, internal pressure and tensile axial loads increase the capacity of the pipe to accommodate bending strain, while compressive axial loads cause the instability to occur at lower bending strains. Analyses such as this can also be used to assess the impact of the material properties of the pipe on pipe buckling. For example, investigators in reference [6] have shown that pipe materials with high strain hardening capacity perform much better in resisting buckling than pipe materials with low strain hardening or pipes with a significant plateau in its stress-strain curve. Analyses such as these have also been used by ExxonMobil and others [7] to study the impact of initial geometric imperfections in the pipe or the presence of girth welds on the overall capacity of the pipe to resist buckling failures.

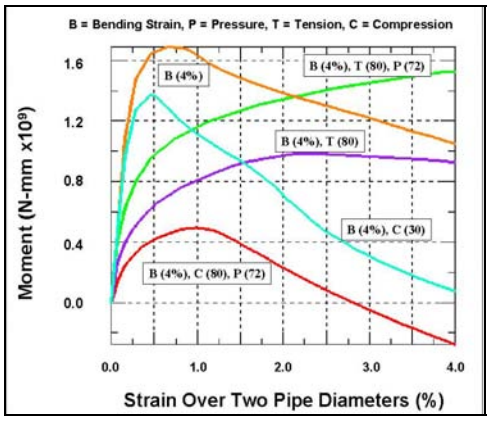

Figure 9. Bending Moment vs Bending Strain for Different Loading Conditions

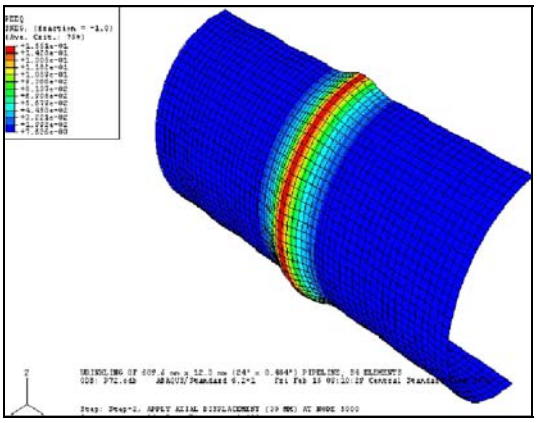

Figure 10. Finite Element Model to Assess Wrinkling Capacity of Pipe

Assessment of Wrinkling Capacity of Pipe

Finite element models such as the ones described above can also be used to assess the wrinkling capacity of buried pipelines. This failure mode occurs when the ground movements are such that the pipe sees significant axial compressive loads with little or no bending. These types of failures have been observed on several occasions in the past following major seismic events.

Figure 10 shows how the deformation in the pipe under compressive loads can localize in a weak or imperfect area of the pipe, causing a wrinkle to form there. Once such a wrinkle forms, the axial stiffness in this area of the pipe is reduced, causing pipe from either side of the wrinkle to feed into this area. This can result in multiple wrinkles or folds forming in the pipe. Understanding the physics of such instabilities has allowed ExxonMobil to develop design strategies to prevent them.

Assessment of Other Failure Modes

Nonlinear finite element methods can also be used to assess the **burst capacity** of the pipe, as well as the **upheaval buckling** resistance of buried pipelines subjected to high compressive loads. In addition, such models can also be used to assess the lateral **"global buckling"** response of unburied pipelines subjected to high axial and lateral seismic loads. The term "global buckling" as used here refers to a global beam-column type of instability causing the pipe to move laterally over a significant length, and not a local instability occurring in the cross-section of the pipe.

For seismic areas, it is also very important to be able to prevent **brittle fracture failures** at pipeline girth welds, when the pipe is subjected to significant plastic strains. In general, the strength of girth welds for pipelines in seismic areas must overmatch the strength of the adjacent pipe to prevent strain localization in the weld zone and heat affected areas. The welds must also have adequate toughness and ductility to prevent brittle fractures at the joints - one of the most prevalent failure modes observed in older pipelines following large seismic events. Ideally, the welds must be able to sustain high tensile strains in the pipe, with weld defects growing slowly

with increasing strain in a ductile tearing mode and not in a brittle fracture mode. Such welds are technically feasible with existing welding technology.

ExxonMobil is currently conducting research programs to develop analytical methods and tools to assess the capacity of girth welds to accommodate plastic strain. These elasto-plastic fracture models focus on predicting the tearing resistance of weld defects for pipe reeling and seismic applications, where the pipe may be subjected to large plastic strains. Initial results from these studies look very promising, with tests planned during 2003 to validate these models.

TESTS TO VALIDATE ANALYTICAL MODEL PREDICTIONS

As indicated earlier, ExxonMobil has already completed or is currently planning large scale test programs in several areas, to better understand pipe failure modes associated with seismic loads, and validate analytical models developed by ExxonMobil to study these failure modes.

In 2000, ExxonMobil completed a wide plate test program at Ghent University in Belgium, to assess the strain capacity of X-70 and X-80 girth welds. During this program, welds from six different welding procedures were tested. The tests covered a wide range of weld properties and weld defect sizes. A picture of the experimental setup used for these tests is shown in Figure 11. The overall goal of these tests was to demonstrate the feasibility of accommodating tensile strains in buried pipelines of up to 4% without weld failures leading to leaks or ruptures. This goal was easily achieved, and the tests yielded very valuable insight on how to properly design girth welds to accommodate large plastic strains.

Figure 11. ExxonMobil Wide Plate Tests to Assess Strain Capacity of Girth Welds

In 2003 ExxonMobil plans to conduct a series of large scale tests at C-FER in Canada, to better understand the buckling and wrinkling behavior of pipelines subjected to large loads, such as those anticipated when buried pipelines are subjected to large ground movements during large earthquakes. Similar tests have been conducted before by others [7] for pipelines buried in permafrost areas, but these tests did not simulate the range of loads anticipated under large seismic events. Results from the 2003 ExxonMobil tests will be used to validate the analytical models described earlier for assessing the buckling and wrinkling behavior of pipelines in seismic areas, and validate our overall seismic design philosophy. In 2003, tests are also planned for

validating our analytical methods for assessing the ductile tearing resistance of weld defects for pipes subjected to large plastic strains.

CONCLUSIONS

Over the last several years, ExxonMobil has undertaken several research studies to develop the technologies needed to predict the static and dynamic response of pipelines subjected to seismic hazards, and to assess the capacity of the pipe and its welds to accommodate the deformation resulting from these hazards. The knowledge gained from these programs has allowed us to develop safe and cost effective design practices for such pipelines.

Even in highly seismic areas such as Japan or Alaska, our studies show that pipelines can be made robust enough to accommodate the anticipated seismic hazards without catastrophic failures that can impact health, safety and the environment. Furthermore, our studies show that such pipelines can be designed to maintain high operability standards, thus preventing undue service interruptions following seismic events.

Because existing Industry Codes and Standards are not always adequate to address pipeline seismic issues, very often project specific design criteria are developed to supplement existing local Standards. ExxonMobil has participated in several such efforts around the world. We recently worked jointly with the appropriate regulatory agencies in Russia to develop a Project Specific Design Code (PSDC) for our Sakhalin pipelines in Russia. A similar effort is currently in progress in Japan to develop a PSDC for a proposed future pipeline from Sakhalin to Japan.

REFERENCES

1. O' Rourke, T.D. and Palmer, M.C., "Earthquake Performance of Gas Transmission Pipelines", Earthquake Spectra, Volume 12, No. 3, August 1996.
2. Audibert, J.M.E, Nyman,D.J.and O'Rourke, T.D., "Differential Ground Movement Effects on Buried Pipelines", Guidelines for the Seismic Design of Oil and Gas Pipeline Systems, ASCE Technical Council on Lifeline Earthquake Engineering, 1984.
3. Thenhaus, P.C. and Campbell, K.W., "Seismic Hazard Analysis", Earthquake Engineering Handbook, Edited by Wai-Fah Chen and Charles Scawthorn, CRC Press, 2003.
4. Wells, D.L. and Coppersmith, K.J., "New Empirical Relationships among Magnitude, Rupture Length, Rupture Width, Rupture Area, and Surface Displacement", Bulletin of the Seismological Society of America, Vol. 84, No. 4, August 1994.
5. Japan Gas Association, "Recommended Practices for Earthquake Resistant Design of Gas Pipelines", Earthquake Resistant Design Codes in Japan, Chapter 6, January 2000.
6. Suzuki,N., Endo, S., Yoshikawa, M., and Toyoda, M., "Effects of Strain Hardening Exponent on Inelastic Local Buckling Strength and Mechanical Properties of Line Pipes", OMAE Proceedings, June 2001.

Dorey, A.B., Cheng, J.J.R., and Murray, D.W., "Critical Buckling Strains for Energy Pipelines", Structural Engineering Report No. 237, University of Alberta, April 2001.

NUMERICAL STUDY FOR RUPTURE BEHAVIOR OF BURIED GAS PIPELINE SUBJECTED TO SEISMIC FAULT DISPLACEMENT

Yasuo OGAWA, Yusuke FUJITA , Yasunari YANOU, Tomohisa MEKATA,
Makoto KAWAKAMI and Kazuhiko WATANABE

ABSTRACT

Nonlinear finite element analysis was performed for buried gas pipeline subjected to seismic fault displacement in order to study rupture behavior of the pipeline structure. Pipes of 100mm to 600mm in diameter were studied. According to the calculated results, z-shaped buckling deformation of the pipeline was observed. The analysis model employed in this paper was found to be very simple and useful for gaining overviews of the rupture behavior of gas pipeline subjected to seismic fault displacement.

Yasuo OGAWA, Yusuke FUJITA,Yasunari YANOU, Tomohisa MEKATA Osaka Gas Co. Ltd, 4-1-2 Hiranomachi, Chuo-ku Osaka,541-0046,Japan
Makoto KAWAKAMI, KazuhikoWATANABE KOZO KEIKAKU ENGINEERING Inc. 4-5-3 Chuo, Nakano-ku Tokyo,164-0011,Japan

INTRODUCTION

On September 21, 1999, the Chichi earthquake occurred in Taiwan. It was reported that buried gas pipelines underwent bending deformation due to ground displacement at a reverse fault near the Wushi Bridge about 10 km south of Taichung[1]. The deformation of a 200mm-size pipeline was Z-shaped, with the pipeline being bent at two points (Photo 1). There have been virtually no cases of substantial deformation comparable to this case in gas pipelines comprised of welded steel pipes.

This report aims to evaluate the safety of buried gas pipelines undergoing fault displacements. Firstly, we conducted a numerical analysis of the bending deformation of gas pipelines that underwent the Chichi earthquake. And then we tried to conduct a numerical analysis of gas piplines which are used in Osaka for case studies. Furthermore, we examined how much ground displacement a gas pipeline can withstand. The profiles of the pipelines are shown in Table 1 and Table 2.

The tool we used for the analysis was ADINA[2], which is a finite-element analysis program. Material non-linearity and geometrical non-linearity were taken into consideration.

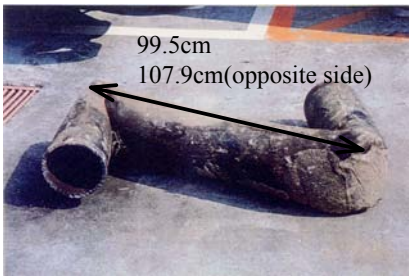

Photo 1 Z-shaped deformation in 200mm-size gas pipeline

Table 1 Profile of Gas Pipelines Undergoing Bending Deformation in the Chichi Earthquake

Pipeline	Material	D(cm)	t(cm)	D/t	Name in This Report
200mm	API X52	21.63	0.90	24	200A-J

Table 2 Profile of Gas Pipelines for case studies

Pipeline	Material	D(cm)	t(cm)	D/t	Name in This Report
150mm	SGP	16.52	0.50	33	150A
200mm	SGP	21.63	0.58	37	200A
300mm	SGP	31.85	0.69	46	300A
400mm	SGP	40.64	0.79	51	400A
600mm	API X52	60.99	1.20	51	600A-1
600mm	API X42	60.99	1.03	59	600A-2
600mm	STPY	60.96	0.95	64	600A-3

ANALYSIS METHOD

Finite-Element Model

We developed an analysis model as shown in Fig. 1.
A fault was assumed to be present within the piping model. A ground displacement was applied to one part of the piping. The other part of the piping was free of the effect of the ground displacement, with the boundary being placed at the fault displacement. Modeling of the pipeline incorporated pipe elements with two nodal points. The pipeline was broken as shown in Fig. 1, into discrete elements of approximate dimension 0.5D in sections near the fault where the pipe would undergo substantial deformation and also approximate dimension 3D in other sections.

Springs representing the ground (ground spring) were applied to each nodal point of the pipe elements in each direction as follows: the horizontal direction perpendicular to the pipe axis (X direction), the axial direction of the pipe (Y direction), and a vertical direction perpendicular to the pipe axis (Z direction). Each ground spring was modeled as a spring element with two nodal points. Regarding the cross-sectional areas of spring elements, the pipe element was multiplied by the pipe diameter to determine values for vertical and horizontal springs. The pipe element length was multiplied by the peripheral length of the pipe to determine the cross-sectional area of the axial spring.

In selecting the lengths for the analysis models, we took into consideration that there were areas of large and small pipe element deformation.

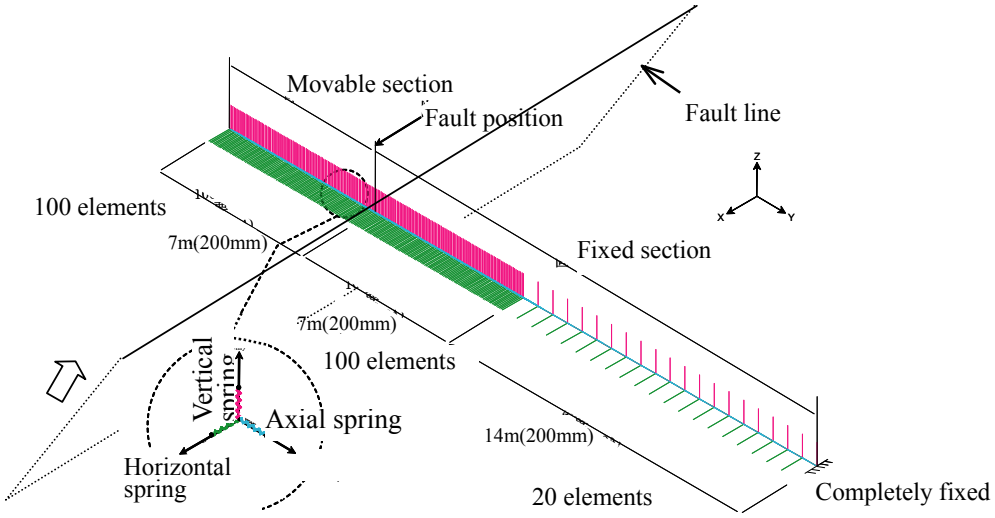

Fig. 1 Analysis Model

Fault Displacement and Boundary Conditions

In the area undergoing ground displacement, displacements were applied to the nodal points on the ground side of spring elements simultaneously in the pipe's axial direction, the horizontal direction perpendicular to the pipe axis, and the vertical direction perpendicular to the pipe axis, as shown in Fig. 1. The actual amounts of displacement were not precisely known at the fault in the ground where the buried gas pipes shown in Photos 1 was located. In this report, therefore, the maximum displacements were assumed to be 300 cm in the pipe's axial direction, 200 cm in the horizontal direction perpendicular to the pipe axis, and 80 cm in the vertical direction perpendicular to the pipe axis.

The boundary condition at the end of the pipeline undergoing the ground displacement was the same amount of displacement as the ground displacement. The boundary condition at the end not undergoing the ground displacement was fixation.

Properties of Pipeline Material

The pipeline material was assumed to present the nonlinear stress-strain characteristics in Table 3.

We developed the numerical analysis model below, to show degradation in strength at bends in the pipeline and bending deformation. Pipe elements located at bends were deleted when the angles of bend reached the angle achieved at the instant of the maximum bending moment of pipe elements. The relationship between the maximum bending moment and the angle of bend is given in Recommended Practice for Design of Gas Transmission Pipelines in Areas Subject to Liquefaction [3]. We used this relationship for the identification of the angle of bend achieved at the instant of the maximum bending moment. More specifically, the angle of bend (ω) achieved at the instant of the maximum bending moment was determined by testing, and we approximated the relationship between this angle and the ratio of pipe diameter to wall thickness (D/t), using a hyperbolic curve. It is shown in Fig. 2. Then, this hyperbolic curve was used to plot the D/t values of the pipelines for determination of their ω values.

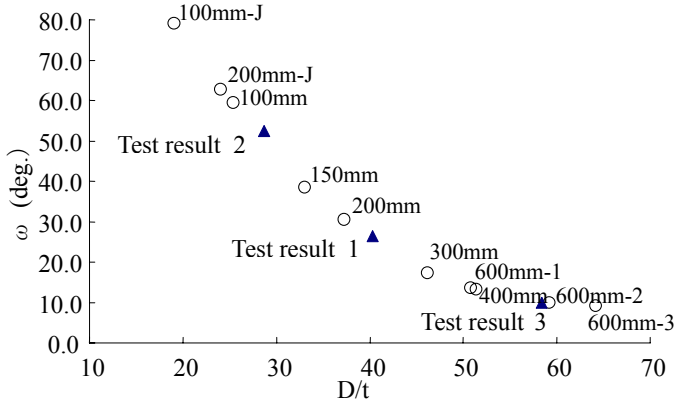

ω : the angle of bend achieved at the instant of the maximum bending moment(deg.)

Fig. 2 Angle of bend achieved at the instant of the maximum bending moment (ω), versus ratio of pipe diameter to wall thickness (D/t)

Table 3 Stress-Strain Characteristics of Pipeline Material

Material	$\sigma y(N/cm^2)$	$E_T(N/cm^2)$	Name in This Report
SGP	$2.872x10^4$	0.00177E	100A ~ 400A
STPY	$3.963x10^4$	0.00245E	600A-3
API X42	$4.093x10^4$	0.00252E	600A-2
API X52	$4.510x10^4$	0.00278E	200A-J , 600A-1

Ground Spring Characteristics

We used the spring characteristics specified in Seismic design guideline of high-pressure gas pipelines [4] and Recommended Practice for Design of Gas Transmission Pipelines in

Areas Subject to Liquefaction [3] as ground spring characteristics. Figure 3 through 5 show the spring characteristics. The spring constants specified in Seismic design guideline of high-pressure gas pipelines [4] were applied to the spring in the pipe's axial direction and the spring in the horizontal direction perpendicular to the pipe axis. In the area where the pipeline drives the ground above it in an upwards direction, the spring specified in the Guidelines for Liquefaction and Earthquake-Resistant Designs of High-Pressure Gas Pipelines[3] was used as the spring in the vertical direction perpendicular to the pipe axis. In the area where the ground below the pipeline drives the pipeline up, a linear spring was used, as shown in Fig. 5.

In the area where the pipeline undergoes Z-shaped deformation, it is appropriate to consider that a large relative displacement occurs between the pipe and the ground, resulting in loss of the binding force of the ground. Accordingly, in our modeling, the ground springs attached to the pipe elements in such areas were deleted at the moment the pipe reached an angle of 45 degrees with respect to the horizontal direction.

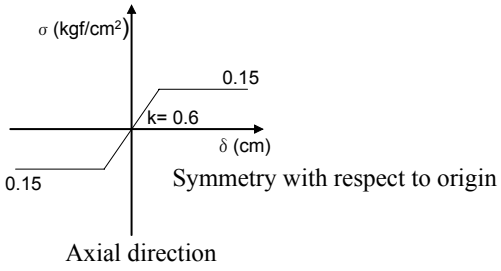

Fig. 3 Ground Spring Characteristics(Axial direction)

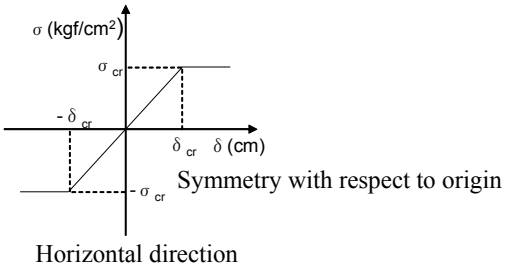

Pipeline	σ cr(N/cm^2)	δ cr(cm)
150mm	51	2.6
200mm	48	2.6
300mm	41	2.7
400mm	39	2.8
600mm	34	2.9

Fig. 4 Ground Spring Characteristics(Horizontal direction)

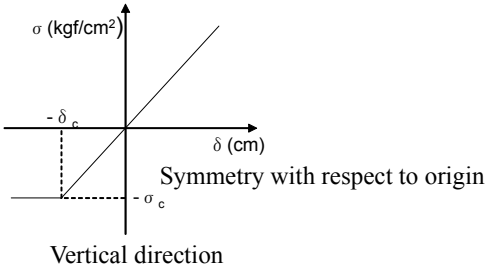

Pipeline	σ c(N/cm^2)	δ c(cm)
150mm	24	0.9
200mm	20	0.9
300mm	15	0.9
400mm	13	0.9
600mm	10	1.0

Fig. 5 Ground Spring Characteristics(Vertical direction)

RESULTS OF ANALUYSIS OF GAS PIPELINES UNDERGOING BENDING DEFORMATION IN THE CHICHI EARTHQUAKE

Figures 6 show 200mm-size pipeline undergoing deformation.

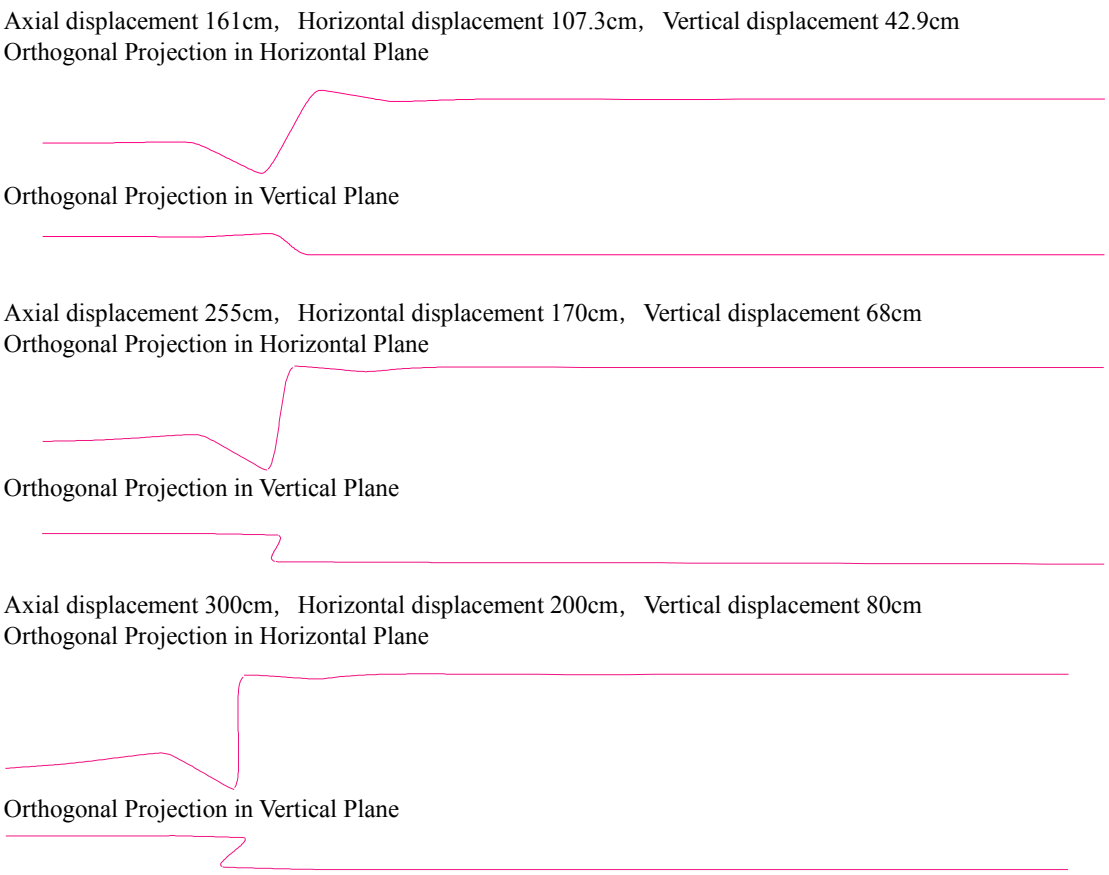

Fig. 6 200mm-Size Pipeline Undergoing Deformation

The 200mm-sized pipeline deformed in the following manner: 1) The maximum moment was reached at an axial displacement of 161 cm, the angle of bend being 63 degrees. 2) The bending deformation began to form a Z shape at an axial displacement of 255 cm. 3) Z-shaped deformation with two bends was completed at the maximum axial displacement of 300 cm. The length between the bends was 250 cm.

The shapes of deformation in pipe obtained through the analysis approximate the actual shapes of deformation shown in Photo 1.

Thus, the analysis method presented in this report has been proven to be effective for the analysis of bending deformation in buried pipelines undergoing substantial fault displacements.

RESULTS OF CASE STUDIES

We applied the analysis method described in the previous section to various pipelines in actual use. Figure 7 shows the final shapes of deformation. These diagrams are drawn as an orthogonal projection of the deformation in a plane containing straight pipeline sections on the right and left of the point of deformation.

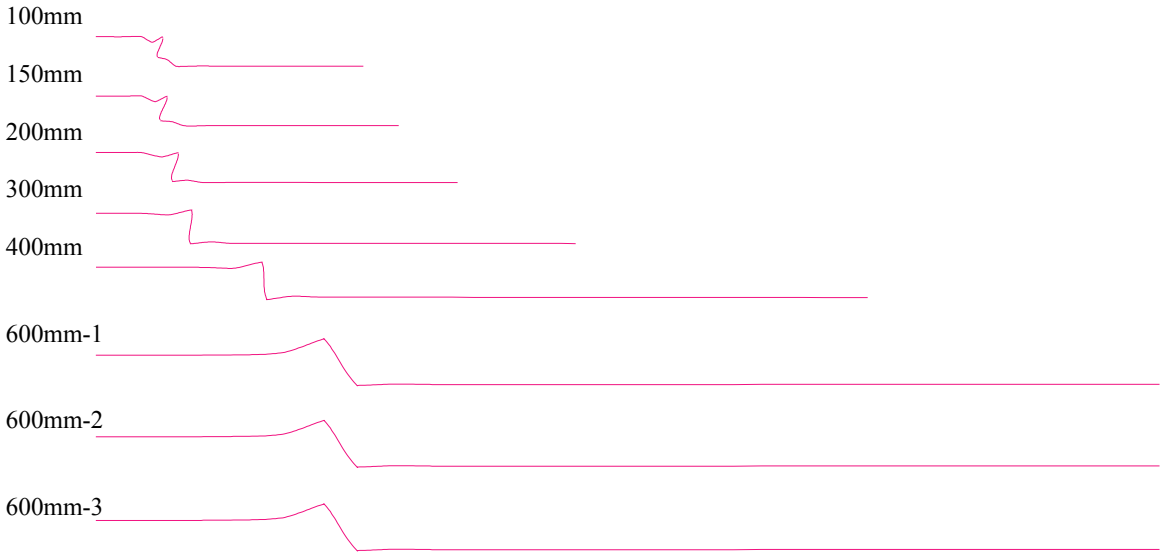

Fig. 7 Final Shapes of Deformation
(axial displacement: 300 cm; horizontal displacement: 200 cm; vertical displacement: 80 cm)

The smaller the pipe diameter, the greater the number of bends, the more complicated the deformation, and the shorter the length between the bends. Conversely, the larger the pipe diameter, the fewer the number of bends, the simpler the deformation, and the longer the length between bends.

Figure 8 shows the relationship between bend-to-bend length and the ratio of pipe diameter to wall thickness(D/t). The broken lines in the diagram link materials of the same stress at yield. According to Fig. 9, the larger the ratio of pipe diameter to wall thickness, the longer the bend-to-bend length. Also, it indicates a tendency for the bend-to-bend length to increase with increasing stress at yield.

SAFETY EVALUATION OF PIPELINES

It is important for our business to ascertain how much ground displacement the pipelines currently in use can withstand in the event of a ground displacement of similar magnitude to that discussed in this report.

Fault displacement at the instant of maximum moment

Figure 9 shows the relationship between fault displacement and ratio of pipe diameter to wall thickness. This relationship is seen when a bend in the pipeline reaches the angle of bend achieved at the instant of maximum bending moment.As shown in Fig. 9, there is a hyperbolic relationship between fault displacement and ratio of pipe diameter to wall thickness ratio at the instant of maximum bending moment. In other words, the smaller the ratio of pipe diameter to wall thickness, the larger the fault displacement, and vice versa.

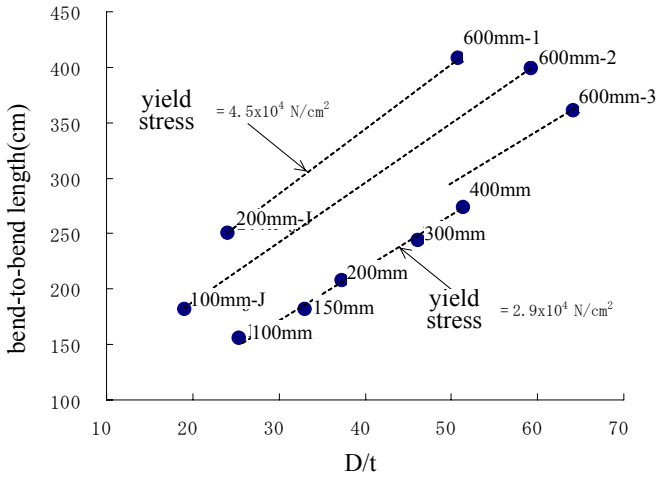

Figure 8 Relationship between bend-to-bend length and ratio of pipe diameter to wall thickness

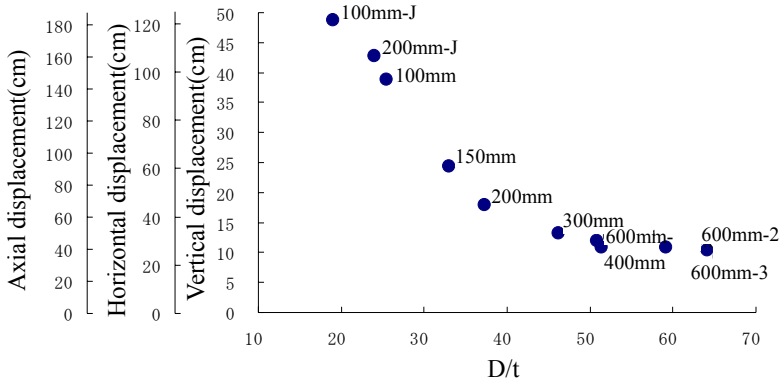

Fig. 9 Relationship between Fault Displacement and D/t at the Instant of Max Bending Moment

Fault displacement at the instant of critical angle of bend

Figure 10 shows the relationship between fault displacement observed when a bend in the pipeline reaches the critical angle of bend (hereinafter referred to as the "critical fault displacement"), and the ratio of pipe diameter to wall thickness. The critical angle of pipeline bend was calculated by the equation (1) proposed in the Guidelines for Earthquake-Resistant Designs of High-Pressure Gas Pipelines[4]

There is an approximately linear relationship between the fault displacement observed when a bend in the pipeline reaches the critical angle of bend, and the ratio of pipe diameter to wall thickness, as shown in Fig. 10. In other words, fault displacement increases with increasing ratio of pipe diameter to wall thickness.

$$\omega_{sc} = \left\{ \frac{44 t_s}{100 D} \left(8k - \frac{2k^2}{3} \right) + \frac{3.44}{\sqrt{2} \cdot \sqrt{D/t_s}} \left(1 + \frac{\varepsilon_f}{2} \right) \right\} \cdot \frac{180}{\pi} \qquad (1)$$

where,

ω_{SC}: critical angle of bend of straight pipe (deg.)

D: outside diameter of straight pipe (cm)

t_S: nominal wall thickness of straight pipe (cm)

L_S: reference length for determination of axial compression deformation and angle of bend of straight pipe (= 64・D)

ε_f: 0.35

k: ratio of $L_S/2$ to outside diameter D (= 3.2)

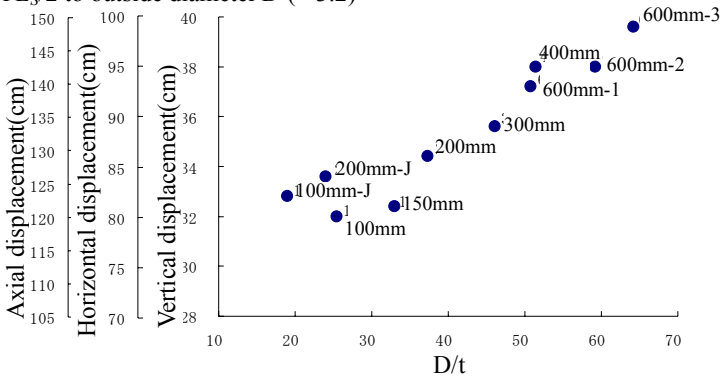

Fig. 10 Relationship between Fault Displacement at the Instant of Critical Angle of Bend and Ratio of Pipe Diameter to Wall Thickness

CONCLUSION

(1) We have developed an analysis method used to express bending deformation subjected to fault in pipelines for numerical calculation.

(2) This method is effective for reproducing the bending deformation in 100mm- and 200mm-size pipelines observed in the Chichi earthquake.

(3) According to the investigation of the relationship between bend-to-bend length and D/t through this analytical model, it indicates a tendency for the bend-to-bend length to increase with increasing stress at yield.

(4) We have ascertained how much ground displacement a pipeline can withstand, through calculation of the ground displacement occurring at the instant of a pipeline's critical displacement.

It is necessary to make further study of ground spring characteristics, amounts of fault displacements and their directions, and deletion methods for pipe elements in bends and ground springs presented in this report.

REFERENCES

[1]Chichi (Taiwan) Earthquake Study Team. , April 2000,*The 1999 Chichi (Taiwan) Earthquake Study Report — On Gas Transmission Pipelines*.

[2]ADINA R&D, Inc. , August 2000, *ADINA Theory and Modeling Guide, Report ARD 00-7*.

[3]Gas Facilities Engineering Standards Investigation Committee, Japan Gas Association. , December 2001,*Recommended Practice for Design of Gas Transmission Pipelines in Areas Subject to Liquefaction*.

[4]Gas Facilities Engineering Standards Investigation Committee, Japan Gas Association. , March 2001,Seismic design guideline of high-pressure gas pipelines.

[5]Proceedings of the Fourth China-Japan-USA Trilateral Symposium on Lifeline Earthquake Engineering, October 2002,*NUMERICAL STUDY FOR RUPTURE BEHAVIOR OF BURIED GAS PIPELINE SUBJECTED TO SEISMIC FAULT DISPLACEMENT*.

Design Considerations to Ensure Pipeline Integrity at Fault Crossing

Nobuhisa Suzuki, Hiroya Kishino, Koji Yoshizaki and SusumuYasuda

ABSTRACT

A design aspect of welded pipelines across a surface fault is presented in this paper focusing on pipe-soil interaction and workhardenability of a high-strength linepipe. A series of strike-slip mode shear model tests were conducted using a split box to investigate the pipe-soil interaction near the surface fault. Based on the test results, three types of soil spring models were employed to compare their effects on deformation of the high-strength pipeline buried across the surface fault. Also, workhardening properties of the pipe were taken into account for finite element analyses for the comparison. Pipeline integrity is evaluated based on the bending moment capacity and critical longitudinal compressive strain associated with local buckling of the buried pipeline pressurized.

INTRODUCTION

Fault crossing is one of the most important issues for seismic design of buried pipelines as well as liquefaction-induced permanent ground deformation (PGD). Damage to the buried pipelines across a fault has been highlighted after the 1999 Chichi earthquake in Taiwan and the 1999 Kocaeli earthquake in Turkey, because such kind of damage caused by the surface fault rupture had not been reported after recent earthquakes before the two big earthquakes. Fortunately, a small diameter gas pipeline survived a normal-slip fault appeared during the 1987 Edgecumbe earthquake in New Zealand. According to the latest reports, we had cosmetic effects on an above ground large diameter pipeline due to another big earthquake in Alaska, the 2002 Denali Fault earthquake.

Especially, high-strength and high-pressure pipelines should be ensured their pressure integrity even under the effects of the fault movements. In order to obtain useful data for the seismic design of the buried pipelines, a series of model tests was conducted using a split box in which a small diameter copper pipe was buried and the effect of a right-lateral strike-slip fault was simulated. Based on the test results, multi-linear soil springs considering reduction of subgrade reaction were introduced for finite element analyses to compare with a bilinear spring model, which has been taken into account in the current seismic design codes of the buried pipelines in Japan. Finite element analyses were also conducted to compare the effects of the workhardenability on the pipeline at the fault crossing. The pipeline integrity was investigated based on the results of the finite element analyses regarding deformability and resistance of the high-strength linepipes.

Nobuhisa Suzuki, Senior Researcher, Research & Development Division, JFE/NKK Corporation, 1-1 Minami-Watarida, Kawasaki, Japan 210 -0855

Hiroya Kishino, Manager, Pipeline Maintenance Technology Group, Pipeline Div., Tokyo Gas Corporation, 1-5-20 Kaigan, Minato-ku, Tokyo, Japan 105-8527

Koji Yoshizaki, Senior Researcher, Pipeline Technology Research Center, Tokyo Gas Corporation, 1-7-7 Suehiro-cho, Tsurumi-ku, Yokohama, Japan 230-0045

Susumu Yasuda, Professor, Dept. of Civil and Environmental Engineering, Tokyo Denki University, Hatoyama, Hiki-Gun, Saitama 350-0394 Japan

SURFACE FAULT RUPTURE OBSERVED AFTER RECENT EARTHQUAKES

The 1999 Kocaeli Earthquake in Turkey

A belt of alluvial lowland extends from the south coast of Izumit Bay to Adapazarı City through Lake Sapanca. A surface fault appeared during the 1999 Kocaeli earthquake and run from the east to the west through the lowland region. After the earthquake, several kinds of damage to lifeline facilities were observed, which were associated with the surface fault rupture. And loss of coastal lands and ground subsidence were also reported in this lowland region. A welded water transmission line, 2.4m in diameter, was damaged at several sites at Kullar due to the surface fault rupture in a right-lateral strike-slip mode. Figure 1 and Photo.1 show a schematic illustration and the surface fault rupture at the site near the pipeline was damaged, respectively. The lateral displacement of the fault rupture was reported as large as 3.2m based on of the discrepancy of a split wall. And the observed crossing angle between the fault and the transmission line was about 60 degrees.

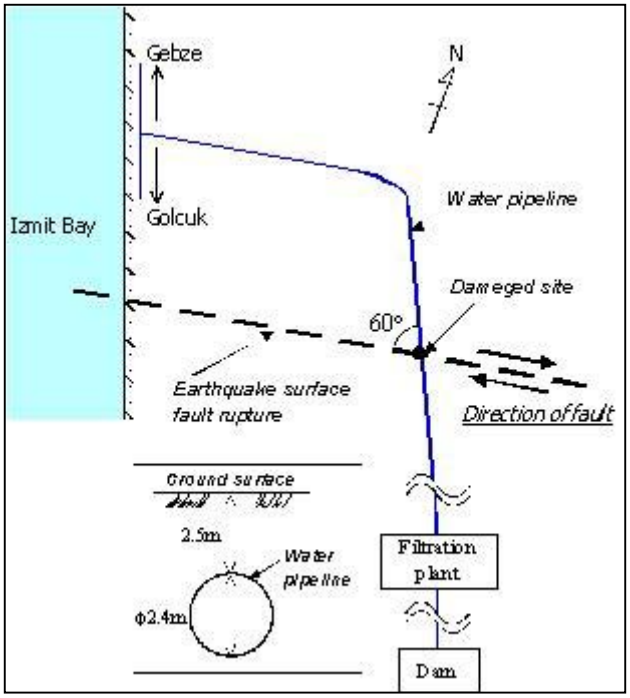

Fig.1 Schematic illustration at the site where the damage to a water main observed, Turkey

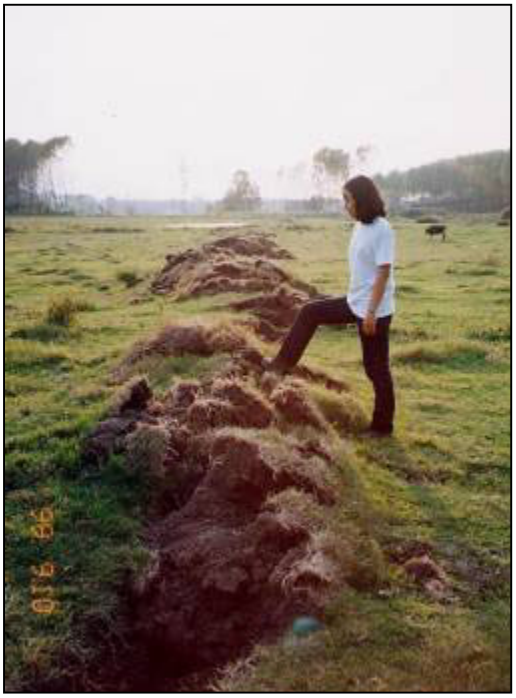

Fig.2 Surface fault rupture near the site near the water main damaged

The 1999 Chichi Earthquake in Taiwan

A lot of huge surface fault ruptures appeared during the 1999 Chichi earthquake, which moved in an oblique thrust mode. The total length of the fault rupture was estimated as long as 125km. According to the report, the maximum vertical displacement reached almost 10m, due to which a dam, several road bridges, many buried pipelines, transmission towers were severely damaged. Also a number of damage to water pipelines and gas pipelines were reported. As shown in Photo.2, two

welded gas pipelines were deformed largely due to the surface fault rupture on an approach road to Wu-Xi Bridge, whose diameters were 6 and 8 inches. Photo.3 represents the fault rupture associated with the damage to the two pipelines, which was taken one month after the earthquake.

Photo.2 Deformation of a buried gas pipeline near Wu-Xi Bridge in Taiwan

Photo.3 Surface fault associated with the damage to the buried gas pipelines

The 1987 Edgecumbe Eearthquake

A surface fault rupture was observed after the 1987 Edgecumbe earthquake at Whakatane in New Zealand, which was a normal-slip fault as shown in Photo.5. According to a report (Berrill, 2001) regarding the fault, the vertical and horizontal dislocations were estimated to be 2.2 and 1.2m, respectively. Despite the large displacement of the surface fault rupture, the welded gas pipeline of 4in. (114mm) diameter survived the normal-slip fault as shown in Photo.4 owing to a crossing angle between the pipeline and the fault plane, which was estimated to be about 45 degrees.

Photo.4 Buried gas pipeline survive the surface fault rupture at Wakatane in New Zealand

Photo.5 Surface fault rupture observed at the site shown in Photo.4

EXPERIMENTS ON SUBGRADE REACTION AT SURFACE FAULT CROSSING

Model Shear Test

Model shear tests were conducted to investigate pipe-soil interaction or subgrade reaction at the fault crossing. A split box shown in Fig.2 and Photo.6 were used, in which a fixed box and a movable box can be seen. Photo.6 represents the split box showing shear deformation at the fault plane. The soil used for the experiments was medium sand with 3.4% of fines content and the grain-size distribution curve is represented in Fig.3. Small diameter copper pipes were used for the experiments. Wire strain gauges were attached on the outer surface of the model pipes as shown in Photo.8. Each model pipe was buried in the model ground with various burial depths. Then, horizontal displacement was introduced up to 10cm by pulling the movable soil box to induce shear rupture.

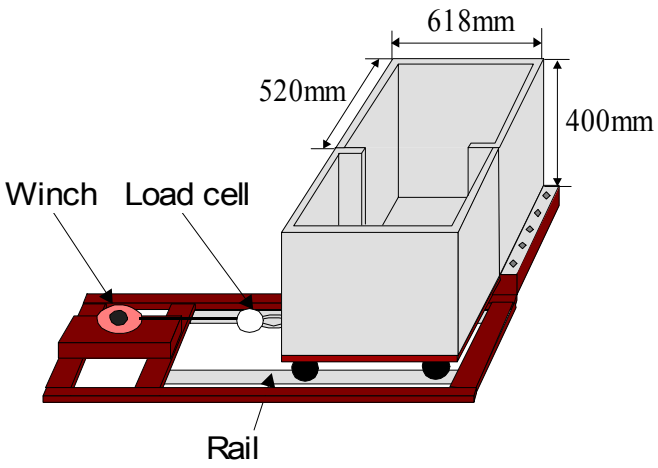

Fig.2 Shear box and test equipment

Photo.7 Shear deformation of the soil box with a buried pipeline

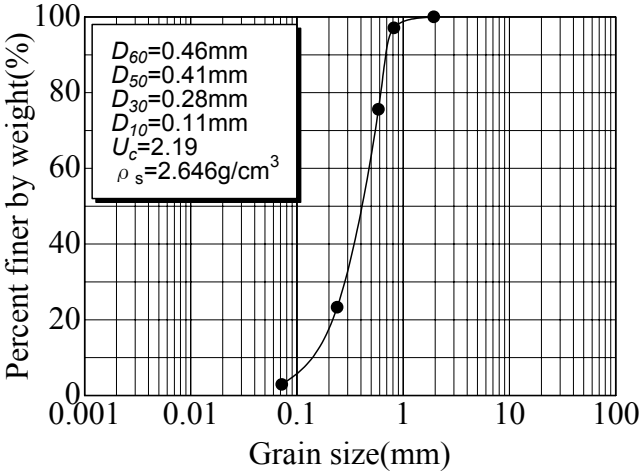

Fig.3 Grain-size distribution curve of tested sand

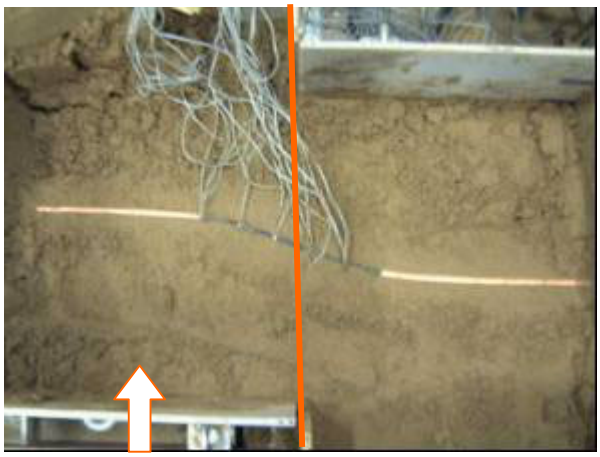

Photo.8 Deformed pipe after a shear test (Solid line represents a fault line)

Pipe diameters of 10.0, 15.9 and 19.1mm and burial depths of 2 to 20mm were employed in the experiments. And crossing angles between the pipe and the fault plane were set to be 60, 90 and 120 degrees. Furthermore, degrees of compaction of the model ground were 95 and 100%. Photo.8 shows a deformed pipe for an example, in which we can observe the maximum bending deformation at about 10cm from the shear plane, the fault rupture plane.

Subgrade Reaction

Longitudinal strains of the tested pipes were measured at several points by wire strain gauges, based on which the deformations of the tested pipes were calculated. As shown in Photo.8, displacements at both ends of the tested pipes coincided with those of the sand boxes. Therefore, we can estimate the relative displacements between the pipe and the sand box. Then the subgrade reactions along the pipes were estimated based on the deformations (Yasuda et al., 2002).

Figures 4 and 5 show relationships between the subgrade reaction and the relative displacement of the tested pipes with different burial depths. Figure 4 represents the subgrade reaction of the cases with the burial depth of 2cm, the shallow models. As shown in Fig.4, the subgrade reactions increase with increasing relative displacement up to 0.7 to 1.0cm, where they show their own peaks. The subgrade reactions tend to decrease with increasing relative displacement after showing their own peaks, and become to be stable where the subgrade reactions were estimated to be about 40 to 60% of the corresponding peak value of the subgrade reactions.

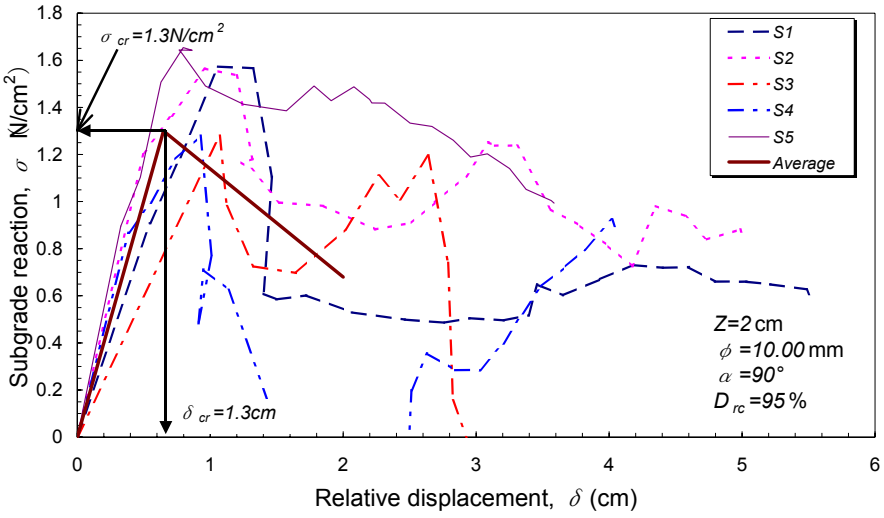

Fig.4 Relationships between relative displacement and subgrade reaction (Z=2cm)

Figure 5 shows the relationships between the subgrade reaction and the relative displacement regarding the experiments with the burial depth of 20cm, which are consistent with the deep model. The subgrade reactions increase with increasing relative displacement and show their peaks where the relative displacements are greater then 4cm. The relationships represented in Fig.5, the deep models, can be idealized by bilinear models, which are different from those of the above-mentioned shallow models. The difference between the relationships can be explained such the effect of the burial depths that slip lines appeared to the ground surface for the shallow model cases however the slip lines could not appear to the surface in the cases of the deep model.

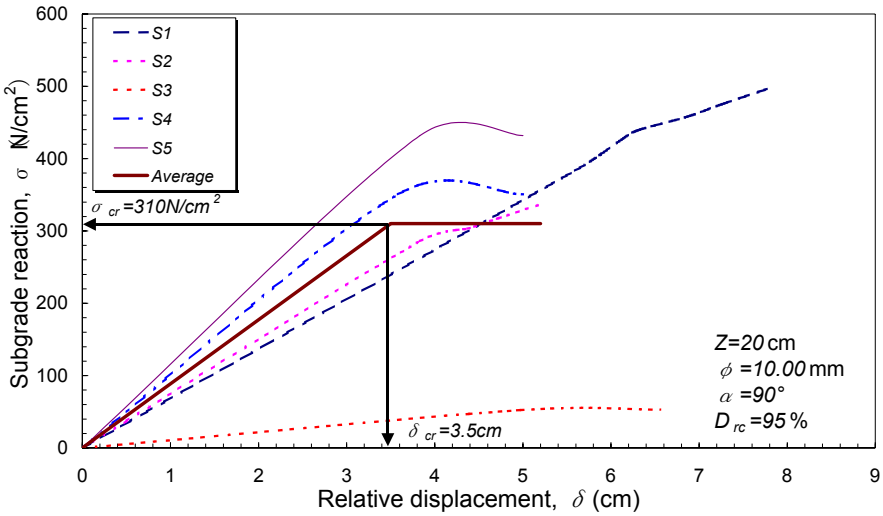

Fig.5 Relationships between relative displacement and subgrade reaction (Z=20cm)

DEFORMATION OF A BURIED PIPELINE ACROSS A STRIKE-SLIP FAULT

Assumptions for Finite Element Analyses

Finite element analyses of a buried pipeline were conducted providing 610mm OD, 12.2mm WT, API 5L X80 grade linepipe, the burial depth of 1.5m and the design factor of 0.8. In the finite element analyses, the pipe was idealized by four-node shell elements and the subgrade reaction was modeled by truss elements. Mesh idealization using the shell elements with a uniform size of 39.1mm wide and 50.0mm long was used for the finite element analyses, where the circumference of the pipe was divided into 48 segments and the aspect ratio of the shell elements became 1.28.

As for the subgrade reaction, two types of the relationship in terms of the relative displacements were obtained through the experiments, the shallow and the deep models. The subgrade reaction models shown in Fig.6 were used for the finite element analyses, in which shallow models show the reduction of the subgrade reaction and the bilinear model of the deep model. In spite of the shallow burial depth of the finite element model, 1.5m, the bilinear model consistent with the deep model was applied to the analyses because that had been defined in several seismic design codes in Japan even for the pipelines buried in comparatively shallow depths. Therefore, three soil springs are given in the figure, in which SPR1-spring is a bilinear model defined by JGA (2000). SPR2 and SPR3 are the soil spring models having reduction of the subgrade reaction, which initiate from the relative displacements equal to the pipe diameter and 50% of the pipe diameter, respectively.

Besides the three types of the subgrade reaction model, two types of the stress-strain relationship of the X80 pipe, shown in Fig.7, are assumed in order to discuss the effect of the workhardenability on the deformability of the high strength pipeline. The notations of HD and ST in the figure represent the stress-strain relationships of High Deformability pipes (Y/T=0.77) and STandard pipes (Y/T=0.89), respectively, in which the Y/T ratio represents the yield-to-tensile stress ratio of the pipe. The higher strength pipes tend to have the higher values of the Y/T ratio, which may decrease the deformability.

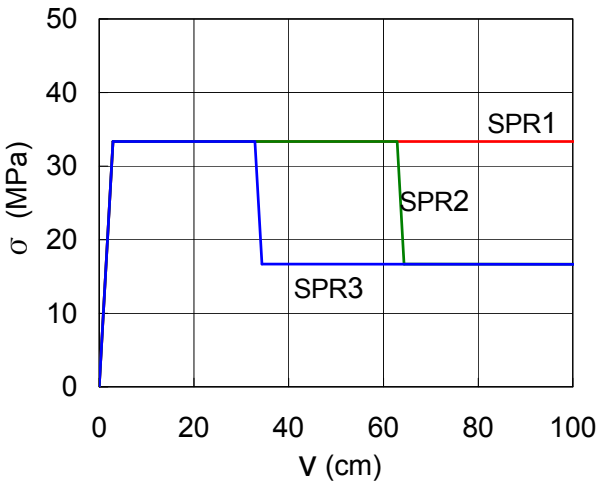

Fig.6 Subgrade reaction models applied to finite element analyses (24in.OD pipe and burial depth of 1.8m)

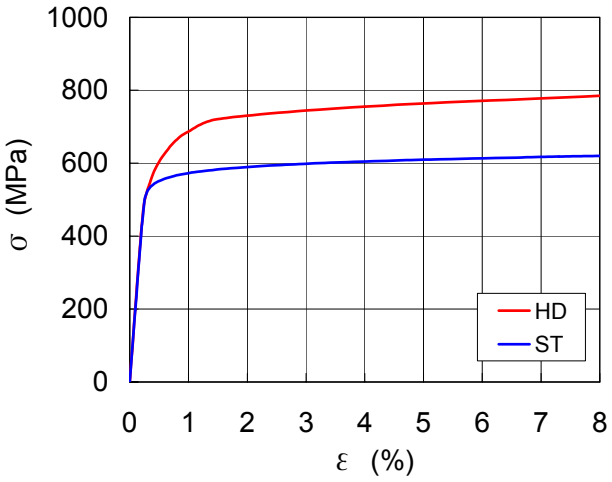

Fig.7 Stress-strain curves of X80 grade linepipes with high-deformability material (HD) and standard material (ST)

Deformation of the Buried Pipeline

Figure 8 shows deformation of the buried pipeline obtained by one of the finite element analyses. The fault plane locates at the center of the figure and the bending deformations of the pipe are concentrated at the both sides of the fault. Figure 9 represents the deformation of the HD-material pipeline with the SPR1-spring, in which the bending deformation of the pipeline propagates 10m from the fault plane when the dislocation is 5m. Figure 10 shows the results of the HD-material and the SPR3-spring, in which the deformations are almost the same as those in Fig.9 at a glance.

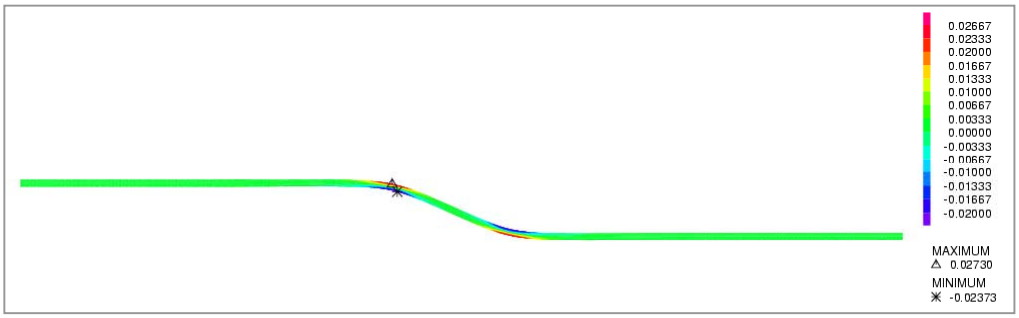

Fig.8 Deformation of the buried pipeline

Figure 11 shows a comparison of the deformations of the HD-material pipeline with the three spring models. As shown in the figure, the deformations are almost the same. Furthermore, a comparison of the deformations of the HD and the ST-materials is represented in Fig.12. As shown in the figure, the difference is not significant, however the deformation of the HD-material pipeline is slightly smaller than that of the ST-material pipeline. Then, as for the deformation of the pipeline represented in this paper, we can conclude that the effects of the soil springs are not so significant.

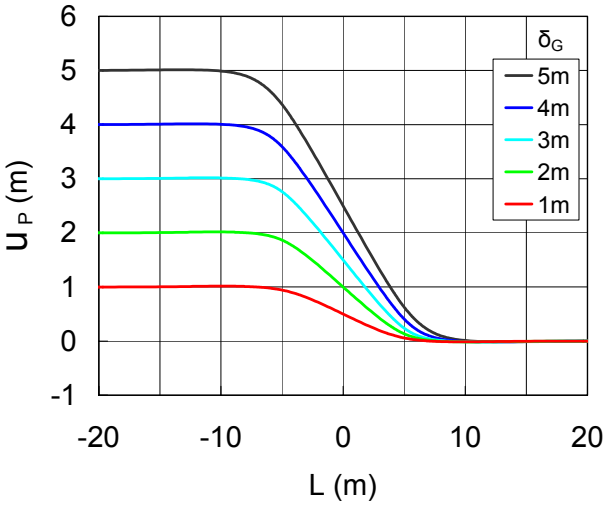

Fig.9 Deformation of buried pipeline (HD-material, SPR1)

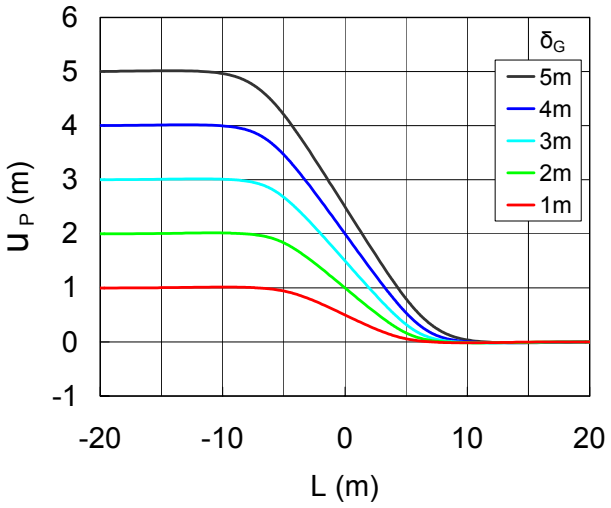

Fig.10 Deformation of buried pipeline (HD-material, SPR3)

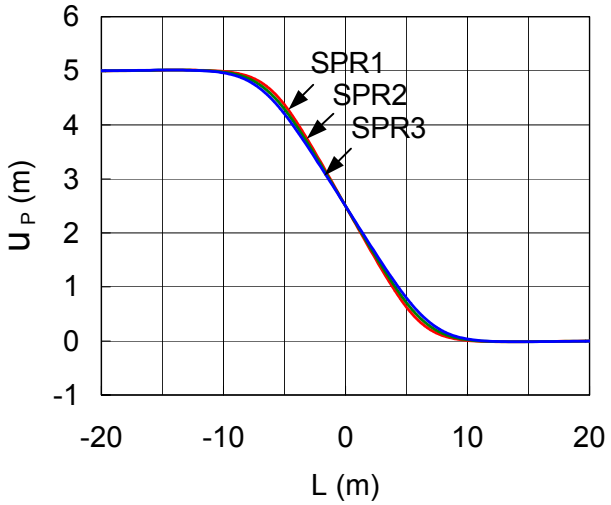

Fig.11 Deformation of buried pipeline (HD-material, Dislocation=5m)

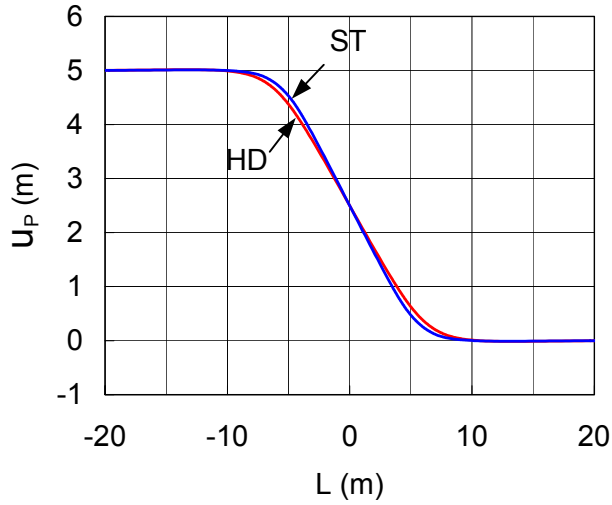

Fig.12 Deformation of buried pipeline (SPR1, Dislocation=5m)

Longitudinal Strain Distributions

Longitudinal strain distributions of the buried pipeline with the dislocations at 3 and 5m are represented in Fig.13, in which we can observe the longitudinal strain spreads over a wide range in the longitudinal direction with increasing dislocation of the surface fault. Max and Min in the figure represent the locations of the maximum longitudinal tensile strain and the maximum longitudinal compressive strain, respectively.

Figures 14 and 15 give the longitudinal strain distributions of the HD and ST-material pipelines with the SPR1-spring, respectively. Figure 16 compares the longitudinal strain distributions of the HD- and the ST-material pipelines at dislocation of 5m, where the maximum longitudinal strain of

the HD-material pipeline is less than that of the ST-material pipeline. Figure 17 shows a comparison of the strain distribution of the three spring models when the dislocation is 5m. The maximum longitudinal strain of the SPR1-spring becomes the largest among them because the large constraint due to the SPR1-spring may be expected compare with the other two soil spring models.

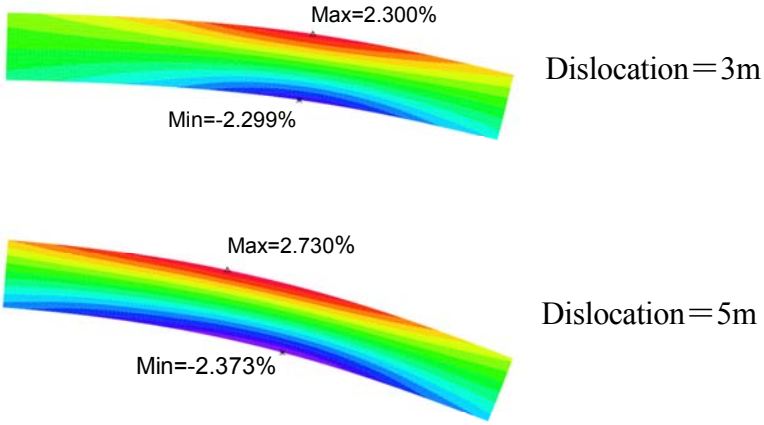

Fig.13 Deformation and longitudinal strain distribution of buried pipeline

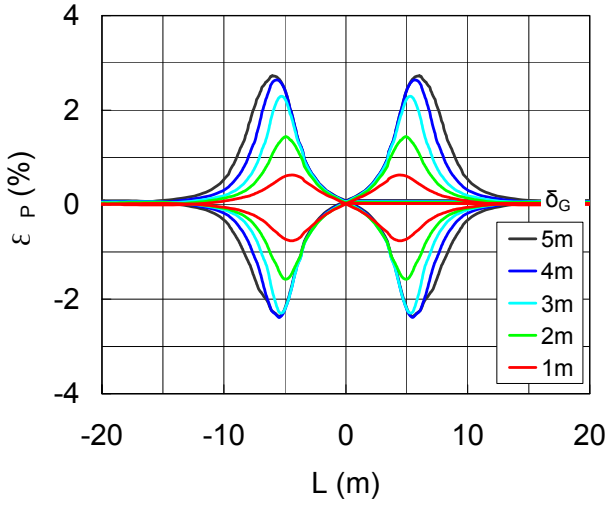

Fig.14 Longitudinal strain distribution (HD-material, SPR1)

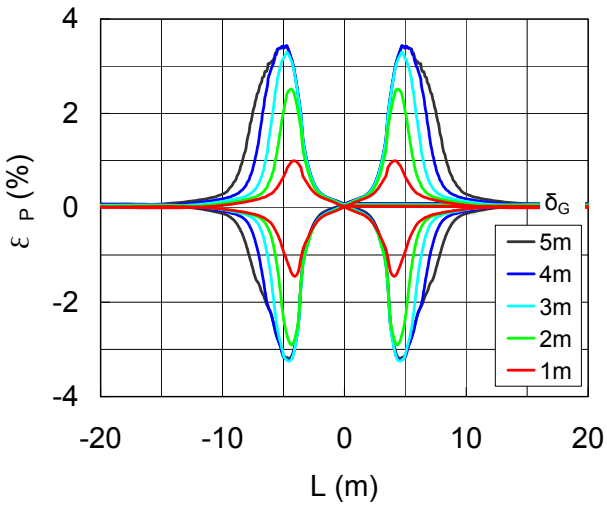

Fig.15 Longitudinal strain distribution (ST-material, SPR1)

Discussion of Pipeline Integrity Regarding the Maximum Longitudinal Strain

Figure 18 gives relationships between the maximum longitudinal strain of the HD-material pipeline and the surface fault dislocation. The maximum compressive strain increases linearly until the dislocation is 3m, and the strain becomes constant with the fault dislocations ranging from 3 to 4m. The maximum tensile strain behaves almost the same as the compressive strain. And the maximum longitudinal strain seems to be slightly dependent on the soil spring models defined in this paper.

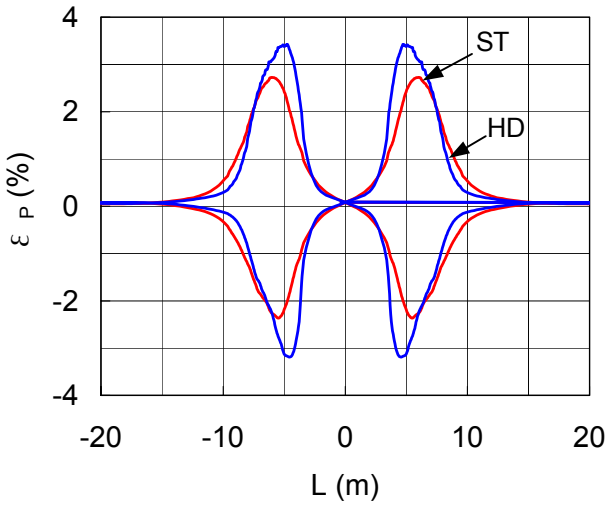

Fig.16 Longitudinal strain distribution (SPR1, Dislocation=5m)

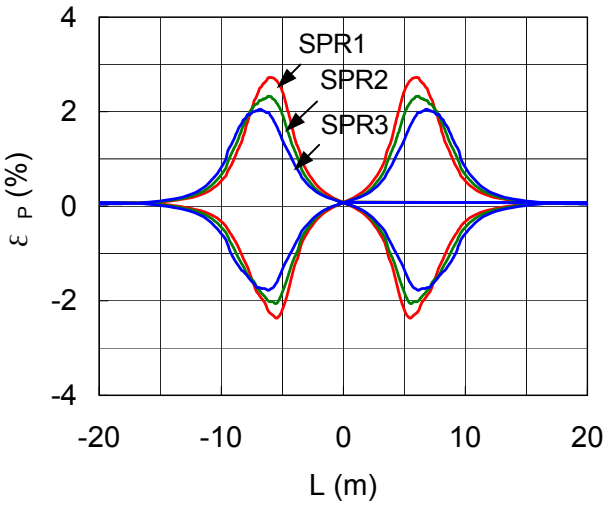

Fig.17 Longitudinal strain distribution (HD-material, Dislocation=5m)

Figure 19 shows a comparison between the maximum longitudinal strains of the HD-material and the ST-material pipelines. The variation of the longitudinal strains of the HD-material pipeline was as mentioned above, however the strains of the ST-material increase linearly until the dislocation is less than 2m and become constant beyond the critical dislocation.

The maximum longitudinal compressive strains of the HD- and the ST-material pipelines are 2.3% and 3.2%, respectively. On the other hand, the critical longitudinal strains of the HD- and the ST-material pipelines can be estimated to be 5.5% and 2.8%, respectively, in accordance with Suzuki and Toyoda (2002). Therefore, pipeline integrity can be assured for the HD-material case however the ST-material may collapse at the fault crossing with the dislocation less than 2m in this case. Then we can conclude that the workhardenability is a significant parameter to ensure the pipeline integrity.

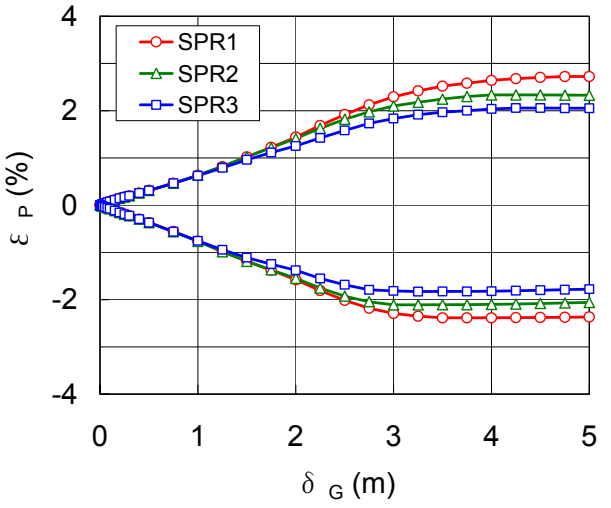

Fig.18 Maximum longitudinal strain vs. dislocation of surface fault (HD-material pipeline)

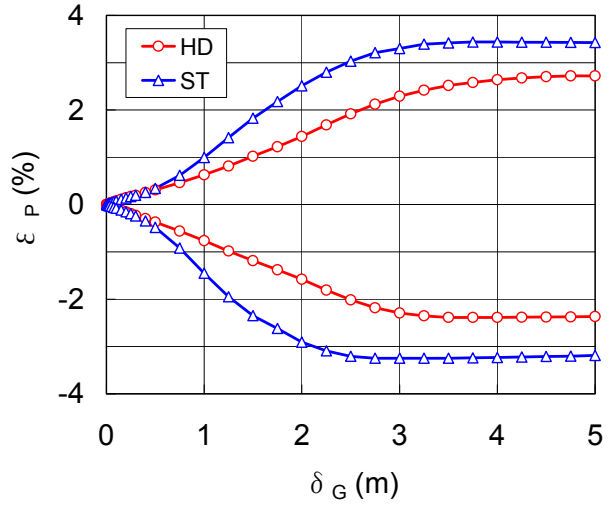

Fig.19 Maximum longitudinal strain vs. dislocation of surface fault (SPR1-spring)

CONCLUSIONS

Damage to the buried pipelines was introduced in connection with the surface fault movements in order to show the background of our research in this paper. In order to investigate the subgrade reaction, model tests were performed. Pipeline integrity of a 24in. OD, X80 high-pressure pipeline was discussed taking the subgrade reaction models and the workhardenability of the pipe into account. Our study in this paper can be summarized and concluded as follows.

The subgrade reaction reduces after showing peak resistance when a burial depth is shallow, in which the coverage is from one to two times larger than the pipe diameter. The subgrade reaction reduces and become to be stable where the value is approximately 50% of the peak resistance. On the other hand, when a burial depth is ten to twenty times deeper than the pipe diameter, the subgrade reaction can be represented by a bilinear function in terms of the relative displacement.

The comparisons regarding the deformations and the longitudinal strains of the buried pipeline employing different subgrade reaction models, which are the bilinear model and the reduction models, present the following tendencies. The difference of the deformations of the pipeline were not so significant however the maximum longitudinal strain of the pipeline with the bilinear soil spring model was 30 to 40% larger than that of the reduced spring models. This tendency coincides with the general comprehension concerning the fact that the bilinear model gives a conservative solution.

As for the effect of the workhardenability of the pipe, the deformations and the longitudinal strains of the pipeline were compared considering the high and the low values of the Y/T ratio, which were 0.89 and 0.77. Similar tendencies to the effect of the soil spring models were observed in terms of the deformation and the longitudinal strain. The deformations of the pipe with the two Y/T ratios were almost the same however the maximum longitudinal strain of the pipeline with the Y/T ratio of 0.89 is 30 to 40 % larger than that of the pipeline with the Y/T ratio of 0.89. This tendency regarding the effect of the Y/T ratio on the pipeline integrity is informative for us because we can increase or improve the pipeline integrity without increasing wall thickness of the pipeline.

ACKNOWLEDGEMENTS

The experiments were conducted by both of Mr. K. Kazami and Miss C. Ihara, former students at Tokyo Denki University. Test results were discussed in a technical committee organized by the Association for Development of Earthquake Prediction (ADEP). The authors would like to express their appreciation to the former students and the members of the technical committee. The authors also wish to thank Mr. I. Kubo of Japan Industrial Testing Co., Ltd. for the finite element analyses.

REFERENCES

JGA (2000): Recommended Practices of the Seismic Design for High-Pressure Gas Pipelines.

ADEP (2001) (Association for the Development of Earthquake Prediction) : Study on the large deformation of the ground (No.4). (in Japanese)

ADEP (2002) (Association for the Development of Earthquake Prediction) : Study on the large deformation of the ground (No.5). (in Japanese)

Suzuki, N. and Toyoda, M. (2002): Seismic Loadings on Buried Pipelines and Deformability of High Strength Linepipes, Application and Evaluation of High-Grade Linepipes in Hostile Environments.

Yasuda, S., Sutani, Y., Suzuki, N. and Isoyama, R. (2002): Countermeasures of Buried Steel Pipes Against Surface Fault Rupture, U.S.-Japan Seminar on Seismic Disaster Mitigation in Urban Area by Geotechnical Engineering.

Centrifuge Modeling of PGD Response of Buried Pipe

Michael O'Rourke, Vikram Gadicherla and Tarek Abdoun

ABSTRACT

Fault crossing, lateral spreads and other types of permanent ground deformation (PGD) are arguably the most severe seismic hazards for continuous buried pipelines. Current analysis and design procedures, to a great extent, are based upon Finite Element (FE) modeling. There are, unfortunately, relatively few full-scale case histories which could be used to benchmark or confirm the applicability of FE assumptions. That is, full-scale field verification of the predicted behavior of buried pipeline subject to PGD is, at best, sparse.

In the paper, a new, centrifuge based, method for determining the response of continuous buried pipe to PGD is presented. Laboratory equipment, similitude relations as well as centrifuge model results are presented. Specifically described are the physical characteristics of RPI's 100 g-ton geotechnical centrifuge and the current lifeline experiment split-box. The split-box contains the model pipeline and surrounding soil and is manufactured such that half can be offset, in flight, simulating PGD. Governing similitude relations which allow one to determine the physical characteristics (diameter, wall thickness, material modulus of elasticity) of the model pipeline are presented.

Finally, recorded strains induced in two buried pipes with prototype diameters of 0.63 m and 0.95 m (24 and 36 inch) subject to 0.6 and 2.0 meters (2 and 6 feet) of full scale fault offsets are presented and compared to corresponding FE results.

Michael O'Rourke, Professor, Civil and Environmental Engineering Department, JEC 4049, Rensselaer Polytechnic Institute, 110 8th Street, Troy, NY 12280-3590
Vikram Gadicherla, Graduate Student, Civil and Environmental Engineering Department, JEC 4049, Rensselaer Polytechnic Institute, 110 8th Street, Troy, NY 12280-3590
Tarek Abdoun, Research Assistant Professor, Civil and Environmental Engineering Department, JEC 4049, Rensselaer Polytechnic Institute, 110 8th Street, Troy, NY 12280-3590

EXPERIMENTAL EQUIPMENT

The Rensselaer Geotechnical Centrifuge facility is located at the basement level of the Jonsson Engineering Center. The centrifuge itself is located in a belowground closed circular roof with a diameter of roughly 6 m (18 feet). Operation of the centrifuge and data acquisition is performed in the adjacent control room. The centrifuge is an acutronic model 665-1.

The in-flight radius of the centrifuge is 3m. The centrifuge is capable of carrying a maximum payload of 1 metric ton at 100 g (i.e. 100 g ton). The maximum speed of the centrifuge is 200 g. The soil model sits on the testing platform which is located at the end of the centrifuge arm. The maximum model or payload dimensions are 100 cm x 80 cm x 80 cm. The transfer of data is enabled by wireless DAQ system and the control signals is enabled by 64 electric slip rings; 50 for analog signals, 12 for power and two for video signals. The hydraulic rotary joints have a total of six passages, two of which are hydraulic oil passages rated at 3000 psi and the remaining four are air/water passages rated at 300 psi.

Split Box

As noted above the split box allows simulation of fault offsets and the relative horizontal displacement at the margins of a lateral spread. The split box has inside dimensions of 1 m x 0.354 m x 0.203 m. It consists of two halves, one is fixed while the other can move horizontally on rollers to simulate an offset. The moving portions of the container are supported and guided using roller bearings to provide precise movement with minimal friction. The sliding interface between fixed and movable portions of the container utilizes low friction Teflon seals protected by steel shields.

A hydraulic cylinder is used to displace the moveable half of the split box. The driving shear force is provided by a 3000 psi hydraulic actuator system, which includes a flow-metering valve, a solenoid valve for remote operation, and hoses for connecting to the centrifuge's quick connects. The load cell, located between the actuator and the movable portion of the split box, measures the force applied by the actuators. The maximum relative displacement of the movable section is 8 cm, simulating 4m offset at 50 g. The flow-metering valve controls the rate of movement of the split box. The motion of the actuator is controlled by a servo valve and a feedback control system, while an LVDT measured the offset

Anchor Points

The connection between the pipe model and the split box end walls consists of a steel rod that sits in one of the metal plates attached to the split box wall. This assembly allows the pipe to rotate freely about the vertical axis. The assembly also has space for two LVDTs, which can measure the rotation of the pipe model at the support. This assembly is covered by a plastic enclosure and rubber sheeting to prevent the entry of sand near the LVDTs.

Instrumentation and Data Acquisition System

Strain gauges were installed on the pipe model to measure the axial and bending strains at various points. The strain gages were model CEA-032UW-120 from the Measurements Group

Inc. Ten strain gauges were set in a quarter bridge configuration and the remaining four strain gauges in a half bridge configuration.

The data acquisition system is capable of recording 128 channels of data at a 10 kHz sampling rate per channel. A Pentium 4 PC generates the digital input signal, which causes the split box to move by the desired offset. The servo controller on the centrifuge arm receives the signal through the slip rings. A hydraulic pump is used to pressurize the actuator in the split box before sending the signal.

CENTRIFUGE MODELING

For problems in which soil-structure interaction forces are dominate, small-scale models by themselves cannot replicate similar stresses at comparable points on the model and the prototype. This is because soil loading and stiffness at a particular depth are related to the self-weight of the soil above. For example, the vertical stress at a depth of 10 m for a soil having a density of 10 KN/m^3, would be 100 KPa. However, in a tenth scale model, the stress at the corresponding location (i.e. 1 m depth in the model) in the same soil is only 10 KPa. As a result, the similitude of soil-structure interaction forces is not maintained. This difficulty can be overcome by effectively increasing the weight of soil by a factor of 10. In a centrifuge, this is accomplished by spinning at a speed corresponding to a centrifugal acceleration of 10 times the earth's gravity (10 g). This is the underlying concept behind centrifuge modeling of soil and soil- structure systems. A partial list of scaling law in terms of a centrifugal acceleration Ng is presented in Table I.

TABLE I SELECTED SIMILITUDE RELATIONS FOR CENTRIFUGE MODELING

Parameter	Model units	Prototype units
Length	1/N	1
Strain	1	1
Stress	1	1
Axial rigidity	$1/N^2$	1
Flexural rigidity	$1/N^4$	1

This concept has been used extensively to study the effect of explosions on soil, the response of piles subjected to earthquake effects and a number of other geotechnical problems. The purpose of the experiments described herein, is to study the response of a continuous buried pipeline subjected to fault movements.

When modeling the response of the buried pipe to fault movement, care must be taken to maintain similitude. In terms of soil, soil similitude is maintained by using the same type of soil in the model as exists for the prototype. This ensures that both the soil density and friction angle in model and prototype match. For buried pipe, the longitudinal forces at the soil-pipe interface are influenced by the roughness of the pipe surface. Hence, this quantity should be similar in both model and prototype. Finally, since the soil forces acting on the pipe are linearly proportional to the pipe diameter, the pipe diameter needs to scale as N.

In relation to the buried pipe, the similitude of axial force effects is maintained if the axial rigidity, EA, (the product of modulus of elasticity and cross section area) scales by a factor of $1/N^2$, when the model is subjected to a centrifugal acceleration of Ng. Note, that stress has the same dimensions or units as modulus of elasticity (psi, ksi, etc.) and hence from Table I both have a scaling factor of 1. However, again from Table I, area (having units of length squared) scales by a factor of N^2. Hence, axial rigidity, which is the product of modulus of elasticity and area, scales as

$$\frac{E_p A_p}{E_m A_m} = N^2 \tag{1}$$

where E is the modulus of elasticity, A is the cross-sectional area while m and p refer to model and prototype respectively. When the wall thickness to diameter ratio, t/d, is small, the area may be approximated as $A = \pi dt$. Hence, the scaling relation to maintain similitude for EA becomes

$$\frac{E_p t_p d_p}{E_m t_m d_m} = N^2 \tag{2}$$

As noted above, the ratio of diameters d_p/d_m scales with N to ensure similitude of soil forces on the pipe interface, hence Equation (2) becomes

$$\frac{E_p t_p}{E_m t_m} = N \tag{3}$$

which is the scaling relation for EA.

In order to maintain the similitude of bending moment in the buried pipe the flexural rigidity, EI, needs to be scaled as

$$\frac{E_p I_p}{E_m I_m} = N^4 \tag{4}$$

where I is the moment of inertia for the pipe. When the t/d ratio is small, the moment of inertia may be approximated as $I = \pi d^3 t/8$. Hence, EI similitude requires

$$\frac{E_p d_p{}^3 t_p{}^3}{E_m d_m{}^3 t_m{}^3} = N^4 \tag{5}$$

However as noted before, d_p/d_m scale as N, hence the similitude relation for EI is identical to that for EA as given in Equation (3).

CENTRIFUGE TESTS

Two pipelines were tested in the Rensselaer centrifuge. The diameter and wall thickness of the steel prototype lines are listed in Table II. The diameter and d/t ratios are common for larger gas and liquid fuel pipe in the U.S.

Commercially available small diameter pipe typically do not have such large d/t ratios. For that reason, aluminum was chosen as the model pipe material. That is, since E_m/E_p for the aluminum model and steel prototype is about 0.30, the scale factor for wall thickness was 0.3 (50) or 15 in order that equations (3) and (5) are satisfied. The resulting diameter and wall thickness for the models are also presented in Table II.

Figures 1 through 4 show the axial and bending strains along the pipe as measured by strain gauges on the Pipeline #1 model. The strains in Figure 1 are for an offset of 0.4 cm while the offsets for Figures 2 through 4 are 0.8, 1.2 and 1.6 cm respectively. The largest of these correspond to a prototype offset of 0.8 m at 50 g.

As one would expect, the bending and axial strains are increasing functions of the offsets. For these tests with a 90° interaction angle between the pipe axis and the fault trace, the bending strains dominate. Also note that the fault location is a point of counter flexure (i.e. zero bending moment) due to the asymmetric nature of the offset.

TABLE II. PIPELINE PROPERTIES

Property	Pipeline #1		Pipeline #2	
	Prototype	Model	Prototype	Model
Diameter	0.64 m (25 in)	1.27 cm (.5 in)	0.95 m (37 in)	1.9 cm (.75 in)
Wall thickness	1.1 cm (.43 in)	0.71 mm (.0279 in)	1.85 cm (0.73 in)	1.27 mm (0.05 in)

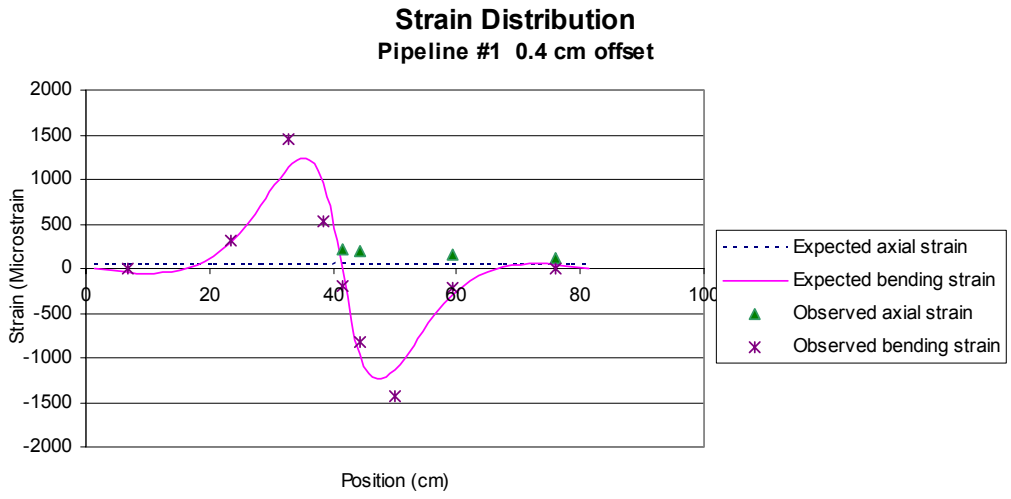

Figure 1. Measured and Simulated Strains for Pipeline #1 Model Subject to an Offset of 0.4 cm

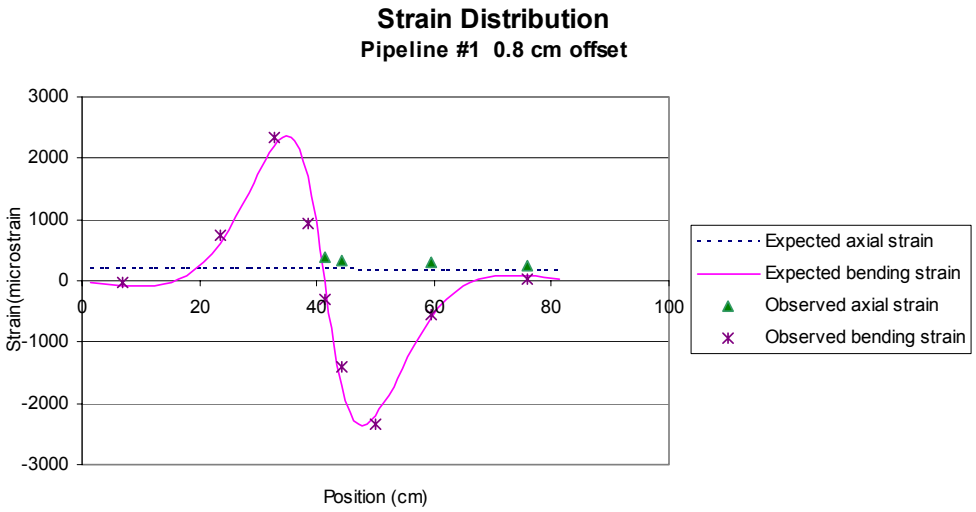

Figure 2. Measured and Simulated Strains for Pipeline #1 Model Subject to an Offset of 0.8 cm

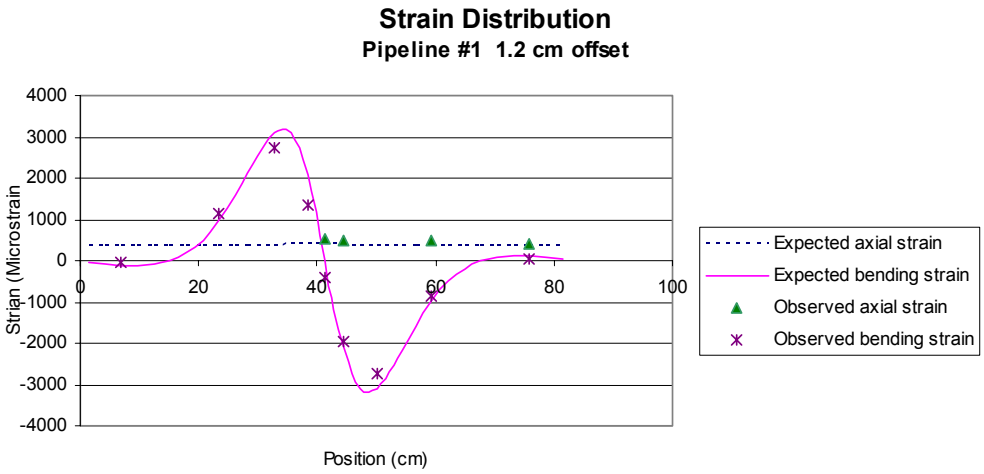

Figure 3. Measured and Simulated Strains for Pipeline #1 Model Subject to an Offset of 1.2 cm

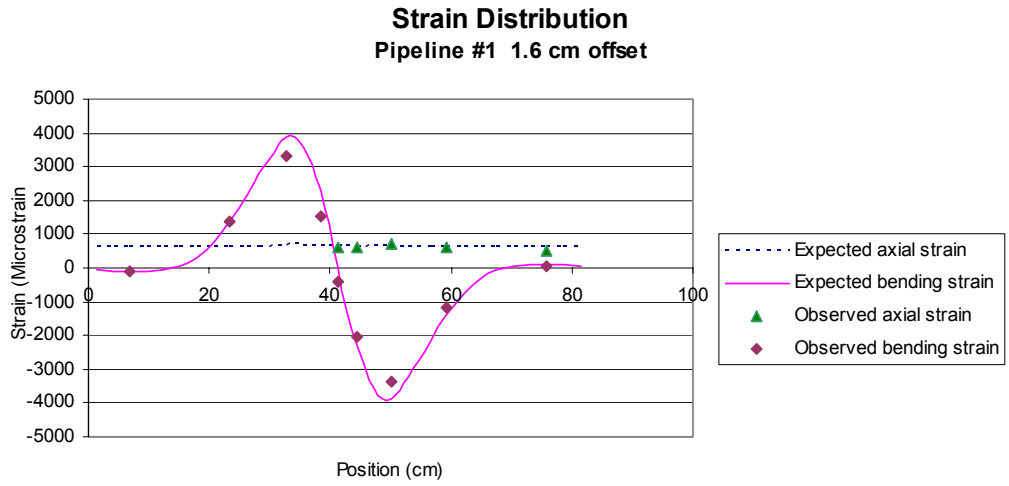

Figure 4. Measured and Simulated Strains for Pipeline #1 Model Subject to an Offset of 1.6 cm

Figures 5 through 9 present similar information for the Pipeline #2 model, specifically axial and bending strains for model offsets of 1, 2, 3 and 4 cm respectively. For these tests at 50 gs, the largest of these offsets correspond to 2 m in prototype scale.

FINITE ELEMENT MODEL

A finite element idealization of the centrifuge model was constructed. The pipe was modeled with beam elements while the soil was modeled as elasto-plastic springs. The burial depth for the pipeline models was 2.4 cm (little under 1 inch) which corresponds to 1.2 m (~4 feet) in prototype scale. The corresponding maximum soil spring resistances, with units of force per unit length of pipe and "yield" displacement were based upon the ASCE Guidelines [1]. Since the burial depth was constant across the model, and the offset had no vertical component, there was no need for vertical soil springs. That is, the FE model was two dimensional in nature. The pipe model was taken to be pinned at the split box wall (i.e. end of FE model located 40 cm (20 m in prototype scale) each side of the fault location). The offset was simulated by displacing the base of all the soil springs located on one side of the fault as well as the pin end on that side of the fault.

The results of the FE simulation are also shown in Figures 1 through 8. For Pipeline #1 (see Figures 1 through 4) the axial and bending strains from the FE simulation match well the measured strains. The match is remarkably good for offsets of 1.2 and 1.6 cm (0.6 and 0.8 m in prototype scale) while somewhat less remarkable at lower offsets. For Pipeline #2 (see Figures 5 through 8) the match between measured strains in the centrifuge experiments and corresponding values from the FE simulation is quite good for offsets of 2 cm or less (1 m in prototype scale). As the offset increases beyond 2 cm, the correspondence between measured and simulated strains deteriorates. It should be mentioned in this regard that peak pipe strains were larger than the yield strain for Pipeline #2 offsets greater than 3 cm (1.5 m prototype scale).

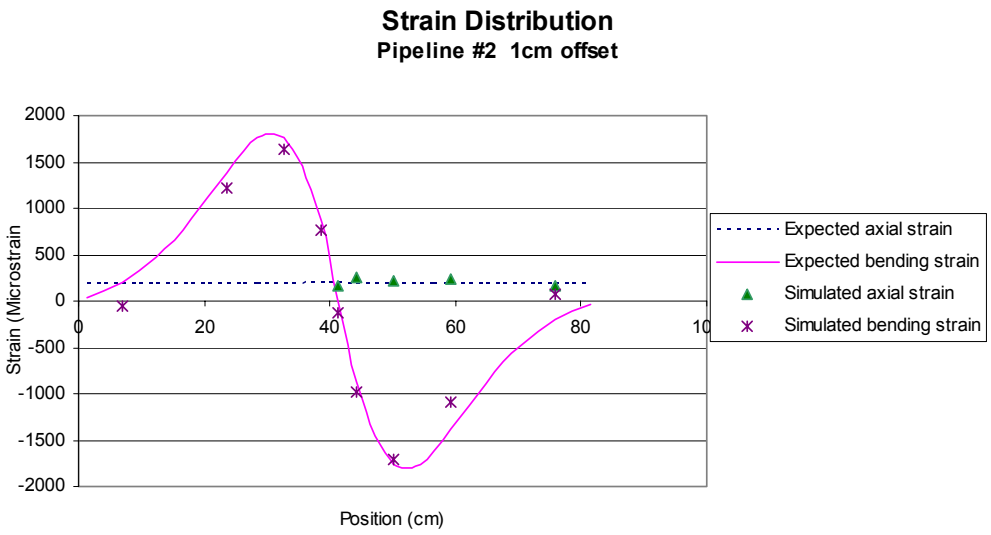

Figure 5. Measured and Simulated Strains for Pipeline #2 Model Subject to 1 cm Offset

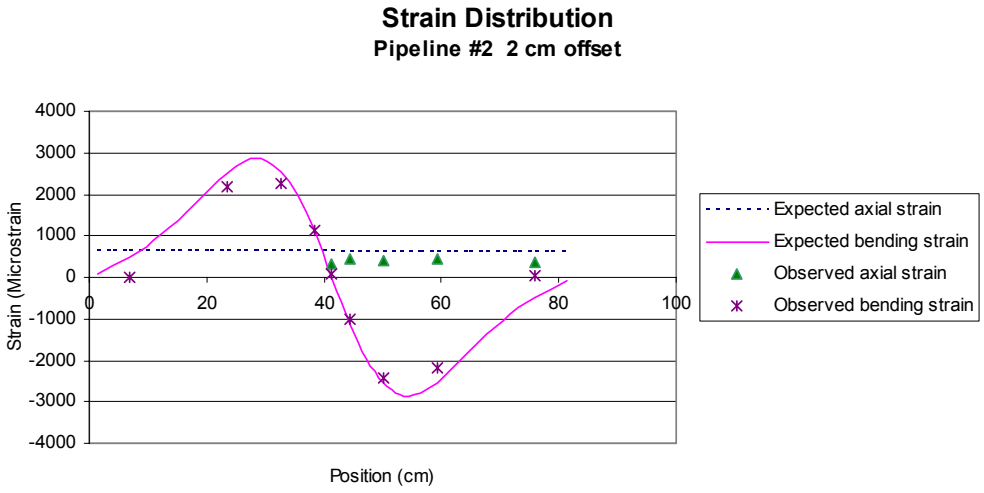

Figure 6 Measured and Simulated Strains for Pipeline #2 Model Subject to 2 cm Offset

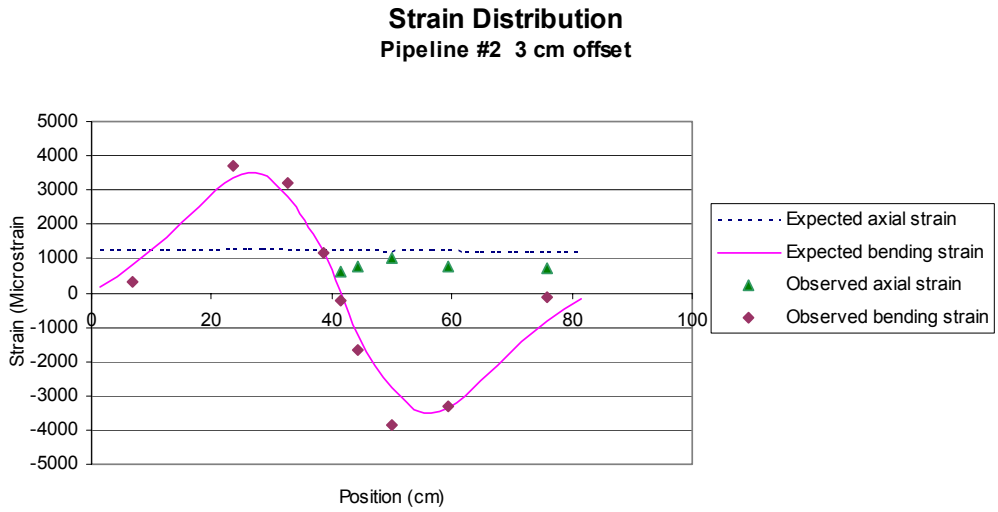

Figure 7. Measured and Simulated Strains for Pipeline #2 Model Subject to 3 cm Offset

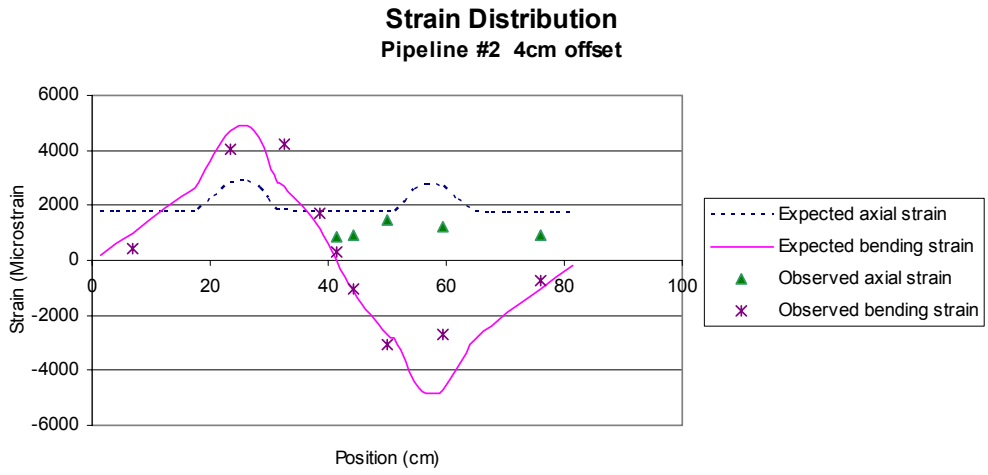

Figure 8. Measured and Simulated Strains for Pipeline #2 Model Subject to 4 cm Offset

CONCLUSIONS

The paper describes the first known attempt to use centrifuge modeling to determine pipe strains induced by PGD. The tests were successful in the sense that the experimental equipment apparently functioned properly and strains were measured as the split box was being offset in-flight. Furthermore, the measured pipe strains matched analytical results from a FE simulation for offsets wherein the pipe remained in the linear elastic range.

ACKNOWLEDGEMENTS

The research work described herein was sponsored by the National Science Foundation through Award No. CMS-0085256. The original NSF program manager was Vijaya Gopu, who was succeeded by Peter Chang. The construction of split box was sponsored by the National Science Foundation through the George E. Brown, Jr. Network for Earthquake Engineering Simulation program (NEES). This support is gratefully acknowledged. However, all statements, results and conclusions are the authors and do not necessarily reflect the views of NSF.

REFERENCES

[1] American Society of Civil Engineers (ASCE), 1984, Guidelines for the Seismic Design of Oil and Gas Pipeline Systems, Committee on Gas and Liquid Fuel Lifelines, ASCE.

Seismic Effect for Submarine Pipelines by Active Fault Movement

Osamu. Kiyomiya, Masayuki. Ichihashi, and Toshinori. Kikuchi

ABSTRACT

There is a possibility that the submarine pipelines to be constructed at present around the Japanese Archipelago might be placed crossing faults. In consideration of the submarine pipelines crossing faults, safety is estimated with the submarine pipelines dependent on the forced displacement of the faults. In this study, safety is examined with the problematic points shown below by means of the analysis based on the finite element method: (1) Safety estimation of the pipelines placed on the seabed subjected to the forced displacement caused by faults. (2) Safety estimation of the buried pipelines subjected to the forced displacement caused by faults.

1. Introduction

Around East Japan, a project concerning the submarine pipelines for transportation of natural gas is at present under way. Several active faults are in existence on the continental shelf in Japanese waters, and there is a high possibility that submarine pipelines will be placed to cross these faults. In recent years, controversy is provoked with respect to the safety of the constructions crossing the faults with the earthquakes in Turkey, Taiwan, etc. as a momentum. Meanwhile with the submarine pipelines exposed to the danger of the forced displacement caused by faults, many of examples of damages are reported in the United State, an advanced country of submarine pipelines. Therefore attention should be paid in this study especially to the submarine pipelines crossing faults in examining its safety. Thus calculation is made with the two examples shown below in accordance with the finite element method of which material nonlinearity is taken account.

a) Safety estimation of the pipelines placed on the seabed exposed to the danger of the force displacement caused by faults.
b) Safety estimation of the buried pipelines exposed to the danger of the forced displacement caused by faults.

2. Faults

2.1 Fault location

Osamu Kiyomiya, Professor of civil engineering, Waseda university, Tokyo ,Japan(k9036@waseda.jp)
Masayuki Ichihashi, Student of civil engineering, Waseda university, Tokyo ,Japan
Toshinori Kikuchi, Student of civil engineering, Waseda university, Tokyo ,Japan

There are many active faults in a planned region of the submarine pipelines. Submarine pipelines around the Japanese Archipelago are always prevented from being placed by the existence of many of active faults, and there is a high possibility that the submarine pipelines in the project will be placed crossing the active faults. On the other hand, most of the active faults existing around the Japanese archipelago are low-angle reversed faults. Details are hereunder shown with respect to the topographical features and active faults.

2.2 Calculation of the fault movement

Proposal is made with several methods to estimate displacement of the ground obtained from fault parameters. This time, fault movement during an earthquake is obtained in accordance with a method proposed by Yoshimitsu Okada.The displacement field Δu_i (ζ_1、ζ_2、ζ_3) in the bed caused by the step Ui (X_1,X_2,X_3) crossing the Σ plane can be calculated by means of the equation shown below..

$$U_i = \frac{1}{F}\iint_{\Sigma} \Delta u_j \left[\lambda \delta_{jk} \frac{\partial u_i^j}{\partial \zeta_n} + \mu \left(\frac{\partial u_i^j}{\partial \zeta_k} + \frac{\partial u_i^k}{\partial \zeta_j} \right) \right] \nu_k d\Sigma \qquad (1)$$

where δ:the Kronecker delta,λ and μ: Lames's constants,ν:the direction cosine of the normal to the surface element d∑

(1) Displacement in a vertical direction

Maximum displacement in a vertical direction is 626.40cm with the model conceived by Kantamori in Sanriku Earthquake (1896/6/15), and a distance between the points where the maximum and minimum values can respectively be obtained is 22km. Meanwhile as an example, a displacement map in a vertical direction with the model conceived by Aki in Niigata Earthquake is calculated. The maximum displacement difference calculated based on the individual parameters with this fault is 364cm in a vertical direction.

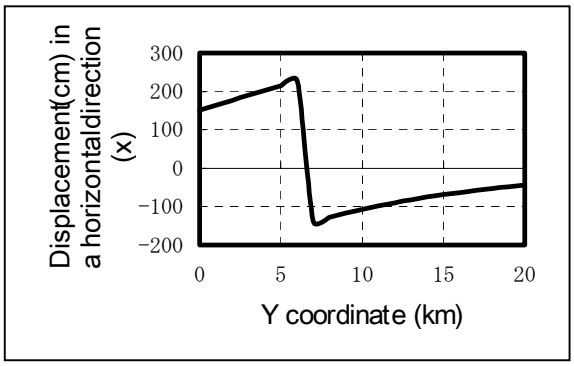

Figure 1. Horizontal displacement by Kantamori in Sanriku Earthquake

(2) Displacement in a horizontal direction

The maximum displacement in a horizontal direction is 583.47cm with the model conceived by Kantamori in Sanriku Earthquake (1896/June/15). The result of the calculation concerning the above description is shown in Fig. 1.

3. Submarine pipeline

3.1 Outline of pipe

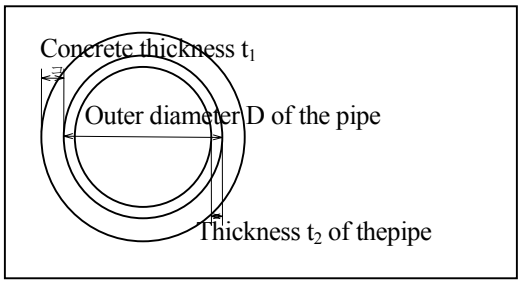

Figure 2. Cross-section of a pipe

Cross-sectional configuration of a pipe is shown in Fig. 2. Concrete is coated onto the surface of the steel materials for weight adjustment in settling the materials and protection from the damage caused by external force. It is necessary to consider the heaviness

of them for weight assessment. The value, which is obtained by subtracting the buoyancy from the weight is dealt with as the weight of the steel materials, is used. On the other hand, unit volume weight has to be assessed in a moistened state. Therefore the weight of the steel materials is to be expressed by Equation (2). On the other hand, the buoyancy acted onto the steel materials can be expressed by Equation (3) when the pipe is submerged.

$$W = \pi\{(D - t_1)t_1\rho_1 + (D + t_2)t_2\rho_2\} \quad (2)$$

$$B = \frac{\pi}{4}(D - t_1 + t_2)(t_1 + t_2)W_0 \quad (3)$$

where W: weight (kN/m^3) of the steel materials per unit length B: buoyancy (kN/m) per unit length D: outer diameter (m) of the pipe t_1: steel material thickness (m) t_2: coating thickness (m) ρ_1: unit volume weight (kN/m^3) of the pipe ρ_2: unit volume weight (kN/m^3) of the coating Wo: unit volume weight (kN/m^3) under seawater

4. Safety estimation of the pipelines placed on the seabed

4.1 Analytical model

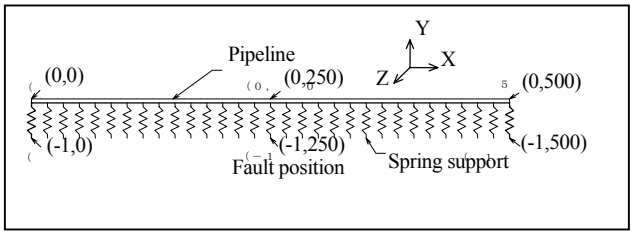

Figure 3. Analytical model

An analytical model of the pipeline not deeply placed on the seabed or in the close vicinity of the seabed is shown in Fig. 3. The length of the submarine pipeline as a calculation model is 500m. On the center, a fault is in existence. The submarine pipeline is substituted with the one-dimensional beam element of total node number 501 and total element number 500. Furthermore on the individual nodes, ground springs are attached in a vertical direction, horizontal direction and axial direction.

Analytical parameters are shown in Table 1. The submarine pipeline (outer diameter of the pipe), internal pressure, ground strength (N value in a standard penetration test), forced displacement direction (types of the fault) are dealt with as analytical parameters

(1) Pipeline

Table 1. Analytical parameters

Outer diameter of the pipe (thickness t_2)	Internal pressure	N value	fault
101.6cm (1.19cm)	ignored	1	Reverse fault
		10	
76.2cm (1.91cm)	In consider--ation	40	Strike fault

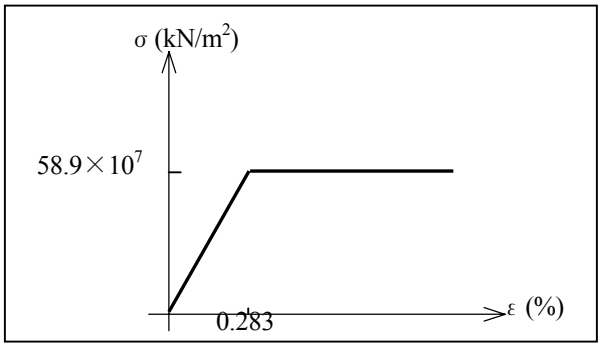

Figure 4. Nonlinearity of the steel

Thickness of the concrete portion around the steel material is 15cm. Furthermore on the assumption that concrete has already had cracks, exclusively the weight was considered without taking account of the strength. The submergible unit volume weight was determined to be 12kN/m^3. Nonlinearity of the material of the submarine pipeline is shown. In Fig. 4. The properties of the steel material is determined to be as follows: Young ratio is 2.1 $\times$ 10^{8}kN/m^2 and yield stress is 58.9 $\times$ 10^{7}kN/m^2 at API5LX80. Meanwhile the outer diameter of the steel material was 101.6cm and 76.2cm respectively with the thickness 1.91cm.

In Table 2, destruction values of the submarine pipeline are listed. The yield moment of the outer diameter D = 101.6cm is 8.6 $\times$ 10^{3}kN・m, whereas the plastic moment is 1.2 $\times$ 10^{4}kNm. Meanwhile it is determined that allowable strain complying with the level 1 earthquake is 2%, whereas the allowable strain complying with the level 2 earthquake is temporarily 4%.

Table 2. Mechanical properties of the pipe

Outer diameter D of the steel material	Yield moment	Inertia moment	Allowable strain
101.6cm	8.6MN·m	12MN·m	Level1:2%
76.2cm	4.6MN·m	6.2MN·m	Level2:4%

(2) Internal pressure

Natural gas flows through the inside of the steel material of the submarine pipeline, and internal pressure is applied onto the steel material. On the assumption that the ratio of the allowable stress degree complying with the internal pressure to the standard lower bound yield stress (design coefficient) is 0.4, models with which the internal pressure is taken into account and not taken into account were considered.

(3) Ground

A ground reactive force coefficient k$_\nu$(kN/m^3) was obtained in accordance with the equation expressed in Road Corporation's Manual as shown below.

$$kv = kv_0\left(\frac{B_v}{30}\right) \quad (4)$$

$$kv_0 = \frac{1}{30}\alpha E, B_v = \sqrt{A_v} \quad (5)$$

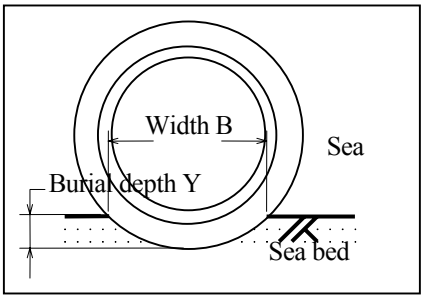

Figure 5. Burial of the pipeline

where B ν : converted foundation width of the foundation,A ν : load area in a vertical direction At that time, Young modulus of the ground was obtained at E = 2.8N N/mm^2 (Road Corporation's equation) from the N value of the standard penetration test. The coefficient α was determined to be 1.

The ground spring k ν in a vertical direction was obtained in consideration of the penetration Y (the width B contacting with the ground) directed toward the ground of the submarine pipeline using the result of Equation 4 as illustrated in Fig. 5.

$$Kv = kvA_v \quad (6)$$

$$A_v = 1 \times B = 1 \times \sqrt{\left(\frac{D}{2}\right)^2 - \left(\frac{D}{2} - Y\right)^2} \qquad (7)$$

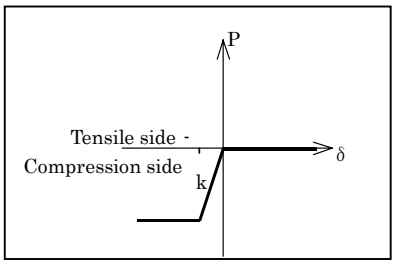

(a) Ground spring in a vertical direction

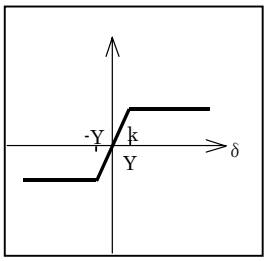

(b) Ground spring in horizontal direction

Figure 6. Nonlinearity of the ground

Nonlinearity of the ground spring in a vertical direction is shown in Fig. 6(a). With the yield force in case that the ground were in a compressed state, the value obtained in case that the submarine pipeline which sunk into the ground to the extent as low as the radius of the submarine pipeline was used. Meanwhile in a tensile state, supposition was made that no spring was in existence. Likewise nonlinearity of the ground spring in a horizontal direction is shown in Fig. 6(b). On the supposition that the constant of the ground spring in a horizontal direction is 1/3 of the one of the ground spring in a vertical direction, the value of the burial depth to the submarine pipeline was used for the yield force. Under the condition shown above, the N value of the seabed was considered in a range from 1 to 40.

4.2 Analytical result and consideration

4.2.1 Analytical result of the vertical movement

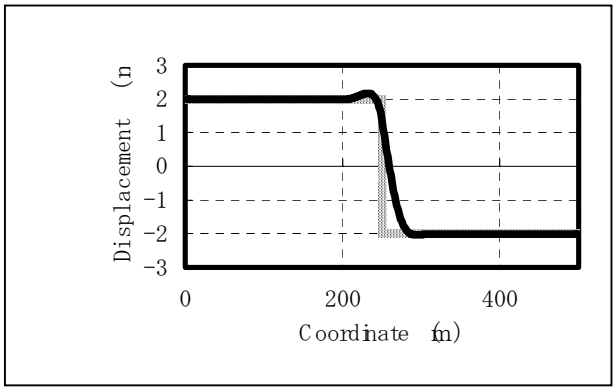

Figure 7. Displacement distribution of the vertical movement

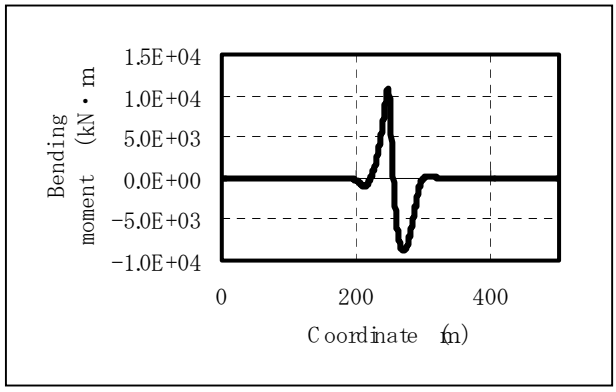

Figure 8. Bending moment distribution of the vertical movement

Vertical movement is introduced by normal fault or reverse fault. In Fig. 7, displacement in a vertical direction of the pipeline is shown in case that the outer diameter D of the steel material = 101.6cm and forced displacement is applied 4m in a vertical direction ignoring the internal pressure at the N value = 1. The pipeline was separated from the seabed in a range of approximately 30m in the side of the ground upper than the fault position driven into a floating state. Contrarily in the lower side of the ground, the pipeline was placed on the seabed biting into it. Distribution of the bending moment calculated for the pipeline at that time is depicted in Fig. 8. The maximum bending moment was calculated on a position 4m in the side of the ground upper than the fault, and almost none of the bending moment was calculated on a position approximately

50m distant from the fault in case of both the upper and lower ground directions.

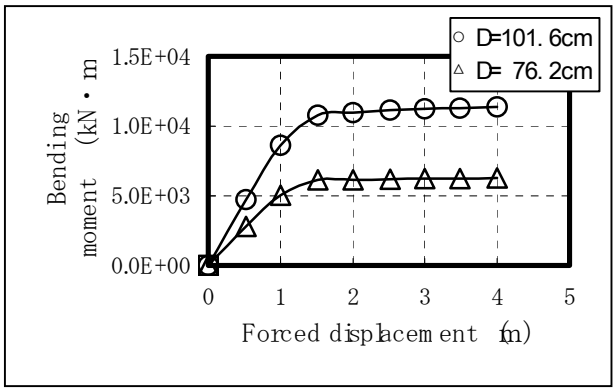

(a) Relationship between the maximum bending moment and the forced displacement

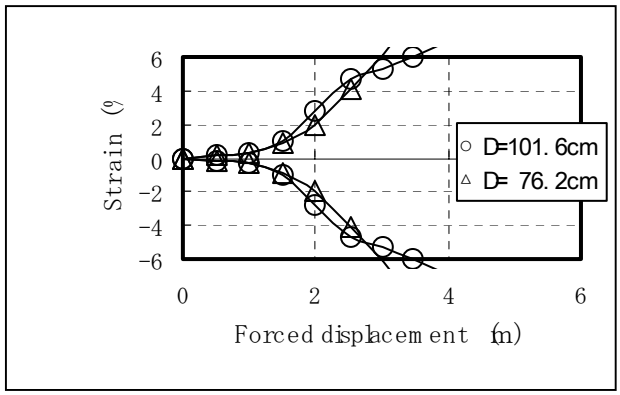

(b) Relationship between the maximum axial strain and the forced displacement

Figure 9. Effect of the outer diameter of the pipe

4.2.2 Seismic effect of the individual parameters for the analytical result of the vertical movement

(1) Effect of the outer diameterof the pipe

A relationship between the maximum bending moment in case that the forced displacement is given at the N value = 10 in a vertical direction and the forced displacement is shown in Fig. 9(a). In the meantime, a relationship between the maximum strain and the forced displacement is shown in Fig. 9(b). When the outer diameter of the steel material was made smaller, the spot where the maximum bending moment and the maximum axial strain are calculated comes closer to the fault position on the seabed. With the steel material with an outer diameter D = 101.6cm, greater bending moment was calculated at the same forced displacement at that time than with the steel material with an outer diameter D = 76.2cm. However the forced displacement to the extent that the axial strain becomes 3% makes almost no change in case that the outer diameter D = 101.6cm of the steel material and in case that the outer diameter D = 76.2cm of the steel diameter, and just a slight amount of the seismic effect of the outer diameter of the steel material was exerted on the axial strain.

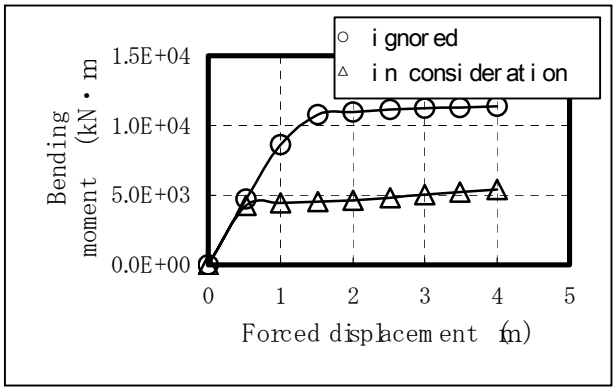

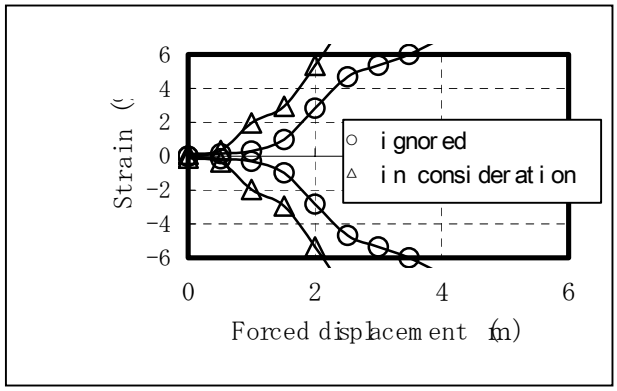

Figure 10. Relationship between the maximum axial strain and the forced displacement

(2) Seismic effect of the internal pressure

A relationship between the maximum bending moment in case that forced displacement is given in a vertical direction under the condition that steel material outer diameter = 101.6cm and N value = 10 and the forced displacement is shown in Fig. 10. In the meantime, a relationship between the maximum axial strain and the forced displacement is shown in Fig. 10.

When the internal pressure is considered, the spot where the bending moment and the maximum axial strain are calculated approached the fault on the seabed. Meanwhile when the internal pressure is considered, the moment came closer to the maximum value under the condition that the forced displacement 1m. Furthermore when the internal pressure is ignored, the moment approached the plastic moment under the condition that the forced displacement is 2m. On the other hand, the forced displacement in case that the axial strain became 3% was 2.04m when the internal pressure was ignored. The amount became 1.58m when the internal pressure was considered. Thus it is explained that the seismic effect of the internal pressure exerted on the axial strain was large.

(3) Seismic effect of the ground strength

A relationship between the maximum bending moment in case that the forced displacement in a vertical direction is given by ignoring the internal pressure and the forced displacement is shown in Fig. 11(a). In the meantime, a relationship between the maximum axial strain and the forced displacement is shown in Fig. 11(b). When the ground strength became large, the spot where the maximum bending moment and the maximum axial strain were calculated approached the fault position on the seabed. At that time, the forced displacement until it reached the plastic moment became small when the ground strength became large. Meanwhile when the forced displacement in case that the axial strain became 3% was 1.35m when N value = 40. The amount became more than 4m when N value = 1. Thus it is explained that the seismic effect of the ground strength exerted on axial strain was a large one.

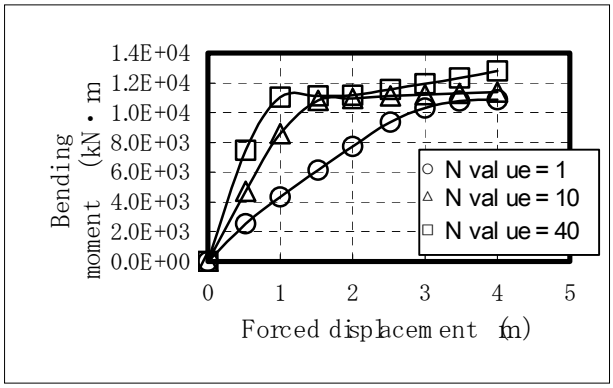

(a) Relationship between the maximum bending moment and the forced

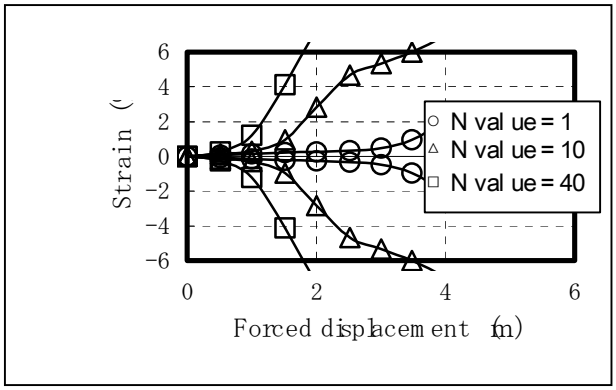

(b) Relationship between the maximum axial strain and the forced displacement

Figure 11. Seismic effect of the ground strength

4.2.3 Analytical result of the horizontal movement

Horizontal movement is introduced by strike fault. In Fig. 12, displacement in a horizontal direction of the pipeline is shown in case that the diameter D = 101.6cm of the steel material at N value = 1 by ignoring the internal pressure. The pipeline deviates itself throughout the interval of

500m. At that time, a distribution of the bending moment calculated for the pipeline is shown in Fig. 15. The calculation was made on a spot where the maximum bending moment is 250m distant from the fault position.

4.2.4 Seismic effect of the parameters for the analysis result of the horizontal movement

(1) Effect of the outer diameter of the pipe

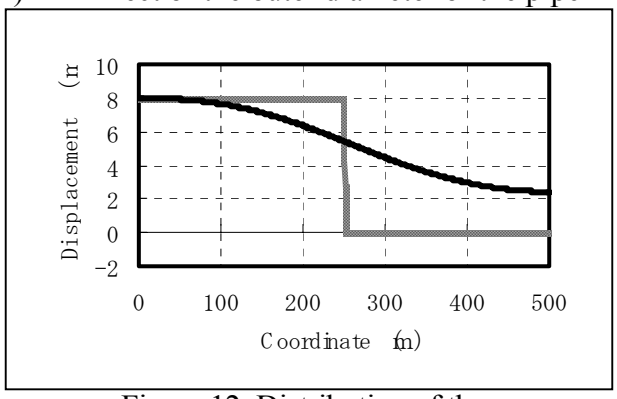

Figure 12. Distribution of the horizontal movement

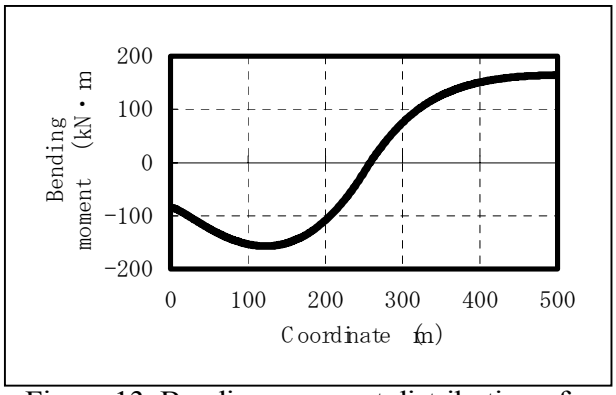

Figure 13. Bending moment distribution of the horizontal movement

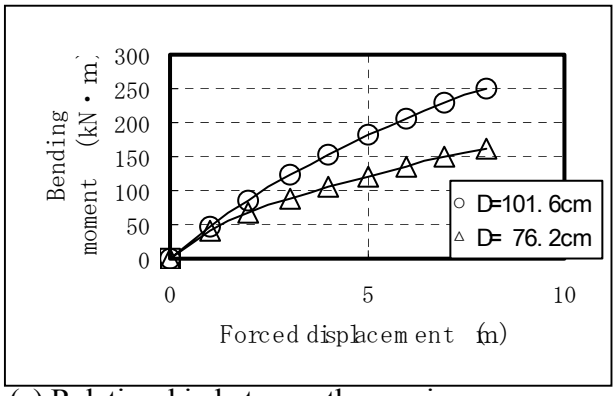

(a) Relationship between the maximum bending moment and the forced displacement

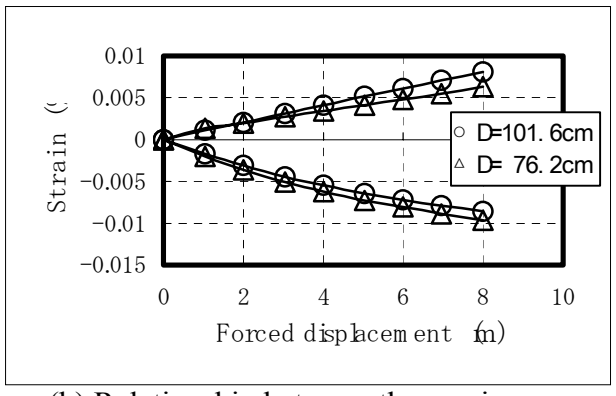

(b) Relationship between the maximum axial strain and the forced displacement

Figure 14. Seismic effect of the steel material outer diameter

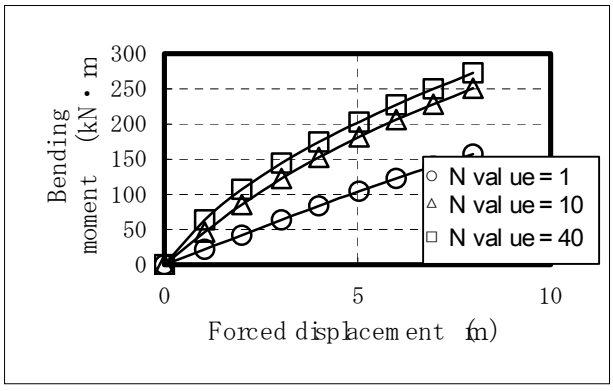

(a) Relationship between the maximum bending moment and the forced displacement

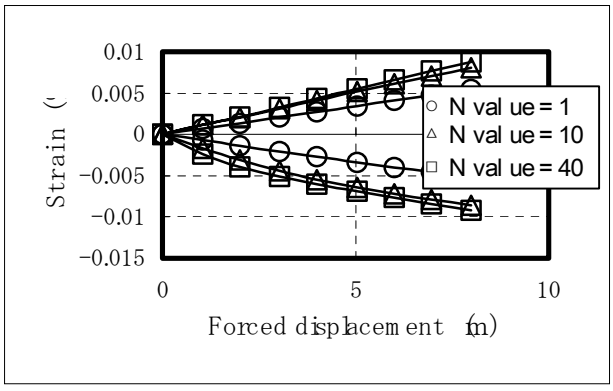

(b) Relationship between the maximum axial strain and the forced displacement

Figure 15. Relationship between the maximum axial strain and the forced displacement

A relationship between the maximum bending moment of the pipeline in case that the forced displacement is given in a horizontal direction and the internal pressure is ignored under the condition that the N value is 10 and the forced displacement is shown in Fig. 14(a). In the meantime, a relationship between the maximum strain and the forced displacement is shown in Fig. 14(b). Larger bending moment was calculated with the same forced displacement in case that the steel material outer diameter D = 101.6cm than in case that the steel material outer diameter = 76.2cm. However the value of the axial strain remained almost unchanged in case that the steel material outer diameter D = 101.6cm and in case that the steel material outer diameter D = 76.2cm, and just an exceedingly small amount of seismic effect of the steel material outer diameter was exerted on the axial strain. The maximum bending moment obtained to the extent that the forced displacement became 8m takes a value of not smaller than 1/30 of the yield moment. Thus the maximum axial strain was 0.009% at the largest, and did not reach the allowable strain.

(2) Seismic effect of the internal pressure

A relationship between the maximum bending moment of the pipeline in case that the forced displacement was given in a vertical direction under the condition that the steel material outer diameter D = 101.6cm and N value = 10 and the forced displacement is calculated. In the meantime, a relationship between the maximum axial strain and the forced displacement is obtained. The bending moment distributions were quite the same. This is due to the fact that regardless of the presence or absence of the internal pressure, the deformation of the submarine pipeline remains within a linear range. Meanwhile with the axial strain, a model in consideration of the internal pressure became stronger in the axial strain by an amount of the seismic effect of the internal pressure in comparison with the model not in consideration of the internal pressure. The maximum bending moment where the forced displacement reached 8m takes a value of less than 1/30 of the yield moment at the largest. Thus the maximum axial strain was 0.14% even when the internal pressure was considered, and failed to reach the allowable strain.

(3) Seismic effect of the ground strength

A relationship between the maximum bending moment and the forced displacement in case that the diameter of the steel material is 101.6cm, the internal pressure is ignored, and the forced displacement is applied in a horizontal direction is shown in Fig. 15(a). In the meantime, a relationship between the maximum axial strain and the forced displacement is shown in Fig. 15(b). As the N value became larger, the maximum bending moment was made larger. Meanwhile although the value of the axial strain was larger than the steel material diameter D = 101.6cm and the steel material diameter D = 76.2cm, its seismic effect was scanty. The maximum bending moment to the extent that the forced displacement became 8m took a value of less than1/30 of the yield moment at the largest. Meanwhile the maximum axial strain became 0.009% at the largest, and never reached the allowable strain.

5. Safety evaluation of the buried pipeline

5.1 Analytical model

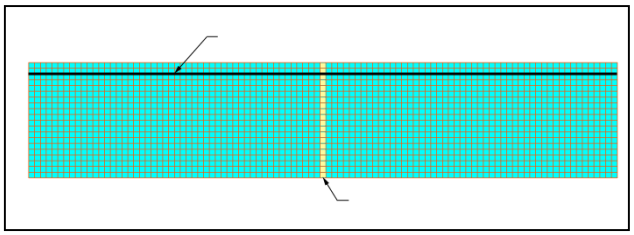

Figure 16. An analytical model

The analytical model used this time is shown in Fig. 16. On the assumption that the length of the submarine pipeline on the

calculation model is 100m, a fault is located on the central portion. The buried pipeline was substituted by means of the one-dimensional beam element of the node number 101 and element number 101, and was inserted onto the subsurface layer standardized into a specific model in accordance with the finite element method. On the assumption that the subsurface layer is a plane strain element, the subsurface layer thickness is 20m and longitudinal length is 5m. On the assumption that deformation coefficient is 1.0×10^4KN/m^2 and the deformation coefficient of the relatively soft layer on a fault position (hereafter called fault plane) is 1.0×10^3KN/m^2, none of nonlinearity of the ground is considered this time. Meanwhile on the assumption that the outer diameter D = 101.6cm of the steel material and the internal pressure are ignored. The structure and quality of the pipeline are the same as those in case of the safety evaluation of the pipeline placed on the undersea ground.

Under the condition referred to above, a half side of the base rock was fixed and another side was provided with forced displacement in a horizontal direction in a style of steps holding the fault plane between the two.

Meanwhile on the assumption that the analysis parameters in case that the analysis was made this time were inclination of the fault dip angle and width of fault rupture zone. The inclination was 45° , 63.3° , and 90° . Also the width of the fault plane is 1 and 2 meters.

5.2 Analytical result and consideration

5.2.1 Analytical result of the vertical movement

Seismic effect caused by the inclination of the fault plane

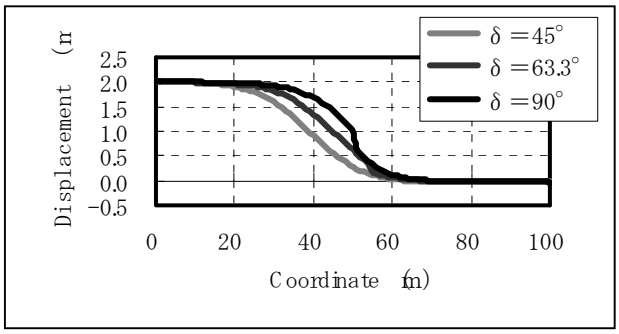

Figure 17. Displacement distribution of the vertical movement

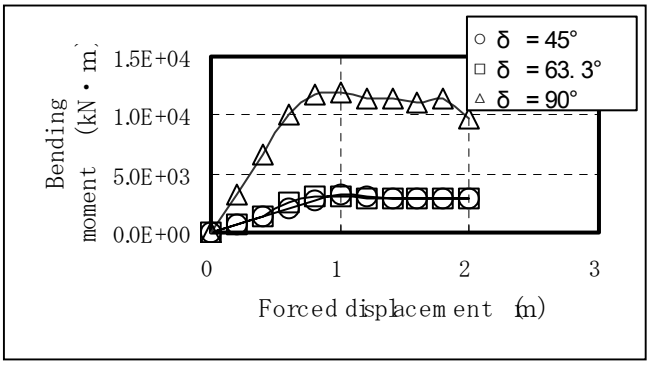

Figure 18. Relationship between the maximum bending moment and the forced displacement, seismic effect caused by the inclination of the fault plane (the fault width 1m)

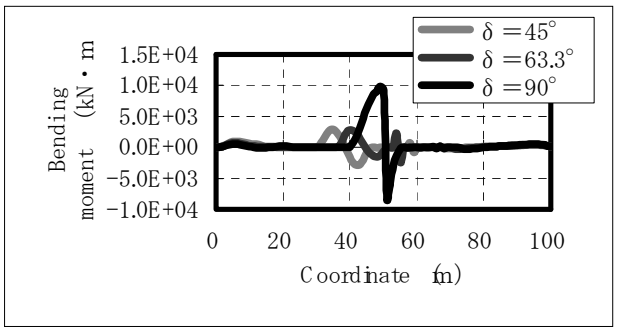

Figure 19. Bending moment distribution of the vertical movement

Fig. 17 shows with displacement of the pipeline in a vertical direction in case that forced displacement was given 2m in a vertical direction at the fault width 1m. The pipeline made displacement in a range of approximately 30m individually in the side of the layers upper

and lower than the fault position. In case that the inclination δ of the fault plane = 90° , the maximum bending moment was calculated on the position of the upper layer side 2m. In case that the pipeline left 10m from the fault with both the upper and lower layer directions, the bending moment could be hardly calculated. In the vicinity of the inclination $\delta = 63.3°$ and the inclination $\delta = 45°$, relatively irregular bending moment distribution was calculated. In case that the pipeline left 15m from the fault with both the upper and lower ground directions, the bending moment could hardly be calculated.

A relationship between the maximum bending moment of the pipeline in case that the forced displacement was given in a vertical direction at the fault width 1m and the forced displacement is shown in Fig. 18. When the inclination of the fault plane was made larger, the spot where the maximum bending moment was calculated approached the fault position. With the inclination $\delta = 90°$, larger bending moment was calculated by the same forced displacement than with the inclination $\delta = 63.3°$ of the fault and the inclination $\delta = 45°$ of the fault plane. The distribution of the subsurface layer in case that $\delta = 45°$ is shown in Fig. 20(a). The subsurface layer in case that the inclination $\delta = 63.3°$ is shown in Fig. 20(b). The subsurface layer in case that the inclination $\delta = 90°$ is shown in Fig. 20(c).

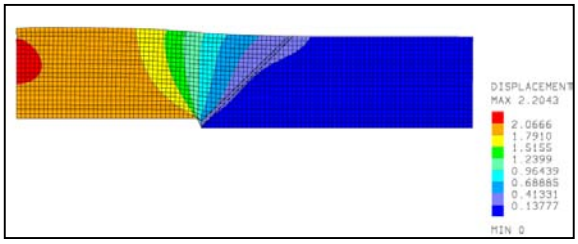

(a) The subsurface layer in case that the inclination δ =45°

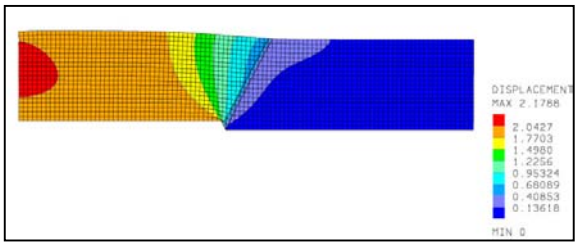

(b) The subsurface layer in case that the inclination δ =63.3°

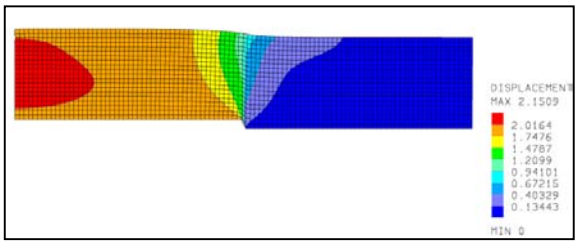

(c) The subsurface layer in case that the inclination δ =90°

Figure 20. Seismic effect caused by the inclination of the fault plane (the fault width 1m)

6. Conclusions

In this study, the safety evaluation was made with the submarine pipeline complying with the forced displacement of the fault. As a result, conclusions are obtained as shown below respectively in connection with the pipeline placed on the seabed and the buried pipeline.

6.1 Pipeline placed on the seabed

(1) Vertical movement by fault

Owing to increase of forced displacement, the pipeline reached the allowable strain. On the other hand, cross section force became the maximum in the vicinity of the fault on the upper layer side. On that occasion, the seismic effect exerted on the strength of the seabed and the pressure in the

pipeline was large with the axial strain of the pipeline. That is to say, the harder the seabed was, the larger the strain was. Meanwhile in consideration of the internal pressure, it is made clear that the strain became large.

(2) Horizontal movement by fault

Since the pipeline slipped on the ground, strains are very small within the allowable strain. On the other hand, the location where the cross section force became large was located on a place considerably distant from the fault position. On that occasion, the seismic effect complying with the internal pressure in the pipe was large with the axial strain of the pipeline. That is to say, in consideration of the internal pressure, the strain became large.

6.2 Buried pipeline[i]

The strains this time reached the allowable strain owing to a considerable forced displacement. On the other hand, the cross section force became the maximum in the vicinity of the upper layer side. On that occasion, the bending moment of the pipeline was subjected to great seismic effect of the inclination of the fault plane. When the fault plane inclined, the bending moment was lowered. The seismic effect caused by the fault plane width was relatively scanty this time.

Acknowledgments

The calculation of the fault movement was conducted in accordance with the computer program offered by Professor Shimazaki of the University of Tokyo. The authors wish to express their sincere gratitude to the professor who was kind enough to provide the authors with an opportunity to make the calculation of the fault movement. The authors are also grateful to Mr. H. Azuma, former graduate student of Waseda University who was cooperative to authors in executing the calculation of the spring model.

References

[1] Hiroki AZUMA and Osamu KIYOMIYA:Evaluation of pipe strain due to active fault,Second Symposuim of Eathquake Disaster based on Failure Process of Structures,pp.147-152, March 2001

[2] Yoshimitsu OKADA: Surface deformation due to shear and tensile faults in half-space, Bullitin of the seismological society of America,Vol.75.No.4,pp.1135-1154, Augst 1985

[3] Shiro TAKADA,etc:Shell-mode Response of Buried Pipelines to Large Fault Movements,Journal of Structual Engineering,Vol.44A,pp.1637-1645,March 1998

Recommended Practice for Design of Gas Transmission Pipelines in Areas Subject to Liquefaction

Takashi Kobayashi, Kazunori Shimamura, Noritake Oguchi, Yasuo Ogawa, Takayoshi Uchida, Seiji Kojima, Tetsuji Kitano and Kazuto Tamamoto

ABSTRACT

Following the studies of the magnitude of liquefaction-induced ground displacements, restraint forces exerted upon pipelines, simplified and useful deformation formulas for evaluating large-scale pipeline deformations caused by liquefaction-induced ground displacements and critical pipe deformations capable of satisfying the seismic performance criterion of "no leakage of gas", the Recommended Practice for Design of Gas Transmission Pipelines in Areas Subject to Liquefaction was established. This paper describes the fundamental principles and a part of the design practice of the Recommended Practice.

Takashi Kobayashi, Tokyo Gas Co., Ltd., Pipeline Department, 5-20, Kaigan 1-Chome, Minato-Ku, Tokyo 105-8527, JAPAN
Kazunori Shimamura, Tokyo Gas Co., Ltd., Pipeline Department, 5-20, Kaigan 1-Chome, Minato-Ku, Tokyo 105-8527, JAPAN
Noritake Oguchi, Tokyo Gas Co., Ltd., Pipeline Department, 5-20, Kaigan 1-Chome, Minato-Ku, Tokyo 105-8527, JAPAN
Yasuo Ogawa, Osaka Gas Co., Ltd., Engineering Department, 1-2, Hiranomachi 4-Chome, Chuou-Ku, Osaka 541-0046, JAPAN
Takayoshi Uchida, Osaka Gas Co., Ltd., Transmission Department, 1-2, Hiranomachi 4-Chome, Chuou-Ku, Osaka 541-0046, JAPAN
Seiji Kojima, Toho Gas Co., Ltd., Distribution Planning & Administration Department, 19-18, Sakurada-Cho, Atsuta-Ku, Nagoya 456-8511, JAPAN
Tetsuji Kitano, Toho Gas Co., Ltd., Distribution Planning & Administration Department, 19-18, Sakurada-Cho, Atsuta-Ku, Nagoya 456-8511, JAPAN
Kazuto Tamamoto, Saibu Gas Co., Ltd., Production & Piping Planning Department, 17-1, Chiyo 1-Chome, Hakata-Ku, Fukuoka 812-8707, JAPAN

INTRODUCTION

After the 1995 Hyogoken-nanbu (Kobe) Earthquake, the Japan Gas Association, commissioned by Agency of Natural Resources and Energy, Ministry of Economy, Trade and Industry (METI), launched studies to establish the Recommended Practice for Design of Gas Transmission Pipelines in Areas Subject to Liquefaction. The studies included experiments and numerical analyses involving:

- the magnitude of liquefaction-induced ground displacements,
- the restraint forces exerted upon pipelines due to liquefaction-induced ground displacements[1 - 3],
- simplified and useful deformation formulas and FEM based analysis method used to evaluate large-scale pipeline deformations caused by liquefaction-induced ground displacements[4 - 8],
- the critical pipe deformations[9 - 10].

Following the studies, the Recommended Practice was established. The fundamental principles and a part of the design practice are described below.

FUNDAMENTAL PRINCIPLES OF THE DESIGN

Seismic Performance

The seismic performance criterion set in the Recommended Practice is "no leakage of gas". Although pipeline deformation is permissible, gas leaks must not occur.

Liquefaction Effects to be Considered

The effects of the following liquefaction-induced ground displacements shall be considered:

1) horizontal displacements in sloping ground,
2) horizontal displacements in ground behind quay walls,
3) settlements in areas in which pipelines are provided with rigid supports such as abutments.

Design Seismic Motion and Design Ground Displacements

Level 2 design seismic motion shall be used to identify the presence and severity of liquefaction. While the probability of an occurrence is small, the intensity of such an event is very high. Design ground displacements are set to be large enough when they are compared with those obtained by case studies in previous earthquakes.

Pipe Deformation Mode

Four pipe deformation modes shall be considered in the design, as follows:

1) straight pipe – uniaxial compression,
2) straight pipe – bending,
3) pipe bend – in-plane bending in the closing direction,
4) Pipe bend – in-plane bending in the opening direction.

Figure 1 shows these four deformation modes.

Load and Resistance Factor Design

Figure 2 shows the design flow diagram. For the seismic performance criterion, Equation 1 must be satisfied for any of the considered deformation modes. In this design methodology, a safety margin is assigned to each individual design component in the form of a partial safety factor, as is shown in Equation 2 and Equation 3.

$$S_d \leq R_d \tag{1}$$

where S_d : Design pipeline deformation evaluated by pipeline deformation analysis,

R_d : Design critical deformation. Beyond this critical deformation, gas leaks.

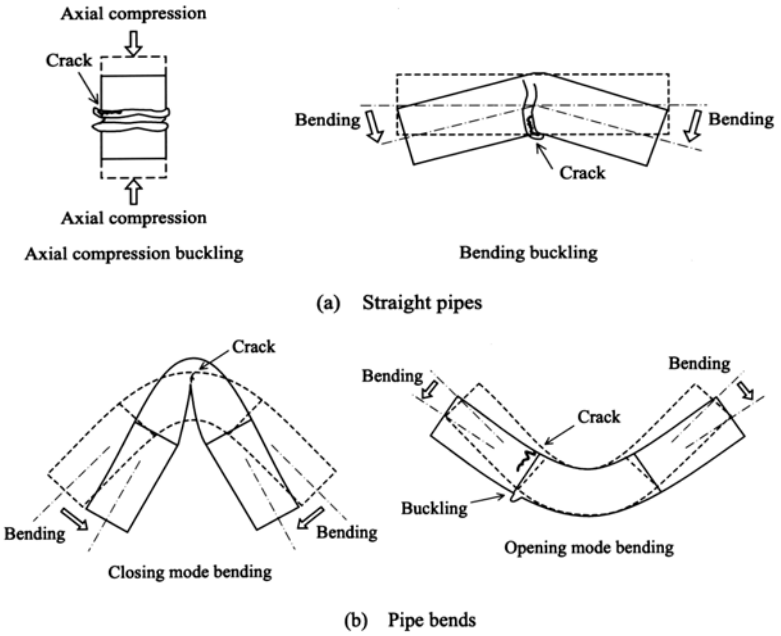

Figure 1. The deformation modes for straight pipes and pipe bends

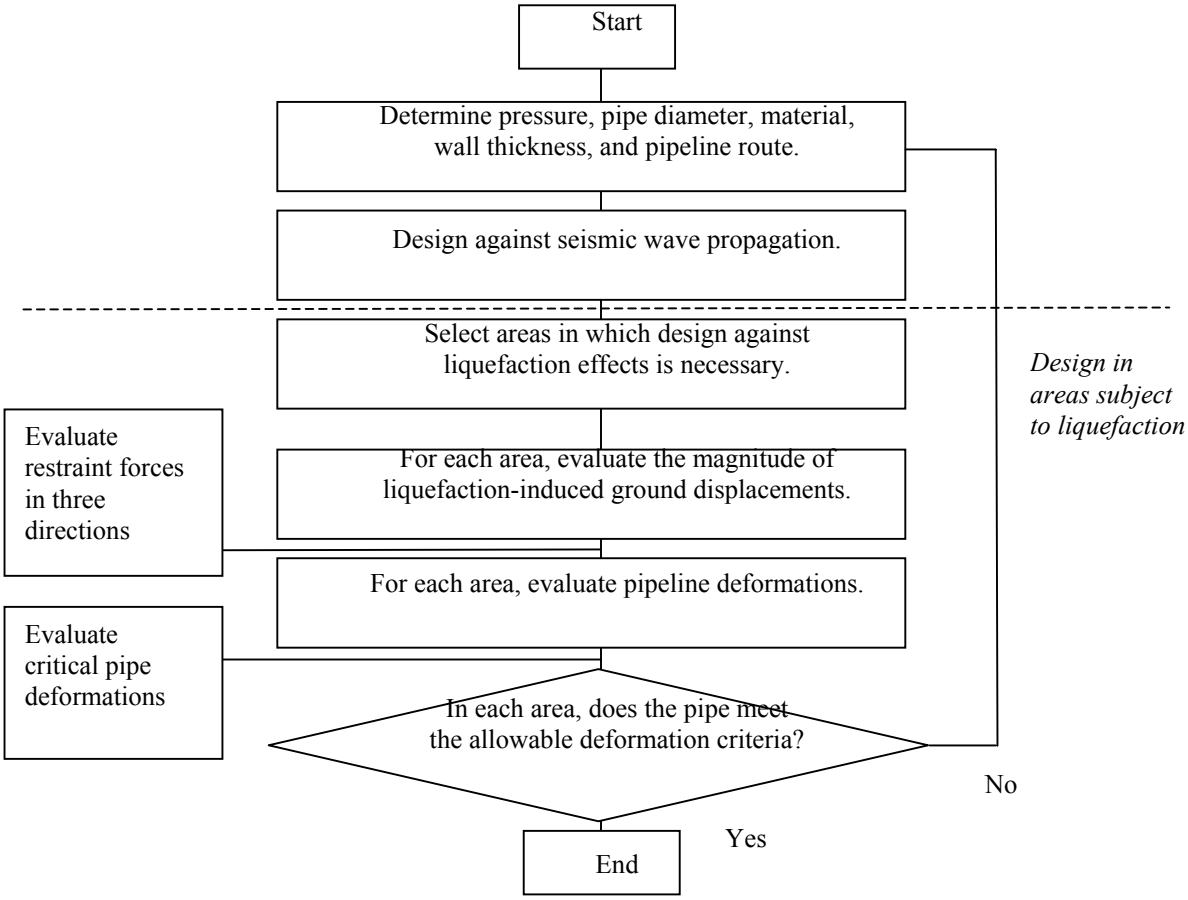

Figure 2. Design flow diagram

$$S_d = \gamma_a \cdot S(\gamma_\delta \cdot \delta, L, \gamma_K \cdot K) \quad (2)$$

$$R_d = R(\varepsilon_u / \gamma_m) / \gamma_b \quad (3)$$

where $S(*)$: Function used to evaluate design pipeline deformation.

δ : Liquefaction-induced ground displacement.

L : Length of the area in which liquefaction-induced ground displacements occur.

K : Restraint force exerted upon pipelines due to liquefaction-induced ground displacements.

$R(*)$: Function used to evaluate design critical pipe deformation.

ε_u : Critical pipe strain. Beyond this critical strain, gas leaks occur.

γ_* : Partial safety factor.

AREAS IN WHICH DESIGN AGAINST LIQUEFACTION IS NECESSARY

Geomorphological Conditions

The areas in which design against liquefaction effects is necessary is selected through the three phases.

In the first phase, the geomorphological condition of an area is investigated to obtain a preliminary estimate of liquefaction potential. Mountain districts, hills, plateaus, terraces and alluvial fans whose gradient of ground surfaces is greater than a few degrees are exempted, since they present negligible liquefaction potential.

Pipeline Damage Potential

In the second phase, the following areas are selected among those not exempted at the first phase in principle. In other areas, the pipeline damage potential is not considered to be large.

1) The gradient of sloping ground surfaces is greater than or equal to 1.0%.
2) The height of the quay walls is greater than or equal to 5m, and the pipeline is buried within 100m of the quay wall.
3) The pipeline has rigid supports such as abutments.

Resistance Ratio for Liquefaction FL and Liquefaction Index PL

The resistance ratio for liquefaction FL is evaluated using a design horizontal seismic coefficient and soil data for each area selected in the second phase.

The methodology as well as the design horizontal seismic coefficient to evaluate FL is drawn from "Specifications for Highway Bridges Part V Seismic Design" [11]. Then, the liquefaction index PL is evaluated at each area using Equation 4.

$$PL = \int_0^{20} F \cdot (10 - 0.5x) dx \quad (4)$$

where PL : Liquefaction Index.

$F = 1 - FL$ if $FL < 1.0$.

$F = 0$ if $FL \geq 1.0$.

x : Depth from the ground surface (m).

Areas in which design against liquefaction effects is necessary are selected as follows:

1) PL is greater than or equal to 5 when pipelines are buried in sloping ground.
2) PL is greater than or equal to 5, and the thickness of the liquefying layer is greater than or equal to 1/2 of the height of the quay wall when pipelines are buried in the ground behind quay walls.
3) PL is greater than or equal to 5 when pipelines are provided with rigid supports such as an abutments.

LIQUEFACTION-INDUCED GROUND DISPLACEMENTS

Horizontal Ground Displacements in Sloping Ground

Equation 5 is a semi-empirical and semi-theoretical formula used to evaluate horizontal ground displacements in sloping ground [12]. Equation 5 was obtained from consideration of the flow of liquefying layers as one-dimensional steady state viscous flow. Multiple liquefying layers were supposed to exist. The proportional constant was determined by the regression analysis using the data of case studies of horizontal ground displacements during the 1964 Niigata Earthquake, the 1983 Nihonkai-chubu Earthquake and the 1995 Hyogoken-nanbu (Kobe) Earthquake. Figure 3 provides a comparison of the horizontal displacements evaluated by Equation 5 with ones measured during previous earthquakes.

$$\delta_h = 36 \cdot c \cdot \left\{ \sum_{i=1}^{n} \frac{1/2 \cdot \gamma_i \cdot H_i^2 + \sigma_{vi} \cdot H_i}{\left(1/2 \cdot \gamma_i \cdot H_i + \sigma_{vi}\right)^{\frac{3}{2}} \cdot N_{bi}} \right\} \cdot \theta_g \qquad (5)$$

$$N_{bi} = N_{1i} + \Delta N_{1i}$$

$$N_{1i} = \frac{1.7 \cdot N_i}{\sigma_{vi}' / 98 + 0.7}$$

$$\Delta N_{1i} = \begin{cases} 0 & \text{if } 0\% \le FC < 10\% \\ 5 & \text{if } 10\% \le FC < 20\% \\ 10 & \text{if } 20\% \le FC \end{cases}$$

where δ_h : Horizontal ground displacement (m).

c : Urban area coefficient. 0.5 if the pipeline is buried in an urban area in which buildings are supported by underground piles or they have basements. 1.0 if not.

H_i : Thickness of the i-th liquefying layer (m).

γ_i : Unit weight of the i-th liquefying layer (kN/m^3).

N_{bi} : Corrected SPT blow value of the i-th liquefying layer accounting for the effect of grain size.

σ_{vi} : Total overburden pressure exerted upon the upper surface of the i-th liquefying layer (kN/m^2).

N_{1i} : SPT blow value of the i-th liquefying layer corresponding to effective overburden pressure of 98 kN/m^2.

N_i : SPT blow value of the i-th liquefying layer.

ΔN_{1i} : Correction of SPT blow value of the i-th liquefying layer accounting for the effect of grain size.

FC : Clay and silt fraction (%). Transit weight percentage of the soil grains with a diameter less than 75 μ m.

σ_{vi}' : Effective overburden pressure exerted upon the middle surface of the i-th liquefying layer (kN/m^2).

θ_g : Gradient of sloping ground surface (%).

The load effect factor was determined to be 1.8 to make the factored design horizontal displacements evaluated by using Equation 5 at each of 1 – 3 m displacement measured site larger than the measured horizontal displacement at 90% of measured sites. The maximum factored design horizontal displacement was determined to be 3m. This was because 95% of the measured horizontal displacements of greater than 1m in the inland area during the 1964 Niigata Earthquake and the 1983 Nihonkai-chubu Earthquake were less than or equal to 3m.

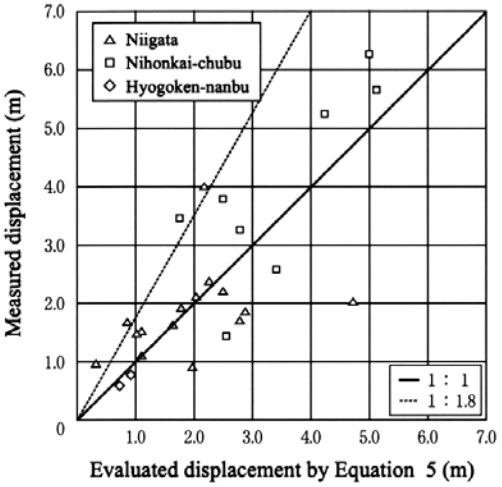

Figure 3. Comparison of the horizontal displacements evaluated by Equation 5 with ones measured during previous earthquakes

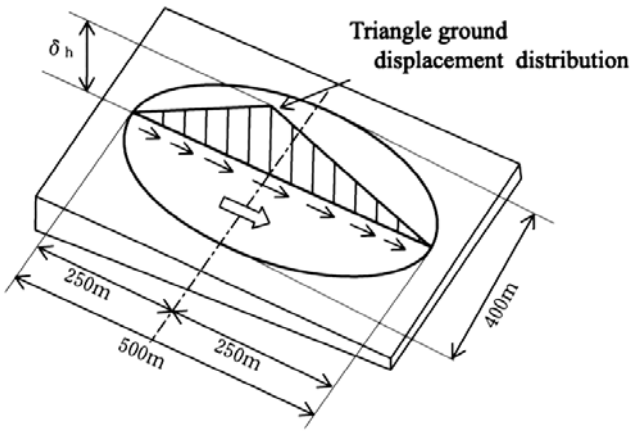

Figure 4. Distribution of liquefaction-induced ground displacements

The distribution of liquefaction-induced ground displacements should be evaluated based on liquefying layer distribution and the gradient of sloping ground surfaces at each site. Instead, the triangle distribution shown in Figure 4 may be used. This distribution was obtained from investigations of case studies during previous earthquakes.

Horizontal Ground Displacements at Ground behind Quay Walls

The movement of quay walls is evaluated by Equation 6. The horizontal movement ratio of quay walls, as shown in Table 1, was determined according to case studies during previous earthquakes [13].

$$\Delta_w = F_w \cdot \frac{H_w}{100} \tag{6}$$

where Δ_w : Horizontal movement of quay walls (m).

F_w : Horizontal movement ratio of quay walls. Shown in Table 1 (%).

H_w : Height of quay walls (m).

The depth of areas in which ground displacements occur is evaluated by Equation 7. Equation 7 was obtained from case studies during previous earthquakes [13].

$$L_{w0} = 250 \frac{\Delta_w}{N_1} \tag{7}$$

where L_{w0} : Depth of areas in which ground displacements occur (m).

N_1 : SPT blow value corresponding to effective overburden pressure of 98 kN/m^2.

$$N_1 = \frac{1.7 \cdot N}{\sigma_v' / 98 + 0.7}$$

TABLE 1. THE HORIZONTAL MOVEMENT RATIO OF QUAY WALLS

Quay wall type	Liquefaction severity		Movement ratio (%)
Gravity type	Only background liquefies.		15
	Background and foundation ground liquefy.		30
Sheet pile type	Background liquefies.	Ground around anchor piles does not liquefy.	20
		Ground around anchor piles liquefies.	40
	All of background, foundation ground and ground around anchor piles liquefy.		75

Horizontal displacements at pipeline sites are evaluated by Equation 8. Equation 8 was obtained from case studies during previous earthquakes [13].

$$\delta_h = \Delta_w \cdot \exp(-3.35 \cdot L_{wp} / L_{w0}) \tag{8}$$

where δ_h : Horizontal displacement at pipeline sites (m).

L_{wp} : Distance from the quay wall to pipeline sites (m).

The load effect factor was determined to be 1.3 to make the factored design horizontal displacements nearly equal to the upper limit of those obtained from case studies.

Settlements

The magnitude of settlements is evaluated by multiplying liquefying layer thickness by 5%. A figure of 5% was determined based on soil element tests [14]. The load effect factor was determined to be 1.0, since 5% was nearly equal to the upper limit in the element tests.

RESTRAINT FORCES EXERTED UPON PIPELINES

Soil spring characteristics were modeled by a bilinear relationship between restraint forces exerted upon pipelines and the relative displacements of the ground and the pipelines. Figure 5 shows the bilinear relationship.

The depth of the crown of pipelines is generally 1.5m – 1.8m. At this depth, pipelines may be or may not be buried in the liquefying layer. Therefore, pipelines were assumed to be buried in the non-liquefying layer above a liquefying layer, since restraint forces exerted upon pipelines are larger in this case.

Restraint Force by Axial Ground Displacements

Table 2 shows critical shear stress, a yield displacement and a soil spring coefficient for pipelines buried at the depth of 1.8m from ground surface to the crown. Critical shear stress was investigated by centrifuge model experiments [2]. Measured critical shear stress was nearly equal to that specified in Recommended Practice for Earthquake Resistant Design of High Pressure Gas Pipelines [15] which is the design guidelines against wave propagation and in which a liquefying layer is not supposed to exist. As a result, the same critical shear stress, yield displacement and soil spring coefficient were adopted as in reference [15].

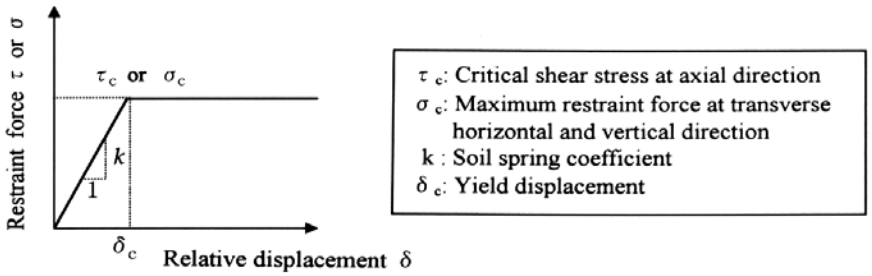

Figure 5. A bilinear relationship between the restraint forces exerted upon pipelines and the relative displacements of the ground and the pipelines

TABLE 2. CRITICAL SHEAR STRESS, A YIELD DISPLACEMENT AND A SOIL SPRING COEFFICIENT IN AN AXIAL DIRECTION (PIPELINE DEPTH : 1.8m)

Critical shear stress τ_c (N/cm^2)	Yield displacement δ_c (cm)	Soil spring coefficient $k = \tau_c / \delta_c$ (N/cm^3)
1.5	0.25	6.0

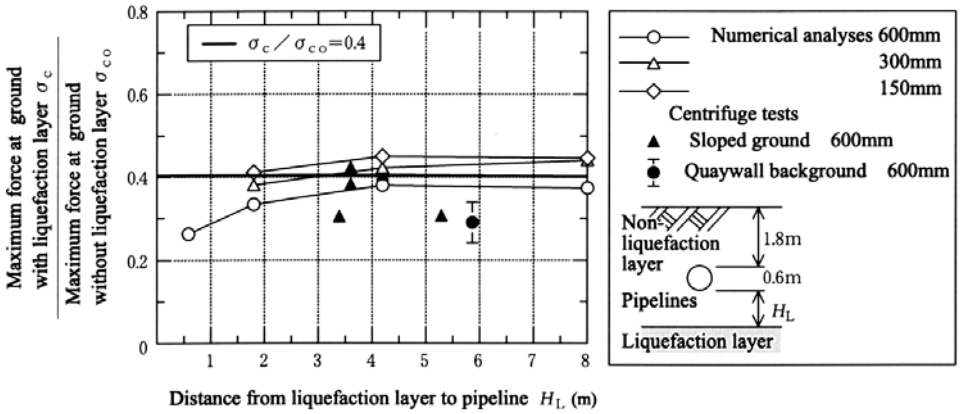

Figure 6. The maximum restraint force ratio in a transverse horizontal direction

The load effect factor was determined to be 1.2 to make the factored design critical shear stress nearly equal to the upper limit of those obtained in the experiments.

Restraint Force by Transverse Horizontal Ground Displacements

Maximum restraint forces were investigated by centrifuge model experiments [3], numerical analyses and shaking table experiments. As shown in Figure 6, they were nearly equal to 0.4 times those specified in reference [15]. As a result, maximum restraint forces of 0.4 times those in reference [15] were adopted. Soil spring coefficients of 0.4 times those in reference [15] were adopted, either. Yield displacements were identical.

The load effect factor was determined to be 1.2 to make the factored design restraint forces nearly equal to the upper limit of those obtained in the experiments and the numerical analyses.

Restraint Force by Settlements

Maximum restraint forces per unit area, yield displacements and soil spring coefficients presented at reference [16] were adopted. The load effect factor was determined to be 1.1 to make the factored design restraint forces nearly equal to the upper limit of those in the experiments in the reference [16] et al..

PIPELINE DEFORMATION ANALYSIS

Deformation Formulas

Table 3 shows pipeline deformation evaluation methods. During the development of the deformation formulas, the severest conditions that resulted in largest deformations and deflection angles were considered. These conditions involved the input direction of ground displacements, the position of a pipe bend, the length and the width of liquefaction areas, initial pipe bend angles, and the number of pipe bends in the pipeline system.

TABLE 3. PIPELINE DEFORMATION EVALUATION METHODS

Liquefaction effects	Pipelines uniformly supported by the ground	Pipelines whose supporting condition changes along their course
Horizontal displacements in sloping ground	Deformation formulas: ・ straight pipe-compression, ・ straight pipe- bending, ・ pipe bend-closing mode [7], ・ pipe bend-opening mode [7].	Non-linear FE analysis with beam element or shell/beam hybrid model.
Horizontal displacements in ground behind quay walls	The same as the above.	
Settlements	May be omitted.	

An Example of Deformation Formulas

Equation 9 is the deformation formula used to evaluate pipe bend deflection angles due to horizontal displacements in the ground behind quay walls. Figure 7 shows the model from which Equation 9 was obtained.

$$\omega_{bo} = \frac{180}{\pi} \cdot \frac{150 \cdot \gamma_\delta \cdot \delta_h}{L_{p01}} \cdot \left(0.81 \cdot \frac{D}{D_{600}} + 0.43 \right) \tag{9}$$

$$L_{p01} = \sqrt[4]{\frac{1200 \cdot E \cdot I \cdot \gamma_\delta \cdot \delta_h}{P_l}}$$

$$P_l = D \cdot \gamma_k \cdot \sigma_c$$

where ω_{bo} : Pipe bend deflection angle (degree).

L_{po1} : Hinge length at opening mode (m).

D_{600} : External diameter for normalization. =60.96cm.

D : External diameter of pipes (cm).

If $D > D_{600}$, then $D = D_{600}$.

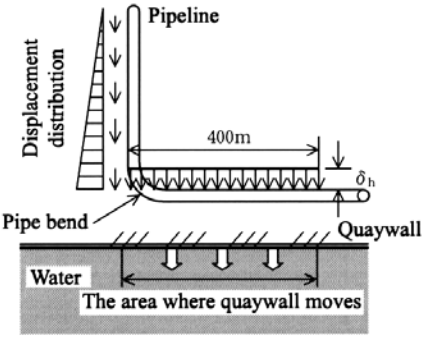

Figure 7. A pipeline model including a pipe bend in the ground behind quay walls

Non-linear FE analysis with shell/beam hybrid model was assumed to give precise deformation and its structural analysis factor was determined to be 1.0. Other structural analysis factors were determined to make the factored pipeline deformations larger than those evaluated by the non-linear FE analysis with shell/beam hybrid model. In case of deformation formulas, they are 1.1.

CRITICAL PIPE DEFORMATION

Equation 10 is the critical deformation formula used to evaluate pipe bend critical deflection angles in closing mode. Equation 11 and 12 are the formulas for opening mode.

Closing Mode Bending

$$\omega_{bsc} = 0.9 \cdot \frac{\sqrt{D/t_b} \cdot \sqrt{\phi}}{R_c/D} + \omega_{sc} \tag{10}$$

Opening Mode Bending

$$\omega_{boc} = 2.24 \cdot \frac{\phi}{\sqrt{D/t_b} \cdot (R_c/D)^{0.25} \cdot \eta} \qquad \text{if} \quad \phi \geq 22.5 \tag{11}$$

$$\omega_{boc} = 2.24 \cdot \frac{22.5}{\sqrt{D/t_b} \cdot (R_c/D)^{0.25} \cdot \eta} \qquad \text{if} \quad \phi < 22.5 \tag{12}$$

where ω_{bsc} : Pipe bend critical deflection angle in closing mode (degree). The maximum is 71 degrees.

ω_{sc} : Straight pipe critical deflection angle. k=1 (degree).

ω_{boc} : Pipe bend critical deflection angle in opening mode (degree). The maximum is 71 degrees.

t_b : Nominal wall thickness of pipe bends (cm).

ϕ : Initial pipe bend angle (degree).

R_c : Pipe bend radius (cm).

η : Coefficient accounting for the strain hardening effect. =0.62 – 0.93.

Due to the limited number of full scale tests and numerical analyses, the use of Equation 10, 11 and 12 should be restricted to the conditions shown in Table 4.

The critical deformation of pipe bends was investigated by full scale tests of twenty one pipe bends and FE analyses using shell element [10]. Figure 8 shows deformation by bending at the final stage. Figure 9 shows cut samples of the pipe after tests. In most tests and analyses, the internal pressure that produced a hoop stress of 0.4 times the specified minimum yield strength of the material was applied by water.

TABLE 4. THE CONDITOINS TO WHICH EQUATION 10, 11 and 12 CAN BE USED

Material	X42, X46, X52, X60, X65, STPG370, STPG410, STPT370, STPT410, STPT480 and STPY400
Design factor*	Less than or equal to 0.4
Nominal diameter of pipes (mm)	Greater than or equal to 100, and less than or equal to 750
Ratio of the external diameter of pipes to the nominal wall thickness of pipes	Greater than or equal to 15, and less than or equal to 60
Initial pipe bend angle (degree)	Greater than or equal to 0
Ratio of the pipe bend radius to the external diameter of pipes	Greater than or equal to 1.5

*The ratio of the hoop stress due to internal pressure to the specified minimum yield strength of the material

(a) Closing mode bending
(X65, Dn=600mm, D/t=40, R=3D, ϕ=90°)

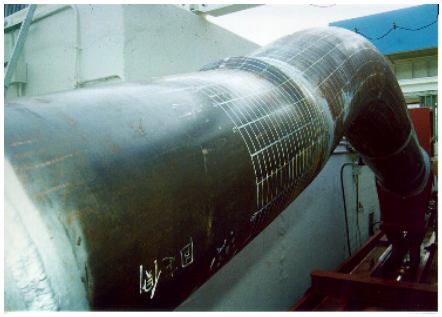

(b) Opening mode bending
(X65, Dn=600mm, D/t=40, R=3D, ϕ=45°)

Figure 8. Deformation by bending at the final stage

(a) Closing mode bending
(X52, Dn=400mm, D/t=51, R=1.5D, ϕ=90°)

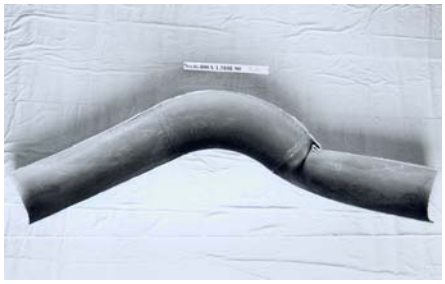

(b) Opening mode bending
(X52, Dn=400mm, D/t=51, R=1.5D, ϕ=22.5°)

Figure 9. Cut samples of the pipe after tests

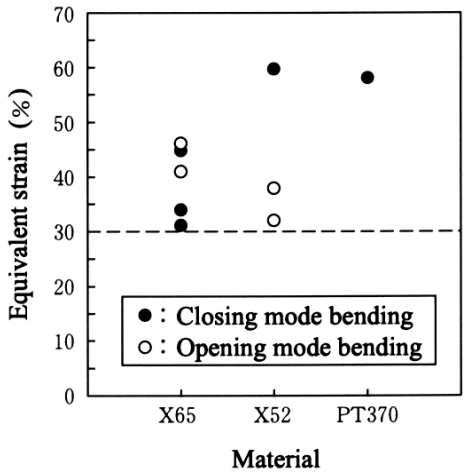

Figure 10. Estimated critical equivalent plastic strains

In closing mode bending tests, a stress release process for both internal pressure and applied load was introduced because a crack was not initiated even up to the maximum displacement of the loading apparatus capacity under monotonic increasing loading. Cracks first appeared during the stress release process. In opening mode bending tests, cracks first appeared under monotonic increasing loading.

Figure 10 shows the estimated critical equivalent plastic strains defined by Equation 13. Only the strain in the test in which the crack was initiated on the pipe surface is plotted in the figure. From Figure 10, the critical equivalent plastic strain was determined to be 30% under the scope of the conditions described in Table 4. The material resistance factor was determined to be 1.0 since all estimated critical equivalent plastic strains exceeded 30%. In the next step, the pipe bend deflection angle for which the maximum equivalent plastic strain reached 30% was estimated in closing mode by FE analysis with a shell element. In the case of opening mode, the maximum equivalent strain for the estimation of the pipe bend deflection angle was 10% rather than 30% due to the occurrence of notable buckling when the strain exceeded 10%. In the last step, the critical deformation formula was obtained from estimated deflection angles by the regression analysis using the parameters including initial pipe bend angles, external diameters, pipe bend radii and the ratio of external diameter to nominal wall thickness. In the case of the opening mode bending, the strain hardening parameter was also considered. The pipe element factor was determined to be 1.0 since critical deflection angles evaluated by formulas were less than all of those obtained in the full scale tests in which the crack was initiated on the pipe surface.

$$\varepsilon_{eq} = (\sqrt{2}/3) \cdot \{ \ (\varepsilon_x - \varepsilon_y)^2 + (\varepsilon_z - \varepsilon_x)^2 + (\varepsilon_y - \varepsilon_z)^2 \ \}^{1/2} \tag{13}$$

where ε_{eq} : Equivalent plastic strain.

$\varepsilon_{x,y,z}$: Plastic part of the principal axial, hoop and radial strain.

CONCLUDING REMARKS

Following the studies of the magnitude of liquefaction-induced ground displacements, restraint forces exerted upon pipelines, deformation formulas for evaluating large-scale pipeline deformations and critical pipe deformations capable of satisfying the seismic performance criterion of "no leakage of gas", the Recommended Practice for Design of Gas Transmission Pipelines in Areas Subject to Liquefaction was established.

ACKNOWLEDGMENTS

After the 1995 Hyogoken-nanbu (Kobe) Earthquake, Agency of Natural Resources and Energy, Ministry of Economy, Trade and Industry (METI) commissioned the Japan Gas Association to investigate gas pipeline

behavior in the event of liquefaction. Begun in 1996 and taking five years to complete, this investigation was supervised by the committee for the investigation of the effects of liquefaction on gas pipelines, chaired by Dr. Tsuneo Katayama, Director-General, National Research Institute for Earth Science and Disaster Prevention. The authors wish to express their gratitude to all those at METI for their permission to publish this paper. They also wish to express their gratitude to committee members for their invaluable suggestions.

REFERENCES

[1] Shimamura, K., M.Hamada, S.Yasuda, S.Kojima, Y.Fujita, and T.Kikuchi. 2000. "Experimental and analytical study of the floatation of buried gas steel pipe due to liquefaction," *11th European Conference on Earthquake Engineering*.

[2] Shimamura, K., M.Hamada, S.Yasuda, K.Ohtomo, Y.Fujita, S.Kojima, and Y.Taji. 2000. "Load on pipes buried in a non-liquefaction layer due to liquefaction-induced ground displacement," *12th World Conference on Earthquake Engineering*.

[3] Shimamura, K., Y.Fujita, S.Kojima, Y.Taji, and M.Hamada. To be published in Feb. 2003. "Transverse horizontal load on buried pipes due to liquefaction-induced permanent ground displacement," *Soils and Foundations*, Vol.43, No. 1.

[4] Takada, S., Y.Ogawa, K.Yoshizaki, T.Kitano and T.Kuwajima. 1998. "A large-scale deformation analysis technique for buried pipes exposed to lateral displacement due to liquefaction," *11th European Conference on Earthquake Engineering*.

[5] Takada, S., T.Suzuki, T.Koike, J.Ueno, Y.Ogawa, N.Hosokawa, T.Kitano, and T.Kuwajima. 2000. "A simplified estimation method of elasto-plastic deformations of buried pipelines caused by lateral spreading due to liquefaction," *12th World Conference on Earthquake Engineering*.

[6] Takada, S., Y.Ogawa, N.Hosokawa, T.Kitano, K.Okamura, and T.Kuwajima. 2000. "Analysis of casual factors generating large-scale deformation patterns in buried pipeline under the influence of lateral flows by liquefaction," *12th World Conference on Earthquake Engineering*.

[7] Suzuki, T., S.Takada, T.Koike, Y.Ogawa, and M.Matsumoto. 2002. "Plastic hinge analysis for buried pipeline under lateral displacement caused by subsoil liquefaction," *J. of Structural Mechanics and Earthquake Engineering*, JSCE, No. 710 / I – 60 (in Japanese).

[8] Sato, K., M.Matsumoto, S.Takada and Y.Ogawa. 2002. "Large deformation of buried pipeline due to ground displacement caused by lateral flow," *J. of Structural Mechanics and Earthquake Engineering*, JSCE, No. 710 / I – 60 (in Japanese).

[9] Miki, C., N.Oguchi, T.Uchida, A.Suganuma and T.Inoue. 2000. "Deformation and fracture properties of straight steel pipe with internal pressure under uniaxial compressive and bending load." *12th World Conference on Earthquake Engineering*.

[10] Miki, C., T.Kobayashi, N.Oguchi, T.Uchida, A.Suganuma, and A.Katoh. 2000. "Deformation and fracture properties of steel pipe bend with internal pressure subjected to in-plane bending," *12th World Conference on Earthquake Engineering*.

[11] Japan Road Association. 1996. "Specifications for Highway Bridges Part V Seismic Design."

[12] Hamada, M., K.Wakamatsu, K.Shimamura and T. Nire. 2001. "A study on the evaluation of horizontal displacement of liquefied ground," *Proceedings of 26th Earthquake Engineering Conference*, 2001.8, pp.649 – 652(in Japanese)

[13] Ishihara, K., S.Yasuda and S.Iai. 1997. "Simple evaluation method of the lateral flow in ground behind quay walls caused by liquefaction," *Proceedings of 24th Earthquake Engineering Conference*, 1997.7, pp.541 – 544(in Japanese)

[14] Ishihara, K., M.Yoshimine. 1992. "Evaluation of settlement in sand deposits following liquefaction during earthquake, *Soils & Foundations*, Vol.31, No.2, pp.173 – 188.

[15] Japan Gas Association. 2000. "Recommended Practice for Earthquake Resistant Design of High Pressure Gas Pipelines," (in Japanese).

[16] Trautmann, C.H., T.D.O'rourke and F.H.Kulhawy. 1985. "Uplift force-displacement response of buried pipe," *J. of Geotechnical Engineering,* ASCE, Vol.111, No.9.

Design, Mitigation, and Rehabilitation of Lifeline Systems

Pipeline Seismic Mitigation using Trenchless Technology

Le Val Lund, P.E.

ABSTRACT

Water, wastewater and natural gas utilities are usually limited in funds for seismic mitigation of their pipelines. A number of methods are discussed which can be used for lifeline pipeline rehabilitation and enhancing the seismic performance of pipelines used for water, wastewater and natural gas, as well as improving the flow capacity and in the case of a water pipeline water quality. These methods use the trenchless technology, which minimizes disruption to traffic, business and residents; impact on the environment; reduces costs and the time of construction. All the methods use the annular space in an existing pipe for the pipeline rehabilitation avoiding trench excavation.

Le Val Lund, P.E., M. ASCE, Civil Engineer, 3245 Lowry Road,
Los Angeles, CA 90027

INTRODUCTION

Lifelines

A lifeline pipeline can convey water, wastewater, storm drainage, natural gas and liquid fuels and a lifeline conduit can contain power and communication cables. Lifelines are those systems and facilities necessary for the functioning of an industrialized society and also necessary for emergency response and recovery after a natural disaster, such as an earthquake. The seismic hazards that may impact pipelines and conduits are faulting, shaking, liquefaction, lateral spreading, and landslides. Also they may be damaged by another lifeline system, which is damaged and is co-located with the pipeline or conduit.

Seismic Mitigation

The pipeline seismic mitigation is based on the facts that using trenchless technology an almost complete overhaul is made of the pipeline by the following activities:

1. All the old fittings (bends, tees, crosses, valves and other obstructions) are removed from the pipeline.
2. After the pipeline is cleaned a thorough physical and closed circuit television inspection is made of the pipeline at the launch pits and locations where the fittings have been removed.
3. Laboratory testing of the materials may be made to determine there physical characteristics.
4. All the fittings are replaced with new units and in some cases this involves replacing the fire hydrants, service connections and meters.
5. The insertion of a liner of generally flexible materials provides for some seismic movement of the pipeline.
6. In some cases the liner provides for the seismic strengthening of the pipeline and make it available for higher internal pressure.

Temporary Repairs

Temporary repair of pipelines and conduits are necessary to restore utility service to medical facilities, police and fire stations, and emergency operating centers. Also necessary is water for public fire protection, natural gas for cooking and space heating and liquid fuel for operation of emergency equipment and lifeline facilities. Temporary repairs are made to prevent floods from broken water lines, fires and explosions from broken gas and fuel lines, and sewers and storm drains to

prevent pollution and the spread of disease. Restoration of power and communications facilities is necessary for emergency response and recovery. Eventually pipelines
and conduits are repaired to provide service to homes, business and industry.

Permanent Replacement

Permanent pipeline replacement is made to increase seismic resistance, improve or increase capacity, improve water quality and minimize leaks of gas, fuel oil, water and wastewater. These leaks result in unaccounted for gas, fuel oil and water and result in loss of revenues. This report is concentrating on water and wastewater systems; however, the methods can be applied to the other lifeline systems.

Financial Impact

Difficulties in implementing seismic mitigation or rehabilitation of pipelines and conduits are normally financial, which requires management and sometimes public and political support. However, in some cases the lack of good information on the condition of pipes, and the operational restraints necessary to maintain service may impact the decision process. Financing the program may come from normal rates charged for the quantity of product used, emergency surcharges, taxes approved by the governing body, general obligation or revenue bonds, insurance, government grants or loans. Underground permanent replacement, if repair is not feasible, and seismic mitigation if desired, can be done by two methods, trench excavation or trenchless technology.

TRENCH EXCAVATION

Replacement of pressure pipelines using trench excavation method, using welded steel pipe with welded joints and ductile iron pipe with rubber gasket joints has shown good performance in past earthquakes. Both of these types of pipe can be joined by various types of mechanical couplings, which provide flexibility during a seismic event. Trench excavation in an urban area with busy roadways causes disruption of traffic and disturbs the residents and businesses and may have an impact on the environment. The type of joints used in this pipe is important for good seismic performance. Joint types will be discussed later in this report.

TRENCHLESS TECHNOLOGY

Trenchless technology rehabilitation of pipe has increased in popularity in urban areas, because of its lessened impact on traffic, residents, businesses and environment. The pipe or conduit rehabilitation has some value towards seismic mitigation; however, it cannot be specifically quantified. Also important is the fact

generally new pipe occupies the existing space among other substructures in a somewhat crowded area with other utilities. Also trenchless technology can reduce the cost and time of construction. All of the methods require a drained and cleaned pipe and temporary supply of water to implement. The rehabilitation of existing water mains by cleaning and lining insitu permanently improves the hydraulic capacity, seals joints and pinhole leaks and improves water quality by minimizing taste and odor problems associated with unlined pipe.

Temporary Bypass

Temporary bypass or sideling systems maintain customer water service prior to the cleaning and lining operation used in trenchless technology. The quick connect pipeline is usually laid in the gutter along the curb line on each side of the street. Connections to the active water system are made at the fire hydrants or in some cases by a wet tap to the pressurized water main. Normal installation requires 50 and 100-millimeter (mm) (2 and 4-inch) diameter lines. Temporary hose connections are made to the existing meters for residential, commercial and in some cases for fire service. Wastewater system can be bypassed by pumping from an upstream manhole to a downstream manhole. Temporary supply of water, although rarely done, can be provided by tank trailers, tank trucks, bottled water or portable hose.

Pipeline Cleaning

After the bends, valves and other obstructions are removed, the pipe is cleaned by using one of the following methods:

1. Hydraulic-A steel frame in the form of a piston with protruding metal scrapper blades is propelled through the pipeline by water pressure.
2. Mechanical-The cleaning scrappers are pulled through the pipe by a winch.

In both cases water is used to flush debris out of the pipe. The scrapper is pulled back and forth until the pipe wall is cleaned for lining.

Closed Circuit Television Inspection

Closed circuit television inspection is done to observe the condition of the interior of the pipe and identify any unknown obstructions or connections. After the pipe has been cleaned a self-propelled television camera photographs the interior of the pipe. The camera has lights to illuminate the interior of the pipe. The image is transmitted to a monitor in van located outside the launching pit, where an operator observes the condition of the pipe and makes videotape for future reference.

REHABILITATION METHODS

Cement Mortar Lining

. After inspection and the pipeline is cleaned, a cement-mortar is premixed above ground and pumped to the lining machine through high-pressure rubber hoses inside the pipe. The cement mortar lining machine consists of a rapidly spinning dispensing head that centrifugally applies a uniform coating of cement, sand and water to the pipe wall as the lining machine is winched through the pipe. As the cement-mortar is applied, a flexible conical troweling device follows behind to produce a smooth hydraulically efficient surface. In large diameter pipes the smoothing of the cement-mortar is done with rotating trowels instead conical troweling device. Cement mortar lining is specified by American Water Works Association (AWWA) Standard AWWA C-602. The mortar is 1:1 mixture of Portland cement and silica sand with water added for proper placement. Cement-mortar lining is generally not considered a seismic improvement; however, the fact the fact that old valves, fittings and service connections are upgraded during rehabilitation, it provides some seismic improvement. In the 1994 Northridge earthquake, field personnel observed old cast iron and steel pipe which had been cement mortar lined in place appeared to have a lower frequency of leaks; however, this has not been scientifically documented.

Pipe Insertion

Pipe insertion method is done in existing larger diameter pipes, where retaining the diameter for flow capacity is not critical. The existing pipe requires inspection, cleaning and the removal of valves and sharp bends. Prefabricated welded steel pipe is installed within the annular space of the old pipe and joints are welded. The annular space between the old pipe and the new pipe is filled with cement grout.

Slip Lining

Slip lining method using high density polyethylene (HDPE) pipe is done on existing pipe in both the small and large sizes mainly for gas, water and wastewater lines. The HDPE pipe is laid out along a roadway, joints are fused together under high temperature and pressure The HDPE pipe is pulled through the existing host pipe. Connections are made to existing pipe by a specially fabricated bolted flanged connection. The HDPE pipe can either be smaller than the existing pipe or through a special process (pipe bursting or splitting to be discussed later) maintain the same inside or increase the inside diameter the host pipe.

The British gas industry has been the pioneer since the 1970's, in using slip-lining technologies to rehabilitate gas mains. Later wastewater agencies started using the slip lining method for sewer mains. Gas mains rehabilitated with HDPE pipe performed well in the 1994 Northridge earthquake. The use of HDPE pipe for water service has lagged due to the approval process for the material to be used in potable water systems.

Expanded Molecular Reoriented PVC

The Expanded Molecular Reoriented Poly Vinyl Chloride (PVC) method is a patented system for water pipelines, which guarantees a working water pressure of 1000 kilopascal (kPa) (150 pounds per square inch (psi)). The manufacturer of this piThe method lines the host pipe with a standard AWWA) C-900 class PVC pipe. After the existing pipe has been cleaned and inspected, a slightly smaller diameter standard new PVC pipe is pulled through the host pipe and each end is sealed. Joints are fused together with heat and pressure similar to the joints in the slip lining method. A boiler makes steam and a compressor injects the high-pressure steam into the PVC pipe, gradually expanding the PVC, so that fits tight against the host pipe. The integrity of the host pipe is not important for maintaining pressure, since the PVC pipe is structurally sound.

Insituform Technologies, Inc. Methods

There are several methods available for gravity and pressure pipe systems, which are trade names of the Insituform Technologies, Inc.

The Paltem System ® uses continuous woven polyester hose with an elastomer coating and can be used in pipelines up to 1000-mm (40-in) in diameter and through bends up to 90 degrees. The uncoated side of the liner is covered with an epoxy resin. Compressed air or water pressure is then used to invert (turn inside out) and propel the liner through the pipe from the access pit. This is called the inversion process. Heat or ambient temperature is used to cure the epoxy resin and adhere the liner to the inside of the pipe. The ends of the liner are then cut off and the end seals are installed before the line is placed back into service.

Pressure Pipe Liner ® is like the Paltem System for structurally sound pipe system. The system uses a reinforced felt tube and modified resin system. It can be installed in diameters 200- to 1200-mm (8- to 48-in) in diameter and uses the same inversion process as the Paltem.

The Thermopipe System ® is used for rehabilitating small distribution mains, 100- to 200- mm (4- to 8-in), and has a long-term hydraulic pressure rating of 1000 kPa (150 psi). The system is polyethylene tube reinforced woven polyester fiber and is factory folded in a "C" shape. It is then wound onto a reel, which enables it to be transported to a job site. The liner is winched into the pipe and is re-rounded using

steam and air pressure, so that it closely fits the existing inside diameter of the pipe. End seals are installed before the line is placed back into service. It can be used to rehabilitate pipes of all common materials and can be used through slight bends.

Pipe Bursting

The Pneumatic Pipe Bursting Process simultaneously breaks the old pipe pushing it into the surrounding soil while the new pipe is pulled into place. This method is mainly used for cast iron, concrete, and vitrified clay pipe. Again this is done after a television inspection and removal of gate valves and sharp bends and the cleaning of the pipe. An expander on the pipe-bursting tool increases the diameter of the hole. The pneumatic tool (Grundocrack ®) is guided through the old pipe by a cable, and an internal reciprocating piston breaks the pipe and supplies the force for most of the forward motion.

The HDPE pipe is laid out along a roadway; joints are fused together under high temperature and pressure as in the slip lining process. The HDPE pipe is attached and immediately follows the expander tool into the existing host pipe. A large capacity portable compressor is used to drive the pneumatic tool. Sometimes an extension in front of the expander tool, called a schnoze, is used to help guide the expander tool in the host pipe. A Bentonite solution is sometimes used to reduce friction for larger diameter HDPE to maintain the annular space created as the tool travels through the host pipe.

Connections are made to existing pipe by a specially fabricated bolted flanged connection. The new pipe is a high-density polyethylene (HDPE) material, which can be up to 50-mm (2-in) thick depending on system pressure. Even with the same diameter this new pipe reduces the hydraulic friction and automatically increases the flow capacity. Also this process provides an opportunity to increase the pipe diameter from 0 to 25% in diameter to further increase flow capacity of the pipe.

While most pipe bursting jobs use the pneumatic type of bursting tools there are other types. There is static bursting which pulls a splitting head into the host pipe and fractures the host pipe by the constant pulling by the chain or cable attached to the splitting head. The other method used is the hydraulic actuated bursting head to fracture the pipe. A cable attached to the front of the bursting head pulls the devise through the pipe. Again the new HDPE is immediately pulled through the expanded pipe. These systems can be used for water, wastewater, storm drainage and gas systems, as well as upgrading telephone and power circular conduits.

Pipe Splitting

The Pipe Splitting System is somewhat similar to the Pipe Bursting Process, which simultaneously breaks the old pipe pushing it into the surrounding soil while the new pipe is pulled into place. This method is mainly used for steel pipe. Again this is done after a television inspection and removal of gate valves and sharp bends and the cleaning of the pipe. A launch pit is required at each end of the pipeline to be

lined. The Grundoburst ® System consists of a hydraulic power unit, hydraulic flow control and Grundoburst ® hydraulic bursting unit. Quicklot ® bursting rods are pushed through the host pipe with the Grundoburst ®, until they reach the launch pit at the other end of the pipeline. A flexible guide rod out front helps the rods navigate the existing line.

Once at the launching pit, the guide rod is removed and bladed cutting wheels, a bursting head, an expander and new HDPE pipe are attached. The entire configuration is pulled back through the host pipe. The bladed cutting wheels split the existing pipe. The bursting head and expander displace the fragmented host pipe into the surrounding soil while the new HDE is pulled through the host pipe. An expander on the pipe bursting tool increases the diameter of the hole. The especially design bladed rollers split the host pipe instead of ripping or tearing it. Various bladed rollers are available to split a wide range of pipe diameters.

The HDPE pipe is laid out along a roadway; joints are fused together under high temperature and pressure as in the slip lining process. The HDPE pipe is attached and immediately follows the expander tool into the existing host pipe. Connections are made to existing pipe by a specially fabricated bolted flanged connection. The new pipe is a high-density polyethylene (HDPE) material, which can be up to 50-mm (2-in) thick depending on system pressure. Even with the same diameter this new pipe reduces the hydraulic friction and automatically increases the flow capacity. Also this process provides an opportunity to increase the pipe diameter from 0 to 25% in diameter to further increase flow capacity of the pipe.

JOINT SYSTEM

In the trenchless technology method to improve the seismic performance of the joint system requires the excavation of each joint and may prove to be as much inconvenience to the residents, business and the environment. The costs and time of construction would increase.

The joint system is critical in the seismic performance of segmented piping systems. Butt-welded joints have shown better performance in past earthquakes than bell and spigot welded joints. One of the better joint systems is one that permits both transverse and longitudinal movement of the joints for water, wastewater and industrial pipelines. This type of joint is available in sizes up to 1500-mm (60-in) in diameter, and is about 30% more expensive than conventional pipe joints. It performed very well in the 1995 Kobe earthquake. This joint is normally used for inlet/outlet connection to tanks and reservoirs, and at large service connections, but it may be used at other critical locations, such as, fault crossings.

The butt-welded joint system avoids the eccentricity of the conventional bell and spigot joints. Butt-welded joints on gas lines performed well in the 1994 Northridge earthquake. Studies at the Cornell University, New York are being performed to improve the performance of the bell and spigot joint, by changing the

configuration of the bell and spigot or by applying a reinforcing plastic wrap around the joint. The ductile iron seismic joint (S1 and S2) with rubber gaskets used in Japan performed very well in the 1995 Kobe earthquake.

CONCLUSION

Pipeline rehabilitation using trenchless technology is used by utilities to minimize the impact of construction on residents, business and the environment at a reduce cost and time of construction to provide improved flow capacity, water quality and enhance the seismic resistance of pipelines.

Implementation of seismic mitigation program should be done after completion of a seismic vulnerability analysis of the entire utility system. The mitigation program also requires an updated and practiced emergency response and recovery plan. Pipeline utilities in areas of seismic activity should maintain an inventory or locate, list and continuously update emergency resources of temporary bypass piping, pipe, fittings, repair clamps, equipment and construction industry specialized trained personnel.

REFERENCES

[1] American Society of Civil Engineers, Pipelines in the Constructed Environment, Proceedings of the 1998 Pipeline Division Conference, August 23-28, 1998, San Diego, California, Edited by Joseph P. Castronovo and James A. Clark, Reston, VA, 1998

[2] Insituform Technologies, Inc., Technical Bulletins, Chesterfield, MO, 1998

[3] Insituform Technologies, Inc., Grundocrack ® Pneumatic Pipe Bursting System, Aurora IL 1996

[4] J. Fletcher Creamer and Son, Inc., Pipe Cleaning and Lining Services, Hackensack, NJ, 2000

[5] Insituform Technologies, Inc., Grundoburst ® Static Pipe Bursting System, Aurora IL 2001

[6] Personal contact with Richard Nieman and Mark Smith, Duraliner, New Orleans, LA; Welfredo Paz and Kathy Harada, Los Angeles Department of Water and Power; George Mallakis, J. Fletcher Creamer and Son, Inc., Sylmar, CA; Collins K. Orton, TT Technologies, Inc., Aurora, IL; 2002.

L.L. 8US/J 02Wksp 112802

Earthquake-Resistant Design for Pipelines Subjected to Permanent Ground Deformation using EPS Backfill

Koji Yoshizaki and Takashi Sakanoue

ABSTRACT

Earthquake-induced Permanent Ground Deformation (PGD), occurring as surface fault deformation, liquefaction-induced soil movements, and landslides, can affect significantly underground lifelines, such as buried gas and water pipelines. There is substantial evidence of gas and water supply pipeline damage caused by PGD from past major earthquakes. To design pipelines against earthquakes, the pipelines should have enough stiffness against force conveyed from adjacent ground. For the pipelines constructed in areas where such PGD is expected, the pipe stiffness should be increased with larger diameter, thickness or strength, or the soil-pipe interaction should be reduced. In this paper, the effect of EPS (Expanded Poly-Styrene) for backfill on reduction of soil-pipeline interaction was evaluated for earthquake-resistant design.

Full-scale experiments were conducted to evaluate the effect of EPS for reduction of soil-pipeline interaction. 100-mm-diameter pipeline was buried in the ground assuming a pipeline buried under roads. The pipe was then pushed into the ground horizontally with a hydraulic jack for 300 mm, and the reaction force was measured to evaluate the soil-pipe interaction in the transverse horizontal direction.

The results showed that the EPS backfill had significant effect to reduce the soil-pipe interaction. For the case when EPS was used for backfill, the peak value of the measured reaction force was approximately half of that of the case when compacted sand was used for backfill.

Effect of EPS backfill on large deformation behavior of buried pipelines with elbows subjected to PGD was also evaluated using Finite Element analytical model with the reduction in soil-pipe interaction.

Koji Yoshizaki, Senior Researcher, Pipeline Technology Center, Tokyo Gas Co., Ltd., 1-7-7 Suehiro-cho, Tsurumi-ku, Yokohama, Japan 230-0045

Takashi Sakanoue, Researcher, Pipeline Technology Center, Tokyo Gas Co., Ltd., 1-7-7 Suehiro-cho, Tsurumi-ku, Yokohama, Japan 230-0045

INTRODUCTION

Earthquake-induced Permanent Ground Deformation (PGD), occurring as surface fault deformation, liquefaction-induced soil movements, and landslides, can affect significantly underground lifelines, such as buried gas and water pipelines. There is substantial evidence of gas and water supply pipeline damage caused by PGD from past major earthquakes, such as the 1906 San Francisco[1], the 1964 Niigata, the 1971 San Fernando[1], the 1979 Imperial Valley, the 1983 Nihonkai-chubu[2], the 1989 Loma Prieta, the 1994 Northridge[3], and the 1995 Hyogoken-nanbu[4] earthquakes. More recent earthquakes, including the 1999 Kocaeli and Duzce earthquakes in Turkey, and the 1999 Chi-chi earthquake in Taiwan[5], have provided additional evidence of the importance of liquefaction, faults rupture and landslides through their effects on a variety of electrical, gas and water supply lifelines.

To design pipelines against earthquakes, the pipelines have to have enough stiffness against force conveyed from adjacent ground. For the pipelines constructed in areas where such PGD is expected, the pipe stiffness should be increased with larger diameter, thickness or strength, or the soil-pipe interaction should be reduced.

In this paper, the effect of EPS (Expanded Poly-Styrene) for backfill on reduction of soil-pipeline interaction was evaluated for earthquake-resistant design. Effect of EPS backfill on large deformation behavior of buried pipelines with elbows subjected to PGD was also evaluated using Finite Element analytical model with the reduction in soil-pipe interaction.

EXPERIMENTS ON THE EFFECT OF EPS BACKFILL

Experimental condition

Full-scale experiments were conducted to evaluate the effect of EPS backfill on soil-pipe interaction. 100-mm-diameter pipe section was installed and backfilled in a test compartment that had inside dimensions of 3.1 m by 2 m by 1.56 m deep, and pushed into the test compartment by a hydraulic jack through two 65-mm-diameter pipes. Figure 1 (a) shows a plan view of the experimental setup. Two kinds of tests were conducted: Tests 1 and 2 were performed with backfill of compacted sand only, and EPS backfill was used for Test 3. Side views of both kinds of the tests are shown in Figures 1 (b) and (c), respectively.

The pipeline was installed at a 0.9 m depth to top of pipe in each of three experiments: Approximately 18 tons of sand was moved into the sand box for each experiment. The sand is called “Chiba Sand”, which is clean sand (3.4 % by weight of fines). The properties are summarized in TABLE I and satisfy the standard for backfill sand specified by Bureau of Construction of Tokyo Metropolitan Government. The grain size curve for Chiba Sand is shown in Figure 2. The sand was placed and compacted in 150-mm lifts with strict controls on water content and in situ density, which are summarized in TABLE II. In this table, internal friction angles obtained from triaxial compression tests with strain rate of 5%/min were determined from dry unit weight using the relationship shown in Figure 3.

The backfilled pipe section was pushed into the test compartment for 300 mm in the horizontal direction. The rate of displacement of the hydraulic jack was approximately 3 mm/sec.

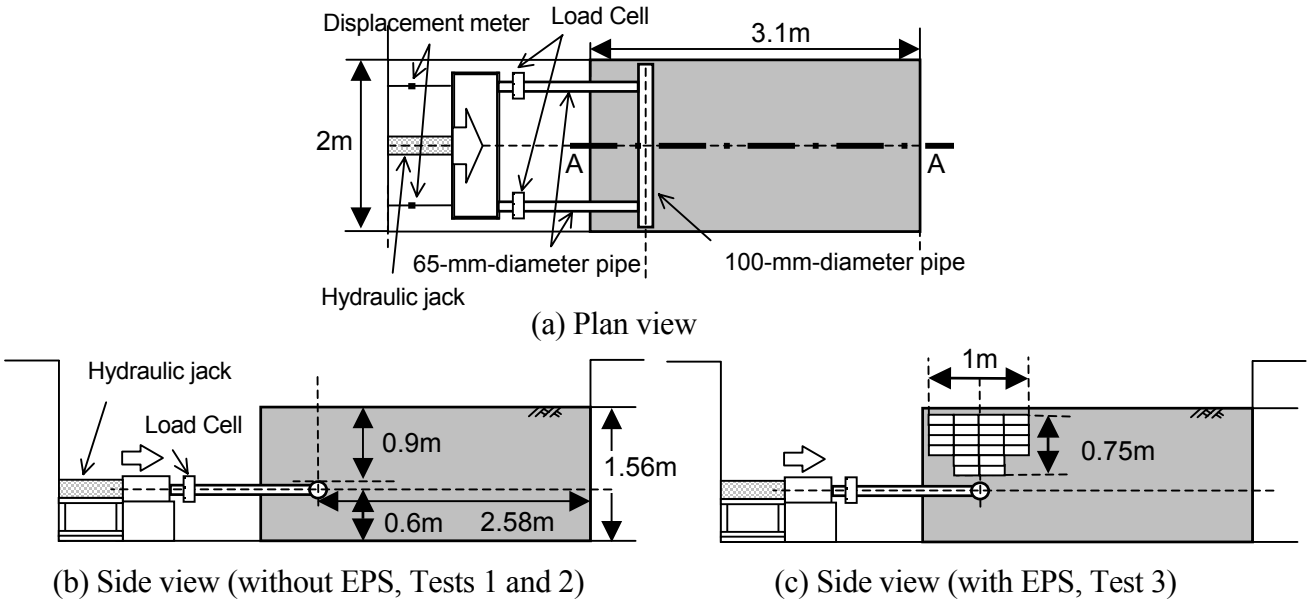

Figure 1. Experimental setup for evaluation of soil-pipe interaction

TABLE I. PHYSICAL PROPERTIES OF CHIBA SAND

Specific gravity (Mg/m^3)		2.65
Grain size distribution	Gravel (%)	0
	Sand (%)	96.6
	Silt (%)	3.4
Maximum dry unit weight (kN/m^3)		17.0
Optimum water content (%)		17.2

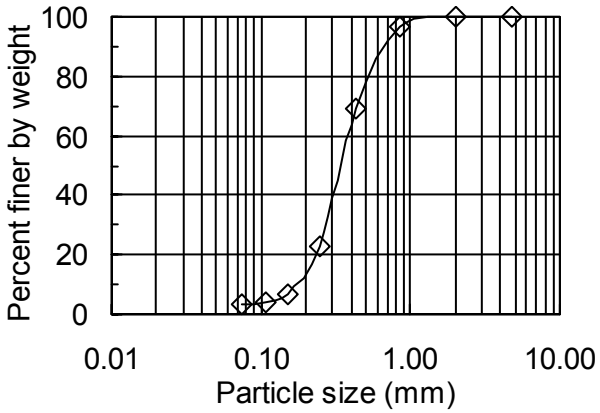

Figure 2. Grain size distribution of Chiba Sand

TABLE II. EXPERIMENTAL CONDITIONS

Test Number	1	2	3
EPS backfill	No	No	Yes
Water content (%)	16.6	17.6	16.9
Wet unit weight (kN/m^3)	17.8	18.1	17.9
Dry unit weight (kN/m^3)	15.2	15.4	15.3
Degree of compaction (%)	96	96	96
Internal friction angle (degree)	41.3	42.2	41.8

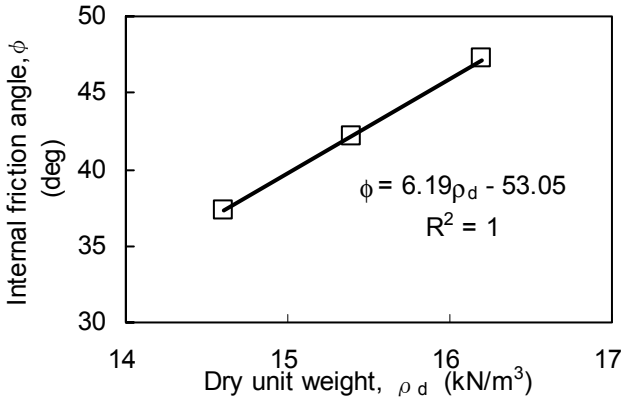

Figure 3. Relationship between dry unit weight and internal friction angle

TABLE III. PHYSICAL PROPERTIES OF EPS BLOCK

Unit weight (kN/m^3)	0.3
Ultimate compressive strength (kN/m^2)	180
Allowable compressive stress (kN/m^2)	90
Allowable temperature (ºC)	80

For Test 3, EPS blocks with dimensions of 0.5 m by 0.25 m by 0.125 m were used for backfill. EPS block is a light-weight material and generally used for embankment on soft ground or slopes where landslides are expected. The properties of the EPS block are summarized in TABLE III. The sand was placed for 0.1 m from the top of the pipe section, and then the EPS blocks were installed on the assumption that the trench is 1m in width, as shown in Figure 1 (c).

Experimental results

Figure 4 (a) shows the ground surface of the test compartment after Test 1. Surficial having could be seen after the test. Figures 4 (b) and (c) show the plane of soil slip observed at the Section A-A, which is shown in Figure 1 (a), by removing half of the sand in the test compartment after the test. The horizontal distance between the original pipe position and the point where the cracking reached the ground surface was 1.4 m as shown in Figure 4 (c). On the other hand, for Test 3, the plane of soil slip reached the EPS block, and then the slip occurred between the EPS and sand, as shown in Figures 5 (b) and (c). The horizontal distance between the original pipe position and the point where the cracking reached the ground surface was 0.5 m, which was less than half of that of Test 1.

(a) Ground surface (b) Slip surface at Section A-A (c) Sketch of ground deformation at Section A-A

Figure 4. Ground deformation after experiment（Test 1， without EPS）

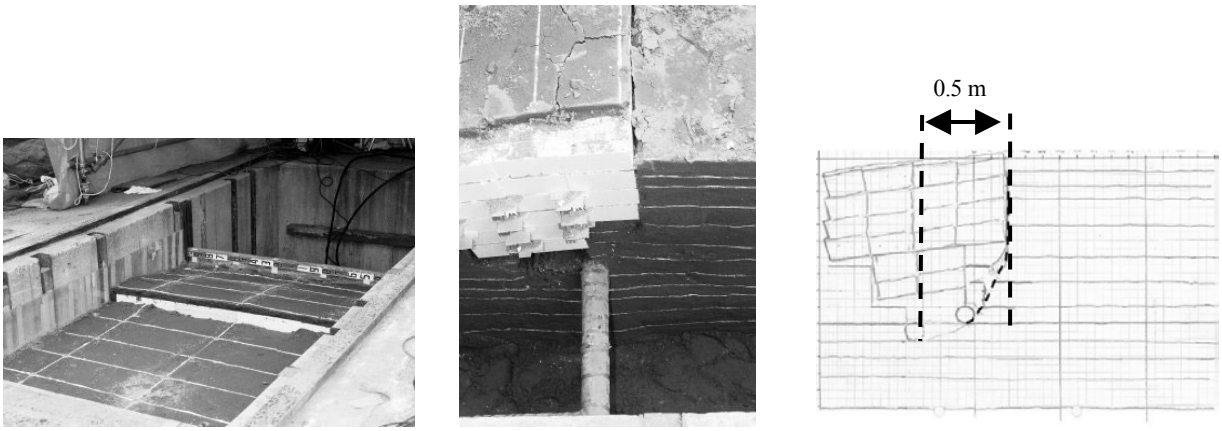

(a) Ground surface (b) Slip surface at Section A-A (c) Sketch of ground deformation at Section A-A

Figure 5. Ground deformation after experiment（Test 3， with EPS）

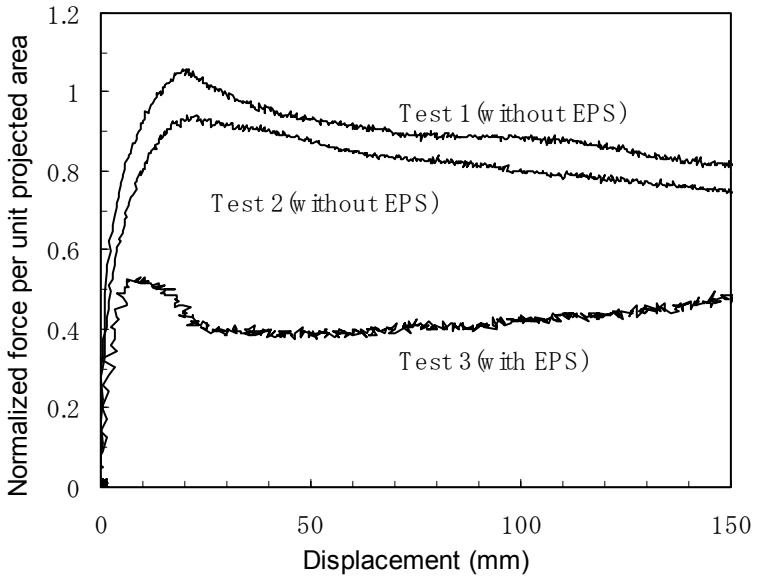

Figure 6. Experimental results

Figure 6 shows the experimental results: normalized force per unit projected area vs. relative displacement of pipe in the ground. Here, the normalized force per unit projected area was calculated from the force per unit projected area, which was adjusted so that the internal friction angles of the three tests are equal using the relationship proposed by Trautmann and O'Rourke[6], and also was normalized with the average of the maximum values recorded during Tests 1 and 2. Both the soil properties for Tests 1 and 2 in TABLE II and the close agreement in maximum forces (13 % difference) provide evidence that similar conditions were achieved in the three tests.

The maximum force recorded during Test 3, which used EPS backfill, was 54 % of the average of the maximum values recorded during Tests 1 and 2, as shown in Figure 6. From these experimental results, when EPS is used for backfill, the lateral force on pipes with the movement of the ground during earthquakes can be reduced to approximately half of that of normal backfill. Quantitative evaluation of the reduction in forces can be achieved by eliminating the effect of loading rods and the edges of the pipe section, and by considering other conditions of the ground.

ANALYSES OF EPS BACKFILL EFFECT ON ENHANCEMENT OF EARTHQUAKE-RESISTANCE OF BURIED PIPELINES

Using the obtained experimental data, finite element analyses were conducted to evaluate the effect of EPS backfill on enhancement of the resistance of buried pipelines against PGD during earthquakes.

Gas and other types of pipelines must often be constructed to change direction rapidly to avoid other underground facilities or to adjust to the shape of roads under which the pipelines are buried. Because elbows are locations where flexural and axial pipeline deformations are restrained, concentrated strains can easily accumulate at elbows in response to PGD, as shown in Figure 7 (a). Therefore, a model of a buried pipeline with an elbow subjected to PGD, as shown in Figure 7 (b), is assumed for evaluation of the effect of EPS backfill.

A modeling technique named HYBRID MODEL was developed for simulating large-scale pipeline and elbow response to PGD in the previous work[7, 8]. The model uses shell elements for the elbow and its neighboring part where large, localized strains occur. As shown in Figure 8 (a), the shell elements are located over a distance equal to 40 times the diameter from the center point of the elbow. The shell elements are linked to beam elements that extend beyond the distance of 40 times the diameter. Continuity of deformation between the shell and beam elements is enforced by the use of Multi-Point Constraint in ABAQUS, as shown in Figure 8 (b).

The analytical model was verified and calibrated in the previous work[9]. Figure 9 (a) shows the large-scale experiments of PGD effects on steel pipelines with elbows. The test compartment has dimensions of 10 m by 5 m by 1.5 m approximately. L-shape 100-mm-diameter pipeline with 90-degree elbow was backfilled with compacted sand with cover depth of 0.9 m, and was subjected to ground displacement of 1 m by pulling a part of the test compartment using a crane. Figure 9 (b) shows the measured and predicted longitudinal strains under maximum ground deformation on both the extrados and intrados surfaces along the pipeline. There was good agreement for both the magnitude and distribution of measured and analytical strains.

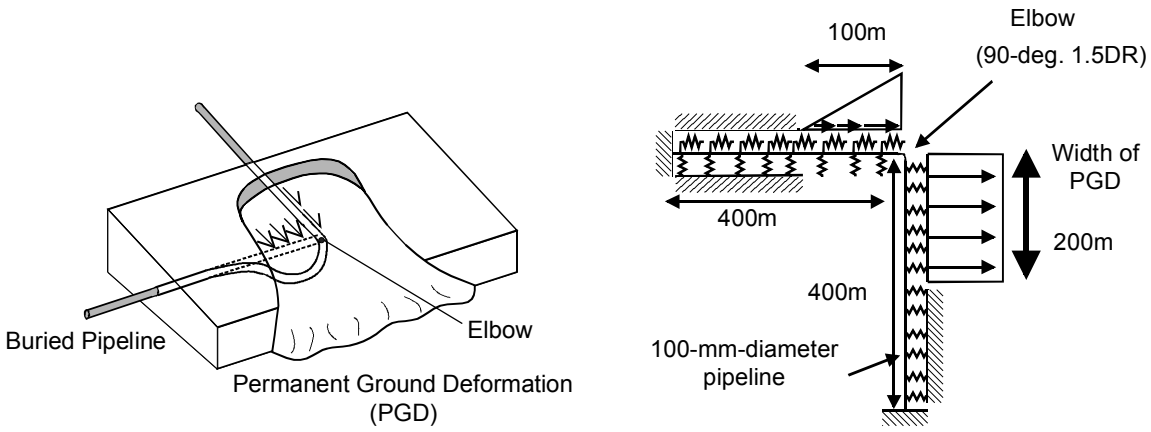

(a) PGD effect on buried pipelines with elbows (b) Assumed model

Figure 7. Assumed model of a buried pipeline with an elbow subjected to PGD

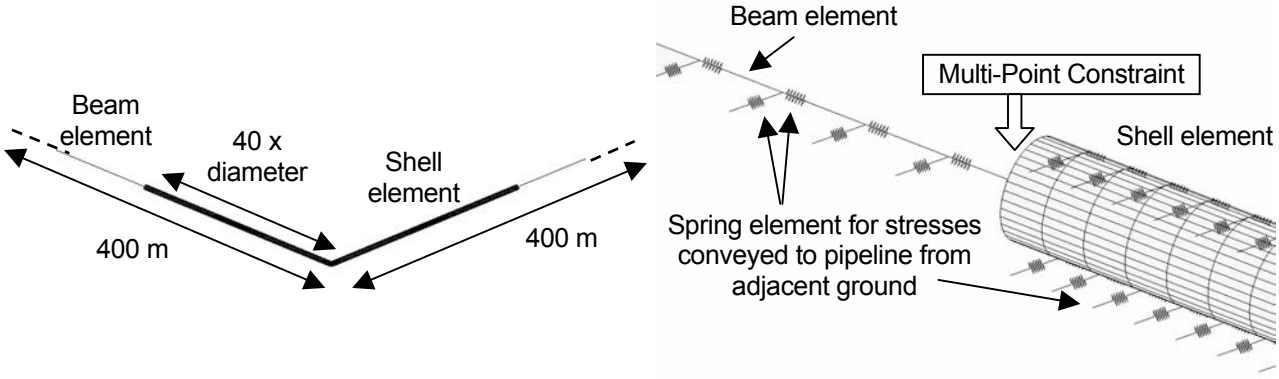

(a) Analytical model around elbow (b) Modeling for connection between shell elements and beam elements

Figure 8. HYBRID MODEL used for analyses of buried pipelines

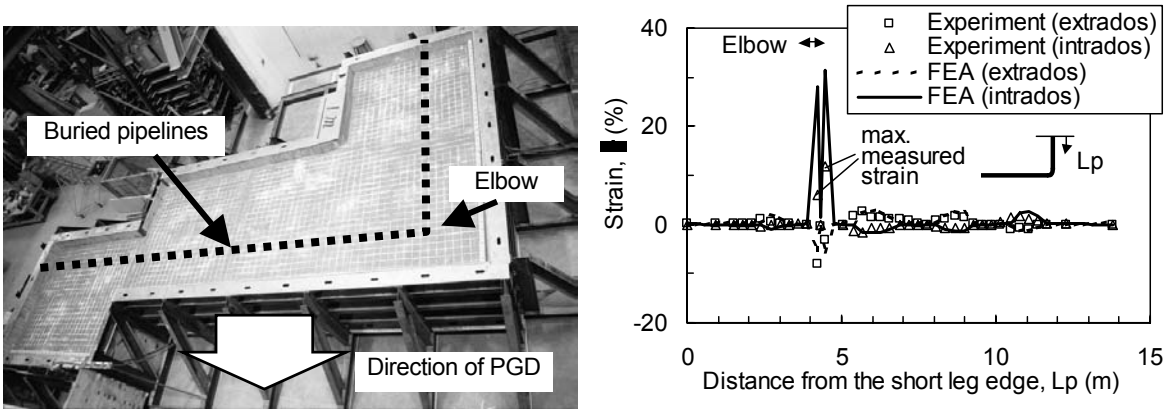

(a) Experimental setup (b) Comparison between analytical and experimental results (longitudinal strain)

Figure 9. Large-scale experiment on large deformation behavior of buried pipelines with elbows subjected to PGD[9]

100-mm-diameter pipeline with a 90-degree elbow was used to evaluate the effect of EPS on large deformation behavior subjected to PGD, as shown in Figure 7(b). SGP steel (Japanese Industrial Standard, JIS-G3452) with a minimum ultimate tensile strength of 294 MPa is used for straight pipe, and STPT 370 (JIS-G3456) with a specified minimum yield stress of 215 MPa and a minimum ultimate tensile strength of 370 MPa was used for the elbow.

The pipeline was modeled with isotropic shell elements with reduced integration points. ABAQUS Version 5.8 was used as a solver for the analyses with geometric nonlinearity and large strain formulation. The von Mises criterion and associated flow rule were applied to the model. Since the straining is in the same direction in strain space throughout the analyses, isotropic hardening was used in the model.

Soil-pipe interaction was modeled with discrete spring elements in both the longitudinal and circumferential directions for the shell elements, and in the longitudinal direction for the beam elements, as shown in Figure 8 (b). The force-displacement relationships were modeled in accordance with JGA guideline[10] and the data presented by Trautmann and O'Rourke[6]. Figure 10 (a) shows the force per unit area vs. relative displacement plot used to model soil-pipe interaction in the axial direction. Figure 10 (b) shows the force per unit projected area vs. relative displacement plot in the lateral direction. The effect of EPS backfill was modeled with the reduction of the peak value of the force per unit projected area in the lateral direction, as shown in Figure 10 (b).

Figure 11 shows the analytical results, where maximum strain in either the longitudinal or circumferential direction is plotted vs. ground displacement. When the ground displacement is 2 m, the maximum strain of the case without EPS was 24.2 %, whereas that of the case with EPS was 13.3 %, which had 45 % of reduction. Therefore, EPS backfill showed significant effect for enhancement of earthquake-resistance of buried pipelines with elbows subjected to PGD.

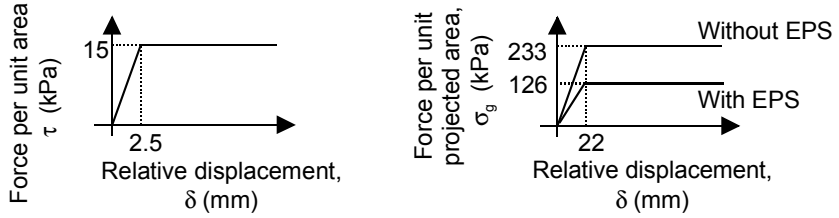

(a) Axial direction (b) Lateral direction

Figure 10. Model of soil-pipe interaction for 100-mm-diameter pipe with cover depth of 0.9 m and internal friction angle of 40 degrees

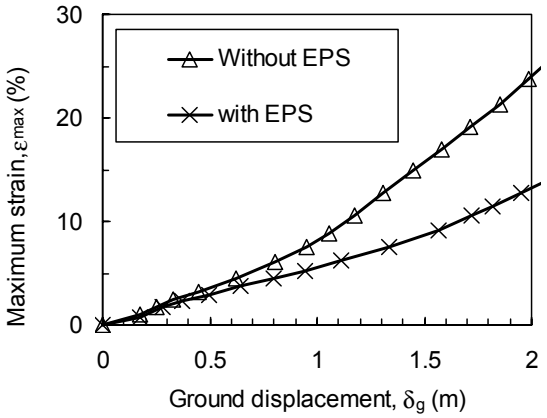

Figure 11. Analytical results of EPS effect on earthquake-resistance of pipelines with elbows

CONCLUSIONS

This paper investigated the effect of EPS for backfill on enhancement of earthquake-resistance of buried pipelines. Full-scale experiments were conducted to evaluate the effect of EPS backfill on the reduction of soil-pipe interaction. Effect of EPS backfill on large deformation behavior of buried pipelines with elbows subjected to PGD was also evaluated using Finite Element analytical model with the reduction in soil-pipe interaction. The following conclusions are drawn in this study:

(1) When EPS is used for backfill, the lateral force on pipes with the movement of the ground during earthquakes can be reduced to approximately half of that of normal backfill.
(2) Analytical results showed that EPS backfill had significant effect for enhancement of earthquake-resistance of buried pipelines with elbows subjected to PGD.

ACKNOWLEDGMENT: The authors wish to thank Messrs. Kazunori Shimamura, Tomoki Masuda, Takahito Watanabe, Hiroshi Sugawara, Naoto Hagiwara, Masato Nakayama and Daisuke Ujiie of Tokyo Gas Co., Ltd. and Messrs. Takehiko Suzuki and Yasuyuki Takahashi of Kanpai Co., Ltd. for their assistance in conducting the experiments. Thanks are extended to Professor Thomas D. O'Rourke, Mr. Timothy K. Bond and Mr. James Mason of Cornell University, and Professor Masanori Hamada of Waseda University for their invaluable assistance on the large-scale experiment of buried pipelines with elbows subjected to Permanent Ground Deformation. Professor Ikuo Towhata of Tokyo University, Professor Susumu Yasuda of Tokyo Denki University, and Dr. Nobuhisa Suzuki provided suggestions, which led to significant improvement in the research.

REFERENCES

[1] O'Rourke, T. D. and Lane, P.A. 1989. "Liquefaction Hazards and Their Effects on Buried Pipelines," Technical Report, NCEER-89-0007, NCEER, Buffalo, NY.
[2] Hamada, M. 1992. "Large Ground Deformations and Their Effects on Lifeline: 1989 Nihonkai-Chubu Earthquake," Proceedings, Case Studies of Liquefaction and Lifeline Performance During Past Earthquakes Volume 1 Japanese Case Studies, MCEER-92-0001, NCEER, Buffalo, NY.
[3] O'Rourke, T. D. and Palmer, M. C. 1996. "Earthquake Performance of Gas Transmission Pipelines," *Earthquake Spectra*, Vol. 20, No. 3, pp. 493-527.
[4] Oka, S. 1996. "Damage of Gas Facilities by Great Hanshin Earthquake and Restoration Process," Proceedings, 6th Japan-U.S. Workshop on Earthquake Resistant Design of Lifeline Facilities and Countermeasures Against Soil Liquefaction, NCEER-96-0012, MCEER, Buffalo, NY, pp.111-124.
[5] Japan Society of Civil Engineers. 1999. "The 1999 Ji-Ji Earthquake, Taiwan, Investigation into the Damage to Civil Engineering Structures," Investigation Report, pp. 7.13 - 7.21.
[6] Trautmann, C. H. and O'Rourke, T.D. 1985. "Lateral Force- Displacement Response of Buried Pipe," Journal of Geotechnical Engineering, ASCE, Reston, VA, Vol.111, No.9, pp. 1077-1092.
[7] Yoshizaki, K. and Oguchi, N. 1996. "Estimation of the deformation behavior of elbows for an earthquake-resistant design," Proceedings, 11th World Conference on Earthquake Engineering, Acapulco, Mexico, Paper No. 1783, Elsevier Science.
[8] Yoshizaki, K., O'Rourke, T. D. and Hamada, M. 2001. "Large Deformation Behavior of Buried Pipelines with Low-angle Elbows Subjected to Permanent Ground Deformation," Journal of Structural Mechanics and Earthquake Engineering, Vol. 18, No. 1, No. 675/I-55, pp. 41-52.
[9] Yoshizaki, K., O'Rourke, T. D. and Hamada, M. 2002. "Large Scale Experiments of Buried Steel Pipelines with Elbows Subjected to Permanent Ground Deformation," Proceedings, Seventh U.S. National Conference on Earthquake Engineering, No. 217.
[10] Japan Gas Association. 2000. *Recommended Practice for Earthquake Resistant Design of High Pressure Gas Pipelines*, Japan Gas Association (in Japanese), Tokyo, Japan.

EFFECTS OF GROUND MOVEMENTS ON CONCRETE CHANNELS

Craig A. Davis, J.P. Bardet, and Jianping Hu

ABSTRACT

Herein we present case studies on the performance of eight concrete lined channels in the Northern San Fernando Valley of Los Angeles, California, which were shaken by strong ground motions during the 1971 San Fernando and 1994 Northridge earthquakes. We also investigate the usefulness of several techniques that evaluate the performance of two unique channels, i.e., the High Speed Channel (HSC) and Bypass Channel (BC) located in the Los Angeles Department of Water and Power's Van Norman Complex. The various performances of the eight channels, which pass through different subsurface materials, are useful to identify important aspects of the seismic performance of channels. The case studies point out the need for further research for understanding (1) the differences in the responses of channels to separate earthquakes of similar magnitude, (2) the effects of weak clay soils on permanent ground movement and channel performances, (3) the inter-relation between ground movements and liner damage, and (4) the relative contribution of transient and permanent ground movements on channel damage. The case studies on HSC and BC are instructive to assess the effects of transient and permanent ground movement on liner damage. Preliminary evaluations of channel cracks, permanent ground movements, subsurface profiles, and nearby strong ground motion recordings from the 1994 Northridge earthquake show that the channel liners might be severely damaged from transient motions before large permanent movements take place, a result which is consistent with other studies on a nearby large diameter pipe. The case studies also indicate the need for improving the aerial methods used to determine permanent ground movements and the MLR modeling of permanent ground movements in weak non-liquefiable soils.

Craig A. Davis, Waterworks Engineer, Geotechnical Engineering Group, Los Angeles Department of Water and Power, 111 N. Hope Street, Room 1368, Los Angles, CA, 90051.
J.P. Bardet, Professor, Civil Engineering Department, University of Southern California, Kaprielian Hall 230B, University Park, Los Angeles, CA 90089-2531.
Jianping Hu, Graduate Student, Civil Engineering Department, University of Southern California, Kaprielian Hall 230B, University Park, Los Angeles, CA 90089-2531.

INTRODUCTION

The seismic performance of concrete lined channels is not well understood because they are strongly dependent on complicated interactions between concrete liners and the soil and rock in which they are constructed. Channels constructed in stable ground are expected to perform well during strong earthquake shaking, whereas those in marginally stable ground are more susceptible to earthquake damage. This trend is also found for other lifeline components, such as pipes. However, the response of channels to transient and permanent ground deformations is much more difficult to predict than for pipes because channels have more variable parameters including geotechnical considerations, construction methodology, and channel structure geometry. A recent fragility study for water supply conduits [1] clearly identified these difficulties in predicting channel performance and pointed out the lack of case studies, which impinges our present predictions of channel performance.

This paper attempts to improve our understanding and predictions of the seismic performance of channels by presenting case studies of several concrete lined channels in the Los Angeles Department of Water and Power's (LADWP) Van Norman Complex (Complex), located in the Northern San Fernando Valley. These channels were severely shaken by the M_w 6.7 February 9, 1971 San Fernando and M_w 6.7 January 17, 1994 Northridge Earthquakes. The Complex is located approximately 11 km from both the epicenters of the 1971 and 1994 earthquakes.

TABLE I. CONCRETE LINED CHANNELS ON VAN NORMAN COMPLEX.

Channel	Function	Year Placed	Shape	Material	1971 & 1994 Performance
1a. High Speed Channel (HSC)	Aqueduct	1912	Curved triangle	Alluvium	Damaged
1b. Energy Dissipater Structure (EDS)	Aqueduct	1941/ 1969	Rect.	Alluvium, Fill	Damaged
2. Bypass Channel (BC)	Aqueduct	1941	Trap.	Alluvium, Fill	Damaged
3. Tailrace	Aqueduct	1922/ 1941	Trap.	Alluvium	Damaged
4. Sepulveda Storm Channel (SSC)	Storm control	1960's	Trap.	Bedrock, Fill	Damaged
5. Bull Creek Branch Concrete Channel (BCB)	Storm control	1941	Trap.	Bedrock, Fill	Minor cracking
6. Upper San Fernando Spill Channel (USFC)	Reservoir spill control	1921	Rect.	Bedrock, Alluvium, Fill	Damaged
7a. L.A. Reservoir 850 cfs channel (LARC)	Storm control	1977	Trap.	Bedrock	No damage
7b. L.A. Reservoir Spill Channel (LARC)	Spill control & storm	1977	Rect.	Bedrock	No damage
8. Lakeside Storm Channel (LSC)	Storm control	1950's/ 1960's	Trap.	Bedrock, Alluvium	No damage

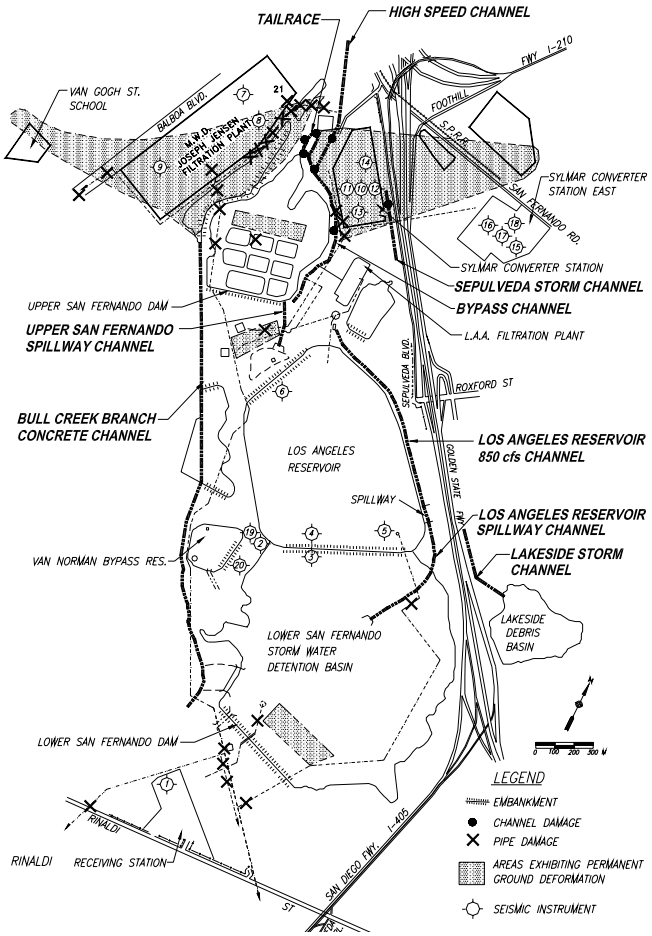

Fig. 1. Van Norman Complex showing channel locations, pipe and channel damage, seismic recording instruments, and regions of observed permanent ground movement.

CHANNELS

Table I summarizes general information on eight concrete lined channels in the Complex. Figure 1 shows the channel locations. Hereafter, the channels are referenced according to the abbreviations in the first column of Table I. HSC/EDS and LARC channel subtypes are presented to help identify performance of different construction. The aqueduct channels are normally full of water whereas the other channels are normally empty, or nearly empty, until large storms occur. Table I indicates the general ground conditions in which the channels are located. Alluvium and fill correspond to sandy, silty, or clayey soils. Fills may be compacted or loose. All bedrock is sedimentary.

Figure 1 shows the locations of pipe and channel damage after the 1994 earthquake (refer to [2] and [3] for detail). As shown in Fig. 1, most of the pipe damage and all the channel damage resulted on the Complex northern end. Table I identifies the channel performances during the 1971 San Fernando and 1994 Northridge earthquakes. The channels sustained significantly more damage in 1971. Figure 2 shows the HSC, BC, Tailrace, and SSC damage from the 1994 Northridge earthquake, which is also described in Table II. Detailed locations and descriptions of the 1971 damage are not available. The item 20 of Table II is the only channel damage not shown in Fig. 2.

TABLE II. DAMAGE TO CHANNELS FROM THE 1994 NORTHRIDGE EARTHQUAKE.

Item	Channel	Damage
1	High Speed	Small cracks, minor damage.
2	High Speed	Limited cracking, spalling, and soil settlement. Large cracks across from Penstock P.S. and S.F.P.P. Receiving Station (compression).
3	High Speed	Rupture and deformation of concrete liner.
4	High Speed	Separation and cracking of liner, settlement, lateral movement. Some soil foundation erosion. Spilling at high flow rates.
5	High Speed	0.3 m (1 ft) vertical scarp from slope failure.
6	High Speed	Seepage through soil at high flow rates/elevations.
7	Energy Dissipater	Active failure of EDS retaining structure; inadequately reinforced.
8	Bypass	Bridge abutment seating failure, cracking of channel walls.
9	Bypass	Ruptures in concrete channel.
10	Bypass	Longitudinal cracking on west shoulder.
11	Bypass	Leaking through patched ruptures at higher flow rates.
12	Bypass	Longitudinal and transverse cracking, separation of concrete liner, settlement, lateral movement. Erosion of soil foundation.
12a		Largest ground deformation.
13	Tailrace	Dike failure; piping from transverse cracks and liquefaction induced differential lateral spreading.
14	Tailrace	Slope failure; liquefaction and lateral spreading.
15	Tailrace	Crushing of concrete riser; liquefaction and lateral spreading.
16	Tailrace	Cracking of concrete turbine chambers, flow of soil into chambers.
17	Tailrace	Settlement and lateral movement (southward) of soil around Power Plant.
18	Tailrace	Liquefaction of Tailrace banks, settlement, lateral soil movement, crushed concrete liner.
19	Sepulveda Storm	Lateral displacement and transverse cracks.
20	Upper San Fernando Spill	Large fractures from settlement and lateral movement of hydraulic fill soils. No damage in channel constructed within natural ground.

For the sake of conciseness, all channels will not be described in detail. However the conditions surrounding the channels, which may be associated with damage or no damage, are summarized below. Table II includes the causes of damage when those are clearly identifiable. BCB, LARC, and LSC are within stable rock and soil, which may be responsible for the good performances of these channels. Soils around HSC, BC and SSC and Tailrace were observed to have undergone some permanent ground movements. Davis and Bardet [4] described the 1994 performance of the Tailrace summarized in Table II. Youd [5] reported information on permanent ground deformations after the 1971 earthquake, and attributed damage to HSC, BC, and SSC to liquefaction induced lateral movements. Davis and Scantlin [6] summarized ground movements from the 1994 earthquake, and reported that HSC and BC are surrounded mainly by weak clayey soils, which are unlikely to be susceptible to liquefaction.

Channel Performance Assessment

The channel performances in Tables I and II indicate:

1. The channels in firm ground, natural and well-compacted fill, perform favorably and consistently in different earthquakes of similar magnitude.
2. The channels in weak ground, natural and fill, can sustain significant damage and perform inconsistently in different earthquakes of similar magnitude.

3. The damage to channel structural liners appear to result from transient and permanent ground movements and other geotechnically related problems; structural inertia forces do not appear to cause any significant damage.
4. The vertical retaining walls of channels can perform poorly if they are not properly designed to resist lateral earthquake forces.
5. Embankment fills forming channels can fail as embankment dams.
6. Erosion through soil cracks (piping) and separations between soil and liner can cause significant secondary damage, with a time delay after the initial damage occurring at the time of the earthquake.
7. The performance of channels, which are in weak ground susceptible to large transient and permanent ground movements, is not well understood.

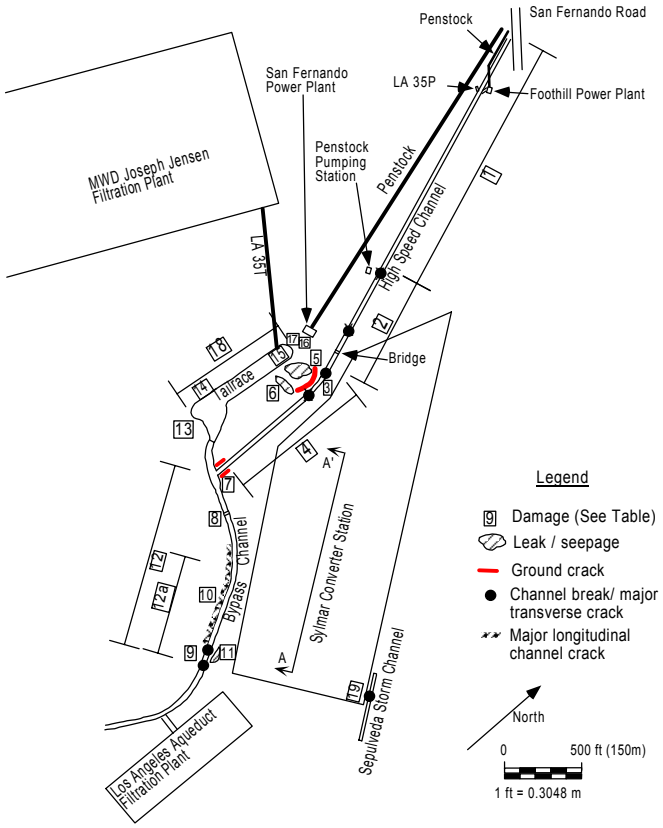

Figure. 2. Northridge Earthquake channel damage, see Table II for descriptions.

These remarks confirm the complicated seismic behaviors of channels and identify many geotechnical, structural, and hydraulic issues, which are interrelated and must be considered in designing channels. These remarks also indicate that geotechnical issues are of primary concern as they may lead to major subsequent structural and hydraulic issues. Many concerns identified above can be handled with current engineering practices. However, some issues warrant further investigations especially on: (1) the differences in 1971 and 1994 performances, (2) the geotechnical conditions leading to permanent ground movements (i.e., sand liquefaction versus clay failures), (3) the inter-relation between ground movement magnitude and liner damage, and (4) the differences in damage resulting from transient and permanent ground movements.

Hereafter, HSC and BC 1994 case studies are presented to assess the effects of ground movements on channel performance.

NORTHRIDGE EARTHQUAKE STRONG GROUND MOTION RECORDINGS

The January 17, 1994 Northridge Earthquake occurred on an unmapped blind thrust fault with a M_w of 6.7 [7]. Its epicenter was approximately 11 km south of the Complex. The Complex overlies the north-easterly boundary of the fault, which ruptured toward the north and subjected the HSC and BC to strong near source pulses [8]. Figure 1 shows the location of 20 seismic instruments that recorded the 1994 ground motion [8]. Stations 10 and 13, which are located at the Sylmar Converter Station a few meters east of the HSC and BC, are the most pertinent to this investigation. Free-field Station 10 recorded 0.90g peak ground acceleration (pga), 130 cm/s peak ground velocity (pgv), and 41 cm peak ground displacement (pgd). The ground below Station 10 consists of approximately 10 m of firm silty sand to sandy silt soil having an average shear wave velocity β = 263 m/s [9]. Station 13 is located in a concrete building basement and recorded 0.58g pga, 116 cm/s pgv, and 38 cm pgd. [10][8]. The ground below Station 13 consists of approximately 14 m of weak clayey silt with average β = 135 m/s shear wave velocity [11].

HIGH SPEED CHANNEL (HSC) AND BYPASS CHANNELS (BC)

Figures 3 and 4 show the round-bottomed triangular section of HSC and the trapezoidal cross section of BC, respectively. Figures 5 and 6 show a plan and profile for portions of the HSC and BC, respectively, with the horizontal dimension given as stationing of 30.48 m.

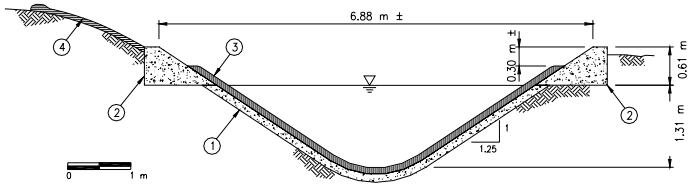

Figure 3. High Speed Channel cross-section. ① Original 1912 channel with 12.7 cm thick unreinforced concrete, ② 1969 unreinforced concrete channel enlargement, ③ 7.6 cm thick wire mesh reinforced concrete gunite overly for post-1971 earthquake repair, and ④ 7.6 cm gunite 1972 drainage improvement.

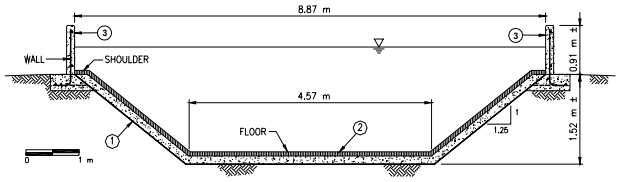

Figure 4. Bypass Channel cross-section. ① Original 1941 channel with 15.2 cm thick unreinforced concrete, ② 7.6 cm thick wire mesh reinforced concrete gunite overly for post-1971 earthquake repair, and ③ post-1971 earthquake channel enlargement.

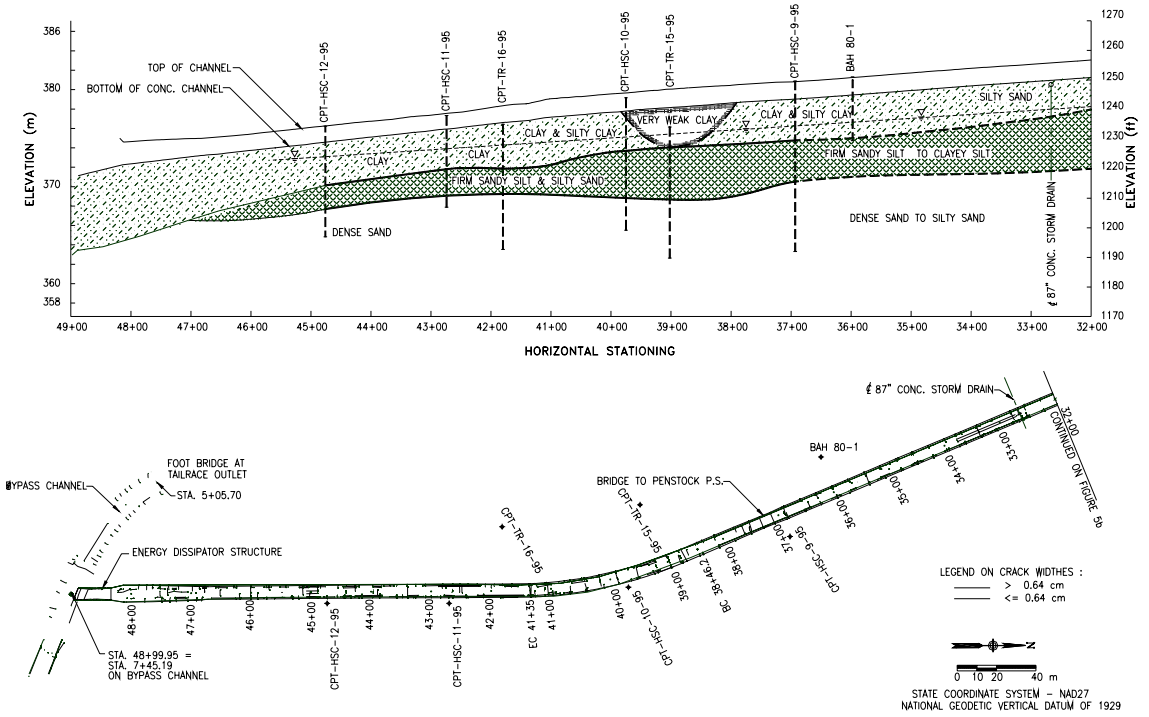

Figure 5. High Speed Channel plan and profile showing crack locations, CPT locations, and interpreted subsurface soil conditions.

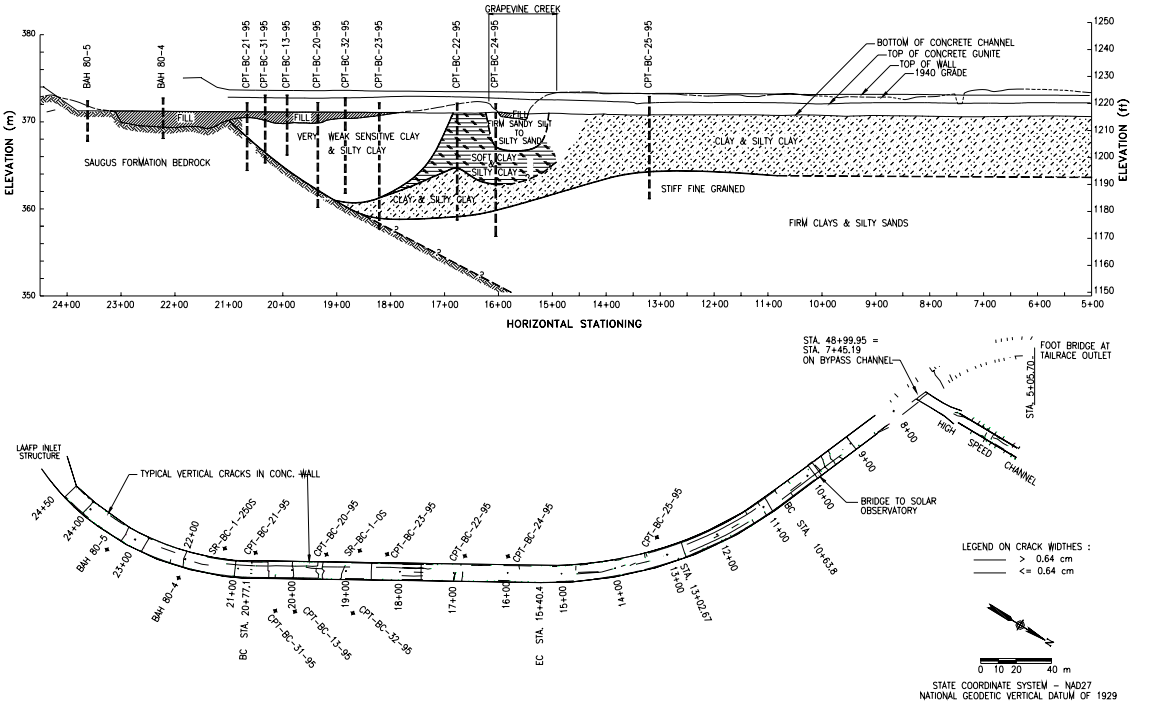

Figure 6. Bypass Channel plan and profile showing crack locations, CPT locations, and interpreted subsurface soil conditions.

Subsurface conditions

Figures 5 and 6 show soil profiles along the HSC and BC. These profiles were determined using results of Cone Penetration Testing (CPT) and boring logs obtained in the HSC and BC vicinity [12][4]. The CPT soundings and boring logs were supplemented with ground surface profiles along the HSC and BC, which were documented in 1913 and 1940, respectively.

As shown in Figs. 5 and 6, the soil conditions vary under the HSC and BC. Much of the soils consist of interbedded sandy silts, silty clay, and clay alluvial deposits, underlain by stronger alluvial soils above Saugus Formation bedrock. In a few places, the channels were constructed in fill. There are two zones of very weak clays, one under the HSC (Fig. 5), and one under the BC (Fig. 6). The locations of these weak soils correlate with the areas of most severe damage presented in Fig. 2 and greatest cracking in Figs. 5 and 6.

The groundwater condition around the HSC and BC is influenced by water seeping from the channels, which are not completely watertight. The natural groundwater has a general downward gradient to the south along the HSC and southwest along the BC. Figure 5 shows the groundwater surface around the HSC measured from subsurface investigations within 10 m of the channel. Groundwater around the BC was measured a little below ground surface, and is not shown in Fig. 6. Channel seepage influences the groundwater elevation locally, causing a mound in the groundwater surface, which matches the natural water levels, at approximately 6 m deep, away from the channels. Seepage from the BC influences natural water levels in the soft clay soils at distances greater than 18 m. Seepage from the HSC dissipates rapidly within 10 m of the channel, except for a localized condition in soft clay soils where the groundwater is observed to remain near the ground surface.

1994 Damage

Figures 5 and 6 show crack locations surveyed after the 1994 earthquake. Cracks were grouped into two categories (1) wider than 0.63 cm and (2) smaller than 0.63 cm, which are referred to as major or minor cracks. Davis and Scantlin [6] describe the methods used to obtain the crack data. As shown in Figs. 2 and 5, the HSC sustained numerous transverse cracks and separations along its alignment. Many cracks extended through the original concrete liner and the gunite overlay that was placed in 1971. Most of the larger longitudinal cracking in the HSC occurred at the top of the gunite overlay, indicating separation between the top curb and the channel. In many locations the HSC gunite overlay began to separate from the original liner. One overlay section, approximately 9.1 m long, was lifted off by flowing water after it ruptured due to ground movement. Some of the damage to both channels was due to the continued water flow across broken sections immediately after the earthquake.

Figure 6 shows numerous cracks along the BC, which separated in many locations. In some places, the overlay began to delaminate from the original channel. There are 7 major BC transverse cracks wider than 0.63 cm wide. Two major cracks occurred near the BC south end over soil fill. Many major transverse cracks over the clay soils were wider than 1.3 cm. The greatest transverse cracking resulted above soft clayey soils between BC Stations 17+50 and 20+50 (corresponding to location 9 in Fig. 2) rupturing across the entire channel section and displacing the lining and walls. The two transverse cracks between BC Stations 20+00 and 20+50 had a noticeable vertical offset, down to the north, and left lateral offsets having a minimum movement of 7.6 cm.

The BC bottom heaved in some areas and subsided in other areas, which caused longitudinal cracking and permanent channel deformations. Figure 2 and Table II show extensive longitudinal cracking along the of BC west shoulder where large separations resulted between the soil and concrete walls and allowed water to flow between them.

Most of the BC major longitudinal cracks, noted in Fig. 6 to be wider than 0.63 cm, were actually wider than 1.3 cm. One crack between Stations 18+00 and 19+00 reached at least 10 cm in width. Most longitudinal cracking in the BC floor had a measurable vertical offset averaging 0.63 cm. Some of the longitudinal shoulder cracking on the BC west side had vertical offsets of approximately 2.5 cm, down to the west, possibly indicating differential movement between the wall and channel slopes.

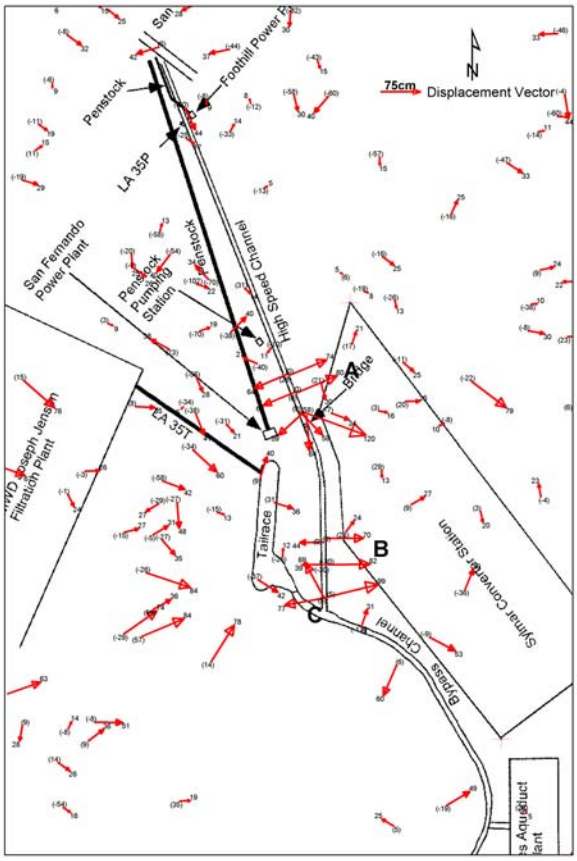

Fig. 7. Measured permanent ground movements from aerial photogrammetry. Vectors represent horizontal movement, numbers in parentheses are vertical movement (cm).

PERMANENT GROUND DEFORMATIONS

Figure 1 shows the locations of permanent ground deformation. The two largest ground deformation areas affected the aqueduct channels. Most soil deformations occurred in these areas, although deformations were not continuous within these areas as noted in [2] and [3]. Figure 1 shows the locations of breaks and displacements on pipes and channels around the Complex. The most significant channel breaks occurred within zones of documented permanent ground deformation. As shown in Figures 1, 2, 5, and 6, most of the HSC damaged portions and all the BC damaged portions are within the ground deformation zones.

Figure 7 shows movement vectors, which were measured by aerial photographs taken shortly before and after the 1994 earthquake, and corrected for tectonic deformation. The measurements were obtained from aerial photogrammetry as described in [13]. As shown in Figure 7, the horizontal ground movement is negligible on the northern part of the HSC. Vectors at "A" and "B" indicate that the HSC widened as longitudinal cracks opened (Fig. 5). Vectors at

"C" show that the EDS retaining walls failed and moved up to 99 cm into the channel. Unfortunately, no horizontal measurements were made in the area where the largest deformations were observed. However, the closest lateral measurements on the HSC (i.e., 54 cm) and the BC (i.e., 60 cm) are a lower bound of horizontal movements. All horizontal ground movements were obtained from aerial photographs; none were surveyed on the ground.

Measured Settlement

Figures 8a and 9a show the settlement profiles of the HSC and BC, respectively. The settlements were measured on the concrete surfaces. In zones of large settlement, the channels could bridge the ground movement and create gaps between underlying soil and channel. Consequently, the settlement measurements reported in Figures 8a and 9a are lower bounds of deformation in the underlying soil. The HSC profile was obtained by comparing the results of surveys carried out in 1964 and 1994. The BC profile was obtained from surveys in 1971 and 1994. The HSC profile of Fig. 8a combines the settlements from both the 1971 and 1994 earthquakes and does not account for changes in channel liner (e.g., Fig. 3) following 1971 and 1994 repairs, and thus it underestimates the liner settlement. No surveys of the HSC after the 1971 earthquake and of the BC before the 1971 earthquake could be found. As shown in Figures 8a and 9a, the channels underwent large settlements with the largest settlement in the areas of soft clayey soils (Figs. 5 and 6). Figure 8a does not show the largest HSC settlement occurring at the same location as the weakest clay soils in Fig. 5. This is believed to result from the settlement calculations being affected by a larger than normal concrete repair thickness in this region; field observations indicate the HSC had greatest settlements in the vicinity of weakest soils. Differential settlements as large as 15 cm were measured across the width of BC, which indicated that the liner tilted down to the west.

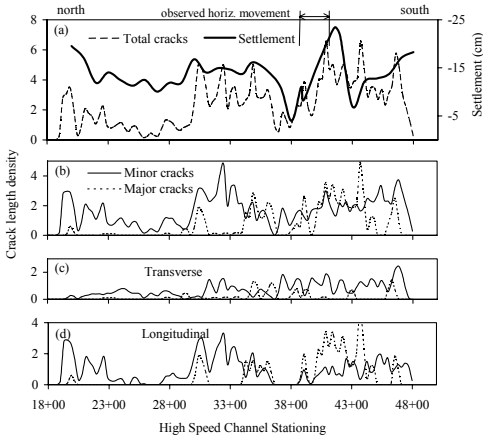

Figure 8. HSC settlement and crack density.

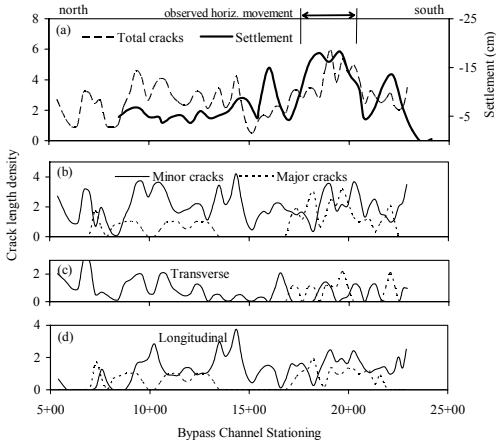

Figure 9. BC settlement and crack density.

EVALUATION

Figures 8 and 9 present the crack density over the lengths of HSC and BC, respectively, and compare crack density to channel settlement. The crack density is defined as the number of cracks per unit length of channel. Figures 8a and 9a show the calculated crack density using all cracks. There is a trend for cracking to increase with settlement, but there is no consistent pattern over the entire channel lengths. As shown in Figs. 5 and 6, the cracks are mostly transverse (perpendicular) or longitudinal (parallel) to the channel axes. Figures 8b-d and 9b-d depict major and minor cracks, and show a reasonably good correlation of major cracking with settlement, but no correlation of settlement with minor cracking. Longitudinal cracks in the HSC and transverse

cracks in the BC have very good correlations with settlement in Figs. 8d and 9c, respectively. Figures 8 and 9 also show that the crack density magnitudes for any crack subcategory are similar for HSC and BC.

As shown in Figures 8 and 9, the approximate regions of observed large lateral movements generally correspond to areas of large settlements, when accounting for the HSC settlement limitations described in the previous section. The minor cracks appear uncorrelated with permanent horizontal or vertical ground movements, soil conditions, and channel type. Except for some longitudinal cracks, most of the major cracks correspond to large permanent ground movements. The better correlation of major transverse cracks with permanent movement may result from the nearly perpendicular crossing of HSC and BC through deformations regions, which would tend to cause larger strain concentrations from differential ground movements. The cracks that did not result from permanent ground strains were presumably caused by transient strains. Therefore, most of the minor cracks and some of the major cracks resulted from transient motions. Questions remain as to whether some of the major cracks within the areas of large permanent ground deformation resulted from transient motions before permanent ground deformations occurred. This condition was encountered for a large diameter pipe damaged east of the Tailrace [14]. The channels may have been damaged in a similar manner. Additional evaluations are required to address this problem.

A preliminary analysis was undertaken to correlate horizontal permanent ground movement with channel damage. Since no direct measurements are available in the areas of greatest damage, an empirical evaluation was performed using a MLR model that predicts permanent ground deformation [15]. The MLR model was first tested at 9 locations where subsurface conditions and horizontal movements coexisted near the channels. The predicted ground movements were significantly smaller than the measured values, with differences ranging from 8 to 50 cm. The MLR model predicted little variation in permanent ground deformation, typically 5 to 10 cm [15]. This discrepancy between observed and predicted deformations is expected since the MLR model was calibrated from permanent ground deformation due to soil liquefaction and that the clayey soils below the channels are unlikely susceptible to liquefaction. Unfortunately, there are no existing empirical methods for predicting clay soil movements. This preliminary analysis points out the need for improved empirical ground deformation methods.

A preliminary analysis was also undertaken to evaluate transient strains. Peak transient strain γ is determined from: $\gamma = \alpha \cdot pgv / \beta$, where α is a proportionality constant. The recorded motions from Stations 10 and 13 represent the variation in transient ground motions between the soft and firm soils under the HSC and BC. It is clear that strains in the weaker clay soils were about twice as large as those in the other surrounding soils; the pgv in both soils were nearly the same, but β in weak clay is about half. This may explain the greater number of major cracks within the weak soil regions. However, Figs. 8 and 9 indicate that the minor crack density is relatively independent of ground strain.

CONCLUSIONS

We have presented case studies of the performance of concrete lined channels shaken by the 1971 San Fernando and 1994 Northridge earthquakes in the Van Norman Complex in Los Angeles, California. The comparative studies of channel performances identify many issues to account for in seismic resistant design of channels, and point out that liner damage may result from both transient and permanent ground movements. The case studies of the performances of the High Speed Channel (HSC) and Bypass Channel (BC) after the 1994 earthquake, using aerial and ground survey measurements, provided valuable insight into the relative contributions of transient and permanent movements. The case studies on the HSC and BC imply that additional studies are required to fully understand the problem. The investigation was based on lateral ground movement obtained from aerial photographs, which are useful for understanding global

movements over large areas. The accuracy of these displacements needs to be improved before they become useful for evaluate the performance of specific facilities (e.g., HSC and BC). Empirical models for predicting permanent ground deformations also require improvements to account for deformations in non-liquefiable soils. These case studies provide valuable information for improving our understanding of the seismic performances of channels and help identify new research needs in geotechnical and lifeline earthquake engineering.

ACKNOWLEDGMENTS

The support from the Los Angeles Department of Water and Power is gratefully acknowledged. J. C. Chen helped prepare drawings.

REFERENCES

[1] American Lifelines Alliance (ALA), 2001, "Seismic Fragility Formulas for Water Systems," Parts I and II, ASCE and FEMA, available at www.americanlifelinesalliance.org.

[2] Davis, C.A., and J.P. Bardet, 1995a, "Seismic Performance of Van Norman Water Lifelines," *Proc. 4th U.S. Conference on Lifeline Earthquake Engineering,* ASCE, San Francisco, Aug., pp. 652-659.

[3] Davis, C.A., and J.P. Bardet, 1995b, "Northridge Earthquake - Van Norman Complex Ground Movement," *Proc. 3rd International Conf. on Recent Advances in Geotechnical Earthquake Engineering and Soil Dynamics*, Vol. 3, 14.09, St. Louis, MO.

[4] Davis, C.A., and J.P. Bardet, 1996, "Performance of Two Reservoirs During the 1994 Northridge Earthquake," *Journal of the Geotechnical Engineering Division,* ASCE, 122(8), pp. 613-622.

[5] Youd, T.L. (1973), "Ground Movements in Van Norman Lake Vicinity During San Fernando Earthquake," NOAA Spec. Rpt., Vol. III, pp. 197-206.

[6] Davis, C.A., and P.S. Scantlin, 1997, "Response of the High Speed and Bypass Channels to the 1994 Northridge Earthquake and Recommended Repairs," *Los Angeles Department of Water and Power, Water Supply Division, Report No. AX 215-47*.

[7] Wald, D.J., and T.H. Heaton, 1994, "A Dislocation Model of the 1994 Northridge, California, Earthquake Determined from Strong Ground Motions," *USGS,* Open-File Report 94-278.

[8] Bardet, J.P. and C.A. Davis, 1996a, "Engineering Observations on Ground Motion at the Van Norman Complex after the Northridge Earthquake," *Bull. Seism. Soc. Am.*86, 1B, pp. S333-S349.

[9] Gibbs J.F., Tinsley, J.C., and W.B. Joyner, 1996, "Seismic Velocities and Geol. Conditions at 12 Sites Subjected to Strong Ground Motions in the 1994 Northridge, CA, Earthquake," *USGS* OFR 96-740.

[10] Lindvall Richter Benuska Associates, 1995, "Processed LADWP Power System Strong-Motion Records from the Northridge, California Earthquake of January 17, 1994," P*repared for the Los Angeles Department of Water and Power,* LRB 007-027.

[11] Dames and Moore, 1995, "Cone Penetration Testing and Seismic Velocity Surveys LADWP Van Norman Complex, Los Angeles, California," *Project No. 00138-093-015*.

[12] Los Angeles Department of Water and Power (LADWP), 1981, "Van Norman Pumping Station #2 Discharge Lines - Geologic Exploration," LADWP Memorandum Dated March 4.

[13] O'Rourke, T.D., B.L. Roth, and M. Hamada, 1992, "Large Ground Deformations and Their Effects on Lifeline Facilities: 1971 San Fernando Earthquake," Vol. 2, *NCEER-92-0002*.

[14] Davis, C.A., 2001, "Retrofit of a Large Diameter Trunk Line Case Study of Seismic Performance," *Proc. of 2nd Japan-US Workshop on Seismic Measures for Water Supply*, AWWARF/JWWA, Tokyo, Japan, Aug. 6-9, 2001, American Waterworks Association Research Foundation Project No. 2786.

[16] Bardet, J. P., Mace, N., Tobita, T. and J. Hu, 2002, Regional modeling of Liquefaction-induced ground deformation, *Earthquake Spectra*, EERI, Vol. 18, No. 1, pp. 19-46.

Effectiveness of remedial measures by shear deformation constraint method

Nozomu Yoshida[1] and Hiroyoshi Kiku[2]

ABSTRACT

Effectiveness of remedial measures against soil liquefaction by a shear deformation constraint method is examined through finite element analyses, because at present, there is no relevant design method. At first, mechanism of stress transfer from the rigid wall to the nearby ground is investigated, and it is shown that the soil element deforms in the vertical direction by shear when shear deformation in horizontal direction is constrained by the stiffer underground structure. This effect weakens the effectiveness of remedial measures. Then finite element analysis using a model ground with underground walls is conducted in order to confirm this idea and in order to evaluate the effect. It's effect is significant when overburden stress is small, i.e., near the ground surface, but the effect decreases at deep depths. The easiest way to use average stiffness between the soil and underground wall, which is sometimes used in the engineering practice, is shown to mislead actual behavior significantly to the dangerous side. As an conclusion, remedial measures by shear deformation constraint method works as expected to reduce the horizontal displacement of the ground by which many underground structures suffer damage, but it does not work to reduce excess porewater pressure generation near the ground surface.

[1] Nozomu Yoshida, Chief Engineer, Oyo Technical Center, Oyo Corporation, Toro-cho 2-61-5, Saitama-shi 330-8632, JAPAN

[2] Hiroyoshi Kiku, Associated Professor, Kanto Gakuin University, Rokuura-higashi 1-50-1, Kanazawa-ku, Yokohama, Kanagawa 236-8501, JAPAN

INTRODUCTION

It is empirically recognized that an underground wall and lattice shaped ground improvement work as remedial measures against soil liquefaction. Shear deformation of the ground is expected to become small because much shear stress is carried out by the underground wall or improved ground. This method is called remedial measures against soil liquefaction by shear strain constraint method.

In spite of the facts that this method worked in the past earthquakes and in the laboratory test such as shaking table test, a design method to evaluate the effectiveness of this method is not established [1]. Therefore, they have been used to give additional ability to constrain the onset of soil liquefaction, but were not used in practice as only remedial measures purpose.

In this method, stiffness changes in the horizontal direction, and stiffer parts such as underground walls and improved ground are expected to constrain deformations of softer parts or ground. Therefore, interaction between stiffer parts and softer parts should be considered relevantly. A first idea as a practical engineer may be a method to use an average stiffness in evaluating the deformation of the overall ground including the wall; this method is reported as an case history in the text (JGS, 1993).

However, as pointed out in this paper, this simple assumption does not consider the interaction between the stiffer part and the softer part, and will mislead the behavior of overall ground. In this paper, we propose a mechanism to explain what happens between the stiffer part and the softer part in the ground, and to show the effect of this method as remedial measures against soil liquefaction through an example case study.

MECHANISM OF SHEAR STRESS PROPAGATION

Recently, a laminar box began to be used in shaking table tests and centrifugal tests, but a rigid box had been a popular test apparatus in the past and even at present in investigating the liquefaction behavior of ground. There are significant differences in behavior of the ground between a laminar box test and a rigid box test. In the test using a laminar, a surface layer may sometimes does not liquefy when liquefaction occurs at deep depths, because shear wave does not propagate through the liquefied layer. On the other hand, liquefaction occurs in the whole ground in the rigid box test because waves also propagate through the walls. This indicates that existence of the rigid underground structure cannot be said to constrain the onset of soil liquefaction; liquefaction can occur in the ground even with several tens centimeters width. Moreover, it indicates that evaluation of the ground behavior by average stiffness between stiffer parts (underground wall) and softer parts (ground) may lead bad result.

Figure 1 shows two infinitesimally small elements: the one is at the surface of the underground wall and the other is a soil element adjacent to the underground wall. Shear stress acting on each element and deformation caused by the shear stress are also drawn schematically. Since shear stress is carried mainly by shear wall, large shear stress will be produced in the shear wall. As shown in Figure 1, if shear stress appears at the edge of the wall, the same amount of shear stress should work in the soil element from the equilibrium condition in order to carry this kind of shear stress. In the case of horizontal deposit, shear deformation occurs in the horizontal direction. However, since horizontal displacement is constrains by the existence of the underground wall, shear deformation occurs in the vertical direction as shown in Figure 1. Therefore liquefaction can occur in the ground by the shear waves traveling in the underground wall. The same behavior will happen in the ground improvement such as a sand compaction pile method and rod compaction method. As a result of this behavior, vertical movement appears in the ground even in the case that the ground is shaken only in the horizontal direction.

It is noted that shear stress at the surface of the wall is zero based on beam theory. This is true if the wall is placed in the air because air does not carry shear stress. However, in the ground, shear stress appears at the surface of the wall as adjacent soil can carry shear stress. This implies that shear stress at the surface of the wall can increase up to shear strength of the surrounding soil. Therefore, above discussion is valid even in beam type behavior of wall.

As shown in the preceding, a complicated interaction takes place between the underground wall and the interior ground, which affects the liquefaction characteristics of ground. It is also noted that this interaction cannot be considered by the analysis considering only horizontal displacement. Moreover, verification of this mechanism cannot be made in the total stress analysis such as FLUSH because shear stress transferred from the wall to the ground depends on the shear strength of the ground that will reduce during shaking because of excess porewater pressure generation. The effect of this mechanism to overall behavior of ground is investigated in this paper through a case study based on an effective stress dynamic response analysis.

MODEL

Ground and underground wall

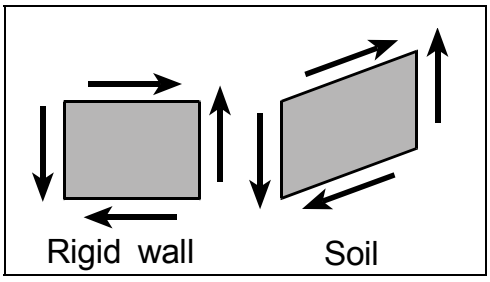

Figure 1 Shear stress transfer from rigid wall to ground.

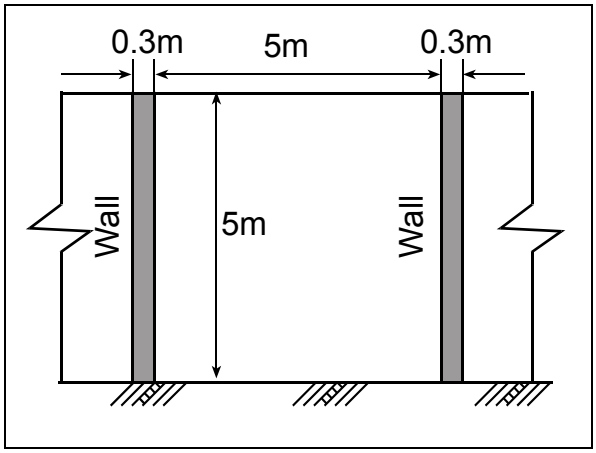

Figure 2 Ground and underground wall

A simplified model shown in Figure 2 is used so that mechanism can be easily recognized.

The SPT *N*-value of the ground is 10, and the water table coincides with the ground surface. The base layer is located at GL-5m.

Underground walls are placed every 5.3 meters (interior width of the ground is 5 m). The 30 cm thick wall behaves in an elastic manner. The stiffness of the wall is set 100 times larger than the concrete considering the existence of the wall parallel to the shake plane. Moreover, unit weight of the underground wall is set 10 times larger than the concrete considering a weight of the superstructure that is not modeled in this study.

A repeated boundary is used in the horizontal direction; displacement at the left end of the wall is set equals to be the one at the right end of the ground. A rigid base is assumed and a half of the 1940 El-Centro NS component is applied.

MATERIAL PROPERTY OF SOIL AND ITS MODELING

A constitutive model proposed by the authors [2] is used under the simple two-dimensional condition. This model can simulate arbitrary defined dynamic deformation characteristics perfectly. A Ramberg-Osgood model is used for equivalent stress *s* versus equivalent strain *e* relationships for the skeleton curve. Volumetric strain caused by dilatancy is evaluated by modifying a bowl model [3] into simple two-dimensional condition. They are summarized in the followings:

$$\text{Shear deformation: } \gamma = \eta\left(1+\alpha\eta^{\beta-1}\right) \tag{1}$$

where

$\gamma = e / e_r$: Equivalent strain normalized by reference equivalent strain

$\eta = s / \tau_{\max}$: Dimensionless equivalent stress

$e_r = \tau_{\max} / G_{\max}$: Reference strain, and

$\tau_{\max} = c\cos\phi + \sigma'_{\mathrm{m}}\sin\phi$: Shear strength

$$\text{Dilatancy model: } \varepsilon_{vd} = Ae^{B} + \frac{\int de}{C + D\int de} \tag{2}$$

Here c is cohesion, ϕ is internal friction angle, G_{max} is elastic shear modulus, and α and β are parameters to define the *s*-*e* relationships. Volumetric strain caused by dilatancy ε_{vd} is determined by four parameters A, B, C and D.

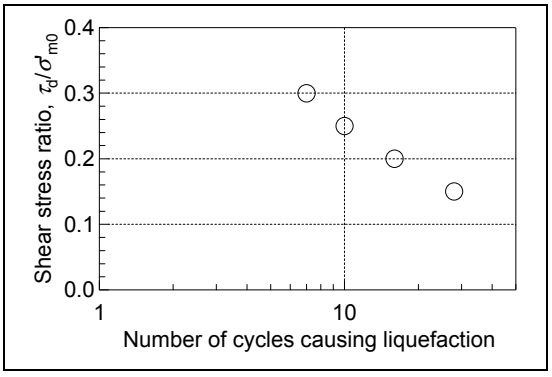

Figure 3 Liquefaction strength (initial confining stress = 100kPa)

Internal friction angle is set 35 degrees, cohesion is set 1 kPa, and $G_{\max} = 4700\sigma'^{0.5}_{m}$. The small cohesion is considered in order to control the shear strength after the onset of liquefaction.

Liquefaction strength of the model is shown in Figure 3. Stress-strain relationships and stress paths are drawn in Figure 4 as an example.

RESULT OF ANALYSIS AND DISCUSSION

A computer code STADAS [4] is employed to analyze the model. Reduced integration with an anti-hourglass stiffness is used in building an element stiffness matrix of a solid element. Therefore, bending behavior of a wall can be simulated well.

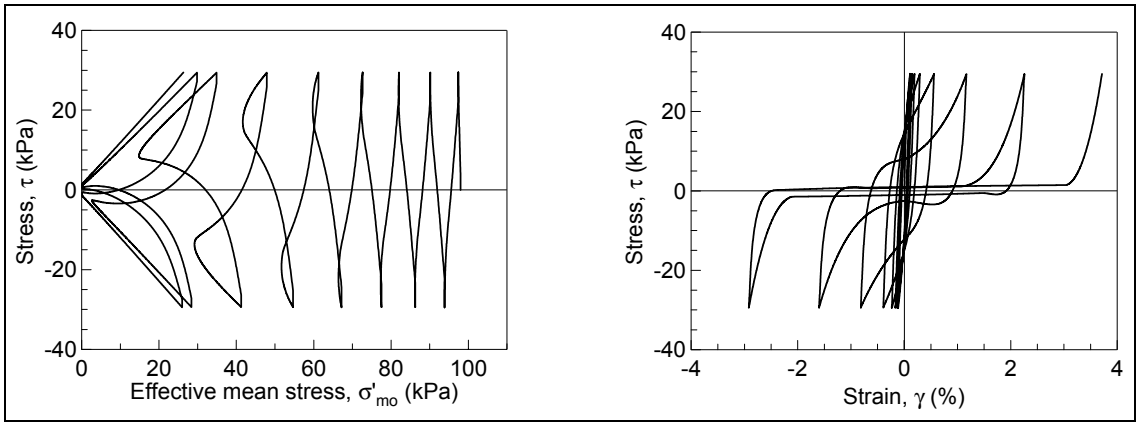

Figure 4 An example of stress path and stress-strain relationships

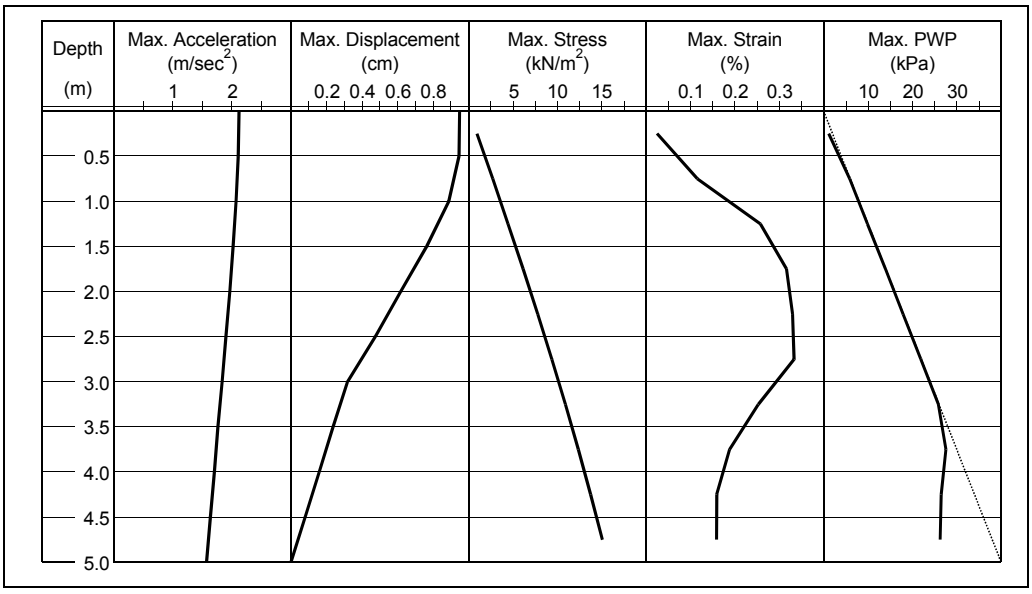

Figure 5 Maximum response by one-dimensional analysis

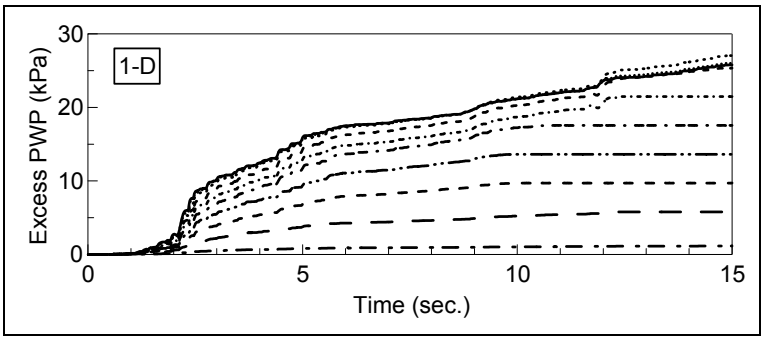

Figure 6 Excess porewater time history

Both one-dimensional analysis and two-dimensional analysis are conducted. A horizontally layered deposit is assumed in the one-dimensional analysis.

One-dimensional analysis

A horizontally layered deposit is analyzed first in order to obtain the behavior of the bare ground without remediation. Peak responses are summarized in Figure 5, Excess porewater pressure time histories are shown in Figure 6 for all layers, and acceleration and displacement time histories at the ground surface are shown in Figure 7. Maximum displacement at the ground surface relative to the base layer is about 1 cm, and peak acceleration at the ground surface is about $2m/s^2$.

In the excess porewater time history shown in Figure 6, lines with smaller excess porewater pressure belongs to the shallower location. From Figures 5 and 6, one can recognize that liquefaction occurred between GL-0.5 and 3.5m. Liquefaction occurred at the shallow depth first, then extends gradually to the deep depths.

A maximum strain is about 0.3%. This value seems very small compared with the ordinary definition of liquefaction by shear strain (double shear strain amplitude = 7.5%), which will be discussed later. Excess porewater pressure generates quicker under random loading as can be seen in Figure 8. Maximum displacement occurs at about 12 seconds which is much later than main amplitude of ground shaking. This delay of displacement has been frequently seen in past analyses using the same wave as input motion. Unfortunately, since liquefaction occurs from the element near the ground surface, phenomena that liquefaction do not occur near the ground if liquefaction occurs earlier in the deep depths cannot be seen.

Two-dimensional analysis

Two-dimensional analysis is conducted to investigate the behavior of the ground-underground wall system. Maximum displacements are shown for one-and two-dimensional analyses in Figure 9. Since the direction of the maximum displacement depends on nodes (they can take either positive or negative sign), absolute values are used. Therefore, although the figure is drawn as if it is a deformed shape, only absolute values have meaning.

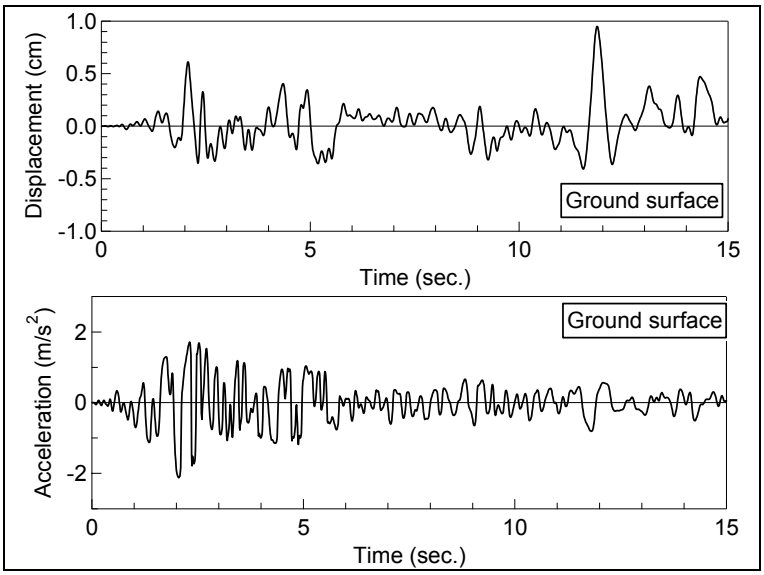

Figure 7 Acceleration and displacement time history at ground surface

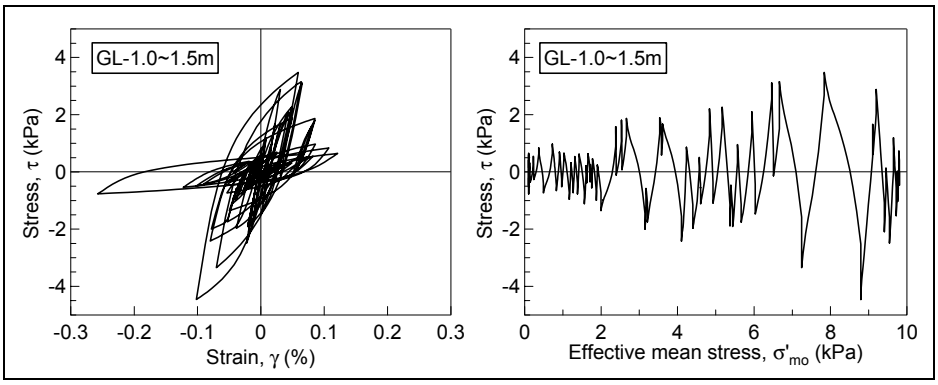

Figure 8 Example of behavior during liquefaction test (GL-1~1.5m)

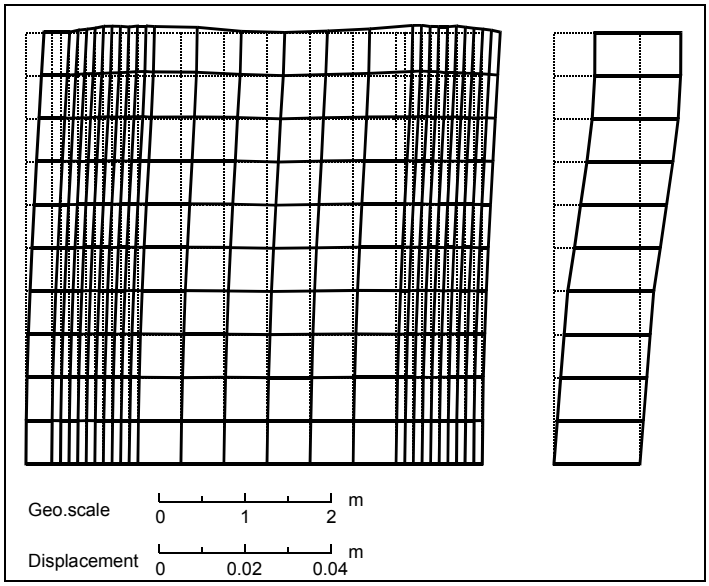

Figure 9 Absolute value of maximum displacement by two- and one-dimensional analyses.

Three features can be easily seen in the figure.

At first, maximum horizontal displacement at the ground surface is about 1 cm in the one-dimensional analysis whereas it is about 0.4 cm in the two-dimensional analysis; displacement by the two-dimensional analysis is less than a half of that by the one-dimensional analysis. Therefore, the underground wall worked in order to reduce the horizontal displacement of the ground as expected. It is however noted that the displacement of 0.4 cm is very large compared with the displacement of the ground when average stiffness is used as shown later. In this sense, the underground wall does not work as expected.

Next, as seen in Figure 5, large deformation is observed at the middle depth and deformation near the ground surface is small in the one-dimensional analysis. On the other hand, shear strain seems to increase towards the ground surface in the two-dimensional analysis. Deformation constraint effect by underground wall also seems to appear.

Finally there appears vertical displacement, especially near the boundary of the underground wall. As discussed in the previous section, vertical displacement appears even in the horizontal shaking. Since vertical displacement near the center is nearly zero, inverse symmetric shapes of displacement is implied to occur in the whole ground. This deformation pattern agrees with the mechanism described in the previous section.

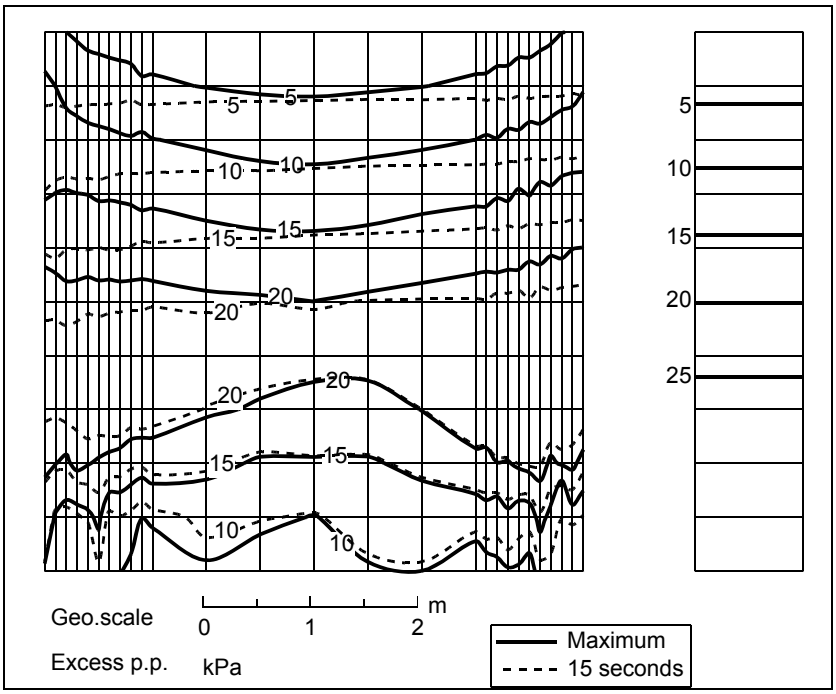

Figure 10 Contour of excess porewater pressure by two- and one-dimensional analyses.

Contour lines of the excess porewater pressure are shown in Figure 10; both maximum values and residual values (excess porewater pressure at the end of shaking) are shown for two- and one-dimensional analyses as dashed and solid lines. It is noted that excess porewater pressure increases nearly monotonically in the one-dimensional analysis as seen in Figure 6, maximum value and residual value are nearly the same. This indicates that cyclic mobility behavior did not occur in the one-dimensional analysis. Considering the nature of the input earthquake motion, waves with large amplitude comes at about 2 seconds, but stress point does not path phase transform region at this stage. Then amplitude becomes small. In such a situation, excess porewater pressure can generate without causing cyclic mobility behavior and without causing large strain. Similar behavior is seen in the test [5].

Residual excess porewater pressures are nearly identical for both one- and two-dimensional analyses in the layers above GL-3m. This fact clearly indicates that onset of liquefaction cannot be prevented by the underground wall.

On the other hand, excess porewater pressure generation is clearly smaller in the two-dimensional analysis than in the one-dimensional analysis at depths larger than 3 m. It is noted that vertical displacement becomes more difficult to occur at deep depth than at shallow depth, and vertical displacement is zero at the base. These facts prove that the mechanism shown in this paper is important.

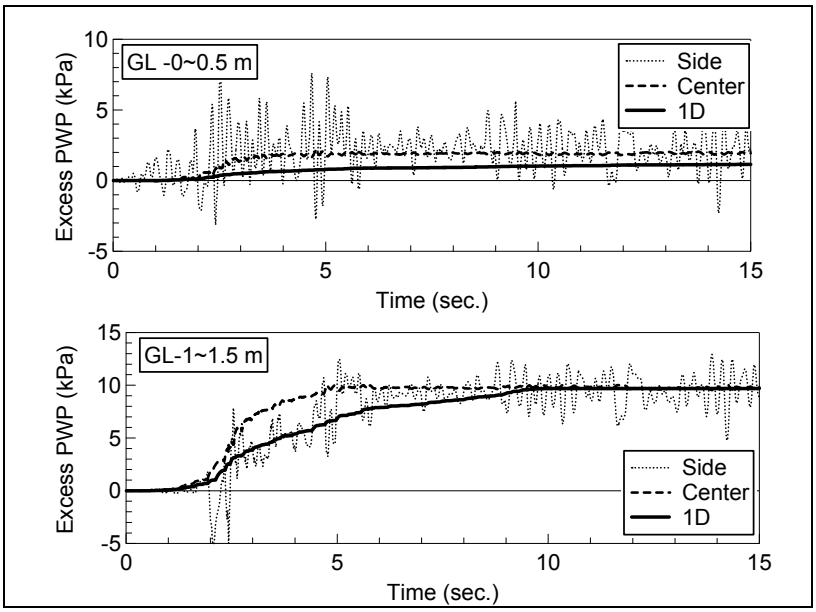

Figure 11 Comparison of excess porewater pressure time history

The maximum excess porewater pressure is nearly the same with the residual excess porewater pressure along the centerline of the ground. Differences between the maximum excess porewater pressure and the residual excess porewater pressure become large towards the wall. As can be seen in Figure 5, region above GL-3m liquefy in the one-dimensional analysis. Therefore, if excess porewater is larger than the one in the one-dimensional analysis as seen above, total overburden stress must be increased, which is possible only when vertical movement occurs.

This can also be recognized from the excess porewater pressure time history in Figure 11, in which excess porewater pressures time history by the one-dimensional analysis are compared with the one at the elements adjacent to wall (shown as side in the figure) and at the center of the ground (shown as center) by the two-dimensional analysis are shown at depths GL±0~0.5m and GL-1~1.5m.

Liquefaction does not occur at the ground surface in the one-dimensional analysis as shown in the left figure. Significant vibration is observed at the element near the wall in the two-dimensional analysis, but excess porewater pressure increases monotonically at the center. In spite of these difference, residual values at the end of the earthquake are nearly the same and they are nearly equal to initial overburden stress; element at the ground surface liquefy in two-dimensional analysis, which is different with the result of one-dimensional analysis. Same with the element at the surface, excess porewater pressure vibrates at the element adjacent to wall at depth between GL-1~1.5m, but amplitude of vibration becomes much smaller. Excess porewater pressure monotonically increases same with the element at the ground surface at the center, too. Compared with the one-dimensional element, generation of excess porewater pressure occurs earlier in the two-dimensional analysis. These observations also imply that existence of underground wall does not reduce excess porewater pressure in the ground; it contributes excess porewater pressure.

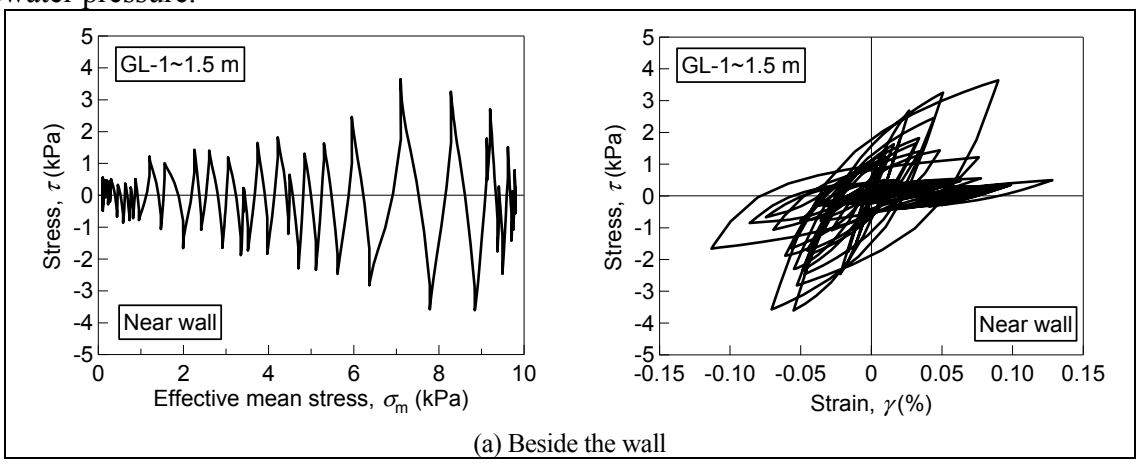

(a) Beside the wall

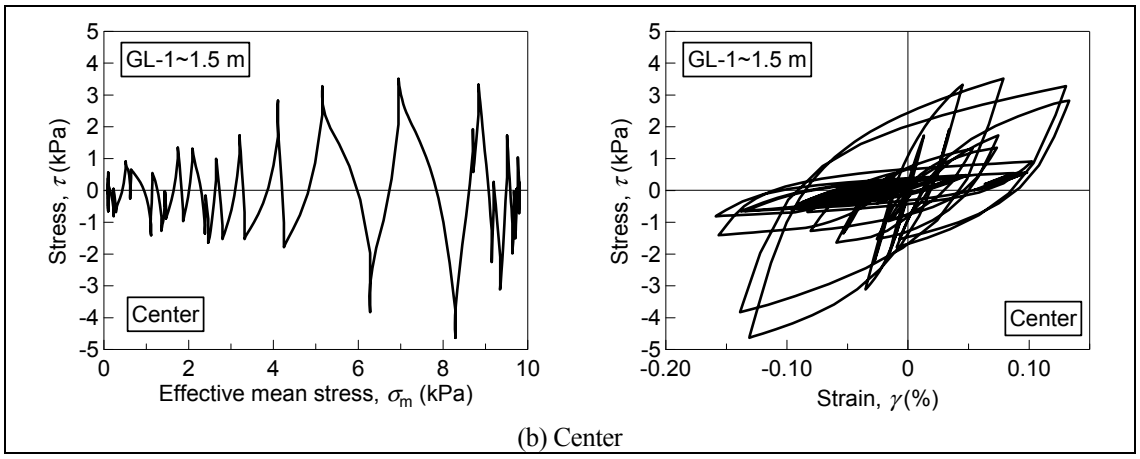

(b) Center

Figure 12 Behavior of soil element at GL-1~1.5m

Behavior of elements at the side and at the center is shown in Figure 12 at GL-1~1.5 m depth, which can be compared with the behavior at the same depth in one-dimensional analysis in Figure 8. General behaviors do not differ very much. It is noted that shear stresses and shear strains are the ones in horizontal plane. Therefore, shear strain is the largest in one-dimensional analysis, then at the center of ground and finally adjacent to wall. This again implies that deformation in horizontal direction is constrained. This also explains why excess porewater generates larger at the center element than at the element adjacent to wall as shown in Figure 11.

Figure 13 shows displacement time histories at the ground surface for both one- and two-dimensional analyses. As shown in Figure 13(a), displacement in the one-dimensional analysis is larger at about 2 second where the largest wave comes. It is also larger at about 12 second where displacement becomes the largest. Since behaviors in the two-dimensional analysis cannot be distinguished well in Figure 13(a), they are enlarged in Figure 13(b). Waveforms are nearly identical at the center and at the side of wall except that displacement at the center drifts at about 6 seconds. Elastic behavior of wall is supposed to cause the difference.

Effect of vertical displacement constraint

Through the preceding discussions, it becomes clear that vertical displacement accelerates excess porewater pressure generation. The idea to use average stiffness, however, does not consider vertical displacement presented in this paper. In order to investigate the effect of vertical

displacement to the excess porewater pressure generation, two-dimensional analysis is conducted by constraining the vertical displacement; only horizontal displacement is allowed. Figure 14 compares displacements at the center of two-dimensional analyses and one-dimensional analysis. Solid line indicated "Horizontal" is the result of this case (no vertical displacement) whereas dashed line indicated "Free" is the result in the preceding (free of vertical displacement). Displacement under vertical displacement constraint is much smaller than other cases; Solid line seems horizontal line or no horizontal displacement. Related to this, excess porewater pressure hardly generates. When vertical displacement is constrained, earthquake load is distributed depending on shear stiffness. Shear stiffness of the underground wall is much larger than that of soil. Therefore almost all earthquake load is carried by the underground wall, which result in almost zero excess porewater pressure generation.

An analysis to constrain displacements of nodes that belong to underground wall is also conducted, whose result is not shown in this paper. Displacement is also very small compared with ordinary two-dimensional analysis even in this case although it is larger than the case that vertical displacement allowed. This fact also validates the mechanism proposed here.

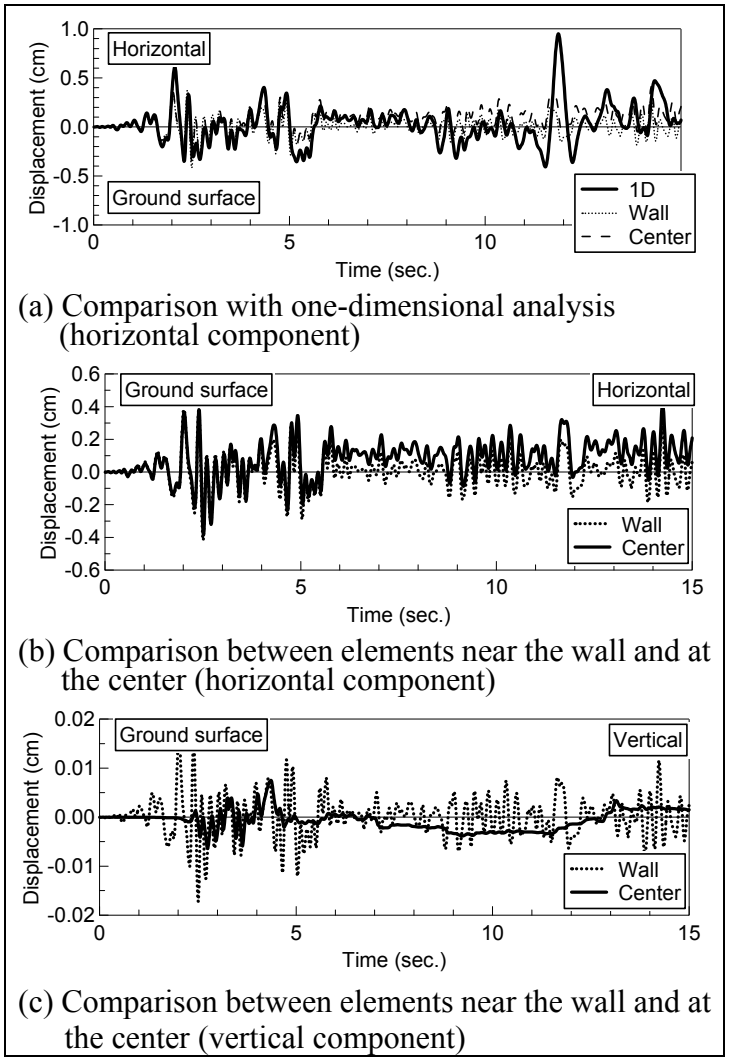

(a) Comparison with one-dimensional analysis (horizontal component)

(b) Comparison between elements near the wall and at the center (horizontal component)

(c) Comparison between elements near the wall and at the center (vertical component)

Figure 13 Comparison of displacements at the ground surface.

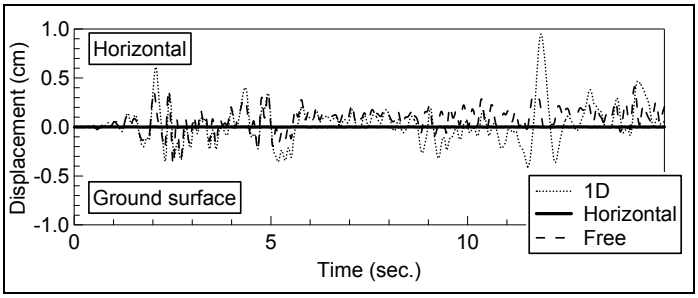

Figure 14 Comparison of horizontal displacement at the ground surface

CONCLUDING REMARKS

Discussions are made in order to make the mechanism how remedial measures against soil liquefaction by shear strain constrained method works. Following conclusions are obtained from the case study using a simplified model.

The ground vibrates vertically by the shear stress transmission from the underground wall to the ground, which generates additional shear deformation in the ground, resulting in excess porewater pressure generation. Therefore, it cannot be said that existence of the rigid or stiffer underground wall constrains onset of soil liquefaction. A simple method to use average stiffness in evaluating the shear strain of the ground results in too small shear deformation, which is a critical side evaluation in design.

This kind of vertical deformation is easier to occur near the ground surface, and is difficult to occur at deep depth. Existence of nonliquefied layer above the liquefied layer will also work to make vertical deformation difficult although it is not proved in this paper.

It is, however, noted that horizontal displacement becomes much smaller by the existence of the underground wall. Since much damage to underground structures is caused by the ground displacement but not by the excess porewater pressure generation, remedial measures by shear deformation constraint method works because horizontal displacement of the ground is much smaller than the one of a bare ground.

It is possible to reduce shear stress acting on the wall by reducing the shear stress transmitted from the wall. One example is an existence of underground wall parallel to the place of shaking.

Inertia force from the superstructure also causes shear stress in the underground wall; therefore it will affect onset of soil liquefaction.

A mechanism that has not been known or discussed is made clear to accelerate excess porewater pressure generation. Since a simplified model is used in the case study, quantitative evaluation how underground wall works cannot be made in this paper. Establishment of the design method remains a future problem.

REFERENCES

[1] Japanese Geotechnical Society (1993): Investigation, design and application of remedial measures against soil liquefaction

[2] Yoshida, N. and Tsujino, S. (1993): A simplified practical stress-strain model for the multi-dimensional analysis under repeated loading, Proc., The 28th Japan National Conference of Soil Mechanics and Foundation Engineering, pp. 1221-1224

[3] Fukutake, T. and Ohtsuki, A. (1993): Analysis by ALISS, Proc. Symposium on Remedial Measures against Liquefaction, JCSMFE, pp. 125-134

[4] Yoshida, N. (1993): STADAS, A computer program for static and dynamic analysis of ground and soil-structure interaction problems, Report, Soil Dynamics Group, The University of British Columbia, Vancouver, Canada

[5] Kusakabe, S. (1996): A study of dynamic behavior of ground by on-line earthquake response test, Theses submitted to Yamaguchi University for partial fulfillment of Doctor of Engineering

Seismic Risk Management of Lifeline Systems

Kinya Yamamoto, Masaru Hoshiya and Haruo Ohno

ABSTRACT

Basic consideration is made on how comprehensively we can evaluate potential seismic risk of lifeline systems and gain an insight into the safety by way of information entropy, which transmits information of various kinds under uncertainties. It is clarified that a redundancy index R_E defined via Shannon's information entropy [1] can be an index to represent redundancy of a system and whose value plays a role to choose the best alternative for designing a system or for finding the best damage mitigation measure against earthquake hazard. A redundancy index R_E [2] is defined by the entropy of a subset of damage modes of a system of m components conditioned on some damage occurrence. The redundancy index R_E takes between zero and unity. When R_E takes zero, a system has no redundancy. And if R_E is unity, the redundancy of the system is maximum.

A study of reliability and redundancy of engineering systems has been carried out by many researchers. De et al [3] have proposed the redundancy index R_R. And Ziha [4] [5] has also defined a redundancy index of engineering systems via Shannon's information entropy. Redundancy index R_R is a conditional probability of event D_m which is an event of failure of all m components conditioned on some damage occurrence. And Ziha's redundancy index R_Z is defined by the entropy of a subset of operational modes conditioned on any operational state.

Hoshiya and Yamamoto [6] justified the validity of R_E to represent a redundancy measure by numerical analyses. First, with highly indeterminate parallel cable systems subject to a pullout loading, these redundancy indexes have been compared, and their characteristics have been discussed and clarified. Then the redundancy indexes R_E and R_Z have been applied to a water supply network in a regional zone and have been compared. And it was found that R_E is superior to other indexes R_R and R_Z.

Finally, a case study is conducted on basis of R_E for a Kobe water supply system which was affected the 1995 Hyogoken-Nanbu earthquake.

Kinya Yamamoto, Assistant Professor, Department of Civil Engineering, Kogyokusha College of Technology, 5-14-2 Nishigotanda , Shinagawa-ku ,Tokyo Japan 141-0031
Masaru Hoshiya, Professor, Department of Civil Engineering, Musashi Institute of Technology, 1-28-1 Tamazutsumi, Setagaya-ku, Tokyo Japan 158-8557
Haruo Ohno, Professor, Department of Civil Engineering, Kogyokusha College of Technology, 5-14-2 Nishigotanda, Shinagawa-ku, Tokyo Japan 141-0031

INTRODUCTION

Many engineers were interested in system safety and reliability again by 1995 Hyogoken-Nanbu earthquake, since not only building structures but also many lifeline facilities were damaged or destroyed. Many engineering systems, for example an indeterminate structure, a lifeline network system etc., are composed of many components. If some components should be damaged, systems may still be functional. Since partial damages do not necessarily lead to the overall failure of a system, reserve capacity of a system, called redundancy of a system, becomes of vital importance when the reliability and the safety of a system are discussed. Thus, rational evaluation of the safety is not easy, and the reliability and the reserve capacity of the system must be investigated after defining the physical interpretation.

The reliability and redundancy have been investigated extensively in the past. To mention a few among many others, early time studies were carried out by Freudenthal et al. [7], Yao et al. [8], Moses et al. [9], Cornell [10] and Hoshiya [11], where they dealt with static problems and a system consisting of many components were taken up as a basic model to discuss the reliability and redundancy. Recently, De et al. [3] defined the redundancy index R_R as the probability of overall system failure conditioned on any first component failure. And using this redundancy index R_R, Wen et al. [12] proposed a framework for quantifying redundancy for a parallel system under dynamic loading. Ziha [4] [5] also discussed redundancy of engineering systems, and proposed a redundancy index R_Z based on Shannon's information entropy [1] [13] [14].

Hoshiya [2], Hoshiya and Yamamoto [15], Yamamoto et. al. [13] and Hoshiya and Yamamoto [6] were motivated by Ziha's studies and proposed a redundancy index R_E. In these studies, characteristics of three redundancy indexes namely R_E, R_Z and R_R to be used for evaluation of system redundancy is comparatively discussed, where a highly indeterminate parallel cable system subject to a pullout loading and a water supply network system to earthquake ground motion are employed. And it is shown that the proposed index R_E can indicate redundancy of a system more distinctly than other indexes by Ziha and De et al, and it can be a tool to gain the insight and read more into the reliability and redundancy.

In this paper, the redundancy index R_E is applied to a Kobe water supply system as a case study, where the 1995 Hyogoken-Nanbu earthquake is used as the input hazard.

REDUNDANCY INDEX

The Venn's diagram for sample space of an engineering system composed of m components is shown in Figure 1. In lifeline network models, the redundancy index is applied to each demand node with multiple paths from supply nodes. And since the network consists of nodes and links, component means link for a network model.

The universe of sample space is defined as follows.

$$U = \{D_0, D_1, D_2, \cdots, D_{m-1}, D_F\} \tag{1}$$

$$U = O \cup NO = D \cup ND \tag{2}$$

In Eq.(2), O is a subset of operational modes, NO is a subset of non-operational mode, D is a subset of damage modes and ND is a subset of no component failure. They are defined respectively as follows.

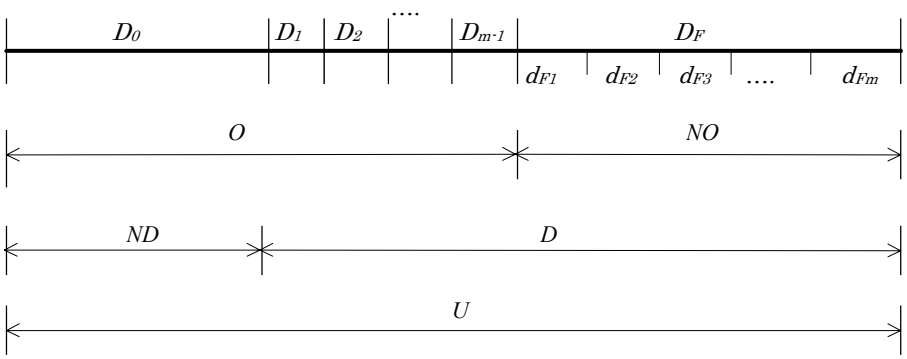

Figure 1. Venn's diagram for sample space of engineering system.

$$O = \{D_0, D_1, D_2, \cdots, D_{m-1}\} \tag{3}$$

$$NO = \{D_F\} \tag{4}$$

$$D = \{D_1, D_2, \cdots, D_{m-1}, D_F\} \tag{5}$$

$$ND = \{D_0\} \tag{6}$$

In these equations, D_0 is an operational mode without any component failure. D_i , in which i takes 1 to m-1, is an operational mode with failures of any i components. And D_F is a non-operational mode. It notes that a lifeline network in general may not be able to supply water to a particular demand node, even if only a few of components fail, and therefore for a lifeline network, D_F is composed of non-operational modes defined by Eq.(7), where d_{Fi}, is a non-operational mode due to failures of i components.

It notes that these modes are mutually exclusive and collectively exhaustive.

$$D_F = \{d_{F1}, d_{F2}, \cdots, d_{Fm-1}, d_{Fm}\} \tag{7}$$

In Eq.(7), d_{Fi}, whose i takes 1 to m, is a non-operational mode with any components failure.

Redundancy Index R_E

Redundancy index R_E [2] [6] is defined as Eq.(8).

$$R_E = H_{D|D} / \log_2(m) = \frac{\{-\sum_{i=1}^{m-1} P_{D_i|D} \log_2 P_{D_i|D} - P_{D_F|D} \log_2 P_{D_F|D}\}}{\log_2(m)} \tag{8}$$

In Eq.(8), $H_{D|D}$ is an entropy of a subset of operational modes conditioned on operational state. And $P_{D_i|D}$ is a conditional probability of an event D_i conditioned on damage state, which is defined as follows.

$$P_{D_i}|_D = \frac{P(D_i)}{P_D} \tag{9}$$

$$P_{D_F}|_D = \frac{P(D_F)}{P_D} \tag{10}$$

where P_D is a probability of a damage state D.

The numerator in Eq.(8) is the information entropy of subsystem of partial damages conditioned on any first component failure, and the denominator is introduced as a normalization factor such that R_E takes 0 to 1. The numerator, that is the entropy of the subsystem becomes larger when these probabilities of damage modes are not zero and they scatter widely. Then, it may be interpreted that redundancy index R_E is a reserve distance from initial failure of any one component (state D_1) to the overall functional loss (state D_F). It is clear that if R_E is closer to 1, the redundancy is higher, and otherwise smaller.

Redundancy of the Whole System R_{ES}

To evaluate the redundancy of not only each demand node but also the whole system, an index R_{ES} is defined as Eq.(11).

$$R_{ES} = \sum \frac{w_j}{\sum w_j} R_{Ej} \tag{11}$$

where R_{Ej} is a redundancy index of demand node j, and w_j is an weight of demand node j in the system. In Eq.(11), R_{ES} is defined as the weighted mean value of R_E of all demand nodes within the system, which is defined as Eq.(8), and shows the redundancy of the whole system.

A CASE STUDY - WATER SUPPLY NETWORK

It is shown that the redundancy index R_E could indicate redundancy of a system more distinctly than other indexes R_Z by Ziha and R_R by De et al, and it could be a tool to gain the insight and read more into the reliability and redundancy by numerical examples with a parallel cable model and a water supply network model [2] [15] [13]. And it is clarified that the redundancy index R_E could be an index to represent the overall redundancy and this index value plays a role to choose the best alternative for designing engineering systems or for finding damage mitigation measures against natural hazards [6].

In this paper, the redundancy index R_E is applied to evaluate the seismic risk mitigation for the water supply system of Kobe city. To mitigate the seismic risk, Kobe water supply department is constructing the new transmission pipe through the town area [17]. This new transmission pipe can supply water to existing links and demand nodes directly, and be the water storage facilities, when the earthquake occurred. The water supply system of Kobe employs a gravity flow system and has more than 120 service reservoirs [18] on basis of the geographical characteristic of the location of Kobe city which sprawls in a narrow band from the east to the west direction surrounded with mountains in the north and sea coast in the south.

For calculation, we consider the water supply network with 6 service reservoirs, whose water distribution areas are mutually independent, in the down town area of Kobe city in Figure 2. To evaluate an effect of the new transmission pipe, a water supply network model is expressed at each service reservoirs area. And in this study, we show the result of calculation on one of 6 water distribution areas.

Network Model

In order to make a simplified analytical model, the system is first divided into 6 independent areas as in Figure 2. For a demonstration purpose, the distribution area A is herein taken up in Figure 3, and a corresponding model of present system and model of after mitigation with new transmission pipes are shown respectively in Figures 4(a) and (b), where node 1 is a supply node and nodes 2 to 15 are demand nodes. And in figure 4, the model of present system means that the new transmission pipe hasn't been laid yet, and the model of after mitigation means that the new transmission pipe has already been laid. The model of after mitigation has two additional supply nodes via the transmission pipes, one of them supplies water to node 6, and the other one directly to links 1,2 and 3.

On the model of after mitigation in Figure 4(b), demand node 6 is supplied water from new supply node, which is an imaginary source from the new transmission pipe, through the new link without any damages, and links 1, 2 and 3 are supplied through dummy nodes attached to each link and dummy links, whose probabilities of damage are 0. After that, probabilities of damage of links 1, 2 and 3 are decreased to about one half or one third of origin.

Assume that when water is supplied from a supply node to demand nodes through links, water flows in the directions shown by arrows attached to links. And even after earthquake occurrence, the directions of water flow are kept unchanged. Referring to past data of earthquake damage in this area [19], damage rate is assigned to each link [20], and assuming Poisson distribution of damage along a link, probabilities of failure of a link with at least more than or equal to one spot of damage are estimated. These probabilities of links in Table 1 are failure probabilities conditioned on occurrence of the 1995 Hyogoken-Nanbu earthquake. Based on the probabilities of failure of each link, Monte Carlo simulation was carried out to obtain 2×10^6 sample fields. With these sample fields, the universe of sample space defined as Eq.(1) and Eq.(2) is estimated. And numerical values for link lengths, pipe materials with diameter as well as probabilities of failure of links are summarized in Table 1, too.

And redundancy indexes R_E of each demand node, which is defined by Eq.(8), and an index R_{ES} defined by Eq.(11) are calculated. When R_{ES} is calculated, water consumption in m^3/day (cubic meter per day) of each node shown in Table 1 is used as the weight of demand node. Since link in the network consists of nodes and links, number of components *m* in Eq.(8) becomes number of links except new links.

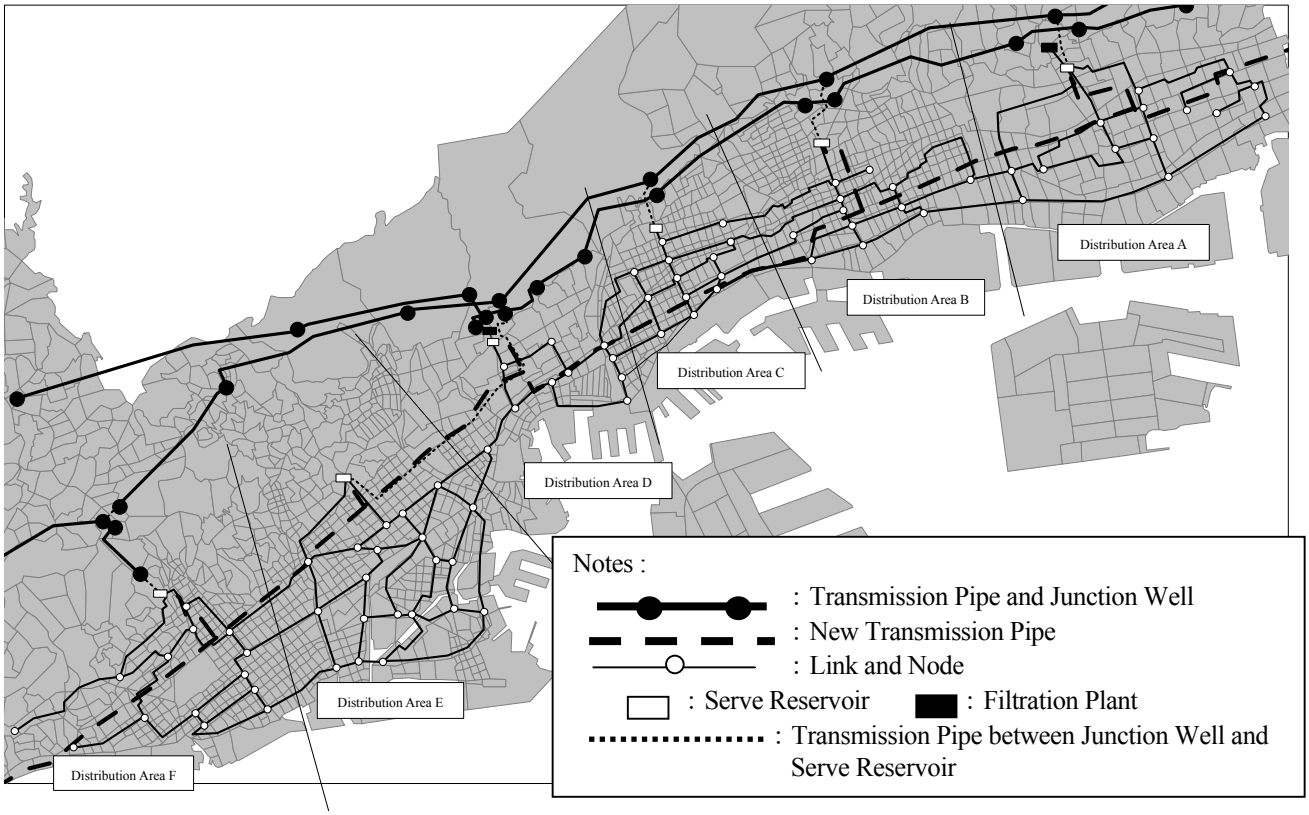

Figure 2. Water supply network in the town area of Kobe city.

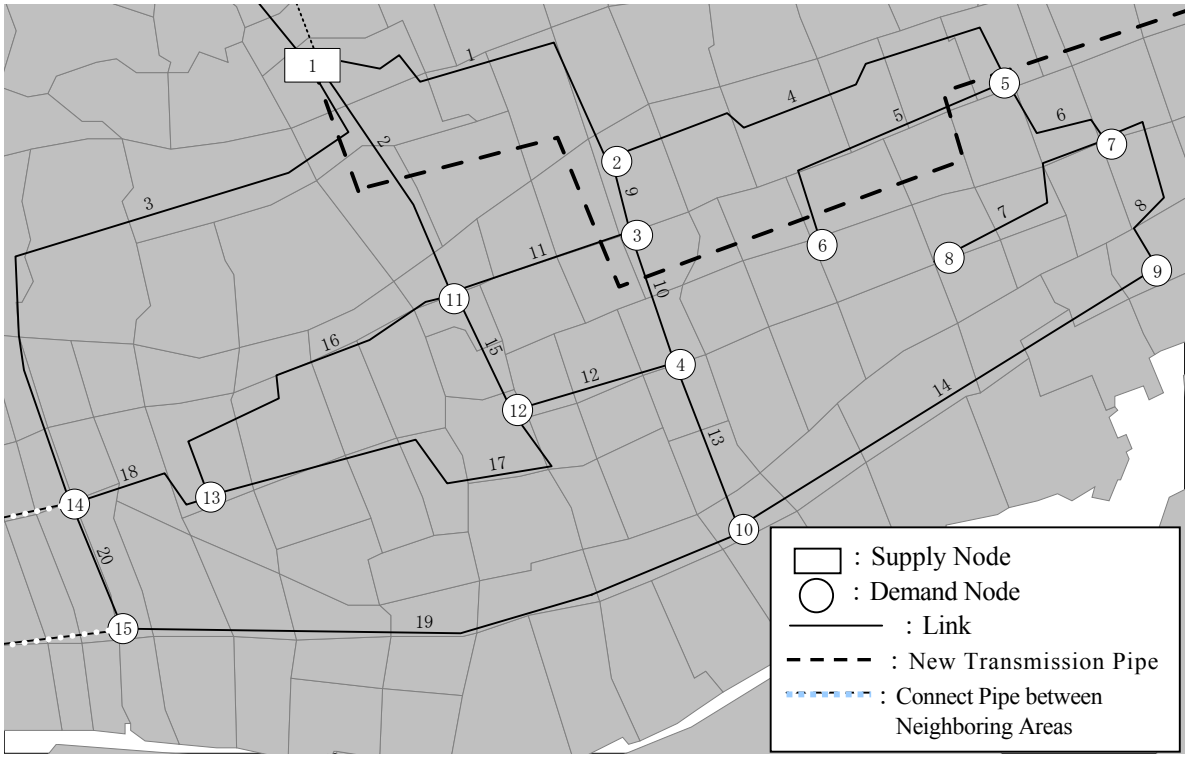

Figure 3. Water supply network of distribution area A.

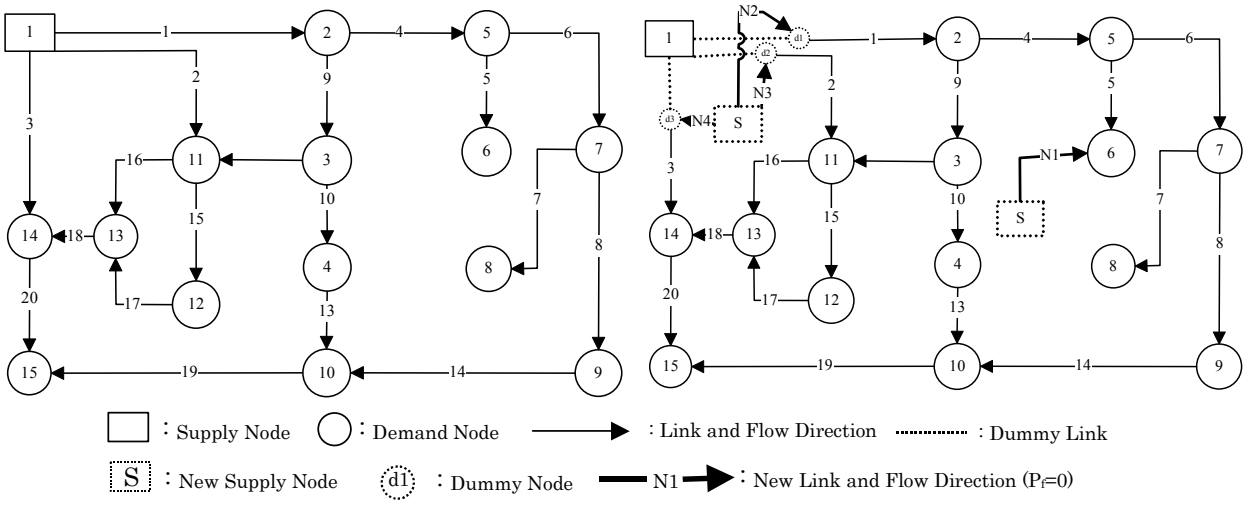

(a) model of present system **(b) model of after mitigation**

Figure 4. Network model of the water distribution area A for calculation.

TABLE 1. LINK AND DEMAND NODE DATA OF NETWORK MODEL OF THE WATER DISTRIBUSION AREA A

Link No.	Length (km)	Kind of Pipe	Diameter (mm)	P_f
1	1.183	DIP	400	0.2844
2	0.818	DIP	400	0.2084
3	2.193	DIP	800	0.3474
4	1.472	DIP	400	0.5721
5	0.973	DIP	400	0.4211
6	0.474	DIP	400	0.2126
7	0.726	DIP	400	0.4049
8	0.673	DIP	400	0.2717
9	0.248	DIP	800	0.0855
10	0.440	DIP	800	0.1514
11	0.616	DIP	400	0.1751
12	0.522	DIP	400	0.1621
13	0.562	DIP	800	0.1677
14	1.559	DIP	400	0.3930
15	0.411	DIP	400	0.1155
16	1.230	DIP	400	0.3099
17	1.409	DIP	400	0.3429
18	0.524	DIP	400	0.1492
19	2.033	CIP	400	0.8942
20	0.437	DIP	400	0.1490

Kind of Pipe DIP：Ductile Iron Pipe,
CIP：Cast-Iron Pipe, SP：Steel Pipe

Node No.	Water Consumption (m^3／day)
2	2237
3	1678
4	3356
5	4475
6	2797
7	2237
8	3356
9	3356
10	5593
11	2237
12	5593
13	3915
14	3915
15	5034
Total	49780

Node 1 is a supply node.

OPTIMAL SOLUTIONS FOR MITIGATION

Here, a risk management measure to find optimal solution for mitigation is discussed.

The redundancy index R_E of each demand node of the water distribution area A and the value of an index R_{ES}, which shows the redundancy of the whole system, are shown in Figure 5.

In Figure 5, the value of R_{ES} of the model of present system is 0.563, and the value of R_{ES} of the model of after mitigation is 0.598. This means that the effect of the new transmission pipe is represented.

In the water distribution area A, demand node 6 and links 1, 2 and 3 are supplied water by the new transmission pipe directly. Discuss about the effect of the new transmission pipe to each demand node, the redundancy index R_E of demand node 6 is increased from 0.268 to 0.662. And the redundancy indexes R_E of demand nodes 5, 7, 8 and 9 are increased a little, which are from 0.459 to 0.405, from 0.339 to 0.387, from 0.226 to 0.261 and from 0.265 to 0.304 respectively. Here Table 1 indicates that links 1, 2 and 3 have probabilities of 0.2844, 0.2084 and 0.3474, which are not so high probabilities.

The index of node 6 is remarkably improved in the model of after mitigation, obviously due to the newly laid transmission pipes. In the water distribution area A, link 4 has probability of 0.5721, which is not so low probability. And link 4 is on a route from supply node 1 to demand

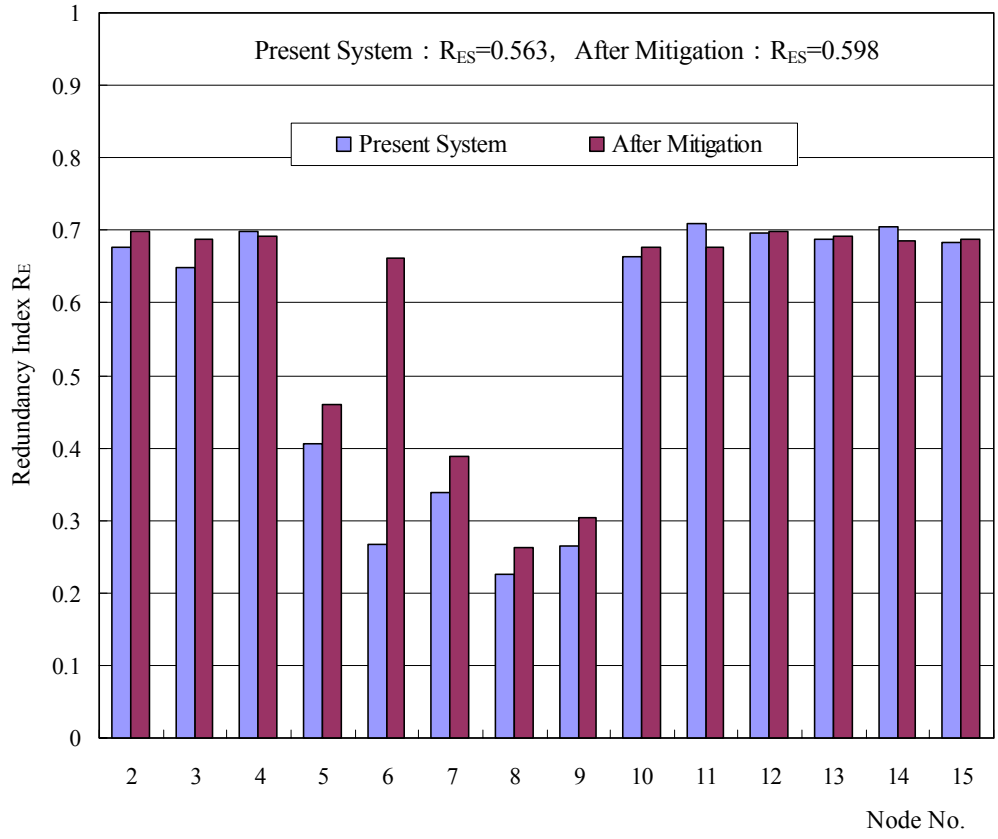

Figure 5. Simulation results of network model of the water distribution area A. (2×10^6 trial)

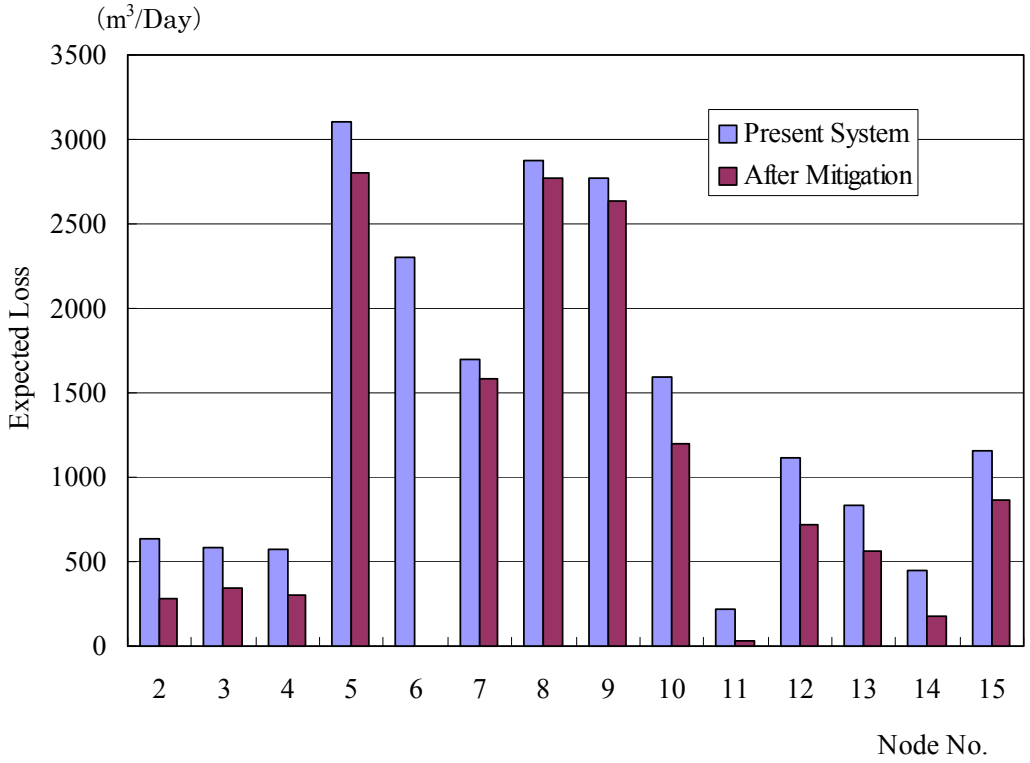

Figure 6. Expected loss of each demand node of the water distribution area A.

nodes 5, 6, 7, 8 and 9, whose redundancy indexes R_E are low values not only in the model of present system but also in the model of after mitigation. So the redundancy indexes R_E of these demand nodes except demand node 6, which is supplied water directly, take low values. But this means that the effect of the new transmission pipe is represented, too.

Figure 5 shows that redundancy index R_E of some demand nodes have smaller index values than before. However, this does not mean that these demand nodes have become unsafe, but simply due to the relative distributions of P_f values of demand nodes over the links of the network. In fact, since the index is defined based on entropy, it indicates a relative value of redundancy of each node compared to other nodes of a whole system. Redundancy improvement of the model of after mitigation is clearly observed if the expected losses of each demand node are compared for the model of present system and the model of after mitigation shown in Figure 6.

CONCLUSIONS AND FUTURE STUDY

(1) Attention is paid to the information entropy in conjunction with reliability and redundancy of engineering systems. And the redundancy of a network system is expressed by using information entropy. We proposed the redundancy index R_E to measure the reserve capacity of an engineering system with information entropy. And the redundancy of the network is formulated which includes the effect of the network configuration. The redundancy index R_E may play a major role in evaluation of the safety level requirements of current seismic design codes of lifeline system.

(2) The redundancy index R_E may play a major role in evaluation of an optimal alternative of a lifeline network for earthquake damage mitigation.
(3) As a case study, the redundancy index R_E is applied to evaluate the seismic risk mitigation for the water supply system of Kobe city. And the effect of the seismic risk mitigation for the water supply system of Kobe city is evaluated.
(4) Lifeline system like a water supply system has a network deployed in the wide area, which is composed of many components, and there are correlations among the probabilities of failure of these components, which are due to the specificity of both component properties and their regional locations. Then, it may be interpreted that a lifeline system is of a portfolio characteristic. As a matter of fact, the proposed redundancy index R_E involuntarily reflects the notion of portfolio stemmed from the field of finance engineering. For a future study, contribution of correlation characteristics among probabilities of failure of system components to the redundancy may be clarified from a point of view of a portfolio.

ACKNOWLEDGEMENTS

We thank the Kobe Water Supply Department for giving us data of Kobe water supply network for the case study.

REFERENCES

[1] Shannon, C.E. and W. Weaver. 1949. "The mathematical theory of communication", Univ. of Illinois Press., Urbana.
[2] Hoshiya, M. 1999. "Reliability vs. uncertainty in structural safety." Proc., 8th International Conference on Application of Probability and Statistics, Sydney, Australia, pp. 1131-1134.
[3] De, R.S., A. Karamchandani and C.A.. Cornell, 1989. "Study of redundancy in near-ideal parallel structural systems." Proc., 5th International Conference on Structural Safety and Reliability, San Francisco, Calif., pp. 975-982.
[4] Ziha, K. 2000. "Event oriented system analysis." *Probabilistic Engineering Mechanics*, Elsevier, England, Vol.15, No.3, pp. 261-275.
[5] Ziha, K. 2000. "Redundancy and Robustness of Systems of Events." *Probabilistic Engineering Mechanics*, Elsevier, England, Vol.15, No.4, pp.347-357.
[6] Hoshiya, M and K. Yamamoto. 2002. "Redundancy Index of Lifeline Systems." *Journal of Engineering Mechanics*, ASCE, Vol.128, No.9, pp.961-968.
[7] Freudenthal, A.M., J.M. Garrelts, and M. Shinozuka. 1966. "The analysis of structural safety." *Journal of the Structural Division*, ASCE, Vol.92, No.ST1, pp. 267-326.
[8] Yao, J.T.P. and H.Y. Yeh. 1969. "Formulation of structural reliability." *Journal of the Structural Division*, ASCE, Vol.95, No.ST12, pp. 2611-2620.
[9] Moses, F. and D. E. Kinser. 1967. "Analysis of structural reliability." *Journal of the Structural Division*, ASCE, Vol.93, No.ST5, pp. 147-164.
[10] Cornell, C.A. 1967. "Bounds on the reliability of structural systems." *Journal of the Structural Division*, ASCE, Vol.93, No.ST1, pp. 171-200.
[11] Hoshiya, M. 1971. "Reliability of redundant cable system" *Journal of the Structural Division*, ASCE, Vol.97, No.ST11, pp. 2773-2776.
[12] Wen, Y.K., C.-H. Wang and S.H. Song. 1999. "Structural redundancy under stochastic loads." Proc., 4th Imternational Conference on Stochastic Structural Dynamics, Notre Dame, Indiana, pp. 213-220.
[13] Khinchin, A.I. 1957. "Mathematical foundations of information theory", Dover Publications, New York.
[14] Kullback, S. 1959. "Information theory and statistics", Dover Publications, New York.
[15] Hoshiya, M. and K. Yamamoto. 2000. "Information entropy for redundancy of engineering systems." Proc., International Conference on Monte Carlo Simulation, Monte Carlo, pp. 273-278.

[16] Yamamoto, K., H. Ohno and M. Hoshiya. 2001. “Redundancy and reliability of engineering systems with information entropy.” Proc., ICOSSAR’01 (CD-ROM), Los Angels, Calif.
[17] Kobe Water Supply Department. 1995 “Aseismic basic plan for facilities of Kobe water system”.
[18] Kobe Water Supply Department. 2000 “General map of Kobe Water Network”.
[19] Kobe Water Supply Department. 1996 “Hanshin-Awaji Great Disaster, Document of Restoration of Water System”.
[20] Isoyama, R., E. Ishida, S. Yune and N. Shiraki, 1998 “Study of estimation of earthquake damages of water pipes”, *Journal of Japan Water Works Association*, Vol.67, No.2, pp. 25-40.

Development of Earthquake Resistance Evaluation Method for Buried Pipeline Networks

Yoshihisa SHIMIZU, Kenichi KOGANEMARU and Nobuhisa SUZUKI

ABSTRACT

In this paper, a new method is developed for evaluation of earthquake resistance of buried pipelines. Not only the strength of pipeline materials but also the shape of pipeline networks, the seismic response of the ground, and the effect of liquefaction are taken into consideration to evaluate actual earthquake resistance of existing buried pipeline networks. Using this evaluation method, weak points of pipeline networks can be picked up and rational measures against earthquakes can be achieved for existing pipelines.

Yoshihisa SHIMIZU, Senior Manager, Center for Supply Control and Disaster Management, Tokyo Gas Co., Ltd. 1-5-20, Kaigan, Minato-ku, Tokyo, JAPAN, 105-8527

Kenichi KOGANEMARU, Engineer, Center for Supply Control and Disaster Management, Tokyo Gas Co., Ltd. 1-5-20, Kaigan, Minato-ku, Tokyo, JAPAN, 105-8527

Nobuhisa SUZUKI, Reseach & Development Division, NKK Corporation, 1-1, Minamiwatarida-cho, Kawasaki-ku, kawasaki, JAPAN, 210-0855

INTRODUCTION

The seismic resistance of buried pipeline was conventionally evaluated only by the strength of material used for the pipeline. Consequently, the buried pipeline with weak-strength material was recognized as the pipe to be replaced or to be reinforced. However, after the analysis on the damaged city gas buried pipes in 1995 Kobe Earthquake, it became clear that even in the strongly shaken area, only some of the pipes with weak-strength material were damaged, which were seemed to be effected by the soil conditions or the network shapes. Therefore, the conventional method could be over-investment if it is used for the determination of replacement / reinforcement plan.

Here, it is obviously important to develop the new seismic resistance evaluation method for buried pipes where both the soil conditions and the network shapes are taken into consideration, in order to make the replacement / reinforcement plan to be effective. In addition to it, the new method can be introduced into real-time damage mitigation systems such as "SUPREME"[1], to conduct accurate damage estimation. This paper introduces the recent advances of the development and the actual utilization case conducted by Tokyo Gas Company.

OUTLINE OF THE NEW EVALUATION METHOD

In this new method, the seismic resistance of the buried pipes can be evaluated reasonably through comparison between the strength of the buried pipes and the external forces on the pipes induced by design earthquake motion, as shown in Fig.1.

Here, SUPREME[1] (**Sup**er High Density **Re**al-time **M**onitoring of **E**arthquakes) is the real-time city gas damage mitigation system which has been developed by Tokyo Gas and in operation at Tokyo metropolitan area since July, 2001. SUPREME has detailed GIS database such as 60,000 bore-hole logging data, geological classification data and 48,000km – length pipeline data. In addition, the "Seismic Design Guideline for High Pressure Gas Pipeline"[2] was published in 2000 and the "Seismic Design Guideline for High Pressure Gas Pipeline Buried in Liquefiable Soil Areas"[3] was set in 2001. Utilizing these guidelines and SUPREME database, the external forces on the buried pipes can be accurately calculated. Moreover, a fast analytical method for seismic responses of buried pipeline networks[4] has been newly developed. Utilizing this method and the strength database obtained by experiments, the strength of the buried pipeline can be accurately calculated.

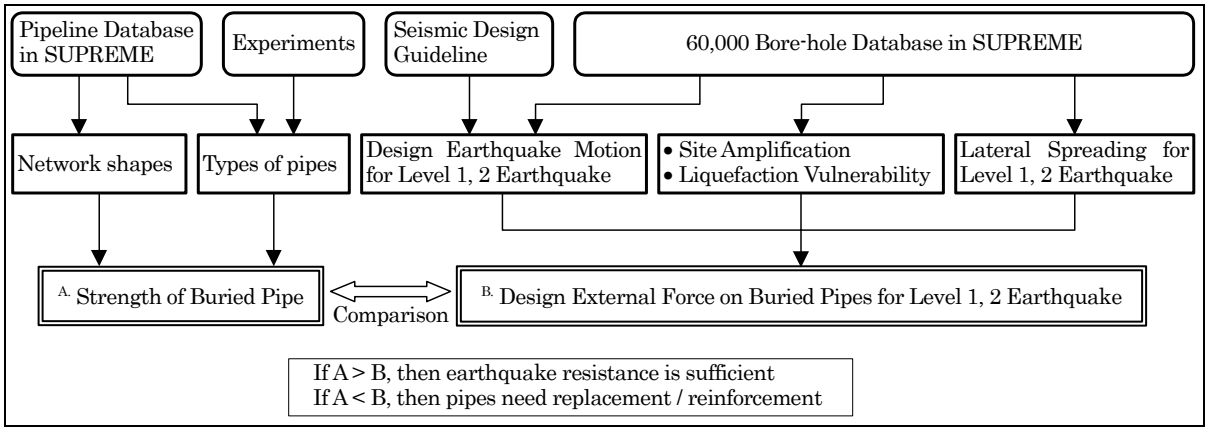

Figure 1. Basic Concept of the New Method

DESIGN EXTERNAL FORCE

The design external force can be assumed according to any seismic design guidelines. Here, for the example, the procedure to calculate the external force induced by "Shaking" based on the "Seismic Design Guideline for High-Pressure Gas Pipeline" is introduced.

According to the "Seismic Design Guideline for High-Pressure Gas Pipeline", the velocity response spectrum at the engineering baserock is defined as shown in Fig.2, respectively for Level 1 and 2 Earthquakes.

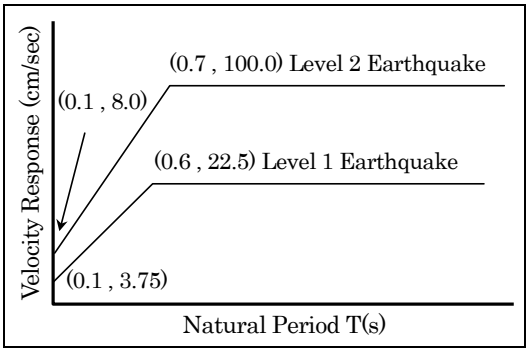

Figure 2. Velocity Response Spectrum for Level 1 and 2 Earthquake[2)]

In SUPREME, the natural period database is prepared on GIS with 50m×50m pixels as shown in Fig.3, utilizing a total of 60,000 borehole logging data (Fig.4).

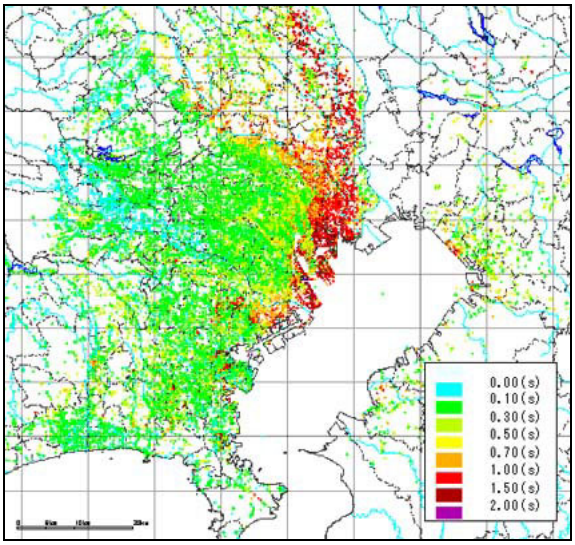

Figure 3. Natural Period Database in SUPREME

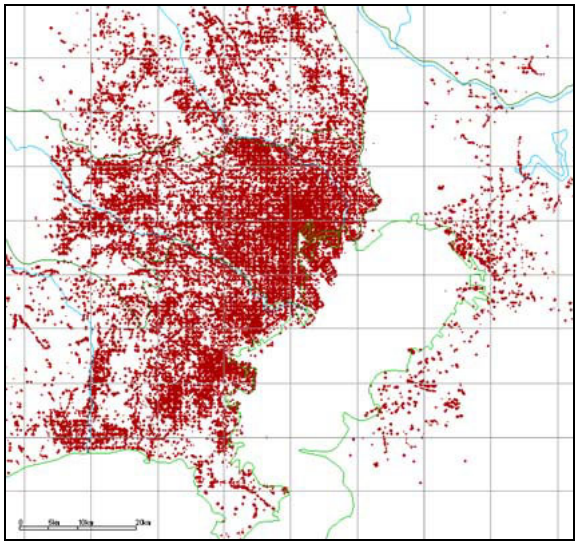

Figure 4. Sites of bore-holes employed in SUPREME.

Based on Fig.2 and Fig.3, the velocity response on the engineering baserock at any points can be estimated. then, utilizing the design guideline, the external forces or the strain of the buried pipe may be of course calculated. Here, to make the procedure as simple as possible, the design external forces is expressed as design SI values at any points on the surface ground. The SI value on the engineering rock (SI_B) can be expressed by Eq.1.

$SI_B = 1.18 \times Sv$ (Eq.1)

The conversion factor from the engineering rock to surface for SI values was defined in the guideline as $4/\pi$.

Then the design SI values on the surface ground (SI_S) can be obtained by Eq.2.

$$SI_S = \frac{4}{\pi} \times SI_B \quad \text{(Eq.2)}$$

STRENGTH OF THE BURIED PIPE

STRENGTH DATABASE OBTAINED BY EXPERIMENTS

Tokyo Gas's medium pressure pipeline networks contains welded steel pipes, ductile cast iron pipes, welded steel valves, ductile cast iron valves and cast iron valves. For all these elements, the compression and tensile strength data were obtained through vast volume of experiments.

For example, the results of tensile strength tests for cast-iron valves with different diameters are shown in Fig.5, Photo.1 and Table.1.

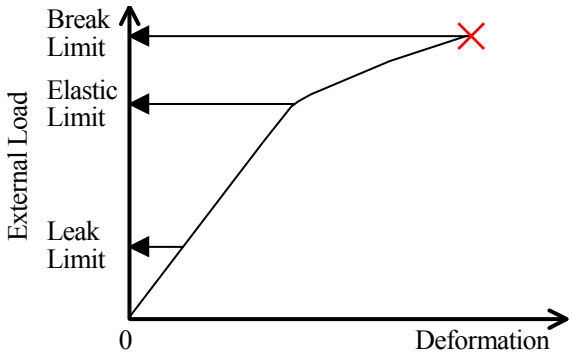

Figure 5. Tensile Strength Tests for Cast Iron Valves

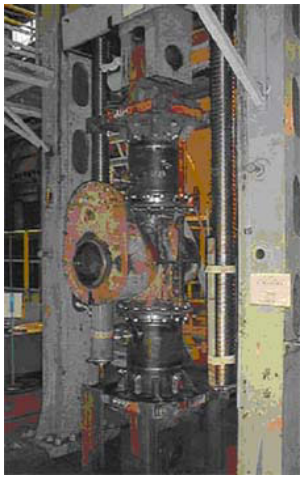

Photo 1. Tensile Strength Tests for Cast Iron Valves

Table 1. Tensile Strength of Cast Iron Valves

Diameter (mm)	100	200	300	600
Elastic Limit (tf)	26	35	39	188
Break Limit (tf)	46	72	136	439

Here, 3 tensile strengths are defined as follows. “Leak Limit” is the tensile strength where leakage starts to occur at the flange joint. “Elastic Limit” is the tensile strength where plastic deformation starts to occur. “Break Limit” is the tensile straight where valves break. These strength data has been used for selection of valves to be replaced or reinforced and determination of priority.

DEVELOPMENT OF NeEX

The maximum strain or the maximum axial force induced by “Shaking” depends on the ground surface deformation (Uh) and the network shapes. The exact answer can be obtained if FEM calculation is conducted for vast spatial pipeline network but the calculation volume will be too large to be practical (Fig.6). Then. the fast analytical method for seismic responses of buried pipeline networks, namely NeEX[4], has been developed to reduce the calculation volume. In this method, to neglect the effect of distant pipe, the network is divided into many small pipe elements which contain a straight pipe and boundary elements such as bend, as shown in Fig.7. If FEM calculation is conducted for all these small elements, the calculation volume cannot be reduced. Then, in advance, the strength database such as “stress-strain curve” is prepared for each boundary elements such as bends or Tees, by using FEM calculation results or experiment results. Then, for each small pipe element, non-linear equation with a condition of force equilibrium and deformation consistency will be solved (Fig.8). Note that a beam element is used in this calculation to be simple.

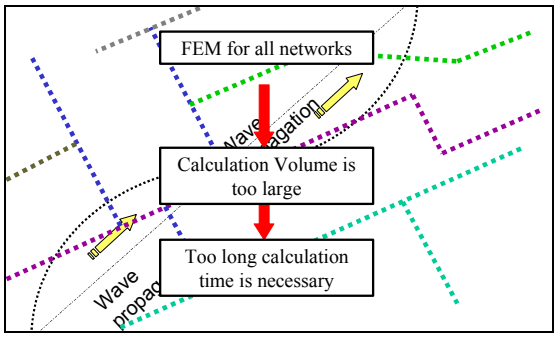

Figure 6. FEM for All Networks

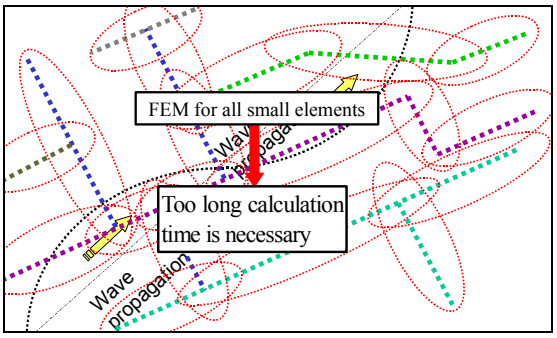

Figure 7. FEM for all networks which are divided into many small

This new method and conventional FEM method were applied into the medium-pressure pipeline networks in Koto-ku area of Tokyo which were divided into 3,000 elements, to compare their calculation volume. For conventional FEM by super-computer, it took 15 days. On the other hand, for NeEX with desk-top PC, it took only 2 minutes to complete the calculation. Then, it was proved that the calculation time in the new method is only 1/10,000 of the one of the conventional FEM.

With regard to the accuracy of calculation, it was proved that the calculation result by the NeEX coincides with the one of FEM for axial force calcution.[4)]

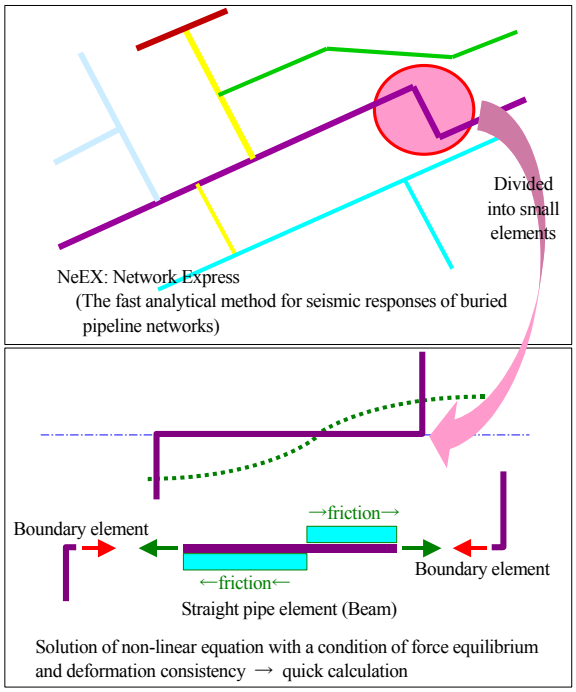

Figure 8. Development of NeEX

DETRMIMINATION OF CRITICAL SI VALUE

At first, the vast volume of Tokyo Gas's medium pressure network, with 6,000 km length in total, was to be divided into small pipe elements, utilizing pipe data base, valve data base and soil database in SUPREME. After dispersion work, the number of elements reached 230,000.

Secondly, for each dispersed element, the NeEX was applied to calculate the maximum axial force or the maximum strain according to the ground surface deformation (Uh) by shaking.
Uh can be obtained by the following equation[2].

$$Uh = SI \times T / (1.18 \times 2\pi) \qquad \text{(Eq.3)}$$

where Uh:Ground surface deformation (cm)
SI: Spectrum intensity (cm / sec)
T: Natural period of ground at the element (sec)

Here, Uh depends on SI.
Then, if the calculated maximum axial force or the maximum strain exceds the strength of material used for the element, the element is judged as "damaged". Therefore the "critical" condition can be defined where the calculated values are equal to the strength of the element. Consequently the critical Uh, in other word, critical SI value, SIc, can be obtained, for each element, as shown in Fig.9.

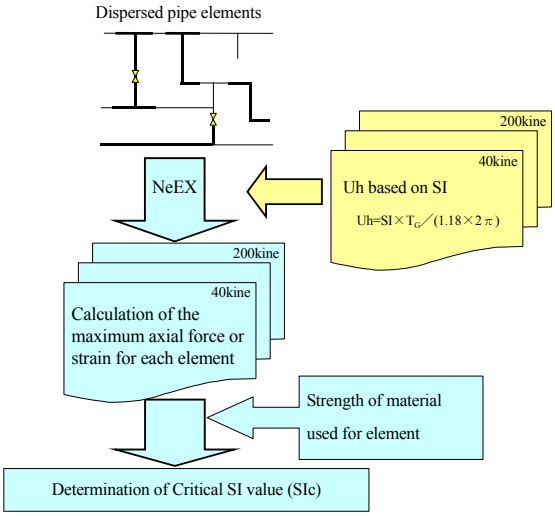

Figure 9. Determination of Critical SI Value

SEISMIC RESISTANCE EVALUATION METHOD

The seismic resistance evaluation for buried pipeline can be conducted easily to compare the design SI value on the surface ground (SIs) with the critical SI value (SIc) for each element.

If SIs $\geqq$ SIc, then the pipe element is judged to have poor seismic resistance and the replacement or reinforcement is to be planned.

If SIs $\leqq$ SIc, then the pipe element is judged to have sufficient seismic resistance.

This method has been already applied to Tokyo Gas's medium pressure pipeline network. One of the results is shown in Fig.10. For example, there are 1,500 cast iron valves in Tokyo Gas and after this evaluation, only 10% of them was proved to be replaced or reinforced and the rest of them was judged to have sufficient seismic resistance. Tokyo Gas has already started to replace them and plans to finish the work by 2003. Thus, utilizing the new seismic resistance evaluation method, the over-investment can be avoided.

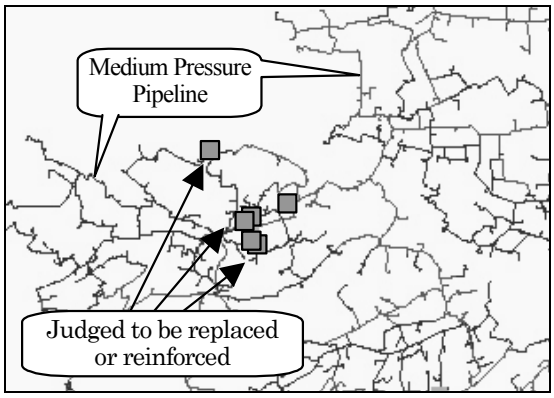

Figure 10. Seismic Resistance Evaluation

UTIIZATION IN SUPREME

Conventionally, the fragility curve based on the pipe damage experience in past earthquakes has been used for the real-time damage assessment. It seems to be practical for low pressure ctiy gas networks because there are ample damage cases in past earthquakes. However, for medium pressure or high pressure city gas networks, this method is not suitable because in the past earthquake, there was not much pipe damage case and the accuracy of the fragility curve cannot be assured.

Here, the new method to evaluate the seismic resistance of buried pipeline networks has been developed and the database of "critical SI value, SIc" for all 230,000 elements has been prepared. On the other hand, in SUPREME, the SI distribution (SIr) can be determined very precisely on GIS with 1.4 million 50m×50m maps in real-time just after earthquakes, utilizing 3,700 new SI sensors and site amplification database shown in Fig.11[5]. Then, it is quite easy to conduct accurate damage assessment for medium pressure pipeline if comparison between SIc and SIr is conducted.

This method has been already installed in SUPREME and the damage assessment will be conducted as shown in Fig.12 and 13 when a big earthquake happens. The results of damage assessment will be big assistance for decision making of emergency response.

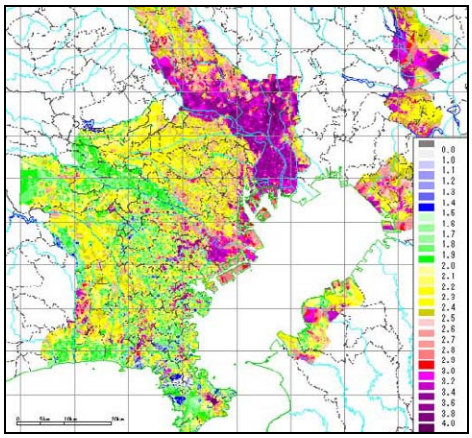

Figure 11. SI Amplification Database in SUPREME

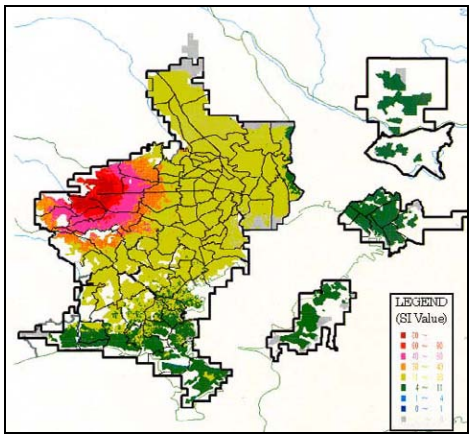

Figure 12. Real-time SI value distribution (SIr) under assumption of Tachikawa Earthquake

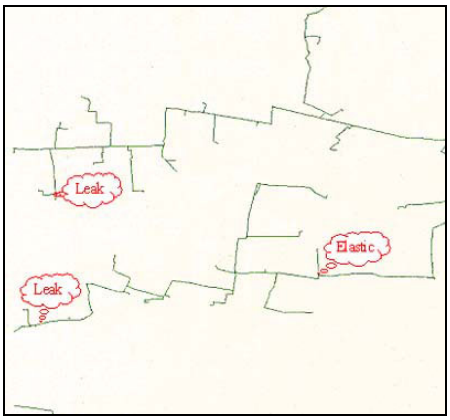

Figure 13. Results of damage assessment for medium pressure pipeline in SUPREME, under assumption of Tachikawa Earthquake

CONCLUSION

The new evaluation method for earthquake resistance of buried pipeline networks has been developed. Utilizing this method, the over-investment for the replacement of medium pressure pipes can be realized. The major achievements are described in what follows.

[1] The seismic design external forces based on the "Seismic Design Guideline for High-Pressure Gas Pipeline" has been expressed as the "Design SI value on the surface ground (SIs)", utilizing a total of 60,000 bore-hole logging database in SUPREME.

[2] The database of compression and tensile strength for all materials used in medium pressure gas pipeline has been prepared through lots of experiments.

[3] The new and vast analytical evaluation method for seismic responses of buried pipeline networks, namely NeEX (Network Express), has been developed.

[4] After dispersion of 6,000km length medium pressure pipeline networks, the NeEX was applied to calculate the "critical SI value (SIc)" "for all 230,000 elements, utilizing material strength database and soil database.

[5] The simple and accurate seismic resistance evaluation for buried pipeline has been realized with comparison between SIs and SIc.

[6] The accurate real-time damage assessment for medium pressure pipeline has been realized through comparison between the "Real-time SI value (SIr)" obtained in SUPREME monitoring system and SIc. This logic has been already installed in SUPREME and it will be a great assistance for decision making on emergency response.

REFERENCES

[1] Shimizu, Y., Yamazaki, F., Nakayama, W., Koganemaru, K., Ishida, E., and Isoyama, R., 2002, "Development of Super High-density Realtime Disaster Mitigation System for Gas Supply Networks", 12th European Conference on Earthquake Engineering, Paper No.858, 10p

[2] Japan Gas Association, 2000; "Seismic Design Guideline for High Pressure Gas Pipeline"

[3] Japan Gas Association, 2000; "Seismic Design Guideline for High Pressure Gas Pipeline in Liquefiable Soil Areas"

[4] Suzuki, N., Horikawa, H., Mori, K., Mayumi, T., Shimizu, Y., Koganemaru, K., Yoshizaki, K. and Hatsuta, Y., 2002; "A Fast and Effective Solver for Responses of Buried Pipeline Networks",11th Japan Earthquake Engineering Symposium, (Under submission)

[5] Shimizu, Y., Ishida, E., Isoyama, R., Koganemaru, K., Nakayama, W., and Yamazaki, F., 2000; "Development of SUPREME, Super High-Density Realtime Disaster Mitigation System for Gas Supply System", Proceedings of the 6th International Conference on Seismic Zonation, pp. 1181-1186

Advancing the State-of-the-Art of Liquefaction Hazard Mapping

Application of the Liquefaction Potential Index to Liquefaction Hazard Mapping

Thomas L. Holzer , Selcuk Toprak, and Michael J. Bennett

ABSTRACT

Cumulative distributions of the liquefaction potential index (LPI) measured within geologic units were used to prepare quantitative liquefaction hazard maps of the cities of Alameda, Berkeley, Emeryville, Oakland, and Piedmont, California. LPI values were computed from a total of 210 cone penetration test soundings conducted in different geologic units in the study region. For an **M**7.1 earthquake on the nearby Hayward Fault, LPI predicts that 73 % of the area underlain by artificial fill and 3 % of the area underlain by Holocene alluvial fan can be expected to show surface effects of liquefaction. The predictions are consistent with recent experience where similar deposits experienced near-source ground motion.

Thomas L. Holzer, Research Geologist, U.S. Geological Survey, 345 Middlefield Road, Menlo Park, CA 94025
Selcuk Toprak, Visiting Research Engineer, Waseda University and Advanced Industrial Science and Technology (AIST)**,** Department of Civil Engineering**,** Waseda University, 3-4-1 Okubo, Shinjuku-ku**,** Tokyo, Japan 169-8555 (Asst. Prof., Pamukkale University, Kinikli, Denizli, Turkey, 20070)
Michael J. Bennett, Operational Geologist, U.S. Geological Survey, 345 Middlefield Road, Menlo Park, CA 94025

INTRODUCTION

Quantification of liquefaction hazard is an important challenge encountered in the preparation of regional liquefaction hazard maps. Because most liquefaction maps are based on geologic maps, the problem ultimately reduces to the classification of the liquefaction potential of geologic units. While blow counts may be collected and used to evaluate relative liquefaction potential, the hazard of geologic units as described in maps is commonly described in general terms ranging from low to very high [1], and thus show only relative liquefaction potential. This report describes the application of the liquefaction potential index (LPI) to quantify the hazard potential of geologic units. The application is illustrated with mapping done in the San Francisco Bay area, California.

LPI, as originally defined by Iwasaki and others [2], predicts the liquefaction performance of the soil profile to a depth of 20 m at a specific site. It provides an estimate of the severity of liquefaction at a specific location unlike the simplified procedure [3], which provides an estimate of the liquefaction potential only for a soil element. Investigations in both Japan and the United States of liquefaction occurrences in historic earthquakes suggest that in general surface manifestations of liquefaction—sand boils, ground cracking, and lateral spreading—occur where values of LPI exceed about 5. By conducting field surveys that permit computation of the distribution of LPI for specific geologic units, the percentage of the area that will exhibit surface manifestations of liquefaction can be estimated for each geologic unit.

LPI

LPI was originally developed in Japan to estimate the potential of liquefaction to cause foundation damage [2]. The index assumes that the severity of liquefaction is proportional to the:

(1) thickness of the liquefied layer;
(2) proximity of the liquefied layer to the surface; and
(3) amount by which the factor safety (FS) is less than 1.0, where FS is the ratio of the liquefaction resistance to the load imposed by the earthquake.

It was defined as:

$$LPI = \int_0^{20m} F\, w(z)\, dz \qquad (1)$$

where

$F = 1 - FS$ for $FS \leq 1$, and
$F = 0$ for $FS > 1$, and
$w(z) = 10 - 0.5\, z$, where z is the depth in meters.

Values of LPI for eq. 1 range from 0 for a site with no liquefaction potential to a maximum of 100 for a site in which the factor of safety is zero over the entire 20-m-depth range. Although

LPI relies on the simplified procedure to estimate factors of safety, the prediction by LPI is more comprehensive than that made by the simplified procedure. The simplified procedure predicts the performance of a soil element whereas LPI predicts the performance of the whole soil column to a depth of 20 m.

Iwasaki and others [4] and Toprak and Holzer [5] have compiled case histories that compare LPI with observed severity of liquefaction. Iwasaki and others [4] concluded that severe liquefaction is likely at sites with LPI > 15 and that severe liquefaction is unlikely at sites with LPI < 5. Toprak and Holzer [5] correlated surface manifestations of liquefaction with LPI for the 1989 Loma Prieta, California, earthquake and concluded that sand boils and lateral spreading, respectively, occur primarily where LPI $\geq$ 5 and 12.

GEOLOGY AND DATA

The surficial geology of the study area is shown in Figure 1. The study area is near the eastern shore of San Francisco Bay and includes the cities of Alameda, Berkeley, Emeryville, Oakland, and Piedmont, California. The surficial geology can be geographically subdivided into three broad categories. The area west of the original natural shoreline—the landward extent of artificial fill—is primarily underlain by artificial fill that rests on Holocene younger bay mud that was deposited in San Francisco Bay. Immediately east of the natural shoreline is the central area where the surficial geology consists of Holocene and Pleistocene alluvial fan deposits. East of the central area, bedrock is exposed at the land surface. The artificial fills in the western area are extensive and consist primarily of sand, which were hydraulically emplaced before 1964 without consideration of their vulnerability to liquefaction. Fill thickness ranges from about 11 m to zero where the fill pinches out along the original shoreline. The average thickness is about 3 m. The Holocene alluvial fan deposits in general consist of fine-grained deposits, although sands locally may be present. The fan complex was active until modern urban development covered the land surface and channelized the modern streams. These deposits rest on older Pleistocene alluvial fan deposits that were last active during the previous interglacial period. The upper surface of the Pleistocene alluvial fan deposits is heavily dissected as the result of tectonic uplift and stream incision caused by the lowering of stream base level when sea level retreated during the last glaciation. Merritt Sand, which is primarily a wind-blown deposit, locally overlies the Pleistocene alluvial fan. The Merritt Sand was deposited near the end of the Pleistocene Epoch when sea level was below its current level.

The Hayward Fault is the most important seismic source in the study area [6]. Recent studies of earthquake recurrence on the Hayward Fault indicate there is a 32 % probability of a **M** $\geq$ 6.7 earthquake in the period 2000-2030 [6]. These studies also indicate a **M**7.1 earthquake can be expected on the Hayward Fault with an estimated recurrence time of 523 yr. This earthquake assumes both the north and south segments of the fault rupture in a single event. Rupture of the northern segment alone, which is in the study area, would produce an **M**6.6 earthquake. Its estimated recurrence time is 387 yr. The last major earthquake on the Hayward Fault was in 1868. Its estimated magnitude was 6.8 and it ruptured the northern segment of the fault.

A total of 210 cone penetration tests (CPT) soundings were conducted in artificial fill and Holocene and Pleistocene surficial units (Figure 1). In addition to penetration testing, shear-wave velocity was measured in each sounding and used to help identify the geologic units. Sampling

adjacent to selected CPT soundings was conducted to ensure soils were classified properly from the CPT measurements. The CPT data and shear-wave velocity travel times are available at http://quake.usgs.gov/prepare/cpt/.

METHODOLOGY

LPI values were computed for each CPT sounding using **M**6.6 and 7.1 earthquakes on the nearby Hayward Fault; factors of safety were computed using Robertson and Wride [7]. These two earthquakes dominate when the shaking hazard in the Oakland region is deaggregated for magnitude (see http://geohazards.cr.usgs.gov/eq/). Peak horizontal ground accelerations (PGA) of 0.4 and 0.5 g were used at each sounding, respectively, to compute factors of safety in the LPI for the **M**6.6 and 7.1 earthquakes. These values of PGA were estimated with the attenuation relation of Boore and others [8] and are based on average distance of the study area from the fault and average soil conditions. Depths to ground water at each sounding were either measured or inferred from a regional map of the water table prepared for the study.

To identify the hazard level of each geologic unit for the **M**6.6 and 7.1 earthquakes on the Hayward Fault, LPI values were grouped by surficial geologic unit and cumulative distributions of LPI were prepared (Figure 2). Although the mapping of surficial geology by Helley and Graymer [9] identified subunits within the Holocene alluvial fan, these subunits were not geotechnically distinguishable in the CPT soundings. Accordingly, LPI computed for soundings in the Holocene alluvial fan were assigned to a single geologic unit. Based on the calibration of LPI by Toprak and Holzer [5], it was assumed that surface manifestations of liquefaction occur where LPI $\geq$ 5. Thus, the percentage of soundings with LPI $\geq$ 5 for each geologic unit indicates the approximate percentage of surface area underlain by that unit that will exhibit surface manifestations of liquefaction. For the **M**7.1 earthquake, Figure 2a indicates that 73 % and 3 %, respectively, of the areas underlain by artificial fill and Holocene alluvial fan will exhibit surface manifestations of liquefaction. As will be discussed, 38 % of a portion of the area underlain by Merritt Sand is predicted to exhibit liquefaction effects (see the Merritt Sand (subunit) in Figure 2). Surface manifestations of liquefaction are not anticipated for the areas underlain by the Pleistocene alluvial fan and most of the Merritt Sand because LPI < 5. For the **M**6.6 earthquake, Figure 2b indicates that only the artificial fill will exhibit surface manifestations of liquefaction; 56 % of the area underlain by the fill will be affected.

The grouping of LPI by surficial geologic units ignores the contribution to LPI of underlying older geologic units where the surficial unit is less than 20 m thick. Fortunately, within the present study area, liquefaction potential tends to be dominated by the unit exposed at the land surface, at least where the surface unit is saturated.

LIQUEFACTION HAZARD MAPS

Liquefaction hazard maps based on the LPI distributions plotted in Figure 2 are shown in Figures 3 and 4, respectively, for the **M**7.1 and 6.6 earthquakes on the Hayward Fault. The maps show the percentage of area for each geologic unit that will exhibit surface manifestations of liquefaction as predicted by Figure 2. Although the percentage estimated in Figure 2 for each geologic unit implies a high degree of accuracy, the map was subdivided into 10 % categories. For example, the area underlain by the artificial fill was placed in the category where the area expected to exhibit surface effects from liquefaction ranges from 70 to 80 %, rather than assign a

73 % prediction to it. Units without a demonstrable hazard based on the LPI data, but which locally might have some hazard based on geologic considerations were assigned to the 0-1 % category. In addition to using mapped boundaries of geologic units to outline areas with different degrees of hazard, the eastward extent of saturated Holocene alluvial fan sediment was determined and used as an additional boundary. East of this boundary the Holocene alluvial fan is above the water table and does not contribute to the liquefaction hazard. The liquefaction hazard east of the boundary derives from the deeper underlying saturated Pleistocene sediment. To delineate this hydrogeologic boundary, the thickness of Holocene alluvial fan deposits was mapped using thickness values determined from the CPT soundings and subsurface borings collected by the California Geological Survey as part of its preparation of seismic hazard zone maps of the area (see http://www.consrv.ca.gov/CGS/). The depth to ground water was also mapped based on water-level measurements in the holes created by the CPT soundings. The intersection of these mapped surfaces—the zero saturated thickness boundary—was computed by a geographic information system.

The liquefaction hazard of the Merritt Sand is not geographically uniform. Three areas with different degrees of hazard were recognized. Soundings in most of the area underlain by Merritt Sand yield LPI values less than 5, which indicate the hazard is low. However, soundings in the western part of northernmost exposure of Merritt Sand (see area ***A*** in Figure 3), yield many LPI values greater than 5 for the **M**7.1 earthquake. Detailed exploration of this western area that included subsurface sampling revealed that two subsurface conditions contribute to the elevated LPI values. First, the area is underlain by an approximately 1-m-thick laterally contiguous layer of liquefiable soil at a depth of about 5 m. About 38 % of the soundings yield LPI $\geq$ 5 in this area for the **M**7.1 earthquake. Second, the upper part of the Merritt Sand near the northern boundary of the western area is reworked and loose (see area ***B*** in Figure 3). Soundings in this small area yield LPI $\geq$ 10 for the **M**7.1 earthquake. Geologic cross sections indicate this area is south of a buried channel that was incised during the last low stand of sea level. Until the channel filled with Holocene sediment, we speculate that the Merritt Sand on the southern bank of this channel was exposed to surface processes and reworked by surface runoff and landsliding into the channel. The small area was lumped in the hazard map with the area underlain by artificial fill.

A small, but finite, hazard level (<1 %) was assigned to the areas underlain by Pleistocene alluvial fan deposits and most of the Merritt Sand because liquefaction cannot be completely precluded at regional scale hazard mapping. The low LPI values in soundings in Pleistocene alluvial fan deposits and most of the Merritt Sand indicate these units are generally not susceptible to liquefaction.

CONCLUSIONS

Computation of the LPI distributions of geologic units offers a quantitative approach for regionally mapping liquefaction hazard. By calibrating the LPI scale with observations of ground performance in previous earthquakes, LPI distributions of geologic units can be used to estimate how much of the area underlain by each geologic unit can be expected to show surface effects of liquefaction. The methodology was applied to an area along the eastern shore of San Francisco Bay using calibrations of LPI from the 1989 Loma Prieta, California, earthquake. The percentages of areas that are predicted to exhibit surface manifestations are generally consistent

with experience in recent earthquakes where deposits have experienced near-source ground motion. For example, the large percentage of the artificial fill that is predicted by this investigation to liquefy is consistent with the extensive liquefaction of loose fills during the 1995 earthquake in Kobe, Japan [10]. Similarly, the small, but nevertheless significant, area predicted to liquefy in areas underlain by Holocene alluvial fan deposits is consistent with U.S. experience in the 1994 Northridge, California, earthquake, where a small percent of the alluvial fan liquefied [11]. The minor hazard of Pleistocene alluvial fan units is also consistent with historical experience. The prediction that 38 % of part of the area underlain by Merritt Sand will liquefy, however, is high for Pleistocene-age deposits. Reports of modern liquefaction of Pleistocene-age deposits are rare.

ACKNOWLEDGMENTS

We appreciate the assistance of Amy C. Padovani in preparing Figures 1, 3, and 4, and geologic insights from John C. Tinsley, III. Thomas E. Noce conducted the CPT soundings. Coyn Criley preformed the laboratory tests. Manuel G. Bonilla and Raymond C. Wilson reviewed drafts of the manuscript. Portions of the investigation were supported by PG&E through a CRADA with the USGS.

REFERENCES

[1] Power, M.S., and T.L. Holzer. 1996. "Liquefaction Maps," Applied Technology Council, Redwood City, Calif., ATC TechBrief 1, 12 p.

[2] Iwasaki, T., F. Tatsuoka, K. Tokida, and S. Yasuda. 1978. "A practical method for assessing soil liquefaction potential based on case studies at various sites in Japan," 2nd International conference on microzonation, San Francisco, pp. 885-896.

[3] Seed, H. B., and I.M. Idriss. 1971. "Simplified procedure for evaluating soil liquefaction potential," *J. Soil Mechanics and Foundation Engineering*, 97 (9):1249-1273.

[4] Iwasaki, T., K. Tokida, F. Tatsuoka, S. Watanabe, S.Yasuda, and H. Sato. 1982. "Microzonation for soil liquefaction potential using simplified methods," 3rd International Earthquake Microzonation Conference, Seattle, pp. 1319-1330.

[5] Toprak, S., and T. L. Holzer. 2003. "Liquefaction potential index–a field assessment," *J.Geotechnical and Geoenvironmental Engineering*, in press.

[6] Working Group on California Earthquake Probabilities. 1999. Earthquake probabilities in the San Francisco Bay region: 2000-2030–A summary of findings. *U. S. Geological Survey Open-file Report 99-517*, 36 p.

[7] Robertson, P. K., and C.E. Wride. 1997. "Cyclic liquefaction and its evaluation based on the SPT and CPT." in *Evaluation of Liquefaction Resistance of Soils, Technical Report NCEER-97-0022*, National Center for Earthquake Engineering Research, Buffalo, pp. 41-87.

[8] Boore, D.M., W.B. Joyner, and T.E. Fumal. 1994. "Estimation of response spectra and peak accelerations from western North American earthquakes: an interim report, Part 2," *U.S. Geological Survey Open-file Report 94-127*, 40 p.

[9] Helley, E.J., and R.W. Graymer. 1997. "Quaternary geology of Alameda County, and parts of Contra Costa, Santa Clara, San Mateo, San Francisco, Stanislaus, and San Joaquin Counties, California: A digital database," *U.S. Geological Survey Open-file Report* 97-97.

[10] Hamada, M., R. Isoyama, and K. Wakamatsu. 1995. "The 1995 Hyogoken-Nanbu (Kobe) earthquake, liquefaction, ground displacement and soil condition in Hanshin area," Association for Development of Earthquake Prediction, The School of Science and Engineering, Waseda University, Tokyo, Japan, 194 p.

[11] Holzer, T. L., M.J. Bennett, D.J. Ponti, and J. C. Tinsley, III. 1999. "Liquefaction and soil failure during the 1994 Northridge earthquake," *J. Geotechnical and Geoenvironmental Engineering*, 125(6): 438-452.

[12] Lienkaemper, J.J. 1992. "Map of recently active traces of the Hayward Fault, Alameda and Contra Costa Counties, California," *U.S. Geological Survey Miscellaneous Field Studies Map MF-2196.*

[13] Holzer, T.L., M.J. Bennett, T.E. Noce, A.C. Padovani, and J.C. Tinsley, III. 2002. “Liquefaction hazard and shaking amplification maps of Alameda, Berkeley, Emeryville, Oakland, and Piedmont, California: A digital database,” *U.S. Geological Survey Open-file Report. 02-296 (version 1.0)*, 11 p. (http://geopubs.wr.usgs.gov/open-file/of02-296)

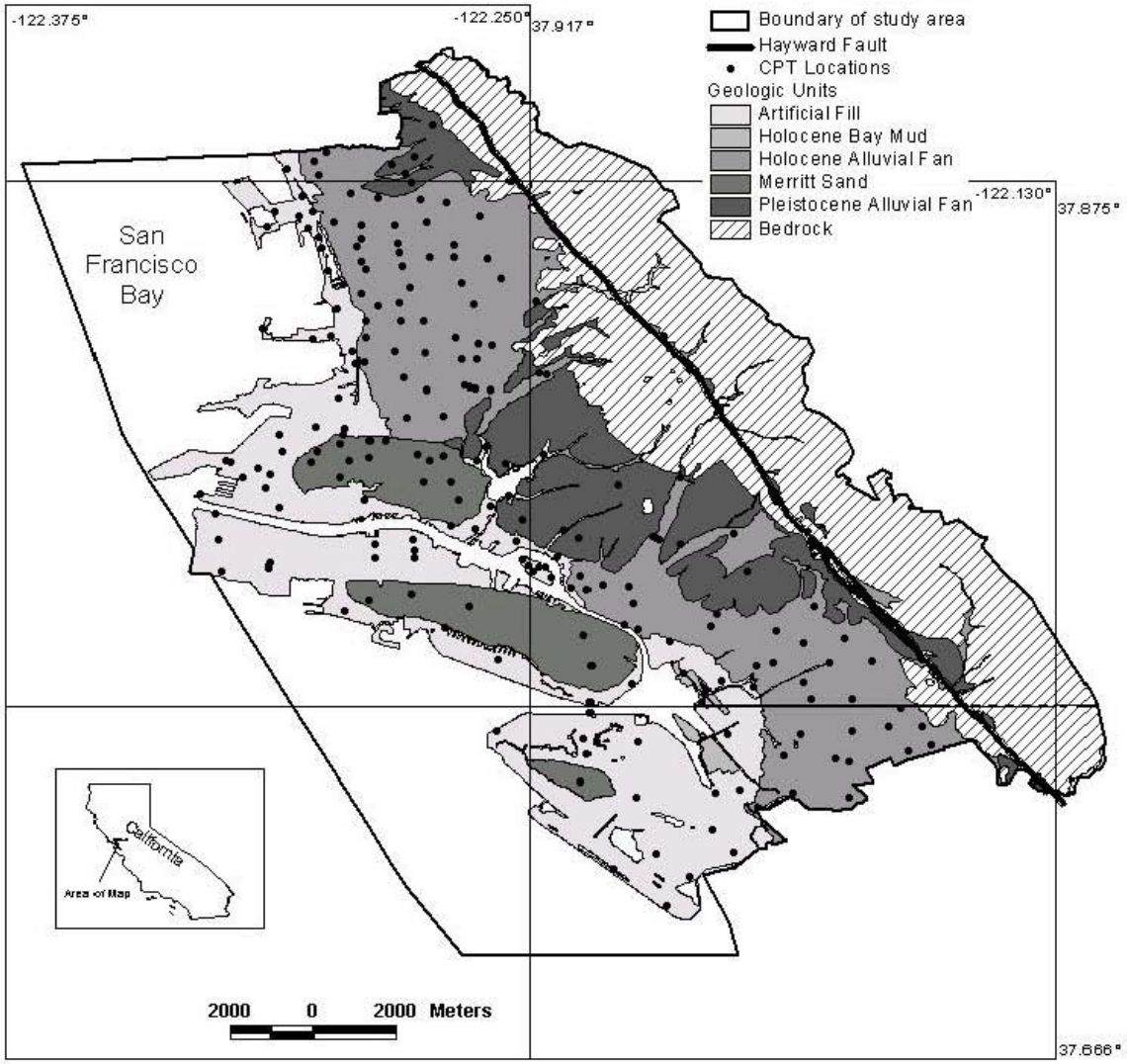

Figure 1. Generalized map of surficial geology of Alameda, Berkeley, Emeryville, Oakland, and Piedmont, California (modified from Helley and Graymer [9]). Trace of Hayward Fault is from Lienkaemper [12]. Original shoreline is the eastern boundary of the artificial fill.

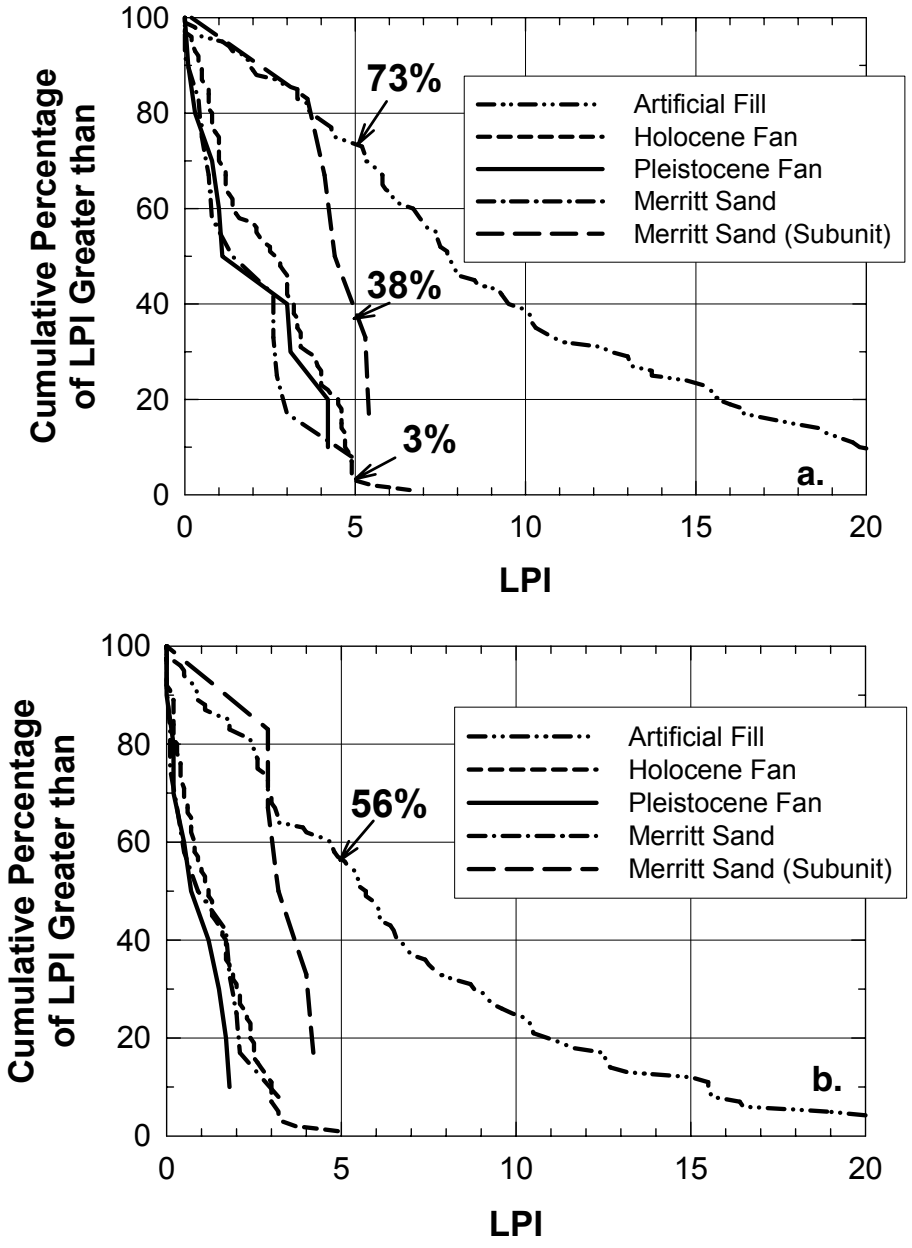

Figure 2. Cumulative percentage distributions of LPI for surficial geologic units in Alameda, Berkeley, Emeryville, Oakland, and Piedmont, California, for (**a**.) **M**7.1 and (**b**.) **M**6.6 earthquakes on the Hayward Fault.

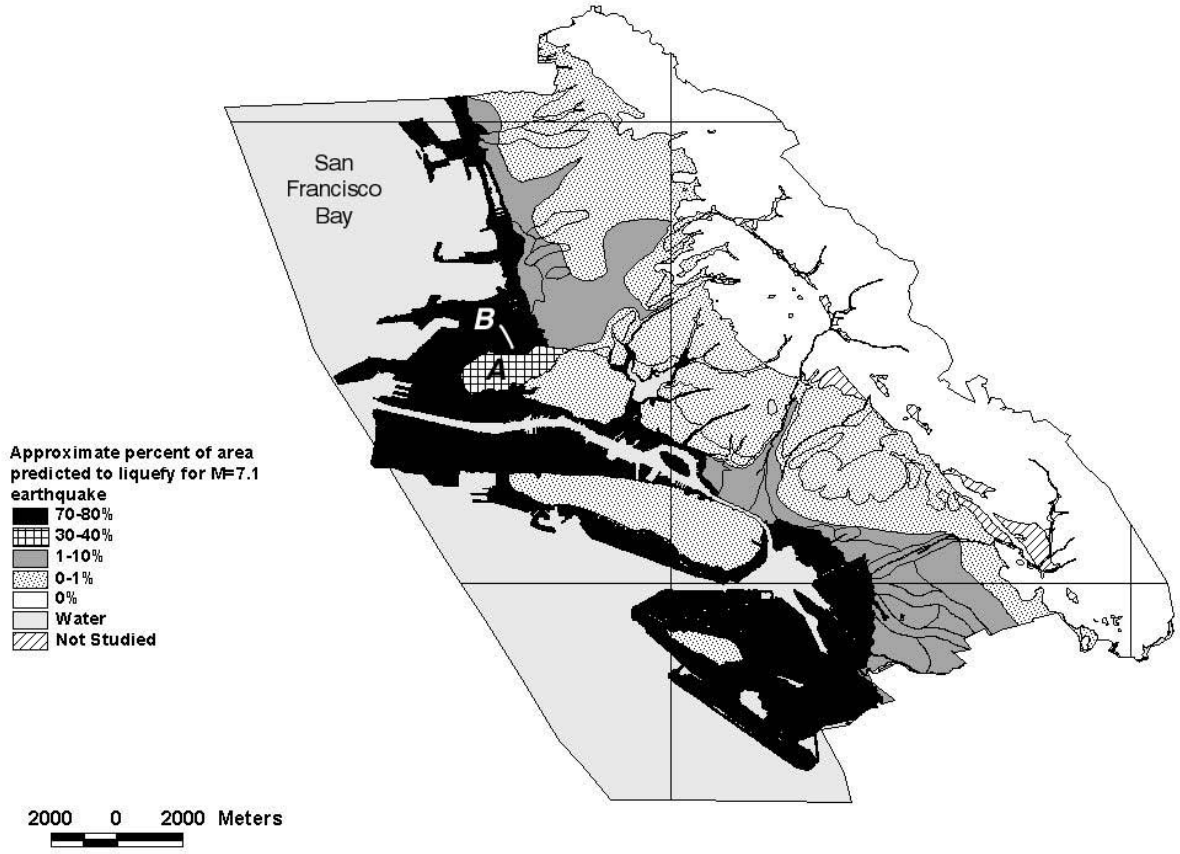

Figure 3. Liquefaction hazard map of Alameda, Berkeley, Emeryville, Oakland, and Piedmont, California, for an **M**7.1 earthquake on the Hayward Fault (Modified from Holzer and others [13]). Map shows areas where different percentages of the land area will exhibit surface manifestations of liquefaction.

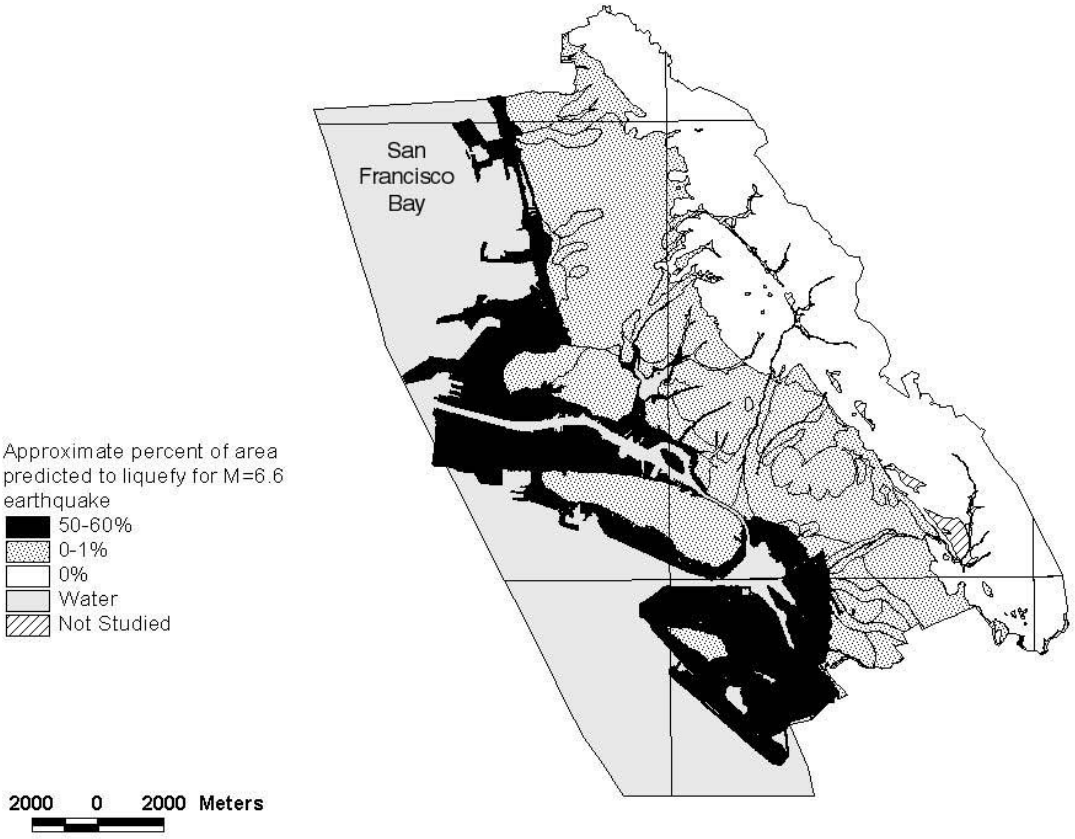

Figure 4. Liquefaction hazard map of Alameda, Berkeley, Emeryville, Oakland, and Piedmont, California, for an **M**.6.6 earthquake on the Hayward Fault. Map shows areas where different percentages of the land area will exhibit surface manifestations of liquefaction.

SPATIAL MODELING OF LIQUEFACTION-INDUCED GROUND DEFORMATION IN KOBE PORT-ISLAND

Jean-Pierre Bardet[1] and Jianping Hu[2]

ABSTRACT

Herein we propose a methodology for mapping the liquefaction-induced ground deformations which earthquakes may generate over large areas. The methodology uses multiple linear regression (MLR), geostatistics and geographic information system (GIS). Geostatistics and GIS are combined to generate and filter over extended areas the parameters of a recently developed ground-deformation MLR model. The proposed methodology, which is intended for the microzonation of liquefaction hazards worldwide, is applied to the case history of ground deformation that took place in Port Island, Kobe, during the 1995 Hyogoken-Nanbu, Japan earthquake. The comparison of predicted and observed results shows that the methodology is capable of predicting the ground deformation observed in 1995, even though the ground deformation model was calibrated from earthquake case histories prior to 1994.

INTRODUCTION

After earthquakes, liquefaction-induced ground deformation was observed to cover areas as large as a few square kilometers, to have amplitude ranging anywhere from a few centimeters to several meters, and to cause substantial damages to lifelines and pile-foundations of buildings and bridge piers (e.g., Hamada et al., 1996; Hamada and O'Rourke, 1992). Liquefaction-induced ground deformation was studied using different approaches, including empirical models, centrifuge models, shake table models, and computational models (e.g., Bardet 2003). Empirical models offer a pragmatic approach for predicting liquefaction-induced ground deformation over large areas due to a limited number of model parameters. Present empirical models include Hamada et al. (1986); Youd and Perkins (1987); Bartlett and Youd (1992, 1995); Rauch and Martin (2000); Bardet et al. (1999 and 2002); and Youd et al. (2002). Empirical models predict liquefaction-induced ground deformation in terms of seismic, topographical and geotechnical parameters. They can be applied for mapping areas prone to deformation due to liquefaction during future earthquakes. Such a liquefaction hazard mapping, which is under evaluation by the California Geological Survey, has far-reaching implications in assessing and mitigating the risks to lifeline networks and civil infrastructures.

The use of empirical models for mapping ground-deformations hazards raises many questions. For instance, what are the limitations and uncertainties of empirical model in predicting liquefaction-induced ground deformation? Can empirical models, although calibrated from case histories prior to

[1] Professor, Civil Engineering Department, University of Southern California, Los Angeles, CA 90089-2531.

[2] Research Assistant, Civil Engineering Department, University of Southern California, Los Angeles, CA 90089-2531.

1990, describe case histories after 1990? Can empirical models, although based on spatially unrelated data, describe the spatial variation of ground deformation? In an attempt to answer some of these questions, the present paper proposes a methodology for predicting liquefaction-induced ground deformation, which is based on geostatistics (e.g., Chiles and Delfiner, 1999; and Wackernagel, 1995) and the ground deformation model of Bardet et al. (2002).

Following the introduction, the first section reviews the model of Bardet et al. (2002), and describes the proposed methodology. The second section illustrates the methodology in a case study in Port Island of Kobe city, Japan, after the 1995 Hyogoken-Nanbu earthquake, and attempts to examine the performance of MLR model for an earthquake from which it was not calibrated. Based on the case history, the last section investigates the uncertainties in predicting ground deformations, and makes some recommendation for improving liquefaction hazard mappings.

METHODOLOGY FOR PREDICTION OF GROUND DEFORMATION

Figure 1 summarizes the proposed methodology for predicting liquefaction-induced ground deformation, which includes the extraction and generation of model parameter values over areas under consideration.

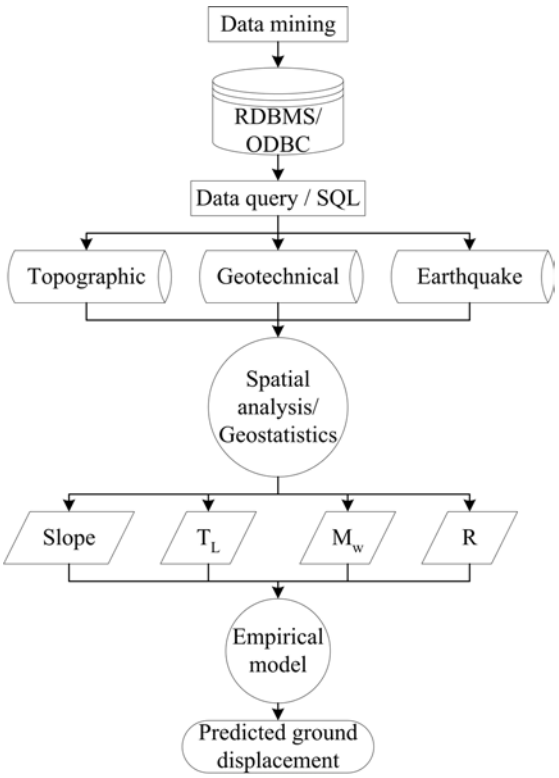

Figure 1. Methodology for extracting/generating model parameters and predicting liquefaction-induced ground deformation.

Ground deformation Model

For predicting liquefaction-induced ground deformation in gently sloping grounds free of topographic irregularities, Bardet et al. (2002) proposed the following four-parameter MLR model:

$$Log_{10}(D+0.01) = -6.815 + 1.017M_w - 0.278Log_{10}R$$

$$-0.026R + 0.454Log_{10}S + 0.558Log_{10}T_L \quad (1)$$

where D is the predicted displacement (m); M_w is the moment magnitude; R is the distance to earthquake source (km); S is the ground slope (%); and T_L is the thickness of liquefiable layer (m). The development of Eq. 1 is detailed in Bardet et al. (2002). The coefficients of Eq. 1 were calibrated from the Bartlett and Youd (1992) database, which contains data from earthquakes that occurred before 1990, and which excludes data from the 1994 Northridge, California, earthquake and 1995 Hyogoken-Nanbu, Japan, earthquake. In theory, other empirical models (e.g., Youd et al, 2002) could also be considered in the present study. Such comparative studies will be the subject of future work.

Generation of model parameters

Equation 1 requires three types of data, i.e., topographic, stratigraphic and seismic data. The data within the areas under study are queried from a recently developed RDBMS database (Bardet et al., 2002), which has ODBC capability (Open DataBase Connectivity) and is usable by a large number of RDBMS platforms. The data on ground deformation, topography, and soil stratigraphy, which are referenced with geographic coordinates, are scattered in space and have different density and location. For instance, boreholes and measured displacements have different locations. Boreholes are not aligned with the grid of digital elevation models (DEM). Geostatistics is useful to generate continuous fields of model parameters (e.g., S and T_L) from scattered data, and is critical for determining model parameters and applying the MLR model for ground deformations. The methodology of Fig. 1 was implemented in a geographic information system (GIS) framework, which provides users with a graphical environment for identifying data in the study area, querying input data, generating continuous fields of model parameters, predicting ground displacements, and comparing predicted and measured ground displacements when those are available. The methodology of Fig.1 can be extended for mapping liquefaction hazards and risks to lifeline networks, provided that fragility curves are available for assessing damage to lifelines components. Using this methodology, engineers and planners can map the hazards of liquefaction induced ground deformation, better understand the amplitude and extent of liquefaction, and perform relevant mitigation to lifelines and civil infrastructures.

Spatial analysis using GeostastisTics

The model parameters S and T_L of Eq. 1 vary depending on the topography and soil stratigraphy. Their values are usually known only at scattered locations. The proposed methodology uses geostatistics (e.g., Chiles and Delfiner, 1999; Wackernagel, 1995) to interpolate fields of model parameters over the study area. It assumes that the expected value $\hat{Z}(X_k)$ of variable Z at location X_k can be interpolated as follows:

$$\hat{Z}(X_k) = \sum_{i=1}^{m} \lambda_i Z(X_i) \quad (2)$$

where $Z(X_i)$ represents the known value of variable Z at point X_i; λ_i is the interpolation weight function, which depends on the interpolation method; and m is the total number of points used in the interpolation. Most GIS software (e.g., ArcGIS, 1999; and GoldenSoftware, 1996) include three types of spatial interpolation, i.e., Inverse Distance Weighting (IDW), Spline, and Kriging (e.g., Chiles and

Delfiner, 1999). The IDW method assumes that λ_i decreases with the distance d_i between points X_k and X_i:

$$\hat{Z}(X_k) = \sum_{i=1}^{m} Z(X_i) / d_i^{\alpha} \tag{3}$$

where α is a positive factor controlling the decrease in λ_i with d_i. IDW works best with evenly distributed points, but generates errors for unevenly distributed data clusters. The Spline method uses polynomial functions to fit a smooth and gradual surface through known points. It may however produce interpolated values outside the range of measured values. Both Spline and IDW methods are vulnerable to outliers, which corresponds to "bull eyes" contours centered about unusually large or small values, and cannot assess the uncertainties of estimated values.

Kriging overcomes the shortcomings of IDW and Spline methods by minimizing the variance of estimation. Kriging uses a semivariogram (also referred to as variogram) for the interpolation between spatial points. In the case of isotropic conditions, the experimental variogram is:

$$\hat{\gamma}(h) = \frac{1}{2n} \sum_{i=1}^{n} \left[Z(X) - Z(X+h) \right]^2 \tag{4}$$

where n is the total number of observations separated by the distance h. In practice, Eq. 4 is evaluated for evenly spaced values of h using a lag tolerance Δh, and n is the number of points falling between h- Δh and h+Δh. As shown in Fig. 2, a typical variogram saturates to a constant value (i.e., sill) for a distance called *range*. The range represents the distance beyond which there is no correlation between spatial points. In theory, $\gamma(h) = 0$ when $h = 0$. However, the variogram often exhibits a nugget effect at very small lag distance, which reflects usually measurement errors (e.g., Bailey and Gatrell, 1996). Experimental variograms can be fitted using spherical, exponential or Gaussian models (e.g., Chiles and Delfiner, 1999). Based on an isotropic variogram, ordinary Kriging determines the coefficients λ_i by solving the following system of $n+1$ equations:

$$\sum_{j=1}^{n} \lambda_i \hat{\gamma}(h_{ij}) + \beta = \hat{\gamma}(h_{ik}) \quad i = 1,2,\cdots,n \quad \text{and} \quad \sum_{i=1}^{n} \lambda_i = 1 \tag{5}$$

where β is a Lagrange multiplier. The isotropic variogram of Eq. 4 can be generalized for anisotropic cases when data depend not only on distance but also on direction:

$$\hat{\gamma}(\mathbf{h}) = \frac{1}{2k(\mathbf{h})} \sum_{i=1}^{k(\mathbf{h})} \left[Z(\mathbf{x}_i + \mathbf{h}) - Z(\mathbf{x}_i) \right]^2 \tag{6}$$

where $\mathbf{h}$ is the vector that separates point $\mathbf{x}_i$ and $\mathbf{x}_k$; $k(\mathbf{h})$ is the number of pairs of variables at distance $\mathbf{h}$ apart. In practice, anisotropic variograms are determined by partitioning data in directional bins. Anisotropy is detected when the range or sill changes significantly with direction. Geostatistics is useful for understanding the distribution of model parameters in the study areas, and to build parameter fields from other parameter fields, e.g., ground slope from elevation data. For instance, the present analysis calculates the ground slope $S_{i,j}$ at grid point i,j from the elevation $z_{i,j}$ at neighboring grid points as follows:

$$S_{i,j} = \sqrt{X_{i,j}^2 + Y_{i,j}^2} \tag{7}$$

where $X_{i,j}$ and $Y_{i,j}$ are the slopes in the EW and NS-direction, respectively, which are calculated using a 3x3 moving average, i.e.:

$$X_{i,j} = \frac{z_{i-1,j-1} + 2z_{i-1,j} + z_{i-1,j+1} - z_{i+1,j-1} - 2z_{i+1,j} - z_{i+1,j+1}}{8\Delta x}$$
$$Y_{i,j} = \frac{z_{i-1,j-1} + 2z_{i,j-1} + z_{i+1,j-1} - z_{i-1,j+1} - 2z_{i,j+1} - z_{i+1,j+1}}{8\Delta y} \quad (8)$$

In Eq. 8, Δx and Δy are the grid spacing in the EW and NS directions, respectively.

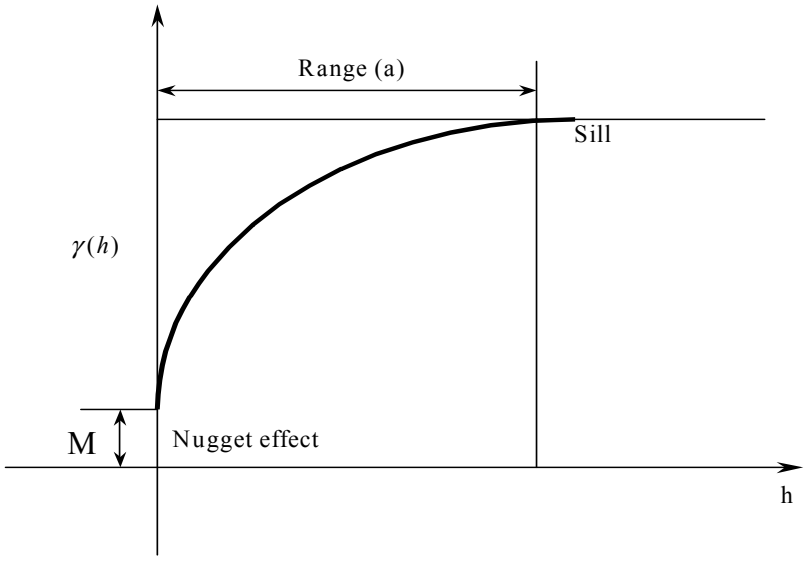

Figure 2. Example of variogram with a nugget effect (e.g., Chiles and Delfiner, 1999).

Errors in prediction

The uncertainties in predicting ground deformations with Eq. 1 originate mainly from two types of error, i.e., (1) inaccurate determination of model variables, and (2) limitations inherent to the ground deformation model.

As any data sets, the data sets required to predict liquefaction-induced ground deformation contain systematic and nonsystematic (random) errors on topographic information and underground soil conditions. Systematic errors originate from the operations, equipment and recording procedures in field measurements; they can be reduced with accurate calibration of equipment, adequate training of operators and careful documentation. In some cases, systematic errors can even be corrected if data acquisition and processing are properly documented. In contrast to systematic errors, random errors are largely unpredictable and unavoidable. The present methodology is mainly concerned with random errors. Using statistical methods, it examines the random errors attached to two model parameters, i.e., S and T_L, which are likely to generate the largest modeling errors. Other sources of errors are not included hereafter. The present analysis assesses the combined errors of spatial interpolation and model parameters using the minimum error variance (e.g., Chiles and Delfiner, 1999). In the case of ordinary Kriging, the estimated interpolation error at location x_0 is the standard deviation of the error estimate:

$$\sigma_{OK}^2(x_0) = \sum_{i=1}^{n} \lambda_i \gamma(x_0 - x_i) - \beta \tag{9}$$

where n, x_i, λ_i and β are defined as in Eqs. 2 and 5.

After the introduction of variable $D' = \log_{10}(D + 0.01)$, Eq. 1 predicts the mean value of ground deformation as follows:

$$\hat{D}' = b_0 + b_1 X_1 + \ldots + b_p X_p \tag{10}$$

where b_0, …, b_p are constant coefficients, X_1 ,…, X_p are the model variables and p the total number of model variables. In the particular case of Eq. 1, $p = 5$ and the coefficients b_i and variables X_i are:

$$\begin{aligned} &b_0 = -6.815, \quad b_1 = 1.017, \quad b_2 = -0.278, \quad b_3 = -0.026, \quad b_4 = 0.454, \quad b_5 = 0.558 \\ &X_1 = M_w, \quad X_2 = Log_{10}R, \quad X_3 = R, \quad X_4 = Log_{10}S, \quad X_5 = Log_{10}T_L \end{aligned} \tag{11}$$

The variance of $\hat{D}'$ can be written as follows:

$$Var(D') = s^2 \mathbf{X}_0^T \mathbf{C} \mathbf{X}_0 + b_1^2 Var(X_1) + \ldots + b_p^2 Var(X_p) \tag{12}$$

where $\mathbf{X}_0^T = (1 \quad X_1 \quad X_2 \quad \ldots \quad X_p)$ is the components vector of model variables, and s^2 is the residual mean square:

$$s^2 = \frac{1}{n - p - 1} \sum_{i=1}^{n} \left(\hat{D}_i' - D_i' \right)^2 \tag{13}$$

In Eq. 13, D_i' is the i[th] observed value of D', and $\hat{D}_i'$ is i[th] predicted value corresponding to D_i' (i = 1,…,n). The value of s^2 is 0.084 and that of the covariance matrix **C** is (Bardet et al., 2002):

$$\mathbf{C} = 10^{-3} \times \begin{pmatrix} 0.46 & 0.14 & 0.00 & 0.08 & -0.03 & -0.40 & 0.02 & 0.01 \\ & 46.52 & -0.77 & -0.25 & 0.13 & -39.92 & -11.30 & -5.13 \\ & & 0.60 & -2.25 & 0.00 & -0.39 & 0.63 & -1.19 \\ & & & 24.74 & -0.53 & 6.07 & -2.71 & -5.63 \\ & & & & 0.03 & -0.18 & 0.06 & 0.11 \\ & \textit{Symmetric} & & & & 46.84 & 0.04 & -0.16 \\ & & & & & & 44.29 & 10.62 \\ & & & & & & & 22.33 \end{pmatrix} \tag{14}$$

The variance and standard deviation of variables D and D' can be approximately related through:

$$\sigma^2(D) = Var(D) \approx \left(\frac{\partial \hat{D}}{\partial D'} \right)^2 Var(D') = 10^{2D'} Var(\hat{D}') \text{ and } \sigma(D) \approx D\sigma(D') \tag{15}$$

CASE STUDY IN PORT ISLAND, KOBE

Study Area

In theory, the proposed methodology applies to all seismic regions within the world. Hereafter, it is illustrated in a particular case history in Port Island, Kobe, which took place during the 1995 Hyogoken-Nanbu, Japan earthquake. Port Island is a manmade island, the construction of which started in 1967 (Hamada and Wakamatsu, 1996). The island is about 17 km far from the epicenter of the Hyogoken-Nanbu earthquake, and about 7 km from the surface fault rupture (e.g., Wald, 1996; and Yoshida et al., 1996). As shown in Fig. 3, the central part of the island contains schools, hospitals, high-rise residential buildings and hotels, and the ground surface in this area is elevated about 3-4 m higher than the surrounding area. As shown in Fig. 3, the 1400m x 800m study area is delineated with a dashed line. The area is made of improved and unimproved ground. It was selected about 200m far away from the waterfront to avoid interactions with the displacements of quaywalls (e.g., Hamada et al. 1996).

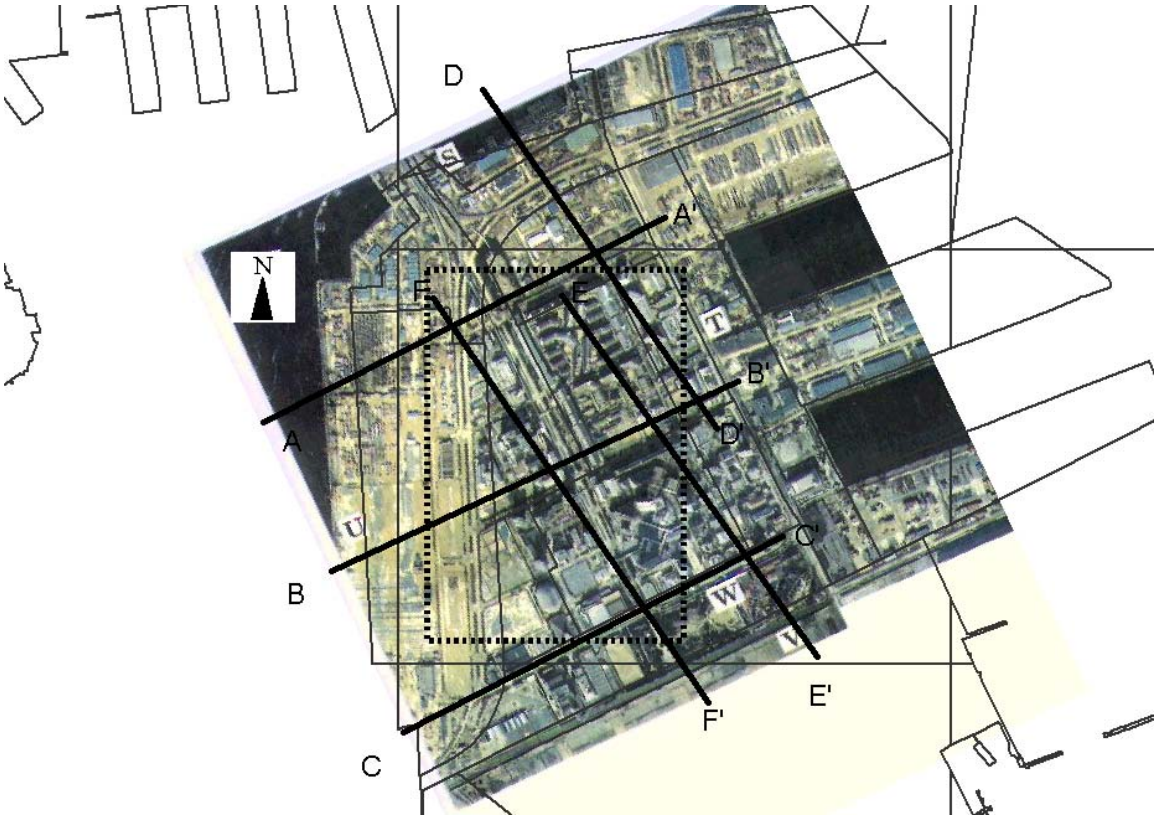

Figure 3. Aerial photo of Port Island after 1995 Kobe earthquake showing study area (dotted line) and location of two-dimensional soil profiles across the study area.

Available data set

The information required for predicting earthquake-induced ground deformation (i.e., ground water table, topography, and soil conditions) is available from Jibankun, a geotechnical database which was created after the 1995 Kobe earthquake and includes about 5000 boreholes (Tanaka and

Okimura, 2001). During a collaborative research program between the University of Southern California and Kobe University, the geotechnical, topographic and displacement data were converted into a RDBMS-GIS platform (Bardet et al., 2002). This database include compiled raw data, e.g., borehole logs, soil tests, SPT-N values, water table, ground elevations, ground displacements from the 1995 Kobe earthquake.

Figure 4 shows the location of borehole data in Port Island and the ground displacement vectors obtained using aerial photographs (Hamada et al., 1996). As shown in Fig. 4, the quaywalls in Port Island typically displaced 1-3 m toward the sea due to liquefaction. Near the center of the island, the ground displacements are not oriented toward the sea, which implies that the ground deformation relates not to the movement of quaywalls, but to sloping ground. This remark justifies the selection of the study area and the modeling of ground deformation using Eq. 1.

Figure 4. Displacement vector and borehole location in Port Island (data after Tanaka and Okimura, 2001)

Table 1 summarizes the available data in the study area. There are 330 displacement vectors, including 221 vectors on free ground; the other vectors are on non-ground locations, e.g., buildings and trees. SPT borehole data were obtained between 1970 and 1995. There are 69 boring tests available in the study area, 19 of which include information on the ground water elevation at the time of the field tests.

Table 1. Available information in study area in Port Island, Kobe.

Type	Amount
Measured displacements (total)	330
Measured displacements (ground)	221
Elevation	221
SPT	69
Ground water table	19

Figure 5 shows six two-dimensional soil profiles, which were constructed using SPT boreholes. These profiles are located in Fig. 3. Port Island is a reclaimed man-made island which has soil deposits made of three uniform layers. The upper 10 ~ 15 m thick layer is mostly made of artificial fill, and is underlain by a layer of clayey soil up to a depth of 30 m. The bottom layer is made of alternating sandy and clayey soils. The soil profiles of Fig. 5 are in good agreement with those independently obtained by Hamada et al. (1996).

Regional parameter estimation

The study area was divided into a 20m x 20m grid. The parameters M_w, R, S and T_L were determined at grid points. The earthquake magnitude M_w was set to 6.9 at all grid points. The distance R between grid points and earthquake source was calculated using the spatial positions of grid points and distance to fault rupture. The values of R vary between 6.4 and 7.4 km in the study area. The mean values of the model parameters S and T_L were determined using ordinary Kriging.

The ground elevation model in the study area is based on 221 elevation points. Figure 7 shows the directional variograms, which characterize the spatial variation of elevation data along six different directions. The zero direction corresponds to East-West in Fig. 7. The directional variograms are obtained for a lag interval of 30 m and a lag tolerance of 6 m. As shown in Fig. 7, the ground elevation is slightly anisotropic. The variograms of Fig. 7 were fitted using an exponential function with a nugget close to 0.6. This fitted variogram filters the high-frequency noise on measured elevations, which result from a 53-cm measurement error on elevation (Hamada et al., 1996).

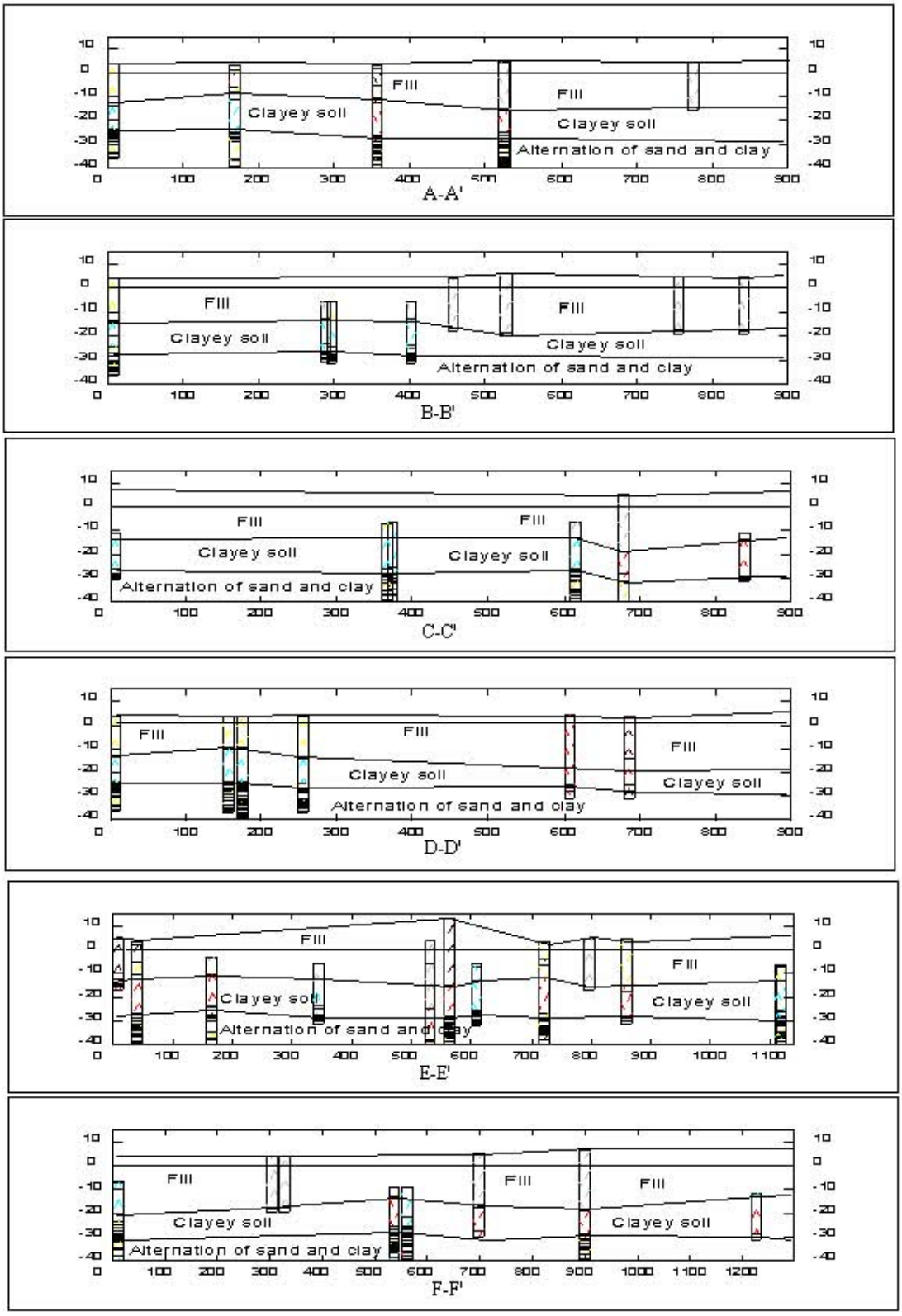

Figure 6. Two-dimensional soil profiles in Port Island along lines AA', BB', CC', DD' EE', and FF' of Fig. 3.

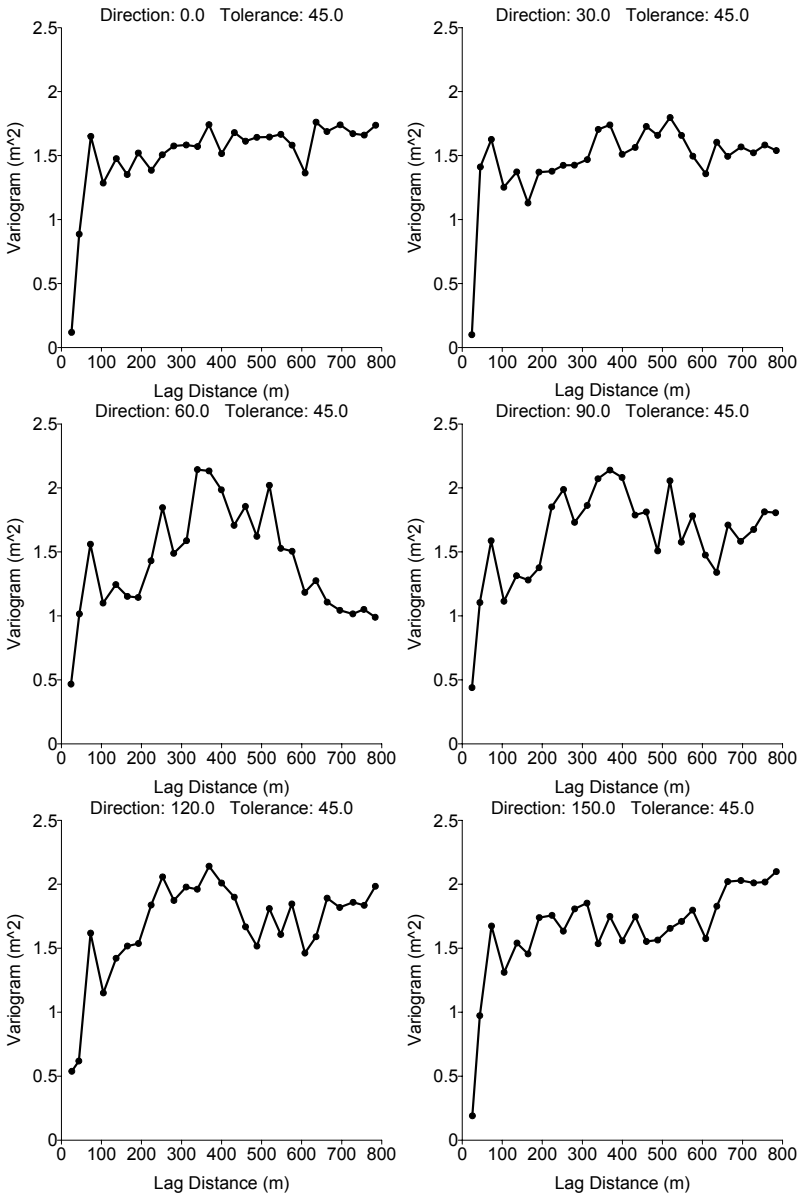

Figure 7. Directional variograms showing spatial continuity and anisotropy of elevation data.

Figure 8 shows the ground elevation generated using ordinary Kriging with and without filtering. Both IDW and Kriging without filtering produce typical "bulleyes," which are detectable in the concentration of contour lines around extreme values. As shown in Fig. 8c, the maps of filtered elevation are physically more meaningful. Figure 8d shows the standard deviation (Eq. 9) on elevation corresponding to Fig. 8c. Figure 9 displays the ground surface elevation using TIN (Triangulated Irregular Network). The eastern part of the study area has higher elevation than the western part. Covered with residential facilities, it has been elevated for various reasons including landscaping and drainage. The ground slope S in the study area was calculated from the elevation model of Fig. 8c using Eqs. 7 and 8. Figure 10a shows the map of ground slope, which ranges from 0.01% to 5%. The steeper slope values are observed in the eastern part of the study area.

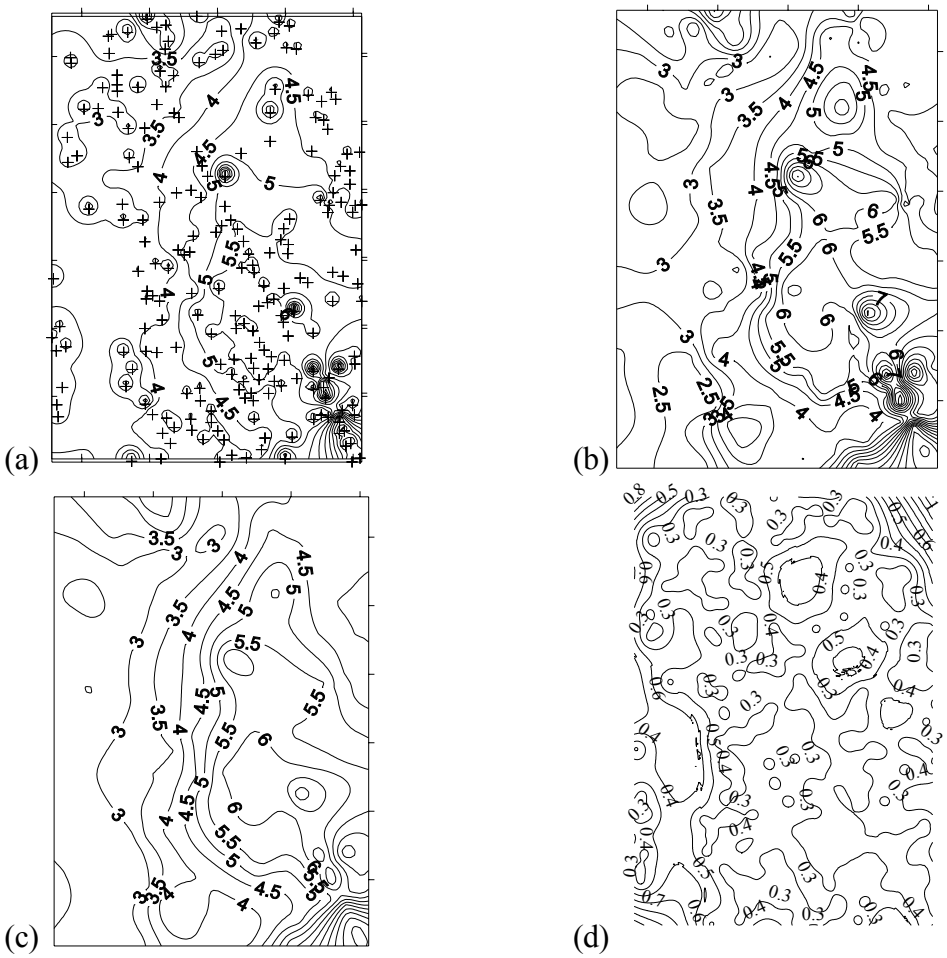

Figure 8. Elevation models in study area (elevation in meter) using three spatial interpolation techniques: (a) IDW ($\alpha = 2$); (b) Kriging without filtering; (c) Kriging with filtering; and (d) Standard deviation of elevation.

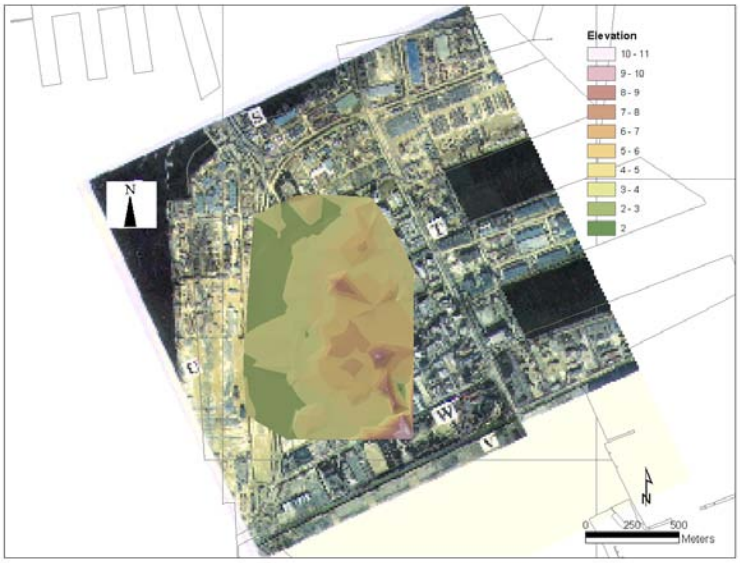

Figure 9. Elevation model in study area corresponding to Fig. 8c.

The value of T_L is determined from the cumulative thickness of layers, which satisfy three conditions: (1) below the ground water table, (2) $(N1)_{60}$ less than 15, and (3) clay content less than 15%. T_L depends on the elevation of the ground water table, which was assumed to be constant at the sea level at the time of the 1995 Hyogoken-Nanbu earthquake. The elevation of ground water table could not be assessed from the 19 boreholes including information on the water table. The ground water table in Port Island varies with time and changes with the sea tide and rainfalls. Its elevation could not be inferred from the information on water table from boreholes because these field tests were performed at various times between 1970 and 1995. The SPT blow counts were corrected following the procedure of Seed et al. (1986), which accounts for different rod energy ratio, hammer frequency and borehole diameter. In the case of sands having $(N_1)_{60} < 20$, N_{60} in the U.S. and Japan are related through:

$$(N_{60})_{US} \approx 0.9(N_{60})_{Japan} \tag{16}$$

The T_L values were interpolated using ordinary Kriging with filtering. As shown in Fig. 10b, the values of T_L in the study area range from 2 m to 14 m. The eastern part of the study area shows smaller liquefied thickness than the northwest part, which results from the ground improvement performed in this area before the 1995 Hyogoken-Nanbu earthquake (Hamada et al., 1996).

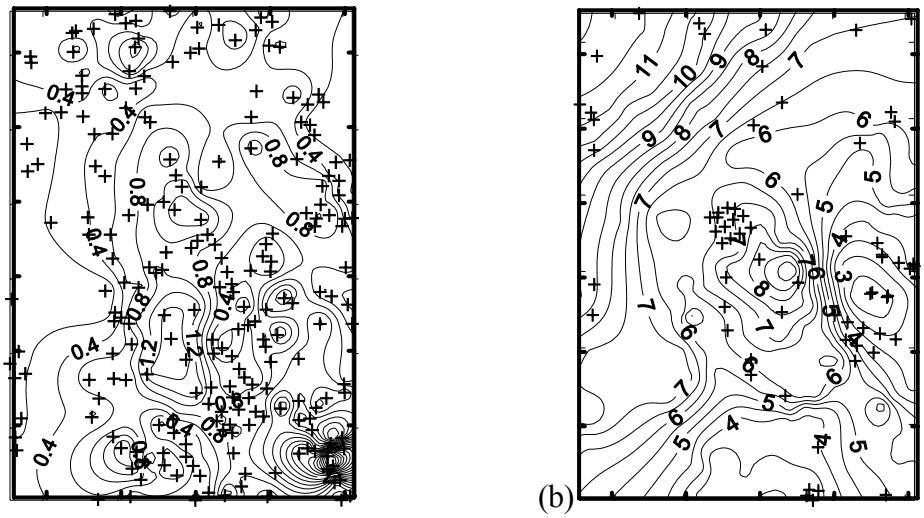

Figure 10. Values of model parameters interpolated using ordinary Kriging in study area: (a) slope S and (b) thickness T_L.

Predicted displacement

As shown in Figs. 11a and b, measured displacements vary rapidly over short distance, which results from the 33-cm errors in processing aerial photographs in the horizontal direction (Hamada et al., 1996). The measurement errors were filtered out using the same Kriging technique as for elevation. The nugget was found to be about 276 cm^2, which corresponds to the errors in processing aerial photographs. As shown in Fig 11c, the filtered displacements are smoother than those obtained using IDW and Kriging without filtering. As indicated in Table 2, the values of T_L and S in Figs. 10 fall within the ranges that are acceptable for the MLR model (i.e., Eq. 1). Figure 12 show the maps of measured displacement, predicted displacement and corresponding residual. As shown in Figs. 12a and 12b, predicted and measured displacements are in good agreement, provided that high-frequency

noises are filtered out. Most residuals fall between –20 cm and 20 cm. As shown in Fig. 13, the predicted and measured displacements are also in good agreement after filtering.

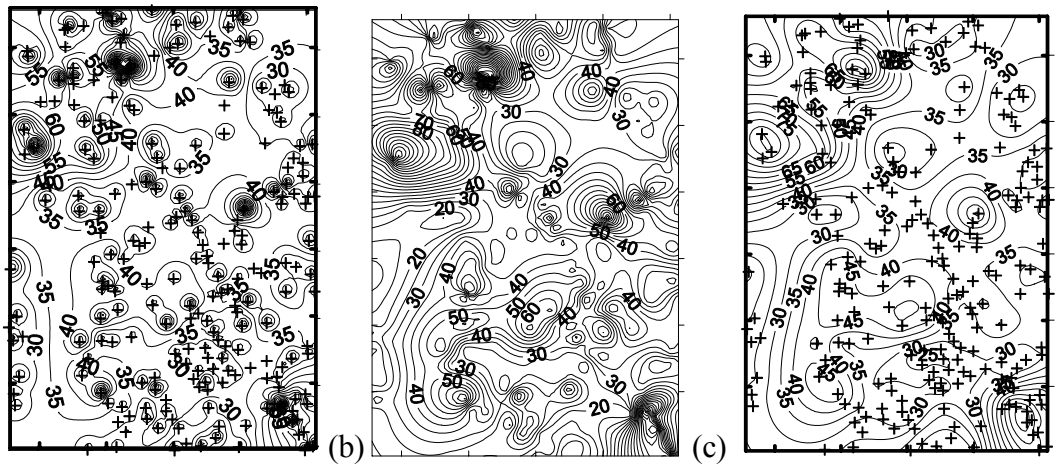

Figure 11. Maps of displacement amplitudes measured in study area (after Hamada et al., 1996) and interpolated using different techniques: (a) IDW (α=2); (b) Kriging without filtering; and (c) Kriging with filtering.

Table 2. Value range of MLR model parameters in study area.

Notation	Parameter	Range
M_w	Earthquake Magnitude	6.9
R	Source distance (km)	6.4 ~ 7.4
T_L	Liquefied layer thickness (m)	2 ~ 14
S	Slope (%)	0.01 ~ 5

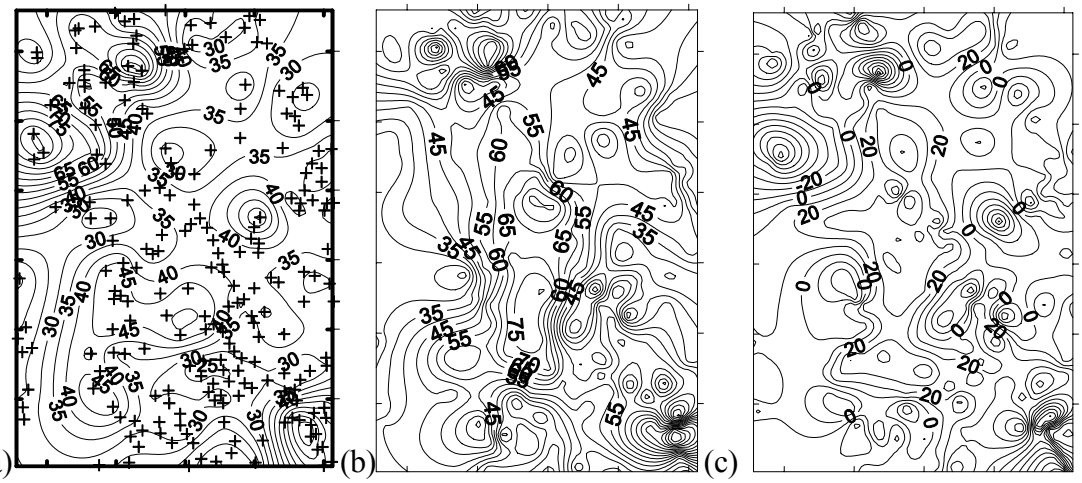

Figure 12. Maps of measured and predicted displacements: (a) Measured and filtered (10- 100 cm); (b) Predicted (15- 110 cm); and (c) Residual (-60 – 40 cm).

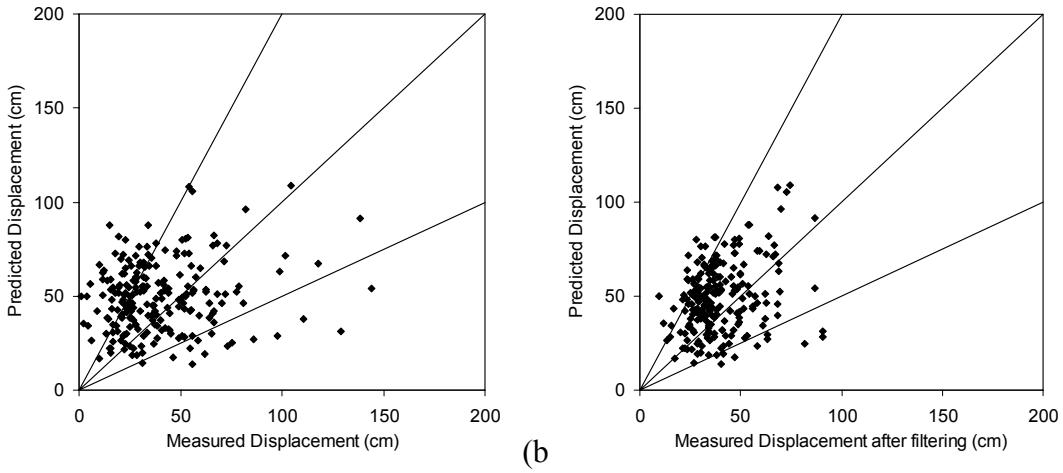

Figure 13. Comparison of predicted displacement and measured displacement: (a) without filtering and (b) with filtering.

Uncertainties on model parameters and predicted displacements

The proposed methodology, which was so far applied to predict mean values of liquefaction-induced ground deformation, can be used to examine model uncertainties and to assess possible deviations from predicted mean values. The present analysis assumes that the parameters S and T_L cause the largest uncertainties, and that M_w and R produce smaller uncertainties.

Figure 14a shows the spatial distribution of the standard deviation of ground slope S, which is generated by ordinary Kriging, i.e., Eq. 9. The standard deviation of S is about 0.01 – 0.5%. The values of T_L depend on the ground water elevation and $N1_{60}$ profiles. The errors on $N1_{60}$, which are complicated to evaluate in the present study, are neglected hereafter. The errors on the ground water elevation are also neglected; the water table is assumed to be flat at mean sea level at the time the Hyogoken-Nanbu earthquake. Figure 14b shows the spatial distribution of the standard deviation of T_L, which is generated using ordinary Kriging. The maximum standard deviation of T_L is about 1 m.

Assuming that the modeling errors can only originate from the MLR model calibration and from the model parameters S and T_L, the variance of $\hat{D}'$ (i.e., decimal logarithm of D) is approximated as follows:

$$Var(D') = s^2 \mathbf{X}_0^T \mathbf{C} \mathbf{X}_0 + b_4^2 Var(Log_{10} S) + b_5^2 Var(Log_{10} T_L) \tag{17}$$

The first item in the right hand side of Eq. 17 indicates the variance of MLR model, and the other two terms represent the variance originating from parameters S and T_L, respectively. The standard deviation of D can be approximated from Eq. 17 using Eq. 15. Figure 14c shows the standard deviation of D which results solely from the errors on model parameters S and T_L as depicted in Figs. 14a and b. Figure 14d displays the standard deviation of D which include both the errors on S and T_L and the MLR modeling errors. As shown in Figs. 14, the model itself and the model parameters generate comparable errors for the predicted displacement. In view of the similarity of Figs. 14b and d, the slope errors appear to be control the predicted displacement errors.

Table 3 summarizes the maximum standard deviations on the values of T_L, S and predicted displacements. The predicted displacement error is about 45 cm because of uncertainty in T_L and S, and about 30 cm from the MLR model error. Overall the maximum predicted displacement error exceeds 75cm.

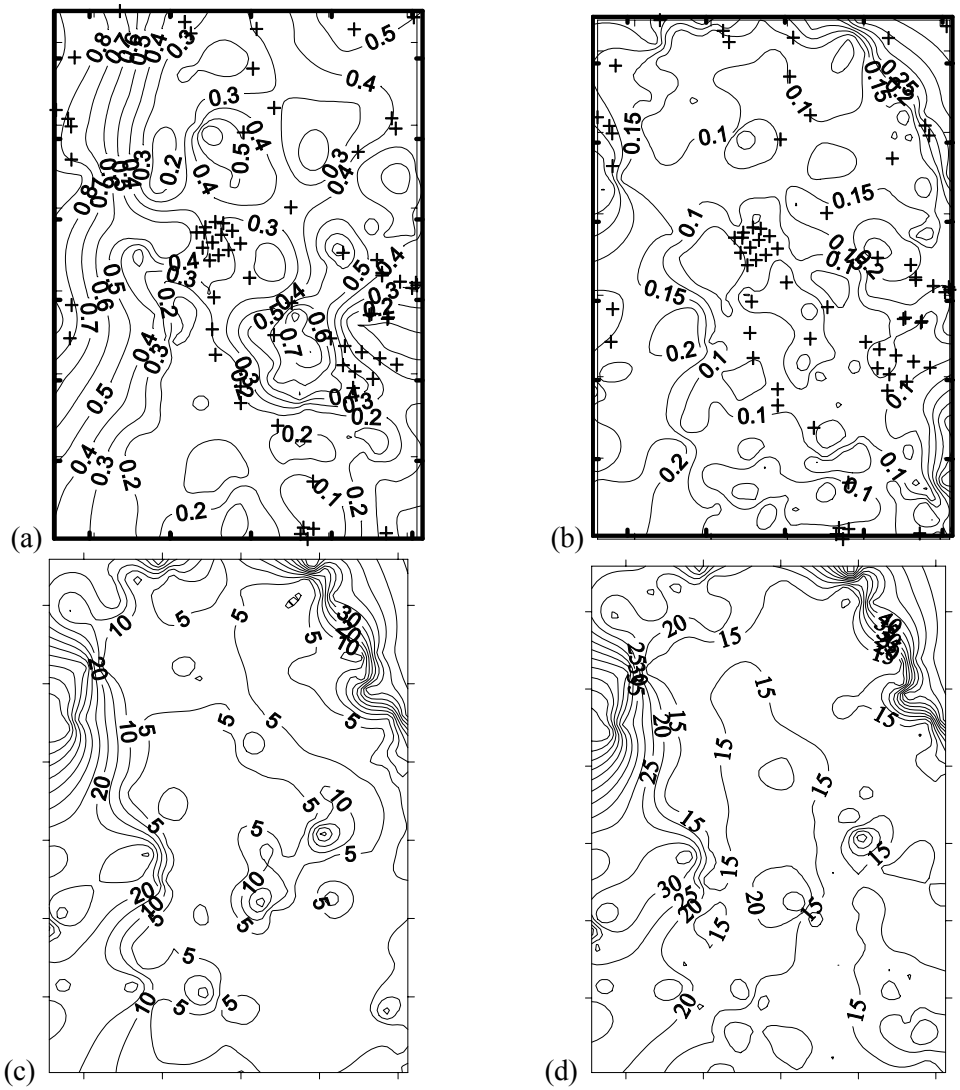

Figure 14. Standard deviations for model parameters and predicted displacements: (a) T_L (m) (b) S (%); (c) predicted displacement (cm) including only model parameters standard deviation; and (d) predicted displacement (cm) including all standard deviations.

DISCUSSION

The model uncertainties were attributed to soil parameters and topography in a particular case study in Japan. More research is needed to examine the effects of other parameters, e.g., depth of water table, SPT blow counts, distance to earthquake source, moment magnitude, and heterogeneity of soil deposits. The present case study in Port Island only requires the use of ordinary Kriging with a slight directional anisotropy. The soil deposits in Port Island are rather uniform, which simplifies the generation of model parameters in the study area. The analysis of more heterogeneous soil deposits

and complicated topography may required advanced Kriging techniques, e.g., drift filtering, universal Krigging, cluster Kriging across discontinuities (e.g., Chiles and Delfiner, 1999). The proposed methodology is based on an empirical MLR model. Modeling advances are likely to originate from models which are rooted in mechanics and physics.

Table 3. Maximum standard deviations of model parameters and predicted displacements.

Type of uncertainty	Standard deviation
Liquefied layer thickness (T_L) (m)	1
Slope S (%)	0.5
Displacement resulting from S and T_L (cm)	45
Displacement resulting from MLR model (cm)	30
Displacement (cm)	75

CONCLUSION

A methodology for predicting liquefaction-induced ground deformation over large areas has been presented and illustrated using a case study in Port Island after the 1995 Hyogoken-Nanbu earthquake. The methodology relies upon the ground-deformation model of Bardet et al. (2002), geostatistics and geographic information system (GIS). The prediction of liquefaction-induced ground deformation over large regions requires data on soil boreholes, topography and ground water surface elevation. Geostatistics and GIS are combined to generate the model parameters over extended areas, and to examine the standard deviations of model parameters and results. The comparison of predicted and observed results shows that the methodology is capable of predicting the ground deformation observed in 1995, even though the ground deformation model was calibrated from earthquakes prior to 1990. The proposed methodology is intended for the microzonation of liquefaction hazards worldwide.

ACKNOWLEDGEMENTS

The authors thank Profs. Y. Tanaka and T. Okimura of Kobe University and Prof. M. Hamada for their contribution to this collaborative research. The financial support of the National Science Foundation is acknowledged.

REFERENCES

1. ArcGIS, 2001, "ArcGIS™ Geostatistical analyst: Statistical Tools for data exploration, modeling, and advanced surface generation", *ESRI White Paper*, ESRI, Redlands, CA.
2. Bailey, T. and A. Gatrell, 1995, "*Interactive spatial data analysis*," Longman Scientific & Technical, England.
3. Bardet, J. P., 2003, "Advances in Analysis of Soil Liquefaction during Earthquakes," in International Handbook of Earthquake and Engineering Seismology (Edited by W. H. K. Lee, H. Kanamori, P. C. Jennings, and C. Kisslinger), Chapter 77, in press.
4. Bardet, J. P., J. Hu, T. Tobita and J. Swift, 2002, "Liquefaction Ground Deformation Database," A report to PG&E-Caltrans-PEER Program of Applied Earthquake Engineering Research on Life-lines, Task 3A04, Civil Engineering Department, University of Southern California.

5. Bardet, J. P., N. Mace, T. Tobita, and J. Hu, 2002, "Regional modeling of Liquefaction-induced ground deformation," *Earthquake Spectra*, Earthquake Engineering Research Institute, Vol. 18, No. 1, pp. 19-46.
6. Bardet, J. P., N. Mace, and T. Tobita, 1999, Liquefaction-induced ground deformation and failure, *A report to PEER/PG&E,* Task 4 – Phase 1, Civil Engineering Department, University of Southern California.
7. Bartlett, S. F. and T. L. Youd, 1992, Empirical analysis of horizontal ground displacement generated by liquefaction-induced lateral spreads, *Technical report NCEER-92-0021.*
8. Bartlett, S. F. and T. L. Youd, 1995, "Empirical Prediction of Liquefaction-Induced Lateral Spread," *Journal of Geotechnical Engineering, ASCE,* Vol. 121, No. 4, pp. 316-329.
9. Chiles, J. P. and P. Delfiner, 1999, *"Geostatistics – Modeling Spatial Uncertainty,"* John Wiley & Sons, New York.
10. GoldenSoftware, 1999, "Surfer 7.0", GoldenSoftware Inc., Golden, Colorado.
11. Hamada, M. and K. Wakamatsu, 1996, "Liquefaction, Ground Deformation and their Caused Damage to Structures," *The 1995 Hyogoken-Nanbu Earthquake-Investigation into damage to Civil Engineering Structures, Committee of Earthquake Engineering, Japan society of Civil Engineers*, pp45-92.
12. Hamada, M., R. Isoyama, and K. Wakamatsu, 1995, "The Hyogoken-Nanbu (Kobe) Earthquake, Liquefaction, Ground Displacement and Soil Condition in Hanshin Area," *Association for Development of Earthquake Prediction, The school of Science and Engineering, Waseda University, Japan Engineering Consultants*.
13. Hamada, M., and T. D. O'Rourke, 1992, "Case histories of liquefaction and lifeline performance during past earthquakes," *Technical report NCEER-92-0001,* National Center for Earthquake Engineering Research, State University of New York, Buffalo, 2 Vols.
14. Rauch, A. F., and J. R. Martin II, 2000, "EPOLLS model for predicting average displacements on lateral spreads," *J. Geotechnical and Geoenvironmental Engineering, ASCE*, Vol. 126, No. 4, pp. 360-371.
15. Seed, H. B., K. Tokimatsu, and L. F. Harder, 1985, "Influence of SPT Procedure in Soil Liquefaction Resistance Evaluation," *Journal of Geotechnical Engineering,* ASCE, Vol. 111, No. 12, pp. 1425-1445
16. Tanaka, Y. and T. Okimura, T., 2001, "In-depth Geotechnical Database, Kobe Jibankun, for Seimic Hazard Study", COSMOS Workshop on Archiving and Web Dissemination of Geotechnical Data, Richmond, CA
17. Wackernagel, H., 1995, "*Multivariate Geostatistics*," Springer-Verlag, Berlin Heidelberg, Germany.
18. Wald, D. J., 1996, "Slip history of the 1995 Kobe, Japan, earthquake determined from strong motion, teleseismic and geodetic data," *J. Phys. Earth*, 44, pp. 489–503.
19. Yoshida, S., K. Koketsu, B. Shibazaki, T. Sagiya, T. Kato, and Y. Yoshida, 1996, "Joint inversion of the near- and far-field waveforms and geodetic data for the rupture process of the 1995 Kobe earthquake," *J. Phys. Earth*, 44, pp. 437–454.
20. Youd, T. L. and D. M. Perkins, 1987, "Mapping of Liquefaction Severity Index," *Journal of Geotechnical Engineering Division*, ASCE, No. 11, pp. 1374-1392.
21. Youd, T.L., C. M. Hansen, and S. F. Bartlett, 2002, "Revised MLR Equations for Prediction of Lateral Spread Displacement," *Journal of Geotechnical and Geoenvironmental Engineering*, ASCE, Vol. 128, No. 12, pp. 1007-1017.

Ground Deformation and Questionnaire Survey for Witnesses of Liquefaction During the 2000 Tottori-ken Seibu Earthquake

Masakatsu Miyajima, Masaho Yoshida and Masaru Kitaura

ABSTRACT

The 2000 Tottori-ken Seibu Earthquake occurred at 1:30 p.m. (local time) on October 6, 2000 in a western part of Tottori Prefecture in Japan. Liquefaction occurred extensively, especially at the reclaimed land such as Takenouchi industrial estate in Sakaiminato City. First, ground deformation induced by liquefaction was studied in relation to the soil conditions. Next, a questionnaire survey was conducted for the witnesses of liquefaction in Takenouchi industrial estate. It was supposed that many people saw the liquefaction phenomenon during and after the earthquake because the earthquake occurred in the daytime on a weekday. The conditions of sand boil, time history of ground deformation, and ground motion during liquefaction were discussed on the results of the survey.

INTRODUCTION

The photographs and video movies of liquefaction during the 1964 Niigata earthquake were well known. Although liquefaction occurred repeatedly during past earthquakes, there were few visual records and witnesses. During the 1995 Kobe earthquake, extensive liquefaction occurred at coastal reclaimed land and liquefaction-induced large ground displacements were caused. However, there were few people who saw the liquefaction phenomenon directly because it occurred in an early morning at no residential area.

At 13:30 on October 6, 2000, an earthquake of magnitude 7.3 in the scale of Japan Meteorological Agency hit a western part of Tottori Prefecture in Japan. A serious damage was caused by liquefaction in Takenouchi industrial estate that located in east of Sakaiminato City in Tottori Prefecture. The Takenouchi industrial estate was reclaimed land that was constructed from 1978 to 1985 and its gross area was 128 hectares [1]. As this earthquake occurred in the daytime on a weekday, it was supposed that many people saw the liquefaction.

A questionnaire survey was conducted to collect information about witnesses of liquefaction, such as occurrence of sand boil caused by liquefaction, characteristics and time history of ground deformation and ground motion at liquefied sites in this study. The questionnaires were delivered to the people who were working in Takenouchi industrial estate when the earthquake happened. The relationship between characteristics of liquefaction and geological conditions in Takenouchi industrial estate was also investigated.

Masakatsu Miyajima, Professor, Dept. of Civil Engineering, Kanazawa University, 2-40-20 Kodatsuno, Kanazawa, Ishikawa, Japan 920-8667
Masaho Yoshida, Associate Professor, Dept. of Civil Engineering, Fukui National College of Technology, Geshi, Sabae, Fukui, Japan 916-8507
Masaru Kitaura, Professor, Dept. of Civil Engineering, Kanazawa University, 2-40-20 Kodatsuno, Kanazawa, Ishikawa, Japan 920-8667

OUTLINE OF QUESTIONNAIRE SURVEY

The questionnaire survey for liquefaction phenomenon during the 2000 Tottori-ken Seibu earthquake was conducted. One hundred eight questionnaires were delivered to eleven companies in Takenouchi industrial estate on March 13, 2001, five months after the earthquake. Fifty-seven questionnaires were collected from eight companies, so the withdrawal rate of questionnaires was 53%. The effective questionnaires were, however, forty because the answerers who stayed in another place or rode in a car during the event were excepted. Locations of companies at which questionnaires were collected were shown as circled number in Figure 1.

The total number of questions is 55, such as location at which answerers stayed (11 questions), earthquake ground motion (7), knowledge of liquefaction (5), damage caused by liquefaction (14), awareness for disaster prevention before and after the earthquake (5) and generic character of answerers (3).

LIQUEFACTION AND SOIL CONDITIONS

Sites, which were obtained the answers, were divided into two areas in order to compare the degree of liquefaction. The sites of Nos. 8, 9 and 10 are called as shore side and the sites of Nos.5 and 6 are called as sea side in this paper. The number of effective answers was 14 in each area. All of answerers felt the earthquake ground motion in the building made by reinforced concrete or steel, which was built about 10 years ago. Figure 2 shows the geological section along D-line in Figure 1 [2]. The top 10m is composed of reclaimed layer (R in Figure 2) made by loose sandy silt mixed with shells at the No.3-line near the sea side. At the No.5-line near the shore side, alluvial sand layer (Ad) lies beneath the reclaimed layer made by silt and sand. A research report shows the extreme sand boil, crack and uneven settlements of ground surface occurred in shore side rather than sea side owing to the liquefaction of alluvial sand layer [3]. There were many people in the shore side who saw the sand boil just after the earthquake rather than the people in the sea side. It suggests that sand boil easily spouted out in the shore side because the sand layer lied near the ground surface.

RESULTS OF QUESTIONNAIRE SURVEY AND DISCUSSIONS

Generic Character of Answerers

Figure 3 shows generic character of answerers. The number of men was slightly more than that of women and their ages were 50s and 60s. Although the damage of their companies was very serious, the rate of answerers whose houses were damaged was about 20%.

Knowledge of Liquefaction

Since the damage caused by liquefaction has gone into headlines during the 1995 Kobe earthquake, researchers connected with liquefaction have felt that the meaning of liquefaction filtered into people. However, the degree of understanding of liquefaction was not very high before this earthquake as shown in Q.19 and Q.20 of Figure 4. However, people who experienced this earthquake deepened their understanding of liquefaction. Someone said

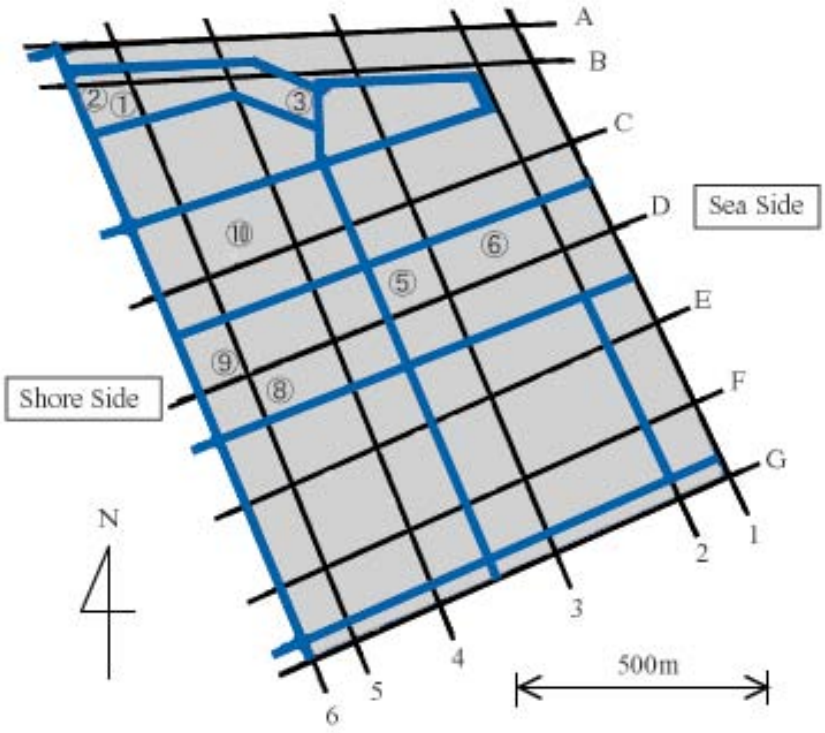

Figure 1. Plane view of Takenouchi industrial estate

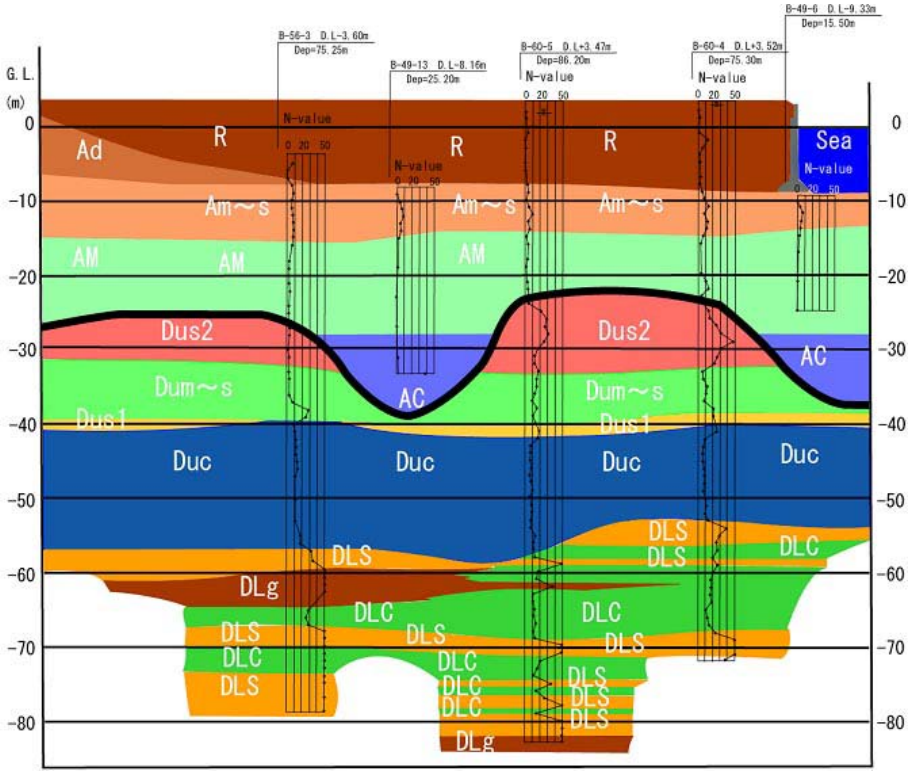

Figure 2. Geological section along D-line in Figure 1

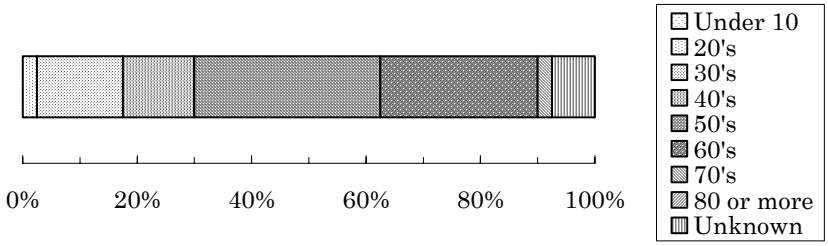

Q.54 What is your age?

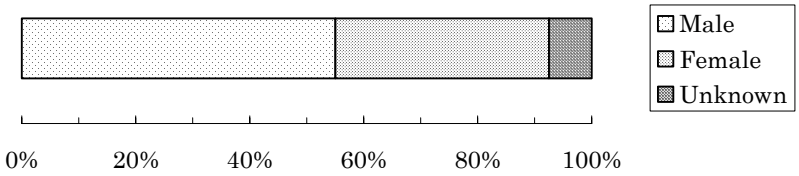

Q.55 What is your sex?

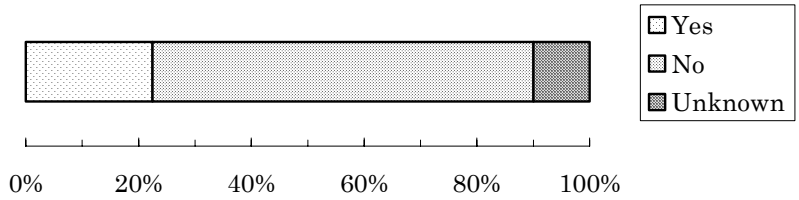

Q.53 Were there any damages to your house?

Figure 3. Attribution of answerers

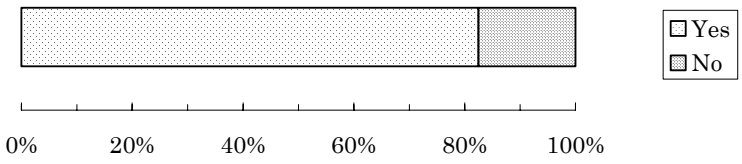

Q.19 Have you ever heard a word “liquefaction”?

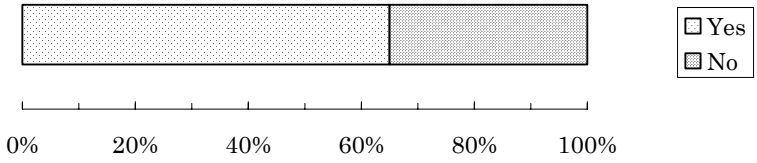

Q.20 Have you ever known what “liquefaction” was before the earthquake?

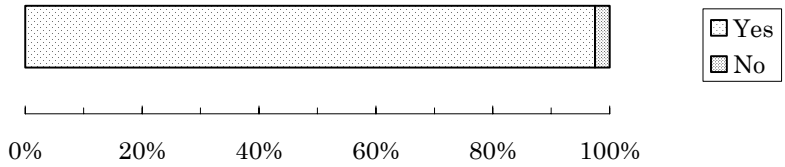

Q.21 Did you understand what “liquefaction” was after the earthquake?

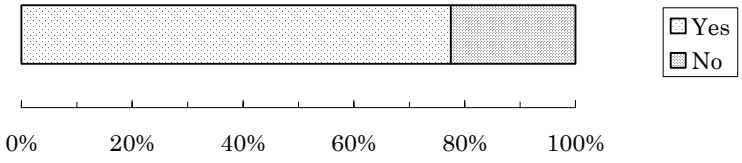

Q.22 Are you afraid of “liquefaction”?

Figure 4. Knowledge of liquefaction

"Please teach me about liquefaction in detail". Many people felt a fear against the liquefaction as shown in Q.22. An interesting answer was "I felt that my body sank into the ground due to sand boil."

Sand Boil

Since all of answerers stayed in buildings of their companies, it is considered that people saw the sand boil directly after stop of the earthquake ground motion. The answers concerning with the time when the people saw a sand boil were divided into two groups as shown in Q.26 of Figure 5. One was just after the earthquake, and the other was some minutes later. The people, who saw it instantaneously when the sand and water spouted from a ground surface first, answered Q.26. It seems that the degree of liquefaction, existence of pavement and crack of ground surface influenced the start of sand boil.

There are three answers of eyewitness that the water spouted out from the ground surface first, and then the sand with water spouted out. It was observed at three different places. It is very interesting that the spouted material was changing as time went by. It is estimated from the answers of Q.28 to Q.30 that the dark-grayed muddy water spouted out with a height from 10cm to 30cm, just as the water coming out from a tap. Three groups of answers were obtained uniformity about the viscosity of sand and water as shown in Q.30 of Figure 5. It is considered that they depend on the soil conditions and the time when they saw. There were a few answers about the time when the spouting of sand and water finished. Fastest time was 10 minutes later, longest time was 10 hours over and the majority of answers were from one to two hours later.

Ground Deformation Induced by Liquefaction

Figures 6 and 7 show the results of questionnaire survey about vertical and horizontal displacements of ground and structures. It is clear that answerers of 85% saw the displacements. The vertical relative displacement was from 20cm to 50cm. There were two groups of answers concerning with the time when the displacements occurred. One was just after the earthquake, and the other was some minutes later as same as the time when the sand boil occurred. The majority of answerers were 30 minutes later. The answer that the displacement gradually became large with the lapse of time was obtained from 78% of the answerers. The fastest time was a few minutes later and the latest time was a few days later. The answer said that it became large by aftershock. The horizontal displacement was smaller than the vertical displacement. The direction of displacements was distinguished along the direction of east and west. This direction was coincided with the predominant direction of strong ground motion.

RELATION BETWEEN PHOTOGRAPHS AND RESULTS OF QUESTIONNAIRE SURVEY

Photographs 1 to 4 show a progress of liquefaction, which was taken by a staff stayed at the site No.3 in Figure 1. The shooting time was accurate because the time was get from the internal watch of his digital camera. It can be seen that there was no change in the front gate from Photograph 1, which was taken at 10 minutes after the earthquake. However, it can be seen from Photograph 2, which was taken at 25 minutes later, that the sand and water were spouted from the cracks of ground surface. These photographs correspond with the answer of Q.26 in Figure 5, that is, the sand boil occurred after some minutes. Photograph 3 shows

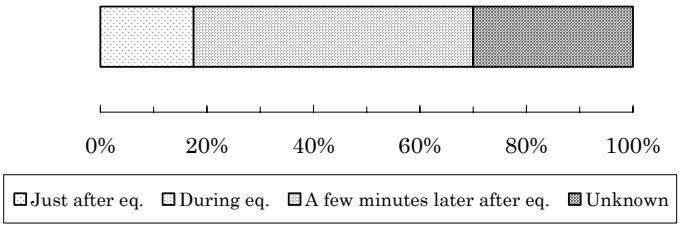

Q.26 When did you see the sand boil?

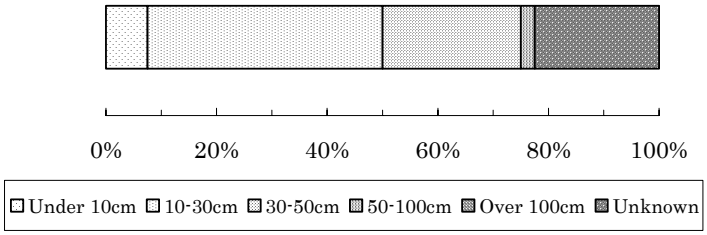

Q.28 How high did the sand and water spout out?

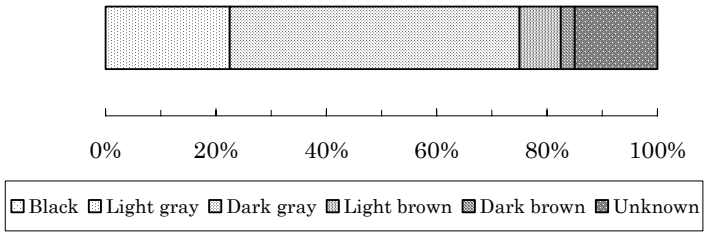

Q.29 What was the color of sand boil?

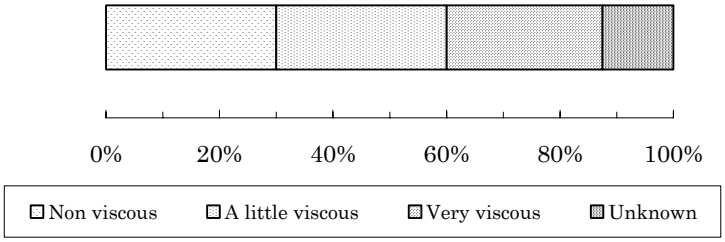

Q.30 How viscous the sand boil was?

Figure 5. Appearance of sand boil

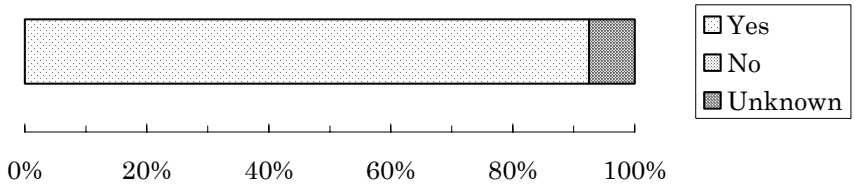

Q.35 Was a vertical gap between building and ground caused?

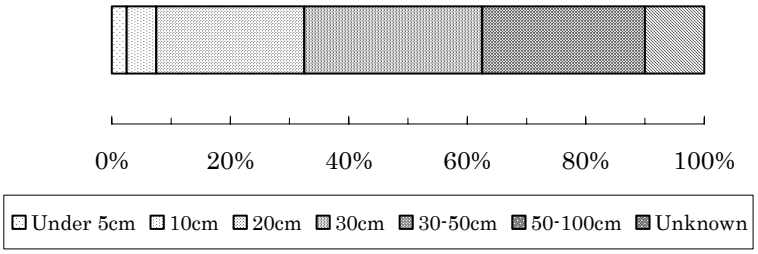

Q.36 How large the maximum gap was?

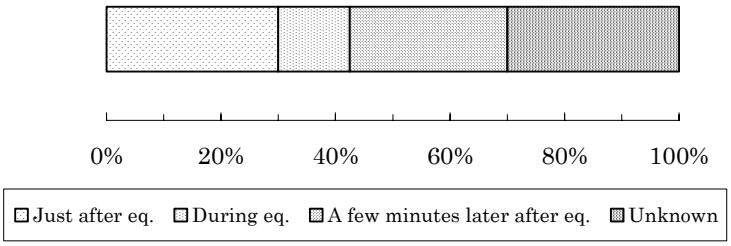

Q.37 When did the gap occur?

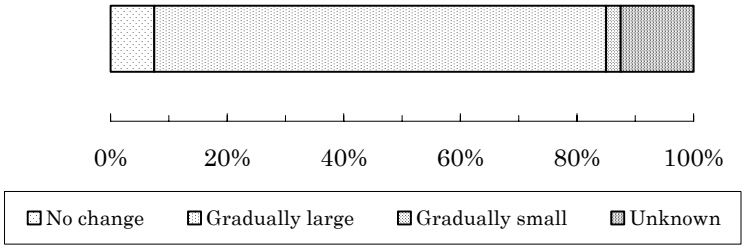

Q.38 Did the gap change as time went by?

Figure 6. Vertical displacement induced by liquefaction

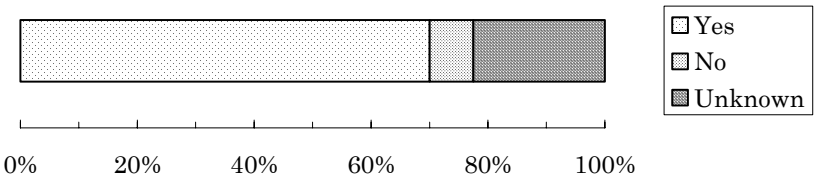

Q.40 Was a horizontal gap between building and ground caused?

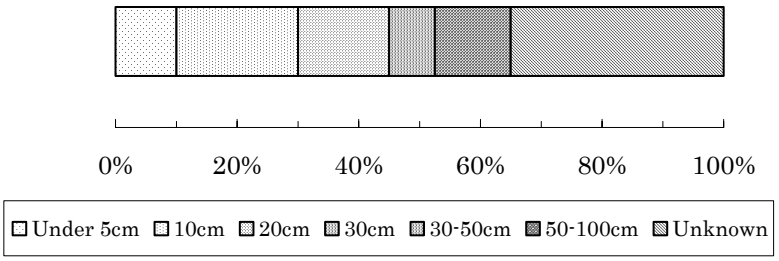

Q.41 How large the maximum gap was?

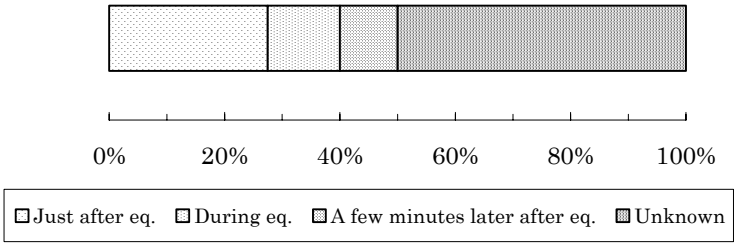

Q.43 When did the gap occur?

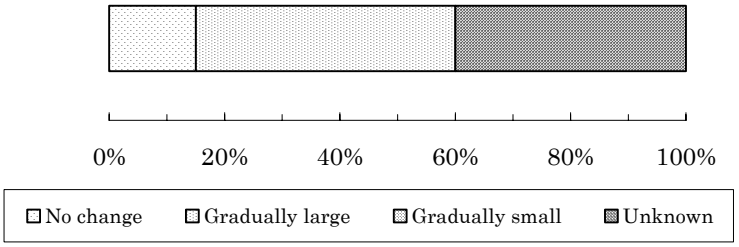

Q.44 Did the gap change as time went by?

Figure 7. Horizontal displacement induced by liquefaction

Photograph 1. Front gate and road (10 minutes after the earthquake)

Photograph 2. Sand boil from crack of road (25 minutes after the earthquake)

Photograph 3. Wavy sand boil (26 minutes after the earthquake)

Photograph 4. Increase of settlements of road (1 week after the earthquake)

the dark-grayed muddy sand, which spouted out up to about 10cm in height. This also corresponds with the answers in Figure 5. Photograph 4 shows the ground deformation of the same site, which was taken one week later. It can be seen that the ground at which the man was standing settled relatively as compared with the road behind him. According to an evidence of a staff in the company, it was confirmed that the ground settlements increased day by day. This also corresponds with the increasing of ground displacement as mentioned in Figure 6.

CONCLUSIONS

A questionnaire survey was conducted to collect information about witnesses of liquefaction, such as occurrence of sand boil caused by liquefaction, characteristics and time history of ground deformation and ground motion at liquefied sites. The following conclusions may be drawn from the present study.

(1) People felt afraid of liquefaction and did not understand rightly about it, especially before this earthquake.
(2) There were two groups of answers concerning with the time when the sand boil spouted out from the ground surface. One was just after the earthquake and the other was some minutes later. The answers about ground deformation were similar. The ground displacement, however, increased day by day after the earthquake.
(3) The dark-grayed muddy water spouted out with a height from 10cm to 30cm, just as the water coming out from a tap. There were various answers concerning with the time when sand boil stopped. The spouting materials occasionally changed as time went by.

ACKNOWLEGMENTS

The authors wish to acknowledge the western enterprise bureau in Tottori Prefecture for their offering geological data and the fisheries experimentation laboratory in Tottori Prefecture for their offering digital photographs. For the questionnaire survey, the authors are very grateful to the companies in the Takenouchi industrial estate. This study supported in part by the Grant-in-Aid for Ministry of Education, Science, Sports and Culture in Japan (No.13555129).

REFERENCES

[1] Enterprise Bureau of Tottori Prefecture. 1983. "Summary of Reclamation Project in Takenouchi Area of Sakai Outer Port" (in Japanese).
[2] Enterprise Bureau of Tottori Prefecture, 1985, "Geological Cross Section for Reclamation Project in Takenouchi Area of Sakai Outer Port " (in Japanese).
[3] Public Works Research Institute, 2000, "Urgent Research Report on the 2000 Western Tottori Prefecture Earthquake", Technical Memorandum of PWRI, No.3769, p.40 (in Japanese).

Discriminant Technique of Liquefaction by Use of Observed Earthquake Records

Junji Kiyono, Kenzo Toki and Masahiro Morishita

ABSTRACT

This paper proposed a discrimination method of liquefaction induced by the strong ground motion by using monitored records of surface ground accelerations. Many online observation systems of strong ground motions and immediate response systems have been installed and implemented in recent Japan. The early estimation of damage to the structures and casualties is very important to prevent the disaster from spreading. The detection of the liquefaction is also useful to estimate the damage to the structures. When the liquefaction occurs, a predominant period of the earthquake time history tends to lengthen. But the phenomena that the predominant period becomes long occur also when the earthquake record includes surface waves. In this paper, we improve the existing technique by taking into account the period characteristics of the up-down component. As this technique adopts non-stationary spectrum, the judgment can be carried out without gathering all time history of the earthquake data. It is suitable for the real-time earthquake disaster prevention.

INTRODUCTION

Severe ground deformation induced by widespread liquefactions was occurred during the 1964 Niigata earthquake. Several apartments were tilted, bridges were collapsed, harbors, railways and airports were damaged. The lifeline facilities such as electricity, gas, and water supply systems also sustained severe damage. In the 1995 Kobe earthquake, destructive damage to a waterfront area induced by the liquefaction was reported. As the direct damage to the lifeline facilities triggers the second and the third disasters, we have to cut a chain of the disasters by the immediate response.

Many earthquake monitoring systems and early damage assessment systems such as UrDAS for JR, CUBE for Caltech/USGS and SIGNAL for Tokyo Gas Co. Ltd. have already worked [1]. The Japan Meteorological Agency (JMA) monitors the seismic intensity at more than hundred locations throughout Japan and determines the hypocenter and magnitude within a few minutes after an event [2]. CUBE (The Caltech-USGS Broadcast of Earthquake) system [3] determines earthquake locations and magnitudes just after the earthquake based on the data recorded by the Southern California Seismic Network. With the 1995 Kobe earthquake as a turning point, these kinds of systems are being developed especially in a local government.

The countermeasures to the earthquake disaster undertaken are roughly divided into two parts. The first is pre-earthquake countermeasure and the second is post-earthquake countermeasures. The an earthquake prediction by various observations of natural phenomena in scientific viewpoints,

Junji Kiyono, Associate Professor, Graduate School of Civil Engineering, Kyoto University, Yoshida-honmachi, Sakyo, Kyoto, Japan 606-8501

Kenzo Toki, Professor, Faculty of Science and Engineering, Ritsumeikan University, 1-1-1 Nojihigashi, Kusatsu,, Shiga, Japan 525-8577

Masahiro Morishita, Graduate Student, Graduate School of Civil Engineering, Kyoto University, Yoshida-honmachi, Sakyo, Kyoto, Japan 606-8501

the former is the countermeasure based on the seismic observations both for short and long terms, namely improvement of the earthquake resistant standard and strengthening of structures, construction of earthquake disaster prevention structures, earthquake resistant systems and so on in engineering view points. In the latter countermeasure, various activities are undertaken according to the respective time steps of emergency response, restoration, recovery and reconstruction. These kinds of earthquake disaster prevention systems are relatively well explored in Japan.

The UrEDAS (Urgent Earthquake Detection and Alarm System) of the Railway Technical Research Institute is the first alarm system used in practice [4]. Judging from the information of the P-wave arrival, the system estimates the location and magnitude of an earthquake very quickly. Then the system forces bullet trains to stop before the arrival of S-wave. EPEDAT (the early Post-Earthquake Damage Assessment Tool) was developed to estimate building and lifeline damage in Southern California by using the geographical information system (GIS) [5]. Similar real-time damage assessment systems were also developed in Japan. SIGNAL (the Seismic Information Gathering and Network Alert) of Tokyo Gas Company performs damage estimation of a natural gas network using earthquake monitoring and GIS [6]. The system has 331 SI sensors, 5 seismometers on bedrock and 20 liquefaction sensors in Tokyo area. As a part of emergency management system, Kawasaki City has developed a damage assessment system for the city with a population of about 1.2million [7]. The system is unique in the sense that it not only predicts damage statistics but also serves as an emergency operation manual. Yokohama City [8] started a project to deploy a very dense strong ground motion accelerometer network with 150 instruments and three control centers. Tokyo Fire Department [9] also developed an early damage assessment system for fire fighting and rescue operations. The system is basically a computer package of a damage assessment tool for scenario earthquakes. The system has a database for soil condition, buildings, fire occurrence risk, and time dependent population. In Public Works Research Institute, Ministry of Construction, is developing a real-time earthquake damage estimation system for road facilities [10]. By providing rough estimation on damage states and damage distributions in a short time, the system supports decision-makers to facilitate emergency responses immediately after an earthquake. The JMA is responsible for broadcasting earthquake information in Japan. In 1993 and 1994, several damaging earthquake occurred in northern Japan. After the Kobe earthquake, in order not to miss localized heavily damaged areas, the number of stations was further increased to 574 as of April, 1996. The National Research Institute for Earth Science and Disaster Prevention of the Science and Technology Agency [11] deployed a total of 1,000 strong ground motion accelerometers called "K-net" throughout Japan. Recently the Fire Defense Agency of Japanese government also ventured upon a project to deploy on accelerometer in each municipality (3,255 in total) in Japan excluding municipalities having JMA's or K-NET's instruments. An algorithm in order to update estimated physical values by using the measurement data obtained after the first estimation of damage is developed [12].

Frequency characteristics of liquefied ground markedly change especially in the horizontal component, and the horizontal amplitude attenuates stronger than up-down component. Considering these special phenomena, several discriminant techniques of the liquefaction are proposed. Miyazima et al. [13] paid attention to the frequency characteristics and time variation of the ratio of horizontal to vertical peak accelerations. Takada et al. [14] calculated the intensity ratio of the original Arias Intensity and high-cut one. Nakayama et al. [15] judged the liquefaction from the relation between the predominant period and the ground displacement calculated by the spectral intensity and peak acceleration. Kostadinov et al. [16] propose a detection method, which simultaneously analyzes the instantaneous frequency content of the horizontal and vertical ground acceleration. These existing

techniques, however, make a judgment mainly by use of horizontal components of the earthquake records. This causes the misjudgment of the liquefaction when the surface waves appear in the seismic records.

In this study, we introduce the discriminant technique of liquefied ground that is taking into account the frequency characteristics of the vertical component of the record. The judgment by this technique can provide useful information for the liquefaction monitoring and immediate response just after the earthquake.

DISCRIMINANT TECHNIQUE OF LIQUEFIED GROUND

Estimation of Non-stationary Predominant Period

In order to grasp the temporal variation of the predominant period, we here use the developing spectrum using Maximum Entropy Method (MEM) proposed by Hino [17]. Consider the frequency dependent range, t-2πm/ω, for the component wave of frequency, ω. The energy of the component wave is written as

$$X_\omega(t) = \frac{1}{2\pi}\int_{t-2\pi m/\omega}^{t} x(\tau)e^{-i\omega\tau}d\tau \tag{1}$$

The ensemble average of component energies is expressed by

$$\left\langle \left|X_\omega(t)\right|^2 \right\rangle = \frac{1}{(2\pi)^2}\int\int_{t-2\pi m/\omega}^{t} \left\langle x(\tau_1)x(\tau_2)\right\rangle e^{i\omega(\tau_1-\tau_2)}d\tau_1 d\tau_2 \tag{2}$$

As the component energy is calculated by averaging the values of the range, 2πm/ω, the averaged energy can be defined as power spectrum, ϕ(ω, t),

$$\phi(\omega,t) = \frac{\omega}{2\pi m}\left\langle 2\pi\left|X_\omega(t)\right|^2 \right\rangle = \frac{1}{4\pi^2 m}\int\int_{t-2\pi m/\omega}^{t} \left\langle x(\tau_1)x(\tau_2)\right\rangle e^{i\omega(\tau_1-\tau_2)}d\tau_1 d\tau_2 \tag{3}$$

Figure 1 (a), (b), (c) show the observed wave, non-stationary spectrum and variation of predominant period for UD-component of the Port Island record in the 1995 Kobe earthquake. As the contribution of the component frequency is found from the non-stationary spectrum, this information can be introduced in the algorithm of online estimation of liquefaction.

Period Characteristics of Liquefied Ground

Saturated loose sandy deposits tend to liquefy during earthquake. Grain size distribution and N-value are the key factors of the liquefaction. However, the results judging from the above simple procedure before earthquake is not sufficient. When the liquefaction occurred during earthquake, a long period component is dominant in the horizontal record. Because the generation of excess pore water pressure causes the weakening of the soil that lost the shear strength. When the shear wave velocity decreases with a deterioration of the soil rigidity, the predominant period is elongated.

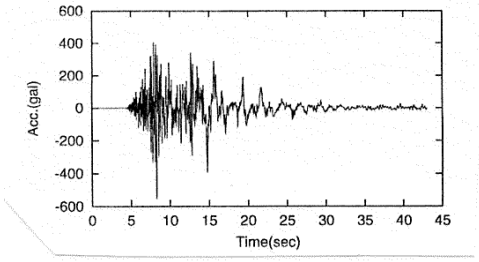

(a) Earthquake motion

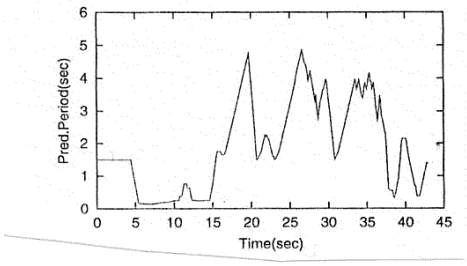

(c) Time history of predominant frequency

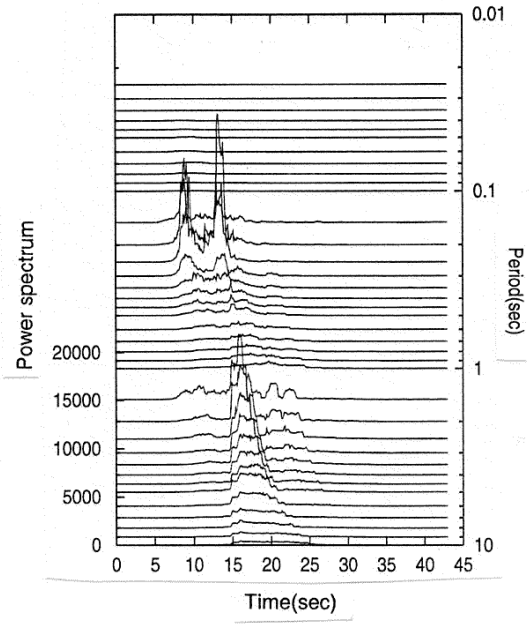

(b) Non-stationary power spectrum

Figure 1. Observed wave, non-stationary spectrum and variation of predominant period for UD-component of the Port Island record in the 1995 Kobe earthquake

In the past earthquakes, long period waves can be seen in the horizontal acceleration records observed on the liquefied grounds. But this significant feature can be observed in the records on the non-liquefied grounds. The earthquake records that contain a surface wave are the cases. The typical examples are the records observed at Shimizu-miho during the 1978 Near Izu Ohshima earthquake, at Osaka city sites during the 1995 Kobe earthquake, at Shizukuishi during North Iwate Pref. Earthquake. As Rayleigh wave can often be seen in the strong ground motion with the surface waves, elongation of the period appears not only in the horizontal but also in the vertical component.

We here propose the technique which judges the existence of the liquefaction by discriminating the cause of the period elongation.

Discriminant Technique

The transmission characteristics of the shear wave are governed by the soil structure such as grain size, shape, density, and so on. On the other hand, the transmission characteristics of the compressional wave are affected by the bulk modulus of pore water. When the liquefaction occurs, the shear wave velocity decreases with the rigidity deterioration but the compressional wave does not drastically change. Consequently the long period waves in the horizontal component predominate after the time liquefaction has occurred but not in the vertical component. For Rayleigh wave, the long period waves predominate both in horizontal and vertical components when the body waves begin to attenuate. We consider these wave and soil characteristics and propose the following discriminant technique.

The first predominant period, T, of a two-layered medium (bedrock and surface layer) is

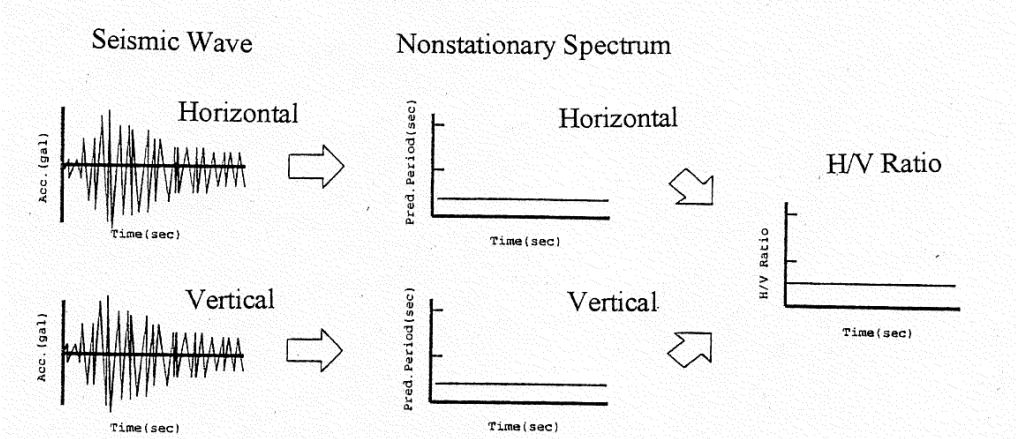

(a) No liquefaction (without surface wave)

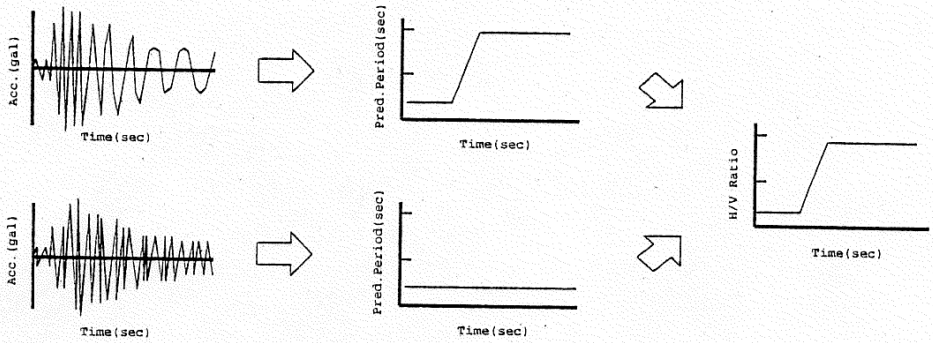

(b) Liquefaction (without surface wave)

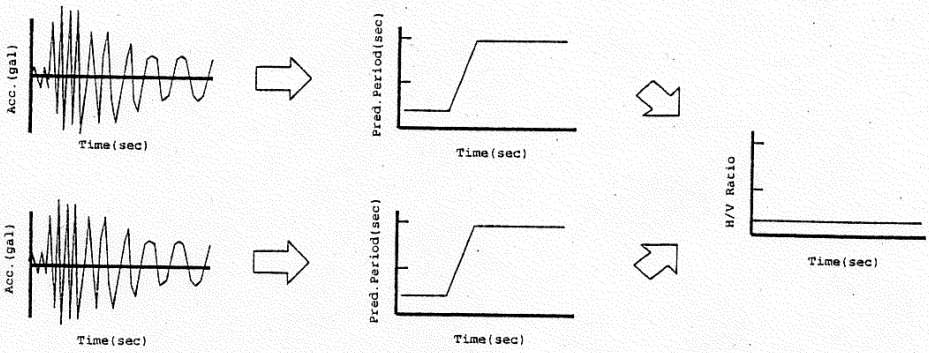

(c) No liquefaction (with surface wave)

Figure 2. Schematic figures for discriminat technique of liquefaction by the use of observed records

$$T = \frac{4H}{V_s} \tag{4}$$

in which H is depth of a surface layer, V_s the shear wave velocity. In case of plural layers,

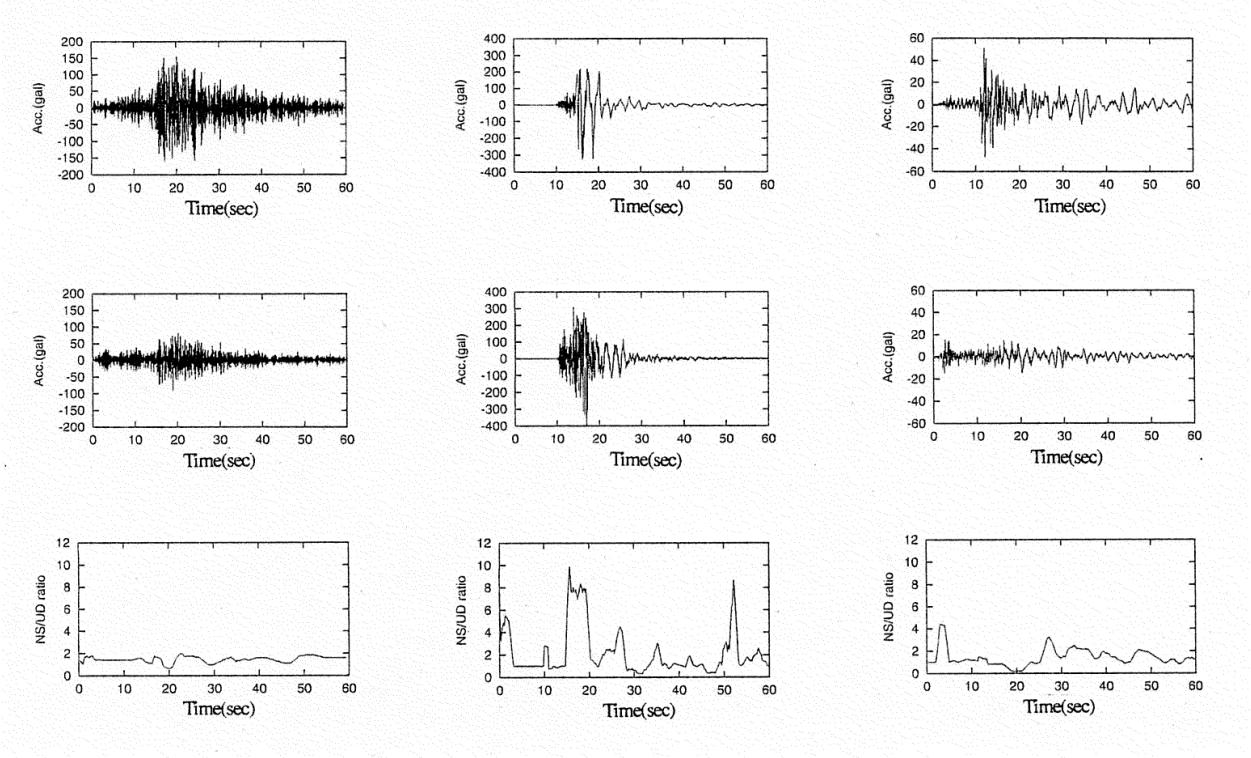

(a) Miyako (MYK) (b) Higashi-Kobe Bridge (HGS) (c) Shimizu-miho (SMZ)

Figure 3. Examples of observed data corresponding to Figure 2; (a) MYK record in the 1978 Off-coast Miyagi Pref. Earthquake, (b) HGS record in the 1995 Kobe earthquake, and (c) SMZ record in the 1978 Near Izu Ohshima earthquake.

$$T = \sum_{j=1}^{N} \frac{4H_j}{V_{sj}} \tag{5}$$

The relation between P-wave velocity, V_p, and V_s is

$$V_p = \sqrt{\frac{\lambda + 2G}{\rho}} = \sqrt{\frac{2(1-\nu)}{1-2\nu}}\, V_s \tag{6}$$

Consider the body wave with the small incident angle. Predominant periods for the horizontal and vertical motions of the ground could relate to the S- and P-wave velocity respectively. When the ground does not liquefy, the ratio of the predominant periods for horizontal and vertical motion is proportional to the ratio of S-wave to P-wave velocity. Therefore the ratio of the predominant periods keeps constant through the all duration time.

When the ground has liquefied, the rigidity of the ground decreases and the predominant period elongates. But as the P-wave transmits directly, the period components of the vertical motion do not markedly change. Therefore the ratio of the predominant periods increases just after the liquefaction occurs.

When the surface wave, especially Rayleigh wave, is included in the observed records, the long period wave can be seen at the latter half of the record in not only horizontal but also vertical motion. Consequently the ratio of the predominant periods keeps constant through the all duration time. The schematic explanation is shown in Figure 2 (a), (b), (c). Figure 3 (a), (b), (c) are the examples of observed data corresponding to Figure 2; (a) Miyako record in the 1978 Off-coast Miyagi Pref. Earthquake, (b) Higashi-Kobe Bridge record in the 1995 Kobe earthquake, and (c) Shimizu-miho record in the 1978 Near Izu Ohshima earthquake. The long period component appeared in the Shimizu-miho record is reported to be the surface wave [18].

In order to judge the occurrence of liquefaction by a common scale factor, the ratio of horizontal and vertical predominant period, T_H/T_V, should be generalized without distinction of the site. This is because the ratio tends to depend on the value of S-wave velocity, V_s, as V_p is almost constant, (1500m/s) in a surface layer even if T_H/T_V is non-dimensional. In this study, we multiply the ratio by kV_s (k is constant and set to be 1/200) to normalize the value of vertical axis.

$$\frac{T_H}{T_V} kV_s \cong \frac{V_p}{V_s} k'V_s = k'V_p \rightarrow const. \tag{7}$$

TABLE I. EARTHQUAKE DATA ANALYZED AND LIQUEFACTION REPORT

Report	Observation site	Earthquake	Vs (m/sec)
○	Port Island (KPI)	1995 Kobe EQ.	198
○	Higashi Kobe Brdg. (HGS)	1995 Kobe EQ.	180
○	Aomori Port (AOM)	1968 Tokachi Off-shore EQ.	165
○	Wildlife (WIL)	1987 Superstition Hills EQ.	(200)
○	Kushiro Port (KSH)	1993 Kushito Off-shore EQ.	154
○	Hakodate Port (HKD)	1993 Hokkaido SW Off-shore EQ.	176
△	JR Takatori (TKT)	1995 Kobe EQ.	172
△	Amagasaki (AMA)	1995 Kobe EQ.	145
×	Miyako (MYK)	1978 Off-coast Miyagi Pref. EQ.	(200)
×	Shimizu-miho (SMZ)	1978 Near Izu-Oshima EQ.	(200)
×	Sakai (SKI)	1995 Kobe EQ.	139
×	Tadaoka (TDO)	1995 Kobe EQ.	(200)
×	Kobe- motoyama (KBM)	1995 Kobe EQ.	150
×	Sendai (SND)	1997 NW Kagoshima Pref. EQ.	184

JUDGMENT OF LIQUEFACTION BY OBSERVED RECORDS

The earthquake records used and existence of liquefaction reported are shown in TABLE I. In this table, symbols of ○, △, and × mean "liquefaction", "liquefaction suspicion", and "no liquefaction". "Liquefaction suspicion" site is that there are no evidence of the liquefaction at the just point but the liquefaction was observed at the vicinity of the site within 50m [13].

The proposed method is implemented according to the following steps.

1) The total duration time of the predominant period ratio, $T(r)$, that exceeds a level, r, is counted.

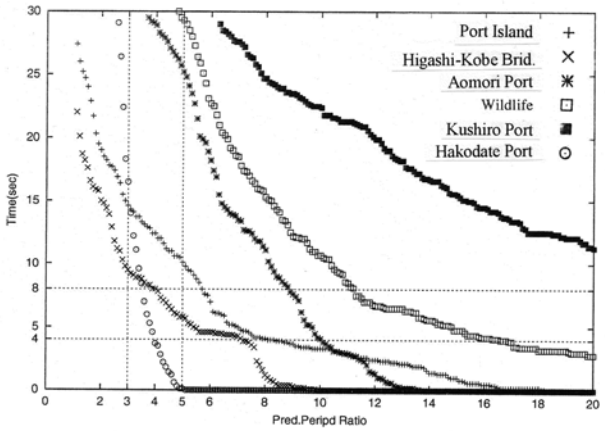

(a) Field report: ○ (No Liquefaction)

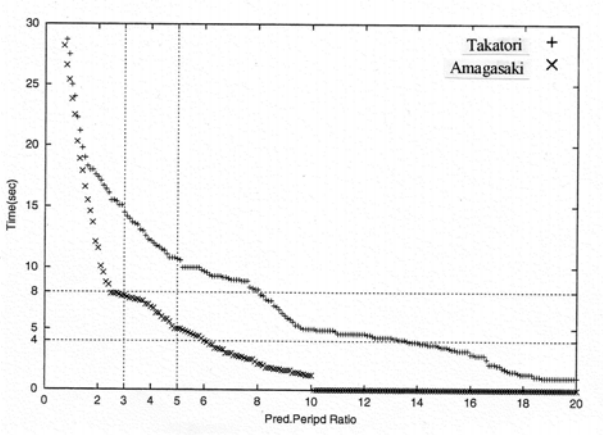

(b) Field report: △ (Liquefaction suspicion)

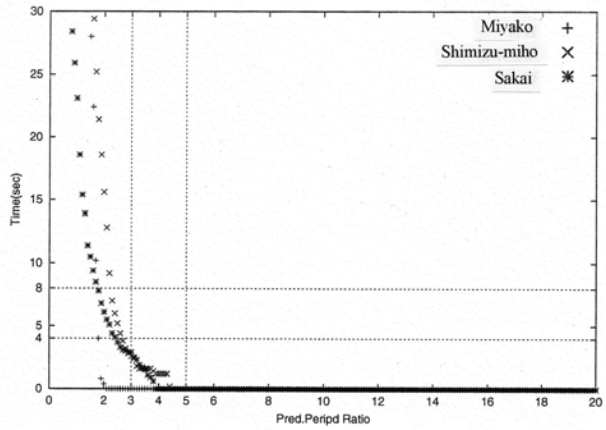

(c) Field report: × (No liquefaction)

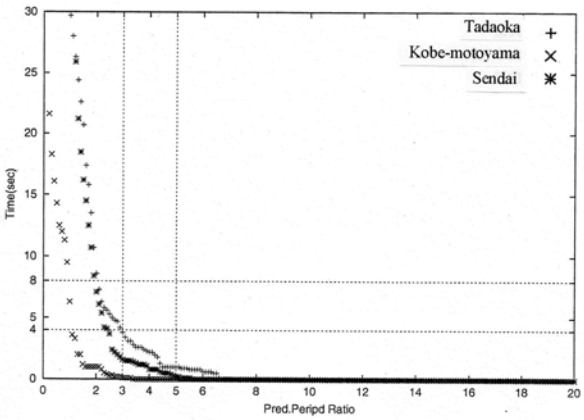

(d) Field report: × (No liquefaction)

Figure 4. Relations between *T(r)* and *r* for the fourteen sites

2) The predominant period ratios, *r*, and the total duration times, *T(r)*, are determined for "liquefaction", "liquefaction suspicion", and "no liquefaction".

The relations of *T(r)* and *r* for the fourteen sites are shown in Figure 4. Figure 4 (a) corresponds to "○: liquefaction", (b) "△: liquefaction suspicion", and (c)-(d) "×: no liquefaction". The duration time, *T(r)*, gradually decreases with the increase of the predominant period ratios, *r* in "liquefaction" sites. On the other hand, the *T(r)'s* of "no liquefaction" sites rapidly decrease.

Occurrence of liquefaction is judged according to the following two conditions; (i) *T(5) >4sec*, and (ii) *T(3)>8sec*. When the *T(r)* time history satisfies both conditions, the ground is judged "liquefaction". When *T(r)* satisfies neither (i) nor (ii), it is judged "no liquefaction", and otherwise "liquefaction suspicion".

By using above criteria, the fourteen earthquake records are analyzed to detect the liquefaction. The results of the detection are given in TABLE II. Although the Hakodate Port is judged "liquefaction suspicion" against the report of "liquefaction" and the JR Takatori is "liquefaction" against the report of "liquefaction suspicion", most of the results are in good agreement with the

reports. Especially the record at Shimizu-miho site, which includes the effect of surface wave, are distinguished from the liquefaction.

The characteristics of this discriminat technique are that the calculation procedure is sequential and on-line processing is possible. This is the useful tool for the real time detection of liquefaction and damage estimation.

TABLE II. COMPARISON OF JUDGMENT RESULTS AND LIQUEFACTION REPORT

Judgment	Report	Observation site	Earthquake
○	○	Port Island (KPI)	1995 Kobe EQ.
○	○	Higashi Kobe Brdg. (HGS)	1995 Kobe EQ.
○	○	Aomori Port (AOM)	1968 Tokachi Off-shore EQ.
○	○	Wildlife (WIL)	1987 Superstition Hills EQ.
○	○	Kushiro Port (KSH)	1993 Kushito Off-shore EQ.
△	○	Hakodate Port (HKD)	1993 Hokkaido SW Off-shore EQ.
○	△	JR Takatori (TKT)	1995 Kobe EQ.
△	△	Amagasaki (AMA)	1995 Kobe EQ.
×	×	Miyako (MYK)	1978 Off-coast Miyagi Pref. EQ.
×	×	Shimizu-miho (SMZ)	1978 Near Izu-Oshima EQ.
×	×	Sakai (SKI)	1995 Kobe EQ.
×	×	Tadaoka (TDO)	1995 Kobe EQ.
×	×	Kobe- motoyama (KBM)	1995 Kobe EQ.
×	×	Sendai (SND)	1997 NW Kagoshima Pref. EQ.

CONCLUSIONS

Earthquake monitoring and real time damage assessment systems in Japan have rather long history. As introduced in the preceding section, triggered by the Kobe Earthquake, so many new strong motion monitoring networks and early damage assessment systems are being developed. In order to avoid a lack of information just after an earthquake, early damage assessment systems with intensive earthquake monitoring are expected to play a vital role in the near future.

In this study, we introduce the discriminant technique of liquefied ground that is taking into account the frequency characteristics of the vertical component of the record. The judgment by this technique can provide useful information for the liquefaction monitoring and immediate response just after the earthquake. The significant feature of this discriminat technique is that the calculation procedure is sequential. Thus the real time detection of liquefaction and immediate damage estimation are possible by introducing the on-line processing system.

REFERENCES

[1] Noda, S. and Meguro, K. 1995. "A New Horizon for Sophisticated Real-time Earthquake Engineering," *Jour. of Natural Disaster Science*, 17(2): 13-46.

[2] JMA. 1996. *JMA Intensity –Basic Knowledge and its Application–*, Gyosei (in Japanese).

[3] Kanamori, H., Hauksson, E., and Heaton, T. 1991. "TERRA Scope and CUBE Project at Caltech," EOS.72, 564.

[4] Nakamura, Y. and Ueno, M. 1986. "Development of Urgent Earthquake Detection and Alarm System," *Proc. of the 7th Japan earthquake Engineering Symposium*: 2095-2100 (in Japanese).

[5] Eguchi, R., Goltz, J.D., Seligson, H., and Heaton, T. H. 1984. "Real-time Earthquake Hazard Assessment in California, the early Post-earthquake Damage Assessment Tool and the Caltech-USGS Broadcast of Earthquake," *Proc. of the 5th U.S.-Japan national Conference on Earthquake Engineering*, II: 55-63.
[6] Yamazaki, F., Katayama,T. and Yoshikawa, Y. 1994. "On-line Damage Assessment of City gas Networks based on Dense earthquake Monitoring," *Proc. of the 5th U.S.-Japan national Conference on Earthquake Engineering*, IV: 829-837.
[7] Ohta, Y. 1994. "Seismic strong motions as key information for earthquake disaster prevention," *Zisin*, 47(1): 113-136 (in Japanese).
[8] Yokohama City. 1996. *High-concentration Seismograph Network –Seismometry System in Yokohama City*.
[9] Fire Research Institute of the Fire Defense Agency. 1996. *User's Guide of Simplified Earthquake Damage Assessment System* (in Japanese).
[10] Sugita, H. and Hamada, T. 1997. "Development of real-time damage estimation system for road facilities," *Proc. of 7th U.S.-Japan Workshop on Earthquake Disaster Prevention for Lifeline Systems*.
[11] National Research Institut for Earth Science and Disaster Prevention, Science and Technology Agency. 1995. *Kyoshin Net*.
[12] Kiyono,J. and Miura, F. 1997. "Estimation of Spatial Distribution of Ground Deformation Just after Earthquakes," *Proc. of 7th KAIST-NTU-KU Tri-lateral Seminar/Workshop on Civil Engineering*: 251-256.
[13] Miyajima, S., S. Nozu and M. Kitaura. 1997. "A detection method for liquefaction using strong ground records," *Proc. of the 24th JSCE Earthquake Engineering Symposium*, JSCE (in Japanese)
[14] Takada, S. and R. Ozaki, 1997. "A judgment for liquefaction based on strong ground motion," *Proc. of the 24th JSCE Earthquake Engineering Symposium*, JSCE (in Japanese)
[15] Nakayama, W., Y. Shimizu and T. Suzuki. 1998. "A judgment for liquefaction based on strong ground motion," Proc. of the 53th Annual Conf. of JSCE, Vol.1-B, JSCE (in Japanese)
[16] Kostadinov, M. V. and F. Yamazaki. 2001. "Detection of soil liquefaction from strong motion records," *Proc. of EESD,* 30, 2: 173-193.
[17] Hino, M. 1977. *Spectrum Analysis*, Asakura-Shoten.
[18] Sugito,M., H. Goto and F. Aikawa. 1984. "A detection method for liquefaction using strong ground records," *Proc. of JSCE Structural Eng./Earthquake Eng.*, Vol.1, No.2.

Estimation of the Zones Susceptible to Liquefaction-induced Flow in Tokyo.

Susumu Yasuda, Yoshihisa Shimizu, Kenichi Koganemaru,
Ryoji Isoyama, Eisuke Ishida and Kouichi Matsumoto

ABSTRACT

Liquefaction-induced ground flow brings severe damage to structures. In Tokyo, alluvial loose sand layers and reclaimed loose soil layers are widely deposited in lowland area. These layers are susceptible to liquefaction during earthquakes. Moreover, there are many rivers and canals in the lowland. Therefore, it is anxious about the damage to structures due to liquefaction-induced flow during future earthquakes.

The authors tried to estimate the susceptible zones for the liquefaction-induced ground flow in Tokyo. Two types of flow were evaluated: flow at gentle slopes and the flow at the ground behind river walls. Many boring data were collected and liquefiable layers were estimated. Data on the river walls and water depth for rivers were collected also. Then the estimation for the liquefaction-induced ground flow was conducted by the analytical code "ALID". Relationships among the displacement at the ground surface, thickness of liquefiable layer, fines contents and etc were derived.

INTRODUCTION

Liquefaction-induced ground flow brought severe damage to many structures during past earthquakes. For example, bridges, buried pipes, buildings and other structures were damaged due to the flow during the 1964 Niigata earthquake, the 1983 Nihonkai-chubu earthquake and the 1995 Hyogoken-nambu (Kobe) earthquake in Japan. In Tokyo, alluvial liquefiable loose sand layers and reclaimed loose soil layers are widely deposited in lowland area. Moreover, many rivers and canals flow in the lowland, and gentle slopes exist at several sites. In fact, liquefaction-induced flow occurred at several sites during the 1923 Kanto earthquake. Therefore, it is concerned the similar damage to structures due to liquefaction-induced flow will occur in Tokyo during future earthquakes. The authors developed a simplified procedure for the analysis of liquefaction-induced large deformation. Then the authors tried to estimate the susceptible zones for the liquefaction-induced ground flow in Tokyo based on the simplified procedure. Special attention was paid for the effect of fines content of alluvial sand layer on the liquefaction-induced displacement of the ground, because the alluvial sand contain much fines and quite different from the clean sands which caused large displacement during the Niigata and Nihonkai-chubu earthquakes.

Susumu Yasuda, Professor, Tokyo Denki University, Hotoyama, Hiki-gun, Saitama JAPAN 350-0394
Yoshihisa Shimizu and Kenichi Koganemaru, Engineer, Tokyo Gas Co., Ltd., 1-5-20, Kaigan, Minato-ku, Tokyo, JAPAN 105-0022
Ryoji Isoyama and Eisuke Ishida, Engineer, Japan Engineering Consultants Co., Ltd., 5-33-11 Honmachi, Nakano-ku, Tokyo JAPAN 164-0012
Kouichi Motsumoto, Graduate student, Tokyo Denki University, Hotoyama, Hiki-gun, Saitama JAPAN 350-0394

GEOMORPHOLOGIC CONDITION AND POSSIBLE TYPES OF FLOW IN TOKYO

Geomorphologic Condition in Tokyo

Tokyo is divided into four areas in geomorphologic condition from east to west: mountain, hill, terrace and lowland areas. Liquefiable loose sand layers are deposited in the lowland area. The lowland area is subdivided into four zones: a large alluvial lowland formed by Arakawa River and Edogawa River, a narrow lowland formed by Tamagawa River, a beach along Tokyo Bay and artificially reclaimed lands constructed along Tokyo Bay. Tokyo Station is the boundary of the hill area and the large lowland zone.

Alluvial loose sand layers are deposited in the lowlands formed by the rivers and beach. Reclaimed loose sand layers are filled in the reclaimed lands. These loose sand layers are sensitive to liquefaction during earthquakes. However, the loose sands contain fairly much fines such as 10 to 40%. The ground surface of the lowland area is almost flat. But some gentle slopes are existed at several sites.There are many rivers and canals retaining by walls in the lowland area. Moreover, reclaimed lands are protected by sea walls and quay walls.

Type of Liquefaction-induced Flow

According to the previous studies, liquefaction-induced ground flow can be divided into two classes, as illustrated in Figure 1: ①ground flow on gentle slopes, and ②ground flow behind quay walls. Damage to buried pipes and other structures occurred in the first situation during the 1964 Niigata and the 1983 Nihonkai-chubu earthquakes in Japan. The maximum horizontal displacement was about 5 m in Noshiro City during the Nihinkai-chubu earthquake. In contrast, second type of flow occurred during the 1964 Niigata and the 1995 Hyogoken-nambu (Kobe) earthquakes in Japan. The maximum horizontal displacement near quay walls was about 10 meters in Niigata and 4 meters in Kobe, respectively. The maximum distance of ground flow was about 300 meters and 150 meters back from the river or the sea in Niigata and Kobe, respectively. Many structures such as road bridges, buried pipes and buildings were severely damaged by the ground flow. Similar damages

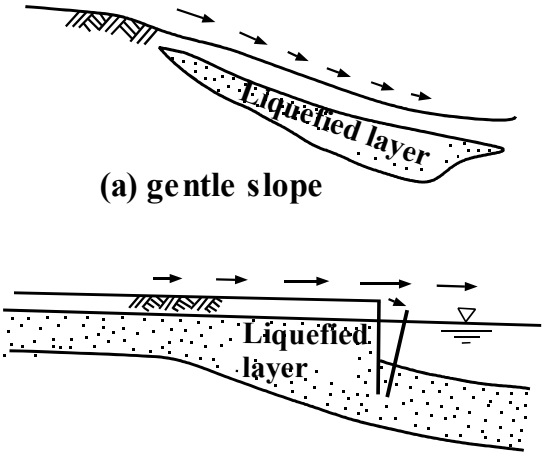

Figure 1 Two types of liquefaction-induced flow

were reported during the 1990 Luzon, Philippines and the 1991Telire-Limon, Costa Rica earthquakes. (e.g. Yasuda & Berrill, 2000[1])

Liquefaction-induced Damage during the 1923 Kanto earthquake

The most recent earthquake which brought liquefaction in Tokyo was the 1923 Kanto earthquake with the magnitude of 7.9 in JMA scale. Liquefied sites during the Kanto earthquake was studied by Kuribayashi and Tasuoka(1975)[2] and others. Literature survey and hearing from inhabitants prevailed the occurrence of liquefaction-induced flow at several sites. Moreover, aerial photos taken just after the earthquake proved the occurrence of the flow. According to these studies, the two types of flow occurred at the following sites:

(1) Ohmori district: ground flow occurred on a gentle slope at a beach along Tokyo Bay.

(2) Nihonbashi and Nishikameari districts: river walls collapsed and the ground behind the walls flowed towards the rivers.

In the present circumstance, gentle slopes and river walls are existed at many sites in the lowland areas and reclaimed land areas in Tokyo. Moreover, liquefiable loose sand layers are deposits in these areas. Therefore, the occurrence of the two types of liquefaction-induced flow and associated damage to urban facilities are concerned.

ESTIMATION METHOD OF SUSCEPTIBLE SITES FOR LIQUEFACTION-INDUCED FLOW

Outline of the ALID (Analysis of Liquefaction-Induced Deformation)

There are three classes of method to estimate the flow-associated displacement:

1) by use of an empirical formula,

2) by a residual deformation analysis, and

3) by an effective stress response analysis.

Several empirical formulae to estimate the ground displacement have been proposed recently based on the damage during the Nihonkai-cubu, Niigata and Kobe earthquakes. These methods are simple and easy to apply to a wide area. However, these methods are difficult to apply to Tokyo because the liquefiable sands have much fines in Tokyo as mentioned above. The displacement of the liquefied ground is greatly influenced by the fine content. The liquefied sands in Niigata and Noshiro cities were very clean and the liquefied sand in Kobe has not much fines.

Effect of fines content can be analyzed by the effective stress response analysis, but is difficult to apply to a wide area because of huge cost. Then a residual deformation analysis method named “ALID (Analysis for Liquefaction-induced Deformation)”developed by the authors (Yasuda et al., 1999[3]) was applied in this study. The outline of the method is as follows:

Finite element method is applied twice as follow:

i) In the first step, the deformation of the ground is calculated by the finite element method using the shear modulus before earthquake.

ii) The finite element method is applied again by using the decreased shear modulus due to liquefaction with the condition of no volume change.

iii) The difference in the deformation measured by the two analyses is supposed to equal the residual ground deformation.

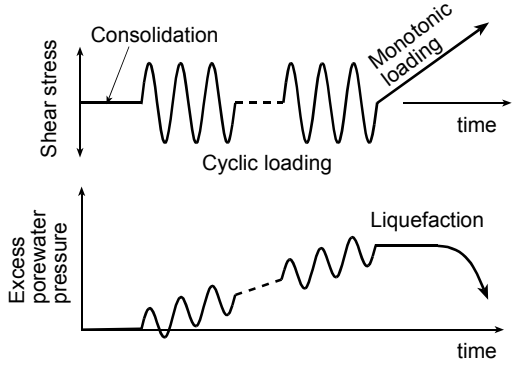

Figure 2 Procedure of cyclic and monotonic loading

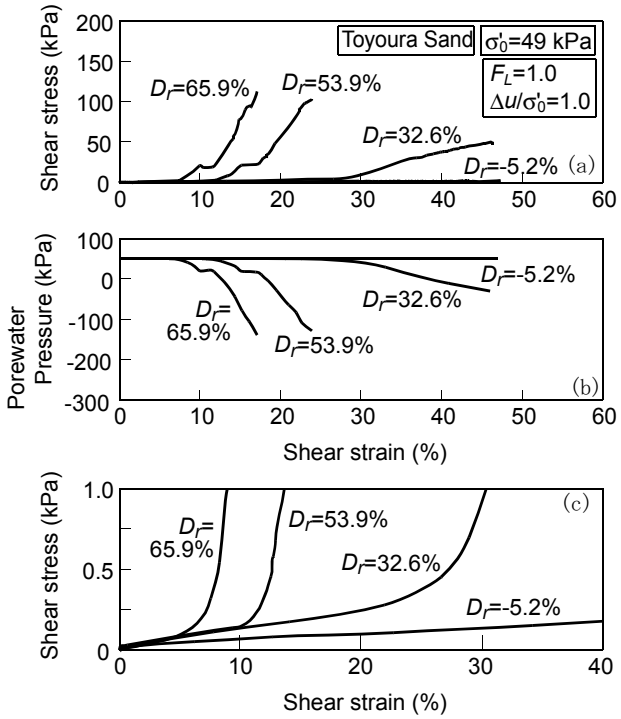

Figure 3 Stress-strain curves of liquefied Toyoura sand (Yasuda et al., 1999 [3])

The authors conducted torsional shear tests to obtain the reduction rate of shear modulus due to liquefaction (Yasuda et al., 1998[4]). A prescribed number or prescribed amplitude of cyclic loadings was applied to samples in undrained condition as shown in Figure 2. Safety factor against liquefaction, F_L, which implies severity of liquefaction was controlled by the number of cycles or amplitude of the cyclic loadings. After that, a monotonic loading was applied under undrained condition.

Figure 3 shows stress-strain curves and excess porewater pressure-strain curves in the case of Toyoura sand with different relative densities, *Dr*. Scales of axes in Figure 3(c) are enlarged one of Figure 3(a). Shear strain increased with very low shear stress up to very large strain. Then, after a resistance transformation point, the shear stress increased comparatively rapidly with shear strain, following the decrease of pore water pressure. As shown in Figure 3(c), shear strain up to the resistance transformation point increased with the decrease of *Dr*. And, shear modulus up to the resistance transformation point decreased with the decrease of *Dr*.

In the liquefied specimen, shear strain increased with very low shear stress up to very large strain as schematically shown in Figure 4. Then, after a resistance transformation point (turning point), the shear stress increased comparatively rapidly with shear strain, following the decrease of pore water pressure. The amount of strain up to the resistance transformation point is called the "reference strain at resistance transformation, γ_L" as shown in Figure 4. Stress-strain curves before and after the reference transformation point can be presented approximately by a bilinear model with G_1, G_2 and γ_L:

$$\tau = G_1 \gamma \quad \text{for } \gamma < \gamma_L \tag{1}$$

$$\tau = G_1 \gamma_L + G_2(\gamma - \gamma_L) \quad \text{for } \gamma \geqq \gamma_L \tag{2}$$

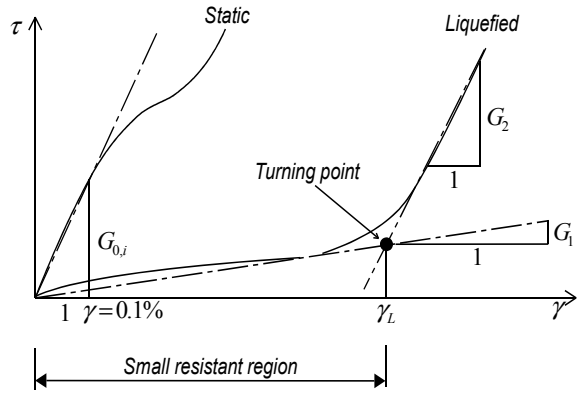

Figure 4 Definition of $G_{0i,}$ G_1 and γ_L

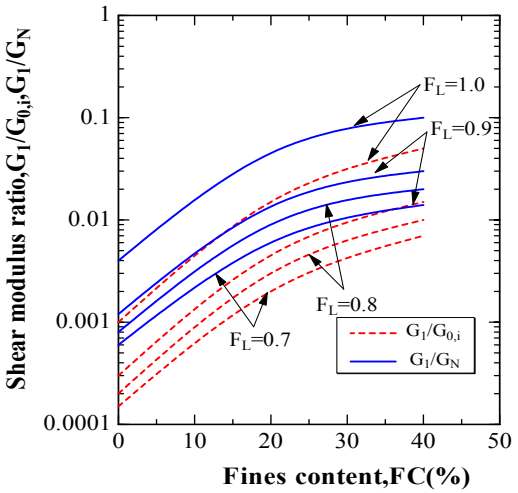

Figure 5 Summary of relationships among shear modulus ratio, F_L an Fc (Yasuda et al., 1999[3])

where G_1 and G_2 are the shear moduli before and after the reference transformation point, respectively. To know the reduction rate of shear modulus due to liquefaction, the rate of shear modulus G_1/G_0, which is the ratio of shear modulus after and before liquefaction, was calculated. Relationships among the shear modulus ratio, G_1/G_0 and fines content less than 75 μ m, Fc, in the range of F_L =0.7 to 1.0 were summarized as shown in Figure 5.

Several Analyses to Demonstrate the Effectiveness of the ALID for Liquefaction-induced Flow

The proposed method "ALID" was applied to several structures which were damaged during past earthquakes, to demonstrate the adaptability of the method (e.g. Yasuda et al., 1999[3]). Among them three cases in which estimated liquefaction-induced displacements were compared with the actual displacements, are shown below. In the analyses, shear modulus before the earthquake were estimated by SPT N-values, and F_L was evaluated by the method introduced in the Specification for Highway Bridges (1996).

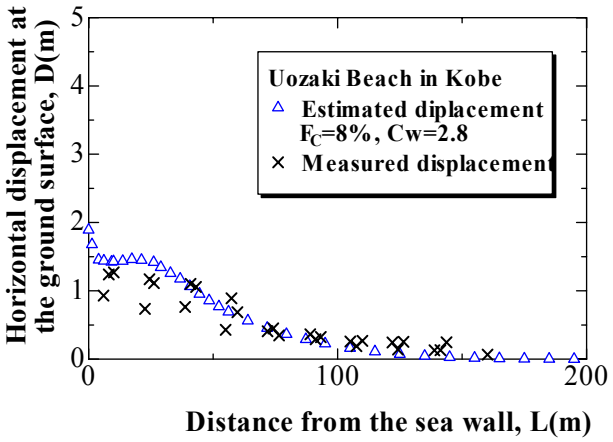

Figure 6 Measured and estimated displacement at Uozaki Beach in Kobe

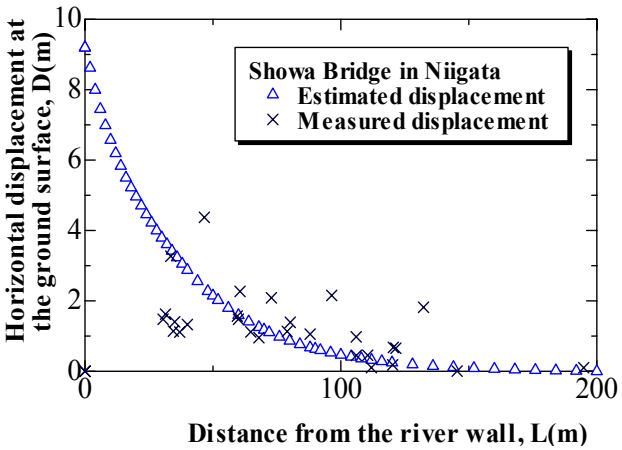

Figure 7 Measured and estimated displacement near Showa Bridge in Niigata

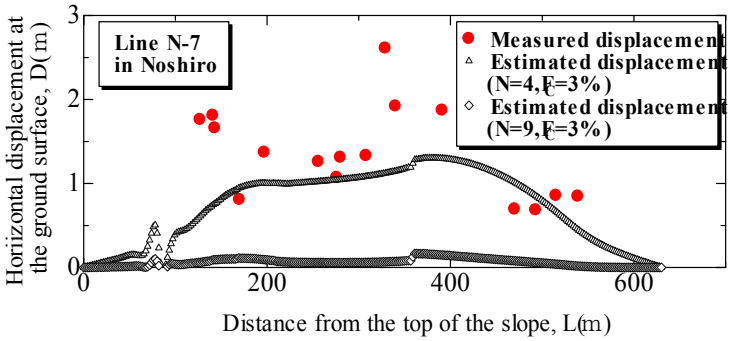

Figure 8 Measured and estimated displacement in Noshiro

A caisson type quay wall moved toward the sea and the ground behind the wall flowed at Uozakihama in Kobe during the 1995 Hyogoken-nambu earthquake. Horizontal displacement of the wall was 2.0 m and the flow extended to more than 100 m from the wall. Figure 6 shows the analyzed result. Estimated horizontal displacement and extended area were similar as the actual values.

Many sheet type walls moved and tilted toward Shinano River and brought severe ground flow behind the walls during the 1964 Niigata earthquake. Several meters movement occurred near Showa Bridge as shown in Figure 7. Estimated displacement agreed well with the measured displacement as shown in Figure 7.

A very gentle slope with the gradient of about 1 % flowed due to liquefaction in Noshiro City during the 1983 Nihonkai-chubu earthquake. Two values of SPT N-value were assumed in the analyses because only few Standard Penetration Tests have not been conducted in this area. Analyzed deformation showed that estimated displacement is fairly coincided with the measured displacement if small SPT N-value is assumed as shown in Figure 8.

ESTIMATION OF SUSCEPTIBILITIES FOR LIQUEFACTION-INDUCED FLOW IN TOKYO

Estimation of Safety Factor against Liquefaction

As huge number of soil investigation has been conducted in Tokyo, the authors collected the boring data in the lowland and reclaimed land zones. Liquefiable layers and safety factor against liquefaction, F_L at the boring sites were estimated by the simple method introduced in the specification for Highway Bridges in Japan (1996)[5]. Though huge numbers of SPT N-values were collected, only few data on fines content were collected. Then the authors tried to estimate the fines content based on the relationship between SPT *N*-value and fines content as shown in Figure 5. There is a unique relationship between SPT *N*-value and fines content for alluvial sands in Tokyo. And the alluvial sand layers contain much fines such as 10 to 30 % as shown in Figure 9.

Estimated Displacement at Gentle Slopes

By assuming the maximum surface acceleration as 400 gals, the distribution of liquefaction potential, P_L (Iwasaki et al. 1978 [6]) was evaluated. Then the sites where P_L is greater than 5 were assumed to be the prone sites for the flow if the ground surface is inclined more than 1 %. The gradient of the ground surface was measured by contour lines on a detailed topographic map. The

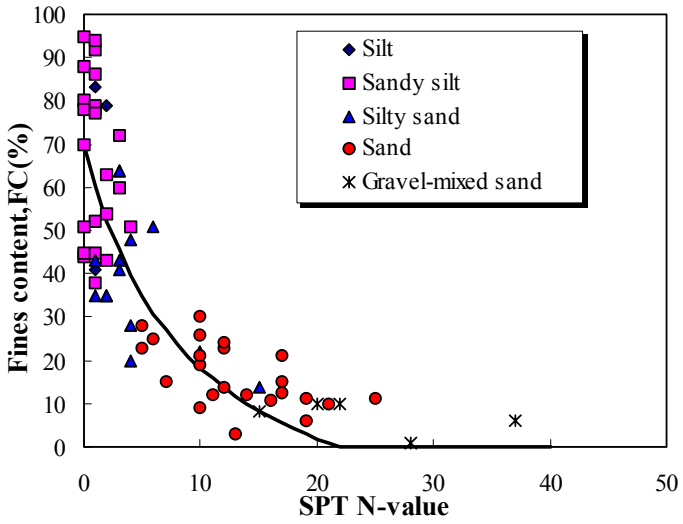

Figure 9 Relationship between SPT *N*-value and fines content of alluvial sands in Tokyo

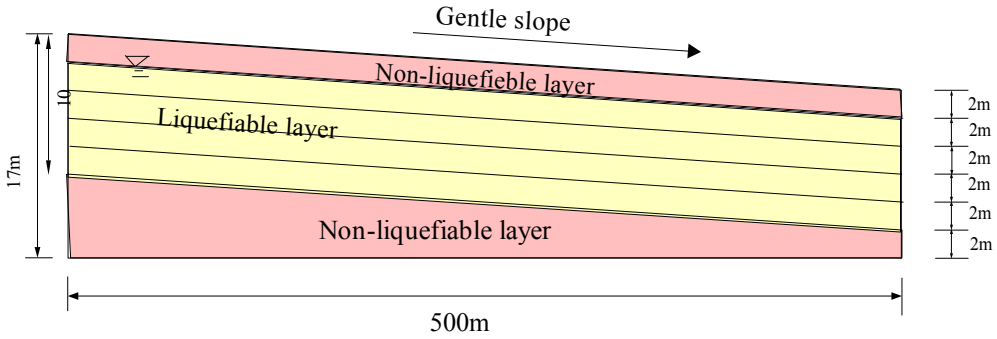

Figure 10 Model ground for gentle slope

gradient of the selected sites was 1 % to 3 %. Estimated thickness of the liquefiable layer was 2 m to 8 m. Then the model ground as shown in Figure 10 was assumed. Fines content, F_c of the liquefiable layer was assumed as 0 % to 40 % based on the data shown in Figure 10. Then the analyses for liquefaction-induced deformation were carried out by the "ALID" under the condition of several gradient, fines content, thickness of liquefiable layer and safety factor against liquefaction.

Figures 11 and 12 show the relationship among the analyzed horizontal displacement at the ground surface, thickness, F_L and F_c of the liquefiable layer under the gradient of 1%. The horizontal displacement increased with the thickness of the liquefiable layer and decreased with F_c and F_L. Though figures are not shown here, the horizontal displacement increased with the gradient of the ground surface.

Base on these figures, horizontal displacements at the selected sites were estimated. Figure 13 shows the distribution of displacements at Ohmori district where flow was occurred during the 1923 Kanto earthquake mentioned before. The estimated horizontal displacements in this district were 0.08 m to 0.14 m. These displacements are quite smaller than the displacements which occurred in Noshiro City during the 1983 Nihonkai-chubu earthquake. Main reason of the difference must be attributed to the difference of fines content of the sands in each city. To assist this assumption, additional analyses were carried out for clean sand layer by using the same model shown in Figure 10.

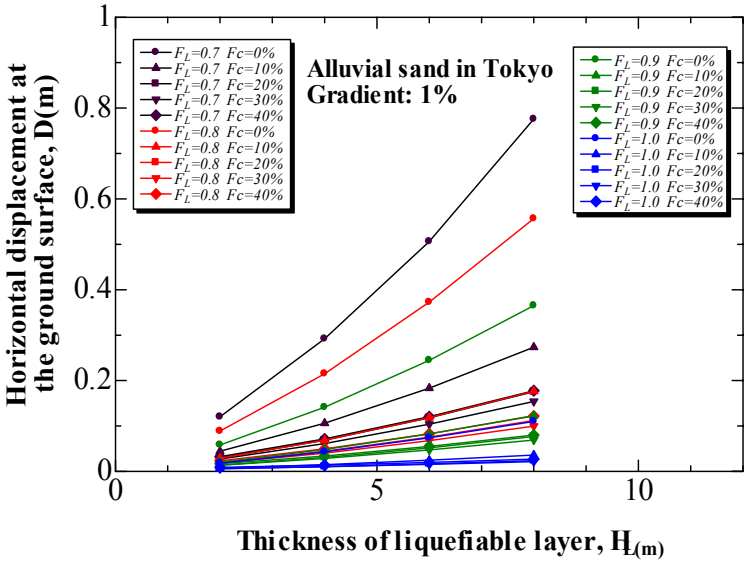

Figure 11 Relationship between thickness of liquefiable layer and horizontal displacement in Tokyo

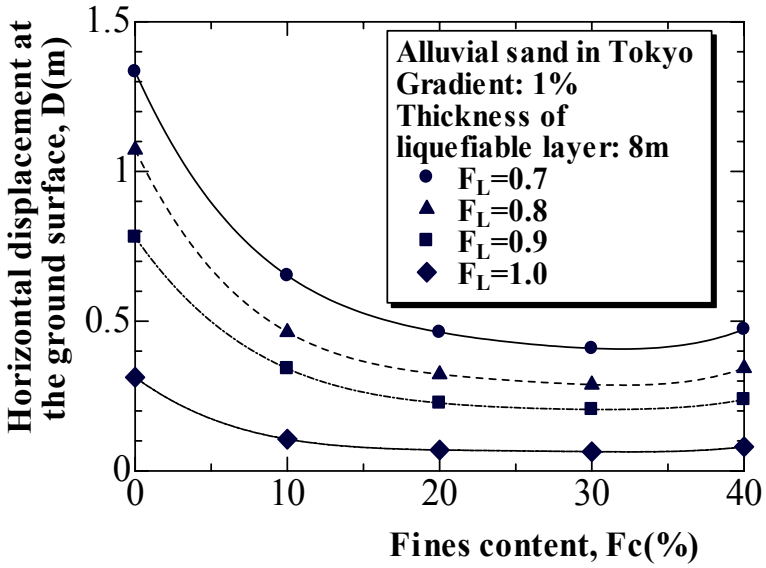

Figure 12 Relationship between fines content of liquefiable layer and horizontal displacement in Tokyo

The analyzed results were shown in Figure 14. In the analyses, SPT *N*-value was assumed as not related with fines content. As shown in Figure 14, the displacement at the ground surface is large as 1 to 4 m if liquefiable layer does not contain fines.

Based on the analyses, the following simple formula for alluvial sand in Tokyo was derived:

$$D=0.0225(H_L)^{1.18}(\alpha)^{0.871}(F_L)^{-4.31}(Fc)^{-0.578} \quad (3)$$

(*Fc* must be assumed as 2.16 if *Fc* is less than 2.16)

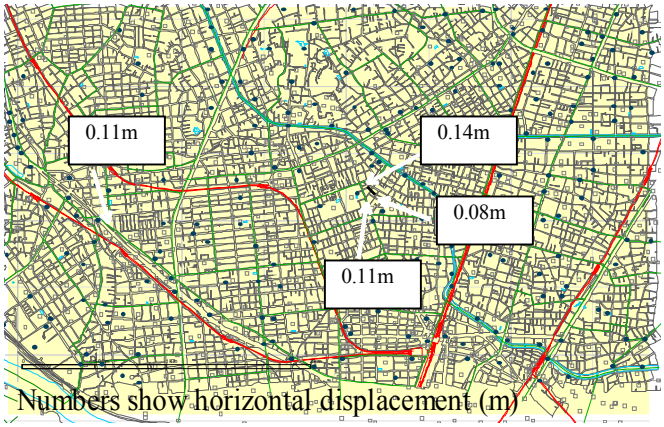

Figure 13 Estimated distribution of horizontal displacements at Ohmori district

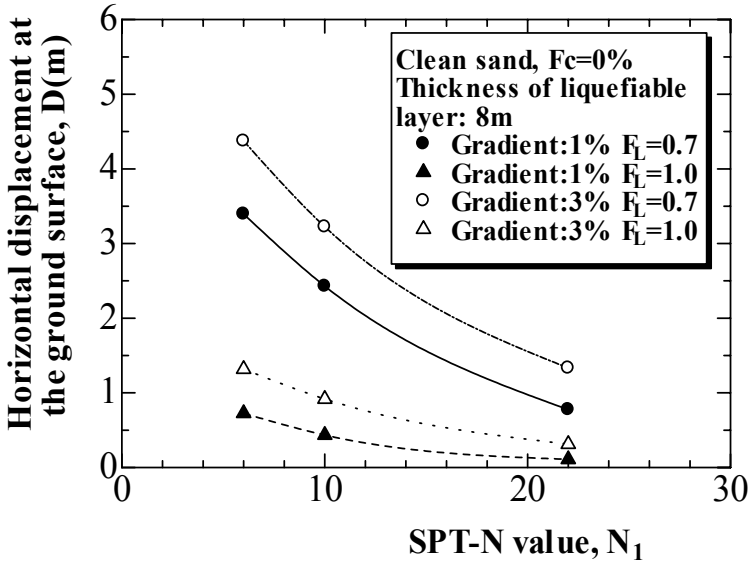

Figure 14 Estimated relationship among displacement, SPT N-value, gradient and F_L for clean sand

Where, D: displacement at the ground surface (m), H_L: thickness of liquefiable layer (m), α: gradient (%), F_L: safety factor against liquefaction and Fc: fines content (%).

Estimated Displacement behind River Walls

Almost all of quay walls for ships along Tokyo Bay have been designed by considering liquefaction. Deep river and sea walls have been treated to strengthen against liquefaction. Therefore, shallow river walls have the possibility of the damage due to liquefaction-induced ground flow. Then the analyses were carried out on the shallow river walls.

There are two types of river walls in Tokyo: gravity type of wall and sheet pile type wall. Figures 15 and 16 show typical cross sections of the gravity type wall and the sheet pile type wall, respectively. In the gravity type wall, a L type concrete wall is supported by pile foundations. The analyses were carried out for two depths of water, 1 meter and 3 meters. Thickness, F_c and F_L of

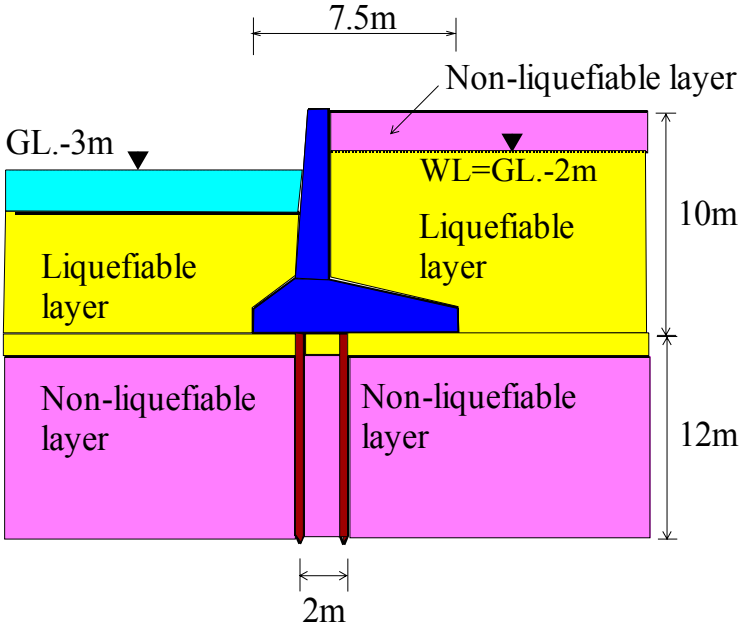

Figure 15 Typical cross section of gravity type wall in Tokyo

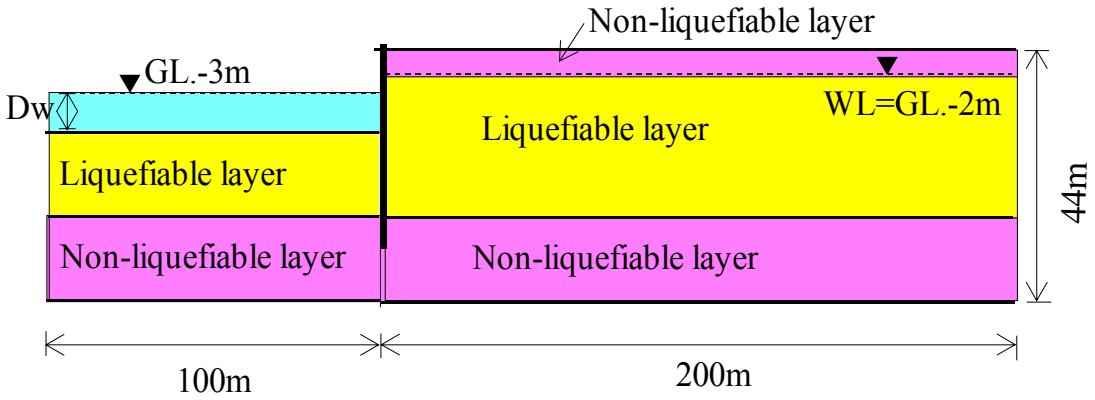

Figure 16 Typical cross section of sheet pile type wall in Tokyo

liquefiable layer were varied as 4 meters to 12 meters, 0 % to 30 %, 0.7 to 1.0, respectively. The analyses for the sheet pile type wall were conducted under the similar conditions of the water depth and the liquefiable layer.

Figures 17 and 18 show horizontal displacement at the ground surface behind the wall under the conditions of 3 meter of the water depth and F_L=0.7. The horizontal displacement decreased with the distance from the wall. Displacement at a distance increased with the thickness of the liquefiable layer and decreased with F_c. According to Figures 17 and 18, displacement near river wall is 0.5 to 2.5 m.

Based on the analyses, the following simple formulae for alluvial sand in Tokyo were derived:

For gravity type wall: $D_{max}=0.000607(H_L)^{2.99}(Hw)^{0.125}(F_L)^{-0.466}(Fc)^{-0.365}$ (4)

(Fc must be assumed as 5.79 % if Fc is less than 5.79 %)

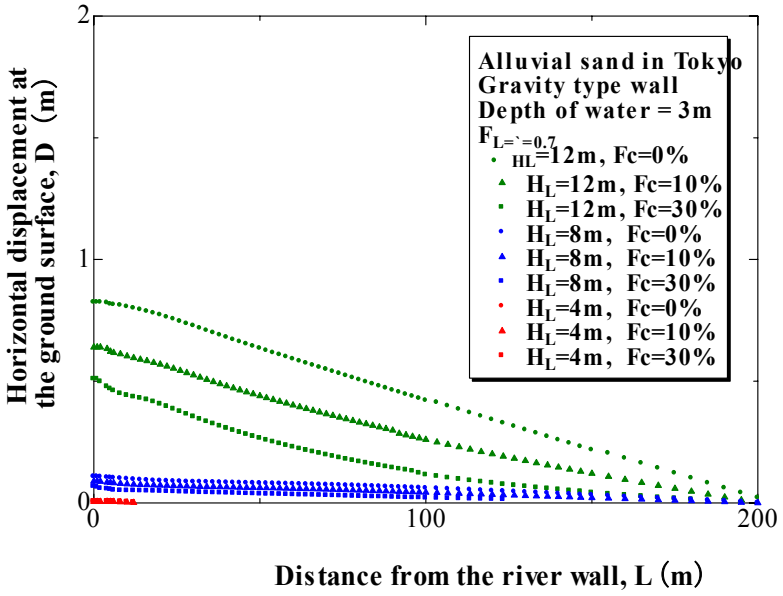

Figure 17 Horizontal displacement at the ground surface behind the gravity type wall in Tokyo

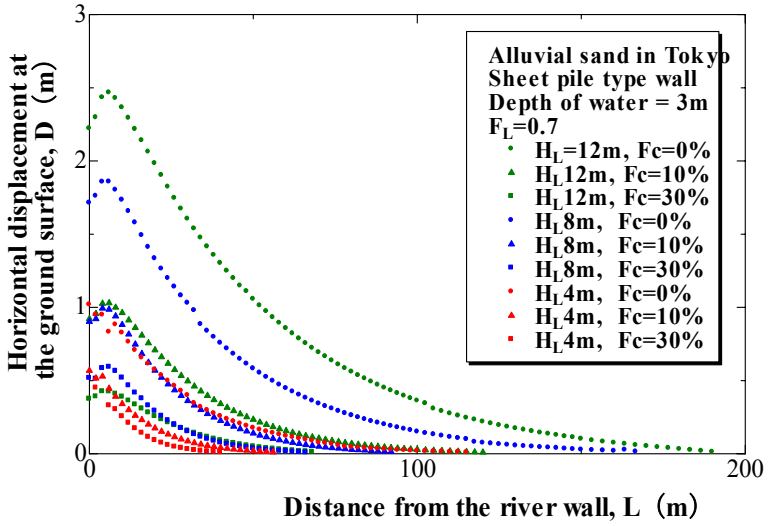

Figure 18 Horizontal displacement at the ground surface behind the sheet pile type wall in Tokyo

For sheet type wall: $D_{max}=0.23\ 7(H_L)^{0.692}(Hw)^{0.178}(F_L)^{-3.17}(Fc)^{-0.461}$ (5)

(*Fc* must be assumed as 3.27 % if *Fc* is less than 3.27 %)

Where, D_{max}: displacement at the ground surface near wall (m), H_L: thickness of liquefiable layer (m), *Hw*: depth of water (m), F_L: safety factor against liquefaction and *Fc*: fines content (%).

CONCLUSIONS

Distribution of horizontal displacements due to liquefaction-induced flow in Tokyo during future earthquakes was estimated based on a simple analytical method "ALID." The following conclusions were derived through the analyses:

1. Two types of liquefaction-induced flow, flow on gentle slopes and flow on the ground behind river walls were estimated to have been induced in Tokyo.
2. The horizontal displacement due to the flow on the gentle slope is not so large e.g. less than 0.5 m, and is affected by thickness of liquefiable layer, gradient, Fc and F_L.
3. The flow behind river walls is 0.5 m to 2.5 m and is affected by type of the wall, thickness of liquefiable layer, Fc and F_L

ACKNOWREGEMENT

This study was organized by the Association for Development of Earthquake Prediction. The authors would like to express sincere appreciations to the members in the committee for the fruitful discussion and suggestions.

REFERENCES

[1] Yasuda, S. & J. Berrill 2000. "Observation of the earthquake response of foundations in soil profiles containing saturated sands." *1st International Conference on Geotechnical and Geological Engineering –GeoEng2000*, Issue Lecture, pp.1441-1470.
pp.885-896.

[2] Kuribayashi, E. & F. Tatsuoka 1975. "Brief review of liquefaction during earthquakes in Japan," *Soils and Foundations,* Vol.15, No.4, pp.81-92.

[3] Yasuda, S., N. Yoshida, K. Adachi, H. Kiku & S. Gose 1999. "A simplified analysis of liquefaction-induced residual deformation." *2nd International Conference on Earthquake Geotechnical Engineering*, pp.555-560.

[4] Yasuda, S., T. Terauchi, H. Morimoto, A. Erken & N. Yoshida 1998. "Post liquefaction behavior of several sands," *Proc. of the 11th European Conference on Earthquake Engineering.*

[5] The Japan Road Association. 1996. "Specification for Highway Bridges." (in Japanese)

[6] Iwasaki, T., F. Tatsuoka, K. Tokida & S. Yasuda 1978. "A Practical method for assessing soil liquefaction potential based on case studies at various sites in Japan," *Proc. of the 2nd International Conference on Microzonation*, Vol.2,

Fault Ruptures, Ground Movement and Their Effects on Structures

Actual observations and numerical simulations of surface fault ruptures and their effects on engineering structures

Ömer Aydan

ABSTRACT

As observed after each large earthquake resulting in surface fault breaks through cities and towns, the authorities and engineers are severely critisized by particularly some disciplines of earth science and mass media for the development of cities, infra structures as well as industrial facilities in regions with active fault zones. If the points of their critization and suggestions are taken into account, it should not be possible to build any structure in seismically very active countries such as Turkey, Japan, India, Taiwan, the Western part of USA while the societies of these countries demand better living environments. Therefore, the ways for dealing with the designing and building structures in active fault zones must be found by the scientists and engineers rather than just turning their heads other way. The main purpose of this article is to illustrate surface fault ruptures and their effects on structures for the fundamental modes of faulting during earthquakes through actual observations and numerical simulations, which may be useful in developing some guidelines for the seismic design associated with surface fault ruptures.

INTRODUCTION

Recent large earthquakes in Turkey and Taiwan resulted in a paramount concern in earthquake engineering how to design such structures in the events of surface faulting, which takes place just beneath the structures. An extensive survey of types of damage to structures by faulting are presented by Aydan et al. 1999 and Ulusay et al. 2001. Various model tests on the occurrence and propagation of ground breaks induced by fault beneath the thick sedimentary deposits have been now carried out in various institutes in USA and in Japan. Experimental tests and numerical simulations are also carried out to investigate how surface fault ruptures develop and their effects on structures. For the assessment of their effects on structures, several numerical models have been utilized which have been originally developed in the field of rock mechanics and rock engineering. These methods are finite element methods with joint or interface elements (FEM-J, FEM-I), Distinct Element Method (DEM), Displacement Discontinuity Analysis method (DDA), Displacement Discontinuity Method (DDM) and Discrete Finite Element Method (DFEM). Kawamoto and Aydan (2000) gave an extensive summary of these methods.

This particular study is concerned with the actual observations and numerical simulations of surface fault ruptures and their effects on structures, associated with normal, strike-slip and thrust faulting events. DFEM is used for the simulation of fault propagation and fault-structure interaction. In the simulations of fundamental faulting modes such as normal, thrust and strike-slip faulting mechanisms are considered. The fault-structure interaction problem is studied by simulating the behaviour of a simple truss structure under normal and thrust

Ömer Aydan*, Professor, Tokai University, Marine Civil Eng. Dept. , 3-20-1 Orido, Shimizu ,Japan 424-8610
ditto * Adjunct Professor, Istanbul Technical University, Mining Faculty, Maslak, Istanbul ,Turkey

type faulting conditions. The main intention of this study is illustrate the effects of surface fault ruptures on structures for the fundamental modes of faulting during earthquakes through actual observations and numerical simulations, which may be useful in developing some guidelines for the seismic design associated with surface fault ruptures.

ACTUAL OBSERVATIONS ON FAULT RUPTURES

The fault is geologically defined as a discontinuity in geological medium along which a relative displacement took place. Faults are broadly classified into three big groups, namely, normal faults, thrust faults and strike-slip faults as seen in Figure 1. A fault is geologically defined as active if a relative movement took place in a period less than 2 millions years. On the other hand, the service life of engineering structures could not generally be greater than 100-150 years. Taking this fact into consideration, there were new attempts to define active faults for engineering purposes by various US government agencies defined the active faults.

However, these diverse definitions, based on the agency's perception of risk, also lead to confusion. It is well known that a fault zone may involve various kinds of fractures and it is a zone having a finite volume (Aydan et al.1997). In other words, it is not a single plane. Furthermore, the faults may have a negative or positive flower structure as a result of their trans-tensional or trans-pressional nature and the reduction of vertical stress near the earth surface (Aydan et al. 1999). For example, even a fault having a narrow thickness at depth may cause a broad rupture zones and numerous fractures on the ground surface during earthquakes. In addition to that, it is impossible to say the same ground breaks will re-rupture in the next earthquake in regions with thick alluvial deposits. The ground breaks may be caused by the relative motions of the faults beneath these sedimentary deposits. The appearance of ground breaks is closely related to geological structure, characteristics of sedimentary deposits, their geometry, the magnitude of earthquakes and fault movements. Although this problem was studied in the field of structural geology, there is a great interest in the ground break propagation in sedimentary deposits above the active faults in earthquake engineering. Many model tests in laboratory and field observations on actual fault breaks are carried out by various researchers under mostly constant velocity field. There is still a sufficient room for further studies on fault propagation under constant acceleration field which may be more relevant to the actual conditions.

(a) Normal faulting (b) Strike-slip faulting (c) Thrust faulting

Figure 1: Some examples of faulting

ACTUAL OBSERVATIONS ON THE INTERACTION BETWEEN FAULT RUPTURES AND STRUCTURES

In this section, various typical examples of damage to structures induced by the fault-breaks observed in recent large earthquakes in Turkey, Japan and Taiwan are presented.

Roadways and Railways

The Trans-European Motorway (TEM) was damaged at three different locations by the earthquake fault caused by the 1999 Kocaeli earthquake. The motorway with east and west bounds having 3 lanes each is slightly elevated through embankments in the earthquake affected region. The surfacing of the motorway was damaged by rupturing and buckling as seen in Figure 2. The railways were also built on the existing ground surface. The railways were buckled near Tepetarla station where the earthquake fault crossed the railways at an angle of 50-55^0 with well known 'S' shape (Figure 3).

Figure 2: Buckling of roadway surfacing

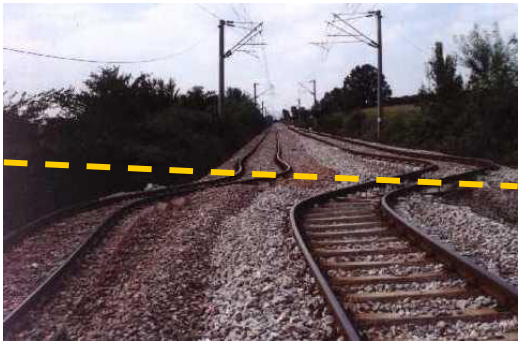

Figure 3: Buckled railways

Bridges and Viaducts

Along the damaged section of the TEM motorway, there were several overpass bridges. Among them, a four span overpass bridge at Arifiye junction collapsed as a result of faulting (Figure 4). The fault rupture passed between the northern abutment and the adjacent pier. The overpass was designed as a simply supported structure according to the modified AASHTO standards and girders had a elastrometric bearings. However, the girders were connected to each other through prestressed cables. The angle between the motorway and the strike of the earthquake fault was approximately 15^0 while the angle between the axis of the overpass bridge and the strike of the fault was 65^0. The measurements of the relative displacement in the vicinity of the fault ranges between 330 and 450 cm. Therefore an average value of 390 cm could be assumed for the relative displacement between the pier and the abutment of the bridge. The Pefong bridge collapsed due to the fault break due to thrust faulting, which passed between the piers near its southern abutment as seen in Figure 5.

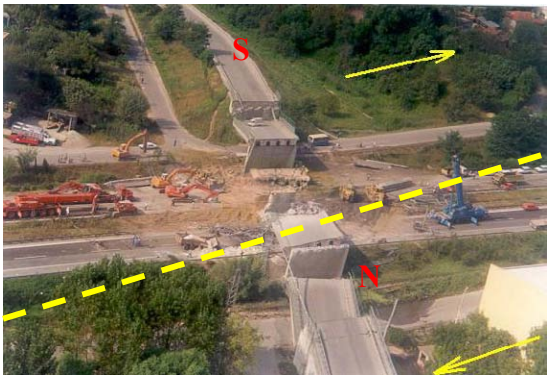

Figure 4: The collapse of the overpass bridge at Arifiye

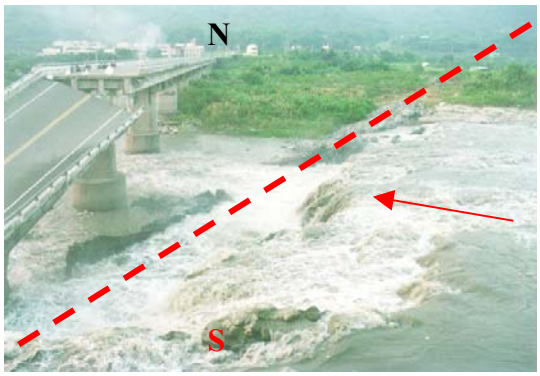

Figure 5 Collapse of Pefong Bridge (note the uplifed ground on RHS)

Dams

The nearest dam was Yuvacık dam in the earthquake affected area in the 1999 Kocaeli earthquake, which is an earthfill dam with a height of 40m. Although this dam was at a distance of 10km to the earthquake epicenter, no failure was observed. The Shihkang dam, which is a concrete gravity dam with a height of 25m, was ruptured by the thrust type faulting during the 1999 Chi-Chi earthquake (Figure 6). The relative displacement between the uplifted part of the dam was more than 980cm. Liyutan rockfill dam with a height of 90m and a crest width of 210m, which was on the overhanging block of Chelongpu fault was not damaged even the acceleration records at this dam showed that the acceleration was amplified 4.5 times of that at the base of the dam (105 Gal).

Figure 6: Failure of Shihkang dam due to faulting

Figure 7: Collapse of Bolu tunnel in squeezing ground

Tunnels

The past experience on the performance of tunnels through active fault zone during earthquakes indicates that the damage is restricted into certain locations. Portals and the locations where the tunnel crosses the fault may be damaged as it occurred in the 1999 Chi-Chi earthquake. A section nearby Elmalık portal of Bolu Tunnel was collapsed. This section of the tunnel was excavated under very heavy squeezing conditions (Aydan and Dalgıç 1999) The well known examples of damage to tunnels at locations, where the fault rupture crossed the tunnel, are mainly observed in Japan. The Tanna fault ruptured during 1977 Izu earthquake caused damage to a railway tunnel and the relative displacement was about 100cm. Similar type damage with a small amount of relative displacements due to motions of Rokko, Egeyama and Koyo faults to the tunnels of Shinkansen and subway lines through Rokko mountains were also observed (Aydan 1996). During the 1999 Chi-Chi earthquake, the portal of the water intake tunnels was ruptured for a distance of 10m as a result of thrust faulting. Except this section, the tunnel was undamaged for its entire length.

Figure 8 The collapse of Daikai station

Subways

The behaviour of subways in active fault zones are basically quite similar to that of tunnels. the Daikai station of the subway line in Kobe was caused by the lateral strike-slip movement of Egeyama fault just beneath this station although some tried to associate the collapse of the station with the intensity of shaking (Figure 8). The investigation of the collapse of this station by the first author showed that the collapse was not

due to shaking as the central columns of the station were subjected to torsional failure due to the permanent ground displacement, which was consistent with the lateral strike-slip movement of Egeyama fault (Aydan 1996). As the cities in the earthquake affected regions had no subways lines during the 1999 Kocaeli and Chi-Chi earthquakes, it is difficult to draw any further conclusion.

Power Transmisson Lines

Power transmission lines generally consist of pylons and power transmission cables. The design of pylons and cables are generally based on the wind loads resulting from typhons or hurricanes. Additionally, the possibility of slope failure of the pylon foundations is considered in the design of pylons. The cables do not fail during earthquakes unless the pylons are toppled due to faulting, shaking or slope failure. During the 1999 Kocaeli earthquake, only one pylon was damaged nearby Ford-Otosan automobile factory at Kavaklı district of Gölcük town. At this site a normal fault, which is a secondary fault to the main lateral strike-slip faulting event, crossed through the foundations of the pylon and its vertical throw was about 240cm . One of the foundations of the pylon was pulled out of the ground and was exposed as seen in Figure 9(a). Some of its truss elements were slightly buckled. Nevertheless, the damage to the pylon was quite limited and this damage could not hinder its function. Similar type damage to pylons straddling the Nojima fault break in the 1995 Kobe earthquake (Figure 9(b)) and the Chelungpu fault during the 1999 Chi-Chi earthquake were observed as shown in Figure 9(c).

(a) 1999 Kocaeli earthquake (b) 1995 Kobe Earthquake (c) 1999 Chi-chi Earthquake

Figure 9 Damage to pylons due to faulting

Line-like & Tubular Structures

Tubular structures may be specifically designated as petrol and gas pipe-lines, water pipes and sewage systems. They can be also classified as line-like structures. These structures may fail either by buckling or separation during a faulting event. Five such incidents were observed during the 1999 Kocaeli earthquake (Figure 10). One of the incidents involved the separation of a ductile iron pipe as a result of faulting near the collapsed overpass bridge. The second incident took place at the pumping facility of the Seka papermill plant at Sapanca Lake. The third incident occurred near Tepetarla village where the railways were buckled. The fourth and fifth incident took place at Arifiye and nearby Başiskele. The fifth incident was quite important since the fault caused a heavy damage to the main water-pipe having a diameter of 2m. Similar type of failures took place in the sewage pipe networks whenever faulting breaks were observed. The natural gas pipelines lines crossing the İzmit Gulf between Yalova and Pendik was undamaged. Some brittle asbestos water pipes were also damaged in Kaynaşlı and Fındıklı due the fault rupture of the 1999 Düzce earthquake. Although it is difficult to prevent damage to tubular structures, the use of flexible joints may be effective in such active fault zones when they are embedded.

Figure 10 Damage to pipes in the 1999 Kocaeli and 1999 Düzce earthquakes

Buildings

Many buildings along the earthquake faults of the 1999 Kocaeli, Düzce and Chi-Chi earthquakes behaved in various manner. During the site investigation of the 1999 Kocaeli earthquake one could see either totaly collapsed, severly damaged or intact buildings just on or next to the traces of the fault breaks. The examples are many and it is quite difficult to quote all of them. Two typical examples are given and briefly discussed. Nevertheless, this topic deserves more thorough investigations. The first example is a single story reinforced concrete house with a raft foundation in Fındıklı village. The fault passed just underneath the building (Figure 11). The relative displacement of the fault break was about 200cm with a 100cm downthrow. The building was tilted but no damage to this building was observed. A very peculiar behaviour of an apartment complex consisting of 8 five story apartment blocks was observed in Kullar village as shown in Figure 12. Seven apartment blocks failed in a pancake mode while one apartment block remained self-standing. One of the failed apartment blocks just crossed by the fault break which has a relative horizontal displacement of 240cm and 20-25cm vertical throw (north side down). The ground surface was sloping to north. One of two apartment blocks on the southern side was damaged while the other one collapsed towards east in a pancake mode in accordance with the movement of its foundation. The 5 blocks on the northern side were competely collapsed in a pancake mode towards west in accordance with the direction of shaking. Except the apartment block over the fault break, the failure of 5 blocks on the northern side of the fault break may be considered to be purely due to shaking. Although the intensity of shaking on the southern side of the fault break should be the same, the damaged self-standing apartment block should deserve some special consideration. Whatever the reason is, it

is of great interest that the most vulnerable buildings may also survive within a distance of 5 to 6m to the fault break during the in-land earthquakes.

Figure 11: The behaviour of a single story reinforced building at Fındıklı

Figure 12: The collapse of apartment blocks at Kullar village

NUMERICAL SIMULATIONS

Fault Propagation Simulations

Aydan and Mamaghani proposed the discrete finite element method (DFEM) for blocky systems which is based on the principles of the finite element method (Aydan et al., 1996, Mamaghani et al., 1994, 1998). It is possible to handle deformable blocks and contacts that specify the interaction among them. Small displacement theory is applied to intact blocks while blocks can take finite displacement, Blocks are polygons with an arbitrary number of sides which are in contact with neighboring blocks, and are idealized as a single or multiple finite elements. Block contacts are represented by a contact element, which has a finite thickness.

In this study, a pseudo-dynamic procedure of this method is employed so that intact blocks and block contacts can behave elasto-plastically. The method of analysis is a pseudo time stepping incremental procedure. To model the elasto-plastic response of materials and contacts in numerical analysis, the initial stiffness method was employed together with the use of *Updated Lagrangian Scheme*.

Table 1 gives the materials properties used in discrete finite element method simulations. The thickness of the fault plane was selected as 10mm in view of past experiences. In the simulations the fault plane was modeled through contact elements. The fault plane behaves elastically when the normal and shear stresses are below its yield strength. However, if yielding takes place, its behaviour is simulated as an elastic-perfectly plastic behaviour. In normal and thrust faulting the displacements having an amplitude of 10cm are imposed at the boundary nodes as indicated in Figure 13 both in x and y directions. As for the strike-slip faulting simulation, the prescribed displacements of 10cm are imposed only in y-direction at selected points shown in Figure 13(b). Figures 14(a)-(c) show the deformed configurations of the model at computation step 1 and 10. The computed results for Step 1 correspond to initial elastic responses after the prescribed displacement conditions being imposed. Results at computation Step 10 correspond to the fault propagation if yielding along the fault plane takes place. After a certain number of computation steps, the deformation of the fault tends to become stationary for the prescribed displacement boundary conditions. The propagation of faults start at the bottom side and migrates towards the ground surface as expected. These three specific examples clearly show that the method used is capable of simulating the fault propagation processes for three different faulting modes.

Table 1 Materials properties used in discrete finite element method simulations.

Material	λ (MPa)	μ (MPa)	γ (kN/m^3)	c (MPa)	ϕ (^{o})	σ_t (MPa)
Solid	2000	2000	26	-	-	-
Fault	50	50	-	0.0	40	0.0

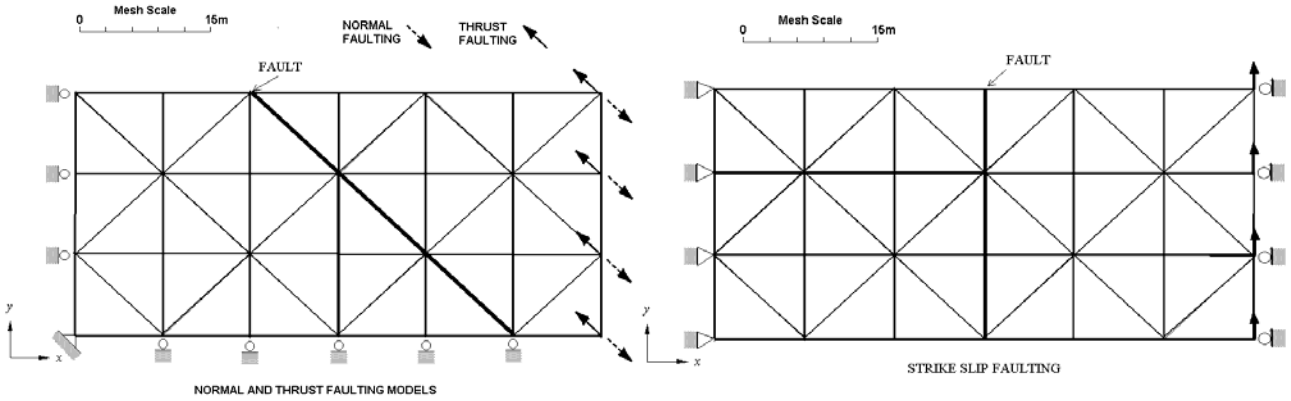

(a) Normal faulting and Thrust faulting mesh (b) Strike-slip faulting mesh

Figure 13 Finite element meshes and boundary conditions used in simulations

(a)

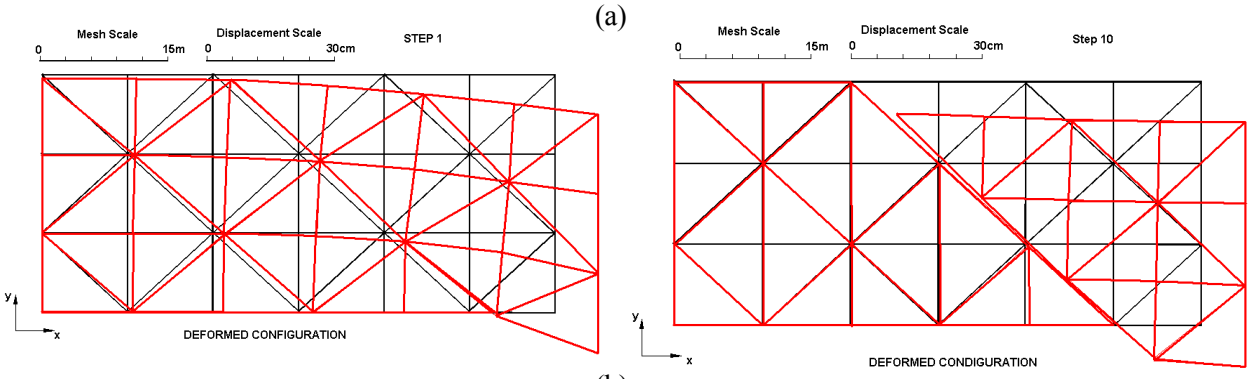

(b)

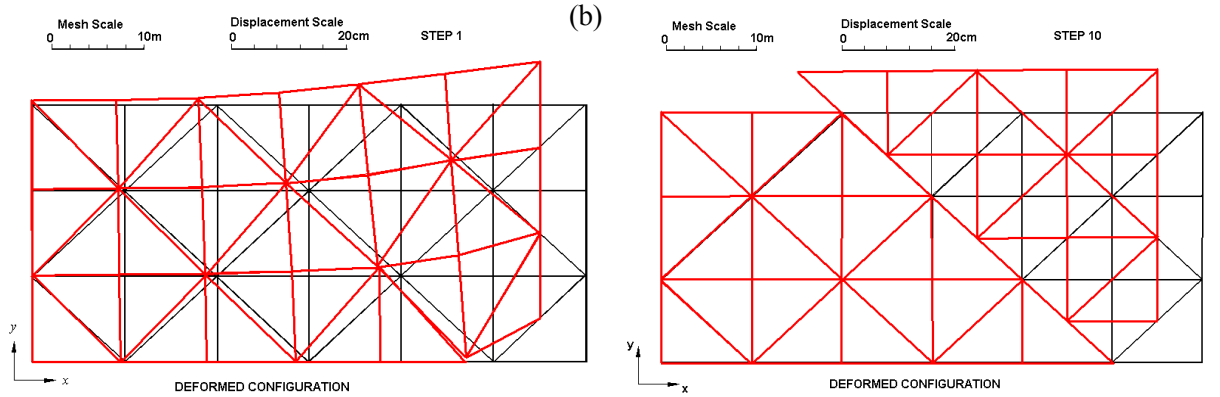

(c)

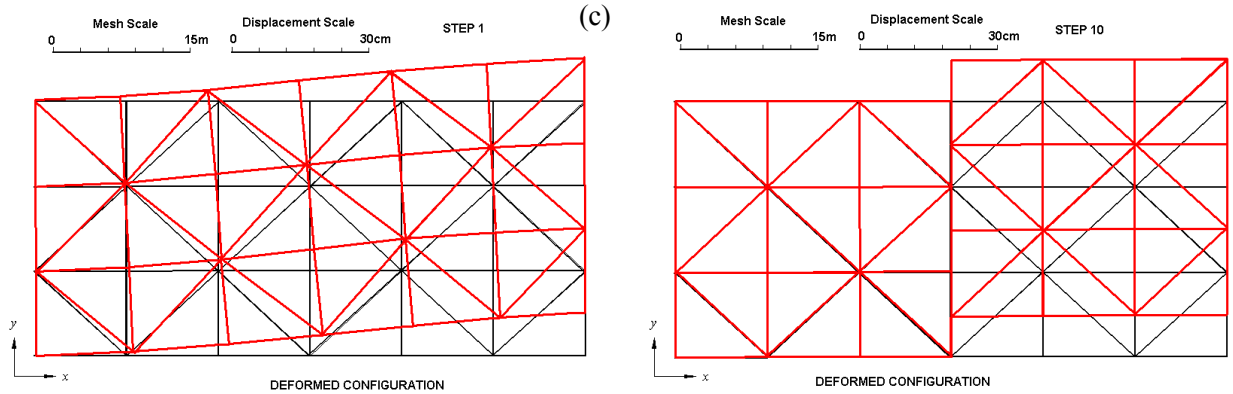

Figure 14 Deformed configurations at Steps 1 and for (a) normal faulting; (b) thrust faulting; (c) strike-slip faulting simulations

Fault-Structure Interaction Simulation

The most important aspect in earthquake engineering is the interaction between structures and fault breaks. For this purpose, a truss structure straddling over the projected fault trace on the ground surface was considered, and normal faulting and thrust faulting conditions are imposed through prescribed displacement at selected points as in the previous computations. The material properties for solid and fault are the same as those given in Table 1. The elastic modulus and the cross-section area of a typical truss were chosen as 90 GPa and 0.1 m^2 and their behaviour was assumed to be elastic. Figure 15 shows the finite element meshes and boundary conditions used in simulations. Figure 16 shows the deformed configurations at computations steps 1 and 10 for normal and thrust type faulting modes. In both cases, the truss structure tilts. While the thrust type faulting causes the contraction of trusses, the normal faulting condition results in the extension of trusses and separation of the supporting members fixed to the ground. These responses resemble to those shown in Figure 9. Although trusses were assumed to be behaving elastically in these simulations, it is quite easy to implement their elasto-plastic behaviour within the DFEM.

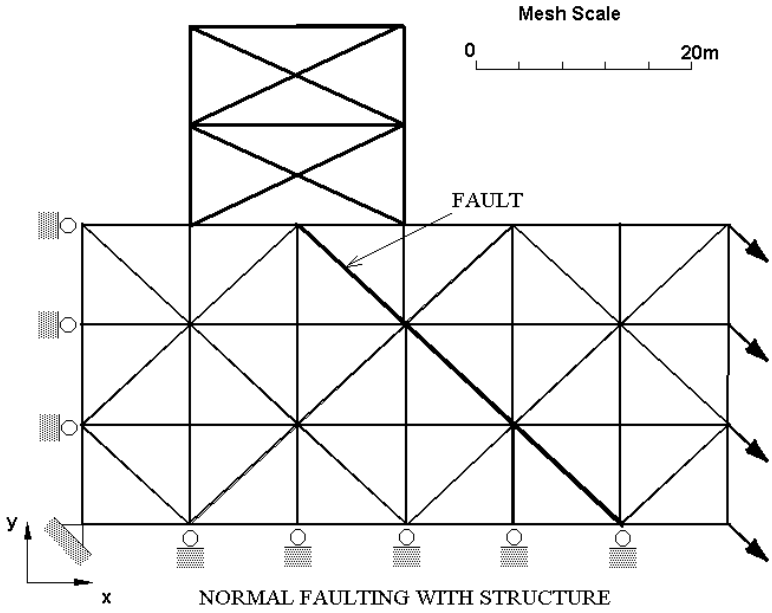

Figure 15 Finite element meshes and boundary conditions for fault-structure interaction simulations

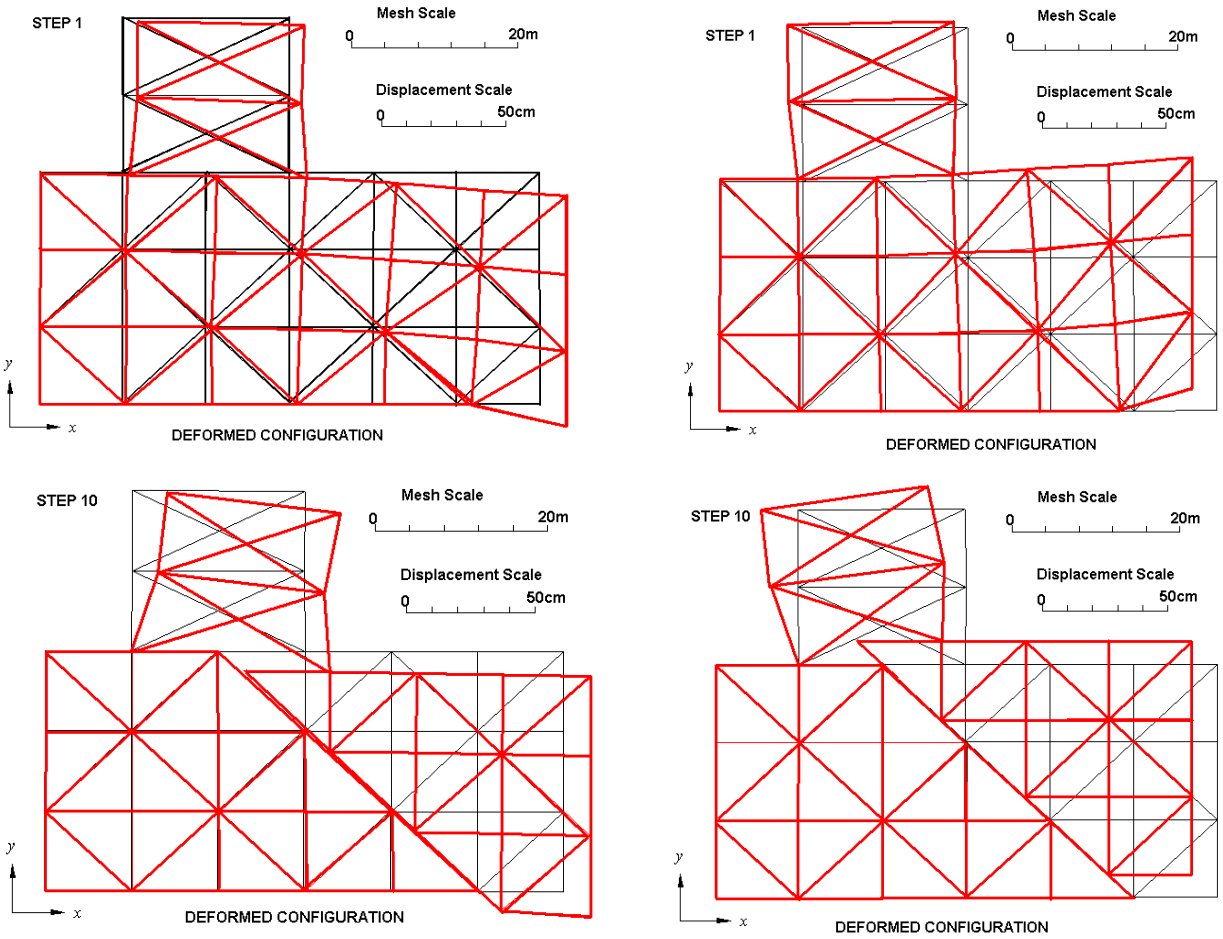

(a) Normal faulting (b) Thrust faulting

Figure 16: Simulations of the fault-structure interaction for normal faulting and thrust conditions

CONCLUSIONS

In this article, the actual observations surface fault ruptures and their effects on structures, associated with normal, strike-slip and thrust faulting events have been described. As for numerical simulations, Discrete Finite Element Method (DFEM) is used for the simulation of fault propagation and fault-structure interaction. In the simulations fundamental faulting modes such as normal, thrust and strike-slip faulting mechanisms are considered. The computational results clearly demonstrated that the DFEM is capable of simulating both the fault propagation and fault-structure interaction, although a simple version of this method is used. Nevertheless, it is possible to use the other versions of the DFEM depending upon the available information on the characteristics of solid and fault planes. It is hoped that actual observations and numerical simulations described in this article may be useful in developing some guidelines for the seismic design associated with surface fault ruptures.

REFERENCES

Aydan, Ö., I.H.P. Mamaghani, T. Kawamoto 1996. Application of discrete finite element method (DFEM) to rock engineering structures, *NARMS '96*, 2039-2046.

Aydan, Ö., Ulusay, R., Hasgür, Z., and Taşkın, B., 1999. *A site investigation of Kocaeli Earthquake of August 17, 1999*". Turkish Earthquake Foundation, **TDV/DR 08-49**, 180pp.

Aydan, Ö., Ulusay, R., Kumsar, H. and Tuncay, E., 2000a.. *Site investigation and engineering evaluation of the Düzce-Bolu Earthquake of November 12,, 1999*. Turkish Earthquake Foundation, **TDV/DR 095-51,** 307pp.

Aydan, Ö., Ulusay, R., Hasgür, Z., and Hamada, M., 1999. The behaviour of structures built in active fault zones in view of actual examples from the 1999 Kocaeli and Chi-chi Earthquakes. ITU-IAHS International Conference on the Kocaeli Earthquake 17 August 1999: A Scientific Assessment and Recommendations for Re-building, İstanbul.

Aydan, Ö. and S. Dalgıç, T. Kawamoto (2000): Prediction of squeezing potential of rocks in tunnelling through a combination of an analytical method and rock mass classifications.*Italian Geotechnical Journal, Vol.34, No.1, 41-45*.

Mamaghani, I.H.P., S. Baba, **Ö. Aydan,** S. Shimizu 1994. Discrete finite element method for blocky systems, *Computer Methods and Advances in Geomechanics*, IACMAG, Morgantown,1, 843-850.

Kawamoto, T. and **Aydan, Ö.** (1999): A review of numerical analysis of tunnels in discontinuous rock masses. International Journal of Numerical and Analytical Methods in Geomechanics, Vol. 23, 1377-1391

Ulusay, R. **Aydan, Ö.,** Hamada, M. (2001): The behaviour of structures built on active fault zones: Examples from the recent earthquakes of Turkey. A Workshop on Seismic-Fault Induced Failures – Possible Remedies for Damage to Urban Facilities. 1-26, Tokyo, Japan.

Dynamic Simulation of Base Fault Motion for Studying Ground Surface Deformation

Kimiro Meguro and Pradeep Kumar Ramancharla

ABSTRACT

Over the past few decades, significant effort has been devoted to understand the problem of ground shaking. Accordingly, numerous design and construction procedures have been developed to minimize damage due to strong ground motion. However, the efforts towards improving our understanding of the problem of surface faulting have been relatively modest. In the conventional attenuation relationship, peak ground acceleration shows maximum values at the closest distance from the fault. However, in the real observations, sometimes it is found that the damage near to the surface fault is not maximum; instead it is high little away from the surface rupture zone. The common practice with important facilities such as dams, nuclear power plants, and public buildings has been to avoid construction across the recognized trace of an active fault. However, in case of the buried faults, our ability to delineate the possible potential hazard that can be caused due to the future rupture activity is far from complete.

Catastrophic earthquakes in the recent times have posed many new challenges to the engineering profession. To understand the phenomena of surface failure, many researchers conducted experiments. Cole and Lade have tried to determine the location of surface fault rupture and width of the affected zone in alluvium over dip-slip fault using fault test box. They hypothesized that the results may be applicable to cohesive materials. Lade et al. studied to determine the multiple failure surfaces by conducting the experiments on sand using fault test box. The results of the sand box model tests concluded that the observed displacement fields were nearly the same in different materials. Onizuka et al. have modeled the deformation of ground using aluminum rods. Through experiments, they investigated bedrock stresses induced by reverse dip-slip faults. Bray investigated the pattern of ruptures in clay models under 1-g subjected to dip-slip faulting. Tani et al. conducted a 1-g model study of dip-slip faulting using dry Toyoura sand as model material. Results from their tests indicated that the base offset necessary for the rupture to propagate to the ground surface varied with fault orientation. These observations are in agreement with those from the study of Cole and Lade.

Using the above experimental methods, we can find the affected length on the surface. However, replicating the actual field conditions using experiments is very difficult, especially, controlling the material properties and modeling the boundary conditions. Moreover, large amount of data is necessary to establish a relationship between seismic fault parameters and resulting surface deformation.

On the other hand, studying this phenomenon using numerical model has the advantage of controlling the parameters like material properties, size of the model, boundary condition, dip angle, etc. Numerical model allow us to investigate a number of aspects of the fault rupture propagation phenomenon, which are difficult to study from the examination of case histories and the conduct of physical model tests. It allows for the behavior of the soil and the imposed boundary conditions. However, the adopted numerical model should have adequate capacity to study non-linear large deformation analysis.

In this paper, a new application to Applied Element Method (AEM) is proposed and numerical modeling of fault rupture propagation in dynamic condition is done using 2D AEM. It is found from the results that the PGA very near to the fault trace becomes relatively smaller and increases to peak value and then attenuates towards the hanging wall side. This information can give some insights to the actual phenomenon.

Kimiro Meguro, Associate Professor, Institute of Industrial Science, The University of Tokyo, Komaba 4-6-1, Meguro Ku, 153-8505 Tokyo, Japan

Pradeep Kumar Ramancharla, Post doctoral researcher, Institute of Industrial Science, The University of Tokyo, Komaba 4-6-1, Meguro Ku, 153-8505 Tokyo, Japan

INTRODUCTION

Over the past few decades, significant effort has been devoted to understanding the problem of ground shaking. Accordingly, numerous design and construction procedures have been developed to minimize damage due to strong ground motion. However, the efforts towards improving our understanding of the problem of surface faulting have been relatively modest. The common practice with important facilities such as dams, nuclear power plants, and public buildings has been to avoid construction across the recognized trace of an active fault. However, in case of the buried faults our ability to delineate the possible potential hazard that can be caused due to the future rupture activity is far from complete. But, the occurrence of the catastrophic earthquakes i.e. Kocaeli, Turkey, Chi-Chi, Taiwan and etc., in the recent times has posed many new challenges to the engineering community. Therefore, the engineering profession should develop techniques to mitigate the damaging effects of surface faulting.

Two enormously disastrous earthquakes occurred during the year 1999. The first one was an earthquake of magnitude 7.4 (Mw) occurred in Turkey on 17th August 1999 [1], and immediately following that, another event of magnitude 7.3 (Mw, Central Weather Bureau, Taiwan) occurred in Taiwan on 21st September 1999 [2]. The earthquake fault (North Anatolian Fault) in Turkey was traced over 100 km. The magnitude of right lateral movement of the fault on the ground surface was measured to be 2 to 4 m. And in Taiwan, severer effects were observed. The earthquake fault (Cher-Lung-Pu Fault) was traced for about 80 km, here the fault movement directly caused severe damage. The magnitude of maximum vertical differential movement was measured to be nearly 10.0 m. From the above two events, it is clear that the severe damage can be caused not only by the strong ground motion but also due to large surface deformations lying directly over the seismic faults. Hence, it is necessary to direct our efforts to study the relation between seismic fault characteristics, thickness of soil deposit and surface deformation.

Many researchers conducted experiments to understand the phenomena of surface failure, Cole and Lade [3] have tried to determine the location of surface fault rupture and width of the affected zone in alluvium over dip-slip fault using fault test box. They hypothesized that the results may be applicable to cohesive materials. Lade et al. [4] studied to determine the multiple failure surfaces by conducting the experiments on sand using fault test box. The results of the sand box model tests concluded that the observed displacement fields were largely the same for the different materials. Onizuka et al. [5] have modeled the deformation of ground using aluminium rods. Through experiments, they investigated bedrock stresses induced by reverse dip-slip faults. Bray [6] investigated the pattern of ruptures in clay models under 1-g subjected to dip-slip faulting. The range of bedrock's dip angle varied from 600 to 900 for both normal and reverse faults. Tani et al. [7] conducted a 1-g model study of dip-slip faulting using dry Toyoura sand as model material. Results from their first series of tests indicated that the base offset necessary for the rupture to propogate to the ground surface varied with fault orientation. These observations are in agreement with those from the study of Cole and Lade [3].

Using the above experimental methods, we can find the affected length on the surface. However, replicating the actual field conditions using experiments is very difficult, especially, controlling the material properties and modelling the boundary conditions. Moreover, large amount of data is necessary to establish a relationship between seismic fault parameters and resulting surface deformation. On the other hand, studying this phenomenon using numerical model has the advantage of controlling the parameters like material properties, size of the model, boundary condition, dip angle, etc. Numerical model allow us to investigate a number of aspects of the fault rupture propagation phenomenon, which are difficult to study from the examination of case histories or the conduct of physical model tests. It allows for the precise control and the model used to represent the behaviour of the soil and the imposed boundary conditions. Of course, the accuracy and reliability of any numerical approach depends on the validity of the mathematical conceptualisation of the critical aspects of the problem [6]. If the limitations of the assumptions imposed in the problem definition are understood, the numerical analyses can assist the engineer in attempting to understand the problem in question.

The discrete element approach can be used to model soil, since a soil mass is not a continuum. Instead, it is an assemblage of finite-sized particles. Inter-particle forces fundamentally determine the observed macroscopic behaviour of soil. Moreover, once a shear or tension cracks develops within the soil mass it typically becomes difficult to reliable apply a numerical approach based on the principles of continuum mechanics. The EDEM, however has a serious drawback in that it requires an enormous

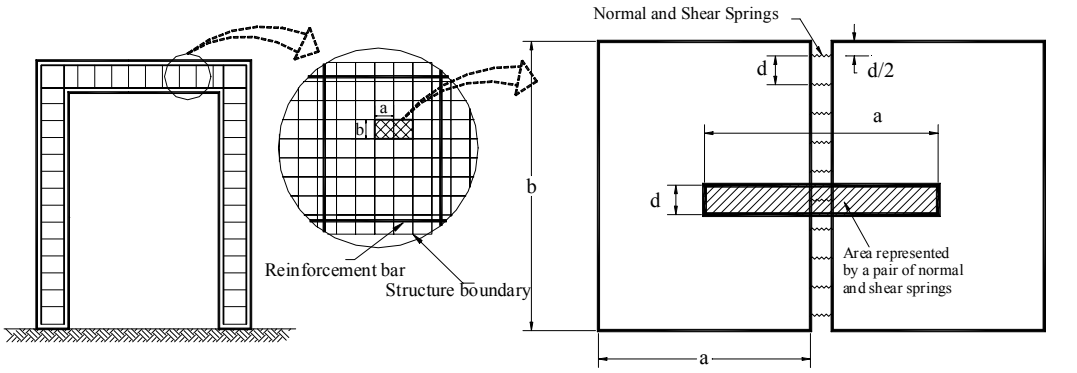

(a) Element generation for AEM (b) Spring distribution and area of influence of each pair of springs

Figure 1. Modeling of structure in AEM

amount of calculation time because explicit numerical integration is unstable unless the time step used is very short (Hakuno and Meguro [8]).

APPLIED ELEMENT METHOD (AEM)

With the AEM [9, 10, 11], structure is modelled as an assembly of small elements that are made by dividing of the structure virtually, as shown in Figure 1(a). The two elements shown in Figure 1(b) are assumed to be connected by pairs of normal and shear springs located at contact locations that are distributed around the element edges. Each pair of springs totally represents stresses and deformations of a certain area (hatched area in Figure 1(b)) of the studied elements. The spring stiffness is determined as shown in Eq. (1):

$$K_n = \frac{E \times d \times T}{a} \text{ and } K_s = \frac{G \times d \times T}{a} \quad (1)$$

where, *d* is the distance between springs, *T* is the thickness of the element and *a* is the length of the representative area, *E* and *G* are the Young's and shear modulus of the material, respectively. The above equation indicates that each spring represents the stiffness of an area (*d* x *T*) with length *a* of the studied material. In case of reinforcement, this area is replaced by that of the reinforcement bar. The above equation indicates that the spring stiffness is calculated as if the spring connects the element centerlines.

In 2D AEM, three degrees of freedom are assumed for each element. These degrees of freedom represent the rigid body motion of the element. Although the element motion is a rigid body motion, its internal stresses and deformations can be calculated by the spring deformation around each element. This means that although the element shape doesn't change during analysis, the behavior of assembly of elements is deformable.

The two elements shown in Figure 2 are assumed to be connected by only one pair of normal (stiffness: K_n) and shear (stiffness: K_s) springs. The values of (dx and dy) correspond to the relative coordinate of the contact point with respect to the centroid. To have a general stiffness matrix, the location of element and contact springs are assumed in a general position. The stiffness matrix components corresponding to each degree of freedom are determined by assuming a unit displacement in the studied direction and by determining forces at the centroid of each element. The element stiffness matrix size is only (6 x 6). Eq. (2) shows the components of the upper left quarter of the stiffness matrix. All used notations in this equation are shown in Figure 2. It is clear that the stiffness matrix depends on the contact spring stiffness and the spring location.

The stiffness matrix in Eq. (2) is for only one pair of contact springs. However, the global stiffness matrix is determined by summing up the stiffness matrices of individual pair of springs around each element. Consequently, the developed stiffness matrix is an average stiffness matrix for the element

according to the stress situation around the element. This technique can be used both in load and displacement control cases. The governing equation is:

$$[K_G][\Delta] = [F] \quad (2)$$

$$\begin{bmatrix} \begin{matrix}\mathrm{Sin}^2(\theta+\alpha)K_n \\ +\mathrm{Cos}^2(\theta+\alpha)K_s\end{matrix} & \begin{matrix}-K_n\mathrm{Sin}(\theta+\alpha)\mathrm{Cos}(\theta+\alpha) \\ +K_s\mathrm{Sin}(\theta+\alpha)\mathrm{Cos}(\theta+\alpha)\end{matrix} & \begin{matrix}\mathrm{Cos}(\theta+\alpha)K_sL\mathrm{Sin}(\alpha) \\ -\mathrm{Sin}(\theta+\alpha)K_nL\mathrm{Cos}(\alpha)\end{matrix} \\ \begin{matrix}-K_n\mathrm{Sin}(\theta+\alpha)\mathrm{Cos}(\theta+\alpha) \\ +K_s\mathrm{Sin}(\theta+\alpha)\mathrm{Cos}(\theta+\alpha)\end{matrix} & \begin{matrix}\mathrm{Sin}^2(\theta+\alpha)K_s \\ +\mathrm{Cos}^2(\theta+\alpha)K_n\end{matrix} & \begin{matrix}\mathrm{Cos}(\theta+\alpha)K_nL\mathrm{Cos}(\alpha) \\ +\mathrm{Sin}(\theta+\alpha)K_sL\mathrm{Sin}(\alpha)\end{matrix} \\ \begin{matrix}\mathrm{Cos}(\theta+\alpha)K_sL\mathrm{Sin}(\alpha) \\ -\mathrm{Sin}(\theta+\alpha)K_nL\mathrm{Cos}(\alpha)\end{matrix} & \begin{matrix}\mathrm{Cos}(\theta+\alpha)K_nL\mathrm{Cos}(\alpha) \\ +\mathrm{Sin}(\theta+\alpha)K_sL\mathrm{Sin}(\alpha)\end{matrix} & \begin{matrix}L^2\mathrm{Cos}^2(\alpha)K_n \\ +L^2\mathrm{Sin}^2(\alpha)K_s\end{matrix} \end{bmatrix} \quad (3)$$

where, $[K_G]$ is the global stiffness matrix; $[\Delta]$ the displacement vector and $[F]$ the applied load vector. In load control case, the vector, [F], is known before the analysis. In displacement control case, the load is applied by unit virtual displacement for one or more degrees of freedom. By using the advantage of AEM's simplicity in formulation and accuracy in non-linear range, fault rupture zone shown in Figure 3 is modeled.

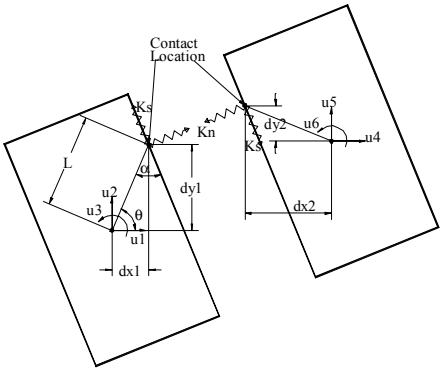

Figure 2. Spring connectivity

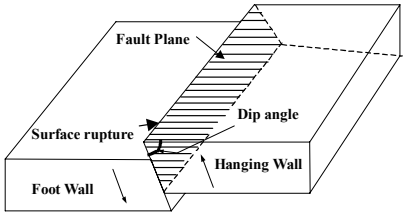

Figure 3. Fault terminology

MODEL PREPARATION

The mechanism shown in Figure 3 is called Reverse Dip-Slip Faulting. This is one of the types of fault where the hanging wall moves upward relative to the footwall. If the direction of the movement of the hanging wall is downward then it is called normal faulting. To analyse the mechanism of fault rupture zone near dip-slip faults, the numerical model shown in Figure 4 is prepared. Length of the model is assumed as 1 km and depth is 150 m. The location of the base fault is assumed to lie exactly at the centre of the model.

Generally, soil strata and bedrock extend upto tens of kilometres in horizontal direction. Numerical modelling of such a large media is a difficult task and moreover, for studying the surface behavior near the active fault region, it is necessary to model the small portion of the region that includes all the effects when the bedrock moves. For studying the selected region numerically, we assumed the boundary on left side to be fixed in horizontal direction. In order to avoid the interference of boundary condition on numerical results, left side boundary is kept at sufficient distance from the fault zone. The bottom of the bedrock is assumed as fixed.

When the model is set with no loading except the self-weight, which is applied as gravity load, the model exhibits free vibrations across the equilibrium position. These vibrations will decay consuming the large amount of CPU time. Hence, the static analysis is performed first and the self-weight is applied in increments. After the total self-weight is applied in static way, the model for performing dynamic fault rupture analysis is ready.

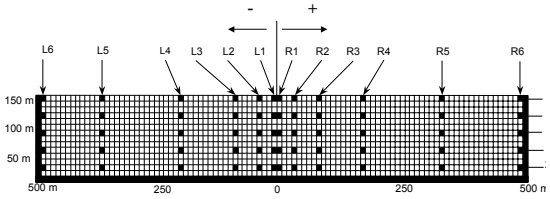

Figure 4. Numerical model for fault rupture study

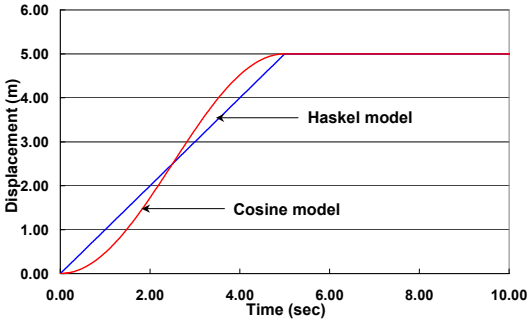

Figure 5. Slip function

SLIP RATE OF FAULT

After setting the model to perform dynamic analysis, it is necessary to know the influence of the slip rate of the fault on the vibration. The slip rate of the fault is one of the five source parameters that are important for discussion while dealing with the dynamic characteristics of fault rupture propagation. These parameters are; the fault length (L), the fault width (W), rupture velocity (VR), the final offset (D), and rise time (t). Since we are dealing with 2D model, length of the fault is not considered and width of the fault is kept constant in all the cases of analysis. The remaining three parameters are observed varying their values. Slip velocity is dependent on the last two parameters i.e. final offset (D) and rise time (t).

To understand the effect of slip rate, linear elastic analyses were first performed. Two kinds of slip functions as shown in Figure 5 were observed. First, the ramp model [12, 13] is observed and later cosine model is used in the analysis. Figure 6(a) shows the horizontal and vertical displacement time history of the element "R5" on the hanging wall, Figure 6(b) is showing the kinetic and potential energy changes in the system and Figures 6(c) and (d) show the horizontal and vertical velocity time histories of element "R5" on hanging wall and element "L5" on footwall, respectively. From the set of figures, it can be easily seen that the effect of input base displacement is affecting the vibration, especially from Figure 6(c), sudden rise and drop in the velocity exactly at the starting and ending of the constant rate displacement. The reason for this behavior is due the input displacement function, which has sudden rise at the start of input and constant velocity till 5 seconds and then sudden drop at 5 sec. Hence, to remove this effect, the input base displacement following Cosine model is considered (see Figure 5). Set of Figures 7(a) ~ (d) are showing the similar results as discussed. From this, it can be easily seen that there is no effect of input base displacement.

CASE STUDY

Permanent ground displacements that accompany a seismic event are the consequence of the fault slip and are referred as the static displacement field of that event or as coseismic displacements [14,15]. This displacement field differs from the ground displacements induced by the seismic waves, which are generated during earthquakes rupture propagation and referred as dynamic displacement field. Despite their name, near–fault static displacements are developed rapidly, within short period of the time that is related to the slip rise time. The shortness of this development turns the coseismal displacement into a dynamic phenomenon. Since they are likely to be non-reversal and continuous, their time history will appear as a pulse of motion with a ramp-type shape. On observing the seismic records (see Figure 8) obtained during the Chi-chi earthquake [16]. It can be obtained during the Chi-chi earthquake [16]. It can be understood that the permanent relative ground displacement was responsible for most of the damage near the fault zone. For comparing the numerical analysis results with near field seismic records obtained during 1999, Chi-chi, Taiwan, a 2D microscopic model shown in Figure 4 is used. Response is measured at 6 observation points on the left and right side of the point exactly above the location of the underlying base fault. These points (L1 ~ L6 and R1 ~ R6) are located unevenly (i.e. at 5m, 25m, 65m, 145m, 305m, 485m) on each side.

For comparing the results with real near field records with large displacement, closed form approximation of static displacement is assumed. Pulse-like displacement time history that represents the base motion is considered (see Figure 9) referring to Mladen [17]. As an approximation, the corresponding displacement pulse can be assumed as Gaussian-type function

$$d_{sp}(t) = \frac{\sqrt{2\pi}}{n} V_{sp} T_p \Phi\left[\frac{(t - t_c)}{T_p / n}\right] \tag{4}$$

where V_{sp} is the amplitude of static velocity pulse, T_p, Velocity pulse duration, t_c time instant, at which the pulse is centered, n constant equal to 6 and t is the time. The term T_p/n has the meaning of standard deviation and controls the actual spread of the pulse with respect to the given pulse duration and Φ is the normal probability function. For more details, refer to Mladen [17]

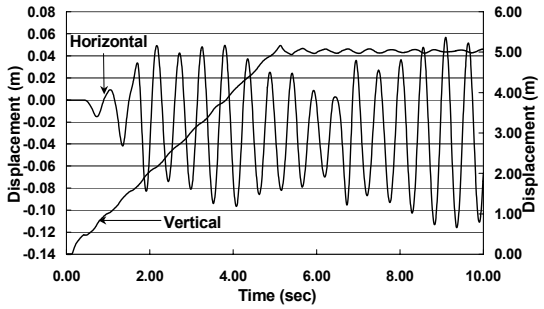

(a) Horizontal and vertical displacement time history (Haskell model)

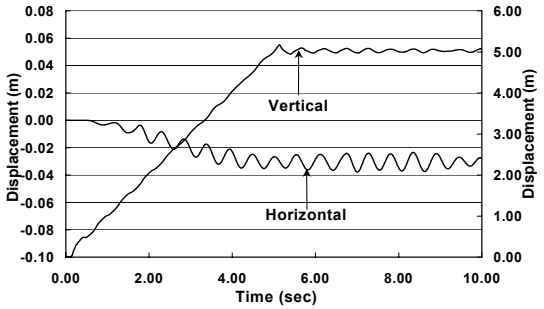

(a) Horizontal and vertical displacement time history (Cosine model)

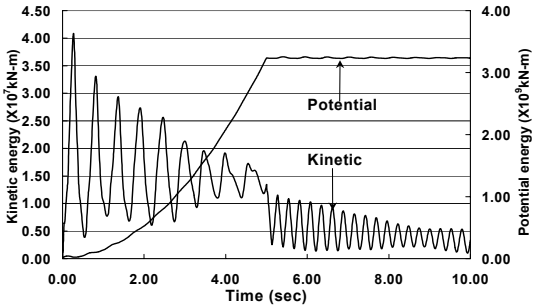

(b) Kinetic and potential energy changes in the system (Haskell model)

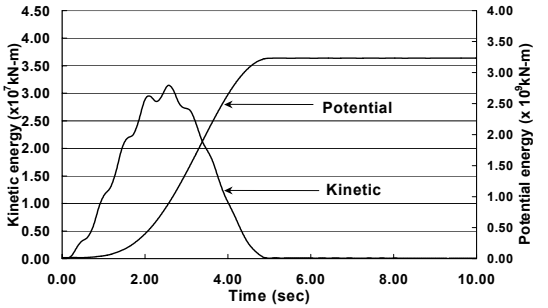

(b) Kinetic and potential energy changes in the system (Cosine model)

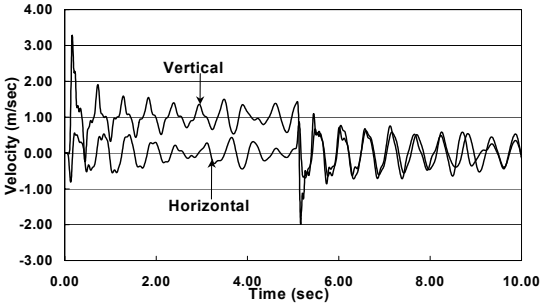

(c) Velocity time history of element "R5" on hanging wall (Haskell model)

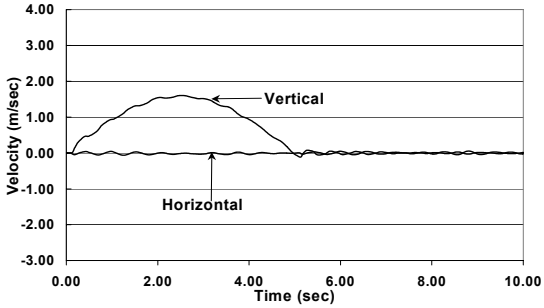

(c) Velocity time history of element "R5" on hanging wall (Cosine model)

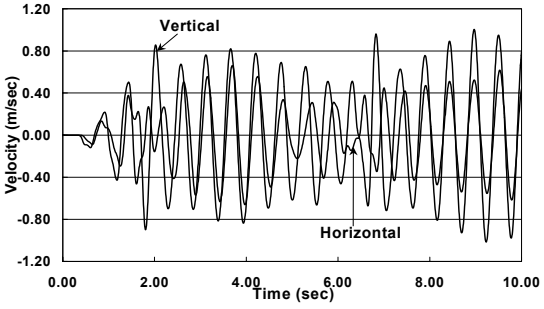

(d) Velocity time history of element "L5" on footwall (Haskell model)

Fig. 6 Effect of slip function on the response of soil deposit (case study using Haskell)

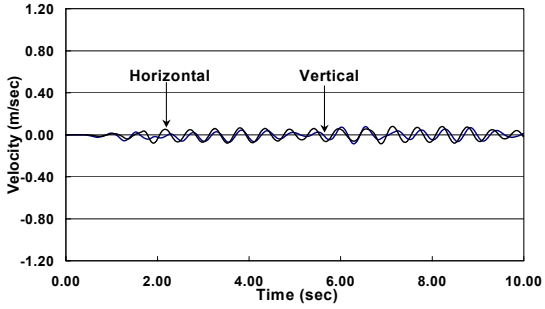

(d) Velocity time history of element "L5" on footwall (Cosine model)

Fig. 7 Effect of slip function on the response of soil deposit (case study using Cosine model)

In general, the amplitude of wave attenuates because the material damping absorbs some of the elastic energy of the stress wave; the specific energy (energy per unit volume) decreases as the wave travels through a material. The reduction of specific energy causes the amplitude of the wave to decrease with distance. In purely elastic materials, the energy is conserved (no conversion to other forms of energy takes place), this reduction in amplitude due to spreading of the energy over a greater volume of material is often referred to as radiation damping (or geometric attenuation). It should be distinguished from material damping in which elastic energy is actually dissipated by viscous, hysteretic, or other mechanisms18). The above explanation says that the attenuation takes places from the shortest distance from the fault towards the farther distances. This is true when we discuss in large scale but when we look at the places very near to the fault trace, the scenario becomes different.

Figures 10(a) and (b) show the vertical and horizontal displacement time histories respectively. From Figure 10(a) it can be seen that from R5 to R3, the displacement is same as the input displacement. However, from R3 to R2 it decreases and finally it reaches to zero towards footwall side. From Figure 10 (b), it can be seen that the effect of hanging wall displacement on the horizontal surface deformation is significant in the near fault region and towards the footwall. Figures 11(a) and (b) show the vertical and horizontal acceleration time histories. It can be seen from this figure that the acceleration on surface attenuates when we move towards the farther distances from the fault. Spatial distribution of the final surface deformation in horizontal and vertical directions is shown in Figure 12. From this figure, it can be seen that the vertical displacement on the surface is proportional to the hanging wall displacement on the hanging wall side. However, on the footwall side there is a slight negative displacement. When we look at the horizontal displacement on the surface, it can be easily said that the deformation is occurred in the wider region on footwall side. However, on the hanging wall side its effect is not much. This is due to the opening of tension crack. Figure 13(a) ~ (c) show the attenuation of peak ground acceleration, velocity and displacement respectively. In all the figures, two dotted lines are shown. On is indicating the location of the base fault and the other is showing the possible location of surface rupture. It can be seen from the Figure 13(a), that the PGA increases first and attains the peak value and then attenuates towards hanging wall direction. In general, the amount of destruction exactly on the fault is more because of the large relative permanent displacement. However, little away from the fault the damage is less because the amplitude of strong ground motion is not so high. And at farther distances, PGA attains greater magnitude and then decreases with distance. This phenomenon is sometimes observed during the past earthquakes. However, due to the sparse distribution of the seismometers, this could not be represented by actual recorded data. But with the help of the newly developed numerical model, we can show this phenomenon. Figure 13(b) shows the attenuation of Peak ground velocity (PGV) with distance. From this figure, it can be said that the vertical velocity component

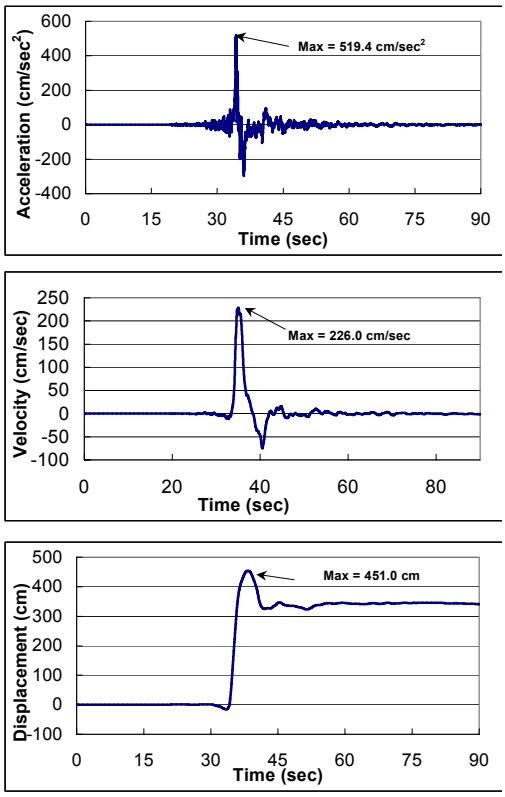

Figure 8. Acceleration Velocity and displacement time history of the records obtained at Shihkan (TCU068) during the 1999 Chi-chi, Taiwan earthquake

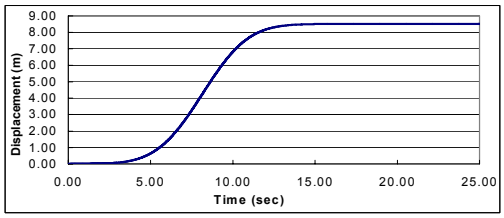

Figure 9. Assumed static input displacement

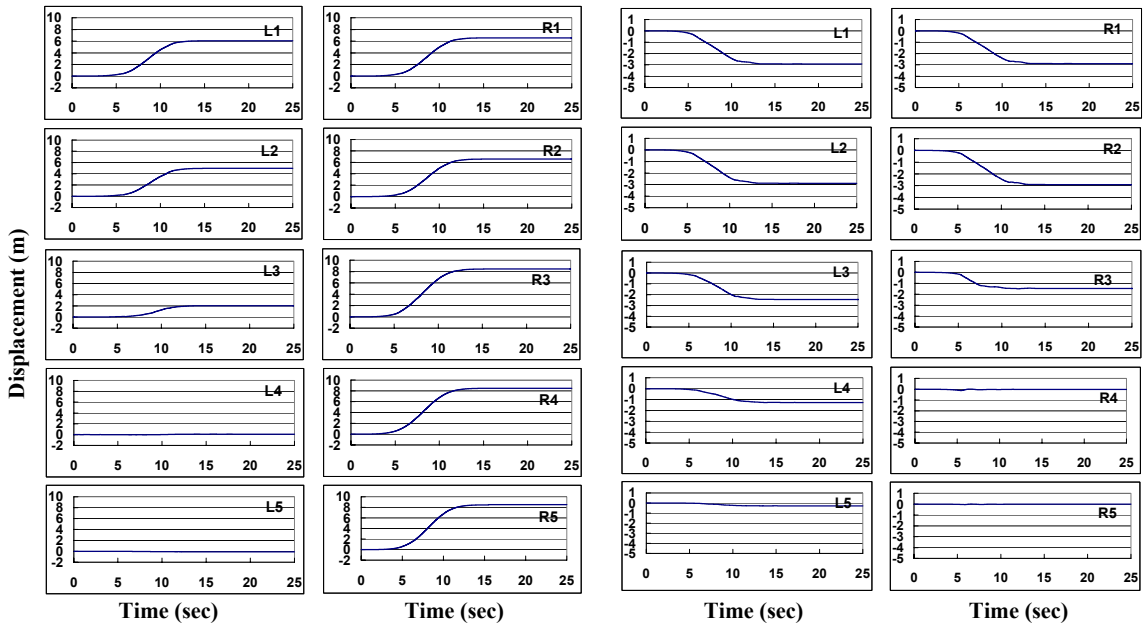

(a) Vertical surface displacement (b) Horizontal surface displacement

Figure 10. Vertical and horizontal displacement time histories (at L1~L5 and R1~R5)

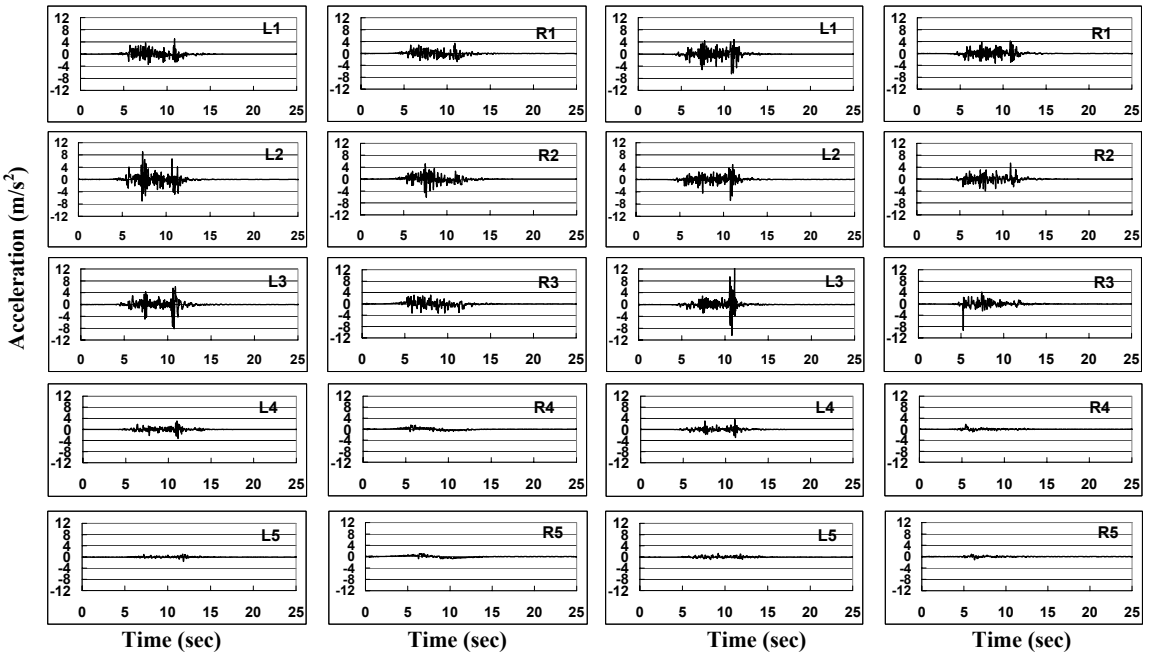

(a) Vertical acceleration time histories (b) Horizontal acceleration time histories

Figure 11. Vertical and horizontal acceleration time histories (at L1~L5 and R1~R5)

is having maximum values on the hanging wall side and reduces towards footwall. However, the horizontal velocity is having lower values near the location of surface rupture and increases slightly towards hanging wall direction and then attenuates with distances. Figure 13(c) shows the peak ground displacement (PGD) attenuation with distance. This graph is similar to the final displacement as explained in Figure 12. On observing the Figure 13, it can be easily said that the peak responses are not maximum near the place where surface rupture is taking place. Instead they are maximum little away

from the surface rupture towards the hanging wall direction. The reason for this can be understood when we look at the propagation of cracks from the bedrock towards the surface (see Figure 14). Figure 14(a) shows the element location and Figure 14(b) shows the crack propagation. Near the surface fault rupture, the material becomes highly non-linear and the response of this region becomes low compared to the adjacent areas response.

A parametric study is also conducted to find the influence of the material elastic property on surface deformation and crack propagation. Four kinds of soil properties are used whose shear wave velocities, Vs=745 m/s, 527 m/s, 373 m/s and 264 m/s. Analysis is carried out by giving the displacement shown in Figure 9. Final surface displacement is plotted in Figure 15. From this figure, it can be easily seen that the deformation is absorbed in case of soft soil. And in case of harder soil the influence area on the surface is more. Figure 16 shows the element location and crack propagation in different soil deposits. From this figure it can be concluded that, in soft soil deposits the shear band in narrow, where as in hard soil the shear banding occurs in wider area.

A complete understanding of the phenomenon of fault rupture propagation in soil may remain incomplete because of the numerous governing factors that are highly variable and not well quantified. And hence, the above-discussed study is important because, geological observations of surface ruptures associated with historical earthquakes in the world have indicated that surface ruptures occurred, without any definite exceptions, on pre-existing faults. Moreover, there are lines of evidence indicating that moderate to large-scale faults have moved repeatedly in the geologic past. This is because a fault coalesces other faults and fractures near its edge every time it slips, and approaches to the ground surface with time. Conversely, a map-scale fault cannot be formed in a single event. The repetitive nature of faulting gives us an important basis for predicting future activity of faults by using geologic information. And hence, the study on the fault rupture propagation is necessary to establish the possible locations of the faults appearing on the surface due to future earthquakes because engineers are more concerned about the damage that will be caused when the structures are located on the vulnerable area.

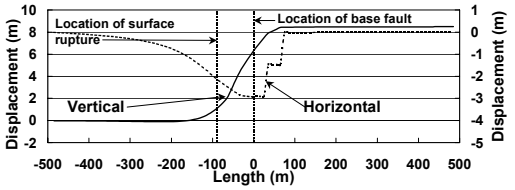

Figure 12. Final surface displacement

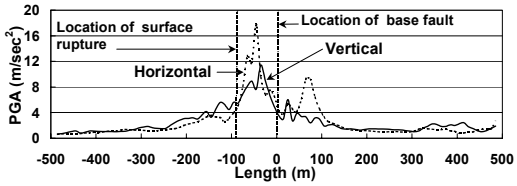

(a) Peak ground acceleration (PGA)

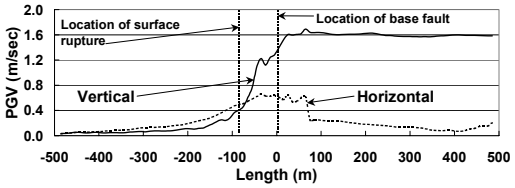

(b) Peak ground velocity (PGV)

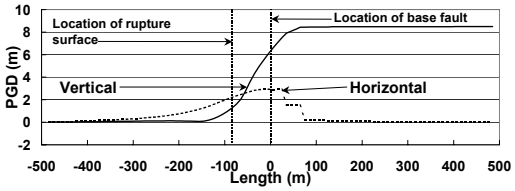

(c) Peak ground displacement (PGD)

Figure 13. Attenuation of peak ground responses

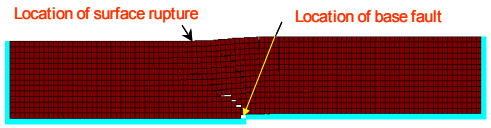

(a) Element location

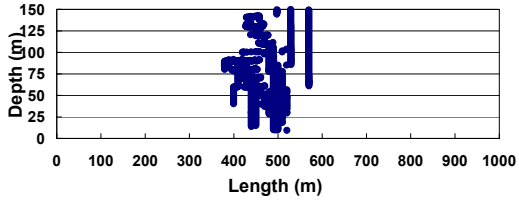

(b) Crack propagation

Figure 14. Element location and crack propagation responses

CONCLUSIONS

A new application to Applied Element Method (AEM) is proposed in this paper. Numerical modelling of fault rupture propagation in dynamic condition is done using 2D AEM. It is found from the

results, that the peak responses very near to the surface rupture are not maximum. Instead they attain higher values little away from the surface rupture towards hanging wall side.

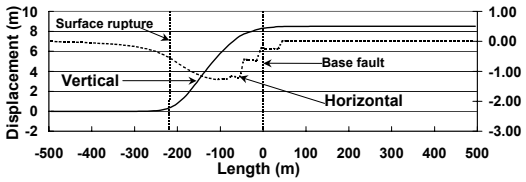

(a) Vs=745 m/s

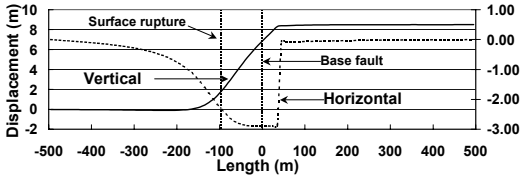

(b) Vs=264 m/s

Figure 15. Final surface displacement for different soil deposits

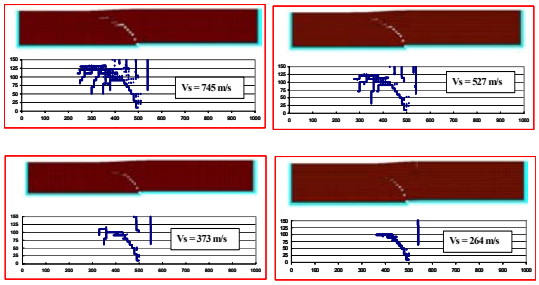

Figure 16. Element location and crack propagation in different soil deposits

REFERENCES

[1] Japan Society of Civil Engineers, *The 1999 Kocaeli earthquake, Turkey, Investigation into damage to civil engineering structures*, Earthquake Engineering Committee, Japan Society of Civil Engineers, 1999 (a).

[2] Japan Society of Civil Engineers, The 1999 Ji-Ji earthquake, Taiwan, *Investigation into damage to civil engineering structures*, Earthquake Engineering Committee, Japan Society of Civil Engineers, 1999 (b).

[3] Cole, D. A., Jr., and Lade, P. V., Influence zones in alluvium over dip-slip faults, *Journal of Geotechnical Engineering*, ASCE, Proc. Paper 18788, Vol. 110, No. GT5, pp. 599-615, 1984.

[4] Lade, P. V., Cole, D. A., Jr., and Cummings David, Multiple failure surfaces over dip-slip faults, *Journal of Geotechnical Engineering*, ASCE, Proc. Paper 18789, Vol. 110, No. GT5, pp. 616-627, 1984.

[5] Onizuka, N., Hakuno, M., Iwashita, K. and Suzuki, T., Deformation in grounds and bedrock stress induced by reverse dip-slip faults, *Journal of Applied Mechanics*, JSCE, Vol. 2, pp. 533-542, 1999 (in Japanese).

[6] Bray, J.D., *The effects of tectonic movements on stresses and deformations in earth embankments*, Dissertation doctor of philosophy, University of California, Berkeley, 1990.

[7] Tani, K., Ueta, K., and Onizuka, N.: Scale effects of Quarternary Ground Deformation observed in Model Tests of vertical Fault, Proceedings 29th Japan National Conference of Soil Mechanics and Foundation Engineering, pp. 1359-1562, 1994 (in Japanese).

[8] Hakuno, M., Meguro, K.: Simulation of concrete-frame collapse due to dynamic loading, *Journal of Engineering Mechanics*, ASCE, Vol. 119, No. 9, September, 1993.

[9] Meguro, K. and Tagel-Din, H., Applied element method for structural analysis: Theory and application for linear materials, *Structural Eng./Earthquake Eng.*, JSCE, Vol. 17, No. 1, 21s-35s, 2000.

[10] Tagel-Din, H., *A new efficient method for nonlinear, large deformation and collapse analysis of structures*, Ph.D. thesis, Civil Eng. Dept., The University of Tokyo, 1998.

[11] Meguro, K. and Tagel-Din H., A new efficient technique for fracture analysis of structures, *Bulletin of Earthquake Resistant Structure Research Center*, Institute of Industrial Science, The University of Tokyo, No. 30, 1997.

[12] Ben-Menahem, A., and M.N. Toksoz: Source mechanism from spectra of long period surface waves, *Journal of Geophysical Research* 68: 5207-5222, 1963.

[13] Haskell, N.A. Radiation pattern of surface waves from point sources in a multi-layered medium, *Bulletin of Seismological Society of America* 54: 377-394, 1964.

[14] Hall, J.F., Heaton, T.H., Halling, M.W. and Wald, D.J., Near-source ground motion and its effects on flexible buildings, *Earthquake Spectra*, 11(4), 569-605, 1995.

[15] Tatcher, W., Geodetic measurement of active tectonic processes,' Active tectonics (studies in geophysics) 155-163, National Academy Press, 1986.

[16] Lee, W.H.K., T.C. Shin, K.W. Kuo, and K.C. Chen, CWB free-field strong motion Data from the 921 Chi-Chi Earthquake: Volume 1. digital acceleration files on CD-ROM, pre-publication version (December 6, 1999), Seismology Center, Central weather bureau, Taipei, Taiwan, 1999.

[17] Mladen V. K., *Utilization of strong motion parameters for earthquake damage assessment of grounds and structures*, A dissertation submitted to the department of civil engineering (Ph.D. Thesis), University of Tokyo, 2000.
[18] Kramer, S.L., *Geotechnical earthquake engineering*, Prentice-hall inc. Upper saddle river, New Jersey, pp.180, 1996.

SEISMIC COMPRESSION: EFFECTS ON LIFELINES AND UPDATED ANALYSIS METHOD

Jonathan P. Stewart, Daniel H. Whang, and Patrick M. Smith
University of California, Los Angeles

ABSTRACT. Seismic compression is defined as the accrual of contractive volumetric strains in unsaturated soil during strong shaking from earthquakes. In this paper, we review well documented incidents of damage to pipelines and structures caused by seismic compression of compacted fills within a subdivision strongly shaken by the 1994 Northridge earthquake. We also describe a simplified procedure for estimating ground displacements from seismic compression in compacted fill. The procedure has three steps: (1) estimation of shear strain amplitude within the fill soil mass from the peak acceleration at the ground surface and other seismological and site parameters; (2) estimation of volumetric strains within the fill mass based on compaction conditions in the fill, the shear strain amplitude, and the equivalent number of uniform strain cycles; and (3) integration of volumetric strains across the fill section to estimate settlement. The framework of the present procedure is similar to that of Tokimatsu and Seed (1987), which is strictly applicable only to clean sands. We update this widely used procedure to incorporate relatively recent material models for clean sands, and to extend the formulation to allow analysis of non-plastic silty sands and low-plasticity clays. The procedure is implemented for three field case history sites with measured settlements, and is found to generally provide reasonable, first-order estimates of ground settlements given the simplifying assumptions associated with this approximate method of analysis.

INTRODUCTION

Ground deformations in compacted fill slopes from seismic compression have been documented following a number of earthquakes (Lawson, 1908; Seed, 1967; McClure, 1973; Pyke et al. 1975; Slosson, 1975; Stewart et al., 2001). However, most of the data is anecdotal in the sense that a few selected sites with deformations were investigated, but systematic surveys of sites within a given region were generally not performed. Such surveys allow variations of damage between fill and non-fill sites to be assessed, which provides a more robust indication of the significance of ground failure in fill. One of the objectives of this paper is to document one such survey for a region strongly shaken by the 1994 Northridge, California earthquake, with particular emphasis placed on the performance of a number of buried pipelines. The data for this case study was originally presented by Stewart et al. (2001).

The current state of practice for estimating the seismic compression of unsaturated compacted fill soils consists of the methodology presented by Tokimatsu and Seed (1987), which is strictly applicable to clean sands. Accordingly, a second objective of this paper is to update this widely used procedure to incorporate relatively recent test data for compacted sandy soils, and to extend the formulation to allow analysis of recently compacted fill soils containing significant fines. Partial motivation for this update comes from laboratory testing by Stewart et al. (2002), which has shown that clean sands can experience up to ten times more vertical strain than soils with fines compacted to a comparable density. Consequently, current methods for estimating seismic

compression may be overly conservative, and may not be applicable to soils containing fines. We present a brief summary of the Tokimatsu and Seed (1987) methodology; discuss advances since 1987 that provide an opportunity to improve the analysis procedure; outline a new analysis procedure similar in format to the 1987 procedure but incorporating recent advances; and apply the procedure to three field case histories.

EFFECTS OF SEISMIC COMPRESSION ON LIFELINES: NORTHRIDGE EARTHQUAKE CASE STUDY

The Santa Clarita Valley area was among the most strongly shaken regions by the Northridge earthquake, and experienced significant ground deformations in compacted fill. Development has often occurred in deeply incised canyon/ridge topography, which requires massive grading operations involving deep canyon fills. Engineered improvements constructed across fill and cut areas are often of fairly uniform design and construction. Such sites provide the opportunity to assess the impact of earth fills on the performance of improvements (such as pipelines and houses) by comparing damage statistics for cut and fill areas.

One such site is the 21,000 acre subdivision shown in Figure 1. At the time of the Northridge earthquake, 645 properties in the subdivision had been developed, with the construction having occurred between July 1986 and October 1987. The site is approximately 9 km from the Northridge fault rupture plane (by Wald and Heaton, 1994), and likely experienced peak ground accelerations on rock on the order of 0.3 to 0.5g (Chang et al., 1996). Original topography at the site consisted of numerous canyons and ridges, with a general increase in elevation to the west. Grading operations involved the construction of fills with maximum depths typically on the order of about 15 to 21 m. The fill soils placed at the site are primarily sands and silty sands, with non-plastic fines contents on the order of 15-30%. Fill placed at the site was required to have a minimum relative compaction by the modified Proctor standard of 90%. Water content was not controlled during construction, and cut areas were not overexcavated.

Stewart et al. (2001) documented the performance of buried pipelines (water, sewer, stormdrain, and gas) and building structures that were in place at the time of the 1994 Northridge earthquake. As shown in Figure 1, 14 breaks were reported in the water distribution system (15, 20, or 25 cm diameter asbestos-concrete pipes), most of which are described as “shear failure.” All the breaks occurred in fill, generally near cut/fill contacts. The gas and storm drain lines primarily consist of relatively flexible PVC pipe, and no breaks were reported. A 152-cm diameter reinforced concrete storm drain, constructed in 2.4 m sections, which passes through the subdivision only had minor damage at grout joints that was uniformly distributed across the length of the pipe (i.e., no concentration of damage in fill areas). The strength and stiffness of the reinforced concrete section was sufficient to resist damage associated with deformations in fill.

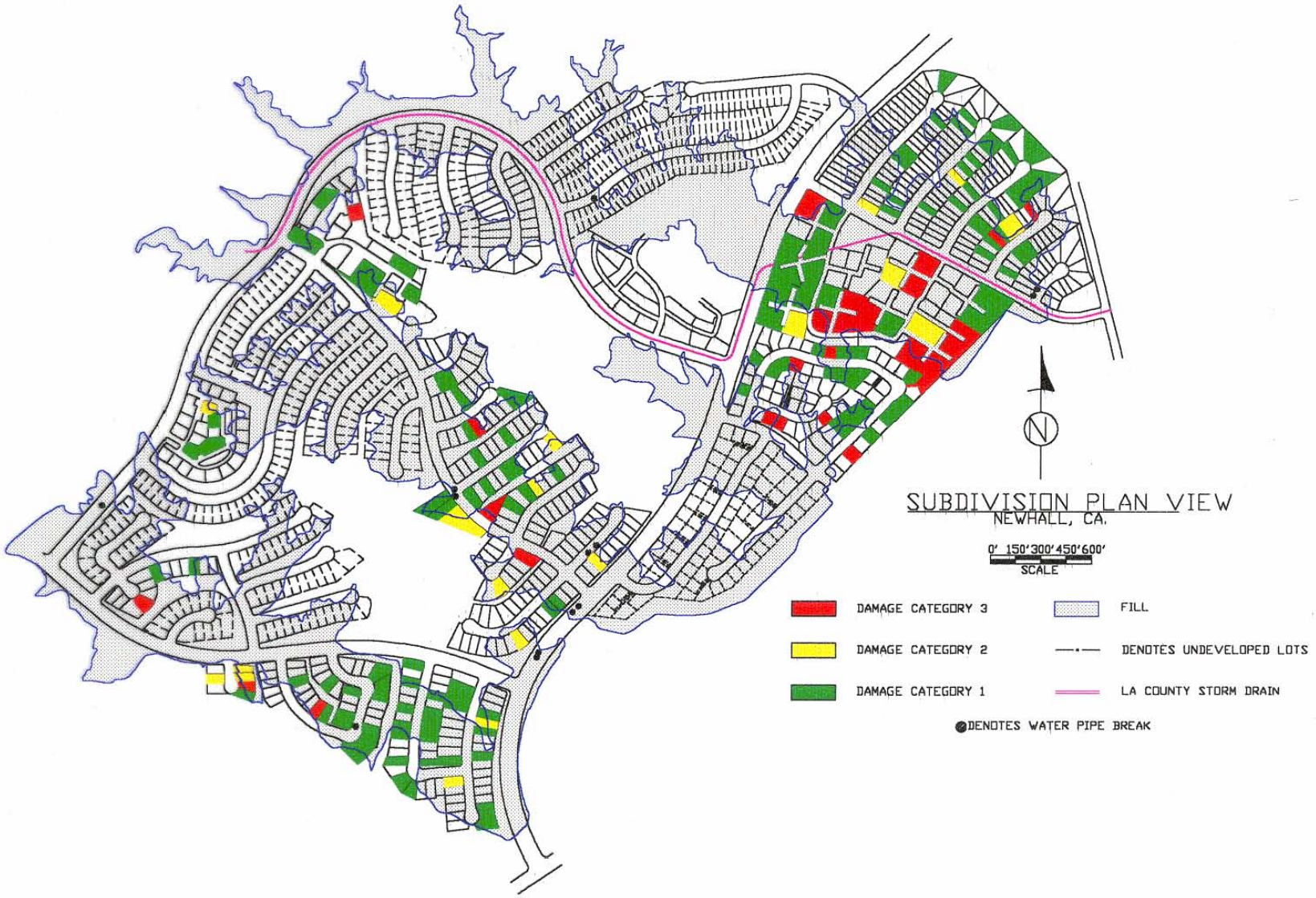

Fig. 1. Plan view of subdivision showing fill and cut zones and locations of damaged water pipes and structures

Damage to structures was evaluated based on inspection reports prepared by Los Angeles County staff within one month of the earthquake. Inspections were made upon the request of property owners seeking earthquake relief. Specific damages were documented (e.g. foundation cracks, wall cracks, collapsed chimneys), and monetary losses were estimated. Some properties were not inspected, presumably because of little or no earthquake damage. As shown in Figure 1, damage at each site was classified according to the four categories in Table 1. Also shown in Table 1 is the frequency with which the various damage levels were encountered in cut, fill, and cut/fill transition lots. These data indicate that the likelihood of significant damage (Damage Category of 2 or 3) on cut/fill or fill lots was more than twice that on cut lots.

Table 1. Damage statistics for subdivision as function of site condition. Indicated are numbers (and percentages in parentheses) of lots within each site category with different damage levels

Site Condition	No Damage* (0)	Cosmetic Damage* (1)	Moderate Damage* (2)	Significant Damage* (3)	Total
Cut	193 (77%)	49 (20%)	3 (1%)	5 (2%)	250
Cut/Fill	159 (66%)	60 (25%)	11 (4%)	12 (5%)	242
Fill	100 (65%)	39 (25%)	8 (5%)	7 (5%)	154
All lots	452 (70%)	148 (23%)	22 (3%)	24 (4%)	646

*0. No damage. No observed distress, or no homeowner request for inspection
1. Cosmetic damage. Cracks in walls and ceilings that do not threaten structural integrity.
2. Moderate damage. Cosmetic damage + damaged roof, chimney, floors, windows, or plumbing suggesting some ground deformation or intense shaking.
3. Significant damage. Moderate damage + cracked foundation and displacements observed in soil, suggesting significant ground deformation.

The reported damage from this subdivision indicates that the presence of fill significantly affected the likelihood of damage to pipelines and building structures, as all reported pipeline breaks occurred in fill near cut/fill transitions, and the likelihood of significant structural damage on fill or cut/fill areas was more than twice that on cut areas.

Two ground failure mechanisms can be postulated to have caused the ground deformations that led to the pipe breaks and likely contributed to the structural damage:

1. *Seismic compression*, i.e., contractive volumetric strains developed during cyclic loading of unsaturated, compacted soil, and
2. *Permanent shear deformations*, either along distinct sliding surfaces or distributed across highly stressed zones in the fill.

Analyses by Stewart et al. (2001) found that for many common fill geometries, the general characteristics of the observed ground deformations could be best explained by the seismic compression mechanism. Permanent shear deformations are most likely at a relatively small subset of sites with large static driving shear stresses relative to the soil strength (i.e., sites with low static factors of safety). As this condition is not present in the subdivision described above, the ground deformations almost certainly resulted from seismic compression.

The following sections describe an analysis procedure for seismic compression, and then apply this procedure to sites where the amount of seismic compression induced settlement is well known or can be reliably estimated. The procedures are not applied to the subdivision site because the amount of settlement in the field is not known from pre- and post-earthquake surveys.

ANALYSIS OF GROUND DEFORMATIONS FROM SEISMIC COMPRESSION

Existing State-of-Practice for Seismic Compression Analysis

The original Tokimatsu and Seed (1987) analysis procedure is based on a simplified representation of the distribution of shear stress with depth in a one-dimensional soil column. If the soil column above a soil element at depth *h* behaves as a rigid body, and the surface peak horizontal acceleration is *PHA*, then the mass of soil above *h* would impose a maximum shear stress of:

$$\tau_{rigid,\max} = \frac{PHA}{g} \cdot \sigma_0 \tag{1}$$

where g = the acceleration due to gravity and σ_o = total overburden pressure at depth h.

Soil flexibility reduces the shear stress to values less than $\tau_{rigid,\ max}$, as a result of vertical incoherence of ground motion. Seed and Idriss (1971) developed a simplified technique to estimate earthquake induced cycle shear stresses at depth. They multiplied $\tau_{rigid,max}$ by a stress reduction factor, r_d (which is the ratio of the actual shear stress at depth vs. the theoretical "rigid body" shear stress). A factor of 0.65 is then applied to reduce the peak cyclic shear stress, τ_{max}, to the effective cyclic stress, τ_{eff}, as:

$$\tau_{eff} = 0.65 \cdot \frac{PHA}{g} \cdot \sigma_0 \cdot r_d \tag{2}$$

Effective shear strain, γ_{eff}, is estimated from τ_{eff} using the effective shear modulus (G_{eff}), as follows:

$$\gamma_{eff} = \frac{\tau_{eff}}{G_{eff}} = \frac{\tau_{eff}}{G_{\max}\left(\frac{G_{eff}}{G_{\max}}\right)} \tag{3}$$

where G_{max} = small strain shear modulus. Combining Eqs. 2 and 3 leads to:

$$\gamma_{eff}\ \frac{G_{eff}}{G_{\max}} = \frac{0.65 \cdot PHA \cdot \sigma_o \cdot r_d}{g \cdot G_{\max}} \tag{4}$$

The product $\gamma_{eff}\ (G_{eff}/G_{max})$ in Eq. 4 can be readily translated to a shear strain amplitude γ_{eff} using published models for soil modulus reduction with increasing shear strain (i.e. models relating γ_{eff} to G_{eff}/G_{max}). Tokimatsu and Seed (1987) recommended using the modulus reduction curves of Iwasaki et al. (1978), which depend on effective stress.

Having estimated γ_{eff} with the above procedure, volumetric strains at 15 cycles of shaking [$(\varepsilon_v)_{N=15}$] are estimated using an appropriate volumetric strain material model (these models relate $(\varepsilon_v)_{N=15}$ to γ_{eff}, and depend on the compaction condition of the fill soil). Tokimatsu and Seed (1987) utilized the volumetric strain material model of Silver and Seed (1971), which are derived from laboratory simple shear testing of clean sands. In that work, the in situ density for sands is represented by relative density (D_r).

The values of $(\varepsilon_v)_{N=15}$ are adjusted to the volumetric strain (ε_v) for the actual number of strain cycles (N) using the factor $C_N = \varepsilon_v/(\varepsilon_v)_{N=15}$. Tokimatsu and Seed (1987) recommended using C_N relations for clean sand derived from testing by Silver and Seed (1971). Parameter N is a ground motion intensity measure (like *PHA*), and Tokimatsu and Seed (1987) recommended that it be estimated using an empirical relationship between magnitude (m) and N proposed by Seed et al. (1975).

The N-adjusted volumetric strain ε_v is multiplied by two to account for multi-directional shaking effects per the recommendations of Pyke et al. (1975). Hence, the final estimate of volumetric strain at a point is represented by $2\times C_N\times(\varepsilon_v)_{N=15}$. These volumetric strains are then integrated over the depth of the soil column to calculate settlement.

Advances Since 1987

Several features of the original Tokimatsu and Seed (1987) procedure for seismic compression analysis can be updated. These include: (1) new relations for r_d developed by Seed et al. (2001); (2) new relations for N by Liu et al. (2001); (3) new models for modulus reduction which incorporate the effects of effective stress, soil plasticity, and other factors, by Darendeli and Stokoe (2001); and (4) new material models relating shear strain to volumetric strain for sandy soils and soils with fines by Stewart et al. (2002). The following sections present the rationale for making these changes and synthesize the critical features of the new model components.

Stress Reduction Factors (r_d)

The original stress reduction factors recommended by Tokimatsu and Seed (1987) are the factors by Seed and Idriss (1971) that have been widely used for soil liquefaction applications. These factors, shown by the solid lines in Figure 2, are based on the results of a limited number of ground response analyses. Seed et al. (2001) found these factors to be biased (generally high) based on a relatively extensive parametric study involving 2153 combinations of site profiles and input motions. Profiles of r_d from that study are also shown in Figure 2. Using these profiles, Seed et al. (2001) regressed r_d against *PHA*, depth (z), magnitude (m), and average soil shear wave velocity in the upper 12 m ($V_{s\text{-}12}$), and recommended the following relationship for the median of r_d:

$$z < 20 \text{ m}: \quad r_d = \frac{\left[1 + a_1/a_2(z)\right]}{\left[1 + a_1/a_3\right]} \tag{5a}$$

$$z > 20 \text{ m}: \quad r_d = \frac{\left[1 + a_1/a_2(z=20)\right]}{\left[1 + a_1/a_3\right]} - 0.0046(z - 20) \tag{5b}$$

where,

$$a_1 = -23.013 - 2.949 \cdot PHA/g + 0.999 \cdot m + 0.0053 \cdot V_{s-12}$$

$$a_2(z) = 16.258 - 0.201 \cdot e^{0.341(z + 0.0785 \cdot V_{s-12} + 7.586)}$$

$a_2(z=20)$ is $a_2(z)$ with z set to 20 m

$$a_3(z) = 16.258 + 0.201 \cdot e^{0.341(0.0785 \cdot V_{s-12} + 7.586)}$$

In all of the above, depth (z) is in meters and velocity ($V_{s\text{-}12}$) is in m/s.

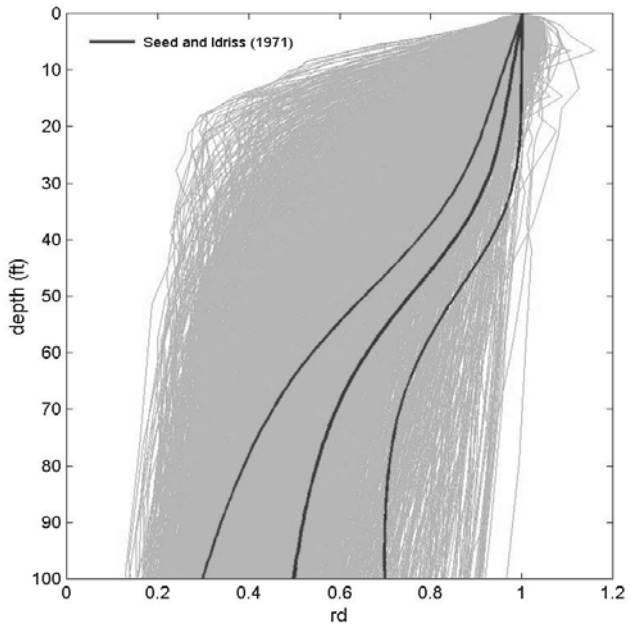

Fig. 2. Stress reduction factors recommended by Seed and Idriss (1971) along with ground response analysis results of Seed et al. (2001)

Equivalent Number of Uniform Strain Cycles (*N*)

Using a strong motion data set for tectonically active regions, Liu et al. (2001) developed empirical regression equations to evaluate the equivalent number of uniform stress cycles of earthquake shaking as a function of magnitude (*m*), site-source distance (*r*), site condition (*S*=0 for rock, *S*=1 for soil), and near-fault rupture directivity effects. The *N* values were derived based on weighting factors specific to the problem of soil liquefaction triggering. However, one of the sets of weighting factors used by Liu et al. was found by Stewart et al. (2002) to be appropriate for evaluation of equivalent number of uniform *strain* cycles (*N*) for the seismic compression of sand. Predictions by that model for non near-fault conditions are shown in Figure 3, and the median model predictions are given by,

$$\ln(N) = \ln\left[\frac{\left(\frac{\exp\left(b_1 + b_2\left(m - m^*\right)\right)}{10^{1.5m+16.05}}\right)^{-\frac{1}{3}}}{4.9\cdot 10^6\,\beta} + Sc_1 + rc_2\right] \tag{6}$$

where *r* is in km, $b_1 = 1.53$, $b_2 = 1.51$, $c_1 = 0.75$, $c_2 = 0.095$, $\beta = 3.2$, and $m^* = 5.8$.

This model is more consistent with the data than the model of Seed et al. (1975), which depends only on magnitude and is tailored to the problem of soil liquefaction. Figure 3 shows significant differences between these models, particularly at large distances.

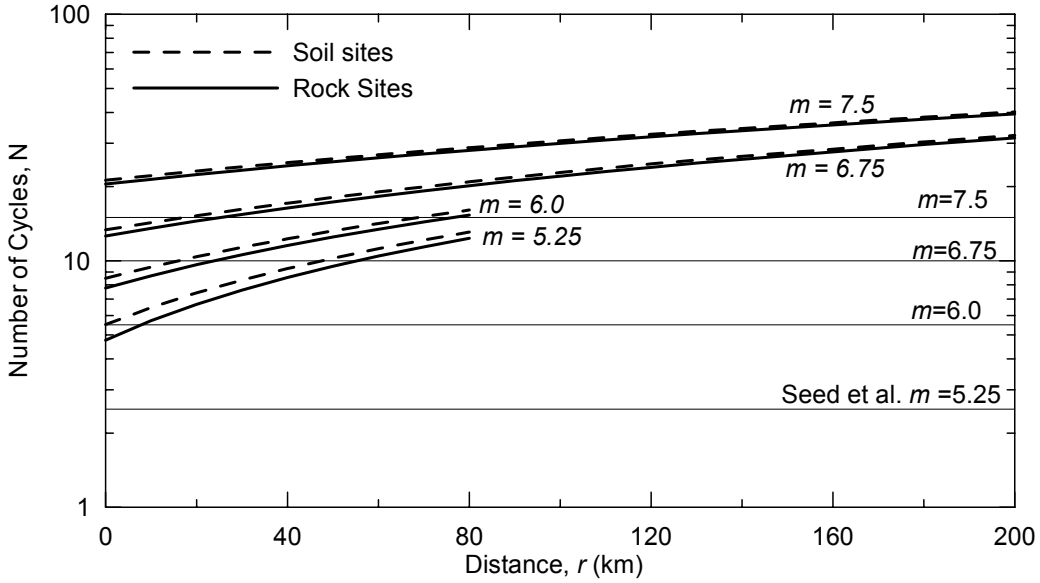

Fig. 3. Variation of median values of *N* with distance and magnitude from Liu et al. (2001) along with recommendations of Seed et al. (1975).

Modulus Reduction Curves

Modulus reduction curves have a critical role in the analysis procedure, as they are used to estimate shear strains per Eq. 4. Tokimatsu and Seed (1987) recommended the use of modulus reduction curves for clean uniform sands by Iwasaki et al. (1978), which vary with effective stress. The model for modulus reduction by Darendeli and Stokoe (2001) is based on a much larger suite of test results, and incorporates effects of effective stress (σ'), soil plasticity (as represented by plasticity index, PI), and overconsolidation ratio (OCR). Figure 4 shows a family of modulus reduction curves (based on the D&S model) for varying PI and σ' (the effects of OCR are generally small, and the plots in Figure 4 apply for OCR = 1, which is generally appropriate for fills at z >3-6 m, Duncan et al., 1991). Note that the plots in Figure 4 are formatted to directly estimate shear strain, γ from the product $\gamma \cdot (G/G_{max})$.

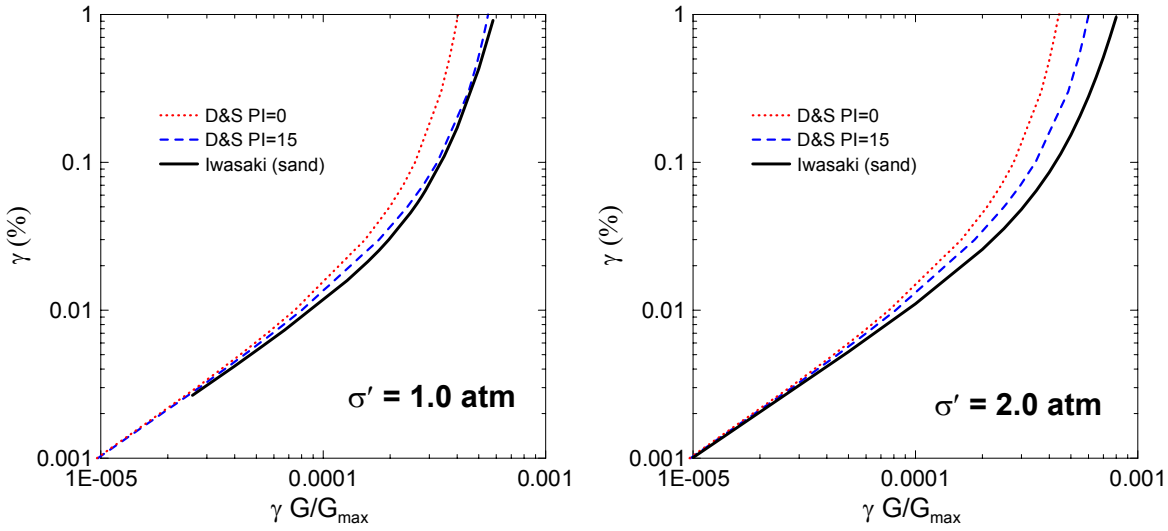

Fig. 4. Modulus reduction curves from Iwasaki (1978) and Darendeli and Stokoe (2001) re-expressed in format for estimation of shear strain amplitude, showing effects of effective overburden stress and soil plasticity

The D&S results show that nonlinearity decreases with increasing PI. At relatively large confining pressures ($\sigma' > 0.5$ atm), the D&S curves for both PI = 0 and 15 are more nonlinear than those by Iwasaki, which can affect significantly the computed shear strains.

Pradel (1998) performed a curve fit to the Iwasaki modulus reduction curves in Figure 4 using the following equation:

$$\gamma = \frac{1 + a \cdot e^{b \cdot R}}{1 + a} R \cdot 100 \ \text{(in \%)} \qquad (7)$$

where R is the product in Eq. 4. Fitting Eq. 7 to the D&S curves, a and b are found to be:

PI ≈ 15: $\quad a = 0.194 \cdot (\sigma'/p_a)^{0.265} \qquad b = 7490 \cdot (\sigma'/p_a)^{-0.418}$

PI ≈ 0: $\quad a = 0.199 \cdot (\sigma'/p_a)^{0.231} \qquad b = 10850 \cdot (\sigma'/p_a)^{-0.410}$

where p_a = 101.3 kPA. Shear strains for PI between 0 and 15 can be interpolated using Eq. 7.

Material Models for Volumetric Strain

A volumetric strain material model is defined as a relationship between (1) cyclic shear strain amplitude, γ_c, and $(\varepsilon_v)_{N=15}$ and (2) C_N and N. Tokimatsu and Seed (1987) recommended the use of volumetric strain material models that were derived from cyclic simple shear testing of clean sands by Silver and Seed (1971). Recent simple shear testing at UCLA has re-examined these relationships for clean sand and has developed models for several fill soils containing fines.

The UCLA test results on clean sands are synthesized in the left frame of Figure 5 at D_r = 60%, and are also compared to the test results of Silver and Seed (1971). The recent testing was performed on 16 sands spanning a range of sand compositional factors (gradation, grain size, grain angularity). No trends in $(\varepsilon_v)_{N=15}$ were found relative to these compositional factors, although the collective results provide insight into the variability associated with volumetric strain material models for sand. The right side of Figure 5 shows median ± two standard deviation results for C_N based on these same tests, which again show no dependence on sand compositional factors. Also shown is the recommended curve by Silver and Seed (1971), which predicts less settlement at earlier cycles ($N < 15$) and more settlement at latter cycles ($N > 15$).

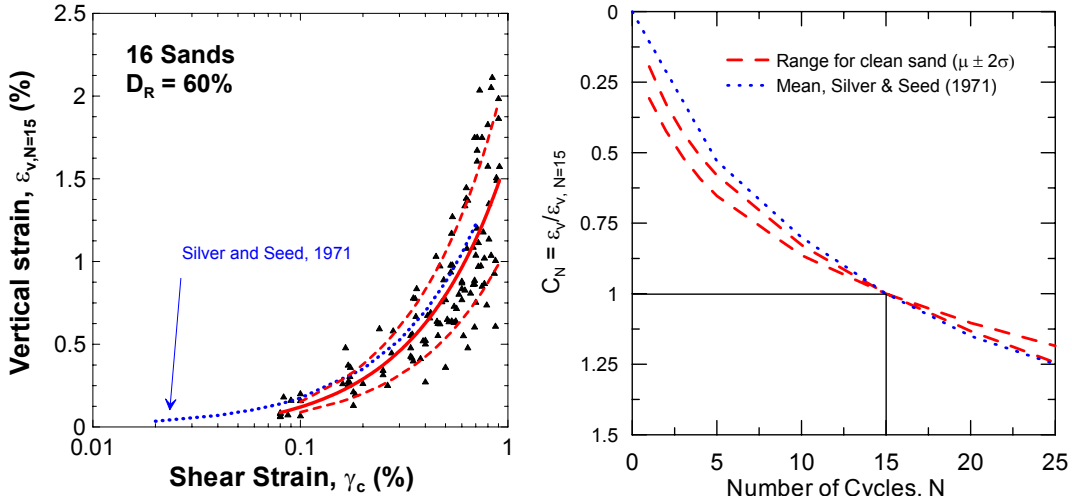

Fig. 5. Volumetric strain material models based on simple shear testing of clean sands

Testing of fill soils with fines has been performed on four specimens from two field sites that were investigated in detail by Stewart et al. (2002). The results provide insight into the effects of essentially non-plastic fines (PI = 2) and low plasticity fines (PI = 15) on the seismic compression susceptibility of compacted soils with large fines content (approximately 50%). Curve fits to these test results are compared to clean sand results in Figure 6, and show that

1. For the same Modified Proctor relative compaction (*RC*), soils with non-plastic fines experience less seismic compression than clean sands for a common set of baseline conditions, but these two materials behave similarly in the sense that *RC* is the principal construction-related factor affecting seismic compression (i.e. degree-of-saturation, *S*, is not important), and
2. Seismic compression in soils with low-plasticity fines decreases not only with increasing *RC*, but also for moderate *RC*s, decreases with increasing as-compacted degree-of-saturation (*S*). At low *S*, volumetric strains from seismic compression are comparable to those for sand (at a common *RC*), whereas at high *S* the strains are approximately one-quarter of those for sand.

The C_N curves for these materials are generally similar to the lower-bound C_N curve shown in Figure 5 (i.e. the curve showing the most rapid decrease with *N*). The results shown in Figure 6 for these materials may not be applicable to other fill soils.

Caution should be exercised in applying these test results to old fills that may be been subject to significant ageing and post-construction wetting, the effects of which on seismic compression are unknown.

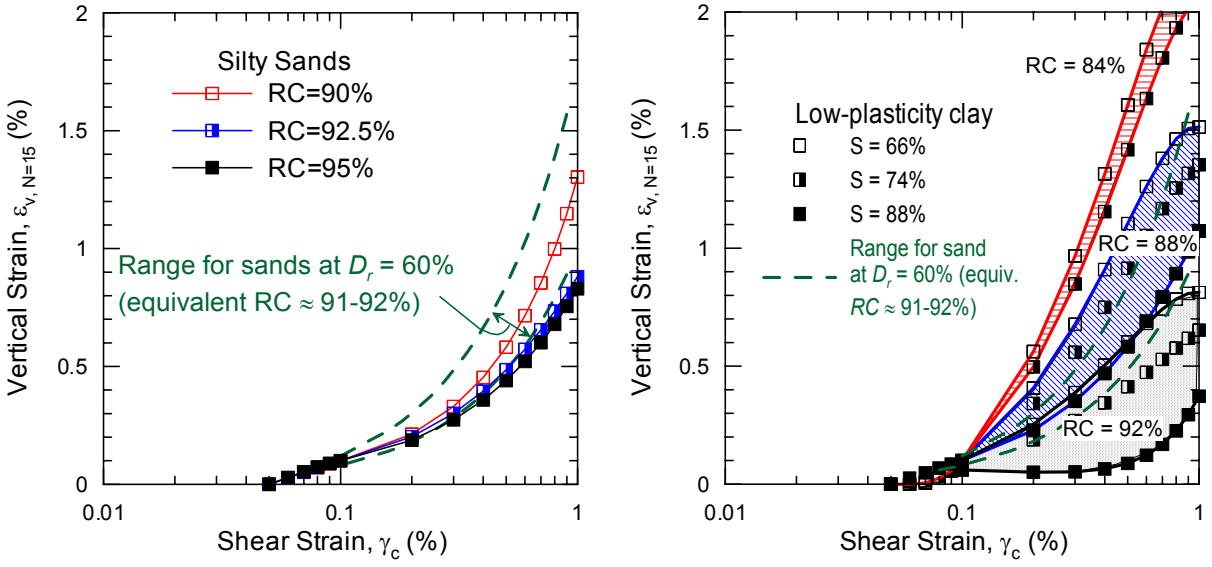

Fig. 6. Volumetric strain material models based on simple shear testing of soils with fines

Recommended Analysis Procedure

The procedure has three general steps: (1) estimation of shear strain amplitude within the fill soil mass from the peak acceleration at the ground surface and other seismological and site parameters; (2) estimation of volumetric strains within the fill mass based on compaction conditions in the fill, the shear strain amplitude, and the equivalent number of uniform strain cycles; and (3) integration of volumetric strains across the fill section to estimate settlement. Details on the first two steps follow:

1(a). Estimate *PHA* and *N* using appropriate seismic hazard analyses. The *PHA* value should apply for the ground condition at the surface of the fill. This will generally require accounting for ground response effects either through site-specific analysis (preferred) or application of an amplification factor. Amplification factor models applicable to the shallow soil over rock configuration of hillside fills are unavailable, but investigations of several specific sites by Stewart et al. (2002) have generally found PHA amplifications of about 1.5 to 2.0 for typical design levels of shaking (i.e. *PHA* on rock ≈ 0.3-0.7 g).

1(b). Measure or estimate shear wave velocity in fill soils, and estimate the maximum shear modulus as $G_{max} = V_s^2 \rho$, where ρ = mass density of soil.

1(c). Estimate stress reduction factors (r_d) as function of depth using the relation in Eqs. 5.

1(d). Estimate the variation of shear strain amplitude (γ_{eff}) with depth using Eq. 4 and Figure 4.

2(a). Estimate $(\varepsilon_v)_{N=15}$ based on γ_{eff} and soil compaction condition using appropriate material models for volumetric strain.

2(b). Estimate C_N and calculate $\varepsilon_v = C_N \times (\varepsilon_v)_{N=15}$. Multiply by two to account for multi-directional shaking effects.

COMPARISON OF ANALYSIS RESULTS TO CASE HISTORIES

In this section, we compare predictions from the above analysis procedure to observed settlements at three sites where such settlements are reliably known from survey measurements. One of the case studies is a fill blanket at the Jensen Filtration Plant shaken by the 1971 San Fernando, California earthquake (Pyke et al., 1975), and the other two (denoted Sites A and B) are canyon fills in Santa Clarita shaken by the Northridge, California earthquake (Stewart et al., 2002). It should be emphasized that these case histories do not provide a sufficient data set against which to calibrate the analysis procedure. We present these comparisons merely to illustrate the general performance of the model for typical design-basis levels of shaking in seismically active regions.

At the Jensen site, the clayey sand fill is up to 17 m thick and overlies 1.5-6 m of alluvium. The water table is located in the alluvium, which liquefied during the earthquake causing lateral spreading. Estimated peak accelerations at the site are 0.5-0.6 g. Observed settlements along a survey baseline were 12.7 cm, although some of these settlements can be attributed to lateral

spreading. Pyke et al. (1975) estimated the settlements from seismic compression to be approximately 9 to 10 cm.

At Santa Clarita Site A, the sandy clay fill is up to 24 m thick and overlies shallow alluvium and rock. Modified Proctor relative compactions of fill are ~88%, and the fill was generally compacted dry of optimum. Peak accelerations at the site have been estimated as 0.5-0.7 g. Settlements as large as 18 cm occurred in a building at the site during the earthquake. Site B has silty sand fill varying from 15 to 30 m thick overlying rock. Modified Proctor relative compactions of near-surface fill soils were approximately 92%, and approximately 95% at depth. Peak accelerations at the site have been estimated as approximately 0.8 to 1.2 g. Observed settlements of the fill ranged from about 2 to 6 cm.

For Santa Clarita Sites A-B, the variability of input parameters V_s and *PHA* was estimated and integrated into the analysis using a logic tree approach. Weighted means and standard deviations were calculated from the distributions of calculated settlements. Best estimate soil properties were used for the Jensen site. We account for matric suction effects on σ' in our analysis of γ. Matric suction does not affect total stress σ_o, but is estimated to add ~1 atm to σ' based on typical soil-water characteristic curves (Fredlund, 1993). As shown in Table 2, calculated settlements are reasonably consistent with observation for Jensen and Site A, but not for Site B. The problem at Site B appears to be the very strong levels of shaking (*PHA* > 1 g), for which Figure 4 provides unrealistically large estimates of γ. Site-specific ground response analysis of Site B provides unbiased estimates (Stewart et al., 2002), and appear to be needed to reliably estimate γ for very strong shaking.

Table 2. Summary of calculated (median ± one standard deviation) and observed settlements

Site	Recommended Procedure (cm)	Observation (cm)
Jensen	8.6	9-10
Site A	6.9 +/- 4.7	6
Site B	14.5 +/- 8.4	5.6

SUMMARY AND CONCLUSIONS

In this paper we first present field performance data from a subdivision strongly shaken by the Northridge earthquake that shows the important effect of fill vs. non-fill site condition on damage patterns for pipeline systems and house structures. The ground deformations causing, or at least strongly contributing to, this damage likely resulted from volumetric strain accumulation in compacted fill, which is referred to as seismic compression.

We present an analysis procedure to estimate ground settlements from seismic compression. The procedure de-couples the calculations of shear strain and volumetric strain, and utilizes recent research results on stress reduction factors (r_d), soil modulus reduction curves, and soil volumetric strain models. The results are generally found to compare favorably to observed field settlements, although problems in shear strain estimation are encountered for very strong levels of shaking (*PHA* values over ~1 g).

ACKNOWLEDGEMENTS

Support for this work was provided by the U.S. Geological Survey, National Earthquake Hazards Reduction Program, Award No. 1434-HG-98-GR-00037; a CAREER grant from the National Science Foundation (NSF Award No. 9733113); and the Pacific Earthquake Engineering Research Center's Program of Applied Earthquake Engineering Research of Lifeline Systems with funding from the Pacific Gas and Electric Company (PEER award number Z-19-2-133-96). This work made use of Earthquake Engineering Research Centers Shared Facilities supported by the National Science Foundation under Award #EEC-9701568. The views and conclusions contained in this document are those of the authors and should not be interpreted as necessarily representing the official policies, either expressed or implied, of the U.S. Government.

REFERENCES

Chang, S.W., Bray, J.D., and Seed, R.B. (1996). "Engineering implications of ground motions from the Northridge earthquake," *Bull Seism. Soc. Am.*, 86(1B), S270-S288.

Darendeli M.B. and Stokoe K.H. (2001). "Development of a new family of normalized modulus reduction and material damping curves," University of Texas, Geotechnical Engineering Report GD01-1.

Duncan J.M., Williams G.W., Sehn A.L., and Seed R.B. (1991). "Estimation of earth pressures due to compaction," *J. Geotech. Engrg.*, ASCE, 117 (12), 1833-1847.

Iwasaki T, Tatsuoka F., and Takagi Y. (1978). "Shear modulus of sands under cyclic torsional shear loading," *Soils and Foundations*, 18 (1), 39-50.

Fredlund, D. G. (1993). *Soil mechanics for unsaturated soils*, Wiley, New York.

Lawson, A. C., ed. (1908). "Minor geologic effects of the earthquake," *California earthquake of April 18, 1906*, Publ. 87, Vol. 1, Part 2, Carnegie Institute of Washington, D.C., 384-409.

Liu A.H., Stewart J.P., Abrahamson N.A. and Moriwaki, Y. (2001). "Equivalent number of uniform stress cycles for soil liquefaction analysis," *J. Geotech. and Geoenv. Engrg.*, ASCE, 127 (12), 1017-1026.

McClure, F.E. (1973). "Performance of single family dwellings in the San Fernando earthquake of February 9, 1971." NOAA, U.S. Dept. of Commerce, May.

Pradel D. (1998). "Procedure to evaluate earthquake-induced settlements in dry sandy soils," *J. Geotech. and Geoenv. Engrg.*, ASCE, 124 (4), 364-368.

Pyke R., Seed H.B., Chan C.K. (1975). "Settlement of sands under multidirectional shaking," *J. Geotech. Engrg.*, ASCE, 101 (4), 379-398.

Seed H.B. and Idriss I.M. (1971). "Simplified procedure for evaluating soil liquefaction potential," *J. Soil Mech. and Foundations Div.*, ASCE, 97(9), 1249-1273.

Seed H.B., Idriss I.M., Makdisi F., and Banerjee N. (1975). "Representation of irregular stress time histories by equivalent uniform stress series in liquefaction analyses," *Rpt. No. UCB/EERC-75-29*, U.C. Berkeley.

Seed, R.B., Cetin, K.O., Moss, R.E.S., Kammerer, A.M., Wu, J., Pestana, J.M., and Riemer, M.F. (2001). "Recent advances in soil liquefaction engineering and seismic site response evaluation," *Proc. 4th Int. Conf. on Recent Advances in Geotech. Eqk. Engrg. Soil Dyn*., Paper No. SPL-2

Silver M.L. and Seed H.B. (1971). "Volume changes in sands due to cyclic loading," *J. Soil Mech. and Foundations Div.*, ASCE, 97(9), 1171-1182.

Stewart J.P., Bray J.D., McMahon D.J., Smith P.M., and Kropp A.L. (2001). "Seismic performance of hillside fills," *J. Geotech. and Geoenv. Engrg.*, ASCE, 127 (11), 905-919.

Stewart J.P., Smith P.M., Whang D.H., and Bray J.D. (2002). "Documentation and analysis of field case histories of seismic compression during the 1994 Northridge, California earthquake," *Report No. PEER-2002/09*, Pacific Earthquake Engineering Research Center, U.C. Berkeley, October.

Tokimatsu K. and Seed H.B. (1987). "Evaluation of settlements in sands due to earthquake shaking," *J. Geotech. Engrg*., ASCE, 113(8), 861-878.

Wald, D.J. and Heaton, T.H. (1994). "A dislocation model of the 1994 Northridge, California, Earthquake determined from strong ground motions," *Open-File Report 94-278*, U.S. Geological Survey.

Fault-inflicted Damage to Civil Infrastructures
-- Lessons Learned and Possible Remedial Measures --

Kazuo Konagai

ABSTRACT

A number of devastating earthquakes took place in rapid succession in the closing year of the International Decade for Natural Disaster Reduction (IDNDR). Among them, Aug. 17, 1999 Kocaeli Earthquake in Turkey and Sept. 21, 1999 Chi-Chi Earthquake in Taiwan were extraordinary. One of the most spectacular aspects of these earthquakes was the damage to structures inflicted directly by faulting, and is posing us difficult problems about minimizing the fault-related damage. A discussion on this issue, thus, must be based on a quite different scenario from those for ordinary designs in which ground accelerations and/or velocities are crucial factors. On November 2000, The Japan Society of Civil Engineers (JSCE) organized a taskforce for establishing remedial measures for damage to civil-infrastructures.

The taskforce aims (1) to investigate previous examples of faulting and fault-related damages, (2) to develop efficient and reliable tools for predicting possible extents of fault-induced soil deformations, (3) to discuss possible measures for minimizing losses of life and damage to a variety of structures, and with all abovementioned, (4) to enable decision makers to better understand the nature of the hazard and to assist them to identify appropriate ameliorative actions**.** The research activity of the taskforce incorporates works of many others, especially with respect to risk identification and analysis, and the taskforce is making up an ***assumed scheme for Seismic-Fault-Zoning Act*** as a chart for integrating these individual works. In this scheme, thrust faults receive due attention because two thirds of active fault systems in Japan are thrust faults. Zoning for thrust faults is in general more difficult than that for strike-slip faults because a bundle of thrust faults often make up a "wider brush" with many fault traces hidden in areas off the most suspicious line recognized from surface configurations. This paper provides an overview of the findings and future problems discussed among the taskforce members.

Kazuo KONAGAI, Professor, Institute of Industrial Science, University of Tokyo, 4-6-1 Komaba, Meguro-ku, Tokyo 153-8505, Japan.

INTRODUCTION

The 1999 ChiChi Earthquake in Taiwan, Kocaeli and Duzce Earthquakes in Turkey were a serious threat of possible destructions of mega-cities that spread over some hidden fault traces, and poses us difficult problems to minimize the fault-inflicted damage. In some less populated regions, limiting development within known and active fault zones would be very effective, and in California, USA, a law to this effect has been enacted since the early 1970s. This law, "Alquist-Priolo Fault Zoning act" (California Geological Survey[1)]), requires the State Geologists to establish regulatory zones (Earthquake Fault Zones) around the surface traces of active faults. Before a project is permitted, a geological investigation is required, and the construction of a building is permitted only if the building is located more than 50 feet off a fault trace. A similar zoning act has been enacted in Auckland, New Zealand [2)] as well.

It is, however, noted that the laws in California and New Zealand deal with strike-slip faults, while about two thirds of active faults in Japan are thrust faults. As contrasted with strike-slip faults, a bundle of thrust faults make up a "wider brush" with many fault traces hidden in areas off the most suspicious line recognized from surface configurations. In addition, these areas are often densely populated in such overpopulated countries as Taiwan and Japan.

To discuss possible remedial measures, a taskforce was organized in the Japan Society of Civil Engineers. The taskforce aims (1) to investigate previous examples of faulting and fault-related damages, (2) to develop efficient and reliable tools for predicting possible extents of fault-induced soil deformations, (3) to discuss possible measures for minimizing losses of life and damage to a variety of structures, and with all abovementioned, (4) to enable decision makers to better understand the nature of the hazard and to assist them to identify appropriate ameliorative actions**.** The details follow next.

OVERVIEW OF THE TASKFORCE ACTIVITIES

The research activity of the taskforce incorporates the work of many others, especially with respect to risk identification and analysis. Examples follow as:

Digital database of previous examples of faulting and fault related damages

Materials for the following examples were collected:

(a) ShihKang area (1999 ChiChi Earthquake, Taiwan): In the Chi-Chi earthquake, Taiwan, the activated fault appeared branching east off the recognized trace of the Chelungpu fault in the vicinity of Feng-Yuan City, and crossed the Shih-Kang area. One branch of this fault crossed the northern end of Shih-Kang dam causing its three spillways to be completely destroyed. The maximum vertical offset of about 10 meters was reached there. Materials collected include a survey map of Sihkang area, a crack map of the dam etc. (from collaborators in Taiwan incl. Kung ChenShan, SINOTECH)

(b) Yalova-Izmit areas (1999 Kocaeli Earthquake, Turkey): The earthquake that originated at a shallow depth of about 17 km produced spectacular right-lateral faulting over the western part of the North Anatolian fault. The fault ran across Gölcük city facing the Izmit Bay of the Marmara Sea. Some waterfront areas of Gölcük were flooded due to a down drop movement of soil of several meters along the fault. -- Materials collected include those from R. ULSAY, Haceteppe Univ., D., URAL, Istanbul Technical Univ. and the Japan Geotechnical Society team)

(c) Outlet tunnel of Kakkonda hydropower station (**Figure 1**, 1998 Mid-North Iwate Earthquake, Japan): An earthquake of M=6.1 shook north-western area of Iwate prefecture, Japan, at 16:58, September 3, 1998, injuring 10 people. The focal depth of this earthquake was quite shallow enough for one of the activated faults to appear across a paddy field; the fact is quite unusual for earthquakes of this magnitude. One of the fault planes that appeared as the straight rising mark in a paddy field, crossed a concrete outlet tunnel of the second Kakkonda hydroelectric power station. The circular tunnel wall was cracked up into several large pieces. Some pieces of the cracked wall were pushed in the tunnel reducing the tunnel's cross-section. One cracked piece of about 2 m high and 2 m wide completely fell down onto the invert allowing the soil with big boulders (30 - 50 cm) to be squeezed into the tunnel. -- Materials collected include a crack-map of the damaged tunnel etc. (from Tohoku Electric Power Co. Ltd)
(d) Tanna Tunnel (1930 North Izu Earthquake, Japan): A crack map of the tunnel etc. from RTRI.
(e) Inatori Tunnel (1978 Off the IzuOshima island Earthquake.): A crack map of the tunnel, Buckled rail: Even off the fault rupture plane, buckling of rails can occur, and cause derailment etc. from RTRI.
(f) Rokko Tunnel (1995 Kobe Earthquake): Crack maps etc. from RTRI.
(g) Bol viaduct (1999 Duzce Earthquake, Turkey): Materials from Kawashima, K., Tokyo Inst., Technology.
(h) Traces of faulting found at ruins (many earthquakes. In Japan): Materials from Sangawa, A., Active Fault Research Center, National Research Institute of Advanced Industrial Science and Technology.
(i) Active fault maps (digital, 1/25,000) published by Nakata, T., Hiroshima Univ. and Imaizumi, T., Yamanashi Univ.

Efficient and reliable tools for predicting possible extents of fault-induced soil deformations

Experiments:

(j) Dry sand models were sheared at their bases. The models were then CT-scanned to visualize shear bands formed in their interiors. (by Central Research Institute of Electric Power Industry, and Tani, H., Yokohama National University)
(k) Experiments by Taniyama, H., Saitama University
(l) Experiments by Bray, J., UC Berkeley.
(m) Both dry and water-saturated sand models were sheared at their bases. For the saturated case, negative pore pressure built up was remarkable at around the corner wedge of the base rock as the base rock cut further deep in the surface sand, and the surface sand deformation differed remarkably from the dry case (by Konagai, K. and Johansson, J., IIS, University of Tokyo).

Numerical tools: (all files will be open to public)

Tools that the taskforce members have been developing will allow for discussions of large deformations of soils, (liquefaction, landslides etc). As long as we stay within small deformation range, natural hazards are not thoroughly described nor understood by many stakeholders. Tools will require two sets of data, one for experts, the other for decision makers.

(n) Applied Element Method (Ramancharla, P. and Meguro, K.[4])
(o) Stochastic Finite Element Method (Anders and Hori, M.[5])
(p) Lagrangian Particle Finite Difference Method (See **Figure 2,** Konagai, K. and Johansson, J.[6]).
(q) Large Strain Finite Element Analysis of Local Second Gradient Model by Matsushima, T. Tsukuba Univ.

Discussions for minimizing losses of life and damage to a variety of structures (still going on)

(r) Flexible supports for bridges (Iemura, H. and Kawashima, K. etc)
(s) Soft tunnel coating for seismic isolation (Suzuki, T., etc)
(t) Installation of Emergency Valves etc. (East Bay Municipal Utility District (EBMUD), USA).
(u) Slip joint of Clyde dam, (New Zealand)
(v) Analysis of rail buckling (Railway Technical Research Institution)

Figure 1 Outlet tunnel of Kakkonda Hydropower Station (Konagai et al. [3])

Above: Entire view of the cracked tunnel

Below: Soil including boulders of 30-50 cm diameter was squeezed in the tunnel.

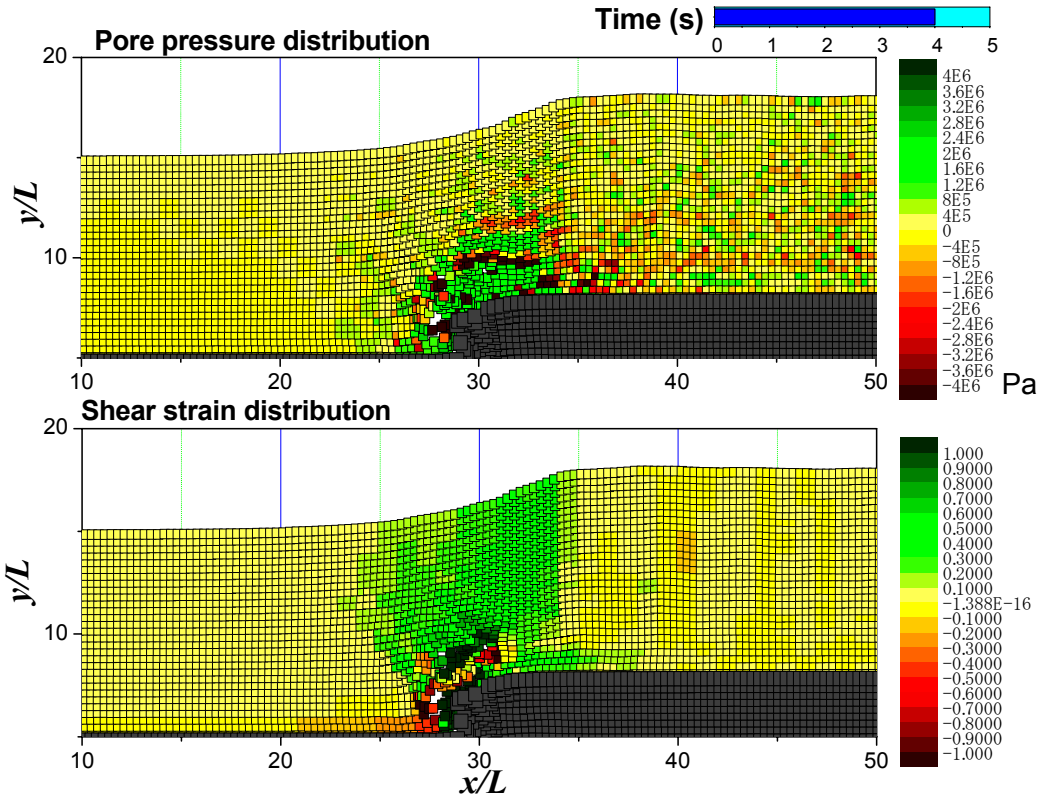

Figure 2 Simulation of Faulting by using Lagrangian Particle Finite Difference Method (Konagai and Johansson[6])

This figure shows simple simulation of reverse faulting. When the soil mass was immersed in water, the pore pressure distribution within the surface soil underwent some drastic changes as the base rock came steadily up in it at the rate of 1m/s. No sooner than the base rock began pushing the soil deposit, positive pore pressure was instantaneously induced along the soil-base rock interface. However, negative pore pressure was then gradually built up at around the corner wedge of the base rock (hanging wall) as the base rock was pushed further up. This negative pore pressure is substantially large enough to reach the cavitation threshold and to cause the surface soil configuration to differ from that without pore pressure effect.

ASSUMED SCHEME FOR SEISMIC FAULT ZONING ACT

To allow for further synthetic integration, the taskforce is making up an ***assumed scheme for Seismic-Fault-Zoning Act***.

Tentative articles for this scheme follow:

A1. Faults to be dealt with

The law deals with 1st and 2nd category active faults. For a fault with a possible slipping rate faster than 1m/1000 years and/or high potential for the next occurrence (>10%), the strictest rule (Rank A, See **Table 1** in **Article 4**) will be applied, while Rank B is applied to the others.

[Explanation]

The Research Group for Active Faults of Japan, which has been organized by the authors of "Active Faults in Japan", University of Tokyo Press, 1980, has confirmed that more than 2000 active faults exist and are classified as follows:

(1) 1st category active faults that have been activated in the past 10,000 years, and have caused some damage to existing structures and/or responsible for earthquake occurrences,

(2) 2nd category active faults that have been known activated in the past 10,000 years, and have deformed diluvial terraces.

Among the 1st category active faults, those having high average slipping rates λ larger than 1m/1000 years are referred to as "Class A" faults, and those with 1m/1000 years $> \lambda >$ 0.1m/1000 years and 0.1m/1000 years $> \lambda$ are "Class B" and "Class C" faults, respectively.

The headquarters for Earthquake Research Promotion has been organized under the Prime Minister's Office to promote research into earthquakes with the goal of strengthening disaster prevention measures, particularly the reduction of damage and casualties from earthquakes. Its sub-committee for Long-term Evaluations provides its estimation of possible recurring times of period for major active faults as well as the potential for the next occurrence of major earthquakes (See **Figure 3**).

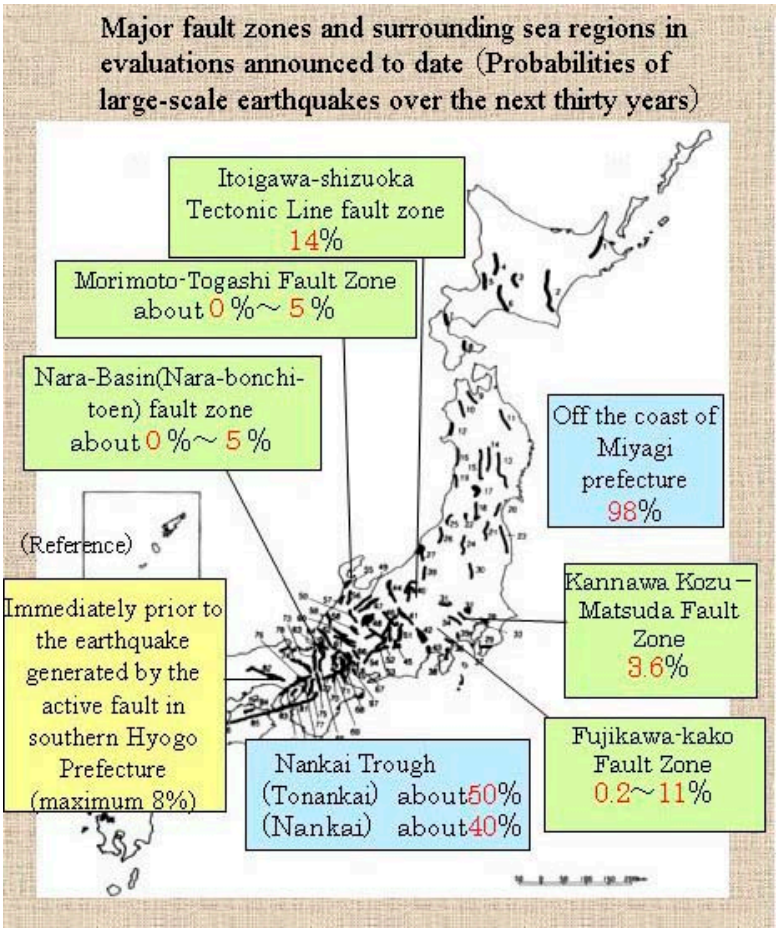

Figure 3 Probabilities of large-scale earthquakes over the next 30 years (Headquarters for earthquake research promotion[7])

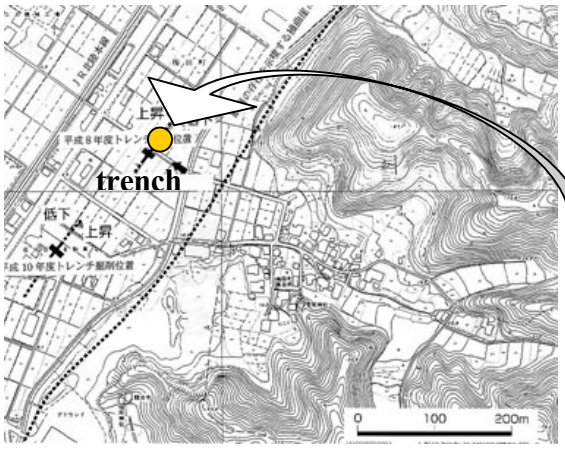

Figure 4. Location of a fault trace found 100 m off the older fault along mountains

Figure 5 Trench wall of Morimoto fault (Photo by Sangawa)

A2. Project defined

"Project" used hereafter means any of the followings:

(1) Structures for human occupancy
(2) Lifelines for human transportation
(3) Important civil-infrastructures such as dams etc.

They determine ***stakeholders***. The stakeholders are colleague researchers, and senior management and practitioners in key enterprises. They also include cities and counties responsible for requiring seismic-retrofitting, permitting constructing buildings for human occupancy etc.

A3. Fault zones

The law requires Prefecture Geologists to establish regulatory zones called "Earthquake Fault Zones" around the surface traces of active faults and to issue appropriate maps. The zones vary in width, but average about 300 m wide with a strike-slip fault trace put in its middle. But as for a thrust fault along a boundary between mountains and a flat land, the fault zone shall cover about 300 m wide the flat land with the fault trace put aside along the zone's edge. This does not necessarily mean the exterior area on the mountains side is safer than that on the flatland side. As for intense shakes are concerned, it is quite often that the shake is very intense on the hanging wall side. It is also to be noted that soft soil deposits are often responsible for amplifying base input motions. "Earthquake Fault Zones" are just for accounting for considerable deformations of soils.

[Explanation]

Differing from strike-slip faults, a thrust fault can appear abruptly in a flat land several hundreds meters off the older fault trace that is recognized from surface geological configurations. **Figures 4** and **5** show respectively the location of a newly found Morimoto fault trace and a photo of a trench excavated across it. The fault was found about 100 m off the recognized old fault trace along the mountainside. A base mud rock is cutting sharp in an overlying soft soil deposit, while the soil deposit is gently bent by the base rock. And there was nothing remaining on the ground surface evidencing the presence of this hidden fault. It is noted here that the right-hand side of the base rock (hanging wall) that came about 1m up into the surface soil deposit was not on the mountain side but on the flat land side. Assuming that a soil wedge was pushed up and we were looking at just one side of the

wedge, this fact suggests the presence of another new fault hidden further away from the mountains, and actually, this new fault was found in 2001 about 500m off the mountains (Nakata and Imaizumi, 2002). This seemingly says that the width of 300m for the Fault Hazard Zone may not be wide enough. The hidden fault, however, will not reach the ground surface through a thick soil deposit. Taking this advantage, some restrictions may be eased.

A4. Restriction:

As a distinct base rock rupture propagates up through overlying soil material, strains will spread and decrease. The overall strain induced within the surface soil deposit will be represented by D/H where D= dislocation of the base rock and H = thickness of the soil deposit. If the material is brittle, the distance that the base rock rupture propagates will be large, while in a soft overlying material strains will be absorbed. Thus, comparing D/H with the soil's failure strain γ_y will provide necessary information for possible remedial measures for fault-inflicted damage to civil infrastructures. The parameter $\zeta = D/\gamma_y H$ thus determines the restriction levels for projects in a fault zone as listed in **Table 1**.

As for important civil infrastructures, numerical simulations are necessary to ensure that the restrictions and/or measures taken will be effective.

A possible D value will be determined from either:

(1) the maximum credible dislocation observed at nearby trenches, outcrops etc., or
(2) the possible maximum dislocation of an asperity that has ever estimated for an event in the concerned fault system.

Table 1. Restrictions for **Rank A** faults

Restriction Level	ζ	Project in **Article 2(1)** (Dwellings etc.)	Project in **Article 2(2)** (Railways, Roads etc.)
1	$1>\zeta$	A structure **can** be placed over a suspicious trace of fault **only if** it has a stiff mat foundation with no or little embedment depth.	**Tunnels:** A tunnel can be constructed across a fault only if expected ξ value is staying below the critical value for the structure. Parameter ξ describes the representative strain induced within a tunnel (See **Section 4.2**).
2	$x>\zeta>1$	If an active fault is found, a structure for human occupancy cannot be placed over the trace of the fault and must be set back by $\alpha \times \zeta \times H$ from the fault. Parameter α differs in different types of faults (Normal, Reverse, Strike-slip).	In principle, it is desirable not to construct a tunnel across a fault. But if unavoidable, necessary measures for keeping its cross-section open as it was must be taken. In this case also ξ determines the details of the measures.
3	$\zeta>x$	Ditto.	Avoid construction

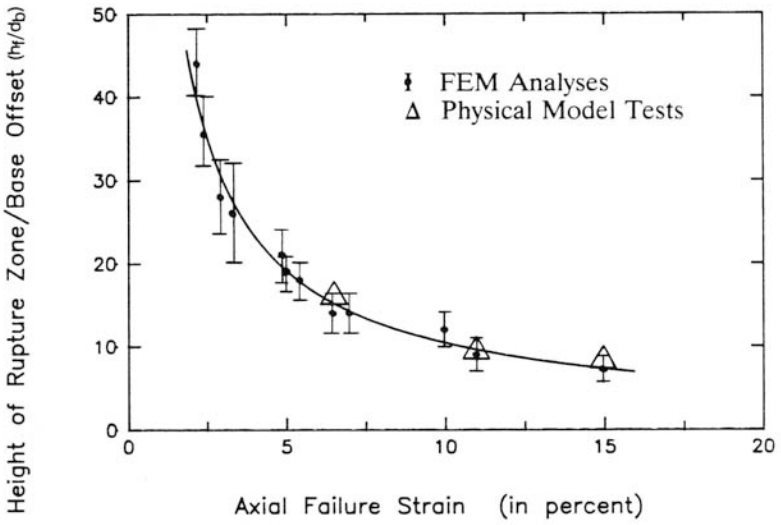

Figure 6 Normalized height of shear rupture zone in soil overlying base rock fault as a function of soil's failure strain (after Bray et al. [8])

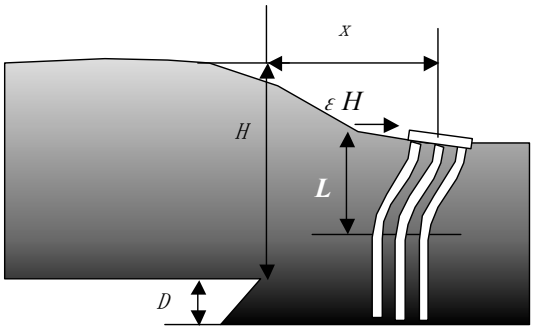

Figure 7 Piles deformed in the overlying soil deposit

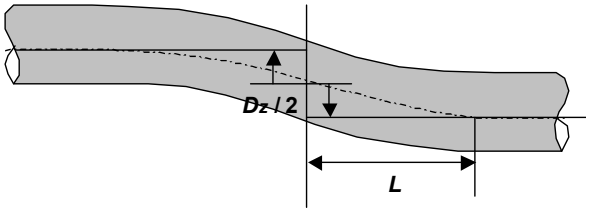

Figure 8 Tunnel experiencing fault dislocation

[Explanation]

Bray (1994) found through both his numerical and experimental studies that at a specified amount of bed rock fault displacement, the height that the shear rupture will propagate up into the overlying soil can be related to the failure strain of the soil as shown in **Figure 6**.

The curve in Fig.6 seemingly exhibits some hyperbolic feature, and the product of the normalized height H/D by the soil's failure strain γ_y is about 100%. This means that the shear rupture reaches the overlying ground surface when $\zeta(=D/\gamma_y H)$=1.0.

A4.1 Countermeasures for Project in Article 2(1):

In principle, avoid construction of structures over a fault trace. If an active fault is found, a structure for human occupancy must be set back by $\alpha \times \zeta \times H$ from the fault. But if unavoidable, it is allowed to do it only when parameter ζ is less than 1.0 and the structure has a stiff mat foundation with no or little embedment depth so that a fault rupture can be diverted around or go beneath the foundation.

A4.2 Countermeasures for Project in Article 2(2):

Underground structures (Tunnels, piles etc.)

Under lateral loading, the horizontal deflection of a pile decreases with increasing depth. In practice, most laterally loaded piles are indeed 'flexible' in the sense that they are not deformed over their entire lengths. Instead, pile deflections become negligible below an active length (or effective length) L (**Figure 7**). The active length, an important parameter in the design of a pile foundation, depends largely on the ratio of the pile stiffness EI (= number of piles grouped together × EI for a single pile) for flexural deformation and the soil stiffness G, and is proportional to:

$$L_0 = \sqrt[4]{EI / G}$$

Assuming that the pile cap displacement is proportional to $H\zeta$, the overall strain induced within the pile will be represented by $H\zeta / L_0$ (=ξ hereafter). Details of countermeasures will be determined depending upon ξ, and it will be useful to summarize a monograph describing pile cap displacements and rotations in terms of $H\zeta$ and ξ.

For tunnels, $H\zeta$ in ξ may be replaced with the fault rupture displacement D_z at the point where the tunnel meets the fault plane (**Figure 8**).

CONCLUSIONS

Surface fault rupture has been more strongly recognized as a principal earthquake hazard since the dramatic Kocaeli (Turkey), Chi-Chi (Taiwan) and Dutze (Turkey) earthquakes of 1999. Damage to bridges, dams and tunnels in these earthquakes motivated the enactment of a fault-zoning act in Taiwan. In some less populated regions, limiting development within known and active fault zones would be very effective. This limitation, however, might be very difficult in overpopulated areas. In Japan, at least 2000 faults inland are known to be active, and some cities of large populations exceeding a million are found just on thick fault traces. They include Kyoto of 1.5 millions population above Hanaori fault, a historical city with a large number of temples and shrines, Osaka with 2.6 millions population above Uemachi fault, Nagoya, 2.2 million, with Tenpaku fault and Kobe spreading over a bundle of faults. Zoning thus necessarily requires extensive discussions with clear scientific evidences provided so that a social consensus is reached. In this discussion, it is noted that soil strain is not always localized on a particular fault rupture plane, but can be distributed within a certain band along the fault. It is, noted that the most faults dealt with fault hazard mapping acts in both California and New Zealand are strike-slip faults, while about two thirds of active faults in Japan are thrust faults. As contrasted with strike-slip faults, a bundle of thrust faults make up a "wider brush" with many fault traces hidden in areas off the most suspicious line recognized from the surface configuration.

A JSCE taskforce has been organized to discuss and establish possible remedial measures for damage to urban facilities. The taskforce has been investigating the previous examples of faulting and fault-related damages, and is archiving them as a digital data set. Based on the collected data, the taskforce is now making up an ***assumed scheme for Seismic-Fault-Zoning Act,*** in which a fault zone is established in different ways for different fault types. The overall strain induced within a surface soil deposit overlying a stiff base rock can be represented by D / H where D= dislocation of the base rock and H = thickness of the soil deposit. If the material is brittle, the distance that the base rock

rupture propagates will be large, while in a soft overlying material strains will be absorbed. Thus, the parameter $\zeta = D/\gamma_y H$ determines the restriction level in an established Fault Zone. Active length, $L_0 = \sqrt[4]{EI/G}$, is also an important parameter. For a flexible structure embedded or buried in soil, L_0 is short. When L_0 is compared with a possible fault dislocation D, it provides an idea of possible strain induced within this structure.

However, the assumed scheme for now is just for integrating works of many individual researchers. Many problems are to be solved for more practical details. Along faults, for example, alluvial soil deposits including large boulders are often found. To see how these large inclusions in a soil matrix affect the soil's overall behavior, an extensive study will be necessary, and is to be addressed in a later publication.

REFERENCES

[1] California Geological Survey: Alquist Priolo Earthquake Fault Zones, California Department of Conservation, http://www.consrv.ca.gov/cgs/rghm/ap/index.htm, 2002.

[2] Wellington Regional Council: Hazard management, http://www.wrc.govt.nz/em/hazrep.htm, 2002.

[3] Konagai, K., Mikami, A., Katagiri, T., Ahsan, R. and Maruyama, D.: Report of damage caused by the Mid-North Iwate Earthquake of September 3, 1998, *Bull., Earthquake Resistant Structure Research Center*, IIS, University of Tokyo, **32**, 3-13, 1999.

[4] Ramancharla, P.K. and Meguro, K: Applied Element Simulation of Non-linear Behavior of Dip-slip Faults for Studying Ground Surface Deformation, *Proceedings of A Workshop on Seismic Fault-induced Failures*, JSPS, 109-114, 2001.

[5] Anders, M. and Hori, M.: Three-dimensional stochastic finite element method for elasto-plastic body, *Int. J. Numer. Meth. Engng*., **51**, 449-478, 2001.

[6] Konagai, K. and Johansson, J.: Two Dimensional Lagrangian Particle Finite Difference Method for Modeling Large Soil Deformations, *Structural Eng./ Earthquake Eng.* **18(2)**, 91s-95s, 2001.

[7] Headquarters for earthquake research promotion: http://www.jishin.go.jp/main/index-e.html, 2002.

[8] Bray, J.D., Seed, R.B. and Seed, H.B.: Analysis of Earthquake Fault Rupture Propagation through Cohesive Soil, Journal of Geotechnical Engineering, ASCE, **120(3)**, 562-580, 1994.

Near-field Effects of the 2000 Western Tottori-prefecture Earthquake on Kasho Dam

Tatsuo OHMACHI[1], Naoyuki KOJIMA[2]
and Atsushi MURAKAMI[3]

ABSTRACT

During the 2000 Western Tottori-prefecture earthquake (M_J7.3), strong motion records at Kasho Dam showed peak acceleration of 2051gal at the dam crest and 531gal at the dam bottom, respectively. Despite such large acceleration, the 46m-high concrete gravity dam escaped from significant damage to the dam body. However, the reservoir water level showed sudden drop of 6cm after the main shock, which was followed by damped free vibration lasting for hours. As for the seismic fault of the earthquake, no trace of the fault rupturing was discovered on the ground surface in the near field including the dam site.

Integration of time histories of the strong motion acceleration at the dam bottom resulted in permanent displacement of 28cm to the north, 7cm to the east and uplift of 5cm. Since the dam site was located just above the hidden fault, the sudden drop of the reservoir water level and the permanent displacement of the ground were near-field effects of the seismic faulting. The free vibration was the seiche of the reservoir water, having such characteristics as the period of 6.5min and a damping ratio of 2%.

Relative displacement between the top and the bottom of the dam was detected by a plumb line vertically installed in the dam body. Apparently, the main shock induced the relative displacement of 2.8mm in the left-bank side (X) direction, and 0.7mm in the upstream (Y) direction, respectively. The small relative displacement is consistent with the fact that the dam body was not damaged by the strong shaking.

INTRODUCTION

At 13h30m (local time) on October 6, 2000, the 2000 Western Tottori-prefecture, Japan earthquake occurred with the magnitude M_J7.3. Kasho Dam is located in the near field of the earthquake, and strong motion records at the dam showed 2051gal and 531gal at the upper and lower parts of the dam, respectively. Despite such large acceleration, the dam

[1] Professor, Interdisciplinary Graduate School of Science and Engineering, Tokyo Institute of Technology, 4259 Nagatsuta-cho, Midoriku, Yokohama, Japan 226-8502

[2] Civil Engineer, Metropolitan Expressway Public Corporation, 6-6-2, Nishi-Shinjuku, Shinjuku, Tokyo, Japan 160-0023. (Formerly, Graduate Student at Tokyo Institute of Technology, Yokohama, Japan)

[3] Graduate Student, Interdisciplinary Graduate School of Science and Engineering, Tokyo Institute of Technology, 4259 Nagatsuta-cho, Midoriku, Yokohama, Japan 226-8502.

escaped from significant damage to the dam body, but minor damage such as concrete cracking on the side-wall of an elevator shaft was observed. There was also no report on the increase in the leakage water after the earthquake. Nevertheless, the reservoir water level recorded at the dam showed sudden drop of 6cm immediately after the main shock, followed by damped free vibration lasting for hours.

As for the seismic fault, no trace of the fault rupturing was discovered on the ground surface in the near field including the dam site. Even with the state-of-the-art knowledge and technology, it is impossible to predict when and where such earthquakes due to hidden faults will take place. To the authors' belief, the first step to cope with this kind of unpredictable earthquakes is a case study on causes and effects of such earthquakes. The case of Kasho Dam in the 2000 earthquake will give us good lessons on what happens to civil engineering structures in the event of seismic rupturing of a hidden fault underlying the structures. This paper was reconstructed from our previous paper [1], excluding detailed description on numerical simulations.

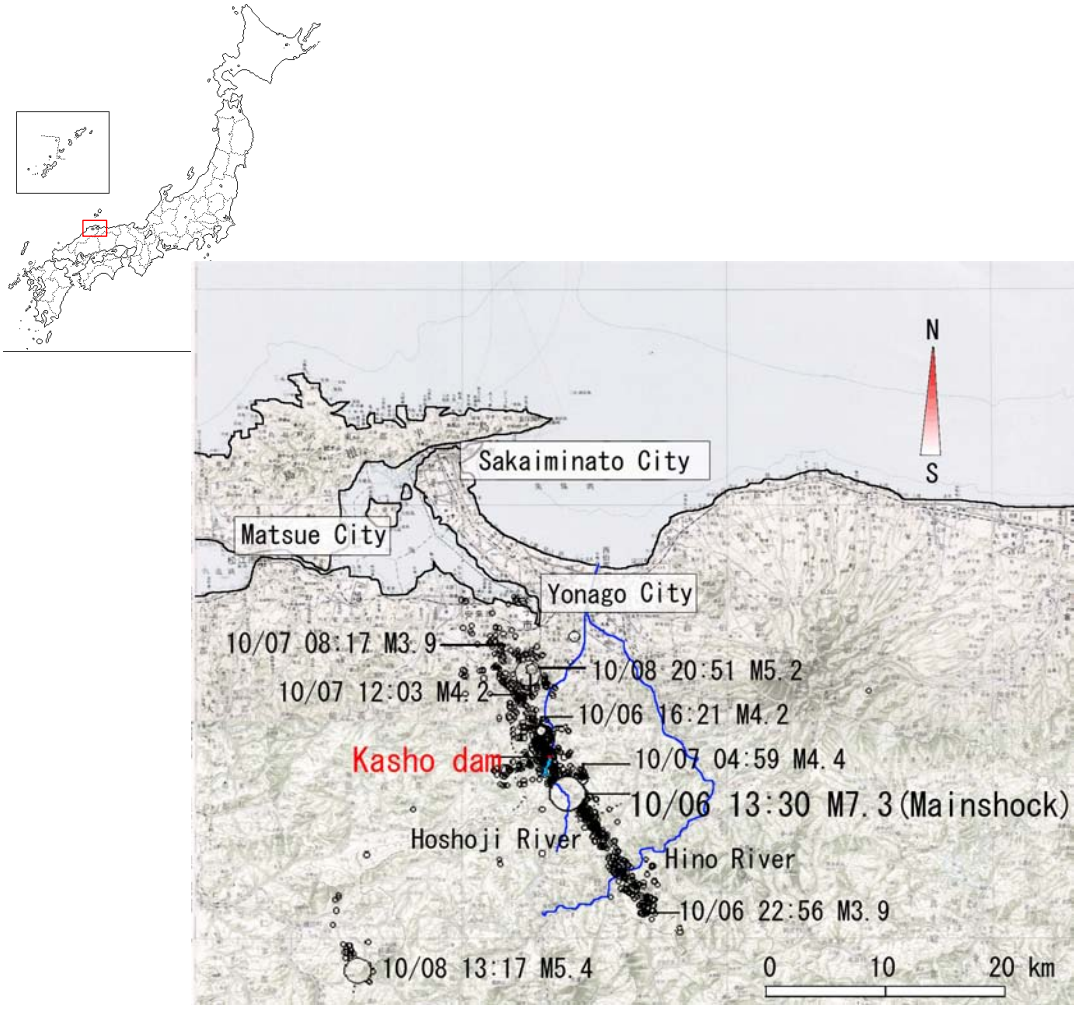

Figure 1 Location map showing the main shock, aftershocks and Kasho Dam

STRONG MOTION RECORDS OBSERVED AT KASHO DAM

Kasho Dam is a concrete gravity dam with the height of 46.4m and the crest length of 174m, constructed in 1989. The location of the dam is shown in Figure 1, in which locations of the main shock and aftershocks of the 2000 Western Tottori-prefecture earthquake are also shown. In Figure 1, it is evident that the seismic faulting took place just below the dam site of Kasho Dam. The full water level of the dam reservoir is EL. 118m, while the water level was EL. 112m when the main shock occurred.

At Kasho Dam, several monitoring systems are installed. Among them, two sets of three-component strong motion accelerometers (seismometers) are installed at two places. One at the upper part is fixed at EL. 124.5m on the concrete floor of the upper elevator room next to the dam crest, and the other at the lower part is at EL. 87.0m on the concrete floor of the lower inspection gallery, as shown in Figure 2. Although the azimuth of the dam axis is N110° E , horizontal components of both seismometers are installed in the N-S and E-W directions. Peak accelerations recorded during the main shock of the 2000 earthquake are listed in Table 1. A reservoir water level meter of a floating type is also installed in a concrete cottage next to the dam crest, as shown in Figure 2.

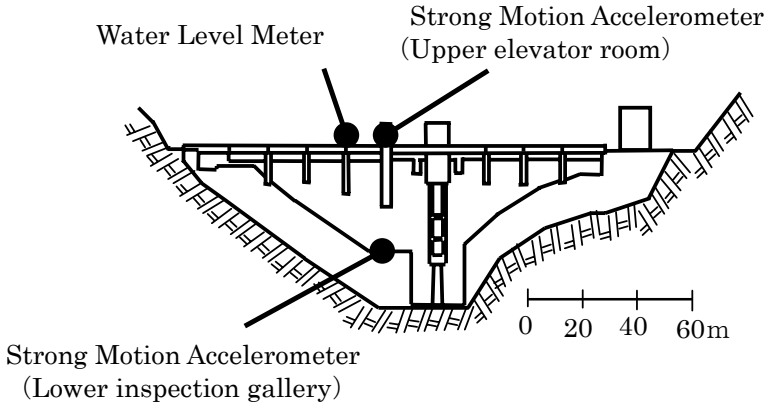

Figure 2 Location of seismometers and water level meter.

Table 1 Peak acceleration at Kasho Dam

	Lower inspection gallery	Upper elevator room
N-S Component	529 gal	2051 gal
E-W Component	531 gal	1406 gal
U-D Component	485 gal	884 gal

Figure 3 Kasho Dam viewed from the downstream right bank.

A downstream view of the dam is shown in Figure 3, in which the above-mentioned elevator shaft and concrete cottage are shown. A standard cross section of the dam is shown in Figure 4, which shows a tunnel spillway equipped at EL. 93.0m. The spillway is provided with two gates. One on the downstream side is a main gate of a radial-gate type, and the other on the upstream face is a sub-gate of a roller-gate type. To operate the sub-gate, there is a sub-gate control room overhanging from the dam crest. The sub-gate control room and the upper part of the elevator shaft suffered concrete cracking on the floor and the walls, respectively, due to the strong shaking of the main shock, which will not be mentioned in more detail here.

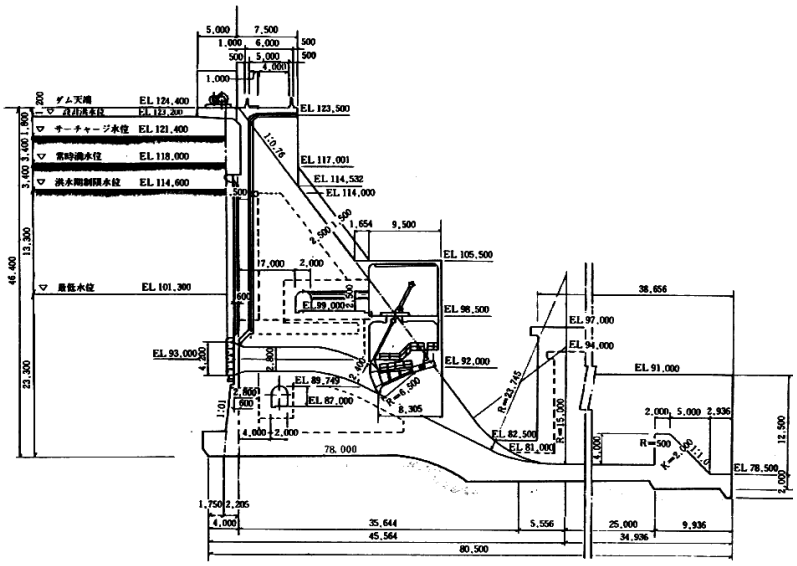

Figure 4 Standard Cross Section of Kasho Dam

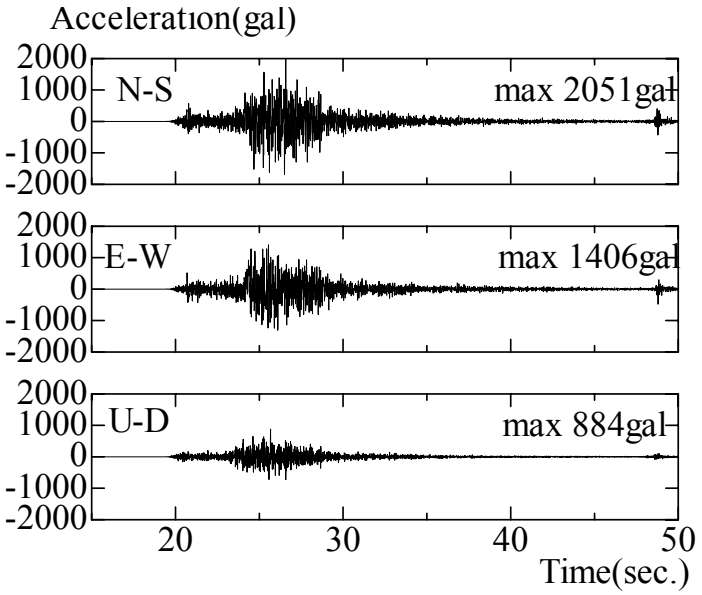

(a) Records observed in the upper elevator room

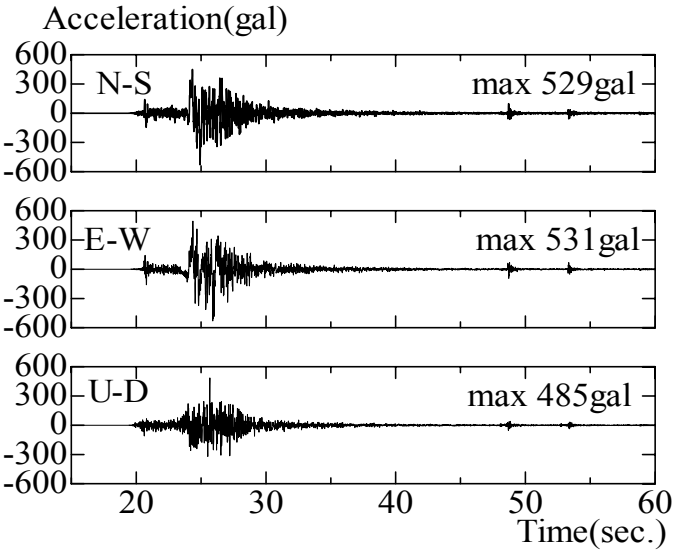

(b) Records observed in the lower inspection gallery

Figure 5 Strong motion records observed at Kasho Dam.

Time histories recorded at the two places of the dam are shown in Figure 5. The acceleration data were sampled at 100Hz with 24bit numbers. A reliable range of frequency is said to be as wide as from DC to 41 HZ.

GROUND DISPLACEMENT CAUSED BY THE SEISMIC FAULTING

To estimate seismic ground displacement, the acceleration time histories shown in Figure 5(b) were integrated twice with respect to time, with the results shown in Figure 6. According to Figure 6, it seems reasonable to think that the dam base was displaced in three directions in different manners. In the N-S direction, the displacement occurred almost monotonously to the north and permanent displacement of 27.6cm to the north remained after the shaking. In the E-W direction, the displacement was like a single sine-wave with a permanent displacement of about 6.5cm to the west. In the U-D direction, the displacement was like a single pulse with a permanent uplift of about 4.7cm.

With the boundary element method, a numerical simulation was conducted to estimate the earthquake-induced ground displacement for the square area of 23km long in the NS direction and 17km wide in the EW direction, in which Kasho Dam and its reservoir are included [1]. Table 1 shows the fault parameters used in the simulation.

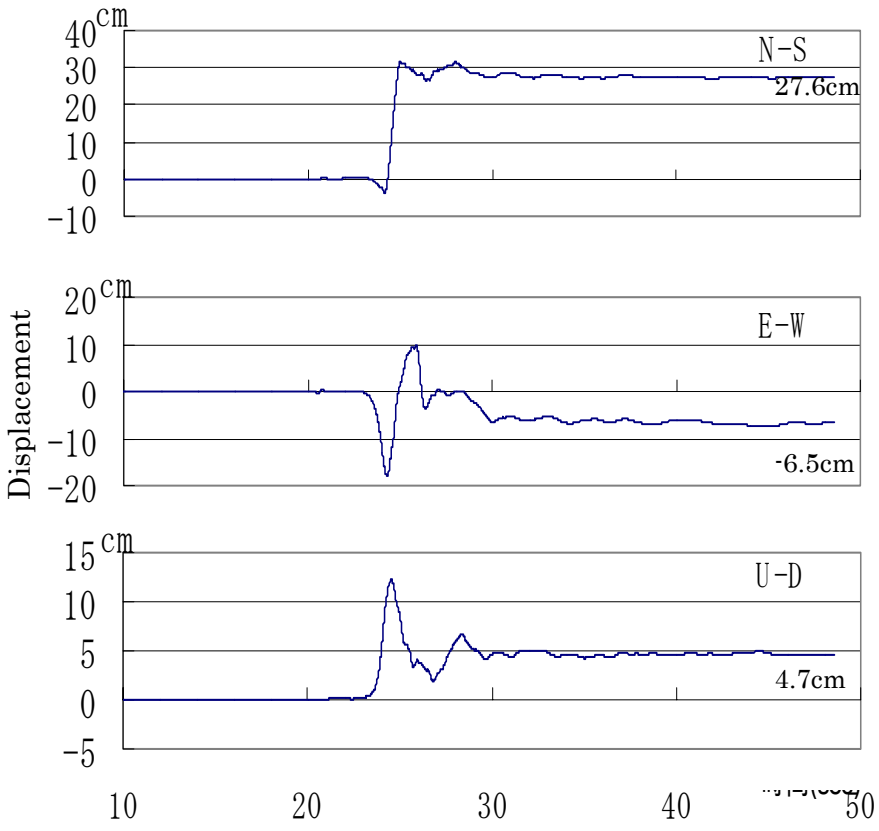

Figure 6 Displacement time histories obtained by integration of acceleration in Figure 5.

Table 2　Fault parameters used in the simulation.

Item	Value
Strike （degree）	152
Dip （degree）	86
Rake （degree）	-7
Dislocation （*m*）	1.4
Depth of the fault （*km*）	1.0
Fault length （*km*）	20
Fault width （*km*）	10

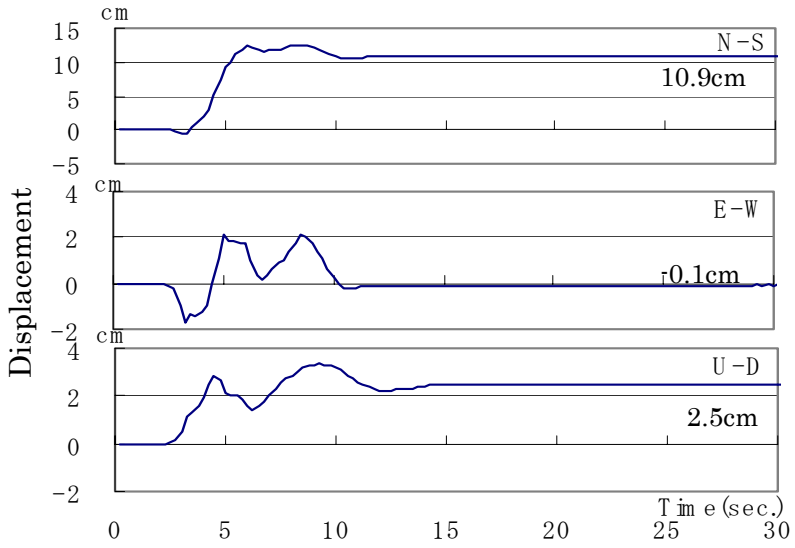

Figure 7　Ground displacement at Kasho Dam estimated from numerical simulation

The simulation indicated a general trend of uplift to the north-east of the reservoir, and settlement to the south-west of the reservoir. This trend was consistent with the result of a ground survey conducted after the main shock. Figure 7 shows time histories of the simulated displacement at the dam, which are roughly similar to their counterparts shown in Figure 6, though they are not exactly the same with one another. The simulated ground displacement at the dam is 10.9cm to the north, 0.1cm to the west, and 2.5cm of uplift.

Based on the similarity between the observation and the simulation as a whole, it seems reasonable to think that the dam site was displaced by the seismic faulting of the main shock, as was inferred from the integration of the strong motion acceleration.

EARTHQUAKE-INDUCED INCLINATION OF THE DAM

To detect relative displacement between the top and the bottom of the dam, a plumb line has been vertically installed in the dam body. The upper end of a steel string is fixed at the floor of the elevator room, next to the strong motion accelerometer, while the lower end connected with a weight is accommodated in a measurement device located in the lower inspection gallery. The measurement is automatically conducted a few times a day. From Figure 8 which shows readings of the plumb line, the main shock induced the relative displacement of 2.8mm in the X- (left-bank side) direction, and 0.7mm in the Y- (upstream) direction, respectively.

By integrating twice the differential strong motion acceleration between the top and the bottom of the dam, the relative displacement was calculated, with a result shown in Figure 9. The relative displacement shown in Figure 9 is 0.1mm at most in both N-S and E-W directions and 0.03mm at most in U-D direction, and converged to zero after the strong shaking. These displacements seem to be consistent with the fact that the dam body was free from significant damage.

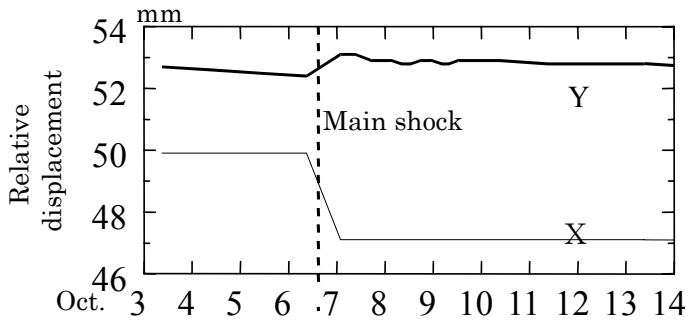

Figure 8 Relative displacement detected with the plumb line

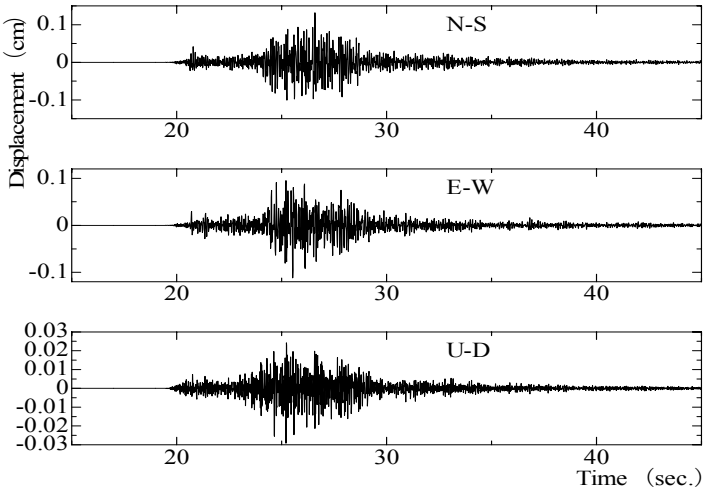

Figure 9 Relative displacement calculated from differential strong motion acceleration

Hence the relative displacement detected with the plumb line can be attributed to the earthquake-induced inclination of the dam as well as of the ground.

CHANGE OF THE RESERVOIR WATER LEVEL

The record of the water level before and after the main shock is shown in Figure 10, in which a sudden drop of the water level amounting to about 6cm is seen on both time histories with high and low resolutions, shown at upper and lower parts respectively. The records also indicate that, following the sudden drop, the water level showed damped free vibration for hours.

To analyze the water level record, it was roughly reproduced from readings of the peaks and troughs as shown in Figure 11(a). From the reproduced records shown in Figure 11(a), the free vibration characteristics such as the period and the damping factor were estimated from the Fourier spectrum of the data shown in Figure 11(b). The period and the damping ratio were found to be 6.5min and 2%, respectively.

As described earlier, the dam site was displaced by the seismic faulting, which gave rise to uplift of the dam body and incremental reservoir capacity resulting from the change in the ground slope under the reservoir. These are regarded as the main causes of the sudden drop of the reservoir water level. A schematic explanation is shown in Figure 12, in which the dam and ground conditions before and after the earthquake are shown by thin and thick lines, respectively.

In Figure 12, $\triangle H_1$ is the water level change due to the incremental water capacity, which is roughly estimable from an average settlement of the reservoir area, and $\triangle H_2$ is the water level change due to the uplift of the dam. When the simulated displacement shown in Figure 7 is used, $\triangle H_1$ and $\triangle H_2$ are found to be –1.5cm and 2.5cm, respectively, as shown in Figure 12. Accordingly, the water level change resulting from the simulation given by $\triangle H = \triangle H_1 + \triangle H_2$ is expected to be –4.0cm, which seems to agree fairly well with the observation.

Free vibration of the reservoir water is often referred to as seiche or seiching. The fundamental period T for a rectangular reservoir is approximately given by

$$T = \frac{2a}{\sqrt{gh}} \qquad (1)$$

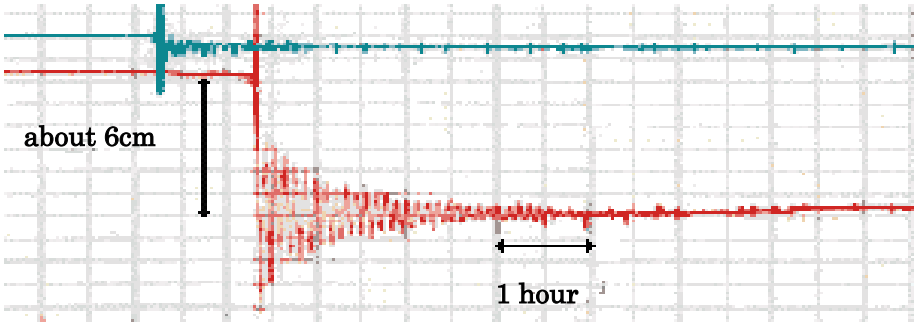

Figure 10 A copy of the reservoir water level record

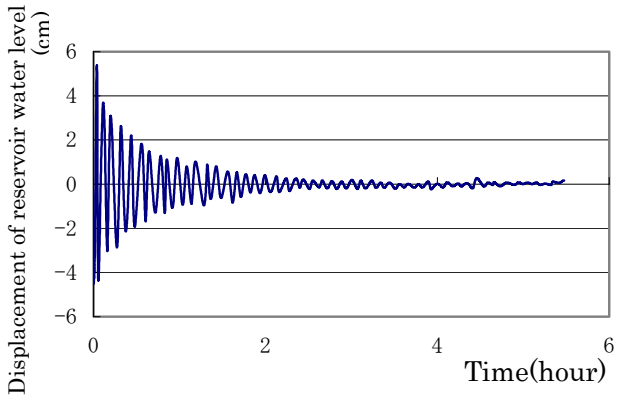

(a)

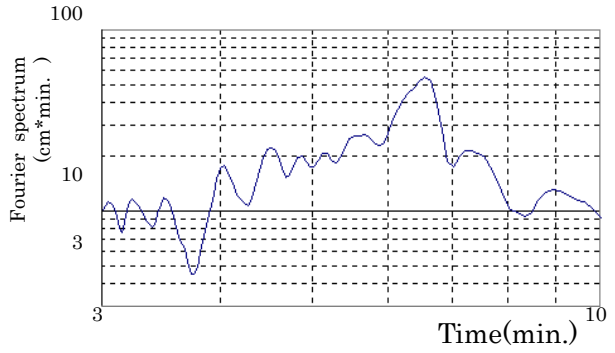

(b)

Figure 11 Reproduced free vibration data of the reservoir water level (a) and its spectrum (b).

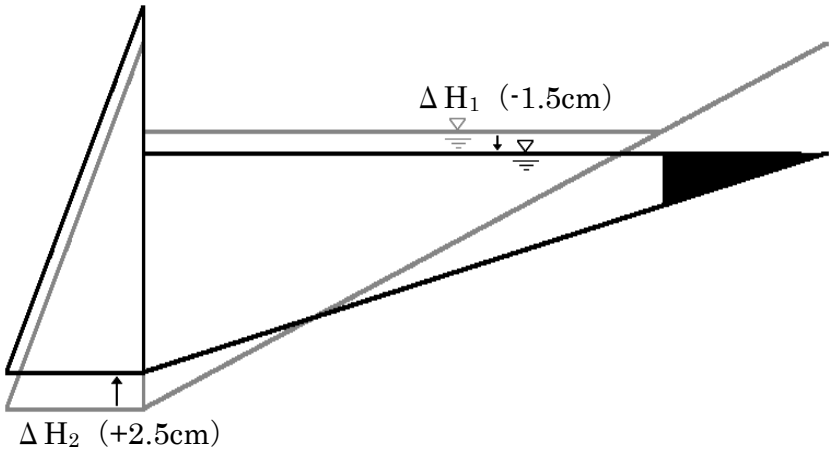

Figure 12 Schematic explanation of the water level change caused by the ground displacement

where a and h are the length and the depth of the reservoir, respectively, and g is acceleration of gravity. Introducing a=2km and h=10m into Equation (1) as approximations for Kasho Dam leads to T=7.0min, which is close to the observed period of the free vibration 6.5min. Hence, it seems highly probable that the free vibration of the reservoir is the seiche. On this basis, the simulation of the seiche was conducted using a numerical technique recently developed for tsunami simulation [2]. The technique is basically to solve the Navier-Stokes equation, using the 3-D finite difference method (FDM). In the simulation, for the sake of simplicity, the dam and the ground were assumed to be rigid.

A result of the simulation is shown in Figure 13, which shows a time history of the reservoir water level at the dam [1]. According to Figure 13, the fundamental period of the simulated seiche is 7.5min (450sec). The change of the water surface in the fundamental mode is like a see-saw movement with an axis at the middle of the reservoir. Although the simulated period is a little longer than the observed one, the difference is understandable and in an allowable range when the roughness of the simulation model is considered.

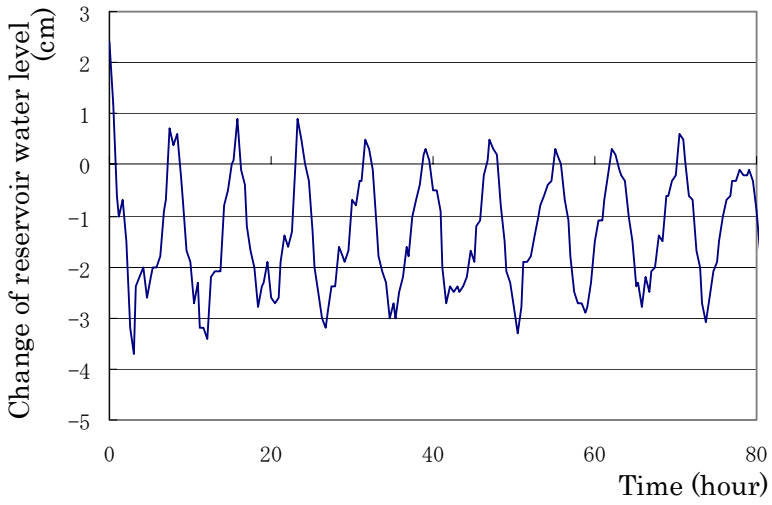

Figure 13 Time history of simulated water level at Kasho Dam

CONCLUSIONS

During the 2000 Western Tottori-prefecture earthquake (M_J7.3), strong motion records at Kasho Dam showed as large acceleration as 2051gal at the top and 531gal at the bottom. Despite such large acceleration, the dam survived the earthquake without damage to the dam body. However, sudden drop of the reservoir water level and slight inclination of the dam to the left bank side were observed immediately after the main shock.

In the meantime, no trace of the fault rupturing was discovered on the ground surface in the near field of the earthquake. Since the dam was located just above the hidden fault, permanent displacement of the ground was observed over the dam site including the dam and the reservoir.

This was confirmed from a fact that, when the strong motion acceleration at the dam bottom is integrated twice with respect to time, permanent displacement at the dam was calculated to be 28cm to the north, 7cm to the west and uplift of about 5cm. The sudden drop of the water level and inclination of the dam body were found to be attributable to the permanent displacement of the ground under the reservoir.

Following the sudden drop of the reservoir water level, free vibration of the water level was observed with the period of 6.5min and a damping ratio of 2%. The free vibration was found to be what is called the seiche of the reservoir water.

ACKNOWLEDGMENT

The authors would like to express his thanks to Department of Civil Engineering, Tottori Prefecture for providing a variety of valuable information about effects of the 2000 earthquake on Kasho Dam. This study was partially supported by the Ministry of Education, Science, Sports and Culture, Grant in Aid for Scientific Research No.13480119 (Ohmachi, T.) and No.12555134 (Kawashima, K.).

REFERENCES

[1] Ohmachi, T. Kojima, N. and Murakami, A. (2002).” Near-field response of Kasho Dam to the 2000 Western Tottori-prefecture , Japan earthquake. (submitted for publication in Journal of Natural Disaster Science).

[2] Ohmachi, T., Tsukiyama, H. and Matsumoto, H.(2001).”Simulation of tsunami induced by dynamic displacement of seabed due to seismic faulting”, *BSSA* Vol. 91, NO.6, 1898-1909.

AN EXPERIMENTAL STUDY ON FAULT RUPTURE PROPAGATION IN SANDY SOIL DEPOSIT

Jea Woo Lee, Ryoichi Iwanaga, Go Tabuchi and Masanori Hamada

ABATRACT

Kocaeli(1999, Turkey) and Jiji(1999, Taiwan) earthquakes revealed that ground surface ruptures, induced by faulting movement in the underlying bedrock, could cause severe damages to the major infra structures in highly populated area. Although a few of researchers in Japan and US have tried to understand this complex phenomenon, much of problems are still remained as unsolved. This paper presents the results of experimental studies to examine the mechanism of the rupture propagation in soil deposits. Based on the results from various cases of faulting tests under 1-g condition, useful information to predict the location and the magnitude of surface ruptures have been provided. Numerical analysis has been also performed to investigate the response of sandy soil subjected to dip-slip faulting using finite difference method and Mohr-Coulomb failure criterion. By the comparison of between the experimental results and the analytical results, it is confirmed that the numerical model can't predict the propagation of ground rupture with an enough accuracy.

Jea Woo Lee, PhD Student, School of Science and Engineering, Waseda University, 3-4-1, Ohkubo, Shinjuku-ku, Tokyo, Japan, 169-8555
Ryoichi Iwanaga and Go Tabuchi, Graduate Student, School of Science and Engineering, Waseda University, 3-4-1 Ohkubo, Shinju-ku, Tokyo, Japan 169-8555
Masanori Hamada, Professor, School of Science and Engineering, Waseda University, 3-4-1, Ohkubo, Shinjuku-ku, Tokyo, Japan, 169-8555

INTRODUCTION

Recent earthquakes occurred at Kocaeli (Mw 7.3, 1999, Turkey) and Jiji (Mw 7.9, 1999, Taiwan) revealed that ground surface ruptures, induced by faulting movement in the underlying bedrock, could cause severe damages to the major infrastructures. Surface rupture along the Chelungpu fault during Jiji earthquake in Taiwan, thrust buildings laterally, and racked buildings and industrial facilities such as concrete dam, lifelines due to differential vertical ground movements (Refer to Figure 1). Similarly a number of buildings and public facilities were injured from the combination of lateral and vertical movement of surface ground during Kocaeli earthquake in Turkey. In spite of harmlessness owing to the extremely low population in Tibet plateau, Central Kunlun (Ms 8.1, 2001, China) earthquake produced 400 km long surface fault rupture zone, the length and maximum displacement of which is the largest among the surface rupture zones reported on so far. These tragic events invoked us the necessities of proper understanding of fault rupture propagation through soil deposits.

A few of seismic researchers in Japan and US have continuously paid their efforts to examine the complex phenomenon through experimental and analytical studies. Roth et al. (1982) performed a series of centrifugal tests to simulate the rupture propagation of sand under more realistic gravity stress condition. Cole et al. (1984) presented a theoretical model to predict the location of surface rupture based on the results from a series of 1-g fault box tests of alluvial sand. Bray et al. (1994) released the experimental and analytical results of studies on the response of saturated clay soils to bed rock displacement. Several series of 1-g fault box test using Toyoura sand and silica sand in dry were carried out to investigate the effect of fault type on the required displacement to form shear rupture by Tani et al. (1994, 1999), who also suggested the modified analytical model to predict the behavior of rupture propagation based on their experimental studies.

In this study a series of model test for dip-slip faulting using 1-g fault test box has been conducted to examine the rupture propagation in dry sand with particular concern on the relationship between the fault type and the affecting factors required to develop complete shear ruptures to ground surface. An improved testing device was prepared to minimize sorts of possible errors during the test. The results from numerical simulation utilizing elasto -plastic theory and finite difference scheme additionally present an appropriate agreement with the experimental results.

SETUP AND PROCEDURE FOR 1-G FAULT RUPTURE TEST

Preparation of Testing Apparatus

Two kinds of testing devices, similar to them used by Cole et al. (1984) and Tani et al. (1994), have been introduced to conduct the dip-slip (normal/reverse) faulting tests under 1-g condition. Both of the devices are not identical in dimension and configuration but have been

designed to function in the same way. The earlier-made device (Apparatus I, Figure 2(a)) was molded with steel frame and acrylic board-walled box of which dimension is 2.0m-0.5m-1.0m in length, width and depth. And a hand-operated hydraulic jack was used to activate the up and down movement of bottom plate in the apparatus.

On the contrary Apparatus II (Figure 2 (b)) was built up using a lager glass-walled box of which dimension is 3.0m-1.0m-1.0m in length, width and depth, one-half of its basal plate could be moved up or down along various angles to relative to the fixed half using a electronically controlled high-capacity motor. The adjustable rolling hopper was also assembled to place the sand in the testing box at a uniform density, whereas it was not available to the earlier device. Figure 2 explains the details of updates of the improved device.

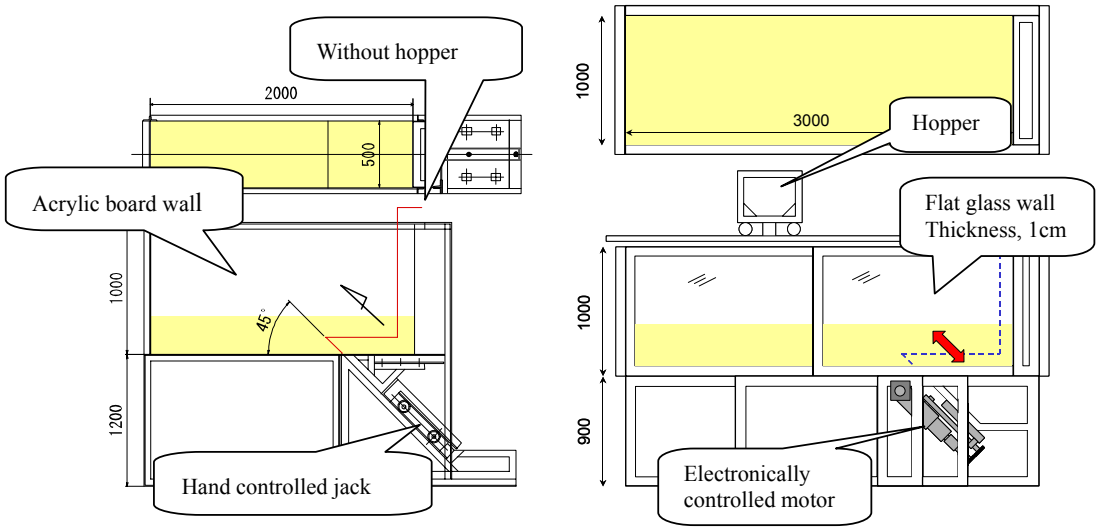

(a) Apparatus I **(b)** Apparatus II

Figure 2. Testing devices used in 1g-fault test

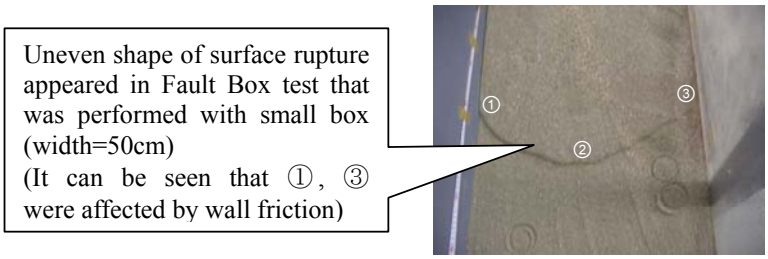

Figure 3. Half-moon shape of surface rupture due to wall friction

While performing sorts of tests using the smaller apparatus, some of troubles such as the leakage of sand, unexpected shape of failure line and the effect of wall friction were encountered. The most serious one among them was thought to be the effect of wall friction which was regarded to be caused by relatively narrow width of testing box and high level of frictional resistance between acrylic board wall and soil comparing with case of glass wall. Since this effect is apt to form a distorted pattern of deformation as shown Figure 3, it makes it difficult to measure the exact location of rupturing point on the surface of soil mass.

It is shown that this problem can be effectively avoided by the use of the glass walled box and sufficient width of testing box for the apparatus, as the experimental results form the improved testing apparatus presents no significant evidence of wall friction such as a configuration similar to a half moon shape of failure surface. (Refer to Figure 5 (c))

Specimen for Test

Basically the specimen used in the experiments is divided into dense and loose granular materials. Silica sand of which D_{50} - that corresponds to the grain size 50% finer - is 0.157mm, was placed in the apparatus at a uniform densities for dense/loose state - its relative density, D_r is about 83±4%, 59±4% respectively - by raining itself into the box with the adjustable hopper. Several number of laboratory tests using small-size aluminum can have been performed to measure the density of sand for each case. The soil parameters related to grain size are summarized in Table 1 and Figure 4.

Table 1. Soil parameters used in tests

Material Type	Silica Sand No. 7
Average Grain size D_{50}	0.157 mm
Uniformity Coefficient Uc	1.55
Coefficient of Curvature Uc'	0.946
Relative Density Dr	Loose : 59±4% Dense : 83±4%

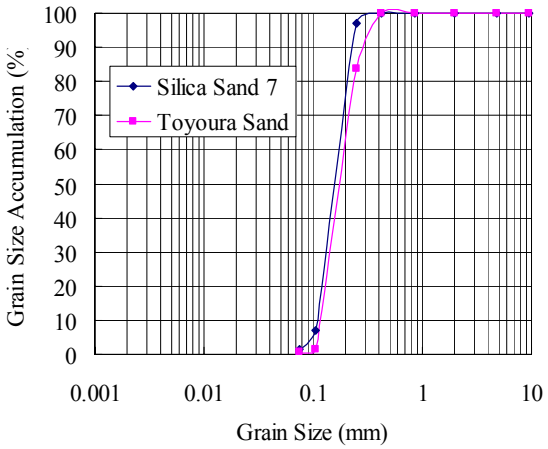

Figure 4. Gradation curve for soil used in test

Testing Procedure

The procedure for 1-g fault test in this study consists of stepwise movement of basal deck of the testing device. The details of the procedure are summarized as bellows;
i) Preparation of uniform sand layer using hopper with installation of black sand grid and target, ii) Activation of up-lifting/down-dragging of moving deck to the vertical displacement in increment with constant speed of 2mm/min. for each faulting angle, iii) Taking photos of both sides of deformed specimen and surface of soil mass at every increment of vertical displacement, iv) Repetition of processes described as ii) and iii) to required offset to form complete shear ruptures.

Testing Cases

Totally 22 cases of experiments were conducted with variation of height of soil layer and dip angle for loose/dense sand. As for a dense/loose sand layer with the height of 20 cm, 3 cases of dip angle ranging as 30°, 45°and 60° were implemented. The effect of height of soil layer was evaluated from the tests on dense sand of which thickness varies from 10cm to 60 cm with dip angle 45°.

OBSERVED BEHAVOUR FROM FAULT TEST

Rupture Pattern Induced by Dip-slip Fault

Propagation of shear failure through sandy soil mass can be obviously seen the successive three photographs shown in Figure 5 (a). The shape of failure surfaces due to dip-slip (up and down) movement of basal plate appeared similar to the results previously presented by Cole et al (1984) and Tani et al (1996) in general. As shown in Figure 5 (a), the failure surfaces for all reverse faults initiate from the contact of the soil mass and movable bottom plate approximately tangent to the fault dip angle. And they gradually move to outward from the initiating point, then finally shape the curve that can be represented by logarithmic spiral.

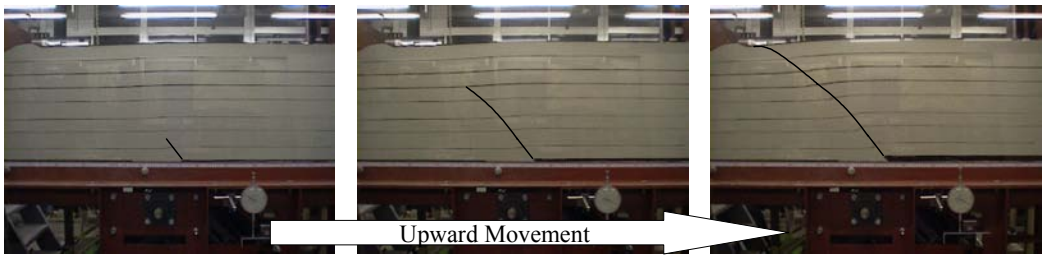

(a) Reserve fault – side view

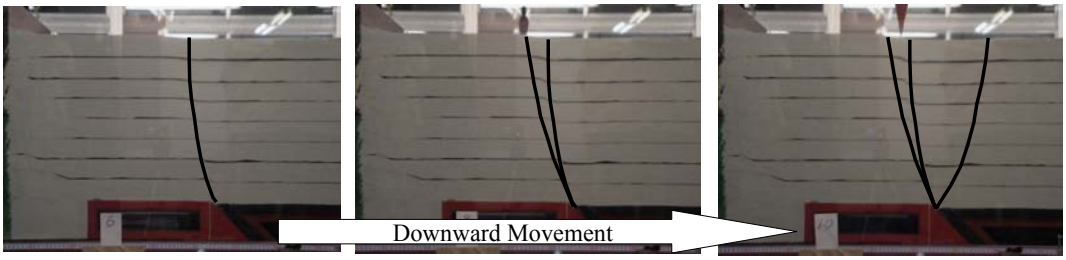

(b) Normal fault – side view

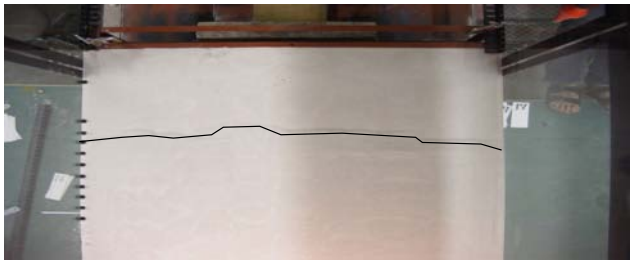

(c) Reserve fault – over view (the shape of surface rupture is almost straight)

Figure 5. Selected photographs corresponding to three stages in reverse/normal faulting test on 40cm of dense sand with dip angle=45°

As for the failure surfaces developed by normal faults, three lines of failure surfaces were taken place successively as the fault displacement continued, which is also close to the previous experimental results presented by Cole et al (1984) and Tani et al (1996). However, Cole et al. classified the failure surfaces into two groups that occurred in order, and Tani et al. suggested 4 stages of development for the failures, whereas this study divided them by 3 categories. As shown in Figure 5 (b), the first failure surface began to propagate directly up to the surface regardless to dip angle, a bit of continuous movement of basal plate formed the

second failure surface in the fore side, then finally the third failure surface developed in opposition to preceded two surfaces, as the continuous faulting configured complete shear band. The detailed location of the surfaces will be mentioned in the following section.

The contours of maximum shear strain at the moment of initial appearance of surface failure were achieved using a digital image processing software, which is capable of capturing the relative displacements of targets installed in soil model. (Refer to Figure 6)

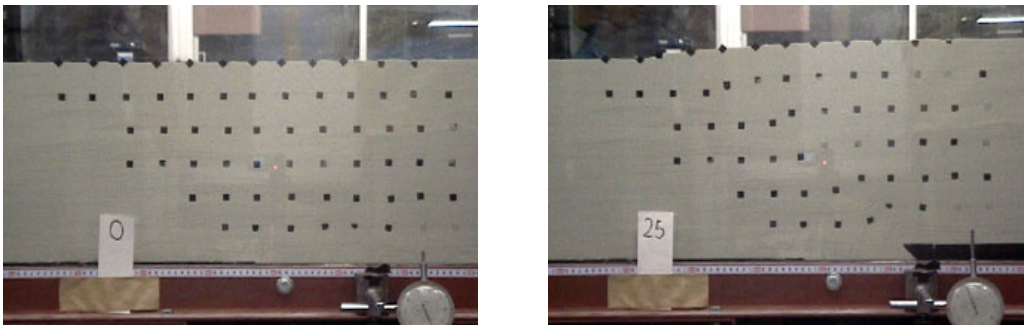

(a) Vertical Offset 0mm, D/H=0.0% **(b)** Vertical Offset 25mm, D/H=8.3%

Figure 6. Development of fault rupture with targets for image processing

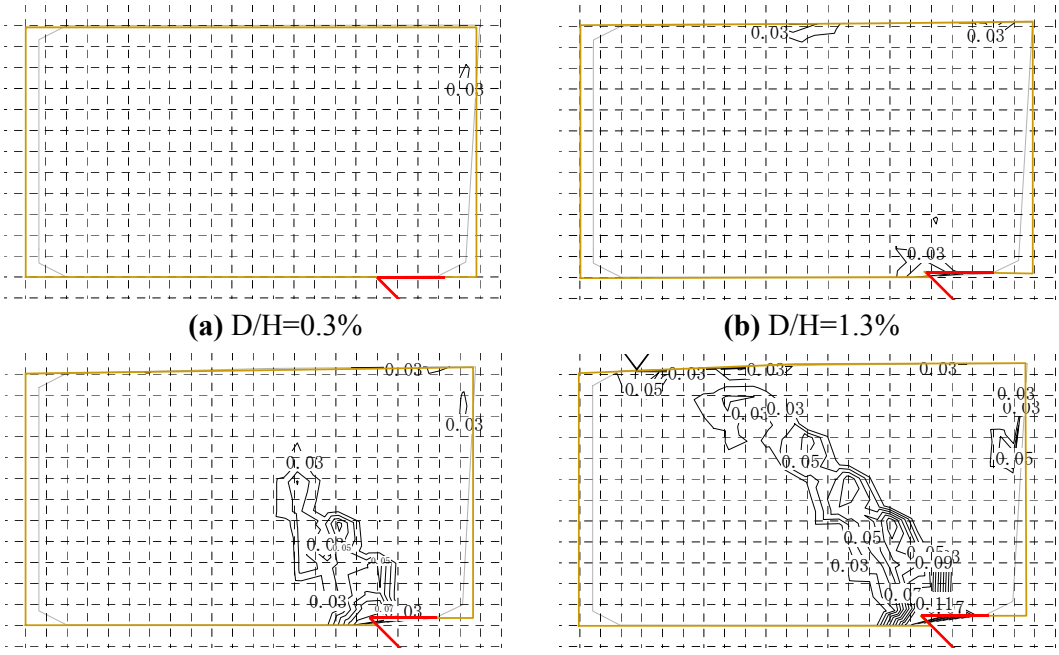

(a) D/H=0.3% **(b)** D/H=1.3%

(c) D/H=2.7% **(d)** D/H=4.0%

Figure 7. Acquisition of maximum shear strain contour using image processing

Based on the achieved increments of displacement at grid points, the maximum shear strain can be calculated using simple equations prevailed in the area of engineering mechanics. Figure 7 shows the distribution of maximum shear strain contours corresponding to the propagation of failure surface. As shown in the Figure 7 (d), it was founded that the normalized vertical displacement, denoted by D/H, was equal to 4.0% as the failure surface

initiating from the bottom of the soil model reached the surface of the model. At the same time, referring to the measured location of surface rupture -marked as reverse triangle in Figure 7 (d)- from the fault box test, the value of maximum shear strain equivalent to the failure surfaces was appeared to be 0.03 when the complete failure surfaces initially constituted in soil mass.

Location of Surface Rupture and Affecting Factors

Based on the testing results described in the previous section, a model for observation of rupture pattern is depicted as Figure 8. Referring to the model, the relationship of the horizontal distance, W, of the rupture surface from the point on the surface vertically above the point where the fault intersects the bottom of the sand mass and its affecting factors involving the faulting dip angle θ, the height of the soil mass H, can be explained as shown in Figure 9.

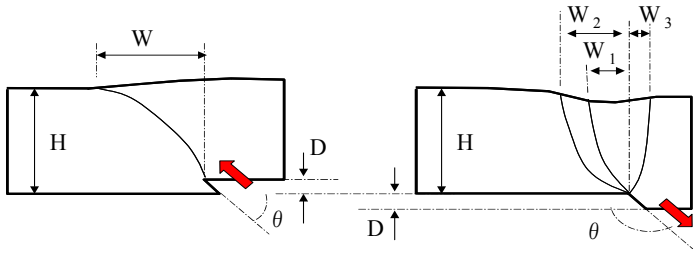

(a) Reverse fault **(b)** Normal fault

Figure 8. Model for the evaluation of rupture patterns

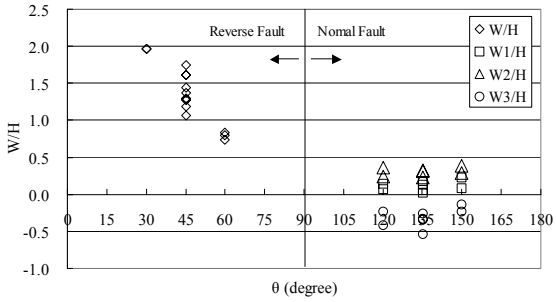

(a) W/H versus θ

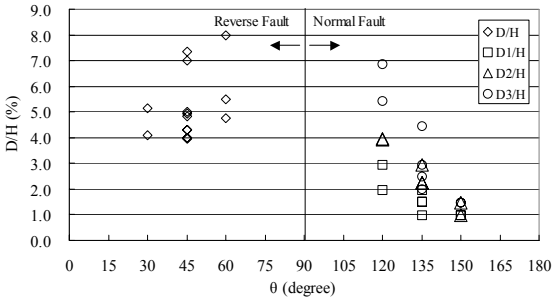

(b) D/H versus θ

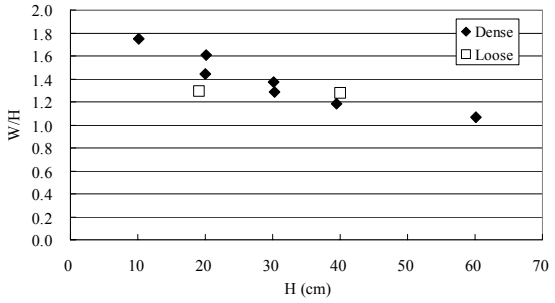

(c) W/H versus H (Reverse fault with θ=45°)

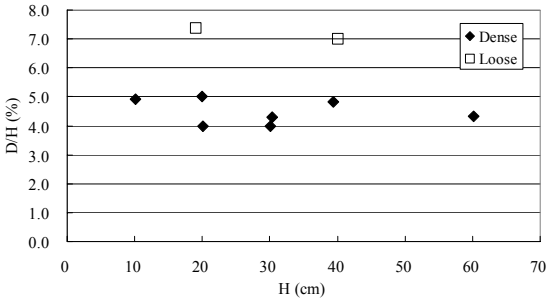

(d) D/H versus H (Reverse fault with θ=45°)

Figure 9. Variation of W/H and D/H as a function of dip angle, θ and height of soil layer, H

Figure 9 (a) and (b) illustrates the variation of W/H and D/H according to the changes of dip angle. For the reverse faults, there happened relatively stiff inclination of the value of W/H to down with increase of the dip angle, but there is only a little change in value for the normal faults. On the contrary, there is a reverse tendency in the variation of D/H. It appeared to be very significant in case of the normal faults, whereas there is only a slight variance in D/H for the reverse faults.

Regarding the effect of height of soil layer, Figure 9 (c) shows that the distance W is coming closer to the point the fault intersects with increase of the height of soil mass. This implies that the rupture pattern changes as the thickness of the soil mass is varied. Besides, it can be seen in Figure 9 (d) that a complete failure surface forms in dense sand mass at a normalized vertical displacement of approximately 4~5% with reverse faulting. And it is also found that the vertical displacement required to form complete shear failure in loose sand mass is approximately 7.0~7.5%, which is greatly larger than that required in dense sand mass.

NUMERICAL SIMULATION

Numerical Model

Numerical analysis has been performed to investigate the response of alluvial soil subjected to dip-slip faulting movement using FLAC Ver. 3.3 (Itasca, 1995). Mohr-Coulomb failure criterion is adopted to allow for the simulation of plastic behavior of the model. And the Lagrangian scheme in which the coordinate of each grid is updated according to the development of plastic increment is utilized to minimize the calculating shock responding to the progress of plastic large deformation. Non associated flow rule was applied to this numerical model. The material properties of the sand used in 1g-Fault Box test were obtained from a series of confined compressive tests (CD) as shown in Table 2.

Table 2. Material Properties used in FLAC Analysis

Items	Unit Weight γ, (ton/m^3)	Elastic Modulus E, (MPa)	Friction Angle ϕ , (°)	Poisson Ratio ν
Value	1.435	67.56	34.12 (Residual Strength)	0.36

Results from Numerical Analysis

15 cases of fault rupture propagation have been simulated in accordance to the variation of dip angle of basement fault and height of a sandy soil(c=0.0). Figure 10 demonstrates the deformed meshes resulted from the cases with vertical offset as much as 10% of height of soil layer regarding dip angle of 30°and 60°. The calculated W/H according to the variation of height of the soil layer is depicted in Figure 11. The value of W was measured form the distribution of calculated maximum shear strain in soil mass. As shown in Figure 11, on the contrary to the results from 1g-fault box tests presented in Figure 9 (c), the value of the ratio W/H with respect to 45 degree of dip angle shows no variation regarding the increase of height of soil layer. The results form the case of 60 degree of sip angle also presents no definite trends as to the variation of dip angle. But with respect to 30 degree of dip angle, the value of the ratio W/H tends to be getting greater according to the increase of height of soil

layer. This tendency somewhat differ from the experimental results that show certain decrease of W/H in accordance with the increase of height of soil mass, even if the tests were limited to the 45°of dip angle. It can be inferred from the results from numerical simulations that with assumption that the material properties of soil mass is not changed depending upon confining stress, the height of soil mass little affects the location of the surface rupture at least where the dip angle is stiffer than 45°.

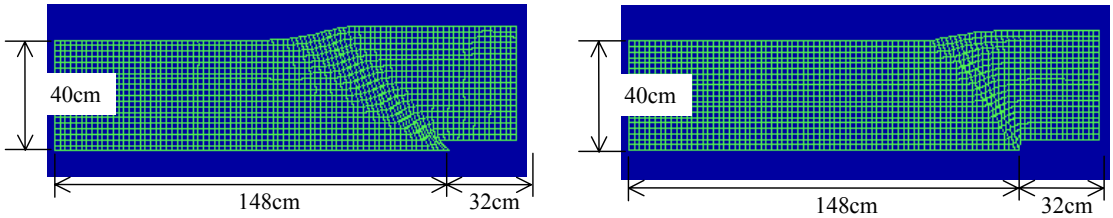

(a) Dip angle = 30° **(b)** Dip Angle = 60°

Figure 10. Deformed Mesh, D/H=10%

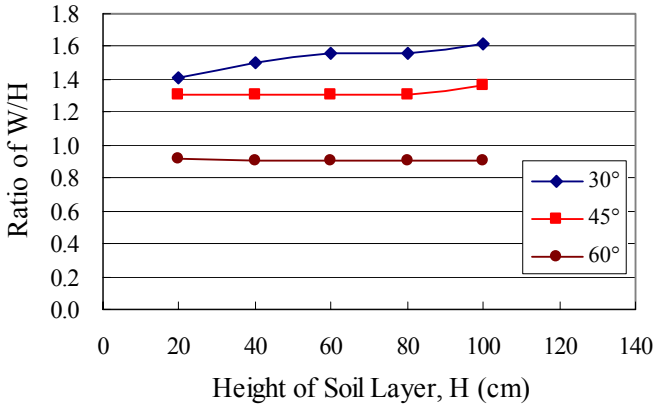

Figure 11. W/H versus Height of soil layer from numerical analysis

DISCUSSIONS

Comparison with the Results from Numerical Simulation

As described in the previous section, numerical analyses using FDM and Mohr-Coulomb failure criterion have been implemented to verify the experimental results in this study. By means of the digital processing of the experimental data, it was acquired that the complete slip line developed in fault box model appropriately coincide with a contour of maximum shear strain with value of 0.03 in soil mass with faulting angle of 45°. Thus, it is worthwhile comparing the experimental results with the numerical simulations to validate a tendency of the soil behavior achieved from the fault box tests.

The maximum shear strain in FLAC is defined as the following equation, which is same as one used in the digital processing of the experimental results.

$$\gamma = \frac{1}{2}\sqrt{(\varepsilon_{xx} - \varepsilon_{yy})^2 + 4\varepsilon^2{}_{xy}} \quad (1)$$

Figure 12 shows the distribution of calculated maximum shear strain with respect to the normalized vertical displacement to develop a complete slip line in dense sand mass. Comaring with the experimental results shown in Figure 7, the entire feature of calculated maximum shear strain contours in numerical model subjected to reverse faulting with dip angle of 45° show good agreement measured one from the 1g-fault box tests.

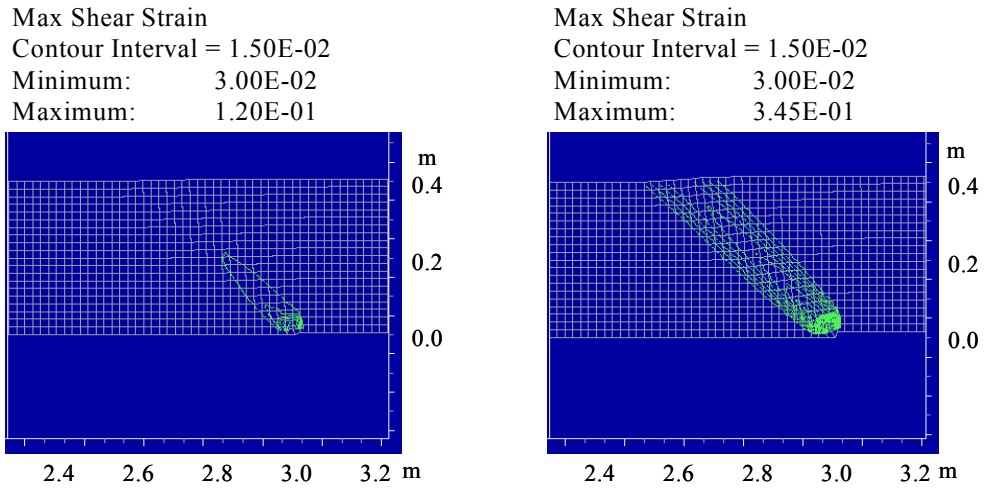

(a) D/H= 2% (b) D/H= 4%

Figure 12. Calculated maximum shear strains in dense sand, H=40cm, dip angle=45°

Comparison with the Previous Studies

Comparison with the experimental results and the theoretical model presented by Tani et al. (1996) invokes much of attention to understanding of the experimental results in this study. Tani et al.(1999) suggested a modified theoretical model to predict the location and pattern of faulting rupture based on their experimental results. Figure 13 presents a diagram in which the author's experimental results, Tani et al's experimental results and calculated value by Tani's modified equation for the updated model have been plotted altogether. It can be obviously seen that there is a significant dispersion in the experimental results of Tani et al's, whereas a distinct tendency inclining to down in value of W/H corresponding to the height of soil mass. Considering the comment mentioned by Tani et al. that the features of fault rupture propagation in model tests are basically identical with various heights of sand layers, the author's founding is somewhat exceptional and noticeable.

Bray et al. (1996) noticed that the angle of dilation of sand under low confinement could differ from that in the larger prototype earth structures. Moreover, the volume change tendencies of a dry sand can very significantly at low confining stress as the thickness of sand in 1g-fault box test is varied. Therefore, given the demonstrated importance of dilation angle of sand and the experimental results come out from this study, it would be reasonable to yield the declining tendency with increase of the height of sand mass in 1-g fault box test.

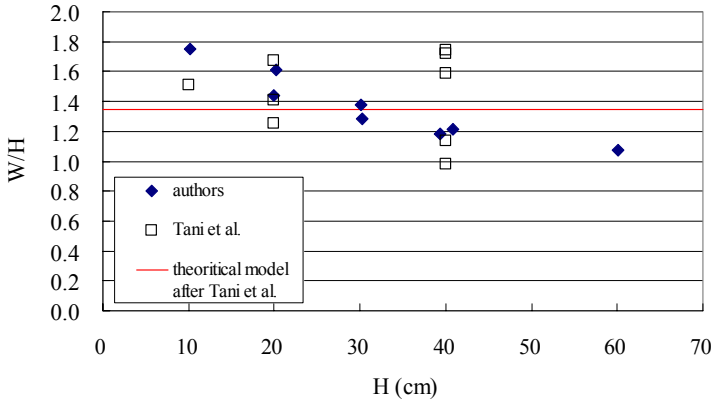

Figure 13. Comparison of experimental results with Tani et al

CONCLUSIONS AND FUTURE STUDIES

The patterns and the location of fault rupture in a sandy soil overlying active dip-slip fault have been studied on the basis of the results from 1-g fault box tests and numerical simulation. The necessity of large-scale testing box and the procedure for preparation of the tests were reviewed. The relationship of the location of surface rupture and its affecting factors were also evaluated. The time dependent variation of maximum shear strain in the sandy soil mass subjected to faulting action was traced to understanding the behavior of finite element in sandy soil using digital processing technique. By the comparison with previous studies, the experimental results and their trends were turned out to be consistent with them on the whole except that change of rupture pattern with various height of soil mass. For the further understanding of the phenomenon, it should be followed to carry out the experiments in various conditions of sandy soils. Considering the tendency achieved from this study, it is strongly needed to verify the effect of thickness of soil mass that can be equivalent to confining pressure on the development of rupture pattern. The centrifugal tests for simulation of dip slip faulting will be thus performed by the authors to investigate the effect of confining stress in sandy soil mass in near future.

REFERENCES

[1] Anon., *FLAC Ver 3.3 User manual*, Itasca, Minneapolis, Minnesota, United States, 1995
[2] Anon., *DIPP-MOTION User manual*, DITECT, Tokyo, Japan, 2000
[3] Bray, J. D., Seed, R. B., and Seed, H. B., Analysis of earthquake fault rupture propagation through cohesive soil, *Journal of Geotechnical Engineering,* ASCE, Vol. 120, No 3., pp. 562-580, 1994
[4] Bray, J. D., Developing mitigation measures for the hazards associated with earthquake surface fault rupture, *Proceedings of A Workshop on Seismic Fault-Induced Failures* pp. 55-77, 2001
[5] Cole, D. A., Jr., and Lade, P. V., Influence zones in alluvium over dip-slip faults. *Journal of Geotechnical Engineering*, ASCE, Vol. 110, No. GT5, pp. 599-615, 1984
[6] Lade, P. V., Cole, D. A. Jr., Multiple failure surfaces over dip-slip failure, *Journal of Geotechnical Engineering*, ASCE, Vol. 110, No. GT5, pp. 616-627, 1984
[7] Lazarte, C. A., The response of earth structures to surface fault rupture, *PhD thesis*, University of California at Berkeley, Berkeley, CA, United States, 1996

[8] Goto, T., Research on prediction of the location and the magnitudes of the ground surface ruptures, *MS thesis*, Waseda University, Shinjuku, Tokyo, 2001

[9] Hamada, M., Research subjects on earthquake resistance of civil infrastructures against fault-induced ground surface ruptures, *Proceedings of A Workshop on Seismic Fault-Induced Failures* pp. 131-134, 2001

[10] Tani, K., Ueta, K. and Onizuka, N., Scale effect of quaternary ground deformation observed in model tests of vertical fault, *Proceeding of 29th Japan National Conference on SMFE*, pp. 1359~1362, 1994 (in Japanese)

[11] W.H.Roth,R.F.scott and I.Austin, Centrifuge modeling of fault rupture propagation through alluvial soils, *geophysical research letters*,vol.8,pp.561-564, 1981

[12] Tani, K., Watanabe, R., Theoretical Model for Location of Ground Surface Break of Shear Plane Developed in Sand Layer due to Dip-Slip Faulting, *Tsuchi-to-Kiso*, vol.536, pp31-31, 2002

[13] Cundall, P. A. and Board, M., A microcomputer program for modeling large-strain plasticity problems, *Proc.,6th Int. Conf.*,Innsbruck,Austria,April 1988, pp.2101-2108, 1988

[14] K. Ueda and K. Tani, Deformation of Quaternary Deposits and Ground Surface Caused by Bedrock Fault Movements (Part2) – Normal and Reverse Fault Model Tests, *Abiko Research Laboratory Rep.,* NO.U98048, 1999

[15] Tani, K., Ueda, K., and Onizuka, N. Discussion to the paper "Earthquake Fault Rupture Propagation", *Journal of Geotech. Eng.*, ASCE, 120, No.3, pp543-561, 1996

Evaluation of Seismic Performance of Lifeline Systems

Seismic Performance Criteria for Lifeline Systems

Masanobu Shinozuka and Xuejiang Dong

ABSTRACT

This paper introduces seismic performance criteria for lifeline systems consistent with the definition of system performance of more societal relevance focusing on its "robustness" and "rapidity in recovery". The robustness represents the capability of the system to continue to function satisfactorily during and after the earthquake, while the rapidity indicates the organizational and technical capability on the part of owner and regulatory agencies to restore function of the damaged system to the original level within an acceptably short period of time after the earthquake. Both robustness and rapidity can only be observed and verified after the fact. Therefore, they should be evaluated by pre-event simulations so that some assurance of compliance with the corresponding performance criteria can be given with high reliability. Such pre-event performance analysis can be carried out on the basis of the probabilistic systems analysis including network flow analysis in general. This paper concentrates on electric power system in particular, and specifically deals with seismic performance of its transmission system. Furthermore, in the systems analysis, only receiving station equipment are considered seismically vulnerable in this first attempt to define and introduce performance criteria. Furthermore, in order to gain more realistic physical insight from the study, the probabilistic systems analysis is performed on the LADWP's (Los Angeles Department of Water and Power's) power system subjected to forty seven (47) scenario earthquakes that are believed to well represent the seismic hazard in the region where the system is located. Considering only the key performance criteria related to the supply of power to customer households, the results of the pre-event probabilistic systems analysis provides an estimated probability that at least x percent of the households will suffer at any year from loss of power immediately after any earthquake. Then, the risk curve is developed by plotting the estimated annual probability as a function of x. The utility of the risk curve is multifold. Typically, comparison of two risk curves, one associated with station equipment seismically retrofitted and the other not retrofitted, can indicate the effect of the retrofit in terms of the reduction in annual probability of having more than any specified rate of households without power, or equivalently, in terms of the reduction in the rate of households without power given a specified level of the annual probability. More importantly, the risk curve can be used to determine whether the system performance complies with the specified criteria defined apriori based on the expert review of the past experience of damage, economic loss, and societal disruption in conjunction with the prevailing level of acceptable risk.

Masanobu Shinozuka, UCI Distinguished Professor, University of California, Irvine
EG-4150, Irvine, CA 92697-2175
Xuejiang Dong, Research Associate, University of California, Irvine
MST 205E, Irvine, CA 92697

Introduction

While emergency repair and power supply were accomplished rapidly in the aftermath of the 1994 Northridge earthquake (one day) and the 1995 Kobe earthquake (three days), the costs of full restoration of their electric power systems were extremely high. Estimated direct costs were said to be approximately $500 million and $4 billion for the Northridge and the Kobe earthquakes, respectively. Since the "big one" appears to be imminent in California, a much longer and more costly interruption of electric power may have to be anticipated, which could have overwhelming socio-economic impacts in the affected region. This research examines seismic system performance measures and criteria from technical and societal point of view.

As a significant updating of research result published in Shinozuka et al (2002), this paper introduces seismic performance criteria for lifeline systems consistent with the definition of system performance of more societal relevance focusing on its "robustness" and "rapidity in recovery". The robustness represents the capability of the system to continue to function satisfactorily during and after the earthquake, while the rapidity indicates the organizational and technical capability on the part of owner and regulatory agencies to restore function of the damaged system to the original level within an acceptably short period of time after the earthquake. Both robustness and rapidity can only be observed and verified after the fact. Therefore, they should be evaluated by pre-event simulations so that some assurance of compliance with the corresponding performance criteria can be given with high reliability.

To develop analysis methodology and gain insight in order to achieve the objective of this research, the seismic performance of electric power source is evaluated using, as a testbed, the Los Angeles Department of Water and Power's (LADWP's) electric power system, particularly its transmission systems. This paper will use the results from the inventory survey and equipment rehabilitation study being performed concurrently primarily by the members of the research team supported by Multidisciplinary Center for Earthquake Engineering Research (MCEER) to examine the extent of mitigation enhancement such rehabilitation work can produce. The analysis requires a somewhat elaborate systems analysis of LADWP's power system with primary emphasis on the receiving station performance under damaging earthquakes such as the 1994 Northridge earthquake.

The MCEER (Multidisciplinary Center for Earthquake Engineering Research) research team on lifeline system performance evaluation has a unique experience and capability of modeling lifeline systems and carrying out a seismic performance evaluation, given inventory data, system configuration and fragility information with or without rehabilitation. The evaluation requires a delicate coordination of various technologies involving interpretation and manipulation of sophisticated and voluminous inventory data, utilization of highly specialized computer codes for systems analysis, estimation of fragility enhancement resulting from advanced rehabilitation technology and integration of all the above into a GIS platform for demonstration. This capability itself represents an advanced technology and the purpose of this research effort is to make use of this technology for the system performance analysis on the Los Angeles Department of Water and Power's (LADWP's) electric power system.

LADWP's Power System

There are two electric power networks serving the Los Angeles region operated by different organizations, Los Angeles Department of Water and Power, and Southern California Edison. Basically, these networks are managed independently. However, for coping with the fluctuating power demand, they cooperate with each other at transmission level operation. In addition, since the networks are a part of the vast Western Systems Coordinating Council's (WSCC's) power transmission network covering 14 western states in USA, two Canadian provinces in Canada and northern Baja California in Mexico, the analysis is performed by taking all the receiving stations and transmission facilities covered by the WSCC network into account. Indeed, the fact that a black-out condition was observed over several states after the Northridge earthquake demonstrates the far-reaching impact of a local system failure throughout the network.

LADWP's electric power service areas and the power supply therein under usual operating conditions are shown in Figures 1 and 2. The areas not colored are serviced by Southern California Edison. Figure 3 is a PGA map under the Northridge earthquake developed on the basis of the contour map provided by David Wald, U.S. Geological Survey and Figure 4 shows the relative average power output (ratio of power supply after damaging earthquake to power supply before earthquake averaged over 20 simuloations) of LADWP's system due to Northridge earthquake under the assumption that only the transformers are vulnerable to the earthquake with the fragility curves to be provided later. This assumption is based on the observation that the transformers represent one of the most critical equipment for the functionality of the power network system, and in addition, they are difficult to repair and/or replace in a short time frame. The average relative power output computed in Figure 4 is based on Monte Carlo simulation with the sample size equal to 20 for each of three cases involving different levels of fragility enhancement. Figure 5 represents five separate simulation results of LADWP system for Case 1 under Northridge earthquake when only transformers are considered vulnerable. The system analysis is performed under the fragility curves provided in Figure 6, in which Case 1 was developed from Northridge earthquake transformers damage data and Case 2 and 3 have enhanced median values by about 50% and 100% respectively with the aid of base-isolation. No change in log-standard deviation is considered. The increasingly improved system performance resulted as fragility curves move to the right (Case 1 to Case 2 and to Case 3). The extent to which the rehabilitation or retrofit of transformers as represented by enhanced fragility curves clearly contributes to improved system performance. The effect of other equipment such as circuit breakers, disconnect switches and buses on the system performance was also studied and will be published elsewhere.

In the present research, FPS (Friction Pendulum System) is considered for enhancing the fragility of the LADWP's transformers. Analytical simulations are performed for a typical transformer weighing 230,000 lbs. subjected to the ground acceleration time histories observed at the Sylmar receiving station during the 1994 Northridge earthquake. To evaluate the effectiveness of FPS for a wide range of earthquake intensities, time histories were linearly scaled up to achieve higher PGA values for the development of fragility information. The result shows (Saadeghvaziri and Feng, 2001) that the degree of reduction in the inertia force exerted on the transformer depends on time histories with differing levels of PGA (0.5 g, 1.0 g, and 1.5 g).

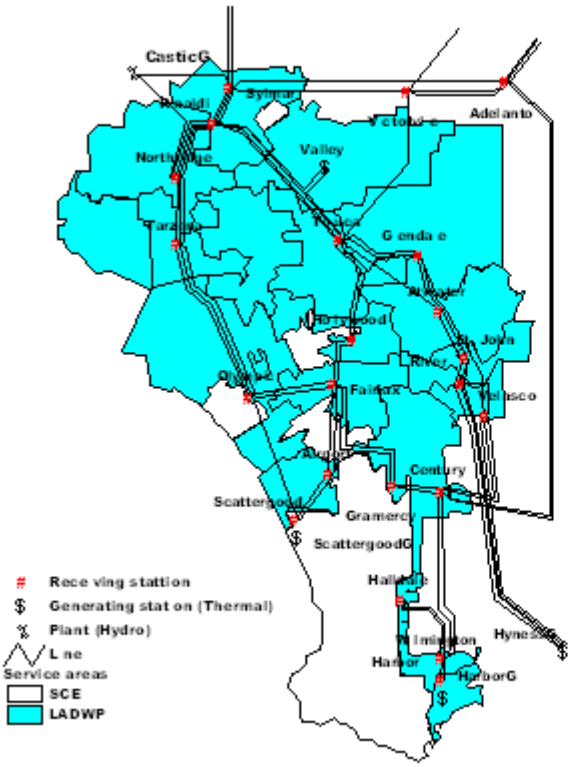

Figure 1. Service areas of LADWP

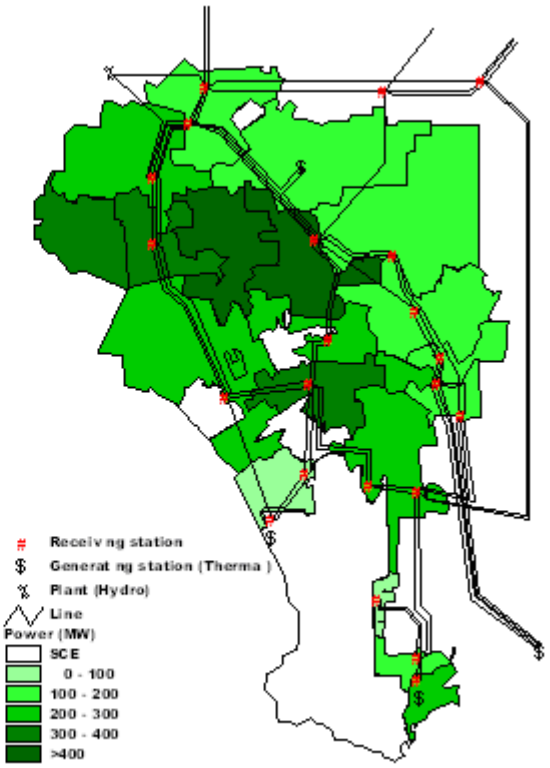

Figure 2. Electric power output for service areas under intact condition

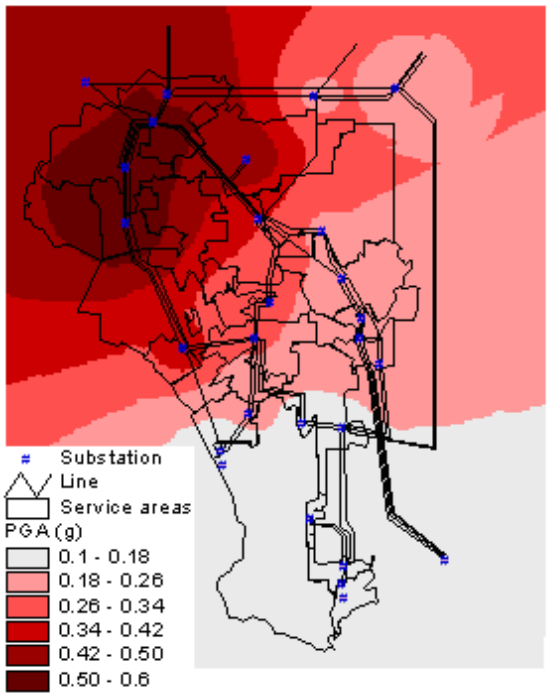

Figure 3. PGA under Northridge earthquake

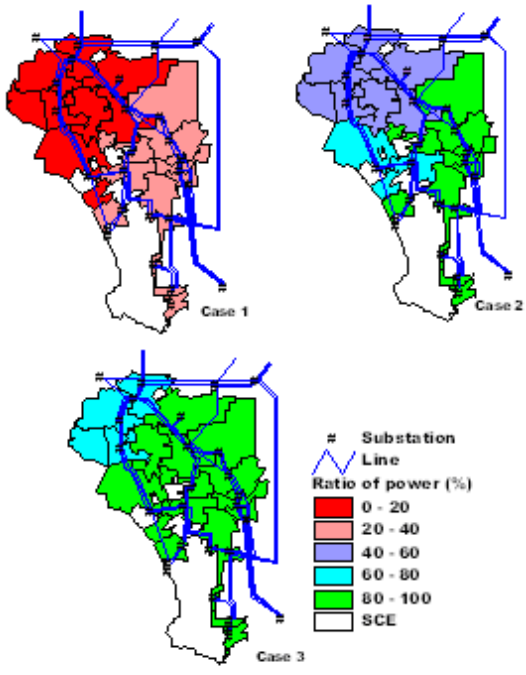

Figure 4. Relative average power output with only transformers being vulnerable

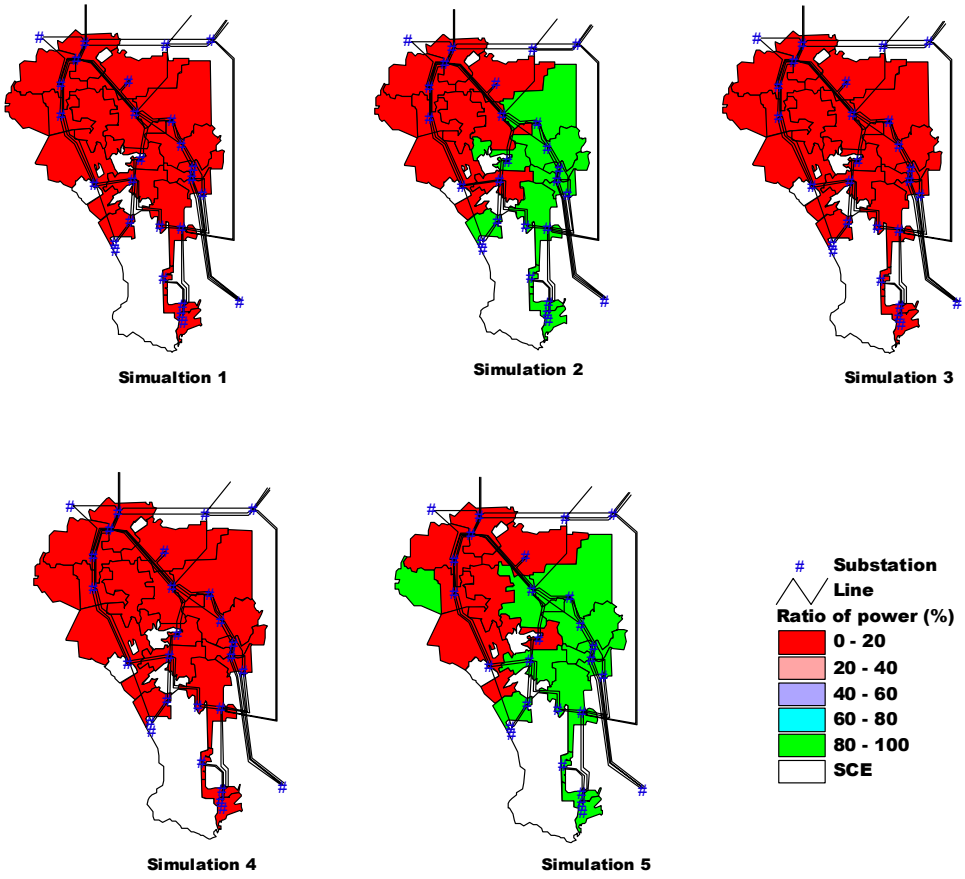

Figure 5. Simulation of power output under Northridge earthquake

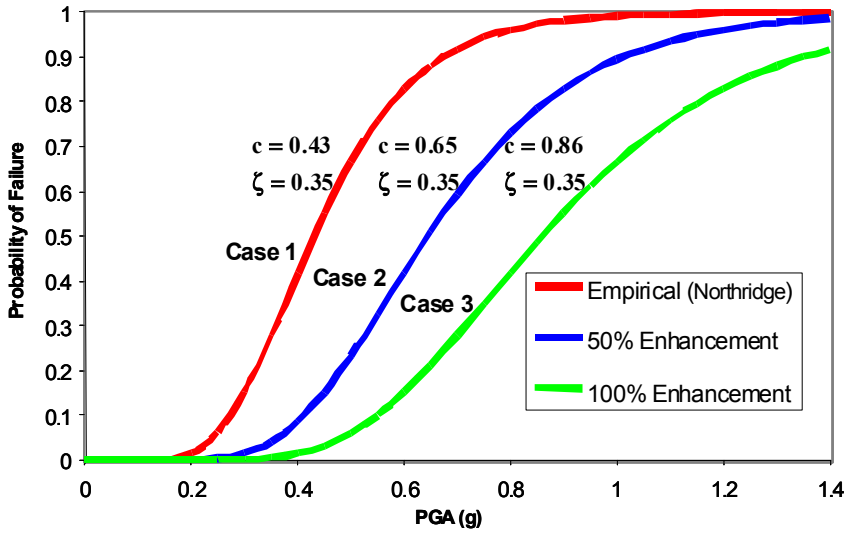

Figure 6. Fragility curves

More specifically, (1) FPS is more effective for earthquakes with larger PGA's; (2) the reduction of acceleration exerted on the transformer is more significant when FPS' radius is larger at the expense of larger displacements. (3) in general, for a reasonable size of radius (say 15 inches), the reduction ranges from 30% to 50% depending on the earthquake intensity between 0.5 g to 1.5 g in terms of PGA. This result is generally consistent with hypothetical fragility curve enhancement introduced in Figure 6. The more recent studies also found in Saadeghvaziri and Feng (2001) confirm similar results.

In analyzing the functional reliability of each receiving station, the following modes of failure are taken into consideration: (1) loss of connectivity, (2) failure of the receiving station's critical components, and (3) power system imbalance. It was noted that most of the transmission lines of the LADWP's power system are aerially supported by transmission towers, although some are through underground. While by no means this implies that the transmission lines are completely free from seismic vulnerability as indicated by a failure of a transmission tower due to land slide resulting from the Northridge earthquake, it was assumed in this study that they are, primarily for the purpose of analytical simplicity and due to insufficiency of damage data. In the systems analysis pursued here, receiving station data were taken from the WSCC's database and used for the systems analysis in conjunction with the computer code IPFLOW, (version 5.0), licensed by the Electric Power Research Institute (EPRI).

Monte Carlo Simulation

Using the ARC/INFO GIS capability, the electric transmission network map was overlaid with the PGA map (Figure 3) to identify the PGA value associated with each receiving station under the Northridge earthquake. The fragility curves provided in Figure 6 were then used to simulate the state of damage involving the transformers at all the receiving stations of the LADWP's power system. For each systems analysis, the connectivity and power flow were examined with the aid of IPFLOW, while treating LADWP's power system as a part of WSCC's overall system.

Loss of connectivity occurs when the node of interest is isolated from all the generators due to malfunction of at least one of the nodes on each and every possible path between this node and any of the generators and other sources of power. Hence, the loss of connectivity can be confirmed on each damage state by actually verifying the loss of connectivity with respect to all the paths that would otherwise establish the desired connectivity.

As for abnormal power flow, it is noted that the electric power transmission system is highly sensitive to power balance and ordinarily some criteria are used to judge whether or not the node continues to function immediately after internal and external disturbances. Two kinds of criteria are employed at each node for the abnormal power flow: power imbalance and abnormal voltage. When the network is damaged due to an earthquake, the total generating power becomes greater or less than the total power demand. Under normal conditions, the balance between power generation and demand is within a certain range of tolerance. Actually, total power generation is between 1.05 and 1.10 times total demand for the system to be operational even accounting for power transmission loss.

In this study, it is assumed that if these conditions are not satisfied, the operator of the electric system must either reduce or increase the power generation to keep the balance of power. However, in some cases, the supply cannot timely follow with the demand because the generating system is unable to respond quickly enough. In this case, it was assumed that the power generation of each power plant cannot be increased or reduced by more than 10% of the current generating power. When the power balance cannot be maintained even after increasing or reducing the generating power by the range of 1.05-1.10, the system was assumed to be down due to power imbalance. In this respect, the effect of the emergency management systems used for power flow management will be taken into consideration in the systems analysis in a future study.

As to abnormal voltage, voltage magnitude at each node can be obtained by power flow analysis. Then, if the ratio of the voltage of the damaged system to the intact system is out of a tolerable range (plus/minus 10% of the voltage in the intact system), it was assumed that a blackout will occur in the area served by the receiving station.

For the Monte Carlo simulation of system performance under the Northridge earthquake, each receiving station was examined with respect to its possible malfunction under these three modes of failure for each simulated damage state. Thus, each simulation identifies the receiving stations that will become inoperational.

The simulation is repeated 20 times on the network. Each simulation provided a differently damaged network condition. Figure 4 shows the ratio of the average power supply of the damaged network to that associated with the intact network for each service area. The average is taken over the entire sample size equal to 20. It is concluded from Figure 4 that rehabilitation that leads to the fragility curve labeled as Case 2 was good enough to protect the transformers, and hence the entire power system, under the assumption that structures and other equipment are not vulnerable to earthquake ground motion.

Risk Curve of LADWP's Power System

Observation of the receiving station locations of LADWP and SCE relative to the faults in and around the Los Angeles area indicates that many receiving stations are constructed near the seismic faults having significantly high possibilities of suffering damage from earthquakes originating from these faults. In the present study, therefore, 47 scenarios earthquakes as developed by Chang et al (2000) are used and the corresponding power flow analyses are performed producing an estimated average reduction in power supply in each service area by means of ratio after and before each earthquake. This ratio is combined with the information of the number of households in each service area obtained from the census tract data as shown in Fig.7. This combination permits a pre-event probabilistic systems analysis and provides an estimated probability that at least x percent of the households will suffer at any year from loss of power immediately after any earthquake. Then, the risk curve is developed by plotting the estimated annual probability as a function of x in Fig.8 for the present analysis. Curves for Case1 and Case2 respectively show risk curves without and with rehabilitation of transformers. The utility of the risk curve is multifold. Typically, comparison of two risk curves, one associated with station equipment seismically retrofitted and the other not retrofitted, can indicate the effect of the retrofit in terms of the reduction in annual probability of having more

than any specified rate of households without power, or equivalently, in terms of the reduction in the rate of households without power given a specified level of the annual probability. More importantly, the risk curve can be used to determine whether the system performance complies with the specified criteria defined apriori based on the expert review of the past experience of damage, economic loss, and societal disruption in conjunction with the prevailing level of acceptable risk.

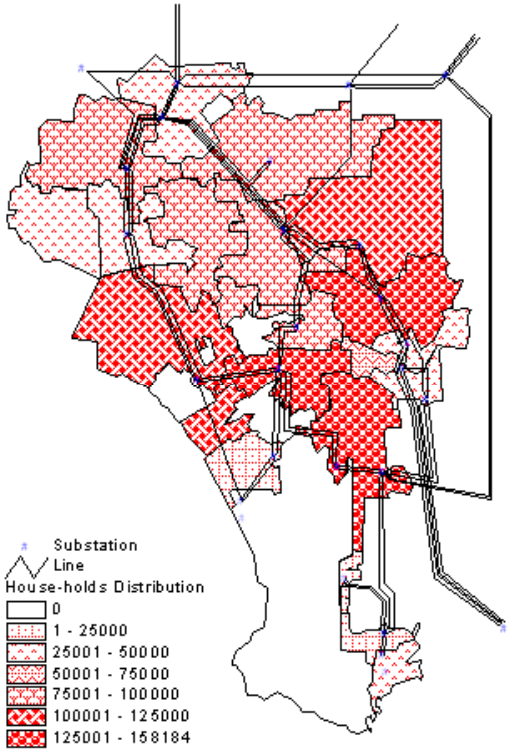

Figure 7. Special Distribution of Households in Service Areas

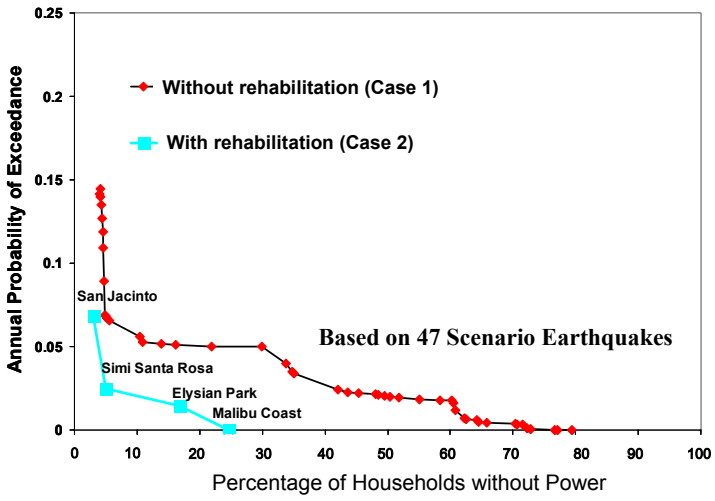

Figure 8. Annual Probability of Exceedance for Households without Power

Table 1 System Performance Criterion I for Pre-event Assessment and Rehabilitation

	Robustness and Resourcefulness	Reliability
Power*	A majority (at least 80%) of households will have continued power supply after earthquake	With a high level of reliability (at least 90% of earthquake events).
Water*	A majority (at least 80%) of households will have continued water supply after earthquake	With a high level of reliability (at least 90% of earthquake events).
Hospital*	A majority (at least 95%) of injured or otherwise traumatized individuals will be accommodated in acute care hospitals for medical care	With a high level of reliability (at least 90% of earthquake events).

* Percentages in parentheses are consistent with site-visit presentation for Electric Power Systems (slide # 25 and 27). Slide 27 shows how rehabilitated system satisfies the criterion for power system above whereas original system does not.

Table 2 System Performance Criterion II for Post-Event Response and Recovery

	Resourcefulness and Rapidity	Reliability
Power*	A majority (at least 95%) of households will have power supply as rapidly as possible within a short period of time (3 days)	With a high level of reliability (at least 90% of earthquake events).
Water*	A majority (at least 95%) of households will have water supply as rapidly as possible within a short period of time (3 weeks)	With a high level of reliability (at least 90% of earthquake events).
Hospital*	All the injured and traumatized will be accommodated in acute care hospitals as rapidly as possible within a short period of time (1 day)	With a high level of reliability (at least 90% of earthquake events).

* Values in parentheses are consistent with site visit presentation for Electric Power Systems (slides # 27 and 25)

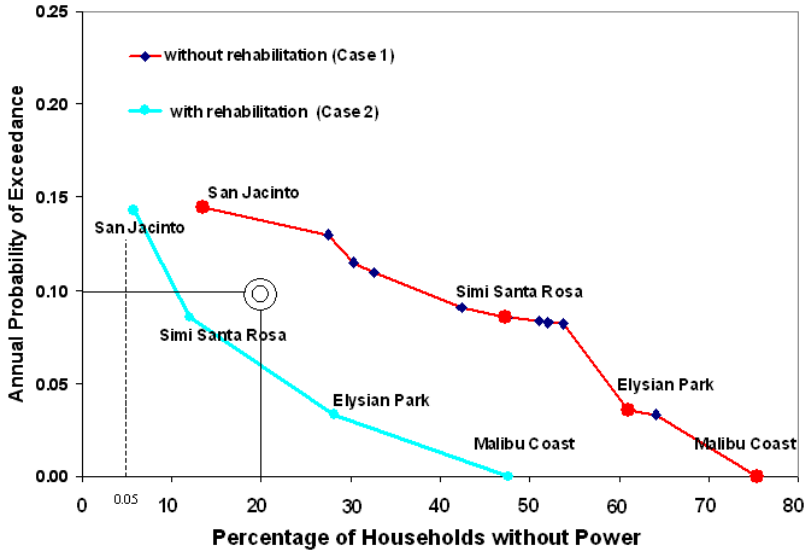

Figure 9. Annual Probability of Exceedance for Households without Power (enlarged view)

System Performance Criteria

The following performance criteria for power systems demonstrated in Tables 1 and 2 are preliminary and limited in scope. Table 1 lists criteria to be satisfied in pre-event assessment, and Table 2 those in post-event emergency response. These Tables also include performance criteria for water and acute care hospital systems. In combination, they conceptually establish the degree of community resilience in terms of robustness, rapidity and reliability. Specific values (in percentages for robustness and rapidity in restoration) are examples for the ease of understanding the concept. The performance criterion for power systems shown in Table 1 is represented by a double-circled point in Fig.9 (enlarged version of Fig.8) where the robustness corresponds to the annual probability of 80% or more households with power after any earthquake is lower than 0.9. The risk curve for Case 1 (without rehabilitation) does not satisfy this criterion, but the risk curve for Case 2 (with rehabilitation) does satisfy it. These criteria can also be used to judge the effectiveness of rehabilitation as carried out in this study. Data collection and modeling for the rapidity in restoration are much more difficult to pursue. Further research is needed to develop analytical models based on the past experience so that the performance criteria such as shown in Table 2 become meaningful in practice.

Future Research

Now that all the analytical tools are in place, the research will continue to proceed on four fronts. The first is to refine the systems analysis methodology by incorporating other significant receiving stations equipment and validating the results of the analysis with data from power interruption experiences caused by the Northridge and other earthquakes. Further effort for closer interaction with LADWP's power and water systems will also be considered. This requires, however, additional effort for inventory and other database development.

The second is to further study seismic vulnerability of the equipment and develop their fragility curves. In this regard, the results from the research carried out by MCEER investigators on fragility information will be used as they become available. Rehabilitation measures can then be expressed as fragility curve enhancements, which can in turn be directly reflected on the systems analysis with the aid of Monte Carlo techniques. In this connection, rehabilitation measures other than those by base isolation will be explored. Possibilities include use of advanced semi-active dampers, and the shaking table tests on transformers equipped with such dampers will be performed at MCEER-NCREE collaboration.

The third area of concern is the level of uncertainly involved in the assessment result. There are many sauces of uncertainty exist. It appears that major contributing sources stem from fragility and hazard estimations. A study is currently under way by the authors to focus on these issues.

The third area of future endeavor involves direct and indirect economic loss estimation arising from physical damage to the system facilities resulting in possible system interruption. In the context of this paper, this is a crucial factor to be investigated for the development of realistic system performance criteria from the " rapidity in restoration" point of view. This endeavor expands the MCEER team's capability in this area demonstrated by the study of the seismic vulnerability of the Memphis area's electricity lifelines (see Shinozuka et al., 1998). To assist the MCEER investigators in loss estimation, the Monte Carlo simulation will be performed in such a way that direct and indirect loss estimation will be pursued by recording a specific inventory of equipment damage observed for each realization of system damage. As detailed in Shinozuka and Eguchi (1997), this allows statistics on direct and indirect losses based on individual states of damage associated with corresponding simulation to be obtained, rather than based on the average of power output taken over the entire sample of simulation.

Acknowledgement

This work was supported by the National Science Foundation through Multidisciplinary Center for Earthquake Engineering Research. The authors also acknowledge for the technical support provided by LADWP, Professor T.C.Cheng. and Dr.X. Jin of University of Southern California and Mr. Don Penn, independent consultant.

References

[1] Chang, E. S., M. Shinozuka and J. Moore (2000). Probabilistic Earthquake Scenarios: Extending Risk Analysis Methodologies to Spatially Distributed Systems, Earthquake Spectra, Vol. 16, No. 3, August, 2000, pp.557-572.

[2] Saadeghvaziri M. A. and M. Feng (2001). Experimental and Analytical Study of Base-Isolation for Electric Power Equipment, Research Progress and Accomplishments 2000-2001, Multidisciplinary Center for Earthquake Engineering Research, May, pp. 29-40.

[3] Shinozuka M. and R. Eguchi (1997). Seismic Risk Analysis of Liquid Fuel Systems; A Conceptual and Procedural Framework for Guidelines Development, Proceedings of The Northridge Earthquake Research Conference, Los Angeles, California, August 20-22.

[4] Shinozuka M., A. Rose and R. Eguchi, (eds.) (1998). Engineering and Socioeconomic Impacts of Earthquakes: An Analysis of Electricity Lifeline Disruptions in the New Madrid Area, Monograph No. 2, Multidisciplinary Center for Earthquake Engineering Research, Buffalo, New York.

[5] Shinozuka M., T.C. Cheng, M. Feng and S. T. Mau (1999). Seismic Performance Analysis of Electric Power Systems, Research Progress and Accomplishments 1997-1999, Multidisciplinary Center for Earthquake Engineering Research, July, pp. 61-69.

[6] Shinozuka M., M. Feng, J. Lee and T. Naganuma (2000). Statistical Analysis of Fragility Curves, Journal of Engineering Mechanics, ASCE, Vol. 126, Issue 12, Dec, pp. 1224-1231.

[7] Shinozuka M., T.C.Cheng, X. Jin, X.Dong, D.Penn(2002). System Performance Analyses of Power Networks, Proceedings of Seventh U.S. National Conference on Earthquake Engineering, July 21-25, 2002

[8] Tanaka S., M. Shinozuka, A. Schiff, and Y. Kawata (1997). Lifeline Seismic Performance of Electric Power Systems during the Northridge Earthquake, Proceedings of The Northridge Earthquake Research Conference, Los Angeles, California, August 20-22.

Damage Assessment of Railway Structures Using Numerical Simulation and Vibration Measurement.

Fumiaki Uehan and Kimiro Meguro

ABSTRACT

The tool for assessing seismic performance (*assessment of future damage*) of RC structures is indispensable to mitigate the earthquake damage to a railway. Also, the tool for the inspection of the damage levels (*assessment of actual damage*) of RC structures is necessary for promptly restoring an earthquake damaged railway. In this study, the authors discuss the methods to assess the future/actual damage of RC structures by using the numerical simulation and the vibration measurement.

Numerical simulation of failure mechanism of RC structures

The *Applied Element Method* (AEM) can follow the total structural behavior from elastic range to collapse. The authors examine the Applicability of the AEM as an assessment tool for the seismic performance of RC structures, by means of the simulation of cyclic loading test and seismic response of RC structures. After the 1995 Kobe earthquake, a great number of RC columns of railway viaduct were retrofitted with steel jacket in Japan. Although the RC viaduct with steel jacket has become one of the popular railway structures, the failure mechanism of jacketed RC structure is not clear at present. The authors propose a 2-D numerical model for investigating the behavior of jacketed RC column, and check its validity.

Improvement of damage inspection method using vibration measurement

In the field of health monitoring of railway structures, the inspection methods using vibration measurement have been used. These methods make use of the natural frequency and/or the mode shape of structure as the index of damage assessment. The authors are hoping to improve the accuracy of the inspection method by using the damage judgment criteria calculated by AEM. So, the accuracy of the AEM on the simulation of the natural frequency of damaged RC structures is investigated.

Through the above-mentioned studies, the authors confirm that the AEM functioned as a high-performance seismic damage simulator for RC structures. Seismic performance check of existing structures, selection of the most effective retrofitting method, and development of judgment criteria for damage inspection can be effectively done by AEM. These results are very useful for the assessment and the mitigation of seismic damage for a railway.

Fumiaki UEHAN, Railway Technical Research Institute, 2-8-38 Hikari-cho Kokubunji-shi, Tokyo, Japan 185-8540

Kimiro Meguro, Institute of Industrial Science, University of Tokyo 4-6-1 Komaba Meguro-ku, Tokyo, Japan 153-8505

INTRODUCTION

In this study, we discuss the methods to assess the future/actual damage of RC structures by using the numerical simulation and the vibration measurement. For earthquake disaster measures of railway in the future, it is indispensable to detect weak points of RC structures correctly and provide effective and economical reinforcement. We study the applicability of *Applied Element Method* (AEM) [1] as an evaluation tool for the seismic performance of RC structure with and without applying seismic strengthening technique. So, the numerical simulations of the failure mechanism of RC columns and railway viaduct are carried out, in order to check whether the weak point of RC structures can be detected correctly by the AEM or not. For promptly restoring an earthquake-damaged railway, the tool for the inspection of the actual damage levels of RC structures is indispensable. In order to assess the degree of damage to a RC structure using the inspection techniques based on vibration measurements, it is necessary to identify the changes of the dynamic characteristics accompanied by damage to the structure in advance. So far the accuracy of the AEM on the simulation of natural frequency of damaged structure is investigated through the comparison of the results of experiments and numerical simulations.

TECHNIQUE OF NUMERICAL SIMULATION

Figure 1 illustrates the modeling of RC structure for the AEM [1]. It is assumed that the structure is modeled as an assembly of small rectangular elements made by dividing the structure virtually. Each element is connected by pairs of normal and shear springs located at contact points, which are distributed around the element edges. In the case of 2-dimensional analysis, each element has three degree of freedoms. The material model of concrete is applied to each distribution spring. At the location of reinforcing bar, two pairs of springs are used one for concrete and another for reinforcing bar. Nonlinear material models of steel and concrete shown in Figure 2 are given to the springs, respectively. If the stress of a spring exceeds its resistance, the spring can yield and cut. In this way, AEM can follow the structural behavior from elastic range to total collapse.

Two-dimensional model of the jacketed column [2] is composed of three different types of elements. The first one is the element for the RC inside jacket (RC element, E_C), the second one is the element for the steel jacket installed in sides of the RC column (Side jacket element, E_{JS}) and the third one is the element for the steel jacket between two-side jackets (Front and rear jacket element, E_{Jb}). First one has a material property of RC and the other two types of elements have the material property of steel. There is no connection between the elements of E_{Jb} and Ec in Figure 3. Because the edge elements of both E_C and E_{Jb} are connected with E_{JS}, the steel jacket can restrain the inside concrete. Inside concrete is permitted to crack and reinforcements are permitted to yield and cut.

NUMERICAL SIMULATION OF FAILURE MECHANISM OF RC STRUCTURES

Numerical Simulation for Earthquake disaster measures of RC Structures

For earthquake disaster measures of railway in the future, it is indispensable to detect weak points of RC structures correctly and provide effective and economical reinforcement. In this chapter, we study the applicability of AEM as an evaluation tool for the seismic performance of RC structure with and without applying seismic strengthening technique.

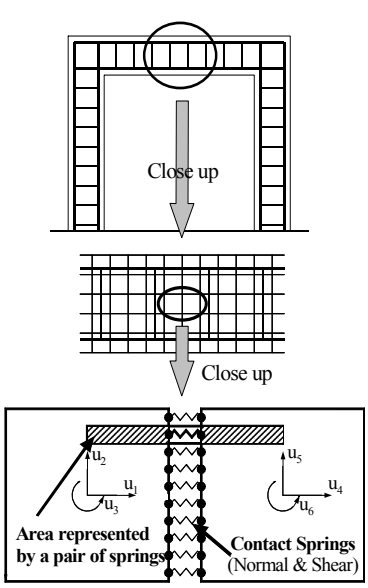

Figure 1. Modeling of RC structure to AEM

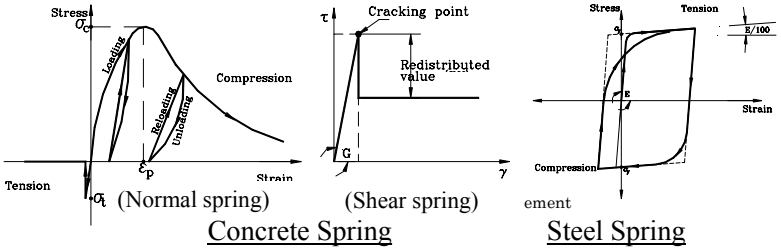

Figure 2. Material model of concrete and reinforcement

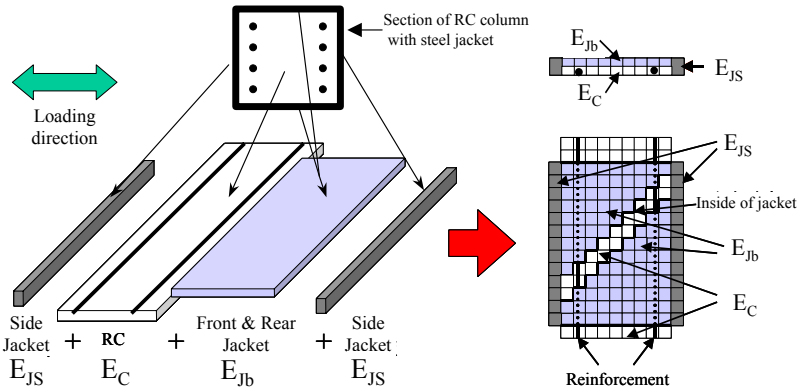

Figure 3. Modeling of RC column with steel jacket

First, the termination of main reinforcements is taken up as a weak point of RC column. The change in the failure mode of RC columns due to the change in the anchorage length of main reinforcements is simulated. Moreover, simulations are also carried out on the effect of the seismic strengthening of the RC columns with steel jacket. Next, in order to check whether the weak point of structure can be detected correctly by the AEM or not, the seismic response simulation of two-storied RC rigid frame viaduct which was collapsed due to 1995 Kobe earthquake is carried out.

Experiment and Numerical Simulation of Vulnerable RC Column

Outline of experiment and numerical simulation

Kawashima *et al.* [3] conducted the loading test of specimens of RC columns that have terminated main reinforcements with inadequate anchorage length. The details of the specimens are shown in TABLE I. The difference among four specimens is the termination height. The termination height means the height of the upper end of terminated main reinforcements from the base. From the viewpoint of design, the standard termination height - just meet the design standard - is 116cm. The height of all main reinforcements of Specimen n-1 is higher than 250cm (no termination). The half numbers of the main reinforcements of Specimen n-2, Specimen n-3, and Specimen n-4 are terminated at the mid-height. The height of the terminated reinforcements of Specimen n-2 is 110cm and it is 6cm lower than the standard termination height. The termination heights of Specimen n-3 and n-4 are 135cm and 160cm, respectively, and they are higher than the standard termination height.

The footings of the specimens are fixed to the reaction floor, and the cyclic load is applied to the head of the specimens by the dynamic actuator. In this case, no axial force is applied. The failure displacement δ_0 (=1.3cm) of the Specimen n-1 is defined as the standard

displacement, the displacements $n \cdot \delta_0$ (n=1,2,3,・・・) are given to the Specimens, making the amplitude increase gradually. The number of loading cycle per 1 loading step (in the same displacement) is 10 times.

The specimens are modeled by 620 square elements whose size is 5×5cm. The models of specimens are *2-D* model and plane stress condition is assumed. The strength of concrete and steel bars of numerical models is same as the strength of real specimens. Although the same loading conditions as the experiment are adopted in the numerical analysis, the number of loading cycle per 1 loading step is one time.

Results and considerations

TABLE II shows the results of the maximum load of the experiment and numerical simulation. The results of numerical simulation are 90-97% of the results of experiment. The maximum strength of main reinforcements in the numerical simulation was assumed 1.75 times of yield strength of real main reinforcements. It is considered that the maximum strength of reinforcement used in the simulation was smaller than actual value.

The results of numerical simulation are compared with the experiment results. Figure 4 shows the failure mode of specimens, and Figure 5 shows the distribution of axial strain of main reinforcement obtained by the experiment and simulation.

Specimen n-1 (No termination): In the both experiment and simulation, the damage to the RC column concentrates on the bottom part of the column. The reinforcements of the column fracture and the column reaches ultimate state, when the inputted displacement is $8\delta_0$ in the experiment, and $9\delta_0$ in the simulation.

Specimen n-2 (Termination height: 110cm): In both the cases, the damage concentrates on the center of the column where the main reinforcements are terminated. The axial strain of the main reinforcement that have no termination, concentrates on the termination point. The column reaches ultimate state, when the inputted displacement is $6.5\delta_0$ in the experiment, and $6\delta_0$ in the simulation.

TABLE I. DETAILS OF SPECIMENS

Specimen No.	n-1	n-2	n-3	n-4
Dimension of cross section（cm）	50×50			
Thickness of concrete cover（cm）	3.5			
Effective height (cm)	250			
Shear span ratio	5.4			
Termination height from base (cm)	-	110	135	160
Yield stress of main reinforcement（MPa）	308			
Yield stress of hoop reinforcement (MPa)	272			
Young's modulus of reinforcement（GPa）	200			
Compressive strength of concrete（MPa）	31.3	32.0	32.5	31.9
Young's modulus of concrete（GPa）	28.0			

TABLE II. COMPARISON OF MAXIMUM STRENGTH

Specimen No.	n-1	n-2	n-3	n-4
Maximum strength obtained by experiment (kN)	167	148	161	166
Maximum strength obtained by simulation (kN)	154	143	145	160

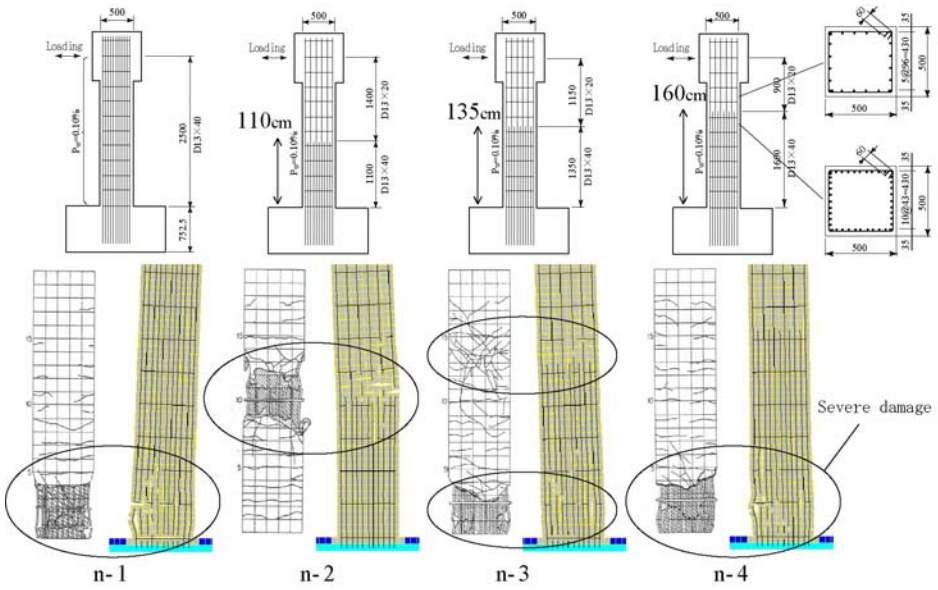

Figure 4. Shape (Upper) and failure mode (Lower: Experiment, Simulation) of specimens

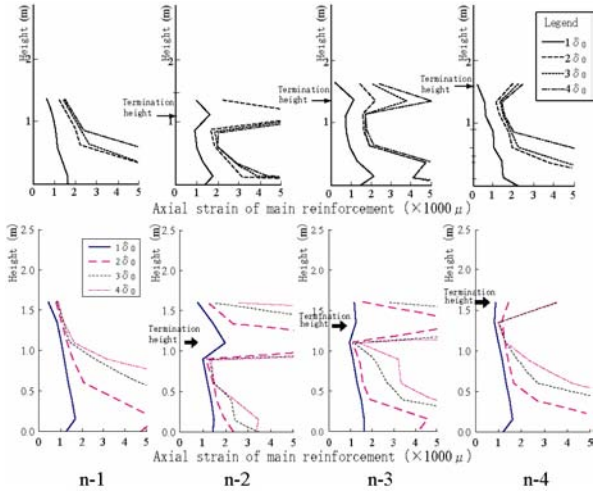

Figure 5. Axial strain of main reinforcement (Upper: Experiment, Lower: Simulation)

Specimen n-3 (Termination height: 135cm): In both the cases, the damage to the RC column concentrates on the bottom part of the column, but termination part of the column is also damaged. In the experiment specimen, the damage begins to concentrate on the bottom part after the $6\delta_0$ is inputted to the column, and when the $8.5\delta_0$ is inputted, the specimen reaches ultimate state at the bottom part. In the numerical model, the hoop reinforcement brakes when the input displacement is $6\delta_0$, after that, the damage is concentrated on the bottom part.

Specimen n-4 (Termination height: 160cm): In both the cases, the damage to the RC column concentrates on the bottom part of the column. When the input displacement is $8\delta_0$, the column reached ultimate state by the fracture of the main reinforcement.

In the experiment, the Specimen n-2 that has the lowest and inappropriate termination height, is damaged at the center of the column where the main reinforcements are terminated. As the termination position becomes high, the damage concentration part shifts to the bottom of the column, and the damage state approaches Specimen n-1 that has no termination. The results of numerical simulation by the AEM can follow well the phenomenon that occurred in

the experiments. The simulated results of the maximum strength and the ultimate displacement, and the experiment results about them are well in agreement. The simulated axial strain of main reinforcements is sufficiently in agreement with the experiment results, and the simulated results can follow well the tendency of change of the strain distribution accompanied by the change of the termination height. It is known well that the measurement of the strain of reinforcement is very difficult in case of the damaged RC structures, and Kawashima *et al.* [3] has also indicated that a certain error might be included in the experiment result of axial strain. So the detailed argument about accuracy of the simulated strain value is avoided.

Experiment and Numerical Simulation of RC Column Reinforced by Steel Jacket

Outline of experiment and numerical simulation

In order to check the effect of earthquake strengthening of RC pier by steel jacketing, Kawashima *et al.* [3] conducted loading test of the RC specimen with steel jacket. TABLE III shows the details of the specimen used in the experiment. The details of those specimens are almost same, but the height of the steel jacket is different. The reinforcements of all specimens are terminated. The termination height is 90cm from the base, and the termination height is 22cm lower than the standard termination height. The Specimen j-1 is not strengthened. The steel jacket of 50cm height is used for the Specimen j-2, and the center of the steel jacket is coincided with the termination height. The steel jacket whose height is 75cm is used for the Specimen j-3, and the position 25cm upper from the bottom of the steel jacket is coincided with the termination height. The tensile strength of steel jacket is 274MPa, and the space between the RC column and steel jacket is filled with the epoxy resin whose thickness is 3mm.

In this experiment, the footings of the specimens are fixed to the reaction wall, and the cyclic load is applied to the head part of the specimens by the dynamic actuator. In this case 282kN of axial force is applied to the specimens. The failure displacement δ_0 (=1.5cm) of the Specimen j-1 is defined as the standard displacement, the displacements $n \cdot \delta_0$ (n=1,2,3,・・・) are given to the Specimens, making the amplitude increase gradually. The number of loading cycle per 1 loading step (in the same displacement) is 10 times.

The every specimen is modeled by about 640 square elements whose size is 5×5cm. The models of specimens are 2-D model and plane stress condition is assumed. The strength of concrete and steel bars of numerical models is same as the strength of real specimens. Although the same loading conditions as the experiment are adopted in numerical analysis, the number of loading cycle per 1 loading step is 1 time.

TABLE III. DETAILS OF SPECIMENS

Specimen No.	j-1	j-2	j-3	(j-4)
Dimension of cross section (cm)	50×50			
Thickness of concrete cover (cm)	3.5			
Effective height (cm)	260			
Shear span ratio	5.6			
Termination height from base (cm)	90			
Yield stress of main reinforcement (MPa)	409	357		
Yield stress of hoop reinforcement (MPa)	433	245		
Thickness of steel jacket (cm)	-	1.0		
Height of steel jacket (cm)	-	50	75	30
Young's modulus of reinforcement (GPa)	200			
Compressive strength of concrete (MPa)	42.0	43.8	35.6	35.6
Young's modulus of concrete (GPa)	28.0			

Results and considerations

TABLE IV shows the results of the maximum load of the experiment and numerical simulation. The results of numerical simulation are 100-105% of the experiment result. The results of numerical simulation are compared with the experiment results. Figure 6 shows the failure mode of specimens, and Figure 7 shows the distribution of axial strain of main reinforcement obtained by the experiment and simulation

Specimen j-1 (Without jacketing): In the both experiment and simulation, the damage to the RC column concentrates on the termination part. The RC column reached ultimate state, when the inputted displacement is $7\delta_0$ in the experiment, and $6\delta_0$ in the simulation.

Specimen j-2 (Height of steel jacket: 50cm): In the both cases, the center of the column near the upper part of the steel jacket, and the bottom of the column are damaged. Finally, the damage to the bottom part becomes severer.

Specimen j-3 (Height of steel jacket: 75cm): In the both cases, the damage to the RC column concentrates on the bottom part of the column. The RC column reached ultimate state, when the inputted displacement is $7\delta_0$ in the experiment, and $6\delta_0$ in the simulation.

Specimen j-4 (Height of steel jacket: 30cm. (Only numerical simulation.)): Numerical model of RC column strengthened by the steel jacket with 30cm height is made in order to check the failure mode of vulnerable RC column with inappropriate steel jacketing. In this case, the damage concentrates on the RC column near the upper part of the steel jacket.

In the experiment, we confirmed that the damage to the Specimen j-1, which is not strengthened, concentrates on the center of the column where the main reinforcements are terminated, and the damage concentration part shifts to the lower part of the column as the height of the steel jacket becomes large.

TABLE IV. COMPARISON OF MAXIMUM STRENGTH

Specimen No.	j-1	j-2	j-3
Maximum strength obtained by experiment (kN)	124	128	126
Maximum strength obtained by simulation (kN)	127	129	133

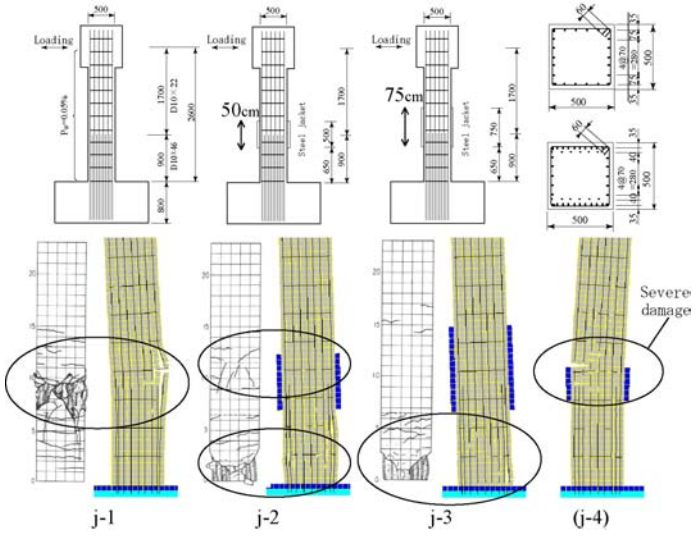

Figure 6. Shape (Upper) and failure mode (Lower: Experiment, Simulation) of specimens

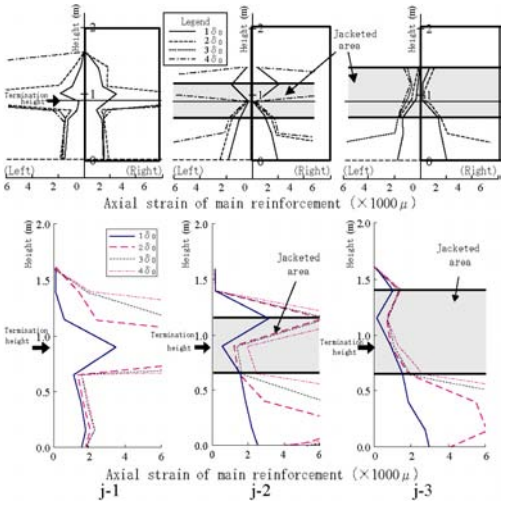

Figure 7. Axial strain of main reinforcement (Upper: Experiment, Lower: Simulation)

The results of the numerical simulation by AEM show the same phenomenon that occurred in the experiments, and the simulated results of the maximum strength and the ultimate displacement have sufficient accuracy. Moreover, the result of the failure mode of the numerical model j-4 suggests that numerical simulation by AEM may be effectively utilizable as the detection method of inadequate earthquake strengthening design.

Simulation of Collapse Behavior of Real Railway Viaduct

Numerical simulation of the JR (Japan Railways) Hansui viaduct that was collapsed due to the 1995 Kobe Earthquake is performed. The damage condition [4] is shown in Figure 8. The viaduct is the double-decked viaduct with 3 spans. The shape of JR Hansui viaduct is shown in Figure 9. The square elements whose side length is 18cm are used to model the viaduct. The number of distributed springs between each two adjacent sides is 10. The material properties of concrete and steel bars are defined by considering the actual strength as showing in TABLE V. The arrangement of reinforcing bars is just as same as the real arrangement shown in Figure 9. The natural frequency of the numerical model that the effect of soil-pail system is taken into consideration is almost same value of the real natural frequency of the undamaged JR Hansui viaduct. The collapse behavior of the model due to the NS component of the JR Takatori ground motion [5] is shown in Figure 10. The damage condition of the numerical model is almost same as the real one.

TABLE V. MATERIAL PROPERTIES OF VIADUCT MODEL

Concrete		Reinforcing bar	
Young's modulus (GPa)	28.0	Young's modulus (GPa)	210
Compressive strength (MPa)	32.0	Yield stress (MPa)	350
Tensile strength (MPa)	2.40		

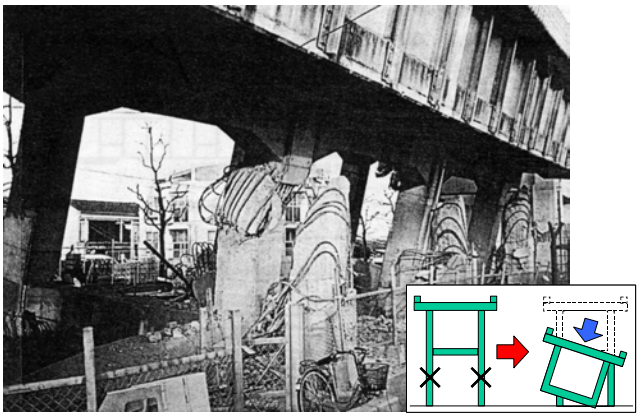

Figure 8. Damage condition of JR Hansui viaduct

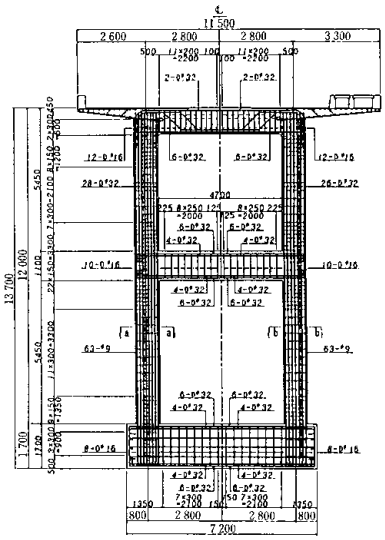

Figure 9. Shape of viaduct and arrangement of reinforcing bars

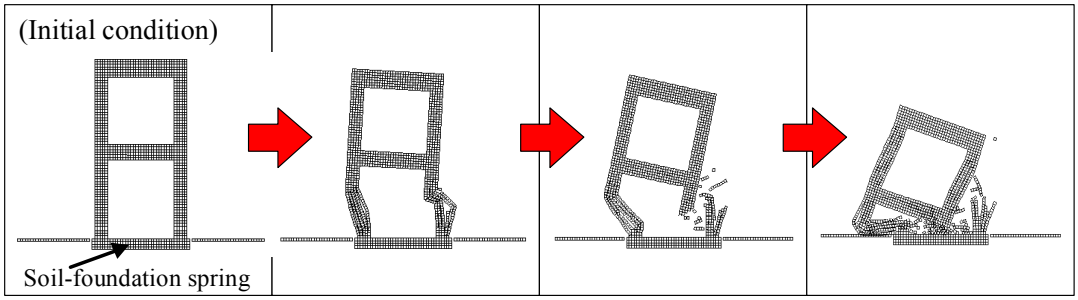

Figure 10. Collapse behavior of numerical model due to ground motion of JR Takatori site

SIMULATION OF THE NATURAL-FREQUENCY CHANGE DUE TO DAMAGE

Application to the Damage Inspection by Using Vibration Measurement

In the field of health monitoring of railway structures, the inspection techniques by using dynamic characteristic of structure have been developed. The methods make use of the natural frequency of structures as the index of damage and/or deterioration levels. The vibration induced by the sources such as the moving train car, impact on the structure and microtremor, is used in order to get the natural frequency of structure (Figure 11). The degree of damage of a RC structure, especially a jacketed structure, cannot be fully grasped by visual inspection. In order to assess the degree of damage to a RC structure using the inspection techniques based on vibration measurements, it is necessary to identify the changes of the dynamic characteristics accompanied by damage to the structure in advance. So, the accuracy of the AEM on the simulation of natural frequency of damaged structure is investigated through the comparison of the results of experimental results and numerical simulations.

Simulation of Natural Frequency of Damaged RC Column

The experiment on the change of natural frequency of RC column due to damage was carried out [6]. The specimen used in the experiment that is the 1/2 model of the column of real railway viaduct is shown in Figure 12. The specimen was damaged step by step due to the cyclic loading. The impact vibration test in order to get the natural frequency of the specimen was performed each damage levels. The material properties of specimen that were gotten by the material test are shown in TABLE VI. The specimen is modeled by the square element that side is 5cm. The number of distributed springs between each two adjacent sides is 10. In case of the experiment, 1 step of cyclic loading is composed 3 cycles, and the impact vibration test was carried out after each steps. The upper section of Figure 13 shows the inputted displacement, and lower section is the comparison between the experimental result and the simulated result of frequency change.

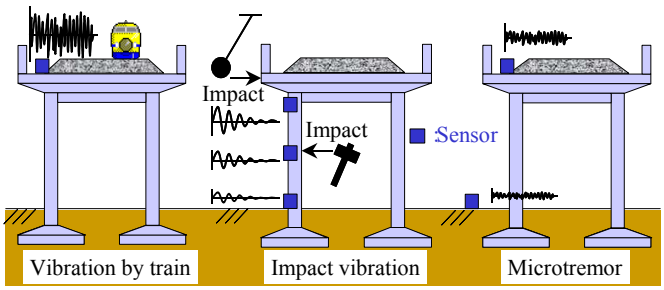

Figure 11. Damage inspection method using vibration measurement

TABLE VI. MATERIAL PROPERTIES OF SPECIMEN

Concrete	Column	Footing
Young's modulus (GPa)	21.9	22.1
Compressive strength (MPa)	28.5	28.7
Tensile strength (MPa)	2.25	2.77
Reinforcing bar	D22	D10

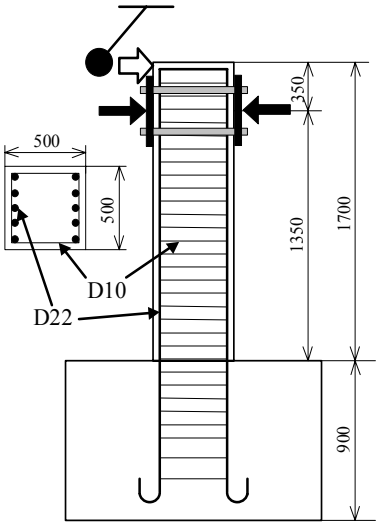

Figure 12. Specimen used in the experiment

Young's modulus (GPa)	193	181
Yield stress (MPa)	421	385

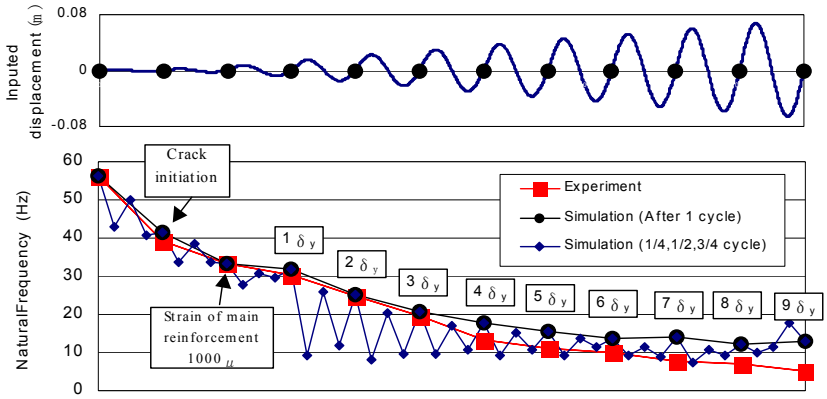

Figure 13. Inputted displacement (Upper) and change of natural frequency due to damage (Lower)

In case of the numerical simulation, the results in case of 1cycle/step are shown in Figure 13 because the difference of the results between in case of 3 cycle/step and in case of 1cycle/step is not big. The simulated natural frequencies of 1/4, 1/2 and 3/4 cycle are also shown in Figure 13. The simulated results can follow the experimental results well.

Simulation of Natural Frequency of Damaged RC Viaduct Reinforced by Steel Jacket

Outline of experiment and numerical simulation

Naganawa *et al*. [7] conducted the loading experiment of a real viaduct reinforced by steel jacket. Daiichi Shinagawa viaduct R13 of the down line, which is removed in connection with Shin-Shinagawa station establishment, was used in the experiment. The structure type of the viaduct is RC rigid frame viaduct supported by 2 columns with 3 spans for single truck. The typical section of the viaduct and the loading equipment are shown in Figure 14. Each column was reinforced by the steel jacket (thickness = 6mm) as shown in Figure 15. The gap between the column and the steel jacket was 30mm, and it was filled up with shrinkage-compensating mortar. Walls were installed in the frame of R12 and R14, which adjoin R13, to act as reaction walls. The slabs between viaducts were cut and the loading jacks were installed there. The cyclic loading test of the R13 along the direction parallel to the track, was carried out by displacement control. After applying cyclic loadings with maximum displacements of ±15mm, ±30mm, ±60mm, ±90mm, ±120mm, ±150mm, ±180mm, ±210mm, and ± 240mm, a monotonic loading of +350mm was imposed as the last step. The impact vibration test of the direction parallel to the track was carried out when each loading step was finished in order to investigate the change of the natural frequency due to damage of the viaduct.

The column of the viaduct was modeled using AEM elements of size 8.25×8.25cm, as shown in Figure 16. It was assumed that the top of the column was restrained against rotation because the viaduct beam was very rigid. The behavior of the whole viaduct was represented with one column carrying one eighth of the total mass of the slab and beams. The design compressive strength of the concrete of the viaduct was 23.5 MPa, and the compression test results, which were obtained at the time of construction, gave a compressive

strength of 32.9 MPa. SD49 was used for the longitudinal reinforcing bars and SS41, for the stirrups.

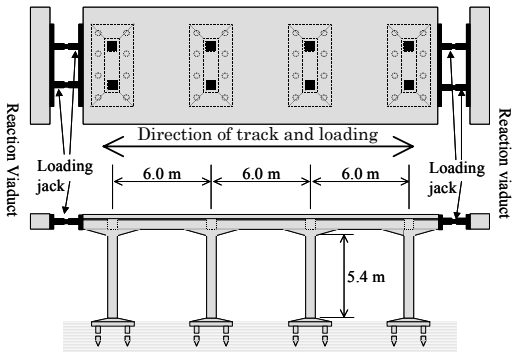

Figure 14. Viaducts and loading equipments

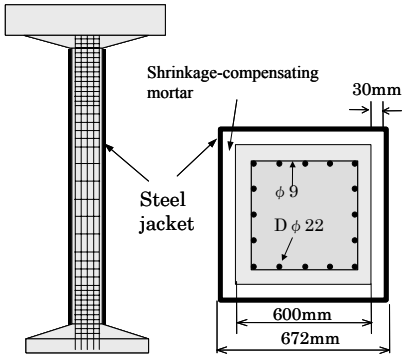

Figure 15. Arrangement of reinforcing bars and cross section of the jacketed column

TABLE VII. COMBINATION OF MATERIAL PROPERTIES

Case	①	②	③	④	⑤	⑥
Concrete	C1	C1	C2	C2	C3	C3
Longitudinal bars	S1	S2	S1	S2	S1	S2

TABLE VIII. MATERIAL PROPERTIES OF NUMERICAL MODEL

	Compressive strength	Young's Modulus		Yield stress	Young's Modulus
Concrete C1	23.5 MPa	24.5 GPa	Longitudinal bar S1	490 MPa	200 GPa
Concrete C2	35.0 MPa	28.0 GPa	Longitudinal bar S2	558 MPa	200 GPa
Concrete C3	17.6 MPa	21.6 GPa	Stirrup	400 MPa	200 GPa

At the first stage of the analysis, the properties of the material of the viaduct were not fixed. Six models with different material properties, as shown in TABLE VII, were created by combining the material properties of the three types of concrete and the two types of longitudinal reinforcing bar shown in TABLE VIII. In addition, by arranging a soil-foundation spring at the bottom of the model, the natural frequency of the column was adjusted so that it became equal to the measured natural frequency of the real viaduct. As a result, the natural frequencies of all the models were equal in the initial state. The changes of the natural frequency of each model due to the structural damage were analyzed and compared with the experimental results.

Results and considerations

The experimental and numerical results are shown in Figure 17. According to the experimental results, the natural frequency reduced to 85% of the original value after the ±30 mm loading. After the ±120mm loading, the natural frequency reduced to 50% and it remained almost constant after that. In the simulation result by AEM, the natural frequency reduced to 79 - 83% after the ±30mm loading, to 55 - 61% after the ±120mm loading, to 50 - 54% after the ±240mm loading, and to 47 - 51% after the +350mm loading. In the numerical simulation results, the difference of the material properties of each model did not have much influence on the natural-frequency change.

CONCLUDING REMARKS

The AEM can simulate the damage behavior of the RC column, the jacketed RC column

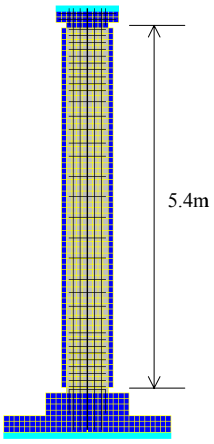

Figure 16. Numerical model of the jacketed column of the viaduct

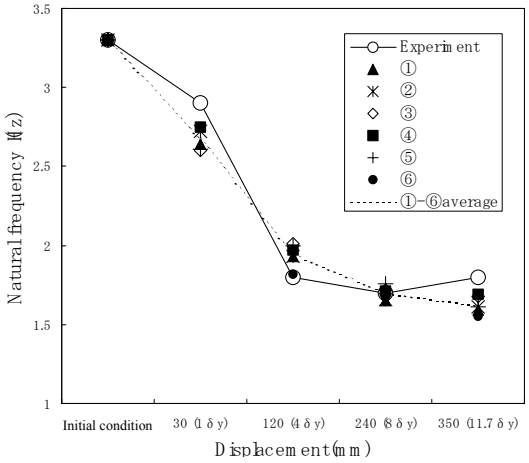

Figure 17. Change of natural frequency of the real viaduct and the numerical models

and the real railway viaduct. The change of natural frequency due to damage of the RC column and the real railway viaduct with steel jacket are also simulated correctly. Through the above-mentioned studies, we confirm that the AEM functioned as a high-performance seismic damage simulator for RC structures and retrofitted RC structures. Seismic performance check of existing pre code-revision structures, selection of the most effective retrofitting method, and development of judgment criteria for damage inspection can be effectively done by AEM. These results are very useful for the assessment and the mitigation of seismic damage for a railway.

REFERENCES

[1] Meguro, K. and Tagel-Din, H. 1997. "A new efficient technique for fracture analysis of structures," *Bulletin of Earthquake Resistant Structure Research Center*, IIS, Univ. of Tokyo, No.30, pp.103-116.

[2] Uehan, F. and Meguro, K. 2000. "Vulnerability assessment of jacketed viaduct using microtremor measurement & numerical simulation," *Proceedings of 12th World Conference of Earthquake Engineering (CD-ROM)*.

[3] Kawashima, K., Unjoh, A., Iida, H. 1993. "Seismic inspection and seismic strengthening methods of reinforced concrete bridge piers at mid-height where main reinforcements are terminated with inadequate anchorage length," *Report of Public Works Research Institute Ministry of Construction*, Vol. 189 (in Japanese).

[4] Editorial committee for the report on the Hanshin-Awaji earthquake disaster. 1996. "Report on the Hanshin-Awaji earthquake disaster, Damage to civil engineering structures, Bridge structure," Maruzen.

[5] Nakamura, Y., Uehan, F. and Inoue, H. 1996. "Waveform and its analysis of the 1995 Hyogo-Ken-Nanbu earthquake II," *JR earthquake information*, No. 23d, RTRI.

[6] Shimono H., Watanabe T. and Satou T. 1997. "A consideration on the damage evaluation of RC members," *Proceedings of the 52th annual conference of the Japan Society of Civil Engineering* I-A, pp. 402-403 (in Japanese).

[7] Naganawa, T. *et al*. 2000. "Experimental study on real RC frame viaduct reinforced by steel (Vol. 2) –Study on soundness diagnosis of RC frame viaduct reinforced by steel after earthquake-," *Proceedings of 55th annual conference of JSCE*, V-501 (in Japanese).

Seismic Performance Evaluation Method for Underground Structures

Tsutomu Nishioka and Shigeki Unjoh

ABSTRACT

Underground structures had been thought to be relatively safe during earthquake ground motions until some of the subway tunnels in Kobe suffered serious damage from the 1995 Hyogoken-nanbu earthquake. It is revealed that underground structures have a wide range of seismic performance according to their ground conditions and structural features. In linear underground structures with long distance such as lifeline systems, the ground conditions and the structural features generally change. It is important from the practical design point of views to simply evaluate the seismic performance of underground structures at a particular site.

This paper presents a simplified seismic performance evaluation method for underground structures. Since the seismic deformation of underground structures is mainly the shear deformation in terms of the whole cross section, the proposed method is based on the shear deformation capacity. The shear deformation capacity is studied through the non-linear frame analyses of five types of common utility boxes (CUBs) with rectangular cross section. In the evaluation method, the ground strain criterion is derived from the shear deformation capacity, using the shear strain transmitting characteristics. The seismic performance is checked by the difference between the ground strain criterion and the peak ground strain on the structure's underground level.

The proposed method is applied to the CUB located at Kobe in Japan that was subjected to the 1995 Hyogoken-nanbu earthquake. The result shows that the CUB has enough ductility with respect to the shear deformation, which coincides with the fact that the CUB suffered only small damage from that earthquake.

Tsutomu Nishioka, Senior Research Engineer, Public Works Research Institute, Earthquake Disaster Prevention Research Group, 1-6 Minamihara, Tsukuba, Ibaraki, 305-8516, Japan

Shigeki Unjoh, Leader, Public Works Research Institute, Earthquake Disaster Prevention Research Group, 1-6 Minamihara, Tsukuba, Ibaraki, 305-8516, Japan

1 INTRODUCTION

The 1995 Hyogoken-nanbu earthquake caused serious damage to some of the subway tunnels at Kobe in Japan [1]. On the other hand, the underground common utility boxes (CUBs) and underground parking structures located at Kobe suffered only minor damage from the earthquake [2]. Underground structures had been thought to be relatively safe during earthquake ground motions until the 1995 Hyogoken-nanbu earthquake. It is revealed that they have a wide range of seismic performance according to their ground conditions and structural features. In linear underground structures with long distance such as lifeline systems, the ground conditions and the structural features generally change. It is necessary from the practical design point of views to simply evaluate the seismic performance of underground structures at a particular site.

The seismic deformation of underground structures is significantly affected by the deformation of the surrounding ground, not by the inertia force acting on the structures. Seismic deformation method (SDM) is commonly applied to practical seismic design of the cross section of underground structures [3-4]. In this method, free-field ground displacement is loaded on the structure through Winkler-type soil springs. One of the problems in the SDM, however, is evaluating the soil spring that is supposed to simulate the soil-structure kinematic interaction. The adequacy of the soil spring and its evaluation method are still under discussion.

The purpose of this paper is to propose a simplified seismic performance evaluation method for underground structures. The main mode of the seismic deformation in the whole cross section is the shear deformation. It is reasonable to evaluate the seismic performance of underground structures in terms of the shear deformation capacity. The ground strain criterion is derived from the shear deformation capacity, using the shear strain transmitting characteristics from free-field ground to the structure. The seismic performance of underground structures is simply checked by the difference between the peak ground strain on the underground structure's level and the ground strain criterion.

The shear deformation capacity is studied through the non-linear frame analysis of five types of the CUBs with rectangular cross section. The ground strain criterion is determined for the types of the CUBs.

Finally, the proposed method is applied to the CUB located at Kobe that was subjected to the 1995 Hyogoken-nanbu earthquake.

2 ANALYSIS OF SEISMIC DEFORMATION CAPACITY

2.1 Analysis cases

Five types of standard CUBs with rectangular cross section are used for the analysis of the shear deformation capacity. The cross sections of the CUBs are shown in Figure 1. In each cross section, 3 kinds of thickness (d=300, 350, 400mm) of the structural members according to the depths of the CUBs are analyzed. Reinforcements D13, D14, and D15 are applied to the thickness d=300, 350, 400mm, respectively. The reinforcements D13, D14, and D15 have 13, 14, and 15mm diameters, respectively. The combination of the thickness and the reinforcements are based on the existing CUBs. Analysis cases are shown in Table 1. Widths and heights of the cross sections indicate the center distances of the structural members. Figure 2 shows the reinforcement bar arrangements. In Section 1 that is around the corners of the cross section the outside reinforcements are 125mm spacing. The other reinforcements including the inside reinforcements in Section 1 and the reinforcements in Section 2 are 250mm spacing, as shown in Figure 2.

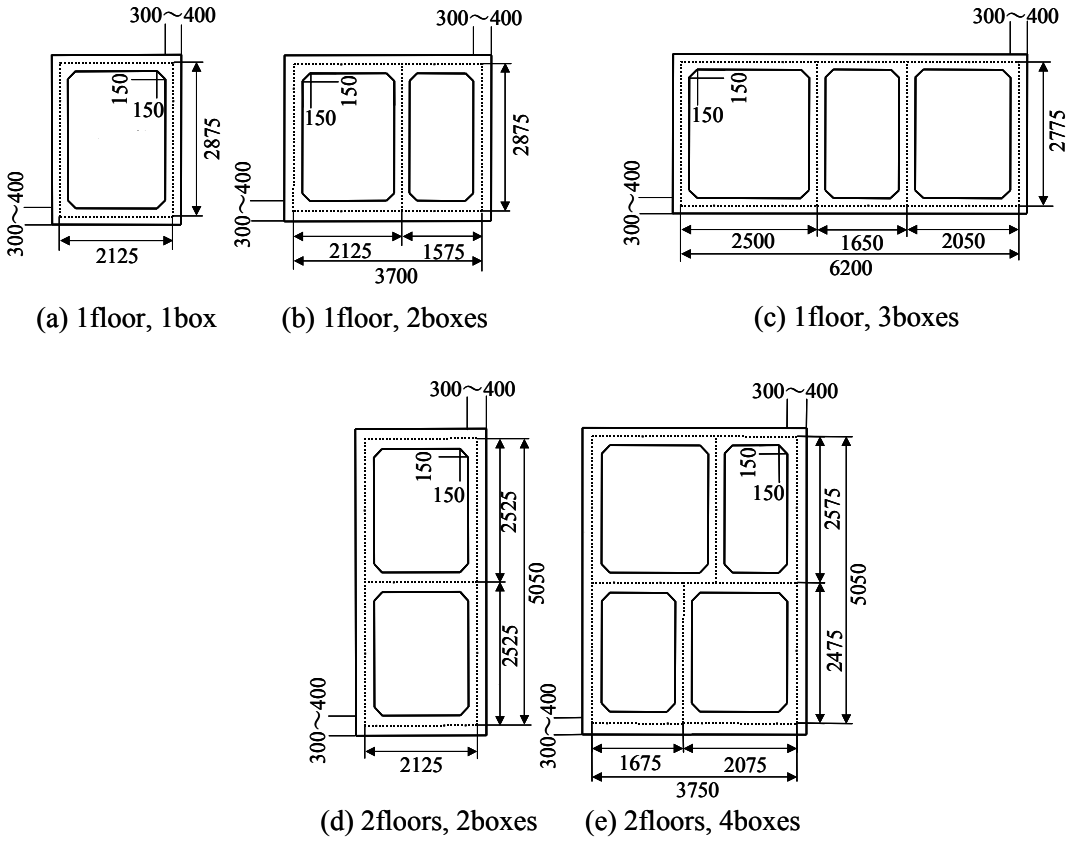

Figure 1. Cross sections of the CUBs (unit:mm)

Table 1. Analysis Cases

Case	Type of CUBs (Floor, Box)	Width b (mm)	Height h (mm)	Thickness d (mm), (reinforcements)	Over-burden D (m)
1	1F,1B	2,125	2,875	300(D13)	4.5
2				350(D16)	8.6
3				400(D19)	15.1
4	1F,2B	3,700	2,875	300(D13)	3.7
5				350(D16)	7.9
6				400(D19)	14.5
7	1F,3B	6,200	2,775	300(D13)	1.9
8				350(D16)	3.8
9				400(D19)	7.2
10	2F,2B	2,125	5,050	300(D13)	4.0
11				350(D16)	7.9
12				400(D19)	13.8
13	2F,4B	3,750	5,050	300(D13)	1.0
14				350(D16)	3.4
15				400(D19)	5.4

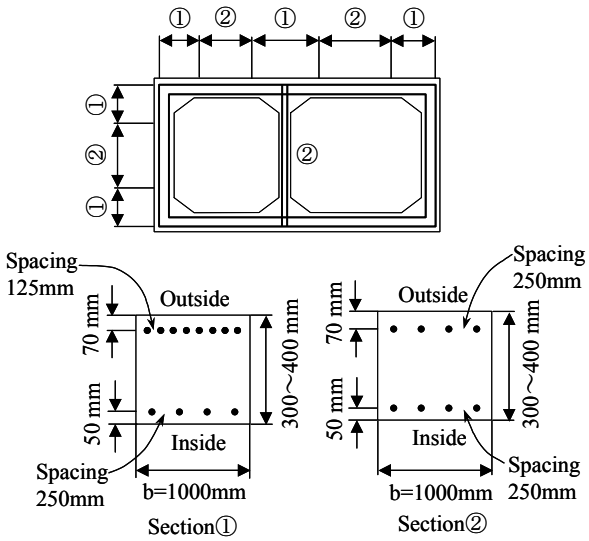

Figure 2. Reinforcement bar arrangements

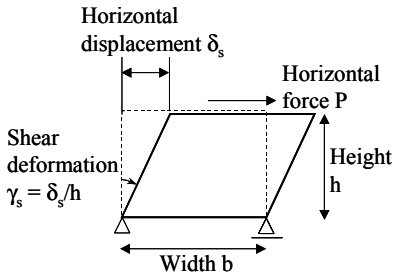

Figure 3. Push-over analysis

2.2 Push-over analysis

Since the seismic deformation of underground structures is primarily the shear deformation, the push-over analysis to increase the shear deformation is conducted for the evaluation of the shear deformation capacity of the CUBs. The simply-supported non-linear frame model is used for the push-over analysis, as shown in Figure 3. The non-linear frame model has the tri-linear moment-curvature relationships as the concrete crack point, the reinforcement yield point, and the ultimate point. The ultimate point is defined as the point where concrete compression strain reaches 0.0035 [5]. Weight per unit volume of the RC, modulus of elasticity, and Poisson's ratio of the concrete are assumed as 24.5 kN/m^3, 2.35×10^4 N/mm^2, and 1/6, respectively. The yield stress of the reinforcements is 295 N/mm^2. The thickness of the outside and inside cover concrete is 70, 50mm, respectively. Initial stress of the non-linear frame model is computed under the conditions that the structures are subjected to the over-burden dead load, the horizontal earth pressure at rest, and the ground reaction force to the lower slab.

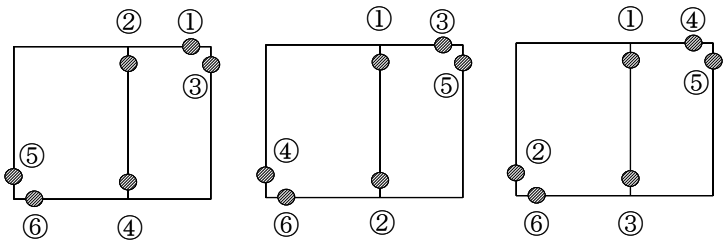

Figure 4. Locations and sequences to reach the ultimate points (Case 4~6)

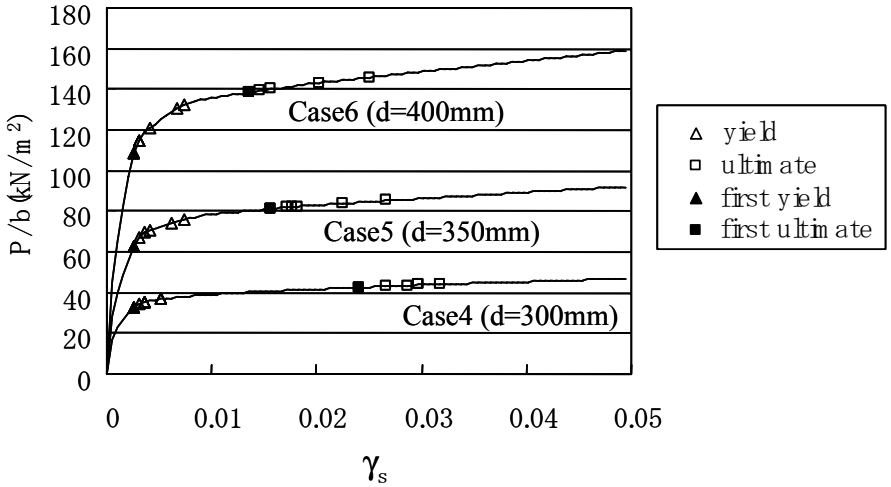

Figure 5. Relationships between γ_s and P/b (Case 4~6)

2.3 Shear deformation capacity

Figure 4 shows the locations and the sequences to reach the ultimate points in Case 4~6. The ultimate points are developed around the bottom left and upper right corners earlier than around the other corners, because the horizontal force is applied to the upper slab in the left-to-right direction from the initial stress condition. Except around the two corners, the ultimate points appear at the upper and lower ends of the partition wall. Case 4~6 have the same locations to reach the ultimate points, but the sequences to reach the ultimate points are not necessarily equal.

Figure 5 shows the relationships between the shear deformation γ_s and the horizontal force per unit width P/b. The six yield points and six ultimate points are located in the curved lines in Figure 5. The larger the thickness d is, the larger the horizontal bearing force is. There are no significant differences among γ_s at the first yield points, but γ_s at the first ultimate points depends on the thickness d. The other cases (Case 1~3, 7~15) show the same tendency as Case 4~6.

The relationships between the thickness d and the shear deformation at the first ultimate points γ_{su1}, are shown in Figure 6. It is found that the larger the thickness d is, the smaller γ_{su1} is and that γ_{su1} of 1 floor type is larger than γ_{su1} of 2 floors type. The push-over analysis for the opposite load direction (the right-to-left direction) is conducted for the CUBs with the dissymmetric cross section,

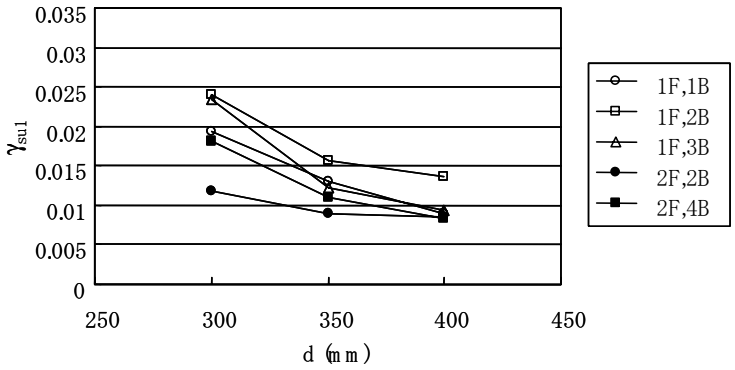

Figure 6. Relationships between d and γ_{su1} (Case 1~15)

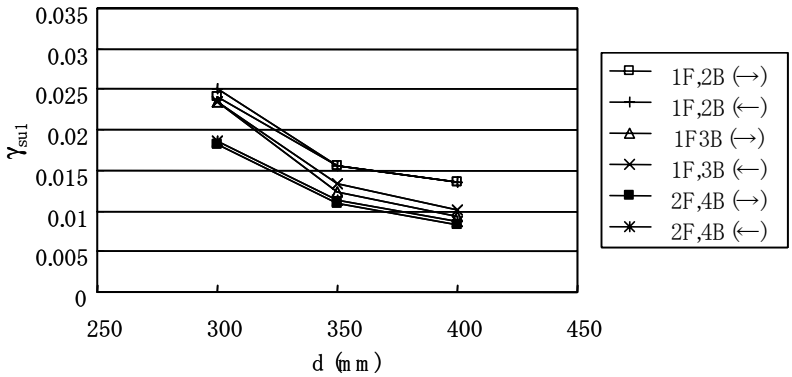

Figure 7. Effect of the load directions (Case 4~9, 13~15)

Table 2. Shear deformation capacity γ_{sa}

γ_{sa}	d=300 mm	d=350 mm	d=400 mm
1 floor type	0.014	0.009	0.007
2 floors type	0.009	0.007	0.006

that correspond to Case 4~9, 13~15. Figure 7 shows the effect of the load directions on the relationships between d and γ_{su1}. Arrows in the legend symbol in Figure 7 denote the load directions. It is found that the load directions do not have much effect on γ_{su1} of the CUBs with the dissymmetric cross section.

As the purpose of the simplified evaluation method is to select vulnerable CUBs that need detailed seismic analysis, the estimation of the shear deformation capacity γ_{sa} of the CUBs should be on the safe side. γ_{sa} is assumed with a safety factor by Equation (1).

$$\gamma_{sa} = \gamma_{sy1} + (\gamma_{su1} - \gamma_{sy1})/\alpha \tag{1}$$

where γ_{su1} = the less shear deformation at the first ultimate point in the two load directions; γ_{sy1} = the shear deformation for the same point as γ_{su1} to reach the reinforcement yield; α = safety factor (=1.5). Table 2 shows γ_{sa} that are the minimum shear deformation capacity estimated in each floor type.

3 SEISMIC PERFORMANCE EVALUATION METHOD

3.1 Ground strain criterion

The authors clarified the shear strain transmitting characteristics from free-field ground to the underground structures [6]. Seismic deformation method (SDM) is commonly applied to seismic design of underground structures, because the deformation of the surrounding ground is a dominant factor for the seismic deformation of the structures. The physical basis of the SDM is explained by the static substructure method, which is derived from the dynamic substructure method [7]. Equation of motion of the SDM are given

$$\begin{bmatrix} K_{SS} & K_{SI} \\ K_{IS} & K_{II}+K_{I0}^{G} \end{bmatrix} \begin{Bmatrix} r_S \\ r_I \end{Bmatrix} = -\begin{bmatrix} M_{SS} & 0 \\ 0 & M_{II} \end{bmatrix} \begin{Bmatrix} \ddot{r}_S \\ \ddot{r}_I \end{Bmatrix} + \begin{Bmatrix} 0 \\ K_{I0}^{G} \cdot r_I^{F} \end{Bmatrix} + \begin{Bmatrix} 0 \\ q_I^{F} \end{Bmatrix} \tag{2}$$

where K = stiffness matrix of the structure, M = mass matrix of the structure, r = displacement vector. The subscripts $_I$ and $_S$ denote the nodes on the soil-structure interface, and the remaining nodes of the structure, respectively. The superscript dots denote time derivation. $K_{I0}{}^{G}$ = ground impedance matrix, $r_I{}^{F}$ = free-field ground displacement vector, $q_I{}^{F}$ = free-field ground internal force on the soil-structure interface.

The second row of Equation (2), the equilibrium on the soil-structure interface, is expressed as

$$(K_{IS} \cdot r_S + K_{II} \cdot r_I) = -M_{II} \cdot \ddot{r}_I + K_{I0}^{G} \cdot (r_I^{F} - r_I) + q_I^{F} \tag{3}$$

Since only the shear deformation of both ground and structure are considered herein, the equilibrium of one-dimensional shear stress in Figure 8 is applied to Equation (3). The equilibrium is given by

$$G_s \cdot \gamma_s = G_g \cdot (\gamma_g - \gamma_s) + G_g \cdot \gamma_g \tag{4}$$

where G_s = equivalent shear stiffness of the whole structure, γ_s = shear deformation (shear strain) of the whole structure, $G_s\gamma_s$ = structure shear stress, G_g = ground shear stiffness, γ_g = ground shear strain on the structure's underground level, $G_g(\gamma_g - \gamma_s)$ = ground shear stress due to the relative shear strain between free-field ground and the structure, $G_g\gamma_g$ = free-field ground shear stress on the structure's underground level. The first term of the right side of Equation (3), the inertia force acting on the structure is ignored, because the effect of the inertia interaction is very small.

The structure-ground shear strain ratio γ_s/γ_g is expressed as

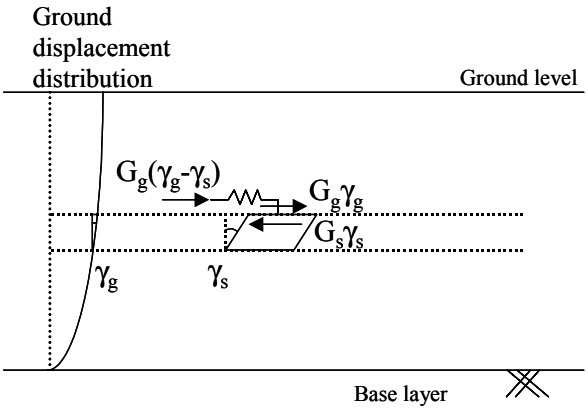

Figure 8. Equilibrium of one-dimensional shear stress of the ground and the underground structure

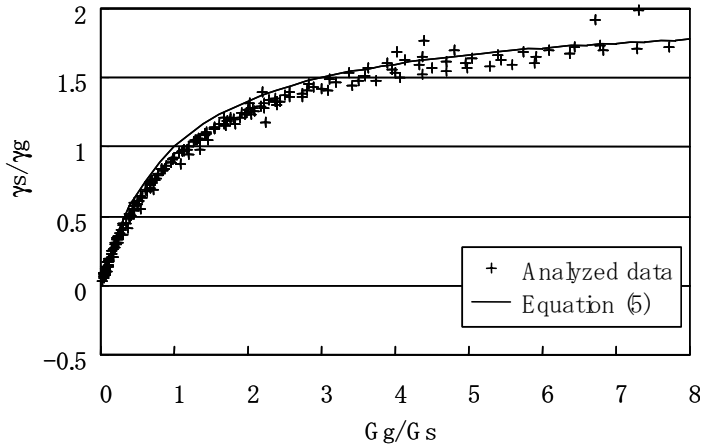

Figure 9. Comparison of Equation (5) and the analyzed data of γ_s/γ_g

$$\gamma_s / \gamma_g = (2G_g / G_s)/(G_g / G_s + 1) \tag{5}$$

Figure 9 shows the comparison between Equation (5) and the data of γ_s/γ_g, which are provided by FEM analyses for the rectangular CUBs with various aspect ratios and underground depths. It is found that Equation (5) estimates the analyzed data of γ_s/γ_g well.

In Equation (5), γ_s/γ_g approaches 2 as G_g/G_s gets large, which means the upper limit of γ_s/γ_g is 2. Therefore, even if the strong ground motion deforms the underground structures into the plastic range, γ_s does not exceed twice as large as γ_g. Additionally, it is explicable that the surrounding soil retains the underground structures ultimately, if the structures have enough ductility. From the upper limit of γ_s/γ_g, the ground strain criterion γ_{gc} is proposed as half of the shear deformation capacity γ_{sa}. The seismic performance of CUBs can be simply evaluated by use of γ_{gc}. If the peak ground strain on the structure's underground level $\gamma_{g,max}$ calculated by the seismic response analysis of free-field ground is smaller than γ_{gc}, the response shear deformation γ_s does not exceed γ_{sa}. Figure 10 shows the flow diagram of the simplified seismic performance evaluation method of the CUBs.

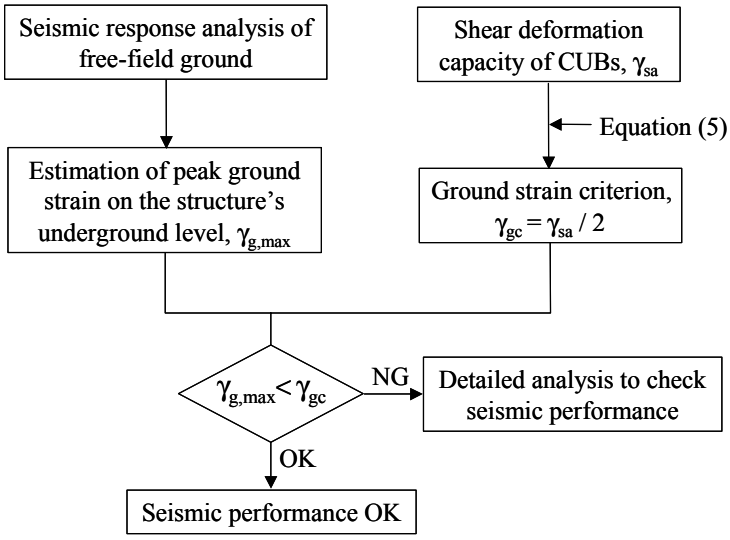

Figure 10. Flow diagram of the simplified seismic performance evaluation method of the CUBs

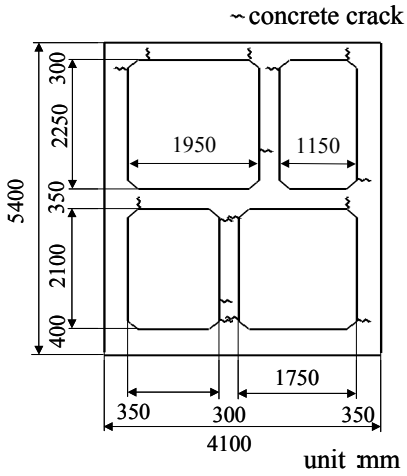

Figure 11. Cross section of the CUB at Kobe

3.2 Practical example

A practical example of the simplified evaluation method is demonstrated as follows. Figure 11 shows the CUB located at Kobe, which suffered small concrete crack damage from the 1995 Hyogoken-nanbu earthquake. Traces of concrete crack obtained by the inside inspection are drawn in Figure 11. Figure 12 indicates the multi-layered ground conditions at the site of the CUB.

The one-dimensional seismic response analysis (SHAKE) is conducted for free-field ground at the site. The ground motion observed in underground (G.L.-83m) near the site is used as the input wave for SHAKE. $\gamma_{g,max} = 1.98 \times 10^{-3}$ is provided by SHAKE.

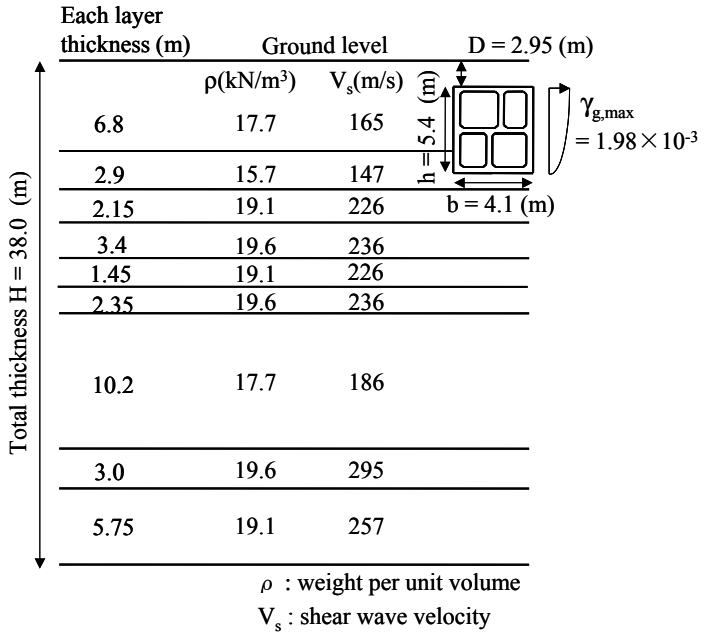

Figure12. Ground conditions at the site of the CUB

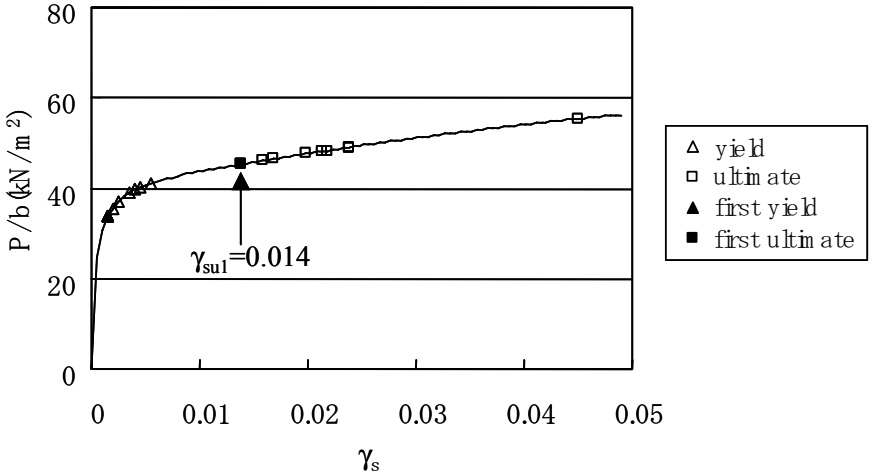

Figure 13. Relationship between γ_s and P/b of the CUB

The thickness of the structural members of the CUB is 300~400mm. The CUB has D13 and D16 reinforcements of which diameters are 13 and 16mm, respectively. In Table 2, the 2 floors type and d=350mm are applicable to the CUB. According to Table 2, γ_{sa} of the CUB is estimated to be 0.007. For the purpose of comparison, the push-over analysis of the CUB is also conducted. The relationship between γ_s and P/b of the CUB is shown in Figure 13. According to the push-over analysis, γ_{su1} is 0.014. Table 3 shows the summary of the evaluation. γ_{sa} from Table 2 is half of γ_{su1} from the push-over analysis. Although γ_{sa} from Table 2 is conservatively estimated, the results of the evaluation are consistent. The response shear deformation γ_s computed precisely by the FEM analysis is about 10% of γ_{su1} from the push-over analysis, which can explain the minor damage suffered from the Hyogoken-nanbu earthquake.

Table 3. Summary of the evaluation

$\gamma_{g,max}$	1.98×10^{-3}	
γ_{sa}	7.0×10^{-3} (Table 2)	$\gamma_{su1}=1.4\times10^{-2}$ (Push-over analysis)
γ_{gc}	3.5×10^{-3}	7.0×10^{-3}
$\gamma_{g,max} < \gamma_{gc}$ (OK)		
γ_s	1.37×10^{-3} (FEM analysis)	

4 CONCLUSION

A simplified seismic performance evaluation method for underground structures is proposed in this paper. The scheme of the evaluation method is shown in Figure 10. The seismic performance of underground structures can be simply checked by the difference between the peak ground strain on the underground structure's level and the ground strain criterion based on the shear strain transmitting characteristics. Finally, the proposed method is applied to the CUB at Kobe that suffered minor damage from the 1995 Hyogoken-nanbu earthquake. The result indicates the CUB has enough seismic performance, which agrees well with the actual damage.

REFERENCES

[1] Samata, S. 1996. "Underground Subway Damage during the Hyogoken-nanbu Earthquake and Reconstruction Technology", *JSCE Journal of Construction Management and Engineering*, No. 534, VI-30, 1-17.

[2] Public Works Research Institute. 1996. "Report on the Disaster Caused by the 1995 Hyogoken Nanbu Earthquake", *Report of Public Works Research Institute*, Japan Ministry of Construction, Vol. 196, 455-470.

[3] Japan Road Association 1992. *Specifications of Design and Construction for Parking Structures*, Maruzen Inc., Tokyo, 155-186.

[4] Railway Technical Research Institute. 1999. *Specifications of Seismic Design for Railway Structures*, Maruzen Inc., Tokyo, 331-341.

[5] Japan Society of Civil Engineers. 1996. *Standard Specifications for Concrete Structures, Design Edition*, Maruzen Inc., Tokyo, 23-24.

[6] Nishioka, T. & Unjoh, S. 2002. "Estimation of the Seismic Shear Deformation of the Underground Structure Based on the Shear Strain Transmitting Characteristics between Ground and Structure", *JSCE Journal of Structural Mechanics and Earthquake Engineering*, No. 710, I-60, 273-282.

[7] Tateishi, A. 1992. "A Study on Loading Method of Seismic Deformation Method", *JSCE Journal of Structural Mechanics and Earthquake Engineering*, No. 441, I-18, 157-166.

Numerical Modeling of Seismic Response of Earth Dams on Liquefiable Foundation

Zhaohui Yang[1], Ahmed Elgamal[2], Korhan Adalier[3], and Michael Sharp[4]

ABSTRACT

Numerical predictions are conducted for two dynamic centrifuge model tests. These centrifuge tests are designed to investigate the effect of foundation densification on the seismic behavior of a zoned earth dam with a saturated liquefiable sand foundation. Model response with and without foundation densification is monitored under dynamic excitation conditions. A solid-fluid fully coupled Finite Element code is employed for conducting the numerical predictions. This code incorporates a plasticity-based soil stress-strain model with the modeling parameters partially defined based on earlier calibration studies. Herein, the computational results are presented and compared with the experimental counterparts. The physical and numerical models both indicate that foundation densification results in reduced lateral and vertical deformations, and increased crest accelerations. Generally, the differences between the computed and recorded dam displacements are within 50%. The observed salient response characteristics such as cyclic mobility effects are highlighted.

1. Research Fellow, Dept. of Structural Engineering, Univ. of California at San Diego, La Jolla, CA 92093.
2. Professor, Dept. of Structural Engineering, Univ. of California at San Diego, La Jolla, CA 92093.
3. Visiting Professor, Dept. of Rensselaer Polytechnic Institute, Troy, NY 12180.
4. Director, Centrifuge Research Center, U.S. Army Engineer Research and Development Center, Vicksburg, MS 39180.

INTRODUCTION

Recently, a series of highly instrumented centrifuge model tests was conducted at Rensselaer Polytechnic Institute [1,2] to experimentally assess the performance of countermeasure techniques for liquefiable earth dam foundations. In this experimental series, seismic behavior of a zoned earth dam with a saturated sand foundation (Fig. 1) was investigated under moderate levels of dynamic excitation. The effect of various parameters on the seismic behavior of the dam, such as the thickness, width, and depth of liquefiable layer, was studied [1]. In all tests, the final permanent displacement field was accurately mapped. Such recorded deformation patterns can serve as the basis of cost-effective remediation measures [1,2,3].

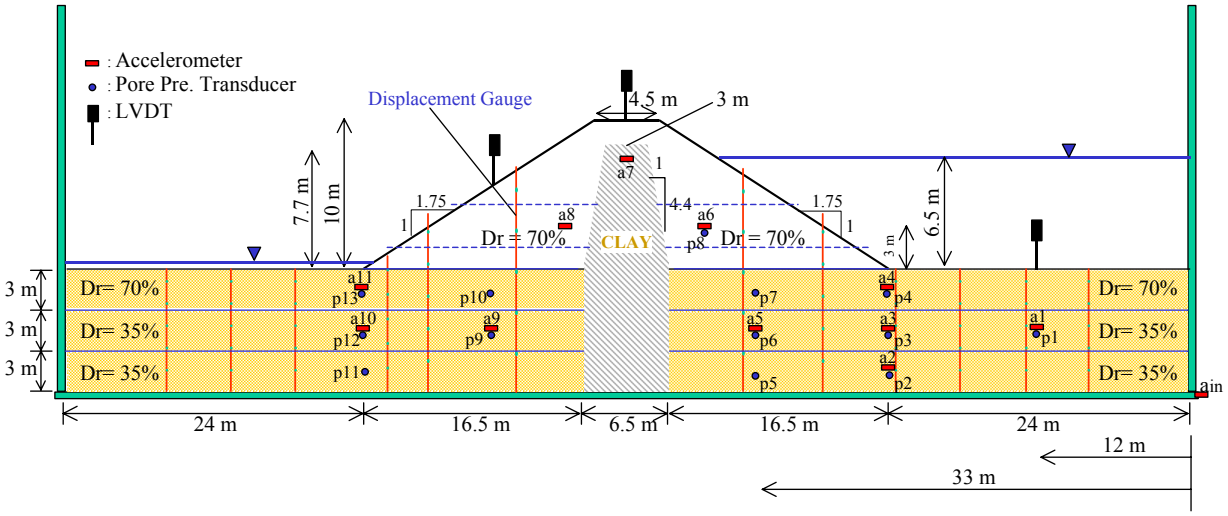

Figure 1. Typical centrifuge model configuration (remediated case) and instrument deployment [1,2].

The complementary data sets generated from this test series shed light on the physical mechanisms underlying the observed dynamic response and deformation patterns, and offer an ideal opportunity for calibration and verification of numerical procedures. Herein, numerical predictions are performed for two of the conducted tests. The first case is the benchmark test with the entire foundation composed of loose Nevada No. 120 sand, at a relative density D_r of about 35%. The second model has the same configuration as the benchmark case, with the 3 m surface layer of the foundation densified to 70% D_r (Fig. 1).

A solid-fluid fully coupled Finite Element program [4,5] was employed in the numerical analysis. This program incorporates a soil stress-strain model that has been calibrated earlier [4] for the same Nevada sand at $D_r \approx 40\%$. This earlier calibration served as the basis for defining the modeling parameters in this study. Blind (Class-A) numerical predictions were conducted, only knowing the physical model configuration and the input motion.

In the following, after a brief description of the experimental and numerical modeling procedures, the blind prediction results are presented and compared with the corresponding experimental data. Throughout, the observed salient response characteristics such as dilatancy and cyclic mobility are highlighted. All computational and experimental results are reported below in prototype scale, unless otherwise specified.

CENTRIFUGE TESTING PROGRAM

The liquefaction countermeasure experimental study [1,2] was conducted at a 100g gravitational acceleration throughout. Under this gravity field, the centrifuge models (Fig. 1) simulated a prototype earth dam of 10 m in height and 39.5 m in base width, resting on a sand foundation deposit of 9 m thickness. The earth dam core was composed of Kaolin clay compacted at about 33% water content, with a dry unit weight of 13.4 kN/m^3 and an estimated unconfined shear strength (s_u) of 16-18 kPa. The embankment was composed of clean Nevada No. 120 sand at a D_r of about 70%. The same sand was also used as the foundation material, at a D_r of about 35% (for the non-densified zone) and 70% (for the densified zone). The foundation layer was saturated with a fluid at a prototype permeability of 1.3x10^{-4} m/s (D_r=35%) and 1.0x10^{-4} m/s (D_r=70%), within the range of fine sands. Water was used to saturate the upstream embankment and as the reservoir fluid (Fig. 1), resulting in a prototype permeability of about 6x10^{-3} m/s (within the range of coarse sands).

Both models were subjected to similar lateral acceleration of about 30 cycles, 0.2g peak amplitude, and 1.5 Hz dominant frequency. Soil response during and after shaking was monitored (Fig. 1) by a large number of miniature accelerometers (in the horizontal direction), pore pressure transducers, Linear Variable Differential Transformers (LVDTs), and a dense mesh of displacement gauges.

NUMERICAL MODELING PROCEDURES

Finite element model

To study the dynamic response of saturated soil systems as an initial-boundary-value problem, a two-dimensional plane-strain Finite Element (FE) program was developed [6,7]. This program implements the two-phase (solid-fluid) fully coupled FE formulation of Chan [8] and Zienkiewicz et al. [9].

The FE mesh for the dam-foundation system is shown in Fig. 2. The boundary conditions for all simulations were:

1) For the solid phase, lateral input motion was specified along the container boundary (base and two lateral sides), as the recorded rigid container acceleration. All nodes on this boundary were fixed in the vertical direction.
2) For the fluid phase, the base and the two sides (i.e., the container boundaries) were impervious. The free water surface (phreatic surface) was assumed to vary linearly within the clay core between the upstream side and the downstream side (dashed line in Fig. 2). For the fluid nodes above and along this surface, zero pore pressure was specified. Finally, at each node along the model surface below the water table, a constant pore pressure was specified equal to the acting hydrostatic pressure.

A static application of gravity (model own weight) was performed before seismic excitation. The resulting fluid hydrostatic pressures and soil stress states served as initial conditions for the subsequent dynamic analysis.

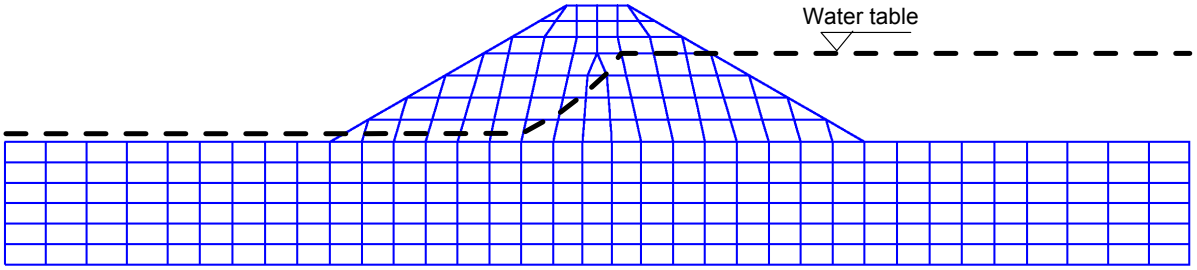

Figure 2. Finite element mesh.

Constitutive model

The FE program incorporates a plasticity-based soil stress-strain constitutive model [6,7,10], in which a number of conical yield surfaces with different tangent shear moduli are employed to represent shear stress-shear strain nonlinearity and confinement dependence of shear strength [11,12]. This soil model was calibrated earlier for the same sand employed in the conducted centrifuge tests, at a $D_r \approx 40\%$. The calibration phase [4] included results of monotonic and cyclic laboratory sample tests [13], as well as data from level-ground and mildly inclined infinite-slope dynamic centrifuge model tests [14,15]. In the following numerical studies, this constitutive model is employed throughout for the foundation and embankment soils.

As mentioned in the Introduction, liquefaction-induced deformation is among the most important criteria for evaluation/remediation of related hazards. In this regard, the employed soil constitutive model was developed with emphasis on simulating the liquefaction-induced shear strain accumulation mechanism in clean medium-dense sands [4,5,10]. Figure 3 depicts the model simulation results of an inclined liquefible loose sand deposit ($D_r \approx 40\%$) subjected to cyclic loading, in terms of shear stress-strain and effective stress path. It shows: 1) an initial phase of gradual loss in effective confinement and thus gradual increase in pore pressure (shear-induced contraction), 2) considerable shear strain accumulating within each load cycle, as the effective confinement approaches zero (i.e., liquefaction), and 3) rapid increase in effective confinement at large cyclic shear strain excursions (shear-induced dilation), which causes increased shear stiffness and strength.

In general, the contraction tendency decreases and the dilation tendency increases with increasing soil density. Therefore, under identical loading conditions, denser sands would experience slower pore-pressure buildup (or confinement loss), less cyclic shear strain accumulation, and stronger instantaneous regain in shear stiffness/strength due to dilation.

Model Parameters Definition

The main modeling parameters include typical dynamic soil properties such as low-strain shear modulus and friction angle, as well as calibration constants to control pore-pressure buildup rate, dilation tendency, and the level of liquefaction-induced cyclic shear strain. For loose Nevada sand (35% D_r), a set of parameter values similar to that calibrated for the 40% D_r Nevada sand [4] was used, with a friction angle of 31.5^o and a phase-transformation angle [16] of 26.5^o. For dense Nevada sand (70% D_r), no formal calibration phase was performed a priori. Hence, the modeling parameters were chosen mainly based on engineering judgment, resulting in higher shear strength and stiffness, stronger dilation tendency, and lower pore pressure buildup rate (35.5^o friction angle and 22^o dilation angle). For the clay core, a simplified version of the same

constitutive model was used, with a cohesion of 17 kPa and zero friction angle (unconsolidated undrained response). This shear strength was chosen based on earlier laboratory testing results [1].

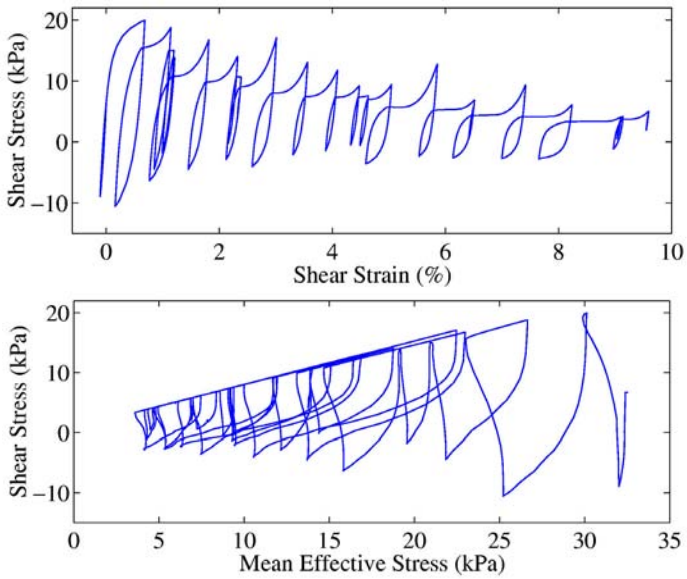

Figure 3. Model simulation of inclined liquefiable soil deposit under undrained shaking conditions showing shear stress-shear strain and effective stress path.

RESULTS AND DISCUSSION

Extensive discussion of the experimental results can be found in [1,2]. In this section, we first summarize the overall deformation pattern (both experimental and computational) of the dam-foundation system, and compare the computed displacements at key locations to the experimental counterparts. Thereafter, computed acceleration and excess pore pressure (u_e) results are presented and compared to the corresponding experimental data at a number of representative locations.

Deformations

Figs. 4a and 4b show the measured along with the computed final configurations, for the benchmark and the remediated cases respectively. In both cases, due to combined action of the imparted lateral excitation and weight of the dam body, foundation soil migrated laterally towards the free field (lateral spreading). Lateral foundation displacements attained maximum values at ground surface, and decreased with depth. In the benchmark case (Fig. 4a), large shear strains developed throughout the entire foundation layer. Furthermore, the large deformations and loss of strength in the foundation material resulted in severe distortion of the overlying dam body (slope instability). On the other hand, the presence of a densified foundation layer in the remediated case (Fig. 4b) restrained the foundation from otherwise excessive straining. The higher shear strength associated with this stiff layer also helped maintain integrity of the dam body.

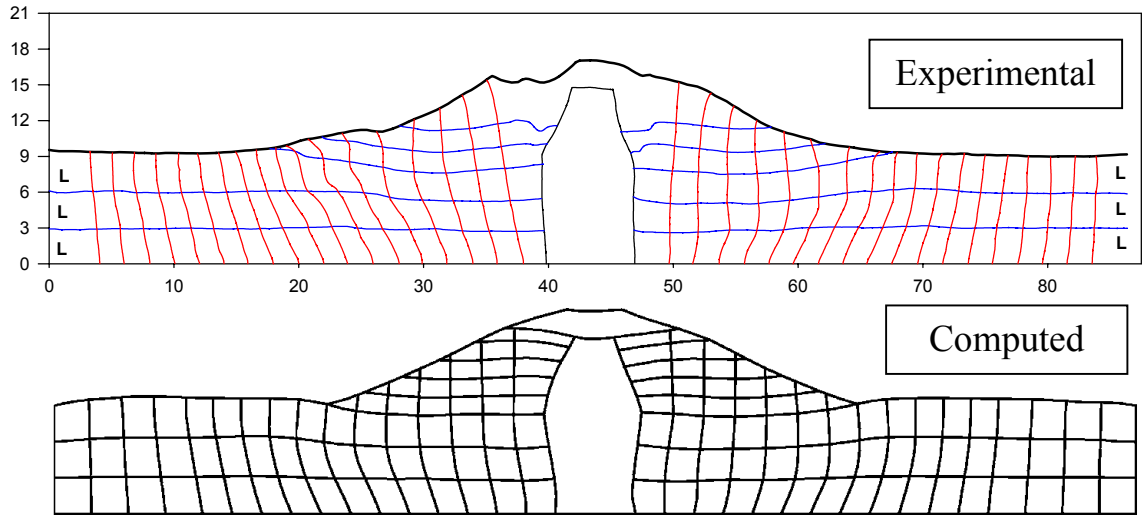

Figure 4a. Recorded and computed deformed configurations (benchmark case).

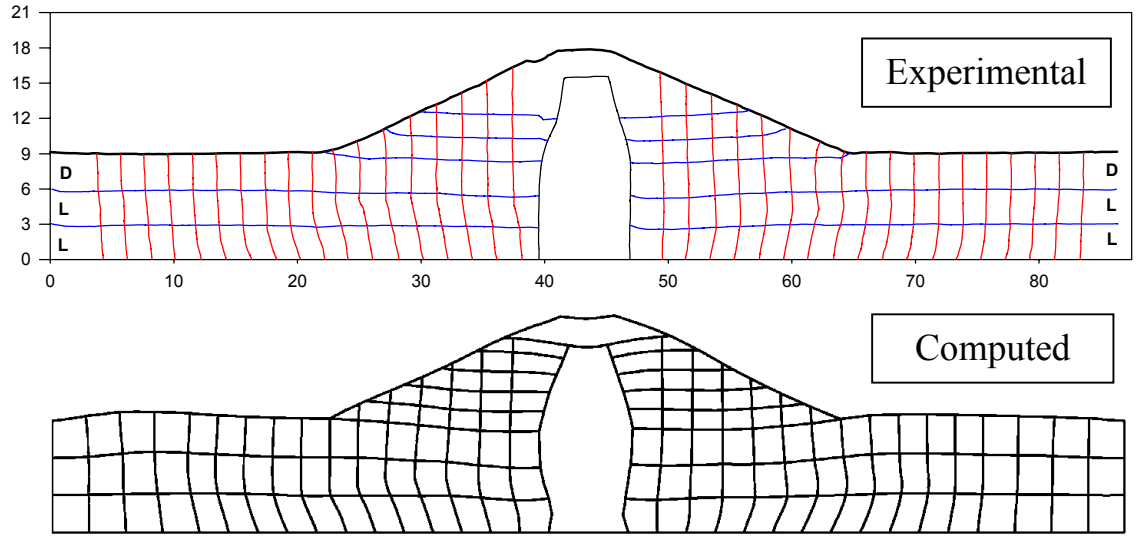

Figure 4b. Recorded and computed deformed configurations (remediated case).

The final lateral displacements at the upstream and downstream dam toes are shown in Fig. 5 for both cases. It is seen that the foundation densification resulted in a significant reduction in the lateral displacements. The final displacements were predicted reasonably well in the remediated case, but was under-predicted by 40-50% in the benchmark case. As mentioned above, considerable lateral deformation in this case was attributed to the failure of the dam slopes, which was not captured by the computational model. It is recognized that better numerical results may be achieved by using a more refined FE mesh.

Fig. 6 depicts computed vertical displacements along with the corresponding LVDT data at the dam slope and crest. In both cases, the settlements are seen to accumulate on a cycle-by-cycle basis, a consequence of the cyclic-mobility response mechanism (Fig. 3). Comparison of the two cases shows that foundation densification has reduced the dam settlement by about 40%.

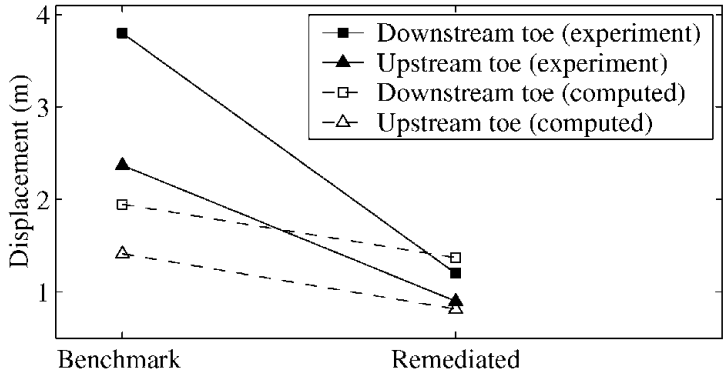

Figure 5. Measured and computed lateral displacements at dam toes.

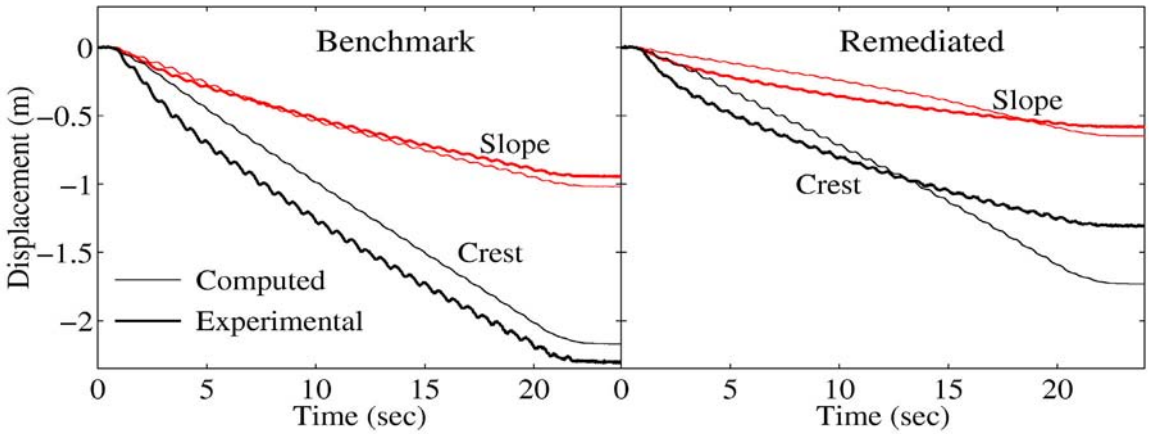

Figure 6. Recorded and computed vertical settlement.

In the benchmark case, the predicted settlement histories are in remarkable agreement with the experimental counterparts at both dam crest and slope. In the remediated case, the predicted slope settlement is also in good agreement with the recorded. The actual crest settlement in this case is seen to accumulate at a gradually decreasing rate, in contrast to the linearly increasing settlement predicted by the numerical models. Hence, the numerical model initially under-predicted but eventually over-predicted the crest settlement by about 30%. The decreasing settlement rate in the physical model may be attributed to: 1) densification of the foundation sand during the shaking, and 2) geometrical nonlinearity due to finite deformations (the computational model is based on small-deformation theory).

Accelerations and excess pore pressures

The acceleration and u_e responses are discussed with focus on three key locations: I) downstream below the dam toe where lateral spreading displacements were most significant, II) upstream below the dam body where the foundation experienced severe lateral elongation, and III) below dam crest, as the acceleration response here is important for any facilities located at the dam crest.

I) Fig. 7 depicts computed vs. recorded acceleration histories (A10) below the downstream dam toe. The phases of dilative response discussed above (Fig. 3) instantaneously increased the soil shearing resistance, resulting in a pattern of strong asymmetric acceleration spikes as exhibited computationally as well as experimentally in both cases. It is seen that the computed

acceleration response agrees very well with the recorded data for both cases. On the upstream side, the acceleration response also exhibited asymmetric spikes but in the opposite direction, in accordance with the direction of foundation lateral spreading thereof.

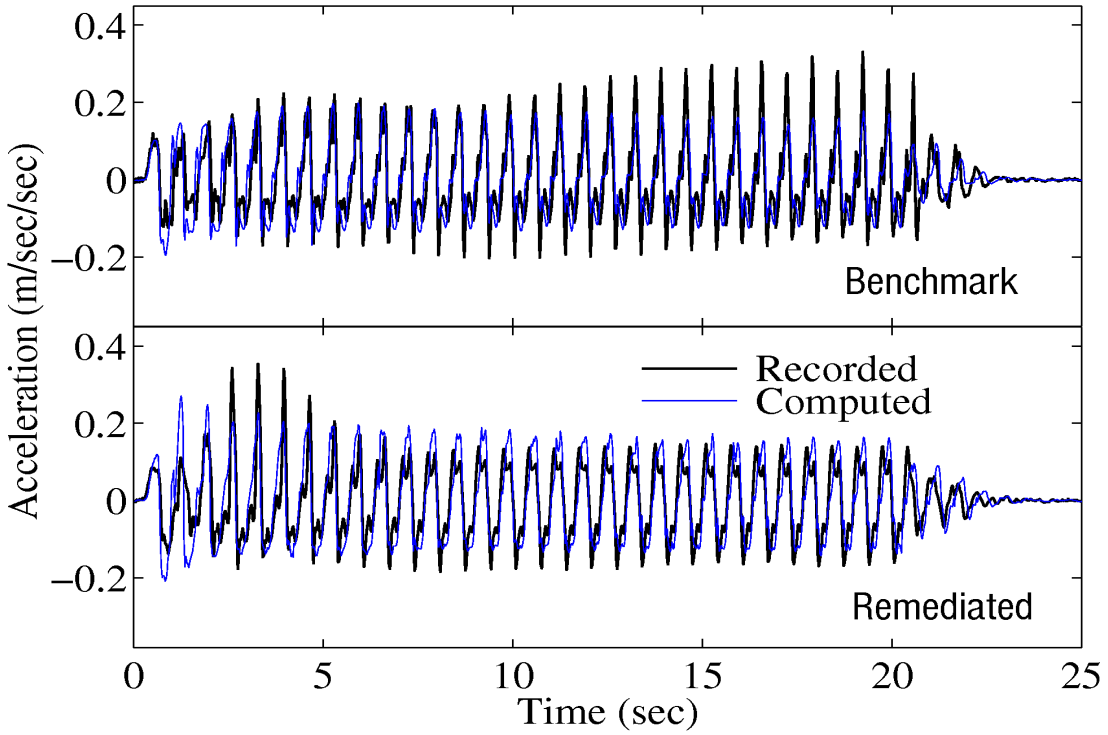

Figure 7. Recorded and computed lateral acceleration histories at downstream below dam toe (ACC 10).

II) Directly below the dam body, stretching of the foundation soil (Fig. 4) led to low or even negative u_e buildup (P7), as depicted in Fig. 8. In particular, the u_e response of the remediated case showed: 1) gradual reduction in u_e during the shaking phase, as soil being stretched, and 2) significant u_e increase after the shaking stopped, as excess pore fluid redistributed into this area. This unique pattern of response was accurately reproduced by the numerical model.

III) Fig. 9 depicts computed vs. recorded acceleration responses near the dam crest (A7), within the clay core. It is clearly seen that the acceleration amplitudes increased in the remediated case, as the denser foundation was able to transmit more seismic energy to the dam crest [1]. In both cases, the numerical model over predicted the actual acceleration amplitudes by about 30-50%.

SUMMARY AND CONCLUSIONS

Blind numerical predictions were conducted to study the seismic behavior of an earth dam-foundation system, without and with foundation densification. Time histories of displacements, accelerations, and excess pore pressures computed at key locations were compared with the recorded counterparts. For the dam displacements (lateral and vertical), the difference between the computed and the recorded results are within 50%. The computed acceleration and pore pressure responses matched the recorded counterparts reasonably well at most locations. Generally, the numerical models captured the predominant cyclic-mobility response mechanism

exhibited in the physical models, in terms of lateral spreading deformations and asymmetric acceleration response. Currently, effort is underway to further calibrate the numerical procedure based on the blind prediction results.

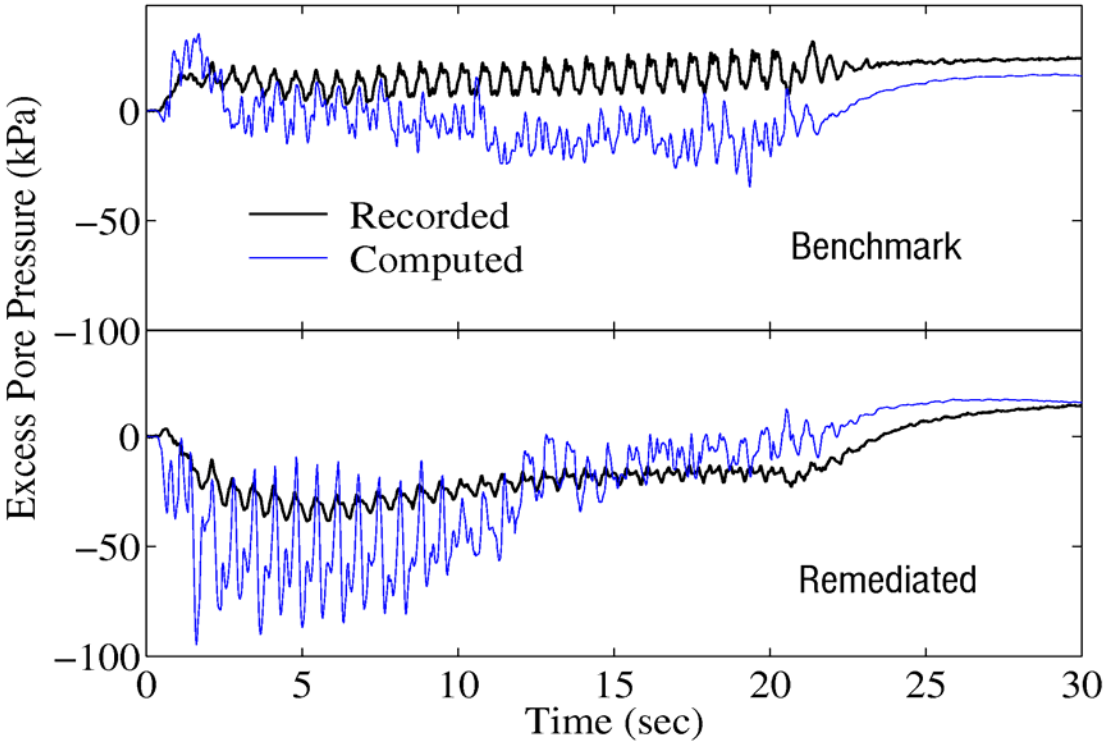

Figure 8. Recorded and computed excess pore pressure histories at upstream below dam body (PPT 7).

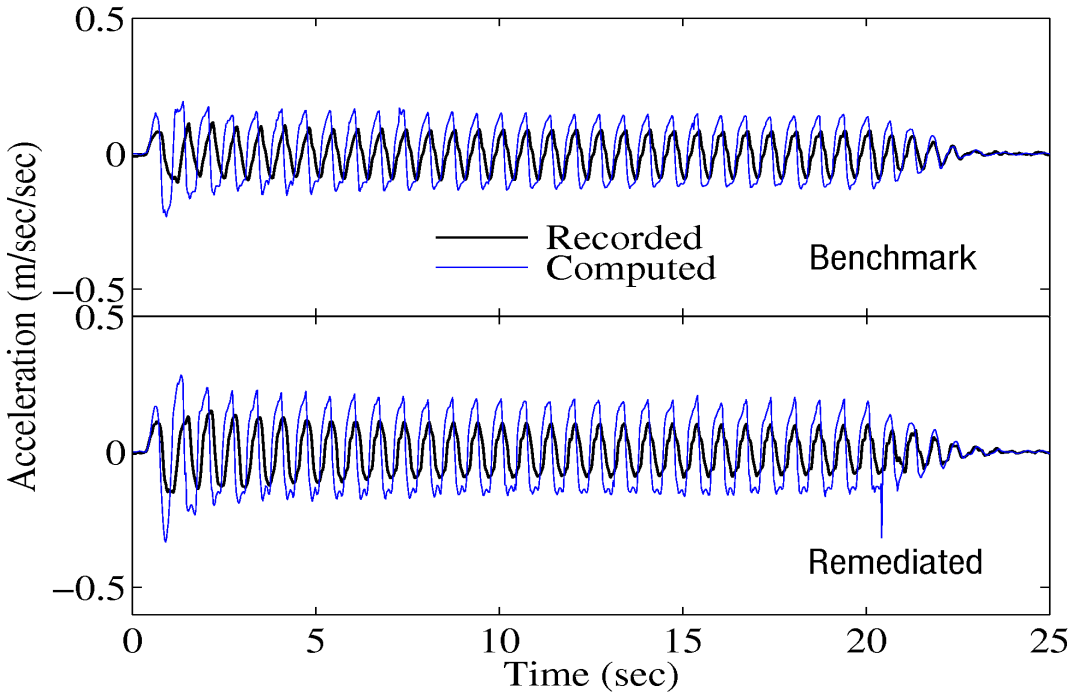

Figure 9. Recorded and computed lateral acceleration histories at top of clay core (ACC 7).

ACKNOWLEDGMENTS

This work was supported by the Office of the Chief Engineers through the Earthquake Engineering Research Program of the U.S. Army Corps of Engineers, and the Pacific Earthquake Engineering Research (PEER) Center, under the National Science Foundation Award Number EEC-9701568.

REFERENCES

[1] Adalier, K. and Sharp, M.K. (2002). "Dynamic Centrifuge Modeling of Earth Dams on Liquefiable Ground," *Invited Paper, 3rd U.S.-Japan Workshop on Advanced Research on Earthquake Engineering for Dams*, June 22-23, San Diego, CA.

[2] Adalier, K. and Sharp, M.K. (2002b). "Embankment Dam on Liquefiable Foundation – Dynamic Behavior and Densification Remediation," *J. Geotechnical and Geoenvironmental Engineering*, ASCE (submitted).

[3] Finn, W.D.L. (2000). "State-of-the-art of Geotechnical Earthquake Engineering Practice," *Soil Dynamics and Earthquake Engineering*, 20, 1-15.

[4] Elgamal, A., Yang, Z. and Parra, E. (2002a). "Computational Modeling of Cyclic Mobility and Post-Liquefaction Site Response," *Soil Dynamics and Earthquake Engineering,* 22(4), 259-271.

[5] Yang, Z. and Elgamal, A. (2002). "Influence of Permeability on Liquefaction-Induced Shear Deformation," *J. Engineering Mechanics*, ASCE, 128(7), 720-729.

[6] Parra, E. (1996). "Numerical Modeling of Liquefaction and Lateral Ground Deformation Including Cyclic Mobility and Dilation Response in Soil Systems," *Ph.D. Thesis*, Dept. of Civil Engineering, Rensselaer Polytechnic Institute, Troy, NY.

[7] Yang, Z. (2000). "Numerical Modeling of Earthquake Site Response Including Dilation and Liquefaction," *Ph.D. Dissertation*, Dept. of Civil Engineering and Engineering Mechanics, Columbia University, New York, NY.

[8] Chan, A. H. C. (1988). "A Unified Finite Element Solution to Static and Dynamic Problems in Geomechanics," *Ph.D. dissertation*, U. College of Swansea, U. K.

[9] Zienkiewicz, O. C., Chan, A. H. C., Pastor, M., Paul, D. K., and Shiomi, T. (1990). "Static and Dynamic Behavior of Soils: A Rational Approach to Quantitative Solutions: I. Fully Saturated Problems," *Proc., Royal Society London*, A 429, 285-309.

[10] Elgamal, A., Yang, Z., Parra, E. and Ragheb, A. (2002b). "Modeling of Cyclic Mobility in Saturated Cohesionless Soils," *Int. J. Plasticity* (in press).

[11] Prevost, J. H. (1985). "A Simple Plasticity Theory for Frictional Cohesionless Soils," *Soil Dynamics and Earthquake Engineering*, 4(1), 9-17.

[12] Lacy, S. (1986). "Numerical Procedures for Nonlinear Transient Analysis of Two-phase Soil System," *Ph.D. Dissertation*, Princeton University, NJ.

[13] Arulmoli, K., Muraleetharan, K.K., Hossain, M.M., and Fruth, L.S. (1992). "VELACS: Verification of Liquefaction Analyses by Centrifuge Studies, Laboratory Testing Program, Soil Data Report," *Report*, The Earth Technology Corporation, Project No. 90-0562, Irvine, CA.

[14] Dobry, R., Taboada, V. and Liu, L. (1995). "Centrifuge Modeling of Liquefaction Effects During Earthquakes," *Keynote Lecture, Proc. 1st Intl. Conf. On Earthquake Geotechnical Engineering* (IS-Tokyo), Ishihara, K. (Ed.), Balkema, Rotterdam, 3, 1291-1324.

[15] Taboada, V.M. (1995). "Centrifuge Modeling of Earthquake-Induced Lateral Spreading in Sand Using a Laminar Box," *Ph.D. Thesis*, Rensselaer Polytechnic Institute, Troy, NY.

[16] Ishihara, K., Tatsuoka, F. and Yasuda, S. (1975). "Undrained Deformation and Liquefaction of Sand under Cyclic Stresses," *Soils and Foundations*, 15(1), 29-44.

Evaluation of Dynamic Earthpressures Acting on Subway Structure Subjected to Earthquake Loading

Che Ailan and Takahiro Iwatate

ABSTRACT

A detailed survey was conducted on the underground structures such as subway structures, mountain tunnels and multipurpose underground ducts in the Hanshin District suffered from the 1995 Hyogoken-Nanbu Earthquake [1,2]. Among them, the damage of Daikai subway station is the first case study of subway structure that completely collapsed by the past earthquakes [3]. In order to clarify the damage mechanism of the subway structure, a series of shaking table tests and simulation analyses were performed with special attention to the dynamic soil-structure interaction and the resultant dynamic forces acting on the structure, especially on the center columns [5,6]. In this paper, the seismic response of the structure and the dynamic forces acting on the structure due to horizontal excitation of sinusoidal and random waves were investigated. These experiment and analysis revealed that significant horizontal forces (shear stress and lateral earth pressure) acted on the structure. In addition, in simulation analyses the relationship between dynamic earth pressures acting on the subway structure and the shear modulus ratio between the structure and the surround ground were evaluated.

1. Introduction

On January 17, 1995, the Hyogoken-Nanbu earthquake in Kobe, Japan, caused serious damage to underground structures that had previously been considered to be resistant to earthquake effects. The most significant damage was caused to subway structures, most of which had been constructed using the cut-and-cover technique. Six underground stations out of the total 21 subway stations in the Kobe area were severely damaged by the earthquake. Among these cases, the Daikai Station was the most seriously damaged. More than half of the center columns at the Daikai station completely collapsed, and the ceiling slab supported by them bent and fell down (Photo 1-1). Figure 1-1shows the schematic diagrams of the damages in the longitudinal section. This collapse of the structure resulted in subsidence at the surface street with a maximum depth of 2.5m [2].

It is important to clarify the damage mechanism of the soil-structure interaction, and the dynamic earth pressures acting on the structure. A series of shaking table tests and simulation analyses were performed due to five different base acceleration (20gal, 50gal, 100gal, 200gal, 400gal) sinusoidal and random (Kobe marine meteorological observatory record of Hyogoken-nanbu earthquake, maximum acceleration 817gal) input excitations [2,4].

Che Ailan, Graduate student, Graduate School of Engineering, Tokyo Metropolitan University, 1-1 Minami-Osawa, Hachoji-shi, Tokyo Japan 192-0397
Takahiro Iwatate, Professor, Graduate School of Engineering, Tokyo Metropolitan University, 1-1 Minami-Osawa, Hachoji-shi, Tokyo Japan 192-0397

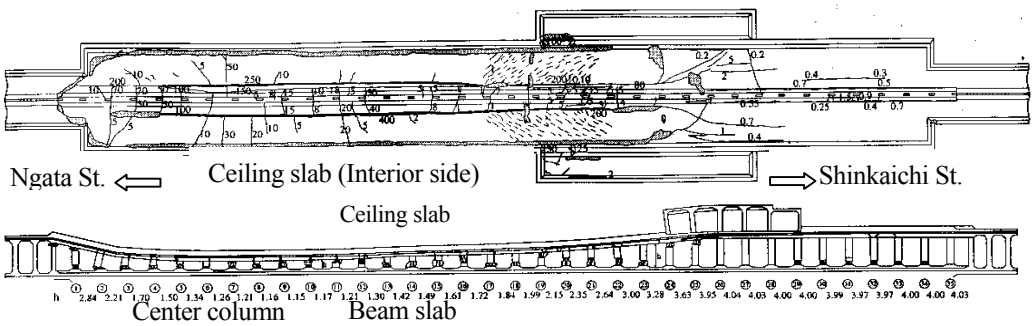

Figure 1-1 Schematic figure indicating damage of the ceiling slab and the center column

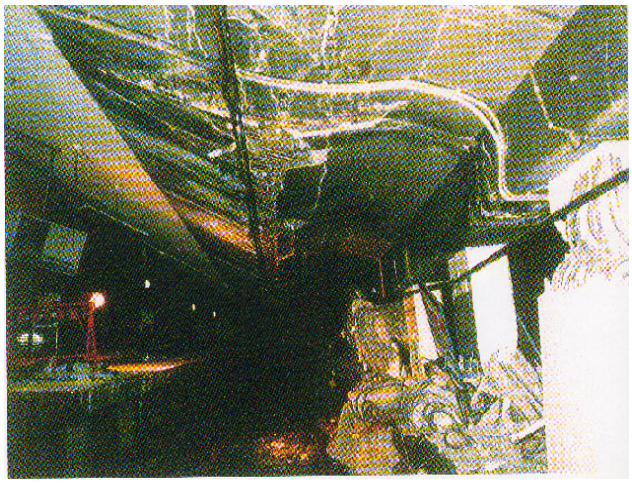

Photo 1-1 Collapse of ceiling slab and center column of Daikai Subway Station

2. Scaled model shaking table tests of the subway structure

In order to clarify the dynamic behavior and the dynamic forces acted on the structure and the damage mechanism of the subway structure, shaking table tests were performed on a 1/30 scale model of Daikai Station (Photo 2-1,2) at the Geotechnical Engineering Laboratory of Tokyo Metropolitan University [9], [10].

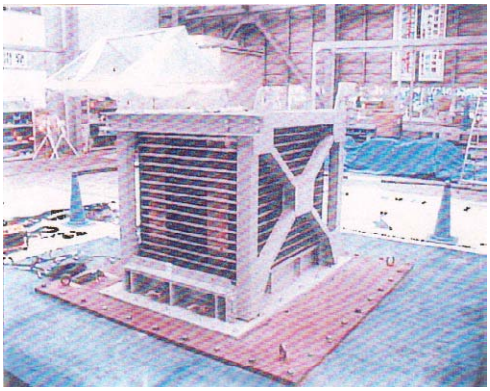

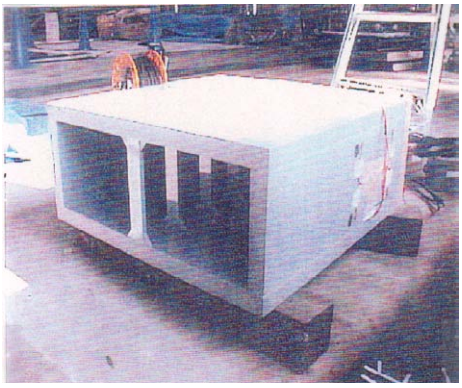

Photo 2-1 Soil container of shaking table tests Photo 2-2 Subway structure model of Daikai station

2.1 Model ground and model subway structure

A new laminar shear box type soil container was developed to reproduce ideal horizontal shear excitation in the ground, as shown in Photo 2-1. The model ground was constructed with fine dry sand (Gifu-Sand D_{60}=0.35mm) in two layers, which are a 0.4 m thick subsurface layer (ρ =1.48tf/m^3) and a 0.6 m thick bearing stratum (ρ =1.60tf/m^3). A 1/30 scale model of the subway structure was placed on the bearing stratum in the surface layer. The subway model was a box type frame structure with seven center columns (three columns were fitted with a pin joint, and the remainder with rigid joints) of dimensions 60 mm × 60 mm × 240 mm constructed from polyvinyl chloride resin (ρ =1.47tf/m^3, Young's modulus G=3.0E+05tf/m^2).

The thickness of the overburden soil was 16 cm (Figure 2-1). A 5 mm thick rubber board was placed between the column and the slabs to represent the pin joints.

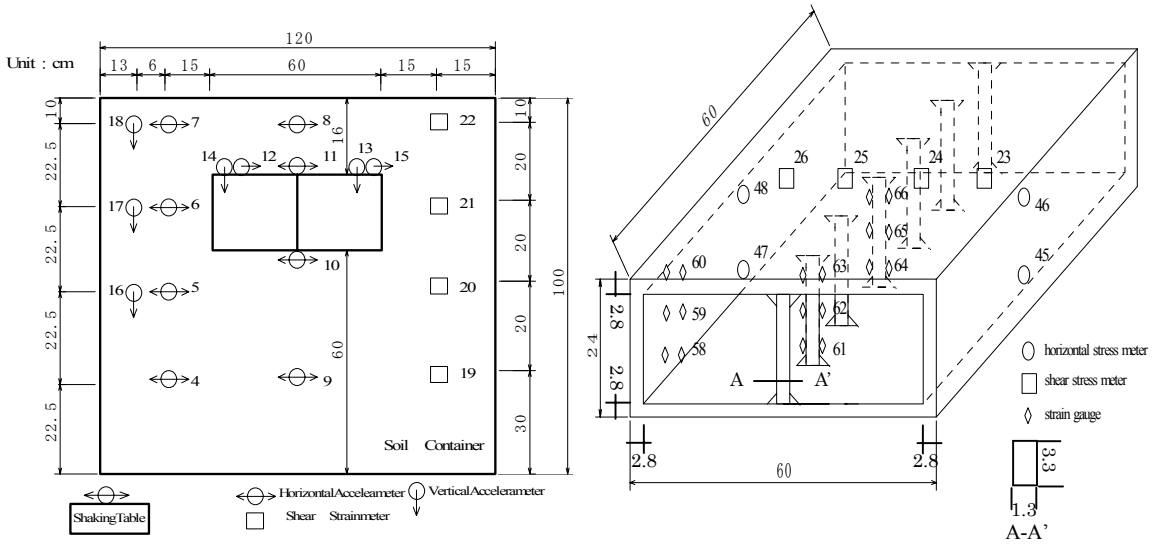

Figure 2-1 Measuring points of the shaking table tests

2.2 Measurements

The acceleration responses of the structure and surrounding ground, shear stress acting on the ceiling slabs, lateral earth pressures acting on the side-walls and dynamic bending strains induced in the center columns (both of that with rigid joints and pin joints) and side walls were measured (Figure2-1).

2.3 Testing programs

The shaking table tests were performed as follows.

(1) Pulse Impact Tests and Free Vibration Tests

The dynamic material properties of the model ground in its lowest natural frequency were estimated by pulse impact tests and free vibration tests.

(2) White-noise Tests

Seven different peak acceleration levels of 10gal, 20gal, 50gal, 100gal, 200gal, 400gal,and 800gal were selected as the horizontal input excitations. From these tests, the shear wave velocity (Vs m/s) (Subsurface: 90m/s, Bearing stratum: 100m/s) and the strain-dependency of the soil properties of the ground structure model were evaluated (Figure 3-2).

(3) Sine Sweep Tests

The sinusoidal vibrations with a constant base acceleration and alternating frequency from 5 Hz to 30 Hz were used as input excitations. Five different base accelerations of 20gal, 50gal, 100gal, 200gal and 400gal were selected as the horizontal input excitations.

(4) Random Vibration Tests

Random vibration tests were conducted, wherein the recorded NS accelerations at Kobe Meteorological Agency Station, during Hyogoken-Nanbu Earthquake were used as the input excitations (Figure 3-3). In the horizontal vibration tests, time scale of 1/1,1/5,1/10.1/20 and 1/30 were adopted. The input maximum acceleration was changed in two cases of 1/2 (50%), and 1/1 (100%).

3. Numerical simulations of shaking table tests

3.1 Numerical Method

A schematic diagram of the numerical simulation is shown in Figure 3-1. The first step is the analysis of the ground response only, and the second step is the analysis of the combined response of the subway structure and the ground.

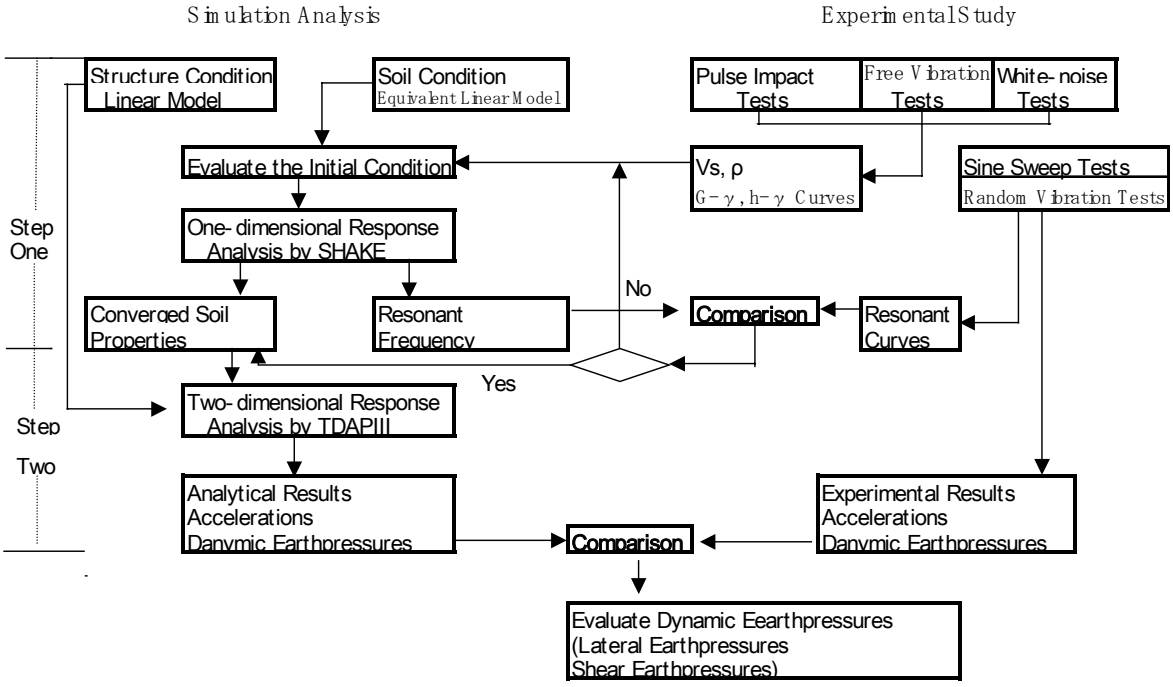

Figure 3-1 Analysis Flow Chart

3.2 Numerical procedure

(1) Earthquake ground response analysis

The dynamic response of the model ground during an earthquake was evaluated by one-dimensional seismic response analysis using multiple-reflection theory, which considered the non-linearity of soil properties by equivalent linear properties from G-γ and h-γ curves estimated from the experimental results (Figure 3-2) [7,8]. In general, the shear wave velocity (Vs m/s) from white noise tests is considered larger than the actual one [4]. Therefore, the value is decreased to 85%

of what observed in the experiment. Using these G- γ and h- γ relations, the acceleration response of the ground when subjected to 5 different sinusoidal and random excitations (Hyogoken-Nanbu Earthquake, time reduction scale 1/10, amplitude 100%) was evaluated (Figure 3-3). The converged values of shear modulus and damping constants of the ground were calculated and used in the two-dimensional analysis below.

(2) Simulation analysis

The two-dimensional dynamic response of the subway structure was conducted using TDAP (Time Domain Dynamic Analysis Program), which used New mark's β method in non-delta form denoted by equations (3-1,3-2). The ground was modeled as two-dimensional finite elements in which the aforementioned converged values of the soil properties were used. The structure was modeled as a set of elastic beams elements. Here, the average acceleration method ($\alpha = 0.25$) was used. The dynamic behavior of the structure and the dynamic forces (shear earth and lateral earth pressures) acting on the structure were evaluated, and the results were compared with experimental measurements.

$$\dot{U}_{t+\Delta t} = \dot{U}_t + \left[(1-\delta)\ddot{U}_t + \delta\ddot{U}_{t+\Delta t}\right]\Delta t \qquad (3-1)$$

$$U_{t+\Delta t} = U_t + \dot{U}_t\Delta t + \left[\left(\frac{1}{2}-\alpha\right)\ddot{U}_t + \alpha\ddot{U}_{t+\Delta t}\right]\Delta t^2 \qquad (3-2)$$

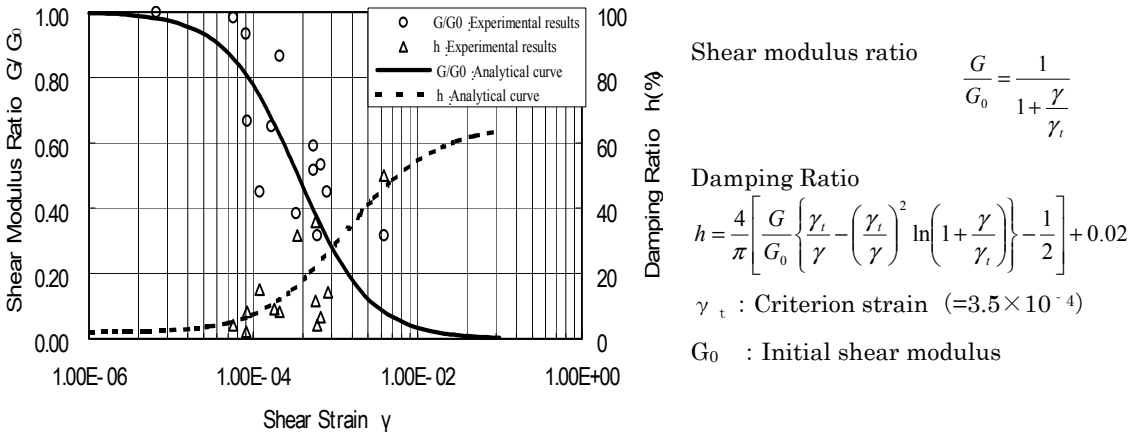

Figure 3-2 Strain-dependency curves of the ground

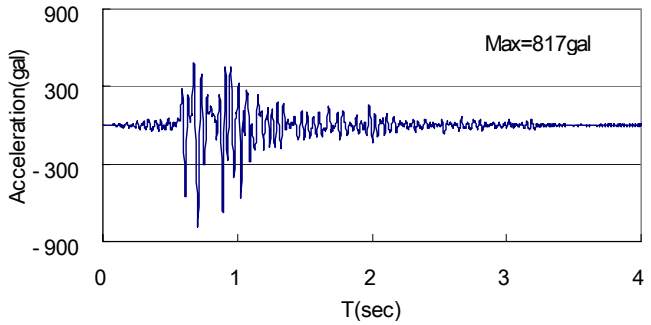

Figure 3-3 Kobe Marine Meteorological Observatory record of Hyogoken-Nanbu earthquake

4. Results

4.1 Dynamic Behaviors of the Ground Model

Comparing the one-dimensional analysis with the experimental results, the distribution of the curves, resonant frequency and acceleration response ratio show close agreement as shown in Figure 4-1. Therefore, it can be concluded that the analytical model and the initial material properties of the ground (shear modulus and damping constants) were appropriate.

The response characteristics of the model ground were determined from the resonance curves shown in Figure 4-1. The resonant frequency of the model ground was 20 Hz for weak excitations (20 gal) and 8 Hz for large excitations (400 gal). Increasing the base acceleration, the decrease in amplification and resonant frequency are shown both in the experiment and the analysis. The model ground exhibited strong nonlinear properties from low levels of strain.

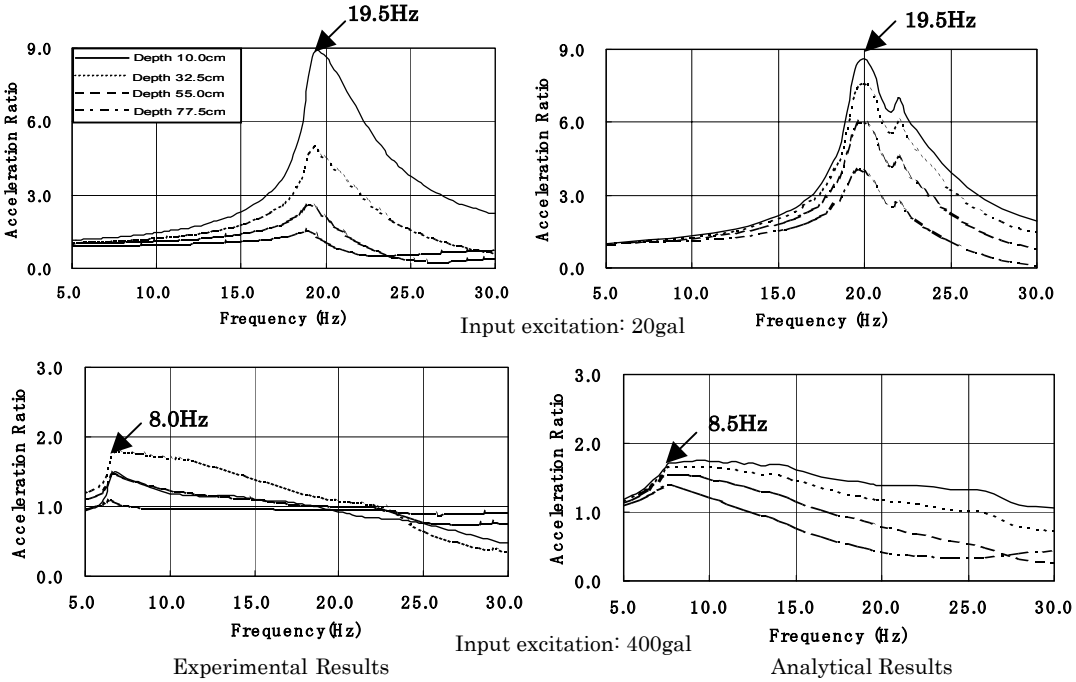

Figure 4-1 Resonant curves of the model ground due to horizontal excitations of sinusoidal waves

4.2 Dynamic Earthpressures acting on the Subway Structure

In order to evaluate the dynamic earth pressures acting on the subway structure, the dynamic lateral earth pressures and the dynamic shear earth pressures at the moment when the displacement of the structure became greatest at the resonant frequency were investigated. It was observed that the subway structure was significantly deformed in shear and rocking modes by horizontal excitations at the resonant frequency (Figure 4-2).

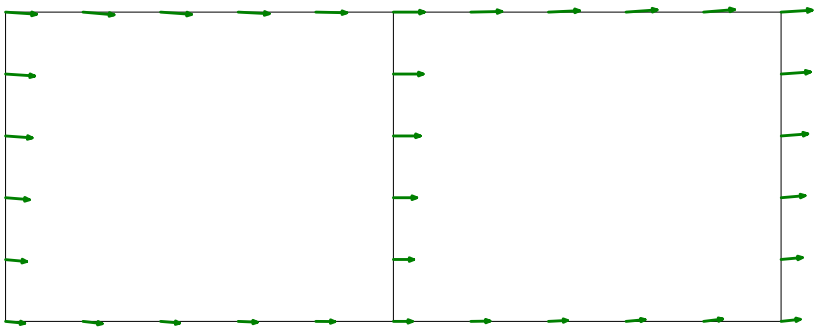

Figure 4-2 The acceleration distribution of the structure when its displacement became greatest

(1) Dynamic shear stress

Figure 4-3 shows the shear earth pressure distributions acted on the structure, at the resonant frequency subjected to sinusoidal input excitations with base accelerations 50gal, 200gal, 400gal and Kobe excitation (maximum acceleration 817gai), respectively. As the results, these values increased with input level. Figure 4-4 shows the relation between input accelerations and the shear earthpressures acted on the ceiling slab by experimental results and numerical ones. From these figures, the non-linear responses occurred remarkably from 200gal input excitation and slide phenomenon occurred at the interface between the ceiling slab and the surrounding ground. Therefore, it may be concluded that these phenomenon can't be simulated by the linear equivalent model and method.

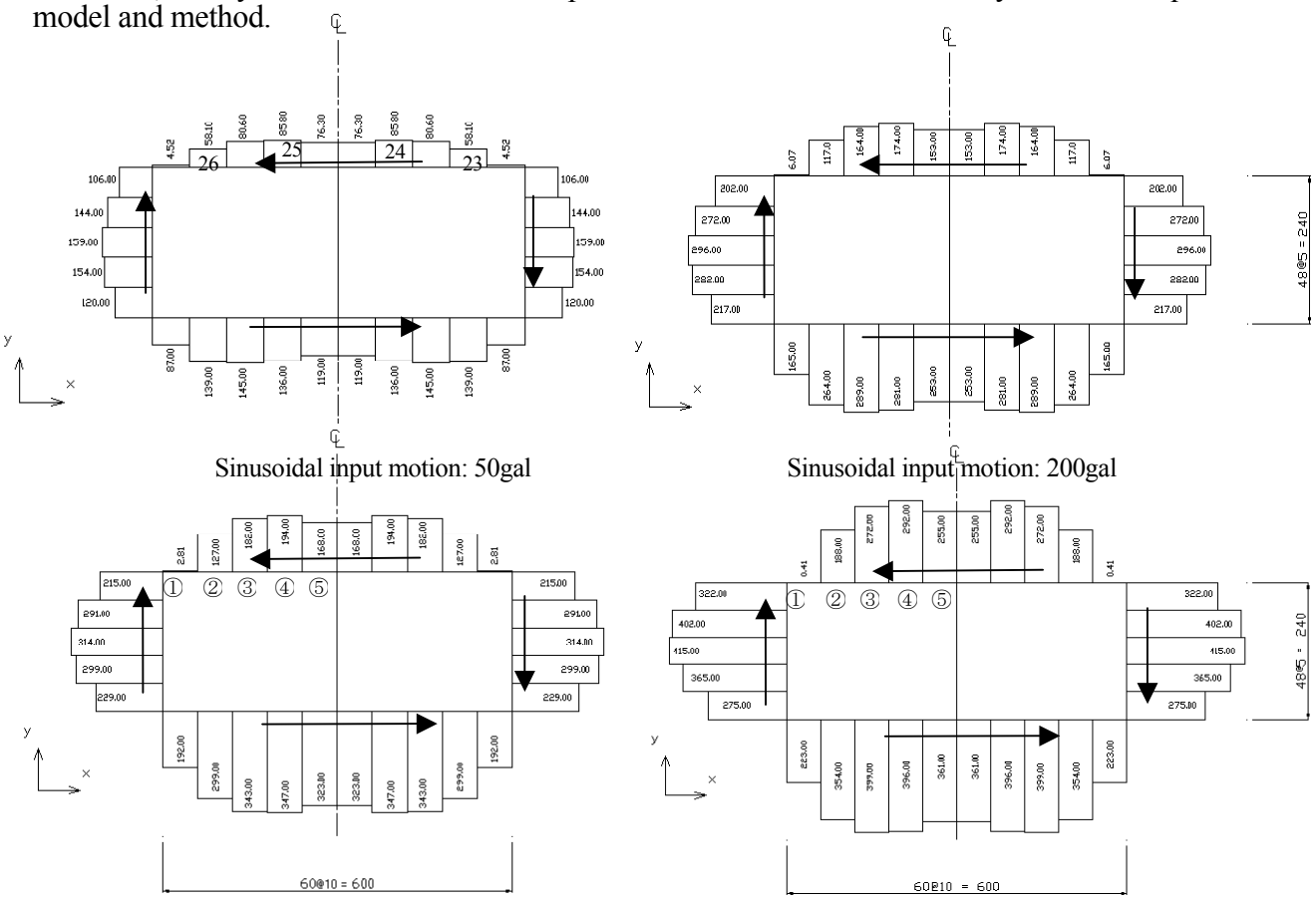

Figure 4-3 The shear earth pressures acted on the structure in the analytical results

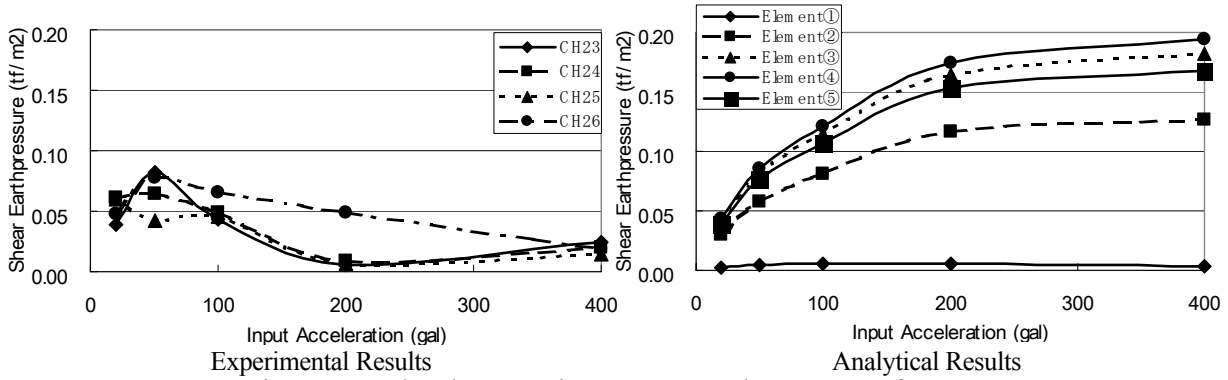

Figure 4-4 The shear earth pressures at the resonant frequency

(2) Dynamic lateral earth pressures

Figure 4-5 shows the lateral earthpressure distributions acted on the structure, at the resonant frequency subjected to sinusoidal input excitations with base accelerations 50gal, 200gal, 400gal and Kobe excitation (maximum acceleration 817gai), respectively. As the results, the dynamic lateral stress acted on the structure increased with input level, and the distributions in depth were out of phase because of the rocking vibration of the structure. The results of the numerical simulations for dynamic lateral earthpressures showed good agreement with the experimental ones (Figure 4-6).

In order to clarify the relationship between dynamic earthpressures acted on the subway structure and the shear modulus ratio between the structure and the surrounding ground, in simulation analyses four kinds of shear modulus ration between the structure and the surrounding ground (Gs/Gg=100, 10, 1, 0.1) were evaluated. As the results, the dynamic lateral earth pressures are dependent on the modulus ration. Decreasing the shear modulus ration, the distribution of the dynamic lateral earth pressures was lost its consistency. The lateral earth pressures acted on both sides of the structure were increased because of stress concentration; on the other hand the lateral earth pressures acted on the center of the structure were decreased（Figure4-7）.

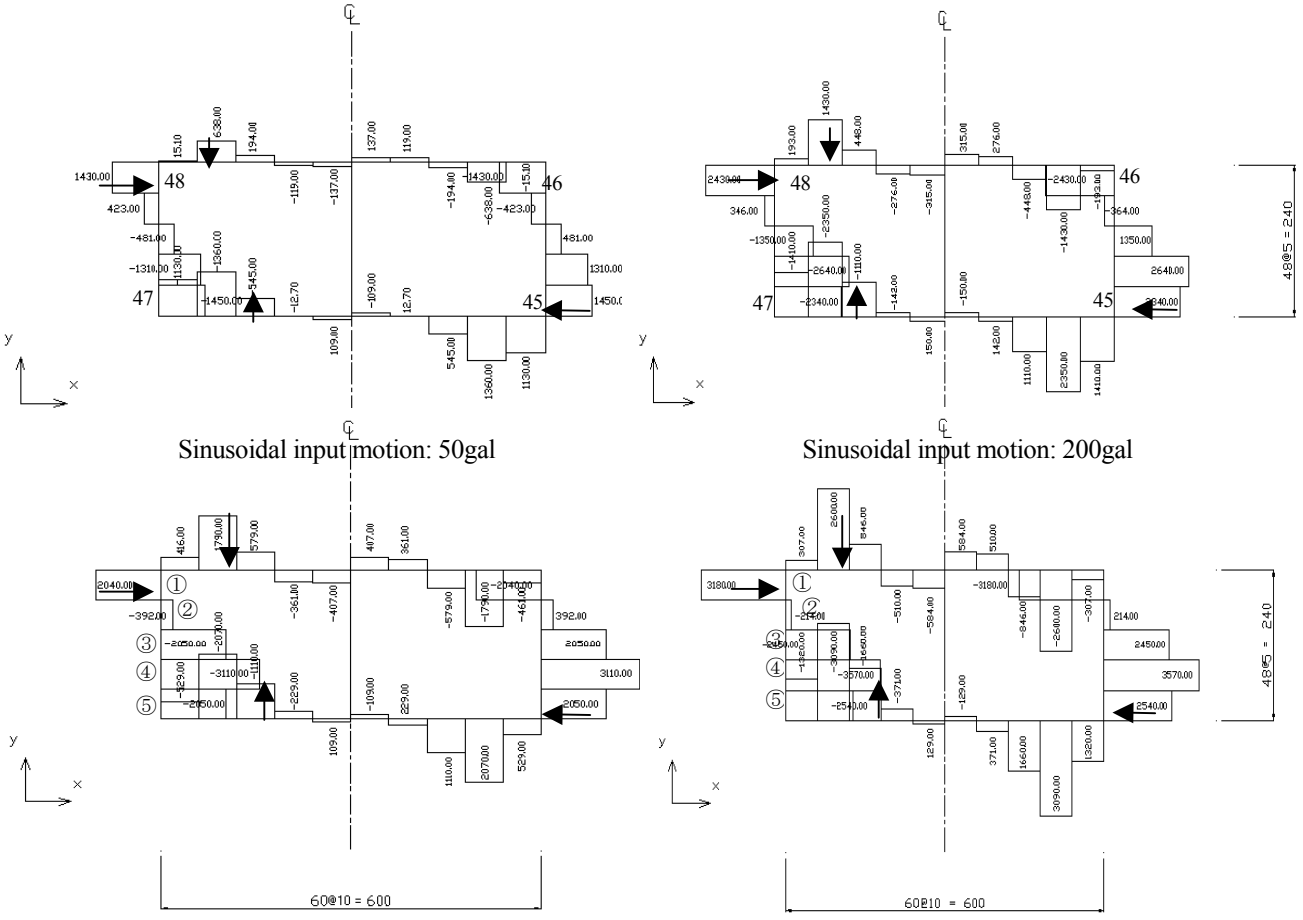

Figure 4-5 The lateral earthpressures acted on the structure in the analytical results

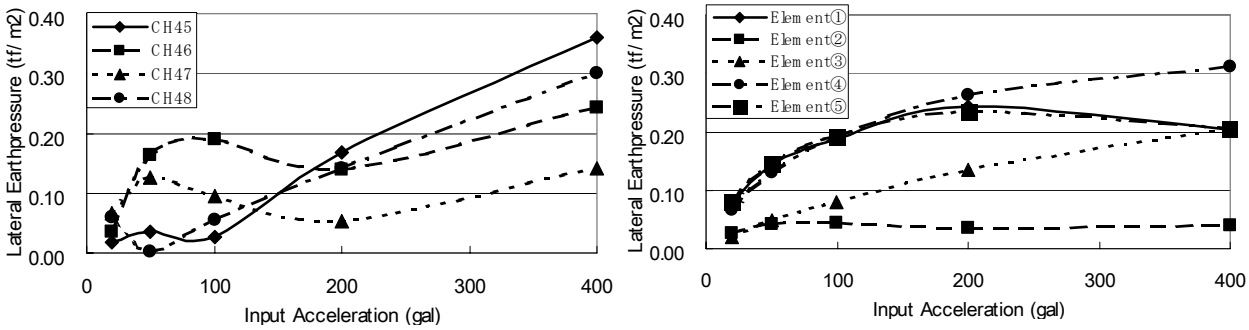

Experimental Results Analytical Results

Figure 4-6 The lateral earthpressures at the resonant frequency

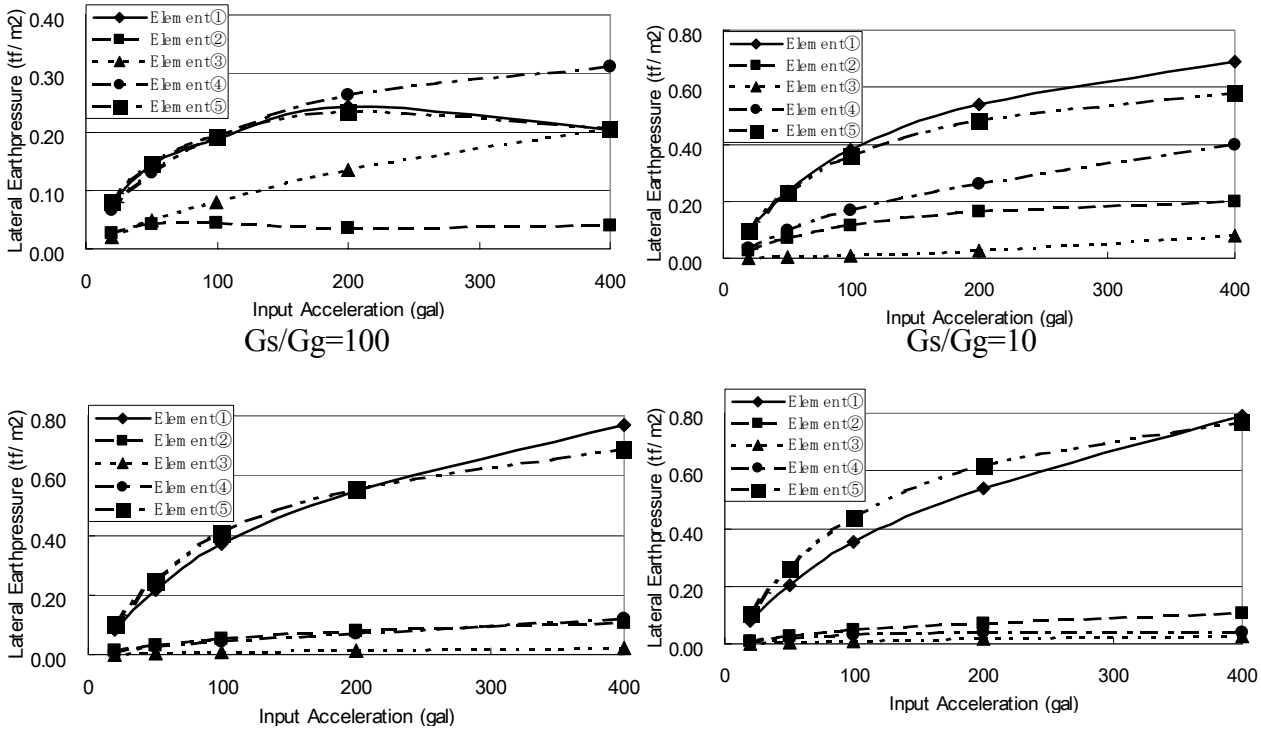

Gs/Gg=100 Gs/Gg=10

Gs/Gg=1.0 Gs/Gg=0.1

Figure 4-7 The relationship between the shear modulus ratio and the dynamic lateral earthpressures

5. Conclusions

The dynamic behaviors and the failure mechanism were clarified experimentally and numerically. It was obtained that the subway structure was significantly deformed in shear and rocking modes by horizontal excitations at the resonant frequency. The dynamic shear earthpressures acted on the structure show deferent responses between experimental results and analysis ones. Therefore, it may be concluded that dynamic shear earthpressures can't be simulated by the linear equivalent model and method. The results of the numerical simulations for dynamic lateral earthpressures showed good agreement with the experimental ones. The dynamic lateral stress acting on the structure increased with input level, and the distributions in depth were out of phase because of the rocking vibration of the structure. The dynamic lateral earthpressures were strongly dependent on the shear modulus

ration between the structure and the surrounding ground. Decreasing the modulus ratio, the lateral earthpressures acted on both sides of the structure were increased because of stress concentration; on the other hand the lateral earthpressures acted on the center of the structure were decreased.

6. References

[1] Committee of Earthquake Engineering, JSCE. 1996. "The Hyogoken-Nanbu Earthquake of 1995 Investigation into Damage to Civil Engineering Structure", pp256-295.

[2] Editorial Committee for the Report on the Hanshin-Awaji Earthquake Disaster. 1998. "Report on the Hanshin-Awaji Earthquake Disaster-Damage to Civil Engineering Structures"

[3] Hiroomi I. Toshio H. Nozomu Y. Masahiko I. 1996. "Damage to Daikai Subway Station", Special Issue of Soils and Foundations 283-300.

[4] T.Iwatate, H.kusu, K.Rin, and T.Tanaka. 1999. "Scaled Model Vibration Tests and Simulation Analyses on Nonlinear Response of Subway Structure", Proceedings of the 25th JSCE Earthquake Engineering Symposium, pp481-484.

[5] A.Che, T.Iwatate. 2002. "Shaking Table Tests and Numerical Simulation of Seismic Response of Subway Structures, Seventh International Conference on Structures Under Shock and Impact", SUSIVII, p367-376.

[6] A.Che, T.Iwatate, (2003), "Shaking Table Tests and Simulation Analyses of Subway Structures Subjected Earthquake Loading, Earthquake Engineering and Engineering Vibration, Publishing.

[7] T.Iwatate, Y.kobayashi, H.kusu, and K.Rin (2000), ""Investigation and Shaking Table Tests of Subway Structures of the Hyogoken-Nanbu Earthquake", The 12th World Conference Earthquake Engineering, (12WCEE2000), p1043.

[8] T.Iwatate, T.Iino, M.Takeuchi, S.Samata, Y.Sato, (1998), ""Investigation and Shaking Table Tests of Subway Structures of the Hyogoken-Nanbu Earthquake", The World Tunnel Congress'98 on Tunnels and Metropolises, ISBN905410936x.

[9] Japan Society of Civil Engineers, January 2000, 'Earthquake Resistant Design Codes in Japan'.

[10] T.Kokusyo, T.Iwatate 1979. Scaled Model Vibration Tests and Numerical Analysis on Nonlinear Dynamic Response of Subway Structure. Proceedings of the 24th JSCE Earthquake Engineering Symposium: pp233-236.

Interpretation and Visualization of Model Test Data for Slope Failure in Liquefying Soil

Bruce L. Kutter, Erik J. Malvick, Ramachandran Kulasingam, and Ross W. Boulanger

ABSTRACT

The upward hydraulic gradient that is characteristic of liquefaction leads to upward flow of water. The presence of an impermeable barrier can lead to the accumulation of water beneath the boundary, with a corresponding increase in void ratio (dilation). As dilation proceeds, the shear resistance of the soil decreases and shear deformations are expected to increase. If the dilation proceeds until the undrained steady state strength is smaller than the driving shear stress, collapse may be expected. To account for this in design, a better understanding of the mechanisms of volumetric and shear deformation under the impermeable boundary is required.

Several model tests conducted in a small centrifuge to investigate the effect of an impermeable layer on the deformation behavior of a slope are summarized in the introduction. One large centrifuge test was conducted to enable use of a larger number of sensors to define the pore pressure and pore water flow mechanisms. In this paper, data from these sensors is used to visualize the pore pressure regime. The methods for producing contour plots of pore pressure and pore pressure ratio based on experimental data are described. The experimental distribution of pore pressure with depth is analyzed to calculate the volumetric strain rate as a function of depth. The calculated volumetric strain rates show volumetric dilation directly beneath the impermeable layer and consolidation in deeper zones.

The extensive data set produced in a highly instrumented model test can be extremely valuable, but organization and comprehension of all the information in a large data set is challenging. New tools for data visualization and data management need to be developed.

Bruce L. Kutter, Professor, University of California, Davis, Department of Civil and Environmental Engineering, One Shields Avenue, Davis, California, USA, 95616, 530-752-8099, fax 530-752-6758, blkutter@ucdavis.edu.
Erik J. Malvick, University of California, Davis, Department of Civil and Environmental Engineering, One Shields Avenue, Davis, California, USA, 95616, 530-752-4617, fax 530-752-7872, ejmalvick@ucdavis.edu.
Ramachandran Kulasingam, University of California, Davis, Department of Civil and Environmental Engineering, One Shields Avenue, Davis, California, USA, 95616, 530-752-4617, fax 530-752-7872, rkulasingam@ucdavis.edu.
Ross W. Boulanger, Professor, University of California, Davis, Department of Civil and Environmental Engineering, One Shields Avenue, Davis, California, USA, 95616, 530-752-2947, fax 530-752-7872, rwboulanger@ucdavis.edu.

INTRODUCTION

In general terms, earthquake-induced slope deformations in sandy soils may be considered to develop due to cyclic mobility of the soil (limited shear strains induced by cyclic loading), flow instability if the soil reaches critical state under the imposed shear stresses, or additional shear and volumetric strains associated with the flow of pore water under shaking-induced excess pore pressure gradients. Cyclic mobility only occurs during shaking. Flow instability may occur during or after shaking, with the timing potentially being affected by the timing of void redistribution if it occurs. Deformations due to pore water flow (void redistribution), which may cause void ratio increases (such as below an impeded drainage boundary) or void ratio decreases (such as in contracting zones undergoing reconsolidation), can occur during and after shaking (Malvick et al.[1]).

A potential situation, similar to "Mechanism B" defined by Whitman in NRC [2], is illustrated in Figure 1. This example consists of an infinite slope with a groundwater table parallel to the ground surface, an impermeable surface layer of thickness H_t and a relatively permeable uniform liquefiable layer of thickness H_b. A hypothetical distribution of excess pore pressure, Δu, is also shown. The flow rate of the water is proportional to the gradient of excess pore water pressure. The inflow to a point such as B is equal to the outflow as long as the second derivative of excess pore pressure is zero at that point. At C, there is a curvature of excess pore pressure distribution, thus one would expect volume change according to the diffusion equation. At A, there is a discontinuity in the permeability so that the water flowing up from the base cannot easily escape, and hence void ratio increases at A. Because there is a shear stress present at A, however, the influx of water may be absorbed by shear-induced dilation. Figure 2 illustrates the stress path at points A and C. The pore pressure initially increases at A and C. But when the paths hit the failure line, shear strains increase and the shear-induced dilatant tendency is mobilized.

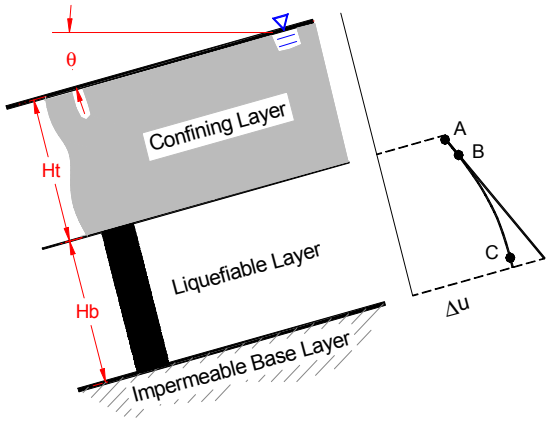

Figure 1. Example of a situation where void ratio may increase locally due to liquefaction-induced pore pressures (Malvick et al. [1[).

If the void ratio at A increases to a critical state where the shear capacity is less than the driving shear stress, flow failure would be expected. At first thought, one may conservatively assume that it would take a very small amount of water from deep layers to cause a shear plane of a dozen grain diameters thickness to expand to the critical state. Recent work (e.g., Malvick et al. [1] and Boulanger [3]), however, has led to a procedure to calculate the thickness of the dilating zone and hence the "dilation capacity" that is available to absorb the influx of water. As it turns out, the dilation capacity is much greater than one would expect based on an assumption that the thickness of the dilating zone is

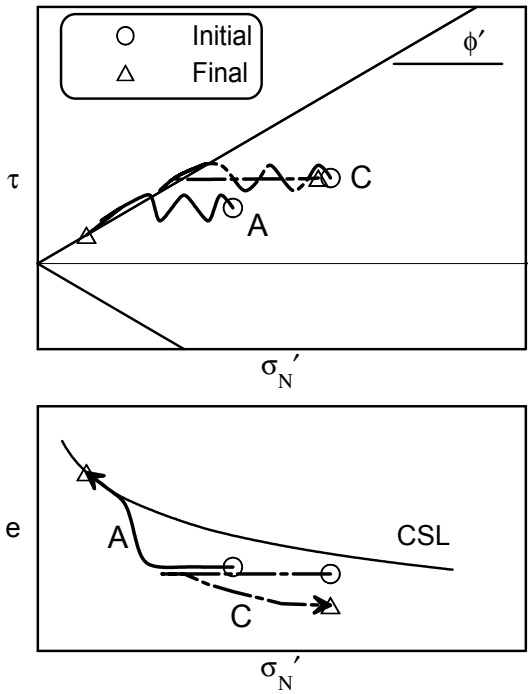

Figure 2. Possible stress path from start of cyclic loading to conclusion of void redistribution (Malvick et al.[1]).

a dozen grain diameters thick. Large shear stresses at points near the impermeable boundary causes points (such as point B) to contribute to the dilation capacity of the deposit.

In recent years, model testing has been carried out to study the potential effects of void ratio increase due to void redistribution. The extreme case of water-interlayer formation on stratified soil layers was observed in shake table tests by Liu & Qiao [5] and Elgamal et al. [6]. Centrifuge tests by Fiegel & Kutter [7] of gentle slopes showed localized deformations near the interface of the liquefying sand and overlying lower permeability layer. Formation of a water-interlayer between an overlying silt and underlying sand layer was inferred from pore pressure records from centrifuge tests by Dobry & Liu [8]. Kokusho [9] showed flow failures that occurred after shaking on shake table tests of slopes consisting of homogeneous sand with thin silt layers and noted the formation of a "water film" beneath the lower permeability layer.

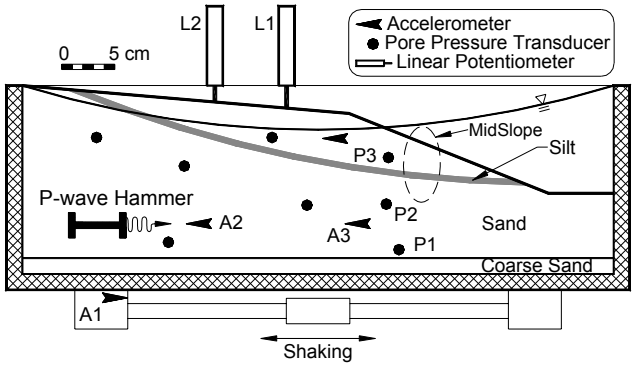

Figure 3. Illustration of the typical model tested on the small centrifuge (after Malvick et al. [4]).

Currently, dynamic centrifuge model tests and laboratory triaxial tests are being conducted to study this problem. Many tests on the 1 m radius Schaevitz centrifuge and one test on the 9 m radius centrifuge have been completed to date.

Figure 3 shows a typical cross section from the model tests on the small centrifuge. A total of about 14 sensors were used to measure pore pressure, acceleration and displacement in the models.

Figure 4 shows photographs from one of the small centrifuge tests. Spaghetti noodles are highlighted on the photographs so one can clearly see that a discontinuity formed, just under the silt arc during motion B, but not during motion A. The models were all subject to a similar protocol of seismic shaking intensity. They were first subject to a short duration earthquake (Motion A) with about 0.32 g accelerations at the base, and then they were subjected to a longer duration motion (Motion B) with a similar peak acceleration. If models did not form a discontinuity after Motion B, the models were subject to a somewhat stronger motion (Motion C).

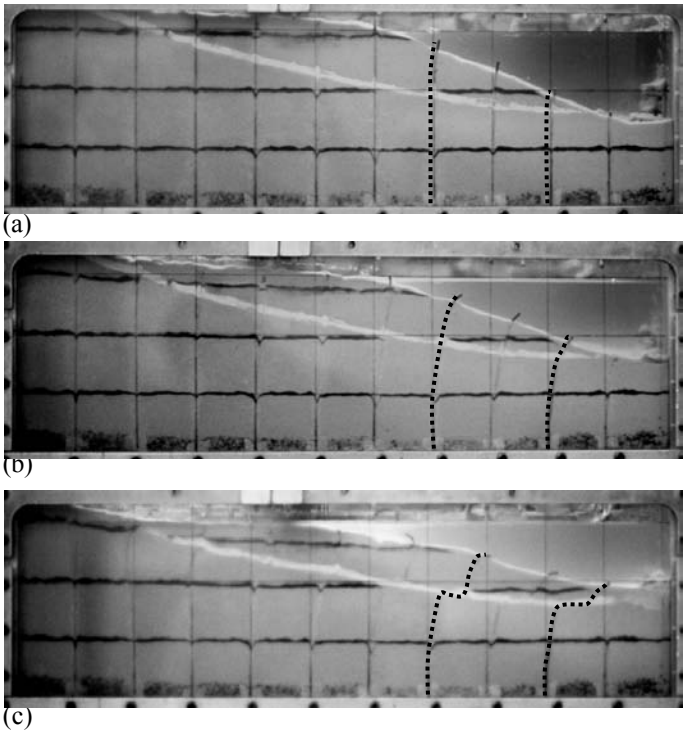

Figure 4. Test 2 photos (a) before (b) after event 1, motion A, a_{max} = 0.32 g (c) after event 2, motion B, a_{max} = 0.32 g (Malvick et al. [4]).

Figure 5 shows a summary of many test results in the small centrifuge. Along the horizontal axis is plotted the relative density of the sand, and along the vertical axis is plotted the cumulative displacement of the sand mass above the impermeable silt layer. The three diamond symbols that show large displacement for low relative density correspond to model tests where a discontinuity of displacement was observed.

From this data, it is apparent that there is a critical relative density, for a given slope geometry and intensity of shaking, below which a discontinuity is formed. From these experiments, it appears that the net amount of permanent deformation of the slope approximately doubled in association with the development of the discontinuity.

Based on these studies, it became clear that the localization of strains beneath an impermeable boundary does have a significant impact upon liquefaction- induced deformation. However, it is difficult to reliably predict when this localization would occur. Important factors influencing localization include the ground motion history, the sand density, the depth of the sand, and permeability of the soils. To clarify the mechanisms at work, a large centrifuge test with more detailed instrumentation was tested.

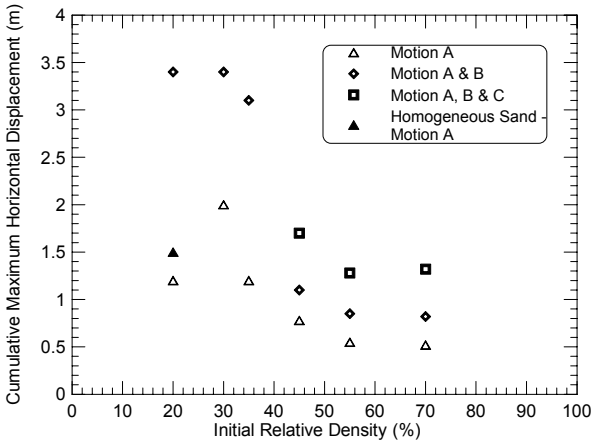

Figure 5. Cumulative movement as a function of Relative Density for small centrifuge models subject to different seismic histories (Kulasingam et al. [10]).

LARGE CENTRIFUGE TEST PROCEDURE

The model contained a 210-mm high, 1V:2H (26.7^o), slope consisting of sand with an embedded silt plane at a slope of 1V:5H (11.4^o). The model was built by placing a 20-mm layer of medium-grained Monterey sand at the bottom of a rigid container as a drainage layer with the remaining sand in the model consisting of loose Nevada sand (D_r = 35%). The buoyant unit weight at this density is 9.1 kN/m^3. The mean grain size of the sand is 0.17 mm and the coefficient of uniformity (D_{60}/D_{10}) is 1.64. The toe of the slope was at an elevation of 160-mm from the bottom of the box, and the toe of the silt plane was 185-mm from the bottom of the box. The model layout is shown in Figure 6 and the instrument locations are indicated in Figures 6 and 7.

All of the soils used in this model were placed by dry pluviation. The 20-mm layer of medium-grained Monterey sand was placed at the base to aid the saturation of the model. The Nevada sand was placed using a barrel pluviator to obtain a 35% relative density above and below the silt plane. This density was obtained by

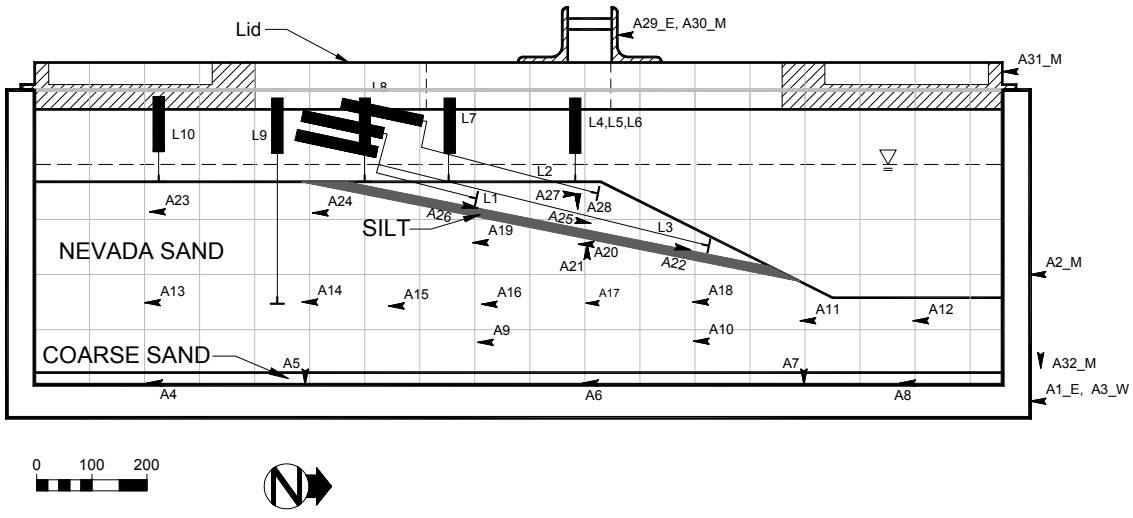

Figure 6. Configuration of the model EJM01 showing container, accelerometer and linear potentiometer locations. A 100 mm square grid is shown to indicate the dimensions of the model.

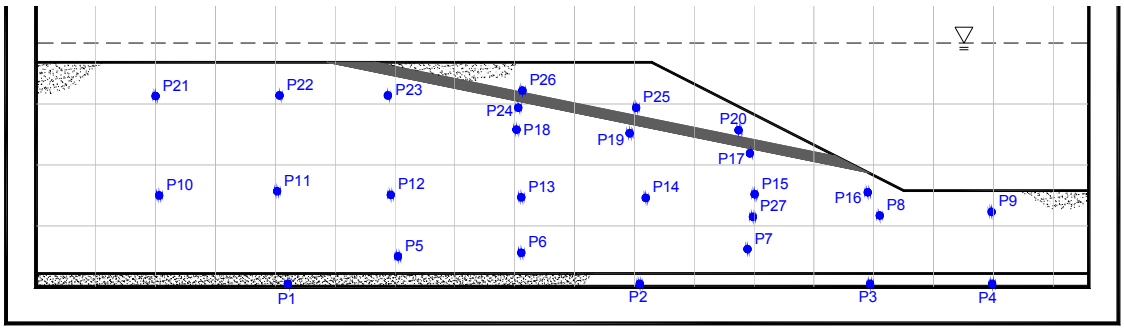

Figure 7. Locations of pore pressure transducers in model EJM01.

calibrating a sieve arrangement on the nozzle of the pluviator and a corresponding flow rate and drop height. The drop height for this test was 860-mm.

The silt plane consisted of silica flour with a mean grain size of 0.02 mm and a permeability of 3×10^{-6} cm/s. The silt plane was prepared by first vacuuming off the top portion of the Nevada sand to the required elevation and slope. The silica flour was then placed in a thin loose lift over the desired plane using small hand shovels. This very loose layer of silt was lightly compacted using a small concrete block to apply a pressure of 1.9-kPa over the whole plane. The finished silt plane had an average thickness of 16-mm.

The remaining sand above the silt plane was pluviated to form the desired finished profile. Embedded in this model was a horizontal grid of black sand at elevation intervals of 100-mm and vertical black sand columns through the nodes of this grid. These grids and columns assist in observing and measuring deformation. In order to maintain a uniform low permeability for the silt plane, small pieces of rolled bentonite were used to construct the vertical grid columns through the silt plane. The model is shown in Figure 8.

The model was then flooded with CO_2 gas and placed under a vacuum of 635-mm (25-in) Hg to remove the air in the sand. A viscous fluid was dripped slowly through tubes to the base of the model until the water level reached the desired elevation of 400-mm from the inside base of the box, which required approximately 5 days. The models were subject to a centrifugal acceleration of 38.1 g during shaking.

A P-wave velocity test was conducted at 1-g prior to spin-up to determine the degree of saturation of the model. The average P-wave velocity between accelerometers A14 and A16 was 1630 m/s, between A16 and A18 was 1760-m/s, and between A14 and A18 was 1700- m/s. The P-wave velocity for water is 1500-m/s, so these measurements in excess of 1500- m/s indicate that saturation is approximately 100%.

Two shaking events were applied to the model at a centrifugal acceleration of 38.1-g. The shaking was applied in the horizontal direction, in the plane of Figures 6 and 7. The shaking events for this test consisted of highly modified and scaled versions of the 908 component (channel 1) of the ground motion recorded at the Los Angeles – UCLA grounds during the 1994 Northridge earthquake. The base acceleration corresponded to about 0.51 g of prototype shaking in both shaking events.

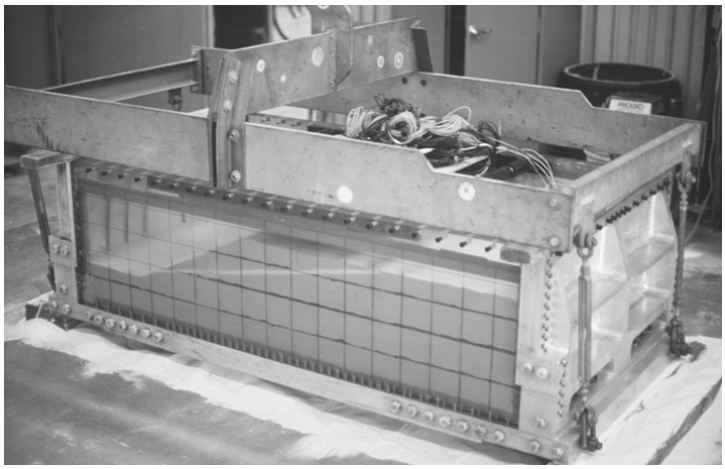

Figure 8. Photograph of the model in the rigid container ready to be weighed prior to moving to the centrifuge.

PORE FLUID PROPERTIES

For dynamic processes, time will scale by a factor of N, where N is the scale factor between prototype and model lengths. For consolidation and seepage problems, if the model is constructed using the same soil that exists in a prototype, time will scale by a factor of N^2 indicating a conflict in scale factors. Alternatively, the diffusion time scale factor is N if the model is constructed of a soil that has a permeability N times smaller than that of the prototype, and the conflict is avoided. Increasing the viscosity of the pore fluid is one way to decrease the permeability of the soil in the model; another way to reduce permeability is to construct the model with soil grains that are smaller than the prototype soil. Stewart et al. [11] have shown that a solution of hydroxypropyl methylcelluose (HPMC) in water is a good viscous pore fluid for centrifuge modeling.

For this test HPMC was used as the pore fluid with a viscosity of 11.6-mm^2/s. For comparison, water has a viscosity of 1-mm^2/s. We chose a viscosity scale factor of 11.6 for a couple reasons. First, the saturation process would have been slower if the viscosity was 38.1, and second we are not attempting to model a specific prototype, so we were not tied by the scaling laws for direct modeling of prototypes. Instead, our goal is to understand the mechanisms of pore water migration; adjustment of the viscosity (i.e., permeability) is considered to be one of the parameters that can be varied to study this mechanism. The model was constructed of Nevada sand, which has a permeability of 0.003 cm/s, as measured in the laboratory. The centrifuge model soil represented a prototype soil with a permeability of 0.003 * 38.1/11.6 = 0.01 cm/s.

The initial and final locations of the instruments with their calibration factors and channel gains are completely documented in the data report by Malvick et al.[12].

RESULTS AND DATA VISUALIZATION

The model was subject to two shaking events while spinning at 38.1 g. The first event had a similar peak acceleration as the second event. Time histories from selected sensor recordings in the second event are shown in Figure 9a. The ground acceleration is unusual. It may be considered as two main shocks, with about 10 seconds of strong shaking each separated and followed by four small, almost identical, "aftershocks". This motion was concocted to investigate the cumulative effect of shaking and void ratio redistribution. Figure 9a also shows two displacements measured in the sand mass above the silt layer, one near the toe and one near the crest of the slope, both measuring relative movement in the anticipated direction of sliding. It is interesting to note that the small aftershocks caused little displacement following the first main shock, but they caused much more displacement following the second main shock. The increase of displacements with successive aftershocks is consistent with the idea that the strength depends on the void ratio and the void ratio of the shear zone is increasing due to void redistribution. The continued displacement after shaking stops is consistent with the idea that an influx of water occurs after shaking due to the liquefaction induced pore pressure gradient that remains after shaking stops. The pore pressure ratio (P23) and acceleration (A24) recorded near the ground surface behind the silt layer show clear evidence that the soil in these regions completely liquefied. Pore pressure ratios are large and the accelerometer is isolated from the shaking. The acceleration of the sand above the silt layer (A27) indicates that this layer was never isolated by liquefaction, in fact motions are amplified ($a_{ma} \approx 0.82$ g). The sensor near the silt arc (A20) is similar in form to that at A27 except it is somewhat smaller. A20 also shows some amplification of accelerations relative to the base motion (base motion at the bottom of Figure 9b indicates $a_{max} \approx 0.5$ g).

Figure 9b shows the base acceleration, which reached 0.51 g, and several pore pressure ratios computed from measurements from the vertical array of transducers near the mid-point of the slope. The pore pressure ratios reached about 0.5 to 0.6 in this vertical array of sensors. The residual pore pressures in this array did not reach 100% pore pressure in this region because it is subject to static shear stresses and has a dilatant tendency.

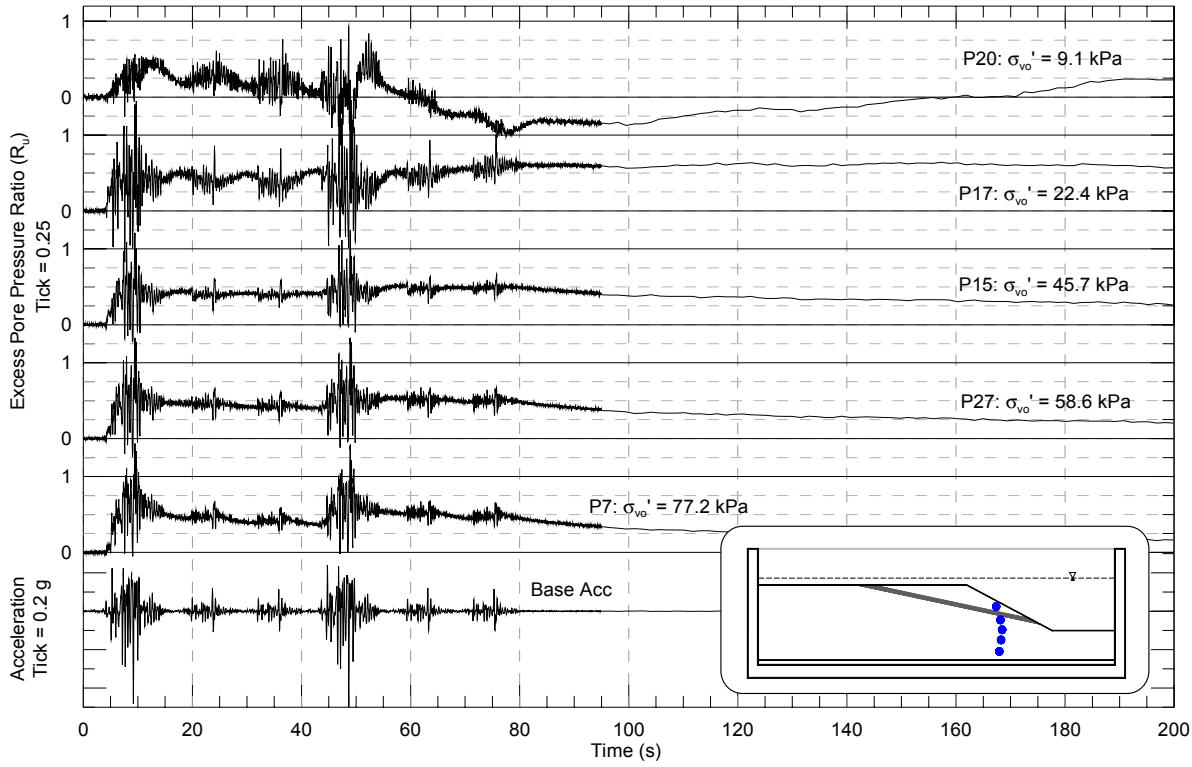

Figure 9b. Excess pore pressure ratios for one vertical array in EJM01 with base acceleration.

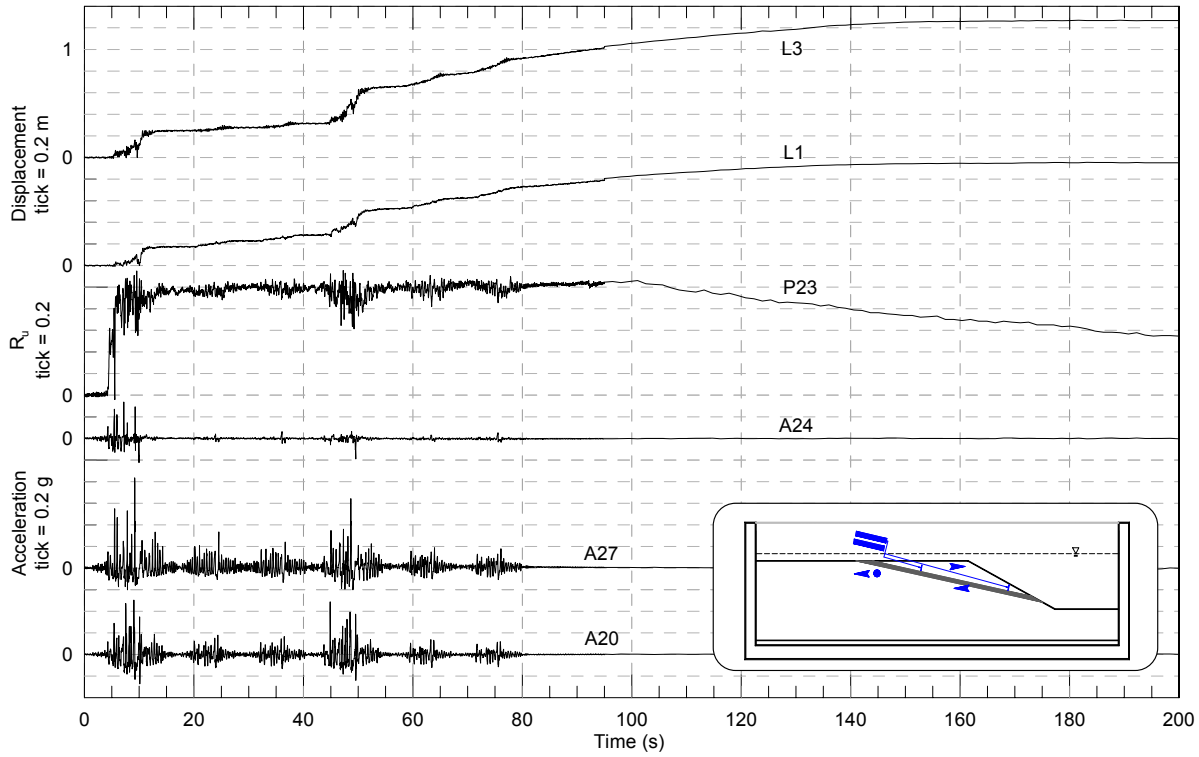

Figure 9a. Comparative response of some accelerometers, pore pressure transducer (R_u), and linear potentiometers.

For an infinite submerged slope, it is straightforward to calculate the maximum pore water pressure that will bring the slope to limiting equilibrium. The relationship is presented in Figure 10. Further injection of pore water does not necessarily increase pore pressures; it may cause volumetric expansion, which is associated with shear displacement, as discussed in relation to Figures 1 and 2. For reference, the silt layer has a slope of 11.4°. For this slope, the limiting pore pressure ratio, r_u, has a value of approximately 0.65.

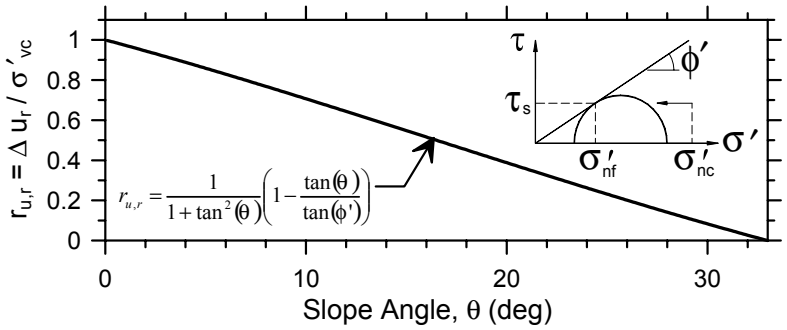

Figure 10. Plot of limiting residual pore pressure ratio in an infinite submerged slope.

Figure 11 shows the deformed shape of the model determined by excavation of the soil after the test when photographs and measurements of the colored sand columns in the interior of the model. The existence of distributed strains throughout the model are apparent as well as a distinct large localized strain directly beneath the silt arc.

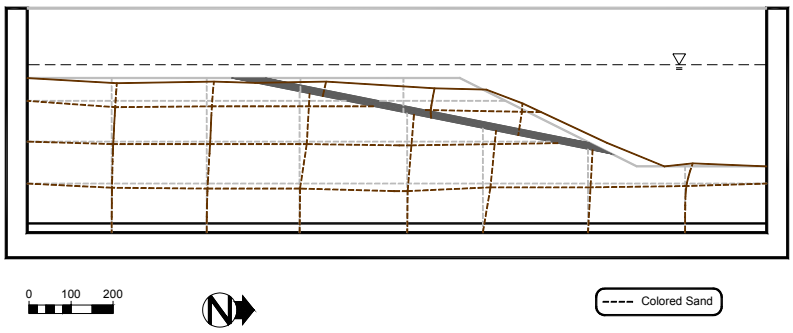

Figure 11. Observed deformed shape of the colored sand grid (West Grid Profile) in test EJM01.

It would be possible now for this paper to proceed to describe data from each of the seventy sensors included in the test. As this does become tedious we present contours of pore pressure and pore pressure ratio and several snapshots of the pore pressure distribution in selected vertical arrays. Animations of the evolution of these contour plots were also produced for presentation at the workshop. Selected frames from these animations are presented below.

Figure 12 presents contours of excess pore water pressure at three different times during the time history. The times are noted on each contour plot and indicated by a circle in the time history at the bottom. The scale for these graphs is indicated by the grey scale in a legend. The model geometry is also indicated by lines indicating the locations of the silt layer and the ground surface. The location of all of the data points upon which these contours are based are indicated by square symbols on the plots. All of the interior points are from actual recordings measured in the experiment. The points indicated on the boundaries of the soil are introduced to approximately force the contours to match the boundary conditions. For example the excess pore pressures at marked points along the container walls are set equal to the pore pressures at the nearest transducer. At the ground surface all excess pore pressures are set to zero, and all pore pressure ratios are set equal to those computed at the nearest transducer. Specifying the boundary conditions is necessary for producing contour plots and it requires an element of judgment. Also note that the contours that extend above the ground surface should be ignored as they are simply an artifact of the contouring algorithm used for these examples.

In the first frame (t = 9.521 s) of Figure 12, high pore pressures appear at the center of the base of the model (maximum pore pressure is in the 120-140 kPa range). In the second and third frames, the highest pore pressures are at the bottom left corner. All of these plots show a steep pore pressure gradient near the silt arc, and low pore pressures above the silt arc, as expected.

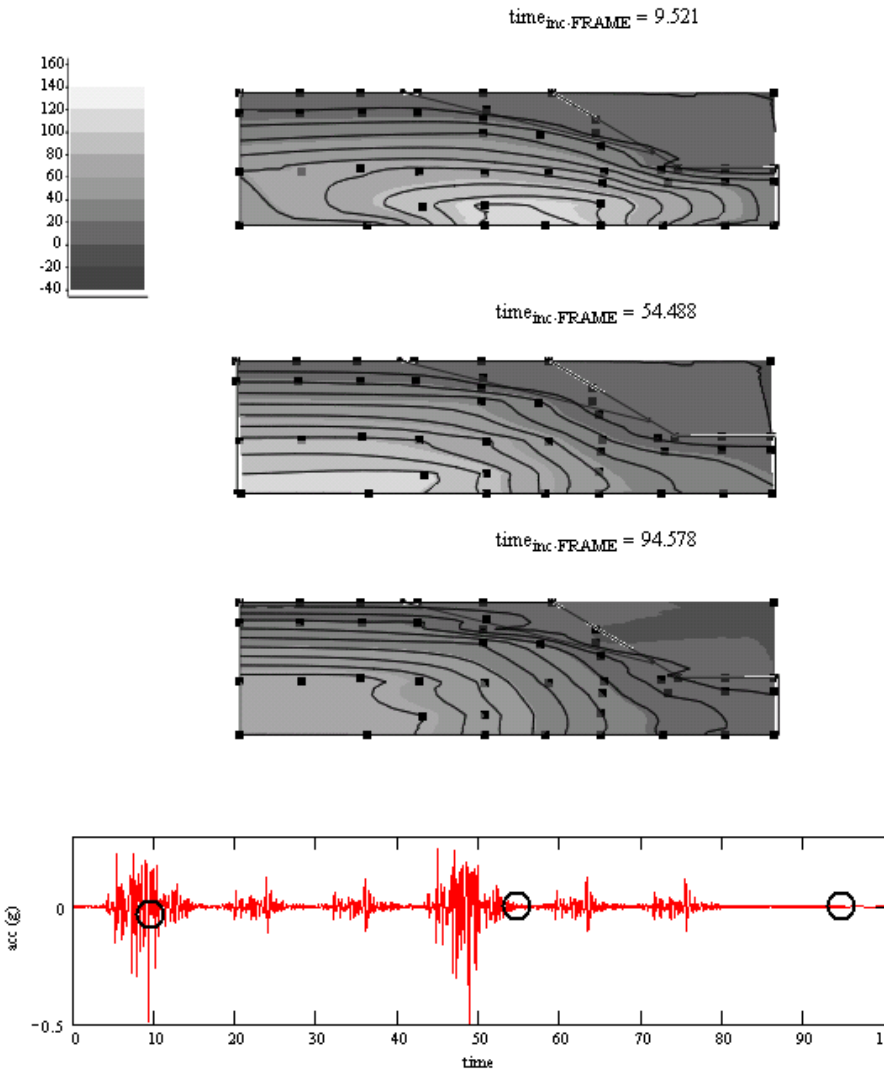

Figure 12. Contours of excess pore water pressure in test EJM01.

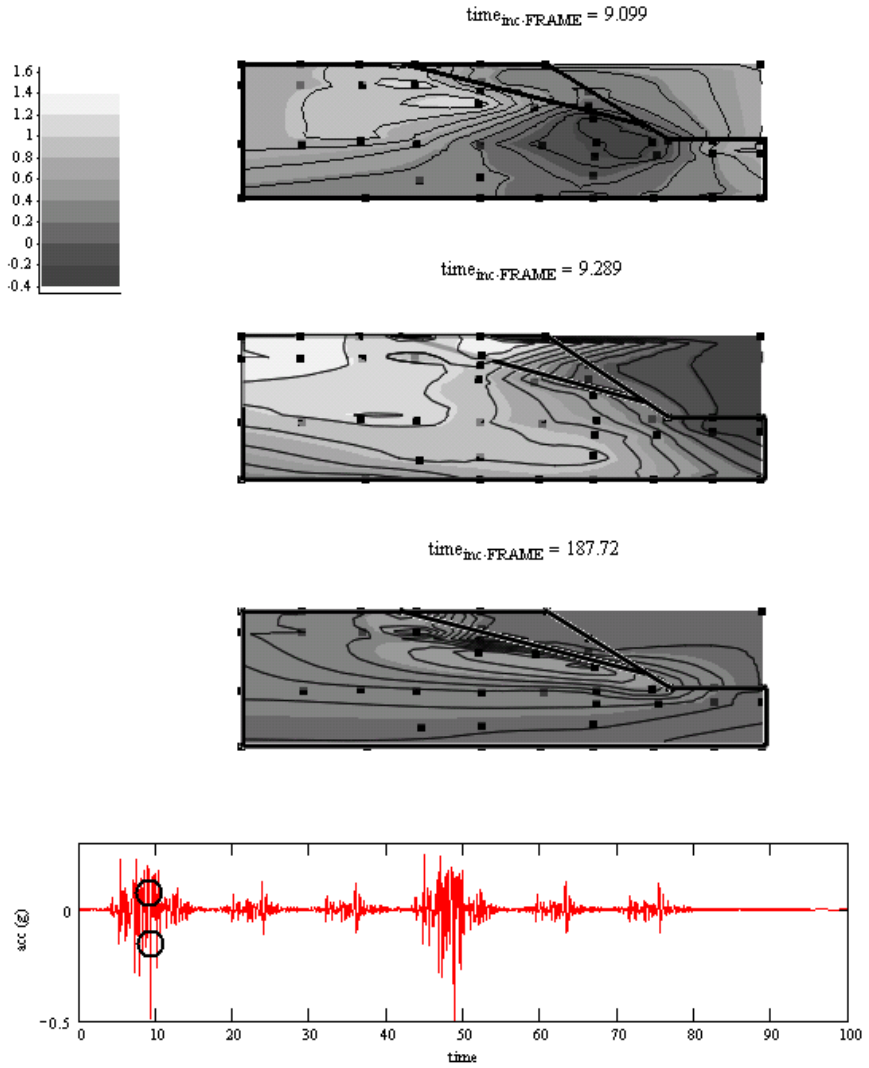

Figure 13. Contours of excess pore pressure ratio, r_u, in test EJM01.

Figure 13 presents contours of pore pressure ratio, which is simply calculated as:

$$r_u = \frac{u_{excess}}{\sigma'_v} \tag{1}$$

where $\sigma'_v = \gamma' z$. σ'_v is the initial vertical effective stress under static (no excess pore pressure) conditions, and z is the vertical depth below the surface. The buoyant unit weight, γ' is 9.1 kN/m^3. The contours of r_u show a lot more detail. Two frames are shown, during the strong shaking in the first main shock. The first frame (t = 9.099 s) is during a positive acceleration pulse (when the base is accelerated to the left). At this time, negative pore pressures are generated beneath the silt near the toe due to the presence of large shear stresses and dilatant tendency. In the second frame (time = 9.289 s) the acceleration is to the right. This unloads the shear stresses beneath the silt and allows the pore pressures to increase. The final frame in Figure 13 is for time = 187.72 s, which is late in the dissipation phase, off the scale of the time history at the bottom of the figure. The final frame clearly shows high pore pressures trapped beneath the silt arc.

Figure 14 presents isochrones of excess pore pressure and computed volumetric strain rate for two vertical arrays of pore pressure transducers. The square points correspond to the array near mid slope (P20, 17, 15, 27, 7) and the circles correspond to an array near the top of the silt arc (P26, 24, 18, 13, 6). For each array, two artificial data points are added: one at the top, representing the boundary condition that the excess pore pressure is zero at the surface, and one at the bottom, where the excess pore pressure is set equal to that of the lowest transducer.

In Figure 14, for a snapshot immediately after the second main shock, the array at mid-slope tends to hover around $r_u = 0.5$ because the shear stresses are large in this region. The array near the top of the silt arc shows higher pore pressures, near $r_u = 0.7$. Pore pressures are lower near the arc, where shear stresses are near failure and strains are larger; pore pressures are greater at depth where the sand is further from the failure state.

The volumetric strain rates in Figure 14 were obtained by first numerically evaluating flow rates toward a transducer assuming 1-dimensional Darcy's law. The velocity of flow in the vertical direction toward transducer i from transducer $i+1$ is calculated by:

$$v_{in} = \frac{k}{\gamma_w} \frac{(u_e)_{i+1} - (u_e)_i}{h_{i+1}} \tag{2}$$

The outflow is calculated similarly. The volumetric strain rate is then approximated by:

$$\frac{d\varepsilon_v}{dt} = \frac{v_{out} - v_{in}}{0.5 \cdot (h_i + h_{i+1})} \tag{3}$$

Here, $0.5 \cdot (h_i + h_{i+1})$ is the tributary thickness of the element (half the distance between the transducers above and below transducer i). The snapshots of volumetric strain rate shown are typical of the entire record. Note that the top data point in the volumetric strain rate plots is for the top transducer; there is no calculated strain rate for the artificial point shown for the drained boundary, thus, there is one less point plotted in the strain rate plot as compared to the excess pore pressure plot. In each case, the impermeable silt layer is between the top two real transducer records. The low permeability of the silt was accounted for in calculation of Equation 2. From the calculations, one can see that densification is occurring at the top transducer (above the silt arc) and volumetric dilation is occurring for the second transducer, just below the silt arc. This is consistent with the idea that the soil is becoming looser below the silt arc. The magnitudes of the computed volumetric strain rates are qualitatively reasonable -- a volumetric strain rate of 0.01 %/s for 100 seconds would produce 1% volume strain. However, we will refrain from making strong quantitative statements about the magnitude of volumetric strain rates until further verification of the accuracy and assumption of the computations. For the array at mid-slope, the third transducer also indicates volumetric dilation. This supports the idea that dilation is

occurring over a thick zone. Dilation is not limited to a thin (e.g., a dozen grain diameters) shear zone directly adjacent to the silt arc.

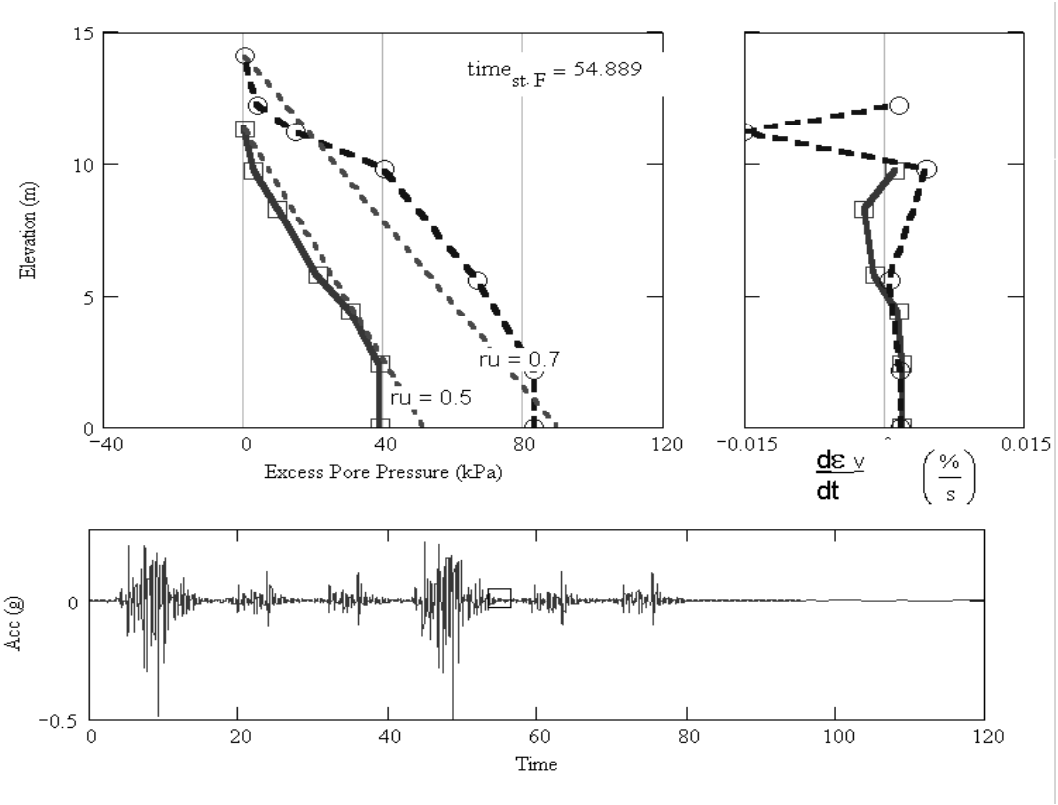

Figure 14. Isochrones of excess pore pressure compared to lines of constant r_u and calculated volumetric strain rate at time = 54.889 s in test EJM01. Two curves correspond to two vertical arrays. Square points are for the vertical array of transducers near mid-slope, and the circles are for the vertical array of transducers near the top of the silt arc.

CONCLUSIONS

This paper focuses on clarifying the mechanisms of deformation and pore fluid migration in sloping ground with the presence of an impermeable boundary that coincides with a potential failure mechanism. A few important points are:

- The presence of a shear stress in a dilatant soil tends to make the stress path stabilize near the phase transformation line. We have calculated the limiting pore pressures as a function of the slope angle for the simple case of a submerged infinite slope.
- Water tends to flow upward during liquefaction and this water may accumulate in a dilating shear zone beneath an impermeable boundary. The thickness of the dilating shear zone is not limited to a dozen grain diameters or so; it can be much larger.
- Excess pore pressure and pore pressure ratio contours obtained from data measured in the large centrifuge test enabled visualization of the pore pressure and flow regimes. The contours are improved by approximately forcing them to be consistent with the known boundary conditions at the ground surface and the container boundaries.
- A new procedure to calculate volumetric strain rate distribution from the experimental data is introduced.

- Calculation of volumetric strain rates, in the proposed manner requires taking the second derivative of the pore pressure distribution with depth. Small errors in water pressure measurement can lead to larger errors in the second derivative. Therefore, it would be useful to take extreme care in accurate calibration.

The use of a large number of sensors in a large centrifuge test makes it possible to obtain somewhat detailed visualizations of pore pressures in the soil profile. We are beginning to be able to compute qualitative volumetric strain distributions based on model test data. The use of even more instrumentation will provide more conclusive evidence to verify the mechanisms of deformation.

ACKNOWLEDGEMENTS

We acknowledge the following contributions. The US National Science Foundation provided funding for this research (Grant # CMS-007011). Dan Wilson provided constant advice in use of MathCAD to produce the contour plots and animations. He also contributed to the planning and conduct of the centrifuge model test. Tom Coker, Chad Justice and Tom Kohnke provided excellent technician assistance in the conduct of the model test. Elizabeth Hausler explained helpful details of procedures that she used to produce contours of pore pressure data.

REFERENCES

[1] Malvick, E. J., R. Kulasingam, R. W. Boulanger, and B. L. Kutter,. 2003, submitted. "Analysis of a Void Redistribution Mechanism in Liquefied Soil," in Proc. 12th Panamerican Conference on Soil Mechanics and Geotechnical Engineering, June 2003, Cambridge, MA.

[2] National Research Council [NRC]. 1985. *Liquefaction of Soils During Earthquake.* Washington, D.C.: National Academy Press.

[3] Boulanger, R. W. 1999. "Void Redistribution in Sand Following Earthquake Loading," in *Physics and Mechanics of Soil Liquefaction*, Lade & Yamamuro, eds., Rotterdam: Balkema, pp. 261-268.

[4] Malvick E. J., R. Kulasingam, B. L. Kutter, and R. W. Boulanger. 2002. "Void Redistribution and Localized Shear Strains in Slopes During Liquefaction," in *Physical Modelling in Geotechnics - ICPMG '02*, R. Phillips, P. J. Guo, and R. Popescu, eds. Lisse: Swets & Zeitlinger, pp. 495-500.

[5] Liu, H., and T. Qiao. 1984. "Liquefaction Potential of Saturated Sand Deposits Underlying Foundation of Structure," in Proc. Eighth World Conference on Earthquake Engineering, San Francisco, 3:199-206.

[6] Elgamal, A.-W., R. Dobry, and K. Adalier. 1989. "Study of Effect of Clay Layers on Liquefaction of Sand Deposit Using Small Scale Models," T. D. O'Rourke and M. Hamada, eds. Proc. 2nd U.S. – Japan Workshop on Liquefaction, Large Ground Deformations and Their Effects on Lifelines, NCEER, SUNY-Buffalo, Buffalo, NY, pp. 233-245.

[7] Fiegel, G.L., and B. L. Kutter. 1994. "Liquefaction Induced Lateral Spreading of Mildly Sloping Ground," *J. Geotech. Engrg.*, ASCE, 120(12):2236-2243.

[8] Dobry, R., and L. Liu. 1992. "Centrifuge Modeling of Soil Liquefaction," Proc. 10th World Conference on Earthquake Engineering, Madrid, July 29-24, 1992, 11:6801-6809.

[9] Kokusho, T. 1999. "Water Film in Liquefied Sand and its Effect on Lateral Spread." *J. Geotech. Geoenv. Engrg.,* ASCE, 125(10):817-826.

[10] Kulasingam, R., E. J. Malvick, R. W. Boulanger, and B. L. Kutter. 2001 "Void Redistribution and Localization of Shear Strains in Model Sand Slopes with Silt Seams: Report on First Year Activities," Proc. U.S.-Japan Joint Workshop and 3rd Grantees Meeting, U.S.-Japan Cooperative Research in Urban disaster Mitigation, Seattle, WA, pp. 117-128.

[11] Stewart, D. P., Y.-R. Chen, and B. L. Kutter. 1998. "Experience with the Use of Methylcelluose as a Viscous Pore Fluid in Centrifuge Models," *Geotechnical Testing Journal*, 21(4):365-369.

[12] Malvick, E. J., R. Kulasingam, R. W. Boulanger, and B. L. Kutter. 2003, submitted. "*Effects of Void Redistribution on Liquefaction Flow of Layered Coil - Centrifuge Data Report for EJM01,"* University of California, Davis, Center for Geotechnical Modeling, *http://cgm.engr.ucdavis.edu.*

Liquefaction Potential and Characteristics of Soils by Field and Laboratory Experiments

Direct Evaluation of the Liquefaction Characteristics of Soil In Situ

Ellen. M. Rathje, Wen-Jong Chang, and Kenneth H. Stokoe, II

ABSTRACT

An in situ dynamic liquefaction test is being developed at the University of Texas at Austin. The essential components of this in situ test are a dynamic loading source and an embedded instrumentation array for simultaneously monitoring the ground response and measuring the pore pressure generation. The dynamic loading system consists of a large mobile shaker (typically called a vibroseis truck in the geophysical exploration industry) that applies dynamic loads to the ground surface and generates waves propagating through the instrumented test area. An instrumentation system and associated data reduction procedures were developed to assess the coupled behavior of the soil skeleton and pore water pressure. The measured response to dynamic loading is used to evaluate the pore pressure generation characteristics of the soil in terms of the induced shear strains and excess pore pressures.

This paper describes the general testing technique used to evaluate liquefaction characteristics in situ. Field results are presented from a site in Austin, Texas where a reconstituted granular material located near the ground surface was tested. For the first time, pore pressure generation curves were measured in situ that describe the relationship between excess pore pressure, shear strain amplitude, and number of loading cycles. These curves are similar to those previously measured in the laboratory. The developed testing technique represents a new testing alternative for the study of liquefaction and potentially will have a significant impact in the field of geotechnical earthquake engineering.

Ellen M. Rathje, Assistant Professor, Department of Civil Engineering, University of Texas, Austin, Texas, 78712
Wen-Jong Chang, Assistant Professor, Department of Civil Engineering, National Chi Nan University, Puli, Taiwan 545
Kenneth H. Stokoe, II, Professor, Jennie C. and Milton T. Graves Chair in Engineering, Department of Civil Engineering, University of Texas, Austin, Texas, 78712

INTRODUCTION

Soil liquefaction is a complicated phenomenon involving the coupled response of the soil skeleton and pore water. Although soil liquefaction has been observed under monotonic or static loading conditions, often the most interesting cases are those caused by seismic or cyclic loading. Simplified procedures using results from in situ tests and laboratory tests have been proposed and used in academic research and practical applications to predict liquefaction behavior [1]. However, these procedures all have intrinsic limitations such as uncertainties in the measured in situ test parameters, the accuracy of empirical correlations, the heterogeneity inherent in field sites, and the size and disturbance associated with laboratory soil specimens. An in situ testing technique that directly measures pore pressure generation and soil response is highly preferred to overcome many of the existing limitations of current techniques.

Few in situ measurements of both dynamic response and pore pressure generation have been reported [2-6]. For these studies, instrumentation systems were installed and researchers waited for an earthquake to load the site. Surface and downhole array accelerometers were used to monitor the ground response and pore pressure transducers were utilized to measure pore pressure generation. The major limitations of these studies include the unknown recurrence of earthquakes, the durability of the sensors after long periods waiting for an earthquake, assumptions regarding the calculation of strains, and validation of the recorded data. Controlled sequential explosions [7-9] is an alternative dynamic loading source and has been used to induce liquefaction.

The main goal of this research is to develop a testing procedure that can directly evaluate the liquefaction potential of soils and study the liquefaction mechanism in situ. Previous research [10] reveals that the liquefaction phenomenon derives from the coupled response between the cyclic shear strain and excess pore water pressure. The proposed testing procedure permits the in situ measurement of the relationship between the induced cyclic shear strain and excess pore water pressure. In this initial developmental stage, a vibroseis truck is used to induce shaking in an instrumented test area by generating surface waves near (within 3.3 m) the test area. The level of shaking is controlled by specifying the vibration levels for the vibroseis. The surface waves induce cyclic shear strains which, in turn, generate excess pore water pressure in the test area. To evaluate shear strain and pore water pressure in situ, a new sensor, called a liquefaction test sensor, has been developed and embedded below the ground surface. This sensor is used to simultaneously monitor the dynamic soil particle velocity and pore water pressure. Shear strain-time histories are calculated systematically from the measured ground velocities. The excess pore water pressure-time histories are measured at the location where the shear strains are calculated using a miniature pore water pressure transducer. Therefore, the full process of cyclic loading is captured, ranging from small-strain loading to significant pore pressure generation. Also, seismic testing techniques are used to characterize the soil conditions before and after liquefaction. The following sections describe the details of the testing and data reduction procedures and the results from a field test series performed on a large-scale reconstituted test specimen that was constructed in a test pit.

DESCRIPTION OF BASIC TESTING TECHNIQUE

The in situ dynamic liquefaction test is designed to measure pore water pressure generation in situ without having to wait for an earthquake. The cyclic loading for the proposed test is similar to earthquake shaking. Also, very importantly, it can be performed over a wide range in strains so that the cyclic threshold strain, γ_t^e, can be evaluated. In the developed testing procedure, a vibroseis truck is used to generate Rayleigh waves that propagate through the test area and induce

a controlled number of cycles of shear strain and shear stress. The shear strains within localized regions can be systematically evaluated using particle velocity data recorded at multiple points in the region. Pore pressure buildup and dissipation are recorded using miniature pore pressure transducers capable of recording both hydrodynamic and residual excess pore pressure. Therefore, the coupled behavior between the dynamic response of the soil skeleton, represented by shear strain, and the excess pore water pressure is measured. Also, the pore pressure generation characteristics of the soil, expressed as excess pore pressure ratio versus mean shear strain amplitude for a specific number of loading cycles, can be measured in the field. This is analogous to the technique developed by Dobry [10] for cyclic strain-controlled laboratory tests. Each component of the basic testing technique is described below.

Dynamic Source

One of the major distinctions between this research and previous in situ liquefaction measurements is the dynamic source. A well-controlled dynamic loading system is used that is capable of generating loads of uniform amplitude at a specific frequency for a specific number of cycles. The dynamic loading system includes a vibroseis truck, a 222-kN (50-kips) load cell, a loading frame, and a rigid circular concrete footing. (The footing was used simply because the loading plate on conventional vibroseis trucks had been removed from the University of Texas vibroseis for other research studies.) The vibroseis truck is used as a vertical vibrator that dynamically loads the rigid footing located at the ground surface. The vertical vibration of this rigid footing generates surface waves that propagate through the test area and induce shear strains and excess pore pressure.

Vibroseis trucks have been widely used in seismic exploration as a wave source. The vibroseis truck owned by the University of Texas at Austin (UT) has been modified for dynamic pavement testing [11,12] and in situ nonlinear soil property studies [13,14]. A photo and schematic drawing of the UT vibroseis truck are shown in Figure 1. The main components of the vibroseis truck include the hydraulic ram (vibrator) and the control system. Limited by the servo valves of the hydraulic system, the UT vibroseis truck can generate sinusoidal waves within a frequency range of 15 Hz to 100 Hz. The maximum applied force is controlled by the weight of the truck, which is 222 kN (50 kips), and the output of the hydraulic ram. An electronic function generator is used to control the loading amplitude, frequency, and number of loading cycles.

Instrumentation Systems

The major instrumentation for the in situ liquefaction test consists of two-dimensional velocity transducers (2D-geophones), accelerometers, pore pressure transducers (PPT), associated signal conditioners, and high-speed data acquisition systems. The 2-D geophones and pore pressure transducers are combined into small packages to create liquefaction test sensors. Two data acquisition systems are employed for different recording lengths. Finally, settlement plates are placed within the test specimen. A general description of each component is presented below.

Liquefaction Test Sensor

The purpose the liquefaction test sensor is to measure soil particle motion and pore water pressure at the same location. Because particle motion and pore pressure are measured by geophones and PPTs, respectively, these two types of sensors must be combined. There are

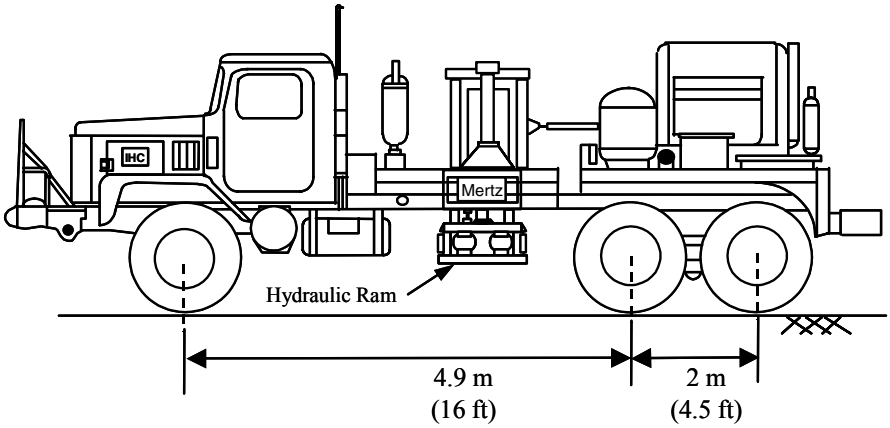

a. Schematic drawing of vibroseis truck [11]

b. Vibroseis truck at field test site in Austin, Texas

Figure 1 Vibroseis truck used as dynamic source

several issues that must be considered in the design. First, the sensor must be small enough to avoid significant interference with the surrounding soil. Second, the unit weight of the sensor package must be similar to the total unit weight of the surrounding soil to avoid floating or sinking of the sensor after significant excess pore water pressure generation. Third, the stiffness of the sensor must be large enough to withstand the stresses during installation and dynamic loading. Fourth, the noise level needs to be small for accurate monitoring and robust data reduction. Fifth, the sensor must be able to be installed vertically (so that it can be pushed into the ground in future applications). Finally, the sensor and cable must be waterproof.

A schematic of the developed liquefaction test sensor is shown in Figure 2. A cylindrical acrylic case was machined with holes to install two perpendicularly oriented 28-Hz geophones and one miniature PPT. The acrylic case is waterproof and provides protection for the sensors. A "shoe", made of thin metal plate, was attached to the bottom of the sensor to provide stability for the sensor during installation. A square aluminum plate with a threaded rod at the center was attached to the top of the sensor to provide a connection with a placement tool. Epoxy was used to fix the sensors within the case at the correct orientations. The epoxy was also used to fill all voids. An individually shielded, four-pair cable was used to provide DC power to the miniature PPT and to connect the two geophones and the PPT with the data acquisition systems.

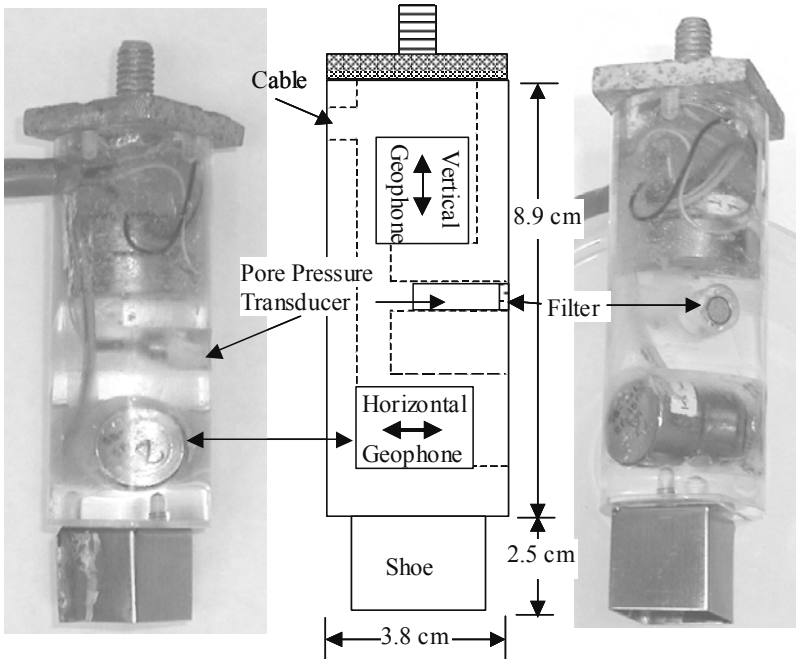

Figure 2 Schematic of liquefaction test sensor

Because the miniature PPT is a relative pressure transducer, which measures the pressure difference between the two sides of the pressure-sensing diaphragm, the side opposite to the water contact surface needs to be vented to the atmosphere to eliminate any pressure difference due to minor changes in atmospheric pressure. A tiny Teflon tube was used to vent the PPT. This tube extends from the back of the PPT to the electrical cable. Venting is achieved through the voids inside the electrical cable, which is open to the air at the end. The unit weight of the liquefaction sensor is about 2.24 g/cm^3 (140 pcf), which is quite close to the total unit weight of the surrounding saturated sand, approximately 2.0 g/cm^3 (130 pcf).

Data Acquisition Systems

Two data acquisition systems, called the transient response data acquisition system (TRDAQ) and the long-term data acquisition system (LTDAQ), are employed in this study. To synchronize the two systems, the function generator signal used to drive the vibroseis loading is recorded by both systems as a reference channel. The TRDAQ consists of a HP 3567A multichannel dynamic signal analyzer (DSA). Because of its limited memory, the TRDAQ records sensors that are only active during dynamic loading. The LTDAQ is composed of a multifunction National Instruments A/D board (PCI-6035E) and *LabView*® software. There are no memory limitations for the LTDAQ, so it is used to acquire the signals from the pore pressure transducers both during and after the dynamic loading.

Settlement Plates

Settlement plates were used to monitor vertical movements within the reconstituted test specimen at different depths. The settlement data was used to construct the settlement profile of the reconstituted test pit, to calculate the permanent vertical stain, and to estimate the in situ density after dynamic loading.

Each settlement plate consists of a square aluminum plate (10 cm by 10 cm). An aluminum rod is fixed to the plate and extends above the ground surface. A sleeve pipe is placed around the rod to allow the plate to settle freely. Settlement plates are installed at different depths to measure the variation of deformation with depth. Optical leveling measurements of the top of the aluminum rod are taken before and after each dynamic test. The vertical settlements for each plate can be obtained by subtracting the original elevation. The accuracy is limited by the resolution of optical leveling equipment, which is about 3 mm (0.12 in).

Small-Strain Seismic Testing

To characterize the dynamic soil properties of the instrumented test area, in situ seismic testing was performed. Specifically, crosshole testing was performed prior to and after each dynamic loading. Also, the measurement of P-wave velocity between embedded sensors was used to verify the saturation of the reconstituted test specimen.

The embedded geophones in the liquefaction test sensors were used as receivers when conducting the crosshole tests. By selecting the appropriately oriented geophones and using an appropriate source, S-wave and P-wave velocities were measured. The crosshole source was placed in a previously installed PVC pipe and was operated at the same elevation as the selected geophones. A portable dynamic signal analyzer was used to acquire and process the signals from the geophones. Because seismic testing is a small-strain test, it can be repeated without affecting the soil properties. Generally, several crosshole tests were performed and the recorded signals were stacked in the time domain to effectively reduce background noise.

FIELD SET-UP

Currently, the in situ dynamic liquefaction test was conducted only on reconstituted soil specimens. These specimens were prepared in a 1.8-m^3 test pit. Reconstituted test specimens were used for the following reasons. First, reconstituted specimens can be reconstructed many times at the same field site, which makes the process repeatable. Second, the physical properties of the test soil, such as relative density, unit weight, and degree of saturation, can be better controlled and more accurately measured using reconstituted test specimens. Third, reconstituted soil specimens can also be constructed in the laboratory for direct comparison with field performance. Fourth, it is easy to install sensors at designated locations within the reconstituted specimen during construction so that soil disturbance is minimized. Finally, it is much easier to perform several "debugging" test series with reconstituted specimens constructed near UT than to travel to several real field sites.

Although analytical studies [15] revealed that the largest strains would be generated at locations close to the footing beneath the vibroseis truck, the reconstituted test pit was placed 3.3 m (11 ft) away from the edge of the footing. This distance was chosen because of safety considerations for the vibroseis truck, such as overturning of the truck when the test pit loses strength and liquefies. A general schematic of the dynamic liquefaction test site is shown in Figure 3. The test pit is lined with a waterproof liner and backfilled soil is deposited under water in the test pit to prepare the specimen. As the soil is deposited, four sensors are placed in a square array, with another sensor placed at the center of the array. A layer of dry sand was placed on top of the test pit to increase the confining pressure in the test specimen. An accelerometer is placed at the top of the overburden layer.

To establish the liquefaction characteristics of the test soil, the test series starts from a low-loading amplitude level. The loading level is gradually increased until significant excess pore pressures are measured or the capacity the UT of vibroseis truck is reached.

DATA COLLECTED DURING LIQUEFACTION TEST

With the current configuration of the test pit and testing sequence, several types of data are collected to determine the dynamic soil properties and pore water pressure generation characteristics of the instrumented test specimen. The fundamental data are listed as follows:

1. The time histories of motion are recorded with the embedded geophones. The shear strain-time histories are evaluated using the geophone records. The geophone data also provide information about the stress waves propagating through the test area during low- and high-level excitation.
2. Excess pore water pressure-time histories are obtained. The pore water pressure-time histories contain both hydrodynamic and residual components. Combined with the shear strain-time histories, the coupled behavior between the induced shear strain and excess pore pressure generation is evaluated.
3. The phase velocity of the stress waves is obtained from the vertical geophones.
4. The pore pressure generation curve of the site is established by compiling the dynamically induced shear strain level and generated excess pore water pressure with respect to a specific number of loading cycles.

Example Test Results

The schematic layout for a typical test series is shown in Figure 3. Five liquefaction sensors were installed, four at the corners of a 0.6 m by 0.6 m square array and one at the center of the array. A PVC pipe was installed along the far side of the test pit, in the same vertical plane as the instrumentation array, and was used as casing for the crosshole source. One settlement plate was placed on top of the specimen to measure the settlement of the specimen. A 0.8-m layer of air-dried sand was placed on top of the specimen as overburden to increase the stresses within the test specimen. With this overburden in place, the vertical effective stress at the center of the array was 19.3 kPa. An accelerometer was placed on top of the overburden to monitor the vertical acceleration.

The initial and final physical properties of the reconstituted test specimen are listed in Table 1. The final values are estimated from the 4.3 cm (1.7 in) of settlement measured at the top of the specimen. The dynamic loads were applied to the footing at a loading frequency of 20 Hz for 1 second. Therefore, 20 cycles of loading were generated. Typical velocity-time histories measured by the two deepest vertical geophones (locations 3 and 4 in Figure 3) are shown in Figure 4.

Two methods were used to evaluate shear strains from the recorded particle velocities. These methods are called the strain displacement matrix (SDM) method and the apparent wave (AW) method. The SDM method uses displacement-time histories, computed from the measured velocity-time histories at the corners of the array, along with the geometry of the array to compute the shear strain at the center of the array. This method uses the strain displacement matrix, as described in finite element formulations, to compute strain [15]. The only assumption incorporated in this calculation is a linear variation of displacement between measurement points. The AW method is a wave propagation-based method for calculating dynamic strains, where strain is calculated as the

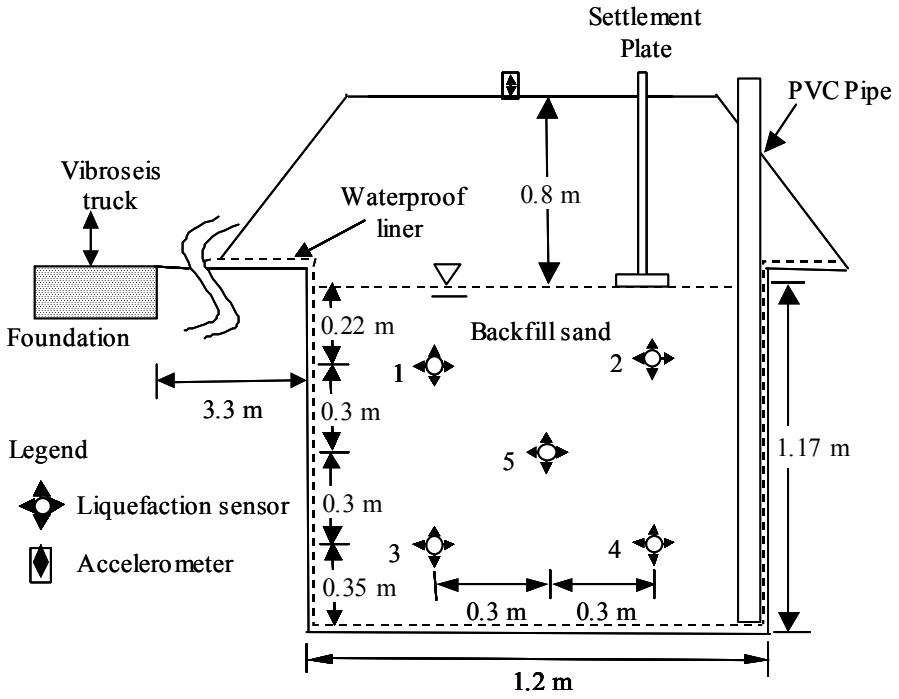

Figure 3 Schematic layout of dynamic source, reconstituted soil in test pit and associated instrumentation used in field tests

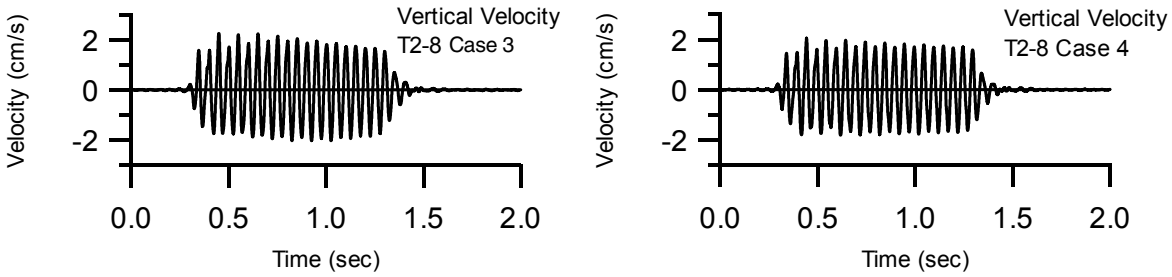

Figure 4 Measured velocity-time histories during testing

Table 1 Physical properties of the reconstituted sand specimen

Soil property		Value
Specific gravity (G_s)		2.68
Maximum void ratio (e_{max})		0.64
Minimum void ratio (e_{min})		0.43
Fines content		0.43%
Initial	Relative density (D_r)	34.7%
	Water content (w)	21.1%
	Total unit weight (γ_t)	20.4 kN/m^3 (129.3 pcf)
Final[(1)]	Relative density (D_r)	61.2%
	Water content (w)	19.0%
	Total unit weight (γ_t)	20.8 kN/m^3 (132.0 pcf)

Note: [(1)] These values are estimated from 4.3 cm (1.7 in.) of settlement

ratio between the particle velocity and wave propagation velocity. For the current test set up, shear strain is computed from the vertical particle velocity and the horizontal wave propagation velocity. The appropriate wave propagation velocity is measured from the phase difference between two adjacent sensors at the same elevation [15]. Because the wave velocity used in the strain computation cannot be attributed to a single type of wave, this strain computation method is called the apparent wave method.

The tests conducted in the test series are divided into two groups according to their mean shear strain levels. The low shear strain level group displayed no or small excess pore pressure during dynamic loading. Also, the shear strain levels are relatively constant during cyclic loading. The large shear strain level group showed significant excess pore pressure generation and the shear strain amplitudes varied during dynamic loading. Example shear strain-time histories evaluated from the liquefaction test sensors at the center of the array are presented in Figures 5a and 5b for the low-strain and high-strain tests, respectively.

The shear strain time-histories at the center of the array from a low strain level test are shown in Figure 5a. The shear strains were computed using the SDM method directly and using the AW method. The shear strain amplitudes during dynamic loading are relatively constant for both methods, and the mean shear strain level is about 0.002%. Shear strain-time histories at the center of the array from a large strain level test are shown in 5b. This test recorded the largest mean shear strain level (0.15%) and the largest excess pore pressure. The shear strain-time history at the center of the array calculated by the SDM method shows significant variation during dynamic loading, indicating a reduction in amplitude during later cycles as pore pressure is generated. This trend is not observed for the AW method.

The pore pressure ratio-time histories from the large strain test are shown in Figure 6. The pore pressure ratio (r_u) is defined as the ratio between the excess pore water pressure and the initial vertical effective stress. In the recording shown in Figure 6, both hydrodynamic and residual pore pressures are observed. The hydrodynamic peak-to-peak amplitude is about 30% and remains approximately constant during dynamic loading. The maximum residual excess pore pressure ratio reaches 46% at the center of the array. For each pore pressure recording, the excess pore pressure dissipated in about 50 seconds.

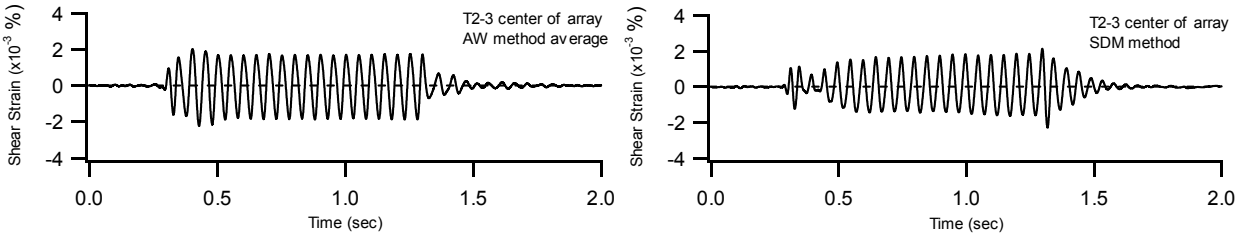

a Shear strain-time histories evaluated at the center of the array for a low strain level test

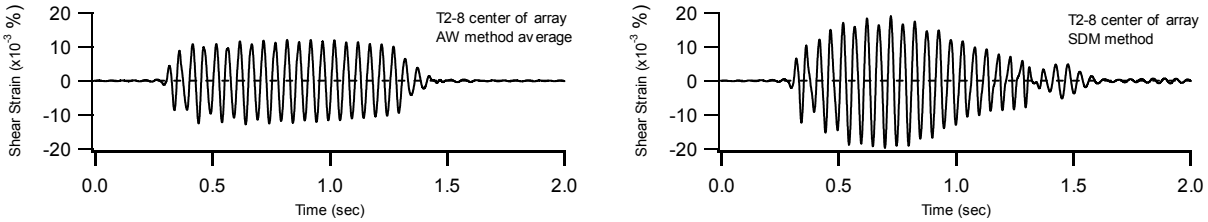

b Shear strain-time histories at the center of the array for a large strain level test

Figure 5 Typical shear strain-time histories

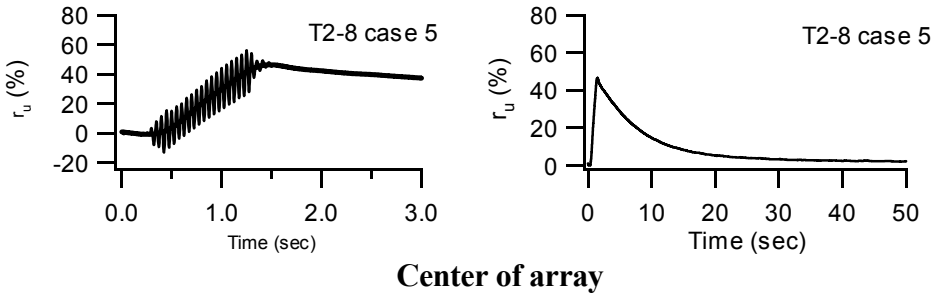

Figure 6 Excess pore pressure ratio-time histories measured during large strain test

Measured excess pore pressure ratio at the center of the array is plotted versus shear strain calculated by the SDM method in Figure 7. The data show little or no pore pressure generation at shear strains below 0.005%. Significant pore pressure is generated at shear strains above 0.01%. At each strain level, more pore pressure is generated as the number of loading cycles increases. The maximum excess pore pressure ratio for this test series was 46.4%, and it occurred after 20 cycles of loading at a shear strain of about 0.015%. The permanent settlement after the large strain test was 4.3 cm, which corresponds to 3.7% volumetric strain.

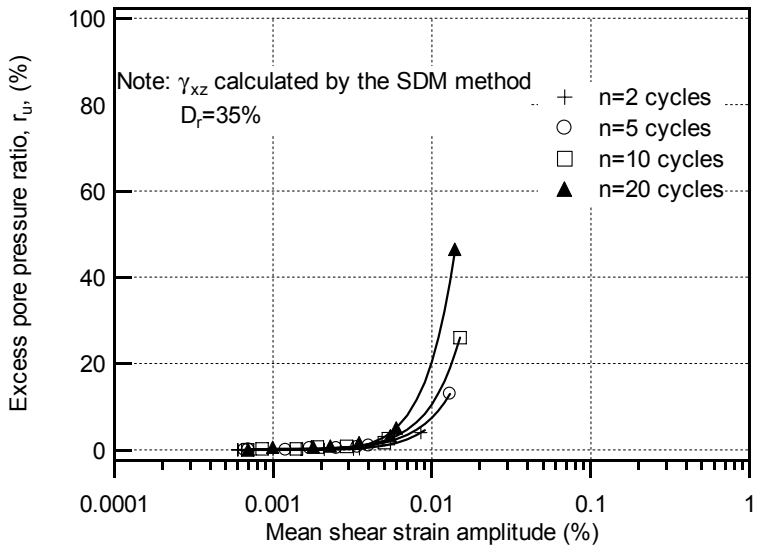

Figure 7 Pore pressure generation curves for different numbers of loading cycles

CONCLUSIONS

To overcome the shortcomings of existing liquefaction evaluation and testing techniques, an in situ dynamic liquefaction test is highly desired. The in situ dynamic liquefaction testing procedure developed at UT measures the pore pressure generation and ground response simultaneously in the field. Therefore, sample disturbance is minimized. Also, by monitoring the full process of pore pressure generation and dissipation in the time domain, the collected data can be applied not only to the identification of initial liquefaction, but also to cases where partial liquefaction occurs. In both of these cases, the consequences of liquefaction can be studied. In addition, the testing procedure can be used to evaluate the effectiveness of various liquefaction remediation techniques. Furthermore, the testing data can be utilized in validation of dynamic numerical analysis. The testing procedure under development will benefit engineering practice, as well as advance the state knowledge regarding liquefaction.

ACKNOWLEDGEMNTS

Financial support was provided through the National Science Foundation under grants CMS-9875430 and CMS-9973717, and the US Geological Survey under grant 01HQGR0036. This support is gratefully acknowledged.

REFERENCES

[1] Youd, T. L., R. D. Andrus, I. Aragon, G. Castro, J. T. Christian, R. Dobry, W. D. L. Finn, L. F. Harder Jr., M. E. Hynes, K. Ishihara, J. P. Koester, S. S. C. Liao, W. F. Marcuson, III, G. R. Martin, J. K. Mitchell, Y. Moriwaki, M. S. Power, P. K. Robertson, R. B. Seed and K. H. Stokoe, II. 2001. "Liquefaction Resistance of Soils: Summary Report from the 1996 NCEER

and 1998 NCEER/NSF Workshops on Evaluation of Liquefaction Resistance of Soils," *Journal of Geotechnical and Geoenvironmental Engineering*, ASCE, 127(10): 817-833.

[2] Holzer, T. L., T. L. Youd, and T. C. Hanks. 1989. "Dynamics of Liquefaction During the Supersition Hills Earthquake (M=6.5) of November 24,1987," *Science*, 244, April 7: 56-59.

[3] Ishihara, K., K.Shimizu, and Y. Yamada. 1981. "Pore Water Pressure Measured in Sand Deposits During an Earthquake," *Soils and Foundations*, 2(4): 85-100.

[4] Ishihara, K., T. Muroi, and I. Towhata. 1989. "In-Situ Pore Water Pressure and Ground Motions During the 1987 Chiba-Toho-Oki Earthquake," *Soils and Foundations*, 29(4): 75-90.

[5] Shen, C. K., Z. Wang and X.S. Li. 1991. ''Pore pressure response During the 1986 Lotung Earthquake,'' *Proceedings, 2nd Int. Conf. on Recent Advances in Geotech. Earthquake Engrg. and Soil Dynamics,* S. Prakash, ed., National Science Foundation, Washington, D.C: 557-563

[6] Youd, T. L. and T. L. Holzer. 1994. "Piezometer Performance at Wildlife Liquefaction Site, California," *Journal of the Geotechnical Engineering Division*, ASCE, 120(GT6): 975-995.

[7] Charlie, W. A., P. J. Jacobs and D. O. Doehring. 1992, "Blast-Induced Liquefaction of an Alluvial Sand Deposit," Geotechnical Testing Journal, 15(1): 14-23.

[8] Gohl, W. B., J. A. Howie, and C. E. Rea. 2001. "Use of Controlled Detonation of Explosives for Liquefaction Testing," *Proceedings, 4st Int. Conf. on Recent Advances in Geotechnical Earthquake Geotechnical Engineering and Soil Dynamics and Symposium in Honor of Professor W. D. Liam Finn*, San Diego, CA, March 26-31.

[9] Rollins, K.M., S.A. Ashford, J. D. Lane. 2001. "Full-Scale Load Testing of Deep Foundations Using Blast-Induced Liquefaction," *Proceedings, 4st Int. Conf. on Recent Advances in Geotechnical Earthquake Geotechnical Engineering and Soil Dynamics and Symposium in Honor of Professor W. D. Liam Finn*, San Diego, CA, March 26-31

[10] Dobry, R., R. S. Ladd, F. Y. Yokel, R. M. Chung, and D. Powell. 1982. "Prediction of Pore Water Pressure Buildup and Liquefaction of Sands During Earthquake by the Cyclic Strain Method," *NBS Builing Science Series 138, National Bureau of Standards*, Gaithersburg, Maryland: 150

[11] Bay, J. A. 1997. "Development of a Rolling Dynamic Deflectometer for Continuous Deflection Testing of Pavements," *Ph.D. Dissertation*, University of Texas at Austin: 75-78.

[12] Bay, J. A., K. H., Stokoe, II., B. F. McCullough and D. R. Alexander. 1999. "Profiling Flexible Highway Pavement Continuously with Rolling Dynamic Deflectometer and a Discrete Points Falling Weight Deflectometer," *Transportation Research Record No. 1665*: 74-85.

[13] Phillips, R. D. 2000. "Initial Design and Implementation of an In Situ Test for Measurement of Nonlinear Soil Properties," M.S. Thesis, The University of Texas at Austin.

[14] Axtell, P. J. 2001. "In-Situ Measurements of Linear and Nonlinear Properties of a Near-Surface, Poorly Graded Sand," M. S. Thesis, The University of Texas at Austin.

[15] Chang, W.J. 2002. "Development of an In Situ Dynamic Liquefaction Test," Ph.D. Dissertation, The University of Texas at Austin.

A MONITORING AND VISUALIZATION TECHNIQUE FOR LIQUEFACTION USING RESISTIVITY

Motoharu Jinguuji, Sunao Kunimatsu, and Selcuk Toprak

ABSTRACT

This paper presents a new technique to monitor and visualize the relative density in saturated sandy soils during liquefaction and post-liquefaction stage. The technique utilizes the unique relation between sands electrical resistivity and porosity. Using the equipment and software developed in this work, the resistivity along the soil depth during liquefaction and post-liquefaction stage can be measured and converted to relative soil density. The relative density results can be viewed on depth versus time plots. The results from the laboratory experiments on homogeneous sands are presented and discussed in this paper. The technique can also be used in large-scale experiments including field tests.

Motoharu Jinguuji and Sunao Kunimatsu, National Institute of Advanced Industrial Science and Technology, AIST West, 16-1 Onogawa, Tsukuba, Ibaraki, Japan

Selcuk Toprak, Visiting Research Engineer, National Institute of Advanced Industrial Science and Technology and Waseda University, AIST West, 16-1 Onogawa, Tsukuba, Ibaraki, Japan (Asst. Prof., Civil Engineering Department, Pamukkale University, Kinikli, Denizli, Turkey, 20070)

INTRODUCTION

Liquefaction is a major concern for structures and lifeline systems in saturated sandy soils. Damage caused by reduced shear strength, settlements and lateral spreads in liquefied soils is commonly reported [e.g., 1, 2]. Among others, one important parameter that affects soil's shearing strength and deformation characteristics is the relative density of soils. Monitoring of relative density in soils during liquefaction and post-liquefaction stage should help clarify the unresolved issues related to the behavior of liquefied soils.

In this study, electrical resistivity of saturated sands is used to determine the relative density. Beginning with Archie [3], the relationship between the electrical resistivity and porosity in saturated soils has been demonstrated by various researchers and its applications to various fields have been suggested [4, 5, 6, 7]. New equipments and software were developed in this work to use the technique in liquefaction research in small laboratory tests, large-scale tests and field experiments. Using the equipment and software, the resistivity along the soil depth during liquefaction and post-liquefaction stage can be measured and converted to relative density [7, 8]. The relative density results can be viewed on depth versus time plots. The technique is being evaluated in small and large-scale laboratory tests and field experiments. The results from the laboratory experiments with homogeneous sands are presented and discussed in this paper.

THE PRINCIPLE AND METHOD OF RESISTIVITY MONITORING

The existing relationship between the porosity and electrical resistivity of sands enables determination of the relative density of sands in liquefaction experiments by measuring resistivity. For saturated sands, the following Archie's law [3] is applicable:

$$F = \phi_t / \phi_w = a n^{-m}. \tag{1}$$

where ϕ_t is the electrical resistivity of soil, ϕ_w is the electrical resistivity of pore water, and n is the porosity of the soil whose resistivity measured. The constants a and m depend on the sand type and are determined from the results of laboratory experiment. The formation factor, F is obtained by normalizing ϕ_t by ϕ_w.

The porosity of sand can be determined from equation (1) using the measured electrical resistivity values for sand and water. Then, the following equations can be used to determine the relative density, D_r:

$$e = \frac{n}{1-n} \tag{2}$$

$$D_r = \frac{e_{\max} - e}{e_{\max} - e_{\min}} \tag{3}$$

where e is the void ratio of soil in its existing state, $e_{\max}$ is the void ratio of soil in its loosest state, and $e_{\min}$ is the void ratio of soil in its densest state.

The following two methods are used for the electrical resistivity measurement of sands in liquefaction experiments.

(1) The first method uses electric current electrodes at fixed position and measures the electric potential between two electrodes by using the commutated direct current. Two different types of potential electrodes can be utilized between current electrodes to measure the potential. One is a set of needle electrodes that are partially inserted into a cylindrical or rectangular vessel at certain depths from the outside, and the other type is a set of line electrodes which are installed at certain depths along the inner walls of a cylindrical or rectangular vessel.
(2) The second method utilizes electrode cable on which electrodes are placed at equal intervals. In this method, the electrodes can be used as current or potential electrode. The electric potential is measured by using different methods, such as 4-pole method.

Figure 1 shows a schematic view of a vessel, electrodes, and the use of Method (1). Two metal mesh electric current electrodes are installed in the top and bottom part of the vessel to transmit parallel current to the soil inside the vessel. The line electrodes shown as circles in the figure are installed at certain depths along the inner wall to serve as potential electrodes. The electric current, I transmitted by the current electrodes and the potential, V at potential electrodes are measured and the distribution of vertical electrical resistivity in the sand is calculated. The resistivity determined in this way is the average soil resistivity between each two potential electrodes. Therefore, it is assigned to the mid-point height between respective potential electrodes. The advantage of this method is that the high-speed sampling can be applied because this method utilizes fixed position of current electrodes. The new equipment developed in this study has capability to pass electric current of 20mA and scan entire 16 potential electrodes into separate data channels in 0.3 seconds. This method is suitable for the laboratory experiments that use small vessel or chamber.

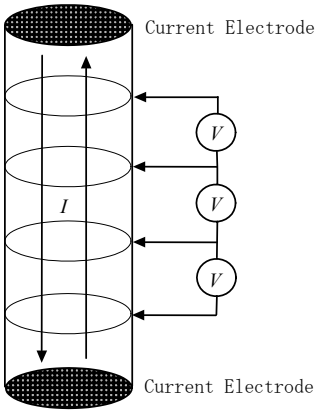

Figure1. Schematic view of the method using current electrodes at fixed position

Figure 2 shows schematic view of an electrode cable, electrodes, and the application of 4-pole method of Method (2). The black solid rectangles on the cable show the location of electrodes. Because electrodes can be used as current or potential electrodes, the distribution of resistivity in the vertical direction around electrode cable is continuously measured by changing a set of 4 electrodes. As shown in the figure, each time a 4-electrode set is selected with top and bottom electrodes serving as current electrodes and intermediate electrodes serving as potential electrodes. The current, I at current electrodes and the potential, V at intermediate electrodes are measured and the resistivity of sand is calculated. The resistivity

determined this way is the average resistivity of the spherical volume between two potential electrodes. Then, the selection moves up or down one electrode, and a new 4-electrode set is selected. This process continues progressively in up or down direction until the measurement is stopped. The new equipment developed for this method can scan entire 32 set of 4-pole electrodes into separate data channels in 0.1 second. Because of the effect of induced polarization, however the sampling time is practically much higher than 0.1 sec. This method is suitable for large scale experiments or field tests.

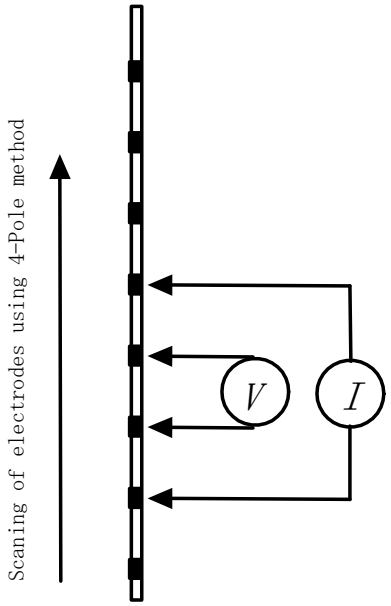

Figure 2. Schematic view of the method using electrode cable

RESISTIVITY CHANGE IN SANDS DURING AND AFTER LIQUEFACTION

To confirm the effectiveness of the resistivity monitoring during liquefaction, laboratory tests were performed. Figure 3 shows the chamber used in the experiments. As a modification to Method (1), there was no mesh electrode at the top. The bottom mesh electrode and the top line electrode were current electrodes that transmit electric current to the sample. To avoid resistivity complicacies associated with this modification, we filled about the bottom half of the box with sand and the top with water. The potential line electrodes along the walls of the chamber were placed at 1.5 cm intervals. Toyoura sand was used in the experiments. The soil sample was prepared using boiling method and the height of the saturated sample in the chamber was about 16 cm. The relative density of Toyoura sand was about 30 %. The box was placed on a small shaking table and 4-second excitation applied. The waveform of the excitation was sine-wave with a frequency of 5 Hz. The amplitude of the acceleration was 150 cm/sec^2.

Figure 4 shows the resistivity results from the experiment. The abscissa and ordinate of the plot are the time in seconds and the height from the bottom of chamber in cm, respectively. The measurement started from 5 seconds before the excitation and the sampling interval was 0.3 sec. The colors on the plot show the resistivity results and the legend is given next to the plot. Increasing resistivity indicates increasing density. Three zones are inferred from the resistivity pattern on the plot. Zone 1 shows the resistivity before the liquefaction starts. Zone 2 shows the resistivity during the liquefaction process. The resistivity in the

upper part of the soil sample during this process decreased, indicating loosening of sand particles. Zone 3 shows the resistivity when sand particles started settling and densification occurred. Densification started from the lower parts of the sample even before the shaking stopped and progressed upward. As shown later in this paper, this state is governed by the dissipation of excess pore pressure. About 13 seconds after the shaking stopped, the resistivity reached constant state in the entire sample. The most significant resistivity change occurred during the transition from liquefied state (Zone 2) to densified state (Zone 3).

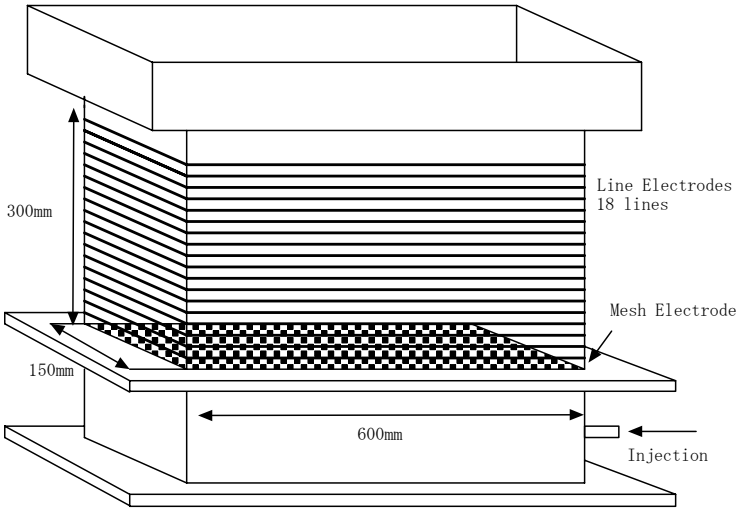

Figure 3. The schematic view of the small rectangular chamber used in the resistivity experiments

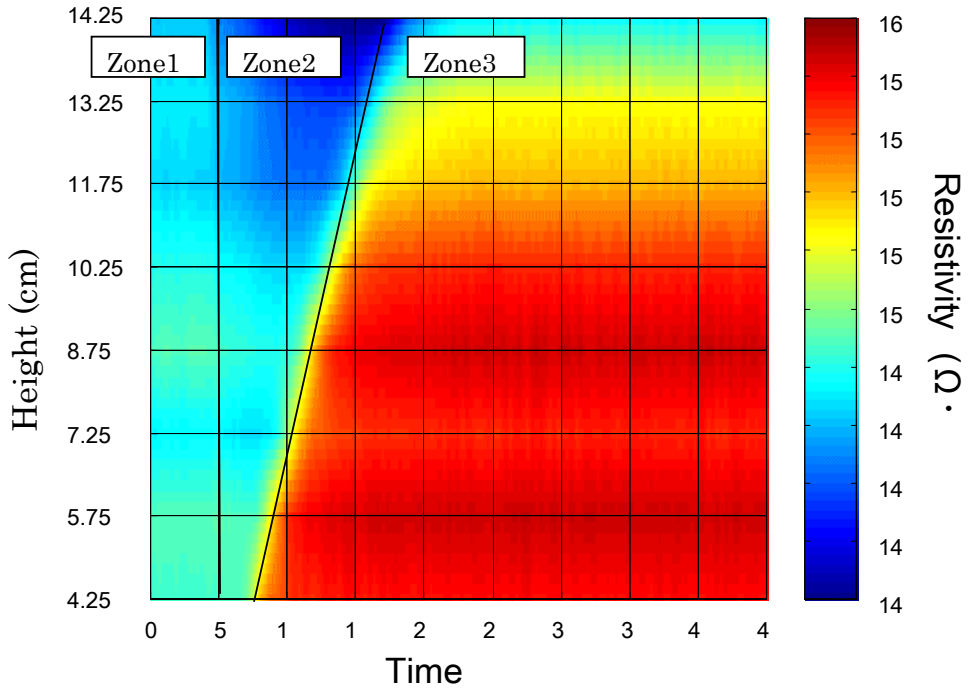

Figure 4. Resistivity measurements of liquefied Toyoura sand

FACTORS THAT AFFECT THE RESISTIVITY BEHAVIOR OF LIQUEFIED SANDS

Some factors are known to affect the liquefaction of sands such as sand type, duration of excitation, and application of successive excitations. The influence of these factors on the resistivity behavior of liquefied sands was tested. The same chamber and shaking table excitation as explained in previous section were used in the following tests.

Toyoura and Keisa No.6 sands were used to test the effect of sand type. Particle size of Toyoura sand is finer than Keisa No.6 sand. The D_{50} values for Toyoura and Keisa No.6 sands are about 0.125 and 0.275 mm, respectively. The sample heights were about 13 cm. The relative density of both samples was about 30 %. Figures 5a and b show the resistivity results from the experiments for Toyoura and Keisa No.6 sand samples, respectively. The legends next to the figures show the color scale for the resistivity change relative to each sample's initial resistivity. Comparison of the figures shows that the resistivity increase, hence the density increase in Keisa No.6 sand progressed upward faster than it did in finer grain Toyoura sand. This is expected as the dissipation of excess pore water pressure is faster in coarse grain sand.

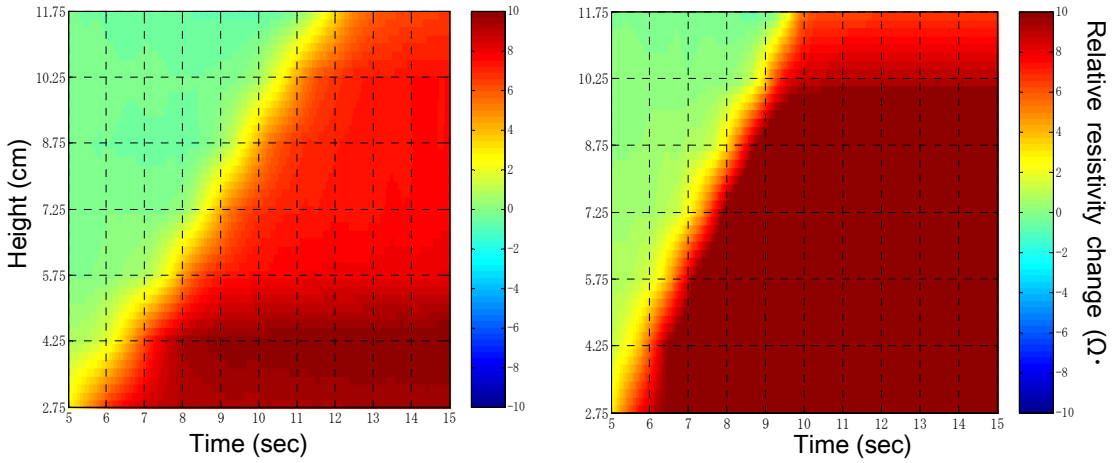

(a) Toyoura sand (b) Keisa No.6 sand

Figure 5. Resistivity changes measured in two different kinds of sand

In order to test the effects of the duration of excitation, Toyoura sand sample was shaken 30 seconds instead of 4 seconds. Figure 6 shows the result of resistivity monitoring starting from 5 seconds before the beginning of the shaking. The results indicate the densification started and completed at lower parts of the sample much before the shaking stopped. The densification process progressed upward and the process reached constant state in the entire sample as soon as the shaking stopped. The comparison of Figures 4 and 6 shows higher resistivities measured in the long duration shaking. For comparison purposes the resistivity scale in Figure 6 was kept the same as the one in Figure 4. The actual resistivity in this test, however reached about 190 ohm-m. levels.

To test the effects of successive excitations, 4-second shaking was applied consecutively six times to Toyoura sand sample. There were about 100 second intervals between each excitation. Figure 7 shows the results from the experiment. The arrows indicate the beginning of each shaking. Each successive excitation resulted in some increase in the resistivity.

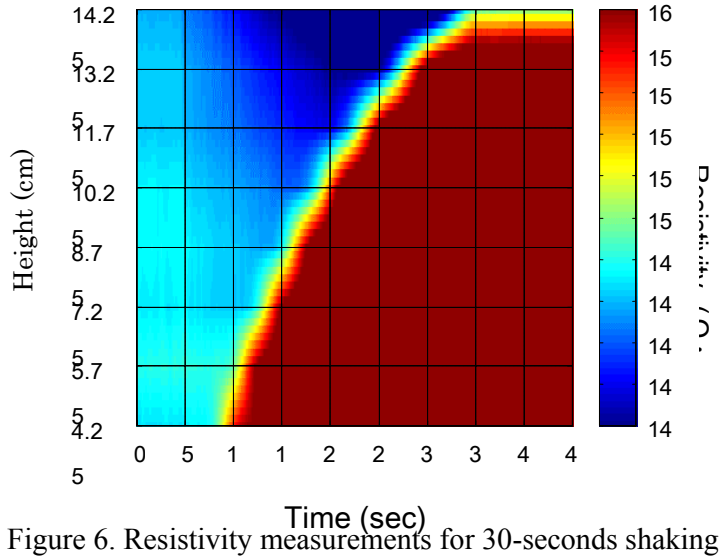

Figure 6. Resistivity measurements for 30-seconds shaking

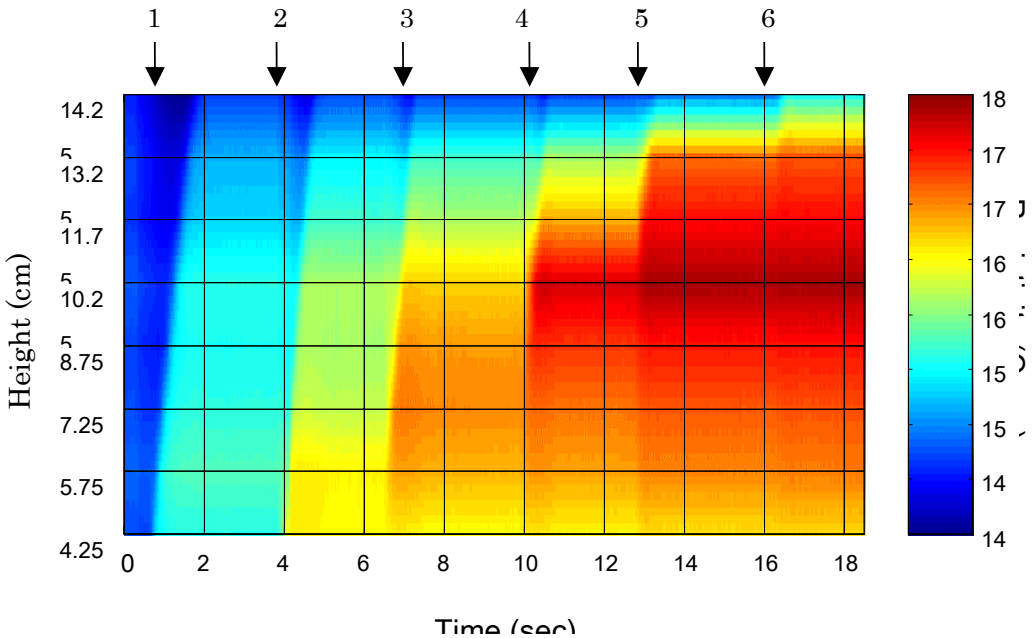

Figure 7. Resistivity measurements during successive six 4-second shakings

MONITORING OF RELATIVE DENSITY

In this section, we present an example of monitoring the relative density in addition to the resistivity measurements in liquefied sands. Pore water pressure and acceleration measurements were also taken during the experiment. Figure 8 shows the cylindrical chamber that was developed for use in the resistivity experiments. The bottom and top mesh electrodes are current electrodes that transmit electric current to the sample. Because of this arrangement of current electrodes, samples about the height of the chamber can be prepared for resistivity measurements. The potential electrodes are needle electrodes that are partially inserted into the chamber from the outside. The locations of the three accelerometers (A1, A2, and A3) as

well as two pore pressure transducers (P1 and P2) on the chamber are shown in Figure 8.

Toyoura sand was used in the experiments. The soil sample was prepared using boiling method. The height of the saturated sample in the chamber was about 50 cm. The remaining 10 cm of the chamber was filled with water. The box was placed on a small shaking table and 4-second excitation was applied. The waveform of the excitation was sine-wave with a frequency of 5 Hz. The amplitude of the acceleration was 600 cm/sec^2. Tests with different shaking accelerations and durations are reported in Jinguuji and others [8].

Figure 9a shows the resistivity results starting from 5 seconds before the beginning of the shaking. The resistivity values are converted to relative density in Figure 9b as explained in *the principle and method of resistivity monitoring* section. Figures 9c and d show the excess pore pressure and acceleration measured during the test. Because the accelerations recorded by three instruments were almost the same, only one recording is provided in the figure.

Higher excess pore pressures were measured at P2 than at P1. The excess pore pressures at both depths reached the initial liquefaction level right after the shaking started. The excess pore pressure at P2 stayed constant at this level until about 5 seconds after the shaking stopped. Then, it decreased to neutral position in 20 seconds. Figure 9b shows that when the excess pore pressure at the depth of P2 started to decrease, the relative density of sand started to increase. This particular time marked the beginning of settling of sand particles and the densification process at this depth. The same process was observed at the depth of P1, that is, the densification started at 20 seconds when the pore pressure at this depth started to decrease. An increase in the relative density was observed in most of the sand sample. The most significant increase was in the upper part of the sample where relative density change from 35 % to 50 % was measured.

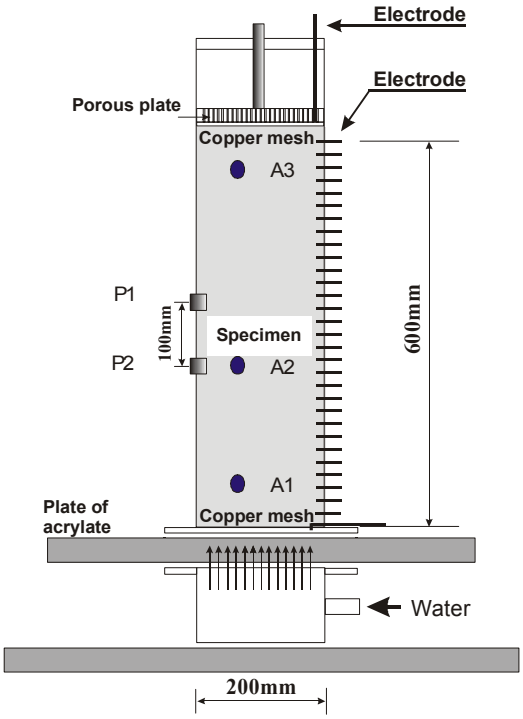

Figure 8. The schematic view of the small cylindrical chamber used in the resistivity experiments

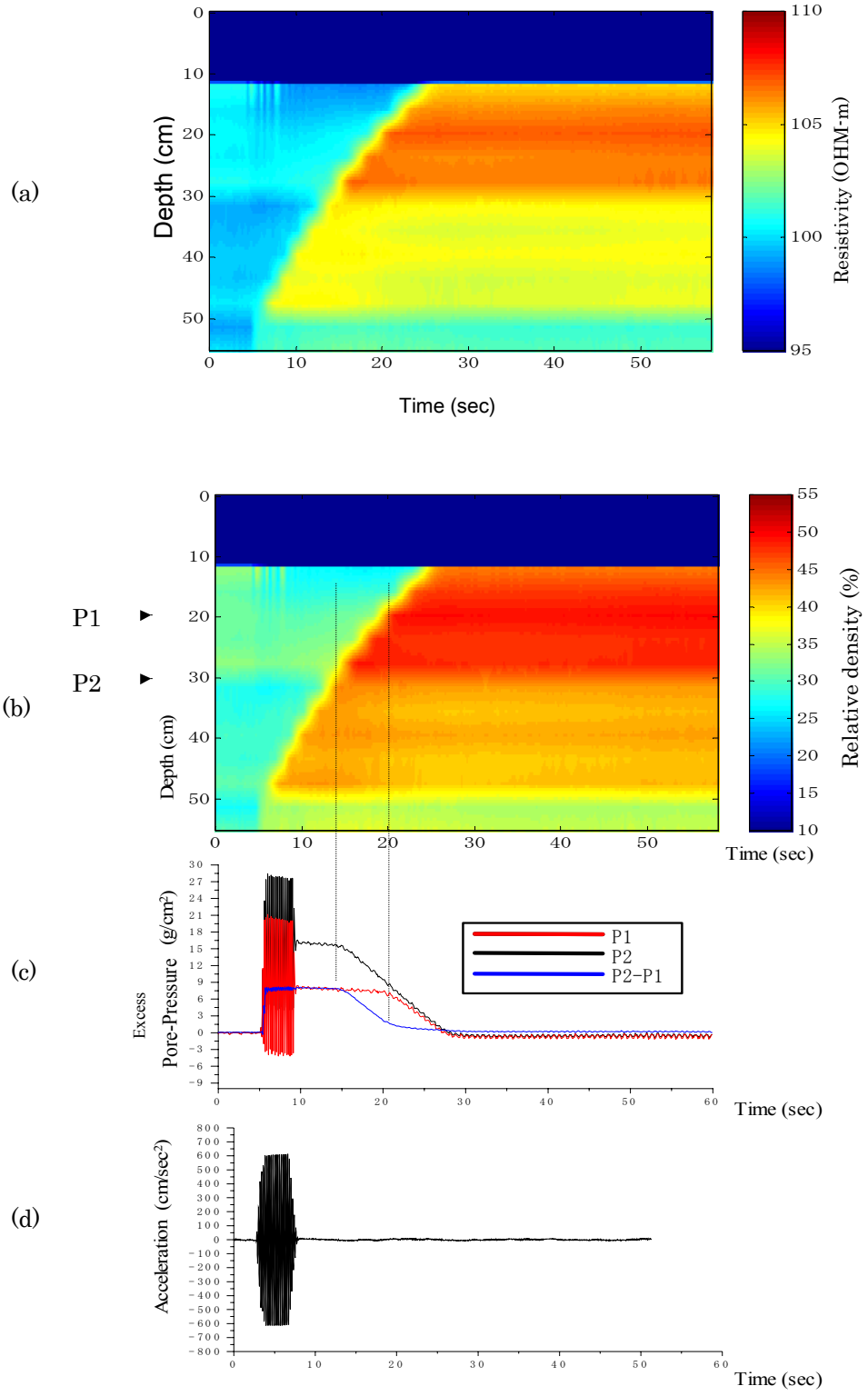

Figure 9. Monitoring of relative density during liquefaction experiment (modified from Jinguuji and others [8])

CONCLUSIONS

This paper presents a new technique to monitor and visualize the relative density in saturated soils during liquefaction and post-liquefaction stage. The technique utilizes the unique relation between soil electrical resistivity and porosity. The results from the laboratory experiments on homogeneous sands show that the resistivity measurements capture the behavior of liquefied sands.

Use of the technique in experiments with silts and silty sands should provide valuable insights into the behavior of these soils. Specially, the behavior of layered soils during liquefaction will be the subject of the future work. The technique is also promising for large-scale laboratory or field tests.

ACKNOWLEDGMENTS

Some of the tests were performed at Waseda University Geotechnical Engineering Laboratory. We thank Prof. Masanori Hamada and his students for the support and assistance.

REFERENCES

[1] Hamada, M. and T. D. O'Rourke. 1992. "Case studies of liquefaction and lifeline performance during past earthquakes," Technical Report NCEER-92-0001.

[2] Holzer, T. L. and S. Toprak. 1999. "Differential building settlements caused by liquefaction during the Izmit, Turkey, earthquake [abs]," Transactions, American Geophysical Union, Fall Meeting Supplement, 80(46): F673.

[3] Archie, G. E. 1942. "The electrical resistivity log as an aid in determining some reservoir characteristics," A.I.M.E. Transactions, 146: 54-62.

[4] Arulmoli, K., K. Arulanandan, and H. B. Seed. 1985. "New method for evaluating liquefaction potential," J. Geotechnical Engineering, 111(1):95-114.

[5] Tonks, D. M, S. D. Hunt, and J. M. Bayne. 1993. "Use of the conductivity probe to evaluate groundwater contamination," Ground Engineering, November: 24-29.

[6] Bellotti, R., J. Benoit, and P. Morabito. 1994. "A self-boring electrical resistivity probe for sands," XIII ICSMFE, New Delhi, India, pp.313-316.

[7] Jinguuji, M. and S. Kunimatsu. 1999. "The measurement of liquefaction phenomena by resistivity and its evaluation," BUTSURI-TANSA, 52 (5): 439-445 (in Japanese).

[8] Jinguuji, M., S. Kunimatsu, H. Izumi, and T. Mochizuki. 2001. "Development of visualization technique of relative density of sand during liquefaction using resistivity and consideration of the results," Japan Society of Civil Engineers, 680(III-55): 201-209 (in Japanese).

Liquefaction Potential of Native Ground in West Kobe, Japan by the Spectral Analysis of Surface Waves (SASW) Method

Robert Kayen, Yasuo Tanaka, Tadahiro Kishida and Shigetoshi Sugimoto

ABSTRACT

We present the results of a shear wave velocity investigation of native ground liquefaction test sites in West Kobe, Japan using a relatively new form of the Spectral Analysis of Surface Waves (SASW) method. This method uses a computer-controlled swept-sine wave source rather than the traditional random noise source consisting of a dropped weight or impact-hammer. This small study was a collaborative effort between the Japan Railway-West (JR), Kobe University, and the United States Geological Survey (USGS) to evaluate the characteristics of ground failure sites along the JR right-of-way in the Wadamisaki District of Kobe. The testing and analysis presented here part of a much larger ongoing liquefaction assessment study using SASW, for which we have already investigated over 230 sites in Japan, Taiwan, and the USA.

In the Wadamisaki District, the native beach soil deposit which suffered liquefaction damage during the 1995 Kobe Eathquake are part of the distal end of a suite of narrow distributary alluvial fans that emanate from the south slope of the Rokko Mountains. The native alluvial zone stretches through the city approximately 20 km in the east-west direction and is about 2 km wide on average. In the Wadamisaki district, the south and north ends of the JR right-of way suffered liquefaction and related settlements, whereas the central portion of the district near the railroad alignment was not damaged.

In November 2001, we investigated 11 sites in the Wadamisaki District, along the JR-West right of way. We found that the liquefied areas in the southern portion of the right-of-way corresponded to a gravely-sand alluvium that is slightly lower in shear wave velocity than the central and northern portion of the right-of-way. These data from liquefied sites plot very close, though rightward of the current recommended NCEER boundary curves. With the larger shear wave velocity data set from Japan, Taiwan, China and the USA, our objective is to gather enough data from high-ground-motion-intensity sites to fully characterize the upper cyclic-stress-ratio region of the shear wave velocity liquefaction-resistance boundary.

Robert Kayen, rkayen@usgs.gov, United States Geological Survey, MS-999, 345 Middlefield Road, Menlo Park, CA 94025, USA & Visiting Professor, Kobe University, RCUSS, Kobe, Japan, 2001-2002.

Yasuo Tanaka, ytgeotec@kobe-u.ac.jp, Professor, Kobe University, RCUSS, 1-1 Rokko Dai, Nada Ku, Kobe, 657-8501 Japan.

Tadahiro Kishida, tkishida@ucdavis.edu, Graduate Student, University of California, Department of Civil and Environmental Engineering, One Shields Avenue, Davis, CA 95616-5294 USA.

Shigetoshi Sugimoto, Graduate Student, Kobe University, RCUSS, Kobe, 657-8501 Japan.

INTRODUCTION

During the Japanese 2001-2002 academic year, we began a field investigation to gather shear wave velocities at liquefaction field performance sites in Asia and the USA with the goal of significantly expanding the worldwide catalog of velocity profiles for liquefaction resistance correlation. Of the many noteworthy observations of Andrus and Stokoe [1], in their assessment of the then available data set, was the paucity of shear wave velocity data in the cyclic stress ratio (CSR) region above 0.3. This is especially the case for sites with high shear wave velocities near the area where the liquefaction resistance boundary likely resides. Historically, liquefaction events of high CSR are concentrated in Japan and Taiwan, especially in the Tohoku region; the island of Hokkaido; Fukui city; Kobe city; and the central-Taiwan cities of Wufeng and Nantou, proximal to the Chi Chi fault. Prior to this study, most of these sites had not been comprehensively evaluated using shear wave velocity.

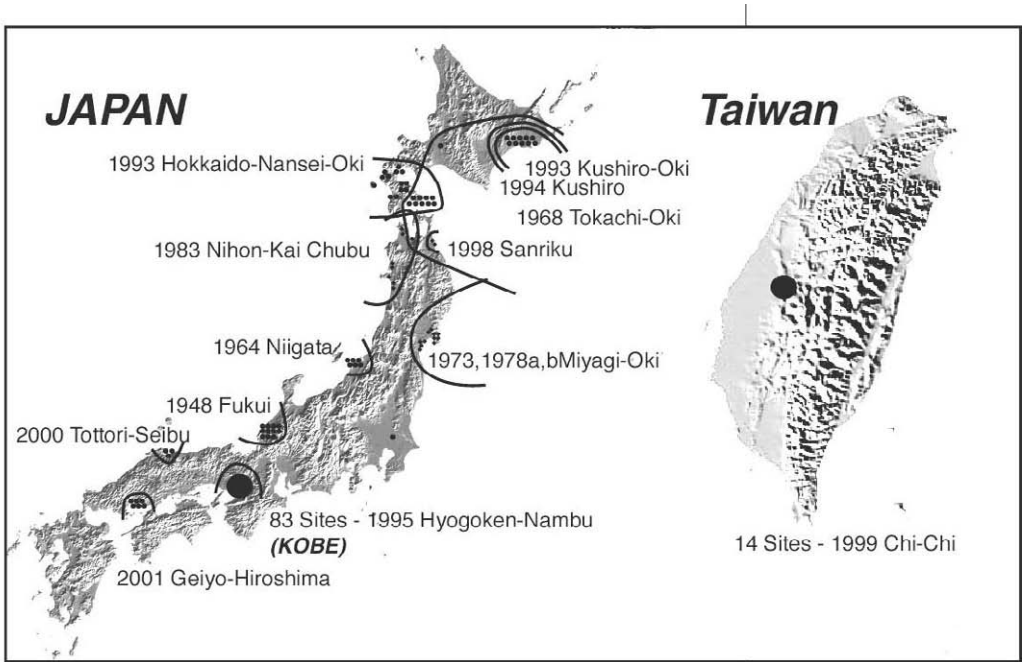

Figure 1. New test locations in Japan (168 sites) and Taiwan (14 sites) visited during 2001-2002 and profiled by the Spectral Analysis of Surface Waves (SASW) method. Many of the liquefaction sites in Tohoku and Hokkaido regions have been affected by 2-4 damaging events in the last 40 years.

To expand the existing shear-wave-velocity data set to include these high-ground-motion-intensity sites, we are using the Spectral Analysis of Surface Waves (SASW) method, a non-invasive, non-destructive test (NDT) for evaluating the shear-wave-velocity characteristics of soil in the field [2]. SASW is particularly useful for rapid, lightweight, high-resolution surveys of the near surface, and can readily profile problematic materials, such as stiff-gravely deposits, and problematic sites, such as very-soft surfaces or sloping ground, where conventional truck-based penetration-methods typically fail. SASW apparatus can easily be deployed at locations impossible to reach by vehicle or truck. The equipment easily fits in an automobile, is deployed by hand, and can be operated by just one person. Using this method it is possible to routinely produce detailed shear wave velocity profiles of the upper 20-30 meters of the soil column.

While the first author was visiting Kobe University on sabbatical in 2001 and 2002, we profiled 182 sites that could be evaluated for liquefaction performance in Japan and Taiwan by SASW (Figure 1). Nearly all of the well-documented post-war liquefaction test sites in the

Japanese and Taiwanese literature, originally evaluated by conventional penetration apparatus, were re-evaluated using SASW in our study. Earthquake-induced liquefaction events in our study date from the most recent large damaging events in Japan and Taiwan (2001 Geiyo and 1999 Chi Chi, respectively), back to the disastrous 1948 Fukui earthquake. These liquefaction events, and the sites tested, represent the majority of the world's well-documented case histories of liquefaction occurrence in modern times. An important focus of our study is to test sites that straddle the liquefaction resistance boundary, and to seek out relatively stiff native soil sites exposed to high intensity motion (e.g. Hyogoken-Nambu 1995; Hokkaido Nansei-Oki 1993; Chi Chi, 1999; Fukui 1948; Kushiro-Oki 1993). The data from this study will allow us to reevaluate the shear wave velocity-based liquefaction resistance curve in light of a more complete and global data set.

PILOT STUDY: WADAMISAKI DISTRICT of WEST KOBE, JAPAN

In this paper, we present a pilot study that helped refine our field and data processing procedures as we acquired of the larger data set. The West Kobe study data represent about 5% of the field sites visited in 2001-2001. The Wadamisaki district is in the Hyogo Ward of Kobe City, an area badly affected by the M_w=6.8 Hyogo-Nambu (South Hyogo Prefecture) earthquake that struck in the early morning of January 17, 1995 [3, 4]. The rupture occurred on a northeast trending structure extending from Awaji Island to the south west, through the Cities of Kobe, Ashiya and Nishinomiya to the Northeast on the main island of Honshu. The fault is several kilometers to the north of our study area. The seismic intensity maximum was JMA-VII (equivalent to MMI = X~XII) in a near-source-zone approximately 2-to-3 km in width, and centered approximately 1-2 km south of the fault trace. This zone stretched 40 km, or so, fault parallel along the margin of Osaka Bay.

Our study area is located on the southern side of the high intensity zone, in a densely populated neighborhood comprised of shoreline industrial and port facilities, multi-storey apartment structures and one- and two-storey residential housing (Figure 2). In the north end of the Wadamisaki District along the Hanshin Expressway, the strong-motion intensity is estimated to have been approximately 0.6g, based on the recorded motion of 0.64g at the JR Takatori Station [3,4]. The district is situated on reworked beach and dune deposits from an alluvial fan distributing eroded granitic soil from the south slope of the Rokko Mountains. The reworked Holocene fan thickness in the study area is typically 6-10 meters and overlies Pleistocene Osaka Bay mud and older alluvium. Due to the steeply dipping granite of the coastal mountains, the soil depth to bedrock is estimated to be in the range of 1000-to-1500 meters [5]. Man-made coastline and islands, south of our study area, have extended the southern reaches of the city into Osaka bay. When unimproved, these deposits are generally highly liquefiable soil-fills.

Our study is focused on the native Holocene reworked alluvial deposits in the uppermost 10 meters of the soil column, above the most recent Pleistocene marine unit. Native soil beneath the southern portion of the district near the JR Wadamisaki Station (test site 106-KOBE and 107-KOBE) and later-built Kobe Wing-Dome (near and south of test site 108-KOBE) and northern portion near and north of the Hanshin Expressway (test site 138-KOBE) suffered marginal liquefaction damage (sand boils and minor fissures) and minor settlements (<10cm). Lateral deformations along the survey line were negligible. The central portion of the district, in the area immediately north and south of the Hyogo Canal (the canal is between sites 113KOBE and 110KOBE), was not affected by liquefaction with the exception of very small and isolated sand vents. The general geotechnical characteristic of the upper 10 meters is of native alluvium that varies slightly in liquefaction resistance, and straddles the liquefaction resistance boundary at very high CSR-levels of earthquake loading.

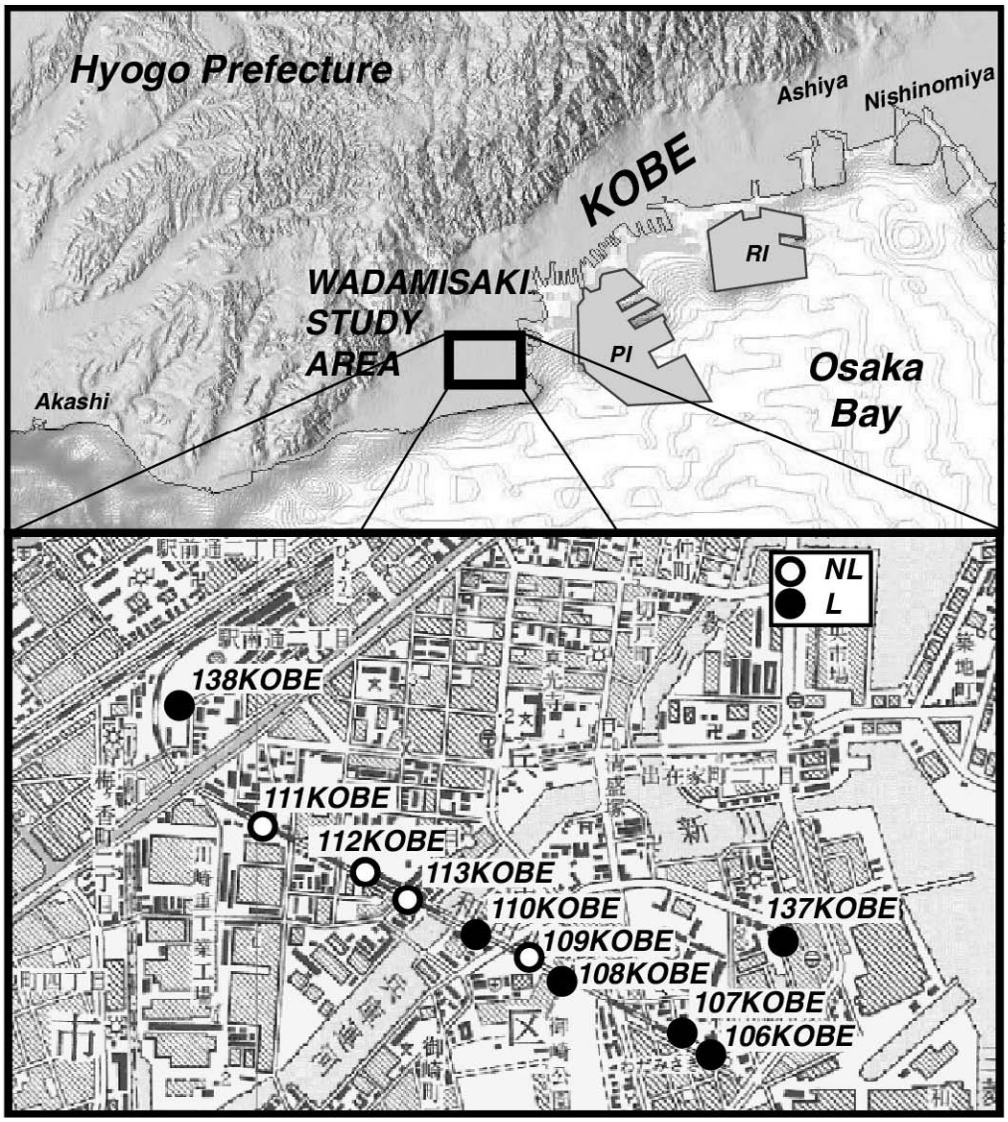

Figure 2. The Wadamisaki district is located in the western-Hyogo Ward of Kobe City, in Hyogo Prefecture. Our numbered test sites fall along the JR-West Wadamisaki railroad feeder-line built in 1890 (Dashed). Sites that experienced liquefaction (L) are solid circles; and sites that did not experience liquefaction sites (NL) are open circles. Many other sites were also tested in Kobe, Port Island (PI), Rokko Island (RI), Ashiya, and Nishinomiya.

METHODS

The Spectral-Analysis-of-Surface-Waves (SASW) method is a relatively new seismic tool to evaluate the stiffness characteristics of soil deposits. SASW is especially useful for profiling gravelly deposits where sampling is difficult and penetration tests fail to characterize or quantify soil properties [6, 7, and 8]. Surface wave methods are highly efficient field tests for profiling the near surface, principally because all measurements are made at the ground surface, are non-invasive, and result in a highly detailed-shear wave model of the ground. Unlike drilling and probing methods, SASW apparatus is lightweight, portable, easily deployable by one or two people, and typically requires no permitting to perform. With vertical excitation of the ground, surface waves carry 67% of the radiated wave energy, and, thus, surface waves carry the highest particle motion amplitudes.

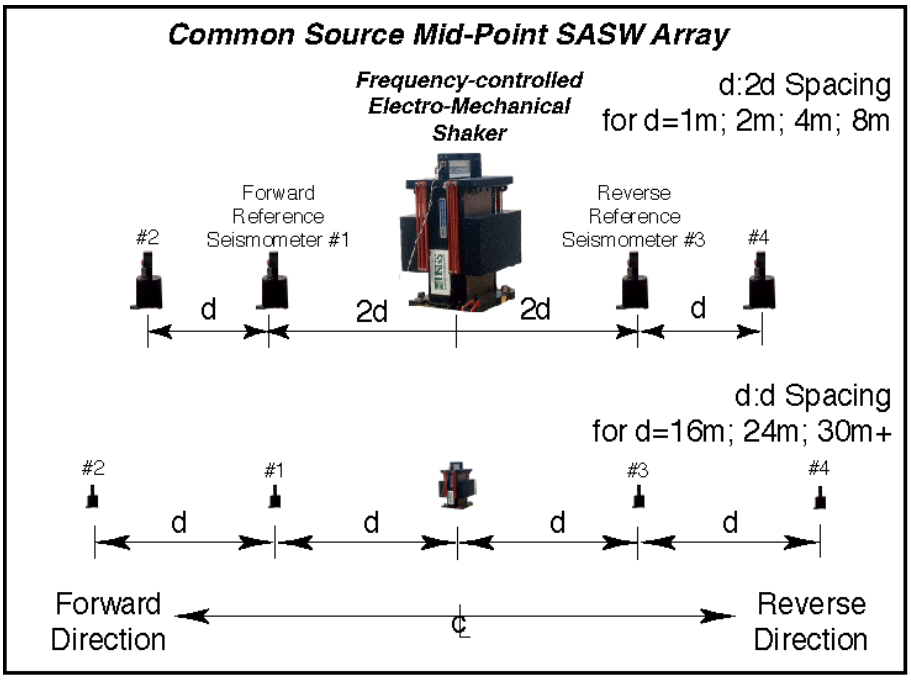

Figure 3. Common source mid-point array for profiling with a 100 kg electro-mechanical shaker. The shaker apparatus allows for controlled-frequency swept-sine SASW analysis. Array separation changes from d:2d to d:d to increase the amplitude of the signal received at sensor 2 and 4 for large array separations.

Dispersive surface waves are waves that vary in velocity with respect to frequency. The dispersive nature of surface waves forms the basis of the SASW method, as the dispersion is a direct result of heterogeneity of the sub-surface velocity structure. During the SASW test, field measurements of surface wave dispersion are recorded using multiple arrays of seismometers. Our field configuration for SASW uses a computer-controlled electromechanical shaker as the mid-point of the array (i.e., Common-Source Midpoint), with four seismometers arrayed in pairs of two and aligned in opposite directions of the source (Figure 3). We use an APS-Dynamics shaker that can produce sinusoidal waves from to 1-1000 Hz (note: any use of trade names or products does not imply endorsement by the U.S. Government). Using a low frequency shaker-source allows for deeper penetration of surface waves and elevated signal-to-noise ratio as compared with a conventional random-noise hammer source. We use the shaker to produce controlled vertical vibrations between 1-150Hz.

The 1-Hz Kinemetrics receivers we use are designed for capturing vertical motions and cover the frequency range of interest in the active-source surface-wave test. For each source-receiver configuration, surface waves are generated by the shaker, controlled by an output waveform from the spectral analyzer. An amplifier boosts the analyzer signal in order to drive the electromechanical motor in the shaker. The receivers measure the waves and a fast Fourier transform (FFT) is performed on each of the four receiver signals. In near-real-time, the linear spectra, cross power spectra, and coherence are computed. The ability to perform near real-time frequency domain calculations and monitor the progress and quality of the test allows us to adjust various aspects of the test to optimize the capture of the phase data. These aspects include the source-wave generation, frequency step-size between each sine-wave burst, number of cycles-per-frequency, total frequency range of all the steps, and receiver spacing.

The common receiver midpoint geometry of Nazarian and Stokoe [2] was not used here, given the weight of the electromechanical shaker. Rather, we adopted common source-midpoint geometry. That is, we placed the source at the centerline of the survey so that the forward and

reverse direction dispersion curves were equidistant from the source for each given array spacing. Several different spacings of receivers are used in the field, and the dispersion curves for each spacing, both in forward and reverse directions, are merged to build a site-dispersion plot. Spacing of receivers used at the Wadamisaki sites stepped geometrically from 1 meter to 24 or 32 meters. The two seismometers are separated by a given distance, d, and the source is usually placed at a distance of 2d from the first [9] seismometer. As the test progresses from capturing high frequency data to lower frequency data, the array separation increases until the d:2d spacing becomes impractical, either due to space limitations, or the attenuation of longer period surface waves. Typically at source distances equal or greater than 16m, the array spacing was changed to d:d. Sanchez-Salinero *et al.* (1987) investigated the variations in the measured dispersion curves given various ratios of d:nd and found that n-values between 1 and 2 were a good compromise between problems associated with near-field effects and distal-wave attenuation.

Given the array separation, the phase of the cross power spectrum is used to calculate the relation between Rayleigh-wavelength and frequency (lambda spectra), and the wavelength and frequency are, in turn, used to compute the phase velocity curve. A simple empirically based method is used in the field to make an initial approximation of the shear wave velocity profile, where one-third the wavelength, λ, is assumed to be the representative depth of the corresponding phase velocity [10]. The shear-wave velocity at $\lambda/3$ is estimated as 1.10 times the computed phase velocity. The actual ratio of V_s / V_R depends on Poisson's ratio and varies from 1.05 to 1.14, and a value of 1.1 is commonly used for saturated soils. For the final velocity profile a numerical approach is used to compute a more accurate estimate of the shear-wave velocity profile by inverting the phase velocities assuming horizontal layering [11, 12]. The empirical and inversion methods compare reasonably well for sites with stiffness properties that vary gradually with depth, slowly and monotonically increase in stiffness, or are uniform in stiffness [13].

LIQUEFACTION ASSESSMENT and VELOCITY DETERMINATION

Preparing data for the liquefaction analysis involves normalizing the shear wave velocity following the standard procedure outline in NCEER-Workshop guidelines [14], and selecting critical layers based on SPT data. The objective of the overall project is to expand the shear-wave-velocity data-set for liquefaction sites. Where it is possible, we also independently estimate the thickness of the liquefied layer and fines contents using penetration data so that there are external controls on the selection of representative shear wave velocities for the critcal layer. At the Wadamisaki district sites, we used a large suite of SPT logs cataloged and available in the KOBE JIBANKUN Geographic Information System (GIS) [15] to independently evaluate stratigraphy, liquefaction potential, and target the depth-range of the representative shear-wave velocity of the liquefaction layer. These logs were also processed using the NCEER-Workshop guidelines [14]. Grain-size distributions for the critical layer were surprisingly uniform along the alignment and had a mean fines-content (<0.074mm) of 8.3% and a standard deviation of 2.8%. We found the association between locations predicted to liquefy using the NCEER-Workshop guidelines for SPT and the actual surface observations presented in the maps of Hamada et al. [16] to be excellent. That is, based on surface observations, the Workshop-SPT guidelines correctly predicted liquefaction potential.

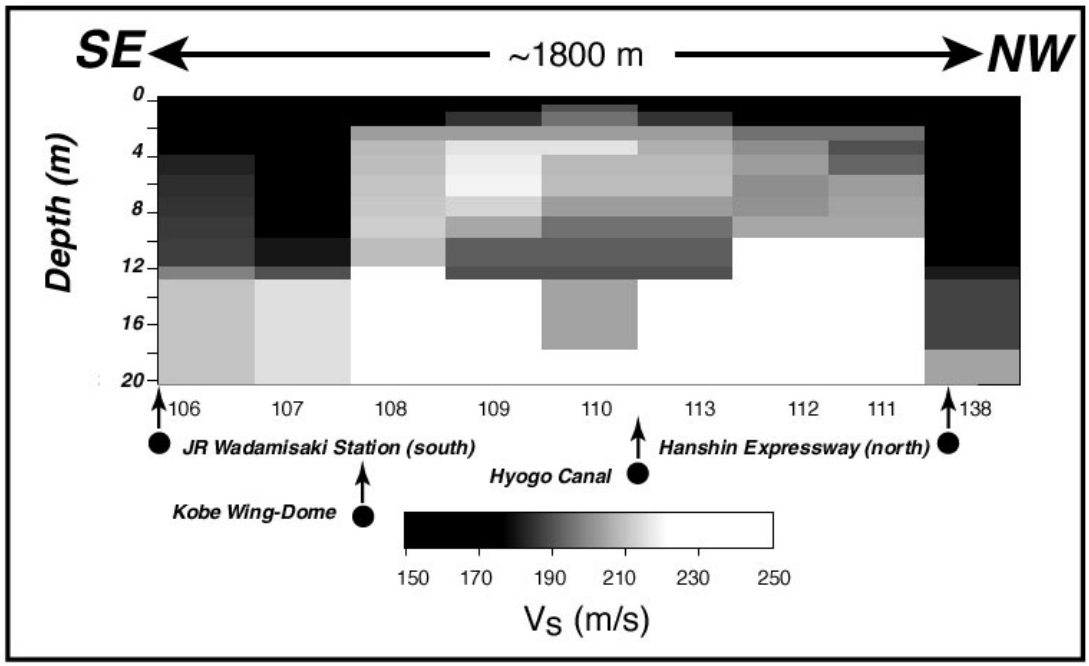

Figure 4. Shear wave velocities for nine sites along the JR-WEST Wadamisaki feeder-line. The profile stretched across slightly less than 2 kilometers of the ground. Numbered test sites are printed below the velocity profile with the KOBE-locator removed. Circles and arrows indicate major structures along the JR right-of-way.

Shear wave velocities along the JR Wadamisaki corridor are plotted as a GIS image in Figure 4. The survey station numbers extend from the south-east end of the line at Wadamisaki Station (Site 106KOBE), to the railroad curve just north of the Hanshin expressway, a distance of 1800 meters (site 138KOBE). The profiles typically show an increase in shear wave velocity to a depth of approximately 3-to-5 meters, and beneath it a somewhat uniform velocity zone within the Holocene sand deposit to a depth of approximately 7-9 meters. Below the Holocene sand is a lower velocity estuarine mud deposit and a deeper and higher velocity Pleistocene alluvium. The shear wave velocities do indicate that the southern portion of the transect have lower velocities in the Holocene sand deposit than does the northern portion. The velocities are consistent with observations that the southern part of the railway right-of way had surface evidence for liquefaction, whereas the portion north of the Hyogo canal and south of the Hanshin Expressway with minor exceptions did not [16]. Thus velocities of the non-liquefied and liquefied ground along the corridor seem to have straddled the liquefaction-triggering boundary during the Hyogo-Nambu event.

The effective stress-normalized velocities of the critical layers identified using the SPT approach are presented in Figure 5. The velocities of the sites are presented as sold (liquefied) and open (non-liquefied) circles, along with ±1 standard deviation ellipses. CSR values are based on the peak ground acceleration recorded at the JR Takatori Station (0.64g) and attenuated for increasing source distance using the model of Boore, et al. [17]. For the Wadamisaki sites, data points transition into the liquefied zone at approximately 215-220 m/s. This velocity range is very close to the range proposed by Andrus and Stokoe [1] for soils having fines contents at or below 5 % (215 m/s).

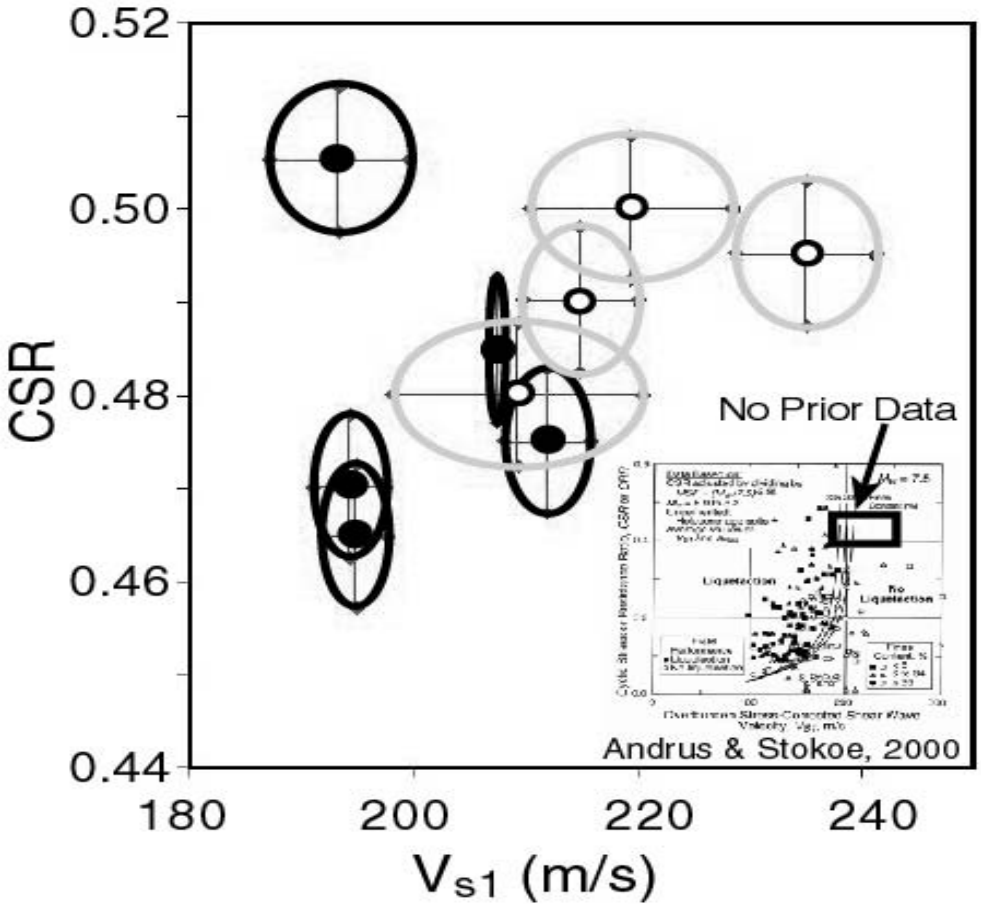

Figure 5. Cyclic stress ratio versus normalized shear wave velocity for the Wadamisaki district sites. The data fall in a high CSR area populated with no prior data. Solid points are the mean velocities of the liquefied layer. Open circles are non-liquefied sites. Ellipses define 1 standard deviation values.

SUMMARY and CONCLUSIONS

This paper presents procedures we are using to expand the world-wide data set of shear wave velocities measured at liquefaction test sites. The elements of the method are to catalog the locations of reported liquefaction test sites and gather available conventional penetration resistance profiles; identify critical layers and their textural characteristics; re-test sites by SASW; and, finally, apply the penetration data-based critical layer range to the SASW velocity profiles to select representative shear wave velocities. The primary objective of our data collection phase is to expand the world-wide data set for shear wave velocities at high CSR sites. Combining the nearly 200 sites in Japan and Taiwan with our USA sites, and prior case histories [1], we are re-evaluating the shear wave-based liquefaction resistance curves within a Bayesian probabilistic framework and methods developed for structural reliability.

Here, we present an example data set, approximately five-percent of our tested sites, and describe how the data are collected and processed prior to the Bayesian updating analysis. The Wadamisaki sites are typical of many locations we tested in Japan and Taiwan that bridge the liquefaction resistance boundary at high CSR. In this study we found that the SASW field and data processing approach worked well to characterize the shear-wave-velocity of the ground, and that the use of an independent data set of penetration logs allow us to select critical layers in an unbiased manner. It is our hope that with the entire data set of nearly 300 US and Asia locations evaluated this way, we will be able to populate enough data points in the region of high CSR and

high shear wave velocity to constrain the boundary curves in this important region of the liquefaction resistance curve.

ACKNOWLEDGEMENTS

Components of this work were supported by the United States Geological Survey; the Pacific Earthquake Engineering Research Center (PEER); Pacific Gas and Electric Company (PG&E); and a USGS Cooperative Research and Development Agreement with Kobe University, Japan. Prof. Ken Stokoe II and Leo Brown provided the USGS with considerable field and data processing advice, as well as SASW hardware recommendations, during Brown's visit to Menlo Park. The thoughtful reviews of Homa Lee and Stephanie Ross are appreciated.

REFERENCES

[1] Andrus, R.D. and Stokoe, K.H., II, Liquefaction Resistance of Soils From Shear-Wave Velocity, *Journal of Geotechnical and Geoenvironmental Engineering, American Society of Civil Engineers*, Vol. 126, No. 11, November 2000, pp. 1015-1025.

[2] Nazarian, S. and Stokoe, K. (1984) In Situ Shear Wave Velocities from Spectral Analysis of Surface Waves, *Proceedings, Eighth World Conference on Earthquake Engineering, San Francisco, California*, Vol. III, pp. 31-39, 1984

[3] Ejiri, J., Sawada, S., Goto, Y., and Toki, K. (1996) Peak Ground Motion Characteristics. *Special Issue on Geotechnical Aspects of the January 17, 1995 Hyogoken-Nambu Earthquake, Soils and Foundations*, p. 7-13.

[4] Oka, F., Sugito, M., Yashima, A. Taguchi, Y. and Sekiguchi, K. (1996) Analysis of strong motion records from the South Hyogo earthquake of January 17, 1995. *Engineering Geology*, V. 43, 85-106.

[5] Fujita, K. and Maeda, Y. (1984) *Geology of the Suma district*. Geological Survey of Japan (in Japanese).

[6] Stokoe, K. and Nazarian, S. (1985) Use of Rayleigh Waves in liquefaction Studies, *in*, R.D. Woods, ed., *Measurement and use of Shear Wave Velocity for Evaluating Dynamic Soil Properties*. ASCE, New York, 1-17.

[7] Stokoe, K., Nazarian, S., Rix, G.J., Sanchez-Salinero, I. Sheu, J.-C., Mok, Y.J. (1988) In situ Seismic Testing of Hard-to-Sample Soils by Surface Wave Method. Earthquake Engineering and Soil Dynamics II - *Recent Advances in Ground-Motion Evaluation*, Geotech. Spec. Pub. No. 20, J.L. Von Thun, ed., ASCE, New York, 264-289.

[8] Tokimatsu, K. (1997) Geotechnical site characterization using surface waves. K. Ishihara, ed. *Earthquake Geotechnical Engineering*, Balkema Press, Rotterdam, p. 1333-1367.

[9] Sanchez-Salinero, I., Roesset, J.M., Shao, K-Y., Stokoe, K.H., Ii, Rix, G.J. (1987) Analytical Evaluation Of Variables Affecting Surface Wave Testing Of Pavements, *Transportation Research Record No.1136*, Pp.86-95.

[10] Gazetas, G. and Yegian, M.K. (1979) Shear and Rayleigh Waves in Soil Dynamics, *Journal of the Geotechnical Engineering Division*, ASCE,105(12), 1455-1470.

[11] Haskell, N.A. (1953) The Dispersion Of Surface Waves On Multilayered Media, *Bulletin Of The Seismological Society Of America*, Vol.43, Pp.17-34.

[12] Thomson, W.T. (1950) Transmission Of Elastic Waves Through A Stratified Solid Medium, *Journal Of Applied Physics*, Vol.21, Pp.89-93.

[13] Heukelom, W., Foster, C.R. (1962) Dynamic Testing Of Pavements *Transactions A.S.C.E.*, Vol.127, Part 1, p.425-451. Discussion, p.451-457.

[14] Youd, T.L., Idriss, I.M. Andrus, R.D. Arango, I., Castro, G., Christian, J.T., Dobry, R., Liam Finn, W.D.L., Harder, L.F., Jr., Hynes, M.E., Ishihara, K., Koester, J.P., Liao, S.S.C., Marcuson, W.F., III, Martin, G.R., Mitchell, J.K., Moriwaki, Y., Power, M.S., Robertson, P.K., Seed, R.B., Stokoe, K.H., II, 2001, Liquefaction Resistance of Soils: Summary Report from the 1996 NCEER and 1998 NCEER/NSF Workshops on Evaluation of Liquefaction Resistance of Soils, ASCE, *Journal of Geotechnical and Geoenvironmental Engineering*, V. 127, No. 10, p 817-833

[15] Tanaka, Y. And Okimura, T. (2001) In-Depth Geotechincal Data Base: Kobe Jibankun For Seismic Hazard Study. Workshop on Archiving and Web Dissemination of Geotechnical Data, Consortium of Organizations for Strong Motion Operating Systems, *Pacific Earthquake Engineering Research Center, PEER*, October 4-5, 2001.

[16] Hamada M., Isoyama, R., and Wakamatsu, K. (1995) The 1995 Hyogoken-Nambu (Kobe) Earthquake: Liquefaction, Ground Displacement and Soil Condition in the Hanshin Area. *Assoc. for Development of Earthquake Prediction*, Tokyo, 194 p.

[17] Boore, D. M. Joyner, W.B. and Fumal, T.E. (1997) Equations for Estimating Horizontal Response Spectra and Peak Acceleration from Western North American Earthquakes: A Summary of Recent Work, *Seismological Research Letters, 68,* January/February.

Experimental Evaluation of Viscid Properties of Liquefied Sand

Jun Kawamura, Kenji Hattori and Hirokazu Akagi

ABSTRACT

Earthquakes cause liquefaction of saturated loose sand. In the great Hanshin-Awaji earthquake of 1995, many revetments and foundations of structures were seriously collapsed by liquefaction in seaside reclaimed ground, and lateral flow damaged buried pipelines of lifeline and foundation piles. Therefore, studies on predicting lateral flow are vital for geotechnical engineering. Recently, the results of model tests are employed to point out that liquefied sand behaves like a viscous fluid. The purpose of this study is to evaluate the physical properties of liquefied sand through changes in the apparent coefficient of viscosity of liquefied sand. The shear resistance of liquefied sand was measured with a hollow cylindrical torsion shear test.

Key Words: Fully saturated sand, liquefaction, torsion, pore pressure, lateral flow

Jun Kawamura, Student, Graduate School of Science and Engineering, Waseda University, 3-4-1 Ohkubo, Shinjuku, Tokyo 169-8555, Japan

Kenji Hattori, Former student, Graduate School of Science and Engineering, Waseda University

Hirokazu Akagi, Professor, Department of Civil Engineering, Waseda University

INTRODUCTION

Earthquakes cause liquefaction of saturated loose sand and lateral flow of liquefied sand. Because of the ground vibration of an earthquake, floating particles of sand in the pore water become like slurry, causing “liquefaction”. Lateral flow implies the soil movement due to even slight inclinations in ground, composed of loose sand that has become liquefied. Hence, liquefaction is often followed by lateral flow, or the phenomenon of ground displacement in a horizontal direction on the order of a meter. The average shear strain of the liquefied layer falls into the several tens to hundreds percentage range. After a seismic vibration, a great displacement is induced that differs from the phenomenon of slope failure in that even the ground beneath a surface that can almost be thought to be horizontal from the engineering view point (1 to 2% or less). Because this great displacement in the ground takes place, many revetments and foundations of structures can be seriously collapsed by liquefaction in seaside reclaimed ground, while lateral flow can damage buried pipelines of lifeline and foundation piles. Because most of the great cities exist on loosely deposited ground, which can easily be liquefied, damage to urban structures by lateral flow is immeasurable. Japan suffers tremendous damage from liquefaction and lateral flow due to her many earthquakes. Therefore, studies on how to predict lateral flow followed by liquefaction are necessary for geotechnical engineering.

Investigating the mechanisms by which lateral displacement of ground by liquefaction occur and finding a way to predict it must begin with the results of case analyses of actual earthquake events, flow tests of model ground, and studies of the engineering properties of liquefied sand (Hamada et al. 2000[1]) . Although the results of ground model tests depend on the velocity and liquefied ground resistance, it has been shown that liquefied sand itself behaves like a viscous fluid. The shear resistance of liquefied sand is measured by performing hollow cylindrical torsion shear testing. Assuming that liquefied sand was a viscous fluid, the viscid properties of liquefied sand were quantitatively evaluated by determining a coefficient of viscosity.

OUTLINE OF TEST

Sample and Testing Apparatus

Toyoura fine sand was used for the samples. Each specimen was a hollow cylinder with a height of 100mm height, an inner diameter of 30mm, and an outer diameter of 70mm. Physical properties of the sample are given in Table.1. In order to reduce friction between the rubber membrane and the specimen, a smooth membrane-sheet 1μm thick was employed to cover around the specimen.

One problem of the hollow torsion shear test is

Table.1 Physical properties of sample

Sample	Toyoura fine sand
Density of soil	2.639 g/cm^3
sand	94.80%
silt	1.82%
clay	3.38%
Max grain size	0.85mm
Max density	1.646 g/cm^3
Min density	1.353g/cm^3

that the tension of the rubber membrane influences the testing data. As a new method of compensating for the rubber membrane tension, the circumference part of the pedestal rotates as well as the top cap simultaneously. Then, the device was improved so that the test might be done without the rubber membrane being twisted. The structure of this device, including the rotating pedestal, is shown in Fig.1.

Axial pressure, axial displacement, torque, rotational displacement, lateral pressure and pore water pressure were measured during the undrained shear test by a digital dynamic strain meter. The measured data were recorded directly into the mobile computer directly. The test apparatus is given in Fig.2

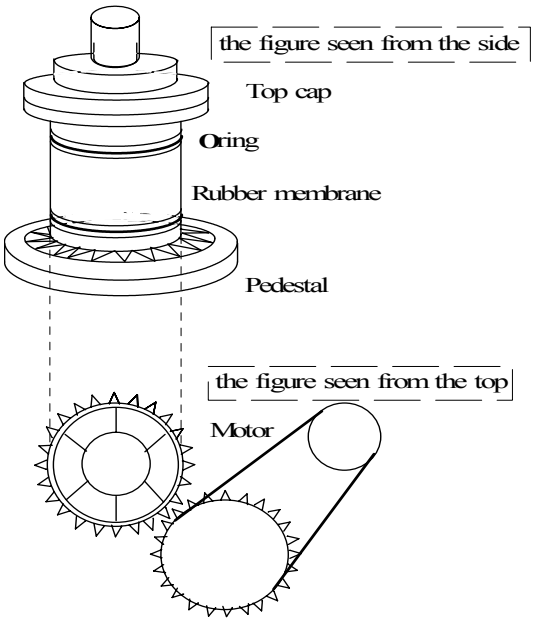

Fig.1 The structure of pedestal

Test Procedure

Specimens were created using the air pluviation method with a relative density of 40%, permeated by water, and frozen in the freezer. After freezing, each specimen was set on the pedestal base and melted in negative pressure. After melting, negative pressure was changed into confining pressure, and the void of the specimen was filled with carbon dioxide. Then, the specimen was permeated by de-aired water and was saturated by using backpressure of 0.2 MPa. The target value of B was over 0.95.

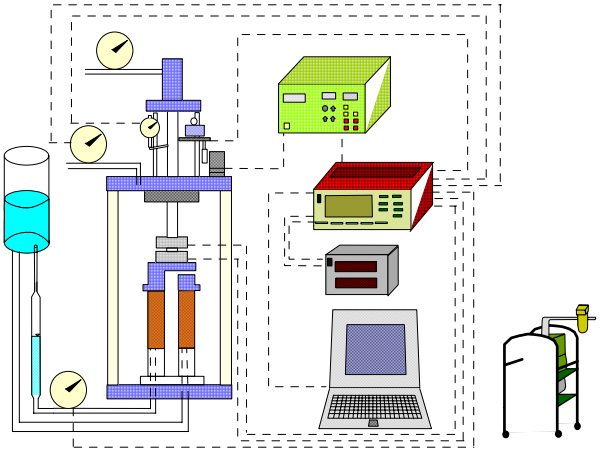

Fig.2 The system of test apparatus

The specimen was consolidated isotropically under constant confining stress. Axial displacement and change in volume of specimen were measured.

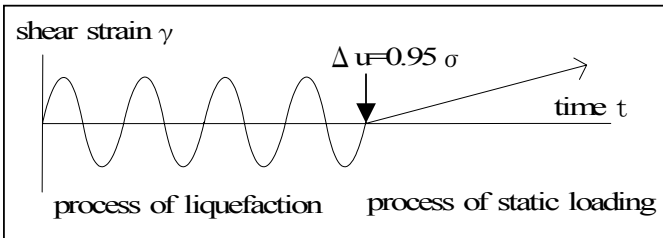

Fig.3 The process of loading

After completion, an undrained cyclic torsion shear test was performed. When excess pore water pressure became 95% of the confining pressure, the specimen was considered to be liquefied, and the cyclic shear test was ended. Then, undrained static torsion shear test was conducted to measure the shear resistance of liquefied sand. The data were analyzed after the undrained static shear test was performed. Each

datum had been recorded in the personal computer.

The loading process of the test at this procedure is shown in Fig.3, and a flow chart of the test procedure is shown in Fig.4. The test was performed with the above process; the coefficient of viscosity of the liquefaction of sand was calculated from the experimental data mentioned above.

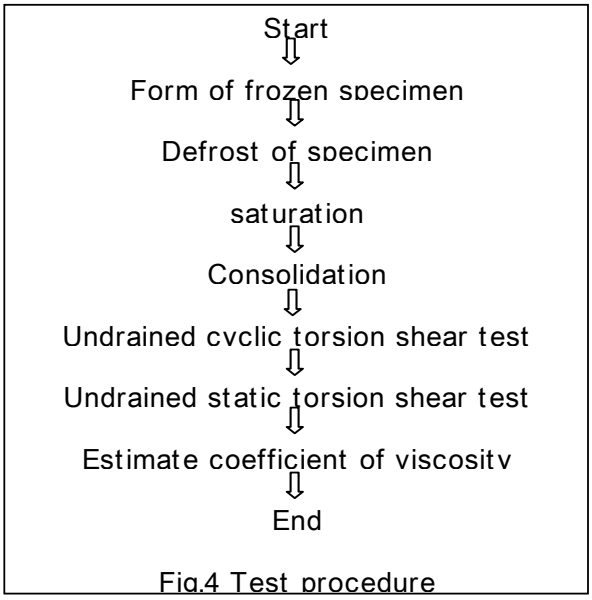

Fig.4 Test procedure

Testing Conditions

Shear strain rate and confining pressure were used as the variable testing conditions. In addition, to evaluate the effect of rubber membrane tension, the tests without pedestal rotation and the blank tests with and without dummy rubber specimen were carried out. The condition of 40% relative density of the specimen was used in all the experiments. Table 2 summarizes the test conditions. The tests were performed several times under each condition to confirm the results.

Table.2 Test condition

Sample	Confining pressure (Mpa)	Strain rate (%/min)	Rotation
Toyoura fine sand	0.05	10	○
	0.1	20	
	0.2	30	
	0.1	30	×
Water	×	30	×
Dammy	0.1	30	×
	0.1	30	○
Only dammy	×	30	×

The rubber membrane filled with the de-aired water was used for the specimen in one of the test conditions in Table 2, indicated by “water”. The dummy specimen is made of rubber, whose dimensions are the same as the sand specimen. Except for the cyclic loading torsion shear for liquefaction, the torsion shear test was performed by the same process as when a sand sample was used. Just the dummy specimen was used in the test, where torsion shear was done without attaching rubber membrane and membrane sheet. Because confining pressure could not be loaded in this case, it is shown with an × in Table 2.

The cases in which rubber membrane tension was compensated by rotation of the pedestal circumference are shown with ○ in the column of Table 2.

The confining pressures used were 0.05, 0.1, or 0.2 MPa, and the strain rates used were 10, 20, or 30% per min. There were a total of nine testing conditions for sand specimens.

RESULTS AND DISCUSSIONS

Rubber membrane tension effects in the pedestal circumference rotation

As shown in Fig. 5, the difference between each value of shear stress and shear strain with the

dummy specimen and the dummy specimen without rotation of the pedestal circumference was measured. This figure depicts the magnitude of tension of the rubber membrane during torsion shear. From the figure, it becomes clear that shear stress is in proportion to shear strain in tension state of rubber membrane.

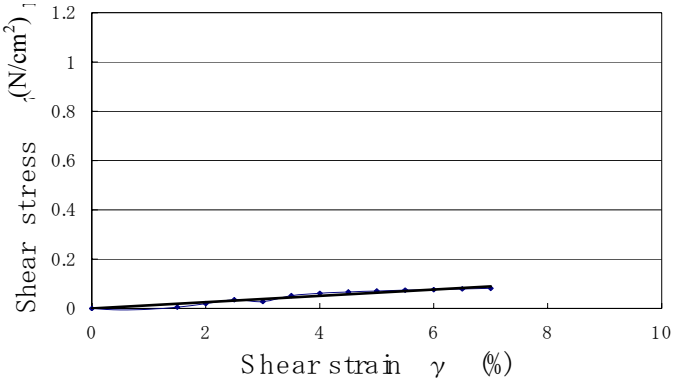

Fig.5 Tension of the rubber membrane by the test of dummy specimen

The results from the dummy specimen with pedestal rotation are shown in Fig.6. They were compared with the results for the blank test using the dummy specimen without pedestal rotation. It was found that the shear stress approached a value that was the same for both. Rotation of the circumference part of pedestal eliminated the influence of the tension of rubber membrane.

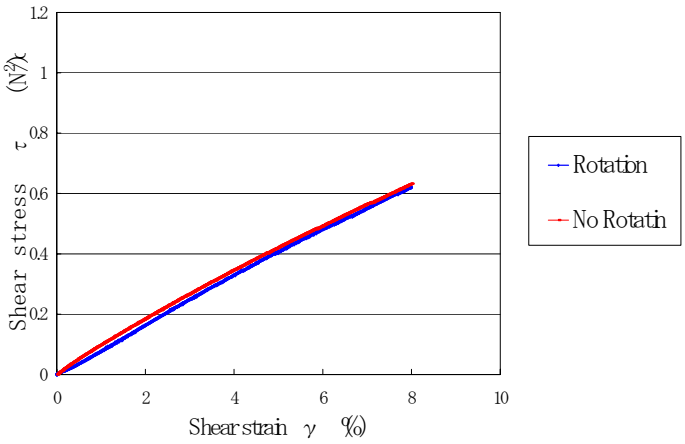

Fig.6 The comparison between the results from the dummy specimen with and without pedestal rotation

The effect of the pedestal circumference rotation under identical conditions of confining pressure 0.1MPa and a strain rate of 30% per min is demonstrated in Fig.7. That figure shows the relations between pore water pressure and shear strain from tests with and without rotation. There was no difference seen between the shear stress and strain relation. However, in tests for which a saturated sand sample was used, considerable differences appeared in the results. With the pedestal rotation, pore

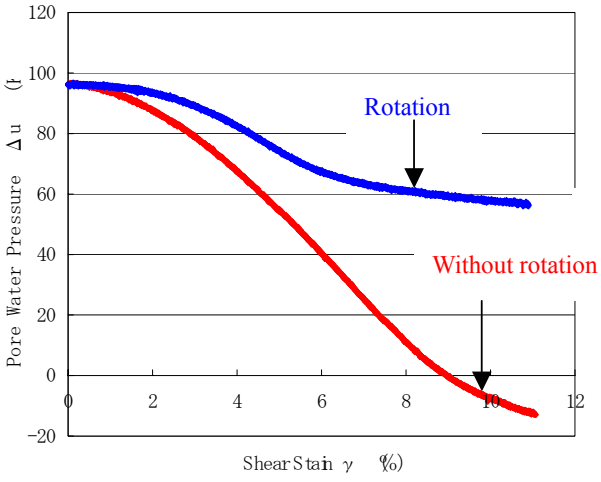

Fig.7 The relations between shear strain and pore water pressure

Fig.8 The comparison of the specimens after testing

water pressure remained at nearly constant value and decreased gradually from the middle. Without the pedestal rotation, it decreased rapidly the moment shear began and ultimately reached a negative value. From the past published experimental results, the shear resistance of liquefied sand shows minute resistance at first; when it is beyond a certain strain, rigidity is recovered, and resistance increases. It is highly unlikely that pore water pressure falls so rapidly at the early stages of shear and that pore water pressure so easily becomes a negative value, suggesting that the result with the pedestal rotation is more appropriate.

What causes the differences that emerge in test results due to the existence of the rotation? When the deformation state of the specimen after test is observed as shown in Fig.8, a change in appearance is hardly seen in cases with the pedestal rotation. But in cases without rotational, the twisting of the rubber membrane clearly transforms the specimen on the side. It can be assumed that deformation due to the twist of the membrane has brought about the change in pore water pressure inside the specimen. Once again, it can be said that results of test performed with the rotation of the pedestal circumference are more accurate or appropriate.

Discussions of Coefficient of Viscosity for Liquefied Sand

The relation between shear stress and shear strain rate was prepared from the experimental results. The apparent coefficient of viscosity for liquefied sand was obtained by the inclination of that relation, as shown in Fig.9. Under the condition of pedestal rotation, the tension of rubber membrane was corrected for, as mentioned before.

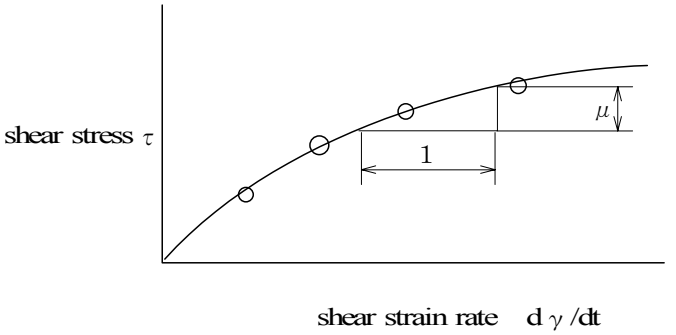

Fig.9 Model of coefficient of viscosity

The following process determined the coefficient of viscosity. When time (1, 3 or 5 sec) passed from the static shear start, the shear stress obtained from the static shear test was plotted on the

coordinates (Fig.10). The inclination of this plot represents the apparent coefficient of viscosity of liquefied sand. Table 3 shows the obtained coefficient of viscosity for each confining pressure.

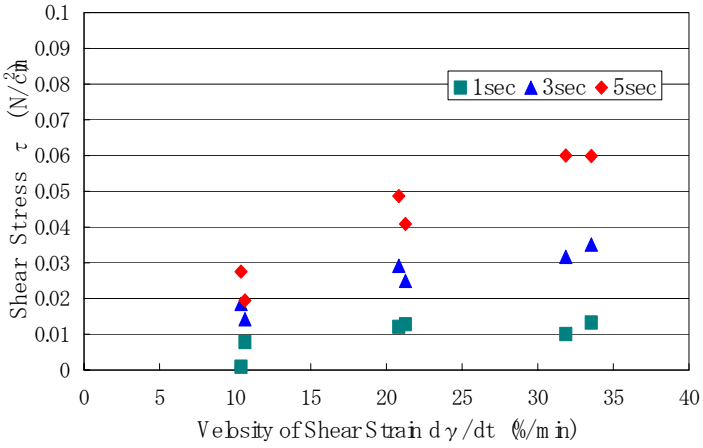

Fig.10 The relationships between shear stress and shear strain rate at the specified elapsed time

In the results of model ground test, it is reported that the coefficient of viscosity of liquefied sand depends on confining pressure. The relationship between the coefficient of viscosity and confining pressure is shown in Fig.11. When confining pressure increased, the coefficient of viscosity was found to increase, as well. The relations shown with log-log plots can be connected with a straight line; the value of the inclination is 0.5 or 0.6.

Table.3 Coefficient of viscosity

Confining pressure (Mpa)	Coefficient of viscosity (N·sec/cm³)		
	1sec	3sec	5sec
0.05	1.8	4.8	9.6
0.1	2.4	9.0	18.0
0.2	3.6	11.4	21.6

In addition, the coefficient of viscosity increases with time after liquefaction (Fig. 12). As for the

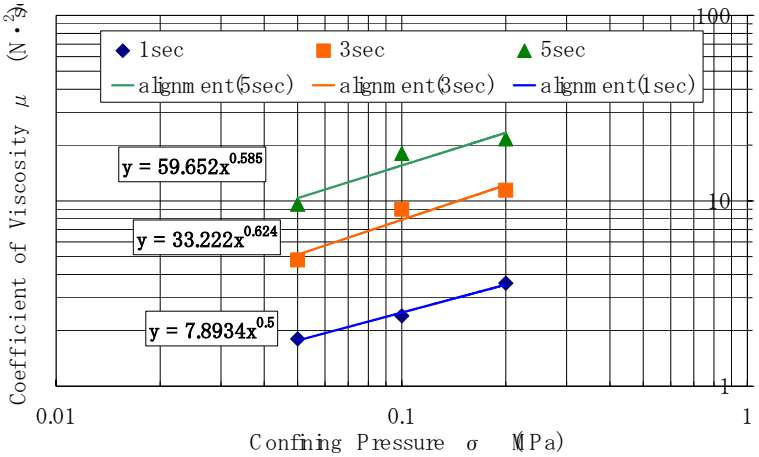

Fig.11 Relations between the coefficient of viscosity and confining pressure

value of inclination as well, it was found that the coefficient of viscosity became greater, as the elapsed time after liquefaction became longer and the confining pressure became larger.

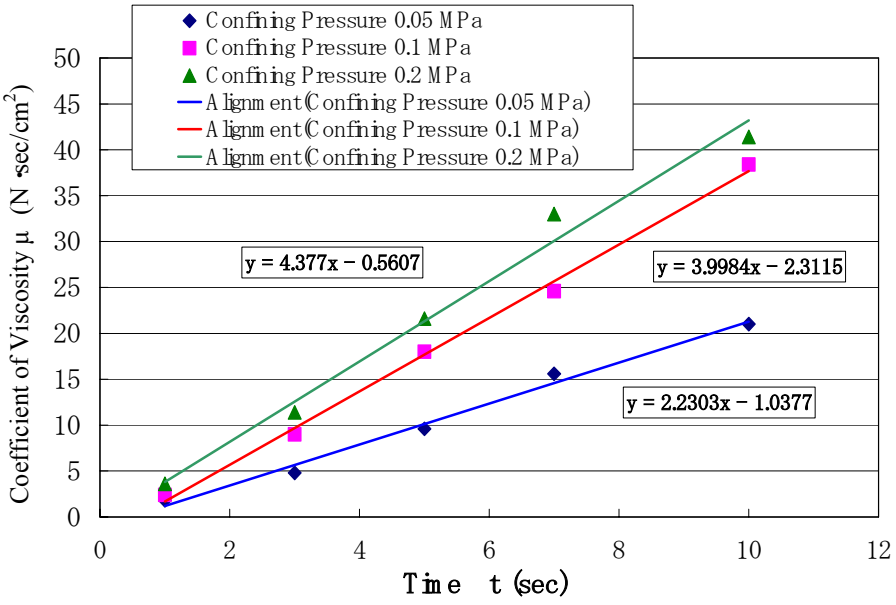

Fig.12 The relationship between the coefficient of viscosity and elapsed time

CONCLUSIONS

1) In the hollow cylindrical torsion test, the tension compensation of the rubber membrane due to the rotation of the part pedestal circumference yields more accurate results than the blank test.

2) The apparent coefficient of viscosity of liquefied sand depends on confining pressure.

3) The apparent coefficient of viscosity of liquefied sand is proportion to the time after liquefaction.

ACKNOWLEDGEMENT

The authors are grateful to the Ministry of Education, Culture, Sports, Science and Technology in Japan for funding this study as a part of the special coordination fund for promoting science and technology in the fiscal year of 2001.

REFERENCE

[1] Masanori Hamada, A. Kono, T. Nasu and K. Yanase: The mechanism of lateral flow of inclined ground and displacement prediction. Proc.2nd Symposium on “Enhancement of Earthquake Performance of Infrastructures Based on Investigation into Fracturing Process”, pp.235-240, March 2000, JSCE

Selection of a Reinforcement Method for Sewage System Structures Based on Earthquake Risk Management

Tetsutaro Kawakami, Kenichi Yamamoto, Tsuneo Ohsumi and Akira Yuasa

ABSTRACT

The deterministic earthquake-resistant design standard has indefinite factors even if a stricter standard is established. We propose a technique for studying effective measures based on functional analysis of the occurrence of an earthquake by introducing the concept of earthquake risk management concerning earthquake-resistant diagnosis and selection of a reinforcement method. Concretely, we selected a water treatment reservoir (element structure) that is one of the major facilities in a sewage system plant as an analysis model. This paper described the present state of the reservoir, damage level after earthquake-resistant reinforcement, methods for calculating reinforcement and repair costs, and methods for evaluating the effect of earthquake-resistant reinforcement using a risk analysis method by showing examples.

As a result of the various examinations, while the conventional earthquake-resistant evaluation is performed considering only the earthquake motion magnitude, this technique shows that the annual risk obtained by adding the risks classified for each earthquake-resistant range and the probability of occurrence of an earthquake can be easily calculated to monistically compare the reinforcement countermeasure plans. Furthermore, it shows that a suitable earthquake-resistant construction method can be objectively selected from multiple candidates. We believe that public investments hereafter require a process similar to "informed consent" adopted in the medical field and sufficient discussions on project necessities and investment effects are essential for the investor, constructor, and beneficiaries. The risk management method proposed by this paper will be effective for this purpose.

INTRODUCTION

In 1995, the Hyogoken-Nanbu Earthquake seriously damaged the sewage systems. The disaster suffered by Kobe City, with more than 90% pervasion of the sewage systems, made us recognize that the system is very important from the viewpoint not only of social infrastructure but also of consideration of the environmental effects.

The Japan Society of Civil Engineering made proposals as [1] concerning the concept of earthquake-resistant design for infrastructure to explain that earthquake-resistant design should include the consideration of earthquake motion at the set location based on the behavior of the active fault. In addition, the design of civil engineering structures for earthquake motion at the set

Tetsutaro Kawakami, Associate Professor, School of Marine Science and Technology, Tokai University, 3-20-1 Orido, Shimizu Shizuoka, Japan 424-8610
Kenichi Yamamoto, Deputy Director, Development Project Analysis Department, Japan Bank for International Cooperation, 1-4-1 Oute-Machi, Chiyoda-Ku, Tokyo, Japan 100-8144
Tsuneo Ohsumi, Senior Researcher, Nippon Koei Co., Ltd. R&D Center, 2304 Inarihara, Kukizaki-Cyou, Inashikiku-Gun, Ibaraki, JAPAN 300-1259
Akira Yuasa, President, Funabashi Analysis Center, 4-7-3-A203 Nishifuna, Funabashi, Chiba, Japan 273-0031

location is shifting to the deformation performance review type that accepts damage as [2] [3] [4] [5]. Therefore, it is necessary to evaluate damage levels of structures quantitatively. One of the methods capable of evaluating the damage level reasonably is the risk evaluation technique that takes risk management into consideration. The risk means the damage caused by the occurrence of something, and risk management means examining and executing ways to reduce or control the possibility of damage before it occurs as [6]. Risk evaluation with risk management has the characteristic that the design engineer can make decisions objectively after considering possible earthquake motion. On the other hand, risk evaluation was not so much examined during the actual activities of design, planning, construction, and maintenance of infrastructure because the purpose of the evaluation was to deal with the earthquake damage risk assuming that absolutely safe structures cannot be built.

Taking the above matters into consideration, we propose a technique for studying effective measures based on functional analysis of the occurrence of an earthquake by introducing the concept of earthquake risk management concerning earthquake-resistant diagnosis and selection of a reinforcement method for sewage system structures and assuming that "the earthquake-resistant design standard has limitations even if a stricter standard is established." More specifically, we selected a water treatment reservoir (element structure), one of the major facilities in a sewage system plant, and describe the present state of the reservoir, damage level after earthquake-resistant reinforcement, methods for calculating reinforcement and repair costs and methods for evaluating the effect of earthquake-resistant reinforcement using a risk analysis method by showing examples.

Furthermore, we propose to handle this technique as an evaluation method used for primary diagnosis. Therefore, it is assumed that the technique can be used in the evaluation in a short period of time in a practical way. When detailed evaluation is needed, the earthquake-resistant performance of the structure concerned will be evaluated by making a secondary diagnosis using the technique considering the damage model as [7] of the structure and the more detailed technique considering the event tree or the fault tree as [8].

SUMMARY OF EARTHQUAKE EVALUATION TECHNIQUE FOR WATER TREATMENT RESERVOIR

Figure 1 shows the flow chart for selecting an earthquake-resistant reinforcement method for an element structure.

The typical construction of the water treatment reservoir is a double covered one where the reservoir as a semi-underground structure and a building slightly protruding from the ground are integrated. The double covered structure has special construction in relation to civil engineering structures.

As to step ① of the selection flow chart, the structure shown in Figure 2 was selected. This cross-section is the largest for sewage systems in Japan and overseas.

As to steps ② and ③, earthquake motion intensity and the probability of occurrence at the object location were calculated using seismic activity records of the location for past years. Although, in the conventional earthquake evaluation, the earthquake motion with a magnitude of zero to infinity was evaluated, this technique assumes three levels of earthquake motion (hereafter earthquake motion level A, level B and level C from small to a significant probability of occurrence are used). Considering the current earthquake-resistant design and practical use, level A earthquake motion is assumed to have a probability of occurrence once or twice during the service life of the sewage treatment plant, a level B earthquake motion has an extremely low probability of occurrence during the service life of the plant, and a level C earthquake motion, the strongest one that ever occurred in

the object location. We proposed the technique for performing risk evaluation using the results of the calculation of these three levels of earthquake motion. In this technique, the earthquake motion risk, which is essentially a continuous amount, is interpolated based on three points. Therefore, the risk in the interpolated section cannot be said to be the risk in the strict meaning. However, since the earthquake motion levels A, B, and C are the ones adopted in the deformation performance review design, the earthquake response analysis of earthquake motion level B or C can be applied to the structure designed according to the deformation review type design method. Since the earthquake load equivalent to the earthquake motion level A was applied to the structures designed before the establishment of the deformation review type design method, the risk evaluation can be performed by considering the earthquake motion levels of B and C again. Therefore the technique has the practical benefit that the risk evaluation can be performed for both cases by using design calculation results obtained by applying this technique.

As to ④ and ⑦, it is necessary to select an analysis technique suitable for special construction for semi-underground structures. In addition, it is desirable to apply a simple technique to the analysis used for the earthquake risk evaluation because the technique is repetitively used to select the most appropriate construction method. Furthermore, it is necessary that the technique takes non-linearity and dynamic coupling of the structure and ground into consideration because it is used to analyze the earthquake motion of level 2 or higher for earthquake-resistant design. In this study, we adopted the non-linear response earthquake motion method as an earthquake-resistant calculation method applicable to a semi-underground structure and satisfy the above conditions.

As to ⑤ and ⑧, we decided to use the calculation based on the response ductility factor used for an index representing the damage level in the deformation performance review type design. More specifically, we will identify the relationship between the response ductility factor and each cost, and find the damage cost from the response

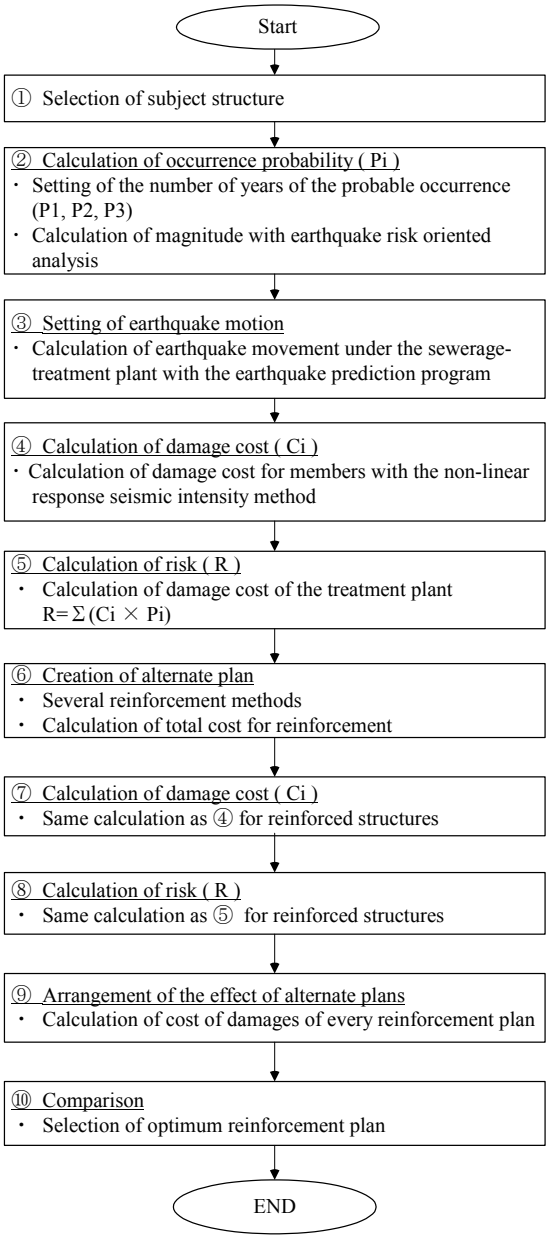

Figure 1. Flow of selection for a seismic reinforcement method.

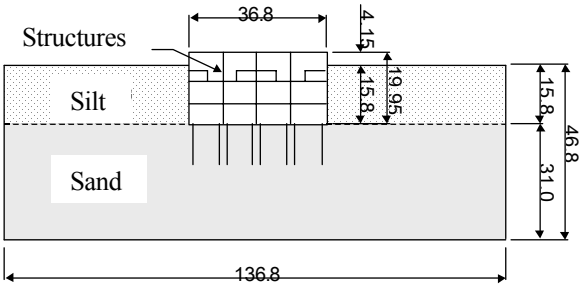

Figure 2. Double covered structure (in m)

ductility factor for each member obtained from the earthquake response analysis to conduct the damage level evaluation. In addition, we will select an earthquake-resistant countermeasure construction method based on the response ductility factor obtained from the earthquake response analysis and perform the damage level evaluation for the case (⑧) provided with the countermeasure in the similar manner.

As to ⑥ and ⑨, the risk for the existing structures and countermeasure plan is calculated from the damage cost to select the optimum earthquake-resistant countermeasure construction method based on the risk evaluation results.

As to ⑩, the cross-section is optimized for the adopted earthquake-resistant reinforcement plan. Here, the response ductility factor for each member is calculated by implementing the earthquake response analysis for the set earthquake motion. By referring to the magnitude and point of occurrence of this response ductility factor, the weak points of the structure can be identified. In addition, the relationship between the reinforced location or strength and the response ductility factor can be identified by modifying the cross-section or strength of members and conducting studies of parameters of the earthquake response analysis. The design engineers can optimize the existing cross-section in the selected countermeasure construction method based on this information. In the following clauses, each step of the above flow chart is described in detail.

SIMULATION OF EARTHQUAKE MOTION BASED ON FAULT MODEL

The earthquake motion was predicted based on the typical earthquake motion classified into three levels consisting of the level A earthquake motion, the level B earthquake motion, and the level C earthquake motion by determining waveform as follows. First, an earthquake risk analysis was carried out to determine the frequency of occurrence (probability of occurrence: P) of the object earthquake and the earthquake magnitude (magnitude M) predicted to occur in the location concerned, where P=30, 300 and 1000 years and M=7.0, 7.9 and 8.3. Then assuming that the earthquake motion waveform is equivalent to that of the Minami-Kanto Earthquake, an artificial earthquake motion waveform was created using the earthquake motion calculation systems as [9] [10] studied and established by a member of the author's team based on the fault model proposed by Harada and Ohsumi as shown in Figure 3. The maximum accelerations in the earthquake-resistant bedrock were calculated to be 99m/s^2, 680 m/s^2 and 800 m/s^2 respectively.

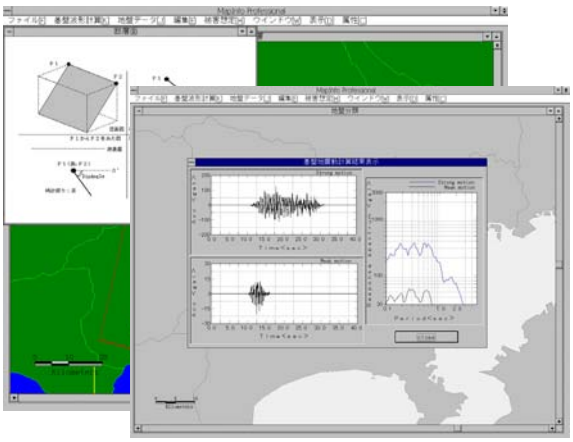

Figure 3. Earthquake motion creation system

ANALYSIS FOR NON-LINEAR RESPONSE SEISMIC INTENSITY METHOD

In order to solve a problem in performing earthquake-resistant calculation for earthquake motion of level 2 or higher where non-linearity of the ground and structure is dominant, it was necessary to take into account the load (seismic intensity) reflected by non-linear characteristics and non-linearity

of the ground and structure. The non-linear response seismic intensity method as [11] used in this technique is the one studied and developed for this study taking this load into consideration as shown in TABLE Ⅰ.

As material models, we applied to the ground a linear model using the minimum secant rigidity obtained by time history calculation from a one-dimensional earth column by applying the modified Ramberg-Osgood model as [12] and to the structure a bi-linear model which assumes the yield moment of the structure to be the bending point, respectively.

In addition, we applied to the seismic intensity, namely load, the acceleration or inertia of the ground at the time of the maximum relative displacement between the upper and lower parts of the structure to be obtained by analysis applying the above one-dimensional earth column model to make them act on the ground.

As to the seismic intensity of the structure, because of the semi-underground structure, the acceleration response spectrum at the position of the structure base was calculated from the analysis applying the one-dimensional earth column model. The response acceleration for the natural period of the structure and the seismic intensity of the ground were assumed to be the seismic intensities of the top and the base of the structure, respectively, to allow the linearly interpolated seismic intensity to act on the portion between the top and the base as load.

TABLE Ⅰ. MODELING OF NON-LINEAR RESPONSE SEISMIC INTENSITY METHOD

	Non-linear model	Load
Ground	Secant rigidity based on one-dimensional R-O model	Response acceleration based on one-dimensional R-O model
Structure	Bi-linear model	Seismic intensity of eigenvalue base on response spectrum

METHOD FOR SELECTING EARTHQUAKE-RESISTANT REINFORCEMENT

Risk Calculation

In this paper, annual risk is evaluated by assuming the expected cost to be the risk. The annual risk is calculated by obtaining the cost of damage for the earthquake motion magnitude for each probability of occurrence set at several points. Figure 4 through 6 show the calculation process of the annual risk as [13]. First, the earthquake motion intensity is set for each probability of occurrence (Figure 4). Then the damage cost for each earthquake motion magnitude in the present state (without

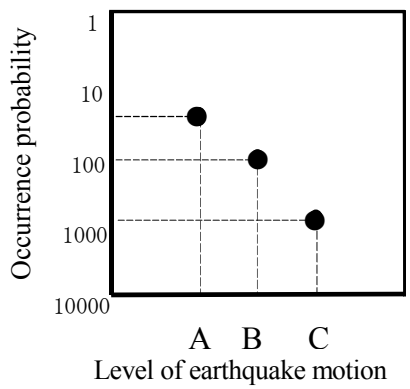

Figure 4. Occurrence probability of earthquake motion

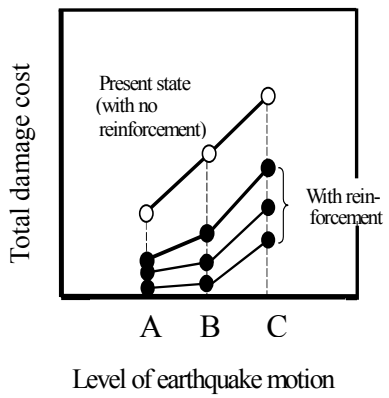

Figure 5. Total cost of damage for each earthquake motion

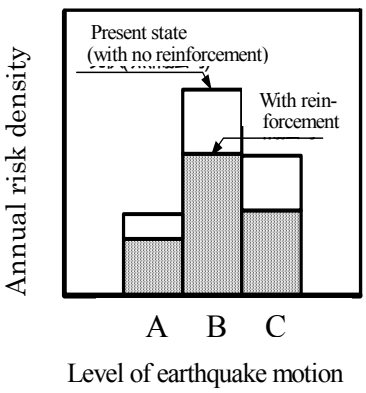

Figure 6. Annual risk density motion for each earthquake

reinforcement) and after the reinforcement (Figure 5). Detailed methods for calculating the cost of damage will be described later.

The risk R in the present state (without reinforcement) and after the reinforcement can be calculated as a summation of each risk shown in Figure 6 and equation (1).

$$R = \sum_{i=1\sim3} (\mathrm{Pi} \times \mathrm{Ci}) + p \times E \quad (1)$$

Where P_i: probability of occurrence of earthquake motion A, B and C (i =1, 2 and 3); C_i: total repair cost for earthquake motion A, B and C in the present state (without reinforcement) or in the state after reinforcement (i =1, 2 and 3); p: probability of performing earthquake-resistant reinforcement (p=0 in the present state and p=1 after reinforcement); and E: earthquake-resistant reinforcement cost. In addition, $P_i \times C_i$ is called annual risk density, which means the risk for each earthquake motion magnitude.

Method for Calculating Damage Cost

The damage cost in the annual risk calculation process is obtained according to the following procedures (i) through (iii):

(i) Set damage level for each member based on Figure 7.

(ii) Calculate response ductility factor for each member by performing earthquake response analysis.

(iii) Set damage cost for each earthquake-resistant performance shown in TABLE Ⅱ to calculate cost of damage.

The damage level shown in Figure 7 represents the state described in TABLE Ⅲ.

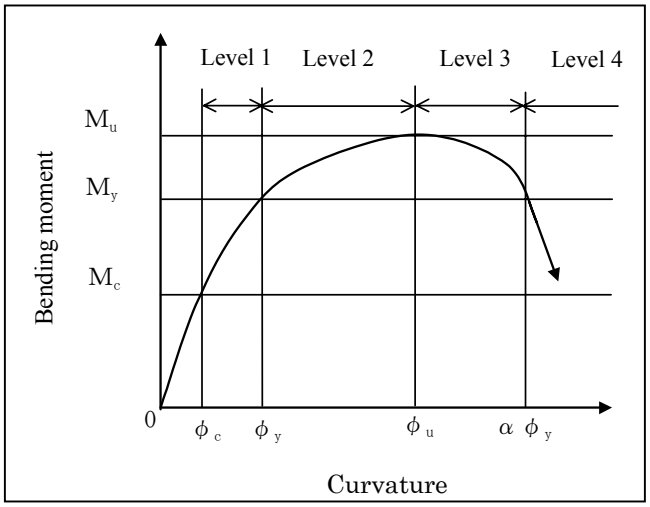

Figure 7. Damage level concept

Method for Selecting the Optimum Reinforcement Construction Method

Here we compare multiple plans for feasible earthquake-resistant reinforcement. The following earthquake equation provides the annual effect of the earthquake resistant reinforcement:

Effect of earthquake-resistant reinforcement＝

Annual risk without reinforcement －Annual risk after earthquake-resistant reinforcement

In addition, considering the cost associated with the earthquake-resistant reinforcement (service period assumed to be N years), we selected the earthquake-resistant reinforcement plan having the largest value obtained from the following formula from the multiple earthquake-resistant reinforcement plans:

Effect of earthquake-resistant reinforcement－earthquake-resistant reinforcement cost/ N

TABLE Ⅱ. RELATIONSHIP BETWEEN EARTHQUAKE-RESISTANT PERFORMANCE AND DAMAGE LEVEL OF EACH MEMBER OF FRAMEWORK

Earthquake-resistant performance	Damage level in bending failure mode		Damage level in shear failure mode
	Member easy to be repaired or reinforced (Slab and beam)	Member difficult to be repaired or reinforced (Wall and column)	
Earthquake-resistant performance 1	Member damage level 1		No damage
Earthquake-resistant performance 2	Member damage level 2 or 3	Member damage level 2	
Earthquake-resistant performance 3	Member damage level 3 (Member damage level 4 for some members)		

TABLE Ⅲ. STANDARD DAMAGE LEVEL OF MEMBERS

Failure mode	Level	Description	Remarks
Bending failure	Damage level 1	Tensile stress of axial reinforcing bar less than yield point (before bending yield)	Range between crack and yield. Between φ_c and φ_v shown in Figure 7.
	Damage level 2	Cover concrete before reaching compressive failure stress (Generated by a load less than the maximum proof stress)	Range between yield and maximum proof stress. Between φ_y and φ_u shown in Figure 7.
	Damage level 3	The member has proof stress higher than the stress at bending yield.	Range between maximum proof stress and response ductility factor 10 (α=10). Between φ_u and $\alpha\varphi_y$ shown in Figure 7.
	Damage level 4	The member has proof stress lower than the load at bending yield	Range where response ductility factor more than 10. More than $\alpha\varphi_y$ shown in Figure 7.
Shear failure	—	When shear force of the member exceeds shear proof stress	—

APPLICATION

The results of the earthquake risk evaluation for the above-mentioned object structure (water treatment plant shown in Figure 2) assuming the magnitude equivalent to the Southern Kanto Earthquake are shown below:

Alternative Proposal

First, TABLE Ⅳ shows the number of members having the response ductility factor of 1 or more obtained from the earthquake response analysis concerning the damage level of the present members (without reinforcement) and its repair cost. It is recognized that the damage of many members results in large repair costs.

Two construction methods that satisfy the earthquake-resistant performance were selected as an earthquake-resistant reinforcement plan for the purpose of increasing the proof stress of the entire structure (Figure 8 and Figure 9). The construction method ① provides columns and beams with additional concrete placement, while construction method ② uses wing walls (including reinforcing walls such as opening walls) and buttresses. The earthquake-resistant reinforcement cost is shown in

TABLE Ⅳ. It is recognized that the reinforcement cost of the construction method ② is about 30% lower than that of construction method ①. Although Figure 8 and Figure 9 are cross-sectional drawing, it should be noted that slabs and beams are arranged in the direction perpendicular to these cross-sections. Each construction method is applied to the object location as a countermeasure.

TABLE Ⅳ also shows the number of members having a response ductility factor of 1 or more obtained from the earthquake response analysis concerning construction methods ① and ②, and the repair cost. The repair cost for earthquake motion A is the one with a response ductility factor of less than 1 (crack). The repair cost for the structure provided with the countermeasure using construction method ① is higher than that of construction ②. This means the damage level of the former is higher than that of the latter.

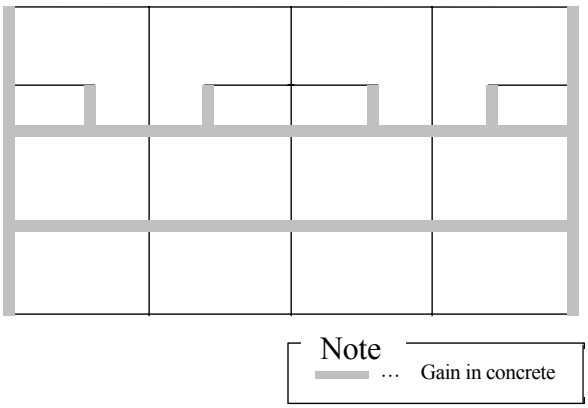

Figure 8. Construction ① method

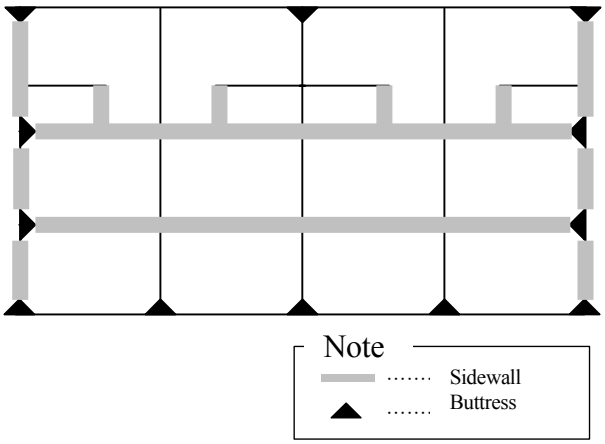

Figure 9. Construction ② method

TABLE Ⅳ. LIST OF DAMAGE AND COST

	Level of earthquake motion	Number of members that have more than ductility factor 1	Total repair cost (yen)	Reinforcement cost (yen)
Present state	Earthquake motion A	0	65,950,000	
Present state	Earthquake motion B	30	3,844,800,000	
Present state	Earthquake motion C	43	6,675,000,000	———
Construction ① method	Earthquake motion A	0	11,480,000	
Construction ① method	Earthquake motion B	4	189,300,000	242,699,000
Construction ① method	Earthquake motion C	6	208,260,000	
Construction ② method	Earthquake motion A	0	2,418,000	
Construction ② method	Earthquake motion B	12	304,244,000	193,296,000
Construction ② method	Earthquake motion C	13	575,357,000	

Selecting the Optimum Reinforcement Construction Method

The relation between the annual risk density and the earthquake motion magnitude is shown in Figure 10. In earthquake motion A, construction method ② is more effective for earthquake-resistant reinforcement than construction method ①. In earthquake motion B, the result is the opposite. Therefore it can be determined that construction method ② is more fragile to earthquake motion magnitude. Thus, it is impossible to decide which of the construction methods ① and ② are better for earthquake-resistant reinforcement from the viewpoint of annual risk density.

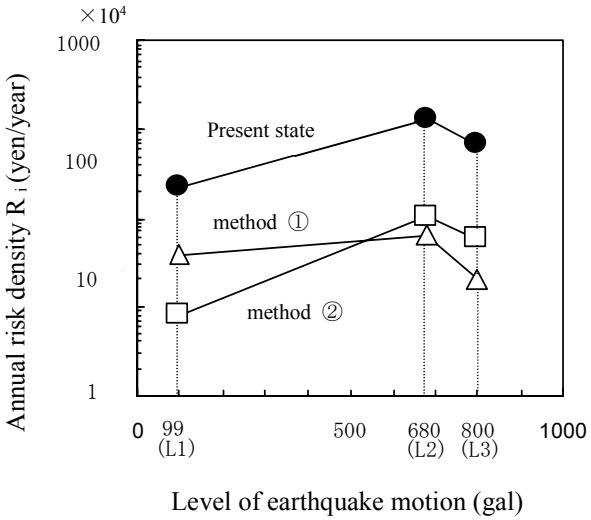

Figure 10. Annual risk density

The annual risk and the effect of the earthquake-resistant reinforcement are shown in TABLE Ⅴ. The number of years in service (N) is determined to be N=40 assuming that the structure was constructed 10 years ago. TABLE Ⅴ shows that construction method ② is better than construction method ① for earthquake-resistant reinforcement.

In the Southern Hyogo Earthquake equivalent to earthquake motion level 2, water treatment plants of five cities and four basins were damaged. Its average damage cost of 3,830 million yen as [14] was almost equal to the damage cost of 3,840 million yen estimated by this technique assuming earthquake motion B.

TABLE Ⅴ. ANNUAL RISK AND THE EFFECT OF A SEISMIC REINFORCEMENT
(UNIT: MILLION YEN/YEAR)

———	①Annual risk without reinforcement	②Annual risk after reinforcement	③Effect of earthquake reinforcement year (①-②)	④Costs of a seismic per reinforcement (unit: million yen)	Effect ③-④/N
Construction method ①	2169	606	1563	242.7	956
Construction method ②	2169	483	1686	193.3	1202

CONCLUSION

This study proposes an earthquake risk evaluation method applicable to sewage treatment plants as an earthquake risk management method and an optimization technique for earthquake-resistant reinforcement design using that method. While the conventional earthquake-resistant evaluation is performed considering only the earthquake motion magnitude, this technique shows that the annual risk obtained by adding the risks classified for each earthquake-resistant range and the probability of occurrence of an earthquake can be easily calculated to monistically compare the reinforcement countermeasure plans. Furthermore, it shows that a suitable earthquake-resistant construction method can be objectively selected from multiple candidates. We believe that public investments hereafter require a process similar to "informed consent" adopted in the medical field and sufficient discussions on project necessities and investment effects are essential for the investor, constructor, and beneficiaries. The risk management method proposed by this paper will be effective for this purpose.

Finally, we recognize the following problems still remain unsolved. First, for practical purposes, this technique takes into account the primary damage (damage to structures) but not secondary damage (damage to auxiliary equipment such as mechanical or electrical system, occurrence of an epidemic due to sewage effluence). The reason is that this technique aims to easily select the optimum countermeasure reinforcement construction method and the secondary damage level can be assumed to be closely correlated with the primary damage level. Secondly, it is necessary to consider the statically indeterminate condition of the structure at the time when failure develops. Thirdly, it is necessary to perform risk evaluation of lifeline systems. The earthquake risk evaluation has two objects, namely an element structure (individual structures such as pumping plant and sewage treatment plant) as in this technique and the lifeline system (entire sewage system including pumping plant, sewage treatment plant, piping connecting these plants, or sewage system linking with other plants) for the occurrence of an earthquake. It is necessary to perform the risk evaluation on these lifeline systems in the strict meaning of functional evaluation. These are the problems to be solved.

REFERENCES

[1] Japan Society of Civil Engineers: Tertiary Proposal and Interpretation related to Earthquake-resistant Design Method for Soil Structure 2000. 6.

[2] Japan Road Association: Road Bridge Specifications (Part V earthquake-resistant design) and Interpretation, 1996.

[3] Japan Society of Civil Engineers: Concrete Standard Specifications (established in 1996), Earthquake-resistant design part, 1996.

[4] Railway Technical Research Institute: Design Standard for Railroad Structures and Interpretation - Earthquake-resistant Design, 1999.

[5] Japan Society of Civil Engineers: Structural Performance Review Guidance for Buried LNG Tank Structure, 1999.

[6] Kusano, N. Necessity of Risk Management in Civil Engineering Field, *Journal of Society of Civil Engineers*, vol. 85, pp. 6-8, July 2000

[7] Hoshitani, M. and Ishii, K. Reliability Analysis of Structures, Kashima Publishing, pp. 50-95.

[8] Nakamura, T. and Mizutani, M. Event Tree Analysis in Earthquake Risk Management, The Third Domestic Symposium concerning Safety and Reliability of Structures, pp.75-80, 1995.

[9] Ohsumi, T., Darama, H. and Harada,T. Engineering simulation of ground motions using a seismological model, *ICOSSAR'97 (7th International Conference on Structural Safety and Reliability),* ISBN9054109785, Vol.3, pp.1471-1478, November, Kyoto, Japan, 1997.

[10] Ohsumi T. and Yamamoto, K. Development of Simplified Earthquake Motion Analysis System, The Japanese Geotechnical Society, The 33rd Conference on Geotechnical Studies, E-8, pp.1131-1132, 1998.

[11] Yuasa, A., Ohsumi, T., Yamamoto, K. and Kawakami, T. Analysis Technique for Non-linear Response Seismic Intensity Method applied to Sewage System, *Structural Engineering Papers*, Vol. 46A, pp345 - 352, 2000.

[12] Jennings, P.C. Periodic response of a yielding structure, *Proc .ASCE*, No. EM2, pp.131-163,1964.

[13] Mizutani, M. Basic Methodology of a Seismic Risk Management (SRM) Procedures, *ICOSSAR'97 (7th International Conference on Structural Safety and Reliability)*, November, Kyoto, Japan, 1997.

[14] Great Hanshin and Awaji Earthquake Investigation Report Committee: Great Hanshin and Awaji Earthquake Investigation Report, Damage of Life Line System and Recovery, Japan Society of Civil Engineers, The Japanese Geotechnical Society, Japan Society of Mechanical Engineers, Architectural Institute of Japan and Seismological Society of Japan, pp. 141-253.

NEW TYPE SIMULATION MODEL FOR SAND DEPOSIT DURING HUGE EARTHQUAKE.
- SHAKING TABLE TEST AND SIMULATION –

Susumu Okamoto, Katsuyuki Sakashita and Ken-ichi Fukushima

ABSTRACT

The conventional simulation models, such as Hardin-Drnevich(H-D) and Ramberg-Osgood(R-O) models, are generally used for evaluating non-linear behavior of non-liquefied sand deposit. But these evaluation methods are not appropriate for non-linear analyses of ground whose shear strain is over 1%. These conventional methods were developed under the allowable stress design method which considers moderate earthquakes. After the 1995 Kobe earthquake, the acceleration of the design earthquakes was changed to be larger one, and the shear strain of ground considered in design procedures was changed to be over 1%. Therefore, new analytical methods for this kind of design earthquake motions are required. A new evaluation method, "Combined Hysteretic(C-H) model", which combines advantages of the H-D and R-O models, is proposed in this paper. The C-H model can simulate the ground behavior with its shear strain over 1%.

The results of shaking table tests and the theory of "Combined Hysteretic(C-H) model" are explained. Then, the simulation results using C-H, H-D, and R-O models are compared with the results of torsional shear tests and the aforementioned shaking table tests. It is clarified that the C-H model is very effective method for evaluating the ground behavior during an extra huge earthquake such as the Kobe earthquake.

Authors will expand this theory to three dimensional analyses, and apply the proposed model to analyze the behavior of many kinds of structures constructed on relatively soft dry sand ground in high seismicity area like Japan.

Susumu Okamoto, Manager, Planning Section, Technology Planning Department, Technology Center, Taisei Corp, 344-1 Nase-cho, Totsuka-ku, Yokohama, Japan 245-0051
Katsuyuki Sakashita, Senior Research Engineer, Civil Structural Engineering Section, Civil Engineering Research Institute, Technology Center, Taisei Corp
Ken-ichi Fukushima , Research Engineer, Civil Structural Engineering Section, Civil Engineering Research Institute, Technology Center, Taisei Corp.

INTRODUCTION

The conventional simulation models, such as Hardin-Drnevich(H-D)[1] and Ramberg-Osgood(R-O) models, are generally used for evaluating non-linear behavior of non-liquified sand deposit. But these evaluation methods are not appropriate for non-linear analyses of ground whose shear strain is over 1%. These conventional methods were developed under the allowable stress design method which considered moderate earthquakes. After the 1995 Kobe earthquake, the acceleration of the design earthquakes was changed to be larger one, and shear strain of ground considered in design procedures was changed to be over 1%. Therefore, new analytical methods for this kind of design earthquake motions are required. These new methods must be able to express the ground response with its shear strain of 1% or more. Kumazaki et al proposed new simulation model which is called as Momentary Deformation Modulus(MDM) model[2]. This model can evaluate dynamic response of liquefied ground and also non-liquefied ground. When this kind of sophisticated model is used, dynamic behavior of ground can be simulated using earthquake motions which are recorded at some types of ground. Anyway, important point to develop such new methods is the hysteretic rule. The hysteretic model using the original Masing rule[3] can not express the hysteretic loop derived from the test results with huge ground strain range over 1%. A new evaluation method, "Combined Hysteretic(C-H) model", which combines advantages of H-D and R-O models, is proposed in this paper. The C-H model can simulate the ground behavior with its shear strain over 1% .

At the first part of this paper, the results of shaking table tests are studied. The sand deposit was made with dry sand, and many kinds of excitation waves with large amplitude were applied in the test series. The maximum shear strain calculated from the experimental results was over 3 %. Fundamental characteristic of sand deposit during a huge earthquake was derived from these shaking table tests

Secondary, the theory of a new evaluation method, "Combined Hysteretic(C-H) model", is explained. Then, the simulation results using C-H,H-D and R-O models are compared with results of torsional shear tests and the shaking table tests. The simulation result using C-H model shows very good agreement with both torsional and shaking test results compared with those using H-D and R-O models.

EXPERIMENTAL STUDY

Sand Deposit

In case of performing a scaled shaking table tests using sand deposit under ordinary gravity condition, the similarity law is usually considered to evaluate the test results. But the applicability of the similarity law has not been confirmed when the input motion is huge, like the motions recorded in Kobe area during the 1995 Kobe earthquake. Since the shear strain of these tests was expected to be over 1 %, the similarity law was not considered. In other words, these tests were performed as very shallow full-scale sand deposit. The model sand deposit was made in a shear box with 2.7m in length, 1.2m in width and 1.5m in depth as shown in Figure 1. Dry silica sand #4 was used, and liquefaction was not considered in these tests.

Experimental Cases

Main objectives of these tests were to clarify the behavior of sand deposit under a huge

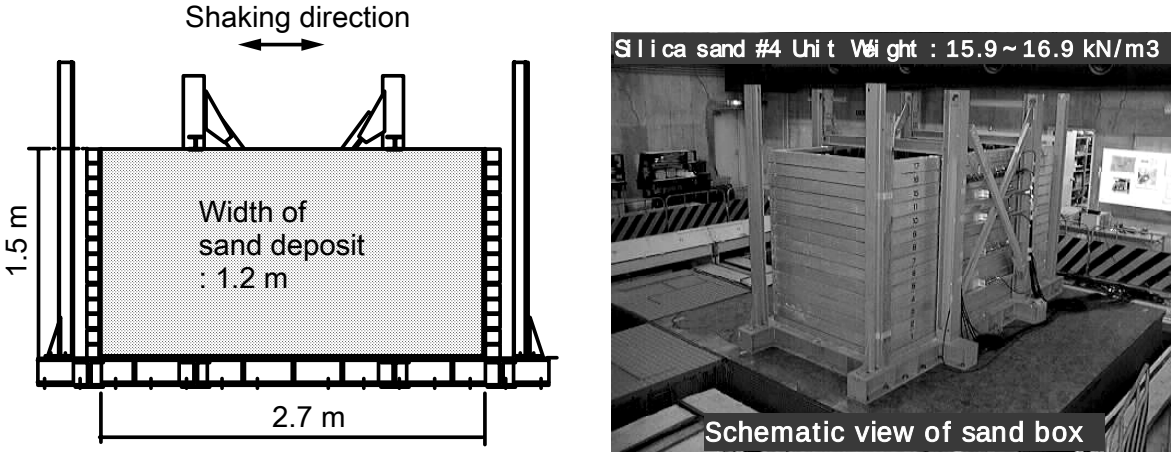

Figure 1. Model of sand deposit

earthquake. The ground motions recorded during the Kobe earthquake and other huge earthquakes were used as excitation waves as shown in TABLE 1. The Kobe wave was the NS component of the ground motions at Kobe Marine Observatory of Japan Meteorological Agency during the 1995 Kobe earthquake. Others were also the famous ground motions recorded at various soil conditions. The Kushiro wave was recorded at rock site during the 1993 Kushiro-oki earthquake. The Tsugaru wave was recorded at soft ground during the 1983 Nihonkai-chuubu earthquake. And the Fukiai wave was recorded at ground with moderate stiffness during the 1995 Kobe earthquake. Time scale of the excitation waves was decreased into 1/5 times of original waves so that the predominant period of the excitation waves were close to the natural frequency of the model deposit. The Kobe wave with time scale of 2/5 and 1/10 were also used. The amplitude of excitation waves was scaled from 0.05 to 2.0 of the original waves.

Ground Condition

The non-linearity of dry sand was very important for evaluating the shaking table test results. Three cases of torsional shear tests were carried out. The test results are shown in Figure 2. The

TABLE 1 INPUT WAVES DURING SHAKING TABLE TEST

Input waves	Amplitude ratio versus original waves	Time scale Ratio to original wave	Number of excitation
Kobe wave	0.05	1/5	1
	0.25		2
	0.50		2
	1.00		3
		2/5	2
		1/10	1
Tsugaru wave	2.00	1/5	1
Fukiai wave	1.00		1
Kushiro wave	0.80		1

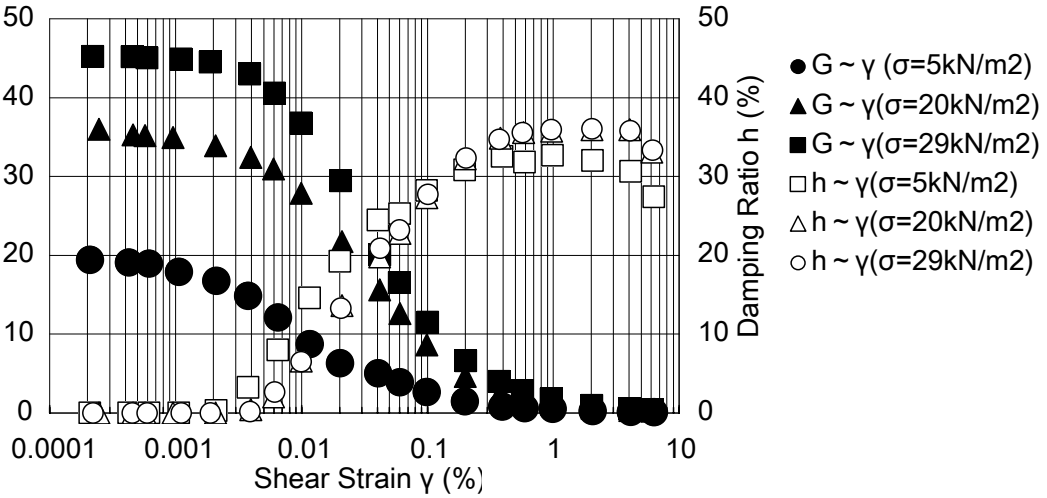

Figure 2. Torsional shear test results of sand : Shear modulus and damping ratio

maximum shear strains were almost 10%. The confined pressures during the tests were set to be 5kN/m2, 20kN/m2, and 29kN/m2, respectively. These confined pressures correspond to the earth pressures at the depth of 30cm, 120cm and 180cm, respectively. The shear stiffness decreased as strain increased, as shown in Figure 2. The shear stiffness at over 1% strain level is very important to clarify the behavior of model ground in these test cases. The damping ratios were over 30% in large strain range over 1%.

Shear velocity distributions in the model sand deposit were evaluated using bender elements. A bender element is a small electrical device with 10mm square and 1mm thickness. It can generates a small amplitude elastic wave, or perceive a tremor, and two elements are used for shear velocity evaluation. Two elements were set apart about 0.1m in a model ground, and one element, called "shaker element", generates a small amplitude wave, while the other, called "receiver element", perceives the tremor. In this way, the shear velocity of the elastic wave in the ground can be evaluated by getting the time histories of shaker and receiver elements. Figure 3. shows the results of the shear velocity derived from the bender elements. The shear velocity before shaking derived

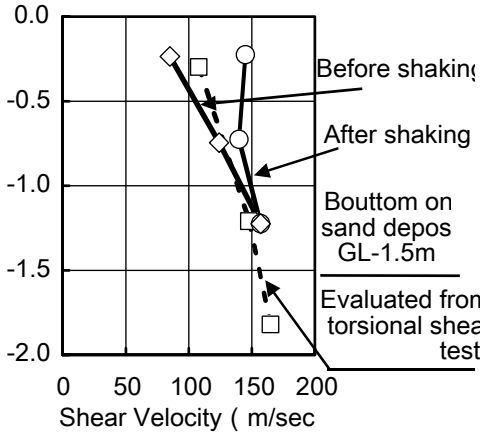

Figure 3. Shear velocity evaluated using bender element

TABLE 2 PREDOMINANT FREQUENCY OF SAND DEPOSIT

	First predominant frequency	Second predominant frequency
Before shaking	19.0 Hz	41.6Hz
After shaking	21.1 Hz	45.9Hz

from the bender elements is almost equal to the one from the torsional shear tests. The shear velocity after shaking is bigger than the one before shaking, because the density of sand deposit was bigger and bigger depending upon shaking. In other words, the soil becomes hard after shaking.

Experimental Result

Predominant Frequency of Model Ground

To clarify the fundamental characteristics of the sand deposit, small amplitude white noise excitation tests were performed. The frequency range of the white noise was between 1Hz and 50Hz, and the targeted amplitude was set to be 40 cm/sec^2. TABLE 2 shows the results of the white noise excitations. The first predominant frequency changed from 19.0Hz to 21.1Hz by shaking.

Time Histories

Figure 4 shows the time histories of input acceleration, ground surface acceleration, and relative displacement of the ground surface versus table at one of the test cases whose input wave was the Kobe wave with original amplitude and 1/5 time scale. The maximum surface acceleration was 493 cm/sec^2, which was less than the maximum input table acceleration, 793cm/sec^2. The reason of this difference is explained later. The maximum surface relative displacement was 11.8mm. It means that the maximum average strain was about 0.8%. The response spectra of the input and surface waves are shown in Figure 5. The predominant period of the input wave was about 0.07sec. But the response of the surface wave at 0.07 sec was much smaller than that of the input wave. And the response of the surface wave between 0.2 and 0.3 sec was much larger than that of the input wave. The predominant frequency of the surface wave was around 3 – 5 Hz, which was less than the predominant frequency of the soil deposit obtained by the small amplitude white noise excitation. This means that the model ground became soft as the shear strain of the model ground increased during shaking.

Shear Strain

Shear strain is very important for evaluating ground behavior. Figure 6 shows the relationships between the maximum acceleration of table and surface, and the maximum table acceleration and the maximum shear strain. The shear strain was calculated considering the difference among displacement of each layer. The displacement of each layer was calculated from double integration of the acceleration record at each layer. The maximum shear strain was over 3% under the Kobe wave with 2/5 time scale. The dotted lines in the figures indicate the results under the Kobe wave with 1/5 time scale. The inclination of the line indicating the surface acceleration decreases as the table acceleration increases. But the inclination of the line indicating shear strain increases as the table acceleration increases. The phenomena occurred because of the non-linearity of the sand deposit. The surface acceleration under the Kobe wave with 1/10 time scale and under the Kushiro wave with 1/5 time scale were larger than that under the Kobe wave with 1/5 time scale. But the trend of the maximum shear strain was opposite. Because the displacement of the Kobe wave with 1/10 time scale and the Kushiro wave with 1/5 time scale were less than that of the Kobe wave with 1/5 time scale while the amplitude of the acceleration was almost the same.

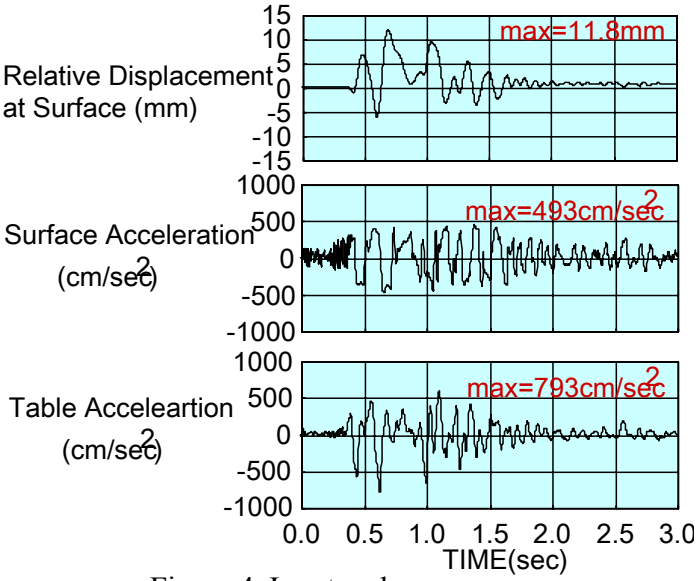

Figure 4. Input and response waves (Kobe100%,T.S.=1/5)

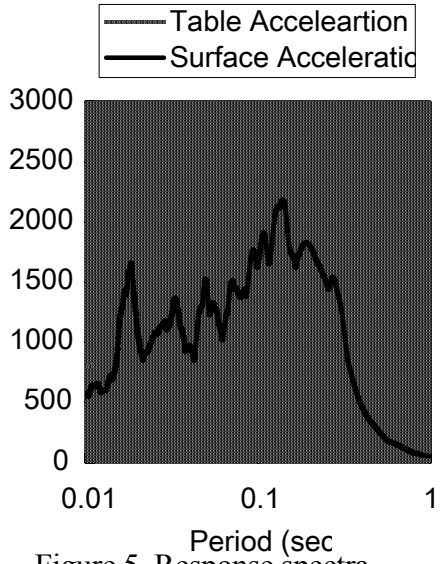

Figure 5. Response spectra (Kobe 100%,T.S.=1/5)

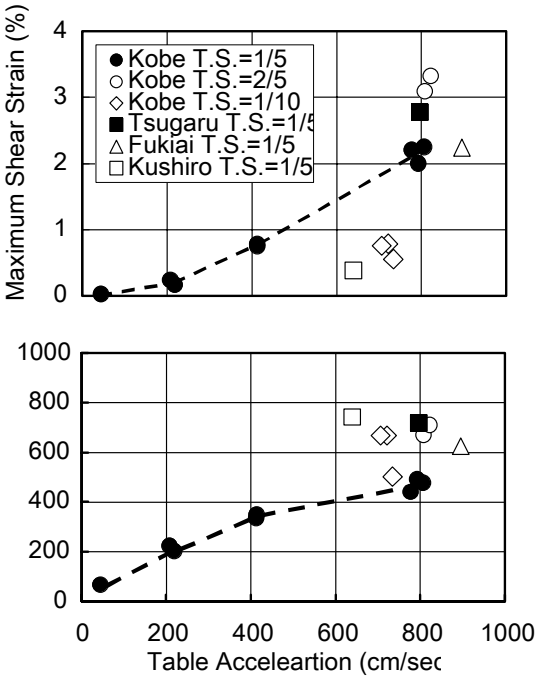

Figure 6. Relationship of table acceleration and response of sand deposit

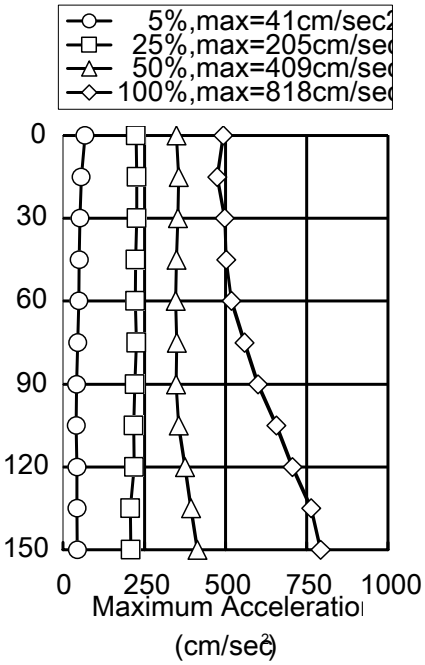

Figure 7. Distribution of maximum acceleration

Distribution of Maximum Acceleration

The distribution of the maximum acceleration under the Kobe wave with 1/5 time scale are shown in Figure 7. The response acceleration along the depth of the sand deposit under waves with 5%, 25% and 50% amplitude were almost constant. Because the predominant frequency of input motions, 15Hz, was a little less than the natural frequency of soil deposit, 19-21Hz. However, the distribution

of the response acceleration along the depth of the sand deposit under the Kobe wave with original amplitude was different from those under smaller amplitude input waves. The maximum acceleration of upper layers were smaller than that of lower layers. The time history of the surface acceleration under the Kobe wave with 100% amplitude in Figure 4 shows trapezoidal shapes around the peak values. This trend is like the time history of a mass on a sliding surface whose frictional coefficient is about 0.5. This behavior occurred when the sand deposit was destroyed. The acceleration when the sand deposit was destroyed was assumed from the shear strength of the model sand. The internal frictional angle of silica sand #4 is about 30 degrees. So shear strength is $\tan 30^\circ$ (=0.58) of the effective confined pressure. In other words, when the horizontal acceleration is about the half of the gravity acceleration, the shear force of the sand over the objective layer is larger than its shear strength, and shear failure occurs at the layer. After the shear failure, the maximum acceleration is limited at the half of the gravity acceleration.

ANALYTICAL STUDY

Objectives

To evaluate the exact ground behavior during a huge earthquake, calculation model which can express the non-linearity of ground must be developed. Hardin-Drnevich(H-D) model and Ramberg-Osgood(R-O) model are generally used to evaluate ground behavior for earthquake resistant design. But these hysteretic non-linear models are not appropriate for applying to non-linear problems under an extra huge earthquake because of the following reasons.

1) Conventional models, e.g. H-D and R-O models, have been confirmed for applying to non-linear problems with relatively large strain up to 1%. But during the Kobe earthquake, ground strain exceeded several percents. So a new constitutive model which can deal with more than 1% ground strain is necessary.

2) In case of evaluating hysteretic behavior with the conventional models, the Masing rule is applied. But damping ratio calculated by the conventional hysteretic rule does not express the real behavior. So we modifyed the Masing rule to fit the hysteretic behavior of sand.

We propose "Combined Hysteretic(C-H) Model" to solve these problems. The outline of the proposed model is explained in the following section. After that, a calculation example analyzing the experimental results is explained.

Combined Hysteretic Model

Skeleton Curve

The H-D model may be used to express the non-linearity of sand deposit under a huge earthquake. But the H-D model does not have enough parameters to fit the torsional shear test results. So the equation of the skeleton curve of the combined hysteretic model is modified as follows.

$$\tau = G_0 \gamma \Big/ \left(1 + \left|\gamma / \gamma_r\right|^{\delta}\right) \tag{1}$$

$$\delta = A \log_{10} \gamma + B \tag{2}$$

where, τ : shear stress, G_0 : initial shear stiffness at small strain range, γ : shear strain, γ_r : reference strain defined as ordinary method, δ : modification parameter to identify the test and model result, A and B : fitting parameter calculated from relationship between δ and γ during torsional shear test.

The parameter δ is specially introduced to fit the model skeleton curve more precisely to the skeleton curve derived from the torsional shear test.

Hysteretic Loop

The hysteretic loop obtained by applying the Masing rule to the skeleton curve defined by the H-D model is bigger than that derived from torsional shear test. So, the parameters α and β in the following equations are introduced to fit the model hysteretic loop to the test results. This equation looks like R-O model.

$$\gamma = \frac{\tau}{G_0}\left(1 + \alpha|\tau|^{\beta}\right) \tag{3}$$

The parameters α and β in this model can be calculated from the maximum damping ratio h_{max} in extra huge strain range.

The initial shear stiffness G_0, the maximum damping ratio h_{max}, and the reference strain γ_r are defined from the torsional shear test results, and finally the hysteretic loop using the "Combined hysteretic(C-H) model" is defined.

Comparison with Torsional Shear Test Results

One example of evaluating the relationship between shear stiffness and shear strain is explained as follows. Confined pressures of this example was 20kN/m^2 as shown in Figure 2. The parameters of the hysteretic model are defined by equation (4).

$$G_0 = 36 \text{ M Pa}, h_{max} = 36\ \%, \gamma_r = 3.20 \times 10^{-2}\ \% \tag{4}$$

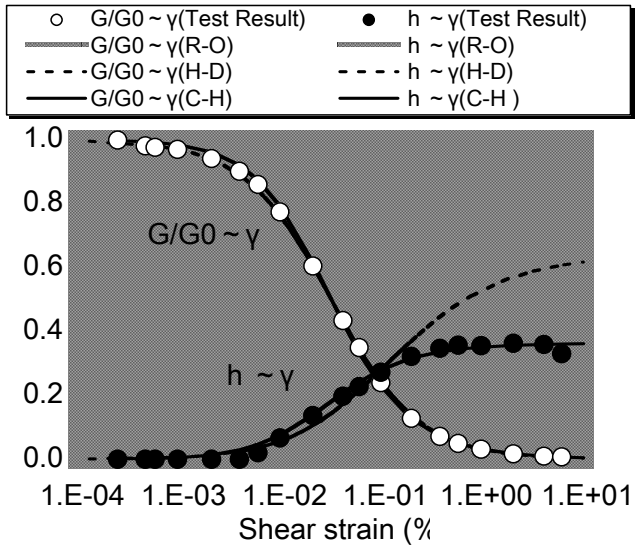

Figure 8. Strain dependency of stiffness and damping ratio

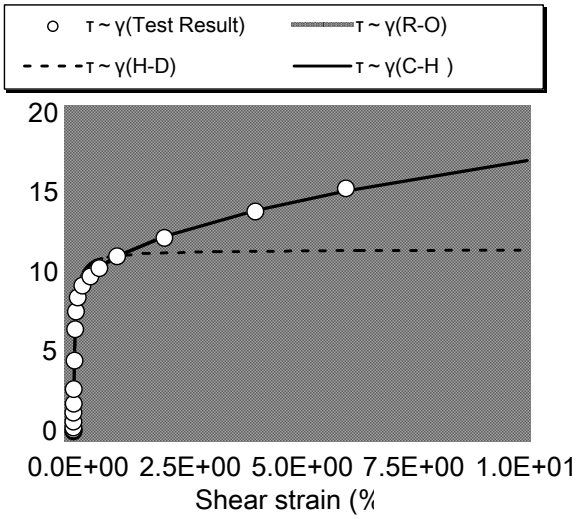

Figure 9. Comparison of skeleton curve

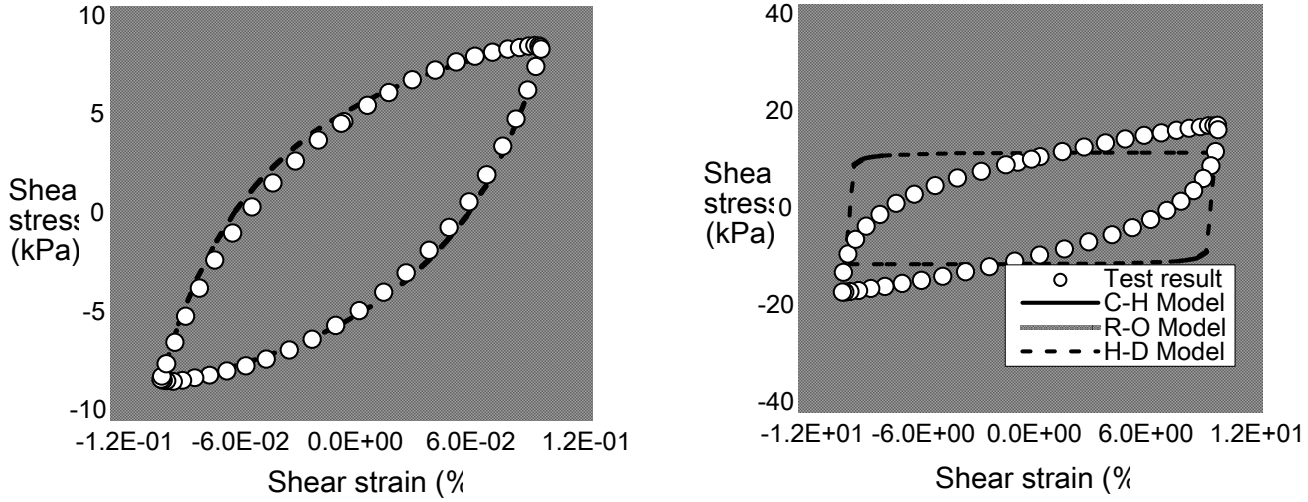

(a) Maximum strain : 0.1% (b) Maximum strain : 10%

Figure 10 Comparison of stress – strain curve at small and large strain amplitude

Strain dependency curve of stiffness and damping ratio are shown in Figure 8. The torsional shear test results, the calculated results using the H-D ,R-O and C-H model are shown in it. The shear stiffness(G/G_0) using the H-D model well fits to the test results, but the damping ratio(h) in huge strain range does not fit to the test results. The damping ratio(h) using the R-O model well fits to the test results, but the shear stiffness(G/G_0) does not fit to the test results. In this kind of situation, the shear stiffness(G/G_0) and damping ratio(h) using the C-H model have very good agreement with the test results. The skeleton curves of each model are shown in Figure 9. The skeleton curve using C-H model is the only one which has very good agreement with test results in wide strain range.

The hysteretic loops with 0.1% strain and 10% strain are shown in Figure 10. The test results, the calculated results using the H-D, R-O and C-H model are shown in it. In case that the shear strain is 0.1%, the stress–strain relationships calculated using each of three type hysteretic model all fit well to the test results. But in case that shear strain is 10%, only C-H model fits to the test results.

Analytical Study Using Combined Hysteretic Model

Simulation Model and Analytical Case

The initial stiffness is calibrated to fit the initial predominant frequency of the analytical model to that of model ground. In calibrating the predominant frequency of the analytical model, the initial stiffness distribution was assumed to be proportional to confined pressure. Figure 11 shows the initial stiffness distribution of the analysis model and the analytical condition. Each element is the plane strain element, and all nodes are fixed in vertical direction. The reference strains of each layer are defined assuming that the reference strains are proportional to half power of the confined pressure. The maximum damping ratios of all layers are defined as constant value, 36%. The fitting parameters A,B in the equation (2), and the parameters α and β in the equation (3) of each element are defined as constant value.

Ground behavior during the Kobe wave with 2/5 time scale was calculated using the Combined-Hysteretic(C-H) model and the Ramberg-Osgood(R-O) model.

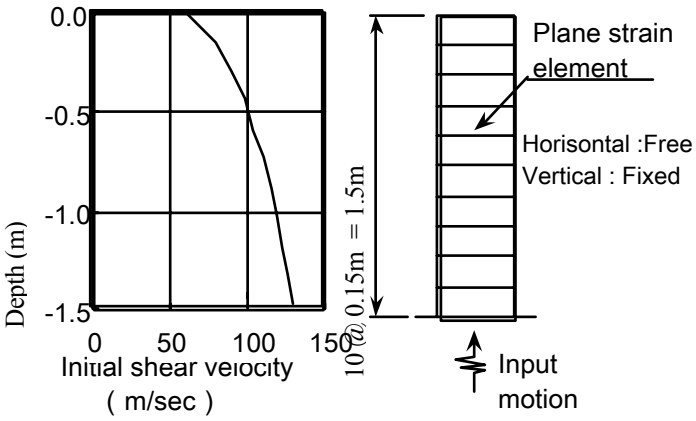

Figure 11. Analytical model and ground stiffness

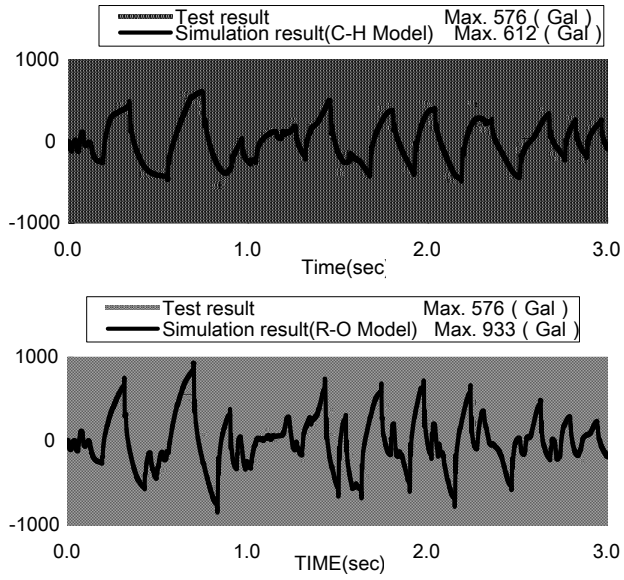

Figure 12 Comparison of experimental and calculated result (Surface acceleration)

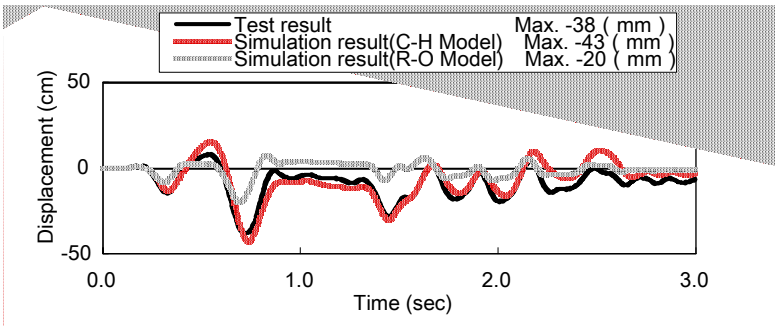

Figure 13 Comparison of experimental and calculated result (Surface displacement)

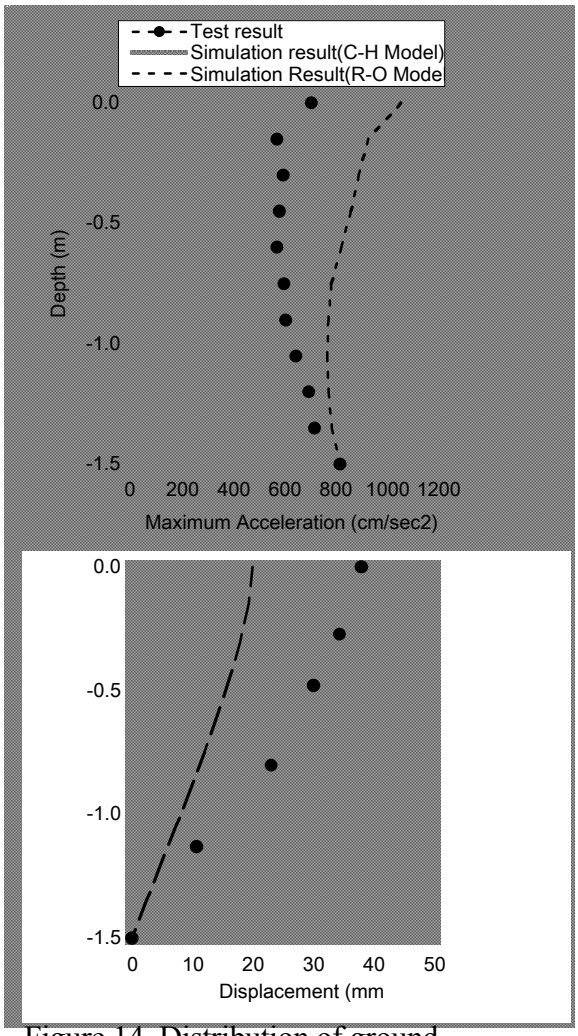

Figure 14 Distribution of ground acceleration and displacement

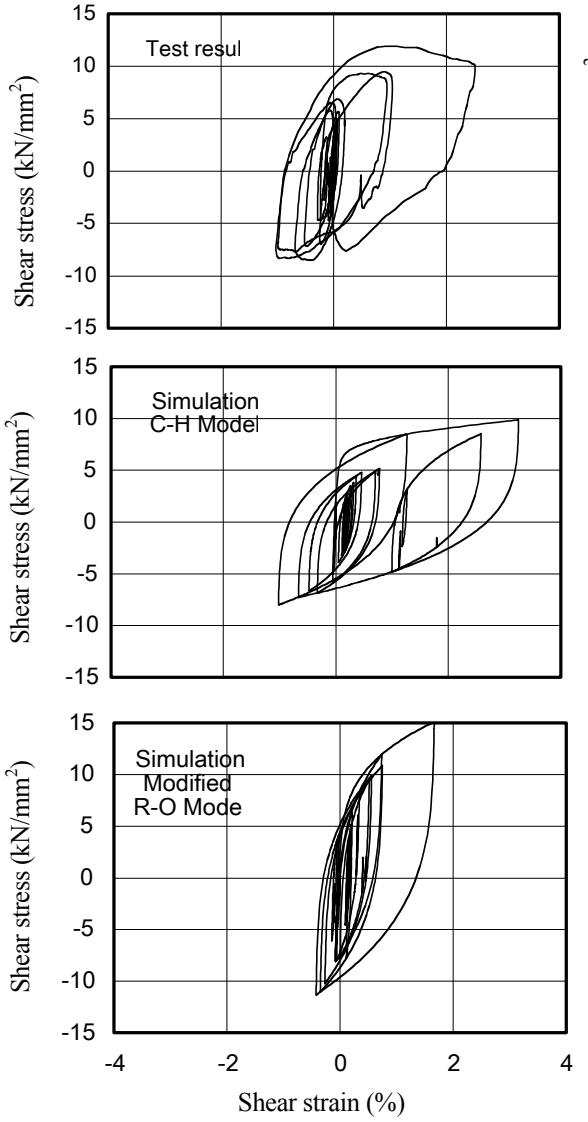

Figure 15. Stress – strain relationship of test and simulation results

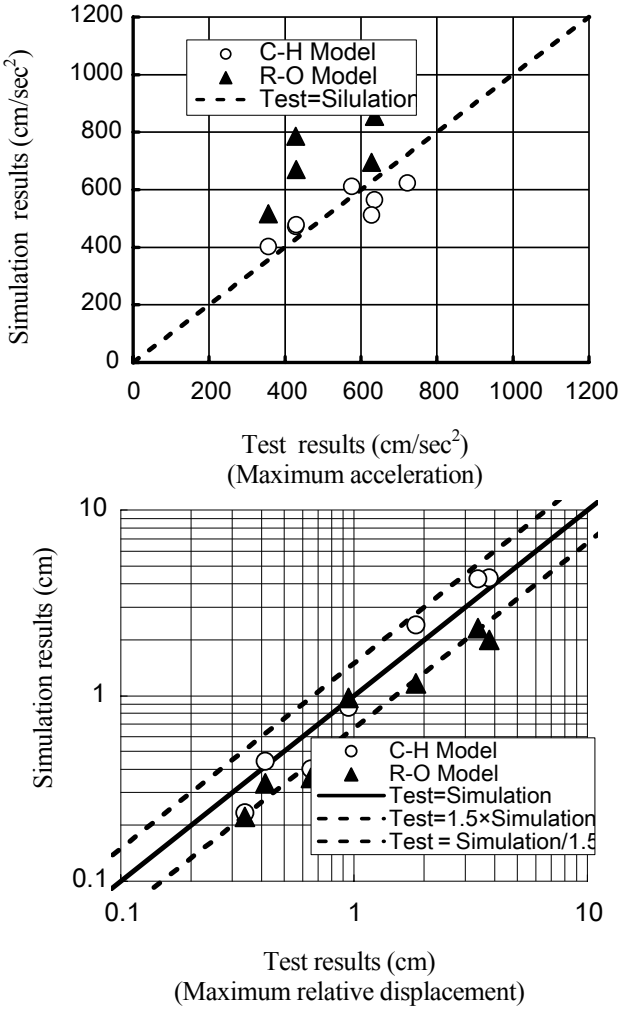

Figure 16. Test and simulation result of maximum acceleration and displacement

Comparison of Response Time Histories

Figure 12 shows the simulated acceleration time histories at the ground surface compared with the test results. The upper figure shows the result using the C-H model, and the lower figure shows the result using the R-O model. For C-H model case, the time history shows trapezoidal shapes at several points. The acceleration values seem to have some limitation, which is almost the same as the limited value of the test results. But the maximum acceleration using the R-O model was larger than that of the test results. The surface relative displacements to the table of the tests and simulations are shown in Figure 13. The simulation results using the C-H model well fit to the test results. The distribution of acceleration and displacement of the test and simulations are shown in Figure 14. The maximum acceleration and relative displacement of each layer calculated using the C-H model fit well to the test results. But the maximum acceleration of each layer calculated using the R-O model is

larger than that of the test results, and the maximum relative displacement of each layer calculated using the R-O model is smaller than that of the test results.

Figure 15 shows the hysteretic stress–strain relationships at the bottom layer of the sand deposit. The hysteretic curve using the C-H model almost coincides with the test result. But the hysteretic curve using the R-O model is different from the test result. In the R-O model, the shear stress has almost the same qualitative characteristics as acceleration, and the shear strain has almost the same qualitative characteristics as the relative displacement.

Figure 16 shows the comparison between the test results and simulation results under several input waves. The maximum accelerations and relative displacements of C-H model were almost the same as those of the test results. But the maximum accelerations of the R-O model are always larger than those of the test results, and the maximum relative displacements of the R-O model were always smaller than those of the test results. These results are similar to the results of the test case under the Kobe wave with 2/5 time scale.

CONCLUSIONS

The shaking table tests using the sand deposit model were performed to clarify the behavior of ground during huge input motion like the 1995 Kobe earthquake. And a new type hysteretic model, "Combined Hysteretic(C-H) model", is proposed in this paper. As results of the tests and simulations using the newly proposed model and the conventional models, following conclusions are derived.

1) Under huge earthquake motion, the surface acceleration decreases from the input acceleration because the inertia force of the sand deposit becomes larger than the frictional strength. This means that shear failure occurs in sand deposit. This failure is very important to express earthquake motion at very shallow layer during a huge earthquake.

2) A new type hysteretic model, "Combined Hysteretic(C-H) model", is proposed considering advantageous points of the H-D and R-O models. The skeleton curve and hysteretic rule are defined as modifications of the H-D and R-O models. Accuracy of the C-H model was confirmed comparing the simulation results with the results of torsional shear tests.

3) The analysis results using the C-H model were compared with those using the R-O model and shaking table test results. It was clarified that the results using the C-H model can well simulate the test results, while the results using the R-O model do not have good agreement with the test results.

It was clarified that the proposed "Combined Hysteretic model" can simulate the ground response during an extra huge motion like the 1995 Kobe earthquake. Authors will expand this theory to three dimensional analysis, and apply the proposed model to analyze the behavior of many kinds of structures constructed on relatively soft ground.

REFERENCES

[1] B.O.Hardin, V.P.Drnevich, 1982.2, "Shear modulus and damping in soils : Dynamic equations and curves", SM7, ASCE, pp.667-692

[2] I.Kumazaki, 1998.3,"Chaos in dynamic deformation properties of nonlinear elements and prediction of their constitutive relations", Doctoral dissertation, Kyoto university,

[3] G.Masing,1926, "Eigenspannungen und verfestigung beim Messing", Proceeding of Second International Congress of Applied Mechanics, Zurich

Rate-dependency of sand under low effective stress as observed in laboratory shear tests

Ikuo Towhata and Chaminda P. Gallage

ABSTRACT

Prediction of liquefaction-induced ground deformation requires that the behavior of sand undergoing very low effective stress is understood experimentally. Previous 1-g model tests revealed the rate-dependent, or viscous, nature of liquefied sand. Since it was therein difficult to evaluate the rate-dependency more accurately, the present study carried out triaxial compression tests in drained manner on Yurakucho sand of Tokyo with fines. The effective stress was maintained very low during shear by supplying high back pressure from the outside. Creep tests in a triaxial compression manner revealed that shear stress consists of an inviscid frictional component and a rate-dependent component, and the study was focused on the latter. The test results demonstrated that the rate-dependent behavior of sand is similar to Bingham model and that the effective stress of sand increases the magnitude of viscous stress, enabling the rate-dependent deformation only under low effective stress. In contrast, the density of sand does not affect the rate-dependent nature significantly. The results of triaxial compression were supplemented by those by triaxial extension as well as tests on special light grains and a scope under lower or null effective stress was obtained. Finally, it is inferred that the cause of the rate-dependency is partly the vortex of pore fluid and partly the grain-to-grain collision during shear deformation.

INTRODUCTION

The prediction of the magnitude of flow displacement of sandy ground which is induced by seismic liquefaction has been attempted by a variety of approaches. Among them those based on elastoplasticity of sand are the most popular and easy to be incorporated in numerical analyses. However, it is often the case that the original elastoplasticity modeling was developed by soil testing which did not pay attention to liquefaction problems. To develop a reasonable soil model, it is essentially important to run laboratory shear tests which

can reveal the stress-strain behavior of liquefied sand that undergoes deformation under extremely low effective stress.

The authors carried out shaking table tests in which an embedded pipe was pulled laterally in liquefied model deposit in the course of strong shaking (Towhata et al., 1999). It was revealed therein that continued strong shaking erased the effects of positive dilatancy, as induced by large shear deformation, which would otherwise increase the effective stress and prevent the development of further shear distortion. Accordingly, the state of low effective stress was maintained and large deformation developed. Moreover, the force which was needed to pull the pipe laterally increased with the velocity of the pipe, showing that liquefied sand has a rate-dependent nature. Although it was further attempted to obtain the viscosity coefficient from those tests, the low level of confining pressure in 1-g model tests made it inappropriate. Another problem was that the stress and strain in the model ground was heterogeneous. Since the nature of soil is nonlinear and strain dependent, the interpretation of data was considered less reliable.

To overcome the above-mentioned problems, the authors carried out laboratory shear tests in which the states of stress and strain are determined more precisely. Also a special care was taken to prevent the positive dilatancy and to keep the state of low effective stress during shear deformation. Certainly, more realistic confining stress was applied to sand and the viscosity coefficient was determined based on the measured stress and strain.

METHOD OF SHEAR TEST

The present study aims at measuring the stress-strain behavior of loose liquefied sand undergoing monotonic deformation. To achieve this goal, the problem is the positive dilatancy of sand which, under undrained shear conditions, increases the effective stress and prevents the development of shear deformation. Not only preventing deformation, the uncontrolled increasing effective stress makes difficult the interpretation of measured stress-strain behavior. To overcome this problem, the authors conducted drained shear tests in which the state of high excess pore water pressure was maintained by externally supplying the equally high back pressure into a tested specimen (Nishimura et al., 2002).

Fig.1 indicates a torsion shear device with a hollow cylindrical specimen. This device can run shear tests either in a torsional or in a triaxial manner. The present study, firstly, ran cyclic “undrained” torsion shear in order to develop high excess pore water pressure. After this stage, the cyclic torsion was terminated, high back pressure which was equal to the developed pore pressure was externally supplied, the drainage valve was opened, and triaxial

compression was conducted.

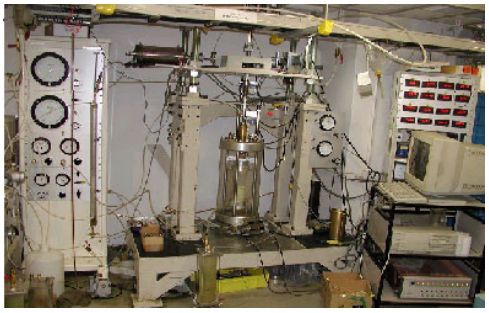

Figure 1 Torsion shear device employed in present study.

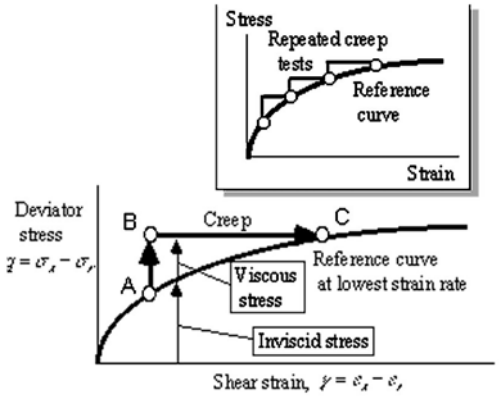

Figure 2 Conceptual illustration of triaxial compression to measure rate-dependency of sand.

The idea of "drained" monotonic shear is illustrated in Fig.2. The reference curve is the static stress-strain relationship which is realized when the rate of strain is very low. In the present study, the rate of strain is faster than this, and the effects of this higher deformation rate is expected to be exhibited in the measured stress. Suppose now that the stress-strain state of a tested specimen lies at the point A. The deviator stress, q, is then suddenly increased to the point B and thereinafter is held constant for a sufficiently long time. The specimen exhibits a creep deformation until reaching the point C and, in the meantime, monitoring is made of the stress, $q=\sigma_a-\sigma_r$, together with the rate of shear strain, $\dot{\gamma} = \dot{\varepsilon}_a - \dot{\varepsilon}_r$.

At present, it is impossible to run shear tests in a stable manner on a completely liquefied sandy specimen. This is because the state of null effective stress makes it impossible that a specimen maintains its cylindrical shape unchanged under loaded deviator stress, q. The sample instability is further promoted by the gravity force acting on sand grains. Although insignificant under higher effective stress, the gravity force can generate large deformation when the effective stress is null. Moreover, the state of effective stress is made substantially heterogeneous by the gravity, because the effective stress at the top of a specimen is null, while higher due to gravity at the bottom; leading to heterogeneous deformation of a specimen. This problem of heterogeneous deformation is significant particularly under torsional shear condition in which shear strain is localized near the top. Consequently, the present study decided to run triaxial compression with low but positive effective stress remaining inside a specimen. To obtain the nature of completely liquefied sand with null effective stress, the obtained experimental data under positive effective stress will be extrapolated towards zero effective stress later on.

The reference curve in Fig.2 is therefore the static stress-strain behavior of sand under

the existing high pore pressure. The terminology of "static" means that the rate of strain is very low. Since the tests are of higher strain rate, the measured stress consists of the static inviscid component and the rate-dependent viscous component. Note that the present study maintains the constant stress for a long time until the creep procedure, BC, is completed. The procedure of *ABC* is repeated several times and the consecutive end points, *C*, of creep are connected with other so that the referenced curve is experimentally obtained; see the inset of Fig.2. Consequently, the inviscid stress is subtracted from the measured deviator stress and the viscous stress is determined. If the test data is interpreted from the view points of Newtonian viscosity, the viscosity coefficient, η, is obtained by

$$\eta = \frac{q_{measured} - q_{inviscid}}{2\left(\dot{\varepsilon}_a - \dot{\varepsilon}_r\right)} \tag{1}$$

TESTED MATERIAL

Tests were run on Yurakucho alluvial sand which is prevalent in the Tokyo area. Fig.3 shows the gradation curve of this sand. The minimum and maximum void ratio of this sand are *0.785* and *1.27*, respectively, while the specific gravity is *2.697*. This sand is non-plastic. However, when the fines content of this sand was separated from coarser grains, liquid and plastic limits were obtained as *PL=54%* and *LL=60%*. This is because the sand is of alluvial origin and a limited amount of clay fraction is contained in the sand.

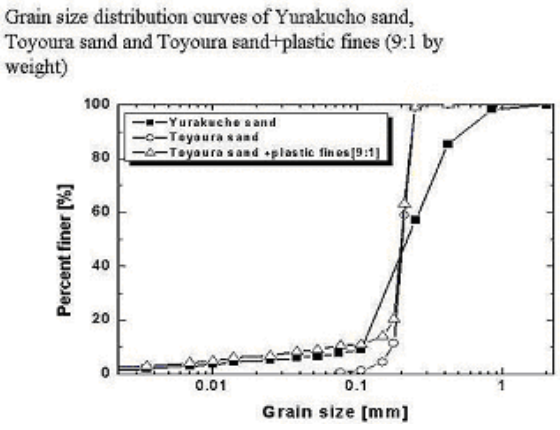

Figure 3 Grain size distribution of Yurakucho sand in Tokyo.

MEASURED STRESS-STRAIN BEHAVIOUR

Fig.4 illustrates a typical behavior of Yurakucho sand specimen during "drained" triaxial compression which followed undrained cyclic loading and decrease of effective stress from *100 kPa* to *10 kPa*. It is noteworthy, particularly in the latter half of the test, that the deviatoric shear strain, $\varepsilon_a - \varepsilon_r$, increased in a creep manner under the constant magnitude of deviator stress. This type of data was employed to determine the viscosity coefficient by means of Eq.1. The deviator stress decreased slightly towards the end of creep due to the increasing cross section of the specimen which finally failed; axial stress being calculated by axial force divided by increasing cross section.

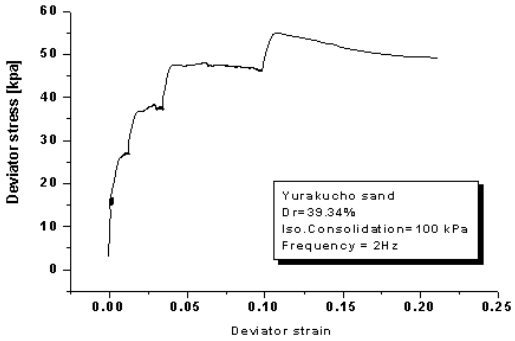

Figure 4 Typical stress-strain relationship of Yurakucho sand during monotonic drained shear after reducing effective stress from 100kPa to 10kPa (relative density=39.3%).

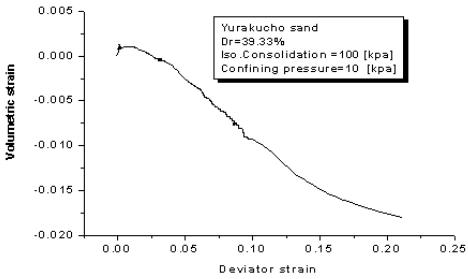

Figure 5 Volume change of Yurakucho sand sample during monotonic drained shear after reducing effective stress from 100kPa to 10kPa (relative density=39.3%).

The volume change of the same specimen in the course of "drained" triaxial compression is illustrated in Fig.5. Since the deviator strain was large, reaching *20%* ultimately, the volume of the specimen expanded. This dilatant behavior is equivalent with increase of effective stress and consecutive hardening under undrained condition. It may be feared that the rate of loading was so high that the water migration into the specimen could not catch up with the required volume increase, decreasing pore pressure undesirably to some extent. In reality, however, five minutes were spent on one stage of creep deformation and the rate of shear strain was less than *0.002%/second* in the most part of creep. Hence, the change of pore pressure due to insufficient water migration occurred for a very short period and did not affect the overall reliability of tests; for a time history of pore pressure during monotonic drained shear, see Fig.6. Note that the pore pressure in this figure was monitored at the top of a specimen, while the specified back pressure was supplied only from the bottom of a specimen. Thus, the pore pressure record in this figure manifests the true time history of pore pressure

inside the specimen in the course of creep deformation.

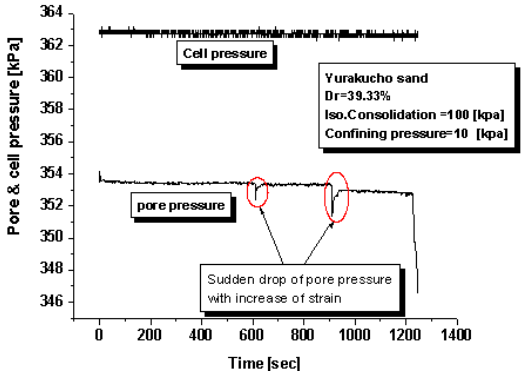

Figure 6 Variation of pore pressure in Yurakucho sand sample during monotonic drained shear after reducing effective stress from 100kPa to 10kPa (relative density=39.3%).

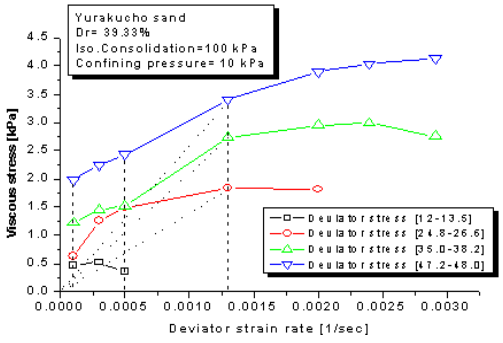

Figure 7 Nonlinear relationship between viscous stress and strain rate.

EQUIVALENT NEWTONIAN VISCOSITY COEFFICIENT

As a nature of soil, the viscous component of stress is not necessarily proportional to the strain rate (Fig.7) as Eq.1 implies. Hence, the calculated viscosity coefficient is not constant, varying with the magnitude of strain rate. For a practical purpose, this section makes use of Eq.1 to calculate the viscosity. This implies that the nonlinearity is replaced by an equivalent linear Newtonian viscosity in which stress and strain rate are proportional to each other. The nonlinearity will be discussed in the next section.

Effects of Mean Effective Stress on Equivalent Newtonian Viscosity

The preceding section described that pore pressure was held constant in the course of "drained" triaxial compression. It should be noted, however, that the mean effective stress increased in the mean time because the axial effective stress increased. Fig.8 summarizes test data for which the preceding undrained cyclic torsion decreased the effective stress from *100 kPa* to *5 kPa*; followed by drained shear. This figure illustrates that the viscous component of deviator stress increases with the increasing effective stress. Note that the viscous stress increases slightly with the strain rate. Consequently, the equivalent Newtonian viscosity coefficient is plotted in Fig.9 for a range of strain rate. The viscosity increases with the mean

effective stress. Moreover, the Newtonian viscosity increases with the decreasing strain rate because the real behavior is nonlinear similar to Bingham viscosity.

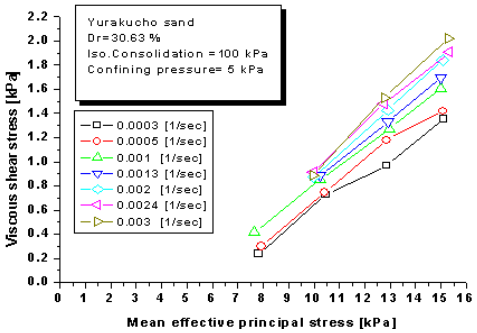

Figure 8 Variation of viscous deviator stress with changing mean effective stress during drained triaxial compression (Dr=30.6%).

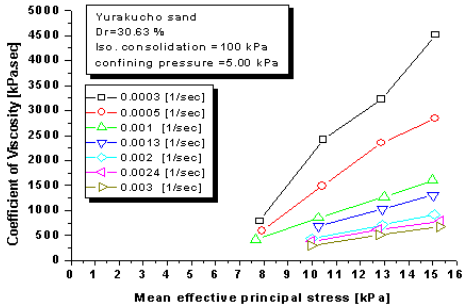

Figure 9 Variation of viscosity coefficient with changing mean effective stress during drained triaxial compression (Dr=30.6%).

Two attempts were further made to study the viscosity under lower effective stress level. Firstly, Fig.10 plots data from triaxial extension tests. Since the axial stress decreased during "drained" extension after pore pressure rise, it was possible to obtain data under *3* to *4 kPa* of mean effective stress. It seems that the viscosity from an extension test is consistent with those from compression. It is probably reasonable to extrapolate these data towards zero effective stress. A second attempt was a use of styrofoam grains whose specific gravity was merely *1.04*. Since the specimen was water-saturated, the buoyancy reduced this value to *0.04* and a specimen was able to maintain stability under lower effective stress level. Fig.11 shows the obtained viscosity. Again, there is a consistency between Yurakucho sand data and styrofoam data except for the lowest strain rate. Thus, the whole data in Figs 10 and 11 are basically consistent.

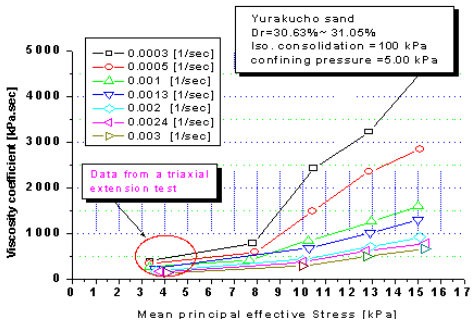

Figure 10 Newtonian viscosity coefficient from drained triaxial compression and extension.

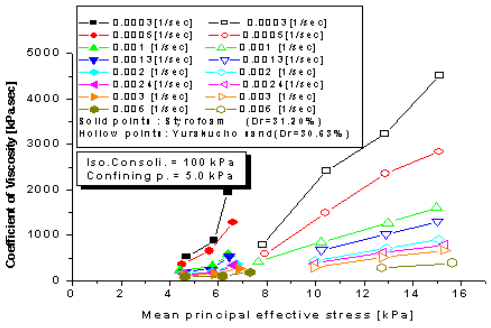

Figure 11 Newtonian viscosity coefficient from drained triaxial compression on styrofoam specimen.

Effects of Relative Density on Equivalent Newtonian Viscosity

Fig.12 shows the variation of Newtonian viscosity with the effective stress at a shear strain rate of 0.002/second. For three relative densities ranging from 30 to 56%, there is no significant difference. This does not mean, however, that loose and medium sands are subjected to similarly large deformation after liquefaction. Denser sand requires more number of shaking cycles to attain the low effective stress and the remaining time period of strong shaking is shorter. Hence, the deformation that can develop during the remaining shorter time is smaller. In other words, the same intensity of cyclic loading results in higher effective stress in denser sand at which viscosity coefficient is greater. Thus, denser sand can develop less magnitude of deformation.

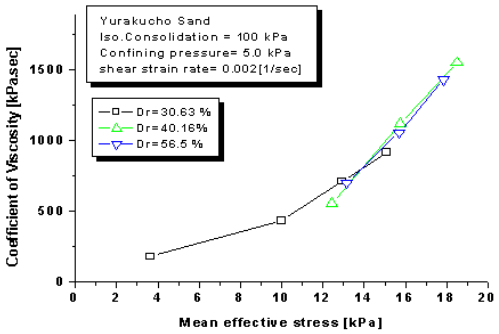

Figure 12 Relationship between Newtonian viscosity coefficient and relative density of Yurakucho sand.修士論文

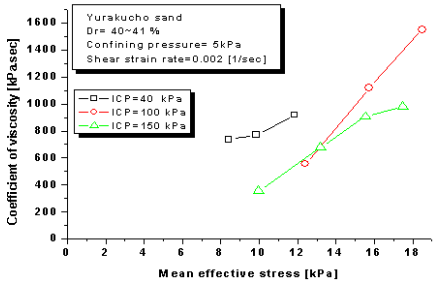

Figure 13 Relationship between Newtonian viscosity coefficient and initial consolidation pressure of Yurakucho sand (mean effective stress during drained triaxial compression being held at 5kPa and strain rate = 0.002/second).

Effects of Initial Consolidation Pressure on Equivalent Newtonian Viscosity

Fig.13 compares viscosity coefficient obtained from three specimens. They were of similar relative density and had the same effective stress of *5 kPa* at the beginning of drained triaxial compression. Their difference lay in the initial isotropic consolidation pressure (*ICP*) which were *40*, *100*, and *150 kPa*, respectively. Obviously different *ICP*s correspond to different depth in the field. The figure reveals that the lower ICP is associated with the greater viscosity. This does not necessarily mean that thinner liquefied deposit develops less extent of deformation. The extent of pore pressure rise prior to triaxial compression was *(40kPa-5kPa) / 40 kPa = 0.875* for *ICP=40 kPa*, while it was *(150-5)/150 = 0.967*. This figure may imply that the greater extent of pore pressure rise is associated with smaller viscosity and more vulnerability to large deformation.

Effects of Fines Content on Equivalent Newtonian Viscosity

Fig.14 compares the Newtonian equivalent viscosity for four types of sand which had different fines content (*<75 microns*). Among these tested materials, Toyoura sand has no fines with uniform fine particle size, Yurakucho sand has fines to some extent (for gradation, see Fig.3), and Toyoura sand which was mixed with either *10%* nonplastic fines, that was made by grinding Toyoura sand itself (npf specimen), or *10%* plastic fines of Yurakucho sand (pf specime). As stated previously, the fines of Yurakucho sand has a plasticity. It is seen in the figure that more fines makes less viscosity.

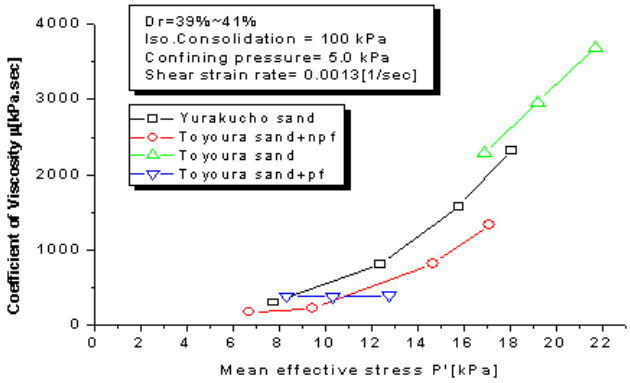

Figure 14　Variation of Newtonian viscosity with fines content. 修

BINGHAM VISCOUS NATURE OF SAND

The present section is addressed to the Bingham viscous nature of Yurakucho sand in place of the equivalent Newtonian interpretation in the preceding sections. Fig.15 exhibits the nonlinear relationship between the measured viscous stress and the strain rate. This nonlinear relationship is somehow similar to what Bingham viscosity suggests. It is noteworthy, however, that this figure depicts only the rate-dependent component of stress and that the frictional and static rate-independent component (Fig.2) is not included. It is further seen in the figure that the viscous stress increased as the mean effective stress was raised by triaxial compression. In more details, not only the magnitude of viscous stress but also the gradient of the plotted curves is increased by the rising effective stress. This implies that both the Bingham strength (vertical offset of the curves) and the Bingham viscosity increase with the effective stress level. Similar points can be made of Fig.16 for a denser sand specimen. Finally, a linear regression was made of the data in the figure and the Bingham strength and viscosity were obtained for further discussion.

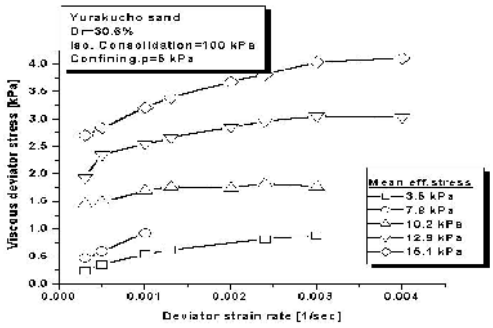

Figure 15 Relationship between viscous stress and strain rate for 30.6% relative density (mean effective stress was reduced from 100kPa to 5kPa by undrained cyclic loading.).

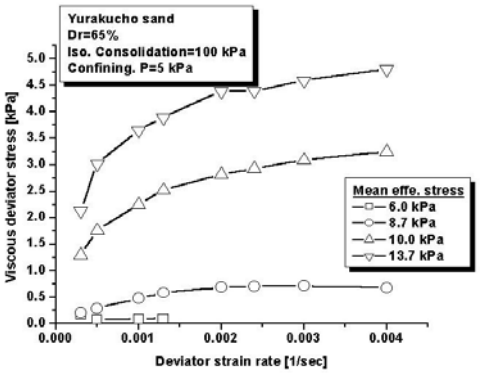

Figure 16 Relationship between viscous stress and strain rate for 65% relative density (mean effective stress was reduced from 100kPa to 5kPa by undrained cyclic loading.).

Fig.17 shows that the Bingham strength increases with the effective stress. It is noteworthy that the magnitude of this strength is not significantly affected by the relative density of sand. Similarly in Fig.18, the Bingham viscous coefficient is nearly independent of relative density as well, although increasing with the effective stress.

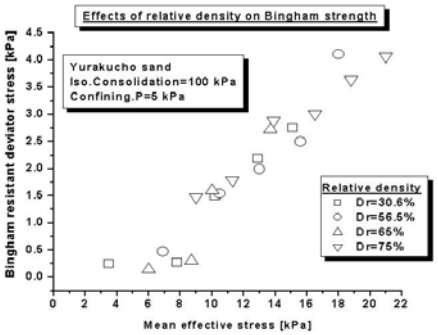

Figure 17 Variation of Bingham strength with effective stress and relative density.

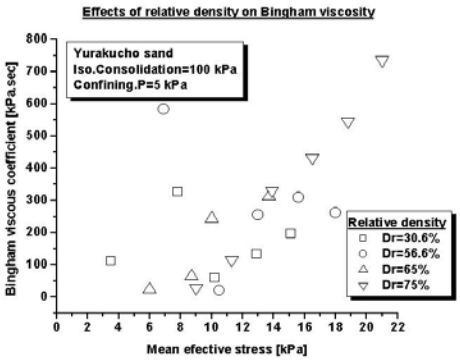

Figure 18 Variation of Bingham viscosity with effective stress and relative density.

CAUSE OF VISCOSITY OF SAND

The experiments so far have revealed that sand undergoing low effective stress has a rate-dependent nature of shear deformation. This raises a question why a mixture of inviscid sand grains and water are so viscous. To answer this question, drained triaxial compression tests were further performed on two special specimens. The first one was a specimen of air-dry Yurakucho sand with pore air and the second one was made of the same sand with vacuum pore. For the second specimen, the external pressure was made negative and the

difference between the external chamber pressure and the pore pressure was made equal to the positive specified effective stress.

The obtained Newtonian equivalent viscosity is indicated in Fig.19. It is important that the air-dry specimen exhibits less extent of viscosity than the water-saturated sand. The viscosity is further reduced in a vacuum specimen. Thus, it seems that the observed viscosity is to some extent accounted for by the action of pore fluid. More clearly, it is possible that vortex energy dissipation of pore water and pore air, to less extent, upon migration of sand grains is the major cause of observed rate-dependency. The remaining rate-dependency of vacuum specimen, however, suggests that there is another source of viscosity which, the authors suppose, is the granular collision in the course of deformation.

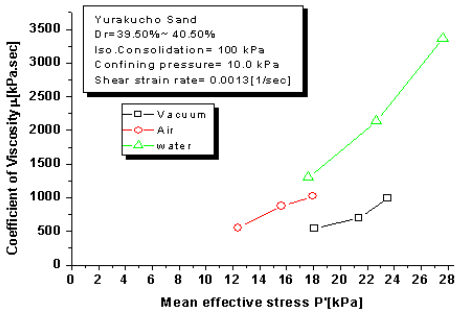

Figure 19 Equivalent Newtonian viscosity of water-saturated, air-dry, and vacuum samples of Yurakucho sand.修士

CONCLUSIONS

Laboratory shear tests were carried out on specimens of loose sand in order to study its rate-dependent behavior under low effective stress. A specially designed “drained” triaxial compression tests were conducted in order to avoid the effects of positive dilatancy and uncertain increase of effective stress on the rate-dependent behavior of sand. Accordingly, the following conclusions were drawn.

1) The viscous component of shear stress varies in a nonlinear manner with the changing strain rate. This behavior is similar to Bingham modelling to some extent. The present paper studied this observed rate-dependency from the view point of both Bingham viscosity modelling and its equivalent Newtonian viscosity.

2) The viscosity increases with the effective stress which is loaded on sand at the time of deformation.

3) the viscosity is affected in addition by the initial consolidation pressure. In other words, the overconsolidation ratio induced by development of excess pore water pressure affects the viscosity.
4) On the contrary, the viscous nature is not affected substantially by the density of sand.
5) It is inferred that the observed viscosity of rate-dependency is generated partly by the vortex of pore fluid, and partly by the grain-to-grain collision.

ACKNOWLEDGMENT

The torsional shear device which was employed in the present study was developed by the grant-in-aid which was supplied by the former Ministry of Education. This assistance is deeply appreciated by the authors.

REFERENCES

【1】Nishimura, S., Towhata, I., and Honda, T. (2002): "Laboratory shear tests on viscous nature of liquefied sand," Soils and Foundations, Vol.42, No.4, pp.89-98.

【2】Towhata, I., Vargas-Monge, W., Orense,R.P. and Yao, M. (1999): "Shaking table tests on subgrade reaction of pipe embedded in sandy liquefied subsoil," Soil Dynamics and Earthquake Engineering Journal, Vol.18, No.5, pp.347-361.

ESTIMATING K_α FOR USE IN EVALUATING CYCLIC RESISTANCE OF SLOPING GROUND

I. M. Idriss and R. W. Boulanger

ABSTRACT

The recently formulated relative state parameter index ξ_R was shown to be a practical index for describing the experimentally observed variation of K_α with both relative density and effective confining stress (Boulanger 2003a). This paper describes the subsequent development of relations that can be used to estimate K_α as a function of both relative density and effective confining pressure. These relationships are also expressed in terms of modified SPT blow count $(N_1)_{60}$ and normalized CPT tip resistance q_{c1N} to facilitate their use in practice for estimating the cyclic resistance of soils beneath sloping ground.

INTRODUCTION

In the initial development of analytical procedures for evaluating the performance of earthdams during earthquakes, the cyclic resistance of the soils comprising the embankment and the foundation was evaluated by conducting cyclic tests on samples of these soils. To accommodate the effects of the initial static shear stress on the cyclic resistance, the cyclic tests were conducted by consolidating the sample under anisotropic loading conditions in a triaxial test prior to applying the cyclic load. Similarly, simple shear tests were conducted by consolidating samples with an initial horizontal shear stress before applying the cyclic load. In both tests, the eventual failure plane had an initial (i.e., static) shear stress, τ_s, and an initial effective normal stress, σ'_{vo}. The ratio $|\tau_s|/\sigma'_{vo}$ has been designated α, and the cyclic resistance for a given number of stress cycles has been related to the initial effective normal stress for various values of α. The earliest tests, which had been conducted on samples of the Sheffield Dam foundation soils (Seed et al 1969), and the subsequent tests on samples of the San Fernando Dams (Seed et al 1975) showed an increase in the cyclic resistance as α increased under all effective confining stresses.

Seed (1983) subsequently introduced the static shear stress ratio correction factor (K_α) as a means for extending the SPT-based liquefaction correlations from level ground conditions to sloping ground conditions. The K_α factor was applied in conjunction with the overburden stress correction factor (K_σ) to adjust the cyclic stress ratio, $(CSR)_{\sigma'_{vo}=1;\alpha=0}$, required to trigger liquefaction at α = 0 and σ'_{vo} = 1 tsf (≈1 atmosphere, P_a). The cyclic stress ratio for α > 0 and σ'_{vo} ≠ 1 tsf is then given by:

$$(CSR)_{\sigma'_{vo}\neq 1;\alpha>0} = K_\alpha K_\sigma (CSR)_{\sigma'_{vo}=1;\alpha=0} \qquad (1)$$

Harder and Boulanger (1997) summarized the available cyclic laboratory test data and confirmed that K_α depends on both relative density, D_R, and effective confining stress. However, Harder

I. M. Idriss, Professor, Department of Civil & Environmental Engineering, University of California, Davis, CA 95616-5294; e-mail: imidriss@aol.com.
R. W. Boulanger, Professor, Department of Civil & Environmental Engineering, University of California, Davis, CA 95616-5294; e-mail: rwboulanger@ucdavis.edu.

and Boulanger suggested that for an initial effective normal stress less than about 3 tsf ($\approx 3 P_a$), the variation of cyclic resistance with α depends primarily on D_R, as shown in Fig. 1. For this range of σ'_{vo}, the ranges shown in Fig. 1 indicate that the cyclic resistance of dense sands can increase significantly as α increases, while the cyclic resistance of loose sands can decrease significantly as α increases.

Vaid and Chern (1985) conducted two series of cyclic triaxial tests on dense (D_R = 0.7) samples of tailings sand; one series of tests was conducted under an initial confining pressure, σ'_{3c} = $2 P_a$, and the other series was conducted under an initial confining pressure, σ'_{3c} = $16 P_a$. The test results showed that the much larger confining stresses produced K_α values that decreased significantly as α increased. The test results conducted with σ'_{3c} = $2 P_a$ produced the opposite trends, i.e., K_α values that increased significantly as α increased. These cyclic triaxial test results will be covered in more detail later in this paper.

This paper describes the derivation of relations that can be used to estimate K_α as a function of both confining stress and denseness (expressed in terms of D_R, normalized SPT blow count, or normalized CPT tip resistance). These relations build on the work of Boulanger (2002, 2003a) who introduced a relative state parameter index, ξ_R, and showed that it could be used as a reasonable and practical index for describing the experimentally observed variation of K_α with both D_R and σ'_{vo}. The specific steps covered in this paper are as follows:

- Review the definition of ξ_R.
- Derive relations between K_α and ξ_R based on cyclic simple shear data at confining stresses of about $2 P_a$.
- Show that the derived relations satisfactorily describe the effect of high confining stresses demonstrated in the tests of Vaid and Chern (1985).
- Use the relations to illustrate the effects of various parameters on K_α over a broader range of conditions.
- Express the relations in terms of SPT $(N_1)_{60}$ and CPT q_{c1N} to facilitate their implementation in practice.

RELATIVE STATE PARAMETER INDEX

The relative state parameter index, ξ_R, as defined by Boulanger (2002, 2003a) is given by:

$$\xi_R = \frac{1}{Q - Ln\left(\frac{100p'}{P_a}\right)} - D_R \qquad (2)$$

in which p' is mean effective normal stress, P_a is atmospheric pressure, D_R is relative density, and Q is an empirical constant. This simple index for representing state was derived from Bolton's (1986) relative dilatancy index. Bolton indicated that the parameter Q depends on the grain type and is approximately equal to 10 for quartz and feldspar, 8 for limestone, 7 for anthracite, and 5.5 for chalk.

Results of cyclic simple shear and cyclic triaxial tests were compiled by Boulanger (2002) and compared in terms of the relative state parameter index, ξ_R, for each test. The relevant test parameters and the value of ξ_R for each test are summarized in Table 1 for the simple shear tests and in Table 2 for the triaxial tests. The test data presented in Tables 1 and 2 indicate that the test conditions that would normally be referenced by an effective normal stress and a relative density need only be referenced by the relative state parameter index, ξ_R. Therefore, the results can now be exhibited in terms of K_α as a function of α for a specific value of ξ_R as shown in Fig. 2 for the simple shear data.

DERIVATION OF RELATIONSHIPS RELATING K_α TO ξ_R

The cyclic simple shear test results shown in Fig. 2 can be interpolated and replotted in terms of K_α versus ξ_R for a selected value of the parameter α. Such plots were prepared at α = 0.05, 0.1, 0.15… 0.35 and used to derive the following general expression relating K_α to ξ_R:

$$K_\alpha = a + b\exp\left(\frac{-\xi_R}{c}\right) \qquad (3a)$$

The parameters (a), (b), and (c) are functions of α and are obtained from the following expressions:

$$a = 1267 + 636\alpha^2 - 634\exp(\alpha) - 632\exp(-\alpha) \qquad (3b)$$

$$b = \exp\left(-1.11 + 12.3\alpha^2 + 1.31Ln(\alpha + 0.0001)\right) \qquad (3c)$$

$$c = 0.138 + 0.126\alpha + 2.52\alpha^3 \qquad (3d)$$

Equations (2) and (3) can then be used to estimate the static shear stress ratio correction factor K_α for any desired combinations of initial static shear stress conditions and state, expressed in terms of (ξ_R).

TABLE 1
CYCLIC SIMPLE SHEAR TESTS
(After Boulanger, 2002)

Relative Density	σ'_{vc} (atm)	K_o	p' (atm)	τ_{cyc}/σ'_{vc}	α	K_α	ξ_R
Tests on Ottawa Sand Conducted by Vaid & Finn (1979)							
0.68	2	0.45	1.27	0.170	0	1	-0.486
0.68	2	0.45	1.27	0.220	0.093	1.294	-0.486
0.68	2	0.45	1.27	0.247	0.192	1.453	-0.486
0.50	2	0.45	1.27	0.107	0	1	-0.306
0.50	2	0.45	1.27	0.099	0.093	0.925	-0.306
0.50	2	0.45	1.27	0.094	0.192	0.879	-0.306
0.50	2	0.45	1.27	0.096	0.291	0.897	-0.306
Tests on Sacramento River Sand Conducted by Boulanger at al (1991)							
0.35	2	0.45	1.27	0.126	0	1	-0.156
0.35	2	0.45	1.27	0.120	0.100	0.952	-0.156
0.35	2	0.45	1.27	0.091	0.200	0.725	-0.156
0.35	2	0.45	1.27	0.080	0.300	0.635	-0.156
0.55	2	0.45	1.27	0.160	0	1	-0.356
0.55	2	0.45	1.27	0.157	0.100	0.981	-0.356
0.55	2	0.45	1.27	0.166	0.200	1.038	-0.356
0.55	2	0.45	1.27	0.183	0.300	1.144	-0.356

Notes for Table 1:

(1) The ratio τ_{cyc}/σ'_{vc} from Vaid & Finn's results was selected at 3% strain reached in 10 cycles.

(2) The ratio τ_{cyc}/σ'_{vc} from Boulanger et al's results was selected at 3% strain reached in 15 cycles.

(3) A value of Q = 10 was used in Eq. (1) to calculate ξ_R for each test.

TABLE 2
CYCLIC TRIAXIAL TESTS
(After Boulanger, 2002)

Relative Density	σ'_{3c} (atm)	K_c	σ'_{fc} (atm)	τ'_{fc} (atm)	p' (atm)	τ_{cyc}/σ'_{fc}	α	K_α	ξ_R
Tests on Tailings Sand Conducted by Vaid & Chern (1985)									
0.7	2	1	2	0	2	0.194	0	1	-0.430
0.7	2	1.5	2.21	0.405	2.33	0.270	0.183	1.390	-0.418
0.7	2	2.0	2.41	0.809	2.67	0.347	0.335	1.786	-0.407
0.7	16	1	16	0	16	0.116	0	1	-0.084
0.7	16	1.25	16.8	1.62	17.3	0.133	0.096	1.151	-0.052
0.7	16	1.5	17.7	3.24	18.7	0.101	0.183	0.875	-0.019
0.7	16	2.0	19.3	6.47	21.3	0.050	0.335	0.431	0.049

Notes for Table 2:

(1) The ratio τ_{cyc}/σ'_{fc} from Vaid & Chem's results was selected at 2.5% strain reached in 10 cycles.

(2) A value of Q = 9 was used in Eq. (1) to calculate ξ_R for each test.

COMPARISONS OF K_α VALUES OBTAINED FROM CYCLIC TESTS WITH VALUES CALCULATED USING DERIVED EQUATIONS

The values of K_α calculated using Eq. (3) are first compared to those obtained from the cyclic simple shear tests of Vaid and Finn (1979) and Boulanger et al (1991). In as much as the cyclic simple shear test data were used to derive the equations, it would be expected that this comparison should provide excellent agreement, as suggested by the information provided in Fig. 3. The values of K_α obtained from the cyclic simple shear tests (Table 1) and the values calculated using Eq. (3) are listed in Table 3. These values are also plotted in Fig. 3 together with the derived curves for α = 0.1, 0.2, and 0.3. As can be noted, the calculated values are very close (in some cases almost identical) to those obtained from the cyclic simple shear tests. The derived curves represent an excellent fit to the test data for α = 0.1 and for α = 0.3, and a reasonable fit to the test data for α = 0.2.

Also shown in Fig. 3 are the derived curves for α = 0.05, 0.1, 0.15… 0.35 to illustrate the variations of K_α with the relative state parameter index ξ_R for a given value of α.

TABLE 3
COMPARING CALCULATED K_α VALUES AGAINST CYCLIC SIMPLE SHEAR DATA

Relative Density	From Cyclic Simple Shear Tests (Table 1)			Calculated K_α
	α	K_α	ξ_R	
Tests on Ottawa Sand Conducted by Vaid & Finn (1979)				
0.68	0	1	-0.486	1
0.68	0.093	1.294	-0.486	1.238
0.68	0.192	1.453	-0.486	1.542
0.50	0	1	-0.306	1
0.50	0.093	0.925	-0.306	0.959
0.50	0.192	0.879	-0.306	0.980
0.50	0.291	0.897	-0.306	0.960
Tests on Sacramento River Sand Conducted by Boulanger at al (1991)				
0.35	0	1	-0.158	1
0.35	0.100	0.952	-0.158	0.876
0.35	0.200	0.725	-0.158	0.788
0.35	0.300	0.635	-0.158	0.626
0.55	0	1	-0.358	1
0.55	0.100	0.981	-0.358	1.014
0.55	0.200	1.038	-0.358	1.095
0.55	0.300	1.144	-0.358	1.127

The values of K_α calculated using Eq. (3) were compared to those obtained from the cyclic triaxial tests of Vaid and Chern (1985). The values of K_α calculated using Eq. (3) and obtained from the tests are listed in Table 4. Using Q = 9, as suggested by Boulanger (2003a) for this tailings sand, the calculated K_α values are about 10 to 25 percent lower than those obtained from the triaxial test data, except for the test result at p' = 21.3 atm and α = 0.335 for which the calculated value is 43% lower. While slightly conservative for these tests, the values of K_α calculated using Eq. (3) capture the relative effect that increasing the confining stress from about

$2P_a$ to about $16P_a$ had on the same D_R = 0.7 tailings sand. The triaxial teats at $\alpha > 0$ were conducted at mean effective stresses greater than that used for the tests at $\alpha = 0$. Thus, some of these differences, between the calculated K_α and K_α based on the results of the triaxial tests, may be attributable to this difference in mean effective stresses (i.e., K_σ effect).

Values of K_α calculated with Q = 9.4 are also presented in Table 4. These calculated K_α values range from 15% lower to 11% higher than the triaxial data, except for the test at p' = 17.3 atm and α = 0.096 where the calculated value is 23% lower. The effects of Q on K_α are illustrated and discussed further in a later section of the paper (see Table 6).

TABLE 4
COMPARING CALCULATED K_α VALUES AGAINST HIGH CONFINING STRESS TESTS

Relative Density	From Cyclic triaxial Tests (Table 2)				Calculated K_α for Q=9	Calculated K_α for Q=9.4
	p' (atm)	α	K_α	ξ_R		
Tests on Ottawa Sand Conducted by Vaid & Chern (1985)						
0.7	2	0	1	-0.430	1	1
0.7	2.33	0.183	1.390	-0.418	1.249	1.350
0.7	2.67	0.335	1.786	-0.407	1.363	1.525
0.7	16	0	1	-0.084	1	1
0.7	17.3	0.096	1.151	-0.052	0.855	0.889
0.7	18.7	0.183	0.875	-0.019	0.733	0.810
0.7	21.3	0.335	0.431	0.049	0.247	0.478

INFLUENCE OF MEAN EFFECTIVE NORMAL STRESS AND RELATIVE DENSITY ON K_α

The variations of K_α with mean effective normal stress, p', are shown in Fig. 4 considering a soil having a relative density of D_R = 0.4 and Q = 10. Similar results are presented in Fig. 5 for a soil having a relative density of D_R = 0.7 and Q = 10. The results shown in Figs. 4 and 5 are for p'/P_a = ½, 1, 2, 4, 8 and 16. These two figures illustrate the strong influence on K_α of both the mean effective normal stress and the relative density of the soil. This influence is also illustrated by the values listed in Table 5, which indicate a decrease in K_α as p'/P_a increases for all values of α and for both D_R = 0.4 and D_R = 0.7. The value of K_α increases with an increase in relative density, all other conditions being the same.

TABLE 5
EFFECT OF MEAN EFFECTIVE NORMAL STRESS AND RELATIVE DENSITY ON K_α VALUES

	K_α at α = 0.1		K_α at α = 0.2		K_α at α = 0.3	
p'/P_a	D_R = 0.4	D_R = 0.7	D_R = 0.4	D_R = 0.7	D_R = 0.4	D_R = 0.7
1	0.899	1.351	0.844	1.717	0.729	1.933
2	0.887	1.265	0.815	1.567	0.677	1.752
8	0.859	1.071	0.745	1.208	0.541	1.288
16	0.845	0.971	0.705	1.005	0.455	0.994

INFLUENCE OF THE PARAMETER Q ON K_α

The values of K_α at p'/P_a = 1 and 8 with Q = 8, 9, and 10 calculated using Eqs. (2) and (3) are listed in Table 6. These results indicate that soils with a higher Q would have a higher value of K_α, especially at high values of α. The results also indicate that the relative effect increases somewhat at higher relative densities and at higher values of the mean effective normal stress.

As noted by Bolton (1986), the parameter Q depends on the grain type and is typically equal to 10 for quartz and feldspar, 8 for limestone, 7 for anthracite, and 5.5 for chalk. Accordingly, for most soils within an embankments or the foundation of an embankment, a value of Q = 9 or 10 would seem reasonable.

TABLE 6
EFFECT OF PARAMETER Q ON K_α VALUES

	K_α at p'/P_a = 1					
	D_R = 0.4			D_R = 0.7		
α	Q = 8	Q = 9	Q = 10	Q = 8	Q = 9	Q = 10
0.1	0.861	0.881	0.899	1.083	1.224	1.351
0.2	0.749	0.801	0.844	1.231	1.494	1.717
0.3	0.550	0.650	0.729	1.319	1.663	1.933
	K_α at p'/P_a = 8					
	D_R = 0.4			D_R = 0.7		
α	Q = 8	Q = 9	Q = 10	Q = 8	Q = 9	Q = 10
0.1	0.826	0.839	0.859	0.837	0.930	1.071
0.2	0.642	0.688	0.745	0.680	0.915	1.208
0.3	0.279	0.413	0.541	0.393	0.851	1.288

RELATING K_α TO SPT BLOW COUNT

The relative state parameter index, ξ_R, is expressed in Eq. (2) as a function of mean effective normal stress, relative density and the parameter Q. Equation (2) can be rewritten by substituting an expression that relates relative density to SPT blow count. Over the past several decades, many researchers have proposed expressions relating SPT blow count to relative density of a cohesionless soil. The relationship developed by Meyerhof (1957) is typical of most available expressions and is given by:

$$N = \left(17 + 24\frac{\sigma'_{vo}}{P_a}\right) D_R^2 \qquad (4)$$

in which N is the SPT blow count (in blows per ft) taken at a depth having an effective vertical stress σ'_{vo}, and D_R (in decimal) is the relative density. The SPT blowcount adjusted for an effective vertical stress of one atmosphere is designated N_1. Thus, Eq. (4) can be rewritten as follows:

$$N_1 = (a+b)\,D_R^2 \qquad (5)$$

The sum $(a+b)$ = 41 in the original Meyerhof relationship [Eq. (4)]. As noted by Cubrinovski and Ishihara (1999), the sum $(a+b)$ is affected by the grain size characteristics and the type of soil under consideration. Cubrinovski and Ishihara included data for high quality undisturbed samples (obtained by in situ freezing) for clean sand and for silty sand. The relative density, fines content, N_1, and median grain size, D_{50}, of each undisturbed sample are tabulated by Cubrinovski and Ishihara, and can be used to calculate the sum $(a+b)$. The calculated values of $(a+b)$ are plotted in Fig. 6, which indicate that the sum $(a+b)$ is higher for the clean sands than it is for the silty sands, but is very weakly dependent on D_{50}. The average values of the sum $(a+b)$ for the soils included in Fig. 6 are summarized in Table 7.

TABLE 7
AVERAGE $(a+b)$ VALUES USING DATA BY CUBRINOVSKI AND ISHIHARA (1999)

Samples	average $(a+b)$**
Silty Sand Samples	19.7
Clean Sand Samples	38.9
All Samples	29.9

** Using N_1 values reported by Cubrinovski and Ishihara (1999)

It may be noted that the SPT blow counts used for calculating the sum $(a+b)$ for the samples presented in Fig. 6 were most likely obtained with a delivered energy of about 80%. If the usual adjustment is made (i.e., multiplying each blow count by the ratio 80/60) to convert the SPT blow counts tabulated by Cubrinovski and Ishihara (1999) to equivalent values of $(N_1)_{60}$, the above averages of $(a+b)$ would be those shown in Table 8.

TABLE 8
AVERAGE $(a+b)$ VALUES AFTER CONVERSION TO 60% ENERGY RATIO

Samples	average $(a+b)$***
Silty Sand Samples	26.2
Clean Sand Samples	51.9
All Samples	39.9

***Values of N_1 reported by Cubrinovski and Ishihara (1999) were multiplied by the ratio 80/60 to convert to $(N_1)_{60}$

It is interesting to note that the value of $(a+b)$ = 39.9 for all samples is very close to that obtained from the original Meyerhof relationship [Eq. (4)].

If the value of $(a+b)$ = 51.9 were used for clean sands, a relative density of only about 76% is obtained for an SPT blow count $(N_1)_{60}$ = 30, which is the limiting value for triggering liquefaction in a clean sand (fines content ≤ 5%) in the currently used SPT-based liquefaction

evaluation procedure. A more realistic value for $(a+b)$ might be 46, which would result in a relative density of about 81% for an SPT blow count $(N_1)_{60}$ = 30. Therefore, a value of $(a+b)$ = 46 seems reasonable to use for clean sands and will be adopted for estimating the variations of K_α with $(N_1)_{60}$.

Equation (2) can be rewritten for clean sands in terms of $(N_1)_{60}$ as follows:

$$\xi_R = \frac{1}{Q - Ln\left(\frac{100p'}{P_a}\right)} - \sqrt{\frac{(N_1)_{60}}{46}} \tag{6}$$

The effective vertical stress, σ'_{vo}, is more widely used in practice and Eq. (6) can be rewritten in terms of σ'_{vo} and the lateral earth pressure coefficient at rest, K_o, as follows:

$$\xi_R = \frac{1}{Q - Ln\left(\frac{100(1+2K_o)\sigma'_{vo}}{3P_a}\right)} - \sqrt{\frac{(N_1)_{60}}{46}} \tag{7}$$

The values of K_α can then be calculated for any given set of $(N_1)_{60}$ and σ'_{vo}/P_a using Eqs. (7) and (3). Values of K_α at σ'_{vo}/P_a = 1 for $(N_1)_{60}$ = 4, 8, 12, 16, and 20 are presented in Fig. 7 and those at σ'_{vo}/P_a = 4 and the same SPT blow counts are presented in Fig. 8. A value of K_o = 0.45 was used for generating these curves. The effects of K_o are covered later in this paper.

Curves such as those presented in Figs. 7 and 8 can be used to estimate K_α, and hence, the cyclic resistance of a soil layer beneath a sloping ground. It is suggested that an equivalent clean sand SPT blow count (i.e., $(N_1)_{60cs}$) be used in Eq. (7) for cohesionless soils with fines contents greater than 5%.

RELATING K_α TO CPT TIP RESISTANCE

Boulanger (2002, 2003b) summarized the solutions completed by Salgado et al (1997a, 1997b) for CPT tip resistance and suggested that these solutions are closely approximated by:

$$\frac{q_c}{P_a} = C_o C_1 \left(\frac{\sigma'_{vo}}{P_a}\right)^m \left(\frac{K_o}{0.45}\right)^{m-0.077} \tag{8a}$$

$$m = 0.7836 - 0.5208 D_R \tag{8b}$$

$$C_o = 25.7 + 39.7 D_R + 212.3 D_R^2 \tag{8c}$$

C_1 = 1	typical soil property set	
C_1 = 0.64	lower bound soil property set	(8d)
C_1 = 1.55	upper bound soil property set	

in which q_c is the CPT tip resistance, and K_o, P_a and σ'_{vo} are as defined earlier in this paper.

The corrected CPT tip resistance (i.e., tip resistance corresponding to an effective vertical stress, σ'_{vo} = atmosphere) is given by:

$$q_{c1} = C_q q_c \tag{9}$$

The coefficient C_q can be expressed as follows:

$$C_q = \left(\frac{P_a}{\sigma'_{vo}}\right)^m \tag{10}$$

in which m varies with D_R as provided in Eq. (8b). The use of a normalized (i.e., dimensionless) corrected tip resistance, q_{c1N}, was suggested by Robertson and Wride (1997) and is equal to:

$$q_{c1N} = \frac{q_{c1}}{P_a} = \left(\frac{P_a}{\sigma'_{vo}}\right)^m \left(\frac{q_c}{P_a}\right) \tag{11}$$

Combining Eqs. (8a), (8c) and (11), provides the following relationship for q_{c1N} as a function of relative density and the coefficient of lateral pressure at rest, K_o:

$$q_{c1N} = C_1 \left(25.7 + 39.7 D_R + 212.3 D_R^2\right)\left(\frac{K_o}{0.45}\right)^{m-0.077} \tag{12}$$

The value of the coefficient $(K_o/0.45)^{m-0.077}$ depends on relative density and on K_o. The variation of this coefficient can have for a range of D_R and K_o values are illustrated in Table 9.

TABLE 9
VARIATION OF COEFFICIENT WITH D_R AND K_o

D_R	m	K_o	$(K_o/0.45)^{m-0.077}$
All relative densities	---	0.45	1.00
0.4	0.575	0.50	1.05
0.5	0.523	0.50	1.05
0.6	0.471	0.50	1.04
0.8	0.367	0.50	1.03
0.5	0.523	0.55	1.09
0.6	0.471	0.55	1.08
0.8	0.367	0.55	1.06
0.6	0.471	0.60	1.12
0.8	0.367	0.60	1.09
0.6	0.471	0.70	1.19
0.8	0.367	0.70	1.14

Thus, the product $C_1 (K_o/0.45)^{m-0.077}$ can vary from 0.64 for the lower bound property set with K_o = 0.45 to possibly over the 1.7 for the upper bound property set, K_o = 0.6 and D_R = 0.6. The wide range of possible values for this product produces a wide variation in the relation between q_{c1N} and D_R described by Eq. (12). This wide variation is, however, similar to the variation observed between $(N_1)_{60}$ and D_R, as represented by the data in Fig. 6.

The product $C_1 (K_o/0.45)^{m-0.077}$ can, however, be reasonably selected to result in a relative density of about 80% at the limiting value of q_{c1N} to trigger liquefaction. The latter value for most of the currently available relationships is $(q_{c1N})_{Lim}$ = 175±. Use of a value for $C_1 (K_o/0.45)^{m-0.077}$ ≈ 0.9 in Eq. (12) results in a value of q_{c1N} = 175 at D_R = 0.8.

Equation (12) can then be rewritten as follows:

$$q_{c1N} = 23.1 + 35.7 D_R + 191.1 D_R^2 \qquad (13)$$

Equation (13) can be inverted to provide an equation relating relative density to the corrected normalized CPT tip resistance. The following approximation is derived:

$$D_R = 0.478 (q_{c1N})^{0.264} - 1.063 \qquad (14)$$

This approach provides the means to calculate the relative state parameter index in terms of q_{c1N} by substituting Eq. (14) into Eq. (2). Thus:

$$\xi_R = \frac{1}{Q - Ln\left(\frac{100 p'}{P_a}\right)} - \left(0.478 (q_{c1N})^{0.264} - 1.063\right) \qquad (15)$$

The latter equation can also be rewritten in terms of the effective vertical stress, i.e.:

$$\xi_R = \frac{1}{Q - Ln\left(\frac{100 (1 + 2K_o) \sigma'_{vo}}{3 P_a}\right)} - \left(0.478 (q_{c1N})^{0.264} - 1.063\right) \qquad (16)$$

The values of K_α can then be calculated for any given set of q_{c1N} and σ'_{vo}/P_a using Eqs. (16) and (3). Values of K_α at σ'_{vo}/P_a = 1 for q_{c1N} = 60, 80, 100, 120, and 160 are presented in Fig. 9 and those at σ'_{vo}/P_a = 4 and the same CPT tip resistances are presented in Fig. 10. A value of K_o = 0.45 was used for generating these curves. The influence of K_o on these calculations is covered in the next section.

INFLUENCE OF LATERAL EARTH PRESSURE COEFFICIENT AT REST, K_o

A value of the lateral earth pressure coefficient at rest, K_o, is required to calculate the relative state parameter index using Eq. (7) or Eq. (16). The variations of K_α with effective vertical

stress and $(N_1)_{60}$ as illustrated in Figs. 7 and 8, or q_{c1N} as illustrated in Figs. 9 and 10, were calculated using a value of K_o = 0.45.

To evaluate the influence of K_o on K_α, values of K_α were calculated for σ'_{vo}/P_a = 1 and 4 and K_o = 0.45 and 0.60 using Eqs. (7) and (3) with $(N_1)_{60}$ = 4, 12 and 20. The results are presented in Figs. 11a and 11b. The values of K_α for σ'_{vo}/P_a = 1 and 4 and K_o = 0.45 and 0.60 using Eqs. (16) and (3) with q_{c1N} = 60, 100 and 120 are presented in Figs. 11c and 11d.

The information presented in Fig. 11 indicates that the lateral earth pressure coefficient at rest, K_o, has little or negligible influence on the calculated values of K_α.

CONCLUDING REMARKS

The relations derived in this paper provide a practical means for estimating the static shear stress ratio correction factor, K_α, for use in evaluating the cyclic resistance of soils beneath sloping ground. The relative state parameter index, ξ_R, provided the framework for describing the experimentally observed dependence of K_α on both relative density, D_R and effective confining pressure, σ'_{vo}. Relations were derived that express K_α as a function of the static shear stress ratio, the mean effective confining pressure, the effective vertical pressure, and the soil's denseness (expressed in terms of D_R, normalized SPT blow count, or normalized CPT tip resistance).

REFERENCES

Bolton, M. D. (1986) "The Strength and Dilatancy of Sands," Geotechnique, 36(1): 65-78.

Boulanger, R. W., Seed, R. B., Chan, C. K., Seed, H. B., and Sousa, J. (1991) "Liquefaction Behavior of Saturated Sands Under Uni-Directional and Bi-Directional Monotonic and Cyclic Simple Shear Loading," Geotechnical Engineering Report No. UCB/GT/91-08, University of California, Berkeley.

Boulanger, R. W. (2002) "Evaluating Liquefaction Resistance at High Overburden Stresses", Proceedings, 3rd US-Japan Workshop on Advanced Research on Earthquake Engineering for Dams, San Diego, CA, June 22-23.

Boulanger, R. W. (2003a) "Relating K_α to a Relative State Parameter Index," Journal of Geotechnical and Geoenvironmental Engineering, ASCE, in press.

Boulanger, R. W. (2003b) "High Overburden Stress Effects in Liquefaction Analyses," Accepted for publication, Journal of Geotechnical and Geoenvironmental Engineering, ASCE.

Cubrinovski, M., and Ishihara, K. (1999) "Empirical Correlation between SPT N-Value and Relative Density for Sandy Soils," Soils and Foundations, Japanese Geotechnical Society, Vol. 39, No. 5, pp 61-71.

Harder, L. F., Jr., and Boulanger, R. W. (1997) "Application of K_σ and K_α Correction Factors," Proceedings of the NCEER Workshop on Evaluation of Liquefaction Resistance of Soils, Report NCEER-97-0022, National Center for Earthquake Engineering Research, SUNY Buffalo, N.Y., pp. 167-190.

Robertson, P. K., and Wride, C. E. (1997) "Cyclic Liquefaction and its Evaluation Based on the SPT and CPT," Proceedings of the NCEER Workshop on Evaluation of Liquefaction Resistance of Soils, Report NCEER-97-0022, National Center for Earthquake Engineering Research, SUNY Buffalo, N.Y., pp. 41-87.

Salgado, R., Mitchell, J. K. and Jamiolkowski, M. (1997a) "Cavity Expansion and Penetration Resistance in Sand," Journal of Geotechnical and Geoenvironmental Engineering, ASCE, Vol. 123, No. 4, April, pp 344 – 354.

Salgado, R., Boulanger, R. W. and Mitchell, J. K. (1997b) "Lateral Stress Effects on CPT Liquefaction Resistance Correlations," Journal of Geotechnical and Geoenvironmental Engineering, ASCE, Vol. 123, No. 8, August, pp 726 – 735.

Seed, H. B. (1983) "Earthquake Resistant Design of Earth Dams," Proceedings of a Symposium on Seismic Design of Embankments and Caverns, Philadelphia, Pennsylvania, ASCE, N.Y.

Seed, H. B., K. L. Lee and I. M. Idriss (1969) "Analysis of Sheffield Dam Failure," Journal of the Soil Mechanics and Foundations Division, ASCE, Vol. 95, No. 5M6, pp. 1453-1490.

Seed, H. B., Lee, K. L., Idriss, I. M., and Makdisi, F. (1973) "Analysis of the Slides in the San Fernando Dams during the Earthquake of February 9, 1971," Report No. EERC 73-2, Earthquake Engineering Research Center, University of California, Berkeley.

Vaid, Y. P., and Chern, J. C. (1985) "Cyclic and Monotonic Undrained Response of Saturated Sands," Proceedings, Session on Advances in the Art of Testing Soils under Cyclic Conditions, ASCE, N.Y., pp 120-147.

Vaid, Y. P., and Finn, W. D. L. (1979) "Static Shear and Liquefaction Potential," Journal of Geotechnical Division, ASCE, Vol. 105, No. GT10, pp 1233-1246.

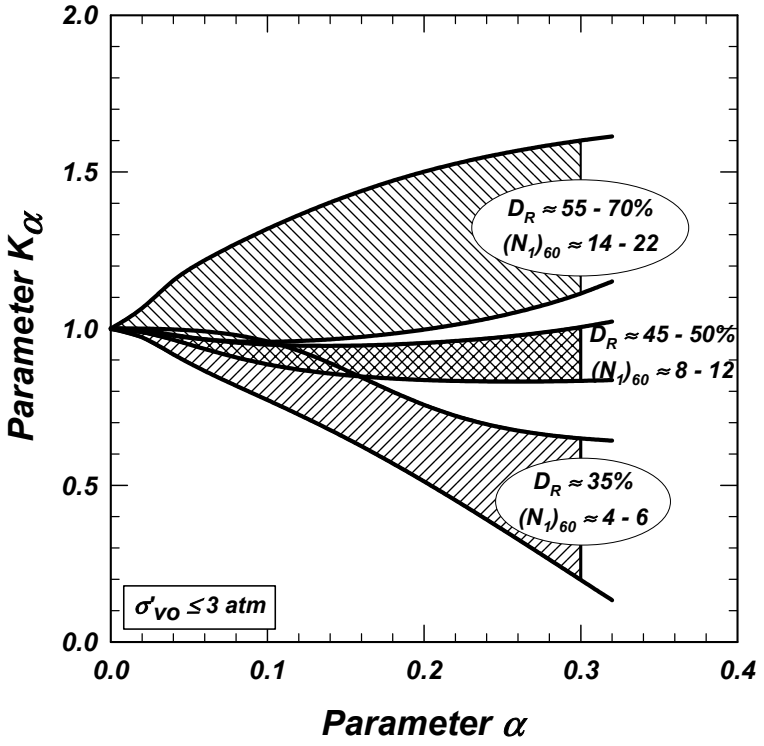

Fig. 1 Values of K_α Recommended by Harder and Boulanger (1997) for Vertical Effective Confining Pressures Less than 3 Atmospheres

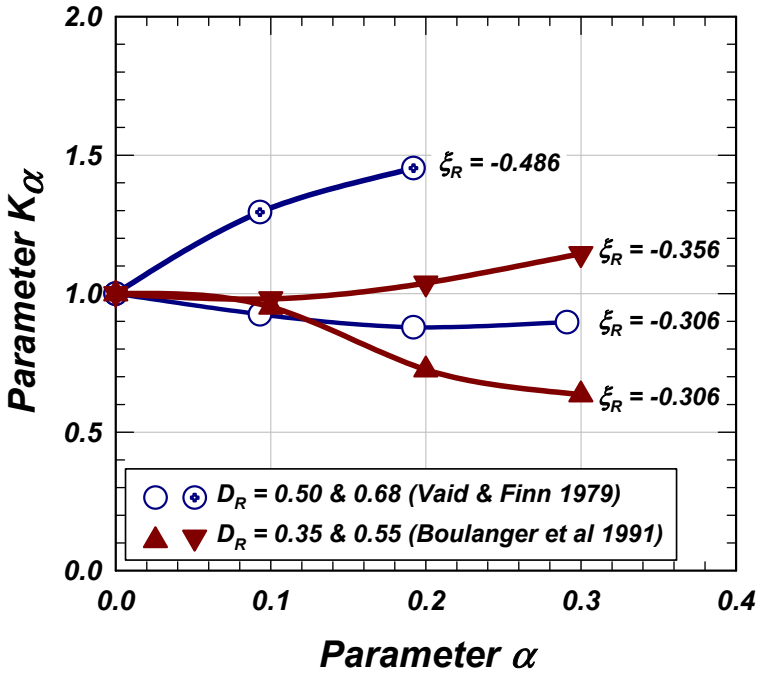

Fig. 2 Cyclic Simple Shear Test Data for a Range of D_R Values at an Effective Confining Pressure of 2 Atmospheres

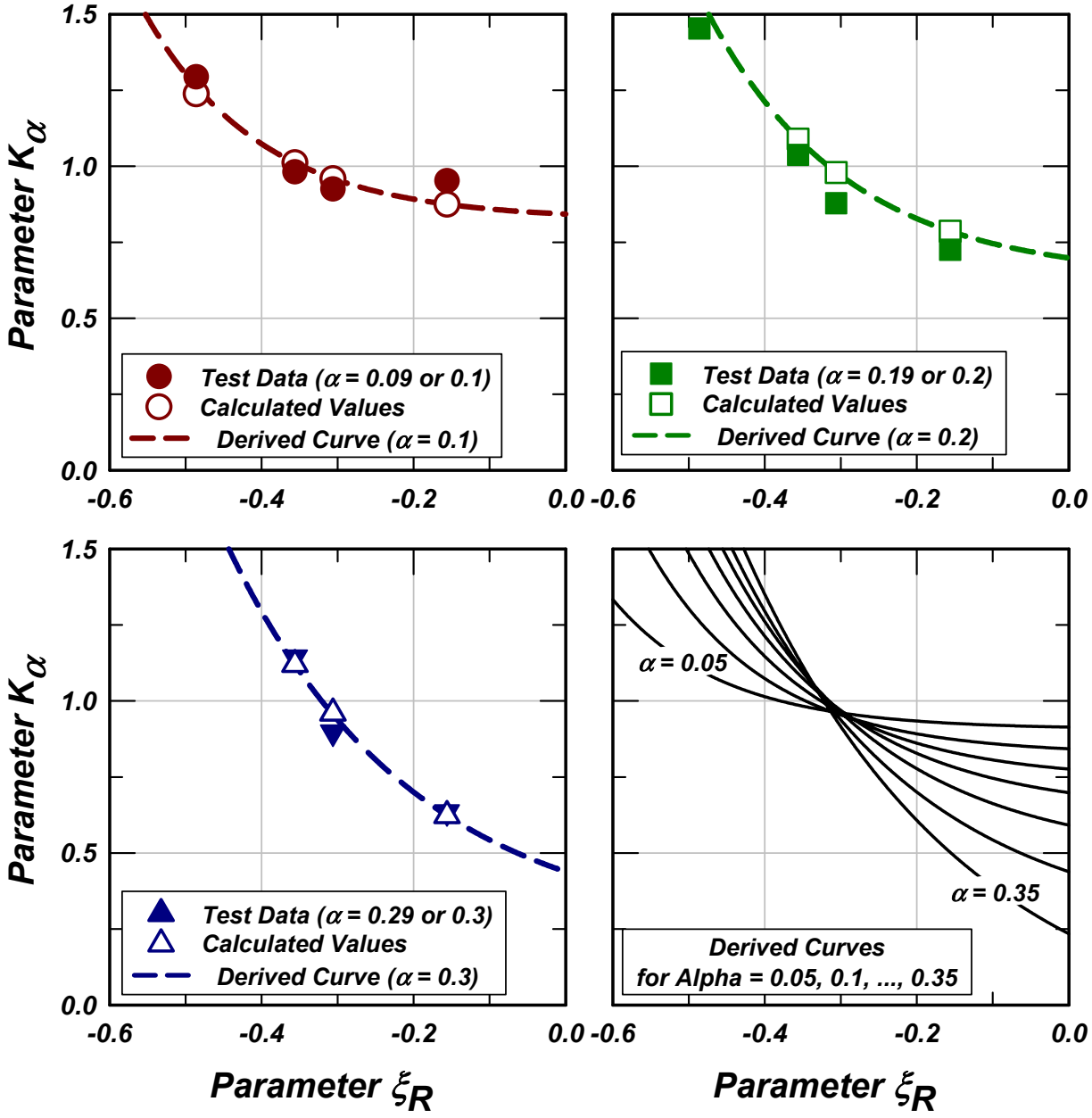

Fig. 3 Comparison of Derived Expressions of (K_α) versus (ξ_R) with Values Obtained from Simple Shear Tests (Table 1) and Corresponding Values Calculated Using Eq. 3 (Table 3)

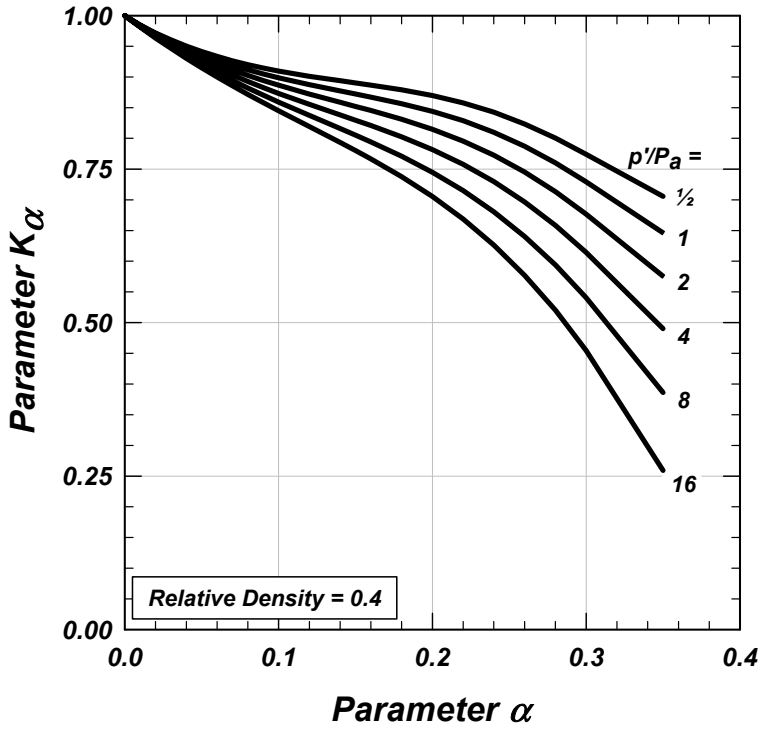

Fig. 4 Influence of p'/P_a on K_α for a Soil with a Relative Density of 40% and Q=10

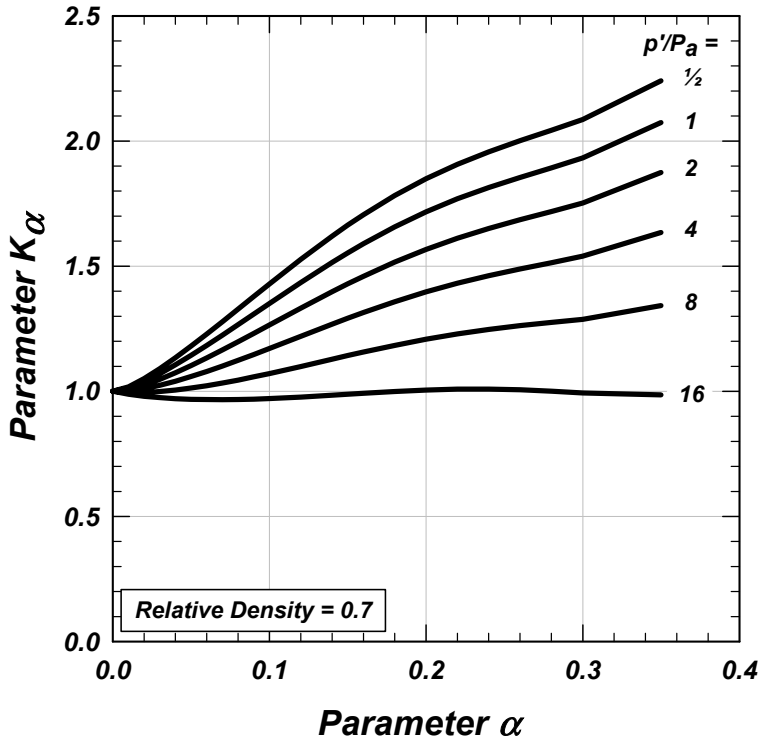

Fig. 5 Influence of p'/P_a on K_α for a Soil with a Relative Density of 70% and Q=10

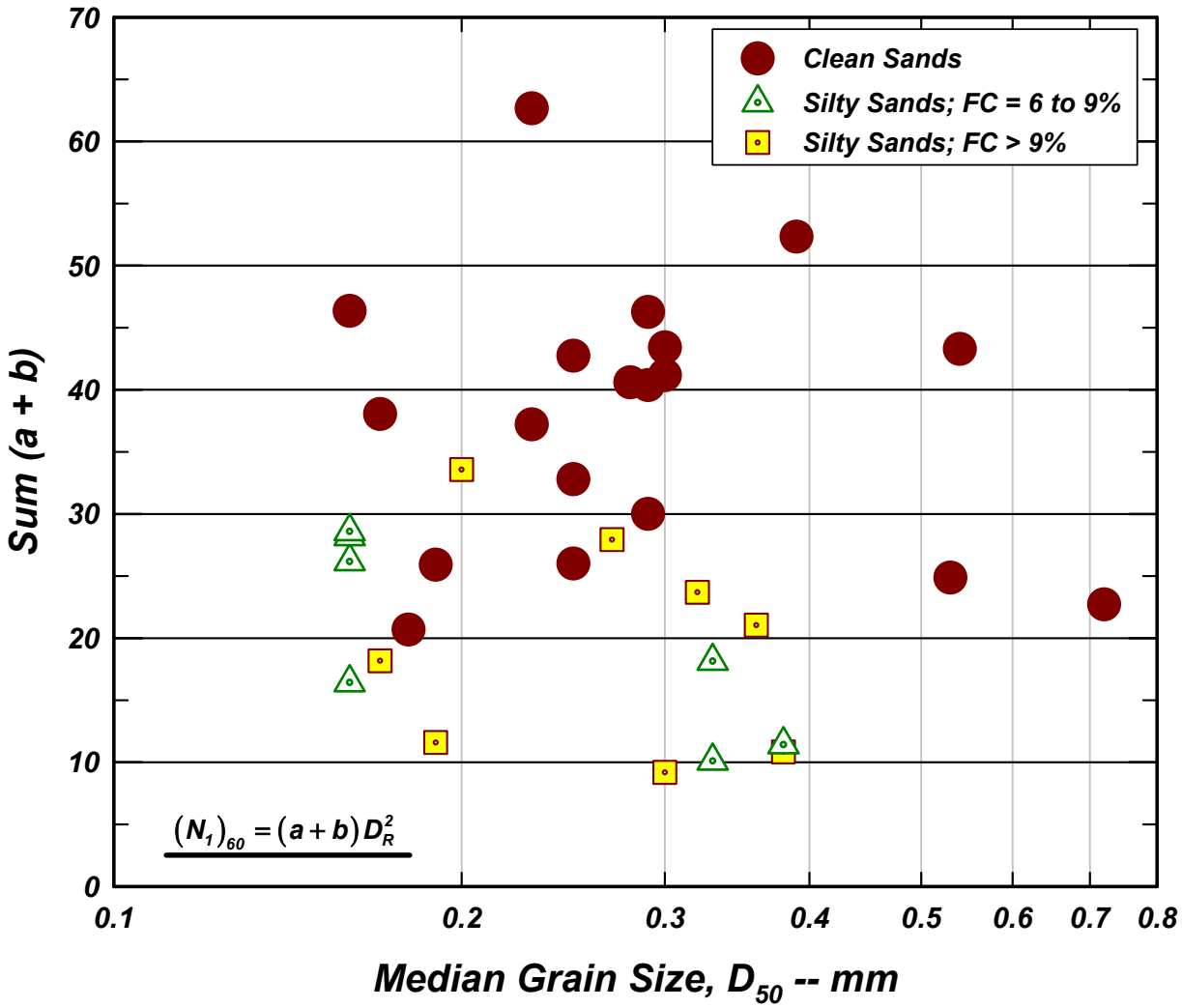

Fig. 6 Variations of the Sum $(a+b)$ with D_{50}

[Values of relative density, N_1, FC, and D_{50} are from Cubrinovski and Ishihara (1999)]

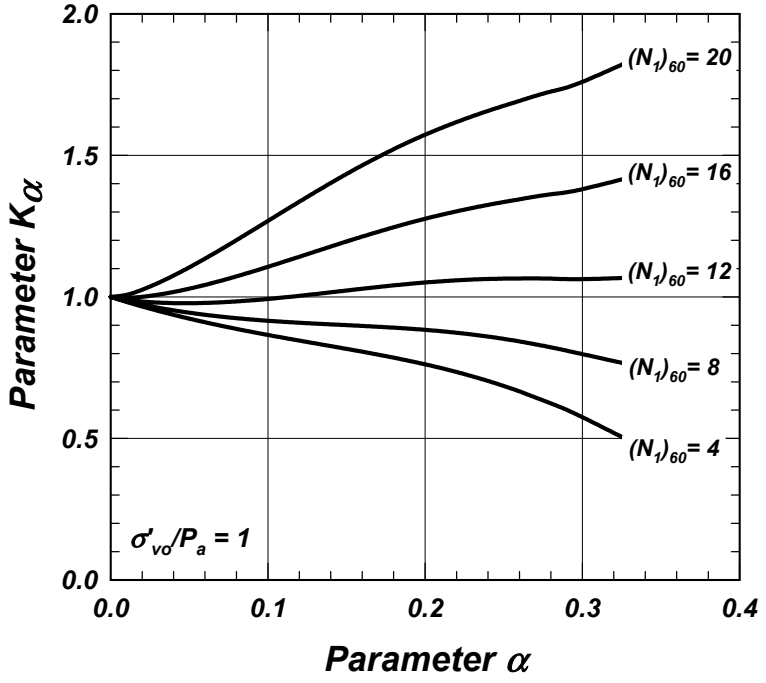

Fig. 7 Variations of K_α with SPT Blow Count $(N_1)_{60}$ at an Effective Vertical Stress, σ'_{vo} = 1 atmosphere

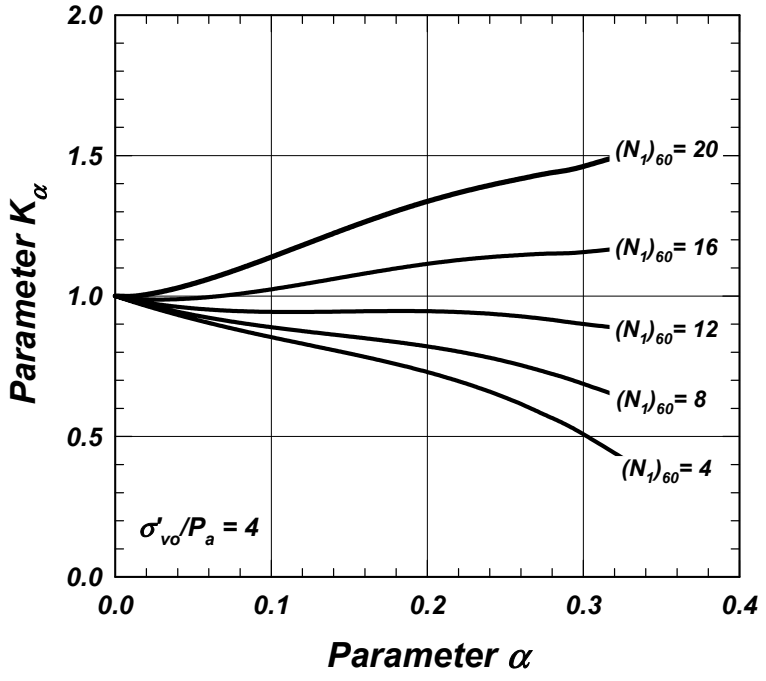

Fig. 8 Variations of K_α with SPT Blow Count $(N_1)_{60}$ at an Effective Vertical Stress, σ'_{vo} = 4 atmosphere

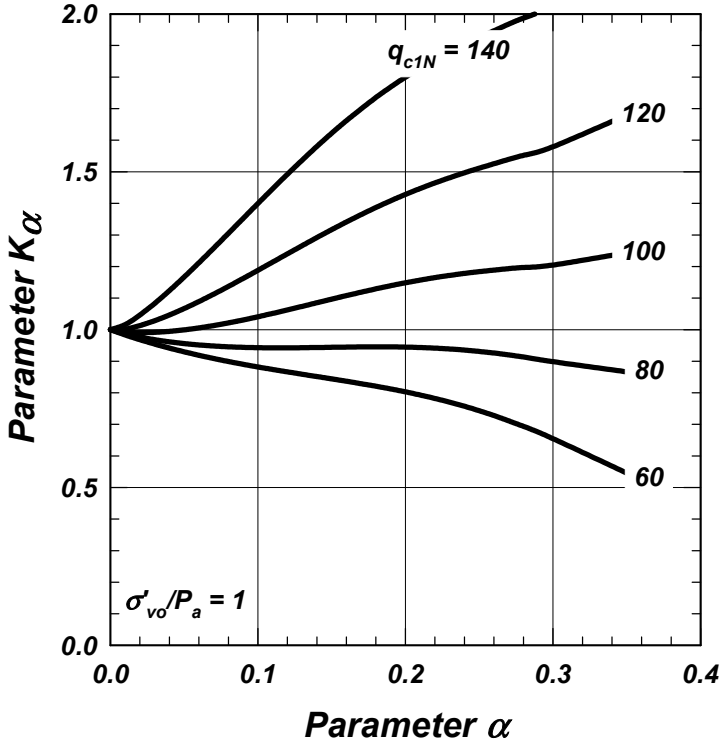

Fig. 9 Variations of K_α with CPT Normalized Tip Resistance q_{c1N} at an Effective Vertical Stress, σ'_{vo} = 1 atmosphere

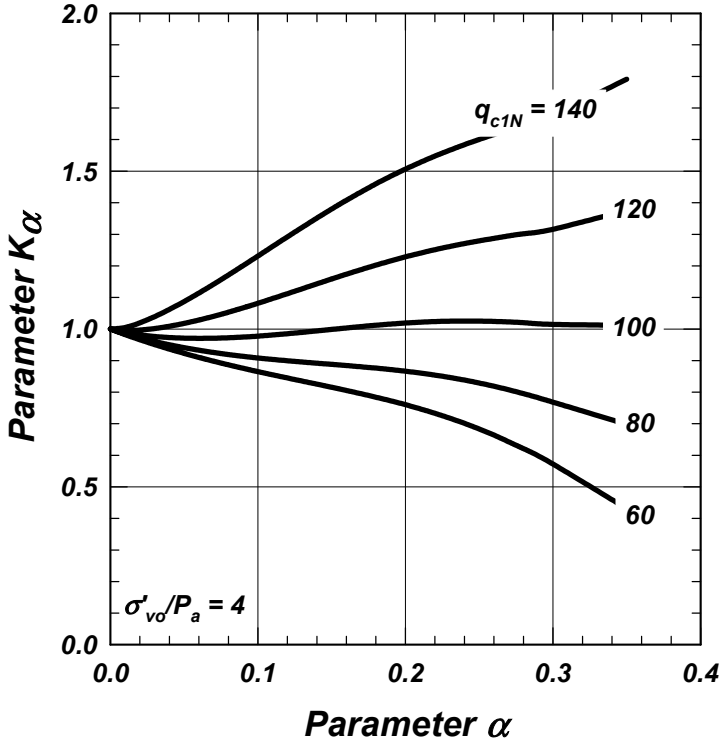

Fig. 10 Variations of K_α with CPT Normalized Tip Resistance q_{c1N} at an Effective Vertical Stress, σ'_{vo} = 4 atmosphere

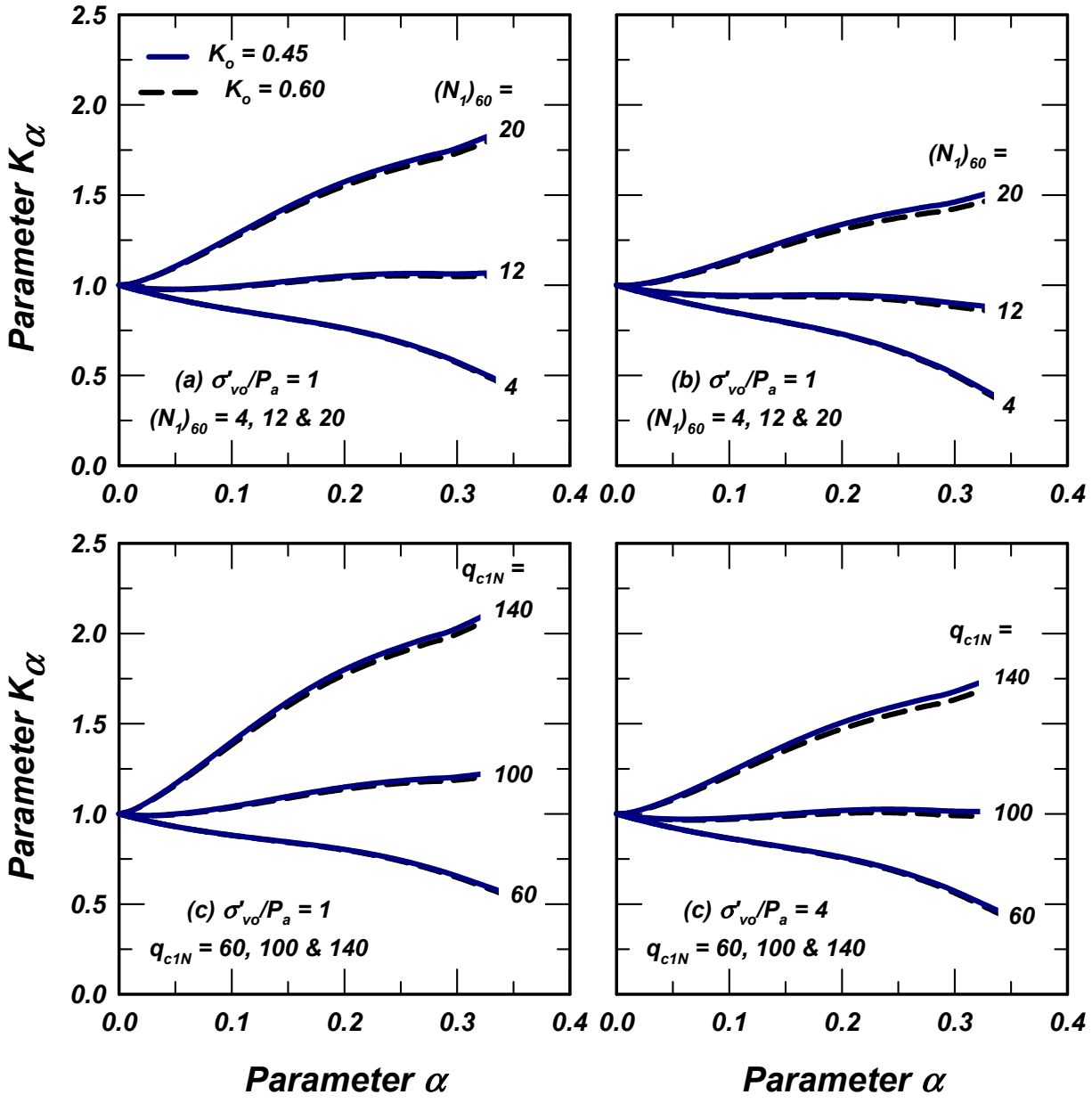

Fig. 11 Influence of Using K_o = 0.45 (Solid Lines) or K_o = 0.60 (Dashed Lines) on Calculated Values of K_α for Various Values of $(N_1)_{60}$ and σ'_{vo}/P_a or Various Values of q_{c1N} and σ'_{vo}/P_a

Behavior of Piles in Liquefied and Laterally Spreading Ground

Performance of Retrofitted Pile Foundations Subjected to Seismically Induced Lateral Spreading

T. Abdoun and Y. Wang

Analysis of Soil-pile Interaction

S. Iai and T. Tobita

Behaviour of Piles in Group Undergoing Lateral Flow in Centrifuge Tests

Shinichiro Imamura, Toshiyuki Hagiwara, Yoshimichi Tsukamoto
and Kenji Ishihara

ABSTRACT

The response of pile groups against seismically induced lateral soil spreading is explored in centrifuge model tests. The influence of number of pile and pile spacing on the total lateral force on piles is especially examined. The silt saturated with water was used to produce geotechnical models in the laminar shear box. The model piles were installed in 1-layer and 2-layer soil models to produce various patterns of pile groups, with different number of pile and pile spacing. In one test series, the pile groups were installed in the direction perpendicular to lateral spreading, while in another test series, the pile groups were installed in the direction parallel to lateral spreading. The instrumented models were then seismically excited at elevated centrifuge gravity. The group effects of closely spaced piles on the total lateral force induced during lateral spreading are evaluated with respect to the number of pile and pile spacing, with a help of a simple theoretical consideration.

Shinichiro Imamura, Research Institute, Nishimatsu Construction Co., Ltd., Japan, 4054, Nakatsu-Sakura-dai, Aikawa-cho, Aiko-gun, Kanagawa, 243-0303, Japan
Toshiyuki Hagiwara, Research Institute, Nishimatsu Construction Co., Ltd., Japan, 4054, Nakatsu-Sakura-dai, Aikawa-cho, Aiko-gun, Kanagawa, 243-0303, Japan
Yoshimichi Tsukamoto, Lecturer, Department of Civil Engineering, Tokyo University of Science, 2641, Yamazaki, Noda-shi, Chiba, 278-8510, Japan
Kenji Ishihara, Professor, Department of Civil Engineering, Chuo University, Mori-kaikan 3F, 1-11-5, Kudan-kita, Chiyoda-ku, Tokyo, 102-8220, Japan

INTRODUCTION

The lateral spreading of sandy soils due to liquefaction during earthquakes has been addressed to exert damaging influence on embedded structures such as lifelines and pile foundations. This issue was vividly manifested during recent strong earthquakes including 1995 Hyogo-ken Nambu Earthquake in Japan, 1999 Kocaeli Earthquake in Turkey, and 1999 Ji-Ji Earthquake in Taiwan. Great efforts have been directed towards physically and numerically modelling the triggering process and consequence of lateral spreading induced during earthquakes, (Hamada et al. 1986, Towhata et al. 1995, Hamada and Wakamatsu 1998, Orense and Towhata 1998, Towhata et al. 1999, Kokusho 1999, Ishihara et al. 1997, Kokusho 2000, Sharp and Dobry 2002). The interactions of laterally spreading liquefied soils with subsurface structures during earthquakes have also been of prime concern in the past studies, (Hamada et al. 1996, Inagaki et al. 1996, Tokimatsu et al. 1996, Iai et al. 1998, Tokimatsu and Asaka 1998, Ishihara and Cubrinovski 1998, Tsukamoto et al. 1998).

Centrifuge model tests have met with success in reproducing phenomena of soil liquefaction and lateral spreading, (Scott et al. 1993, Dobry et al. 1995, Abdoun and Dobry 1998, Taboada and Dobry 1998, Okamura et al. 2001, Imamura et al. 2002). With its technological advances in dynamic centrifuge modelling, the interactions of subsurface structures with seismically induced lateral spreading have also been examined, (Horikoshi et al. 1998, Takahashi et al. 1998, Boulanger et al. 1999). However, there have been few past studies, which are focused on exploring the group effects of closely spaced piles subjected to the lateral pressure induced by lateral spreading.

In this study, centrifuge model tests were carried out to perform some parametric studies on geometrical effects of pile group arrangements which are undergoing seismically induced lateral spreading.

CONDUCT OF CENTRIFUGE TESTS

Centrifuge Facilities

The beam centrifuge facilities located at the Research Institute of Nishimatsu Construction Company were used in this study. This geotechnical centrifuge with an effective radius of 3.8 metres allowed a maximum centrifuge acceleration of 150 g, (Imamura, et al. 1998). The hydraulically activated in-flight seismic shaker, which can generate a maximum horizontal acceleration of 40 g (equivalent to 800 Gal in prototype scale under the condition of elevated centrifuge gravity of 50 g), was located in the swinging platform on which physically scaled geotechnical models were prepared. The geotechnical models were prepared in the instrumented laminar shear box, which has become of common use for dynamic centrifuge model tests, (Whitman et al. 1981, Law et al. 1991, Zeng and Schofield 1996). This model container 650mm long, 400mm wide and 500 mm high in internal dimensions was made up of 33 pieces of 15 mm high rigid aluminum frames stacked one on top of another. Mechanical bearings were placed in between the frames in order that the frames can move horizontally within the limits of ±15 mm, (Imamura and Fujii 2002).

This laminar shear box was developed to satisfy the basic requirement of the plane strain condition in soil deposits in the container. By means of the pre-tension systems with mechanical springs and steel wires, installed at the four corners of the container, the container was pulled up to the pre-tension of 491 N at each corner. This system effectively allowed the self-weight of the frames to be uniformly transmitted to the frames below them, thereby preventing any rocking motions during seismic excitation. The height of the container was chosen to be 350 mm as small as possible to minimize the occurrence of any rocking motions during seismic excitation.

Soil Properties

In order to physically model the occurrence of seismically induced lateral flows of soil, a combination of a non-plastic silt and deaired water was used as model soil and pore fluid, respectively. The physical properties of the silt were specific gravity $G_s = 2.63$, mean particle diameter $D_{50} = 0.06$ mm, maximum void ratio $e_{\max} = 1.586$, and minimum void ratio $e_{\max} = 0.858$. The physical properties of Toyoura fine sand were $G_s = 2.65$, $D_{50} = 0.17$ mm, $e_{\max} = 0.976$, $e_{\min} = 0.606$, and fines content finer than 0.075 mm by weight was $F_c = 0\,\%$. Figure 1 shows the grain size distributions of the silt and Toyoura sand used in this study

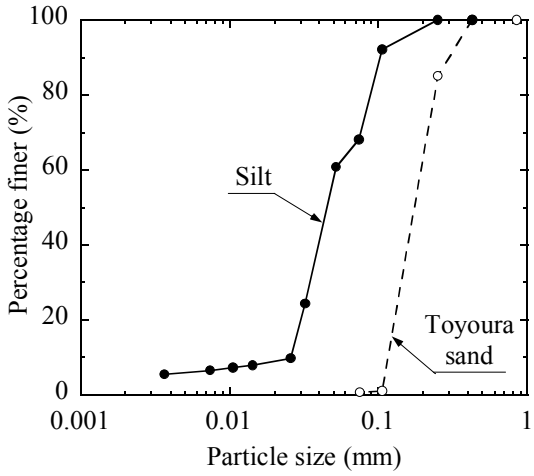

Figure 1 Grain size distribution of model soils.

Model piles

The model piles used in this study were of stainless steel, and are 16 mm in diameter and 0.4 mm in annular thickness. Under the centrifuge gravity of 50 g adopted, this was equivalent to a pile with 80.0 cm in diameter and the flexural rigidity of EI = 744 MN·m^2 in prototype scale. Some of the piles were instrumented in which a pair of strain gauges were attached at 8 positions along the length of the piles. All the piles were tightly fixed to the floor of the laminar shear box, and the top ends were left free.

Model Preparation and Test Series

The details of the centrifuge model test series are shown in Table 1. The test code is defined to indicate "model type", "number of pile", and "spacing between piles". For example, the test code S-2P-2D indicates the single-layered test using two piles spaced at a two-times pile diameter distance. The pile group was installed in the direction perpendicular to lateral flow, except for the test series coded with "-L", in which the pile groups were installed in the direction parallel to lateral flow.There were two model types of soil layering examined in this study. In the single-layer model, a 300 mm deep (equivalent to 15.0 m in prototype scale) soil layer was prepared with water saturated silt of $D_r = 45\%$ by the method of water sedimentation. In the double-layer model, a 240 mm deep (12.0 m in prototype scale) soil layer was first prepared with water saturated silt of $D_r = 45\ \%$ by the method of water sedimentation and a 60 mm deep (3.0 m in prototype scale) soil layer was then prepared over the saturated silt layer with dry Toyoura sand of $D_r = 70\ \%$ by the method of air pluviation. Figures 2(a) and (b) show typical side views of single-layer and double-layer models, respectively. The Linear Variable Displacement Transducer (LVDT) was set up at one side of the laminar box to measure the lateral displacements through the depth of the container, and also on the top surface of the models to monitor the settlement.

The accelerometers and pore pressure transducers were installed at appropriate positions within the models. Figure 3 shows the side view of all the models except for the tests coded with "-L". Varying number of piles was installed at different pile spacing L. The spacing is defined as the closest distance between two adjacent piles; 0, 1 and 2×D, where D is the pile diameter. In the tests with the piles installed in a wall-like manner (S-WP and D-WP), the silicon rubber sheet was placed in between the piles to prevent any seepage while the liquefied soil flows during and after seismic shaking. The model tests with 2D-spaced 4 piles in the single-layer (S-4P-2D) were carried out twice. In the first test, the piles located outside were found to experience the lateral pressure greater than those located inside. Therefore, to reduce the influence of excessive lateral flow near the side wall of the container, the supplementary piles were installed in the second test as shown in S-4P-2D of Figure 3, and it is the results of the second test that are reported in this paper

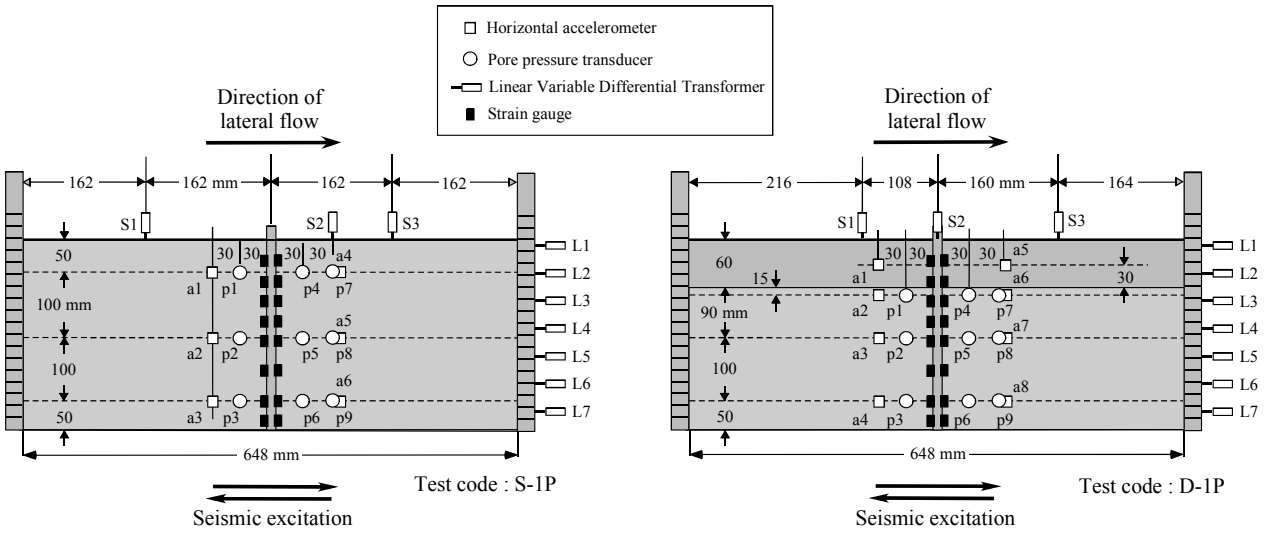

(a) Typical elevation view of single-layer models

(b) Typical elevation view of double-layer models

Figure 2 Model configuration in elevation view.

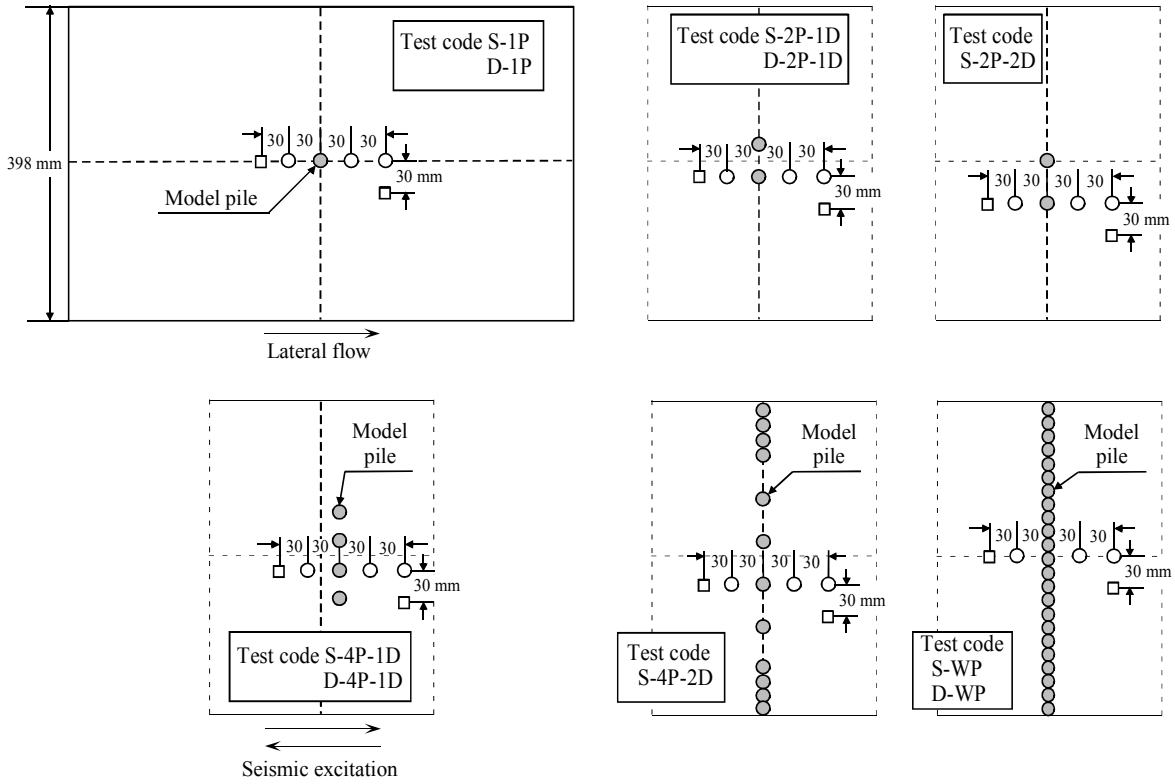

Figure 3 Model Configuration in plan view for all models except for tests coded with "L".

Centrifuge Operations

Figure 4 shows a series of procedures for the centrifuge operations during the centrifuge flight. The models were prepared and instrumented in the laminar shear box located on the swinging platform, before the centrifuge was put in flight. The centrifuge gravity was gradually increased. At the nominal centrifuge gravity of 18 g, the swinging platform was allowed to hold back and to be fixed to the floor of the beam centrifuge. By this procedure a 2° inclination was produced in the models, ($q = 3.5\ \%$). The inclination of the models was determined to comply with the past studies, (Taboada et al. 1998). The centrifuge gravity was again increased up to 50 g. after a reasonable interval to recover a hydrostatic condition within the models at a stable 50 g, the laminar shear box was seismically excited by the in-flight hydraulic actuator with a sinusoidal motion of 9 g in horizontal acceleration and 100 Hz in frequency lasting for 0.2 seconds, (equivalent to 180 Gal, 2 Hz for 10 seconds in prototype scale). All the data outputs from the instrumentations were recorded for 15 sec with a rate of 2 kHz, and stored in PC data files. Hereafter, discussions will be made first on the soil and pile behaviour observed in the tests with piles installed in the direction perpendicular to the lateral flow of soil. The group effects of closely spaced piles on the lateral pressure are then described for the piles installed in the direction perpendicular as well as parallel to the lateral flow of soil. All the model test results are denoted in prototype scale, unless otherwise stated.

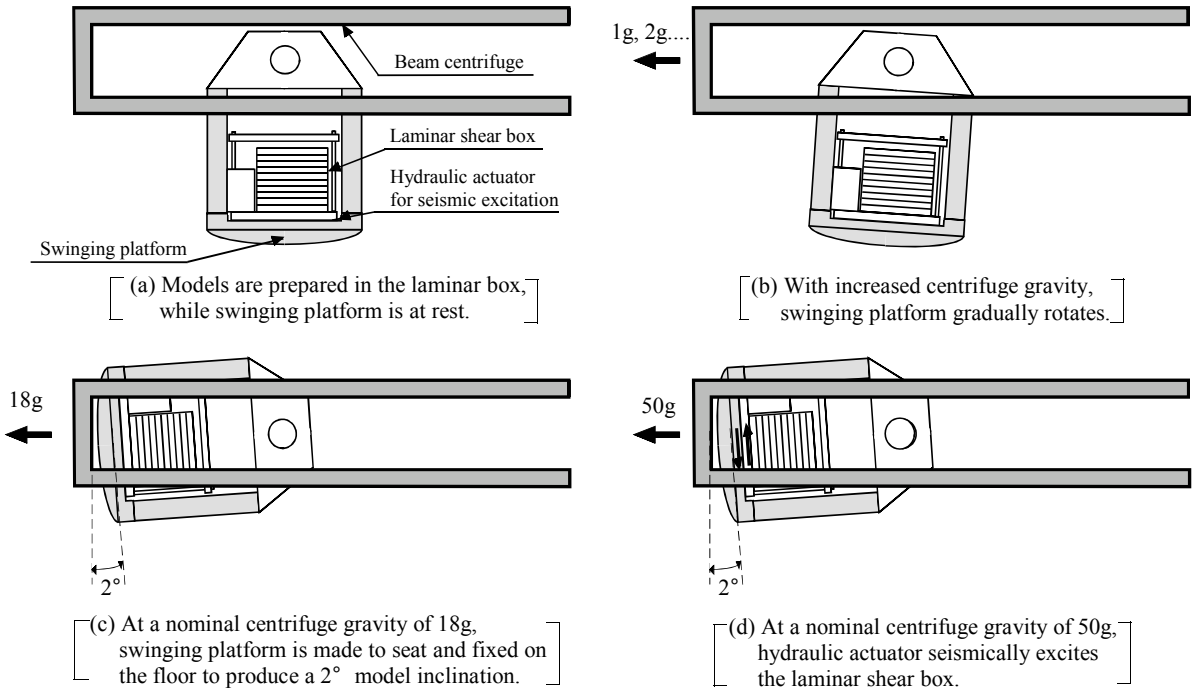

Figure 4 Centrifuge operation for the setting of a model inclination and seismic excitation during increased centrifuge flight.

RESULTS OF CENTRIFUGE TESTS OF SOIL DEPOSITS IN THE MODELS

Behavior of Soil Deposits in the models

Figures 5(a) and (b) show time histories of the excess pore pressure ratio observed in the single-layer models at the depths of 2.5 m and 12.5 m, respectively. In the left diagram, the same data are shown by enlarging the time scale from $t = 0$ to 30 sec. Herein, the excess pore pressure ratio is defined as the excess pore pressure divided by the initial effective overburden stress. At the depth of 2.5 m, the pore pressure rises rapidly and reaches peak values after about 4 cycles of seismic shaking ($t = 2$ to 3 sec), and sustains loosened states of soil liquefaction for a long period after seismic shaking. This occurs due to the pore water mitigating upwards from the lower layer. On the other hand, at the depth of 12.5 m, the pore pressure builds up relatively slowly, and the excess pore pressure ratios achieve values of 0.8 - 1 towards the end of seismic shaking. The pore pressure then reduces after seismic shaking. It is therefore reasonable to assume that the single-layer models experience soil liquefaction down to the depth of at least 12.5 m.

Figures 6(a) and (b) show time histories of the excess pore pressure ratios observed in the double-layer models at the depths of 5.0 m and 12.5 m, respectively. At the depth of 5.0 m, which is immediately below the boundary between the upper and the lower layers, the excess pore pressure ratios are seen achieving peaks of 0.55 - 0.8 around $t = 5$ sec, and reducing to about 0.4 around the end of seismic shaking, except for the test of D-WP. It is most conceivable that the excess pore pressure induced at this depth mitigates relatively rapidly upwards into the upper non-saturated sand layer with the pore pressure not completely developed there.

However, at the depth of 12.5 m, the excess pore pressure ratios achieve a value of about 0.8 at the end of seismic shaking. Therefore, it is reasonable to consider that the double-layer models have experienced liquefaction down to the depth of at least 12.5 m, however, the pore pressure dissipates faster at the upper portion of the lower saturated silt layer due to the relatively rapid mitigation of excess pore water upwards into the upper non-saturated sand layer.

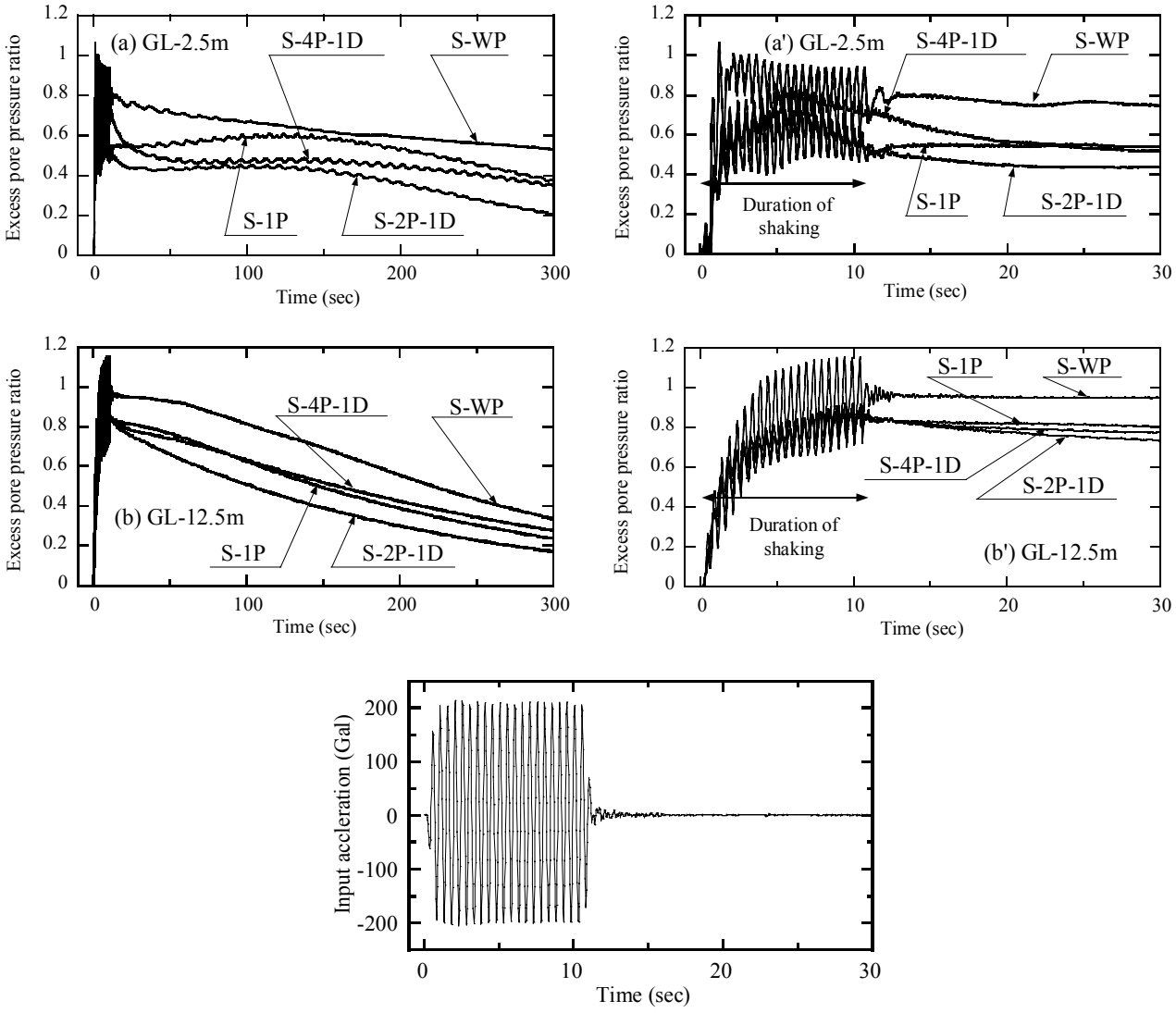

Figure 5 Time histories of excess pore pressure development (single-layer models).

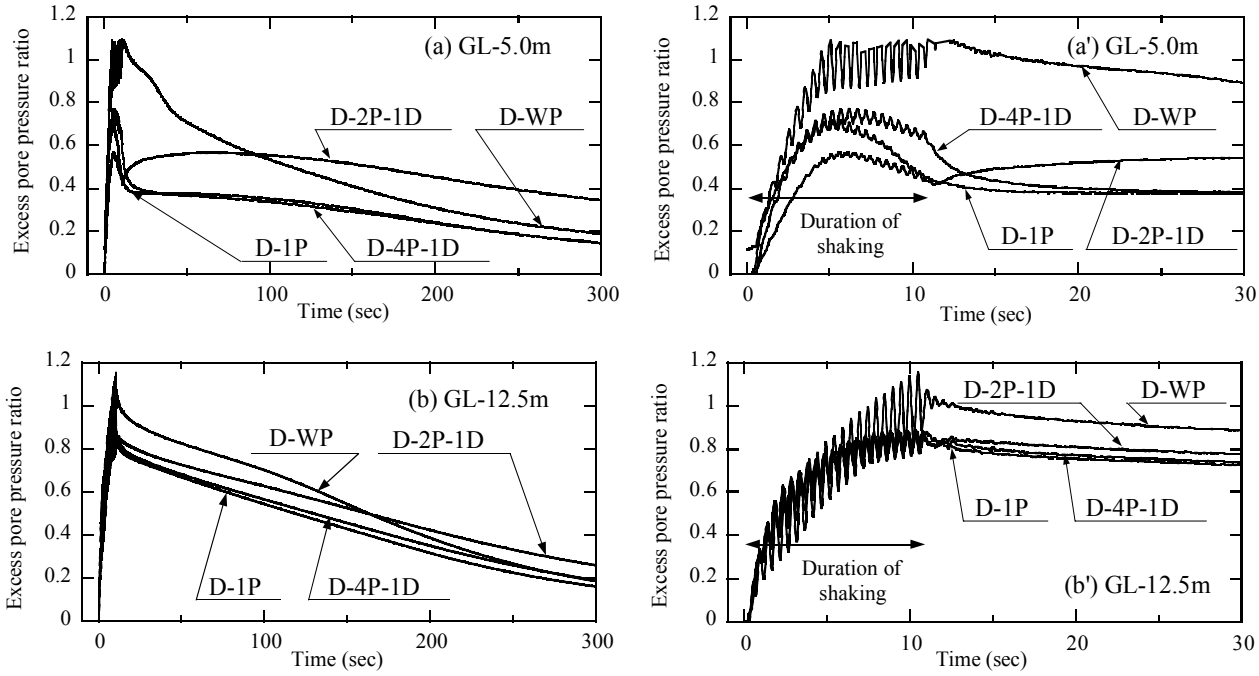

Figure 6 Time histories of excess pore pressure development (double-layer models).

Figure 7 shows the comparison of the profiles of the lateral displacements with depth for the single-layer models. The lateral displacements are seen occurring uniformly down to the depth of about 7.5 m, and gradually reducing with increasing depth. It is also of interest to see that as the number of pile increases and the spacing between adjacent piles becomes narrower, the lateral displacements generally become smaller. The lateral displacements observed in S-WP almost halve those in S-1P.

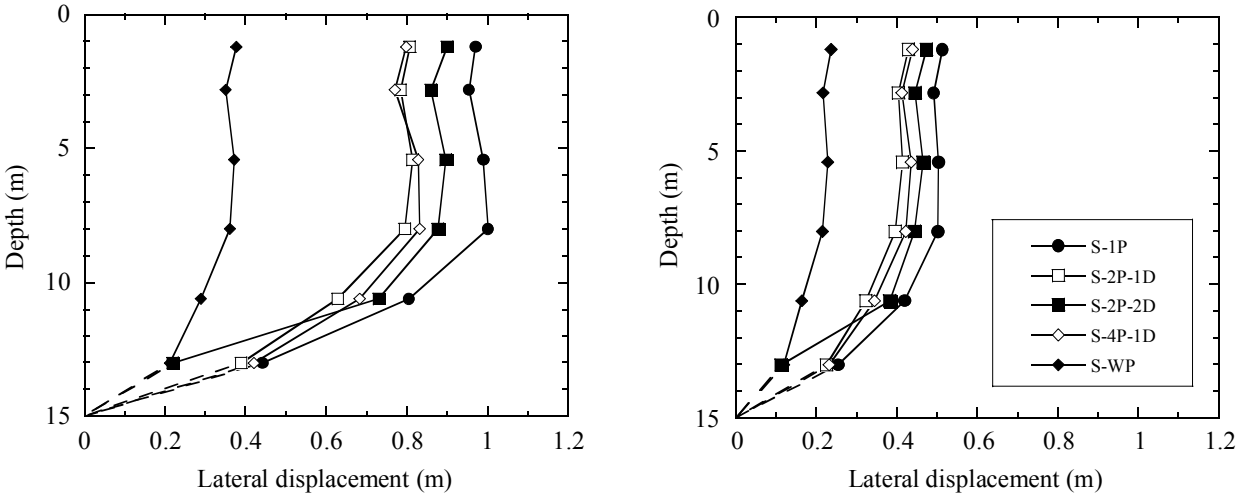

Figure 7 Profiles of lateral soil displacements with depth (single-layer model).

To allow some comparisons with other past studies with respect to lateral soil displacements, the centrifuge model test without piles is also conducted, and coded as S-NP. The centrifuge model tests performed by Taboada et al.(1998) used Nevada sand of D_r = 40 – 45 %, (D50 = 0.15 mm, coefficient of permeability k = 0.0021 cm/s), which were saturated with water as pore fluid, and modeled a soil layer with a depth of 10.0 m and a slope angle of 2 °subject to the seismic excitation of 0.18 – 0.23 g and 2 Hz lasting for about 11 sec in prototype scale. Since the depth adopted in this study was 15.0 m and different from Taboada et al.(1998), the lateral displacements normalized by the full model depth might be appropriate for comparing the two studies. It was found that the lateral displacement at the soil surface is well comparable to that observed by Taboada et al.(1998). However, the centrifuge tests with the silt and water conducted in this study appeared to induce larger lateral displacements at deeper portions of the models. The lateral displacements observed in the tests were found to be approximately 6 – 7 % of the full depth of the liquefiable saturated soil layer.

Figure 8 shows the profiles of the lateral displacement with depth for the double-layer models. The lateral displacements are also found to occur uniformly down to the depth of about 8.5 m, and gradually reduce with increasing depth. It is also interesting to notice here that the lateral displacements observed in the double-layer models are generally smaller than those in the single-layer models. This fact might be related to the relatively rapid dissipation of the excess pore pressure at the upper portion of the lower liquefied silt layer in the double-layer models, as shown in Figure 6(a).

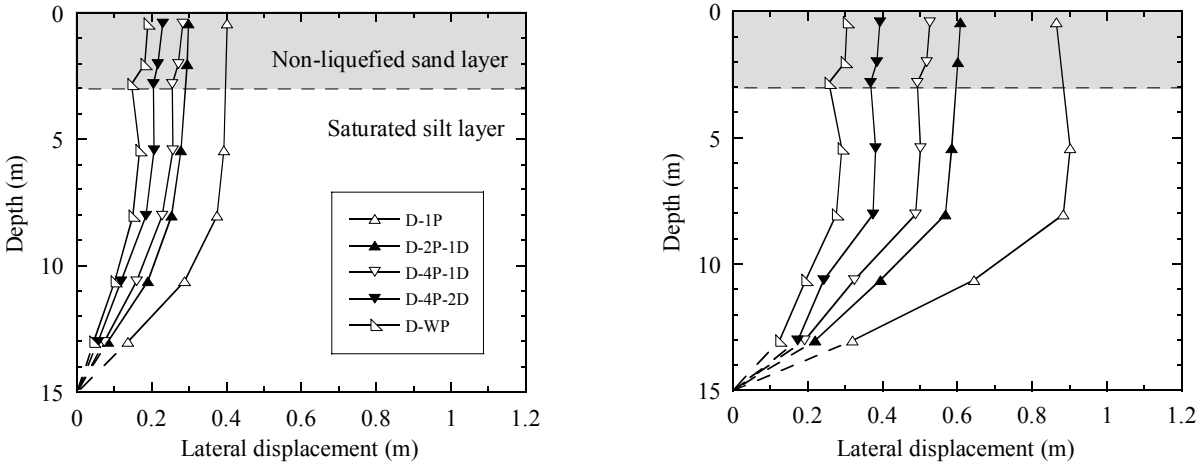

Figure 8 Profiles of lateral soil displacements with depth (double-layer model).

Pile Behaviour

The pile behaviour can be evaluated by analysing the outputs of strain gauges pasted along the piles. The calculation procedure to derive parameters related to pile bending is summarized as follows. The curvature ϕ_i at location i along the pile is calculated from the strain gauge output ε_i. The moment is then calculated as $M_i = EI\,\phi_i$, where *EI* is the flexural rigidity of the pile. The lateral shear force *P* is calculated by taking the differentials to the moment distribution. The distribution of the lateral shear force *P* with depth *z* is then approximated with a 4th order algebraic equation. The distribution of the lateral pressure *p* with depth *z* is then obtained by differentiation of the 4th order algebraic equation divided by the pile diameter *D*. The deflection of the piles, *d(z),*

is calculated as double integral of the curvature ϕ, with a boundary condition given at the bottom of the piles, $d = 0$ and $\phi = 0$, and is calibrated to give the same displacement as that measured by the Laser-reflection-type displacement transducer placed at the top of the pile.

Figures 9(a) and (b) show the profiles of pile deflection with depth, which were observed at the end of seismic shaking, $t = 10$ sec, in the single-layer and double-layer models, respectively. Similar to the lateral displacements shown in Figures 7 and 8, the pile deflection is found to change with the model configurations represented by the number of pile and pile spacing. It would be reasonable to assume that in the double-layer models, the lateral pressure acts towards the direction of lateral flow at the lower liquefied silt layer, since the lateral displacements are larger than the pile deflection. However, since the pile deflection observed within the upper non-liquefied sand layer is almost identical to the lateral displacements, the upper non-liquefied sand layer might have provided a resistant passive zone to the pile in the centrifuge model tests.

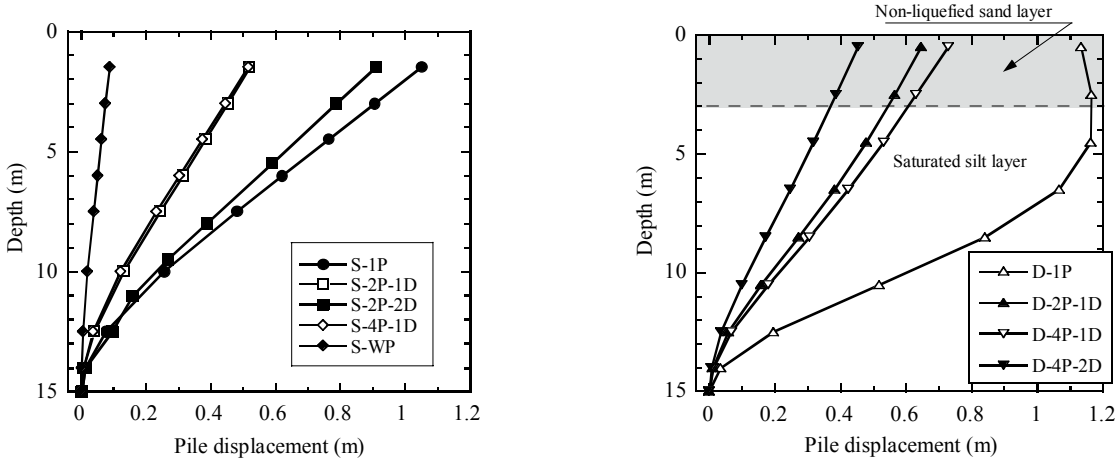

Figure 9 Profiles of pile displacements with depth.

Figures 10(a) and (b) show the distributions of the pile bending moment with depth observed at the end of seismic shaking, $t = 10$ sec. It is seen that in the double-layer models, the pile bending moment is negative from the soil surface to the depth of about $3H_1$ and then turns positive from the depth of 3 H_1, where H_1 is the thickness of the upper non-liquefied sand layer.

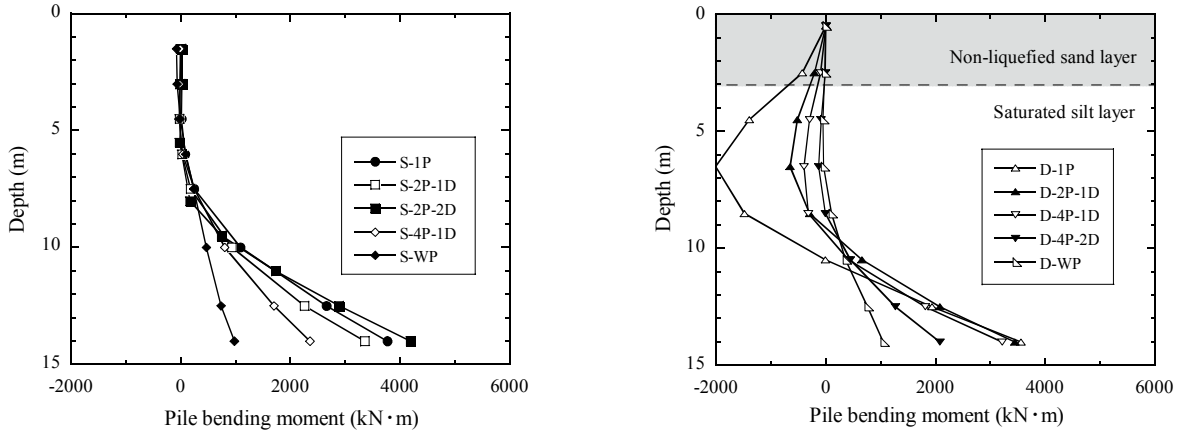

Figure 10 Profiles of pile bending moment with depth.

Figures 11(a) and (b) show the distributions of the lateral pressure with depth in the single-layer and double-layer models, respectively. Also shown in these diagrams are the linear approximations of the relations between the lateral pressure and depth. It may be seen that the lateral pressure subsides at the lower portion of the lower saturated silt layer accompanied by the reduction in the lateral displacements.

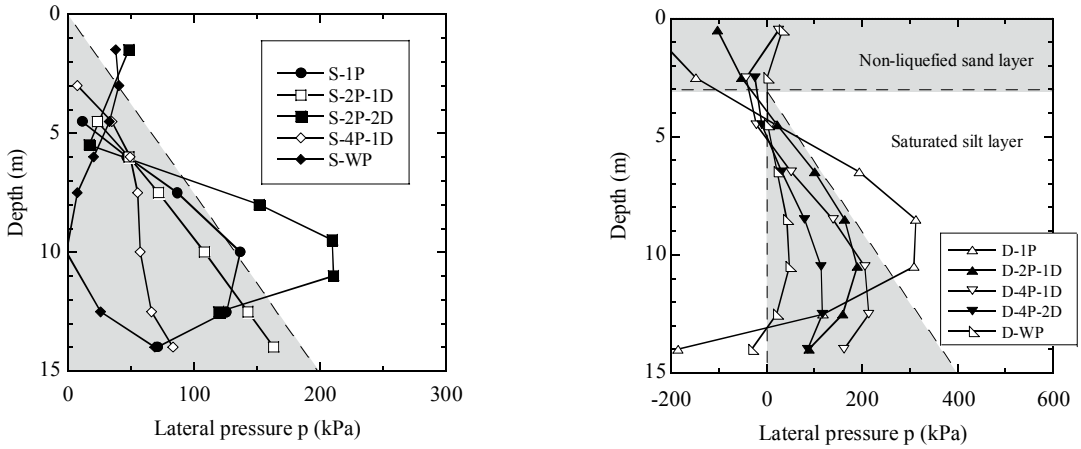

Figure 11 Profiles of lateral pressure with depth.

INTERACTION OF PILES IN GROUP

In interpreting the interaction between piles under lateral loading, the reduction of soil resistance due to the presence of adjacent piles is characterized by the "edge-effect", which is influenced by pile spacing. For piles installed in alignment in the direction of lateral loading, the reduction of soil resistance is characterized by the "shadow-effect", which is also influenced by pile spacing (Reese and van Impe 2001). It is most conceivable that the "edge-" and "shadow-" effects would arise also in the pile group undergoing lateral spreading of liquefied sand, and it is the main aim to examine these effects in this section.

Pile Proximity Ratio

The measured values of the total lateral force per pile P are shown plotted against the number of pile in Figure 12. In the case of the single-layer model tests, the total lateral force P is calculated as a summation of the lateral pressure times the pile diameter D integrated throughout the depth of pile embedment, whereas the summation was made only for the lower silt layer for the case of the double-layer model tests, as shown in Figure 12(b). Also shown with shaded zones in these diagrams are reasonably assumed ranges of the data points, which give a smaller value for the total per pile lateral force with increasing number of pile. It may be seen that the total lateral forces P_w obtained from wall-like pile arrangements are almost the same both in the single-layer and double-layer models. However, the total lateral force P_1 for the single pile in the single-layer model is found to be smaller than that for the single pile in the double-layer model. It is conceivable that this difference arises from the pore pressure being fully developed and sustained for a long period of time in the single-layer models, even after seismic shaking is discontinued. On the other hand, in the double-layer models, the pore pressure at the upper portion of the lower saturated silt layer is

considered not to have been fully developed due to the rapid migration of the excess pore water upwards into the upper unsaturated sand layer.

In order to understand the above test results in a different context, a parameter called "pile proximity ratio", η, is introduced as follows,

$$\eta = \frac{D}{L}, \tag{1}$$

where L is the centre-to-centre distance between two adjacent piles as shown in the inset of Figure 12 The total lateral force per pile P, shown in Figure 12, is now displayed in terms of η in Figure 13. Also shown in these diagrams are reasonably assumed ranges in which the data points fall. Looking over the data points, it may be envisioned that the total lateral force acting on a pile becomes smaller as the pile proximity ratio η increases. It is also found that even with the same spacing between adjacent piles, the total lateral force on the individual pile becomes smaller with increasing number of pile.

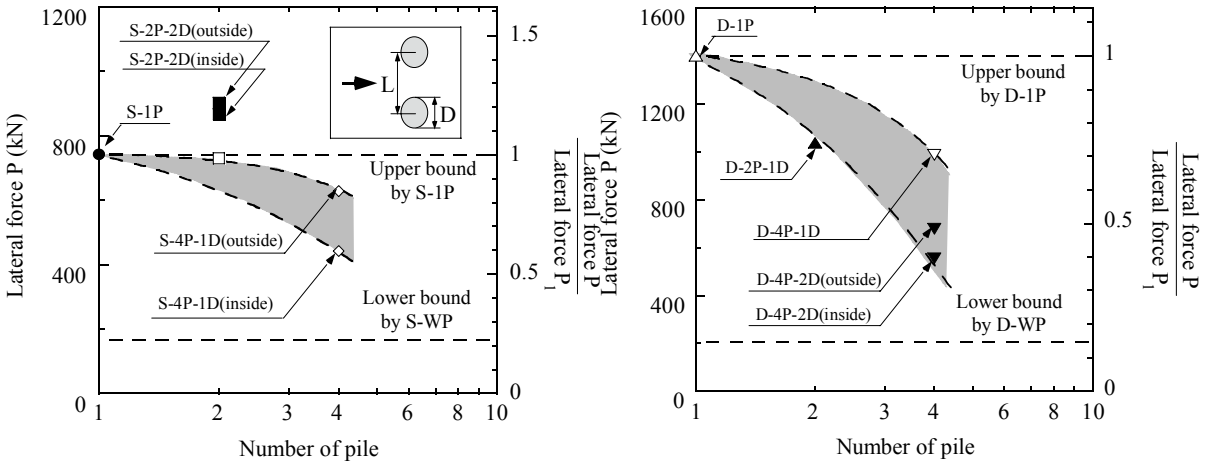

Figure 12 Lateral force on pile against number of pile used in the tests.

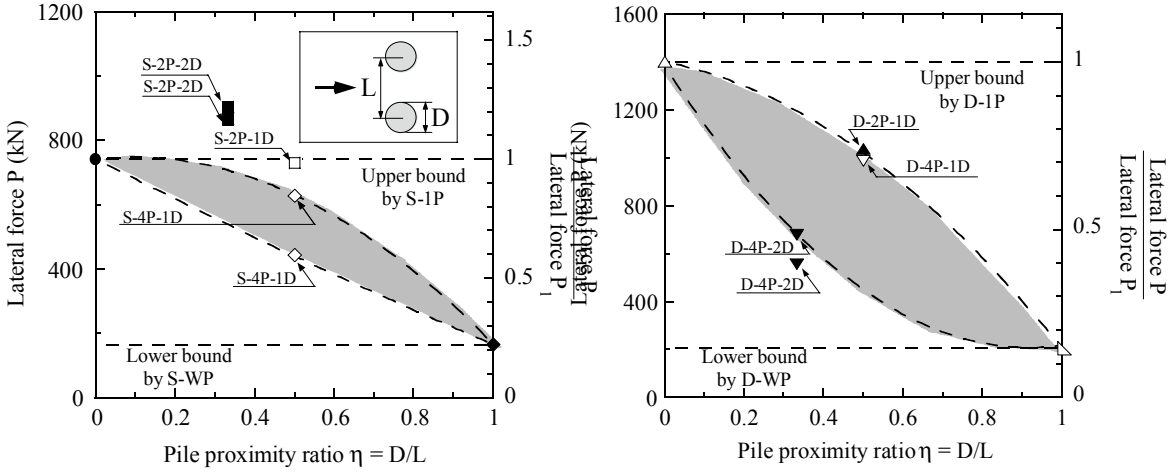

Figure 13 Lateral force on pile against pile proximity ratio η.

Simple Concept for Pile-to-Pile Interaction

A simple physical interpretation may be offered for the group effects by introducing the concept of an influence zone, which is developed behind the pile, when it is subjected to the lateral flow.

The group effects of closely spaced piles on the lateral pressure induced during lateral spreading might be a problem requiring three dimensional considerations. However, for the sake of simplicity, the zone of influence viewed in plan will be considered herein. The zone of influence is also assumed to develop uniformly through the depth, rendering the problem to be two-dimensional.

First, consider the lateral force acting on a continuous wall-like arrangement of piles, which is subjected to the lateral spreading. A soil element behind the wall at any depth would be deformed largely as shown in Figure 14(a), whereby mobilizing the residual strength or steady-state strength τ_f Therefore, the lateral force per pile P_w in such a condition would be given by,

$$P_w = \tau_f D \ , \tag{2}$$

where D is the pile diameter. As another extreme case, let a single pile be considered which undergoes the lateral flow as shown in Figure 14(b). The lateral force per pile is denoted by P_1. The soil mass behind a single pile is assumed to produce what might be termed a zone of influence having a fan shape with an apex angle of ψ. The size of this influence zone is determined by the length of the side, λD, which might be governed by the thickness of a liquefied soil layer, soil properties and pile bending stiffness. By considering the equilibrium of the forces at both ends of the influence zone, the following equation holds valid,

$$P_1 = \left\{ 2\lambda D \sin\frac{\psi}{2} + D \right\} \tau_f \ , \tag{3}$$

Therefore, with reference to the equation (2), one obtains,

$$\frac{P_1}{P_w} = 2\lambda \sin\frac{\psi}{2} + 1 = \Omega \tag{4}$$

The parameter Ω in the equation (4) indicates the ratio of per-pile force between the single pile and the continuously arranged wall-like pile group.

It is to be noted that even with multiple piles, there would be no interaction between two adjacent piles, if these are installed at a sufficiently large spacing. Denoting the centre-to-centre distance between the two piles by *L*, the condition of no overlapping of the influence zone is expressed as,

$$\frac{L - D}{2} \geq \lambda D \sin\frac{\psi}{2} \ . \tag{5}$$

Referring to the definition of Ω given by the equation (4), the equation (5) is rewritten as,

$$\frac{L}{D} \geq \Omega \text{ , or } \eta \leq \frac{1}{\Omega} \text{ .} \tag{6}$$

This implies that if the centre-to-centre distance between two piles, *L,* is larger than Ω times the pile diameter *D*, there will be no interaction between them and each pile is considered to be a single independent pile. For this case, even though there are *N* piles, the lateral force per pile, P_N, is estimated through the relation of the equation (4). Thus, one obtains,

$$\frac{P_N}{P_w} = \frac{P_1}{P_w} = \Omega \text{ . for } \eta \leq \frac{1}{\Omega} \text{ .} \tag{7}$$

When the adjacent piles are close enough to produce overlapping of the zone of influence, as shown in Figure 14(c), the equilibrium of the forces is given as,

$$N P_N = \left\{ 2\lambda D \sin\frac{\psi}{2} + D + (N-1)L \right\} \tau_f \text{ ,} \tag{8}$$

therefore, with reference to $P_w = \tau_f D$ and the equation (4), the following relation is obtained,

$$\frac{P_N}{P_w} = \frac{\Omega}{N} + \frac{N-1}{N}\frac{1}{\eta} \text{ .} \tag{9}$$

This relation holds valid when the pile spacing is close enough to satisfy the following relation,

$$\frac{1}{\Omega} \leq \eta \leq 1 \text{ .} \tag{10}$$

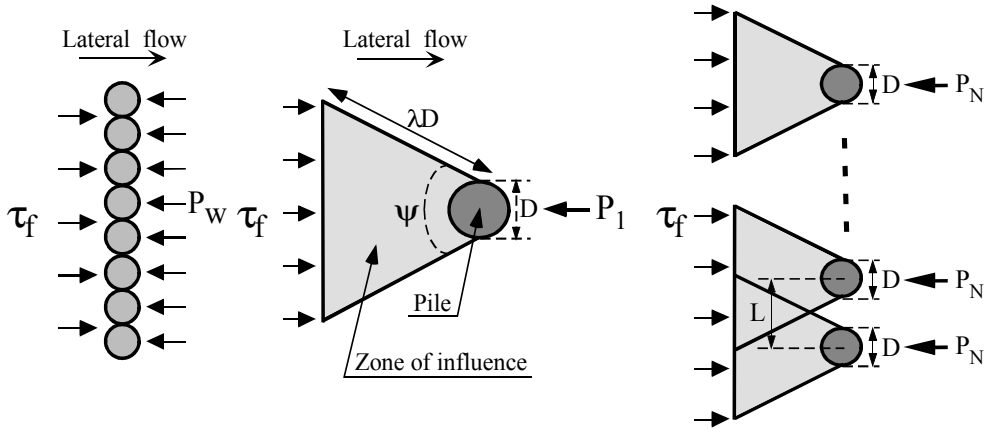

(a) N=∞ , η=1 (L=D) (b) N=1, η=0 (L=∞) (c) N piles, η=0.5 (L=2D)

Figure 14 Simple evaluation of pile group effect against lateral flow.

The significance of the equations (7) and (9) lies in the fact that the parameter $\Omega = \frac{P_1}{P_w}$ is now a sole parameter necessary to determine the per-pile lateral force P_N for a given group consisting of *N* piles. It is also noteworthy that the range of the proximity ratio η, within which the effects of pile-to-pile interaction is manifested, is given as a function of the parameter Ω. Therefore, once the parameter Ω is properly evaluated by way of tests in the laboratory or in-situ, there would be no need to determine individual value of the parameters λ and ψ, which are related to the definition of the influence zone. The equations (9) and (10) imply that when the centre-to-centre distance between piles becomes less than Ω times the pile diameter *D*, the lateral force per pile P_N tends to decrease with increasing number of pile and it eventually reaches a limiting value, which is given by $P = P_w$ at η=1.0.

At this point, it would be of use to define a parameter, α_S, given as follows,

$$\alpha_S = \frac{P}{P_w} \ , \tag{11}$$

where *P* is the lateral force acting on a pile in any arrangement of a pile group. This parameter will be referred to as "load partition parameter". With reference to the relations of the equations (1), (6) and (7), and to the equations (9) and (10), the load partition parameter α_S can be displayed schematically in a form of a diagram as shown in Figure 15.

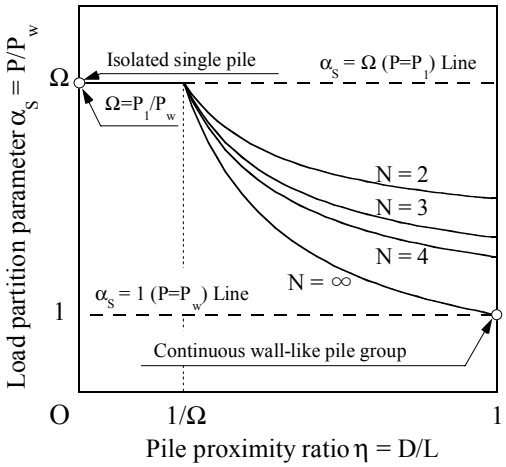

Figure 15 Load partition parameter α_S-pile proximity ratio η relation.

Evaluation of Soil-pile Interaction

It will be of interest to revisit the test data shown in Figure 13, and to interpret them in the light of the theoretical framework displayed in Figure 15. The load partition parameter α_S obtained in the tests is plotted versus the pile proximity ratio η for the cases of the single-layer and double-layer model experiments in Figures 16(a) and (b), respectively. The set of curves displayed in Fig.15 is shown again superimposed in Figure 16, so that best-balanced fitting can be achieved

overall to the measured data points. In Figure 16(a), where the results of the single-layer model tests are shown, $\alpha_S = 4.0$ may be read off as a reasonably chosen value for the case of a single pile from the viewpoint of the best-balanced fitting. Therefore, from the equation (4), the value of Ω is evaluated as $\Omega = 4.0$. For the results of the double-layer model tests, the value of $\alpha_S = 5.0$ may be read off similarly for the case of a single pile based on the best-balanced fitting concept. Thus, the value of Ω is calculated as $\Omega = 5.0$. With reference to the definition given by the equations (6) and (10), the value of $\eta_c = 1/\Omega$ is interpreted as giving a threshold value of the pile proximity ratio differentiating between conditions of pile interaction and non-interaction. Thus, the threshold value, η_c, is obtained as 1/4 to 1/5. This implied the fact that the edge-to-edge spacing between two piles, which is given by *L - D*, should be 3 to 4 times larger than the pile diameter, in order for each of the piles to be considered as an independent single pile without any interaction between them.

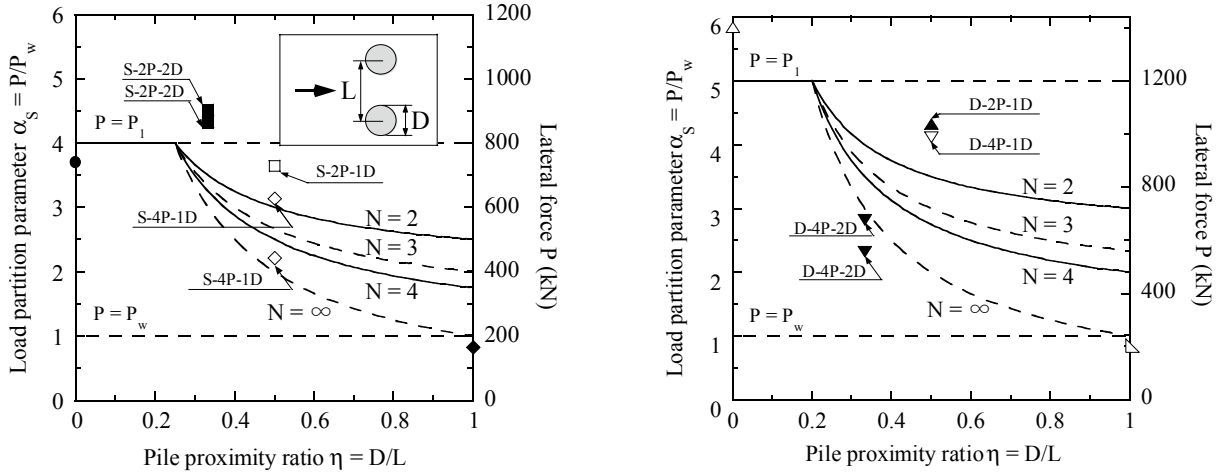

Figure 16 Load partition parameter α_S against pile proximity ratio η.

Lateral force in Continuous Pile Arrangement

The total lateral force P_w is herein assumed to provide the basis for understanding the lateral pressure induced on various types of pile groups. The total lateral force P_w associated with the effective coefficient of lateral pressure K_f' would be expressed as,

$$P_w = K_f' \gamma' D \int_0^H z dz = \frac{1}{2} K_f' \gamma' H^2 D \ , \tag{12}$$

where γ' is the submerged unit weight of soil and *H* is the depth of a liquefied layer subjected to lateral flow. Based on the centrifuge test results of Figures 13(a) and (b), the coefficient of lateral pressure can be calculated by using the equation (12). The outcome of such calculation is shown to yield a value of $K_f' = 0.26$ for the single-layer test and 0.32 for the double-layer test.

When the lateral flow hits an obstacle such as a continuous wall, the liquefied soil may develop large deformation as illustrated in Figure 17, leading to the steady-state strength or residual strength, which is mobilized when sandy soils are loosely deposited exhibiting contractive behaviour. The residual strength S_{us} normalized to an initial confining pressure σ_o' was shown by

Ishihara (1996) and Tsukamoto et al. (1998) to be expressed as,

$$\frac{S_{us}}{\sigma_o'} = \frac{\cos\phi_s}{2}\frac{M}{r_c} \ , \tag{13}$$

$$M = \frac{6\sin\phi_s}{3-\sin\phi_s} \ , \tag{14}$$

where r_c is the initial state ratio defined as $r_c = \frac{\sigma_c'}{\sigma_s'}$, with the effective confining stress σ_s' at the state of phase transformation or at the time when the minimum shear stress is encountered in undrained loading. The angle ϕ_s in the equations (13) and (14) denotes the angle of internal friction at phase transformation. It was also shown by Ishihara (1996) that, in order for a sand to exhibit contractive behaviour, the value of r_c needs to be greater than about 2.0. Introducing r_c=2.0 and a typical value of $\phi_s = 30°$ in the equations (13) and (14), this condition is expressed as,

$$\frac{S_{us}}{\sigma_o'} \le 0.26 \ . \tag{15}$$

This implies the fact that for the sand exhibiting contractive behaviour thereby mobilizing the residual strength, the maximum possible value of the normalized residual strength would be 0.26. Needless to say, the normalized residual strength will take a value less than 0.26 depending upon the soil density.

Coming back to the state of stress behind the continuous wall shown in Figure 17, the total lateral force P_w divided by $\gamma' H^2 D/2$ gives the value of K_f' as defined by the equation (12). Based on the measured value of P_w, the value of K_f' was calculated and shown to be 0.26 for the single-layer model test and 0.32 for the double-layer model test, as mentioned above. It is to be noted that the coefficient K_f' thus obtained has the same physical meanings as the normalized residual strength, which is generally obtained by means of the triaxial compression tests. In comparison of the outcomes from the two independent tests, it may be remarked that the coefficient K_f' obtained from the centrifuge model tests using the silt with $D_r = 45°$ is roughly coincident with the maximum possible value of the normalized residual strength hitherto obtained using the triaxial tests on Toyoura sand.

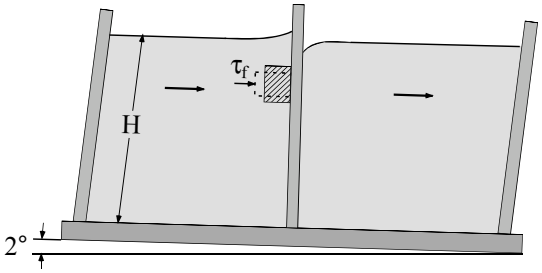

Figure 17 Deformation pattern of a soil element behind the continuous wall undergoing lateral flow of liquefied sand.

CONCLUSIONS

The centrifuge model tests were carried out to examine the group effects of closely spaced piles against seismically induced lateral flow. One-layered and two-layered soil models were prepared in the laminar shear box with the water-saturated silt as a liquefiable soil layer and dry sand as an upper non-liquefiable unsaturated soil layer. A series of pile groups were installed in the direction perpendicular or parallel to the lateral spreading, with varying numbers of pile and pile spacing. The slope angle is provided to the model during centrifuge flight, and seismically excited at the centrifuge gravity of 50 g. With sufficient centrifuge model test data, the group effects of piles on the total lateral force on piles were clarified and interpreted with the help of a simple theoretical consideration with reference to the number of pile and pile spacing. It was found that when the spacing between adjacent piles is more than 3 to 4 times the diameter of piles, there are no interactions among piles and an individual pile behaves as if it were an isolated single pile. However, as the spacing becomes small, the group effects start to emerge, and the total lateral force on the individual pile becomes small. It was also found that with the same spacing between adjacent piles, the total lateral force on the individual pile becomes also small, as the number of piles increases. A simple method for evaluating the group effects of closely spaced piles on the total lateral force per pile was presented based on the test results and simple theoretical considerations. In another series of the tests in which multiple piles were arranged in the same direction as that of the lateral flow, the trailing piles were shown to undergo the lateral force about 85 % of the lateral force acting on the frontal pile.

REFERENCES

[1] Abdoun, T.H., and Dobry, R. (1998) "Seismically induced lateral spreading of two-layer sand deposit and its effect on pile foundations", Proceedings of Centrifuge 98, Kimura, T., Kusakabe, O. and Takemura, J. (eds), Balkema, pp.321-326.

[2] Boulanger, R.W., Curras, C.J., Kutter, B.L., Wilson, D.W., and Abghari, A. (1999) "Seismic soil-pile structure interaction experiments and analysis", Journal of Geotechnical and Geoenvironmental Engineering., ASCE, Vol.125, No.9, pp.750-759.

[3] Dobry, R., Taboada, V. and Liu, L. (1995) "Centrifuge modeling of liquefaction effects during earthquakes", Earthquake Geotechnical Engineering, Ishihara, K. (eds), Balkema, pp.1291-1324.

[4] Hamada, M., Yasuda, S., Isoyama, R. and Emoto, K. (1986) "Study on liquefaction induced permanent ground displacements", Association for the Development of Earthquake Prediction in Japan.

[5] Hamada, M., Isoyama, R. and Wakamatsu, K. (1996) "Liquefaction-induced ground displacement and its related damage to lifeline facilities", Soils and Foundations, Special Issue, Journal of Japanese Geotechnical Society, pp.81 – 97.

[6] Hamada, M. and Wakamatsu, K. (1998) "Liquefaction-induced ground displacement triggered by quaywall movement", Soils and Foundations, Special Issue, Journal of Japanese Geotechnical Society, pp.85 – 95.

[7] Iai, S., Ichii, K., Liu, H. and Morita, T. (1998) "Effective stress analyses of port structures", Soils and Foundations, Special Issue, Journal of Japanese Geotechnical Society, pp.97 – 114

[8] Inagaki, H., Iai, S., Sugano, T., Yamazaki, H. and Inatomi, T. (1996) "Performance of caisson type quay walls at Kobe port", Soils and Foundations, Special Issue, Journal of Japanese Geotechnical Society, pp.119 – 136.

[9] Imamura, S., Hagiwara, T. and Nomoto, T. (1998) "Nishimatsu dynamic geotechnical centrifuge facility", Proceedings of Centrifuge 98, Kimura, T., Kusakabe, O. and Takemura, J. (eds), Balkema, pp.19 - 24.

SEISMIC RESPONSE OF LARGE DIAMETER CAST IN PLACE CONCRETE PILES IN LAYERED LIQUEFIABLE SOILS

W. D. Liam Finn[1] and N. Fujita[2]
[1]*Anabuki Professor and* [2]*Research Assistant, Anabuki Chair of Foundation Geodynamics, Kagawa University, 2217-20 Hayashi-cho, Takamatsu, Kagawa, 760-0396 Japan*

ABSTRACT

Seismic response of large diameter cast in place reinforced concrete (CIPRC) piles is often evaluated by applying the "fixed base" seismic moment and shear from the superstructure to the pile head and conducting a static analysis using a Winkler spring model for pile soil interaction. This pseudo-static approach neglects some important features of seismic response: inertial interaction between structure and foundation, kinematic moments and deflections, and the effects of ground shaking and soil-pile structure interaction on the base shear and moment. Liquefaction introduces more complex problems for analysis and design. All these issues are studied using a nonlinear effective stress simplified 3-D continuum analysis.

1. INTRODUCTION

This paper presents some results from a major research project on the seismic response of cast in place reinforced concrete (CIPRC) piles with diameters ranging from 1m-2m in liquefiable soils during strong earthquake shaking. Two cases are of particular interest. The first case is when the liquefied zone extends from the surface to some depth. This is the most common case in reclaimed land. The second case is when there is a thick non-liquefiable layer at the surface. This case is considered to be the most damaging for the pile in the event that lateral spreading occurs after liquefaction because the unliquefied layer can exert passive lateral pressure against the pile. There are many case histories where this effect was not taken into account and many piles, designed to control settlement only, were badly damaged by lateral spreading following liquefaction. The effects of an unliquefied surface layer on the pile, during the ground shaking phase, are being investigated as part of the research study and some preliminary results on this are presented here.

2. METHODS OF ANALYSIS

The pile foundation-structure system vibrates during earthquake shaking as a coupled system. Logically it should be analyzed as a coupled system. However this type of analysis is not feasible in engineering practice. Many of the popular structural analysis programs do not include the pile foundation directly into a computational model. Even when it can be done, the computational demands are excessive. Therefore various approximate methods are used.

The most common approach to the analysis of pile foundations is to use Winkler springs to simulate soil-pile interaction. The springs may be elastic or nonlinear. Some organizations, such as the American Petroleum Institute (API 1995), gives specific guidance for the development of nonlinear load-deflection (p-y) curves as a function of soil properties to represent nonlinear springs. The API (p-y) curves, which are the most widely used in engineering practice, are based on data from static and slow cyclic loading tests in the field.

Seismic analysis of a pile foundation is often conducted by applying the base shears and moments from a fixed base analysis of the structure to the pile head and using static analysis to estimate moments, shears and displacements in the piles. This static analysis neglects many important factors that affect seismic response of the structure-soil-foundation pile system. Inertial interaction between structure and foundation are neglected. This interaction increases the nonlinear behavior of the soil and reduces pile head stiffnesses. These effects increase the period of the system and change the spectral response and hence the base shears and moments. The kinematic moments are also neglected. These moments arise from the pressures generated against the pile to ensure that the seismic displacements of soil and pile are compatible at points of contact along the pile. These moments, which can be captured by a full dynamic analysis can be very significant. Finally the effects of high pore water pressures and liquefaction on the base moments and shears are also neglected.

An alternative to the Winkler type computational model is to use a finite element continuum analysis based on the actual soil properties. Dynamic nonlinear finite element analysis in the time domain using the full 3-dimensional wave equations is not feasible for engineering practice at present because of the time needed for the computations. However, by relaxing some of the boundary conditions associated with a full 3-D analysis, Finn and Wu (1994) found it possible to get reliable solutions for nonlinear response of pile foundations with greatly reduced computational effort. The results are accurate for excitation due to horizontally polarized shear waves propagating vertically. Wu and Finn (1997a, b) give a full description of this method and of numerous validation studies. The method is incorporated in the computer program PILE-3D. An effective stress version of this program, PILE-3D-EFF, has been developed by Finn and Thavaraj (1999) and validated by Finn et al (1999) and Finn and Thavaraj (2001) in cooperation the geotechnical group at the University of California at Davis.

Seismic response analysis is usually conducted assuming that the input motions are horizontally polarized shear waves propagating vertically. The PILE-3D model retains only those parameters that have been shown to be important in such analysis. These parameters are the shear stresses on vertical and horizontal planes and the normal stresses in the direction of shaking. The soil is modeled by 3-D finite elements as shown in Fig.1. The pile is modeled

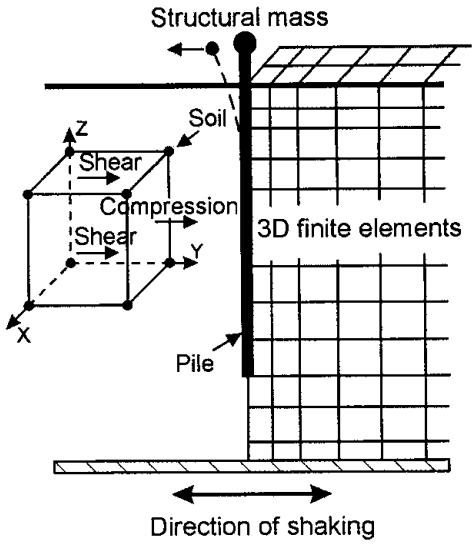

Figure 1 Model for analysis of pile foundations

using beam elements or block elements. The pile is assumed to remain elastic, though cracked section moduli are used for concrete piles, when displacements exceed specified threshold values. This assumption is in keeping with the philosophy that the structural elements of the foundation should not yield.

The inclusion of full inertial interaction would require a coupled analysis of the superstructure and all supporting pile foundations. This is not feasible. However the inertial interaction can be included in approximate ways.

One way is to mount a mass on the CIPRC pile foundation corresponding to the reaction load carried by the pile. This mass is mounted on a massless cantilever in a single degree of freedom system (SDOF) at the effective height of the modal mass in the first mode. The cantilever stiffness is selected so that the period of the SDOF is the same as the rigid base fundamental period of the structure. This model assumes that most of the inertial interaction occurs in the first mode of the structure. This approach was first suggested for the analysis of pile foundations for bridges by Abgari and Chai (1995). More general stick models of the column can be used to give more accurate results

The time history of lateral stiffness shown in Fig. 2, which includes the inertial mass, was calculated for another project using this type of model. The time history of stiffness when inertial interaction is neglected is also shown. The differences between the two time histories are significant. Clearly inertial interaction should be taken into account. The variation of stiffness with time makes it difficult to select a priori a single discrete spring stiffness to represent the lateral stiffness of the pile foundation.

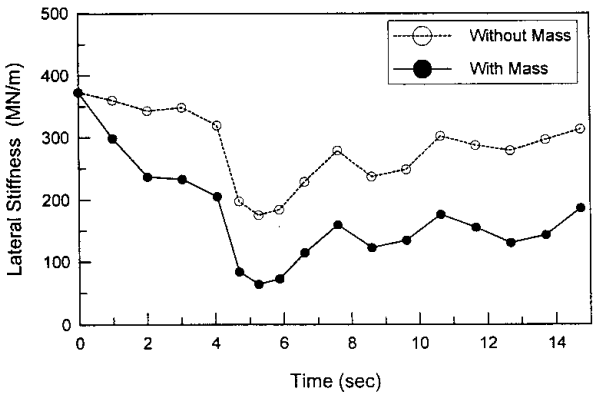

Figure 2 Time dependence of lateral stiffness

3. TYPES OF ANALYSES

During the research project, analyses will be conducted on 6 and 14 storey apartment buildings and on a 6 storey base isolated apartment building. At the present time, analyses are underway on the 14 storey apartment building. Results from these analyses are presented here to illustrate the concepts discussed above and to show the effects of soil layering and kinematic interaction on the moments and deflections in the pile. Seismic analyses were conducted on a 1.5 m diameter cast-in-place reinforced concrete pile supporting a column of the 14 storey building. The soil conditions and pile are shown in Fig. 3. Slightly idealized site conditions are shown in Fig. 4. The upper 10m are expected to liquefy during the design earthquake. The mass mounted on the pile in Fig. 4 represents the mass equivalent of the reaction force carried by the pile. The purpose in placing the mass on the pile is to model approximately the inertial interaction between the

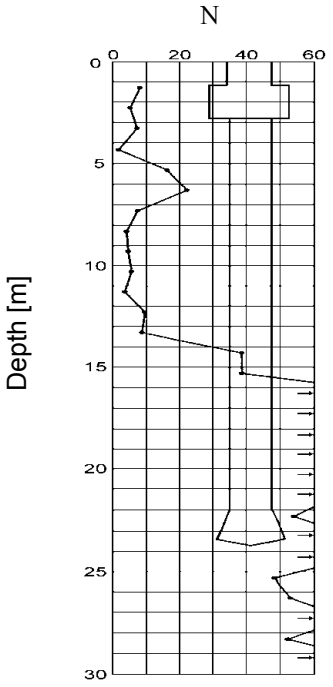

Figure 3 Site in reclaimed land

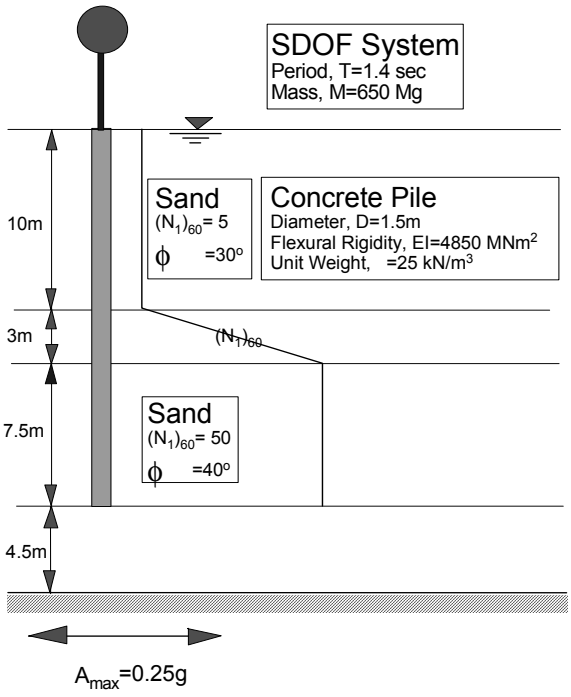

Figure 4 Model of soil-pile-structure system

superstructure and the pile foundation. It is mounted on the pile head by a flexible support that gives a period of vibration of 1.4s that is the estimated fundamental period of the prototype structure. Dynamic effective stress analyses of this system include both inertial and kinematic interactions and the effects of high pore water pressures and liquefaction. Analyses were also conducted without including the mass of the superstructure. These latter analyses give the kinematic deflections and moments. In all these analyses, the nonlinearity of the soil and the effects of seismic pore water pressures are taken into account. In general, soil properties are adjusted continuously for current pore water pressures and shear strains.

The peak acceleration of the input acceleration record is 0.25g and is amplified to 0.4g at the surface. The surface accelerations become negligible after liquefaction has occurred.

4. RESULTS OF ANALYSES

4.1 Analyses with inertial interaction

Pile displacements and moments for the 14 storey building, at the instant of maximum pile head displacement, are shown in Fig. 5 and Fig. 6 respectively. Approximately the top 10 m liquefy or develop very high pore water pressures during earthquake shaking. Results are shown for two conditions; the pile head is essentially fixed against rotation because of the large grade beams used to tie together the pile foundations of the building and the pile head is essentially free to rotate which is closer to North American practice which uses much lighter grade beams. The large grade beams are very effective in controlling displacements because the end fixity against rotation mobilizes much higher inherent pile stiffness. The displacements are more than twice as large when the lighter grade beams are used. The maximum moment occurs at the pile

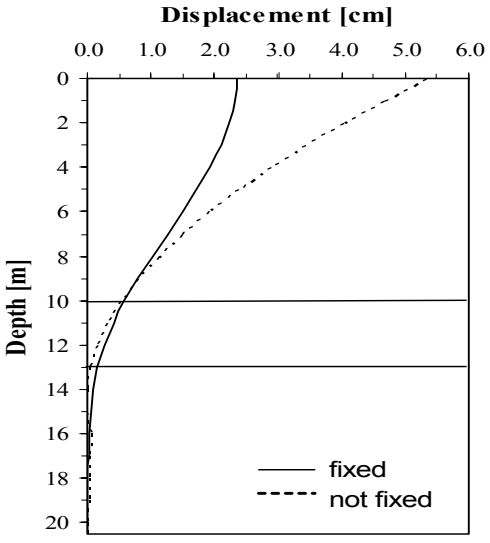

Figure 5 Deflections along pile

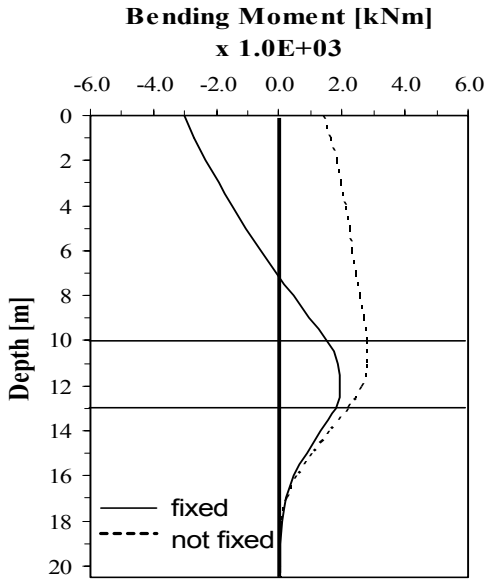

Figure 6 Moments along pile

head, when the pile head is fixed against rotation, but very significant moments also occur at the boundary between the softer and stiffer soils. When the pile head is not fixed against rotation, the maximum moment occurs at the boundary between the stiffer and softer soils. This moment is approximately equal to the pile head moment, when the pile head is fixed against rotation. The results show that when designing piles or evaluating pile foundations in potentially liquefiable soils for earthquake loading, it is important to make a realistic assessment of pile head restraint against rotation and to be aware of the potential for large moments at the interfaces between soft and hard layers.

At some sites a thick surface layer of non-liquefiable soil may lie over the liquefaction zone. A stiff upper layer is incorporated in the original site of the 14 storey building.. Deflections and moments for this case, at the instant of maximum pile head displacement, are shown in Fig.7 and Fig.8 respectively. As before, the results are shown for two pile head conditions, no rotation and essentially free to rotate.

Notice that, in this case, the pile head displacements are about the same whether the pile head is fixed against rotation or not. Also the deflection of the pile head, when the pile head is fixed against rotation, has more than doubled compared to the previous case of no stiff upper layer. This is due to the restraint of the pile by the upper layer and the movement of the layer as a rigid body after liquefaction develops. The stiff upper layer greatly increases the moment demand on the pile during earthquake shaking. The moments at the pile head and at the interface between the soft and stiff soils has increased by 30%, compared to the case without the upper layer. When the pile is fixed against rotation the moments at the pile head and the interface are about the same. The behavior of the upper layer is clarified further in the next section which presents results from kinematic analyses.

4.2 Kinematic Analyses

Kinematic analyses were conducted on the 1.5 m diameter pile to assess the importance of kinematic interaction. Analyses were conducted with and without the stiff surface layer and, in each case, the pile head was considered either fixed against rotation or not. The kinematic analyses were conducted by removing the super-structural mass in Fig. 4.

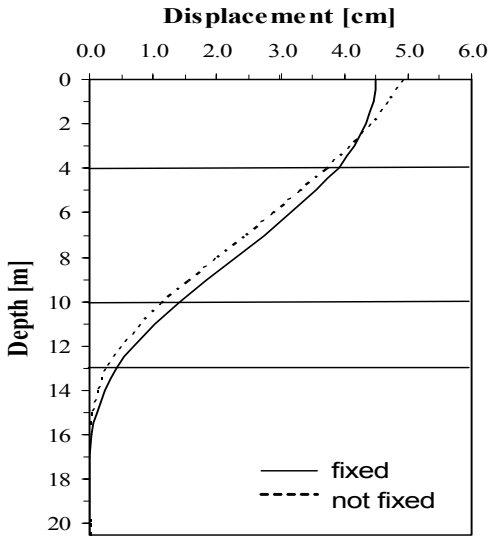

Figure 7 Maximum deflections along pile

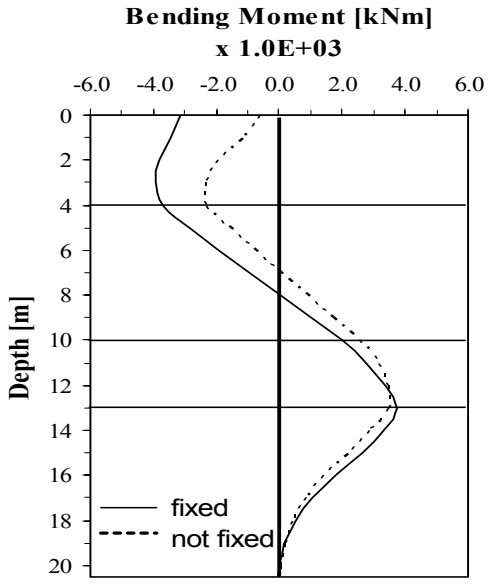

Figure 8 Maximum moments along pile

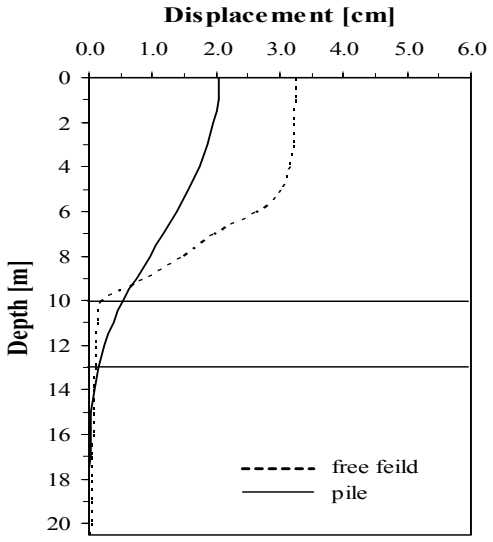

Figure 9 Displacements of pile and free field

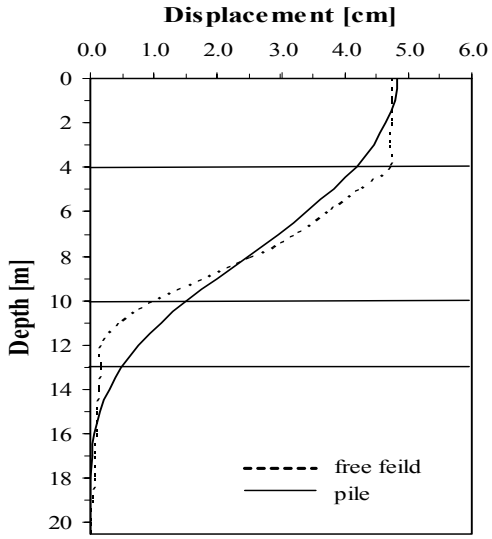

Figure 10 Displacements of pile and free field

The free field displacements of the foundation soils and the pile displacements, both at the instants of maximum pile head displacement, are shown in Fig. 9 and Fig.10. It is evident from Fig. 10 that the stiff upper layer is moving at this time as a rigid body. The displacement patterns of the soil in the free field and the pile are very different. However the compatibility of displacements must be preserved along the interfaces, wherever the soil and pile maintain contact during earthquake shaking. Significant moments and shears may develop in the pile in order to maintain this compatibility requirement as shown in Fig.11 and Fig.12. In the case of the stiff upper layer, the moments are about twice as large as for the case with no such layer. In both cases, the moments are of the same order as when the inertial mass is included. This indicates that, in this case, the kinematic moments dominate the moment response of the foundation.

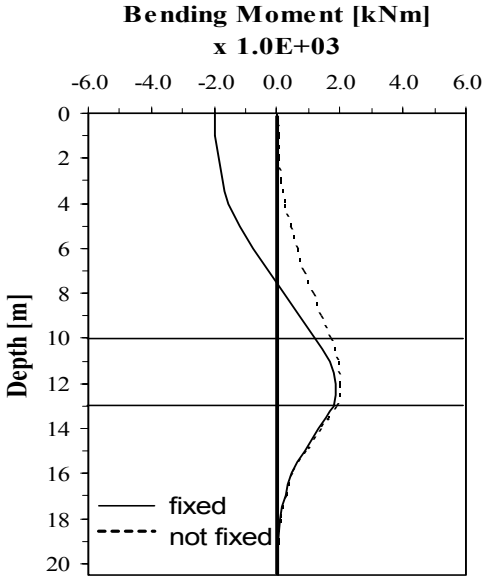

Figure 11 Kinematic moments along the pile with no stiff upper layer

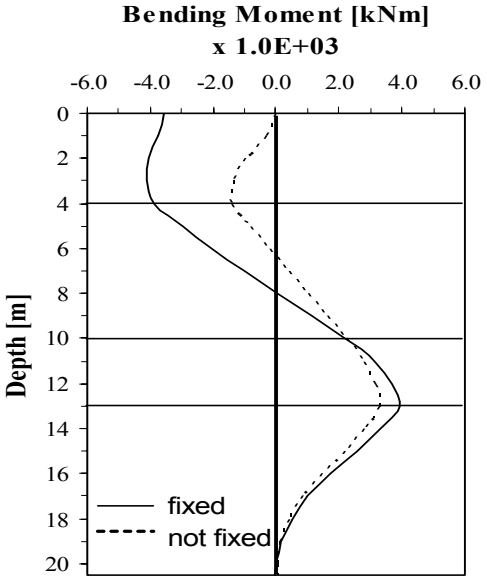

Figure12 Kinematic moments along the pile with stiff upper layer

Clearly analyses that neglect kinematic effects may underestimate significantly design moments and shearing forces in foundation piles.

5. CLOSING REMARKS

This paper gives a general overview of the important factors that affect the seismic design of large diameter cast in place reinforced concrete piles in potentially liquefiable soils during earthquakes. The analyses show that large bending moments develop in critical areas such as at the pile head, when it is fixed against rotation, and the boundary between liquefied and nonliquefied layers. The analyses also demonstrate that if a stiff upper layer overlies the liquefied zone, then the moment and deflection demands on the pile are substantially increased over the case when the stiff upper layer is not present. The keys to good design are reliable estimates of environmental loads, realistic assessments of pile head fixity and the use of methods of analysis that can take into account adequately all the important factors that control the response of the pile-soil-structure system to strong shaking.

.

ACKNOWLEDGEMENTS

The research project on the seismic design and analysis of pile foundations is funded by Anabuki Komuten, Takamatsu, Japan. The support of the company is gratefully acknowledged.

REFERENCES

Abghari, A. and Chai, J., (1995). Modeling of soil-pile superstructure interaction for bridge foundations, Performance of Deep Foundations under Seismic Loading, *ASCE Geotechnical Special Publication* No.51, 45-59

API, (1995). Recommended practice for planning, designing, and constructing fixed offshore platforms, American Petroleum Institute,

Finn, W. D. Liam and Wu, G., (1994). Recent developments in the static and dynamic analysis of pile groups. Proceedings of the Annual Symposium of the Vancouver Geotechnical Society. Vancouver, B. C. Canada , 1-24.

Finn, W. D. Liam and Thavaraj, T. (1999). Pile-3D-EFF A program for nonlinear dynamic effective stress analysis of pile foundations, Anabuki Chair of Foundation Geodynamics, Kagawa University, Japan

Finn, W. D. Liam, Thavaraj, T., Wilson, D. W., Boulanger, R. W.,and Kutter, B., (1999). Seismic analysis of piles and pile groups in liquefiable sand, Proceedings, 7th International Symposium on Numerical Models in Geomechanics, NUMOG VI, Graz, Austria, September, 287-292

Finn, W. D. Liam and Thavaraj, T. (2001). Deep foundations in liquefiable soils: Case histories, centrifuge tests and methods of analysis, CD-ROM Proceedings, 4th Int. Conf. on Recent Advances in Geotechnical Earthquake Engineering and Soil Dynamics, San Diego, CA, March 26-31,

Matsui, T. (1993). Case studies on cast-in-place bored piles and some considerations for design, Proceedings, 2nd International Geotechnical Seminar on Deep Foundations on Bored and Augered Piles, Ghent, 77-102

Matsui, T. and Oda, K. (1996). Foundation damage of structures, Special Issue, *Soils and Foundations,*
Japanese Geotechnical Society, January, 189-200

Murchison, J. M. and O'Neill, M. W. (1984). An evaluation of p-y relationships in cohesionless soils, Proceedings of the ASCE Symposium on Analysis and design of Pile Foundations, ASCE National Convention, San Francisco, California, Oct 1-5, Edited by J. R. Meyer, 174-191

Thavaraj, T. and Finn, W. D. Liam, (2000). A program for dynamic analysis of a single pile using a Winkler model and p-y curves, Anabuki Chair of Foundation Geodynamics, Kagawa University, Japan.

Thavaraj, T. and Finn, W. D. Liam, (2001). A program for dynamic analysis of bridges incorporating foundation springs with specified time histories of stiffnesses, Anabuki Chair of Foundation Geodynamics, Kagawa University, Japan.

Wu, G. and Finn, W. D. Liam, (1997a). Dynamic elastic analysis of pile foundations using the finite element method in the frequency domain, *Canadian Geotechnical Journal*, (34), 34-43

Wu, G. and Finn, W. D. Liam, (1997b). Dynamic nonlinear analysis of pile foundations using the finite element method in the time domain, *Canadian Geotechnical Journal*, (34), 144-152

Characteristics of the External Force acting on a Pile during Liquefaction-induced Lateral Flow of the Ground

Shunichi Higuchi and Takashi Matsuda

ABSTRACT

The purpose of this study is to investigate the behavior of a pile installed into a liquefable sandy ground during the earthquake. To evaluate the performance of pile foundations during severe earthquake, it is necessary to find the characteristics of the external force acting on the pile resulting from the seismic response of the ground. Especially, the behavior of the pile installed into the liquefied ground is very complicated because the physical properties of the soil may change every moment. This paper presents the characteristics of the external force acting on the pile during the lateral flow of the ground investigated by a series of centrifuge experiments.

INTRODUCTION

After the Great Hanshin Earthquake, many research projects were focused in the seismic performance of foundations constructed in the alluvial soft ground. To clarify the behavior of pile foundations in that type of ground during the, it is necessary to find the characteristics of the external force acting on the pile resulting from the seismic response of the ground. Especially, the behavior of the pile installed into the liquefied ground is very complicated because the physical properties of the soil may change every moment. Although many researchers have made efforts to explain the mechanisms of the lateral flow of the liquefied ground and proposed physical models (Hamada et al., [1], Tokida et al., [2]), no consistent conclusion may exist. In this study, the characteristics of the external force acting on the pile during the lateral flow of the ground were investigated by the centrifuge experiments.

CENTRIFUGE TESTS

Test program

Shaking table tests were carried out under the 30g (294m/s^2) centrifugal gravity field using the Obayashi centrifuge earthquake simulator with table dimensions of 2.2m x 1.07m (Matsuda, [3]). Table 1 shows summary of parameters of the shaking table tests. These parameters were selected to investigate the effect of the ground conditions and the characteristics of input motions. Ground conditions are consisted of the loose samples (Dr=40%) and the dense samples (Dr=75%). Figure 1 show the time histories of the input motions used in the experiments. Maximum acceleration amplitude of these input motions are about 12*g* (118m/s^2), and that corresponds to 0.4*g* (3.9m/s^2) in prototype. These motions are prepared basing on the sinusoidal motions with the frequency of 60 Hz.

Shunichi Higuchi, Deputy Senior Research Engineer, Civil Engineering Department, Technical Research Institute of OBAYASHI Co., JAPAN, 4-640 Shimokiyoto, Kiyose-shi, Tokyo Japan 204-8558
Takashi Matsuda, Senior Research Engineer, ditto.

TABE 1 TEST CASES AND PARAMETERS

Test case	1	2	3	4	5	6
Relative density Dr (%)	40	40	40	75	75	75
Input motion	1	2	3	1	2	3

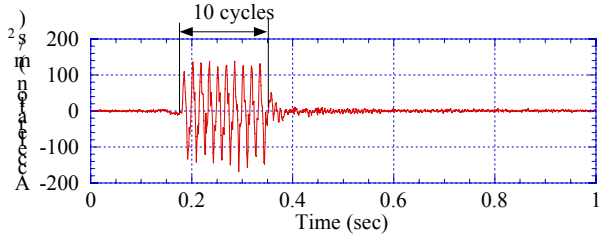

(a) Input motion 1

(b) Input motion 2

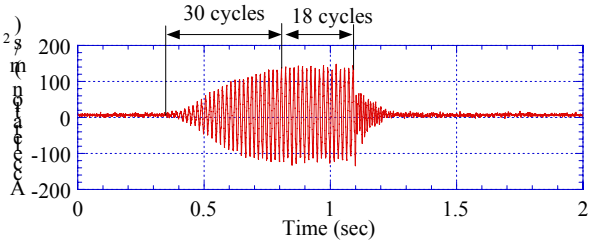

(c) Input motion 3

Figure 1 Time histories of the input motions (Model scale)

Model ground and instrumentation

Figure 2 shows the profile of the model ground and the layout of instruments. Model ground consisted of fine silica sand (D_{50}=0.08mm). Loose samples (Dr=40%) were prepared by the air pluviation method. Dense samples (Dr=75%) were compacted by steel rod after the air pluviation. Dimensions of the model ground are 1000mm in both length and width, 250mm in average depth. Surface of the ground is vacuumed to create the slope, which provides the lateral flow during the shake event. The inclination of the slope is 10%. After the preparation, the model ground was saturated with de-aired water. The level of the water table was set to 250mm from the bottom of the sand layer. In order to minimize the effect of the shaking event on the pile response during the lateral flow, the model ground is set on the centrifuge shake table with its surface slope direction perpendicular to the shaking direction.

Table 2 shows the types and quantity of instrumentation installed into the model ground. Water-resistant LVDTs (ACW-2000) make it possible to directly measure the displacements in the sand layer (Figure 2(c)) during shaking.

TABLE 2. TYPES AND QUANTITES OF INSTRMENTATION

Type	Piezoelectric Accelerometer	Pore Pressure Transducer	Laser Displacement Transducer	Water-resistant LVDT
Manufacturer	NEC (Japan)	Drug (UK)	Keyence (Japan)	RDP Electronics (UK)
Model	A3S	PDCR81	LB-1000 LK-2000	ACW-2000
Range	5500m/s^2	700kPa	0~200 mm 0~30 mm	0~100 mm
Quantity	12	9	5	3

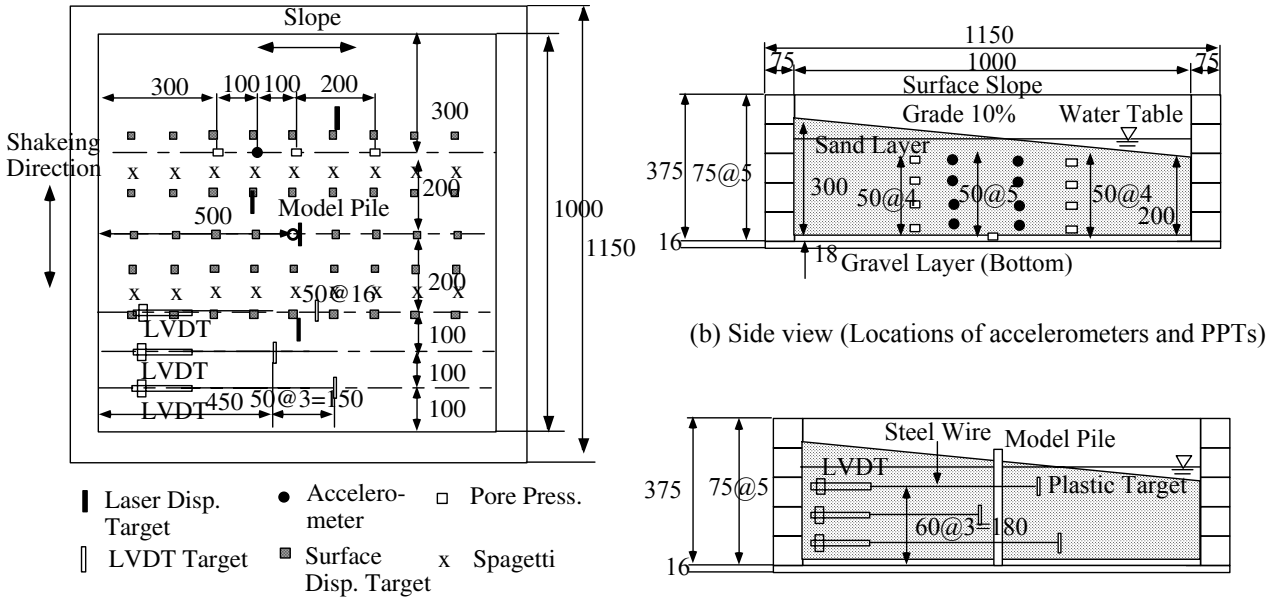

(a) Plain view

(b) Side view (Locations of accelerometers and PPTs)

(c) Side view (Locations of LVDTs)

Figure 2 Model ground and instrumentation

Model piles

Figure 3 shows the profile of the model pile installed into the ground. The pile is made of stainless steel (SUS306) pipe with outer diameter of 20mm and 0.5mm wall thickness. To provide a clear boundary condition of pile behavior, the bottom end of the pile is fixed to the bottom plate of the container. 12 strain gauges (SW-SE sections) are instrumented on the pile to get the distribution of the external force provided by the liquefied soil during shaking. These gauges are installed inside the pile because the existence of gauges and wires outside the pile may affect to the characteristics of the soil-pile interaction.

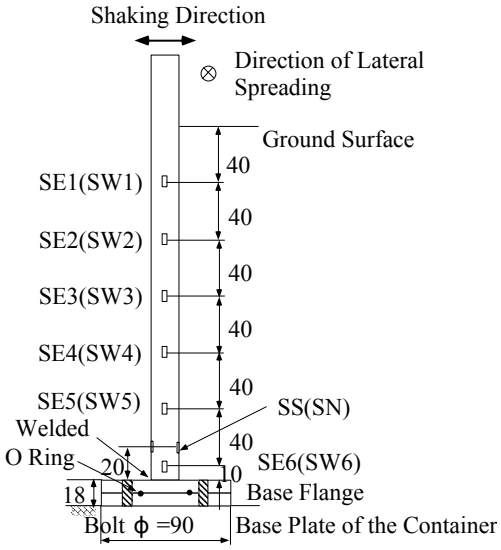

Figure 3 Pile model and instrumentation

TEST RESULTS

Pile response during the lateral flow

Figure 4 shows typical time histories of acceleration, excess pore pressure, bending moment of pile and ground surface displacement from Case 2, in which the sand layer severely liquefied.

Due to the increase of shear stress in the slope caused by centrifugation, pile was subjected to bending moment before shaking. The excess pore pressure starts increasing from t=0.40 sec and the excess pore pressure ratio (u/σ_v') reaches about 1.0 at t=0.57 sec. Surface displacement starts increasing as the excess pore pressure increases as well as the bending moment. At t=0.58 sec, 0.18 sec after start shaking, the bending moment measured at the bottom end of the pile shows its maximum amplitude throughout the time history. After showing the peak value, the bending moment decreases to zero when the surface movement stops. This shows the liquefied soil passed through the model pile during the lateral flow. These facts suggest that there is a strong relation between the external force acting on the pile and the movement of liquefied soil around the pile. Displacement of the ground surface increased faster before the moment at which the peak bending moment appeared.

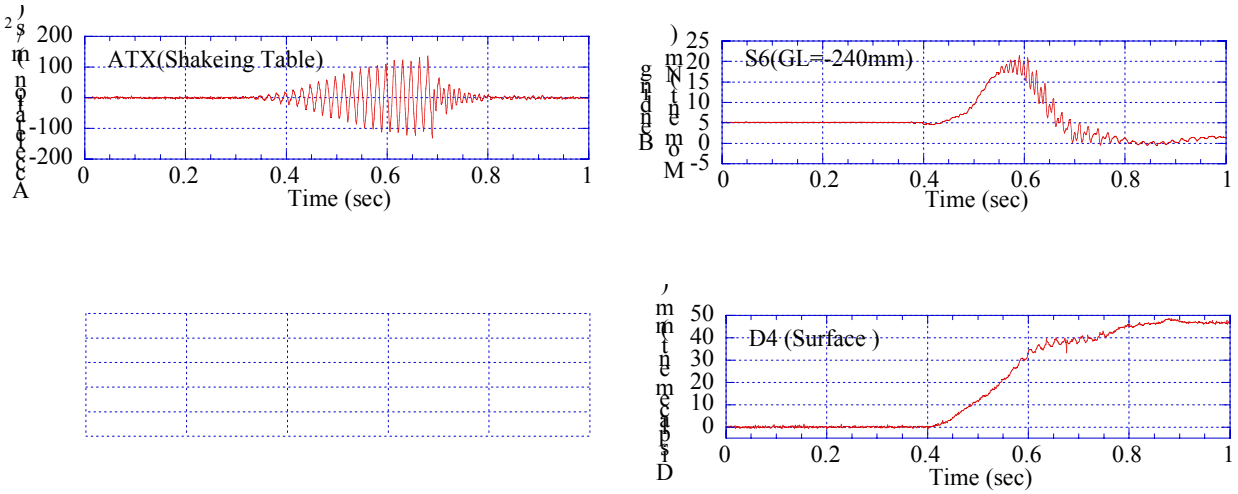

Figure 4 Time histories of acceleration, excess pore pressure ratio, bending moment and displacement from Case 2; loose deposit

Figure 5 shows typical time histories from Case 6, in which the sand layer compacted. Although the responses of the ground and pile are similar to those of Case 2, some differences exist. The peak value of the bending moment of the pile appeared t=0.25sec after start shaking, and decreasing slower after the peak. The maximum amplitude of the bending moment is larger than the maximum bending moment observed in Case 2. Some residual moment remains after the shake event. Displacement of the ground surface constantly increased throughout the shake event in this case. There are small differences in the final displacement of the ground surface between both cases.

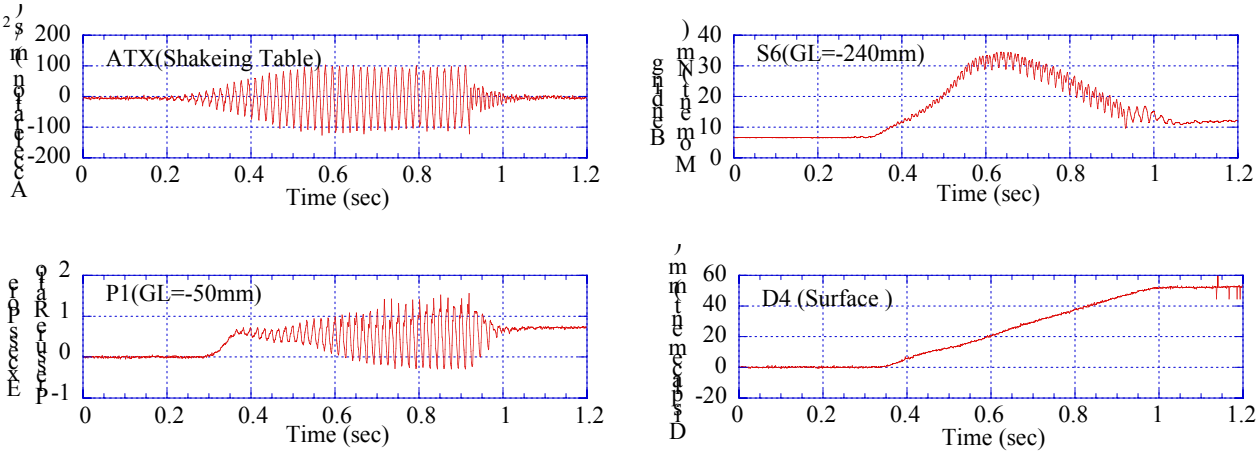

Figure 5 Time histories of acceleration, excess pore pressure ratio, bending moment and displacement from Case 6; dense deposit

Summary of test results

Test results are summarized in this section. The maximum values recorded at typical instrumentation during each experiment are shown in Table 3.

TABLE 3 MAXIMUM VALUES RECORDED AT TYPICAL INSTRUMENTATION

Case	1	2	3	4	5	6
Sand density	Loose (Dr=40%)			Dense (Dr=75%)		
PPR_{max}	1.0	1.0	1.0	0.9	0.8	1.0
DG_{max}	51.1	48.2	47.1	24.7	26.7	55.5
DP_{max}	1.8	1.9	1.8	2.5	1.3	2.9
M_{max}	20.5	21.9	19.2	30.2	18.3	32.8
DG_{Mmax}	24.9	24.1	27.6	22.5	20.5	23.6
DP_{Rm}	0.0	0.0	0.0	1.9	0.9	0.5

PPR_{max} : Maximum excess pore pressure ratio at P4 in Figure.2.
DG_{max} : Maximum ground surface displacement (mm)
DP_{max} : Maximum displacement of the pile top (mm)
M_{max} : Maximum bending moment of the pile at the bottom fixed end (Nm)
DG_{Mmax} : Ground surface displacement when the maximum bending moment of the pile happens (mm)
DP_{Rm} : Residual pile top displacement (mm)
Note: All data indicated in this paper are presented in the model scale.

Followings were observed in the experiments and found from this table.

1 Surface displacement provided by the lateral flow observed in the loose saturated sand deposit (Case 1) is twice as large as that of observed in the compacted sand deposit (Case 3) under the same input motion.
2 Liquefied soil passed through the pile in Case 1 through Case 3, in which grounds were loose. On the other hand, soil kept its strength throughout the shake event and deformation of the pile remained after the lateral flow in Case 4 and Case 5, in which the ground was well compacted.
3 Although the ground was compacted, liquefied soil passed through the pile in Case 6, in which the duration of the input motion was long. Larger surface displacement was observed as well.

4 Relatively larger bending moment on the pile was found on the compacted ground condition (Case 4 and Case 6) than that of the loose ground condition.
5 Maximum bending moment is observed at the moment which the ground surface displacement reaches to about 24mm in each case.

Findings listed above suggest that the ground compaction is not necessary avoiding the damages of the foundation from the lateral flow of the ground initiated by the liquefaction. It may bring about larger section force or residual displacement on the foundations after the earthquake.

CHARACTERISTICS OF THE FORCE ACTING ON THE PILE

Development of the bending moment of the pile during the lateral flow

Figure 6 show the snap shots of the bending moment distribution throughout the pile during the shake event from Case 3 and Case 6.

In Case 3, the curvature of the bending moment distribution may change between the initial stage (t=0.42sec) of the shake event and the instant at which the ground flew (t=0.58 sec). This suggests the mechanism of the external force acting on the pile changes during the shake event. At the beginning of the shake, the pile is subjected the earth pressure caused by change of K-value (σ_h/σ'_v) due to excess pore pressure generation in the soil deposit. On the other hand, the external force during the liquefaction may relate with the lateral flow in the loose deposit.

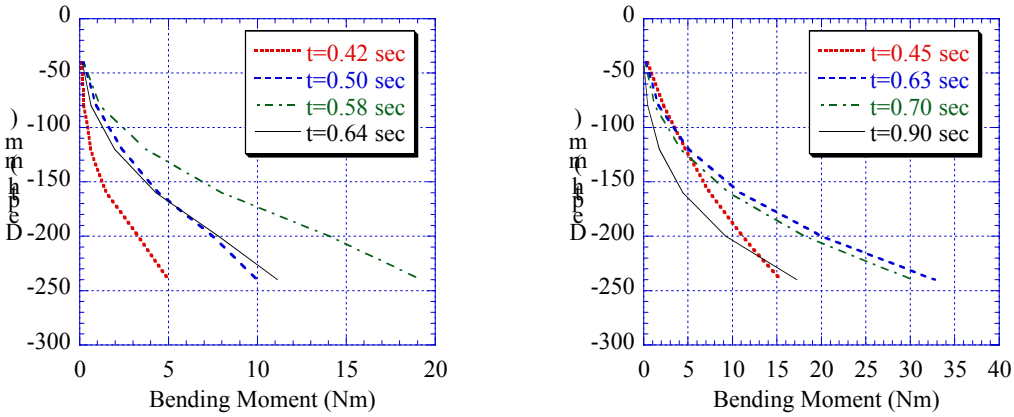

(a) Case 3 (b) Case 6

Figure 6 Snap shots of the bending moment distribution throughout the pile

Evaluation formula of the external force acting on the pile in the liquefied soil

Hamada et al. [4] pointed out that physical property of the liquefied soil is similar to those of fluids. The fact that the liquefied soil passed through the pile during the lateral flow observed in the tests may support this opinion. Therefore, characteristics of the external force acting on the pile installed in the liquefied soil are analyzed based on the fluid mechanics.

The authors proposed the analytical model to predict the external force distribution of the pile from the liquefied soil [5]. That distribution formula $q_t(z)$ is written as,

$$q_t(z) = M_{tb} \cdot (\frac{\pi^2}{4H^2}) \cdot \sin(\frac{\pi}{2H} z) \quad (1)$$

Where,
$q_t(z)$ = external force acting on the pile in terms of z at specific time step (N/m)
z = height from the bottom of the liquefied deposit (m)
M_{tb} = bending moment of the bottom end of the pile at specific time step (Nm)
H = depth of the liquefied deposit (m).

By the assumption that the external force acting on the pile governed by the friction between the pile surface and liquefied soil, following relation is determined.

$$Q_{tb} = \mu_t \dot{\gamma}_t \pi D H = -M_{tb} \frac{\pi}{2H} \quad (2)$$

Where,
Q_{tb} = shear force acting on the bottom end of the pile (N)
μ_t = viscosity of the liquefied soil at specific time (Pa*s)
$\dot{\gamma}_t$ = shear strain velocity at specific time step (1/s) as V_{st}/H (V_{st}: Velocity of the ground surface)
D = pile diameter (m).

Shear strain dependent viscosity of the liquefied soil

Figure 7 shows the relation between viscosity and shear strain velocity of the liquefied soil found in the previous study [5] using the data from Case1 through Case3 in this study. This phenomenon is known as a pseudo-plastic fluid, and same behavior has been reported by Hamada et al. [4].

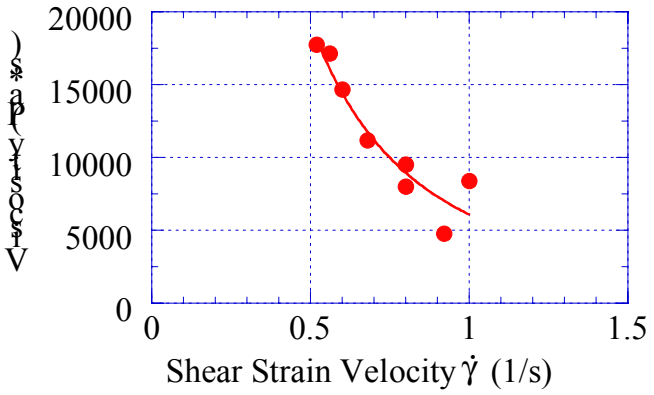

Figure 8 Experimentally determined relation between viscosity and shear strain velocity of the liquefied soil [5]

The solid line in Figure 8 shows the approximation of the relation between viscosity and shear strain velocity by the least square method. This equation can be written in a form of hyperbolic function as,

$$\mu = \frac{\mu_0}{(1+\frac{\dot{\gamma}}{\dot{\gamma}_r})^2} \quad (3)$$

Where,

μ = viscosity (Pa*s), μ_0 = initial viscosity (Pa*s), $\dot{\gamma}_r$ = reference shear strain velocity (1/s).

Here, μ_0 = 398,400 (Pa*s) and $\dot{\gamma}_r$ = 0.1411 (1/s) are determined from this figure.

Prediction of the bending moment distribution of the pile in the dense deposit

Using the equation (1) through (3) the bending moment distribution of the pile in the dense soil deposit is predicted. Because of the same kind of sand used in Case6, the relation illustrated in Figure 8 can be utilized.

Figure 9 shows the time history of the ground surface velocity in Case6. The moment of which the maximum bending moment on the pile observed was t=0.63sec, and the velocity of the ground surface was V=96mm/s.

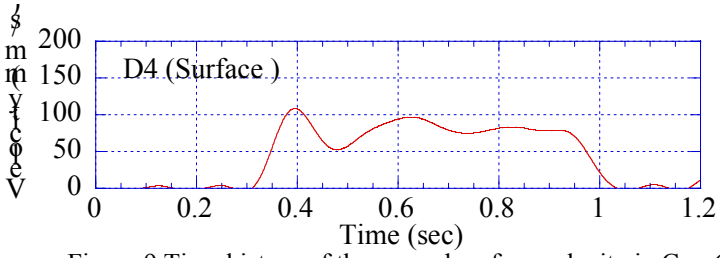

Figure 9 Time history of the ground surface velocity in Case6

The strain velocity can be calculated as $\dot{\gamma}$ =V/H=0.384. By substituting this into the eq.(3), viscosity becomes μ =28,800 Pa*s.

M_{tb} can be derived by eq.(2) as M_{tb} =27.45 Nm. Because the measured bending moment at t=0.63sec is M=32.8 Nm as shown in Table 3, the calculated value is about 15% smaller than the measured value.

Figure 10 shows the moment distribution on the pile at t=0.63sec of Case6.

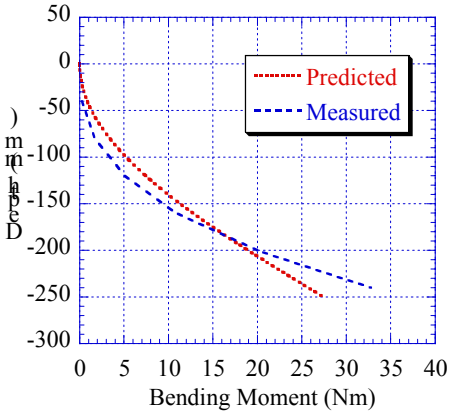

Figure 10 Comparison of the predicted bending moment distribution and measured distribution

Because of the sine approximation on the distribution equation [5], there is some difference in curvature.

CONCLUSION

A series of centrifuge shaking table tests have conducted to investigate the effect of the liquefaction-induced lateral flow on the behavior of single pile. From test results, it is found that characteristics of the external force acting on the pile relate with both the earth pressure and the ground flow depending on the soil condition. Also, the experiment results from the dense ground suggest that the ground compaction is not necessary avoiding the damages of the foundation from the lateral flow of the ground initiated by the liquefaction. It may bring about larger section force or residual displacement on the foundations after the earthquake.

Evaluation formula of the external force acting on the pile in the liquefied soil basing on the fluid mechanics was applied to the dense ground. The predicted bending moment resulted as 15% smaller than the measured value. To apply the proposed model in practice, it is desirable to propose the precise method to evaluate the surface displacement and the flow velocity of the liquefied ground.

Acknowledgments

The authors wish to acknowledge the technical assistance and suggestions of Prof. M. Hamada, Prof. F. Miura and Dr. T. Sugano. Part of this research is funded and charged by the committee named Enhancement of Earthquake Performance of Infrastructures Based on Investigation into Fracturing Process, established by the Japanese Society of Civil Engineers (JCSE).

REFERENCES

[1] Hamada et al. 1994. "An experimental and numerical study on liquefaction-induced ground displacement", *Proc., 5th U.S. National Conference of Earthquake Engineering*, Vol. IV, pp.169-178.

[2] Tokida et al. 1992. "Experimental study on drag acting on piles in ground flowing by soil liquefaction", *Proc., 4th Japan-US Workshop on Earthquake-Resistant Design of Lifeline Facilities and Countermeasures for Soil Liquefaction*.

[3] Matsuda et al. 2002. "Development of the large geotechnical centrifuge and shaking table of Obayashi", *Proc., International Conference of Physical Modeling in Geotechnics*, pp. 63-68.

[4] Hamada et al. 1998. "A study on ground displacement caused by soil liquefaction", *Proc, Japanese Society of Civil Engineers*, No. 596, Vol. III-43, pp. 189-208.

[5] Higuchi et. al. 2002. "Effects of Liquefaction-induced Lateral Flow of the Ground against a Pile Foundation". *Proc., International Conference of Physical Modeling in Geotechnics*, pp. 465-470.

3-Dimensional Simulation of Pile-Ground System During Liquefaction and Following Ground Flow Process

Tadanobu Sato, Takaki Matsumura, Feng Zhang, Yong Moon and Ryosuke Uzuoka

ABSTRACT

Loose saturated sand behaves as a solid before liquefaction but as a fluid when the excess pore water pressure equals the initial confining stress, after which it recovers its strength. Those processes are cannot be treated independently, but should be considered continuous processes that represent change from the solid to fluid state or from the fluid to solid state. Therefore, the total processes of the combined liquefaction-ground flow phenomenon should be treated as a series of processes of phase transformation between the solid and fluid states. In this paper, a simple constitutive equation for loose saturated sand was developed to express the phase transformation between a solid and fluid during liquefaction and the ground flow phenomenon. This constitutive equation was used for a dynamic analysis of a pile-ground system, and its applicability investigated by comparing with the elasto-plastic constitutive equation.

INTRODUCTION

The 1995 Hyogoken-Nambu earthquake, magnitude 7.2 (Richter scale), caused widespread liquefaction of almost all the reclaimed land in Kobe. This liquefaction caused significant damage in Kobe City. In particular, many caisson-type quay walls in Kobe port moved several meters towards the sea due to liquefaction and subsequent ground flow [1,2]. Owing to that movement lateral spreading occurred in the backfill behind the walls after the earthquake. The distribution and range of this spreading extended more than 100m from the caisson-type quay walls [3]. Such large horizontal displacement of soil by liquefaction and the ground flow phenomenon first was reported by Hamada et al. [4] after a detailed aerial photographic survey made in Niigata City which was struck by a large severe earthquake in 1964. Based on reported results, there was horizontal permanent displacement of more than 10m on the bank of the Shinano River in Niigata City. Since then, the ground flow phenomenon caused by liquefaction has been a main topic of liquefaction research.

When saturated sand undergoes cyclic loading, pore water pressure increases until it equals the initial confining stress. As a result, the shear strength of the soil is lost. This is well known as the definition of liquefaction. Further, when liquefied ground undergoes a continuous external

Tadanobu Sato, Professor, Disaster Prevention Research Institute, Kyoto University, Gokasho Uji, Kyoto 611-0011, Japan
Takaki Matsumura, Graduate Student, Dept. of Civil Engineering, Kyoto University, Gokasho Uji, Kyoto 611-0011, Japan
Feng Zhang, Associate Professor, Graduate School of Engineering, Gifu University, Gifu 501-1193, Japan
Yong Moon, Associate Researcher, Disaster Prevention Research Institute, Kyoto University, Gokasho Uji, Kyoto 611-0011, Japan
Ryosuke Uzuoka, Lecturer, Graduate School of Engineering, Tohoku University, Aoba-yama 04, Sendai 980-8579, Japan

driving force, such as that caused by the inclination of its surface, the ground flows like a viscous fluid. As a result, there is large deformation of the surface laterally and damage to structures. This is the ground flow phenomenon [5, 6]. Finally the ground flow phenomenon that accompanies liquefaction ends, the liquefied sand recovers its stiffness, and shear stress increases rapidly as pore water pressure decreases [7].

Consequently, the process of liquefaction and the ground flow phenomenon can be classified in three parts: the solid state before the onset of liquefaction, the fluid state after liquefaction, and the recovered solid state owing to dissipation of the excess pore water pressure and dilatancy caused by development of large shear strain. The analytical approach for studying the liquefaction and ground flow phenomena therefore cannot be treated independently, but should be considered continuous processes that represent change from the solid to fluid state or from the fluid to solid state. Therefore, the total processes of the combined liquefaction-ground flow phenomenon should be treated as a series of processes of phase transformation between the solid and fluid states.

Many numerical algorithms that simulate liquefaction and subsequent processes have been developed that are based on the solid mechanisms [8, 9, 10]. These methods focus mainly on the stress-strain response of pre-liquefaction. And, the ground flow phenomenon that generates a large deformation is not considered. On the other hand, ground flow phenomenon after liquefaction has been studied to give an estimate of the residual large displacement of liquefied ground in terms of fluid or solid mechanisms [11, 12, 13, 14, 15]. Despite many research findings, these methods deal separately with liquefaction or the ground flow phenomenon based on solid or fluid mechanisms. At present, no research has combined solid and fluid mechanisms for simulation of the phase transformation from the solid to fluid states or fluid to solid states.

We have used mechanical and numerical modeling of seismic liquefaction and the ground flow phenomenon in saturated loose sandy soil based on elasto-plastic and viscous fluid constitutive equations. A simple constitutive equation was developed to unify these phase transformations of saturated loose sand. It combines the cyclic elasto-plastic behavior of sand and the Newtonian viscous fluid characteristics of liquefied sand by defining the phase transformation-controlling function. This constitutive equation provides a unified constitutive equation for the characterization of the entire process of liquefaction from the initial to post-liquefaction state. We applied this constitutive equation to analyze the dynamic behavior of a pile-ground system, and to simulate dynamic interaction between a pile and liquefied ground accompanying a flow phenomenon. Its efficiency is investigated by comparing with simulated results obtained by using the elasto-plastic constitutive equation.

CONCEPT OF THE PROPOSED CONSTITUTIVE EQUATION

Based on solid mechanics, the relationship between the total stress and effective stress of a mixture using the component of pore water pressure is

$$\sigma_{ij} = \sigma'_{ij} + p\delta_{ij} \tag{1}$$

where σ_{ij}, σ'_{ij}, p are the total stress tensor, effective stress tensor, and pore water pressure, and δ_{ij} is the Kronecker delta.

When the solid skeleton of a mixture is assumed to be an elasto-plastic body, the effective

stress, σ'_{ij}, in Equation (1) becomes the stress, σ^{ep}_{ij}, of the elasto-plastic body. And Equation (1) becomes

$$\sigma_{ij} = \sigma^{ep}_{ij} + p\delta_{ij} \tag{2}$$

In contrast, the total stress of the viscous fluid in fluid mechanics generally is described as

$$\sigma_{ij} = \sigma^{vf}_{ij} + p\delta_{ij} \tag{3}$$

where σ^{vf}_{ij} is the viscous resistance stress tensor in the viscous fluid.

A comparison of Equations (2) and (3) shows that the component in which the pore water pressure is subtracted from the total stress tensor expresses the effective stress tensor in Equation (2) and the viscous stress tensor in Equation (3). This means that the viscous stress tensor in fluid mechanics coincides with the effective stress tensor concerned with the stiffness of a soil skeleton of a mixture.

Using this relationship, we propose a simple constitutive equation for loose saturated sand that expresses the phase transformation between the solid and fluid states during the liquefaction and ground flow processes. The newly proposed constitutive equation is called the fluidal-elasto-plastic constitutive equation and defined as Equation (4), and a schematic view of the constitutive equation is shown in Figure 1.

$$\sigma_{ij} = (1-\alpha)\,\sigma^{ep}_{ij} + \alpha\,\sigma^{vf}_{ij} + p\delta_{ij} \tag{4}$$

where α is the phase transformation-controlling function. The stress, σ^{ep}_{ij}, is evaluated by the cyclic elasto-plastic constitutive equation [8]. The relationship is written as follows by means of the incremental formulation

$$d\sigma^{ep}_{ij} = D^{ep}_{ijkl}\, d\varepsilon_{kl} \tag{5}$$

where D^{ep}_{ijkl} is the fourth-order isotropic tensor concerned with the stress-strain relationship for the elasto-plastic constitutive equation, and $d\varepsilon_{kl}$ is the strain tensor increment. The stress and strain in Equation (5) are expressed by incremental formulation in order to describe the nonlinear property of the material.

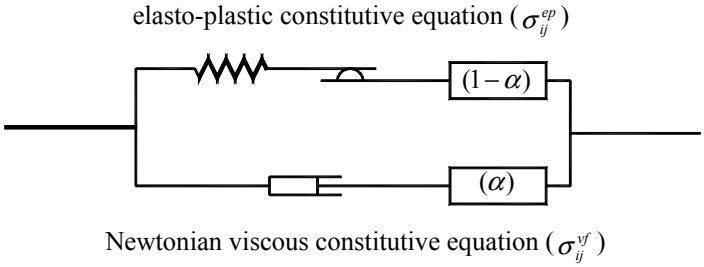

Figure 1. Concept of the fluid-elasto-plastic constitutive equation

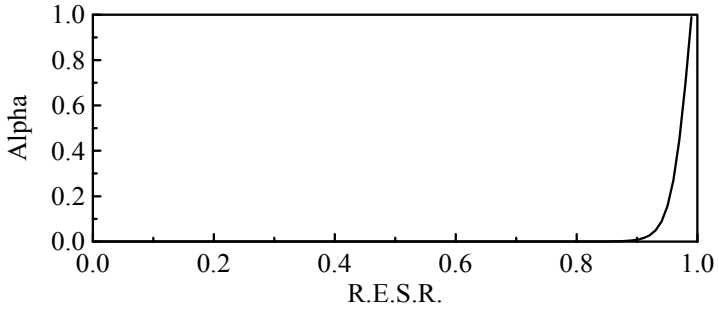

Figure 2. Relationship between α and R.E.S.R.

The stress, σ_{ij}^{vf}, is evaluated by a Newtonian viscous fluid constitutive equation as

$$\sigma_{ij}^{vf} = D_{ijkl}^{vf}\,\dot{\varepsilon}_{kl} = 2\mu'\dot{\varepsilon}_{ij} + \lambda'\dot{\varepsilon}_{kk}\delta_{ij} \tag{6}$$

where D_{ijkl}^{vf} is the fourth-order isotropic tensor concerned with the stress-strain rate relationship for the Newtonian viscous fluid, $\dot{\varepsilon}_{kl}$ is the strain rate tensor, and μ', λ' are the viscous and the second viscous coefficients.

In this paper, the phase transformation-controlling function, α, is a function of the effective stress throughout the process of liquefaction, ground flow and recovery of stiffness. The phase transformation-controlling function is expressed by

$$\alpha = 1.0 + \tanh\left(\mathrm{a}\cdot\left(1-\sigma'_m/\sigma'_{m0}\right)-\mathrm{b}\right) \tag{7}$$

where σ'_m, σ'_{m0} are current and initial mean effective stresses, $1-\sigma'_m/\sigma'_{m0}$ is the relative effective stress ratio (R.E.S.R.) and a, b are parameters.

This relationship between α and R.E.S.R. is shown in Figure 2. When R.E.S.R. is more than 0.9, the value of α rapidly increases, and when the value reaches 1.0, α becomes 1.0 reversibly. α then rapidly decreases with recovery of the mean effective stress caused by seepage and dilatancy. Actuation of the fluid behavior modeled by a Newtonian viscous fluid is limited to a region in which the mean effective stress is very small. The shape of α is controlled by the values of 'a' and 'b' in Equation (7).

NUMERICAL FOMULATION OF THE PROPOSED CONSTITUTIVE EQUATION

A field equation based on the proposed constitutive equation is derived from Biot's mixture theory [16] for a two-phase porous medium composed of the soil skeleton and pore water. The dynamic motion of the proposed constitutive equation is described by the u-p formulation introduced by Oka et al. [17].

The equilibrium equation of the mixture is

$$\rho\ddot{u}_i^s = \frac{\partial\sigma_{ij}}{\partial x_j} + \rho b_i \tag{8}$$

where ρ, $\ddot{u}_i^s$, σ_{ij} are the mixture density, solid skeleton acceleration, and total stress of the mixture, and b_i is the body force.

The derived continuity equation based on the law of mass conservation is

$$\frac{k}{\gamma_w}\left(\rho^f \ddot{\varepsilon}_{ii}^s - \frac{\partial^2 p_d}{\partial x_i^2}\right) - \dot{\varepsilon}_{ii}^s + \frac{n}{K^f}\dot{p}_d = 0 \tag{9}$$

where k, γ_w, ρ^f, $\ddot{\varepsilon}_{ii}^s$, p_d, $\dot{\varepsilon}_{ii}^s$, n are the coefficient of permeability, unit weight of water, density of the fluid, acceleration of the volumetric strain of the solid skeleton, excess pore water pressure, and volumetric strain rate of the solid skeleton, porosity , and K^f is the bulk modulus of the fluid.

The finite element method based on the u-p formulation [17] gives the discretized formulation for the equilibrium equation:

$$[M]\{\ddot{u}_N\} + \left((1-\alpha)[C^{ep}] + \alpha[C^{vf}]\right)\{\dot{u}_N\} + (1-\alpha)[K]\{\Delta u_N\} + \{K_v\}p_{dE} = \{F_d\} - \{R_{d|t}\} \tag{10}$$

Each term in Equation (10) is defined by

$$[M] = \int_V \rho[N]^T[N]dV \tag{11}$$

$$[K] = \int_V [B]^T[D^{ep}][B]dV \tag{12}$$

$$[C^{ep}] = \alpha_0[M] + \alpha_1[K] \tag{13}$$

$$[C^{vf}] = \int_V [B]^T[D^{vf}][B]dV \tag{14}$$

$$\{K_v\} = \int_V \{B_v\}dV \tag{15}$$

$$\{F_d\} = \int_V \rho[N]^T\{b_d\}dV + \int_S [N]^T\{T_d\}dS \tag{16}$$

$$\{R_{d|t}\} = (1-\alpha)\int_V [B]^T\{\sigma^{ep}{}_{|t} - \sigma^{ep}{}_{|t=0}\}dV \tag{17}$$

where $[M]$, $[K]$, $[C^{ep}]$, $[C^{vf}]$ are the mass matrix, stiffness matrix of the elasto-plastic model, Rayleigh damping matrix, and matrix for the relation between the stress and strain rate of the Newton viscous fluid model, and $\{K_v\}$, $\{F_d\}$, $\{R_{|t}\}$ are the transformation vector from nodal displacement to volumetric strain, the vector of the external body force caused by inertia, and vector of the residual force in the previous time step.

In contrast, for the continuity equation (Equation (9)), the pore water pressure is discretized by the finite different method [18] in the space domain, and the discretized formulation for the continuity equation is

$$\rho^f\{K_v\}^T\{\ddot{u}_N\} - \frac{\gamma_w}{k}\{K_v\}^T\{\dot{u}_N\} - \alpha' p_{dE} + \sum_{i=1}^{4}\alpha_i' p_{dE_i} + A\dot{p}_{dE} = 0 \tag{18}$$

where α', α_i' are coefficients of pore water pressure approximated by a finite different mesh between the central and neighboring elements, p_{dEi} is the central pore water pressure on the neighboring element and A is the coefficient for compressibility of the fluid. Furthermore, Equations (10) and (18) can be discretized by the Newmark-β method for the time domain.

PERFORMANCE OF THE PROPOSED CONSTITUTIVE EQUATION

To determine the behavior of the fluidal-elasto-plastic constitutive equation, the large strain response of a liquefied sand specimen was simulated and compared with that found in a torsional shear test in the undrained condition by Yasuda et al. [7]. This torsional shear test was performed on Toyoura sand (Gs=2.64, e_{max}=0.977, e_{min}=0.607, D_{50}=0.12mm, with no finer content) that had a relative density of 50% and the initial effective confining pressure of 98kPa. Viscous coefficients λ'=0.0, μ'=0.3 kPa・s were used to define the Newtonian fluid constitutive equation.

Cyclic loading was terminated when the excess pore pressure ratio reached a certain value. When the number of cyclic loadings reached 20.0 cycles, liquefaction of the soil elements occurred, but loading was continued up to 27.0 cycles then monotonic loading was used. Figure 3 shows the loading process schematically. The cyclic shear stress ratio is 0.153, and the maximum monotonic shear stress 98 kPa.

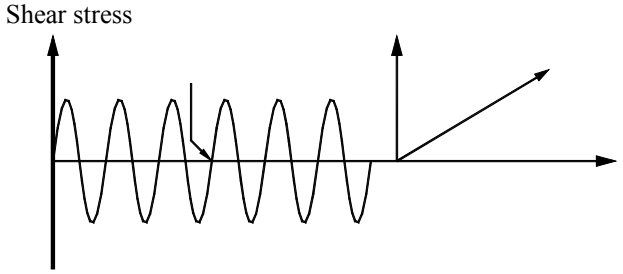

Figure 3. Loading process

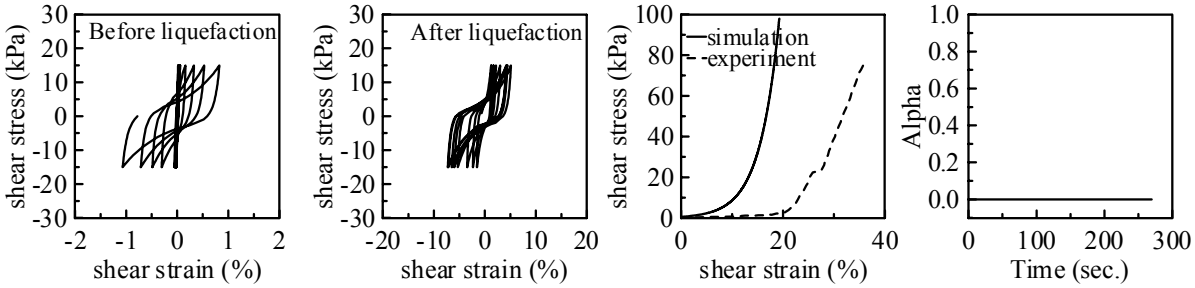

(a) Elasto-plastic constitutive equation

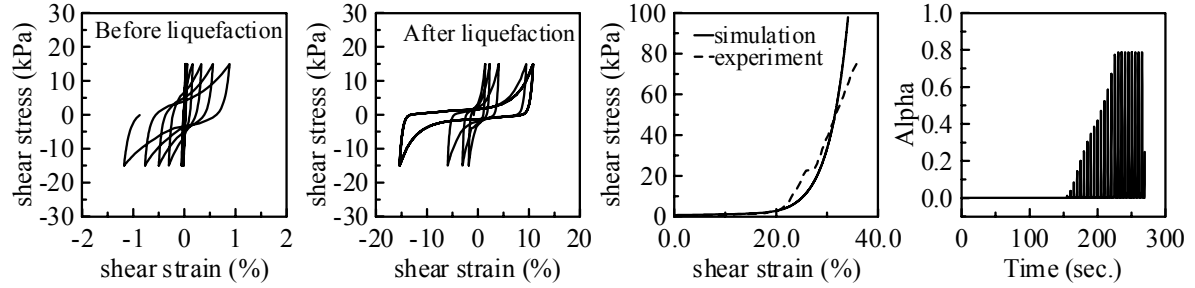

(b) Fluidal- elasto-constitutive equation

Figure 4. Results of the simulation

Numerical results in Figure 4 show comparisons between the elasto-plastic and fluidal-elasto-plastic constitutive equations and the experimental results. This figure also shows the stress-strain relationship during cyclic loading (before and after liquefaction) and monotonic loading, and the history of the phase transformation-controlling function. Before liquefaction occurred, the stress-strain relationships found with the elasto-plastic and fluidal-elasto-plastic constitutive equations are almost the same because the value of α is very small in this cyclic loading range. After the onset of liquefaction, our proposed constitutive equation generates greater shear strain than the elasto-plastic constitutive equation because the value of α increases with the decrease in the mean effective stress. When the mean effective stress increases in the large strain range, α rapidly decreases, and the soil element recovers its strength. Our proposed constitutive equation can analyze the development of large shear strain and the phenomenon of recovery of stiffness from the liquefied to solid phase. Simulated results from the fluidal-elasto-plastic constitutive equation comparing with the elasto-plastic constitutive equation were in good agreement with the experimental results.

NUMERICAL SIMULATION OF A PILE-GROUND SYSTEM

A hybrid element of pile and AFD model

In simulating a pile, the usual method in the finite element analysis is to use a beam element that is known to be a non-volume element. If the area and volume of piles are not considered properly, we face to some difficulties to analyze the interaction between the piles and the ground that is heavily dependent on the geometry of the piles. For this reason, a hybrid element is implemented to simulate the pile behavior. In this paper, a pile (RC member material) is modified a hybrid element that consists of a beam element and column elements as shown in Figure 5, and the stress-strain relations of reinforcement and concrete are shown in Figure 6 [19, 20, 21]. The stiffness of the pile is shared by the beam element and several column elements in such a way that the bending stiffness of pile EI is equal to the sum of the bending stiffness of beam element $(EI)_{beam}$ and solid elements $(EI)_{solid}$. The sharing ratio between the stiffness of beam element and the solid element should be determined in such a way that the mechanical behavior of the cantilever beam simulated by a single beam element and the hybrid element will be the same. In this paper, the sharing ratio between the stiffness of the beam element and the solid elements is selected as 9 to 1 [19].

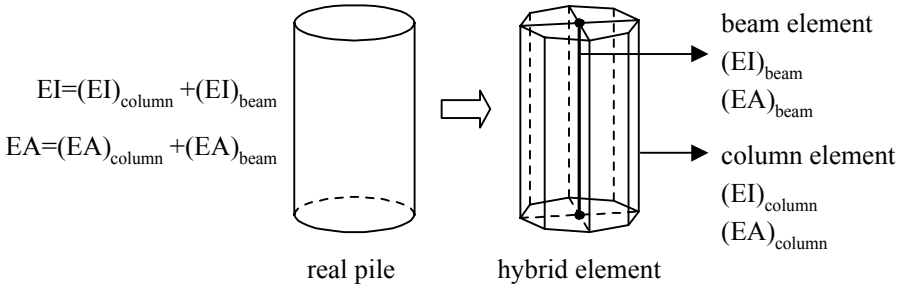

Figure 5. Hybrid element and its mechanism [19, 20]

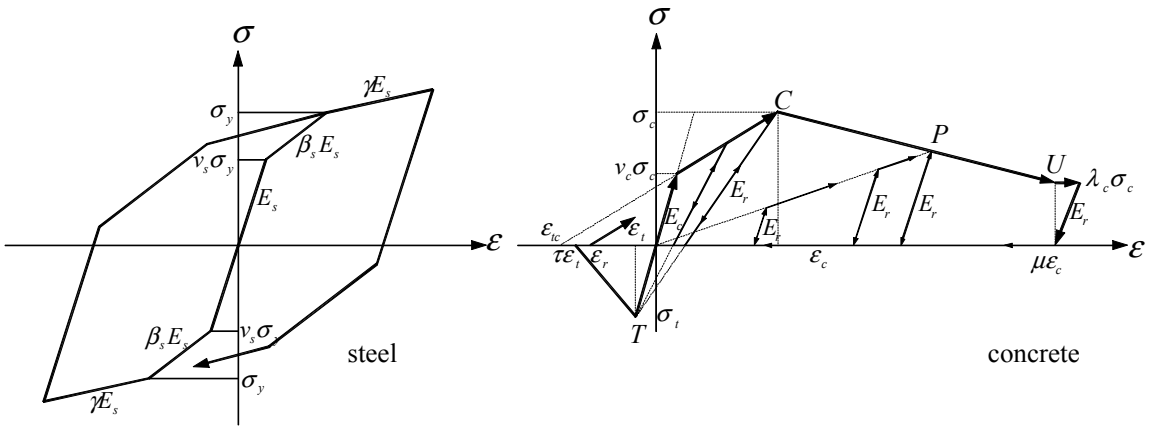

Figure 6. Nonlinear properties of reinforcement and concrete [21]

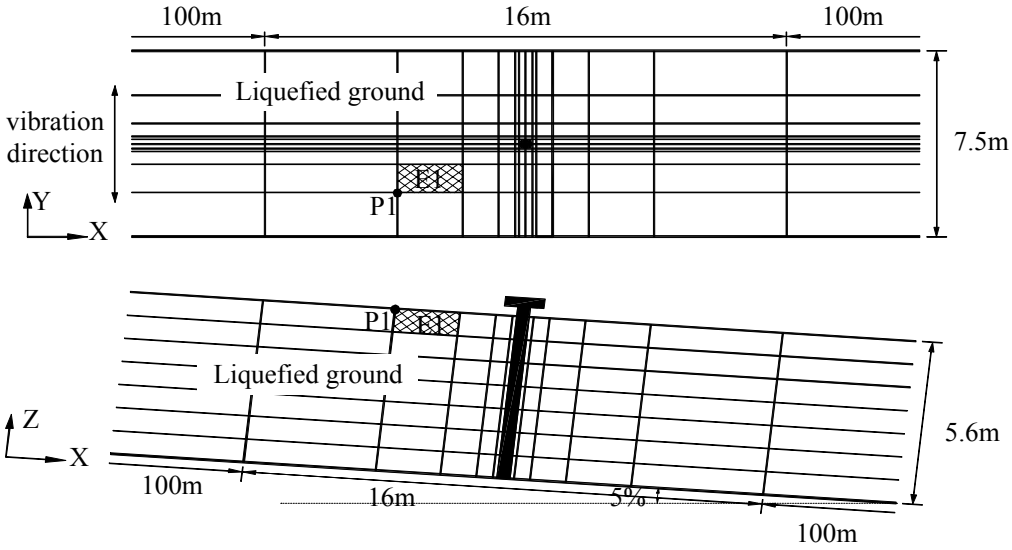

Figure 7. Finite element model

Analytical conditions

For understanding behavior of the proposed constitutive equation, a pile-ground system was simulated by means of the fluidal-elasto-plastic constitutive equation and elasto-plastic constitutive equation under the liquefied ground accompanying the ground flow. Two types of pile-ground system (CASE1; a pile-soil system, CASE2; a footing-pile-soil system) are considered to simulate the dynamic interaction of a pile-ground system under liquefied condition.

Figure 7 shows the finite element model. The liquefiable soil, composed of Silica NO.8 (D_{50}=0.24, uniformity coefficient Uc=1.92, e_{max}=1.251, e_{min}=0.706) with a relative density of about 40% and fully saturated, is assumed to be filled in a model ground with the dimensions of 5.6m high, 16m long by 7.5 width. And the pile (RC material), 0.5m in diameter and 6.4m in length, is placed in the middle/center of the model ground with 5% of inclination. We use an

8-node isoparametric solid elements and beam elements. As a boundary condition, all nodes at the bottom are fixed, and the nodes at the boundary of X-Z plane are fixed only in Y-direction. At the end boundary of X-direction which is the flow direction, equi-displacement elements of 100m were installed, which behave as a uniformly deposited ground at both boundary and decrease the influence of boundary condition. The pile is fixed at the bottom, and the pile rotation is fixed at the top in Case 2.

The input acceleration used is the earthquake motion recorded in Port island of Kobe City during the 1995 Hyogoken-Nanbu earthquake. Figure 8 shows the input acceleration motion. Acceleration is inputted in the Y-direction and the ground is liquefied completely about at 4 seconds after the earthquake motion input. The liquefied ground flows in the direction of X-direction under the influence of the model ground inclination.

The parameters of the piles described by AFD model are listed in Table I. These values are selected from the reference [21]. And Table II gives the constitutive parameters of liquefiable ground. Those parameters were determined from laboratory results and trial and error method for Silica NO.8 with a relative density of about 40%.

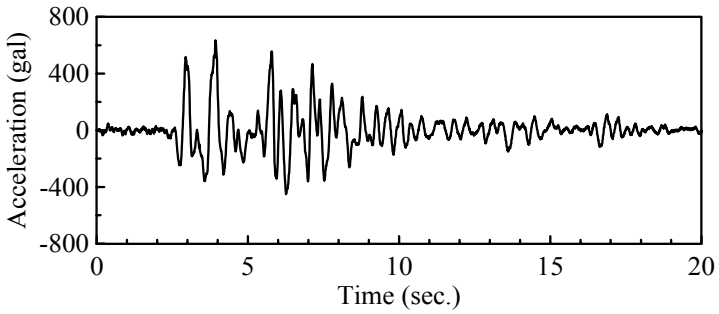

Figure 8. Input acceleration

TABLE I. Parameters (AFD model)

Compressive strength of concrete σ_c	2.4×10^4 kPa	Yielding strength of steel σ_y	3.0×10^5 kPa
Tensile strength of concrete σ_t	3.5×10^3 kPa	Young's modulus of steel E_s	2.1×10^8 kPa
Young's modulus of concrete E_c	3.0×10^7 kPa	Arrangement of the reinforcement	$\phi 22\times12$

TABLE II. Parameters (liquefied ground, Silica No.8)

Initial void ratio (e_0)	1.143	Coefficient for hardening equation (B_1)	32.0
Compression index (λ)	0.025	Coefficient for hardening equation (C_f)	0.0
Swelling index (κ)	0.0025	Coefficient of dilatancy (D_0)	3.50
Normalized initial shear modulus (G_0/σ'_{m0})	443.0	Coefficient of dilatancy (n)	1.10
Phase transformation stress ratio (M_m)	0.909	Reference strain for plastic (γ^P_{ref})	0.001
Failure stress ratio (M_f)	1.308	Reference strain for elastic (γ^E_{ref})	0.006
Coefficient for hardening equation (B_0)	3200.0	The second viscous coefficient (λ')	0.0

RESULTS OF ANALYSIS AND DISCUSSION

Figure 9 shows the simulated results of a CASE1, which are the time histories of the relative effective stress ratio (R.E.S.R.) and phase transformation-controlling function, α, at the point of element E1 (Figure 7) for both cases of using the elasto-plastic and fluidal-elasto-plastic constitutive equations. The simulated result of time history of the R.E.S.R. (Figure 9(a)) indicates that liquefaction occurred at about 4 seconds because the R.E.S.R. is almost reached to 1.0 at this time, and the R.E.S.R. is decreased gradually after 13 seconds. This means that the liquefied ground behaves like a fluid during 3-13 seconds. As the phase transformation-controlling function α in the fluidal-elasto-plastic constitutive equation is increased, the part of the stress contributed from the Newton viscous fluid is increased. In the time history of phase transformation-controlling function (Figure 9(b)), the phase transformation, which starts form solid state, turns to fluid state and returns to solid state, can be rigorously expressed.

Figure 10 shows the simulated results of CASE1, which is the time histories of the horizontal displacement and velocity of lateral flow at the point of node P1 (Figure 7) for cases using the elasto-plastic and fluidal-elasto-plastic constitutive equations. Comparing the simulated results of the displacement and velocity, the values obtained by using the fluidal-elasto-plastic constitutive equation is large than those of the elasto-plastic constitutive equation. This indicated that the fluidal characteristic of liquefied ground is expressed more effectively by the fluidal-elasto plastic constitutive equation than elasto-plastic constitutive equation.

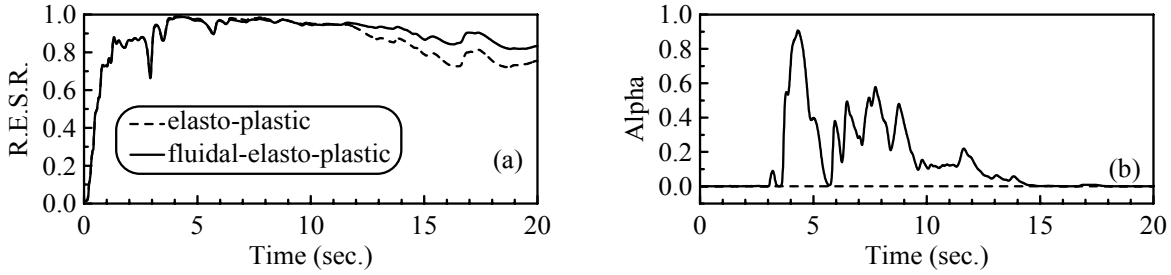

Figure 9. Simulated Results of the R.E.S.R and Alpha (CASE1)

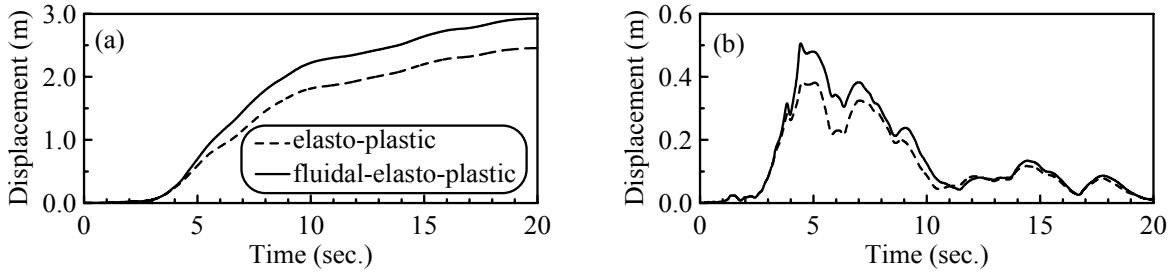

Figure 10. Simulated Results of the displacement and velocity (CASE1)

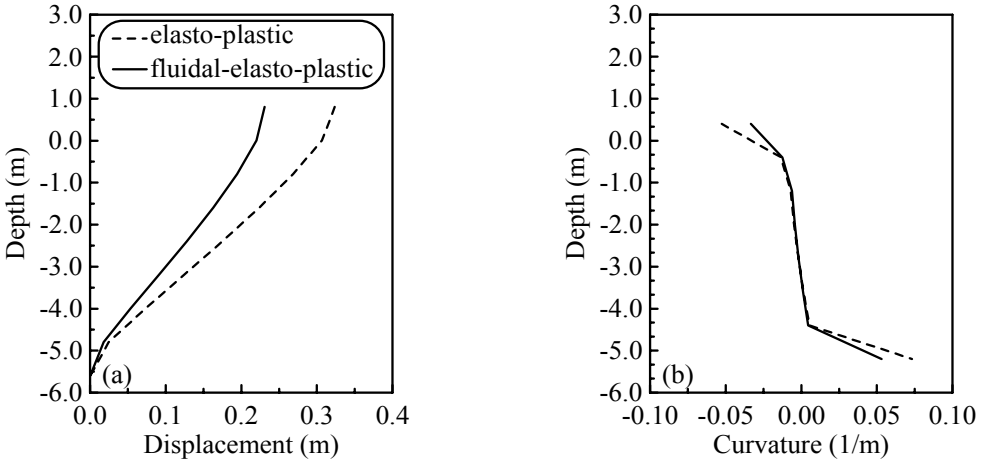

Figure 11. Distributions of horizontal displacement and curvature of the pile (CASE2)

The distribution of horizontal displacement and curvature of a pile, for CASE2, is shown in Figure 11. The horizontal displacement of pile shows that the pile is bent at both the bottom and top. The bending of pile obtained by using elasto-plastic constitutive equation is greater than that by the fluidal-elasto-plastic constitutive equation as shown in the distributions of curvature (Figure 11 (b)). The external force applied to the pile form the liquefied ground is evaluated from Figure 11(a). The residual displacement of the pile calculated by using the fluidal-elasto-plastic constitutive equation is smaller than that of the elasto-plastic constitutive equation. This means that the applied external force to the pile becomes smaller when the ground flows around the pile.

CONCLUSIONS

The process of liquefaction and ground flow phenomenon is divisible into three phases: the solid state before onset of liquefaction, the fluid state of the liquefied soil, and the recovered solid state produced by dissipation of excess pore water pressure. Changes in the three phases are continuous not separate phenomena. Liquefaction and the ground flow phenomenon should both be considered as combination of solid and fluid behaviors. We developed a simple constitutive equation with which to simulate the dynamic response of saturated loose sand by combining a cyclic elasto-plastic constitutive equation based on the solid mechanism and a Newtonian viscous fluid constitutive equation based on fluid mechanism through a phase transformation-controlling function.

The validity of our proposed constitutive equation was tested by a comparison of torsional shear test in the undrained condition and simulated result. The simulated result obtained with the proposed constitutive equation agreed well with experimental results. And phase transformation behavior that goes from the solid through the liquefied state then returns to the solid state can be rigorously expressed by the proposed constitutive equation. And 3-dimensional effective stress analysis was conducted to a pile-ground system. Compared with the results obtained by the elasto-plastic constitutive equation, the maximum displacement and velocity of ground become larger, the displacement and curvature of the pile are smaller when the ground flow phenomenon is taking into account. The results calculated by using the fluidal elasto-plastic constitutive

equation explain better the pile-ground system behavior during liquefaction and following ground flow process.

REFERENCES

[1] Inagaki H, Iai S, Sugano T, Yamazaki H, and Inatomi T. 1996. "Performance of caisson type quay walls at Kobe port," *Soils and Foundations, Special Issue on Geotechnical Aspects of the January 17 1995 Hyogoken-Nambu Earthquake*, 1:119-136.

[2] Kamon M, Wako T, Isemura K, Sawa K, Mimura M, Tateyama K, and Kobayashi S. 1996. "Geotechnical disasters on the waterfront," *Soils and Foundations, Special Issue on Geotechnical Aspects of the January 17 1995 Hyogoken-Nambu Earthquake*, 1:137-147.

[3] Ishihara K, Yasuda S, and Nagase H. 1996. "Soil characteristics and ground damage," *Soils and Foundations, Special Issue on Geotechnical Aspects of the January 17 1995 Hyogoken-Nambu Earthquake*, 1:109-118.

[4] Hamada M, Yasuda S, Isoyama R, and Emoto K. 1986. "Observation of permanent ground displacements induced by soil liquefaction," *Proceedings of the society of civil engineers*, 376(III-6):211-220 (in Japanese).

[5] Ishihara K. 1993. "Liquefaction and flow failure during earthquakes," *Geotechnique*, 43(3):351-415.

[6] Yoshida N. 1998. "The mechanism of a ground flow accompanying liquefaction," *Symposium about the ground flow and permanent displacement of the foundation and the ground structure in case of an earthquake*, *The Japanese Geotechnical Society*, 109:53-70.

[7] Yasuda S, Yoshida N, Masuda T, Nagase H, Mine K, and Kiku H. 1995. "Stress-strain relationships of liquefied sands," *Proceedings of IS-TOKYO'95 / The first international conference on Earthquake Geotechnical Engineering*, 2:811-816.

[8] Oka F, Yashima A, Tateishi A., Taguchi Y, and Yamashita S. 1999. "A cyclic elasto-plastic constitutive model for sand considering a plastic-strain dependence of the shear modulus," *Geotechnique*, 49(5):661-680.

[9] Hashiguchi K, and Chen Z -P. 1998. "Elastoplastic constitutive equation of soils with the subloading surface and the rotational hardening," *International journal for numerical and analytical methods in geomechanics*, 22(3):197-227.

[10] Zienkiewicz O C, and Shiomi T. 1984. "Dynamic behavior of saturated porous media; The generalized Biot formulation and its numerical solution," *International journal for numerical and analytical methods in geomechanics*, 8(1):71-96.

[11] Yasuda S, Yoshida N, Adachi K, Kiku H, Gose S, and Masuda T. 1999. "A simplified practical method for evaluating liquefaction-induced flow," *Journal of geotechnical engineering, Japan society of civil engineers*, 638(III 49):71-89 (in Japanese).

[12] Shamoto Y, Zhang J M, and Tokimatus K. 1998. "New charts for predicting large residual post-liquefaction ground deformation," *Soil Dynamics and Earthquake Engineering*, 17:427-438.

[13] Aydan Ö. 1994. "The dynamic shear response of an infinitely long visco-elastic layer under gravitational loading," *Soil Dynamics and Earthquake Engineering*, 13:181-186.

[14] Tamate S, and Towhata I. 1999. "Numerical simulation of ground flow caused by seismic liquefaction," *Soil Dynamics and Earthquake Engineering*, 18:473-485.

[15] Uzuoka R, Yashima A, Kawakami T, and Konrad J -M. 1998. "Fluid dynamics based prediction of liquefaction induced lateral spreading," *Computers and Geotechnics*, 22(3/4):243-282.

[16] Biot M A. 1962. "Mechanics of deformation and acoustic propagation in porous media," *Journal of Applied Physics*, 33(4):1482-1498.

[17] Oka F, Yashima A, Shibada T, Kato M, and Uzuoka R. 1994. "FEM-FDM coupled liquefaction analysis of a porous soil using an elasto-plastic model," *Applied Scientific Research*, 52:209-245.

[18] Akai K, and Tamura T. 1978. "Numerical analysis of multi-dimensional consolidation accompanied with elasto-plastic constitutive equation," *Proceedings of the society of civil engineers*, 269(III):95-104.

[19] Zhang F, Kimura M, Nakai T, and Hoshikawa T. 2000. "Mechanical behavior of pile foundations subjected to cyclic lateral loading up to the ultimate state," *Soils and Foundations*, 40(5):1-17.

[20] Kimura M, and Zhang F. 2000. "Seismic evaluations of pile foundations with three different methods based on three-dimensional elasto-plastic finite element alalysis," *Soils and Foundations*, 40(5):113-132.

[21] Zhang F, and Kimura M. 2002. "Numerical prediction of the dynamic behaviors of an RC group-pile foundation," *Soils and Foundations*, 42(3):77-92.

Evaluation of Passive Site Remediation against Earthquake induced Liquefaction and its Hazards Effect on Deep Foundations

Ahmet Pamuk, Tarek Abdoun and Patricia M. Gallagher

ABSTRACT

During previous earthquakes serious functional disruption of critical facilities occurred due to the damage of the deep foundations subjected to liquefaction-induced permanent ground lateral displacement. This paper presents a series of centrifuge tests studying the performance of pile foundations prone to lateral spreading and the possible use of colloidal silica as an innovative stabilizing material against liquefaction-induced hazards. Colloidal silica can be used as a non-disruptive mitigation of liquefaction for existing sites. The presented tests simulate a three-layer soil profile of 10 m. An instrumented pile group model was implemented in centrifuge models with and without the colloidal silica stabilizer. A sloping large laminar box was used in the centrifuge tests to evaluate the effectiveness of the proposed passive site remediation method. The response of the free-field liquefiable soil and the group pile subjected to a simulated base shaking were compared for both cases.

The results showed that colloidal silica grout provided significant liquefaction resistance and greatly reduces the free field lateral deformation. The colloidal silica stabilizer reduced the imposed moments on the piles. The measured maximum permanent ground deformation in the colloidal silica-grouted soil model was about 5% of that measured in the untreated soil model. Thus, colloidal silica can be an effective alternative grouting material to the traditional ground improvement methods for existing foundation systems placed in liquefiable soils.

Ahmet Pamuk, Research Assistant, Department of Civil and Environmental Engineering, Rensselaer Polytechnic Institute, Troy, NY 12180, USA
Tarek Abdoun, Research Assistant Professor, Department of Civil and Environmental Engineering, Rensselaer Polytechnic Institute, Troy, NY 12180, USA
Patricia M. Gallagher, Assistant Professor, Department of Civil and Architectural Engineering, Drexel University, Philadelphia, PA, USA

INTRODUCTION

In earthquakes, such as the 1964 Niigata and 1995 Kobe, many buildings and transportation facilities supported on deep foundations were damaged due to the loss of bearing capacity of soils and/or insufficient bending stiffness of piled foundations. Lateral flow movement of liquefied soil in gently sloping areas imposed large bending moments and caused serious damage to exiting deep foundations and their superstructures (e.g., [1, 2, 3]). Lessons learned from those earthquakes increased the understanding of soil liquefaction and allowed engineers to better visualize the causes of structures damages associated with liquefaction induced ground failures. Such experiences have initiated not only a review of current practice of soil remediation, but also a search for better alternatives and more economical remedial measurers and materials. As these new methods/materials are introduced for mitigating soil, it is very important to carefully evaluate their performance during earthquake shaking, and their long-term durability.

There have been many liquefaction studies on non-treated soils, but only a few studying the effectiveness of grouted soils using chemical stabilizers. Dynamic laboratory testing studies done on sands treated with chemical grouts (e.g., [4, 5, 6, 7]), including silicate-grouted sands (e.g., [4, 8, 9]), have proven that chemical stabilization has reduced shear deformation in loose soils. Such tests are useful in understanding the fundamental behavior of treated soil under repeated loads. However, it is important to simulate in-situ stress conditions during an actual earthquake shaking. Accordingly, physical modeling using centrifuge and large shake table tests offer a valuable tool to closely evaluate the performance of the improved soil subjected to simulated earthquake motions. A few dynamic models tests were conducted to investigate the efficiency of chemical grouting as a remedial measure against liquefaction of leveled ground sand [10]. These tests simulated a pile foundation embedded in a level ground sand layer with a super structure on top [11]. The test results showed that the effectiveness of countermeasure increased with the expansion of the remediated area beneath the structures. The dynamic response of the pile foundations were also affected by the magnitude of the input acceleration as well as by the variation in the soil stiffness (e.g., [3, 11]).

One of the well-accepted ground remediation methods for existing structures is cement grouting. This requires the use of drilling or augering machinery, which may cause great disturbance to existing structures. Passive site remediation is a new concept proposed for non-disruptive mitigation of sites susceptible to liquefaction. It involves slow injection of stabilizing materials at the upgradient edge of a site, and delivery of the stabilizer to the target location using natural or augmented groundwater flow. Passive site remediation techniques could have broad application for developed sites where more traditional methods of ground improvement can not be used easily or at all or would disrupt existing infrastructure and facilities. Additionally, access to the entire site would not be required during treatment, so normal site activities would experience only minimal disruption.

Laboratory tests on saturated loose sand samples treated with colloidal silica grout had significantly higher deformation resistance to cyclic loading than untreated sands [4]. Feasibility issues that include the ability of a mass of treated soil to resist deformation and liquefaction during earthquake loading, as well as the ability to deliver the grout uniformly to the formation for centrifuge testing, were studied elsewhere [12].

In this study, colloidal silica treatment is tested as grouting stabilizing grout to reduce the risk of liquefaction-induced damages on a group piled foundation using RPI's in-flight earthquake simulator. The presented tests simulate a three-layer soil profile of 10 m. An instrumented pile group model was implemented in centrifuge models with and without the colloidal silica stabilizer. This was done using a sloping large laminar box to evaluate the effectiveness of the proposed site

remediation method prone to lateral spreading. The response of pile group foundations and free-field behavior of the liquefiable soil under a simulated base shaking were evaluated and compared.

EXPERIMENTAL PROCEDURES

Models Preparation, Testing Materials and Program

The models were constructed in a large laminar rectangular box, with internal dimensions of 71 cm in length, 35.5 cm in width and 22 cm in height, (Fig. 1a). The laminar box was employed to simulate flexible shear beam boundary conditions for the soil and allow soil permanent lateral deformation during shaking (www.ce.rpi.edu/centrifuge). The model dimensions shown in Figure (1a) are in centimeters and the prototype dimensions in parentheses are in meters. A large in-flight computer-controlled centrifuge shaker with a 13.6 metric ton maximum actuation force capacity was used to produce the base dynamic excitation [13]. Nevada No. 120 fine sand was used as the foundation soil. Extensive data regarding the cyclic characteristics of the Nevada sand is reported by [14].

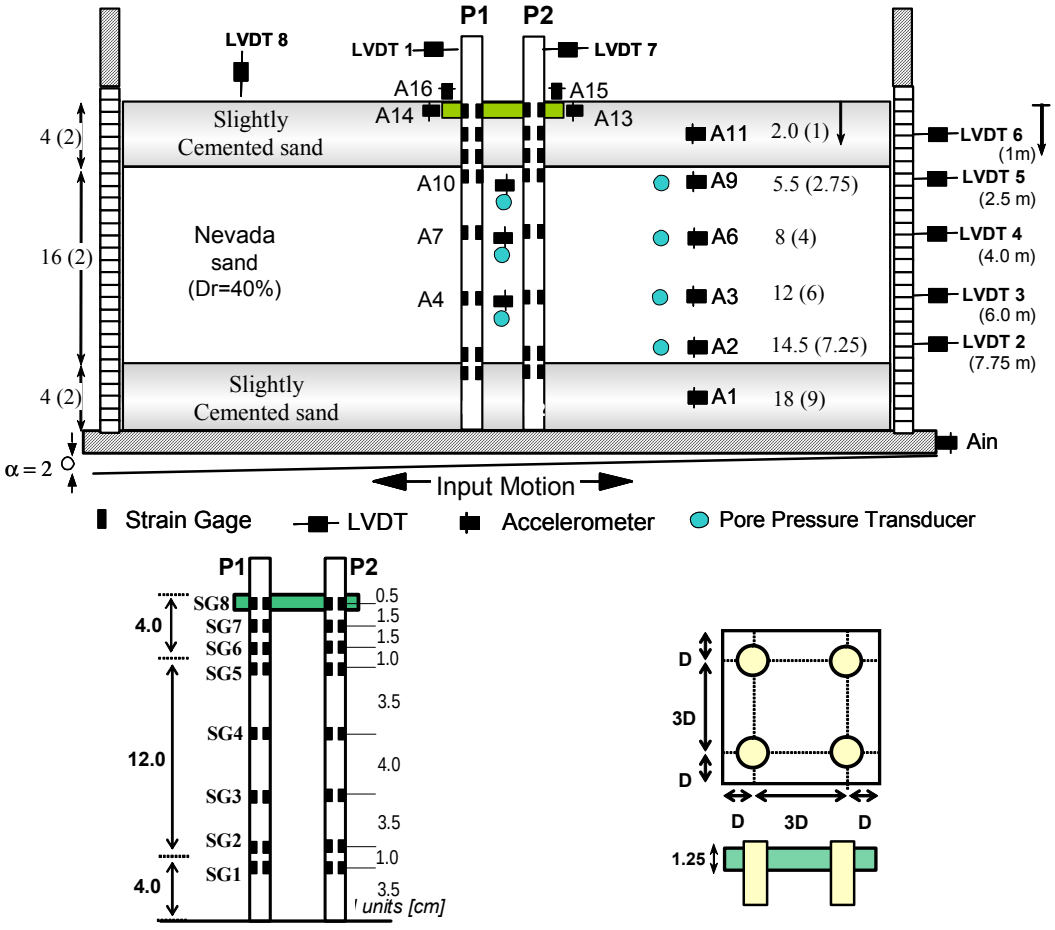

The prototype profile includes a 2 m bottom layer of slightly cemented sand, topped by a 6.0 m layer of uniformly rained Nevada sand at a relative density of about 40%, topped by a 2.0 m of the same slightly cemented sand layer. The prototype soil profile and pile group being simulated in models, as shown in Figure (1a), involves an end-bearing pile group, 2×2, with a pile cap embedded in the top slightly cemented sand layer. Each of the piles in the pile group had a diameter of 0.50 m, length of 10 m and EI = 8000 kN-m^2 (in prototype units), with instrumented strain gages to measure bending moments induced during shaking. A schematic of the detailed instrumentation with strain gages is shown in Figure1b. An aluminum pile cap was rigidly clamped to the top of the model piles with 3D spacing between piles (Fig. 1c).

The centrifuge tests, Model 1 and Model 2, presented in this paper had the same configuration (Fig. 1a), except for the fact that de-aired water was used to saturate the sand layers while a mixture of colloidal silica and water (6 weight percent of colloidal silica grout) was the pore fluid for Model 2. After saturation, the models were spun at 50 g centrifugal acceleration and finally were subjected to 30 cycles of sinusoidal base acceleration having about 0.25 g prototype peak amplitude, and a frequency of 2 Hz, in prototype units.

The colloidal silica used as stabilizing material for Model 2 is an aqueous dispersion of silica particles with an average diameter of 7 nanometers. It is supplied as a 30-weight-percent silica solution with a pH of 10.0 and a viscosity of 5.5 centipoise (cP). After dilution with water, the colloidal silica solution has a density and viscosity similar to water (viscosity ~ 1.5 to 2 cP, water = 1 cP). Colloidal silica also has long, controllable gel times (up to 200 days). The gel time can be adjusted by lowering the pH and by altering the ionic strength of the dilute colloidal silica solution. The gel time, density and viscosity characteristics make colloidal silica attractive as a stabilizer for passive site remediation. Additionally, colloidal silica is nontoxic, biologically and chemically inert, and has excellent durability characteristics [12].

During the induction period, which is the time between mixing and gelling, colloidal silica maintains a low viscosity until just prior to gelling. The ability of the colloidal silica to travel through the formation is a function of its viscosity. Once the viscosity increases ten times above the initial viscosity, travel through the formation becomes extremely slow. Therefore, the travel time, or the time between mixing and an increase in viscosity of 10 times the initial viscosity, is the critical parameter in determining if the grout will be able to travel through the formation. The gel time is the amount of time between mixing and the formation of a firm gel. The curing time is the amount of time between the formation of a firm gel and testing the specimen. The curing time is important because colloidal silica grout continues to gain strength after it forms a firm gel. Sands treated with colloidal silica grouts with different gel times may be compared with respect to strength and deformation properties, provided that the length of the curing time is similar between samples. For example, two samples treated with colloidal silica grout with gel times of 10 hours and 40 hours can be compared, provided the testing is done after curing periods of 40 and 160 hours, respectively. For Model 2, the Nevada sand (Dr=40%) was saturated with the colloidal silica stabilizer (i.e., 6 weight percent of colloidal silica grout). After the completion of the saturation the grouted formation was allowed to cure for two weeks before being tested in the centrifuge.

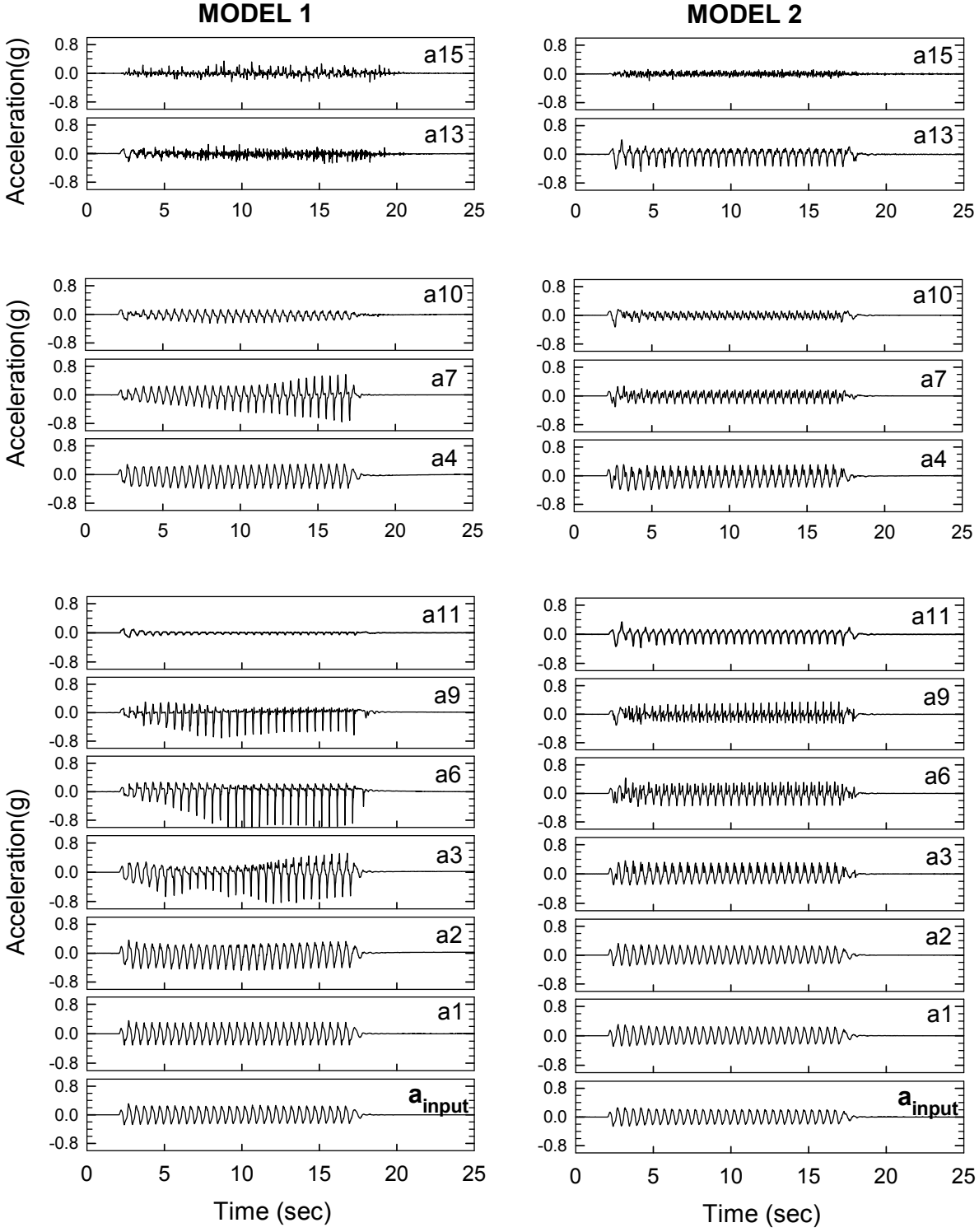
MODEL 1
MODEL 2
Acceleration(g)
a15
a13
a10
a7
a4
a11
a9
a6
a3
a2
a1
a_input
0.8
0.0
-0.8
0
5
10
15
20
25
Time (sec)

TESTING RESULTS

Accelerations

The response of the three-layered soil profile during in-flight shaking was monitored by accelerometers located in the free-field, between individual piles, and on the pile cap. Figure 2 shows acceleration time histories of the soil profile at these locations. In Model 1 (un-treated soil), the acceleration records (A2, 3, 6 and 9) in the free-field within the liquefiable layer revealed asymmetric response (Fig. 2c), indicating that the soil did liquefy and was deforming laterally in the downslope direction.

However, this was not the case in Model 2 (treated with colloidal silica); that is, the response of the treated soil was similar to the input shaking throughout the grouted layer. The accelerations at the bottom cemented layers for both models were similar to the input acceleration, indicating that there was no sliding between the bottom cemented layer and the base of the laminar box. The recorded acceleration of the top cemented layer (A11, Model 1) shows a drop in amplitude after several cycles due to the fact that the top cemented layer gets isolated as the liquefiable layer reached full liquefaction. However, the acceleration at the same location, in Model 2, was very similar to the input shaking, or lateral deformation in the downslope direction.

The recorded accelerations in the middle of the pile group (e.g., A7 and A10, Fig. 2b) is smaller than those in the free-field (A6 and A9), indicating that the presence of the piles limited the lateral deformation of the soil within the pile group system (Fig. 2b). In both models, the recorded horizontal acceleration (Fig. 2a) measured at the pile cap (A13) was similar to that recorded in the top cemented layer (A11, in the free-field). The recorded horizontal acceleration measured at the cap was higher in Model 2, while the recorded vertical accelerations (A15) were less in Model 2.

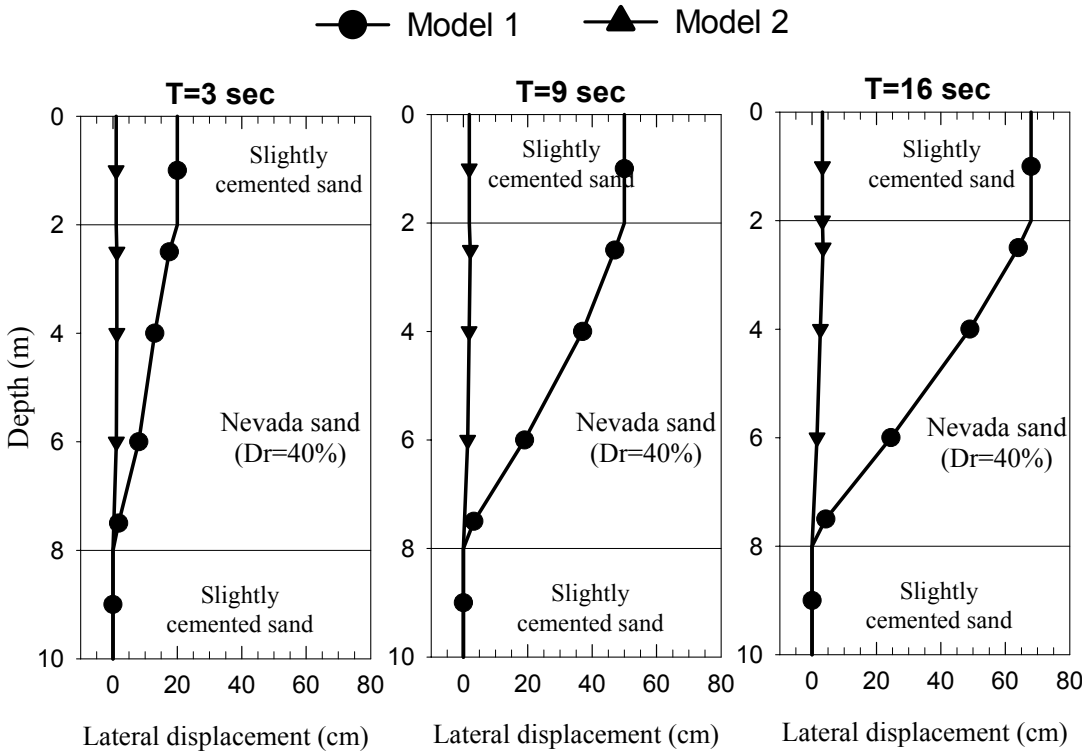

Lateral Deformation

Figure 3 compares recorded free-field lateral displacements at different times during shaking for Models 1 and 2, in prototype units. The lateral displacements increased monotonically as shaking continued. The maximum recorded displacement at the ground surface was about 70 cm in Model 1 (untreated soil) and was only 3.2 cm in Model 2 (treated soil). Figure 4 compares the measured lateral displacement of the ground surface and the pile cap for Models 1 and 2. In both models, the displacement of the ground surface and the pile cap continued increasing during the shaking. The measured lateral displacements of the ground surface and pile cap in Model 1 were approximately 20 times of those measured in Model 2.

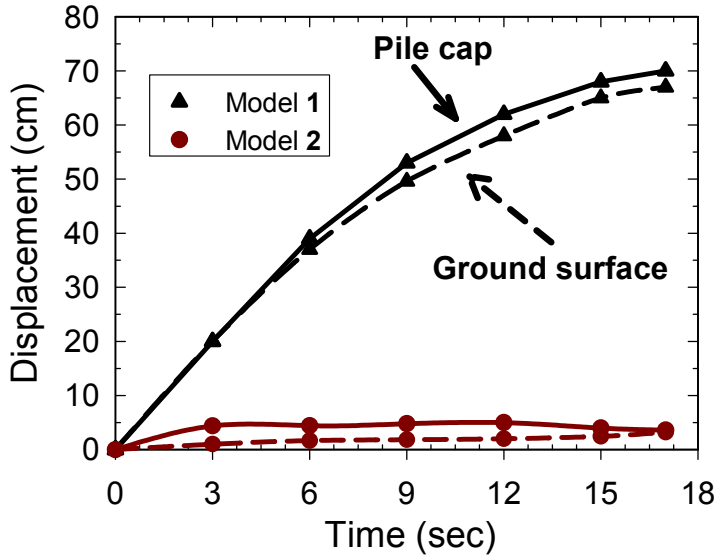

Bending Moments

Figure 5 shows the bending moment time histories in prototype units measured along the piles (P1 and P2, see Figures 1a and 1b). P1 and P2 denote individual piles located in the upslope and downslope direction, respectively. Similar to the measured lateral deformations, the measured moments continued increasing during shaking and stopped at the end of shaking. In Model 1, the maximum bending moment occurred at the upper and lower boundaries of the liquefiable sand layer. As the shaking progressed, the top maximum bending moments shifted upward to the midsection of the top cemented layer indicating that the soil around the pile started to fail, causing a redistribution of the soil lateral pressure along the top of the pile group. The maximum bending moments measured along P1 and P2 in Model 1 (untreated soil) were 225 and 290 kN-m, respectively (Fig. 5). The maximum measured moments along P1 and P2 in Model 2 (treated soil) were significantly lower (approximately 20 times) than those measured in Model 1.

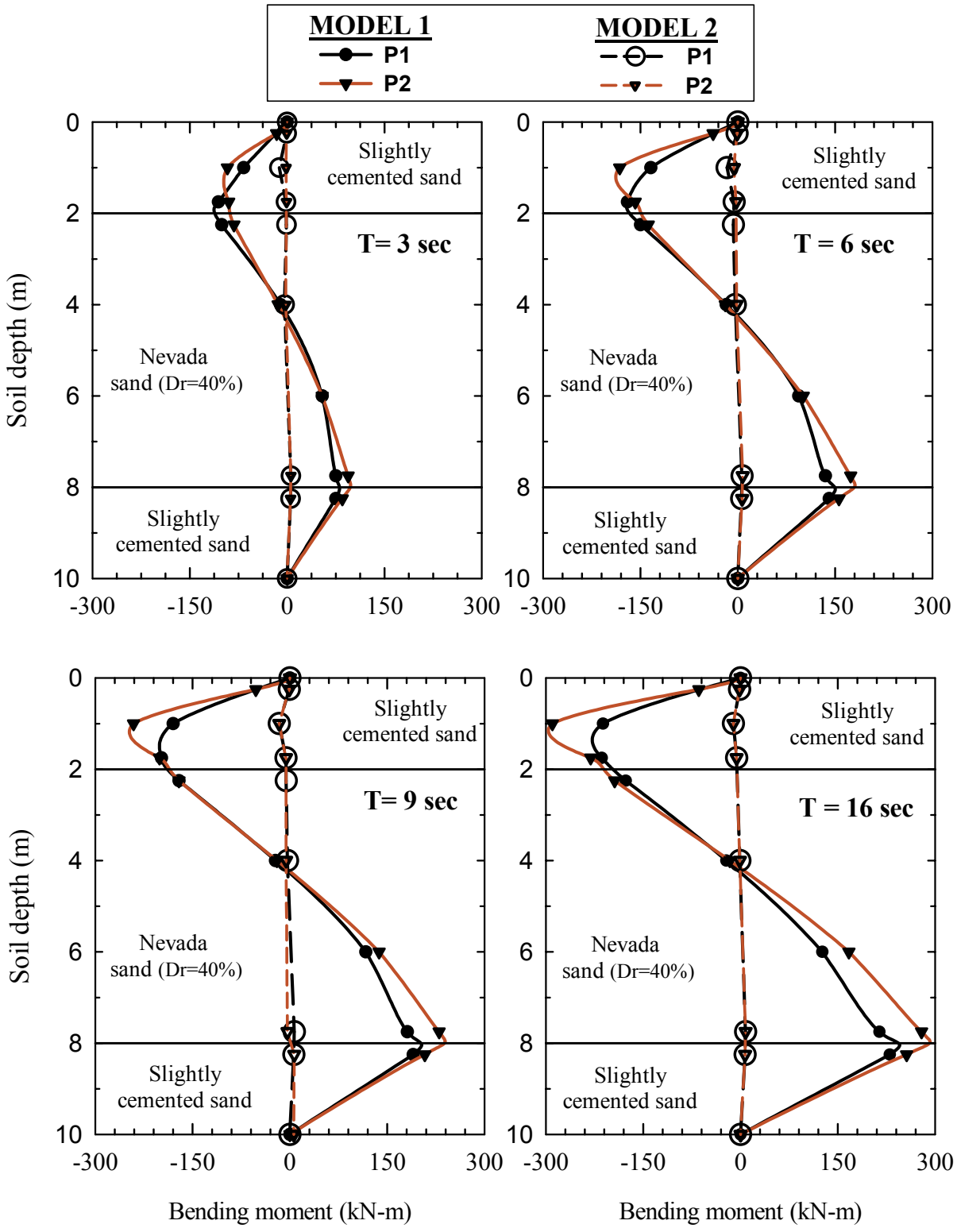

Figure 5. Bending moments in P1 (upslope pile), and P2 (downslope pile) for Model 1 and 2

Soil Conditions around the Pile Cap

Figure 6 shows the condition of the top cemented soil around the pile cap at the end of the shaking for Models 1 and 2. In Model 1 the soil condition around the pile cap indicates that the soil surrounding the pile cap did fail in passive mode (Fig. 6a). On the other hand, in Model 2, there was no indication of any failure around the pile cap (Fig. 6b).

Direction of free-field displacement

CONCLUSIONS

This paper presents dynamic centrifuge model tests conducted on model a group pile to investigate the performance of colloidal silica as a new grouting stabilizer for passive site remediation to mitigate against soil liquefaction and its hazards effects on deep foundations. After comparing the response of the free field and the group pile during shaking of Models 1 and 2, it was concluded that:

1- The liquefiable soil grouted with colloidal silica grout did not liquefy.
2- The lateral deformation of the ground surface for the grouted sand was approximately 5% of the un-grouted soil.
3- The measured bending moments along the model pile group were much smaller for the grouted sand (Model 2). The maximum bending moments appears to be proportional with the lateral ground displacement.
4- Colloidal silica can be a promising chemical stabilizer for site remediation to militate against soil liquefaction and its hazards effects on deep foundations.

ACKNOWLEDGMENTS

This research was supported by the National Science Foundation (NSF), Multidisciplinary Center for Earthquake Engineering Research (MCEER). This support is very gratefully acknowledged.

REFERENCES

[1] Hamada, M. 1992. Large Ground Deformations and their Effects on Lifelines: *1964 Niigata Earthquake*, Ch. 3 of Hamada and O'Rourke, 3-1 to 3-123.

[2] Hamada, M. 2000. Performances of foundations against liquefaction-induced permanent ground displacement, *Proc. 12th World Conf. On Earthquake Engineering*, Paper 1754.

[3] Abdoun, T. and R. Dobry 2002. Evaluation of pile foundation response to lateral spreading, *Soil Dynamics and Earthquake Engineering Journal*, Vol. 22, Issue 9-12, pp. 1069-1076.

[4] Gallagher, P.M. 2000. Passive site remediation for mitigation of liquefaction risk, *PhD Dissertation*, Virginia Polytechnic Institute and State University, Blacksburg, VA.

[5] Maher, M.H., Ro, K.S. and Welsh, J.P. 1994. High strain modulus of damping of chemically grouted sand, *Geotechnical Testing Journal*, ASTM, V.17. (2), 159-170.

[6] Rosenfarb, J.L. abd Hackman, R.E. 1981. The cyclic loading behavior of grouted sand, *Int. Conf. on Recent Advances in Geotechnical Engineering and Soil Dynamics*, Missouri-Rolla, 81-86.

[7] Saxena, S.K., Reddy, K.R. and Avramida, A.S. 1981. Liquefaction resistance of artificially cemented sand, *J. of Geotechnical Engineering*, ASCE, V.114, No.12, 1395-1413.

[8] Maher, M.H., Ro, K.S. and Welsh, J.P. 1994. High strain modulus of damping of chemically grouted sand, *J. of Soil Dynamics and Earthquake Engineering*, (13), 131-138.

[9] Vipulanandan, C and Ata, A. 2000. Cyclic and dappling properties of silicate-grouted sand, *J. of Geotechnical and Geoenvironmental Engineering*, ASCE, V.126, No.7, 650-656.

[10] Imamura, S., Hirano, T., Yoshino, O., Hagiwara, T., Takemura, J and Fuji, N. 2002. Chemical grouting as a countermeasure against liquefaction of sand with existing oil tanks, *Physical Modelling in Geotechnics, ICPMG'02,* 575-580.

[11] Hagiwara, T, Arai, T. and Asega, H. 2002. Large shaking table tests on countermeasures against soil liquefaction for an oil tank with pile foundation, *Physical Modelling in Geotechnics, ICPMG'02*, 563-568.

[12] Gallagher, M.P., Pamuk, A, Koch, A.J. and Abdoun, T. 2002. Centrifuge modeling of passive site remediation *Proc. of the 7th U.S. National Conference on Earthquake Engineering (7NCEE): Urban Earthquake Risk,* Boston, MA, July 2002.

[13] Elgamal, A.W., Dobry, R., Laak, V.P., and Font, J.N. 1991. Design, construction and operation of 100g-ton centrifuge at RPI, *Proc. of Centrifuge 91*, 27-34.

[14] Arulmoli, K., Muraleetharan, K.K., Hossain, M.M., and Fruth, L.S. 1992: Verification of liquefaction analysis by centrifuge studies laboratory testing program soil data. Technical Report, The Earth Technology Corporation, Irvine, California.

AN EXPERIMENTAL STUDY ON EXTERNAL FORCES FROM FLOWING LIQUEFIED SOIL ON FOUNDATIONS PILES

Ji Ho JANG, Atsushi HIRAO, Makoto KURITA, and Masanori HAMADA

ABSTRACT

This paper describes the characteristics of the external loads from flowing liquefied ground on foundation piles based on the results from model tests under the centrifuge conditions. It was obtained from the experiments that the viscous load depending on the flow velocity of liquefied soil was dominant on the piles when the model ground was perfectly liquefied. On the contrary, the external load resulting from ground displacements was governing the pile deformation when the model ground was not liquefied or partially liquefied.

Ji Ho JANG, PhD Student, School of Science and Engineering, Waseda University, 3-4-1, Ohkubo, Shinjuku-ku, Tokyo, Japan, 169-8555
Atsushi HIRAO and Makoto KURITA, Graduate Student, School of Science and Engineering, Waseda University, 3-4-1 Ohkubo, Shinju-ku, Tokyo, Japan 169-8555
Masanori Hamada, Professor, School of Science and Engineering, Waseda University, 3-4-1, Ohkubo, Shinjuku-ku, Tokyo, Japan, 169-8555

INTRODUCTION

Liquefaction-induced ground displacements have caused severe damage to pile foundations, underground structures and pipelines during past earthquakes. In order to establish a rational earthquake-resistant design procedure for pile foundations against liquefaction-induced ground displacement, it is essential to clarify the characteristic of external loads on the piles from the lateral flow in liquefied ground.

Generally, it can be considered that two types of load act on the piles in liquefied ground. One of them is derived from ground displacements and the other from ground velocities. In this study, a series of centrifugal tests have been conducted to investigate the characteristics of the forces on the piles in liquefied soil. Particular concern on the characteristics of loads derived from the ground velocity has been paid. Based on the experimental results, the loads resulting from ground displacement and ground velocity were estimated by the Voigt elasto-viscous model. Besides, the effects of the allocation of grouped piles and the existence of the non-liquefied soil layer overlying the liquefied soil were examined as well.

MODEL EXPERIMENTS UNDER A CENTRIFUGAL CONDITION

Setup and Procedures for the Experiments

The experiment was conducted under a centrifugal acceleration of 30G, by using rigid soil box with a length of 100cm, a height of 37.5cm and a width of 100cm. Figure-1 shows the model of ground, foundation piles, and locations of accelerometers and piezometers. Three cases of the tests shown in Table 1 were carried out. In cases 1 and 2, the whole part of the model grounds with a thickness of 20cm were liquefied, while in case3, non-liquefiable soil with a thickness of 7cm exists over the liquefied. The gradient of the ground surface is 10% and ground water grade is 20cm from the bottom of the center of soil box. The model ground was vibrated by a sinusoidal wave with frequency of 60Hz in the horizontal direction perpendicular to the direction of ground flow.

The liquefiable soil layer was constructed by raining of silica sand No.8 (gravity:2.65, the maximum void ratio:1.40, the minimum void ratio:0.71, average grain size:0.062 relative density:40%) from the hopper, and the non-liquefiable soil layer was formed by silica sand No.6 (gravity:2.65, the maximum void ratio:1.13, the minimum ratio:0.70 and average grain size:0.3 relative density:80%.)

Two sets of accelerometers and piezometers are installed in the model ground with equal spacing as shown in Figure-1 (a) and (b), and a piezometer was placed at the bottom of the model to measure the pore pressure at bottom of the model. Two laser displacement meters were also installed on the surface of the model to trace the time dependant variation of surface movement of the model. Furthermore, the movements of the targets fixed at the ground surface were recorded using a high-speed camcorder.

Stainless steel pipes with a diameter of 20mm and a wall thickness of 0.5mm were used to act as the piles in the model. The bending moments developed along the depth of each pile during vibration were calculated from the measured strains, which were acquired from the strain gauges attached on the inner wall of the pipes. With intention to examine the influences of the allocation of piles in a pile group, 3 piles denoted by C, S, and W respectively were installed as shown in Figure 1 (a) with equal spacing of 2.5D (D :diameter).

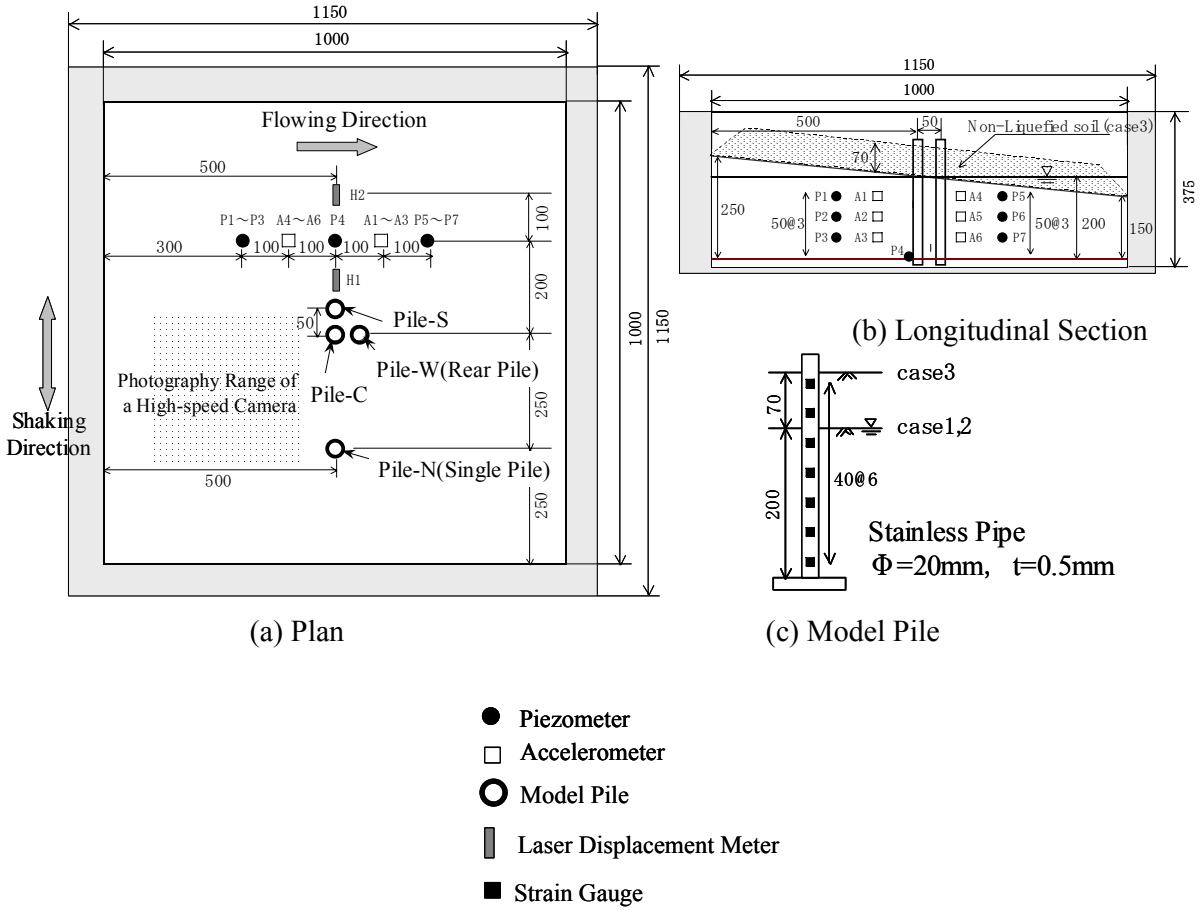

Figure 1 Model Ground, Model Pile and Instrumentation

Table 1 Test Cases and Parameters

	Thickness of Liquefied soil Layer	Thickness of Non-Liquefied soil Layer	Relative Density*	Input Motion	Maximum Amplitude
case1	20cm	—	40%	60Hz10wave	90 m/s^2
case2	20cm	—	40%	60Hz20wave	120 m/s^2
case3	20cm	7cm	40%(80%)	60Hz30wave	150 m/s^2

* () is the relative density of a non-liquefied soil layer.

Pile Deformations, Ground Displacements and Velocities

Figure 2 (a) shows that the time dependant variation of the bending moments at the base of the single pile, the ground displacements and the ground velocities at the surface of model, and the ratio of effective stress and excess pore water pressure, called as excess pore water pressure ratio hereafter, at the level equal to the location of the piezometer P4 which is installed at the deepest level from the surface of model. The ground displacements herein were directly measured from the laser displacement, H2 shown in Figure-1 (a). This ground displacement can be regarded as a free field ground displacement, since the measuring location of it was enough far away from the model pile that may be able to restrict the movement of its surrounding soils.

As plotted in Figure 2 (a) and (b), the time dependant variation of excess pore water pressure ratios in case 1 and case 2 shows that the model ground nearly became liquefied as the elapsed time passed 0.1s from the start of shaking. The bending moment developed at the base of the piles reached to the maximum values at between 0.1～0.2s and then decreased gradually. The ground displacement in case 1 increased to its peak value until 0.2s and stayed constant afterwards. The ground velocity, which can be obtained from the differentiation of the ground displacement with respect to time, in case 2 decreased after reaching a peak value at around 0.1s, but increased again after 0.2s. Both the experiments of cases 1 and 2 were carried out under the mostly same condition besides the input motions. It can be inferred that the model ground recovered its stiffness after the time of the maximum moment in the pile, but was liquefied again because of the lager input motion in case 2.

The time when the bending moment at the base of the single pile (Pile-N) reached the maximum value was at about 0.15s in case 1 and about 0.1s in case 2. At this time, ground surface displacement is still increasing. On the other hand, by the comparison of the variation of bending moment with ground surface velocity, it was found that the time to reach maximum value and the time to begin decreasing were in agreement in general. This result suggests that ground velocity is governing the deformation of the pile

Figure 2 (c) shows the result of case 3, where a layer of non-liquefiable soil is overlaying the liquefied soil. The bending moment in the pile has a similar time history to that of the ground surface displacement, which is increasing gradually during the whole time of excitation. On the contrary, the ground surface velocity recorded its peak value around 0.5s, and gradually decreased afterwards. This result suggests that the ground displacement is governing the deformation of the pile.

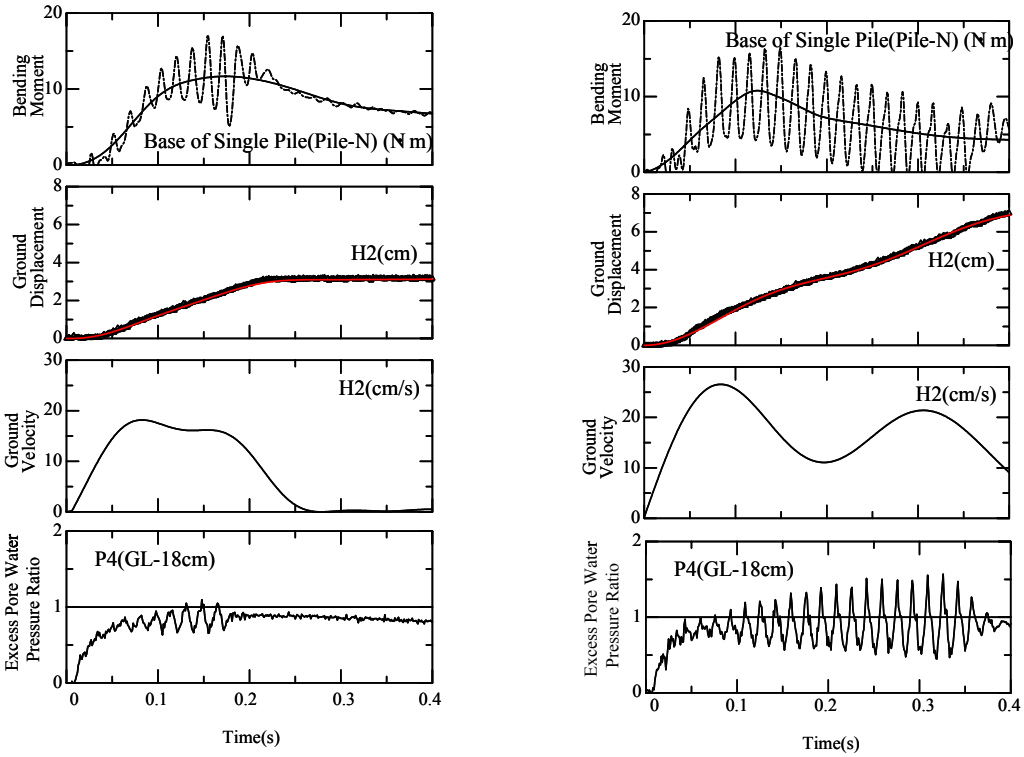

(a) case1

(b) case2

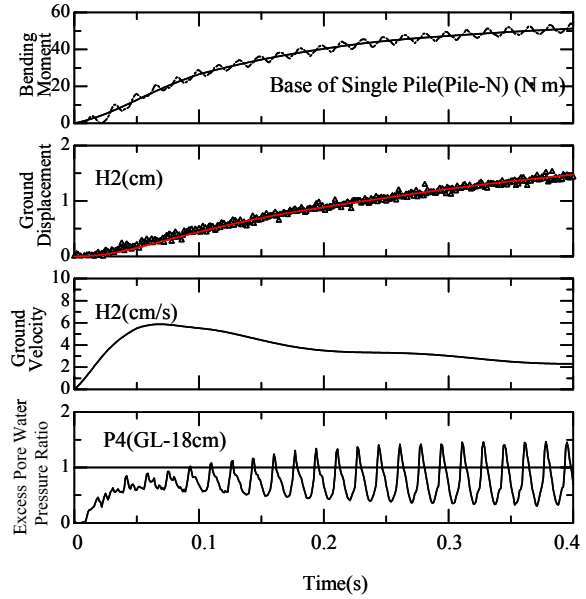

(c) case3

Figure 2 Bending Moment of Piles, Ground Displacements and Velocities, and Excess Pore Water Pressure Ratio

Maximum Bending Moment on Single Pile and Grouped Pile

Figure 3 shows the distribution of bending moment along the pile length for the single pile (Pile-N) and the grouped piles (Piles-C,S,W). In the cases 1 and 2, where the whole part of the model ground was liquefied, the bending moment of the single pile (Pile-N) is much larger than those of the other piles. The lowest value of bending moment in Pile occurred in the pile-W which was installed at the downstream side of the flow. The bending moments of Piles C and S, which were located at the upstream side of the flow were less than that of the single pile (Pile-N). This result suggests that the flow of the liquefied soil around the grouped piles is different from that around the single pile. Figure 3 (d) shows the maximum bending moment of Case 3, where a non-liquefiable soil is overlaying the liquefied soil. In this case the distributions of bending moments along the length of every single pile in the pile group formed in the same trend regardless of its location as shown in Figure 3 (d), whereas there happened definite deviations among the distributions of bending moment according to the location of pile in Cases 1 and 2. It can be inferred that the existence of non-liquefiable layer is regarded as one of governing factors to the generation of pile deformation in the liquefiable soil and gives rise to the almost same trends of load distribution along the piles for both in the single pile and the grouped piles.

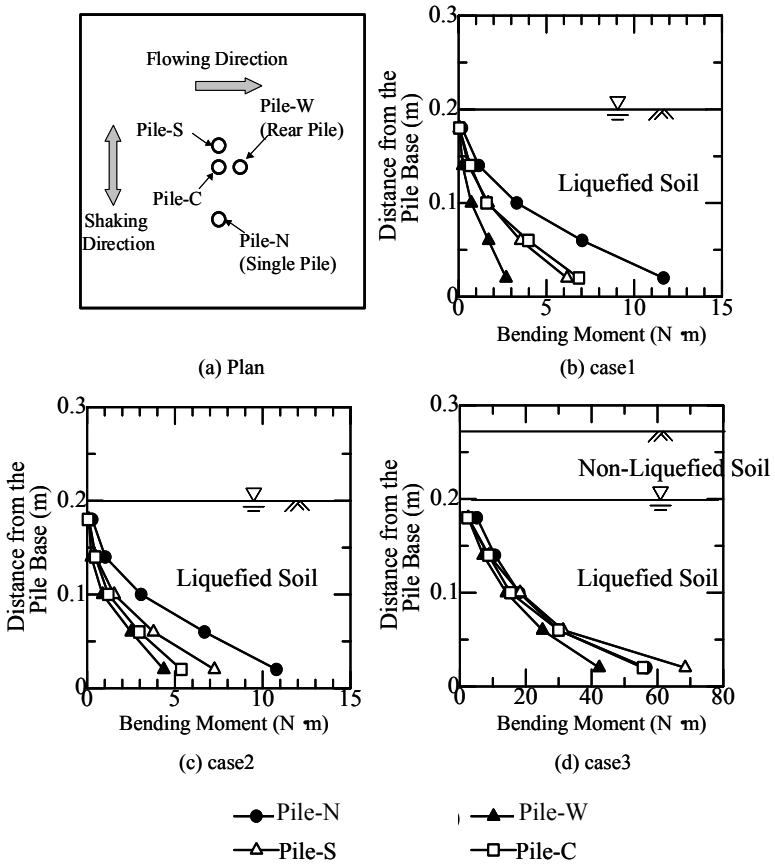

Figure 3 Distribution of Maximum Bending Moment along the Depth of the Pile

EVALUATION OF THE LOADS ON PILES FROM FLOWING GROUNDS

Loads from Lateral Spreading in Liquefied Soil

As shown in Figure 4., the linear distribution of the load acting on the pile was assumed to estimate the effect of lateral spreading and the coefficients of the linear function a and b were determined by the following least mean square method.

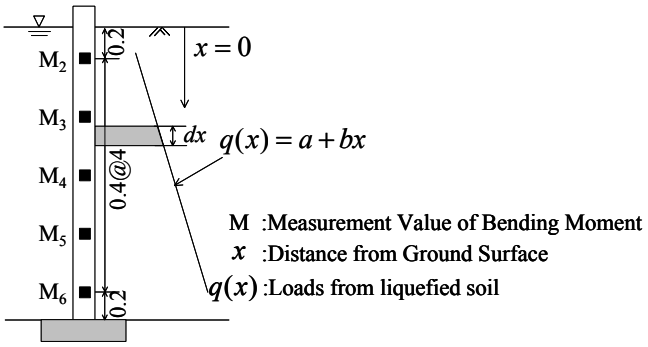

Figure 4. Calculation Model (case1,2)

$$\sum_{i=2}^{6}\left\{M_i - \int_0^{xi} x_i(a+bx)dx\right\}^2 = E, \qquad \frac{\partial E}{\partial a} = 0, \qquad \frac{\partial E}{\partial b} = 0 \tag{1}$$

The time histories of the loads at several depths and their distributions are shown in Figure 5 (case 1) and Figure 6 (case 2). According to the time histories of the load, at the first period (before it passed about 0.1s) the load was larger at the higher elevation (point 2), while the load became lager with a deeper depth at the later period (after 0.1s). This trend is easily observed at the distribution of the load acting at point 6, which is located at close to the base of the pile. This suggests that the characteristics of the load from the flowing ground changed depending upon the elapsed time.

Figures 5 (b) and 6 (b) also illustrate the distributions of the loads at the time of 0.1s and 0.2s. The load marked by the black dots, obtained by direct second order differentiation of the observed bending moment, are scattering but approximately coincide with the load obtained under the condition that the distribution of the load along the pile length was assumed as linear.

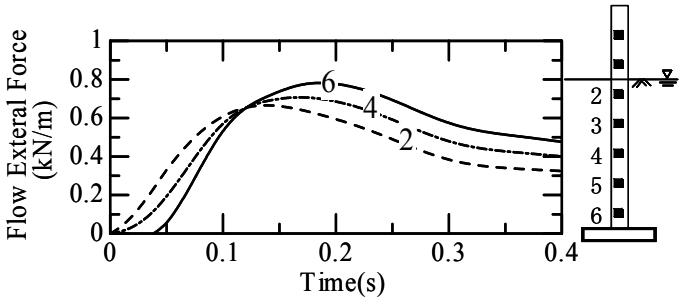

(a) Time history of the loads

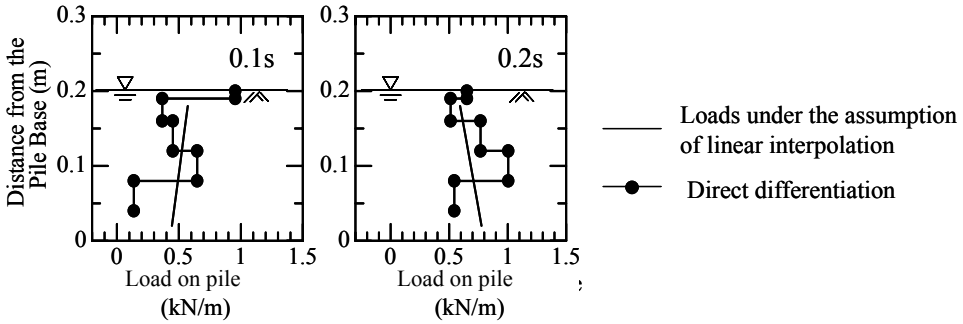

(b) Distribution of the load

Figure 5 Time History and the Distribution of the load on the pile (case1)

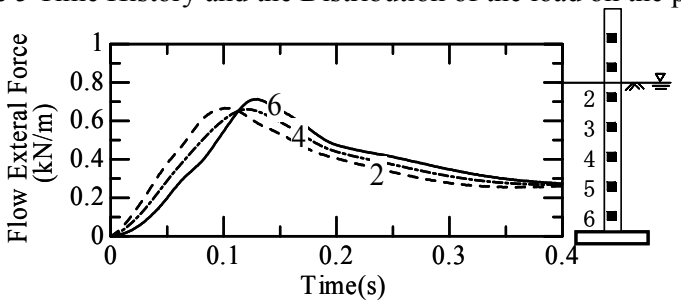

(a) Time history of the loads

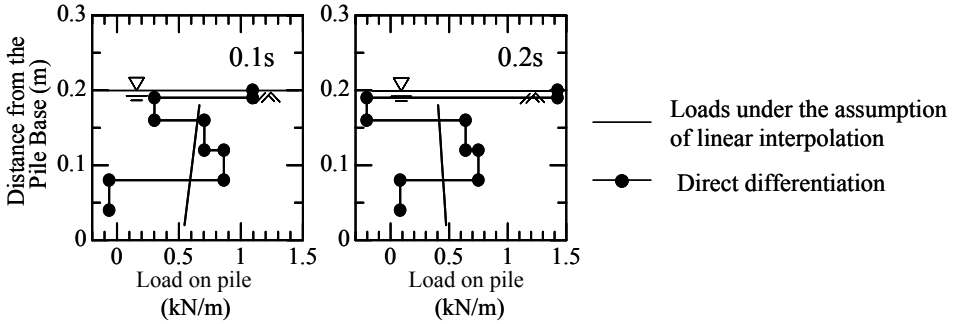

(b) Distribution of the load

Figure 6 Time History and the Distribution of the load on the pile (case2)

Loads from Lateral Flow in Liquefied Soil overlain by Non- Liquefiable Soil

The loads from the lateral flow in liquefied soil overlain by a layer of non-liquefiable soil were estimated from the test results of case 3. As depicted in Figure 7, it was assumed that the load from non-liquefied soil is constant along the pile depth and the load from liquefied soil has a linear distribution. The coefficients a, b and c of the load distributions were determined by the least mean square method.

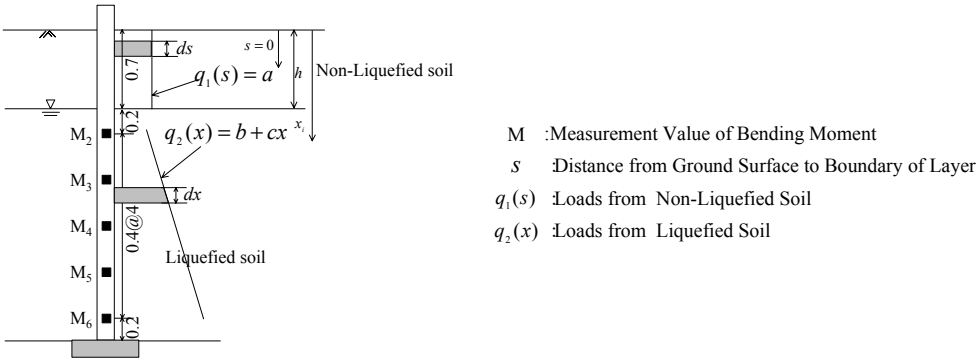

Figure 7 Calculation Model (case3)

Identification of Loads Resulting from Ground Displacement and Velocity

It can be considered that two kinds of load act on the foundation piles from the lateral flow in liquefied ground. One of them is the load resulting from ground displacement and the other from ground velocities. In order to identify these two kinds of load, the Voigt model was adopted as shown in Figure 8. The load on the pile at the depth i was defined as equation (2).

$$q_i = k_i u_i + c_i \dot{u}_i \tag{2}$$

where k_i is the spring coefficient of ground and c_i is the viscous coefficient. u_i and $\dot{u}_i$ can be regarded as the ground displacement and velocity at the depth i respectively under a condition that the pile deformation is negligible because of the relatively large stiffness of the pile.

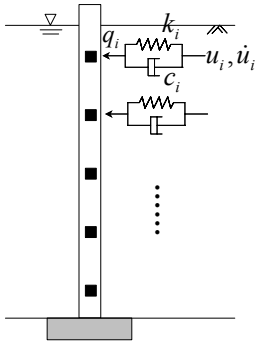

Figure 8 Voigt Model

k_i and c_i can be estimated with the least mean square method as suggested in the formula (3) based on the experimental data. After estimating k_i and c_i, stiffness load ($k_i u_i$) that relies on ground displacement and viscous load ($c_i \dot{u}_i$) that relies on ground velocity can be calculated from the multiplication of two terms by u_i and $\dot{u}$ respectively. As shown in Figure 9, three positions are used for identification.

$$\sum \left\{ q_{(t)} - \left(k_{(t)} u_{(t)} + c_{(t)} \dot{u}_{(t)} \right) \right\}^2 = E, \qquad \frac{\partial E}{\partial k_{(t)}} = 0, \qquad \frac{\partial E}{\partial c_{(t)}} = 0 \tag{3}$$

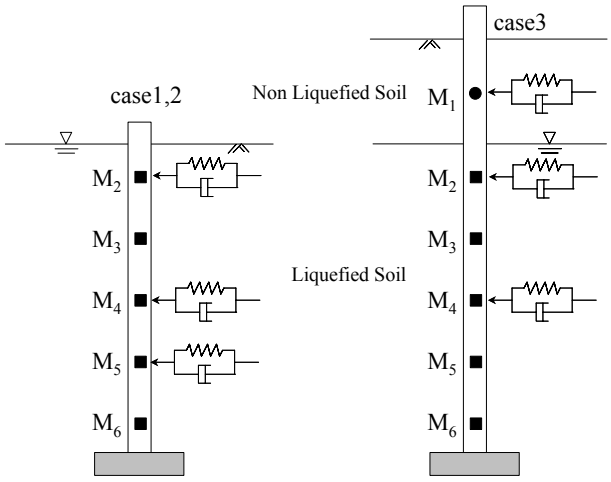

Figure 9 Location of Identification

The results of case 1 and 2 are shown in the Figure 10 and 11. The time histories of the excess pore water pressure ratio, which was measured at almost the same position where load is calculated, are also plotted in the same figure. According to Figure 11 and Figure 12, stiffness load exceeds viscous load while model ground is not liquefied, but viscous load exceeds stiffness load after the occurrence of liquefaction. However, near the ground surface, viscous load always can be found to keep larger than stiffness load. It can be accordingly summarized that viscous load becomes dominant after liquefaction in liquefied soil where the ground model consists of only liquefiable soil.

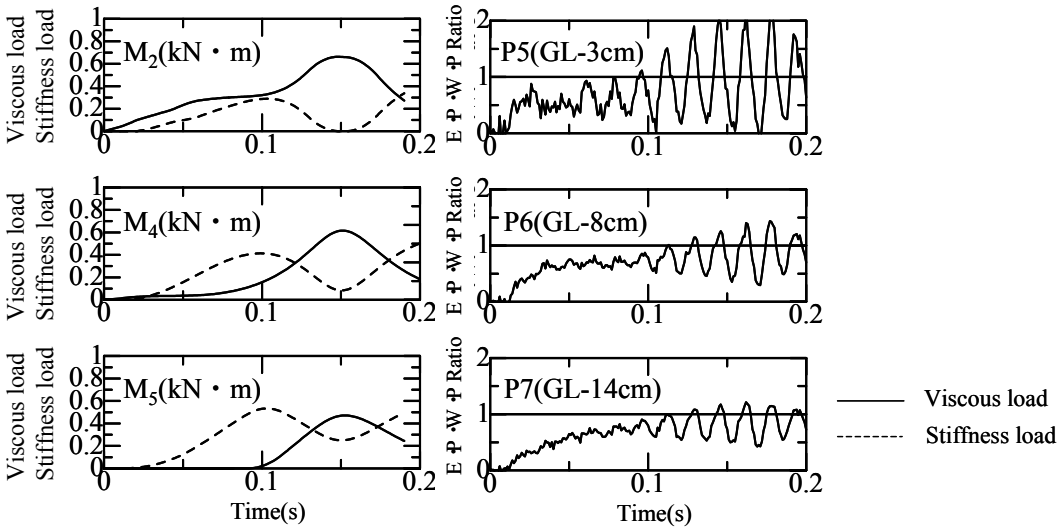

Figure 10 The Result of Identifying in Case 1

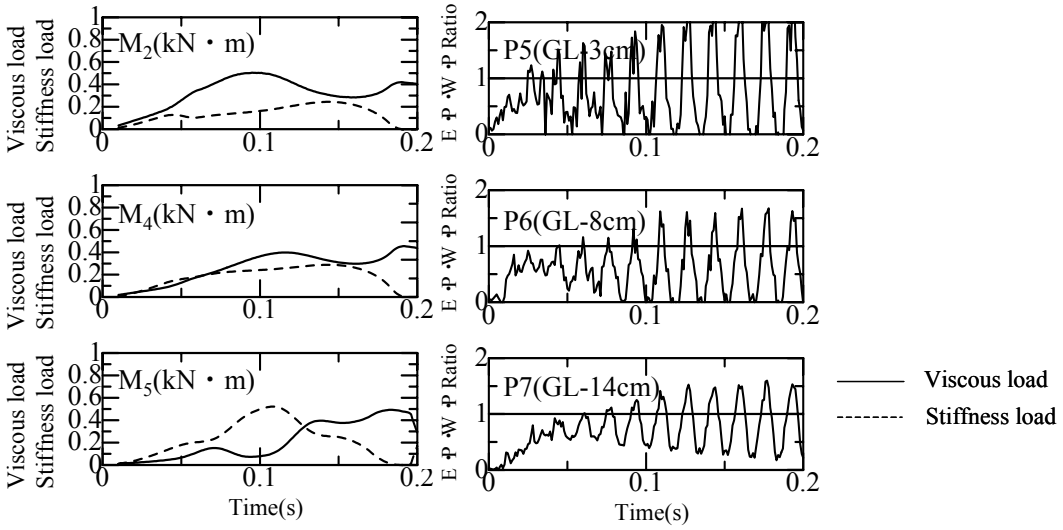

Figure 11 The Result of Identifying in Case 2

The result of case 3 is presented in the Figure 12. According to the time history of M_1, stiffness load is mostly dominant in non-liquefied soil. On the contrary, according to the time history of M_2 and M_3, viscous load exceeds stiffness load after liquefaction, which shows the similar tendency with the results of case 1 and case 2. Consequently, it can be summarized that stiffness load prevails through non-liquefiable layer, while in liquefied soil viscous load is dominant after liquefaction in the case of the existence of non-liquefiable layer.

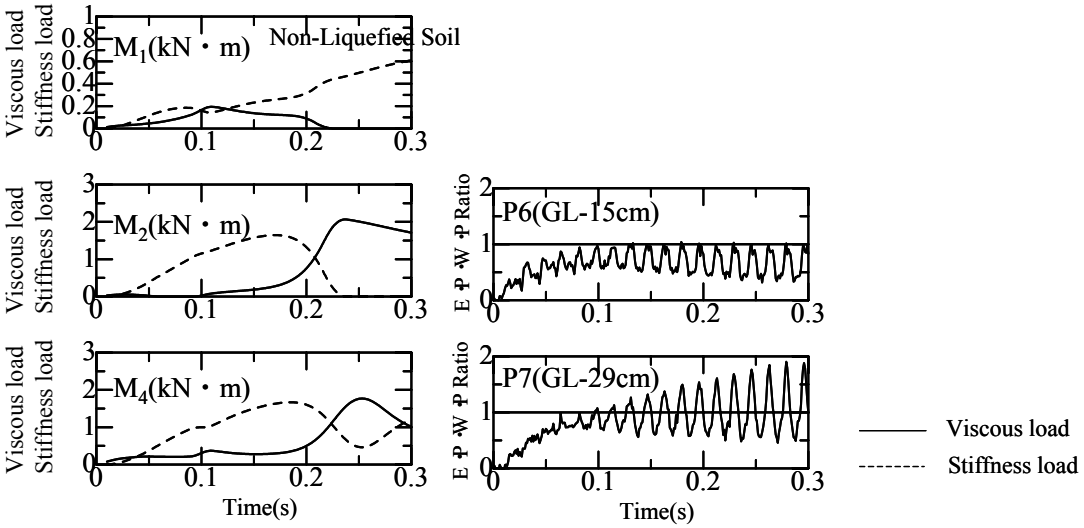

Figure 12 The Result of Identifying in Case

CONCLUSION

The characteristic of the load acting on the piles was evaluated in this study by performing a series of flow experiments of liquefied soil under a centrifugal condition. It was obtained that the viscous load depending on the ground velocity of liquefied soil was dominant on the piles when the model ground was perfectly liquefied. On the contrary, the external load resulting from ground displacements was governing the pile deformation when the model ground was not liquefied or partially liquefied.

ACKNOLEDGEMENT

This work funded under the special coordination funds for promoting science and technology in 2002 and belongs to the part of the accomplishment for “Enhancement of Earthquake Performance of Infrastructures based on Investigation into Fracturing Process.” The authors wish to express their gratitude to the financial support for this work.

REFERENCES

[1] Hamada et al. 1994. “An Experimental and Numerical Study on Liquefaction-induced Ground Displacement”, *Proc.,5th U.S. National Conference of Earthquake Engineering,*

[2] Hamada 1999. “Similitude Law for Liquefied-Ground Flow”, *Proc.,7th U.S.-Japan Workshop on Earthquake Resistant Design of Lifeline Facilities and Countermeasures Against Soil Liquefaction, pp191-205*

[3] M.Hamada, K.Wakamatsu 1998. “A Study on Ground Displacement caused by Soil Liquefaction” *Proc Japanese Society of Civil Engineering No.596, Vol.3, pp189-208*

Measurement of Ground Deformation Induced by Liquefaction and Faulting in the Earthquake Area of the 1999 Kocaeli Earthquake

ABSTRACT

This study was undertaken as the quantitative measurement of permanent ground deformation and associated strain fields induced by liquefaction and faulting resulted from the 1999 Kocaeli earthquake in Turkey. The permanent ground deformation was measured through aerial photogrammetry technique around the Sapanca Lake and the southern shore of Izmit Bay. For the purpose, aerial photographs taken before and after the quake were compared and the differences between these were interpreted as the liquefaction and /or faulting induced displacements.

Oktay Aksu, Ph.D., Photogrammetry Division, General Command of Mapping, Dikimevi, Ankara, Turkey, Phone: (90)-312-5952275, Fax: (90)-312-3201495, oaksu@hgk.mil.tr
Veysel Okan Atak, M.Sc., Photogrammetry Division, General Command of Mapping, Dikimevi, Ankara, Turkey, Phone: (90)-312-5952277, Fax: (90)-312-3201495, oatak@hgk.mil.tr
Mustafa Onder, Ph.D., Photogrammetry Division, General Command of Mapping, Dikimevi, Ankara, Turkey, Phone: (90)-312-5952270, Fax: (90)-312-3201495, monder@hgk.mil.tr
Omer Aydan, Professor, Deartment of Marine Civil Engineering, Tokai University, 3-20-1, Orido, Shimizu, Japan, Phone: (81)-5-4334-0411, Fax: (81)-5-4334-9768, aydan@scc.u-tokai.ac.jp
Masanori Hamada, Professor, School of Science and Engineering, Waseda University, 3-4-1, Ohkubo, Shinjuku, Tokyo, 169-8555, Japan, Phone: (81)-3-3208-0349, Fax: (81)-3-3208-0359, hamada@mn.waseda.ac.jp

INTRODUCTION

Liquefaction of ground below ground water table is caused by the excess pore pressure due to shaking resulting from earthquakes or blasting. As a result the ground temporarily loses their strength and bearing capacity and it behaves as a viscous liquid rather than a solid. The actions in the soil, which cause liquefaction, are primarily shear waves. Liquefaction occurs in saturated soils, that is, soils in which the spaces between individual particles are completely filled with water [1]. The faults breaks appearing on the ground also produce ground deformation Damages and three dimensional displacements on the ground and structure which are caused by liquefaction and faulting after an earthquake can be determined by using photogrammetry and remote sensing data and methods.

Turkey is one of the most seismically active countries in the world and most of her damaging earthquakes are of inland-type. These earthquakes mostly result in permanent ground deformation as a consequence of faulting and liquefaction. Although the effect of faulting on the permanent ground deformation is known, the effect of liquefaction, which is called lateral spreading, became to be known after the 1964 Niigata earthquake. Liquefaction phenomenon was observed in almost all earthquakes occurred in Turkey when the reports of the past earthquakes are carefully examined. Nevertheless, it did not receive any attention until the recent March 13, 1992 Erzincan earthquake [2]. Furthermore, earthquakes having magnitude greater than 6 often results in surface ruptures due to earthquake faulting. Therefore, the ground deformation induced in large Turkish earthquakes represents almost the extreme conditions and it deserves a careful evaluation of ground deformation induced by both ground liquefaction and surface fault breaks.

The 1999 Kocaeli earthquake (also named by Eastern Marmara Earthquake) produced a fault break of more than 150km long and caused extensive ground liquefaction (Figure 1) [3]. The effect of liquefaction was quite extensive at Adapazarı and Sapanca Lake (Figure 2). A collaborative research project to measure permanent ground deformation due to liquefaction and faulting was initiated by Waseda University (Japan) and General Command of Mapping (Turkey) in 2001. Adapazarı, Sapanca Lake vicinity and south coast of Izmit Bay are the areas of interest in the project.

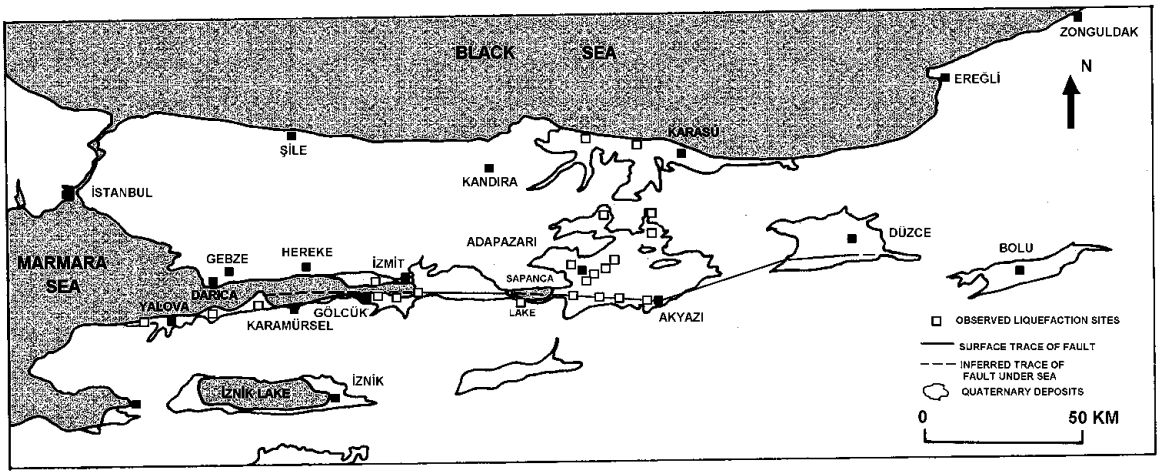

Figure 1. Liquefaction locations observed during Kocaeli earthquake of Aug. 17,1999

Figure 2: Examples of liquefaction in Adapazarı

The permanent ground deformations were measured through the aerial photogrammetry technique at several sites within the quake region as mentioned above. The three-dimensional coordinates of the common points on pre-post earthquake photographs were determined, and the differences between them are interpreted as the liquefaction and faulting induced displacements.

MEASUREMENTS AROUND THE SAPANCA LAKE

Geodetic surveying activities were carried out and aerial photographs were taken in 1:16.000 scale covering the areas Avcilar, Yalova, Izmit, Adapazari by General Command of Mapping on September 8th, 1999 after the Marmara earthquake.

While it is ideal to use aerial photographs pertaining to pre- and post-situation of earthquake in large scales (such as 1:5.000, 1:10.000) for determination of liquefaction, 1:35.000 scale aerial photographs taken in 1994 were to be used instead, as those of 1:16.000 scale taken in 1970 have no triangulation points. Although it seems a disadvantage to use small scale photographs, temporal resolution that is closest dates for the pre- and post-situation aerial photographs is especially preferred in the areas like Marmara region which have dense structuring.

Digital aerial triangulation measurements and block adjustments were implemented using scanned aerial photographs in 21 μm.. Final products were 1:5.000 scale digital orthophoto maps, totally 860 sheets for the earthquake area. So, the exterior orientation parameters of all aerial photographs were already determined. 1:35.000 scale aerial photographs were also processed by means of analytical photogrammetric measurements for the revision of 1:25.000 scale topographic maps. That is why adjusted coordinates of tie points are available. Root mean square error of 6-8 μm. is normally acceptable for topographic mapping in GCM.

As many and well-distributed common points as possible have been selected on the aerial photographs for coordinate measurements. These points are on the features where artificial displacements are minimum, such as junction of roads, bridges and buildings.

Cartesian coordinates at 302 points have been measured in the photogrammetric models including north-coast of Sapanca Lake (Esme). Movement vectors have been calculated by means of coordinate differences of the common points. These vectors show a displacement implies with faulting in the east and southeast direction.

423 points have also been measured at the west corner of Sapanca Lake model. Obtained vectors do not show a unique direction. There is a similar movement with that of Esme in the north of the model, while sparse movement in the south of model because of varying soil structure and locating fault.

418 points have been measured in the area of Sapanca Otel. Displacement vectors have direction mainly to north, upward the Lake because of the liquefaction (Figure 3).

Results about the Sapanca Lake measurements can be seen in Table I.

TABLE I. SAPANCA LAKE AREA MEASUREMENTS AND RESULTS

SAPANCA LAKE AREA		<RESULTANT VECTOR (POST-PRE)(1999-1994)>			
AREA NAME	POINT NUMBER	DE (m)	DN (m)	DL (m)	DV (m)
SAPANCA OTEL	(418 points)				
Mean		0.410	0.835	1.460	-1.714
Detailed Measurement	(219 points)				
Mean_Detailed		0.467	1.207	1.778	-2.041
SAPANCA ESME	(305 points)				
Mean		2.351	-0.428	2.660	0.617
Detailed Measurement	(122 points)				
Mean_Detailed		2.575	0.193	2.849	0.762
SAPANCA LEFT SİDE	(423 points)				
Mean		0.608	0.291	3.036	0.602
Detailed Measurement	(50 points)				
Mean_Detailed		1.304	0.764	2.245	0.131
Detailed Measurement = Detailed Measurements at Coastline Area					

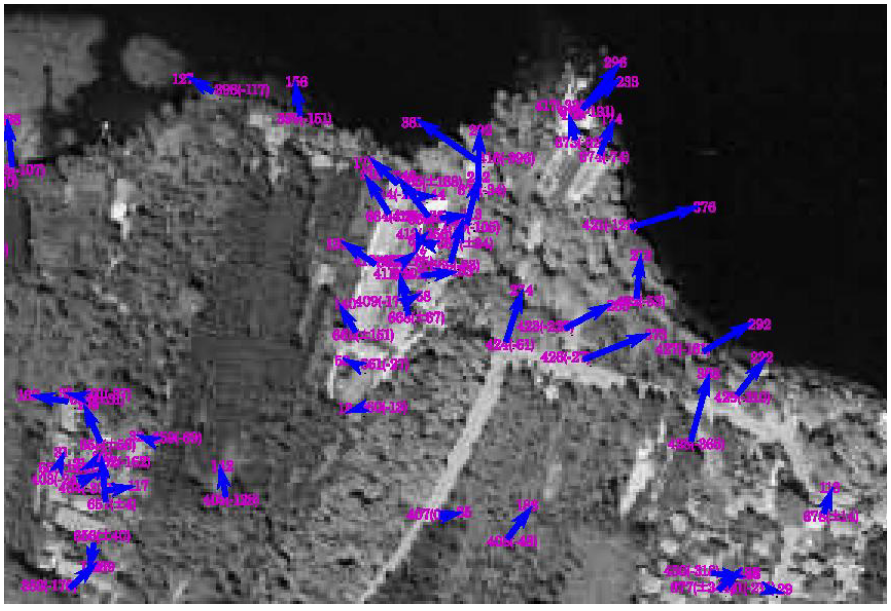

Figure 3. Displacement vectors around the Sapanca Hotel

Some other measurements were also implemented in eight different areas on the coastline of Izmit Bay (Figure 4) in addition to Sapanca Lake. Obtained results can be seen in Table II.

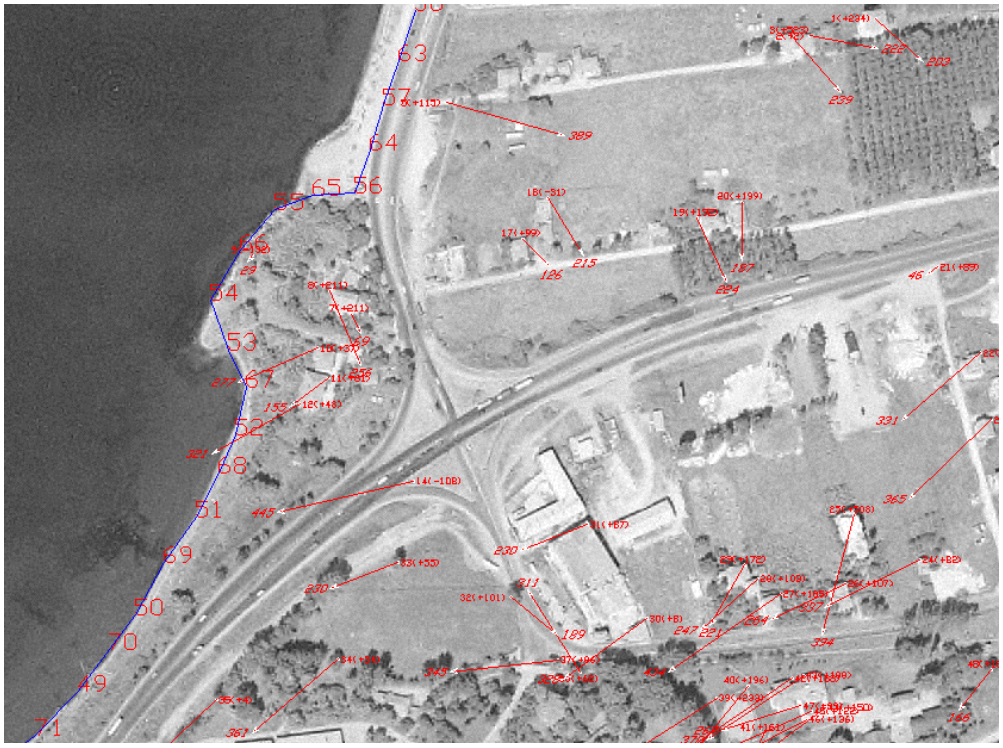

Figure 4. Displacement vectors at Basiskele

TABLE II. IZMIT BAY AREA MEASUREMENTS AND RESULTS

IZMIT BAY AREA		<RESULTANT VECTOR (POST-PRE)(1999-1994)>			
AREA NAME	**POINT NUMBER**	**DE (m)**	**DN (m)**	**DL (m)**	**DV (m)**
BASISKELE	(48 points)				
Mean		-1.389	-1.482	2.766	1.021
SEGMEN	(117 points)				
Mean		-1.064	-1.146	2.317	-0.132
GOLCUK	(92 points)				
Mean		-1.580	-1.259	2.440	-2.481
DEGIRMENDERE	(132 points)				
Mean		-1.354	-1.215	2.445	-0.602
HALIDERE	(66 points)				
Mean		-1.278	0.385	2.058	-1.454
ULASLI	(71 points)				
Mean		-0.438	-0.354	1.399	-0.680
HERSEK	(145 points)				
Mean		-2.069	-1.112	2.881	-1.505
YALOVA	(301 points)				
Mean		1.637	0.709	2.155	1.037

CONCLUSION

Earthquake dated 17th August 1999 has revealed that reliable and rapid information about the effects and affected areas is one of the vital issues. Photogrammetry and remote sensing methods and means provide rapid and reliable information sources. On the other hand, scientific activities on earthquake research can be classified based on geodesy-geology, photogrammetry-remote sensing and geographic information systems. Of these, geodesy and geology deals with plate motion and soil mechanics. GIS based methods provide information for rescue, determination of damaged structures, and rebuilding.

Photogrammetry and remote sensing based methods, in which aerial photographs, satellite images, SAR laser profiling data are used, provide wide opportunities for determination of not only for ground displacement, damaged or collapsed buildings but also resolution and measuring accuracy.

Aerial photographs can be used especially both in detailed analysis studies of the limited comprehensive earthquake effect areas and as a reliable data source for the reconstruction applications by means of orthophoto maps produced in the wide comprehensive effected areas.

On the other side, the laser scanners provide reliable information for the mentioned goals especially in the more limited effect areas more quickly than aerial photographs do. The laser scanners, which are not available in Turkey as for today and require a high cost for establishment, are the systems, of which developments have to be followed closely.

In earthquakes that affect very wide areas like Marmara earthquake, the landsat satellite images are used as a suitable data source abroad, though recently in Turkey. The components, which affect reliability and accuracy, are;

- The images that will be used for determination of changes have to be taken in a limited time range and in the same part of the year, and
- These sensor images have to collect data with the same view angle and resolution.

Based on the aerial photogrammetric evaluations conducted for five sub-areas along the southern coast of the Sapanca Lake, displacement vectors determined confirm the site observations, which were done at liquefaction areas. It is also noted that towards the south part of Sapanca town, where liquefaction has not been observed, some displacement vectors were also determined. These vectors indicate some displacement contributing to the main deformations due to liquefaction induced lateral spreading along the coast of the lake. On the contrary to these, displacement vectors at the northern part of Sapanca Lake, particularly at the north of Esme town, are parallel to the fault, which caused the earthquake. At this part of the site no liquefaction has occurred, and therefore, it can be concluded that the permanent ground deformation is higly associated with the movement of the fault. This part of the study is considered to be valuable for further geotechnical assessments which will be carried out at the second phase by the geotechnical group.

REFERENCES

[1] http://www.eeri.org/earthquakes/EQ_Basics/eq1.html

[2] Aydan, Ö., and Hamada, M. (1992). The site investigation of Erzincan (Turkey) Earthquake of March 13, 1992. 4th Japan-US Workshop on Earthquake Resistant Design of Lifeline Facilities and Countermeasures Against Soil Liquefaction, Honolulu, May, 1992, 17-34.

[3] Aydan, Ö., Ulusay, R., Hasgür, Z., and Taşkın, B. (1999a). A site investigation of Kocaeli Earthquake of August 17, 1999. Turkish Earthquake Foundation, 180pp.

Observed Behavior of Lifelines Subjected to Lateral Spreading: Tokachi Blast Experiment

Scott A. Ashford[1] and Teerawut Juirnarongrit[2]

ABSTRACT

Two full-scale experiments using controlled blasting were conducted in the Port of Tokachi on Hokkaido Island, Japan, to assess the performance of lifeline facilities subjected to lateral spreading. Lifeline specimens in this study included a single pile, a 4-pile group, a 9-pile group, two natural gas pipelines, and one electrical conduit. All of them were extensively instrumented with strain gauges to measure the distribution of moment during lateral spreading. This allowed to compute the loading condition, as well as to conduct the damage and performance assessments on the lifeline facilities. Other instrumentation including pore pressure transducers, GPS units, and slope inclinometers, were also installed to measure the degree of liquefaction as well as the movements of soil and lifelines. This paper presents the test results and provides some discussions on the performance of piles and pipelines observed from the experiments.

Scott A. Ashford, Associate Professor, Department of Structural Engrg., Univ. of California, San Diego, La Jolla, CA 92093-0085

Teerawut Juirnarongrit, Graduate Student Researcher, Department of Structural Engrg., Univ. of California, San Diego, La Jolla, CA 92093-0085.

INTRODUCTION

In past earthquakes, lateral spreading has caused considerable damage to civil infrastructure including port facilities, buildings, bridges, and utilities. Examples are the damage of quay walls and buildings in the 1995 Kobe earthquake; the damage of pile foundations in the 1964 Niigata earthquake; the damage of over 250 bridges and numerous embankments along the Alaskan Railroad and Highway during the 1964 earthquake; the damages of numerous water and gas lines in the 1906 earthquake; and the significant damage in the San Francisco area in 1989 Loma Prieta earthquake [1, 2, 3, 4, 5, 6]. Therefore, it is extremely essential to understand the behavior of soil, as well as lifelines during lateral spreading in order to improve the current design method for lifeline utilities to prevent the catastrophic failure for future earthquakes. Meanwhile, most lateral spreading research to date has focused on small-scale centrifuge studies [7], limited area 1-g shake table tests [8], or case histories [9, 10]. In addition, some full-scale has been carried out to study the behavior of deep foundations in sand liquefied by controlled blasting [11], but these tests do not account for the global translations of the lateral spreading soil mass. In light of this, the full-scale instrumented lifeline components in controlled lateral spreading tests were carried out in order to understand the performance of lifelines and be able to implement the test results in engineering practice. The test results will be a valuable source of data for further development of the empirical methods and/or complex numeral models to use to design lifeline facilities subjected to lateral spreading.

Two full-scale experiments using controlled blasting were conducted in November and December 2001 in the Port of Tokachi on Hokkaido Island, Japan, to study the performance of lifeline facilities subjected to lateral spreading. This research project was the joint collaboration between the University of California San Diego (UCSD) and several Japanese organizations. This overall research effort was lead by the Port and Airport Research Institute (PARI). The primary objective of the test was to assess the performance of quay walls subjected to lateral spreading using controlled blasting. One quay wall was of traditional design and new seismic design criteria was applied to the other. Since the test area was so large, it enabled researchers to include additional experiments in the zone of liquefaction and lateral spreading without interfering with the primary objective of the quay wall test. The University of California, San Diego, together with Waseda University (WU) collaborated with other Japanese researchers to install the lifeline specimens in the zone of lateral spreading through the PEER Lifelines Program with support from Caltrans, Pacific Gas & Electric and the California Energy Commission.

In all, UCSD installed 6 test specimens. The pile specimens in the experiment program consisted of a single pile, a 4-pile group, and a 9-pile group. In addition, two natural gas pipelines and one electrical conduit were installed. The objectives of this study is to conduct damage and performance assessments of those lifelines subjected to lateral spreading, as well as to evaluate loading conditions on the structures during lateral spreading.

SITE CHARACTERIZATION

The test site was a recent man-made land that was completed just a few years ago. The land was built by hydraulically placing fill without any ground improvement; therefore, the soil was very loose and highly susceptible to liquefaction.

A subsurface soil exploration program was carried out in many areas throughout the test site to characterize the soil condition. Generally, the soil condition consisted of 7.5 m of hydraulic fill underlain by 1 m of medium dense sand overlying a very dense gravel layer as presented in Figure 1. The hydraulic fill was comprised of a 4-m layer of very loose silty sand with uncorrected SPT-N values ranging from 1 to 5. This was underlain by a 3.5-m layer of very soft lean to fat clay with sand. Uncorrected SPT blow counts ranged from 0 to 2 blows per 30 cm in this layer. The water table was approximately 1 m below the ground surface. Figure 2 presents the grain size distribution of the hydraulic fill plotted together with

the Japanese standard curves for liquefaction potential evaluation. The first 4 m of the soil fell into a zone of highly susceptible to liquefaction. Below this layer, fine contents increased with depth. Only a thin layer of soil at depths between 7.0 and 7.5 m was not liquefiable. Based on the results of grain size analysis and the soil strength characteristic, the soil at the test site was highly susceptible to liquefaction, and therefore appropriate for conducting the full-scale lateral spreading test.

SITE DESCRIPTION AND TEST SETUP

The UCSD experiments were located in a zone of the unapplied seismic design quay wall where the large global translation of the soil was expected. A layout of the test site for the first experiment is shown in Figure 3. The test site was approximately 25 m wide by 100 m long. The front face was bordered by a water way. The water elevation was approximately +2.00 m on the test day. The sheet pile quay wall was driven to the elevation of -8.00 m and was anchored by the tied rods which were fixed to H-piles to prevent the movement of the quay wall. The quay wall retained approximately 7.5 m of hydraulic fill. The ground surface started to gently slope upwards at 25.2 m away from the quay wall with the embankment slope of 4%. The test site was surrounded by the sheet piles to tip elevations between -5.00 and -8.00 m.

The UCSD pile specimens were located 19.0 m away from the quay wall. The pile specimens consisted of a single pile, a 4-pile group, and a 9-pile group. A group of free head single piles of WU were also located in this region. The pile diameters were 318 mm with wall thickness of 10.5 mm, and a nominal length of 11.5 m. The yield strength of these steel pipe piles was 400 MPa.

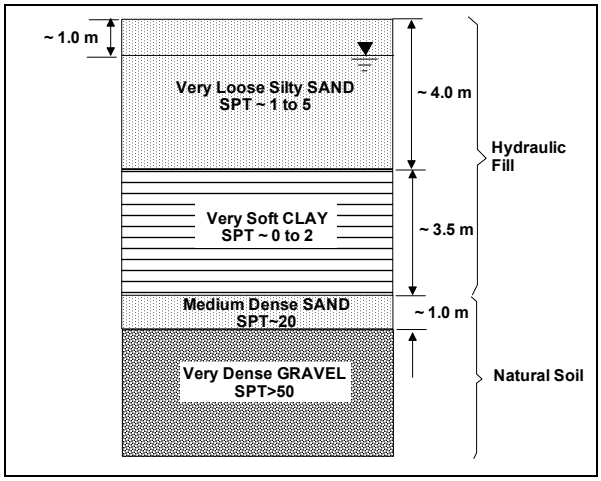

Figure 1. Typical Soil Profile of Test Site.

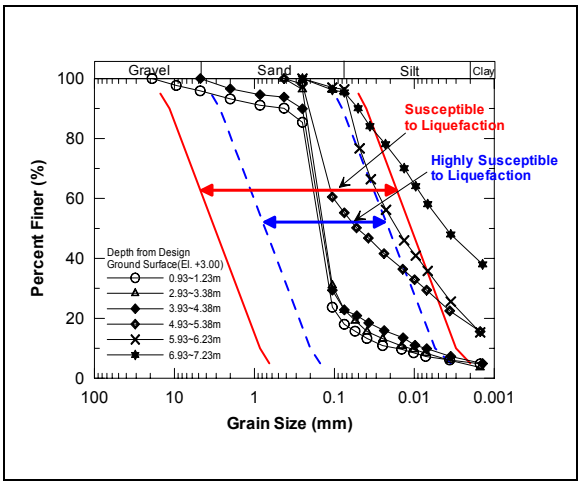

Figure 2. Grain Size Distribution of Soil at Test Site.

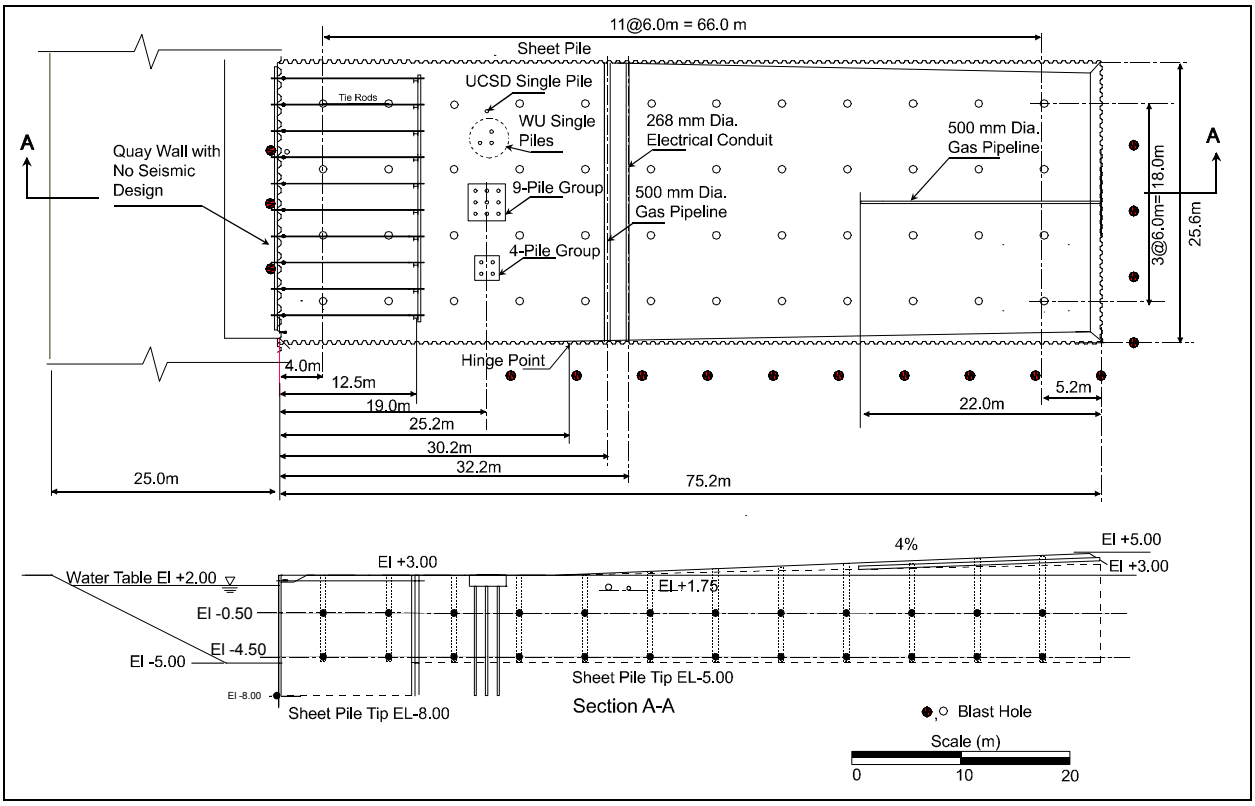

Figure 3. Site Layout of 1st Lateral Spreading Experiment.

In addition, two natural gas pipelines and one electrical conduit were installed. The gas pipeline consisted of a 500 mm diameter pipe with wall thickness of 6 mm and yield strength of 400 MPa. The electrical conduit consisted of a 268 mm diameter with wall thickness of 6 mm and yield strength of 400 MPa. Both pipelines were about 25 m long and located across the test sites at 30 m and 32.2 m away from the quay wall. The bottoms of both pipelines were installed at the elevation of +1.75 m. The other gas pipeline was 22 m long and installed parallel to the direction of the flow. The center of the pipeline was 1 m below the ground surface along its entire length.

Due to the success in using the controlled blasting to induce soil liquefaction in several tests in Japan as well as the full-scale lateral load tests at Treasure Island [11], the same technique was implemented to liquefy the soil at the test site, and thus induce lateral spreading. The blast holes were spaced at 6.0 m on centers in a regular grid pattern. The charges were installed at depths of 3.5 m and 7.5 m below the ground surface. The amount of charges varied from 2 kg nearby the pile specimens to 3-5 kg at other areas. The charge was reduced in the vicinity of pile specimens so as to prevent damage to a large number of instruments installed in the vicinity of pile specimens. The first experiment was carried out on November 13, 2001. The sequence of the blasting started from the back corner of the embankment and then continued to the next holes of the same rows and proceeded successively towards the quay wall. This was followed by the detonation of the secondary blast holes around the perimeter of the test site. The purpose of these explosives was to loosen the soil in the vicinity of the sheet pile to allow unrestricted flow of the soil in such region. Approximately 20 seconds after the completion of the secondary blasting, the additional explosives were used to break the tie rods of the quay wall and allowed the quay wall to move freely to create additional movement of the soil within the test area.

The second lateral spreading test was performed with an attempt to induce additional ground deformations and further evaluate the performance of lifeline facilities subjected to a higher level of soil deformation. The test site for the second lateral spreading test was significantly modified from the first one as presented in Figure 4. The test site was approximately 30 m wide by 40 m long. The quay wall and sheet piles surrounding the test site were removed to allow the soil to move freely. The waterway was excavated on one end of the test site to an elevation of -1.00 m with the slope of 2:1 and then filled with water to an elevation of +2.00 m. However, the actual ground water table during the second test observed from the soil excavation adjacent to the test area was approximately at elevation of +1.00 m. The ground surface was leveled for a distance of 7.5 m away from the edge of the waterway and then started to rise up with an embankment slope of 6% over a distance of 18.0 m. The blast holes were spaced at 6.0 m on centers in a square grid pattern. Charges were installed at depths of 4.0 m and 8.0 m below the design ground surface (El +3.00m). The amount of charges varied from 2 kg to 4 kg. Two additional rows of blast holes were drilled. One was located on the steep slope adjacent to the waterway with the amount of explosives ranging from 1 to 3 kg. The purpose of these explosives was to loosen the soil at the slope toe prior to the primary blasting sequence such that the embankment soil behind it had a high potential to move freely with larger deformation once the primary blasting initiated. The other was located between the pipelines and piles as denoted as blast holes No. 7 to No. 9. Three kilograms of explosives were installed at El. -3.00 m.

The weather condition for the second lateral spreading experiment was quite poor as presented in Figure 5 due to a heavy snowfall of about 0.50 m and wind speed of 100 kph on the test day. The ground was frozen down to depth of approximately 0.20 cm to 0.30 cm below the ground surface at the test site, which would likely impede the global translation of the soil mass. In an attempt to mitigate this, jackhammers were used to break up the frozen ground in the vicinity of test specimens as presented in Figure 6. The second test was carried out on December 14, 2001. The explosives on the steep slopes were detonated initially from S1 to S5. Approximately 15 second later, the primary sequence of the blasting was started. The primary blast began at blast hole No.1 on the rear of the embankment. Then, the blasting proceeded to the next holes of the same rows, and then continued to the next row towards the waterway (i.e., from No.1 to No.17).

INSTRUMENTATION

Piles and pipelines were extensively instrumented with electrical strain gauges. The strain gauges of pile specimens were located at 0.6 m intervals on both upstream and downstream sides of the piles to measure the bending moment along the length of the pile. A series of tiltmeters at various depths were also installed on one pile of each foundation system to use as backup data for strain gauges. Unfortunately, all of them were damaged during the pile installation. Steel channels C 75 mm x 6.92 kg/m with yield strengths of 400 MPa were welded to the steel pipe piles to protect the strain gauges from damage during the pile installation. The strain gauges of the gas pipeline were spaced between 1.0 m and 3.0 m along the top and the side of the pipelines to measure the bending moment along the pipelines in both vertical and horizontal directions, respectively.

Apart from the strain gauges, other instrumentation was also installed to capture behaviors of soil and lifelines in more details. These include pore pressure transducers, soil pressure cells, string-activated linear potentiometers, accelerometers, slope inclinometer casings, and Global Positioning System (GPS) units. A layout of instrumentation for the first experiment is presented in Figure 7. The instrumentation for the second experiment was essentially the same as the first test; therefore, it is not shown in this paper.

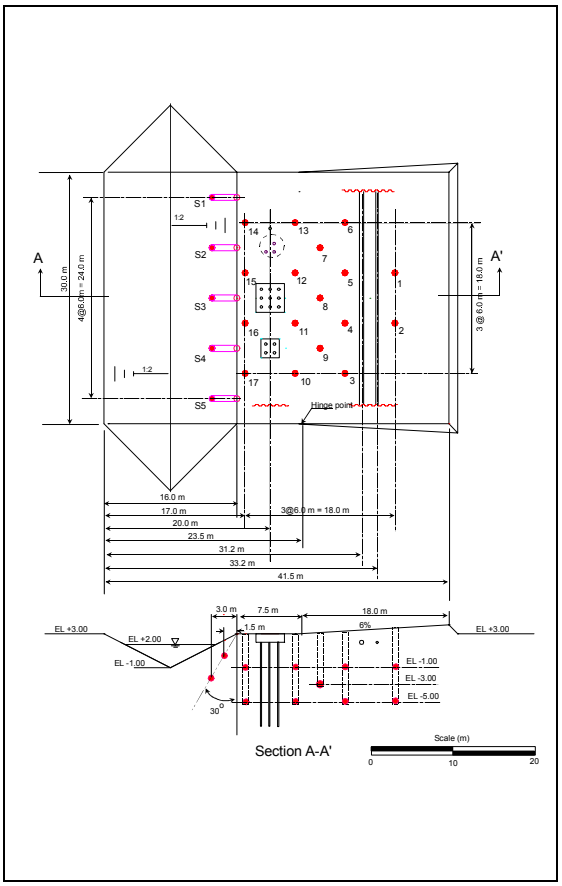

Figure 4. Site Layout of 2nd Lateral Spreading Experiment.

Figure 5. Poor Weather Condition during 2nd Lateral Spreading Experiment.

Figure 6. Breaking up Frozen Ground Surface Using Jack Hammer.

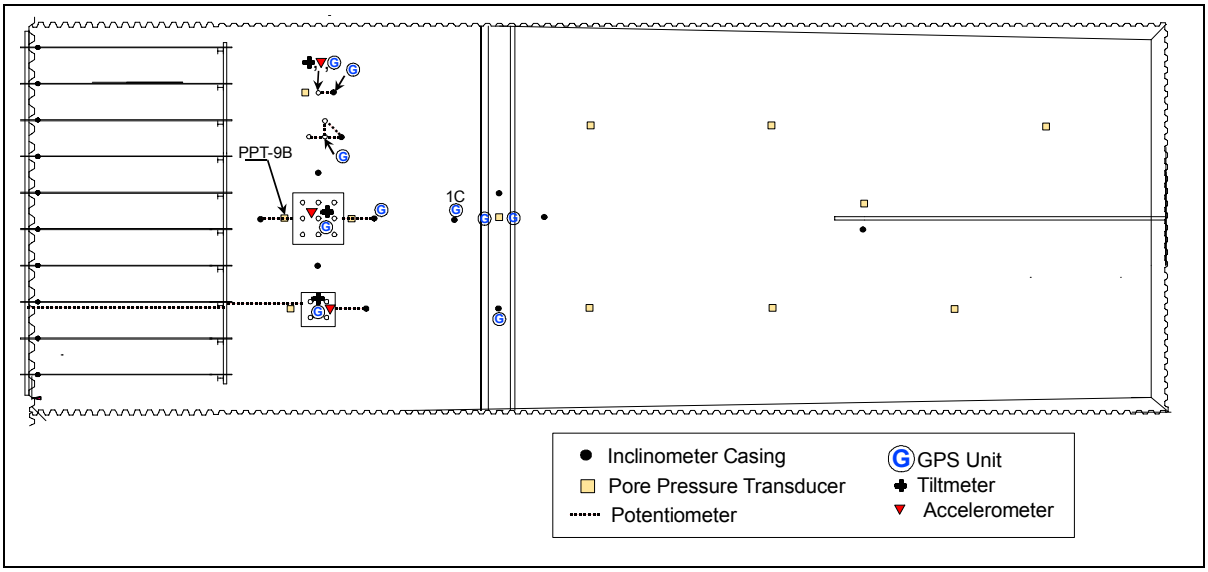

Figure 7. Instrumentation Plan for 1st Lateral Spreading Test.

TEST RESULTS

Excess Pore Water Pressure

An example of excess pore water pressure ratio time-history nearby the 9-pile group at depth of 2 m below the ground surface is presented in Figure 8. The excess pore water pressure ratios built up immediately after the blast though this transducer was located about 50 m away from the first blast hole. The rate of increase in pore water pressure became more rapid as the blast moved closer to the transducers. The increase in pore water pressure ratios proceeded to reach the maximum values at approximately 30 seconds. Fluctuation of pore pressure ratios was obvious as the blasting occurred in the vicinity of the transducer location. The results show that the soil in the vicinity of the 9-pile group was liquefied with the maximum excess pore pressure ratios exceeding 100%. The ratios dropped to about 80% after the blast stopped, then proceeded to dissipate with time. The evidence of increases in excess pore water pressure ratio at times of about 40s and 86s was due to the effect of the secondary blasting and blasting of tied rods, respectively. The characteristics of excess pore water pressure ratios in other locations were basically the same as the one presented herein. The excess pore water pressure ratios throughout the entire test site exceeded 70%. Some of them were slightly over 100%. Sand boil was observed following the blasting as presented in Figure 9 confirming that the ground had indeed liquefied as a result of the blasting.

The excess pore pressure ratios in the 2nd test appeared to be much less than those measured during the first test with values ranging between 30% and 80%. No sand boil was observed in the 2nd test. The lower excess pore water pressure ratio measured in the second test was because the soil condition was less susceptible to liquefaction due to two reasons. First, the soil in the second test was denser because some settlement after liquefaction in the first test took place with the magnitude approximately 20 cm to 60 cm. Second, the ground water table in the second test was lower than that observed in the first test.

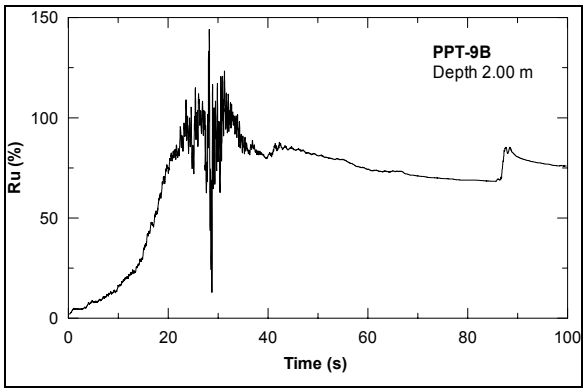

Figure 8. Excess Pore Pressure Ratio vs. Time nearby 9-Pile Group.

Figure 9. Sand Boil after the 1st Experiment.

Deformations of Ground and Lifelines

The GPS units were used to monitor the movements of both ground and lifeline facilities during lateral spreading. The measurements were conducted by a research team from the California Department of Transportation [12]. An example of time history of soil movements on the down slope of the gas pipeline (denoted as unit 1C) in longitudinal, transverse, and vertical directions is presented in Figure 10a. The movements of GPS units were observed at about 10 seconds after blasting initiated. As the blasting moved closer to the GPS location, more movements in all directions were observed. The lateral movements between 10 seconds and 27 seconds were due to not only the liquefaction-induced lateral spreading but also the dynamic forces generated by the blasting. With the blasting past the location of GPS units (at about 27 seconds), the effect of dynamic forces from the blasting was not important as indicated by the insignificant movements in transverse and vertical directions. The longitudinal movement observed after 27 seconds was therefore primarily due to liquefaction-induced lateral spreading. Figure 10b presents the displacement path of GPS unit in the horizontal plane of the gravel surface showing that the horizontal movement mainly occurred in the longitudinal direction towards the quay wall.

The vector displacements in the horizontal plane throughout the test site for the first test are presented in Figure 11a. The largest horizontal displacement was about 43 cm occurring at the pile head of the WU pile. The UCSD single pile moved only 32 cm, which was significantly less than the WU piles. This was likely due to the fact that the WU piles were shorter in length and the pile tips were located just above the dense layer; while the UCSD pile was penetrated about 3.5 meters into the dense soils. The WU piles were therefore likely behaved as rigid piles, in which the rotation and movement at the pile tip were expected. In contrast, the UCSD pile acted as a flexible pile where the rotation and the movement at the pile tip was insignificant. As a result, the displacement at the pile head of the UCSD single pile was less than those of the WU piles. The 4-pile group and the 9-pile group moved significantly less than that of the single pile with the magnitudes of 21cm and 18 cm, respectively. The data from the GPS units in the vicinity of the pipelines show that the movements of the gas pipeline and electrical conduit were similar with a magnitude of about 38 cm. The average of soil movement was about 35 to 40 cm.

As presented in Figure 11b, the horizontal movements occurred in the second test were generally lower than those occurred in the first test, especially in the vicinity of the pipelines. This was mainly due to the soil condition in the second test being less susceptible to liquefaction as mentioned earlier. The movement of the gas pipeline was about 50% of that occurred in the first test. The average soil movement in the second test ranged from 10 cm to 23 cm. One GPS unit installed between two pile caps showed the soil movements as high as 45 cm. However, 10 cm of 45 cm attributed to the movement of slope toe due to the effect of initial blasting along the slope edge. The movement of pile groups in the 2nd test ranged from 16 cm to 18 cm, slightly less than that in the first test. The movements of WU and UCSD single piles at the ground surface were 39 cm and 28 cm, respectively.

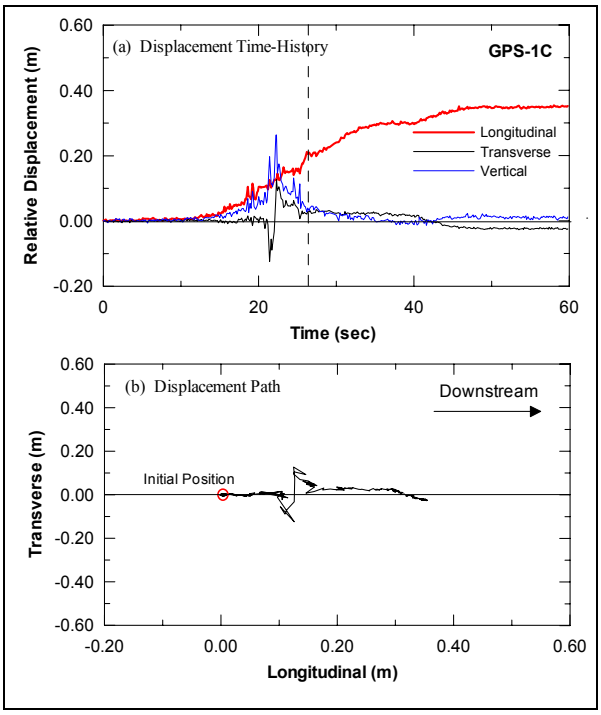

Figure 10. GPS Data (a) Displacement Time-History, and (b) Displacement Path (after Turner 2002).

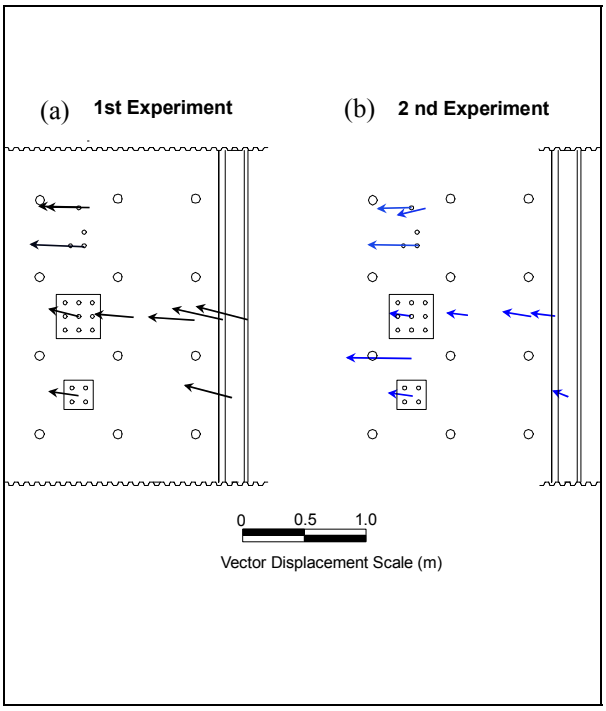

Figure 11. Vector Displacements from GPS Data for 1st and 2nd Experiments (after Turner 2002).

Moment Distribution

Moment distribution along the length of the single pile at the end of the test is presented in Figure 12. The test results indicate that the moments at depths between 0m and 4m were insignificant. One possible explanation for this phenomenon is that after the soil was liquefied, it comes to behave like a viscous fluid material, being able to flow around the pile without significant force acting on the pile. The soil resistance began to increase with depth for the next 3.5 m where a very soft clay layer existed. The maximum moment occurred in a dense soil layer at a depth of about 9 m below the ground surface. The pile was yielded after the second test.

Figure 13 presents the moment distribution of pile No.5 in the 9-pile group. The shape of moment profile from the experiment agreed well with a typical analysis of a pile with fixed head condition showing that the results from the test were reasonable and appropriate for further analysis to estimate the loading distribution of liquefiable soil on the pile. Figure 14 presents the moment profile of each pile in the group after the first experiment. The moment distribution of all piles in the 9-pile group was quite similar, except for pile No. 2 and No.4 where the moments were smaller than the others. This is likely due to the fact that both piles were shorter in length, and had a smaller degree of fixity into the dense soil layer, resulting in a smaller moment in the piles. It is noted that pile No. 2 and No.4 reached refusal during the pile installation, likely due to the presence of a boulder at that particular depth. The similarity of moment distribution of each pile in the group indicates that a shadowing effect was unimportant in liquefied soil. This conclusion was similar to that of a recent research on the behavior of pile group in liquefied soil conducted at Treasure Island [13].

After the second test, all piles in the 4-pile group and the 9-pile group remained elastic with the maximum moment below 70% and 60% of yield moment, respectively. No structural damage was observed on piles to pile cap connections on both pile groups though both pile groups experienced the total movements of nearly 40 cm. In addition, based on the strain gauge data of pipelines (not presented in this paper), all pipelines performed comparatively well without any yielding.

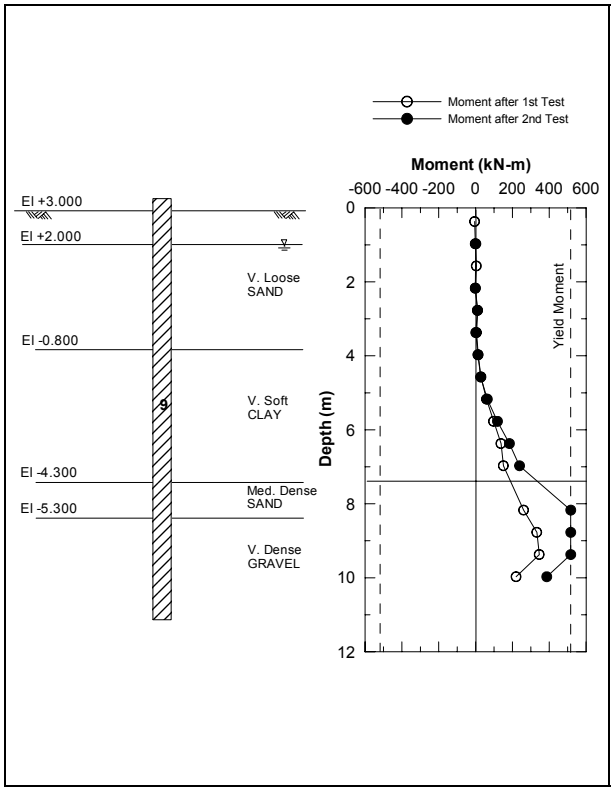

Figure 12. Moment along Single Pile.

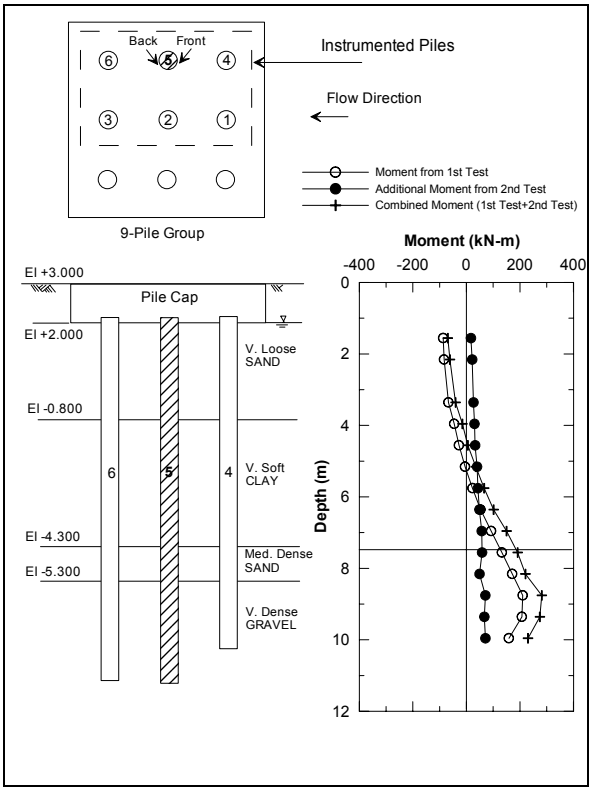

Figure 13. Moment along Pile No.5 of 9-Pile Group.

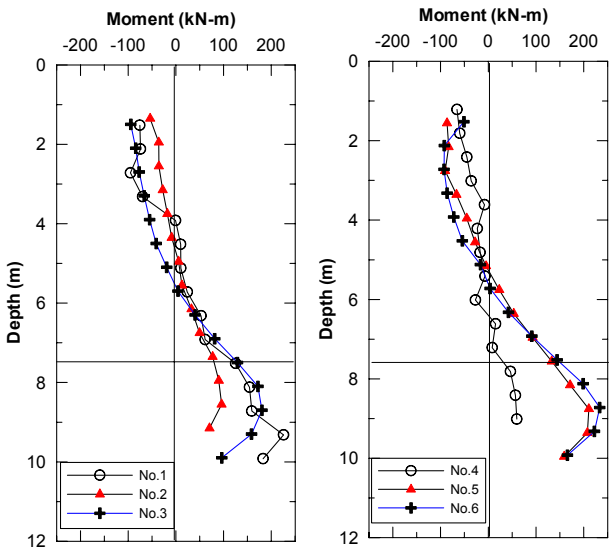

Figure 14. Moment Distribution of Each Pile in the 9-Pile Group (Data Obtained from 1st Experiment).

CONCLUSIONS

Based on the results obtained from two full-scale experiments, the following conclusions can be obtained:

- Controlled blasting successfully liquefied the soil and induced lateral spreading.
- The excess pore water pressure ratios exceeded 70% for the first experiment. The degree of liquefaction in the second experiment was lower than the first one with excess pore pressure ratios ranging between 30% and 80%, likely due to the soil condition in the second test being less susceptible to liquefaction.
- The average soil movements of the first experiment were about 35 cm to 40 cm, while about 9 cm to 22 cm of ground movements were observed in the second test.
- The total movements of the single pile, 4-pile group, and 9-pile group were 58 cm, 39 cm, and 34 cm, respectively.
- The movements of both transverse gas pipeline and electrical conduit were approximately the same.
- Observed moment distribution of the UCSD single pile indicated that global translation of liquefied soil layer provided insignificant force to the pile.
- Shadowing effect of the 9-pile group in liquefied soil was not observed.
- The single pile yielded at the end of the second experiment. Both 4-pile and 9-pile groups performed well during both experiments. Piles remained in elastic range with maximum moments of less than 70% of yield moment. No damaged was observed on piles to pile cap connection.
- All pipelines also performed very well without any yielding.

ACKNOWLEDGEMENT

The authors wish to express their sincere gratitude to the sponsors of the Performance of Lifelines Subjected to Lateral Spreading project, the PEER Lifelines Program with support from Caltrans, Pacific Gas & Electric and the California Energy Commission.

The assistance from Dr. Takehiro Sugano of Port and Airport Research Institute (PARI) and Professor Masanori Hamada from Waseda University(WU), the original leaders of this project, in providing a great opportunity for us to participate in this test, as well as effectively managing the project is gratefully acknowledged. Dr. Akio Abe (Tokyo Soil Research Co.) is acknowledged for providing the test specimens and facilitating the instrumentation work in Japan.

Loren Turner, Cliff Roblee and Tom Shantz from Caltrans' Division of New Technology and Research are gratefully acknowledged for their help in monitoring the movements of soil and lifelines using GPS equipments.

We would like to thank Andrea Martinez and Jeremy Allen, the undergraduate students, for their help in analyzing the data and preparing the figures in this paper.

REFERENCES

[1] Bartlett, S. F. and Youd, T. L., 1992b. "Empirical analysis of horizontal ground displacement generated by liquefaction-induced lateral spreads." *Tech. Rep. NCEER-92-0021*, National Center for Earthquake Engineering Research, Buffalo, N.Y., M. Hamada and T.D. O'Rourke (eds.), August 17.

[2] Seed, H. B., 1987. "Design problems in soil liquefaction." *J. Geotech. Engrg.,* ASCE, Vol. 113, No. 8, August, pp. 827-845.

[3] Youd, T. L., and Hoose, S. N., 1976. "Liquefaction during 1906 San Francisco Earthquake." *J. Geotech. Engrg. Div.*, ASCE, Vol. 102, No. GT5, May, pp. 425-439.

[4] Bardet, J. P., and Kapusker, M., 1993. "Liquefaction sand boils in San Francisco during 1989 Loma Prieta earthquake." *J. Geotech. Engrg.,* ASCE, Vol. 119, No.3, March, pp. 543-562.

[5] Clough, G. W., Martin, J. R., II, and Chameau, J. L., 1994. "The geotechnical aspects." *Practical Lessons from the Loma Prieta Earthquake*, National Research Council, National Academy Press, Washington, D.C., pp. 29-63.

[6] O'Rouke, M. J., and Pease, J. W., 1992. "Large ground deformations and their effects on lifeline facilities: 1989 Loma Prieta earthquake." *Case Studies of Liquefaction and Lifeline Performance During Past Earthquakes, Volume 2: United States Case Studies, Tech. Rep. NCEER-92-0002*, M. Hamada and T.D. O'Rourke (eds.), February 17, 85 pages.

[7] Abdoun, T. Dobry, R., and O-Rourke, T. D., 1997. "Centrifuge and numerical modeling of soil-pile interaction during earthquake induced soil liquefaction and lateral spreading," *Observation and Modeling in Numerical Analysis and Model Tests in Dynamic Soil-Structure Interaction Problems, Geotechnical Special Publication No. 64*, ASCE, New York, pp.64-70.

[8] Tokida, K., Iwasaki, H., Matsumoto, H., and Hamasa, T., 1993. "Liquefaction potential and drag force acting on piles in flowing soils," *Soil Dynamic and Earthquake Engineering*, Computational Mechanics, South Hampton, England, pp. 349-364.

[9] Hamada, M., and O'Rourke, T., Editors., 1992. *Case Studies of Liquefaction and Lifeline Performance During Past Earthquakes, Report No. NCEER-92-0001, Vol.1*, National Center for Earthquake Engineering Research, Buffalo, N.Y.

[10] O'Rouke, T. D., 1996. "Lessons learned for lifeline engineering from major urban earthquakes," *Proceedings, Eleventh World Conference on Earthquake Engineering, Elsevier Science Ltd*., 18 p.

[11] Ashford, S. A., Rollins, K. M., Bradford, S. C., Weaver, T. J., and Baez, J. I., 2000. "Liquefaction mitigation using stone columns around deep foundations: full-scale test results," *Soil Mechanics 2000, Transportation Research Record No. 1736*, TRB, Washington D.C., pp.110-118.

[12] Turner, L. L., 2002. *Measurements of Lateral Spread Using a Real Time Kinematic Global Positioning System*, California Department of Transportation Division of New Technology &Research, April 2002, 94 pages..

[13] Ashford, S. A., Rollins, K. M., 2002. *TILT: Treasure Island Liquefaction Test Final Report, Report No. SSRP-2001/17*, Department of Structural Engineering, UCSD.

Stiffness and Damping of Soil-Pile System in Liquefaction Process

Hatsukazu MIZUNO[1] and Tsutomu HIRADE[2]

ABSTRACT

Shaking table and oscillator tests of soil-pile system are presented. A model of piles and basement (pile cap) models was set up in saturated sand in a big shear box. The tests were composed of shaking table tests and oscillator tests. The shaking table tests clarify dynamic behavior of soil-pile system in horizontal soil in liquefaction process. While the dissipation process of excess pore water pressure in the soil was taking place following the shaking table excitation, the model was exited in sweep mode by an oscillator. Based on the oscillator test results, stiffness and damping of the model are evaluated at various excess pore water pressure ratios and frequencies. Horizontal subgrade coefficients of the pile are also discussed.

INTRODUCTION

Previous earthquakes caused significant pile damage in Japan. The earliest pile damage reports are from 1923 Kanto Earthquake. About thirty cases of pile damage were observed during the period from the 1923 Kanto earthquake to 1983 Nihonkai-Chubu Earthquake. Mizuno(1) discussed the pile damage patterns in these earthquakes and categorized the external direct causes of pile damage such as liquefaction, inertial effects of superstructure to foundation and movement of embankment or filled soil. In the 1995 Hyougoken-Nanbu Earthquake, hundreds of pile damage cases were found. The number of pile damage causes in this earthquake was much larger than the previous ones. However, damage patterns of piles were basically the same as the ones in previous earthquakes Japan, although pile construction methods were changed utterly during about eighty years since the 1923 Kanto Earthquake.

Among the external direct causes of pile damage, liquefaction and liquefaction-induced phenomena such as soil spreading is the main focus of this paper and considered as a soil-structure interaction problem. The objectives of this paper are to clarify dynamic behavior of pile foundations and to evaluate soil properties in liquefaction process.

The experiments reported herein were performed jointly with other teams in the liquefaction related project entitled “Enhancement of Earthquake Performance of Infrastructures Based on Investigation into Fracturing Process”, Special Coordination Funds for Promoting Science and Technology (SCF, 1999-2003 fiscal year). A series of cooperative experiments were performed using NIED (National Institute of Earth Science and Disaster Prevention), BRI

1 Hatsukazu MIZUNO, Research Coordinator of Building Technology, Building Research Institute, 1 Tachihara, Tsukuba City, 305-0802 Japan.

2 Tsutomu HIRADE, Senior Research Engineer, Building Research Institute, 1 Tachihara, Tsukuba City, 305-0802 Japan.

(Building Research Institute) shaking table in the project. Seven institutions joined the experiments-: NIED, BRI (Building Research Institute), Waseda University, PARI (Port and Airport Research Institute), NIRE (National Institute for Rural Engineering), AIST (National Institute of Advanced Industrial Science and Technology) and DPRI (Disaster Prevention Research Institute) of Kyoto University.

TEST SETUP

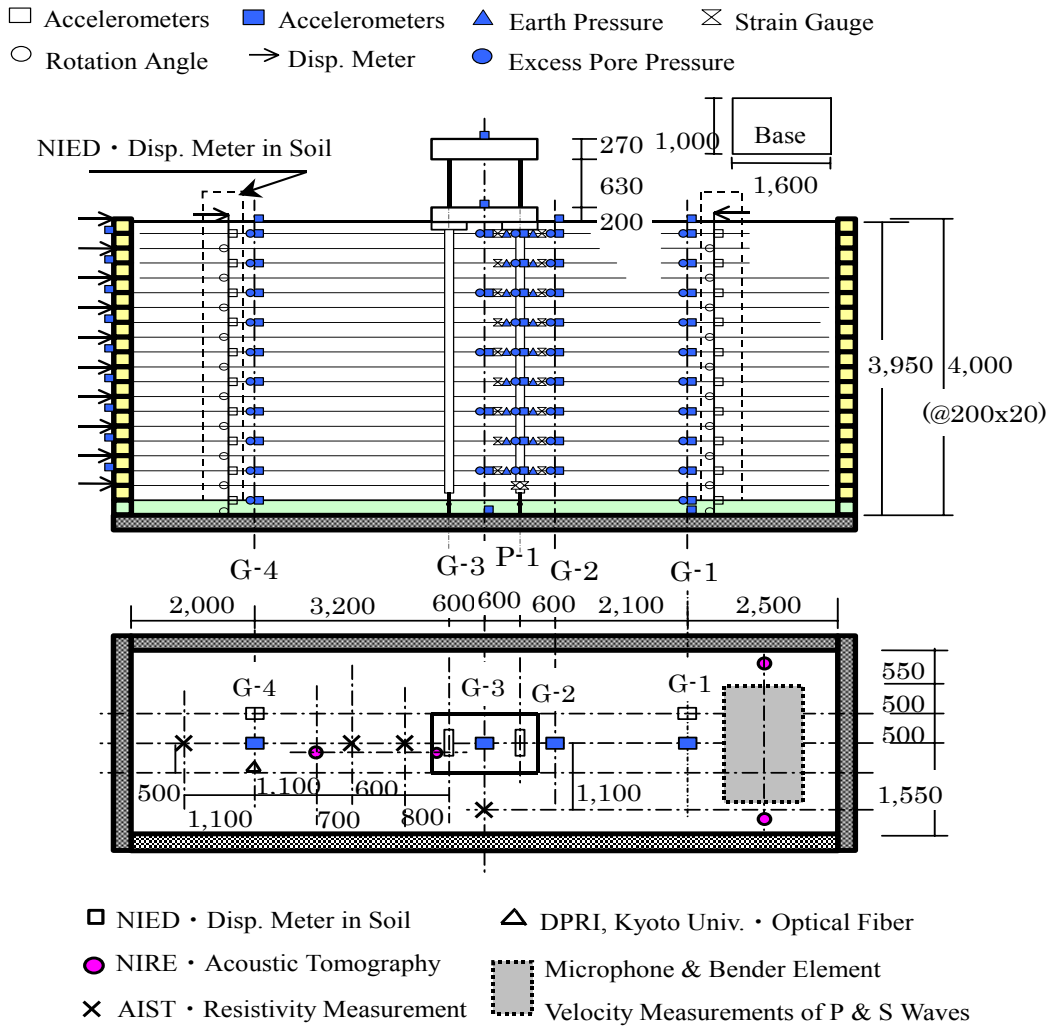

Figure 1. Test setup

Figure 1 shows the test setup including sensor distribution in a big shear box on NIED shaking table. The development and improvement of the box is summarized in Appendix A. The height of the big shear box was 4 meters in the tests. NIED, NIRE, AIST, and DPRI did jointly some measurements using their respective recently developed instruments. Saturated Kasumigaura sand was used for the test soil models herein and Appendix B. The soil model was prepared by pouring sand into water through vibrating screen in water. Mechanical conditions at pile head and pile tip are fixed and hinged, respectively. The fundamental natural

frequency of the building model was adjusted to 5Hz in base-fixed condition. Table I and Table II present test cases and soil conditions including heights of the model soil, respectively.

TABLE I. TEST CASES

Test Case & Sub index		Table Input	Oscillator Test in dissipation process	Water level
Case 1 Soil-Pile Model	-1	Port island G.L.-32m, NS Max.20gal		G.L.-0.5m
	-2	Port island G.L.-32m, NS Max.50gal		
	-3	Port island G.L.-32m, NS Max.100gal		
	-4	Port island G.L.-32m, NS Max.150gal	○	G.L.
Case 2 Soil-Pile Model	-1	Port island G.L.-32m, NS Max.20gal		G.L.
	-2	Sin Wave 3Hz, Max.40gal	○	
	-3	Sin Wave 3Hz, 100gal	○	
Case 3 Soil-Pile-Structural Model	-1	Port island G.L.-32m, NS Max.20gal		G.L.
	-2	Port island G.L.-32m, NS Max.300gal	○	
	-3	Port island G.L.-32m, NS Max.800gal	○	

TABLE II. SOIL CONDITIONS

Test Case & Sub Index		Soil Height (m)	Dry Density ρd (kN/m^3)	Rel. Density Dr (%)
Case 1	-1	3.952	14.9	46.2
	-2			
	-3	3.947	14.9	46.7
	-4	3.875	15.2	54.5
Case 2	-1	3.827	15.3	59.8
	-2			
	-3	3.801	15.4	62.6
Case 3	-1	3.762	15.6	66.8
	-2			
	-3	3.689*	15.9*	74.7*

*Values After Shaking

The big difference between the tests explained in the main body of this paper and the tests shown in Appendix B is the preparation of the soil model in the box. In the tests of Appendix B (the box height: 6m), the model soil in the box was reused several times by injecting pressurized water from the bottom of the box, and thereby boiling the liquefied and settled soil. In the tests in the main body of the paper, the model soil was prepared by pouring sand into water through vibrating screen in water and densifying the sand using shaking without sand boiling.

In each case of the tests, different shaking table excitations were used, as shown in Table I. In each case of the earthquake excitations, the North-South (NS) component acceleration recording at GL-32m depth at Port Island, Kobe during 1995 Hyougoken-Nanbu earthquake was used by scaling to different accelerations. The maximum peak acceleration, 800gal was used in case 3.

One important point of these works is the oscillator tests during and after table shaking. The shaking table tests were done to clarify dynamic behavior of soil and pile in liquefaction process. The oscillator tests during and after the table shaking were done to determine the relation between excess pore pressures and subgrade reaction coefficients of pile, and to evaluate the stiffness and damping of soil-pile system.

DYNAMIC BEHAVIOR OF SOIL IN LIQUEFACTION PROCESS

DYNAMIC CHARCTERISTICS OF SOIL

Dynamic characteristics of tests 1-1, 2-1, 3-1 at 20gal earthquake table excitation, Fourier spectrum ratios of the test soils are summarized in Figure 2. Figure 3 shows fundamental natural modes of test soils. In case 3 with building, a valley of the characteristics is recognized around 5Hz, fundamental natural frequency of building. The valley is caused by energy absorption due to resonance of building model.

CASE 1

In the test 1-2 shown in figure 4, earthquake excitation with peak acceleration 50gal, excess pore water pressures did not increase to excess pore pressure ratio 1.0, and no liquefaction near to soil surface was observed. In test 1-3 shown in Figure 5, earthquake excitation with peak acceleration 100gal, excess pore water pressures reached excess pore pressure ratio 1.0.

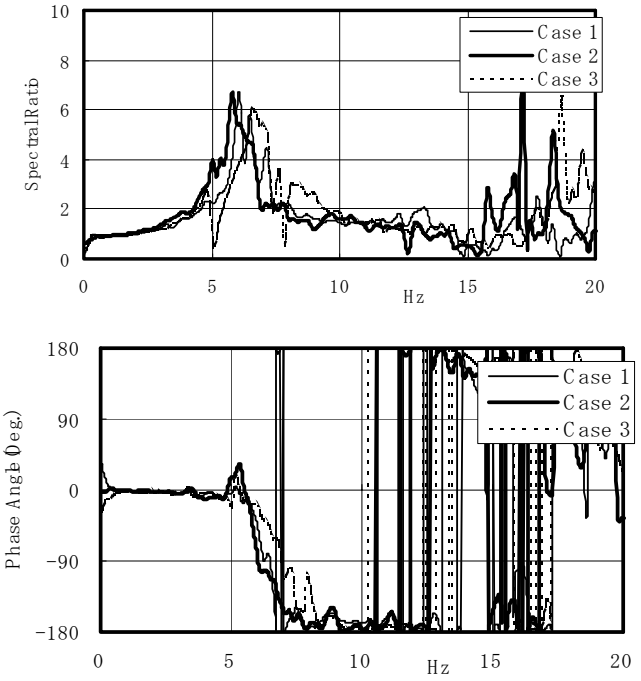

Figure 2. Dynamic characteristics of soil (20gal earthquake excitation)

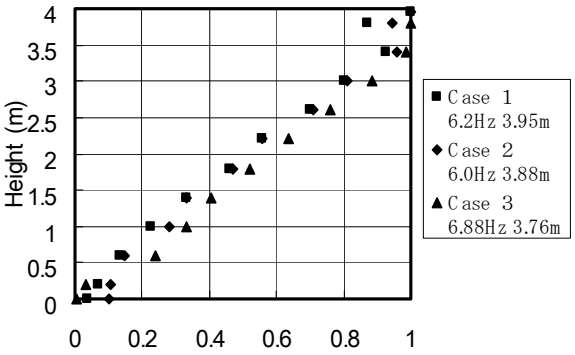

Figure 3. Fundamental natural modes of cases (20 gal earthquake excitation)

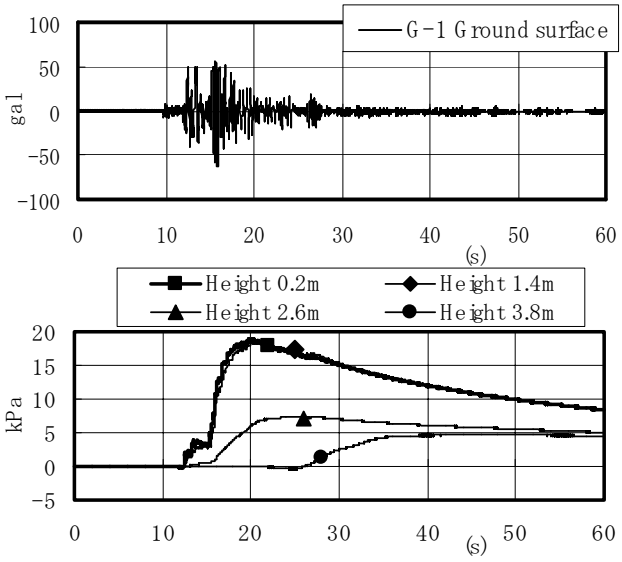

Figure 4. Test 1-2 (50gal earthquake excitation)

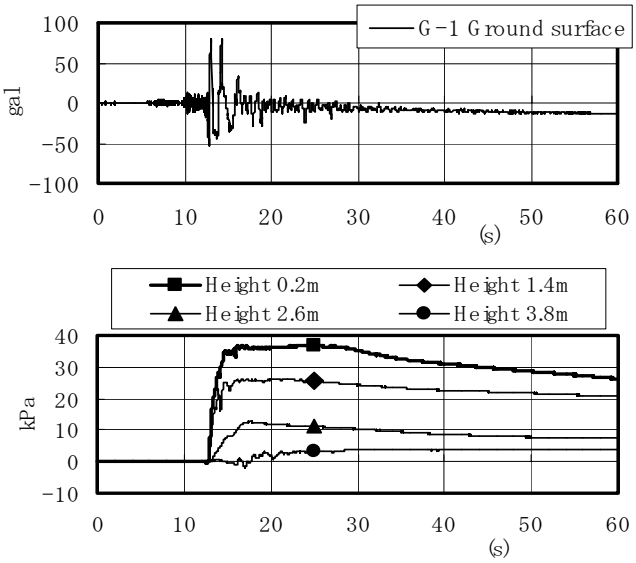

Figure 5. Test 1-3 (100gal earthquake excitation)

CASE 2

In the test 2-3, harmonic 3Hz excitation with 100gal amplitude, accelerations and excess pore pressures in G-1 line (pseudo free field far from pile model) are demonstrated in Figure 6. Accelerations on the soil surface become small, due to liquefaction, compared with table input accelerations.

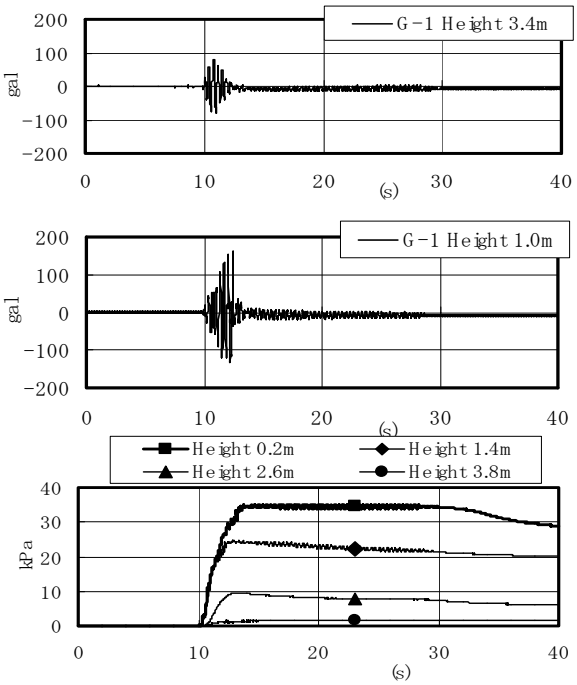

Figure 6. Test 2-3 (Sin wave 3Hz 100gal excitation)

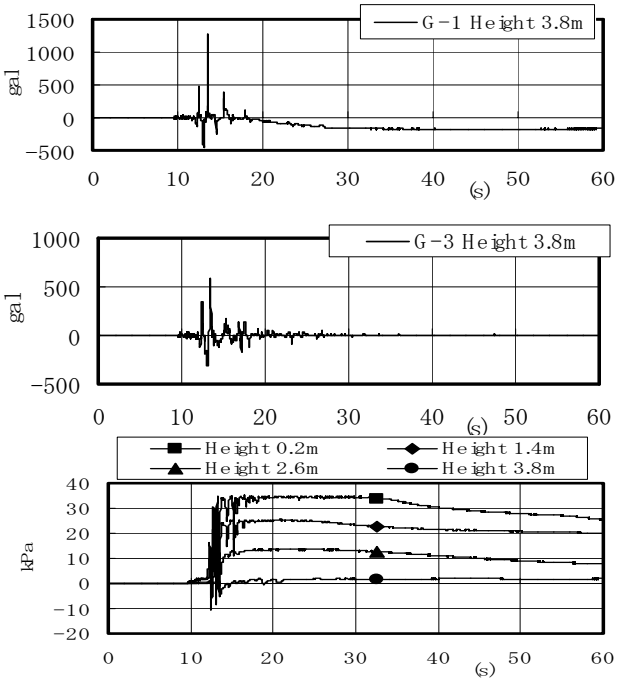

Figure 7. Test 3-3 (800gal earthquake excitation, Building pile model)

CASE 3

In the test 3-3, earthquake excitation with peak acceleration 800gal, accelerations in the soil, at G-1 line (pseudo free field far from pile model) and G-3 line (among piles), and excess pore pressures at G-1 line are demonstrated in Figure 7. At the buildup stage of excess pore pressures, fluctuation of the pressures is observed due to inertia of building model. In comparison of excess pore pressures between G-1 line and G-3 line, excess pore pressures among piles are small due to constraint effects of base.

OSCILLATOR TESTS

Figure 8 shows dissipation process of excess pore pressure on G-4 line after Test 1-4, 150gal earthquake excitation by the table. For the duration of T_1, T_2, T_3, T_4 and T_5 in the figure, unbalanced mass type oscillator excited the base on piles by increasing and decreasing frequencies (sweep up and sweep down). Eccentric mass was adjusted to 100kgfcm. Dynamic forces by the oscillator had almost no influence on the dissipation process of excess pore pressures as shown in the figure. Figures 9 and 10 present average excess pore pressures

on G4 line and on pile (P1) for the duration of T_1, T_2, T_3, T_4 and T_5, respectively. The straight line in the figures corresponds to the overburden pressures.

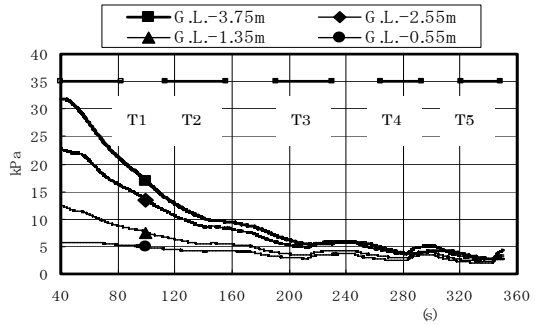

Figure 8. Oscillator tests in dissipation process

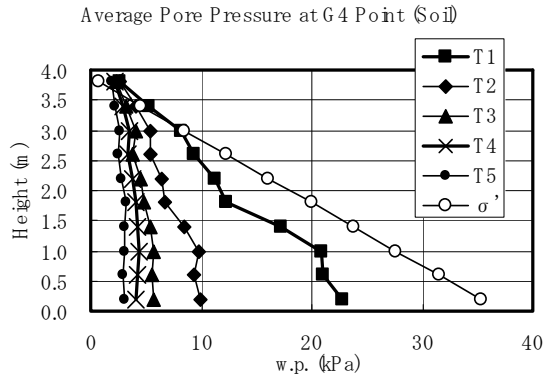

Figure 9. Average pore pressures on G-4 line

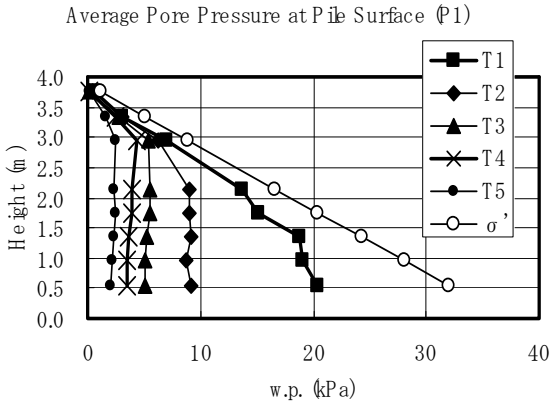

Figure 10. Average pore pressures on pile P1

Figure 11 shows displacement transfer characteristics of the excited base derived from base acceleration. The values in parenthesis represent the excess pore pressure ratio derived from the average value of the excess pore pressures on P-1 line of the pile. The values of the excess pore ratios change from 1.0 to 0.7. Peak frequencies and peak values decrease from the duration of T_1 to the duration of T_5. That indicates change of properties of saturated soil. Peak frequencies derived from phase characteristics in the figure are 4.6Hz, 6.1 Hz, 7.4 Hz, 8.4 Hz and 9.0 Hz, respectively, and moves from lower frequencies to higher frequencies with progress of pressure dissipation. Peaks near to 5 Hz are considered influence of fundamental natural frequency of model soil.

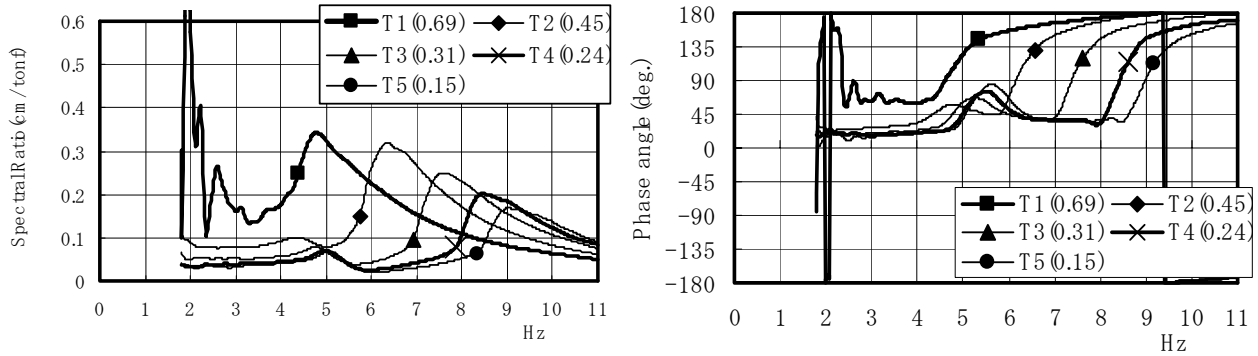

Figure 11. Transfer function of base displacement

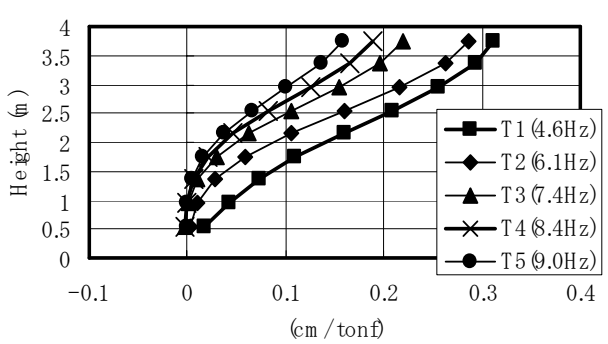

Figure 12. Displacement modes of pile (cm/tonf)

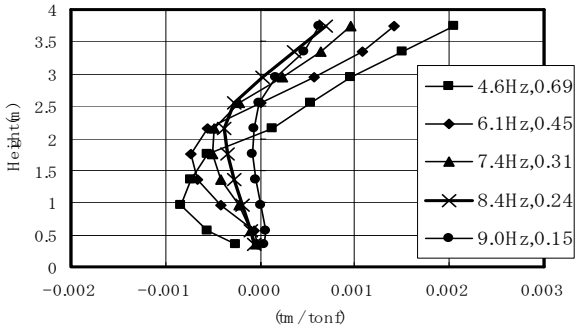

Figure 13. Pile bending moments

Figure 12 illustrates displacement natural modes derived from accelerations at peak frequencies on the pile, P-1. Model soil is confirmed to vibrate in fundamental natural modes in dissipation process of excess pore pressures. Figure 13 shows distribution of pile bending moments at peak frequencies. The points of maximum bending moments in the soil move from the height about 1 meter to the height about 2 meters during the progress of pore water pressure dissipation.

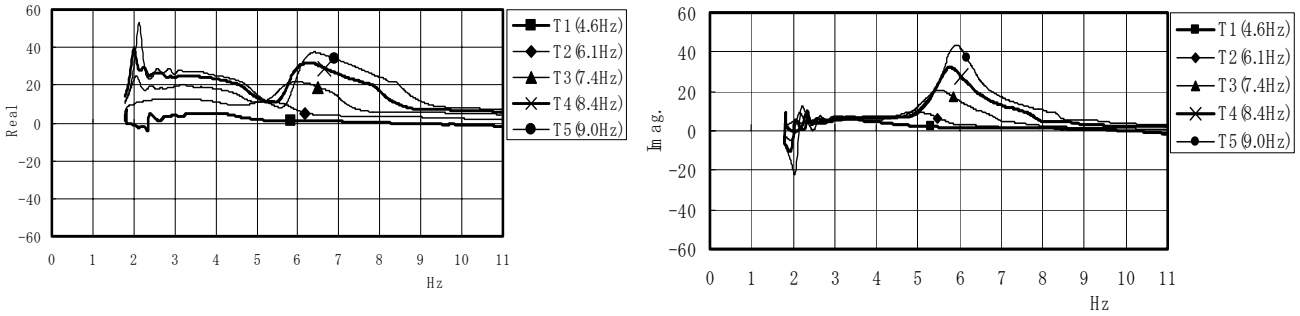

Figure 14. Dynamic impedance (Horizontal)

Figure 14 presents horizontal impedances derived from base displacements. Real parts and imaginary parts of the impedance correspond to stiffness and damping of base-pile-soil system. At T_1 stage with the average excess pore ratio 0.69**,** stiffness and damping are both very small or near to zero at all frequencies. It is important that damping is very small at the higher excess pore pressure ratios from seismic design viewpoint. As the excess pore pressures dissipate, stiffness increases, and fundamental natural frequencies of model soil come into being again near to the frequency 6Hz. It is pointed out that damping also increases with peaks in real parts around 6 Hz.

Figure 15 shows dynamic earth pressure distribution on outside and inside of pile at fundamental natural frequencies. As the excess pore pressures dissipate, maximum values of the pressure move to the upper positions in model soil.

ADDITIONAL OSCILLATOR TESTS

Soil properties at average excess pore pressure ratios higher than 0.69 in Test 1-4 were needed. In tests before Test 2-3, oscillator began to rotate after shaking table excitation. Timing of oscillator start was changed. Oscillator started at frequency 1.8Hz before shaking table excitation, and continued after shaking table excitation. Figure 16 presents displacement

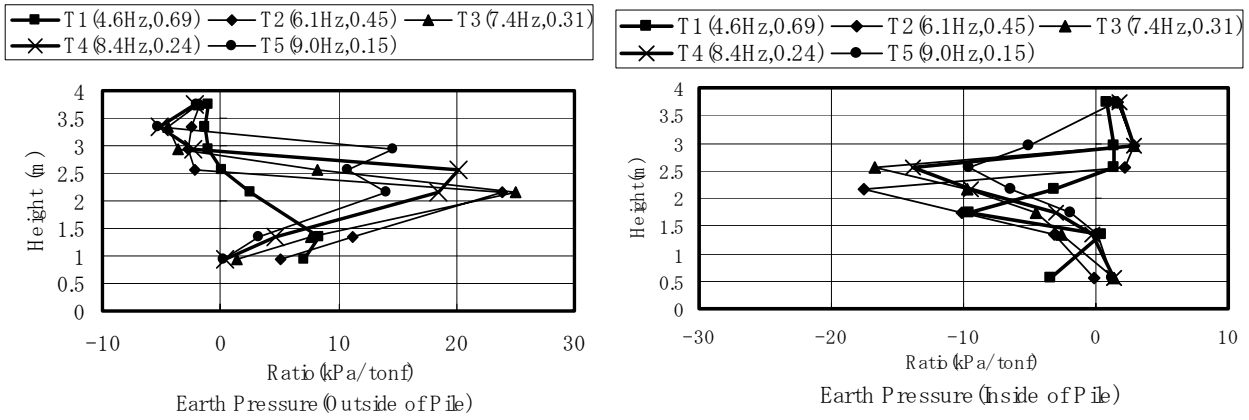

Figure 15. Earth pressures (Left outside, Right inside of pile)

transfer characteristics of the excited base in Test 2-3 just after shaking table excitation stopped. Average value of excess pore pressure ratios on pile, P-1 is 0.82. Judging from phase angle, 90 degree, fundamental natural mode of model soil is 2.7 Hz. However, the amplitude ratio in Figure 16 is almost flat and very small. Figure17 presents dynamic earth pressures distribution derived from the difference pressure on outside and on inside of pile, by adding this data at T_1 of Test 2-3 to those data in Test 1-4. As the excess pore pressures dissipate, maximum values of the pressure mover to the upper positions in model soil. Movement of maximum values of the pressures to the upper positions is considered due to recovery of soil stiffness from the lower positions of model soil.

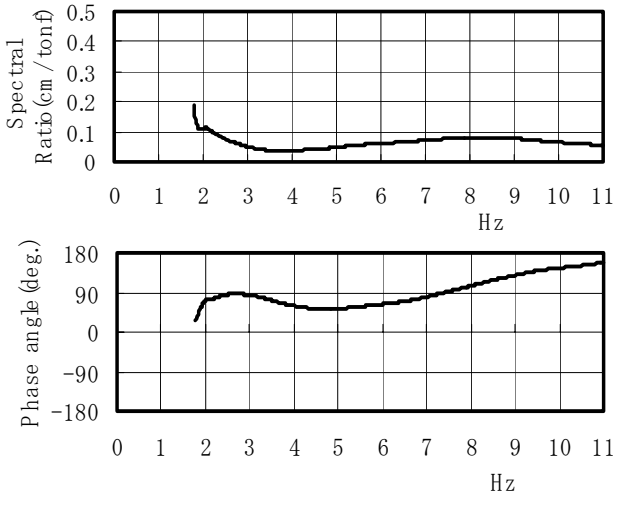

Figure 16. Transfer function of base displacement just after table excitation (Test 2-3)

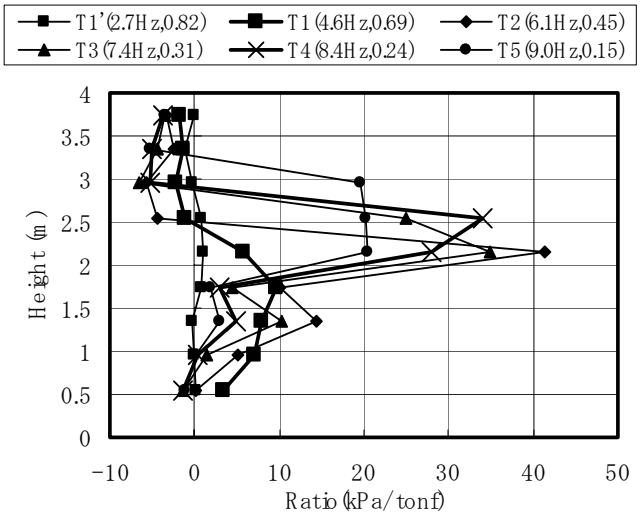

Figure 17. Earth pressures of pile (Difference pressure of outside & inside of pile)

RELATIONSHIP BETWEEN SUBGRADE REACTION COEFFICIENTS AND EXCESS PORE PRESSURES

Figure 18 summarizes distribution of subgrade reaction coefficients. Figure 19 shows relation between subgrade reaction coefficients and average values of excess pore ratios on pile.

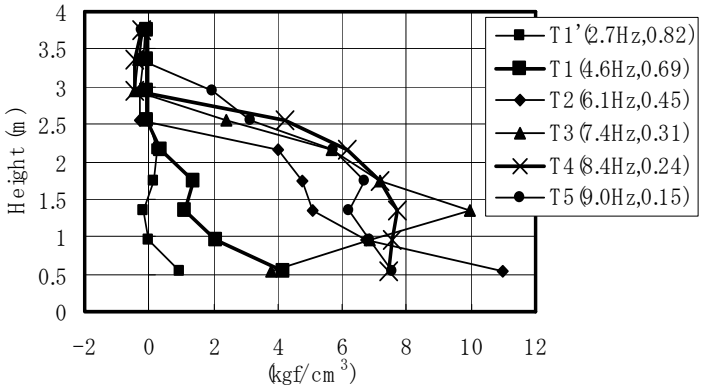

Figure 18. Subgrade reaction coefficients

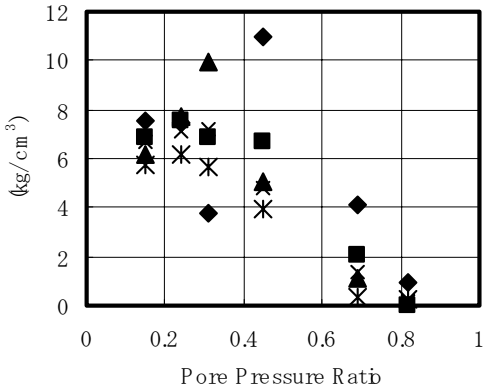

Figure 19. Relation of pore pressure ratio and subgrade reaction Coefficient

CONCLUDING REMARKS

Some concluding remarks are as follows;

1. Combination of large-scale shaking table tests and oscillator tests is an effective tool for clarifying dynamic behavior and the change of saturated soil properties in liquefaction process from viewpoint of soil-structure interaction. Another merit of large-scale shaking table tests is to be able to use prototype of soil and water, and large-scale pile model. As a result, bending moments, earth pressures, etc can be determined.

2. Oscillator tests can clarify some change of soil properties, especially stiffness and damping in dissipation process of excess pore water pressures. When average pore pressure ratio is high, stiffness and damping of soil are very small. With progress of the dissipation from the lower part to higher part of the soil, stiffness and damping of soil both increase, and the fundamental natural frequency of the soil recover.

REFERENCES

[1] H.Mizuno, "Pile Damage During Earthquakes in Japan (1923-1983)," Geotechnical Special Publication, No.11, ASCE, Dynamic Responses of Pile Foundation – Experiment, Analysis and Observation, pp53-78, April, 1987

[2] H.Mizuno, T.Hirade and M.Iiba, "Dynamic Behavior of Pile Foundation – Dynamic Characteristic Determination by Oscilltor Tests," The Third Seminar of "Enhancement of Earthquake Performance of Infrastructures Based on Investigation into Fracturing Process", pp253-258, February 2002

APPENDIX A – BIG SHEAR BOX

BIG SHEAR BOX

Mizuno, BRI and Minowa, NIED carried out shaking table tests of reduced model of base-pile system in liquefaction process of saturated sand about ten years ago. The model was set up in saturated sand soil in small shear box (Approximate height 1m: length 2m: width 1m) on NIED shaking table. Some oscillator tests of pile foundation were done for clarifying the basic relation among excess pore pressure, pile reaction and pile bending moments in dissipation process of excess pore pressure after shaking table excitation. We could not gain satisfied results because of the very rapid increase in shaking table excitation, and rapid dissipation after shaking table excitation in gravity field.

Ogawa and Minowa, NIED, Science and Technology Agency, prepared a plan during the years between 1994 and 1997 to construct a big shear box (Height 6m, Length 12m, Width 4m) , including water injecting and sand boiling facilities for reuse of test soil, and facilities for removing soil from the box. The maximum deformation at the top of the box was designed to be 1.5 meter. The mass ratio of the shear box and soil is evaluated from 0.09 to 0.12. Then, BRI had joined another project of the Construction Technology, Research and Development (Ministry of Construction) entitled "Development of technology for earthquake disaster prevention in large metropolitan areas" from 1992 annual year.

As a part of the projects, in December, 1995, in an intermediate stage of a big shear box completion (box height was about 4m), BRI carried out shaking table tests of base-pile system and building-pile system in dry sand soil, and also as preliminary test, in saturated sand soil at NIED shaking table. Layers of the box were originally designed to slide on fluorocarbon polymers plates powdered by molybdenum chloride. However, even in the condition of no soil, the box did not move with the shaking less than 300gal shaking. To solve the problem, steel pipes of 200 mm diameter were inserted among layers of the box. As a result, the empty box could move when accelerations were more than 70 gals shaking.

After completion of the shear box in 1996, BRI carried out shaking table tests and oscillator tests of base-pile system in saturated sand to clarify the dynamic behavior and change of soil properties in liquefaction process. In 1997, NIED welded on web of H-shape steel layers to increase clearance and to decrease friction among the layers of the box[(1)]. This improvement enabled the layers of empty box move at shaking accelerations as small as 4 gal.

The big shear box has been used about ten times for various test objectives since December 1995. In 2001, seven research institutions carried out shaking table tests to clarify the behavior of lateral spread after liquefaction, pile behavior subjected to lateral land spread, and dynamic behavior in liquefaction process. The tests were part of the project entitled "Enhancement of Earthquake Performance of Infrastructures Based on Investigation into Fracturing Process", Special Coordination Funds for Promoting Science and Technology (SCF).

REFERENCES

[1] K.Ishihara, T.Kagawa, N.Ogawa, C.Minowa K.Sakai and A.Abe, "Design of Large-scale Liquefaction Experiment System," Winds and Seismic Effects, Proceedings of the 28th Joint Meeting oh The US-JAPAN COOPRRATIVE PROGRAM IN NATURAL RESOURCES PANEL ON WIND AND SEISMIC EFFECTS, , NISP SP 904, pp327-329, U.S. Department of Commerce, August 1996

APPENDIX B SHAKING TABLE TESTS IN 1995 AND 1996

This study was conducted as a part of the project entitled "Development of technology for earthquake disaster prevention in large metropolitan areas" (1992-1996 fiscal year, Ministry of Construction) in collaboration with researchers and engineers of universities and private companies. On halfway of the project, we encountered the 1995 Hyogoken-Nanbu earthquake, and found a lot of seismic damage of piles. Shaking table tests utilizing big shear box were planned and prepared before the

earthquake.

The objectives of the tests were to clarify dynamic behavior of pile-soil system, and to evaluate change of soil properties in liquefaction process. Height, length and width of the big shear box were about 6m, 11.6m and 3m, respectively. It is, in principle, impossible for liquefaction process to satisfy similitude ratios in reduced models of prototype water-saturated sands in centrifugally accelerated field. A main reason for using the big shear box was to carry out the experiment in near-to full-scale models of water-saturated sands and piles. The shaking table used in the experiment is large shaking table (maximum specimen weight is 500 tonf) of National Research Institute for Earth Science and Disaster Prevention, Scientific Technology Agency.

Test in 1995

Kasumigaura sand was used for the test soil model. The shaking table test of surface-dry sand deposit (depth: 3.48m) clarified dynamic properties of the soil. Random excitations with maximum acceleration of 60 gals were applied. In the case of surface-dry sand, the mode shape is linear. That means that shear stiffness of soil deposits is proportional to a square root of overburden pressure of soil, namely to a square root of depth. If the shear stiffness is constant with depth, its fundamental mode shape is concave downward in a shape of cosine function. If the shear stiffness is proportional to depth, its fundamental mode shape is convex upward, and motion near to the soil surface increases

Test in 1996

The dimensions of soil deposit in the big shear box used in the experiment were about 6m, 11.6m and 3.lm in height, length and width, respectively. A model of pile foundation was made of steel and was 40cm, 10cm and 5.82m in width, thickness and length, respectively. Table BI shows a series of the experiment cases with their aims. The experiments included shaking table tests of earthquake random excitations, static pulling tests and oscillator tests. In the cases 1, 2 and 3, the aims are to clarify the behavior of pile foundation during liquefaction, and to check soil deposit making, namely dropping sand into water and boiling. In the case 4, the aim is to investigate the effect of a countermeasure against liquefaction, one of excess pore water pressure dissipation method (vertical drains). In the case 5, the aim is to clarify the effect of low ground water table on liquefaction and pile behavior. In each case, an earthquake excitation with 500gals peak acceleration and a random excitation with 30gals peak acceleration were carried out. A NS component acceleration record at GL-32m depth at Port Island, Kobe during 1995 Hyougoken-nanbu earthquake was used in earthquake excitation. Figure B1 shows the setup and measurement points in the experiments. Groundwater levels of all cases and a position of vertical drains in case 4 are also shown in the figure. In the soil deposit, accelerometers and excess pore water transducers were installed on lines G-1 to G-5. Accelerometers, excess pore water transducers and earth pressure transducers (on the both sides perpendicular to vibration direction) were set on pile (P-1). Strain gauges were attached on pile surfaces (P-1 and P-2) to measure bending moments and shear forces. Accelerometers and displacement transducers were installed in the foundation and the shear box.

REFERENCES

[1] H.Mizuno, M.SUGIMOTO, T.MORI, M.IIBA and T.HIRADE, “Dynamic Behavior of Pile Foundation in Liquefaction Process - Shaking Table Testd Utilizing Big Shear Box - ,” Proceedings of The 12th World Conference on Earthquake Engineering (CD) Paper Index Number 1883, January 2000

[2] T.HIRADE, H.Mizuno, M.IIBA, M.SUGIMOTO and T.MORI, ”Oscillator Tests of Pile Foundation in Dissipation Process of Excess Water Pore Pressure After Liquefaction Dynamic ,” Proceedings of The 12th World Conference on Earthquake Engineering (CD) Paper Index Number 1744, January 2000

TABLE BI. TEST SERIES AND OBJECTIVES (Saturated Sand, H: 6m)

Test Case & Test Ground Condition	Shaking Table Test (Input)				Static Load (before shake table)	Oscillator Test	Object
	Random 30gal	Earthquake Shaking, gal (Port island GL-32m, NS)					
		500	200	re-500			
Case1 Drop of Sand into water. Water level G.L.	$O_{2,5}$	O_3			$O_{1,4}$	O_7 In dissipation process	To check liquefaction. Seismic behavior of soil & foundations
		O_6*350gal,time scale=1/2					
Case2 Produced by boiling, Water level G.L.	$O_{2,6}$	O_3		O_7 *600 gal	$O_{1,5}$	O_4 In dissipation process	Seismic behavior of soil & foundations (Comparison with Case1)
Case3 Reproduced by boiling, Water level G.L.	$O_{3,7,9}$	O_4	O_8	O_{10}	$O_{2,6}$	$O_{1,5}$ Before earthquake shaking.	Reappearance of seismic behavior of soil & foundations (Comparison with Case2)
		Measurement of dissipation..					
Case4 Reproduced by boiling with drain, Water level G.L.	$O_{2,4,6}$	O_3	O_5	O_7	O_1		Seismic behavior of soil & foundations in condition under the drain (Comparison with Case3)
		Measurement of dissipation..					
Case5 Reproduced by boiling, Water level G.L.-1.4m	$O_{2,6,7}$	O_3	O_6	O_8	$O_{1,5}$	O_4 In dissipation process.	Seismic behavior of soil & foundations with low water level (Comparison with Case2,3)
		Measurement of dissipation					

Suffix of O : Test Order

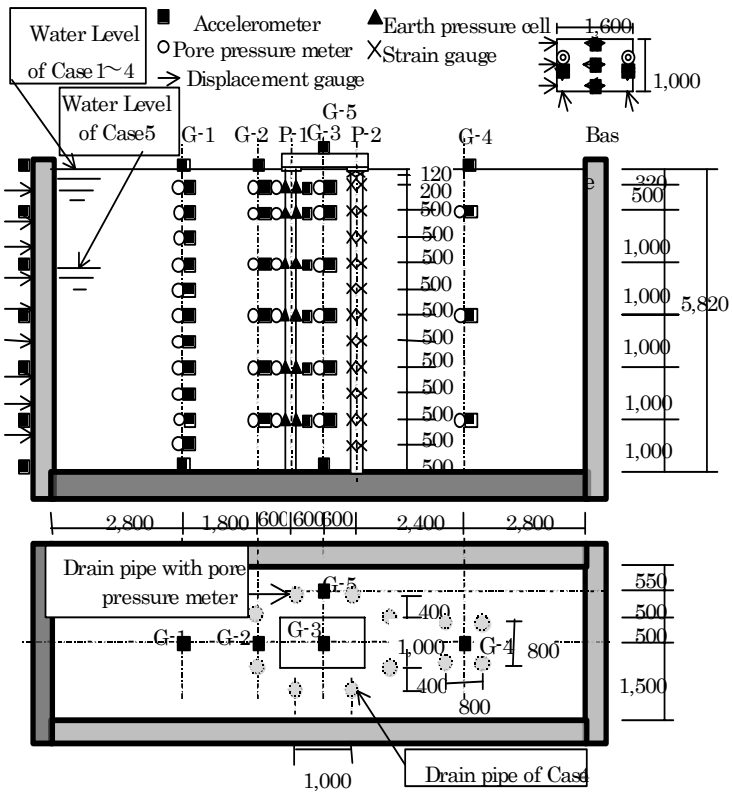

Figure B1. Test setup

TABLE BII. SOIL CONDITIONS

Test Case	Surface Level(m)	Dry density (g/cm^3)	Void ratio	Wet density (g/cm^3)	Relative density (%)	Water Level(m)
1	5.82	1.50	0.81	1.95	38.7	surface
2	5.65	1.59	0.71	2.00	63	surface
3	5.54	1.62	0.68	2.02	71.7	surface
4	5.52	1.62	0.67	2.03	73.3	surface
5	5.39	1.66	0.64	2.05	83.3	surface−1.4

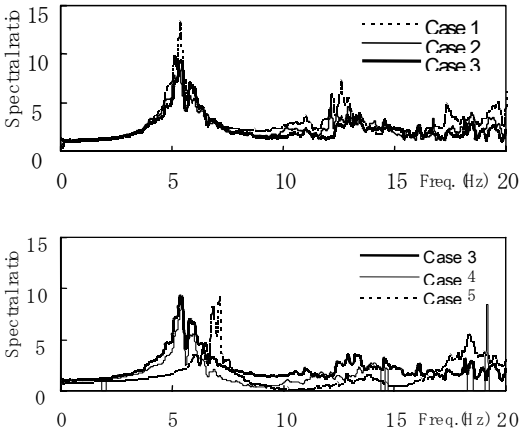

Figure B4. Spectral ratios, random shaking (30gal, H: 6m)

Performance of Retrofitted Pile Foundations Subjected to Seismically Induced Lateral Spreading

Tarek Abdoun, Yingjuan Wang and Ricardo Dobry

ABSTRACT

Experiences from earthquakes and centrifuge models have shown the great importance of the shallow nonliquefiable soil in increasing the forces and moments imposed on the pile cap and pile foundation subjected to liquefaction-induced lateral spreading. This paper focuses on evaluating retrofitting strategies, with emphasis on the placement of a soft or frangible material near the foundation in the shallow nonliquefiable layer. While this shallow soft material reduces the stiffness and the strength of the pile foundation with respect to the superstructure inertia forces, it constitutes an extremely effective way to mitigate the effect of lateral spreading cases in which the resistance to inertia is provided by other foundation elements are one area of application of the proposed retrofitting strategies. Results of three centrifuge tests, Models 2, 2r1 and 2r2, are presented to illustrate the effectiveness of the implemented retrofitting method.

The experimental results for each of the centrifuge pile models are reviewed and compared. After implementing the proposed retrofitting strategies, a dramatic reduction in the maximum bending moment is observed at the upper boundary of the liquefied layer (2 m depth). A reduction of up to 35% in the measured maximum bending moment is also observed at the lower boundary of the liquefied layer (8 m depth). These significant reductions in measured pile maximum bending moments in Model 2r, together with the associated reduction of up to 50% in the measured pile head displacement, demonstrate the effectiveness of the implemented retrofitting method

Tarek Abdoun, Research Assistant Professor, Rensselaer Polytechnic Institute, JEC 4049, 110 8th street, Troy, NY 12180, USA.
Yingjuan Wang, Project Engineer, Mueser Rutledge Consulting Engineers, 225 West 34th St., New York, NY 10122, USA.
Ricardo Dobry, Professor, Rensselaer Polytechnic Institute, JEC 4049, 110 8th street, Troy, NY 12180, USA.

INTRODUCTION

Earthquakes are among the major natural disasters. Case history indicates that in most large earthquakes soil liquefaction-related failures have occurred. For instance, the 1971 San Fernando, California earthquake caused more than five hundred million in damage [1]. In 1976, the Tangshan, China earthquake resulted in collapse and severe damage of many buildings and in the death of several hundred thousand people [1]. The 1995 HyogoKen Nanbu earthquake in Kobe, Japan, caused more than one hundred billion in total damage. The recent Turkey, Taiwan and Greece 1999 earthquakes also caused tremendous destruction. In all these earthquakes, much of the damage was related to liquefaction and associated induced lateral spreading.

Evaluation of case history and physical models reveals the significance of several factors influencing the deformation of deep foundations as well as bending moments and cracking of damaged piles. These factors include: free-field permanent lateral ground displacement; thicknesses and properties of soil strata penetrated by the piles; and the geometry and properties of the pile foundation. The observed damage and cracking to the piles is often concentrated at the upper and lower boundaries of the liquefied sand layer where there is a sudden change in soil properties ([2], [3], [4], [5], [6] and [7]), or at the connections between pile and pile cap (e.g., [2] and [8]).

A series of centrifuge tests were conducted earlier to study the great importance of the shallow nonliquefiable soil in increasing the bending response of the pile foundation ([5], [6] and [7]). This paper presents a promising rehabilitation approach of existing foundations is to replace the shallow soil in a trench around piles and pile cap by a soft material that will yield under constant lateral soil forces (Figs. 1b &1c). This would decrease both bending moments and foundation deformations while allowing the ground lateral spreading to take place without interference from the foundation. As this retrofitting scheme also decreases the lateral resistance of the foundation to inertial loading, a desired material should remain resilient under the transient inertial loading while yielding to static force. In this study, the trench surrounding the foundation will be filled with soft clay. Trenches may be located directly around the foundation (Fig. 1b) or may be located at some distance from the foundation so as to increase the resistance to inertial loading (Fig. 1c).

This paper presents the results of three centrifuge experiments performed to study lateral spreading and its effect on single pile foundations for retrofitted and non-retrofitted piles (Fig. 1). The objectives of this study are accomplished mainly using the centrifuge experiments and corresponding interpretations and comparisons. These objectives can be summaries as follows: i) study the three-layer lateral spreading soil response in the free field during earthquake shaking including the magnitude and profile with depth of the maximum induced lateral displacement; and ii) study the soil-pile interaction in three-layer soil system during liquefaction and lateral spreading, with and without the implementation of retrofitting strategies.

DESCRIPTION OF CENTRIFUGE MODELS

Sketches of RPI's laminar box (0.25 m (W) × 0.46 m (L) × 0.25 m (H), in model units) including the instrumentation used for all the centrifuge models are presented in Figure. 1. The laminar box consists of a stack of up to 39 rectangular rings separated by linear roller bearings, arranged to permit relative movement between rings in the long direction with minimal friction. A relative displacement

of up to 0.006 m between adjacent rings is possible, and the design permits an overall shear strain up to 20%. The laminar box is optimized to accommodate and accurately measure a wide range of cyclic and permanent lateral strains occurring in the soil model. More detailed information on RPI laminar box used in this study is presented by [9] and www.cee.rpi.edu/centrifuge.

The prototype being simulated in Model 2 (Fig. 1a) involves a single solid pile of diameter 0.60 m, length 10 m and EI = 8000 kN-m^2, with a pile cap embedded in the top cemented sand layer. An Aluminum pile cap was rigidly clamped to the to top of the pile model. The pile cap has dimensions of 2 m (W) × 2.5 m (L) × 0.5 m (H), in prototype units. In model units, the model height is approximately 0.20 m, simulating a 10 m prototype soil deposit and pile length at 50g. The prototype profile includes a bottom layer of 2.0 m slightly cemented sand, topped by a 6.0 m layer of uniform Nevada sand placed at a relative density of about 40%, topped by a 2.0 m layer of the same slightly cemented sand. At 50g, the D_r = 40% fine Nevada sand layer in the model simulates a liquefiable, D_r = 40% coarse Nevada sand layer in the prototype. The soil profile is fully saturated with water, inclined 2^0 to the horizontal corresponding to 4.8^0 inclination in the field after the instrumental correction [10], and spun at a centrifuge acceleration of 50g.

The model was excited by 40 cycles of a 100 Hz sinusoidal input parallel to the base of the laminar box, with uniform acceleration amplitude of about 15g. For the 50g centrifuge acceleration of the test, this corresponds respectively, to a frequency of 2 Hz and peak acceleration of 0.3g in prototype units. The horizontal accelerations outside the laminar box and in the soil, excess pore water pressures in the liquefiable sand layer, lateral displacements of the rings, and bending moments along the pile were measured.

The proposed rehabilitation approach of existing foundations by replacing the shallow soil in a trench around piles and pile cap by a soft material that will yield under constant lateral soil forces (Figs. 1b and 1c). Models 2r1 and 2r2 shown in Figs. 1b and 1c, respectively, represent the two strategies used in retrofitting existing single piles with pile cap embedded in a three layer soil system. In Model 2r1 (Strategy 1), the slightly cemented sand directly surrounding the pile cap is replaced by 1m width of a slurry wall made by bentonite and water mixture. The depth of the slurry wall is about 1 m. A 1 m width ring of clay wall is directly surrounding the pile from 1m below the slightly cemented sand surface to the boundary of the cemented sand layer and liquefiable sand layer. In Model 2r2 (Strategy 2), a slurry wall made by bentonite and water mixture was placed around the foundation about 1 m away from the pile cap. The slurry wall has dimensions of 1 m width and 2m depth.

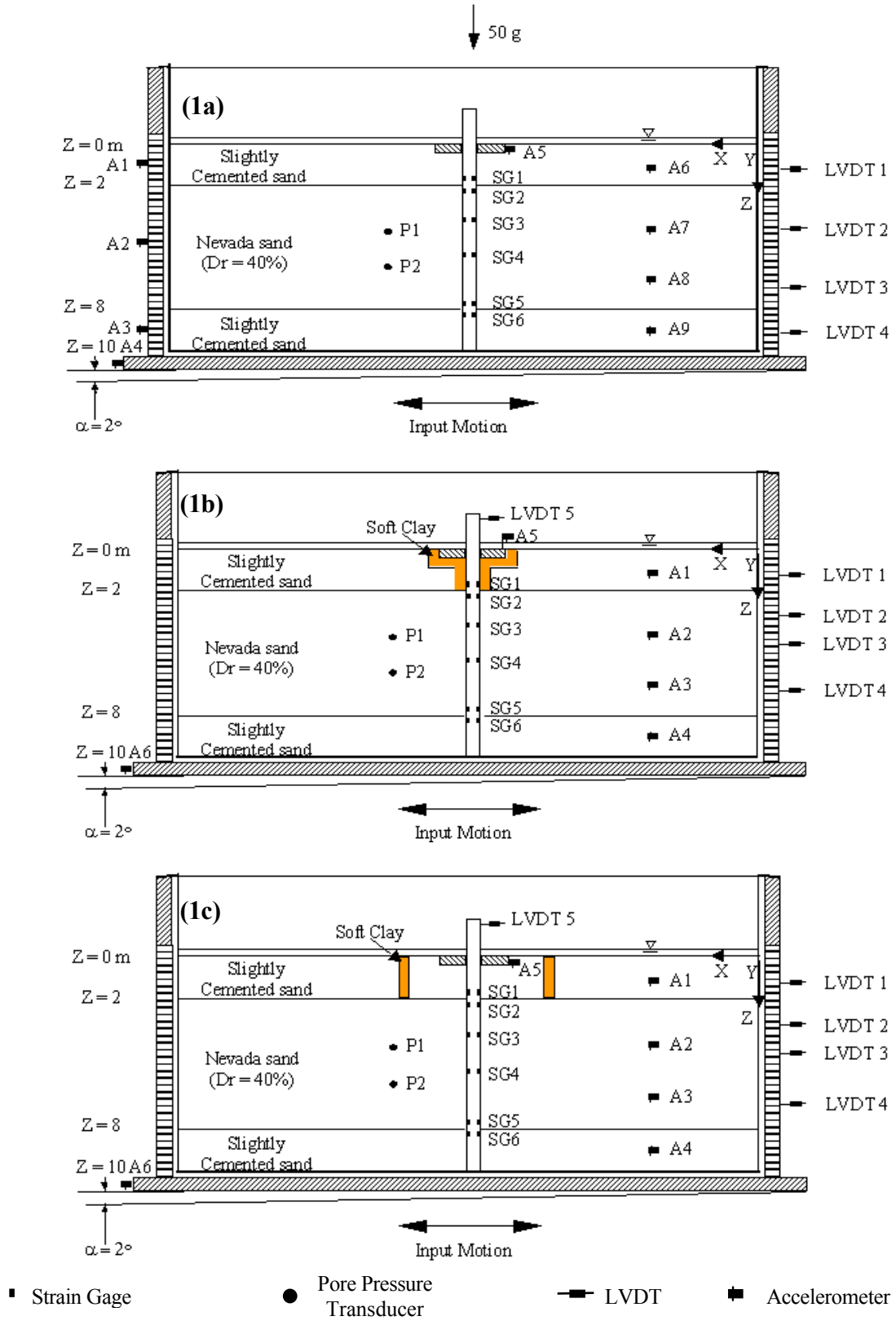

Figure 1: Setups and instrument locations of six centrifuge models; Model 2 (1a), Model 2r1 (1b) and Model 2r2 (1c)

SUMMARY OF CENTRIFUGE TESTS FREE FIELD MEASUREMENTS

It is important to analyze the free field experimental results measured away from the piles to verify tests repeatability. A comparison between excess pore pressure profiles, and soil lateral displacement profiles for all models presented in Fig. 1, at different times during shaking are presented respectively in Figs. 2 and 3. These free field records are very similar, confirming that the presence of the pile did not affect the free field soil response, and also validating the good repeatability of these centrifuge tests. In all models the lateral displacement occurred essentially within the 6.0 m thickness of the liquefiable sand layer (Fig. 3). The permanent ground surface lateral displacements at the end of shaking for all models are listed in Table 1. A similar good comparison, not presented in this paper, was also obtained between the recorded acceleration time histories for the seven centrifuge models [11].

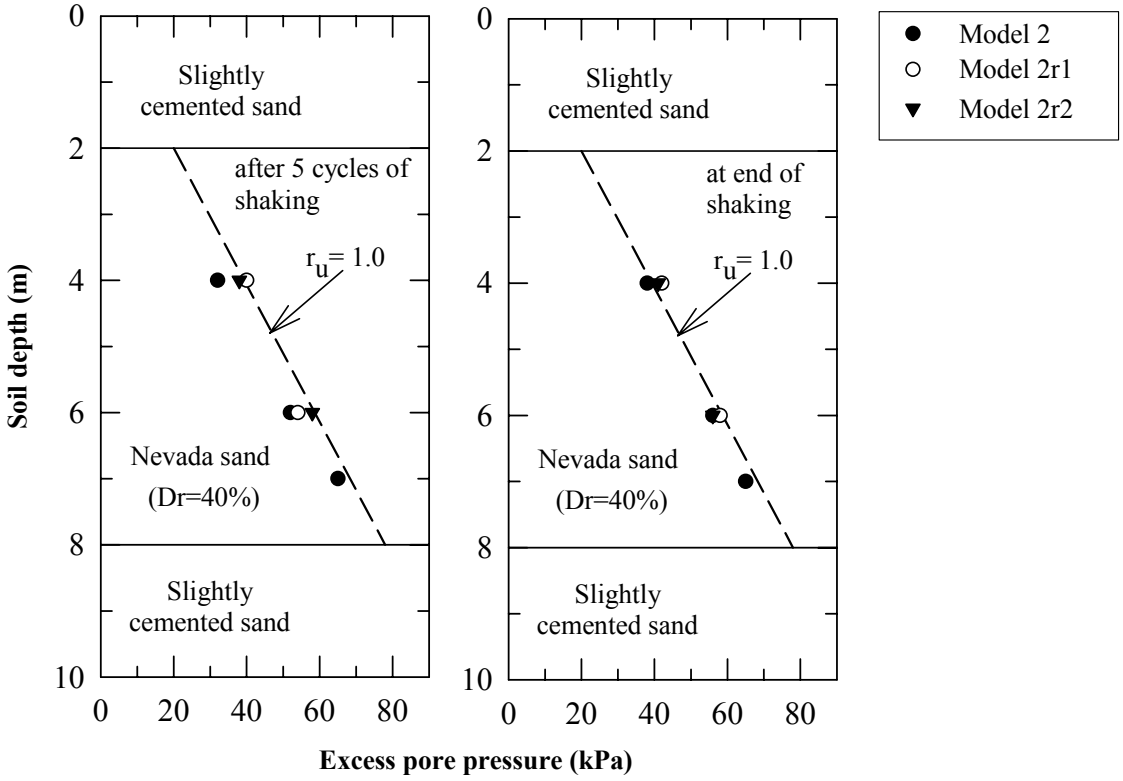

Figure 2: Profiles of free field excess pore pressures measured during and at the end of shaking

COMPARISON OF RESULTS MEASURED IN MODELS 2, 2R1 AND 2R2; PILE RETROFITTING WITH NO INERTIAL EFFECTS

Lateral Displacement: Figure 3 shows the recorded lateral displacements of the soil system at various elevations. The permanent prototype lateral displacements of the ground surface after shaking were about 0.70, 0.74 and 0.78 m for Models 2, 2r1 and 2r2, respectively (Table 1).

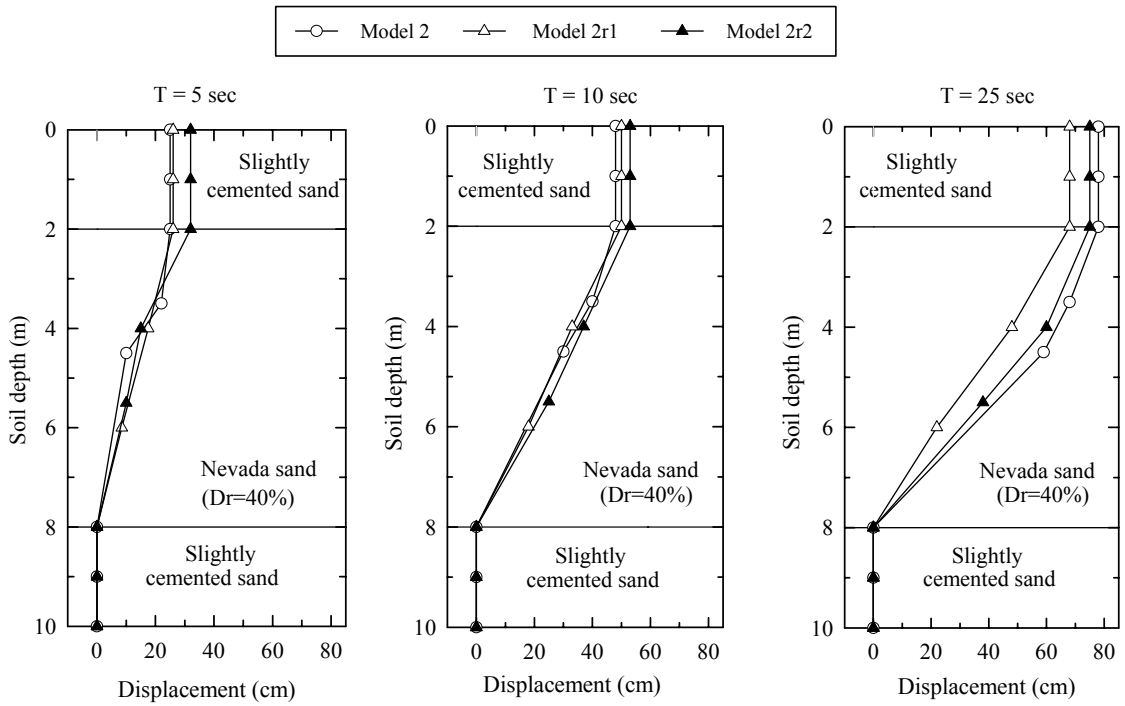

Figure 3: Lateral displacement profiles at different times during shaking, Models 2, 2r1 and 2r2

Table 2: Summary of single pile foundation characteristics and measurements during centrifuge tests (D_r = 40 % in all the tests for the liquefiable layer)

Model No.	No. of soil layers	Pile Cap	Mass	Retrofitting strategy	Measurements on piles			Free field ground surface lateral displacement (m)
					Bending moment, M_{max} (kN-m)		Pile deflection, D_{pmax} (m)	
					Upper boundary	Lower boundary		
2	3	Yes	No	No	270	305	0.85	0.70
2r1	3	Yes	No	Strategy 1	0	220	0.42	0.74
2r2	3	Yes	No	Strategy 2	30	290	0.60	0.78

A comparison of soil and pile lateral displacement profiles of Models 2, 2r1 and 2r2 is presented in Figure 4. Smaller pile head displacements were measured in Models 2r1 and 2r2 than those measured in Model 2. This indicates that the implemented remediation did decrease the pile lateral displacement. Figure 5 presents photos of soil condition around the pile cap after the test of Model 2r1. The pictures indicate that the implemented remediation did decrease the pile lateral displacement as the clay in the upslope of the pile cap was crushed while a gap was left on the downslope side of the cap. The permanent prototype lateral displacements of the pile head at the end of shaking were about 0.85, 0.42 and 0.60 m for Models 2. 2r1 and 2r2, respectively (Table 1).

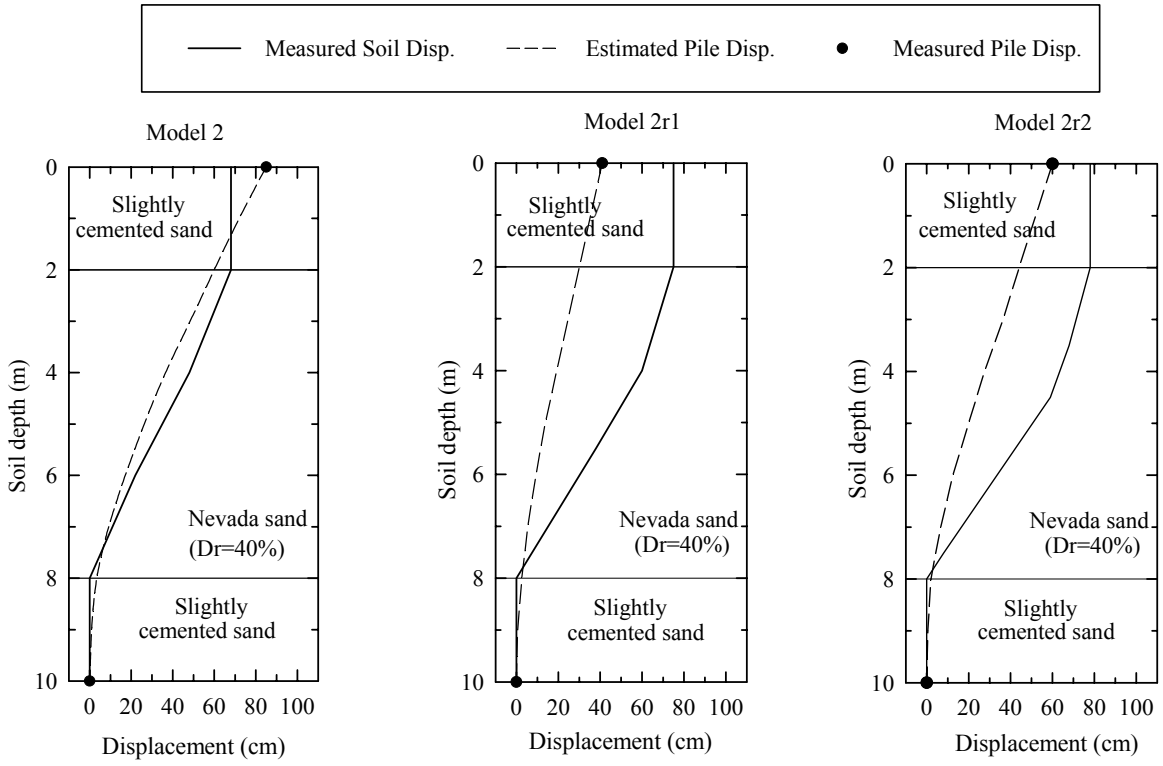

Figure 4: Pile and soil lateral displacement profiles at the end of shaking, Models 2, 2r1 and 2r2, estimated pile displacements were calculated using Beam-on-Winkler springs (BWS)

Bending Moments: The effect of the remediation can be best seen in the comparison of the bending moments. Figure 6 shows the bending moment measured along the pile in Models 2, 2r1 and 2r2 plotted at different times during shaking as the ground surfaces lateral displacement (D_H) was increasing. Before remediation, the measured moments at the interface of the top cemented layer and the liquefiable layer is about 200 kN-m in prototype units. After remediation, it drops to almost zero in Model 2r1 and only 20 kN-m in Model 2r2. Before remediation, the maximum bending moment between the bottom layer and the liquefied layer is about 305 kN-m. It drops to about 200 kN-m in Model 2r1 and drops to about 250 kN-m in Model 2r2.

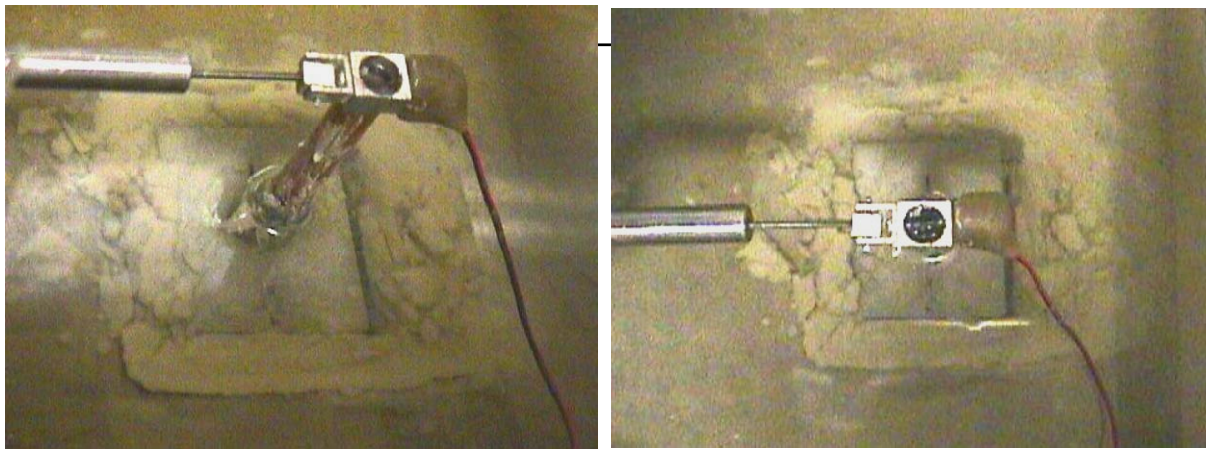

Direction of free field lateral displacement

Figure 5: Photos of soil condition around pile cap after the test, Model 2r1

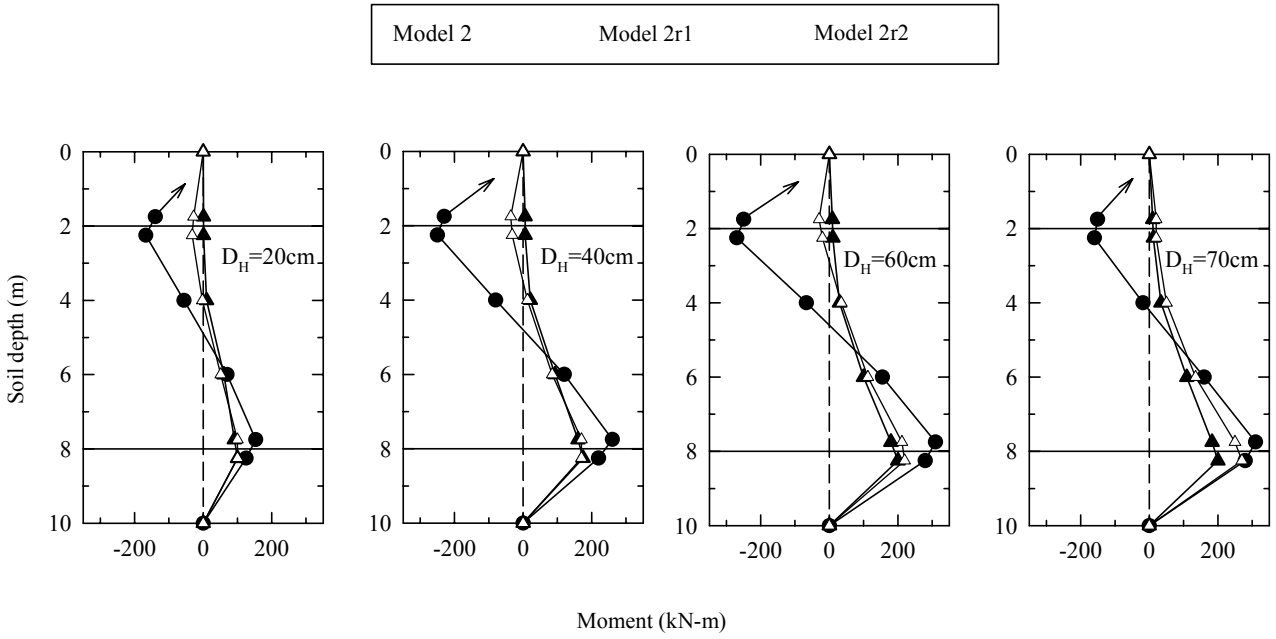

Figure 6: Bending Moments Along the Pile in Model 2, Model 2r1 and Model 2r2

CONCLUSIONS

The results from three centrifuge model tests of sand liquefaction with and without retrofitting strategies for the single pile foundation are reported in this paper, with detailed data interpretations and discussions. Some major conclusions may be drawn from these results as follows:

1 This work demonstrates that centrifuge modeling of soil-pile interaction during liquefaction is both realistic and useful. Consistent results were obtained from all centrifuge model tests, which provided detailed information on bending moment response of single pile foundations subjected to lateral spreading with or without retrofitting.
2 As expected, the maximum bending moment was still measured at the lower boundary between liquefied and nonliquefied soil, while the bending moment at the upper boundaries between liquefied and nonliquefied soil was greatly reduced after retrofitting.
3 Test results indicate that the lateral pressure, exerted by the shallow nonliquefied soil layer controls the bending moments developed along the pile.
4 In the absence of inertia force, a significant reduction of the measured maximum bending moment is achieved by the implementation of the two proposed retrofitting strategies aimed at reducing the lateral pressures exerted by the shallow nonliquefied layer.

ACKNOWLEDGEMENTS

The work reported herein was partially supported by the Multidisciplinary Center for Earthquake Engineering Research (MCEER) and the National Science Foundation (NSF). This support is gratefully acknowledged.

REFERENCES

[1] NRC 1982. Earthquake Engineering Research - 1982, Overview and Recommendations, Report by the Committee on Earthquake Engineering, National Research Council, National Academy Press. Washington, DC.
[2] Hamada, M. 1992. Large Ground Deformations and their Effects on Lifelines: *1964 Niigata Earthquake*, Ch. 3 of Hamada and O'Rourke, 3-1 to 3-123.
[3] Yokoyama, K., Tamura, K. and Matsuo, O. 1997. Design Methods of Bridge Foundations Against Soil Liquefaction and Liquefaction-Induced Ground Flow, 2nd Italy-Japan Workshop on Seismic Design and Retrofit of Bridges Rome, Italy, February 27-28, pp. 109-131.
[4] Tokimatsu, K. 1999. Performance of Pile Foundations in Laterally Spreading Soils, Proc. Second Intl. Conf. on Earthquake Geotechnical Engineering (P. Seco e Pinto, ed.), Lisbon, Portugal, June 21-25, Vol. 3, pp. 957-964.
[5] Abdoun, T. and R. Dobry 2002. Evaluation of pile foundation response to lateral spreading, *Soil Dynamics and Earthquake Engineering Journal*, Vol. 22, Issue 9-12, pp. 1069-1076.
[6] Abdoun, T., R. Dobry, T. D. O'Rourke and S.H. Goh 2002. Pile Response To Lateral Spreads: Centrifuge Modeling, *ASCE Journal of Geotechnical and Geoenvironmental Engineering* (in print).
[7] Dobry, R., T. Abdoun, T. D. O'Rourke, and S.H. Goh 2002. Piles in Lateral Spreading:

Field Bending Moment Evaluation, *ASCE Journal of Geotechnical and Geoenvironmental Engineering* (in print).

[8] Hamada, M. 2000. Performances of Foundations Against Liquefaction-Induced Permanent Ground Displacement, Proc. 12th World Conf. On Earthquake Engineering, Paper 1754.

[9] Van Laak, P., Taboada, V., Dobry, R., and Elgamal, A. W., 1994. Earthquake Centrifuge Modeling Using a Laminar Box, *Dynamic Geotechnical Testing journal*, Second volume, ASTM STP 1213, Ronald J. Ebelhar and Vincent P. Drnevich, and Bruce L. Kutter, eds., American Society for Testing and Materials, Philadelphia.

[10] Taboada, V. 1995. Centrifuge Modeling of Earthquake-Induced Lateral Spreading in Sand Using a Laminar Box, Ph.D. thesis, Rensselaer Polytechnic Institute, Troy, NY.

[11] Wang, Y., 2001. Evaluation of pile foundation retrofitting against lateral spreading and inertial effects during liquefaction using centrifuge models. MS Thesis, Dept. of Civil Engineering, Rensselaer Polytechnic Institute, Troy, NY.

Analysis of Soil-Pile Interaction

Susumu Iai and Tetsuo Tobita

ABSTRACT

As a part of a project for developing a simplified three dimensional analysis method for pile-soil interaction, a two dimensional analysis is performed on a horizontal cross section of a pile-soil system. An effective stress model based on multiple shear mechanism is used through a computer code FLIP. The objective of this two dimensional analysis is to evaluate the effects of soil displacement between the piles and/or soil deformation around the piles. In the conventional simplified analysis, these effects were often idealized as linear or non-linear springs connecting the finite element nodes of beam elements representing a pile and those of solid elements representing soil adjacent to the pile and the analysis was performed on a vertical cross section of a soil-pile system. In this study, the two dimensional analysis of horizontal cross section of a pile-soil system is performed with either a monotonic or cyclic loading applied on an idealized cylindrical rigid body embedded in soil. Soil deformation around a cylindrical cross section of a pile, excess pore water pressures in the soil around the pile, and load-displacement relationship of the pile are computed in drained and undrained conditions for sand.

Major findings from this study are as follows:

(1) The computer code FLIP shows numerical robustness in the nonlinear soil-pile interaction analysis: no difficulty is encountered in the numerical analysis of the soil-pile system involving large displacement/deformation with the order-of-magnitude displacement comparable to that of the pile diameter.

(2) The computed displacement field around a pile shows vortexes in undrained condition. Relative displacement between the piles is concentrated at the interface between the pile and the soil in undrained condition.

(3) The load-displacement relationship of the pile is similar to that of the stress-strain relationship of soil. In drained condition for sand, the load-displacement relationship of the pile is a hysteretic hyperbolic relationship as often assumed in the simplified analysis whereas, in undrained condition for sand, that becomes a hysteretic hardening spring type resembling the stress strain relationship for cyclic mobility of medium to dense sand.

(4) Load distribution among the pile rows depends on the drained/undrained conditions as well as the strain/load level. For the pile spacing of five times the pile diameter, load distribution at a small load/strain level shows minimum at the middle row, whereas that at a large/strain level shows minimum at the back row. Load is approximately equally distributed among the pile rows at the undrained condition.

Disaster Prevention Research Institute, Kyoto University, Gokasho, Uji 611-0011 Japan

INTRODUCTION

In the analysis of soil-pile interaction during strong earthquakes, two dimensional analysis is often performed on a vertical cross section of a soil-pile system. In this analysis, if the finite element nodes of a pile and those of soil adjacent to the pile share the same displacement (i.e. if they move together), the analysis becomes a soil-wall interaction analysis rather than a soil-pile interaction analysis. In the soil-pile interaction analysis, effects of soil displacement between the piles and/or soil deformation around the piles should be adequately evaluated and taken into account in the analysis.

In the simplified two dimensional analysis, these effects are often idealized by linear or non-linear springs connecting the finite element nodes of a pile and those of soil adjacent to the pile. If the springs are adequate, the two dimensional effective stress analysis based on multiple mechanism model, using a computer code FLIP [1], can simulate highly nonlinear soil-pile interaction phenomena, including a case history during the Hyogoken-Nambu earthquake of 1995 (see Figure 1). A procedure to evaluate and idealize the springs, however, has not been well established.

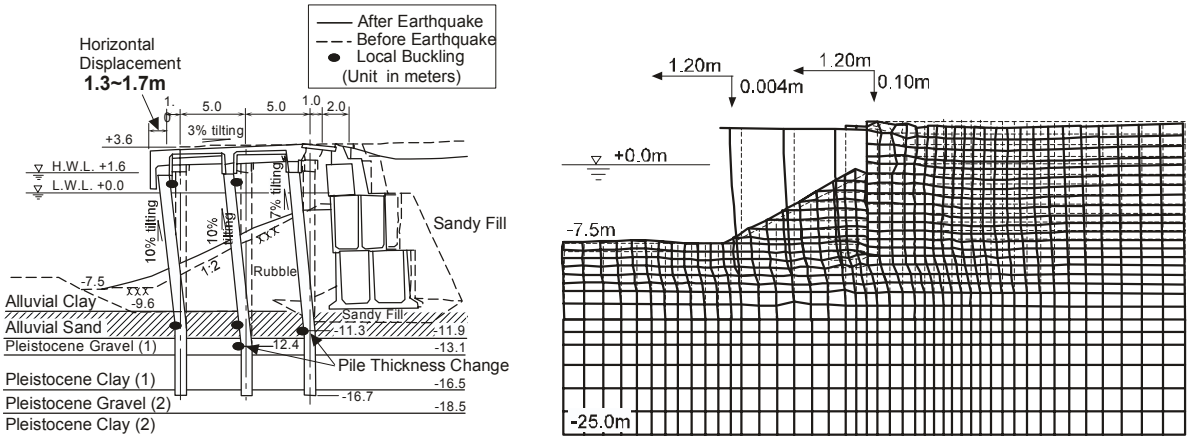

(a) Damage to a pile supported wharf

(b) Computed residual deformation using two dimensional effective stress analysis method (after [2])

Figure 1 Damage to a pile supported wharf at Takahama, Kobe Port, during Hyogoken-Nambu earthquake of 1995 and the computed results based on two dimensional analysis

In this study, a two dimensional analysis is performed on a horizontal cross section of a pile-soil system using the same effective stress analysis method. The objective of this two dimensional analysis is to evaluate the effects of soil displacement between the piles and/or soil deformation around the piles.

TWO DIMENSIONAL ANALYSIS OF A PILE-SOIL SYSTEM IN HORIZONTAL PLANE

The two dimensional analysis of horizontal cross section of a pile-soil system is performed under the pseudo-static condition with either a monotonic or cyclic loading applied on an idealized cylindrical rigid body embedded in soil. In this study, a single row of equally spaced piles deployed perpendicular to the load direction (Figure 2(a)) is idealized into an analysis

domain defined by upper and lower boundaries set at the centers of the pile spacing. These boundaries are periodic, sharing the same displacements at the boundary nodes with the same x-coordinate. At the right and left side boundaries, the x-displacements were fixed.

The finite element mesh used for the analysis for the case of a pile spacing L=5D, with a pile diameter D=1m, is shown in Figure 3. In the analysis, the whole analysis domain is initially consolidated with a confining pressure corresponding to that of the soil layer at a specified depth. The cylindrical pile section is idealized by a linear solid element having a rigidity equivalent to that of concrete but this cross section is replaced by the soil for the initial analysis phase for consolidation. Following this initial analysis phase, the cylindrical pile section is loaded either monotonically or cyclically. Soil deformation around a cylindrical cross section of a pile and load-displacement relationship of the pile are computed in drained and undrained conditions for sand. The parameters for sand used for the analysis are determined referring to the typical properties of clean sand having a SPT N-values of 10 as shown in Table 1.

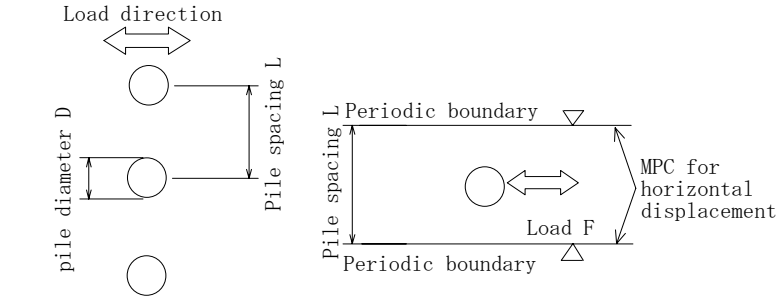

(a) Pile rows (b) Analysis domain for single pile

Figure 2 Two dimensional analysis of a soil-pile system in horizontal plane

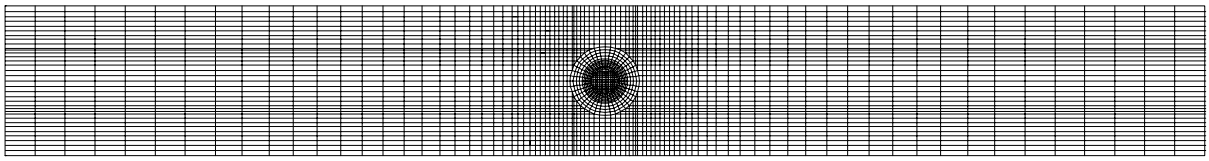

Figure 3 Finite element mesh used for the analysis (L=5D)

Table 1 Parameters for sand

	Parameters for shear mechanism					Parameters for dilatancy					
ρ_t (t/m^3)	G_{ma} (kPa)	ν	σ_{ma}' (kPa)	φ_f (deg)	H_{max}	φ_p (deg)	w1	p1	p2	c1	s1
2.0	84500	0.33	98	39.7	0.240	28.0	3.756	0.5	1.011	1.6	0.005

ρ_t: density; G_{ma}: initial shear modulus at a confining pressure of σ_{ma}'; σ_{ma}': reference confining pressure; φ_f: shear resistance angle; ν : Poisson's ratio; H_{max}; limiting value of damping constant; φ_p :phase transformation angle; w1, p1, p2, c1, s1: parameters for excess pore water accumulation model.

COMPUTED RESULTS FOR SIGLE PILE

The computation was performed in a numerically stable manner even at the large displacements in the order-of-magnitude displacement comparable to that to pile diameter. Numerical instability occurred only when the ultimate state of soil was reached either when the load resistance curve reached the plateau, or when there is instability in the soil under drained condition.

The computed results for the drained condition are shown in Figures 4 through 7. Figure 4 shows the displacement field in deformed mesh. Deformation in the vicinity of the pile is depicted in this figure. The same displacement field is plotted in Figure 5 by displacement vectors. The displacement vectors are mostly directed toward the horizontal direction. In order to clearly shows the relative displacement between the piles, horizontal components of the displacements are plotted in Figure 6. Under the drained condition, the load-displacement relationship shows the shape shown in Figure 7. The computation resulted in divergence at 580kN, presumably reached the ultimate state of soil.

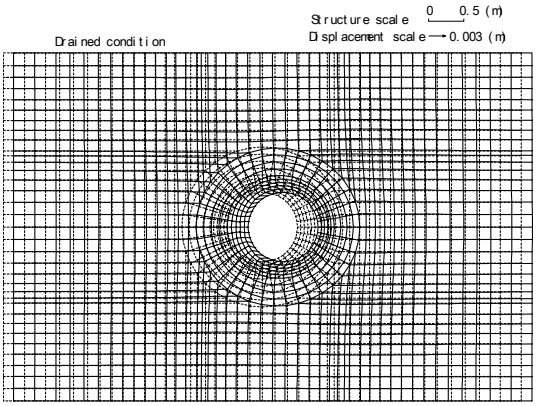

Figure 4 Computed deformation around the pile under drained condition

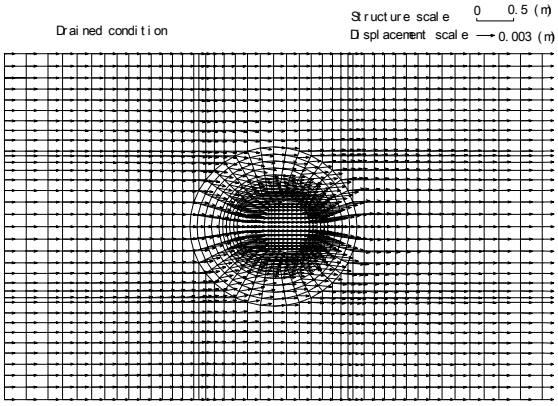

Figure 5 Compute displacement vectors around the pile under drained condition

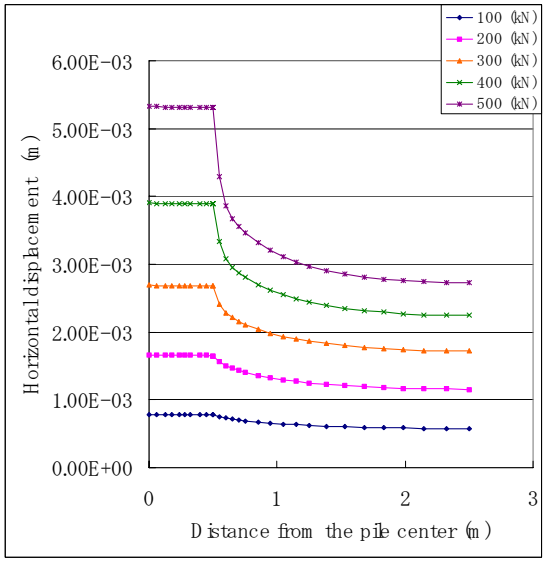

Figure 6 Soil displacement distribution between the piles

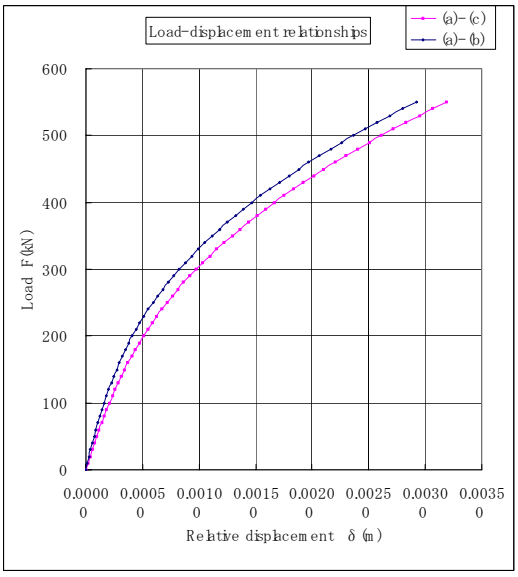

Figure 7 Load-displacement relationships for drained monotonic loading

Computed results for undrained condition are shown in Figures 8 through 10. Figure 4 shows the displacement field for sand under undrained condition. The displacement field is computed for monotonic loading at the load of 3000kN. Soil displacements relative to the pile displacement are clearly shown in Figure 8. The same displacement field is plotted in Figure 9 by displacement vectors. In contrast to the drained condition shown in Figure 5, vortexes can be recognized in Figure 9.

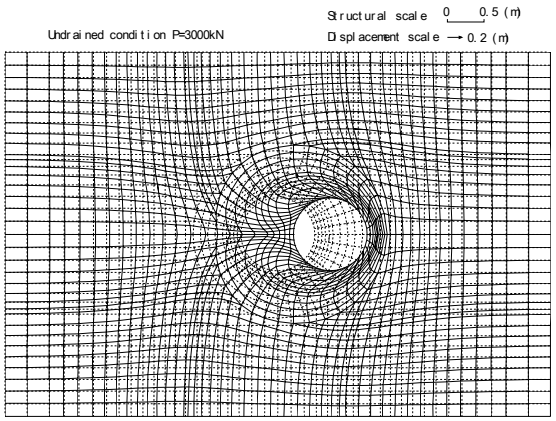

Figure 8 Computed deformation around the pile for undrained condition

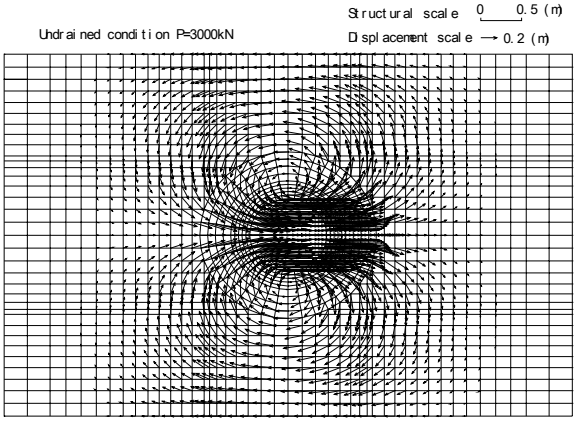

Figure 9 Computed displacement vectors around the pile for undrained condition

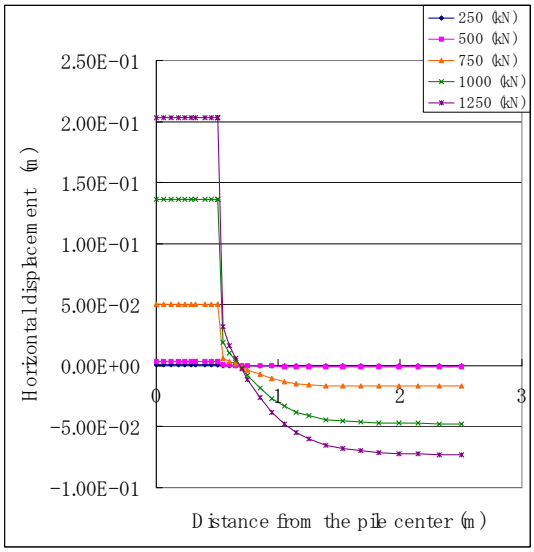

Figure 10 Soil displacement distribution between the piles for undrained condition

Distribution of soil displacement between the piles is shown in Figure 10. In contrast to the drained condition shown in Figure 6, relative displacements are concentrated at the interface between the pile and the soil.

Typical load-displacement relationships computed in undrained condition are shown in Figures 11and 12. The result for P1 is the standard case for sand; others were computed as parametric study. The conditions for other cases are as follows:

P0: excess pore water pressure rise was not allowed.
P4: excess pore water pressure ratio before the cyclic loading was set at 95%
P4-constS0: the same as P4 but the subsequent excess pore water pressure rise during cyclic loading was not allowed.

The initial stiffness of spring defined by the load/relative displacement at small load level was computed as 614000kN/m for P1. The shape of the load-displacement relationships for sand under undrained cyclic condition is similar to those observed for the stress-strain relationships during undrained cyclic loading of sand specimen.

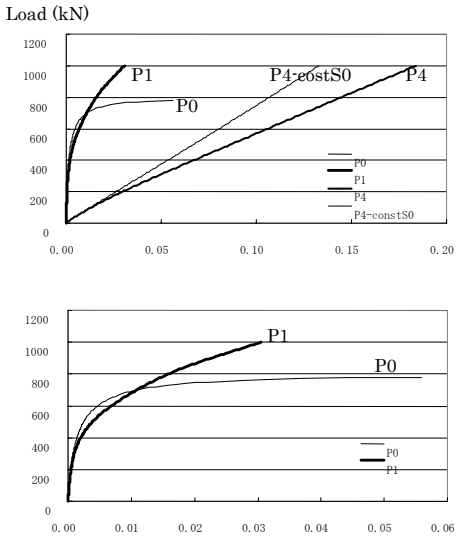

Figure 11 Computed load-displacement relationships for undrained monotonic loading of sand

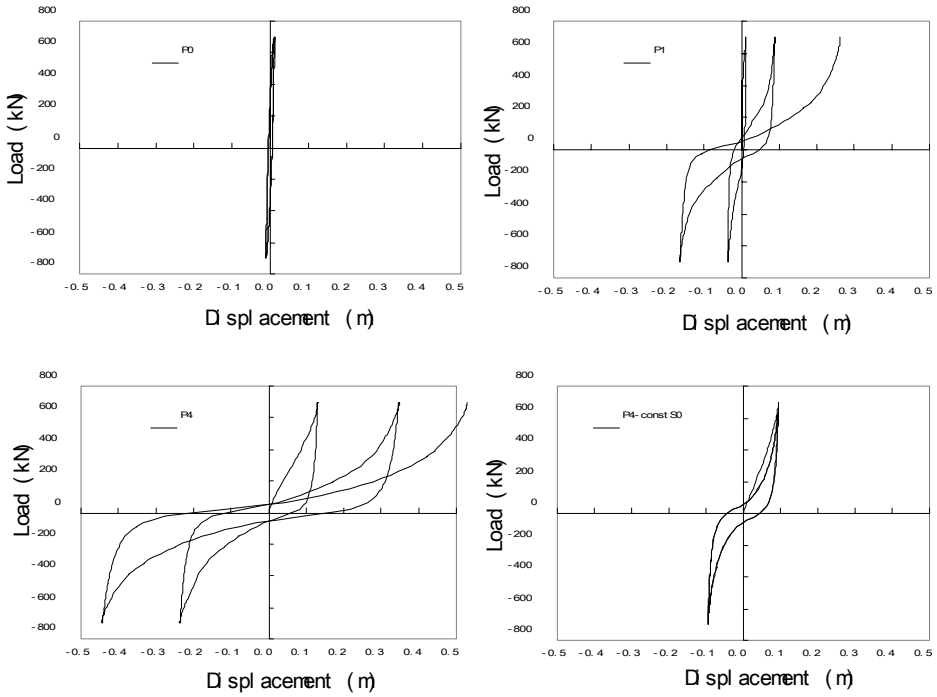

Figure 12 Computed load-displacement relationships for undrained cyclic loading of sand

COMPUTED RESULTS FOR PILE GROUP

Analysis of a pile group of three rows was also performed using the finite element mesh shown in Figure 13. Analysis was performed for both drained and undrained conditions. In the analysis, three rows of piles underwent the same displacement in horizontal direction. As an example of analysis results, deformation and displacement vectors around the pile group computed for undrained conditions are shown in Figures 14 and 15.

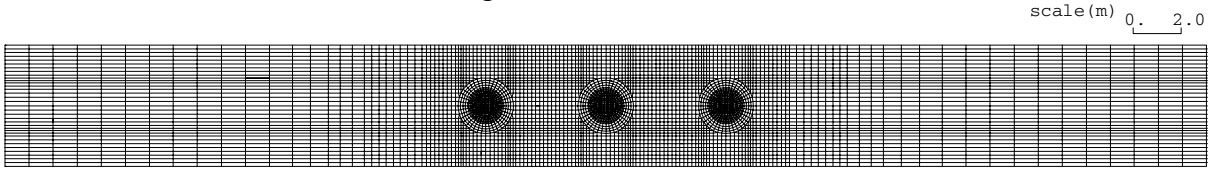

Figure 13 Finite element mesh used for the multiple pile analysis (L=5D)

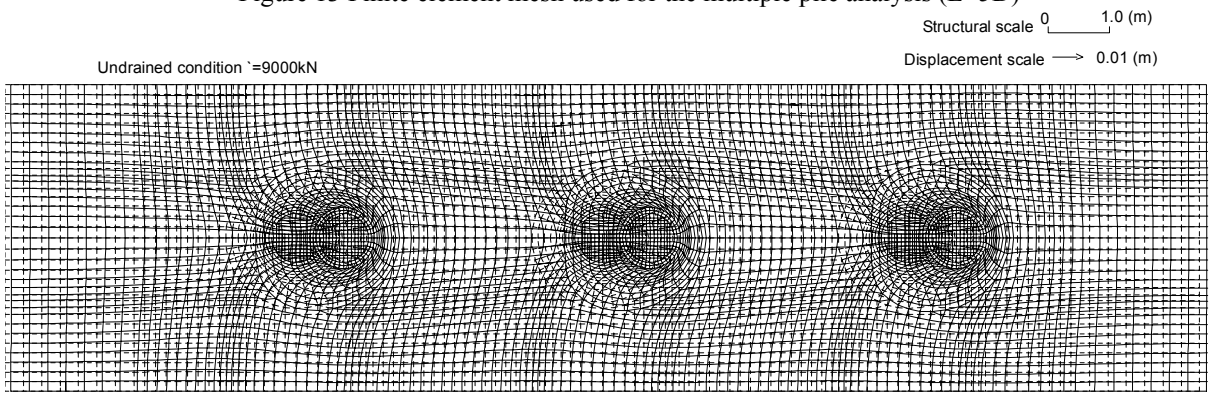

Figure 14 Computed deformation around the pile group for undrained condition

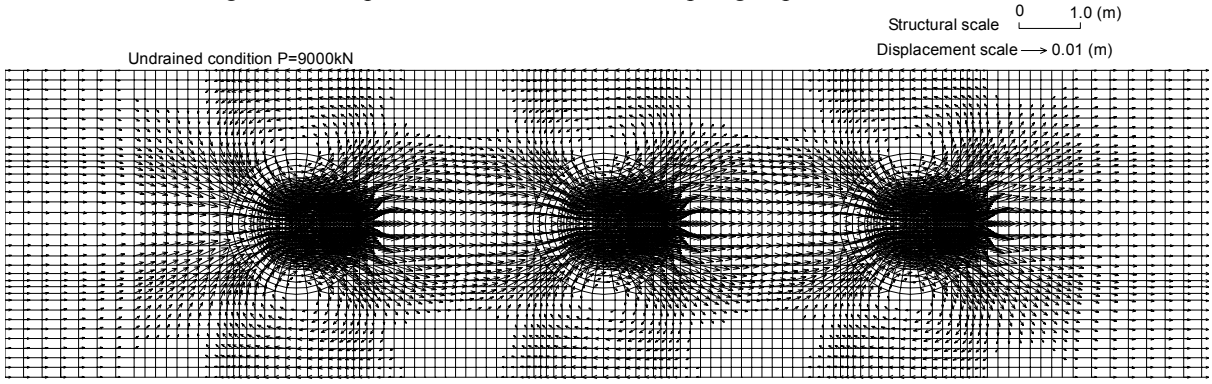

Figure 15 Computed displacement vectors around the pile group for undrained condition

The primary objective of the pile group analysis in horizontal plane was to study the load distribution among the three rows of piles. Figures 16 and 17 show the load distribution among the pile rows for drained and undrained condition. As shown in Figure 16, load distribution at a small load/strain level shows minimum at the middle row, whereas that at a large/strain level shows minimum at the back row. As shown in Figure 17, almost equal load distribution is seen at the undrained condition for the pile spacing of 5D computed in this study.

CONCLUSIONS

Major findings from this study are as follows:

(1) The computer code FLIP shows numerical robustness in the nonlinear soil-pile interaction

analysis: no difficulty is encountered in the numerical analysis of the soil-pile system involving large displacement/deformation with the order-of-magnitude displacement comparable to that of the pile diameter.

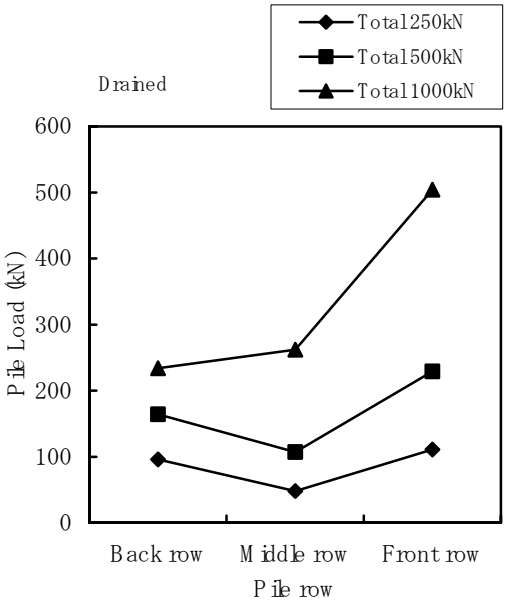

Figure 16 Load distribution for drained condition

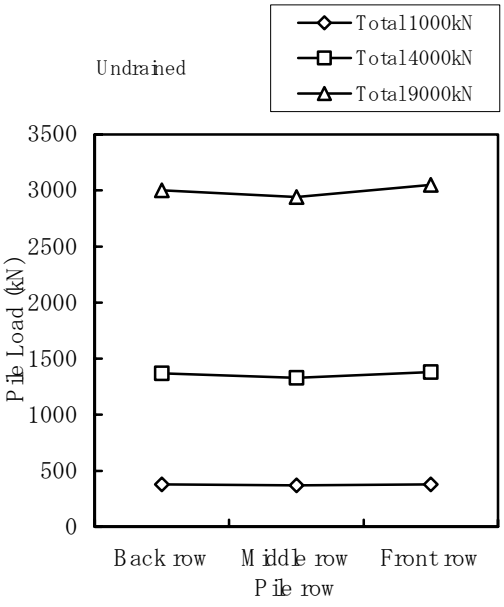

Figure 17 Load distribution for undrained condition

(2) The computed displacement field around a pile shows vortexes in undrained condition. Relative displacement between the piles is concentrated at the interface between the pile and the soil in undrained condition.

(3) The load-displacement relationship of the pile is similar to that of the stress-strain relationship of soil. In drained condition for sand, the load-displacement relationship of the pile is a hysteretic hyperbolic relationship as often assumed in the simplified analysis whereas, in undrained condition for sand, that becomes a hysteretic hardening spring type resembling the stress strain relationship of cyclic mobility of sand.

(4) Load distribution among the pile rows depends on the drained/undrained conditions as well as the strain/load level. For the pile spacing of five times the pile diameter, load distribution at a small load/strain level shows minimum at the middle row, whereas that at a large/strain level shows minimum at the back row. Load is approximately equally distributed among the pile rows at the undrained condition.

ACKNOWLEDGEMENTS

The study has been a part of the project by a technical committee consisting of a consortium for promoting application and modification the effective stress analysis program FLIP.

REFERENCES

[1] Iai, S., Matsunaga, Y., and Kameoka, T. (1992): Strain space plasticity model for cyclic mobility, Soils and Foundations, Vol.32, No.2, pp.1-15

[2] Iai, S. (1998): Seismic analysis and performance of retaining structures, Geotechnical Earthquake engineering and Soil Dynamics III, Geotechnical Special Publication No.75, ASCE, Vol.2, pp.1020-1044

Ground Motion Characteristics and Liquefaction

Statistical investigation of the relationship between building damage and ground performance, including liquefaction, during the 1995 Hyogoken-Nambu (Kobe) Earthquake

Kazue Wakamatsu and Atsunori Numata

ABSTRACT

In response to a bitter experience in the 1995 Hyogoken-Nambu (Kobe) Earthquake, the Level-2 ground motion with the highest level of intensity that would be caused by an earthquake such as the 1995 earthquake, has been considered in seismic design of various kind of structures in Japan, in addition to the Level-1 general ground motion. In evaluating liquefaction potential subjected to the Level-2 ground motion, even medium density sand and gravely sand would result in being liquefiable (liquefaction resistance factor, $F_L \leq 1.0$), which implies that the greater part of low-lying area in Japan would be expose to be risk of liquefaction hazard. However, in engineering purposes, it is not usually important to judge whether or not liquefaction will occur in a certain area, but to evaluate its consequence for damage to structures. It will also be necessary to implement liquefaction countermeasures based on the type and social significance of the structure.

The goal of this study is to evaluate the effects of liquefaction induced by Level-2 ground motion on structural damage. First, data for the Hyogoken-Nambu Earthquake was collected on (1) the state of damage/non-damage to buildings, (2) soil conditions at each site, and (3) occurrence of liquefaction effects such as sand boils and water spouting at each site. Quantitative analyses were then performed on damage level of superstructures and foundations of building, liquefaction susceptibility of the ground, and the condition of observed liquefaction effects. Finally, the results of the analyses were discussed to determine the effects of soil conditions and degree of liquefaction on structural damage.

Kazue Wakamatsu, Research Fellow, Institute of Industrial Science, University of Tokyo, 4-6-1 Komaba, Meguro-ku Tokyo 153-8505 Japan

Atsunori Numata, Manager and Chief Research Engineer, Technical Research Institute, Tobishima Corporation, 5472 Kimagase, Sekiyado-machi, Higashikatsushika-gun, Chiba Pref. 270-0222 Japan

INTRODUCTION

In response to a bitter experience in the 1995 Hyogoken-Nambu (Kobe) Earthquake, the Level-2 ground motion with the highest level of intensity, that would be caused by an earthquake such as the Hyogoken-Nambu Earthquake, has been considered in seismic design of various kind of structures in Japan, in addition to the Level-1 general ground motion. In evaluating liquefaction potential subjected to the Level-2 ground motion, even medium density sand and gravely sand would result in being liquefiable (liquefaction resistance factor, $F_L \leq 1.0$), which implies that the greater part of low-lying area in Japan would be expose to be risk of liquefaction hazard. However, in engineering purposes, it is not usually important to judge whether or not liquefaction will occur in a certain area, but to evaluate its consequence for damage to structures. It will also be necessary to implement liquefaction countermeasures based on the type and social significance of the structure.

The goal of this study is to evaluate the effects of liquefaction induced by level-2 ground motion on ground and structural damage. First, data for the Hyogoken-Nambu Earthquake was collected on (1) the state of damage/non-damage to foundation and superstructures of building, 2) soil conditions at each surveyed building, and (3) occurrence of liquefaction effects such as sand boils and water spouting around the buildings. Quantitative analyses were then performed on liquefaction susceptibility of the ground, damage level of superstructures and foundations of building, and the condition of observed liquefaction effects. Finally, the results of the analyses were discussed to determine the effects of soil conditions on degree of liquefaction and structural damage.

SURVEY METHOD

Data Collected

Many cases of damage to building foundations have been reported in various kinds of reports and research papers [1]. However, the names and locations of the buildings, which are required to collect the information on the site condition such as borehole data, have not been disclosed at the request of property owners. In this study, these buildings were identified through various kind of investigations based on information made available, such as neighborhood descriptions, building photos, and building use, shape, and number of stories. Ultimately, data for 127 cases of foundation damage/non damage were compiled for the database referring to these, literature

Degree of Liquefaction Around Surveyed Buildings

It is extremely difficult to determine the actual degree of liquefaction induced by an earthquake for the local soil under investigation. In this study, it was assumed that surface evidences of liquefaction could be used as indicators of extent and severity and liquefaction of the subsurface. Liquefaction was classified into 5 levels, based on the state of sand and water boiling determined on the basis of information from the maps of ground failures and ground displacement vector diagrams for the Kobe earthquake compiled by Hamada et al. [2], and from reports of liquefaction described in the respective literature for each building site.

TABLE I. DEGREE OF LIQUEFACTION CLASSIFIED BY SURFCE EVIDERNCES OF LIQUEFACTION

Region	Degree of liquefaction	State of sand boils on the ground surface
Coastal region	a	Observed extreme amounts of sand boils in over 50% of the area within a 100-m radius of the subject building
	b	Observed large amounts of sand boils in 20–50% of the area within a 100-m radius of the subject building
	c	Observed sand boils in less than 20% of the area within a 100-m radius of the subject building
	d	No observed sand boils within a 100-m radius of the building but sand boils observed in the surrounding areas.
Inland region	z	No observed sand boils but no obvious sand boils observed in the surrounding areas.

First, the study area was divided into coastal regions that experienced liquefaction over a wide area (zones a–d) and inland regions relative free from liquefaction (zone z). The coastal regions correspond to the area surveyed for ground failures in Hamada et al. [2]. In the inland regions falling outside Hamada's survey map, sand boils occurred only sporadically and on a significantly smaller scale than in coastal zones. The inland regions were thus classified as a single zone "z." Next, the coastal regions were classified into four zones, as summarized in Table 1, based on the state of sand boils.

Assessment of Liquefaction Potential

Liquefaction resistance factor, $F_{L,}$ was calculated using a simplified procedure for liquefaction assessment introduced in the Specifications for Highway Bridges [3] to evaluate liquefaction potential at the ground for each surveyed building. The liquefaction potential index, P_L [4], which is weighted integration of F_L value for depth, was also calculated as an index to represent the degree of liquefaction-induced effects expected on the surface.

Soil layers requiring liquefaction assessment were selected based on the definitions in the Specifications for Highway Bridges [3]. When data on plasticity index, I_P, which is required to determine liquefiable soil layer were not obtained, layers with fines content, FC of < 35% were considered to be "liquefiable" for liquefaction assessment. The soil data collected in the present study were limited to those obtained from borehole logs and the SPT N-values. The soil constants necessary for estimating liquefaction resistance and shear strength during earthquakes were assumed to be equivalent to the standard soil constants determined for the Hanshin region for the respective soil types reported in the borehole logs [5].

In the present study, the design horizontal seismic coefficients, $k_{hc,}$ were assumed as follows in calculations of F_L values for Level-1 and Level-2 ground motions. For calculations of design horizontal seismic coefficients, the formula for Type II (near-field earthquake) earthquakes was used for both Level-1 and Level-2 ground motions, since the subjects of the present study are case histories due to the Hyogoken-Nambu Earthquake. In the 2002 Specifications for Highway Bridges [3], only the design seismic coefficient for Level-2 ground motion is defined. Thus, the design seismic coefficient for Level-1 ground motion was assumed to be 0.18, which is defined in the 1990 Specifications [6], in the calculation of dynamic load induced in a soil element. To enable comparison between the calculated liquefaction ground susceptibilities for Level-1 and Level -2 motions under the same conditions, the horizontal seismic coefficient was varied while ground motion remained fixed as Type II ground motion.

Based on the method specified in the 2002 Specifications for Highway Bridges, the design horizontal seismic coefficient, k_{hc}, for level-2 ground motion was calculated, assuming a modification factor, c_z, for zone A including study area of 1.0 and design horizontal seismic coefficient at ground surface, k_{hG}, of 0.6 (value for ground type III). Dynamic shear strength ratio, R, was calculated using the modification factor based on earthquake motion properties, c_w, obtained with the formula for Type II ground motion.

INDEXS FOR SUSCEPTIBILITY TO LIQUEFACTION

Relationship between Soil Liquefaction and Site Conditions

One important step in evaluating the effect of liquefaction on structural damage is to identify the indexes for liquefaction susceptibility. In this section, various indexes that are considered to be related to liquefaction resistance, such as the minimum SPT N-value of sandy soil layers requiring a liquefaction assessment, the minimum liquefaction resistance factor, F_L, of the ground, the depth to the upper boundary of the estimated liquefiable layer, the liquefiable-layer thickness, and the liquefaction potential index, P_L, will be examined to determine whether significant correlations exist between these indexes and the degree of liquefaction during an actual earthquake.

Figure 1 is a histogram of the minimum SPT N-value of liquefiable soils lying below the groundwater table and above GL-20 m, classified by the degree of liquefaction at each site. Broken lines in the figure indicate the cumulative relative frequencies. In grounds a and b, which had suffered severe degrees of liquefaction, 95% or more of the ground had displayed minimum N-values of 10 or less. In contrast, grounds with minimum N-values greater than 20, though small in number, experienced liquefaction effects of either d or z degrees. In cases in which a layer with N-values of 20 or less is not present at ground levels above GL-20 m, sand boils are not expected to occur even during Level-2 ground motion.

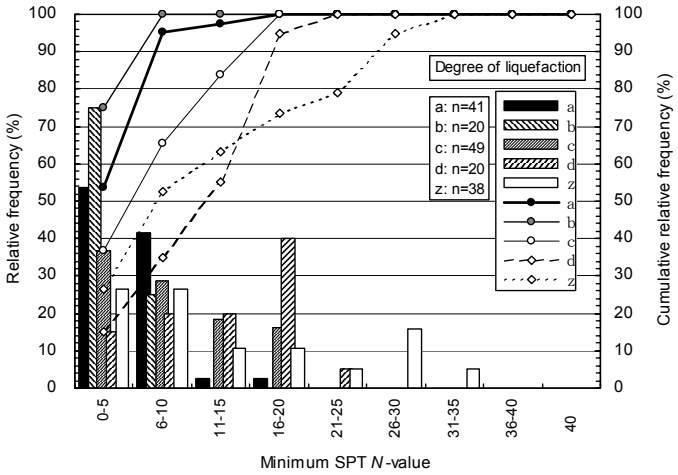

Figure 1. Histogram of the minimum SPT-N value of liquefiable soils classified by the degree of liquefaction

Figure 2 shows histograms of minimum liquefaction resistance factor, F_L, for Level-1 and Level-2 ground motions classified by the degree of liquefaction. Zones a and b, which experienced a severe degree of liquefaction, consist of grounds with $F_L \leq 1$ for Level-1 ground motion in approximately 80–85% of the cases, and $F_L \leq 1.2$ in 90% or more of the cases. On the other hand, zones d and z consist of grounds with $F_L > 1$ in approximately 75–85% of the cases.

For Level-2 ground motion, zones a and b consist of grounds with $F_L \leq 0.4$ in approximately 95% or more of the cases and, zone c consists of grounds with $F_L \leq 0.6$ in approximately 90% of the cases. However, it must be noted that the minimum F_L value is 1 or less in most cases for zone d, without any apparent liquefaction effects, and for zone z, which is unlikely to experience liquefaction. This may indicate that liquefaction had partially occurred within the ground even when its effect is not apparent on the surface. However, it may also suggest that the F_L values calculated for Level-2 ground motions provide results that are excessively on the safe side.

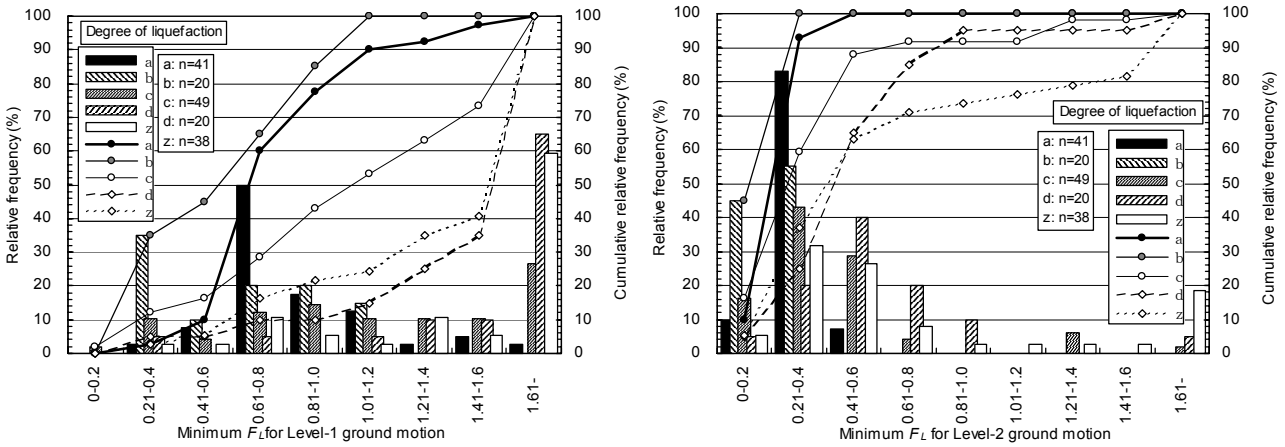

(a) Minimum F_L values for Level-1ground motion (b) Minimum F_L values for Level-2 ground motion

Figure 2. Histograms of minimum liquefaction resistance factor, F_L for Level-1 and Level-2 ground motions classified by the degree of liquefaction

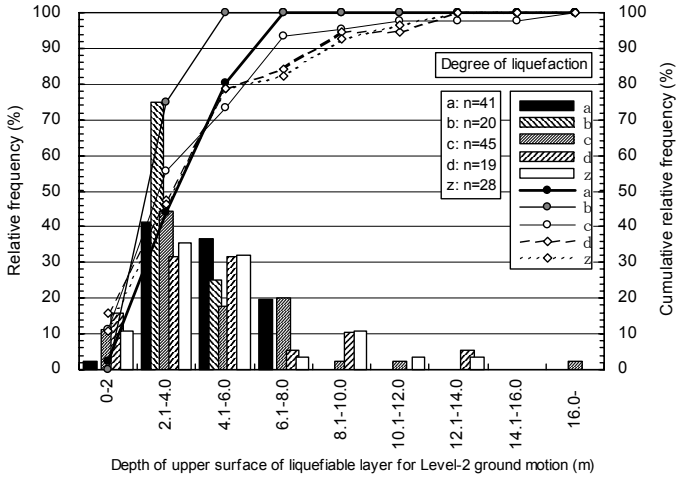

Figure 3. Histogram of the depth of the upper surface of estimated liquefiable layer for Level-2 ground motion classified by the degree of liquefaction

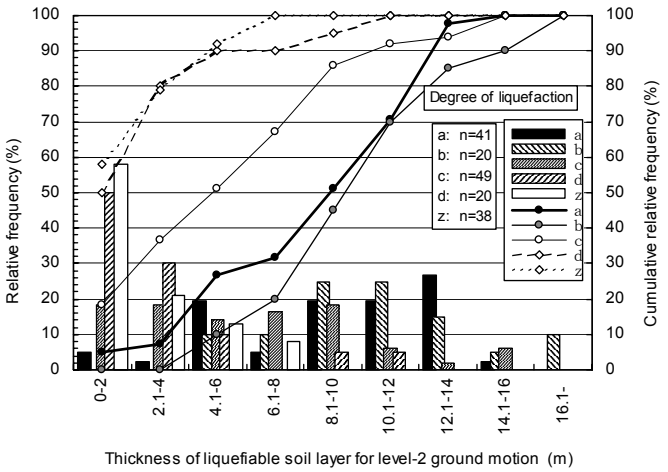

Figure 4. Histogram of the thickness of the estimated liquefiable soil layer for Level-2 ground motion classified by the degree of liquefaction

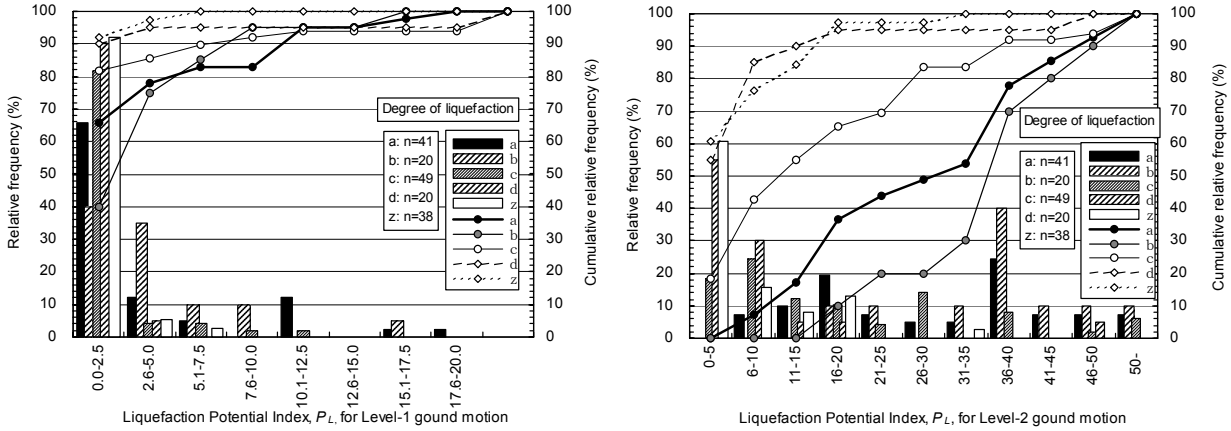

(a) Level-1 ground motion (b) Level-2 ground motion.

Figure 5. Histogram of the liquefaction potential index P_L for Level-1 and Level-2 ground motions classified by the degree of liquefaction

Figure 3 is a histogram of the depth of the upper surface of the estimated liquefiable layer for Level-2 ground motion classified by the degree of liquefaction. Only the results for Level-2 ground motion are shown, as in most of the cases of Level-1 ground motion, none of the soil layers to a depth of GL-20 m displayed an F_L value of 1.0 or less, and the liquefiable soil layer could not be determined. Of the sites predicted to experience liquefaction during Level-2 ground motion, 90% or over had depths to an upper surface of estimated liquefiable soil layer above GL-10 m, with 10% above GL-2 m. However, no clear trend was observed for zones a–z, respectively.

Figure 4 is a histogram of the thickness of the estimated liquefiable layer for Level-2 ground motion classified by the degree of liquefaction. For the same reason as in Figure 3, only the results for Level-2 ground motion are presented. It can be seen that approximate 75–90% of the sites in zones a and b have liquefiable layers that have F_L values of 1 or less are 4 m or over in thickness. In contrast, 50% or more of the sites in zones d and z are 2 m or less in thickness, and 90% of the sites are 6 m or less in thickness. From the above, it can be concluded that the minimum F_L value shown in

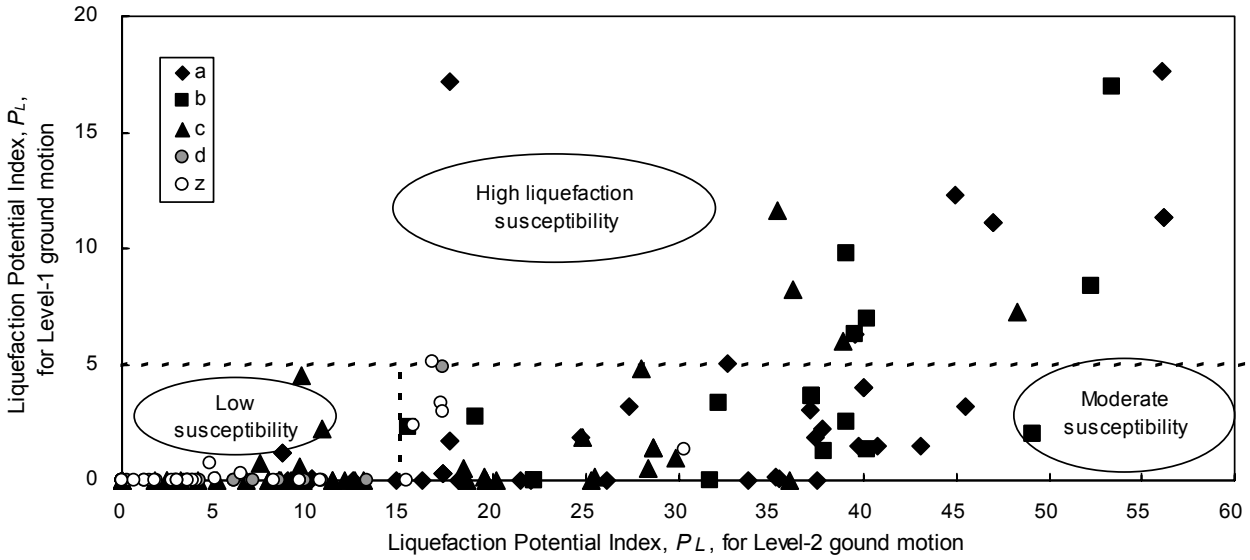

Figure 6. Relationship between P_L values determined for Level-1 and Level-2 ground motions

Figure 2, as well as the thickness of the liquefiable layer, may be effective indexes for liquefaction assessment.

Figure 5 is a histogram of the liquefaction potential index, P_L of the ground classified by the degree of liquefaction for (a) Level-1 ground motion and (b) Level-2 ground motion. It can be seen from Figure 5(a) that the P_L value is less than 2.5 at 90% or more of the sites in zones d and z, and that there are only 2 sites with $P_L > 5$: one in zone z and another in zone d. For zones a and b, the P_L values are greater than 5 at approximately 25% of the sites, suggesting the existence of a thick, loose soil layer. Sites with $P_L \leq 5$ are present in all zones, but sites with $P_L > 5$, which indicates the existence of a thick, loose layer, are virtually restricted to zones a–c. This may indicate that, for Level-1 ground motion, $P_L > 5$ define the lower limit for loose ground that is extremely susceptible to liquefaction.

It can be seen from Figure 5(b) that in zones a and b, which have severe degrees of liquefaction, 85% or more of the sites have $P_L \geq 15$. In contrast, 85% or more of the sites in zones d and z have $P_L \leq 15$. Therefore, it can be concluded that a P_L value of 15 for Level-2 ground motion may define the upper limit for dense ground, which is predicted to be free from the effects of liquefaction.

In the previous section, loose soil having high susceptibility to liquefaction was defined as ground with P_L values > 5 for Level-1 ground motion, and dense soil having low susceptibility to liquefaction as that with P_L values ≤ 15 for Level-2 ground motion. All other grounds correspond to medium-density soils having moderate susceptibility to liquefaction. The dotted lines in Figure 6 shows the boundaries for three ground types. Only the points in zones a–c fall within the high liquefaction susceptibility, while most of the points in zones d and z fall within the low susceptibility. Although approximately 15% of the ground in zones a and b is defined as low susceptibility soil, and 10–15% in zones d and z as high or moderate susceptibility soils, it can basically be concluded that the boundaries defined by liquefaction susceptibility in Figure 6 are sufficiently consistent with the actually observed degrees of liquefaction and, therefore, can be used to assess whether a ground surface will suffer a significant degree of liquefaction.

Relationship Between Ground Subsidence and Site Conditions

Ground subsidence during earthquakes is induced by various kinds of factors such as consolidation and lateral flow due to liquefaction, and also by earthquake ground shaking and displacement by faulting. Among these causes, consolidation and lateral flow due to liquefaction is considered to be the dominant factor in ground subsidence in the liquefied area.

Figures 7 and 8 show relationships between the amount of ground subsidence and the estimated liquefiable-layer thickness and the P_L values, respectively, only the cases of Level-2 ground motion, for the same reason as in Figures 3 and 4. Although a clear correlation is not observed in Figures 7 and 8, there appears to be a basic trend toward larger amounts of ground subsidence for larger P_L values and greater liquefiable-layer thickness. However, there are numerous points with a high liquefiable-layer thickness and large P_L values that have experienced only small amounts of ground subsidence. The amount of ground subsidence presented here is not based on engineering leveling, but are amounts of subsidence relative to a fixed point within the structure premises; this renders detailed analysis difficult.

In the 1995 Hyogoken-Nambu earthquake, soil liquefaction induced large ground displacement in the horizontal direction due to the shift of caisson quay walls, resulting in large

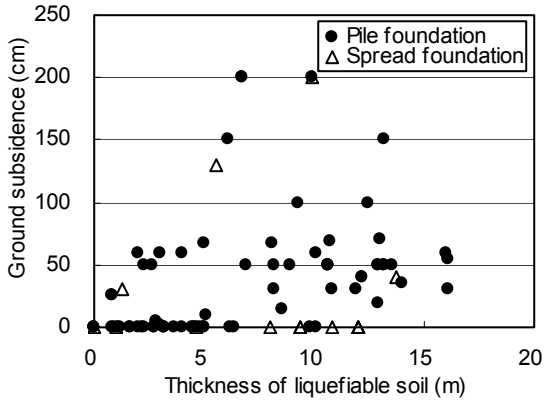

Figure 7. Ground subsidence vs. the thickness of the liquefiable layer for Level-2

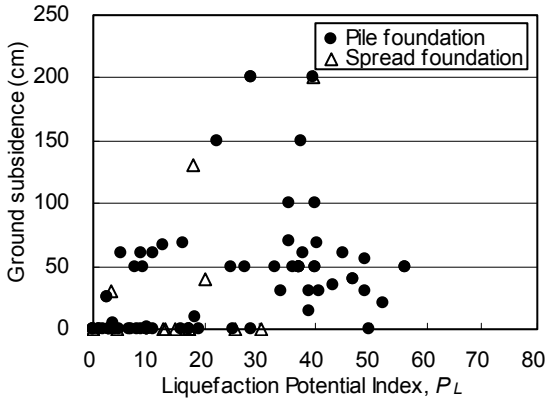

Figure 8. Ground subsidence vs. P_L values for Level-2 ground motion

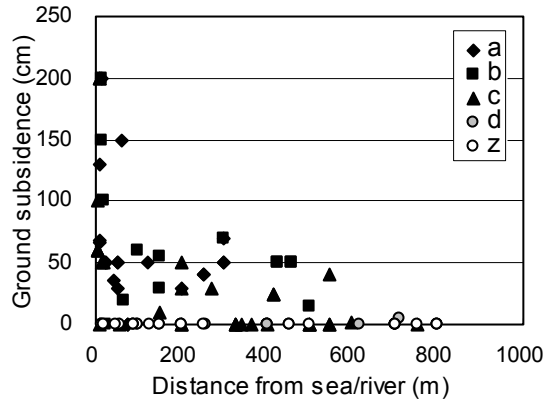

Figure 9. Amount of ground subsidence vs. the distance from the sea or river wall

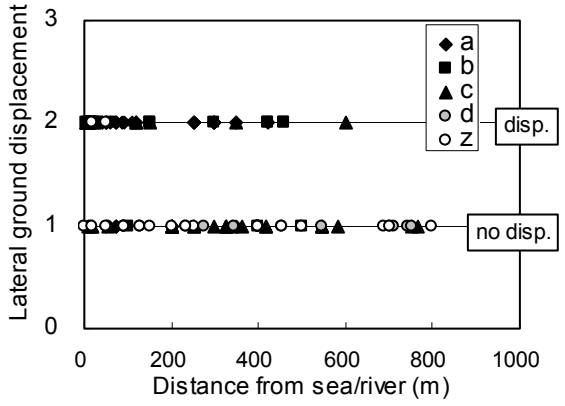

Figure 10. Occurrence of ground displacement vs. the distance from the sea or river wall

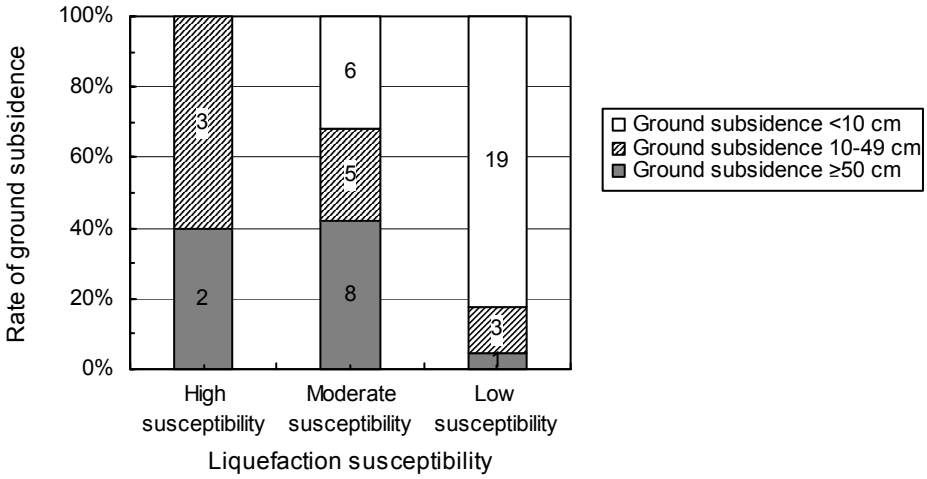

Figure 11. Rate of ground subsidence by liquefaction susceptibility

ground subsidence near the waterline. Figure 9 is a plot showing the relationship between the distance from the sea or river wall and the amount of subsidence, by the degree of liquefaction. It can be seen that ground subsidence was observed in zones a–c, where liquefaction was also observed, and most of cases of subsidence exceeding 50 cm are zones a and b, which experienced severe degrees of liquefaction. It should also be noted that ground subsidence only occurred within a distance of 500 m from sea or river wall, with the severest cases exceeding 100 cm occurring only within a distance of several tens of meters.

Figure 10 shows the relationship between the occurrence of horizontal ground displacement and the distance from sea or river wall, by the degree of liquefaction. Horizontal displacement is observed at most of sites in zones a and b, which are primarily located within a 500-m distance from sea or rivers, which coincides with the area in which ground subsidence was observed. It can be concluded from the above that the primary cause of significant ground subsidence at the survey sites in the present study is the lateral flow caused by liquefaction

Figure 11 shows the rate of ground subsidence by the susceptibility to liquefaction defined based on P_L values, excluding the data points in Figure 10 that are less than 100 m from sea or rivers. It can be seen that the grounds of high susceptibility tend to experience larger subsidence, while only a small percentage of low susceptibility grounds of experience subsidence exceeding 10 cm. Therefore, it can be concluded that susceptibility to liquefaction defined based on P_L values is also an effective index for assessing the amount of ground subsidence.

RELATIONSHIP BETWEEN DAMAGE TO BULDING AND SITE CONDITIONS

Structural damage to buildings is generally caused by a) excessive inertial force on the superstructure (insufficient bearing capacity of the pile), b) difference in ground shaking-induced displacement between strata, c) reduction in the bearing capacity of foundation ground due to liquefaction, d) reduction in the subgrade reaction of a pile due to liquefaction, accompanying pile deformation, and changes in stress on the pile, e) ground failure due to liquefaction (liquefaction-induced lateral flow, landslides, etc.), and f) ground displacement due to faulting. In the Hyogoken-Nambu earthquake, combinations of the above factors are considered to have caused damage to building foundations.

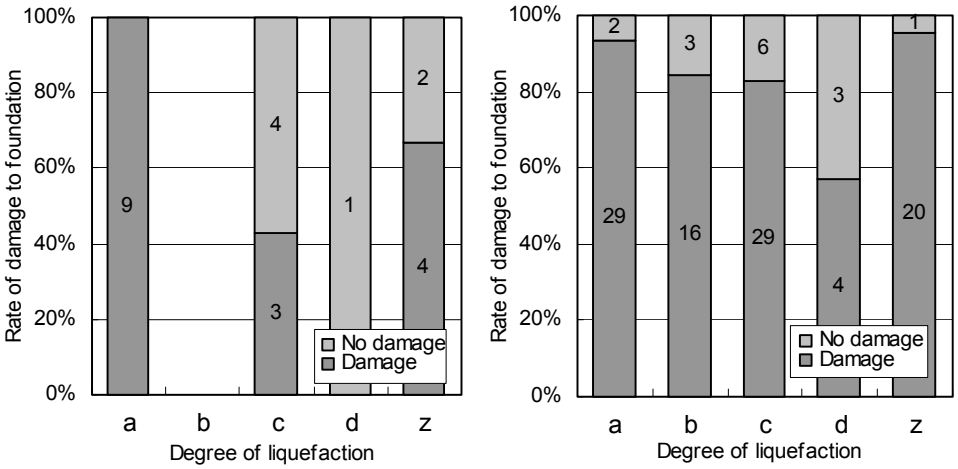

(a) Spread foundation (b) Pile foundation

Figure 12. Rate of damage to foundations by degree of liquefaction

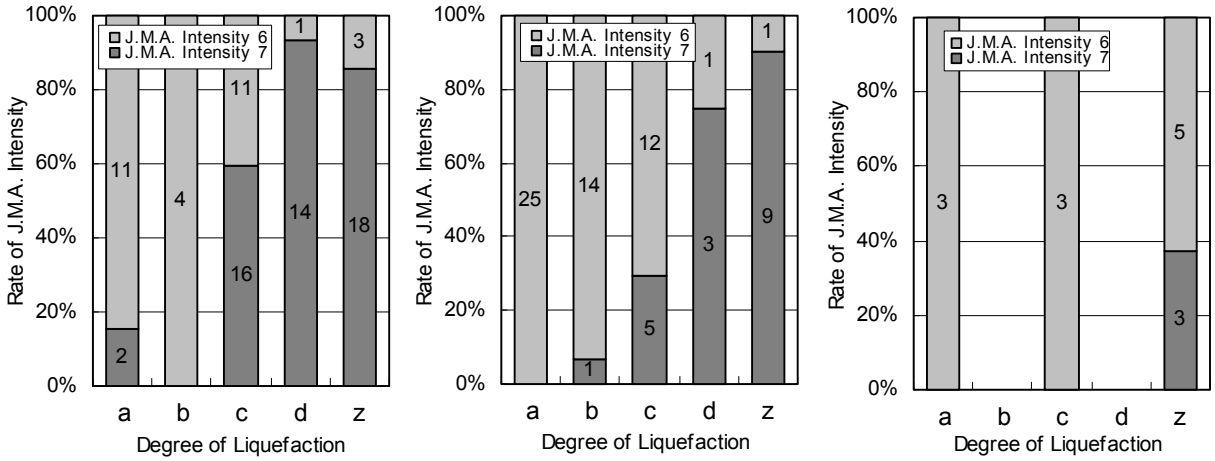

(a) >600 cm/ s^2 (b) 500–600 cm/s^2 (c) 400–500 cm/s^2

Figure 13. Degree of liquefaction classified by JMA intensities for level of ground motion at the engineering base layer

Figures 12(a) and (b) show the relationship between the presence or lack of damage to building foundations and the degree of liquefaction. For both spread and pile foundations, the rate of damage to foundations increases from zone c to a, with increasing degrees of liquefaction. Although both zones d and z are free of liquefaction in the immediate vicinity, zone z, which is nearly free of liquefaction, has a higher rate of damage to building foundations compared to zone d, in which liquefaction was not confirmed within a 100-m radius but was still present in the surrounding regions. This may be due to the lack of nonlinear behavior of the ground due to liquefaction, which may have resulted in stronger ground motions in zone z compared to those in zones a–d. Such stronger ground motions would have subjected the superstructure to excessive inertial force or damaged the piles through earthquake shaking-induced displacement of the ground.

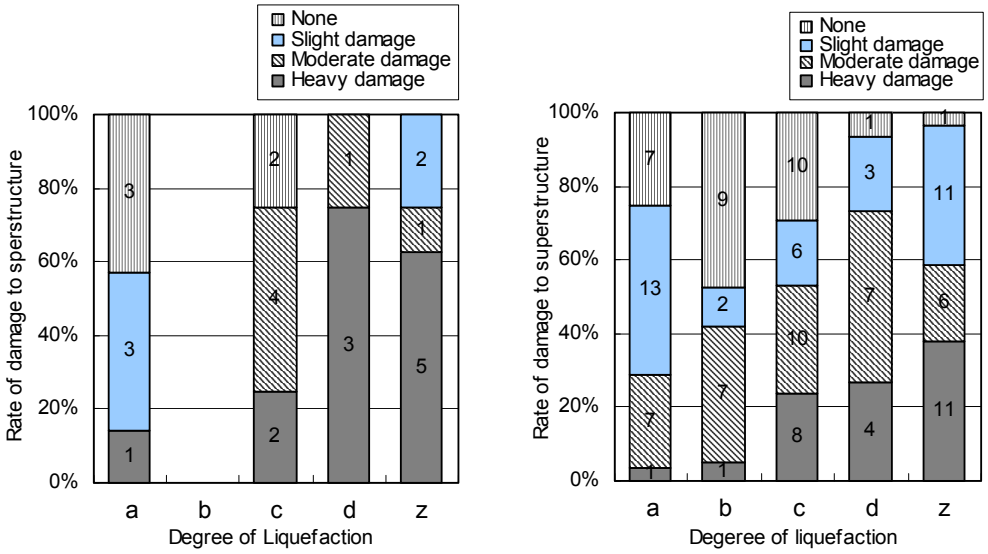

(a) Spread foundation (b) Pile foundation

Figure 14. Rate of damage to superstructures by degree of liquefaction

To verify the above, the relationship between the degree of liquefaction, JMA seismic intensity, and the estimated level of ground motion at the engineering seismic base layer was examined. Figure 13 shows observed JMA intensity of each survey site classified by degree of liquefaction for three levels of ground motion at the engineering seismic base layer [7]. Zones a and b, which have high degrees of liquefaction, primarily experienced ground motion of JMA intensity 6, regardless of the level of ground motion at the base layer. In contrast, zones d and z, which are free of liquefaction, present more areas of JMA intensity 7, with higher levels of ground motion at the base layer.

This implies that the surface ground in zones a and b behaved in a strongly nonlinear manner due to liquefaction, which suppressed the amplification of ground motion. Therefore, in zones d and z, which are free of liquefaction, the observed JMA intensity on the surface correlates well with the level of ground motion at the base. It can be concluded that the so-called "quake-absorbing effect of liquefied ground" has been clearly demonstrated based on the case history of the Hyogoken-Nambu earthquake.

Figure 14 represents rate of damage level of superstructures classified by the degree of liquefaction. For both spread and pile foundations, the rate of heavy damage to superstructures decreases with an increase in the degree of liquefaction. The suppression of the amplification of ground motion due to the quake-absorbing effect of the liquefaction is also reflected in the damage level of superstructures.

CONCLUDING REMARKS

The following conclusions were reached based on a statistical investigation of the cases of damage to buildings due to the 1995 Hyogoken-Nambu earthquake in Kobe and its neighboring cities.

1) The minimum liquefaction resistance factor, $F_{L,}$ and the liquefaction potential index, P_L, are both effective as indexes for assessing the degree of liquefaction at the surface. However, the P_L value seems to be more appropriate.

2) The liquefaction susceptibility classified by P_L value may be used as an index in liquefaction assessment. The ground with low liquefaction susceptibility is defined as ground with a P_L values of > 5 for Level-1 ground motion; the ground with low susceptibility is defined as ground with P_L values of ≤ 15 for Level-2 ground motion. All other grounds are defined as moderate susceptibility to liquefaction.
3) Regions in which significant ground subsidence has been induced by liquefaction generally coincide with regions that generated lateral ground displacement, and are located within approximately 500 m of sea or river wall. In regions within 100 m of a edge of water, high degrees of subsidence exceeding 50 cm have been observed.
4) Based on ground classification by P_L value for Level-1 and Level-2 ground motion, severe cases of ground subsidence exceeding 50 cm due to liquefaction were observed in ground with high and moderate susceptibility to liquefaction but were not observed in ground with low susceptibility.
5) In regions that had experienced liquefaction, the rate of buildings with damaged foundations increases with an increase in the degree of liquefaction for both spread and pile foundations. In contrast, in regions that had experienced no liquefaction, the rate of buildings with damaged foundations is as much as in regions with extensive liquefaction, but this considered to have been induced by strong ground motions rather than by liquefaction.
6) By studying the relationships among the degree of liquefaction, the JMA intensity, and the estimated level of ground motion at the engineering seismic base layer, it has been confirmed that, in regions with extensive liquefaction, the surface ground behaved in a strongly nonlinear manner.
7) With increases in the degree of liquefaction, the rate of heavy damage to superstructures decreases, reflecting the quake-absorbing effect of liquefaction due to the nonlinear behavior of ground.

ACNOWLEDGEMENT

This study was conducted as a part of the activities of the research subcommittee of the Japan Society of Civil Engineers in "Investigation of Liquefaction Caused by Level-2 Ground Motion." The authors would like to thank Chairman, Prof. Kokusho and the other members of the committee for their valuable advice.

REFERENCES

[1] Editorial Committee for the Report on the Hanshin-Awaji Earthquake Disaster. 1998. The Report on the Hanshin-Awaji Earthquake Disaster . Tokyo: Maruzen Publishing Co., pp. 259-547.
[2] Hamada, M., Isoyama, R. and Wakamatsu, K. 1995. The 1995 Hyogoken-nanbu (Kobe) Earthquake, Liquefaction Ground Displacement and Soil Condition in Hanshin Area. Association of for Development of Earthquake Prediction.
[3] Japan Road Association. 2002. Specifications for Highway Bridges Part V Seismic Design.
[4] Iwasaki, T., Tokida, K., Tatsuoka, F., Watanabe, S., Yasuda, S. and Sato, H. 1982. "Microzonation for Soil Liquefaction Potential Using Simplified Methods," Proc., 3rd Int. Conf. On microzonation, Seattle, Vol.3, pp. 1319-1330.
[5] Wakamatsu, K. and Numata, A. 2001. "Soil Constants for Liquefaction Assessment in Hanshin Area," Proc., 56th Annual Meeting of Japan Society of Civil Engineers, Vol.3, pp.216-217 (in Japanese)
[6] Japan Road Association. 1996. Specifications for Highway Bridges Part V Seismic Design.
[7] Sugito S.1996. "Simulation of Near Field Ground Motion by Evolutionary Spectrum Model," Proc., 1st Symposium on the Mitigation of Urban Disasters caused by near-Field Earthquakes, pp.99-102 (in Japanese)

Effects of Ground Motion Characteristics and Fines Content on Liquefaction Resistance Based on Case Histories

Tetsuya Sasaki, Keiichi Tamura, Osamu Matsuo and Shinya Nakamura

ABSTRACT

Liquefaction of soils is one of the major causes of geo-hazards and associated structural damage. Assessments of liquefaction potential of soils are widely used for engineering practice in Japan, the United States and other earthquake prone areas. To verify the current method for assessments of liquefaction potential of soils, many field performance data as possible on liquefaction and non-liquefaction in situ was collected. Also based on the data, the relationships are reviewed.

A total of 846 boring data in liquefied and non-liquefied sites during past eleven earthquakes in Japan was collected. Liquefaction resistance curve was obtained as the liquefaction / non-liquefaction boundary in the relationship between maximum shear stress ratio during an earthquake and the corrected N-value N_1. The lateral seismic coefficient used for the calculation of maximum shear stress ratio during an earthquake was estimated based on a strong motion record or distribution of acceleration.

We studied the influences of ground motion characteristics and soil properties upon liquefaction resistance. The following results were obtained from this study. The liquefaction resistance is large as magnitude is moderate to small or duration is short. The result for ground motion types, which were caused by plate boundary earthquakes with large magnitude, termed as Type I, and inland intra-plate earthquakes, Type II, also coincides with this fact, which suggests that the increment of liquefaction resistance with that of N-value is large in case of inland intra-plate earthquakes. Comparing the results of the same N_1 values, the liquefaction resistance with the fines content of more than 35% increases as the fines content increases. On the other hand, the liquefaction resistance with the fines content of less than 35% decreases as the fines content increases.

Tetsuya Sasaki, Research Engineer, Ground Vibration Research Team, Earthquake Disaster Prevention Research Group, Public Works Research Institute, 1-6 Minamihara, Tsukuba-shi, Ibaraki-ken, Japan 305-8516
Keiichi Tamura, Team Reader, ditto
Osamu Matsuo, Research Coordinator for Earthquake Disaster Prevention, National Institute for Land and Infrastructure Management.
Shinya Nakamura, Senior Research Engineer, Construction Technology Research Department, Public Works Research Institute

INTRODUCTION

Liquefaction of soils is one of the major causes of geo-hazards and associated structural damage. Most of the major cities in Japan are located on the alluvial soils, which are susceptible to liquefaction hazards during earthquakes.

Assessments of liquefaction potential of soils are widely used for engineering practice in Japan, the United States and other earthquake prone areas. The practical procedures are based on soil penetration resistance, typically SPT blow count, and soil gradation data. The assessment procedures are in general summarized as relationships between SPT *N*-value and cyclic strength ratio with a fine content as a parameter.

The Hyogoken Nanbu earthquake of 1995 caused extensive liquefaction over a wide area of offshore-reclaimed lands and inland natural deposits. Liquefaction and its associated ground flow induced destructive damage to various engineering structures. Shortly after the quake, in order to develop the simplified procedure to estimate the liquefaction resistance of in situ soils for severe ground motion, undrained cyclic triaxial tests were run on high quality undisturbed samples retrieved by the ground freezing method and the effect of seismic shear stress irregularity and fines content were reexamined and converted into the method [1]. As the results of the investigation, a revised method to assess liquefaction potential of in situ soils based on SPT *N*-value and soil gradation parameters was proposed [2]. The revised method was calibrated with field performance data during past earthquakes and it showed a good agreement [1].

However, these relationships depend on the data used. Therefore it is aimed in this study that as many field performance data as possible on liquefaction and non-liquefaction in situ be collected. Also based on this data, the relationships are reviewed.

METHODOLOGY

As the first step, as many field performance data as possible on liquefaction and non-liquefaction are collected. The data include boring data (soil profile, SPT *N*-values and soil gradation data), liquefaction evidence map, and strong motion records for past earthquakes in Japan. The number of boring data collected and the earthquakes are summarized in Table 1. Based on this data, the relationships between maximum shear stress ratio during an earthquake and the corrected *N*-value N_1 are reviewed.

(1) Data collection

A total of 846 boring data in liquefied and non-liquefied sites during past eleven earthquakes was collected, which includes from the 1964 Niigata earthquake to the 2000 Western Tottori earthquake. The data collected were critically reviewed from the viewpoint of reliability on judgment whether the site liquefied or not. Judgment of liquefaction occurrence at a boring site was made primarily based on visual observation of surface evidences such as sand boils, cracking, or settlement. For a site where liquefaction occurrence was presumed, liquefied depth was selected according to the following criteria:

a) below the ground water level and within 8 m deep from the ground surface.
b) a mean grain size D_{50} of between 0.02mm and 10 mm.
c) the measured SPT *N*-value is the second lowest.

Table 1. Number of collected boring data

No.	Earthquake	Earthquake motion type	JMA magunitude	Date	Number of boring data
1	Niigata	Type I	7.5	1964/6/16	6
2	Tokachi-Oki	Type I	7.9	1968/5/16	2
3	Miyagi-ken-Oki	Type I	7.4	1978/6/12	1
4	Nihonkai-Chubu	Type I	7.7	1983/5/26	158
5	Kushiro-Oki	Type I	7.8	1993/1/15	77
6	Hokkaido-Nansei-Oki	Type I	7.8	1993/7/12	61
7	Hokkaido-Toho-Oki	Type I	8.1	1994/10/4	3
8	Sanriku-Haruka-Oki	Type I	7.5	1994/12/28	91
9	Hyogo-ken-Nanbu	Type II	7.2	1995/1/17	111
10	Kagoshima	Type II	6.3	1997/5/13	165
11	Gifu	Type II	5.2	1998/4/22	43
12	Tottori-ken-Seibu	Type II	7.3	2000/10/6	128
total					846

(2) Corrected SPT *N*-value

The SPT blow count *N*-value was normalized to an overburden pressure of approximately 100 kPa as

$$N_1 = \frac{170 \cdot N}{\sigma_v' + 70} \tag{1}$$

where N_1 : corrected SPT *N*-value to an effective overburden pressure of 100kPa and
σ_v': effective overburden stress, in kPa.

(3) Cyclic stress ratio

The maximum cyclic shear stress at the depth during the earthquake was first estimated by estimating the peak ground surface acceleration from the neighboring strong motion records or ground surface acceleration distribution maps, and then by using the following equation, which was based on Japanese design specifications for highway bridges [1].

$$L = \frac{\tau_{\max}}{\sigma'_v} = r_d \cdot \frac{\alpha_{\max}}{g} \cdot \frac{\sigma_v}{\sigma'_v} \tag{2}$$

$$r_d = 1 - 0.015z \tag{3}$$

where r_d: reduction factor with depth,
$\alpha_{\max}$: peak ground surface acceleration,
g : gravitational acceleration,
σ_v: total overburden stress,
σ_v': effective overburden stress and
z: depth in meter.

In this study, the peak ground surface accelerations are estimated from a strong motion record or previous peak ground acceleration maps.

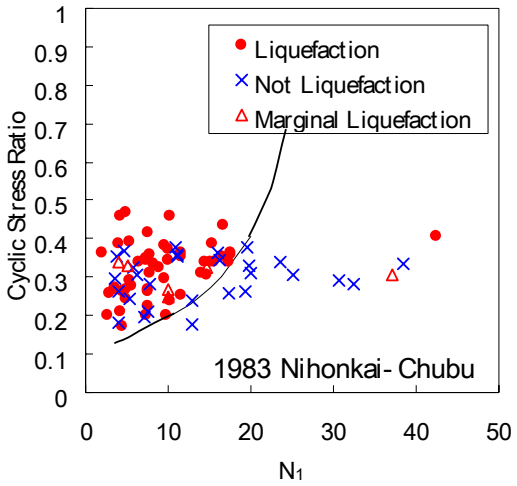

(a) 1983 Nihonkai-Chubu Earthquake

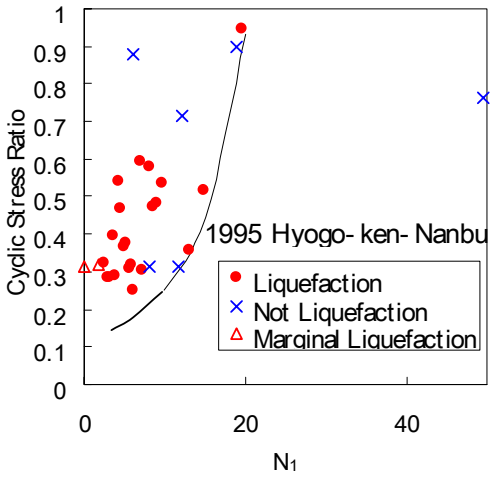

(b) 1995 Hyogo-ken-Nanbu Earthquake

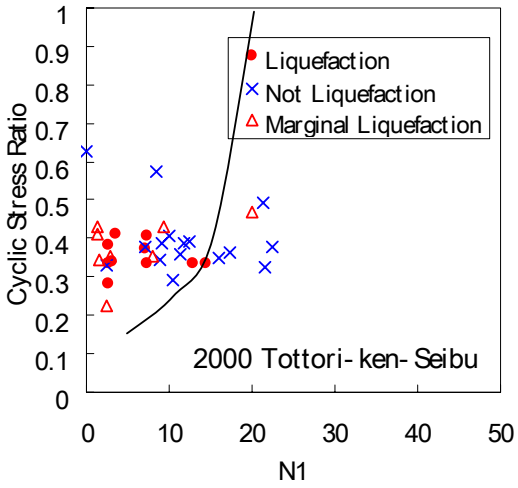

(c) 2000 Tottori-ken-Seibu Earthquake

Figure 1. Relationship between corrected *N*-value N_1 and cyclic stress ratio for typical earthquakes

(4) Liquefaction resistance curve

For each site data, the maximum cyclic shear stress induced at depth and the corrected *N*-value N_1 for the soil were plotted. The data plotted for liquefaction sites and for non-liquefaction sites may form the boundary, which corresponded to the liquefaction resistance curves for a particular soil. Making the data analyses for each data set earthquake, the liquefaction resistance curves were obtained for each earthquake and each soil type.

(5) Examinations on the effect of ground motion characteristics and fines content on liquefaction resistance

Finally, the difference in the liquefaction resistance curves obtained from various earthquake events were analyzed in terms of earthquake motion characteristics and fins contents of soil. Previous studies have shown that liquefaction resistance of soils is affected by the number of cycles, predominant frequency, magnitude and duration of earthquake motions, as well as the soil type and density. These factors affecting liquefaction resistance were examined.

Effects of earthquake motion characteristics on liquefaction resistance of soils

Figure 1 plots the data for typical earthquakes on a maximum shear stress ratio versus corrected *N*-value N_1 plot. Liquefaction resistance curves obtained as the liquefaction / non-liquefaction boundaries in the relationships between maximum shear stress ratio during earthquake and the corrected *N*-value N_1 are also plotted in the figure. The figure shows that the liquefaction resistance curves are different from the each other.

We study the influence of ground motion characteristics upon liquefaction resistance curve, in which earthquake magnitude, duration of ground motion record and ground motion type are chosen for representatives of ground motion characteristics. Ground motion type is classified after the design specifications for highway bridges in Japan [1], i.e., Type I and Type II ground motions represent ground motions caused by plate boundary earthquakes with large magnitude and inland intra-plate earthquakes, respectively.

(1) Effect of earthquake magnitude

Figure 2 shows the relationship between earthquake magnitudes and liquefaction resistances at N_1=10 and 20 and ratio of liquefaction resistance at N_1=20 to that at N_1=20 which were obtained from liquefaction resistance curves for various earthquake events. The moment magnitude M_w is estimated from JMA magnitude M_{JMA}. We see from these figures that the liquefaction resistance is large as magnitude is moderate to small and as N_1 values or liquefaction resistance ratios are large.

In the United States, to adjust the simplified liquefaction resistance curve to different magnitude earthquakes, correction factors called "magnitude scaling factors" were widely introduced [3]. The safety factor against liquefaction can be written in terms of liquefaction resistance ratio, cyclic stress ratio and magnitude scaling factor as follows:

$$FS = \frac{CRR_{7.5}}{CSR} MSF \tag{4}$$

where *FS*: safety factor against liquefaction,

$CRR_{7.5}$: cyclic resistance ratio determined for magnitude 7.5 earthquakes,

CSR: cyclic stress ratio during earthquakes,

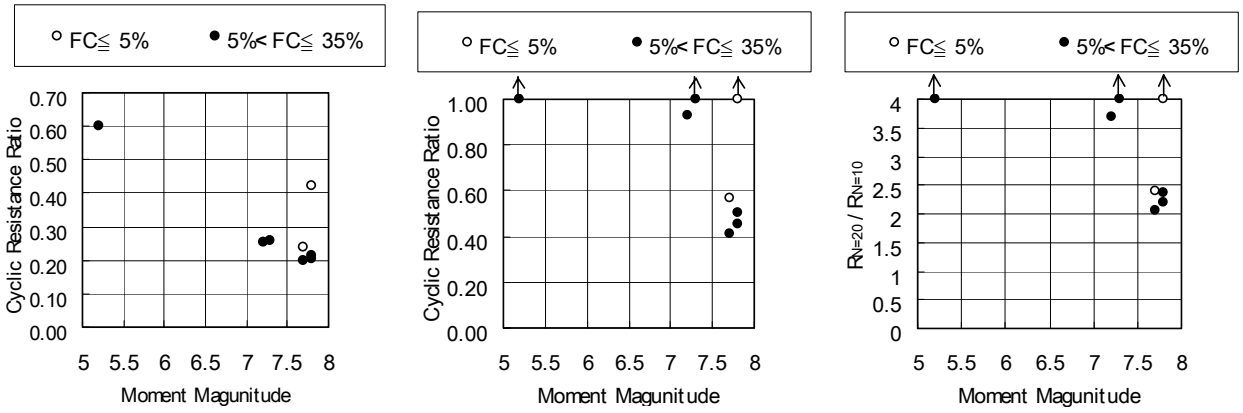

(a)N_1=10 (b) N_1=20 (c) Ratio of cyclic stress ratio N_1=20 to N_1=10

Figures 2. Relationship between earthquake magnitude and cyclic stress ratio

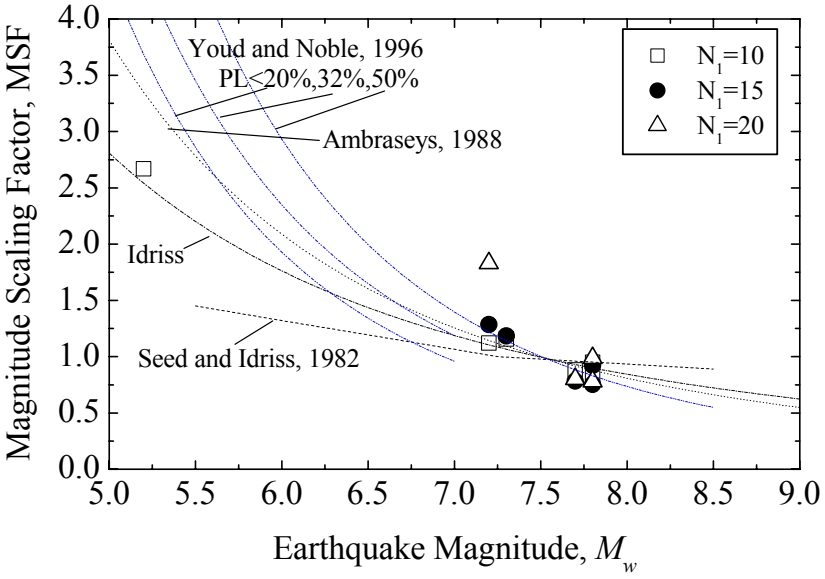

Figure 3. Magnitude scaling factor

MSF: magnitude scaling factor.

Various investigators derived the magnitude scaling factors [3]. In this study, we tried to estimate the magnitude scaling factors from the data collected.

Figure 3 shows the magnitude scaling factors derived from each earthquake. In the figure, magnitude scaling factors proposed by various investigators were also plotted. The magnitude scaling factors in the figure were obtained by following procedures. At first, we obtained the relationship between a liquefaction resistance ratio at specific N_1 values obtained from liquefaction resistance curves for each earthquake and earthquake magnitude (see Figure 2.(a) and (b)). Next, the liquefaction resistance ratio at specific N_1 values (N_1=10, 15 and 20) for magnitude 7.5 earthquake were estimated from the above relation. Finally, we obtained the *MSF* as liquefaction resistance ratio at each N_1 values (N_1=10, 15 and 20) divided by estimated the liquefaction resistance ratio for magnitude 7.5 earthquakes.

We see from Figure 3 that the *MSF* at small N_1 values obtained this study shows similar relation as previous relations. On the other hand, the *MSF* at lager N_1 values is lager than previous relations as magnitude is smaller. This fact indicates that the relationships between *MSF* and earthquake magnitudes might depend on the liquefaction resistance or values of N_1 and as the liquefaction resistance ratio or N_1 value is lager, the increment of *MSF* for decrease in the earthquake magnitude is higher.

(2) Effect of earthquake duration

Figure 4 shows the relationships between earthquake durations and liquefaction resistances at N_1=10 and 20 and a ratio of liquefaction resistance at N_1=10 to that at N_1=20. We see from this figure that the liquefaction resistances and the increment of the liquefaction resistance for the increment of the N_1 values are small as the durations of ground motions are large.

(3) Effect of ground motion type

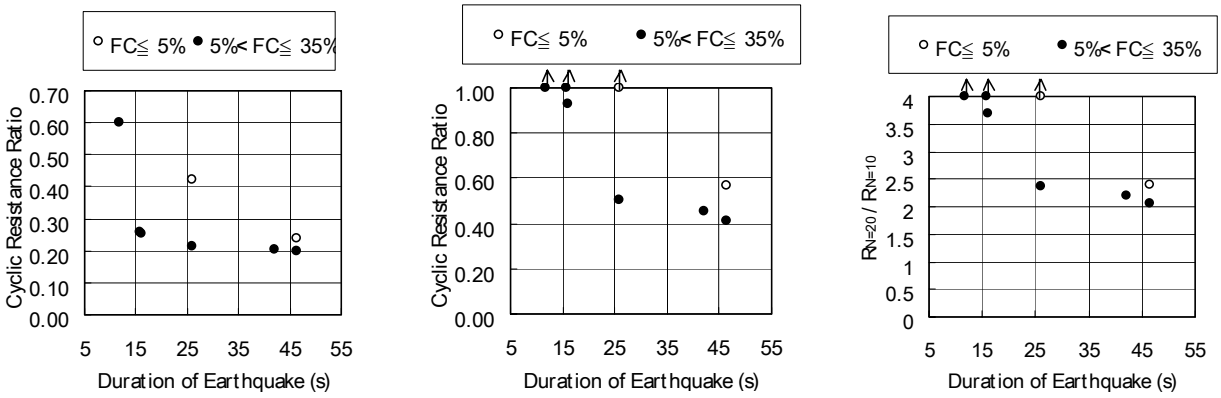

(a)N_1=10 (b) N_1=20 (c) Ratio of cyclic stress ratio N_1=20 to N_1=10

Figure 4. Relationships between duration of ground motion and cyclic stress ratio

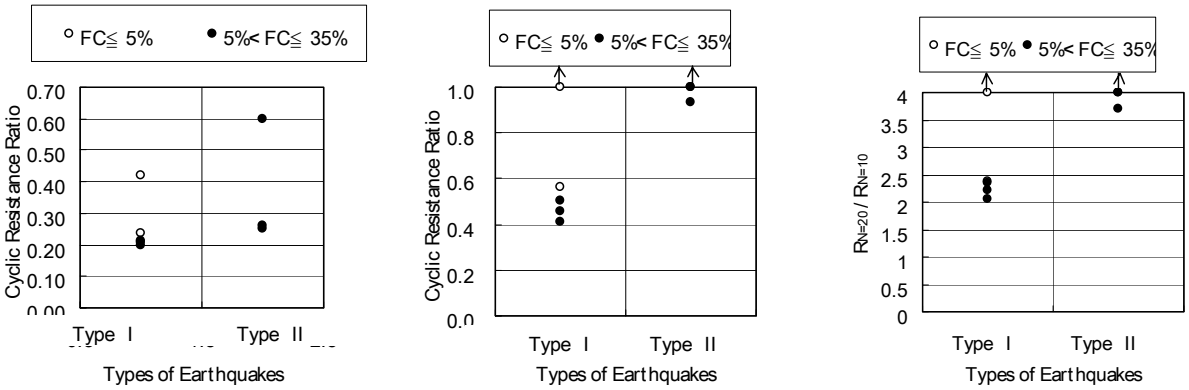

(a)N_1=10 (b) N_1=20 (c) Ratio of cyclic stress ratio N_1=20 to N_1=10

Figure 5. Relationships between ground motion types and cyclic stress ratio

Ground motion type is classified after the design specifications for highway bridges in Japan [1], i.e., Type I and Type II ground motions represent ground motions caused by plate boundary earthquakes with large magnitude and inland intra-plate earthquakes, respectively. In this study, each earthquake is categorized as shown in Table 1.

Figure 5 shows the relationships between ground motion types and liquefaction resistances at N_1=10 and 20 and ratios of the liquefaction resistance at N_1=20 to at N_1=10 for each earthquake. We see from this figure that the liquefaction resistance with that of N_1-value is large in case of inland intra-plate earthquakes, i.e. Type II earthquake. The result for Type I and Type II ground motions also coincides with the above mentioned facts from investigation for earthquake magnitude and duration of ground motion, which suggests that the increment of liquefaction resistance with that of N-value is large in case of inland intra-plate earthquakes.

Figure 6 (a) and (b) separately plot the data for type I and type II ground motion on the maximum shear stress ratio verses corrected N-value N_1 plot, respectively. Liquefaction resistance curves based on "Japanese design specifications for highway bridges" [1] for type I and type II earthquakes are superimposed in the figures respectively. The curves are obtained based on the results of undrained cyclic triaxial tests for high quality undisturbed samples retrieved by the ground freezing method and

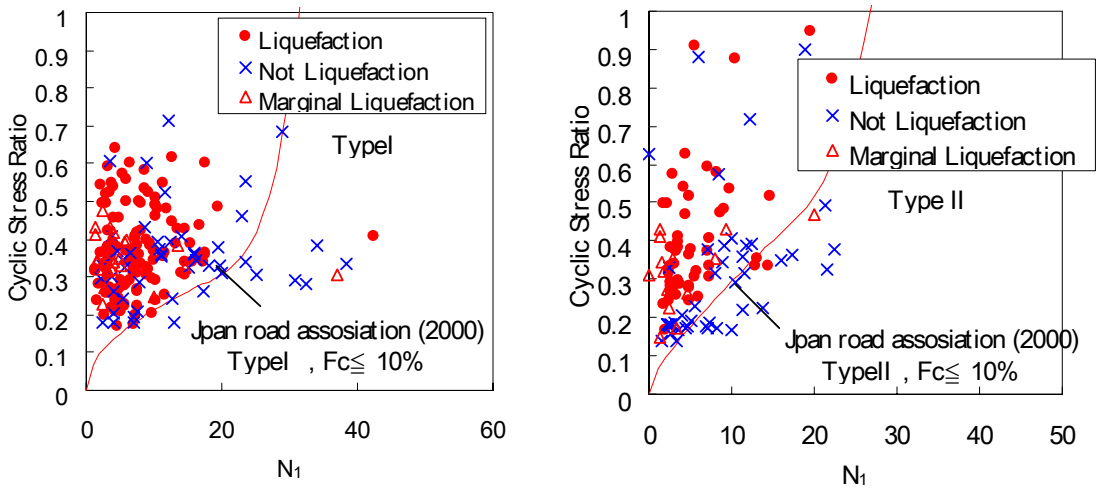

(a) Type I (b) Type II

Figure 6. Relationship between corrected N-value N_1 and cyclic stress ratio for different ground motion types

the reexaminations on the effects of seismic shear stress irregularity and fines content, which were expressed by following equations;

$$R = c_w R_L \tag{5}$$

(for Type I ground motion)

$$c_w = 1.0 \tag{6}$$

(for Type II ground motion)

$$c_w = \begin{Bmatrix} 1.0 & (R_L \le 0.1) \\ 3.3R_L + 0.67 & (0.1 < R_L \le 0.4) \\ 2.0 & (0.4 < R_L) \end{Bmatrix} \tag{7}$$

$$R_L = \begin{Bmatrix} 0.0882\sqrt{N_a/170} & (N_a < 14) \\ 0.0882\sqrt{N_a/170} + 1.6\times10^{-6}\cdot(N_a - 14)^{4.5} & (14 \le N_a) \end{Bmatrix} \tag{8}$$

$$N_a = c_1 N_1 + c_2 \tag{9}$$

where R: liquefaction resistance ratio

c_w: correction factor for shear stress irregularity (which includes a correction for mean confining pressure)

R_L: cyclic triaxial strength ratio

N_a: corrected N value accounting for the effects of grain size

c_1,c_2: parameters expressed as a function of fines content, FC.

Figure 5 show that the liquefaction resistance curves expressed by the equations (5) to (9) based on "Japanese design specifications for highway bridges" are bordering the liquefaction and non-liquefaction data fairly well.

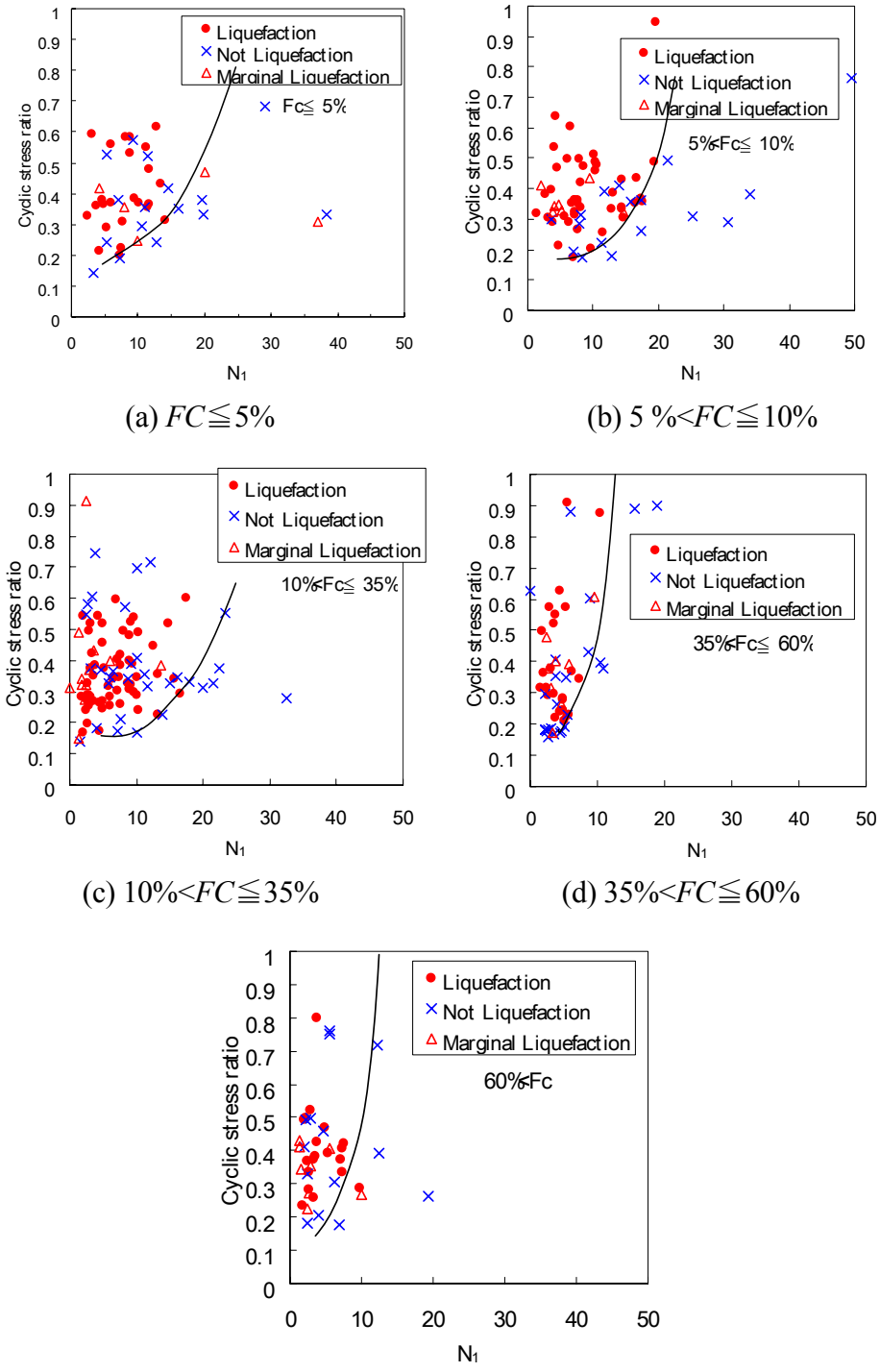

(a) $FC \leqq 5\%$ (b) $5\% < FC \leqq 10\%$

(c) $10\% < FC \leqq 35\%$ (d) $35\% < FC \leqq 60\%$

(e) $60\% < FC$

Figure 7. Liquefaction resistance curves for different fines content

Effect of fines content on liquefaction resistance of soils

In order to see the effect of fines content, the data were separately plotted according to fines content as in Figure 7. We see from this figure that a liquefaction resistance curve is much different in

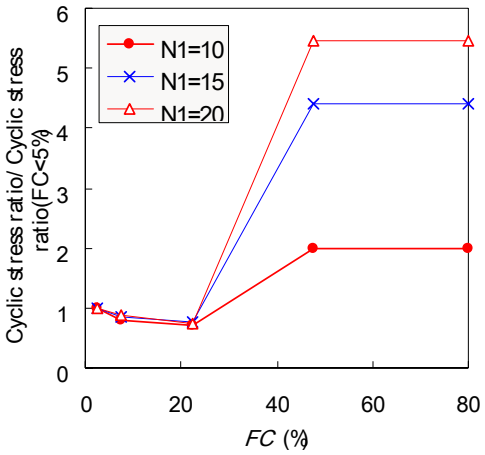

Figure 8. Effect of fines content, *FC*

each other. From this figure, ratios of the liquefaction resistance ratio to that of clean sand (fines content of less than 5%) at N_1= 10, 15 and 20 are plotted in relation to against fines content in Figure 6. Comparing the results of the same N_1 values, the liquefaction resistance with the fines content of more than 35% increases as the fines content increases, and its increment is increase as the N_1 values increase. On the other hand, the liquefaction resistance with the fines content of less than 35% decreases as the fines content increases.

Summary

We collected the field performance data of liquefaction occurrence and studied the influence of ground motion characteristics and fins content upon liquefaction resistance.

The following results were obtained from this study. The liquefaction resistance is large as magnitude is moderate to small or duration is short. The result for Type I and Type II ground motions also coincides with this fact, which suggests that the increment of liquefaction resistance with that of N-value is large in case of inland intra-plate earthquakes. Comparing the results of the same N_1 values, the liquefaction resistance with the fines content of more than 35% increases as the fines content increases. On the other hand, the liquefaction resistance with the fines content of less than 35% decreases as the fines content increases.

REFERENCES

[1] Matsuo, O., Tamura, K., Hamada, T., Azuma, T., Shimazu, T. and Murata, K. 1996 "Revised Liquefaction Potential Evaluation Procedure and Seismic Design Treatment of Liquefaction for Bridge Foundations," Proceedings of 12th U.S.-Japan Bridge Engineering Workshop, pp.137-159.

[2] Japan Road Association 2000. Design Specifications of Highway Bridges Part V Seismic design (English edition). Maruzen Co., pp84-88.

[3] Youd, T. L. and S. K. Noble 1997 " Magnitude scaling factors" Proceedings of the NCEER Workshop on Evaluation of Liquefaction Resistance of Soils, pp149-166.

Influence of Liquefaction on Response Spectra at Wildlife, California and Port Island, Japan Instrument Sites

T. Leslie Youd and Benjamin Carter

ABSTRACT

A primary effect of liquefaction is modification of ground motions as they propagate through layers softened by the liquefaction process. Such modification may be of importance to seismic design of bridges, buildings, pipelines and other constructed works sited over liquefiable layers. To better understand the influences of soil softening and liquefaction on ground response, ground motion records are examined herein from two instrumented sites where ground motions were monitored as liquefaction occurred during recent earthquakes. Those sites are the Wildlife Liquefaction Array (WLA), Imperial Valley, California and the Port Island downhole instrument array (PIDA), Kobe, Japan. The following conclusions are drawn from the study: (1) When significant soil softening or liquefaction occurs early in the sequence of strong ground motions, as occurred at both WLA and PIDA, late arriving short period (<1 sec) strong ground motion pulses are absorbed by the softened layer preventing transmission of strong motions to the ground surface. In this instance the softened layer acts as a natural base isolation system attenuating short-period energy peaks while increasing displacements at longer periods. (2) Soil softening shifts site resonance to longer periods, which may lead to amplification of long-period ground motions. At both WLA and PIDA, ground motions were amplified in the 1.0 sec to 2.0 sec period range. (3) Low-amplitude long-period motions following strong ground shaking may excite long-period ground oscillation over liquefied layers. Such oscillation occurred at WLA where a one-minuted long sequence of oscillations increased spectral accelerations at periods greater than 2.0 sec compared to those expected in the absence of liquefaction. Conditions were not favorable for the development ground oscillation at PIDA. (4) Based on these two case histories, ground oscillation appears to be engendered by resonance between the softened site and late arriving low-amplitude long-period ground motion. At WLA, with a liquefied layer thickness of 4 m and a distant seismic source, amplification of ground motions occurred in the 2.0 sec to 4.0 sec period range due to ground oscillation. At the PIDA site, with a liquefied layer thickness of 15 m and a nearby seismic source, ground oscillation attenuated quickly with only minor amplification of motions at periods greater than 2.0 sec.

Professor, Dept. of Civil and Environmental Engineering, 368 CB, Brigham Young University, Provo, UT 84602
Project Engineer, Construction Inspection and Testing Co., Tempe, AZ 85281

INTRODUCTION

One of the principal effects of liquefaction is modification of ground motions as they propagate through layers softened by the liquefaction process. Such modification may be of importance to the seismic design of bridges, buildings, pipelines and other works constructed over the liquefiable layers. To better understand the influences of soil softening and liquefaction on response spectra, records are examined herein from two instrumented sites subjected to liquefaction during recent earthquakes. Those sites are the Wildlife Liquefaction Array (WLA), Imperial Valley, California and the Port Island downhole instrument array (PIDA), Kobe, Japan. Computed response spectra from these sites indicate that sediment softening during the liquefaction process 1) prevented transmission of large, short-period (less than 1.0 sec) energy pulses through the softened layers; 2) caused lengthening of period and amplification for motions in the 1.0 sec to 2.0 sec range, and 3) in the case of the WLA site generated long-period (2.0 sec to 4.0 sec) ground oscillations that increased or amplified spectral response in this long period range.

INVESTIGATIVE PROCEDURE

To determine the influence of liquefaction on ground motions transmitted through liquefying or liquefied layers, we compared ground motions at and response spectra determined from motions recorded at ground surface (termed actual motions and spectra) with motions and spectra predicted from acceleration recorded by instruments installed immediately below the liquefiable layer (termed predicted motions and spectra). To generate the predicted motions and spectra, the motions recorded at depth were propagated upward to the ground surface using the program PROSHAKE (a modification of SHAKE for of use in a Windows environment). In this analysis, we used shear-wave velocities measured at the sites before the earthquakes with no modulus reductions to account for soil softening. Thus, the motions predicted at ground surface are those that should have occurred in the absence of soil softening and liquefaction.

To check how well predicted motions by this procedure agree with actual motions in the absence of soil softening and liquefaction, we compared measured and predicted motions and spectra determined from the from the 1987 Elmore Ranch earthquake (M=6.2) which shook the WLA site 11 hours before the 1987 Superstition Hills earthquake, but did not generate significant pore water pressures (Holzer et al., 1989). Thus, according to our hypothesis, the predicted and actual ground motions and response spectra should be similar for the Elmore Ranch event. These response spectra are plotted on Fig. 1 for both North-South (NS) and East-West (EW) motions. For the NS motions and response periods greater than 0.4 sec, the predicted spectra are congruent with the actual spectra. Although not congruent in the EW direction for periods greater than 0.4 sec, the predicted spectra closely match the shape of actual spectra with only slightly smaller response values. For periods less than 0.4 sec, actual and predicted spectra have approximately the same shape in both the NS and EW directions, but have significantly different response values at some periods. This comparison indicates that for the WLA site, predicted response spectra closely match the actual spectra for periods greater than 0.4 sec and are generally similar for periods less than 0.4 sec.

As a second check on the procedure, we compared spectra calculated from motions recorded at the 16 m depth during the 1995 Kobe earthquake (M=6.9) (noted as actual spectra on Fig. 2) with predicted spectra at the same depth calculated from ground motions measured at 32 m depth. The 32-m depth motions were propagated upward to the 16 m depth using the program PROSHAKE. Between the 16 m and 32 m depths, the sediments at PIDA are soft, nonliquefiable clays that apparently did not further soften during the earthquake. Although not a perfect fit, the match is rather close between the actual and predicted spectra for periods greater than 0.3 sec for both the NS and EW motions. At periods less than 0.3 sec, the actual and predicted spectra are similar in the NS direction, but a major peak is missed in the predicted spectra for the EW direction relative to the actual spectra.

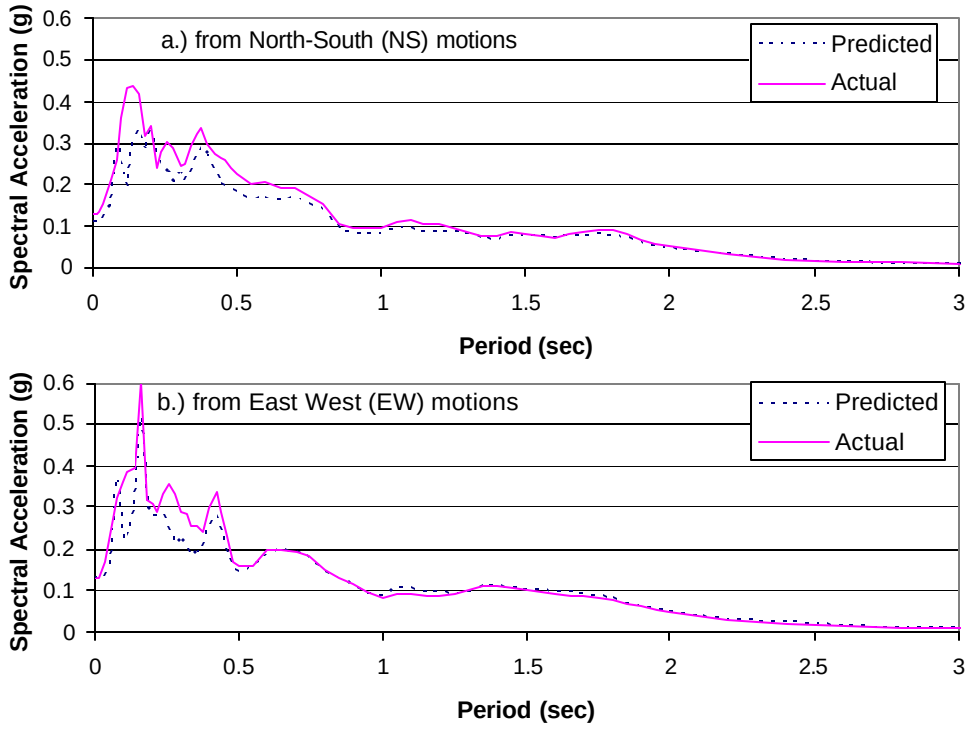

Figure 1. Predicted and actual response spectra at WLA from 1989 Elmore Ranch earthquake (M=6.2)

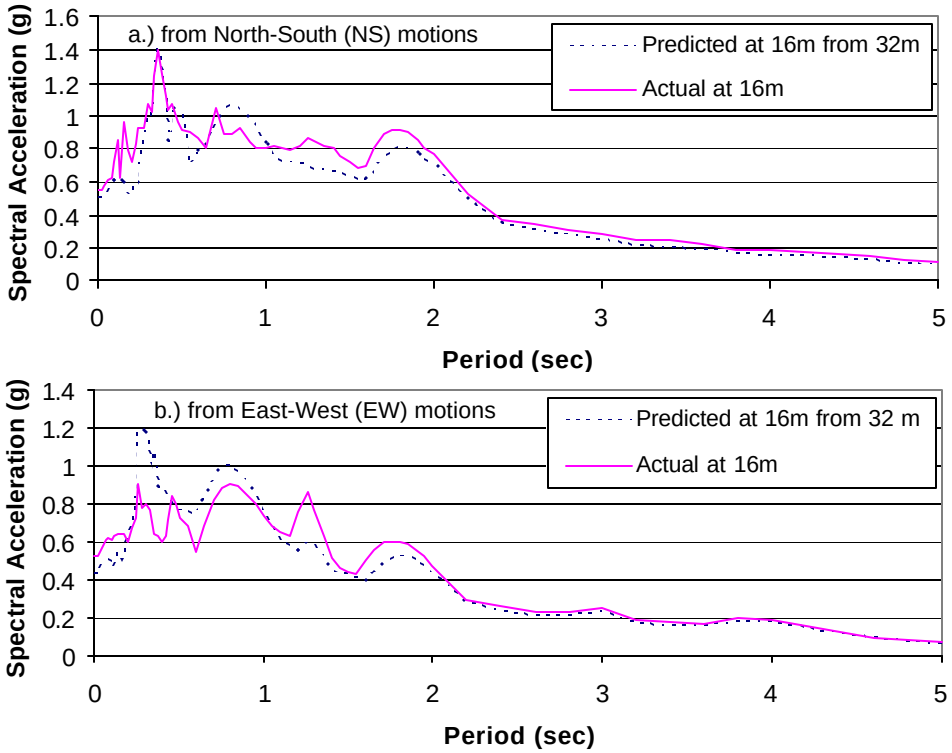

Figure 2. Predicted and actual response spectra at 16 m depth at PIDA from 1995 Hyogoken-Nambu earthquake (M=6.9)

Based on these comparisons, we conclude that actual spectra are adequately matched by predicted spectra to make the desired comparisons, and that major differences between measured and predicted are attributable to soil softening. Thus, major differences between predicted motions and spectra in the following site comparisons are attributed to soil softening during the liquefaction process.

COMPARISON OF GROUND MOTIONS AND RESPONSE SPECTRA FROM THE WILDLIFE LIQUEFACTION ARRAY (WLA)

On November 23, 1987, the Superstition Hills earthquake (M=6.6) shook the WLA site, generating liquefaction of subsurface sands and silty sands lying between depths of 3 m and 7 m. Evidence of liquefaction included sand boils, ground fissures, lateral spread displacement, and instrumentally recorded pore-water pressures. Sediment stratigraphy, soil types, and locations of instruments placed at the site are sketched on Fig. 3. The pore pressure records indicate that pressures began to rise as the peak acceleration pulse of 0.21 g passed through the site 13.6 sec after recording began (Fig. 4). Pore pressures rose rather rapidly at first, but had only risen to pore pressure ratios r_u, ranging from 0.4 to 0.6 when strong ground shaking ceased, about 21 sec after recording began (Holzer et al., 1989; Youd and Holzer, 1994). Pore pressures continued to rise, however, until r_u near 1.0 were reached in the upper part of the layer about 60 sec after triggering.

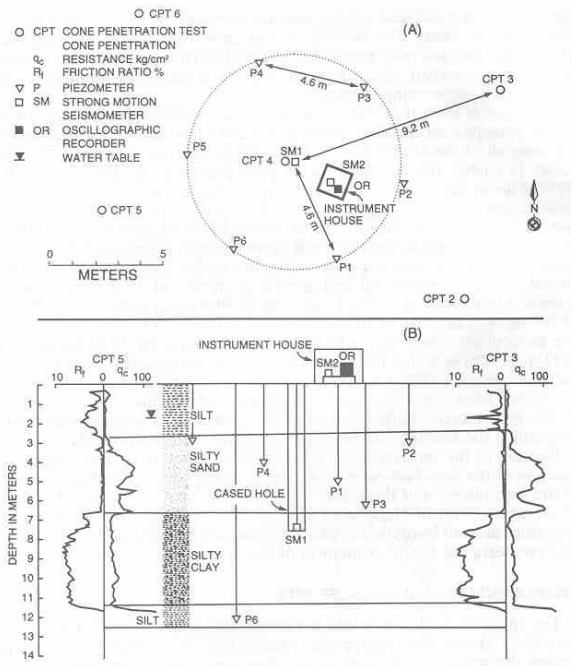

Figure 3. Site plan (a) and cross section (b) showing sediment layers and instrument locations at WLA (after Bennett et al., 1984)

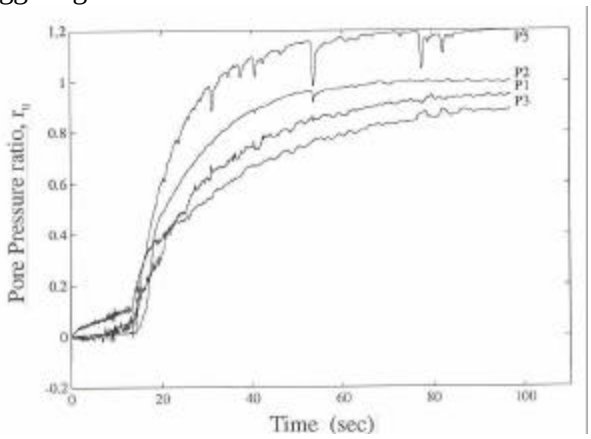

Figure 4. Pore pressure ratio versus time curves calculated from pore pressures recorded at WLA during 1987 Superstition Hills earthquake (M=6.6)

Actual and predicted ground motions at WLA are plotted on Fig. 5 for both the NS and EW directions. These motions are nearly congruent until the 13.6 sec, the time of the arrival of the peak acceleration pulse. At that juncture, pore-water pressures began to rise in the liquefying layer, and the characteristic period of the measured surface motions began to lengthen compared to predicted motions. This lengthening of period is indicative of sediment softening due to increased pore-water pressures. By 16 sec (r_u ranging from 0.2 to 0.3), softening was sufficient that correlation between the actual and

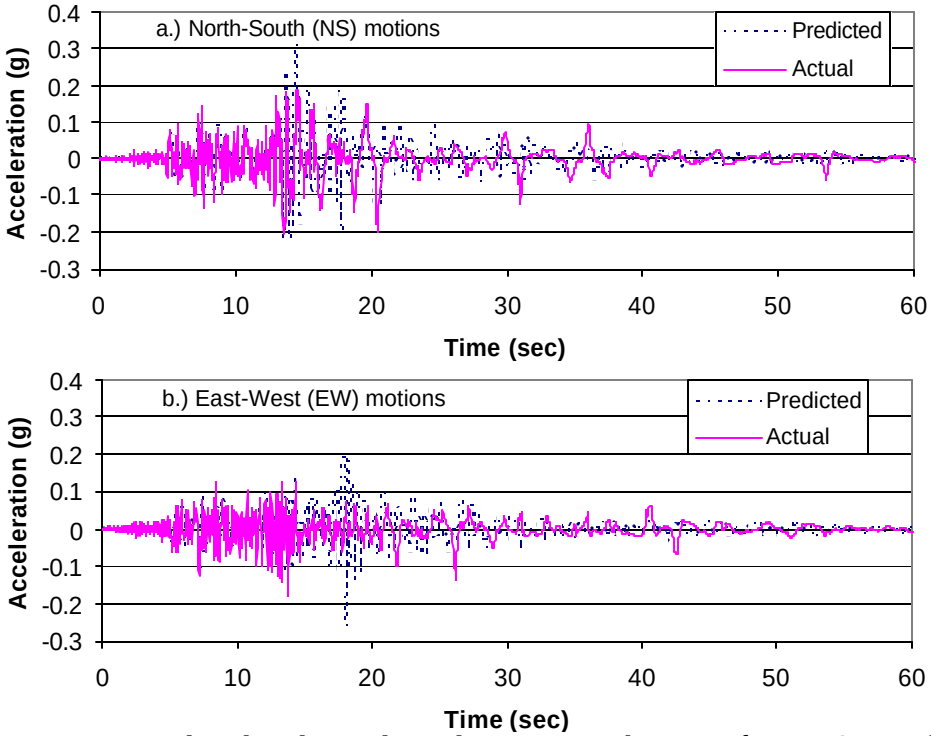

Figure 5. Predicted and actual acceleration time histories for WLA site during WLA during 1987 Superstition Hills earthquake (M=6.6)

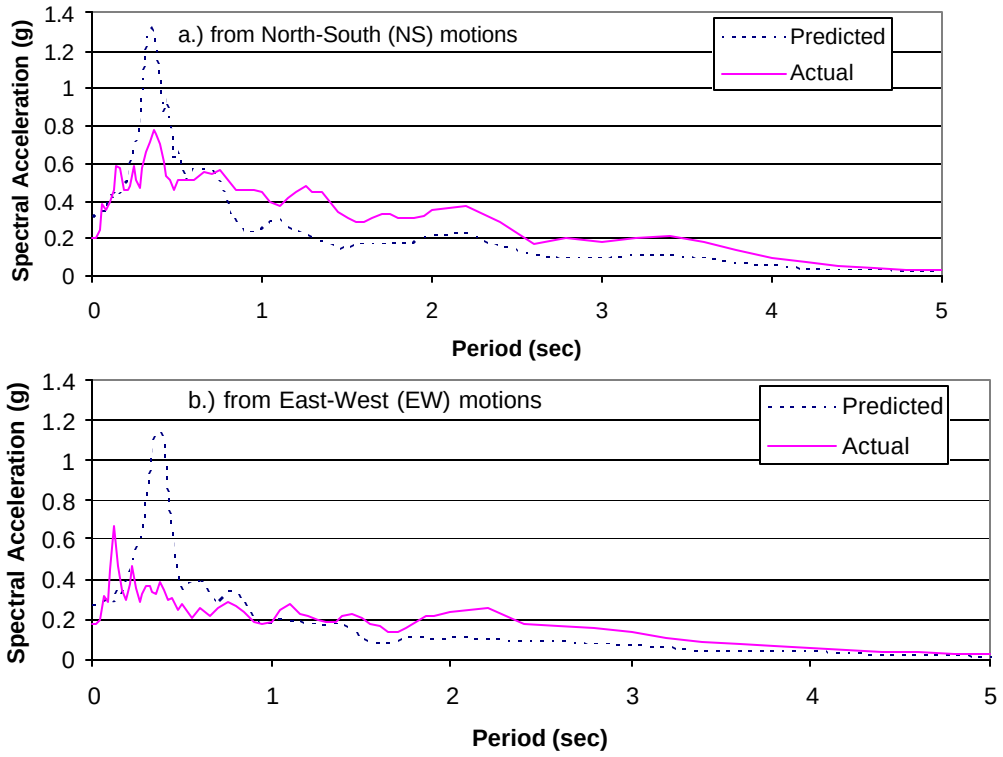

Figure 6. Predicted and actual response spectra for WLA during 1987 Superstition Hills earthquake (M=6.6)

predicted motions was poor. Shortly thereafter, several large acceleration peaks (between 16 sec and 19 sec) arrived at the base, but were not transmitted through the liquefying layer and thus do not appear in the actual surface ground motion record. Pore pressures ratios at this juncture were still less than 0.5.

To examine the influence of soil softening on response spectra, pseudo acceleration response spectra were calculated from the actual and predicted ground motions. Those spectra are plotted on Figs. 6a and 6b for the NS and EW directions, respectively. Large predicted spectral peaks, at periods between 0.2 sec and 0.5 sec, are absent in the actual spectra, indicating that motions causing these expected peaks were absorbed in the softened layer. Conversely, at periods greater than 1.0 sec, the predicted spectra are larger than the actual spectra, indicating amplification of motions in that period range. This amplification was due to ground oscillation that developed at the site. The greater amplification of motions in the 2.0 sec to 4.0 sec range in the NS direction compared to the EW direction was apparently due to greater oscillation in that direction, which is the approximate direction in which lateral spread displacement occurred (Youd and Bartlett, 1989).

To further demonstrate the attenuation of short-period motions and amplification of long-period motions as a function of sediment softening, we computed response spectra from various time segments of the actual and predicted records of ground motion. For example, predicted and actual spectra for the first 13.6 sec, up until the time of the arrival of the peak acceleration pulse and prior to significant pore-pressure rise, are plotted on Fig. 7. These plots show that the predicted and actual spectra were nearly congruent for this increment, an indication that significant sediment softening had not occurred at that time. The plot also indicates that most of the short period energy, periods less than 0.3 sec, had passed though the site by that time.

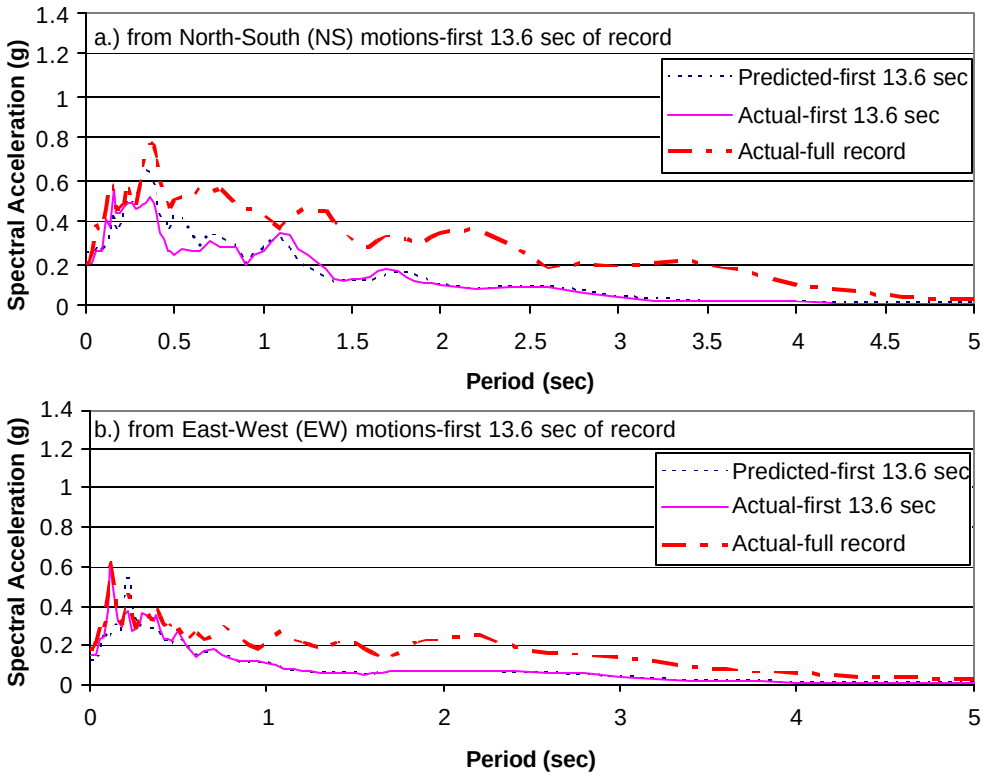

Figure 7. Predicted and actual response spectra calculated from the first 13.6 sec of acceleration record for WLA during 1987 Superstition Hills earthquake (M=6.6)

Fig. 8 contains predicted and actual spectra from the first 20 seconds of record along with the actual spectra from the full record for reference. The predicted spectra on these plots contain large spectral peaks at periods between 0.3 sec and 0.5 sec that are absent on the actual spectra, indicating that large pulses of energy in that period range were absorbed by the softened sediment between 13.6 sec and 20 sec. Also, the predicted and actual spectra are congruent and much lower that the final spectra for periods greater than 1 sec for EW motions and 1.5 sec for NS motions, indication that long-period ground oscillation did not develop prior to 20 sec, the time of approximate cessation of strong ground motion.

The long-period energy that filled the gap between the 20-sec incremental and the final actual spectra (Fig. 8) was due to a series of long-period ground oscillations that developed at the site and continued for about one minute after cessation of strong ground shaking. These oscillations caused greater spectral amplification in the NS direction than the EW direction, apparently due to greater oscillation amplitudes in the NS direction, the direction in which lateral spread displacement occurred. The predicted and actual time histories of acceleration (Fig. 5) indicate a correlation between a series of low-amplitude, long-period motions in the predicted acceleration time history and ground oscillations clearly evident in the actual ground motions. These oscillations, which occurred after strong ground shaking had ceased are roughly in phase and in resonance with the weaker input motions. Thus, it appears that the late arriving long-period seismic waves drove the large and rather persistent ground oscillations that continued after strong motion ceased.

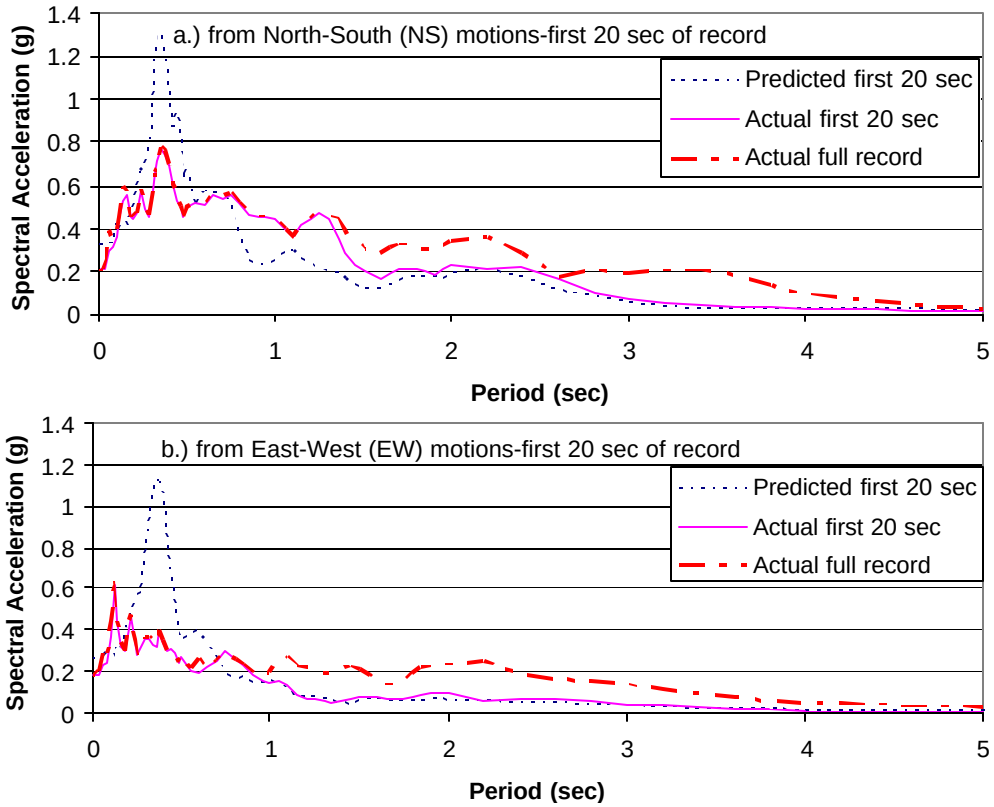

Figure 8. Predicted and actual response spectra calculated form the first 20 sec of acceleration record for WLA during 1987 Superstition Hills earthquake (M=6.6)

COMPARISON OF GROUND MOTIONS AND RESPONSE SPECTRA FROM THE PORT ISLAND ARRAY (PIDA)

On January 17, 1995, the Hyogoken-Nambu earthquake (M=6.9) shook the PIDA site, causing liquefaction of subsurface granular fill between depths of 3 m and 16 m. Evidences of liquefaction included eruption of large sand boils accompanied by vertical (ground settlement) and horizontal (lateral spread) ground displacements at the site of a fraction of a meter each. Sediment stratigraphy consists of 18 m of granular fill underlain by 10 m of soft silty clay (Fig. 9). The soft silty clay is in turn underlain by more than 50 m of alternating layers of diluvial sandy gravels, silts, and silty clays. Blow counts are consistently less than 10 in the fill and upper silty clay, except for a few blow counts as high as 15 in the base of the fill between depths of 15 m and 18 m. Below 18 m, blow counts are consistently greater than 15.

Accelerometers (noted as seismographs on Fig. 9) were installed prior to the earthquake to record upward propagation of seismic waves. The surface accelerometer is above the liquefiable fill and the accelerometer at 16 m depth is near the base of the liquefiable layer. Additional accelerometers were placed at depths of 32 m and 83 m. No piezometers were installed at this site.

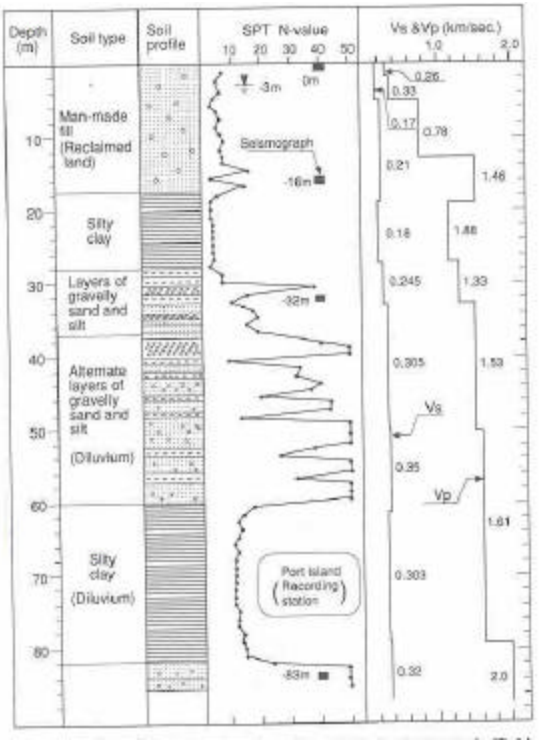

Figure 9. Soil profile and depths of accelerometers (seismographs) at PIDA (after Ishihara et al., 1996)

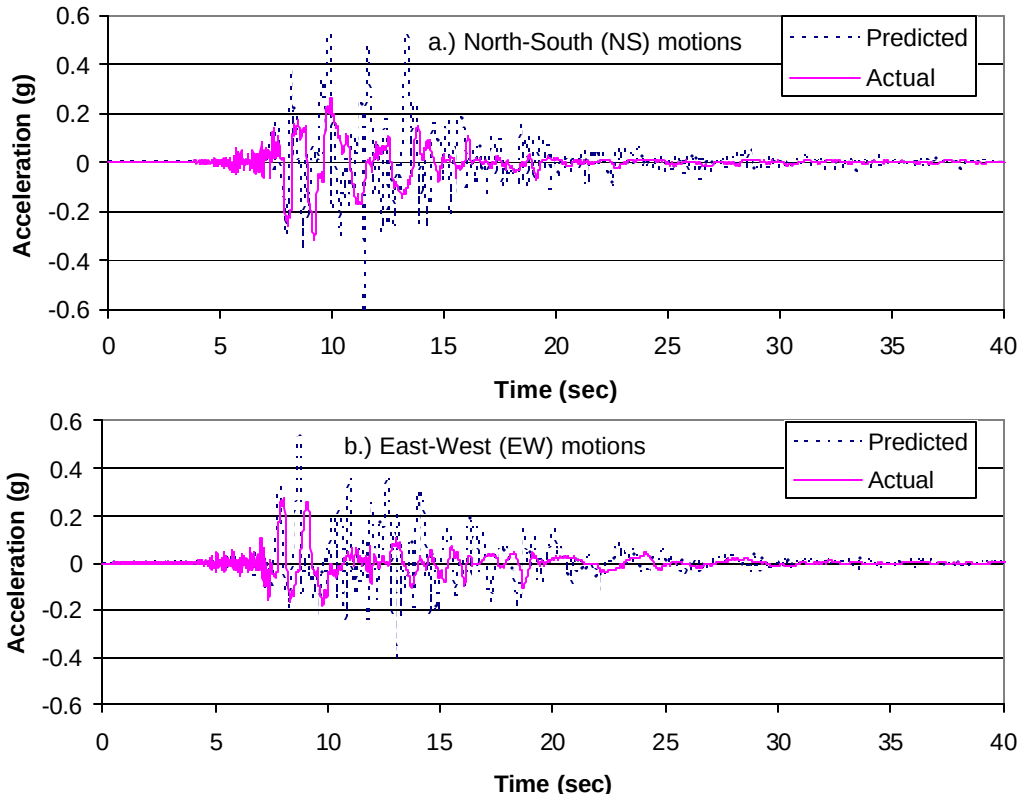

Figure 10. Predicted and actual acceleration time histories for PIDA site during the 1995 Hyogoken-Nambu earthquake (M=6.9)

Time histories of acceleration predicted at ground surface from the 16-m deep accelerometer along with measured or actual time histories are plotted on Fig. 10. These time histories indicate that predicted and measured ground accelerations were congruent until 8.3 sec in the record, when a large, 0.4g , acceleration pulse propagated though the site. At that juncture, the predominant period of the actual ground motions began to lengthen, indicating the onset of pore-pressure rise and sediment softening. From that point on, actual acceleration spikes were greatly attenuated with respect to predicted spikes. Beyond about 10 sec, coherency is lost between predicted and actual ground motions, indicating large pore pressures and major softening had occurred by that time. Although not specifically measured, the following inferences with respect to pore pressures are made from correlations with the behavior observed at WLA. The pore-water pressures apparently began to rise with the arrival of the 8.3 sec acceleration pulse and reached levels sufficient for severe softening ($r_u > 0.5$) by 10 sec. Predicted strong motion pulses, characterized by acceleration peaks grater than 0.1 g, did not propagate to ground surface after 20 sec, indicating that major softening or liquefaction had occurred by that time. After 20 sec, both the predicted and actual ground motions quickly subsided to low levels without continued ground oscillation as occurred at WLA.

Response spectra calculated from the predicted and actual ground motions for the first 8.3 sec of record are plotted on Fig. 11. The predicted and actual spectra at this juncture are not greatly different, indicating the increased pore-water pressures and soil softening had little influence on the transmitted ground motions. However, most of the seismic energy was yet to propagate through the site.

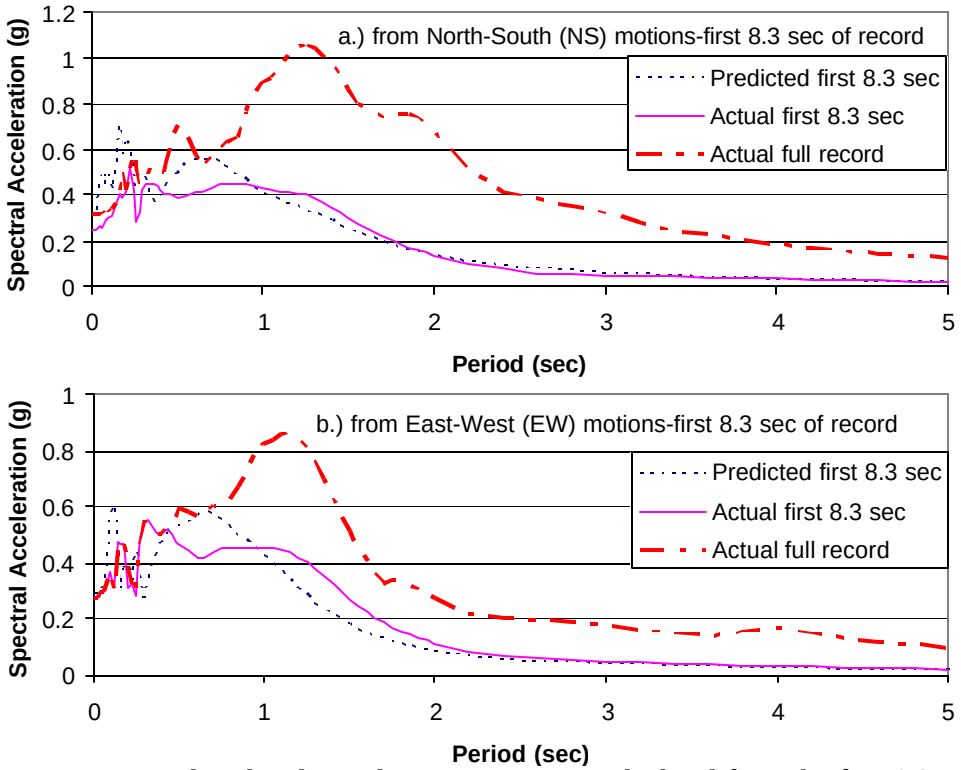

Figure 11. Predicted and actual response spectra calculated form the first 8.3 sec of acceleration record for PIDA during 1995 Hyogoken-Nambu earthquake (M=6.9)

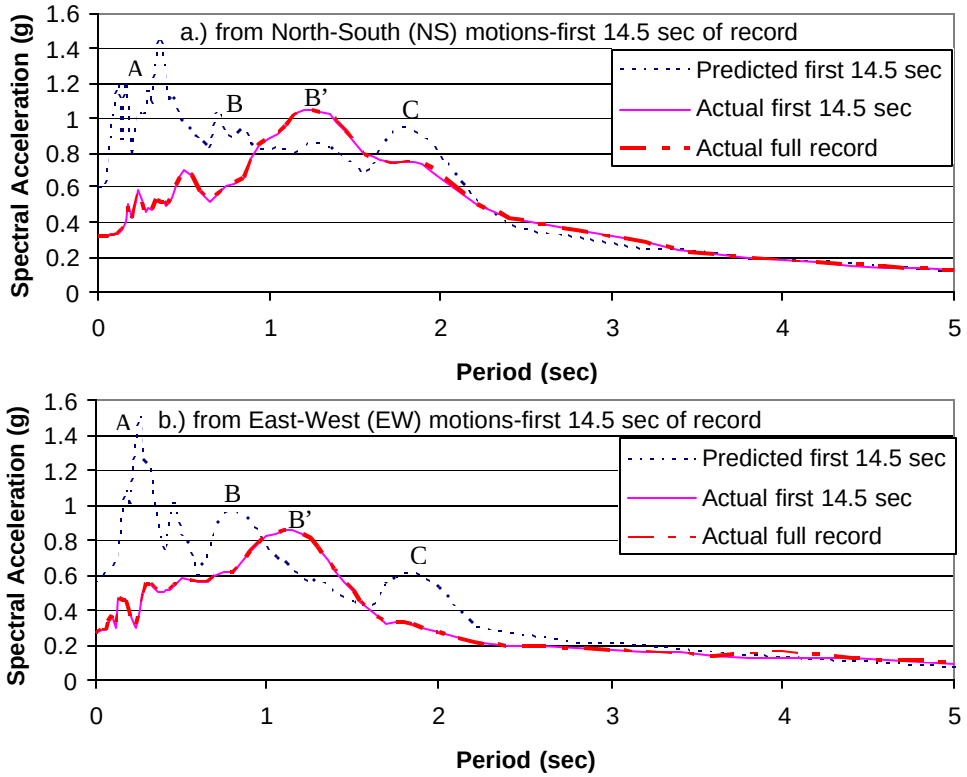

Figure 12. Predicted and actual response spectra calculated form the first 14.5 sec of acceleration record for PIDA during 1995 Hyogoken-Nambu earthquake (M=6.9)

The predicted response spectra for first 14.5 sec of record (Fig. 12) contain major spectral peaks at periods between 0.1 and 0.6 sec that are absent in the actual spectra for both the 8.3 sec and 14.5 sec time increments. These missing peaks (marked by the letter A) indicate that considerable incoming energy in the 0.1 to 0.6 period range was absorbed by the softening layer. Softening also lead to lengthening of period in some ranges. Fore example, predicted spectral peaks in the 0.6 sec to 0.8 sec period range (Peaks B) apparently shifted to periods of about 1.2 sec (Peaks B') in the actual spectra. Peak C, at a period of 18 sec, in the predicted spectra is also missing in the actual spectra, indicating that late arriving energy in this period range was also absorbed in the softening layer.

The actual and final spectra at the 14.5 sec juncture are essentially congruent, indicating that maximum energies at all periods had propagated through the site by 14.5 sec. We also note that predicted spectra at periods greater than 2 sec are less in the actual spectra, indicating that amplification of ground motions did not occur in this period range and that long-period ground oscillation did not develop at PIDA . Possible reasons for the occurrence of amplification and long-period ground oscillation at the WLA but not at PIDA include: 1) Late arriving low-amplitude long-period ground motions were approximately in phase with and apparently drove the long-period ground oscillations that developed at WLA. 2) Although somewhat similar low-amplitude long-period motions occurred until about 30 sec in the predicted PIDA ground motions, they apparently were not in phase or did not cause resonance at this softened site. Consequently, ground motions attenuated rather rapidly after strong ground motions ceased (between 15 and 25 sec). 3) Thicker liquefied layers such as the 15-m layer at PIDA may not be as susceptible to ground oscillation as thinner liquefied layers, such as the 4-m layer at WLA.

CONCLUSIONS

1. When significant soil softening or liquefaction occurs at a site early in the sequence of strong ground motions, as occurred at both WLA and PIDA, later arriving short-period (<1 sec) strong ground motion pulses are absorbed by the softened layer, preventing transmission of strong ground motions to the ground surface. In this instance the softened layer acts as a natural base isolation system attenuating short-period energy peaks. If softening and liquefaction were to develop later in the strong motion sequence, this potentially beneficial aspect would likely be diminished or be of null effect.

2. Soil softening may shift site resonance to longer periods and lead to amplification of ground motions at long periods. At both WLA and PIDA, ground motions were amplified in the 1.0 sec to 2.0 sec period range as indicated by greater actual than predicted spectral values.

3. Where ground oscillation is generated by post-strong-motion low-amplitude long-period seismic excitation, as occurred at WLA, a long sequence of oscillations may occur, greatly increasing long-period (>1 sec) spectral values compared to similar non-liquefied sites.

4. Based on the two case histories examined here, WLA and PIDA, ground oscillation appears to be mobilized by resonance between the softened site and later arriving low-amplitude long-period ground motions. At WLA, with a liquefied layer thickness of 4 m, ground oscillation led to amplification of ground motions in the 1.0 sec to 5.0 sec period range. At the PIDA site, with a liquefied layer thickness of 15 m, ground motions at ground surface attenuated quickly after arriving strong motions ceased and amplification of long-period motions (>2.0 sec) did not occur.

ACKNOWLEDGMENT

Funding for this project was provided by the Utah Department of Transportation (UDOT) under Contract No. 029008. This support is gratefully appreciated and acknowledged.

REFERENCES

Bennett, M.J., McLaughlin, P.V., Sarmiento, John, and Youd, T.L., 1984, Geotechnical investigation of liquefaction sites, Imperial Valley, California: U.S. Geological Survey Open File Report, 84-252, 103 p

Holzer, T.L., Youd, T.L., and Hanks, T.C., 1989, Dynamics of liquefaction during the Superstition Hills Earthquake (M = 6.5) of November 24, 1987: Science, April 7, 1989, v. 244, p. 56-59.

Ishihara, K, Yasuda, S., and Shinkawa, N, 1996, Soil characteristics and ground damage: Soils and Foundations, Special Issue on Geotechnical Aspects of the Hyogoken-Nambu Earthquake, p 109-119.

Youd, T.L. and Bartlett, S.F., 1989, US case histories of liquefaction-induced ground displacement: Proceedings, 1st U.S.-Japan Workshop on Liquefaction, Large Ground Deformation and Their Effects on Lifeline Facilities, National Center for Earthquake Engineering Research, p. 22-31.

Youd, T.L. and Holzer, T.L., 1994, Piezometer performance at the Wildlife liquefaction site: Journal of Geotechnical Engineering, American Society of Civil Engineers, v. 120, no. 6, p. 975-995.

Energy-based Liquefaction Analysis of Earthquake Site Response

Tetsuo Tobita[1] and Jean-Pierre Bardet[2]

ABSTRACT

Herein we propose a method for one dimensional effective stress analysis, which is based on multiple yield surface plasticity, G/G_{max} - γ curves, correlation between dissipated energy and pore pressure buildup, and stress dilatancy. The proposed method takes advantage of the modeling capabilities of a recently developed correlation between pore pressure buildup and dissipated energy, and implements those in a one-dimensional computer program for site response analysis. The lead improvement of the model rests in its engineering calibration and robust simulations. The model implementation is demonstrated for one-dimensional finite difference simulation programs for site response analysis. The simulation results show that the new model is capable of predicting the time histories of acceleration, displacement and pore pressure in centrifuge model tests and in a case history of ground motion recorded in vertical array in Japan.

INTRODUCTION

During past earthquakes, the transient ground motions recorded on soil sites were found to differ from those on nearby rock outcrops. SHAKE [1] is one of the first computer programs for simulating the seismic response of soil sites. SHAKE simulates the cyclic behavior of soils using an equivalent linear model. It simulates reasonably well the weak nonlinearities resulting from an increase in applied shear strain, but simulates poorly the strong nonlinearities arising from soil-water interaction (e.g., liquefaction). Since the 1970s, many researchers have attempted to model soil behavior using effective stress, e.g., [2] and [3], and to incorporate this modeling into site response analysis.

Currently, a number of computer programs are available for simulating the dynamic ground response with the effective stress approach, e.g., DESRA [4], YUSAYUSA [3], DYNA1D [5], FLIP [6], and CYBERQUAKE [7]. The methods used in these site response analysis programs vary from simplified methods based on simplified pore-pressure models, e.g., [4], to more sophisticated techniques using general purpose constitutive models, e.g., [8]. The former methods have generally less parameters, which render them easier to calibrate from available data. The latter methods cover more soil nonlinearities, but their larger number of material constants makes them more difficult to use in practice.

Since the 1990s, methods based on the correlation between dissipated energy and pore pressure buildup have become increasingly used for assessing the effects of pore pressure building during earthquakes. The main advantage of these methods over their predecessors is their logical extension to random cycles and multidimensional loadings. These methods have been examined in the context of experimental laboratory test results, e.g., [9], [10] and [11], centrifuge test modeling [12], constitutive modeling [6] and [13], regional mapping of liquefaction hazards, e.g., [14] and [15].

Results of site response analysis on saturated soil deposits depend largely on the constitutive model used to simulate the stress-strain responses of soils subjected to undrained cyclic loadings. [13] developed an energy-based model for simulating cyclic mobility, which corresponds to alternating large shear strains and regain in shear resistance at low effective mean pressure during undrained cyclic loadings as described in [16].

The objective of the present study is to examine the applicability of the energy-based constitutive model developed by [13] to site response analysis of liquefiable soil deposits. Following the introduction, the

[1] Tetsuo Tobita, Research Associate, Disaster Prevention Research Institute, Kyoto University, Gokasho, Uji, Kyoto 611-0011, Japan

[2] Jean-Pierre Bardet, Professor, Civil Engineering Department, University of Southern California, Los Angles CA 90089-2531

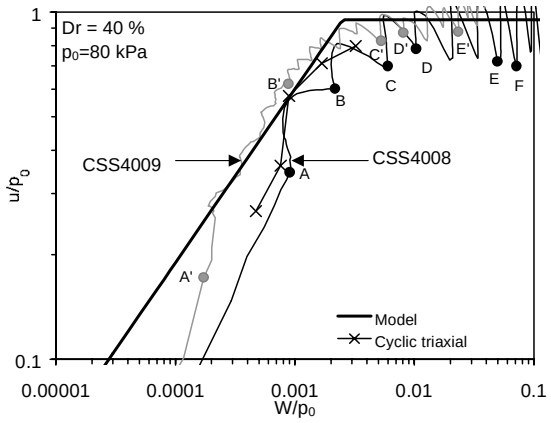

Figure1. Measured variation of normalized pore pressure u/p_0 and dissipated energy W/p_0 during the undrained simple shear tests on Nevada sand [17]

second section reviews the main features of the recently developed constitutive model, and the calibration of its material constants from laboratory test results.
The third section describes the implementation of the model into one-dimensional site response analysis programs. The fourth and fifth sections examine the performance of the model in simulating a centrifuge model test and a real case history relevant to liquefaction analysis. The sixth section is discussion and seventh section is conclusion.

ENERGY-BASED MODELING OF PORE PRESSURE BUILDUP AND CYCLIC MOBILITY

The following reviews the energy model and constitutive model implemented in the present study. Model construction is fully described in [13]. In what follows, stress is taken as the effective stress.

Review of the energy model

Mean effective pressure p and dissipated energy during undrained loadings are correlated as follows:

$$p = p_0 \max\left\{\alpha, 1-\beta\left(W_p / p_0\right)^{\delta}\right\} \tag{1}$$

where W_p is the dissipated energy computed as an area of hysteresis loop; p_0 is the initial effective mean pressure; and α, β and δ are material constants. As shown in Figure 1, Equation 1 simulates that the pore pressure $u = p_0 - p$ increases as a power law of W_p up to $u/p_0 = 1-\alpha$. The values of β and δ for Nevada sand at 40% relative density were determined either by fitting the experimental results with linear regression or specifying the value of energy threshold W_L/p_0 expressed as

$$\frac{W_L}{p_0} = \left(\frac{1-\alpha}{\beta}\right)^{1/\delta} \tag{2}$$

At the energy threshold, the maximum pore pressure ratio specified by $1-\alpha$ is achieved. Compared to other energy-based pore pressure models, e.g., [10], Equation 1 has an additional material constant α, which prevents liquefaction from occurring in dense soils. In theory, the value of α could be defined directly from the minimum effective pressure measured during cyclic test. In practice, it is recommended to select it as a small positive number to prevent complete liquefaction for stability of analysis. The measured variation of u versus W_p during undrained cyclic triaxial tests and simple shear tests (CSS4008 and CSS4009) at 80 kPa effective mean pressure can be found in Figure 1. The model drawn in Figure 1 is for $W_L/p_0 = 0.0025$.

As described in [13] similar approach to [6] has been taken for modeling of stress dilatancy. Namely, stress dilatancy is accounted by modifying Equation 1 as follows:

$$p \leftarrow p + \left(J - p\sin\varphi_p\right)/\sin\varphi_f \qquad \text{if} \quad J > p\sin\varphi_p \tag{3}$$

TABLE 1. Material constants for Nevada Sand at 40% relative density and at 80 kPa initial confining pressure.

Constant	Notation	Value	Unit
Saturated unit weight	γ_{sat}	19.36	kN/m^3
Dry unit weight	γ_d		kN/m^3
Minimum pore pressure ratio	α	0.1	-
Constant for pore pressure model	β	19.0	-
Exponent for pore pressure model	δ	0.5	-
Energy threshold	W_L/p_0	0.0025	
Friction angle at failure	ϕ_f	44	Degree
Shear modulus G_{max} at pressure p_r	G_r	32	MPa
Reference pressure for G_r	p_r	80	kPa

where φ_f is the failure friction angle; φ_p is the angle of phase transformation [16], and J is the second invariant of deviator stress:

$$J^2 = \mathbf{s}:\mathbf{s}/2 \tag{4}$$

In Equation 4, **s** is the deviator stress, and "**:**" denotes the contracted product between two tensors of second order. In the case of simple shear stress conditions encountered for one-dimensional site response, J becomes equal to the absolute value of shear stress τ (i.e., $J = |\tau|$).

Review of the constitutive model

One dimensional multiple yield surface plasticity model, e.g., [18] and [19], is chosen as a constitutive model in the present analysis. The allowable stress space (p, τ) is partitioned using m conical yield surfaces, each having for equation:

$$f_i = \left|\tau - p\alpha_i\right| - pR_i = 0 \quad (i = 1,\ldots, m) \tag{5}$$

where α_i corresponds to the yield surface center and R_i is the slope of the yield surface in the p-τ stress space. The conical yield surfaces are nested in the p-τ stress space, all having their apexes at the stress origin. The largest yield surface is fixed and is the failure surface (i.e,. $\alpha_m = 0$ and $R_m = \sin\varphi_f$) where φ_f is the failure friction angle.

The number m of yield surfaces and their associated parameters, i.e., α_i, R_i, and H_i are calculated from $G/G_{\max}$ - γ curves, where H_i is the tangential shear modulus. If the $G/G_{\max}$ - γ curve is made of n data points (i.e., $G_i/G_{\max}$ - γ_i, $i = 1, \ldots, n$), the modulus H_i and slope R_i are related to $G_i/G_{\max}$ through:

$$H_i = G_{\max}\frac{(G_{i+1}/G_{\max})\gamma_{i+1} - (G_i/G_{\max})\gamma_i}{\gamma_{i+1} - \gamma_i} \quad \text{for } i = 1, \ldots, n\text{-}1, \text{ and } H_n = 0 \tag{6}$$

and

$$R_i = \frac{G_{\max}}{p}(G_i/G_{\max})\gamma_i \quad \text{for } i = 1, \ldots, n \tag{7}$$

The material constants of the constitutive model are listed in Tables 1 for Nevada sand at 40% relative density and at 80 kPa initial effective confining pressure. Figure 2a and 2b show G-γ curve and corresponding backbone curve derived from the resonant column and drained triaxial tests for Nevada sand at the above condition [17]. Figure 3 shows $G_{\max}$-p relation, i.e., pressure-dependency of elastic shear modulus G_{max}, together with results of resonant column tests for Nevada sand. As seen in Figure 3, when the effective confining pressure becomes low, i.e., close to complete liquefaction, more sensitivity to effective confining pressure is given to G_{max} as described in [13].
[13] gives a complete algorithm to integrate step by step the incremental constitutive equation during simple shear, which is the loading encountered in one-dimensional site response analysis. Given an initial stress state (p, τ), the algorithm returns the stress resulting from an applied strain increment $\Delta\gamma$.

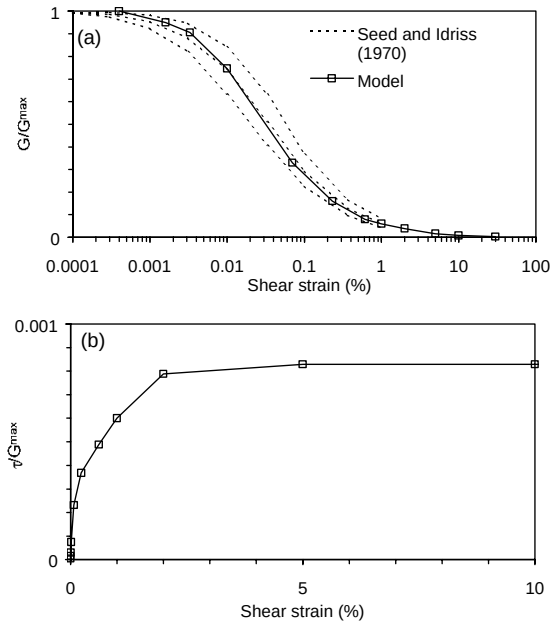

Figure 2. (a) G-γ curve for relative density 40 % and (b) backbone curve [17].

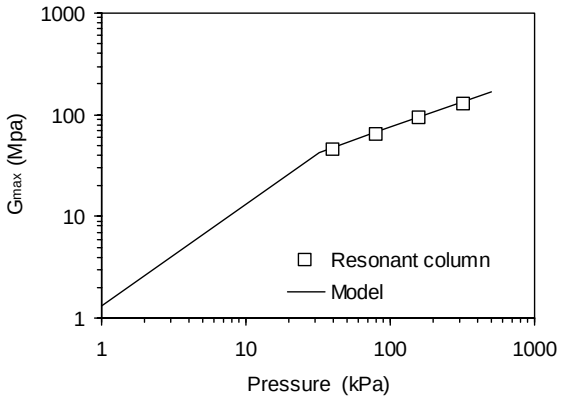

Figure 3. Variation of G_{max} with effective means stress

ONE-DIMENSIONAL GROUND RESPONSE ANALYSIS

The constitutive model presented in the previous section is implemented into LERA, an acronym that stands Liquefaction Earthquake site Response Analysis. LERA adds effective stress capabilities to NERA, a computer program for Nonlinear Earthquake site Response Analysis [20] for pressure independent materials.

Governing equation and boundary conditions

The following assumptions in one-dimensional site response analysis are made. Namely, shear waves propagate vertically in soil layers which are assumed to be (1) horizontally homogenous, (2) of infinite horizontal extent, and (3) subjected only to horizontal motion from bedrock. The governing equation is:

$$\rho \frac{\partial^2 d}{\partial t^2} + \eta \frac{\partial d}{\partial t} = \frac{\partial \tau}{\partial z} \tag{8}$$

where ρ is the soil unit mass; d is the horizontal displacement; z is the depth coordinate; t is the time; τ is the shear stress; and η is a mass-proportional viscous damping coefficient. However, $\eta = 0$ is adapted, i.e., purely hysteretic damping is assumed. The boundary conditions are specified at the ground surface (i.e., z = 0) and at the bottom of soil column (i.e., $z = H$):

$$\tau = 0 \text{ at z = 0 and } \tau = \tau_B \text{ at z = H} \tag{9}$$

The shear stress τ_B at $z = H$, which is usually unknown, can be calculated from the velocity at $z = H$ assuming that the bedrock is elastic as [21],

$$\tau_B = \rho_b v_s (2v_I - v_B) \tag{10}$$

where ρ_b is the unit mass and v_s is shear wave velocity of the bed rock, and v_I is particle velocity of incident wave, v_B is a sum of particle velocity of incident and refracted waves. Equation 10 relates the shear stress and velocity at the soil-column interface; it provides an additional equation to define the shear stress at the lower boundary. Equation 10 also applies to the case of rock outcrop (i.e., $\tau_B = 0$ and $v_B = 2\, v_I$).

Finite difference formulation

Soil deposit is divided into *N-1* layers having various thickness h_i and unit mass ρ_i for $i = 1$ to $N-1$. The displacement d and stress τ are evaluated at N grid nodes. The displacement of node i at time t_n is denoted $d(z_i, t_n) = d_{i,n}$ where z_i is the depth of node i. Similarly the stress and strain at node i at time t_n are denoted $\tau_{i,n}$ and $\gamma_{i,n}$, respectively. $v_{i,n}$ and $a_{i,n}$ denote the velocity $v(z_i, t_n)$ and acceleration $a(z_i,t_n)$ of node i at time t_n. The shear strain in the layer below node i and time t_n is:

$$\gamma_{i,n} = \frac{\partial d}{\partial z} = \frac{d_{i+1,n} - d_{i,n}}{\Delta z_i} \tag{11}$$

Shear strain is constant between nodes i and i+1, which implies that the stress is also constant between nodes i and i+1. Equation 8 at nodes $i = 1, \ldots, N$ at time t_n becomes:

$$\rho_i a_{i,n} + \eta_i v_{i,n} = F_{i,n} \tag{12}$$

where ρ_i and η_i are the unit mass and viscosity of nodes between i and $i+1$, respectively, and $F_{i,n}$ is the stress gradient at node i. Stress gradient at node $i = 2, \ldots, N-1$ at time t_n is evaluated by taking an average of stress at ith and $i-1$th layer as follows:

$$F_{i,n} = \left.\frac{\partial \tau}{\partial z}\right|_{i,n} \approx 2\frac{\tau_{i,n} - \tau_{i-1,n}}{\Delta z_i + \Delta z_{i-1}} \tag{13}$$

At node 1 (surface), the stress should be equal to 0. Therefore a fictitious node 0 and fictitious layer of thickness Δz_1 are introduced above node 1. In this fictitious layer, the stress $\tau_{0,n}$ should be equal to $-\tau_{1,n}$ so that the average stress be equal to zero at node 1 (i.e., $\tau_{0,n} + \tau_{1,n=0} = 0$), which implies that:

$$F_{1,n} = \frac{2\tau_{1,n}}{\Delta z_1} \tag{14}$$

At node N (bottom), the stress should be equal to τ_B. Also, a fictitious node $N+1$ and fictitious layer of thickness Δz_{N-1} are introduced below node N. In this fictitious layer, the stress $\tau_{N,n}$ is equal to $2\tau_{B,n} - \tau_{N-1,n}$ so that the average stress at node N is equal to $\tau_{B,n}$. The stress gradient at node N is therefore:

$$F_{N,n} = \frac{\tau_{N,n} - \tau_{N-1,n}}{\Delta z_{N-1}} = 2\frac{\tau_{B,n} - \tau_{N-1,n}}{\Delta z_{N-1}} \tag{15}$$

Time integration

The central difference method, a particular type of Newmark algorithm where $\beta = 0$, is implemented for time integration of the equation of motion. Table 2 summarizes the calculation of accelerations, velocities and displacements at nodes, and of shear strains and stresses within sublayers. Computation proceeds as follows:

1) The soil deposit is assumed at rest; all variables are initialized to zero.
2) The strain states $\gamma_{i,n}$ and strain increments $\Delta\gamma_{i,n}$ in sublayers are calculated from the nodal displacements.
3) The stresses p and τ are computed from $\Delta\gamma_{i,n}$ through constitutive relation.
4) The velocity of input ground motion is calculated from the time history of input ground acceleration.
5) The predicted nodal velocities at time t_{n+1} are calculated from those at time t_n.
6) The output displacement, velocity and acceleration at time t_n are computed.
7) Displacement, velocity and acceleration are updated.

SIMULATION OF CENTRIFUGE MODEL TESTS

The capabilities of LERA are first investigated by simulating centrifuge model tests that represent the response of soil deposits [22].

Centrifuge model test

The centrifuge test results of VECLAS project [22] are used. The model simulates a 10-m thick soil deposit made of a uniform layer of Nevada sand (D_r = 40 %). The water table is located at the ground surface; the complete layer is saturated. The model is contained in a laminar box, which simulates the one-dimensional kinematical conditions encountered in the field, i.e., which subjects the soil deposit to shear waves propagating vertically.

The time history of the horizontal acceleration is applied at the bottom of the soil layer. The test results are documented using several LVDTs, accelerometers, and pore pressure transducers, which measure the time history of displacement, acceleration and water pressure, respectively, at various depths. Additional details on the experimental procedure can be found in [23]. Nodal acceleration and velocity are not required in the calculation. They are only calculated for displaying the time history of acceleration and velocity at selected nodes.

Calibration of model constants and numerical model

The uniform soil layer is modeled using ten 1-m thick sub-layers. Table 1 lists the model parameters used in the analysis. The initial effective stress, p_0, is computed using $p_0 = (\gamma_{sat} - \gamma_w)\, z$ where γ_{sat} is the saturated unit weight of soil, γ_w is the unit weight of water and z is the depth. The initial pressure therefore ranges from 4.8 to 95.5 kPa in the soil sublayers. All the sublayers are assumed to share the same G/G_{max}-γ curve (Figure 2), which is derived from resonant column tests and drained triaxial tests at 80 kPa effective mean pressure. The values of G_{max} at effective stress 40 and 320 kPa are obtained from resonant column tests [17] as shown in Figure 3. Figure 4 shows the time history of the acceleration prescribed at the base of the laminar box. In the simulation, the input motion has been filtered to eliminate frequency higher that 8 Hz.

TABLE 2. Algorithm for site response analysis.

(1) Initialization

$n = 1, \tilde{v}_{i,n} = 0, a_{i,n} = 0, d_{i,n} = 0, \tau_{i,0} = 0, \gamma_{i,0} = 0, i = 1, \ldots, N$

and $V_{i,0} = 0$, $a_{i,0} = 0$

(2) Calculate strain and strain increment $(i = 1, \cdots, N-1)$

$$\gamma_{i,n} = \frac{d_{i+1,n} - d_{i,n}}{\Delta z_i}, \quad \Delta\gamma_{i,n} = \gamma_{i,n} - \gamma_{i,n-1}$$

(3) Calculate stresses $p_{i,n}$ and $\tau_{i,n}$ from $\Delta\gamma_{i,n}$

(4) Calculate input velocity from prescribed acceleration $a_{I,n}$

$$V_{I,n} = V_{I,n-1} + \tfrac{1}{2}\left(a_{I,n} + a_{I,n-1}\right)\Delta t$$

(5) Calculate predicted velocity

$$\tilde{v}_{N,n+1} = \frac{\tilde{v}_{N,n}\left(\Delta z_{N-1} - v_s \Delta t\right) + 4 v_s V_{I,n} \Delta t - 2\tau_{N-1,n}\Delta t / \rho_b}{\Delta z_{N-1} + v_s \Delta t}$$

at node N (bottom)

$$\tilde{v}_{i,n+1} = \tilde{v}_{i,n} + 2\frac{\tau_{i,n} - \tau_{i-1,n}}{\Delta z_i + \Delta z_{i-1}}\frac{\Delta t}{\rho_i} \quad \text{at node } i = 2,\ldots,N\text{-}1$$

$$\tilde{v}_{1,n+1} = \tilde{v}_{1,n} + \frac{2\tau_{1,n}}{\Delta z_1}\frac{\Delta t}{\rho_1} \quad \text{at node 1 (surface)}$$

(6) Calculate displacement, velocity and acceleration $(i = 1, \cdots, N)$

$$d_{i,n+1} = d_{i,n} + \tilde{v}_{i,n+1}\Delta t$$

$$v_{i,n} = \frac{1}{2}(\tilde{v}_{i,n+1} + \tilde{v}_{i,n})$$

$$a_{i,n} = \frac{1}{\Delta t}(\tilde{v}_{i,n+1} - \tilde{v}_{i,n})$$

(7) $n \leftarrow n+1$ go to (2)

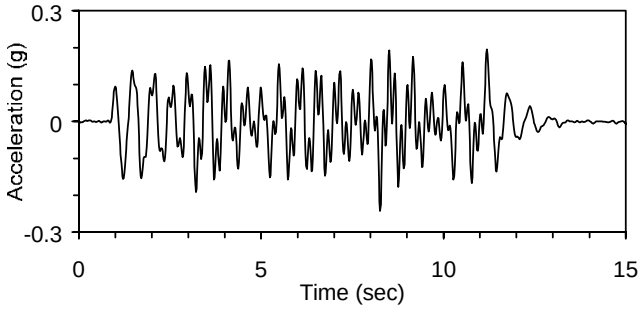

Figure 4. Input acceleration for centrifuge model: VELACS model 1.

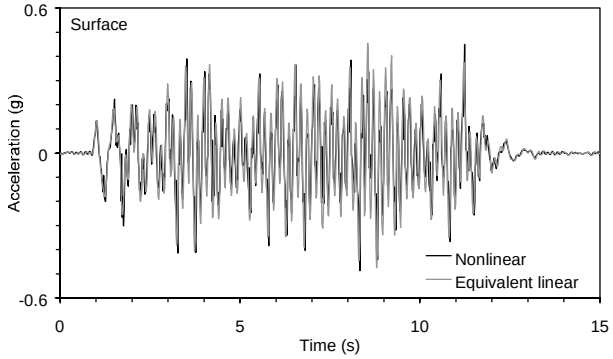

Figure 5. Comparison of surface acceleration obtained from EERA (equivalent linear) and NERA (nonlinear).

TABLE 3. Model parameter for total stress analysis.

	Layer Number	Soil Material Type	Thickness of layer (m)	Maximum shear modulus G_{max} (MPa)	Total unit weight (kN/m^3)	Shear wave velocity (m/sec)	Depth at MIDDLE of layer (m)
Surface	1	1	1.00	47	15.10	175	0.50
	2	1	1.00	82	15.10	231	1.50
	3	1	1.00	106	15.10	262	2.50
	4	1	1.00	125	15.10	285	3.50
	5	1	1.00	142	15.10	304	4.50
	6	1	1.00	157	15.10	320	5.50
	7	1	1.00	171	15.10	333	6.50
	8	1	1.00	183	15.10	345	7.50
	9	1	1.00	195	15.10	356	8.50
	10	1	1.00	207	15.10	366	9.50
Bedrock	11	0		3463	15.10	1500	10

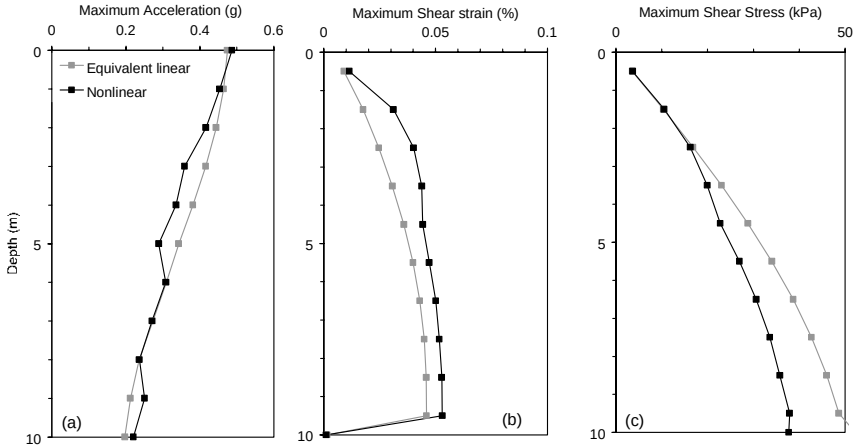

Figure 6. Vertical profiles: (a) maximum acceleration, (b) maximum shear strain and (c) maximum shear stress for total stress analysis.

Total stress analysis

The implementation of LERA is first validated through comparing its results to another site response programs called EERA [24], which is a modern implementation of the equivalent linear concepts embodied in SHAKE [1]. In both simulations, the ground water level is set below the bedrock to simulate the response of a dry soil deposit. EERA and LERA use exactly identical G/G_{max}-γ curves. The EERA's damping curve was calculated so that they coincide with the energy dissipated by hysteretic damping [20]. Table 3 shows parameter for soil deposit. Figure 5 shows the time history of surface accelerations. As shown in Figure 5, the calculation of EERA and NERA agrees well in the case of dry soil deposits. Figures 6a, 6b and 6c show the vertical profiles of maximum acceleration, maximum shear strain, and maximum shear stress, simulated by EERA and NERA, respectively. The difference on the maximum shear strain profile may be originated by the scaling of strain in the equivalent linear model. Based on this EERA-LERA comparison, it can also be concluded that the linear equivalent method simulates reasonably well nonlinearities in dry soil deposits.

Effective stress analysis

Through the use of the model developed in the previous section, LERA extends the capabilities of NERA to saturated soil deposits. The previous analysis was repeated using the same geometry and soil properties, but assuming a saturated soil deposit. The initial effective stress ranges from 4.8 to 95.5 kPa in the saturated soil deposit. Table 4 shows model parameter for the soil deposit.

Figure 7 shows vertical profile of measured and simulated maximum acceleration and maximum relative displacement. As clearly seen on the measured acceleration, the peak ground acceleration is reduced by soil liquefaction, while simulation gives lower acceleration in the middle of soil deposit and similar peak acceleration at the ground surface. This lower acceleration in the middle of deposit in the simulation is due to the loss of soil stiffness caused by liquefaction. The profile of measured displacement shows constant increase of displacement toward surface.

TABLE 4. Model parameter for effective stress analysis.

	Layer Number	Soil Material Type	Thickness of layer (m)	Maximum shear modulus Gmax (MPa)	Total unit weight (kN/m^3)	Shear wave velocity (m/sec)	Location of water table	Depth at MIDDLE of layer (m)	Vertical effective stress (kPa)
Surface	1	1	1.00	6.3	19.36	57	*W*	0.5	4.8
	2	1	1.00	19.0	19.36	98		1.5	14.3
	3	1	1.00	31.6	19.36	127		2.5	23.9
	4	1	1.00	43.3	19.36	148		3.5	33.4
	5	1	1.00	49.1	19.36	158		4.5	43.0
	6	1	1.00	54.3	19.36	166		5.5	52.5
	7	1	1.00	59.0	19.36	173		6.5	62.0
	8	1	1.00	63.4	19.36	179		7.5	71.6
	9	1	1.00	67.5	19.36	185		8.5	81.1
	10	1	1.00	71.3	19.36	190		9.5	90.7
Bedrock	11	0		4439	19.36	1500		10.0	95.5

Figures 8a, 8b and 8c show comparison of the surface acceleration between measured and simulated at the surface (AH3), at a depth of 2.5 m (AH4) and 5 m (AH5), respectively. The measured acceleration record at the surface and the depth of 2.5 m clearly show the reduction of amplitude compared to the one at the depth of 5m. The measured record at 5 m depth shows spiky response after around 8 seconds, whose period is about 0.8 second. This spiky signal may indicate that soil at 5 m depth is dense enough to dilate. In contrast, simulation results show reduction of amplitude of acceleration for all three depths; therefore spiky peaks are not prominent.

Figures 9a, 9b and 9c show measured and simulated relative displacement at the same depth as Figures 8. Measured displacements are obtained by LVDTs which measure the displacement of laminar box, while simulated displacements are obtained by the double integration of simulated acceleration found in Figure 8. Compared with measured displacements, larger permanent displacements can be observed on the simulated displacements for all the depths

To know the cause of these permanent displacements requires further investigation in relation to the accuracy of numerical integration scheme.

Figures 10a, 10b and 10c show time history of pore pressure buildup, effective stress path and hysteresis loop at the depth of –1.5 m, respectively. As it is seen in Figure 10a, soil is not completely liquefied, i.e., pore pressure is not reaching the vertical effective stress. This is because the value of α in the simulation is taken as 0.1 and it may give in an agreement with measured pore pressure buildup. Stress path in Figure 10b shows small dilation in the first few cycles, but it is too small to see the effects on the acceleration record shown in Figure 8a. As seen in Figure 10c, shear strength is greatly reduced as pore pressure builds up and gives large shear strain amplitude about 0.7 %.

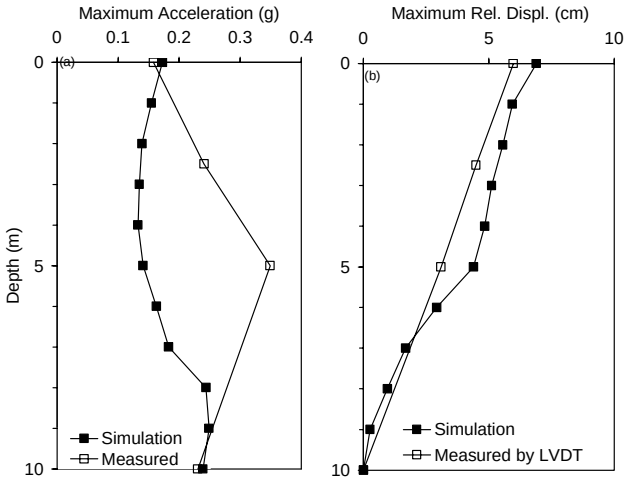

Figure 7. Comparison of vertical profile between measurements and effective stress analysis. (a) Maximum acceleration (b) Maximum relative displacement

SIMULATION OF CASE HISTORY AT THE VERTICAL ARRAY IN KUSHIRO CITY

The Kushiro-oki, Japan, earthquake, which occurred on January 15, 1993, had a 7.8 Richter magnitude. A vertical array of seismograph located in Kushiro city recorded the accelerations [25]. The soil deposits at the site were characterized using nearby soil borings, including density profile, SPT blows counts, and soil classification. Table 5 shows the model parameters for liquefiable layers, i.e. layer number 2 and 3 in Table 6. Table 6 lists the model parameter of the soil deposit. The soil density, maximum shear modulus, failure friction angle, and phase transformation angle are taken from [25]. G-γ curves adapted in the analysis are derived from [26]. Figure 11 shows liquefaction strength curve obtained from the G-γ curve and model parameter shown in Table 5 for layer 2, [13] shows details.

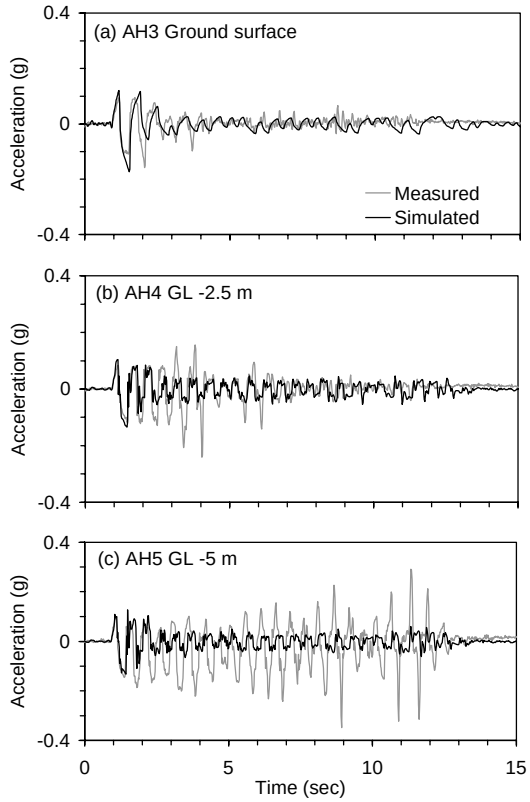

Figure 8. Measured and simulated acceleration (a) ground surface, (b) depth at 2.5 m and (c) depth at 5 m.

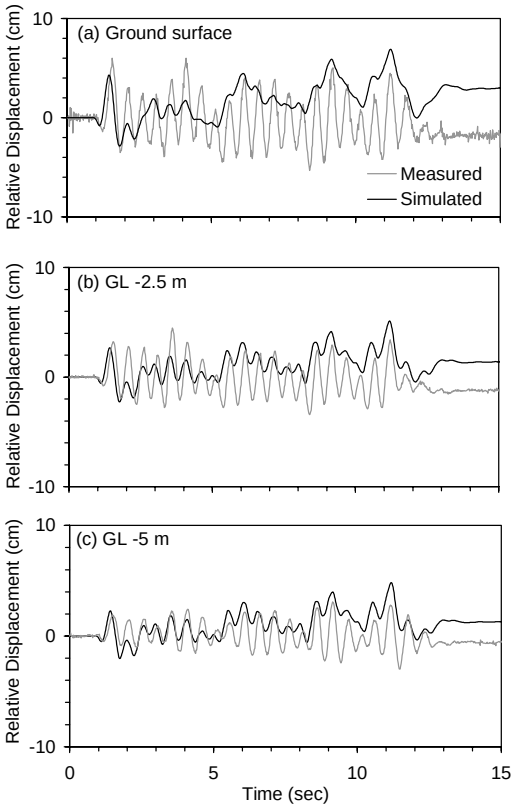

Figure 9. Measured and simulated relative displacement (a) ground surface, (b) depth at 2.5 m and (c) depth at 5 m.

The ground accelerations were recorded at a 77-m depth and at the ground surface. The peak horizontal ground accelerations (i.e., PGA) in the N-S directions at the base and the ground surface were 0.21 g and 0.48 g, respectively. Figure 12 shows the time history of N-S acceleration recoded at the ground surface and at the base of the vertical array, which is prescribed as the input motion to the site response analysis. As shown in Figure 12, the time history of ground surface acceleration displays a pattern characteristic of cyclic mobility with a 1.5 s period spikes.

Figure 13 shows the simulated acceleration at the ground surface and at depths of 2, 9, and 23 meters. Compared the simulated surface acceleration with the measured one in Figure 12, although peak acceleration is not well simulated, high spikes after 30 second is prominent. Figure 14 shows the stress path and hysteresis loop at a depth of 8 m. It is seen on the stress path that soil is dilating, and shear strength is recovered, i.e. mean effective pressure is increasing. It has to be noted, however, that the determination of model parameter, α, β and δ, is not based on the experimental data such as used in the previous section.

DISCUSSION

The present study had for objective to investigate the capabilities of a recently developed constitutive model in the framework of one-dimensional effective stress analysis of site response. The investigation was focused on the modeling of soil-water interaction under undrained conditions and ignored the effects of water diffusion and consolidation. The present approach has to be extended to multi-dimensional site response analysis, especially to see the effects on pore pressure buildup under multi-directional shaking, which is usually ignored by the use of one-dimensional site response analysis

CONCLUSION

A method has been proposed for one-dimensional effective stress site response analysis. The method is based on the multiple yield surface plasticity model, correlation between pore pressure and dissipated energy, and G/G_{max}-γ curves. The main improvement of the constitutive model rests in its engineering calibration and robust simulation. The proposed method takes advantage of these modeling capabilities, and implements those in a one-dimensional computer program for site response analysis.

The code was first examined by comparing results with that of equivalent linear model for the total stress analysis. Then the effective stress analysis is conducted. The simulation results show that the new model is capable of predicting the time histories of acceleration, displacement and pore pressure in centrifuge model test and vertical array case history.

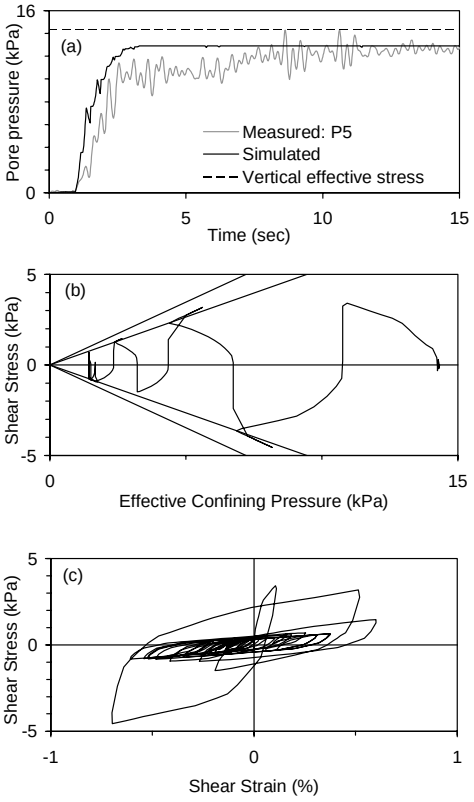

Figure 10. (a) time history of pore pressure buildup measured and simulated, (b) simulated effective stress path, and (c) simulated hysteresis loop, at depth 1.5 m.

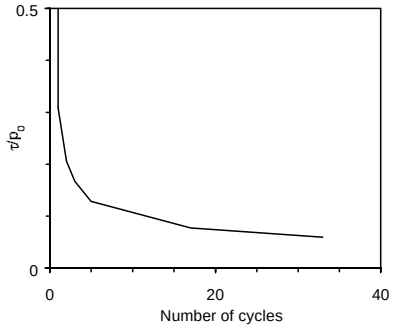

Figure 11. Liquefaction strength curve obtained from the G-γ curve used for layer 2.

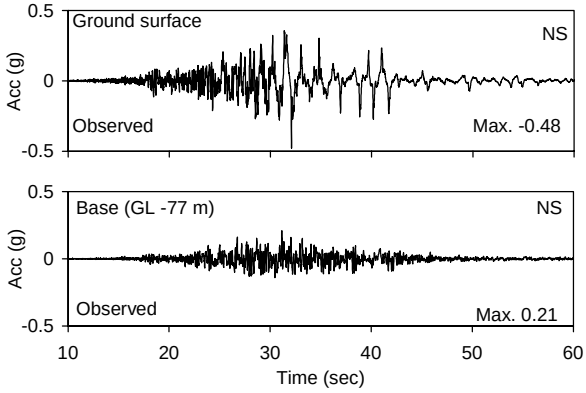

Figure 12. Recorded acceleration at the ground surface and at the depth of 77 m: NS component.

TABLE 5. Model parameter for liquefiable layers at the vertical array in Kushiro city.

	Layer	2	3	
Constant	Notation	Value	Value	Unit
Minimum pore pressure ratio	α	0.01	0.01	-
Constant for pore pressure model	β	18.0	7.5	-
Exponent for pore pressure model	δ	0.44	0.8	-
Energy threshold	W_1/p_0	0.0013	0.080	
Friction angle at failure	ϕ_f	40	48	Degree
Phase transformation angle	ϕ_p	28	28	Degree
Shear modulus G_{max} at pressure p_r	G_r	106.6	210.4	MPa
Reference pressure for G_r	p_r	100	300	kPa

TABLE 6. Model parameter for the Kushiro site.

Layer Number	Sublayer Number		Soil Material Type	Thickness of layer (m)	Maximum shear modulus G_{max} (MPa)	Total unit weight (kN/m^3)	Shear wave velocity (m/sec)	Liquefiable layer	Vertical effective stress (kPa)
1	1	Coarse sand	1	1	106.6	15.1	*263*		8
	2			1					23
2	3	Coarse sand	2	1	106.6	16.9	*249*	*x*	39
	4			2				x	54
	5			2				*x*	68
	6			2				x	82
3	7	Coarse sand	3	2	210.4	19.4	*326*	*x*	99
	8			2				*x*	118
	9			2				*x*	137
	10			2				x	156
	11			2				*x*	176
	12			2				*x*	195
	13			2				*x*	214
4	14	Fine sand	4	3	121.5	17.0	*265*		234
	15			3					256
	16			3					277
5	17	Silt	4	4	204.7	17.2	*341*		303
6	18	Fine sand	4	4	139.1	16.7	*286*		331
	19			4					359
7	20	Gravelly sand	4	4	182.4	19.6	*302*		392
	21			4					431
8	22	Fine sand	4	5	201.2	17.0	*341*		469
	23			5					504
	24			5					540
	25			5					576
	26			5					594

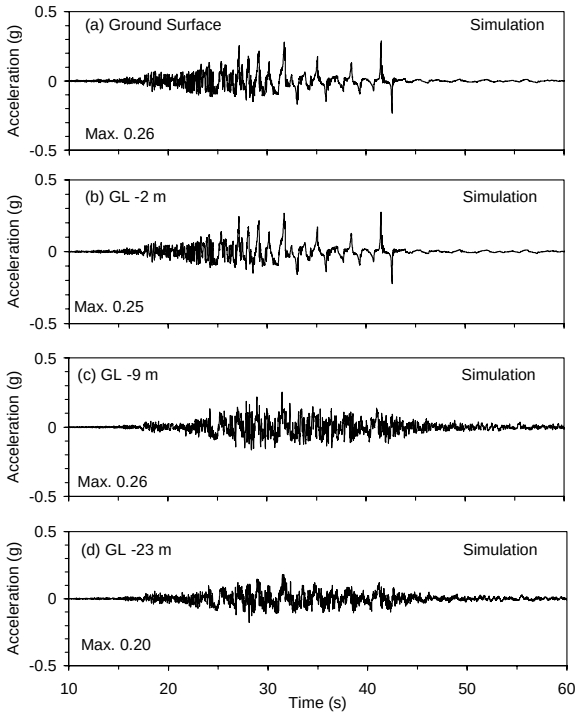

Figure 13. Simulated acceleration at various depth (a) at ground surface, (b) at depth 2 m, (c) 9 m, and (d) 23 m.

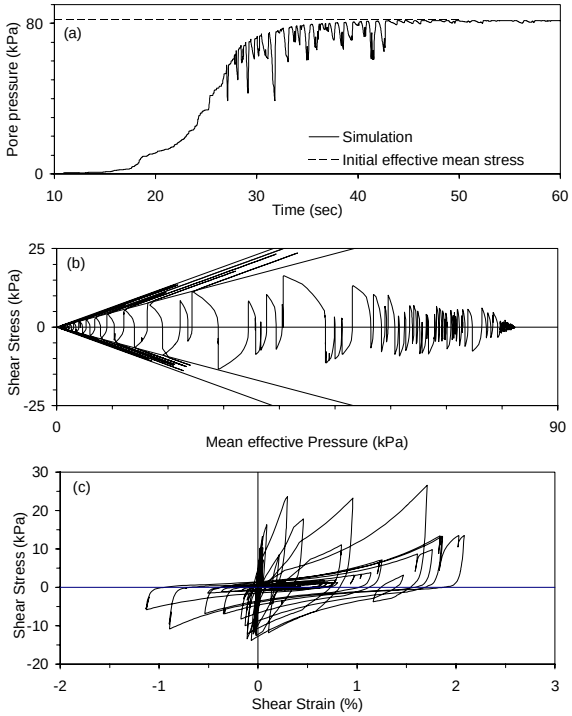

Figure 14. Simulated (a) time history of pore pressure buildup, (b) effective stress path, and (c) hysteresis loop at the depth of 8 m.

REFERENCES

[1] Schnabel, P. B., Lysmer, J., and Seed, H. B. 1972. "SHAKE: A Computer Program for Earthquake Response Analysis of Horizontally Layered Sites," *Report No. UCB/EERC-72/12*, Earthquake Engineering Research Center, University of California, Berkeley, December, 102p.

[2] Martin, G. R., Finn, W. D. L., Seed, H. B. 1975. "Fundamentals of Liquefaction under Cyclic Loading," *Proc. ASCE*, 101(5): 423-438.

[3] Ishihara, K. and Towhata, I. 1980. "One-dimensional Soil Response Analysis during Earthquakes Based on Effective Stress Method," *Journal of The Faculty of Engineering*, The University of Tokyo (B), XXXV(4): 655-700.
[4] Finn, W. D. L., Lee, K. W., and Martin, G. R. 1977. "An effective stress model for liquefaction," *J. Geotech, Engrg. Div., ASCE*, 103(6): 517-533.
[5] Prevost, J. H. 1989. "DYNA1D: A Computer Program for Nonlinear Seismic Site Response Analysis - Technical Documentation," *Multidisciplinary Center for Earthquake Engineering Research*, Report NCEER-89-0025.
[6] Iai, S., Matsunaga, Y. and Kameoka, T. 1992. "Strain space plasticity model for cyclic mobility," *Soils and Foundations*, Japanese Society of Soil Mechanics and Foundation Engineering, 32(2): 1-15.
[7] Modaressi, H., Foerster, E. and Mellal, A. 1997. "Computer-aided Seismic Analysis of Soils," *6th International Symposium on Numerical Models in Geomechanics*, NUMOG VI, Montreal, Quebec, Canada: 427-432.
[8] Aubry, D., Hujeux, J.C., Lassoudière, F. and Meimon, Y. 1982. "A double memory model with multiple mechanisms for cyclic soil behaviour," *Int. Symp. Num. Model. Geomech*., Zurich.
[9] Nemat-Nasser, S., and A. Shokooh, 1979. "A unified approach to densification and liquefaction of cohesionless sand in cyclic shearing," *Canadian Geotechnical Journal*, 16: 659-678.
[10] Davis, R. O., and J. B. Berrill. 1982. "Energy dissipation and seismic liquefaction of sands," *Earthquake Engineering and Structural Dynamics*, 10(2): 59-68.
[11] Figueroa, J. L., A. S. Saada, L. Lian, and M. N. Dahisaria. 1994. "Evaluation of soil liquefaction by energy principles," *Journal of Geotechnical Engineering, ASCE*, 120(9): 1554-1569.
[12] Dief, H. M. and Figueroa, J.L. 2000. "Evaluation of Soil Liquefaction by Energy Principles through Centrifuge Tests," *Proceedings of GeoEng2000*, Melbourne, Australia, November.
[13] Tobita, T. 2002. "Energy-based Modeling of Liquefaction and Earthquake Site Response Analysis," Dissertation submitted to the faculty of the graduate school, University of Southern California.
[14] Trifunac, M. D. 1995. "Empirical criteria for liquefaction in sands via standard penetration tests and seismic wave energy," *Soil Dynamics and Earthquake Engineering*, 14(4): 419-426.
[15] Law, K. T., and Cao, Y. L. 1990. "An energy approach for assessing seismic liquefaction potential," *Canadian Geotechnical Journal*, 27: 213-233.
[16] Ishihara, K. 1996. "Soil Behavior in Earthquake Geotechnics," Oxford Science Publications, Clarendon Press, Oxford, UK.
[17] Arulmoli, K., Muraleetharan, K. K., Hossain, M. M. and Fruth, L. S. 1992. "VELACS: Verification of liquaefaction analysis by centrifuge studies laboratory testing program soil data report," Prepared for National Science Foundation, The Earth Technology Corporation, 13900 Alton Parkway, Suit 120, Irvine, CA 92718.
[18] Mroz, Z. 1967. "On the description of anisotropic workhardening," *Journal of Mechanics and Physics of solids*, 15: 163-175.
[19] Prevost, J. H. 1985. "A simple plasticity theory for frictional cohesionless soils," *Soil and Earthquake Engineering*, 4(1): 9-17.
[20] Bardet, J. P. and Tobita, T. 2001. "NERA: A computer program for Nonlinear Earthquake site Response Analysis of Layered Soil Deposits," University of Southern California, Department of Civil Engineering, http://geoinfo.usc.edu/gees.
[21] Joyner, W. B. and Chen, A. T. 1975. "Calculation of nonlinear ground response in earthquakes," *Bulletin of the Seismological Society of America*, 65(5): 1315-1336.
[22] Arulanandan, K., and R. F. Scott (eds.). 1993 and 1994. "Verification of Numerical Procedures for the Analysis of Soil Liquefaction Problems," *Proceedings of the international conference on the Verification of Numerical Procedures for the Analysis of Soil Liquefaction Problems*, Vols. 1 and 2, A. A. Balkema, Rotterdam, Netherland.
[23] Taboada, V. M. and R. Dobry. 1993. "Experimental results of model No.1 at RPI," *Proceedings of the international conference on the Verification of Numerical Procedures for the Analysis of Soil Liquefaction Problems*, K. Arulanandan and R. F. Scott, eds., Vol. 1, A. A. Balkema, Rotterdam, Netherland, pp. 3-17.
[24] Bardet J. P. and Ichii, K., and Lin, C. H. 2000. "EERA: A computer program for Equivalent-linear Earthquake site Response Analyses of layered soil deposits," University of Southern California, Department of Civil Engineering, http://geoinfo.usc.edu/gees.
[25] Iai S., Morita, T., Kameoka, T., Matsunaga, Y., and Abiko, K. 1995. "Response of a dense sand deposit during 1993 Kushiro-oki earthquake," *Soils and Foundations*, 35(1): 115-131.
[26] PHRI (Port and Harbour Research Institute). 1997. "Handbook on liquefaction remediation of reclaimed land," A. A. Balkema, Rotterdam, Netherland.

Appendices

Working Group Reports

Design, Mitigation and Rehabilitation of Lifeline Systems against Earthquakes

Liquefaction, Lateral Spreads, Fault Ruptures, and Permanent Ground Deformation Effects on Structures

Workshop Technical Program

Workshop Participants

Working Group Report

Design, Mitigation and Rehabilitation of Lifeline Systems Against Earthquakes

1. Develop empirical Multi-Linear Regression (MLR) permanent ground deformation analysis for clays.
2. Develop simplified seismic models for lifeline performance.
3. Develop models for transverse soil/pipe interaction for large permanent ground deformation using a conservative bilinear spring model.
4. Develop models for longitudinal soil/pipe interaction for large permanent ground deformation using a conservative bilinear spring model.
5. Provide information transfer to end users and policy makers, using proceedings, user workshops and executive summaries.
6. Encourage discussion of technical differences on needed research.
7. Contrast and critique current standards of practice versus research findings.
8. Research faulting effect on lifelines.
9. Instrument pipes to monitor their response
10. Develop simplified analysis of liquefaction stages for evaluating the effect to lifeline structures including the pre, post and transient phase and dynamic response.
11. Improve capability for predicting small to moderate transient and permanent ground movement less than 2 m and their consequences.
12. Perform current design analysis on lifeline foundations having successful performances under extreme seismic conditions.
13. Integrate research knowledge from this and other workshops to improve lifeline system performance evaluations.
14. Evaluate most recent lifeline design guidelines with recent research results.
15. Develop design guidelines for fire following earthquakes.
16. Expand invitation to future US/Japan Workshops to other disciplines.
17. Incorporate performance based design in research activities where applicable.

Ll 01-20-03 REV 020203

Working Group Report

Liquefaction, Lateral Spreads, Fault Ruptures, and Permanent Ground Deformation Effects on Structures

Reporters:
J. P. Bardet, S. Ashford, K. Konagai, and T. Sato

Participants:
J. Stewart, B. Kutter, T. Abdoun, Y. Takahashi, T. L. Holzer, I. M. Idriss, K. Wakamatsu, O. Aydan

During the 8th US-Japan workshop on *Earthquake Resistant Design of Lifeline Facilities and Countermeasures against Liquefaction*, a two-hour session was convened on December 18, 2003 on the topic of "Liquefaction, lateral spread, fault rupture, and permanent ground deformation effects on structures." The session was attended by 12 workshop participants, including 4 reporters. The main objective of the session was to identify major research issues and needs on *liquefaction and surface faulting and their effects on civil infrastructures*. The session focused on three major topics:

- Post-earthquake field surveys
- Damage assessment due to liquefaction
- Faulting and its effects on civil infrastructures

Post-earthquake field surveys

Earthquakes provide unique learning opportunities for earthquake engineers. Engineers tend to emphasize investigations of domestic earthquakes because their primary need is to evaluate the performance of structures built to standards and according to practices developed in their own country. Foreign earthquakes, however, often provide special opportunities to validate models and to learn about the performance of specific aspects of the built and natural environments that have implications for risk mitigation in their home country. The workshop recognized that a protocol is needed to facilitate post-earthquake investigations of earthquakes in the United States and Japan by investigators from the non-impacted country. Currently, most visits rely heavily on pre-established personal and professional relationships. The United States National Earthquake Hazards Reduction Program recently has established a plan to coordinate post-earthquake investigations (Holzer et al. 2003). The plan includes a process to accommodate visits by foreign scientists and engineers. The Workshop recommends that NSF remind investigating parties that it supports to follow this process. While the plan emphasizes coordination of investigations of domestic earthquakes, it presents a limited process for coordination of investigations of foreign earthquakes by U.S. investigators. The workshop recommends that NEHRP agencies that support investigations of foreign earthquakes review the process by which they provide support for the purpose of better coordinating their investigations and enhancing the availability of data collected by their investigators. This review should include consideration of the feasibility of making products from U.S. military resources available to investigators.

Post-earthquake investigations yield critical information for improving building codes. Until now, the information collected from post-earthquake surveys has been largely qualitative, with limited quantitative measurements. In view of the advances in remote sensing technologies and portable computers, post-earthquake surveys will yield even more valuable information to research and engineering practice if they were complemented with quantitative measurements performed in the days and weeks after the events. Post-earthquake measurements have become tractable thanks to the development of modern technologies, e.g., accurate global positioning systems (GPS) devices and portable electronic equipments.

Many damage survey technologies that have originated in the military sector may greatly benefit to post-earthquake reconnaissances. For instance, the remote sensing of structural damage, initially developed for assessing weapon impacts, could be useful to estimate rapidly the extent and location of earthquake damage in urbanized areas. It is recommended to establish communication channels with the U.S. Department of Defense to identify the military satellite technologies that are likely to improve rapid damage assessment after having migrated into the civilian sector.

The success of post-earthquake surveys depends on the availability of relevant support data, e.g. high-resolution topographic maps and aerial photographs. At the present, the collection and compilation of relevant maps and aerial photographs are usually performed just after the earthquakes by independent reconnaissance teams. It is recommended to create support websites that identify the sources of maps and aerial photographs in seismic prone areas before the events actually occur. Maps should be available digitally in geographic information systems (GIS) compatible format for easily reporting GPS observations.

Post-earthquake surveys document the evidences rapidly erased by man-made interventions (e.g. cleanup of rubbles and debris, and repair to damaged structures) and natural events (e.g., sand boils erased by rain). Post-earthquake surveys identify new study areas, which need to be later investigated in greater details through follow-up studies in the months after the earthquakes. A successful example of post-event studies is ROSRINE, which stands for ResOlution of Site Response Investigation from the Northridge Earthquake. Post-earthquake surveys only benefit to research and engineering practice if they are complemented with additional in-depth follow-up investigations aimed at implementing our new findings into engineering practice and building codes.

Surveys of damage assessment due to liquefaction

Post-earthquake surveys have identified liquefaction-induced ground deformation as a major source of earthquake damage. Post-earthquake measurements of liquefaction-induced ground deformation are desirable to understand better the relations between ground deformation and damage to civil infrastructure, and to construct fragility curves for a probabilistic assessment of liquefaction hazards. It is recommended to develop guidelines for post earthquake reconnaissance that document the utilization of modern portable GPS technologies and quantitative field survey GIS database.

Most of the case histories of liquefaction-induced ground deformation have been documented using aerial photographs before and after the events, which have typically yielded ground

displacement accurate to 50 cm. The main limitation in processing aerial photographs is the availability of photographs prior to the earthquakes. It is recommended to document a few selected sites using high-resolution low-altitude aerial photographs and laser altimetry (e.g., LIDAR). It is also recommended to complement these remote sensing measurements with field measurements. To this effect, sites of interest need to be instrumented with monuments and inclinometers before the events. A possible way to characterize the extents and severity of liquefaction is to identify changes in fundamental site period using deployable seismic instruments, shortly after the earthquakes. Post-earthquake surveys should not only focus on the sites that display evidence of ground deformation, but should also identify areas with no perceptible ground deformation. There is a lot to learn by comparing the areas that liquefied and did not liquefy.

Faulting and its effects on the built environment

In the aftermath of earthquakes, the surface expressions of faults that ruptured at depth are usually mapped by geologists to understand the mechanisms of fault ruptures. This mapping has yielded valuable information on the rupture types (e.g., strike slip, thrust, and step-over), slip rates and recurrences of earthquakes. The devastating effects of surface faulting was recognized in the past 1971 San Fernando, and prompted the Alquist-Priolo Act which requires all inhabitable structures in California to be built at some distance away from active faults. The 1999 earthquakes in Turkey and Taiwan have shown that surface faulting threaten not only distributed lifeline networks but also buildings and structures, e.g. bridges. There are still unanswered questions about the relation between diffused ground strains and concentrated displacements where surface faulting display complicated geometries, e.g., stepovers. It is recommended to map surface faulting more quantitatively with measurement of distributed and localized ground deformations. From the point of view of solid mechanics, surface faulting may be difficult to describe deterministically because it is governed by material instability in soil deposits, the material properties and geometries of which are not well characterized. From an engineering point of view, it is recommended that future investigations establish databases of ground deformation and surface faulting with the intent of developing statistical models of ground deformation induced by surface faulting.

References

Holzer, T.L., Borcherdt, R.D., Comartin, C.D., Hanson, R.D., Scawthorn, C.R., Tierney, K, Youd, T.L., 2003, "The plan to coordinate NEHRP post-earthquake investigations," *U.S. Geological Survey Circular 1242*, 16 p.

The 8th U.S.-Japan Workshop on Earthquake Resistant Design of Lifeline Facilities and Countermeasures Against Liquefaction

Technical Program

Monday, December 16, 2002

Registration (Room: Chidori) **8:00-**

Opening Session (Room: Chidori) **8:50-10:00**

Opening remarks	***M. Hamada and J.P. Bardet***
Lessons learned from the World Trade Center disaster about critical lifeline systems	***T.D. O'Rourke***

Coffee/Tea Break **10:00-10:15**

Technical Session I (Room: Chidori) **10:15-12:15**

Theme: Response and Design of Pipelines Subject to Permanent Ground Deformations

Chairs: L. Lund and N. Suzuki

(I-1)	Requirements for designing safe and cost effective pipelines in seismic areas	***S.T. Barbas***
(I-2)	Numerical study for rupture behavior of buried gas pipeline subjected to seismic fault displacement	Y. Ogawa, Y. Fujita, Y. Yanou, **T.** ***Meka*****ta**. M. Kawakami and K. Watanabe
(I-3)	Design consideration to ensure pipeline integrity at fault crossing	***N. Suzuki*****,** H. Kishino, K. Yoshizaki and S. Yasuda
(I-4)	Centrifuge modeling of PGD response of buried pipe	***M.J. O'Rourke***
(I-5)	Seismic effect for submarine pipelines by active fault movement	***O. Kiyomiya***, M. Ichihashi and T. Kikuchi
(I-6)	Recommended practice for design of gas transmission pipelines in areas subject to liquefaction	T. Kobayashi, ***K. Shimamura***, N. Oguchi, Y. Ogawa, T. Uchida, S. Kojima, T. Kitano and K. Tamamoto

Lunch **12:15-13:15**

Technical Session II (Room: Chidori) **13:15-15:35**

Theme: Design, Mitigation, and Rehabilitation of Lifeline Systems
Chairs: S. Yasuda and M.J. O'Rourke

(II-1)	Pipeline seismic mitigation using trenchless technology	***L.V. Lund***
(II-2)	Earthquake-resistant design for pipelines subjected to permanent ground deformation using EPS backfill	***K. Yoshizaki*** and T. Sakanoue
(II-3)	Effects of ground movement on concrete channel	***C.A. Davis***, J.P. Bardet and J. Hu
(II-4)	Effectiveness of remedial measures by shear deformation constraint method	***N. Yoshida*** and H. Kiku
(II-5)	Seismic risk management of lifeline systems	***K. Yamamoto***, M. Hoshiya and H. Ohno
(II-6)	Development of earthquake resistance evaluation method for buried pipeline networks	***Y. Shimizu***, K. Koganemaru and N. Suzuki
(II-7)	Rate-dependency of sand under low effective stress as observed in laboratory shear tests	***I. Towhata*** and C.P. Gallage

Coffee/Tea Break **15:35-15:50**

Technical Session III (Room: Chidori) **15:50-17:50**

Theme: Advancing the State-of-the-Art of Liquefaction Hazard Mapping
Chairs: A.W. Elgamal and I. Towhata

(III-1)	Application of the liquefaction potential index to liquefaction hazard mapping	***T.L. Holze***r, S. Toprak, and M.J. Bennett
(III-2)	Consideration of liquefaction in HAZUS regional earthquake loss estimation	***C. Scawthorn*** and H.A. Seligson
(III-3)	Spatial modeling of liquefaction-induced ground deformation in Kobe Port-Island	***J.P. Bardet*** and J. Hu
(III-4)	Ground deformation and questionnaire survey on witnesses of liquefaction during the 2000 Tottori-ken Seibu earthquake	***M. Miyajima***, M. Yoshida and M. Kitaura
(III-5)	Discriminant technique of liquefied ground by use of observed earthquake records	***J. Kiyono***, K. Toki and M. Morishita
(III-6)	Estimation of the zones susceptible to liquefaction-induced flow in Tokyo	***S. Yasuda***, Y. Shimizu, K. Koganemaru, R. Isoyama, E. Ishida and K. Matsumoto

Tuesday, December 17, 2002

Registration (Room: Hako) **8:00-**

Technical Session IV (Room: Hako) **8:30-10:10**
Theme: Fault Ruptures, Ground Movement and Their Effects on Structures
Chairs: K. Konagai and I.M. Idriss

(IV-1)	Actual observations and numerical simulations of surface fault ruptures and their effects on engineering structures	***Ö. Aydan***
(IV-2)	Dynamic simulation of base fault motion for studying ground surface deformation	***M. Meguro*** and P.K. Ramancharla
(IV-3)	Seismic compression: Effects on lifelines and updated analysis method	***J.P. Stewart***, D.H. Whang and P.M. Smith
(IV-4)	Fault-inflicted damage to civil infrastructures – Lessons learned and possible remedial measures.	***K. Konagai***
(IV-5)	Near-field effects on the 2000 western Tottori-prefecture earthquake on Kasho dam	***T. Ohmachi***

Coffee/Tea break **10:10-10:25**

Technical Session V (Room: Hako) **10:25-12:45**
Theme: Evaluation of Seismic Performance of Lifeline Systems
Chairs: J.P. Bardet and M. Miyajima

(V-1)	Seismic performance criteria for lifeline systems	***M. Shinozuka***
(V-2)	Damage assessment of railway structures using numerical simulation and vibration measurement	***F. Uehan*** and K. Meguro
(V-3)	Modeling of soil-structure bridge systems	***A.W. Elgamal***
(V-4)	Seismic performance evaluation method for underground structures	***T. Nishioka*** and S. Unjoh
(V-5)	Numerical modeling of seismic earth dam response on liquefiable foundation	***Z. Yang***, A.W. Elgamal, K. Adalier and M. Sharp
(V-6)	Evaluation of dynamic earth pressures acting on subway structure subjected to earthquake loading	**T.** ***Iwatate*** and A. Che
(V-7)	Interpretation and visualization of model test data for slope failure in liquefying soil	***B.L. Kutter***, E. Malvic, R. Kulasingam and R. Boulanger

Lunch **12:45-13:45**

Technical Session VI (Room: Hako) **13:45-15:45**

Theme: Liquefaction Potential and Characteristics of Soils by Field and Laboratory Experiments

Chairs: T. Sato and T.L. Youd

(VI-1)	Direct Evaluation for the liquefaction characteristics of soil in situ	E.M. Rathje, W.J. Chang and ***K.H. Stokoe, II***
(VI-2)	A monitoring and visualization technique for liquefaction using resistivity	***M. Jinguuji***, S. Kunimatsu and S. Toprak
(VI-3)	Characterization of the liquefaction potential of native ground failure sites in west Kobe, Japan, during the 1995 Hyogo-nambu (great Hanshin) earthquake, by the spectral analysis of surface waves (SASW) method	***R. Kayen***, Y. Tanaka, T. Kishida and S. Sugimoto
(VI-4)	Experimental evaluation of viscid properties of liquefied sand	J. Kawamura, K. Hattori and ***H. Akagi***
(VI-5)	Selection of a reinforcement method for sewage system structures based on earthquake risk management	T. Kawakami, K. Yamamoto, T. Ohsumi and ***A. Yuasa***
(VI-6)	New type simulation model for sand deposit during huge earthquake-shaking table test and simulation	***S. Okamoto***, K. Sakashita and K. Fukushima

Coffee/Tea Break **15:45-16:00**

Technical Session VII (Room: Hako) **16:00-18:20**

Theme: Behavior of Piles in Liquefied and Laterally Spreading Ground-I

Chairs: S.A. Ashford and H. Mizuno

(VII-1)	Effects of spacing on performance of pile groups undergoing lateral spreading	***K. Ishihara***
(VII-2)	Seismic Response of large diameter cast in place concrete piles in layered liquefiable soils	**W.D.L.** Finn and N. Fujita
(VII-3)	Characteristics of the external force acting on a pile during liquefaction-induced lateral flow of the ground	***S. Higuchi*** and T. Matsuda
(VII-4)	Visualization of soil-pile interaction during earthquakes	A. Abe, ***J.F. Meneses*** and F. Kuwabara
(VII-5)	Dimensional simulation of pile-ground system during liquefaction and following ground flow process	***T. Sato***, T. Matsumaru, F. Zhang, Y. Moon and R. Uzuoka
(VII-6)	Evaluation of passive site remediation against earthquake induced liquefaction and its hazards effect on deep foundations	A. Pamuk, ***T. Abdoun*** and P.M. Gallagher
(VII-7)	Report of the reconnaissance of the November 3, 2002 M7.9 Denali Fault Earthquake	***R. Kayen***

Banquet (Room: Hako) **19:00-**

Wednesday, December 18, 2002

Technical Session VIII (Room: Chidori) **8:40-10:20**
Theme: Behaviour of Piles in Liquefied and Laterally Spreading Ground-II
Chairs: N. Yoshida and W.D.L. Finn

(VIII-1)	Measurement of ground deformation induced by liquefaction and faulting in the earthquake area of the 1999 Kocaeli earthquake	***O.*** **Aksu**, J.P. Bardet, V.O. Atak, M. Onder and Ö. Aydan
(VIII-2)	Observed behavior of lifelines subjected to lateral spreading: Tokachi blast experiment	***S.A. Ashford*** and T. Juimarongrit
(VIII-3)	Stiffness and damping of soil-pile system in liquefaction process	***H. Mizuno*** and T. Hirade
(VIII-4)	Performance of retrofitted pile foundations subjected to seismically induced lateral spreading	***T. Abdoun*** and Y. Wang
(VIII-5)	Analysis of soil-pile interaction	***S. Iai*** and T. Tobita

Coffee/Tea Break **10:20-10:40**

Technical Session IX (Room: Chidori) **10:40-12:20**
Theme: Ground Motion Characteristics and Liquefaction
Chairs: T.L. Holzer and S. Iai

(IX-1)	Statistical investigation on relationships between building damage and ground performance including liquefaction during the Hyogoken-Nambu (Kobe) earthquake	***K. Wakamatsu*** and A. Numata
(IX-2)	Effects of ground motion characteristics and fines content on liquefaction resistance based on case histories	**T.** ***Sasaki*** and K. Tamura
(IX-3)	Influence of liquefaction on response spectra at wildlife, California and Port Island, Japan instrument sites	***T.L. Youd*** and B.L. Carter
(IX-4)	Energy-based liquefaction analysis of earthquake site response	**T.** ***Tobita*** and J.P. Bardet
(IX-5)	Probabilistic evaluation of seismic soil liquefaction potential using CPT	R.E.S. Moss and ***R.B. Seed***

Lunch **12:20-13:20**

Group Discussions Led by Workshop Reporters **13:20-15:20**

The following three themes shall be discussed at the group meetings, and the reporters will provide a 10 minute synopsis of important issues raised at the Closing Session.

A. Earthquake Resistant Design of Pile Foundations in Liquefiable Ground (Room: Chidori (A))

Reporters: A.W. Elgamal, T. Abdoun, H. Mizuno, and N. Yoshida

B. Design, Mitigation and Rehabilitation of Lifeline Systems Against Earthquakes (Room: Chidori (B))

Reporters: L.V. Lund, M.J. O'Rourke, Y. Shimizu, S. Iai

C. Liquefaction, Lateral Spreads, Fault Ruptures, and Permanent Ground Deformation Effects on Structures (Room: Bouvardia)

Reporters: J.P. Bardet, T.L. Youd, K. Yoshizaki, M. Miyajima

NEES Presentation and Discussion)(Room: Chidori) **15:50-16:30**

Presentation and discussion on Network for Earthquake Engineering Simulation (NEES).
Presenters/Discussers: J.P. Bardet, B. Kutter, J. Stewart, and K. Stokoe

Closing Session (Room: Chidori) **16:30-17:00**

Thursday, December 19, 2002 (Tentative)

Technical Site Visit **8:30-13:00**

Seismic Reinforcement of Earth Dams, Tokyo Metropolitan Gov.

Note: On this day, one-day-technical tour to Niigata city to see the lateral spread sites and damage caused by the 1964 Niigata earthquake may be organized if there is interest from the workshop participants (The cost of the trip is about 20,000 Yen).

U.S. Participants

Tarek ABDOUN
Rensselaer Polytechnic Institute

Oktay AKSU
General Command of Mapping, Turkish Army

Scott. A. ASHFORD
University of California at San Diego

Serghios T. BARBAS
ExxonMobil Upstream Research Company

Jean Pierre BARDET
University of Southern California

Craig. A. DAVIS
Los Angeles Department of Water and Power

Ahmed. M. ELGAMAL
University of California at San Diego

W.D.Liam FINN
Kagawa University

Thomas. L. HOLZER
United States Geological Survey

I. M. IDRISS
University of California at Davis

Robert KAYEN
United States Geological Survey

Bruce L. KUTTER
University of California at Davis

Le Val LUND
Consultant

Jorge. F. MENESES
University of California at San Diego

Thomas O'ROURKE
Cornell University

Michael O'ROURKE
Rensselaer Polytechnic Institute

Charles SCAWTHORN
EQE International

Raymond B. SEED
University of California at Berkeley

Jonathan P. STEWART
University of California

Masanobu SHINOZUKA
University of California at Irvine

Kenneth STOKOE, II
University of Texas

T. Leslie YOUD
Brigham Young University

J. C. WATSON
Exxon Mobil Development Company

Japanese Participants

Akio ABE
Tokyo Soil Research Co.,Ltd.

Ömer AYDAN
Tokai University

Hirokazu AKAGI
Waseda University

Masanori HAMADA
Waseda University

Shunichi HIGUCHI
Obayashi Corporation

Masaru HOSHIYA
Musashi Institute of Technology

Susumu IAI
Kyoto University

Hirokazu IEMURA
Kyoto University

Kenji ISHIHARA
Chuo University

Takahiro IWATATE
Tokyo Metropolitan University

Motoharu JINGUUJI
National Institute of Advanced Industrial Science and Technology

Hiroyuki KAMEDA
National Research Institute for Earth Science and Disaster Prevention

Tetsutaro KAWAKAMI
Tokai University

Osamu KIYOMIYA
Waseda University

Jyunji KIYONO
Kyoto University

Takaji KOKUSHO
Chuo University

Kazuo KONAGAI
Institute of Industrial Science
University of Tokyo

Sunao KUNIMATSU
National Institute of Advanced Industrial Science and Technology

Takashi MATSUDA
Obayashi Corporation

Kimiro MEGURO
The University of Tokyo

Tomohisa MEKATA
Osaka Gas Co. Ltd.

Shigeru MIWA
Tobishima Corporation

Masakatsu MIYAJIMA
Kanazawa University

Hatsukazu MIZUNO
Building Research Institute

Yoshiyuki MOHRI
National Institute for Rural Engineering

Tsutomu NISHIOKA
Public Works Research Institute

Naoto OHBO
Kajima Corporation

Tatsuo OHMACHI
Interdisciplinary Graduate School of Science and Engineering,
Tokyo Institute of Technology

Tokiharu OHTA
Ashikaga Institute of Technology

Susumu OKAMOTO
Taisei Corporation

Junichi SAKAKIBARA
Kawatetsu Civil Co., Ltd.

Yuichi SANO
Konoike Construction Co., Ltd.

Tetsuya SASAKI
Public Works Research Institute

Tadanobu SATO
Kyoto University

Ryo SAWADA
Railway Technical Research Institute

Yukio SHIBA
Taisei Corporation

Kazunori SHIMAMURA
Tokyo Gas Co., Ltd.

Yoshihisa SHIMIZU
Tokyo Gas Co., Ltd.

Koji SHIMO
Civil Engineering Information Service

Kiyoshi SHINOHARA
Nippon Steel Corporation

Aketo SUZUKI
Taisei InformationSystem Co., Ltd.

Nobuhisa SUZUKI
NKK Corporation

Tomoharu TAJIMA
Sumitomo Metal Industries, Ltd.

Yuji TAKAHASHI
Kajima Corporation

Keiichi TAMURA
Public Works Research Institute

Tetsuo TOBITA
Kyoto University

Koji TOKIMATSU
Tokyo Institute of Technology

Selcuk TOPRAK
Pamukkale University, Waseda University and AIST

Ikuo TOWHATA
The University of Tokyo

Fumiaki UEHAN
Railway Technical Research Institute

Kazue WAKAMATSU
The University of Tokyo

Toshio YAMADA
Shinozuka Research Institute

Kinya YAMAMOTO
Kogyokusha College of Technology

Susumu YASUDA
Tokyo Denki University

Teruhiko YODA
Waseda University

Nozomu YOSHIDA
Oyo Corporation

Koji YOSHIZAKI
Tokyo Gas Co., Ltd.

Akira YUASA
Funabaashi Analysis Center

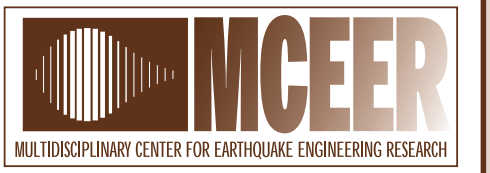

MULTIDISCIPLINARY CENTER FOR EARTHQUAKE ENGINEERING RESEARCH

A National Center of Excellence in Advanced Technology Applications

University at Buffalo, State University of New York
Red Jacket Quadrangle ▪ Buffalo, New York 14261
Phone: (716) 645-3391 ▪ Fax: (716) 645-3399
E-mail: *mceer@mceermail.buffalo.edu* ▪ WWW Site *http://mceer.buffalo.edu*

University at Buffalo *The State University of New York*